KEK Proceedings 2005-20
March 2006
A /H

Proceedings of NANOBEAM2005, 36th ICFA Advanced Beam Dynamics Workshop

Editors
Y. Honda, T. Tauchi and J. Urakawa
KEK, High Energy Accelerator Organization
Y. Iwashita and A. Noda
Kyoto University

Uji Campus, Kyoto University, Japan
October 17-21, 2005

High Energy Accelerator Research Organization

High Energy Accelerator Research Organization (KEK), 2005

KEK Reports are available from:

Science Information and Library Services Division
High Energy Accelerator Research Organization (KEK)
1-1 Oho, Tsukuba-shi
Ibaraki-ken, 305-0801
JAPAN

Phone: +81-29-864-5137
Fax: +81-29-864-4604
E-mail: irdpub@mail.kek.jp
Internet: http://www.kek.jp

KEK Proceedings 2005-20

Proceedings of NANOBEAM2005, 36th ICFA Advanced Beam Dynamics Workshop

Editors
Y. Honda, T. Tauchi and J. Urakawa
KEK, High Energy Accelerator Organization
Y. Iwashita and A. Noda
Kyoto University

Uji Campus, Kyoto University, Japan
October 17-21, 2005

NANOBEAM2005

36th Advanced ICFA Beam Dynamics Workshop on Nano Scale Beams

Photo: Cautesy of Byoudoin

October 17-21, 2005, UJi, Kyoto, Japan

International Advisory Committee:

P. Debu (CEA/Saclay)
J.P. Delahaye (CERN)
S. Ozaki (BNL)
S. Myers (CERN)
D. Trines (DESY)
N. Sasao (Kyoto U.)
D. Burke (SLAC)
S. Holmes (FNAL)
S.I. Kurokawa (KEK)
A. Skrinsky (BINP)
A. Wrulich (PSI)
Y. Kamiya (KEK)
ICFA Beam Dynamics Panel

International Program and Organizing Committee:

R. Assmann (CERN)
G. Blair (Royal Holloway)
P. Burrows (QMUL)
J G.Dugan (Cornell U.)
M. Harrison (BNL)
K.J.Kim (ANL)
M. Mayoud (CERN)
A. Noda (Kyoto U.)
L. Rivkin (PSI)
A. Seryi (SLAC)
V. Shiltsev (FNAL)
S. Mishra (FNAL)
V. Telnov (BINP)
N. Walker (DESY)
L. Zhang (ESRF)
A. Wolski (LBNL)
A. Bay (Lausanne U.)
R. Brinkmann (DESY)
B. Dehning (CERN)
Jie Gao (IHEP)
M. Hildreth (NotreDame U.)
N. Kumagai (SPring-8)
O. Napoly (CEA/Saclay)
T. Raubenheimer (SLAC)
S. Russenschuck (CERN)
T. Shintake (RIKEN)
D. Angal-Kalinin (Daresbury)
J. Urakawa (KEK)
N. Toge (KEK)
K. Yokoya (KEK)
F. Zimmermann (CERN)

Local Organizing Committee:

A. Noda* (Kyoto U.)
Y. Iwashita† (Kyoto U.)
T. Shirai (Kyoto U.)
M. Kumada (NIRS)
T. Sanuki (U. Tokyo)
H. Ogaki (Kyoto U.)
J. Urakawa* (KEK)
T. Tauchi† (KEK)
T. Nomura (Kyoto U.)
Y. Honda (KEK)
T. Yamazaki (Kyoto U.)
K. Masuda (Kyoto U.)

*Chair †Scientific Secretariat

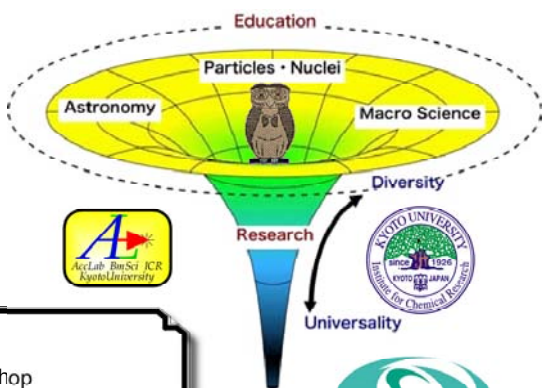

Workshop will look at:
(1) Laserwire mini-workshop
(2) Linear Colliders (ILC and CLIC)
  (a) BDS-design and interaction region
  (b) stabilization and beam control
  (c) Future R&D Plans
(3) Advanced Beam Science
  (a) Low emittance sources
  (b) FELs and radiation generation
  (c) Applications

For further information, please visit: http://wwwal.kuicr.kyoto-u.ac.jp/nanobm

OPENING ADRESS

Akira Noda
Advanced Research Center for Beam Science
Institute for Chemical Research (ICR), Kyoto University
Gokano-sho, Uji-city, Kyoto 611-0011, Japan

On behalf of the organizing committee of the workshop, I would like to present our cordial welcome to all the participants. The first workshop of this series was successfully organized 3 years ago at Lausanne, Co-chaired by Dr. F. Zimmermann, who is here and Dr. R Asmann both from CERN. Following their success, we decided to organize the present workshop almost 1 and half years ago and this is accepted as the 36th ICFA advanced Beam Dynamics Workshop. The main scope of this workshop is, I think, typically the approach to the linear collider although we would like to include also the possible application to other fields such as medical application and material sciences and so on of such a highly developed science and technology originated by the research and developments for linear collider, which is in good harmony with the attitude of our institute created our Advanced Research Center for Beam Science from the April, last year.

At our Institute, an ordinary cyclotron had been operating since 1935 until 1985 at Keage-Laboratory. The cyclotron is now preserved as the monument in front of our building, here in Uji-campus. After the shutdown of the cyclotron, we have constructed 7 MeV proton linac consisting of RFQ and Alvarez as the Research and Developments for High Intensity Proton accelerator Facility. Such a high Intensity Proton Accelerator project had been promoted with the leadership by Late Prof. Hideki Yukawa for overall research related to meson at our university and it is now succeeded as J-PARC project by collaboration between KEK and JAERI and is expected to be completed in a few years from now.

I would like also to mention about our most recent advance briefly. We have been constructing the storage, cooler ring S-LSR for the purpose of beam cooling to realize very fine beam since 2001 and on the 11th, October, we have succeeded in multi-turn injection and realized the beam life of about 200 seconds for 7 MeV protons, on which my colleagues will present the recent results during the workshop. I believe that S-LSR will contribute for creation of very high quality beam through beam cooling.

In Uji-city, one of the 3 campuses of our Kyoto university exists and it is known because of famous novel “Tale of Genji”, which is one of the oldest love stories in the world and the latter 10 chapters is related to Uji. Our workshop aims at the clarification of the fundamental

interaction between elementary particles as the final goal, while the novel treats the fundamental interaction between men and women among the nobles in the courts at Heian Ara more than 1000 years ago. I think both have similarity in dealing with mutual interactions. Uji-city is also famous because of Byodo-in Temple, which appears in our home page and also on the reverse side of Japanese 10 Yen Coin. Near Byodo-in at Uji-gawa river, a famous battle between soldiers groups was made in 1184. Two big groups of Genji soldiers collided between each other. So I think, the place of Uji is one of the appropriate places for our workshop to discuss on linear collider. I hope our discussions in this week here in Uji-campus of our Kyoto University will send out the effective message to the world with good flavor comparable to that of Japanese Green Tea called “Uji-tya”, which is typical product of this area, and can contribute to the improvement of the human culture through realization of linear collider.

Thank you for your attendance to our workshop.

WORKSHOP ORGANIZATION

International Advisory Committee

P.Debu(CEA/Saclay) D.Burke (SLAC) J.P.Delahaye (CERN)
S.Holmes(FNAL) S.Ozaki(BNL) S.I.Kurokawa(KEK)
S.Myers(CERN) A.Skrinsky(BINP) D.Trines(DESY)
A.Wrulich(PSI) N.Sasao(Kyoto U.) Y.Kamiya(KEK)
ICFA Beam Dynamics Panel

International Program and Organizing Committee

R.Assmann(CERN) A.Bay(Lausanne U.) G.Blair(Royal Holloway)
R.Brinkmann(DESY) P. Burrows(QMUL) B.Dehning(CERN)
J.G.Dugan(Cornell U.) Jie Gao(IHEP) M.Harrison(BNL)
M.Hildreth(NotreDame U.) K.J.Kim(ANL) N.Kumagai(SPring-8)
M.Mayoud(CERN) O.Napoly(CEA/Saclay) A.Noda(Kyoto U.)
T.Raubenheimer(SLAC) L.Rivkin(PSI) S.Russenschuck(CERN)
A.Seryi(SLAC) T.Shintake(RIKEN) V.Shiltsev(FNAL)
D.Angal-Kalinin (Daresbury) S.Mishra(FNAL) J.Urakawa(KEK)
V.Telnov (BINP) N.Toge (KEK) N.Walker(DESY)
K.Yokoya(KEK) L.Zhang(ESRF) F.Zimmermann(CERN)
A.Wolski(LBNL)

Local Organizing Committee

A.Noda(Kyoto U.) J.Urakawa (KEK) (Chairmen)
Y.Iwashita(Kyoto U.) T.Tauchi (KEK) (Scientific Secretariat)
T.Shirai(Kyoto U.) T.Nomura(Kyoto U.)
M.Kumada(NIRS) Y.Honda(KEK)
T.Sanuki(U. Tokyo) T.Yamazaki(Kyoto U.)
H.Ohgaki(Kyoto U.) K. Masuda(Kyoto U.)

Working Groups

WG1 for Laser-Wire Mini Workshop

WG1 : Laser-Wire
Conveners : G. Blair, J. Frisch, N. Sasao

WG2 for International Linear Collider (ILC)

WG2a : Beam Delivery System (BDS) Design and Interaction Region
Conveners : D. Angal-Kalinin, A. Seryi, S. Kuroda

WG2b : Stabilization and Beam Control
Conveners : P. Burrows, P. Tenenbaum, R. Sugahara

WG2c : Future R&D Plans
Conveners : F. Zimmermann, M. Ross, M. Kuriki

WG2d : Final Focus Quadrupole (Q) magnet
Conveners : F. Kircher, B. Parker, M. Kumada

WG3 for Nanobeam Sources and Applications

WG3a : Low Emittance Sources
Conveners : F. Stephan, J. Lewellen, J.Clendenin, K. Masuda

WG3b : Free Electron Lasers (FELs) and Radiation Sources
Conveners : G.N. Kulipanov, M. Couprie, H. Ogaki

WG3c : Other Sources
Conveners : Y. Jeong, X. Wang, H. Hanaki

WG4 : Physics with High Intesity Lasers

Conveners : J. Gronberg, T. Takahashi


GANGBEAM 2006

CONTENTS

Plenary Talks

Working Groups Summaries

Closing Remarks and Acknowledgements

WG1: Laserwire

WG2a : BDS Design and Interaction Region

WG2b : Stabilization and Beam Control

WG2c : Future R&D Plans

WG2d : Final Focus Q-magnets

WG3a : Low Emittance

WG3b : FELs/Radiation Sources

WG3c : Other Sources

WG4 : Physics with High Intensity Laser Beam

Summary of Nanobeam'02 and Expectation – 'Stability and Ground Motion Issues in CLIC'

F. Zimmermann, R. Assmann, S. Redaelli, and D. Schulte
CERN, Geneva, Switzerland

Abstract

We £rst review the highlights of the £rst Nanobeam workshop held at Lausanne in 2002, pointing out some open questions and expectations for 2005. In the second part of this paper, we describe the stability and ground-motion issues for the Compact Linear Collider (CLIC) project.

1 OVERVIEW

This invited paper consists of two independent parts. In Section 2 we recall the highlights of the Nanobeam'02 workshop, while Section 3 describes the CLIC project with a special emphasis on ground motion and stability issues. A few open questions for Nanobeam'05 are listed in Section 4.

2 NANOBEAM'02

2.1 Introduction

The 26th Advanced ICFA Beam Dynamics workshop "Nanobeam'02" was the £rst workshop on 'Nanometre-Size Colliding Beams'. Nanobeam'02 was held on the Lausanne University campus from 2 to 6 September, 2002. initiated by the two study groups on CLIC stability and CLIC beam delivery. The workshop was jointly organized by the University of Lausanne (UNIL), the Ecole Polytechnique Federale (EPFL), and the European Organization for Nuclear Research (CERN). The organizers of Nanobeam'02 were Eric d'Amico, Ralph Assmann (chair), Aurelio Bay, Stefano Redaelli, and Frank Zimmermann (chair). About 90 participants from 30 institutes in Europe, Asia and the Americas participated in the event, delivering about 90 scheduled presentations.

The workshop topics were described by Luciano Maiani, the Director General of CERN at the time, as follows [1]:

- production and control of nanometre-size beams,
- component stabilization against disturbing effects such as ground motion,
- an understanding of the achievable limits,
- calibration of the beam energy for precision measurements (integrated mini-workshop, organized by Mike Hildreth and Bernd Dehning),
- laser wire as a novel beam diagnostic (integrated mini-workshop, organized by Grahame Blair).

Prof. Maiani stressed that the road to high-energy nanobeams had been opened. He illustrated the nanometre scale by an example taken from Ralph Assmann: A human hair has a width of 30 μm, while a nanometre is the size of a water molecule.

All future linear colliders aim at vertical spot sizes below 5 nm. This introduces new challenges for accelerator physics (how to generate these beams) and technology (sub-nanometre vibration tolerances). Accelerators can bene£t and further drive strong scienti£c and industrial advances in the nanometre-scale technology. We can pro£t from paralell developments in other £elds of science and industry such as gravitational wave detectors (talk by R. Flaminio [2]), transmission electron microscopy (a 120-keV sub-angstrom electron beam in a scanning transmission electron microscope was described in [3]; see also the talk and paper by S. Isoda at Nanobeam'05 [4]), microchip production, and nanotechnology, to name but a few.

2.2 Particle Physics

John Ellis distilled the particle-physics goals of future colliders [5]. The primary interest is exploring the physics beyond the standard model, which encompasses (1) the problem of mass, (2) the uni£cation of forces, and (3) the origin of ¤avors. Related questions are: Why are there so many particles? Can one explain the numerous parameters of the standard model (19 parameters plus the neutrino masses plus the neutrino mixing angles)? He pointed out that there are many scenarios for the physics lying beyond the standard model, e.g., higgs boson, supersymmetry, extra dimensions, etc. The cross sections for interesting new physics processes decrease as the inverse square of the centre-of-mass energy,

$$\sigma_{\rm interesting} \propto \frac{1}{E_{\rm cm}^2} \ . \qquad (1)$$

Therefore, in order to observe a tangible number of events at a future collider, the collider luminosity must increase as the square of the energy. This implies small beam sizes, and the need for nanobeams.

Figure 1 shows the numbers of supersymmetric particles ("sparticles") which could be found at linear e+e- colliders of various energies and at the LHC, for a number of benchmark scenarios. The higher the energy of the collider, the more sparticles is can discover, again stressing the importance of nanobeams, in view of the cross-section scaling (1).

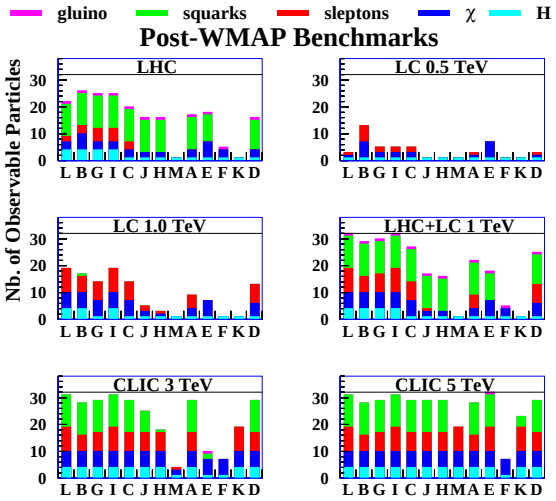

Figure 1: Bar charts of the numbers of different sparticle species which can be observed in a number of beanchmark supersymmetric scenarios at different colliders, including the LHC and linear e+e- colliders with various centre-of-mass energies [6, 5]. The benchmark scenarios are consistent with the cold dark-matter density data from WMAP (WMAP = Wilkinson Microwave Anisotropy Probe - a NASA explorer mission measuring the cosmic background radiation).

2.3 *Gravitational Wave Detectors*

Raffaele Flaminio reviewed the principle, status, and requirements of the gravitational wave detector VIRGO [2]. This detector is a gigantic Michelson interferometer for detecting spin-2 gravitational waves. The interferometer employs a split laser whose light is re¤ected by two distant suspended mirrors, as is illustrated in Figure 2.

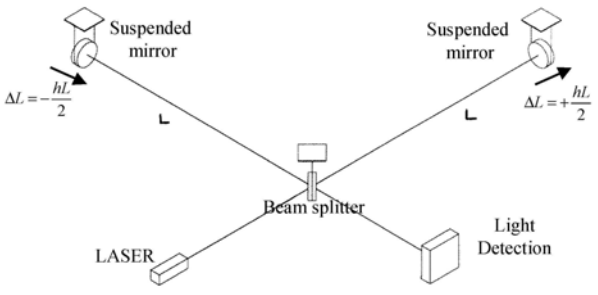

Figure 2: A gravitational wave detector based on a laser interferometer with Fabry-Perot cavities in the arms [2].

The VIRGO detector can measure tiny displacements of the order of 10^{-18} m! To achieve this sensitivity, it includes a 6-stage seismic insulation (see Figure 3), resulting in an attenuation of ground motion by 10 orders of magnitude at 10 Hz. An inertial damping system, using accelerometers, LVDTs, and feedback loops, reduces the mirror motion above 30 mHz to 1 μm. Perturbing effects which need to be taken care of include seismic noise, acoustic noise, photon shot noise, thermal noise, ¤uctuation of the air refraction index, and laser noise.

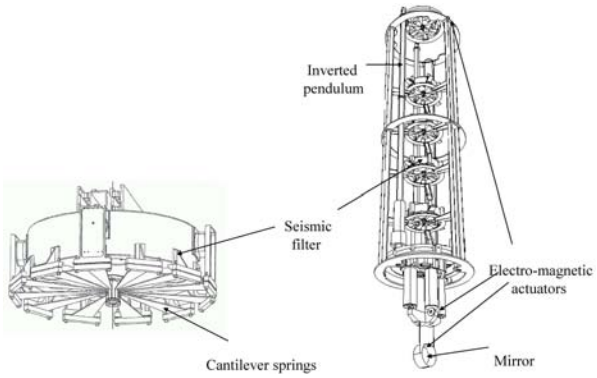

Figure 3: View of the seismic isolator for the VIRGO gravitational wave detector [2].

2.4 *Light Sources and Free Electron Lasers*

Kwang-Je Kim emphasized that future light sources based on X-ray free-electron lasers (FELs) represent a leap in electron-beam and photon-beam technology [7]. Proposals abound across the world for new X-ray and UV facilities, such as LCLS, TESLA-FEL, or SCSS. Figure 4 presents the light-source brilliance as function of year over the last decade on a logarithmic scale. The brilliance, more correctly called 'spectral brightness' [8], refers to the radiated power, or photon emission rate, per unit frequency, per unit solid angle and per unit area normal to the direction of emission. Figure 4 highlights that the increase in light-source brilliance has been much steeper than the increase in computer storage density, which is indicated for comparison. Figure 5 illustrates the enormous improvement in the brilliance which is expected from the next FEL-based generation of light sources.

2.5 *Linear Colliders*

An overview of linear collider was given by S. Chattophadyay with the help of K. Yokoya [9]. Until now there existed only one linear colliders, namely the SLAC Linear Collider or SLC, from which a lot of lessons have been learnt. Figure 6 displays the history of beam sizes in e+e- colliders, circular and linear ones, since about 1970. The spot size achieved at the SLC, about half a micron, was the smallest in any operating collider so far. The Final-Focus Test Beam at SLAC — a £nal focus test facility for future linear colliders — demonstrated a much smaller beam size of about 60 nm. However, the FFTB focused a single beam only, without any collision. The future facilities aim at even smaller spot sizes. The JLC/NLC aimed at a vertical spot size of 3 nm, while the CLIC project foresees an effective beam size at the collision point of 0.7 nm.

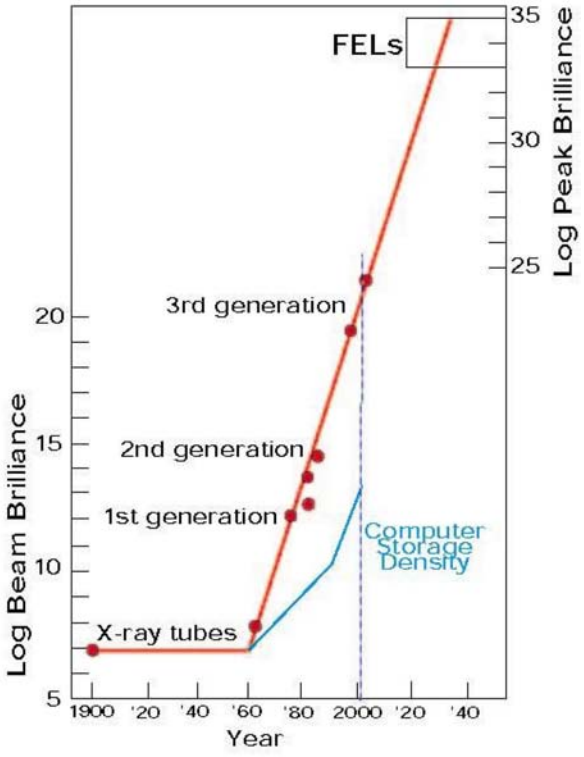

Figure 4: Logarithm of the beam brilliance as a function of year since 1900, compared with the evolution of computer storage density [7].

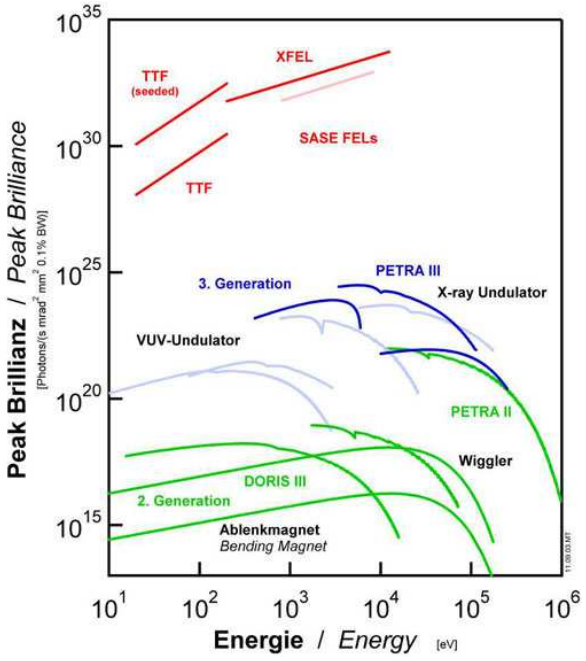

Figure 5: Peak brilliance as a function of photon energy for several 2nd, 3rd and 4th (FEL) generation light sources [7].

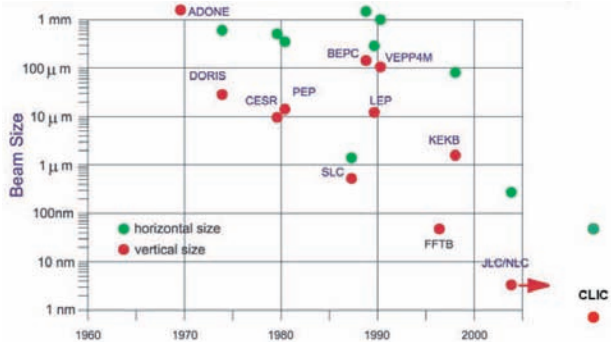

Figure 6: History of beam sizes in e+e- colliders [9]. The point of CLIC was added for completeness.

2.6 Damping Rings

Producing the high-quality beam for the linear collider is a challenging task. Most advanced in this pursuit is the Accelerator Test Facility (ATF) at KEK, which consists of an S-band linac, a prototype damping ring, and an extraction line. The ATF is the largest linear collider test facility in the world. Its beam energy is 1.28 GeV, the electron bunch population $N_b = 10^{10}$, the number of bunches variable between 1 and 20 per train, the repetition rate 1.5 Hz, the horizontal and vertical normalized emittances (in the limit of zero intensity) are about $\gamma\epsilon_x = 2.5$ μm, and $\gamma\epsilon_y \approx 0.02$ μm. The emittances tend to increase with increasing bunch charge due to intrabeam scattering. At a bunch population of $N_b = 8\times10^9$, emittances of $\gamma\epsilon_x = 3.5-4.3$ μm and $\gamma\epsilon_y \approx 13-18$ nm have been demonstrated [10]. Figure 7 compares the emittances achieved at the ATF with those at the SLC and some light sources, as well as with the target damping-ring emittances for some proposed future linear colliders. For example, the CLIC emittance goals are $\gamma\epsilon_x = 0.45$ μm and $\gamma\epsilon_y \approx 3$ nm at the three times lower intensity of $N_b = 2.6\times10^9$.

The Nanobeam'02 workshop featured an interesting comparison of alignment and jitter sensitivities for operating light sources and linear-collider damping rings, provided by T. Raubenheimer and A. Wolski [12]. Their comparison demonstrated that the linear-collider damping rings need to be better than light sources by a factor 3–7 in sextupole alignment (tolerance 10–30 μm), a factor 6–20 in quadrupole roll alignment (40–300 μrad), a factor 3 in quadrupole vertical jitter (75 nm), and a factor 1.5 in magnet-strength stability (10^{-4}). The tighter tolerances quoted in parentheses apply for the TESLA ring, the looser ones for the NLC.

Many problems related to collective effects are awaiting us in the damping rings, — problems like intrabeam scattering, fast ion instability, coherent synchrotron radiation (for which at Nanobeam'02 a new theory was presented by T. Raubenheimer [13]), and electron-cloud instability. Swapan Chattopadhyay reassuringly stated that "we believe we know how to manage" [9].

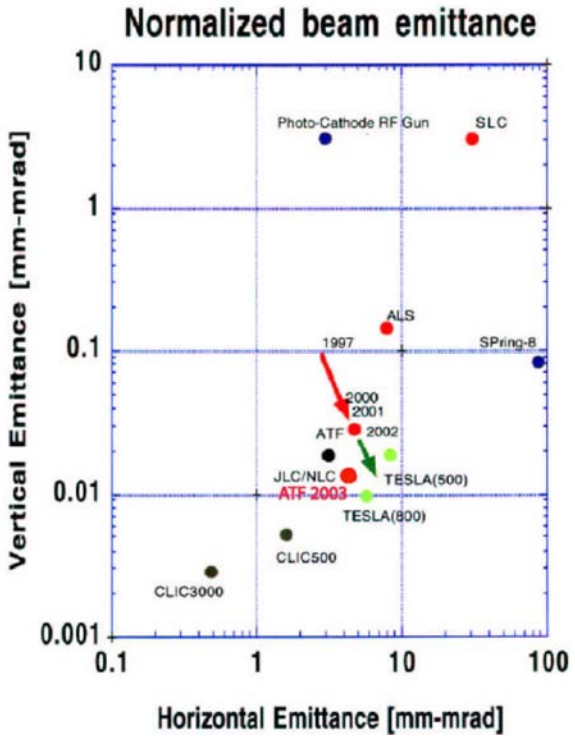

Figure 7: Horizontal versus vertical normalized beam emittances at the ATF, compared with the SLC, some light sources, a photo-cathode rf gun, and various incarnations of damping rings for the JLC/NLC, TESLA and CLIC linear colliders [9, 11].

2.7 *Ground Motion*

Andrei Seryi, surveying grtound motion, distinguished between slow motion and fast motion [14]. The critical frequency separating these two regimes is approximately equal to one twentieth of the collider repetition rate, corresponding to the frequency where the interpulse collision feedback would be effective. For higher frequencies, beam offsets at the collision points cannot be corrected by a pulse-to-pulse feedback. On the other hand, beam offsets due to slow motion can be compensated by feedback. Therefore, at low frequencies, emittance growth is the main concern, and at high frequency the change in beam trajectory.

Andrei's recipe for assessing the impact of ground motion consists of three steps: (1) collect and understand ground motion data, (2) build a model, and (3) simulate the effect for the linear collider. Figure 8 shows ground motion data collected from different locations.

Andrei Seryi stressed the importance of preserving the correlation between the electron and positron beam lines. Figure 9 shows a simulated ground motion amplitude and the resulting orbit for the two sides. The ground motion is continuous, while the two beams collide with an offset.

Vladimir Shiltsev reported observation of orbit motion from the Tevatron proton-antiproton collider [15]. The

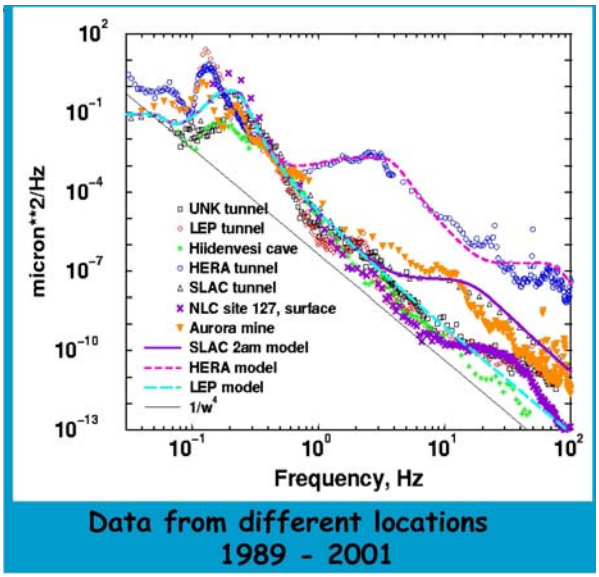

Figure 8: Ground-motion power spectra as a function of frequency from different locations [14].

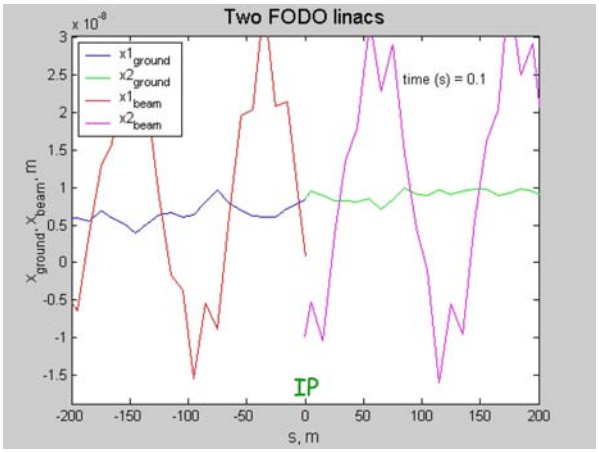

Figure 9: Ground-motion amplitude on either side of the colliation point and the resulting orbits of the electron and positron beams [14].

slow beam motion at the Tevatron exhibits three components: a diurnal movement correlated with outside temperature, a 12-hr period relared to the tides, and a diffusive "ATL" component.

2.8 *Vibration*

Even more important than the natural ground motion are vibrations due to cultural noise and amplifying support resonances. Andrei Seryi presented an example from the SLD detector (the detector of the SLC) where in 1995 Gordon Bowden measured a 30-nm relative motion between the £-nal quadrupole triplets on either side of the collision point up to a frequency of about 7 Hz [14]. Certainly a quieter

detector than SLD could be constructed.

A particular concern for the International Linear Collider (ILC) is the quadrupole stability in the cold linac. At Nanobeam'02, Andrei Seryi addressed this problem for TESLA, the predecessor of the ILC. Although the linac stability requirements in a superconducting linac are apparently looser than in a warm linear collider, the common support of quadrupoles and accelerating cavities (helium return line) may prove a 'shaky ground'. Noise can be excited from the rf pulse (Lorentz force), mechanical coupling to pumps, etc. The vibration coupling to the quadrupoles needs to be appropriately minimized by the mechanical design. Figure 10 shows the measured vibration amplitude as a function of frequency for a cold-linac quadrupole at the Tesla Test Facility (TTF). Clearly visible are frequency lines corresponding to the helium system, vacuum pumps, and mechanical resonances of the cavity. More recent measurements were presented by Andrei at Nanobeam'05, with the latest result being that still a factor of several improvement in quadrupole-vibration amplitude is needed to meet the ILC stability goals.

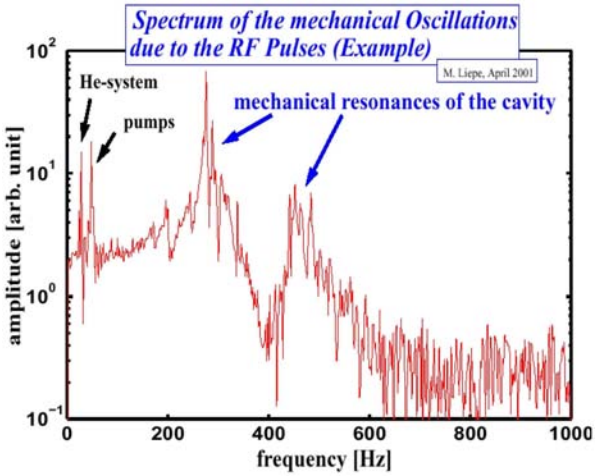

Figure 10: Measured spectrum of mechanical cold-linac quadrupole oscillations in the presence of rf pulses (M. Liepe, 2001) [14].

A vivid illustration of how cold quadrupoles can cause signi£cant beam jitter in existing accelerators came from RHIC. Christoph Montag identi£ed vibrations of the RHIC interaction-region triplet magnets as a source of beam motion at frequencies around 10 Hz, by comparing measured spectra of the beam and the quadrupole cryostat [16]. An example of such a comparison is shown in Figure 11. Christoph made the worrisome observation that, in order to explain the measured beam motion, vibration of the cold masses inside the cryostats must be at the 10-μm level. The measured vibration of the triplet cryostat as a whole has a much smaller amplitude. The induced beam motion results in a modulated beam-beam offset at the collision points, which is thought to be responsible for emittance growth at the start of each RHIC store.

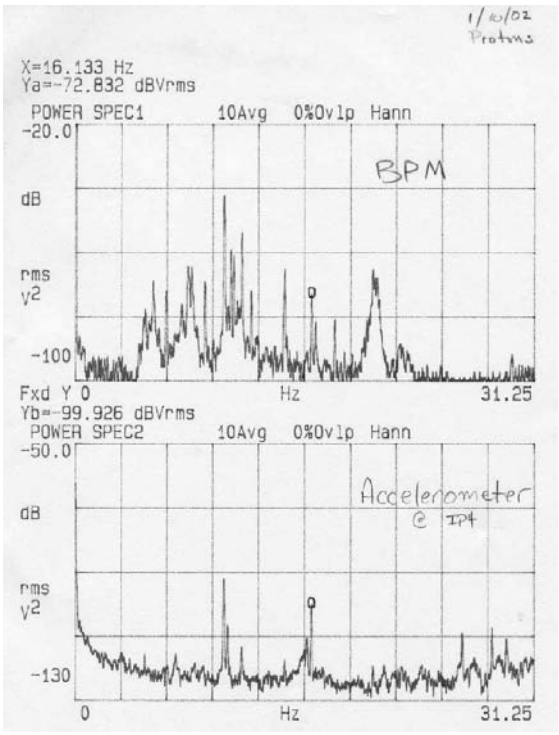

Figure 11: Measured spectra of horizontal beam motion (top) and of the triplet cryostat motion in IP 4 (bottom) [16].

Also fast beam motion at the Tevatron shows peaks at the vibration frequencies of the low-beta quadrupoles, as well as at the frequencies of the central helium lique£er compressors and support resonances. The measured amplitude of the beam motion was more than 10 times the amplitude of the responsible component vibration [15].

2.9 *Stabilization*

Ralph Assmann and Stefano Redaelli reported the progress of the CLIC stabilization study, which has applied latest technology to the accelerator £eld [17, 18]. Quadrupole motion could be stabilized to less than 0.5 nm above 4 Hz, up to ten times better than the supporting ground, so that CERN now has one of the most stable places on earth. Figure 12 shows a photo of the CLIC honeycomb table on its actively stabilized feet.

Andrei Seryi raised some questions on the trade off between mechanical stabilization and £eld correction [14]. Position stabilization via feedback may encounter problems, if the £nal quadrupole is a permanent magnet, vibrating in the £eld of the detector solenoid. The resulting forces would need to be dealt with. The estimated force on a permanent magnet quadrupole can be 300 N to 2500 N, depending on the con£guration (J. Hodgson). The force is due to $\mu < 1$ of the permanent magnet. The alternative is a correction of the magnetic center via a feedforward exciting

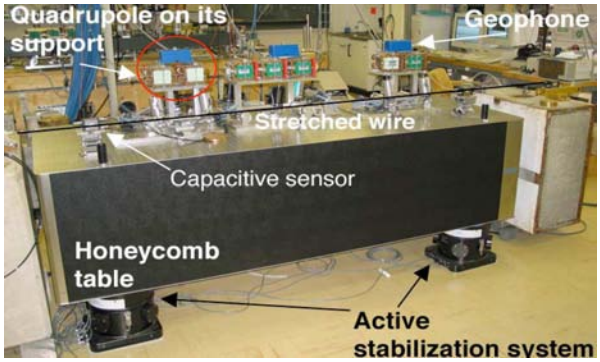

Figure 12: Actively stabilized table of the CLIC stabilization study [17].

a closeby dipole magnet. This feedforward scheme could necessitate the control of many more vibration modes, and, therefore, additional sensors and more complex algorithms. It may prove less effective than the feedback.

Joe Frisch discussed the two alternative approaches to stabilization, namely (1) linking the magnet to the earth by means of lasers and interferometers which measure the motion relative to the ground and correcting the quadrupole position with piezoelectrics, or (2) fully decoupling the magnet from the ground by use of inertial sensors and stabilizing with respect to the '£xed stars' [19]. One problem with most inertial sensors is that they are magnetic and physically large, so that they cannot be used in the detector.

The £rst of these two concepts is referred to as the 'optical anchor'. The optical anchor stiffens the support to simulate a truly rigid connection to the bedrock. Light paths through the detector to the 'bedrock' are required for this approach. Tom Mattison presented pertinent studies at the University of British Columbia [20]. A schematic of the UBC testbench is shown in Figure 13.

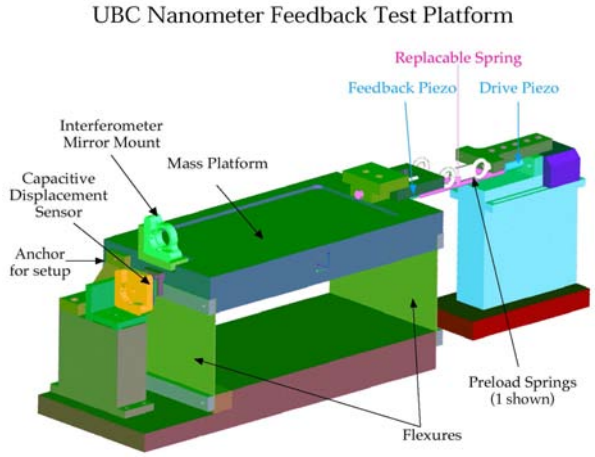

Figure 13: Schematic of the UBC nanometer feedback test platform [20].

At the time of Nanobeam'02, SLAC was developing a compact non-magnetic vibration sensor for intertial stabilization, which is illustrated in Figure 14.

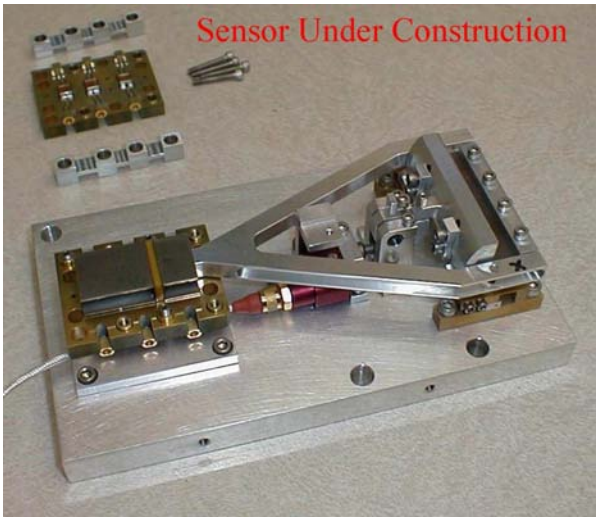

Figure 14: Non-magnetic compact vibration sensor developed at SLAC [19].

2.10 *Feedback*

Nan Phinney described how at the SLC beam-based feedback was used extensively for stabilizing energy, trajectory, intensity, collisions, etc. [21]. A sequence of linac feedbacks used an 'adaptive linear cascade' to avoid overcorrection by multiple systems. Until the end of the SLC, some dif£culties were encountered when attempting to operate the feedback at their full design rates. These dif£culties were mostly understood from experiments or simulation studies. Figure 15 shows a schematic of the SLC with its numerous feedbacks indicated by capital letters.

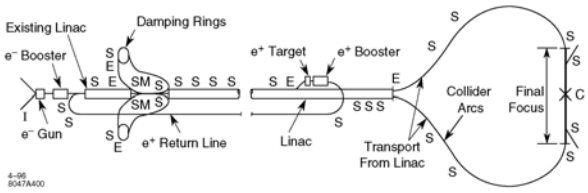

Figure 15: Beam feedback systems in the SLC [21].

Most important is the feedback which keeps the beams in collision. It is based on the huge ampli£cation of an initial offset via the beam-beam collision by a factor 10^5, as explained by Swapan [9]. For example, a 1-nm mis-collision can cause up to 100 mm position shift at a downstream monitor. The collision feedback is illustrated in Figure 16. Related fast-feedback simulations were presented by Glen White [22].

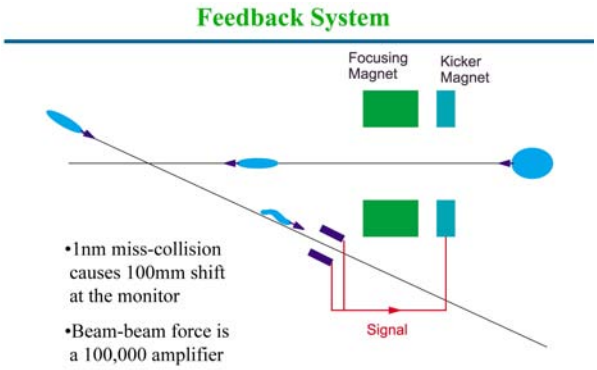

Figure 16: Feedback system for the interaction point [9].

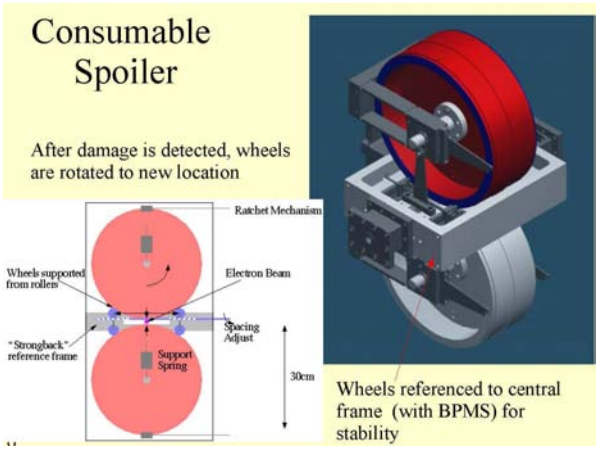

Figure 17: Schematic of a consumable spoiler for a future linear collider and the LHC [19].

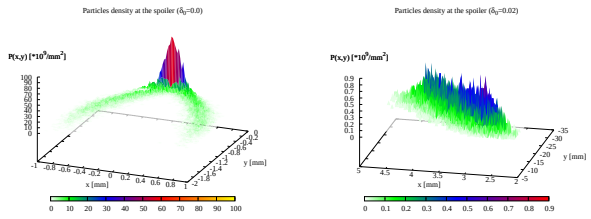

Figure 18: Particle density in the $x - y$ plane at the spoiler location for an energy offset $\delta = 0$ (left) and $\delta = 2\%$ (right) [J. Resta Lopez, A. Faus-Golfe, F. Zimmermann] [27].

2.11 *Collimation*

Peter Tenenbaum reviewed the SLC experience with beam halo, the self-defense against energy oscillations, and the collimator wake-£eld ampli£cation for NLC, TESLA and CLIC [23].

Joe Frisch emphasized that the full linear-collider beam will destroy any solid object at nominal linac beta functions (10 μm spot size) [19]. The surival limit of various materials have been investigated experimentally at SLAC [24]. The beam power at a future linear collider is of order 10 MW, with about 10^{12} electrons per train (NLC). Even a single bunch will cause damage. The usual approach for circumventing this problem is increasing the beta function at the collimator. This can guarantee the collimator survival, but it entails undesirable side effects, such as tight alignment tolerances and wake-£eld problems. Joe described two alternative methods to make the collimators survive a beam impact and to protect the downstream parts of the accelerator, namely solidifying metal spoilers (self-healing) or consumable spoilers based on rotating wheels. A schematic of the latter concept is displayed in Figure 17. A prototype consumable spoiler is presently built at SLAC as part of US-LARP program and it will be installed in the LHC by 2008.

Another scheme is studied at CERN for the CLIC project [25]. Here, a skew sextupole at a dispersive location is used to blow up the vertical spot size at the spoiler. A second skew sextupole placed 180 degrees in bettaron phase behind the £rst cancels all aberrations induced by the £rst sextupole. Figure 18 depicts the particle density at the spoiler location for an on-energy beam and for a beam with 2% energy error. The peak density is much lower for the beam with energy error. The survival limit for a CLIC carbon spoiler corresponds to about 60×10^9 mm^{-2} [26]. As seen in the right picture of Figure 18, the simulated density for an off-energy beam is almost 100 times below this limit, which indicates a signi£cant safety margin of the present optics [27]. The CLIC collimation system was recently improved, as is explained in a companion paper by Angeles Faus-Golfe.

2.12 *Final Focus*

Nick Walker gave a tutorial on the design of £nal-focus systems [28]. The main issue in the £nal-focus optics is the large chromaticity of the £nal lens and its compensation. He contrasted the traditional approach of non-local correction using a dedicated chromatic correction section upstream of the £nal telescope with the novel recipe of local correction at the £nal quadrupole doublet [29]. While the former system has been tested at the SLC and the FFTB, the compact system with local correction has never been demonstrated experimentally. Nevertheless, because of its much reduced length (500 m versus 1800 m) it is currently proposed for all next-generation linear colliders.

The way to design the compact system had escaped everybody but its original inventors plus Shigeru Kuroda until Nanobeam'02, at which two recipes were presented. The procedure for the original design, described by Andrei Seryi, consists of 14 steps. Four programmes — MAD, TRANSPORT, TURTLE and DIMAD — are used in the various steps [30]. An alternative design recipe, which had been employed for the ATF-2 £nal-focus design by Shigeru Kuroda, was presented by Junji Urakawa [31, 32]. The latter is based on 4 analytical expressions and three equations for the matching.

Simulating the performance of a £nal focus is not an

easy task. Stefano Redaelli performed a comparison of results from various tracking codes, namely MAD, DIMAD, PLACET and MERLIN [33]. He found dramatic differences, in particular for beams with a £nite energy spread and with synchrotron radiation. Considering rms values, the differences were as large as 30%. Without synchrotron radiation, MAD showed the largest discrepancies from the other codes, with synchrotron radiation it was MERLIN.

Effects of the solenoid £eld and crossing angle were addressed by Peter Tenenbaum [34], as well as by Daniel Schulte and Frank Zimmermann [35]. The study of the latter two concluded that tilted crab cavities may be necessary.

2.13 *Interaction Region*

Ron Settles, with the help of Tom Markiewicz, explored the interaction region of a future linear collider [36]. Here the issues include vibration, optics, instrumentation, background/masking and engineering. They found that the parameter space is large and the issues highly correlated, as shown schematically in Figure 19.

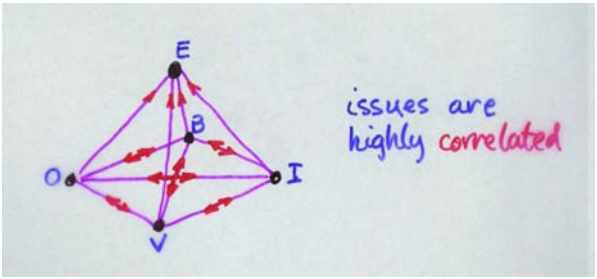

Figure 19: Correlated issues in the design of the interaction region: **V**ibration, **O**ptics, **I**nstrumentation, **B**ackground/masking, and **E**ngineering. [36].

2.14 *Magnets*

Both permanent and superconducting magnet options were explored. M. Kumada, Y. Iwashita, and E. Antokhin presented highlights of permanent-magnet developments, addressing critical issues like temperature stability, radiation damage, variability, interaction with the detector solenoid, and vacuum system [37, 38, 39]. This group had recently built a 4.45 T magnet at $-29°$C and published an article in the CERN Courier [40]. Y. Iwashita presented the idea of a variable-£eld permanent magnet based on a double-ring structure [38]. Figure 20 illustrates the idea of the double-ring variable permanent quadrupole. By rotating the two rings against each other the quadrupole £eld can be switched 'on' or 'off'. In the meantime, he and his colleagues have built a prototype [41]. Its magnetic center was found to shift by as little as 5 μm between the two states.

Also at Nanobeam'02, the use of a superconducting £nal quadrupole for the future linear collider was seriously considered for the £rst time. Brett Parker identi£ed as one of

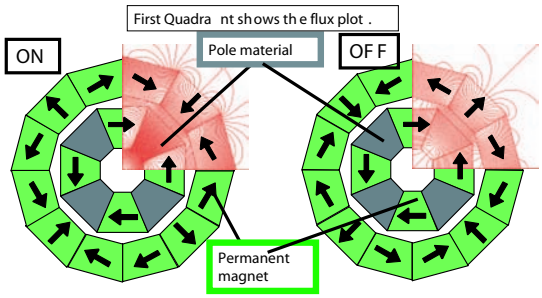

Figure 20: Variable permanent-magnet quadrupole based on a double-ring structure [41].

the main challenges the stabilization of the cold magnetic center to the nanometer level, and he compared traditional massive and novel light-weight magnet designs [42]. Brett also set up a special discussion round on cryogenic vibration. His efforts bore fruit, as at Snowmass 2005 he could present the £rst prototype of a compact superconducting £nal-focus quadrupole (see also [43]), which we may consider a direct outcome of Nanobeam 2002.

2.15 *Diagnostics*

In order to measure the size of nanobeams, new types of diagnostics are required. A spectacular example is the Shintake spot-size monitor, which had been developed for the £nal focus test beam (FFTB) at SLAC [9]. It uses the standing-wave interference pattern created by two parts of the same laser beam intersecting each other at an angle. The period of the fringe pattern can be chosen to be similar to the beam size to be measured, by adjusting the crossing angle of the two laser beams (or the laser wavelength). This monitor successfully measured a 60-nm spot size at the FFTB [44].

Also, the position of a nanobeam needs to be controlled with high precision. To this end, several groups across the globe have developed rf beam-position-monitors with nanometre resolution. Marc Ross reviewed the cavity BPMs in use at the KEK/ATF, which operate at frequencies around 6.2 GHz and are mounted on a movable and tiltable stage [45]. He pointed out that these BPMs can be used for measuring not only the beam position but also the slope of the beam trajectory at the BPM. This is accomplished by separately detecting the two orthogonal components of the induced signal, i.e., the component in-phase with the beam and the one shifted by 90 degrees, respectively. An example measurement of a trajectory slope was presented.

The concept of another novel diagnostics, called the 'slicer/dicer', was presented by Joe Frisch [19]. Here, a combination of bending magnets, transverse rf de¤ectors, and optical transition radiation monitors is employed to decipher the correlation for any pair of the six coordinates (horizontal position and slope, vertical position and slope, bunch length and energy), and, thereby, e.g., to reconstruct

all second moments of the 6D beam distribution.

Yosuke Honda showed multibunch laser-wire results from the ATF, where the bunch-by-bunch beam size is inferred from a single laser-wire scan, with a proper fast detector readout and processing [46].

Grahame Blair presented simulations of halo-related beam loss patterns and of the signal from a laser-wire scan in the CLIC beam-delivery system, using the newly developed code BDSIM, based on GEANT4 [47]. The energy deposited by the photons scattered from a laser wire is of order 7×10^5 GeV, whereas the energy contained in the beam halo is 7×10^{13} GeV, or eight orders of magnitude higher. The enormous difference in magnitude seems to render laser-wire diagnostics extremely challenging. Dedicated quiet locations "in the shadow of the halo losses" must be designed into the beam delivery optics, if laser wires are to be used.

2.16 Sources

Kwang-Je reported exciting results of ¤at-beam generation at the Fermilab A0 beam line using an rf gun immersed in a solenoid £eld and a subsequent skew-quadrupole triplet transformer [48], as had been proposed by Derbenev [49]. A £nal emittance ratio of 41 was demonstrated with individual normalized emittances of $\gamma\epsilon_x = 38.85$ mm mrad and $\gamma\epsilon_y = 0.95$ mm mrad. The emittance prior to the skew-quadrupole channel was measured to be $\gamma\epsilon_{x,y} = 6.44$ mm mrad in both planes.

2.17 Energy Calibration

A topical workshop on energy calibration also was part of Nanobeam'02. Valery Telnov here proposed a new method, based on the spin precession in a dipole £eld of known strength, with two polarimeters located upstream and downstream of this dipole, respectively, and the possibility for arbitrarily varying the initial spin orientation, which is controlled by a spin rotator before the start of the main linac [50]. The set up is sketched schematically in Figure 21. In some sense this is the adapatation of the LEP resonant depolarization technique to a single-pass collider. Valery estimated that the beam energy could be determined with a relative precision of 10^{-5}.

2.18 Test Facilities

An extension of the KEK/ATF so as to include a £nal focus system following the extraction line (ATF-II) was presented by Junji Urakawa at Nanobeam'02 for the £rst time. Figure 22 shows the draft layout and Figure 23 the draft optics by Shigeru Kuroda,which were proposed for this new facility. The rms spot size at the focal point is expected to be 3.4 μm horizontally and 37 nm vertically. The latter would be the smallest ever achieved in an accelerator. Junji quoted Shigeru's assessment that the low energy of the ATF2 of 1.5 GeV makes this a challenging project.

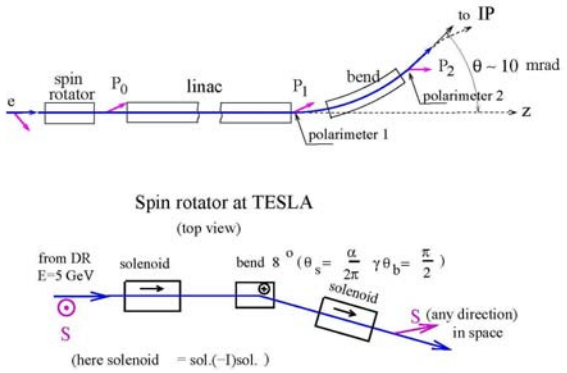

Figure 21: Scheme of the linear-collider energy measurement using the spin precession (top) and schematic of spin rotator (bottom) [50].

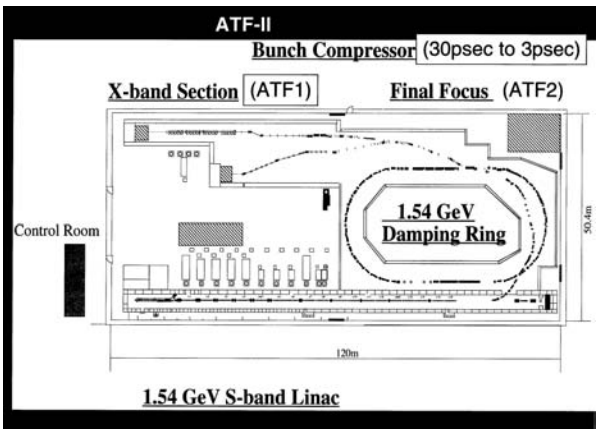

Figure 22: Layout of the ATF-II as proposed in 2002 [31].

Since 2002, this idea has ¤ourished tremendously. The ATF-2 has become a major international project, which now is part of both the ILC global design effort and also the CLIC study, and a complete design proposal has been published [51].

Tor Raubenheimer led a discussion on future collaboration, which he foresaw on 5 different topics, namely

1. beam delivery system and collimation optics, comprising
   - Raimondi/Seryi compact £nal focus optics, for which a beam test would be nice, but not necessary, and which would form a 'nanobeams' test facility, — this is now being realized with the ATF2!
   - tail-folding octupoles, which need a (possibly simple) beam test — they could also be studied at ATF-2,
   - machine background and halo simulation tools, with extensive new tools under development,

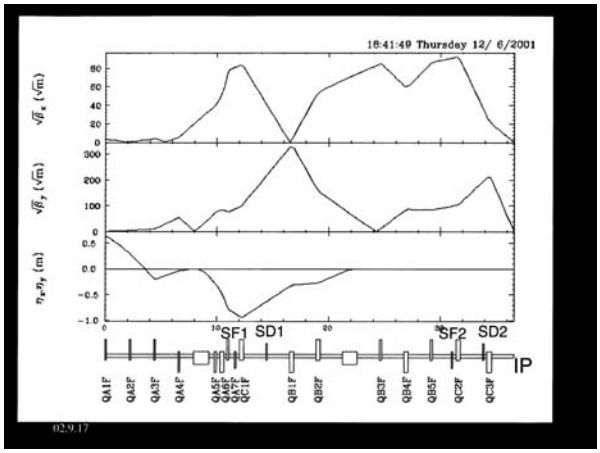

Figure 23: Compact £nal focus designed by Kuroda for the ATF-II proposed in 2002 [31].

simulations of background tuning urgently needed, and the interplay of luminosity and background tuning to be investigated,

2. £nal-doublet magnets (permanent & superconducting ones),
3. stabilization (inertial or optical, mechanical, £eld, and interaction region),
4. instrumentation (BPMs, laser wire, luminosity, energy, polarization)
5. proposed facilities, including
   - an IR girder test stand (non-beam IR magnet mechanical stability test - suf£cient?),
   - the ATF2, i.e., the proposal to construct a compact £nal focus system (plus others) and establish a nanobeam test facility, which is now well underway,
   - LINX, i.e.,a colliding nenabobeam test facility at 30 GeV,
   - extension of CTF2-3 to a multi-bunch nanobeam test facility, and
   - a gamma-gamma IR demonstration, i.e., a photon-collider experiment.

From all these test facilities proposed at Nanobeam'02 only the ATF-2 project has survived, and another one, centered at the SLAC End Station A, has been added [52].

2.19 Proceedings

The Nanobeam'02 proceedings have been published as CERN-Proceedings-2003-001. All presentations and paper are available on the Nanobeam'02 workshp web site *http://icfa-nanobeam.web.cern.ch/icfa-nanobeam/* .

Figure 24: Real landscape at Nanobeam'02: the chateau of Gruyere [photo by Steve Smith] [53].

Figure 25: Real landscape at Nanobeam'05: the byodoin of Uji [photo by Yoshihisa Iwashita] [54].

From Nanobeam'02 to Nanobeam'05 the landscape has changed, as is illustrated in Figures 24 and 25.

More seriously, the collider landscape has changed dramatically as well, as is illustrated in Figures 26 and 27. From the three or four collider projects put forward in 2002, a single one — CLIC — has survived. In addition, a new project, called ILC, is being proposed. Nevertheless, a tremendous number of detailed studies had been conducted for TESLA, NLC and JLC, which were re¤ected in numerous excellent presentations at Nanobeam'02. Even though these projects ceased to exist, their study results are proving invaluable for both the ILC and CLIC.

2.20 Other Nanobeams Applications After 2002

The £eld of nanobeams has greatly expanded since Nanobeam'02.

On 21 May 2005, the ion beam centre (IBC) at the University of Surrey has been awarded a research grant to construct and utilize a new tool for nanotechnology [55]. This tool called the "MeV Nanobeam" will produce an extremely £nely focused beam of protons or other ions accelerated to MeV energy. Professor R. Webb, director of the IBC, enthused that this new tool will further extend the ion

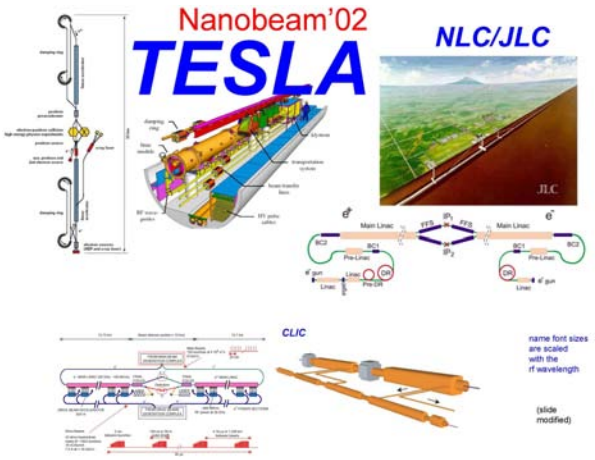

Figure 26: Collider landscape at Nanobeam'02: in 2002 three or four linear-collider projects were proposed, namely TESLA, NLC/JLC, and CLIC; the collider names are scaled with the rf wavelength. Some pictures were taken from [9].

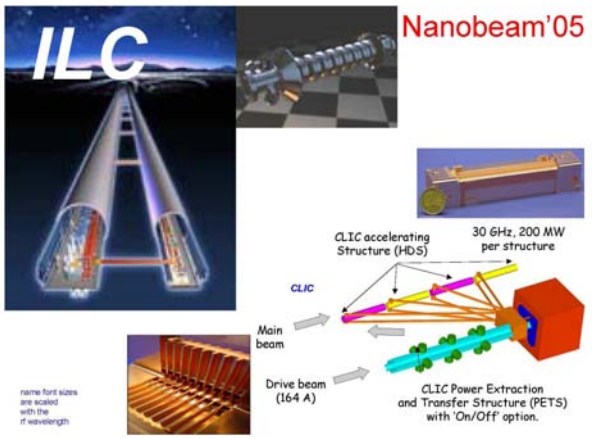

Figure 27: Collider landscape at Nanobeam'05: in 2005 only CLIC remains from the 2002 contenders and there is as a new player the ILC; the collider names are again scaled with the rf wavelength.

beam capabilities into the nanoscale region. He pointed out that the potential applications of this ion nanobeam are almost limitless, as one can both manipulate structures on the nanometre scale as also probe their composition. Of particular interest are applications for the emerging technologies at the life-science interface, e.g., drug delivery devices and the inner working of living cells.

A little earlier, on 13 April 2005, Advanced Nanotech, Inc, a company driving the commercialization of nanotechnology discoveries, has announced that it is investing in the procurement of an electron beam lithograpphy (EBL) tool for the development of nanotechnologies at the University of Cambridge (UK) [56]. The "Nanobeam EBL" boasts impressive throughput due to its large write current of 10 nA at less than 10 nm beam size with a de¤ection rate of 30 MHz. Recently, 50-nm dots and 20-nm lines were drawn with this device, which also features an integrated laser interferometry, automatic alignment and overlay features, for accurate patterning. Errors of less than 40 nm over the length of a 8-inch wafer have been demonstrated.

Another nanotechnology related to nanobeams are carbon nanotubes [57, 58]. These can be used either as a robust collimator material or for the production of nanobeams. Figure 28 shows schematics of a single-wall nanotube lattice and of a multiwall nanotube. Figure 29 shows the simulated improvement factor for LHC collimation ef£ciency using either a single-wall or multi-wall nanotube collimator as compared with an amorphous material [57, 58].

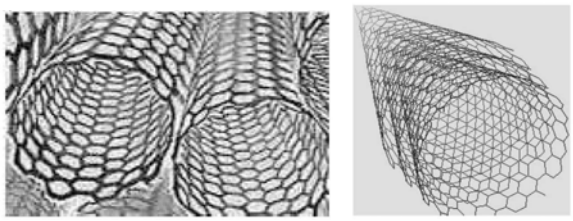

Figure 28: Schematic view of nanostructured lattice made of single-wall nanotubes (left) [57] and picture of a multiwall nanotube (right) [58].

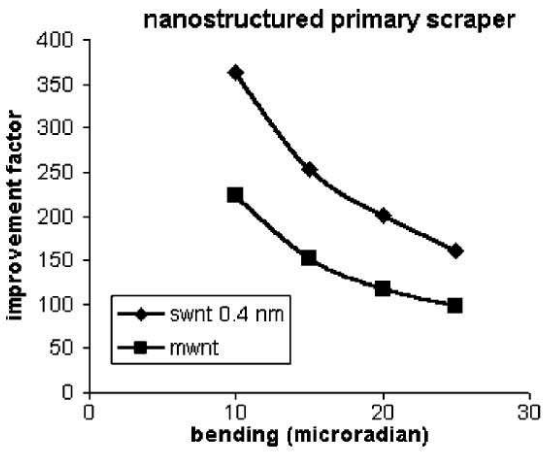

Figure 29: Simulated improvement factor in collimation ef£ciency for an LHC collimator made from either single- or multi-wall nanotubes [57].

3 CLIC - COMPACT LINEAR COLLIDER

3.1 Introduction

CLIC is designed to probe beyond the standard model, and to help understand the origin of mass and the origin of ¤avors [6]. In particular, the physics reach of CLIC not only

is fully complementary with, but it even goes beyond the one of the LHC.

The key features of CLIC [59] are (1) the potential to reach multi-TeV energies in electron-positron collisions, (2) the two-beam acceleration, where energy is stored in a drive beam, transported over long distances with small losses, and rf power generated locally where it is required, and (3) a drive beam produced in a central injector and accelerated in a fully loaded normalconducting linac (with 96% ef£ciency) followed by rf frequency multiplication and power compression.

3.2 CLIC Key Features and Advantages

Two-beam acceleration was £rst proposed by A. Sessler [60] in 1982, and for CLIC by W. Schnell [61] in 1986. Figure 30 shows a schematic of the drive beam and main beam running in parallel. The intense low-energy drive beam is decelerated and its energy converted into rf power, which is transferred to the accelerating rf structures of the higher-energy and less-intense main beam.

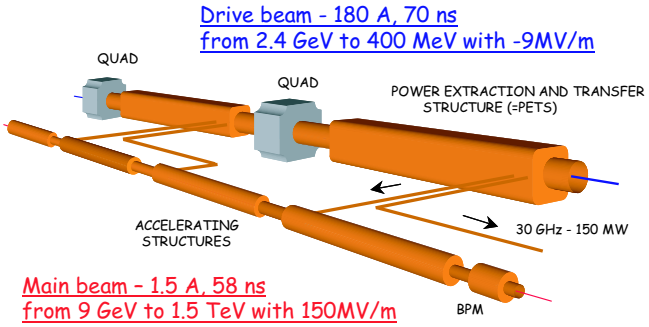

Figure 30: Schematic of CLIC two-beam acceleration module; 6000 such modules are needed for a 3-TeV collider.

Advantages of the CLIC scheme, in addition to the high gradient and short length of the linac, are that it can easily be built in stages, raising the energy simply by the gradual addition of modules, like those shown in Figure 30, and that its tunnel does not house any active elements. A CLIC tunnel cross section is displayed in Figure 31. There are only the two beam pipes, quadrupole magnets, plus the rf & transfer structures, but, e.g., neither klystrons nor modulators. Klystrons and mdoulators are very few in total, comparable in numbers to those in use at the SLAC linac, and they are concentrated in the central injector complex.

Figure 32 present a bird's eye view of the entire CLIC complex for a 3-TeV collider.

3.3 CTF-3

Most key issues of the CLIC concept are being studied and demonstrated at the CLIC Test Facility 3 (CTF-3), which is illustrated in Figure 33. In particular, this facility addresses

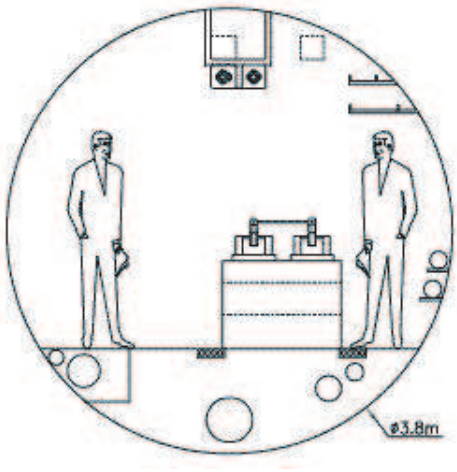

Figure 31: Schematic of the CLIC tunnel cross section. The tunnel is simple, with a diameter of 3.8 m, and no active elements.

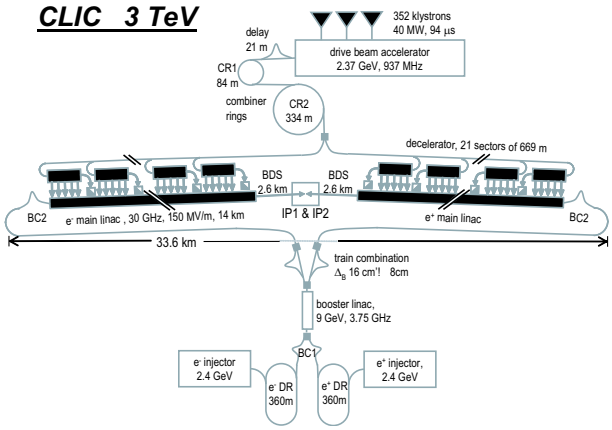

Figure 32: Overall layout of CLIC at 3 TeV [Courtesy H. Braun].

the operation of the drive-beam linac with full beam loading, the frequency multiplication and pulse compression in a delay loop and in a combiner ring, the 30-GHz power generation, and two-beam acceleration.

3.4 Frequency Multiplication

Frequency multiplication by a factor 5 using the combiner ring has been demonstrated already in the "preliminary phase" of CTF-3 [62]. Figure 34 displays streak camera pictures taken on several turns. Newly injected bunches are interleaved with bunches already stored, using rf de¤ectors and a properly tuned ring circumference.

3.5 Drive Beam Linac

Fully loaded operation of the CLIC drive-beam linac is an essential part of the scheme, assuring high overall ef-

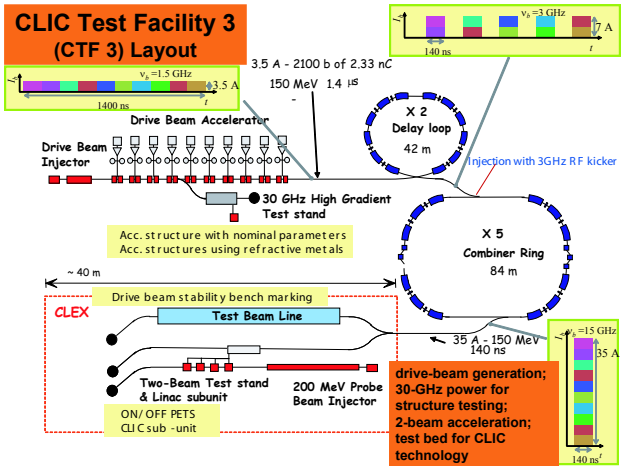

Figure 33: Schematic of the CLIC Test Facility 3 with some further details.

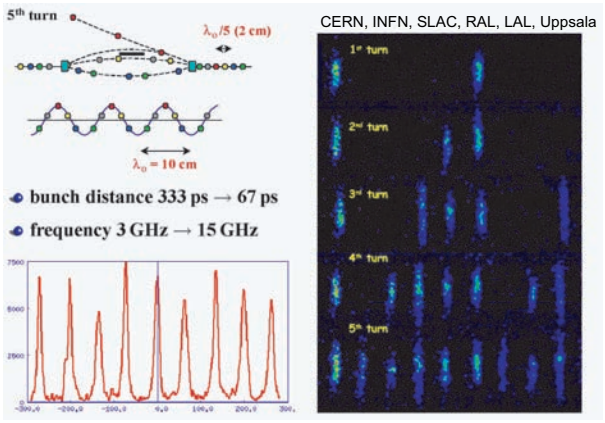

Figure 34: Schematic of bunch combination (top left), streak-camera pictures on successive turns (right), and a cut through the £nal picture (bottom left), documenting the bunch-frequency multiplication in the CTF-3 combiner ring [62].

£ciency. The fully loaded operation has quickly been realized in the CTF-3 linac. Figure 35 shows the £rst demonstration of full beam loading with more than 95% ef£ciency. This level of ef£ciency is higher than achievable by a superconducting system when including cryogenics. The beam was stable in this mode of operation. Table 1 compares the nominal and achieved beam parameters of the CTF-3 linac

3.6 *High Gradient*

Another primary goal of the CLIC scheme is achieving a high accelerating gradient of 150 MV/m or above. In 2002, at the previous facility CTF-2, high gradient tests of structures with molybdenum irises reached 190 MV/m peak accelerating gradient without any damage [63], well above

Table 1: CTF-3 linac parameters.

	nominal	achieved
pulse current	3.5 A	4.5 A
pulse length	1.5 μs	1.5 μs
rms normalized emittance	100 μm	60–90 μm
rms bunch length	5 ps	$<$ 6.5 ps

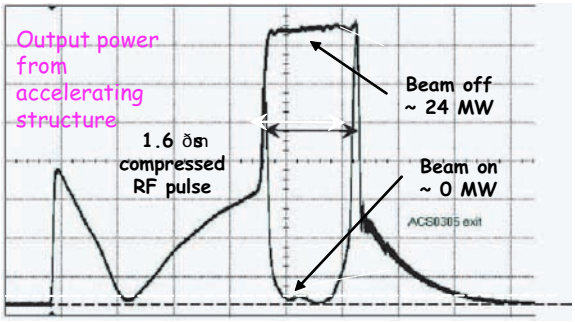

Figure 35: First demonstration of full beam loading in the CTF-3 linac. Shown is the measured output power from an accelerating structure with beam on and beam off as a function of time.

the nominal CLIC accelerating £eld. These spectacular results, which still constitute a world record, are displayed in Figure 36. In 2005, 30-GHz rf pulses of the nominal 70-ns lengths have been produced for structure tests with the design CLIC gradient at CTF-3. This is a remarkable milestone on the path towards CLIC construction.

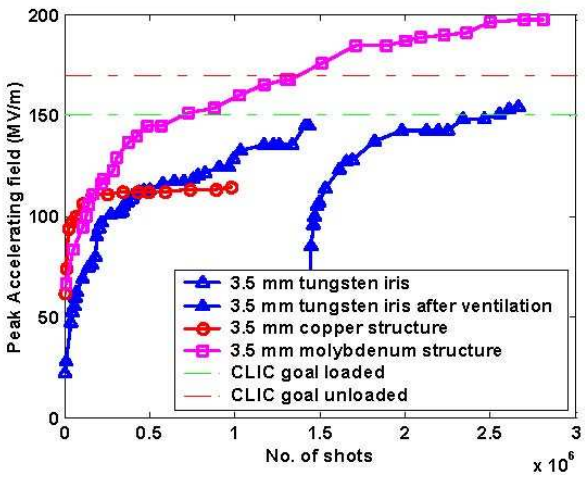

Figure 36: Conditioning history of three copper accelerating structures with either copper, molybdenum or tungsten irises at CTF-2 [63].

3.7 Damping Ring

Work on the CLIC damping ring by Maxim Korostelev has made excellent progress. Now a ring design exists which in simulations produces an emittance even smaller than required. Taking into account the strong effect of intra-beam scattering, the equilibrium emittances are computed to be $\gamma\epsilon_x = 375$ nm, and $\gamma\epsilon_y = 2.3$ nm [64]. The total circumference is only 360 m, and, therefore, the CLIC damping ring is about 20 times smaller than the ILC damping ring. The CLIC ring has a racetrack shape with two straight sections accommodating wigglers. The wiggler parameters were optimized in collaboration with the Budker Institute of Nuclear Physics in Novosibirsk, so as to obtain a high peak £eld with a short period. This is accomplished by adopting superconducting wiggler magnets based on Nb_3Sn technology, providing a period length of 45 mm and a £eld amplitude of 2.5 T [64].

3.8 Positron Source

At Snowmass 2005 a polarized positron source based on laser Compton back scattering was proposed for the ILC by J. Urakawa, E. Bulyak, P. Gladkikh, K. Moenig and others [65]. The ILC proposal foresees a Compton ring with 30 interaction points between the electron beam and the laser beam, and stacking of the produced positrons in the main ILC damping ring. For CLIC a modi£ed, simpler scheme is possible, as 100 times less charge is required per pulse (10 times smaller charge per bunch and 10 times smaller number of bunches per pulse). The needed number of positrons can be produced using a single laser-beam interaction point, and the positrons are stacked in a dedicated compact pre-damping ring. The Compton-based polarized positron source for CLIC is displayed in Figure 37. Simulations by E. Bulyak reveal that the positron yield per turn in the Compton ring is almost constant, close to the ideal maximum value, even without any special rf gymnastics (in the ILC case the yield drops by up to a factor of 3 during the duration of the laser pulse).

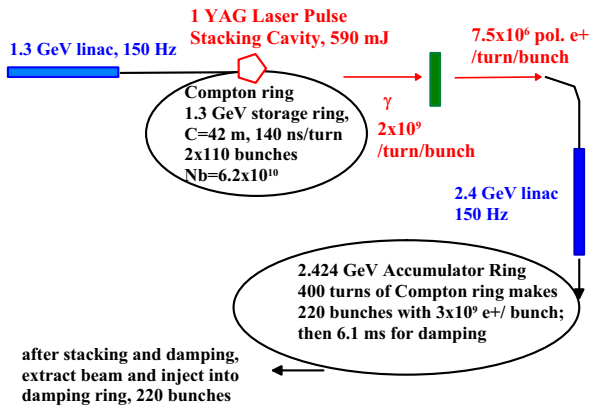

Figure 37: Scheme of CLIC polarized positron source.

3.9 IP Orbit Jitter

If the two beams collide with an offset at the interaction point (IP), the luminosity is reduced. The luminosity reduction depends on the disruption parameter. The vertical rms IP spot size σ_y^* is 0.7 nm for CLIC and about 3.5 nm for the ILC. The offset tolerance is roughly $0.25\sigma_y^*$ or 0.2 nm for CLIC, and $0.1\sigma_y^*$ or 0.35 nm for the ILC. In other words, despite of the nearly six times larger ILC spot size, the jitter tolerance is the same within a factor of two. This is due to the large disruption parameter (bunch length over focal length) of $D_y \approx 18$ for ILC, as compared with $D_y \approx 3.5$ for CLIC.

This increase in sensitivity for ILC (or its predecessor TESLA at the time of Nanobeam'02) is evident in a simulation result of Glen White [66], presented at Nanobeam'02 and reproduced in Figure 38. For small offsets, the luminosity loss is much higher in TESLA than for CLIC or NLC.

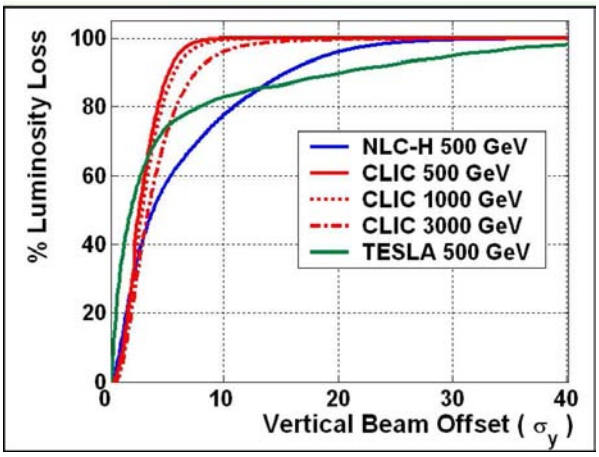

Figure 38: Luminosity loss versus vertical offset in units of the rms beam size at TESLA, CLIC and NLC, as simulated by Glen White for Nanobeam'02 [66].

Another simulation, by Stefano Redaelli, illustrates the desensitizing effect of a moderate disruption for the case of CLIC [67]. This is illustrated in Figure 39. With beam-beam forces present, the luminosity remains signi£cant even for fairly large offsets.

Figure 40 shows the result of a recent beam-beam simulation for the ILC by Daniel Schulte [68]. The luminosity loss for a $0.1\sigma_y^*$ offset normalized to the loss for rigid beams is plotted versus the total luminosity, for different values of bunch length, vertical emittance and vertical IP beta function. There are two groups of curves, differing by the bunch length. A shorter bunch yields higher luminosity before the luminosity loss due to the offset becomes signi£cant. These simulations con£rm the scaling law

$$L \propto \frac{D_{\rm eff} P}{\sigma_z} \ , \qquad (2)$$

with P the beam power and $D_{\rm eff}$ an effective disruption

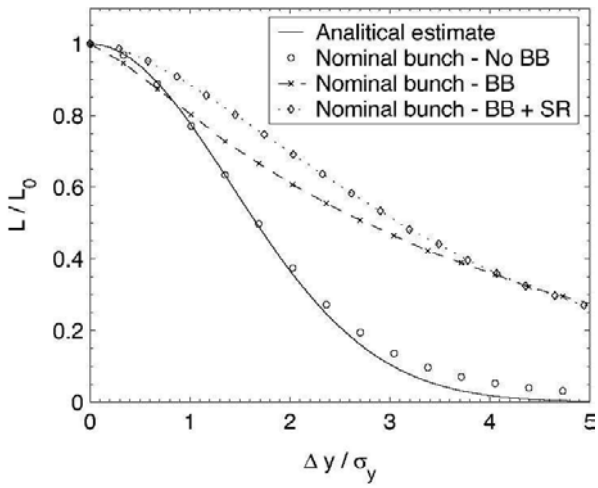

Figure 39: Luminosity loss in CLIC versus vertical offset in units of the rms beam size without or with beam-beam interaction, and with or without synchrotron radiation, as simulated by Stefano Redaelli [67].

parameter. The interesting conclusion is that the luminosity is directly proportional to the disruption. Therefore, ILC could lower its worryingly high disruption parameter only by sacri£cing luminosity.

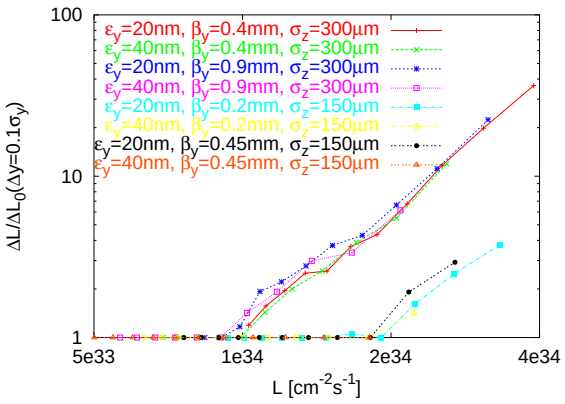

Figure 40: Luminosity loss in ILC for a $0.1\sigma_y^*$ offset normalized to the equivalent loss for rigid beams as a function of luminosity. The curves con£rm that the luminosity is directly proportinal to disruption and inversely proportional to the bunch length [68].

3.10 Ground Motion and Linac Jitter

Table 2 compares parameters related to ground motion and linac jitter in CLIC with those for ILC. A primary difference between ILC and CLIC is the repetition rate of 5 and 150 Hz, respectively. A pulse-to-pulse feedback system can ef£ciently damp the effect of perturbations at frequencies below about a 20th of the repetition rate, which corresponds to 0.25 Hz for ILC and 7.5 Hz for CLIC. The ground

Table 2: Expected ground motion, linac tolerance, and inter-train feedback cutoff frequency for CLIC and ILC.

	ILC	CLIC
repetition rate	5 Hz	150 Hz
feedback cutoff $f_c \approx f_{\rm rep}/20$	0.25 Hz	7.5 Hz
natural ground motion at f_c (site dependent)	300 nm	0.1–1.0 nm
linac quadrupole jitter tolerance	30 nm	1.3 nm

motion power spectrum falling off like the inverse fourth power of frequency, the expected ground motion level at the cutoff frequency is about 300 nm for the ILC (fairly site independent [69]), and 0.1−1.0 nm for CLIC (site dependent [69]). These numbers can be compared with quadrupole jitter tolerances of 30 nm for ILC [70] or 1.3 nm for CLIC. The comparison suggests that for CLIC a feedback correcting on a pulse-to-pulse basis (as for the SLC) is suf£cient to counteract the effect of ground motion, while the ILC must (and can) use a fast intrapulse feedback system.

It is further instructive to compare the linac sensitivity to the wavelength of pertubation for the two colliders. Figure 41 presents the maximum perturbation amplitude of the linac elements giving rise to 1 nm growth in normalized vertical emittance as a function the perturbation wavelength. As expected, CLIC at 3-TeV centre-of-masss energy is about 100 times more sensitive than ILC at 500 GeV (though for CLIC the relevant frequency of ground motion is much higher too), except for wavelengths above about 200 m, where the ILC lattice exhibits resonant behavior.

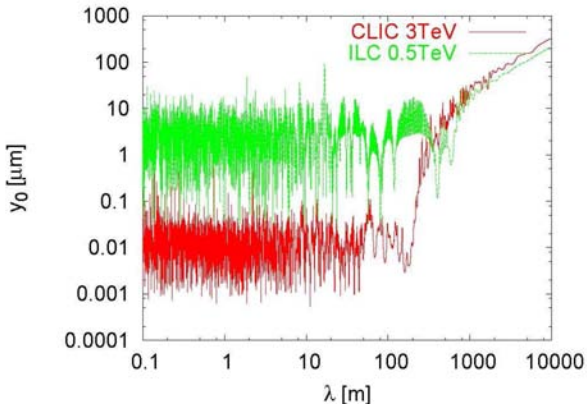

Figure 41: Simulated sensitivity to the scale of a perturbation for ILC at 0.5 TeV and for CLIC at 3 TeV centre-of-mass energy. Shown is the perturbation amplitude corresponding to a growth of the vertical normalized emittance $\gamma\epsilon_y$ by 1 nm as a function of the perturbation wavelength, on a double logarithmic scale [68].

3.11 CLIC Stability Study

The goal of the CLIC stability study was to "demonstrate the feasibility of colliding nanometre-size particle beams in a real accelerator environment for future linear colliders like CLIC". When this study started, meeting the tolerance for the £nal quadrupoles of 0.2 nm uncorrelated rms motion above 4 Hz (now 6–7.5 Hz, thanks to an increase of the CLIC repetition rate) appeared challenging.

The approach taken by the CLIC stability study group was to use state-of-the-art stabilization devices to stabilize CLIC prototype quadrupoles in a normal working environment. Other laboratories had pursued different, mostly home-grown approaches in previous years.

The three steps towards a feasibility demonstration were:

1. establish vibration measurements with sub-nanometre accuracy;

2. investigate modern techniques for stabilizing accelerator magnets; and

3. predict the performance of CLIC achievable with the measured magnet stability.

Measurements were performed not only in a laboratory at CERN, but also at various operating accelerators. Figure 42 displays the measured spectral density of vertical vibrations for a quadrupole and its supporting ground at the Swiss Light Source (SLS), with a circumference of 288 m, beam energy of 2.4 GeV, and a demonstrated beam stability of 1 μm. Clearly visible is the enhanced motion of the quadrupole with respect to ground above about 10 Hz. The total integrated motion above 4 Hz is 30 nm for the ground and 50 nm for the quadrupole. The ratio of the quadrupole spectral power to the ground power represents the so-called transmission function. It exhibits various resonances related to the quadrupole structure and its support.

Simultaneously with the SLS vibration measurement, the beam jitter was detected. A frequency analysis revealed that it is dominated by 50 Hz noise. The resonance peaks of girders and quadrupoles are also seen in the beam motion. The effect of low-frequency ground motion (<15 Hz) is damped by the "lattice response function" [72] since the low-frequency motion corresponds to long wavelengths and is correlated over large distances. The overall rms motion is kept within a few microns. Therefore, magnet vibrations presently are not the limiting factor for the SLS.

The conclusion of this and other similar studies is that the dynamics of low emittance beams can be affected by vibrations. Various ingredients determine the actual effect on the beam:

- amplitude of the ground motion, characterized by a two-dimensional power spectrum $G(\omega, k)$ — this factor is site-speci£c;

- the ground-to-girder-to-quadrupole transmission $TR(\omega)$;

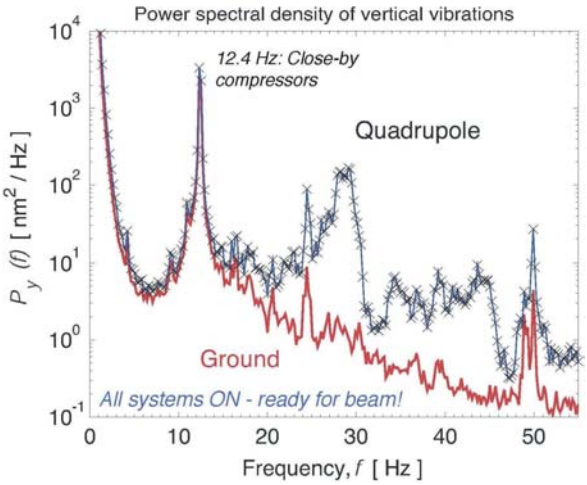

Figure 42: Measured spectral power density for a quadrupole and the ¤oor underneath in the Swiss Light Source [71].

- the lattice response function $R(k)$; and

- the beam-based feedback for beam steering $FB(\omega)$

Multiplying these factors and integrating over frequency and wavelength yields the square of the rms beam jitter,

$$< y^2_{\rm beam} >= \int_0^\infty \int_0^\infty GM(\omega,k)\; TR(\omega)\; R(k)\; FB(\omega)\; \frac{d\omega}{2\pi}\; \frac{dk}{2\pi}\; . \tag{3}$$

The ground-to-quadrupole transmission is determined by how well we can stabilize accelerator magnets.

The solidity of the accelerator ¤oor is a crucial factor in¤uencing the level of ground motion. This was drastically experienced at the SLS, where it was possible to compare ground motion for two ¤oors of different thickness. Namely the ring of the SLS rests on a concrete base two times thicker than the other parts of the building. The comparison of the measured ground motion for the two types of ¤oor, in Figure 43, illustrates that the thicker base reduces the rms ground motion above about 10 Hz by a factor of 5.

The heartpiece of the CLIC stability study was the test stand for vibration measurements and magnet stabilization studies, depicted in Figure 12. In addition, numerous vibration and position sensors were in use, as listed in Table 3.

The most popular type of seismometric sensors are geophones, which can measure in the frequency range from 4 Hz to 300 Hz. The geophones detect velocities with respect to a reference mass at rest. The reference mass is equipped with coils and moves in a magnetic £eld £xed to the outside. The geophone signal derives from the voltage induced in the coils of the reference mass. This voltage is proportional to the mass velocity, the number of coils, and the magnitude of the magnetic £elds. This type of sensor

Table 3: Summary of available vibration and position sensors.

sensor type	model	number	measure	frequency range
geophone	GSV-320 by GeoSig	4	velocity (3 axes)	$\approx$ 1 Hz to 315 Hz
geophone	CMG-40T by Guralp	1	velocity (3 axes)	0.03 Hz – 50 Hz
stretched wire	WPS2-D by Nanotech	3	wire position	$>$ 0 Hz
capacitive distance meter	MCC0.5 by Nanotech	1	distance	up to 10 kHz
accelerometer	JA5L by Sensorex	2	accelertion (tilt angle)	up to 100 Hz
capacitive distance meter	EI-3015 NEMUR, built-in PEPS	3	distance	up to 5 Hz
geophone	TMC-VSV1, built-in PEPS-VX	3	velocity (1 axis)	$\leq$ 7 Hz
geophone	built-in STACIS2000	3	velocity (1 axis)	$\leq$ 5 Hz

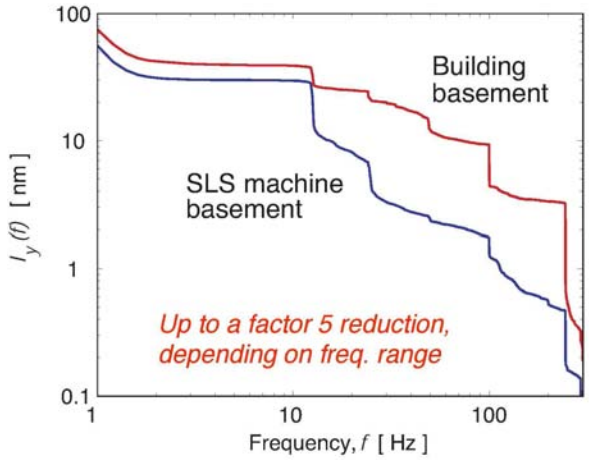

Figure 43: Ground motion amplitude above a certain frequency as a function of this frequency measured at the SLS on two differents grounds. The two sensors were mounted less than a meter apart [71].

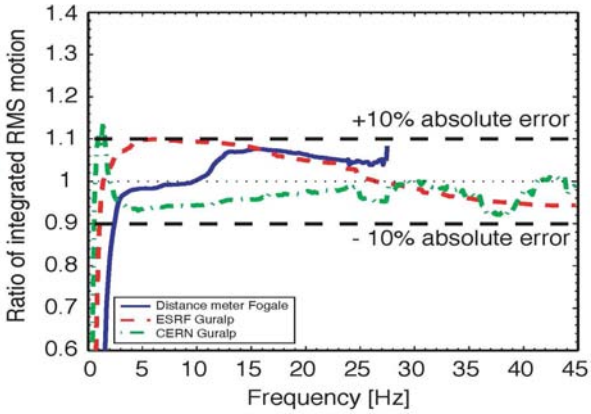

Figure 44: Integrated rms motion measured by three different sensors (based on different physical mechanisms) normalized to that from the geophone of GeoSig as a function of frequency. The picture demonstrates agreement of four sensors within 10% [67].

cannot easily be used in the magnetic £eld of the detector solenoid or the £nal quadrupoles.

The CLIC stability study assessed the error of the measured rms motion by comparing the signal from different sensors and even from different types of sensors. Figure 44 presents the results of a cross-calibration between three different sensors, showing that in the frequency range from 2 Hz to 45 Hz, a measured 1 nm integrated motion equals 1 nm within 10%. The absolute amplitude of the integrated motion varied from 80 nm to 1 nm over the same frequency range.

A crucial problem is the ampli£cation of the ground motion by resonances of the magnet support. Here, active stabilization comes to the rescue, by damping the resonant peak, as is illustrated in Figure 45. The actual actuator implementation depends on the type of stabilization technology chosen, e.g., soft stabilization via air cushion or stiff stabilization using piezoelectrics.

Figure 46 shows a soft air-pressure system, where the magnet is ¤oating on a pillow of pressurized air providing passive damping. Vertical geophones are used for driving an active feedback correction of vibrations by modulating the air ¤ow. The unit is also equipped with a leveling system based on distance meters which keeps the alignment with a 1 μm resolution limit. Figure 47 illustrates the performance of the air-cushion system with and without feedback. Above 8 Hz the rms motion is less than 1 nm, and when the feedback is on, the motion at lower frequencies stays below the natural ground-motion level.

An alternative is a stiff system based on piezoelectric actuators, which is schematized in Figure 48. A photo of this system was shown in Figure 12. It provides a damping of the 3D table vibrations. The performance of thus system is summarized in Figure 49 and in Table 4, which show that a CLIC prototype magnet was stabilized to the subnanometre level. Above 4 Hz, the quadrupole moved by 0.43 nm vertically, while the ground motion was 6.20 nm.

Figure 50 compares the rms quadrupole motion above 4 Hz without and with stabilization, as measured and demonstrated at various laboratories. The £gure visualizes that the CLIC study has advanced magnet stability by more than an order of magnitude compared with previous achievements at DESY or SLAC. At the latter two places, the quadrupole motion was reduced to about 10 nm, whereas the CLIC study reached a stability better than 0.5 nm. It must be

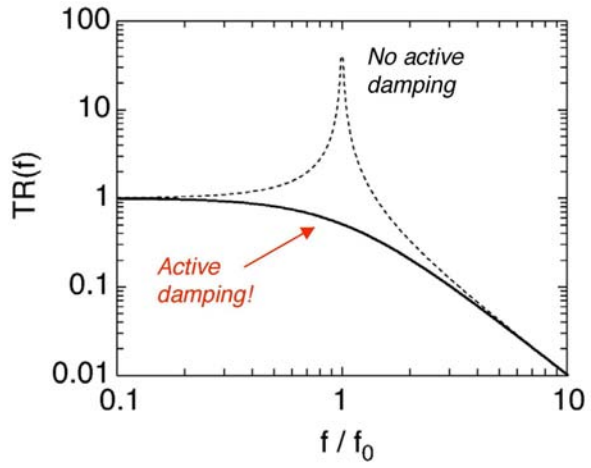

Figure 45: Schematic of transmission function from ground to magnet with and without active damping [67].

Figure 46: Soft air-pressure stabilization system [67].

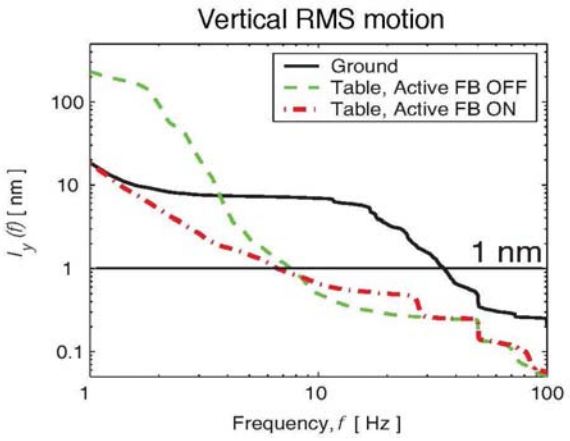

Figure 47: Integrated motion above cutoff frequency as a function of cutoff frequency for the ground and for the air cushion system with or without feedback [67].

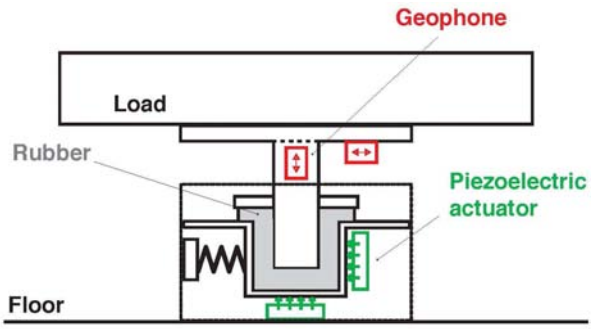

Figure 48: Schematic of a stiff stablization system based on piezoelectric actuators [67].

said that the initial motion without stabilization was also much lower for the CLIC quadrupole than for the others, which could be related to the quietness of the site (though an ordinary CERN laboratory building next to a busy street was chosen for the CLIC measurements), or to the size and structure of the quadrupole, which is much smaller in the CLIC case.

The measured magnet vibration with and without active stabilization system can be used as input for CLIC luminosity simulations, e.g., by assuming that all quadrupole magnets of the beam delivery system vibrate according to the spectrum of motion above 1 Hz measured for a CLIC quadrupole, and, pessimistically, without any correlation between magnets. A further ingredient of the simulations must be the collision feedback at the interaction point, which is essential and which is supposed to act with an exponential time response of 20 or 25 pulses, based on SLC experience.

Table 4: Rms vibration amplitudes above 4 Hz for a quadrupole mounted on the stiff stabilization system compared with the ground.

	quadrupole	¤oor
vertical	0.43 nm	6.20 nm
horizontal	0.79 nm	3.04 nm
longitudinal	4.29 nm	4.32 nm

Figure 51 displays the simulated relative luminosity and the offset between the two colliding beams as a function of time, for the case without magnet stabilization. The luminosity is normalized to the ideal luminosity obtained initially, when all quadrupoles are taken to be perfectly aligned. The luminosity quickly drops almost to zero within a couple of ms, and it never again reaches 50%. Typical beam-beam offsets are 10s of nanometres.

The effect of the active stabilization is illustrated in Figure 52. Here the quadrupoles are supposed to move according to the spectrum measured when the stabilization was switched on. Now the simulated luminosity ¤uctuates

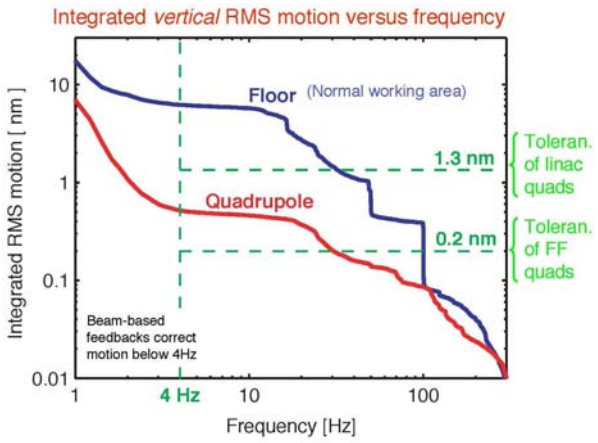

Figure 49: Integrated motion above cutoff frequency as a function of cutoff frequency for the ¤oor and for the stiff stabilization system using piezoelectrics [67].

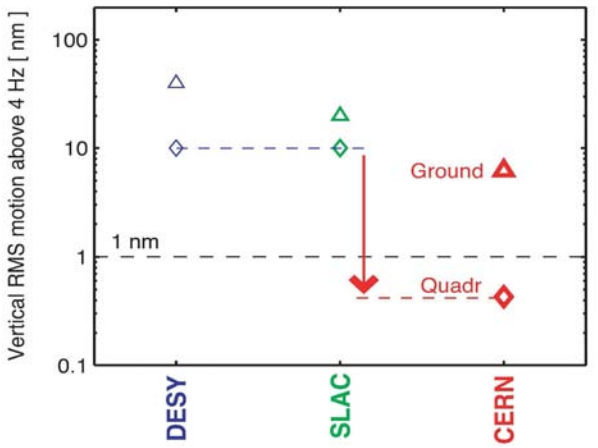

Figure 50: Vertical rms motion of a quadrupole above 4 Hz without and with stabilization demonstrated by the CLIC stabilization study compared with achievements at other laboratories [67].

around an average value of 70%, which is steadily maintained, and the typical beam-beam offset is less than 1σ. This demonstrates how crucial the active stabilization may be at a future collider. It also shows that the stabilization level necessary for satisfactory luminosity can be achieved in practice.

Numerous other systematic studies were conducted in the frame of the CLIC stability study. An interesting investigation concerns the effect of cooling water on the magnet vibrations. This is an issue for the CLIC linac quadrupoles, which must meet a vertical jitter tolerance of 1.3 nm above 4 Hz. Figure 53 presents the measured contribution of the cooling water to the rms quadrupole motion as a function of the water ¤ow. For the nominal ¤ow the contribution of the water was approximately equal to the vertical tolerance.

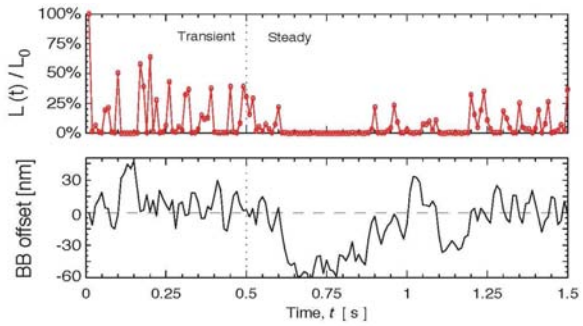

Figure 51: Simulated luminosity and beam-beam offset as a function of time, with quadrupoles moving according to the motion measured for a CLIC quadrupole above 1 Hz without stabilization and assuming a 25-pulse collision feedback [67].

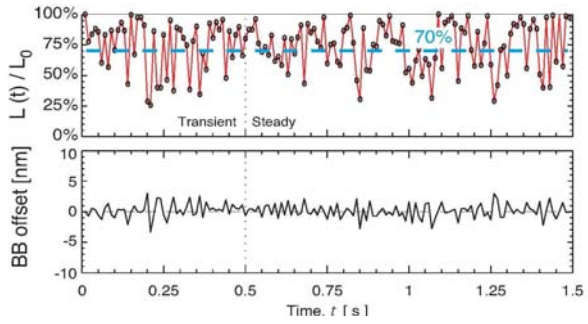

Figure 52: Simulated luminosity and beam-beam offset as a function of time, with quadrupoles moving according to the motion measured for a CLIC quadrupole above 1 Hz with active stabilization and assuming a 25-pulse collision feedback [67].

The systematics were understood, and design changes to the cooling system have been proposed, which will mitigate this effect [73, 74].

The main achievement of the CLIC stability study is the £rst demonstration that colliding nanobeams in CLIC (or any similar collider) are feasible. In particular, the study demonstrated the feasibility of vibration measurements with subnanometre accuracy. Realistic prototypes of CLIC quadrupoles were stabilized to (0.43 ± 0.04) nm vertically and (0.79 ± 0.08) nm horizontally. A full 2D model for time-dependent CLIC simulations shows that 70% of the nominal luminosity can be achieved in a real accelerator environment.

The CLIC stability study is presently continued at LAPP/Annecy [75].

4 SOME EXPECTATIONS FOR NANOBEAM'05

Nanobeam'06 promised to discuss the progress on

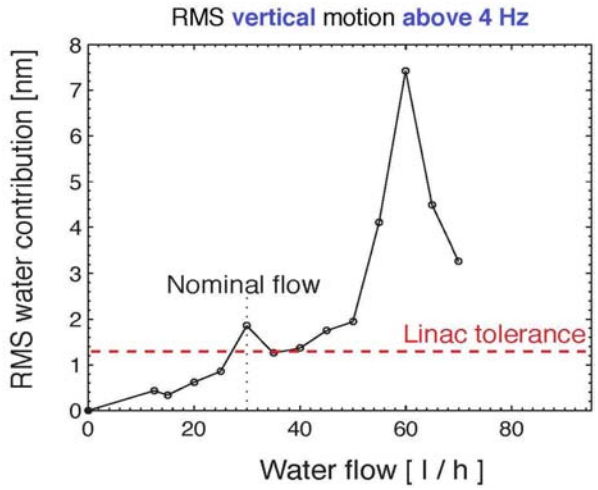

Figure 53: Water contribution to the vertical rms motion of a CLIC quadrupole measured as a function of the velocity of the cooling water [67, 74].

- vibration sensors suitable for a detector environment;
- stability of the quadrupole magnetic £eld center,
- quadrupole vibration in a cold linac,
- advanced applications of RF BPMs and de¤ecting cavities,
- collimation studies,
- fast feedbacks & fast kickers,
- nanobeams at electron microscopes,
- SLAC ESA plans,
- ATF-2 proposal and commissioning plans,
- unexpected proposals and new ideas.

Nanobeam'06 kept its promises, and provided a wealth of additional information fostering a fruitful exchange between various £elds of research.

5 ACKNOWLEDGEMENTS

We would like to thank A. Noda and J. Urakawa for inviting this presentation, and also Y. Iwashita for his reliable assistance.

6 REFERENCES

[1] L. Maiani, "Opening Address," *http://icfa-nanobeam.web.cern.ch/icfa-nanobeam/-slides2.htm*

[2] R. Flaminio, "The Gravitational Wave Detector VIRGO," Proc. Nanobeam'02, CERN-Proceedings-2003-001, p. 7 (2003).

[3] P.E. Batson et al, "Sub-Angstrom Resolution Using Aberration Corrected Electron Optics," Nature 418 (2002).

[4] H. Isoda and H. Kurata, "Electron Microscope as a Nanobeam Analyzer," Proc. Nanobeam'05 (2005).

[5] J. Ellis, "Particle Physics at Future Colliders," Proc. Nanobeam'02, CERN-Proceedings-2003-001, p. 1 (2003).

[6] CLIC Physics Study Group, "Physics at the CLIC Multi-TeV Linear Collider," edited by M. Battaglia, A. de Roeck, J. Ellis, and D. Schulte, CERN-2004-005 (2004).

[7] K.-J. Kim, "Challenges for Future Light Sources and X-Ray FEL's," *http://icfa-nanobeam.web.cern.ch/icfa-nanobeam/-slides2.htm*

[8] US National Institute of Standards and Technology.

[9] S. Chatopadhyay and K. Yokoya, "Challenges in Future Linear Colliders," Proc. Nanobeam'02, CERN-Proceedings-2003-001, p. 15 (2003).

[10] Y. Honda, K. Kubo et al, "Achievement of Ultralow Emittance Beam in the Accelerator Test Facility Damping Ring," Physical Review Letters 92, 5, 054802 (2004).

[11] J. Urakawa, H. Hayano, M.C. Ross, "The Recent Results of the ATF," Proc. Nanobeam'02, CERN-Proceedings-2003-001, p. 223 (2003).

[12] T.O. Raubenheimer, A. Wolski, "Comparison of Alignment Tolerances in the Linear Collider Damping Rings with those in Operating Rings," Proc. Nanobeam'02, CERN-Proceedings-2003-001, p. 243 (2003).

[13] T.O. Raubenheimer, G.V. Stupakov, J.H. Wu, "Coherent Synchrotron Radiation Effect in Damping Rings," Proc. Nanobeam'02, CERN-Proceedings-2003-001, p. 219 (2003).

[14] A. Seryi, "Stability and Ground Motion Challenges in Linear Colliders," Proc. Nanobeam'02, CERN-Proceedings-2003-001, p. 21 (2003).

[15] V. Shiltsev, T. Johnson, X.L. Zhang, "Tevatron Magnets and Orbit Vibrations," Proc. Nanobeam'02, CERN-Proceedings-2003-001, p. 97 (2003).

[16] C. Montag, M. Brennen, J. Butler, R. Bonati, P. Koello, "Observation of Mechanical Triplet Vibrations in RHIC," Proc. Nanobeam'02, CERN-Proceedings-2003-001, p. 93 (2003).

[17] R. Assmann, W. Coosemans, G. Guignard, N. Leros, S. Redaelli, D. Schulte, I. Wilson, F. Zimmermann, "The CLIC Stability Study on the Feasibility of Colliding High Energy Nanobeams," Proc. Nanobeam'02, CERN-Proceedings-2003-001, p. 87 (2003).

[18] R. Assmann, W. Coosemans, S. Redaelli, W. Schnell, "Status of the CLIC Studies on Water Induced Quadrupole Vibrations," Proc. Nanobeam'02, CERN-Proceedings-2003-001, p. 117 (2003).

[19] J. Frisch, "Innovative Technological Solutions for Future Accelerators," *http://icfa-nanobeam.web.cern.ch/icfa-nanobeam/-slides2.htm*

[20] T. Mattison, R. Greenall, T. Downs, "Vibration Control Feedback R&D at University of British Columbia," Proc. Nanobeam'02, CERN-Proceedings-2003-001, p. 81 (2003).

[21] N. Phinney, "Feedback Experience at the SLC and PEP2," *http://icfa-nanobeam.web.cern.ch/icfa-nanobeam/-slides2.htm*

[22] G. White, "Feedback on Nano-Second Timescales: Fast Feedback Simulations," Proc. Nanobeam'02, CERN-Proceedings-2003-001, p. 185 (2003).

[23] P. Tenenbaum, "Overview of Post-Linac Collimation in linear Colliders," *http://icfa-nanobeam.web.cern.ch/icfa-nanobeam/-slides2.htm*

[24] M.C. Ross, R. Iverson, K. Jobe, D. McCormick. P. Tenenbaum, P. Raimondi, "Single Pulse Damage in Copper," LINAC2000 Monterey (2000).

[25] A. Faus-Golfe, F. Zimmermann, "A Nonlinear Collimation System for CLIC," EPAC'02 Paris (2002).

[26] S. Fartoukh, B. Jeanneret, J. Pancin, "Heat Deposition by Transient Beam Passage in Spoilers," CERN-SL-2001-012 AP and CLIC Note 477 (2001).

[27] A. Faus-Golfe et al, "Alternative Design for Collimation System," Proc. Nanobeam'05 (2005).

[28] N.J. Walker, "Beam Delivery Systems for Pedestrians," Proc. Nanobeam'02, CERN-Proceedings-2003-001, p. 25 (2003).

[29] P. Raimondi, A. Seryi, "A Novel Final Focus Design for Future Linear Colliders," Phys. Rev. Letters 86, 3779 (2001).

[30] A. Seryi, "Discussion on Recipe for Design of Compact Final Focus," Proc. Nanobeam'02, CERN-Proceedings-2003-001, p. 69 (2003).

[31] S. Kuroda, J. Urakawa, H. Hayano, K. Kubo, T. Okugi, S. Araki, N. Toge, T. Matsuda, T. Tauchi, "A Plan of KEK-ATF Final Focus Test Beam Line (ATF2)," Proc. Nanobeam'02, CERN-Proceedings-2003-001, p. 247 (2003).

[32] S. Kuroda, "Final Focus Test Optics for the ATF," KEK Appi Seminar (2002).

[33] S. Redaelli, R. Assmann, H. Burkhardt, D. Schulte, F. Zimmermann, N. Walker, Y. Nosochkov, T.O. Raubenheimer, A. Seryi, P. Tenenbaum, "Comparative Assessment of Simulation Tools for Beam Delivery Systems of Linear Colliders," Proc. Nanobeam'02, CERN-Proceedings-2003-001, p. 51 (2003).

[34] P. Tenenbaum, "The Solenoid and the Crossing Angle," *http://icfa-nanobeam.web.cern.ch/icfa-nanobeam/-slides2.htm*

[35] M. Aleksa, R. Assmann, H. Burkhardt, J.-B. Jeanneret, S. Redaelli, T. Risselada, S. Russenschuck, D. Schulte, F. Zimmermann, A. Faus-Golfe, G.A. Blair, "CLIC Beam Delivery System," Proc. Nanobeam'02, CERN-Proceedings-2003-001, p. 35 (2003).

[36] R. Settles, "Interaction-Region Issues," Proc. Nanobeam'02, CERN-Proceedings-2003-001, p. 147 (2003).

[37] M. Kumada, Y. Iwashita, E. Antokhin, "Issues with Permanent Magnets," Proc. Nanobeam'02, CERN-Proceedings-2003-001, p. 149 (2003).

[38] Y. Iwashita, M. Kumada, "Permanent Magnet Quadrupole Lens with Variable Strength," Proc. Nanobeam'02, CERN-Proceedings-2003-001, p. 153 (2003).

[39] E.I. Antokhin, M. Kumada, Y. Iwashita, "The Method of Temperature Compensation for Permament Magnet Final Focus Quadrupole," Proc. Nanobeam'02, CERN-Proceedings-2003-001, p. 157 (2003).

[40] M. Kumada et al, CERN Courier, vol. 41, no. 7, September 2001, p. 9 (2001).

[41] T. Mihara, Y. Iwashita, M. Kumada, C. Spencer, "Variable Permanent Magnet Quadrupole," 19th Magnet Technology Conference 'MT-19', September 2005, Genova (2005).

[42] B. Parker, "Superconducting Magnet Issues," *http://icfa-nanobeam.web.cern.ch/icfa-nanobeam/-slides2.htm*

[43] B. Parker, "Recent Progress Designing Compact Superconducting Final Focus Magnets for the ILC," Proc. Nanobeam'05 (2005).

[44] T. Shintake et al, "Experiments of Nanometer Spot Size Monitor at FFTB Using Laser Interferometry," PAC'95 Dallas (1995).

[45] M.C. Ross, "Instrumentation Development —Test Facilities and Plans," *http://icfa-nanobeam.web.cern.ch/icfa-nanobeam/-slides2.htm*

[46] Y. Honda et al, "Recent Status of Laserwire Monitor Development at KEK-ATF," Proc. Nanobeam'02, CERN-Proceedings-2003-001, p. 165 (2003).

[47] G.A. Blair, "Simulation of Laser-wires at CLIC Using BDSIM," Proc. Nanobeam'02, CERN-Proceedings-2003-001, p. 169 (2003).

[48] K.-J. Kim, "Small Emittance Generation: Flat Beams," *http://icfa-nanobeam.web.cern.ch/icfa-nanobeam/-slides2.htm*

[49] R. Brinkmann, Ya. Derbenev, K. Flottmann, "A Low Emittance, Flat-Beam Electron Source for Linear Colliders," PRST-AB 4, 053501 (2001).

[50] V. Telnov, "Beam Energy Measurement at Linear Colliders Using Spin Precession," Proc. Nanobeam'02, CERN-Proceedings-2003-001, p. 159 (2003).

[51] ATF2 Collaboration (B.I. Grishanov et al), "ATF2 Proposal," SLAC-R-771, CERN-AB-2005-035, KEK-REPORT-2005-2 (2005).

[52] M. Woods et al, "A Test Facility for the International Linear Collider at SLAC End Station A, for Prototypes of Beam Delivery and IR Components," PAC'05 Knoxville (2005).

[53] S. Smith, "Collaborative Discussions - Report from Excursion to Gruyere," *http://icfa-nanobeam.web.cern.ch/icfa-nanobeam/-slides2.htm*

[54] Photo by Y. Iwashita (2005).

[55] *http://www.ati.surrey.ac.uk/news/nanobeam*

[56] *http://www.advancenanotech.com/-050413_research_equip_cam.html*

[57] V.M. Biryukov, S. Bellucci, "Studies of Nanotube Channeling for Ef£cient Beam Scraping at Accelerators," NIM B 230, p. 619 (2005).

[58] V.M. Biryukov, S. Bellucci, "Nanostructures Versus Crystals in Particle Channeling," NIM B 234, p. 99 (2005).

[59] The CLIC Study Team, "A 3 TeV e+e- Linear Collider Based on CLIC Technology," CERN 2000-008 (2000).

[60] A. Sessler, "The Free Electron Laser as a Power Source for a High-Gradient Accelerating Structure," in Laser Acceleration of Particles (P. Channel, ed.), AIP 91, American Institute of Physics, p. 154 (1982).

[61] W. Schnell, "A Two-Stage Linear Collider Using a Superconducting Drive Linac," CLIC Note 13 (1986).

[62] R. Corsini et al., "Experimental Results on Electron Beam Combination and Bunch Frequency Multiplication," PRST-AB 7, 040101 (2004).

[63] C. Achard et al., "A Demonstration of High-Gradient Acceleration," CERN-AB-2003-048, CLIC Note 569 (2003).

[64] M. Korostelev, E. Levichev, P. Vobly, "Progress with Damping Wiggler Design," CLIC Seminar 16.09.2005 (2005).

[65] S. Araki et al, "Design of a Polarized Positron Source Bsaed on Laser Compton Scattering," KEK-PREPRINT-2005-60, CLIC-Note-639, LAL 05-94 (2005).

[66] G. White, "Fast Intra-Train Feedback Systems for a Future Linear Collider," *http://icfa-nanobeam.web.cern.ch/icfa-nanobeam/-slides2.htm*

[67] S. Redaelli, "Stabilization of Nanometre-Size Particle Beams in the Final Focus System of the Compact LInear Collider (CLIC)," CERN-AB-2004-026 (ABP), CLIC-Note 595 (2004).

[68] D. Schulte, private communication (2005).

[69] A. Seryi, "Ground Motion and Vibration Issues for Accelerators," PAC 2001, Chicago (2001).

[70] A. Seryi, "Issues of Stability and Ground Motion in ILC," Proc. Nanobeam'05 (2005).

[71] S. Redaelli, R.W. Assmann, W. Coosemans, M. Boge, M. Dehler, L. Rivkin, "Vibration Measurements at the Swiss Light Source," EPAC 2004 Lucerne (2004).

[72] M. Boge, A. Streun, M. Munoz, "Studies on Imperfections in the SLS Storage Rings," PAC 1999 New York (1999).

[73] W. Schnell, "Cooling and Vibration in the CLIC Main Accelerating Structure," CLIC Note 468 (2001).

[74] R. Assmann, W. Coosemans, S. Redaelli, W. Schnell, "The Effect of Cooling Water on Magnet Vibrations," CLIC Note 531 (2002).

[75] B. Bolzon et al, "Active Stabilization of a Future Linear Collider Final Focus Quadrupole Mock-Up," Proc. Nanobeam'05 (2005).

STATUS OF THE ILC

Kaoru Yokoya, KEK, Tsukuba, Japan

Abstract

The linear collider studies came into a new era of internationally organized form. Since the decision by ICFA in 2004 summer to adopt superconducting technology, two workshps have been held and the design organization called GDE (Global Design Effort) has been created. As the first milestone the BCD (Baseline Configuration Document) was almost completed. In addition, several R&D projects are going on in many countries for the realization of the ILC (International Linear Collider).

HISTORY IN THE PAST ONE YEAR

The design studies of the linear colliders started in mid 1980's. Since then several projects had been in competition and in collaboration. In 2004 August ICFA decided at the ICHEP (International Conference on High Energy Physics) at Beijin that the next linear collider should be based on Superconducting technology and named it ILC. The reason of the choice was

- The machine operation will be easier than X-band warm collider because the larger aperture of the cavities makes the beam motion insensitive to the ground motion and because the larger bunch separation makes the bunch-to-bunch feedback easier.
- The risk will be lower owing to the several-year experience at the TESLA-TTF.
- The European X-FEL can be a prototype and the industrialization is already on-going.
- The power consumption is lower.

At this time it was an urgent issue to reorganize the individual regions (Asia, Europe, Americas) into a form suitable for the international project. This was in particular true for Asia and Americas, where the R&D had been concentrated on the warm technology. The first ILC workshop was held at KEK with the participants over 200. The workshop was organized with 6 working groups (overall design, linac system, injectors, beam delivery system, cavities and communications) and was quite successful in directing the momentum to the unified linear collider.

For the design work and the coordination of the R&D an internation organization was needed so that in March 2005 formation of GDE (Global Design Effort) started. Barry Barish (Caltech) was nominated the director and, as of September 2005, 49 members from Asia (12), Europe (21) and Americas (15) have been decided. These include Regional Directors (F. Takasaki from Asia, B. Foster from Europe and D. Dugan from Americas), Accelerator Desiggn Leaders, Cost Experts, Civil Engineering Experts (1 from each region for these), etc. Latest news is available from the web page [1].

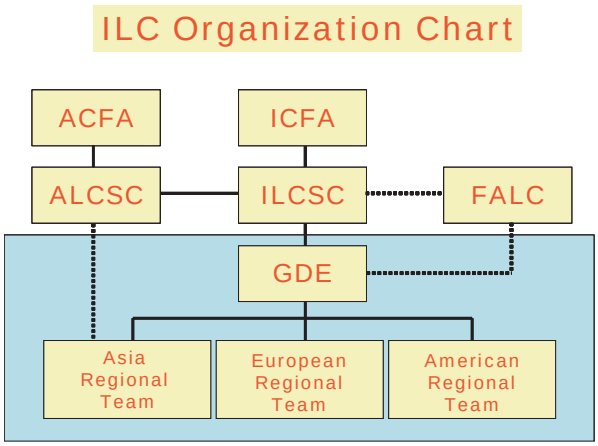

Figure 1: Organization chart of ILCSC, GDE, etc.

ILCSC (ILC Steering Committee) is the overseeing organization of the GDE. It should work also as the contact to the funding agencies. The present schedule is that GDE will be reorganized under' federation of worldwide government agencies 'on the way from RDR to TDR (see below for these two documents) and then ILCSC will hand-off to GDE. M. Tigner (Cornell Univ.) has been the chairperson of ILCSC but S. Kurokawa is going to take over in September 2005. ILCSC is planning to form MAC (Machine Advisory Committee) soon.

GDE made the following plan for the near future.

- Complete the BCD (Baseline Configulation Document) by the end of 2005.
- Complete the RDR (Reference Design Report)
- Create the TDR (Technical Design Report) in 2 or more years after RDR.

BCD will describe the outline of the collider (see below for more detail) and RDR, which contains the rough estimation of the project cost, will be the first document to be shown to the funding agencies.

As the first step to the BCD, the second ILC workshop was held at Snowmass, Colorado, US in 2005 summer. It was a 2-week joint workshop with the

physicists and over 600 people participated. In addition to the 7 subsystem working groups formed at the fiest workshop (the injector group split into two, particle source and damping ring), 6 global working groups were formed which expanded over the subsystems. They included parameters, instrumentation, reliability/availability, civil engineering, cost engineering and the options group (physics other than e^+e^-, e.g., γ-γ collider).

Although the fundamental choice of the machine design, namely normal-conducting or super-conducting, there were still many choices that had to be made for starting detailed design. The important issues include

- Accelerating gradient and the cavity shape
- Positron generation scheme
- Shape and size of DR (Damping Ring)
- Number of bunch compressor stages
- Number of main linac tunnels
- Whether to follow earth 's curvature
- Number of IPs (Interaction Points) and the crossing angle
- Configuration layout of the linac, DR, etc.
- Senario of energy upgrade.

There are two or more possibilities for each of these issues and we have to make choices for these before detailed design.

The BCD will contain the description of the BC (Baseline Configuration) together with the reason of the choice. It should also contain the description of the AC (Alternative Configuration). The latter is a configuration which is still premature but may be completed in the near future and with which one can expect better performance and/or cost reduction. The required R&D for both BC and AC should also be listed in the BCD.

There were some issues for we did not come to conclusions at Snowmass Workshop. For the damping ring problem a mini-workshop was held in Nov.9-11. For other open issues five task forces were created and they wrote so-called 'white papers' by early November. The core members of the GDE (Executive Committee) had a meeting in Nov.17-18 and finally wrote 'Strawman BCD' which was to be finalized in a GDE meeting in early December in Italy. The present text for the proceedings includes the conclusion made by the Strawman BCD (one month after the NanoBeam workshop). Thus, it is slightly different from the presentation at the NanoBeam Workshop.

DESIGN OUTLINE

In this section we describe the results of discussion at the Snowmass workshop on the design choices. There are still more items than listed above but we shall omit them here.

Accelerating Gradient and Cavity Shape

We are eventually aiming at the center-of-mass energy 1TeV. The choice of the accelerating gradient has a strong impact on the site length. The choice of the gradient is closely related to the choice of the cavity shape. According to the recent technology the superconducting breakdown limit due to the surface magnetic field has been considered to be reached for well-treated cavities. The best-treated TESLA-type cavities reached about 41 MV/m (this does not mean it can be operated at this gradient. The operating gradient with safety margin would be 35 MV/m at most). In order to exceeed this value, new cavity shapes are required which has smaller ratio of the maximum surface magnetic field to the accelerating electric field on the beam axis. To this end two different types, namely the Re-entrant type and the LL (low-loss) type have been under development. Single-cell tests for proof-of-principle have been done at Cornell Univ., Jefferson Lab and at KEK. Fig.3 shows results of single-cell tests of re-entrant and LL-type cavities performed at KEK. This shows that the accelerating gradient can in fact be increased by changing the cavity shape.

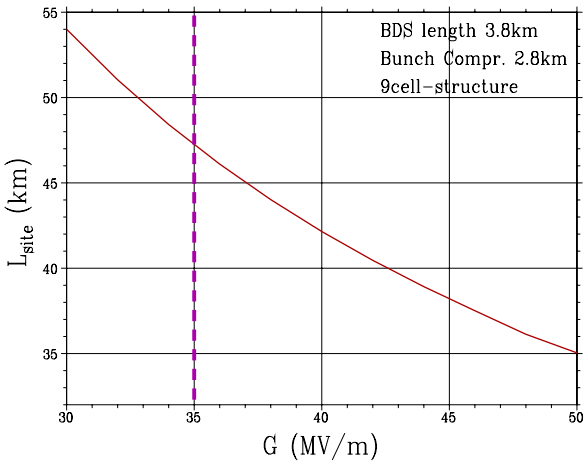

Figure 2: Relation between the accelerating gradient and the required site length. This is subject to many other uncertainties such as the bunch compressor, disgnostics section, etc.

KEK has fabricated four 9-cell LL-type cavities (See Fig. 4) by the Snowmass Workshop but the result of the vertical test of the first one was still poor. The conclusion at the workshop is the following. (Note that the collider will be constructed in two stages, 500GeV in the first stage and 1TeV in the second.) In the 500GeV stage,

- the baseline cavity shape is the TESLA-type and the baseline gradient is 31.5 [35] MV/m. This means that only the cavities which recorded >35MV/m in the vertical test are to be installed

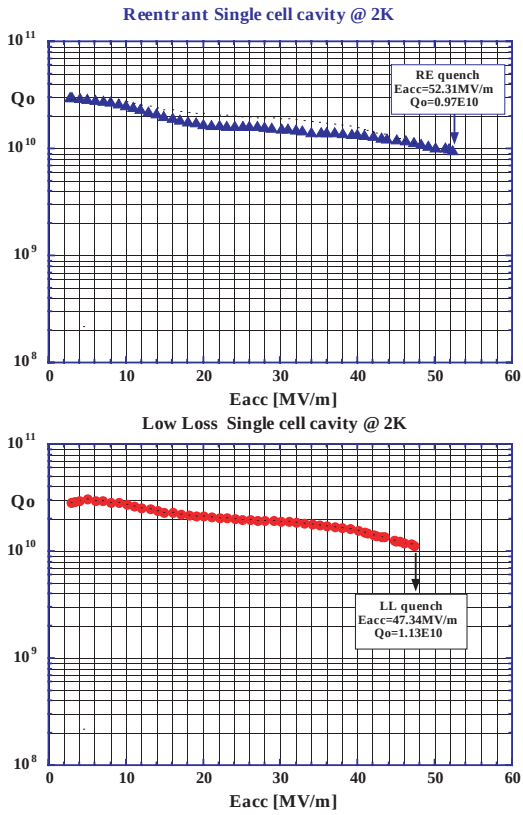

Figure 3: Single-cell test results at KEK. The re-entrant-type cavity (upper) fabricated at Cornell Univ., and surface-treated at KEK reached 52MV/m with $Q_0 \sim 1 \times 10^{10}$. LL-type cavity (lower) fabricated and treated at KEK reached 47MV/m with $Q_0 \sim 1.1 \times 10^{10}$. According to K. Saito, KEK.

in the linac (other are thrown away) and are operated at the average gradient 31.5 MV/m, with 10% margin of actual grdient reduction.

- The required Q_0 value is 1.0 [0.8] $\times 10^{10}$.
- The RF and the cryogenics system should be capable of the gradient 35 MV/m.
- The tunnel length should be calculated grom the value 31.5 MV/m.
- The Alternative Configuration is 36 [40] MV/m with Re-entrant or LL-type cavities. The required Q_0 value is 1.0 [0.8] $\times 10^{10}$.

For the upgrade to 1TeV, the Alternative Configuration for 500GeV stage is adopted as the baseline, taking into account a long R&D time between the two stages.

Figure 4: First LL-type 9-cell cavity fabricated at KEK.

The linac length at 1TeV with the baseline configuration (different gradient between 500GeV portion and the rest) will be around 41km. The required site length including other components, will be about 50km.

Positron Production Scheme

Three schemes for positron generation have been competing:

- Conventional scheme: hit a few GeV electron beam onto a target and capture created positrons.
- Undulator scheme: hit a few tens of MeV photons generated by high energy (>100 GeV) electrons going through an undulator, and capture created positrons. (See Fig. 5)
- Compton scheme: hit a few tens of MeV photons generated by a few GeV electrons in a storage ring going through intense laser beams, and capture created positrons. This is a new scheme proposed at KEK this year.

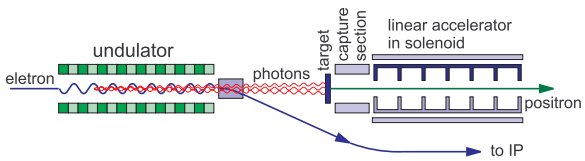

Figure 5: Positron generation scheme using an undulator.

The undulator scheme was chosen at Snowmass Workshop as the baseline. Its major advantage is that a polarized positron beam can be created by using a helical undulator. The disadvantages are that the method has never been tried in actual machines and that the positron beam can be created only when the high energy electron beam is available so that the commssioning of the positron side is not easy. To overcome the last disadvantage, a low-intensity 'keep-alive' source of the conventional method must be attached.

The Compton method requires significant R&D study, though it can produce a polarized positron beam, and was ranked 'Alternative'. The conventional scheme was considered as the backup in case a fatal problem is found in the undulator scheme.

Damping Ring

The beam in the linac consists of about 3000 bunches with the interval 300 to 330ns, thus the total beam length is about 1ms. The damping ring (DR) has to accomodate all these bunches. If the bunches are stored with the same interval, the circumference of the DR has to be 300km, which is unrealistic. Therefore, the bunches must be stored in a compressed form and they must be extracted one by one. To do so, a

kicker magnet with fast rise and fall time is needed as shown in Fig. 6.

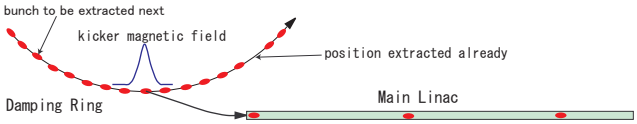

Figure 6: Extraction scheme from the damping ring to the main linac.

There are several different DR designs but they are classified into two categories:

- A small circumferene (less than several km) ring in a separate tunnel
- A large circumference ring most part of which shares the tunnel with the main linac

Fig, 7 shows three of the possible designs. The upper two (circumference 3km and 6km) belong to the first category and the lower one (circumference 17km, called dogbone) to the second. The kicker rise(fall)

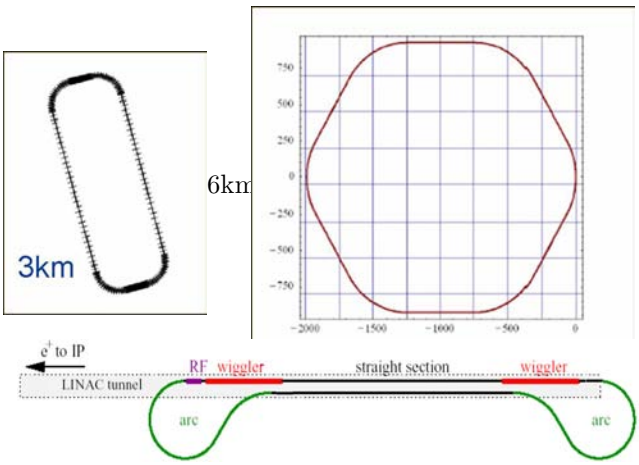

Figure 7: Three designs for the damping ring. The lower one with 17km circumference is called 'dogbone'.

time required for these three cases is 3, 6, and about 20ns when they accomodate 3000 bunches. A new fast kicker has been developed at KEK in 2005. An example of the measurement of the beam kick angle is shown in Fig. 8. The result was quite satisfactory. The rise(fall) time was about 3.6ns, which is enough for 6km ring with 3000 bunches. There is still an issue of the bunch-by-bunch stability of the kick angle (requirement 0.7×10^{-3}) but this can be solved by a feedforward system. Thus, in view of the kicker technology, the dogbone and the 6km ring were thought to be feasible.

The dogbone ring has an advantage that the beam instabilities (in particular the fast ion instability in the electron ring and the electron cloud instability in the positron ring) are less severe owing to the longer bunch distance. But it has disadvantages of complex

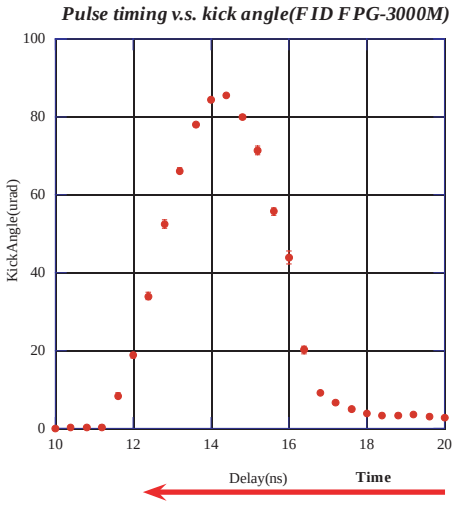

Figure 8: Beam kick measurement by KEK fast kicker. The horizontal axis is the kick timing (ns) and the vertical axis is the kick angle (μrad) by a single kicker. (T. Naito, KEK)

commissioning and operation and of the stray field effect from the linac RF system both due to the tunnel sharing.

In the mini-workshop held in November 2006 the DR working group came to the following conclusion.

- The electron damping ring will be a 6km ring.
- The positron damping ring will be two rings, each 6km circumference.

The reason that two rings were needed for positron was that the electron clound instability was thought to be severe.

Bunch Compressor

The bunch length in the damping rings will be around 6mm. This must be compressed below 300μm for the collision. A bunch length compressor is needed after extraction from the damping ring. It turned out that a single-stage compressor can compress a 6mm bunch into 300μm but this is quite marginal. If the bunch in the damping ring is longer than 6mm or if a bunch shorter than 300μm is needed at the collision point, a single-stage compressor is not enough. The Snowmass workshop adopted two-stage compressor as the baseline, although it is very long (1.4km).

Main Linac Unit

The baseline layout of the main linac unit has been decided as follows. (Fig. 9)

- It consists of one modulator, one klystron, three cryomodules each containing 8 9-cell cavities and one superconducting quadrupole magnet at the center.

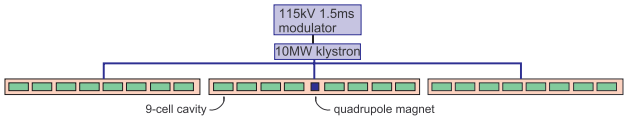

Figure 9: Main linac unit.

- The modulator is the bouncer-type of output voltage 115kV.
- The klystron is the MBK (multi-beam klystron) of output power 10MW with the pulse length 1.5ms.

TESLA design adopted a longer cryomodule containing 12 cavities but a shorter one was chosen as the baseline for easier handling. The packing factor of the linac (including magnet, gaps between modules, etc. but not the sections for beam diagnostics) will be around 69%. This means the 2×250GeV linacs occupy the tunnel length about 250GeV/(31.5MeV/m)/0.69 ≈ 23km. The total length of the first stage tunnel including the beam delivery section (∼4km), the bunch compressors (2×1.4km), etc. is about 30km.

Main Linac Tunnel

The main linac tunnel must accomodate RF system (klystrons and, possibly, modulators) linac cryomodule, and the beam lines from the positron source to the DR. Also, depending on the configuration choice, two DR lines (if the dogbone is selected) and the trasport line from DR to the linac.

The choice had to be made between single and double tunnel designs. In the latter case the RF system will be housed in a separate tunnel running in parallel. TESLA design adopted single tunnel but it is subject to many operational problems (machine repairs are very limited during operation), though it can save the construction cost about 300M Euro according to the TESLA estimation.

Snowmass Workshop selected double tunnel.

Earth's Curvature

When the site length is about 50km, the distance between the straight line and the circle following the earth's curvature amounts to 5km in the middle, and the angle between them 4 mrad. There are three possible choices in the tunnel shape in this respect (see Fig. 10):

- curved tunnel: follow the earth's curvature smoothly. The beam is bent by off-centered orbit in the quadrupole magnets.
- kinked tunnel: follow the earth's curvature by placing bending sections every several kilo-meters.
- laser-straight tunnel

For the first two choices, a shallow tunnel (less than ∼20m deep) is possible, depending on the site. The advantage of the laser-straight tunnel is that the beam

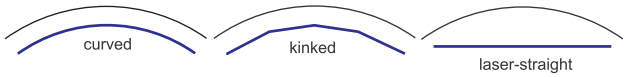

Figure 10: Following the earth's curvature.

dynamics is the simplest. (There was a concern whether curved/kinked tunnel is possible for multiple-TeV case, but this turned at Snowmass out to be no problem.) The disadvantage of the straight tunnel is that the beam has an angle (max 4 mrad) with respect to the water level surface. This makes the design of the cryogenics system complicated and requires R&D.

The baseline choice in the BCD is the curved tunnel because the cost will be the lowest. (The kinked tunnel needs the bending sections and the straight tunnel needs special cryogenics system.)

Energy Upgrade Senario

The project consists of two stages: the first stage with the center-of-mass energy 500GeV and the second stage 1TeV. A few senarios are conceivable for the first stage:

(A) Construct full 1TeV tunnel/linac and run at half gradient

(B) Construct 1TeV tunnel and place linac at upstream

(C) Construct 1TeV tunnel and place linac at downstream

(D) Construct only 500GeV tunnel

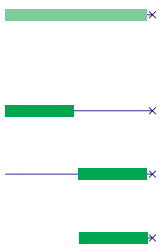

(A) has an advantage of no need to rebuild the production lines in industries. (B) is better than (C) from the view point of beam dynamics (no long transport of low-energy high-quality beams). (D) has an advantage of minimal first stage cost but the overall cost will be larger and the second stage requires to move some of the injectors. (B) allows a smooth upgrade for the second stage.

The discussion was concentrated on (B) and (D).

The task force recommended (B) but the Executive committee chose (D), putting more emphasis on the first stage cost.

Number of Interaction Points

In contrast to ring colliders, to have several interaction points (IP) does not bring about an increase of the total luminosity. Nevertheless, most physicists want two IPs because cross check between detectors would be possible and because a parallel run of different experiments (e.g., e^+e^- and γ-γ) is possible. The motivation to have only 1 IP is in large part the cost. The Snowmass Workshop chose 2IP scheme as the baseline. The Executive committee followed this conclusion but stated that 1IP may be chosen in the future depending on the financial aspect.

Machine Layout

Fig. 11 shows a schematic layout of the collider in the first and second stage according to the choices in the BCD. These figures are not intended to show

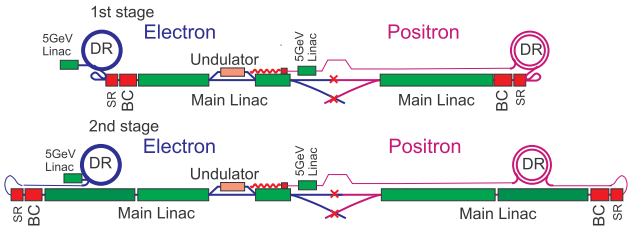

Figure 11: Machine layout in the 'Strawman BCD'. DR: Damping Ring, SR: Spin Rotator, BC: Bunch Compressor.

- the location of the 5GeV injector linacs (e^+ injector may be placed near the e^+ DR)
- the location of the undulator in the stage 2 (may be moved upstream)
- the location of DRs (all the DRs may be placed near the center of the whole system)

SCHEDULE

The expected schedule after the Snowmass workshop will be the following. The next milestone is the completion of the RDR (Reference Design Report), where the first cost estimation will be presented based on the 'sample sites' selected from the three regions (Asia, Europe, Americas).

2005.Nov	BCD Draft by GDE Executive Com.
2005.Dec	Final BCD at GDE meeting at Frascati (Italy)
2006.Jan	Form CCB (Configuration Control Board) to control possible changes after BCD
2006.Mar	GDE meeting at Bangalore (India) with physics WS
2006.Jul	GDE meeting at Vancouber
2006.Nov	GDE meeting in Spain
2006.end	Complete RDR (Reference Design Report) (includes first cost estimation based on 'sample sites')
2007.Jan?	3rd ILC WS (in Europe)
2008-2009?	Complete TDR (Technical Design Report)
?	Site selection
Mid 2010's	Commissioning

We need to define the machine in some more detail for writing the RDR. Intensive discussions will be made towards the meeting in India in March 2006. Then, we have to freeze the machine design at least until RDR for starting serious studies including the cost.

TEST FACILITIES

Various R&D programs for ILC are on-going. Here we briefly summarize the status of only large-scale test facilities.

Three large test facilities exists or are in construction. They are:

- TTF (TESLA Test Facility) at DESY
- SMTF (Superconducting Module Test Facility) at FNAL
- STF (Superconducting Linac Test Facility) at KEK

TTF (Fig. 12) is the test facility to establish the technology of linac for linear colliders and X-ray FEL. Its collaboration organization changed the name from 'TESLA Collaboration' to 'TESLA Technology Collaboration'[2] after the decision by ICFA on ILC. Several-year successful operation up to the accelerating gradient 24MV/m was quite appealing in the decision of ICFA. The accelerating module no.5 was installed in late 2004 and is now being operated around 400 MeV for FEL with the wavelength around 30 Angstrom. The installation of the module no.6 is planned in Spring 2006. This will consist of electropolished cavities only and will be close to the module for the European X-FEL. This will also be the base for the ILC design.

Other two facilities are now under construction. SMTF[3] is being planned at FNAL site. It includes not only the facility for ILC but also for proton driver and for CW linacs. The present construction schedule

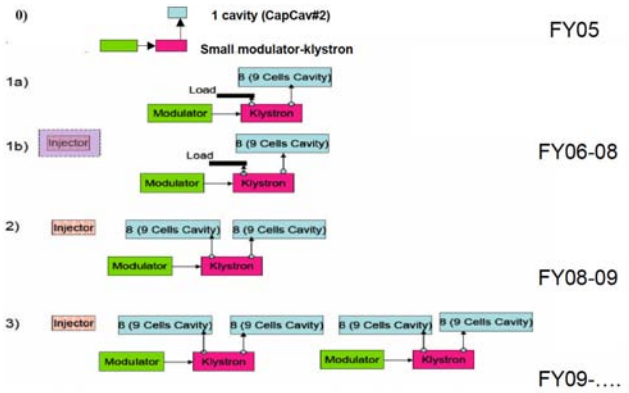

Figure 13: SMTF schedule.

of the ILC part of SMTF is shown in Fig. 13 (subject to change).

STF is being constructed at KEK. The project consists of two phases (see Fig.14). The phase 1 includes two cryostats each containing 4 9-cell cavities. They are the standard TESLA type and LL type. This will

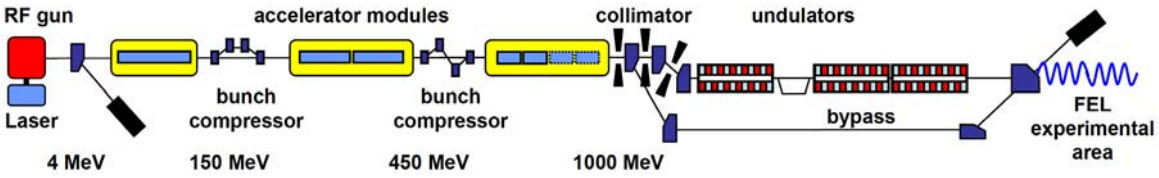

Figure 12: TTF. Up to module no.5 (the first half of the third yellow box) has been installed.

be completed by the end of 2006 and be operated in 2007. The phase 2 basically is to construct one unit of the ILC. The present plan consists of 3 cryomodules each contaning 8 9-cell cavities. The design detail will be studies in 2007 and the whole system including the electron gun is to be completed by the end of 2009.

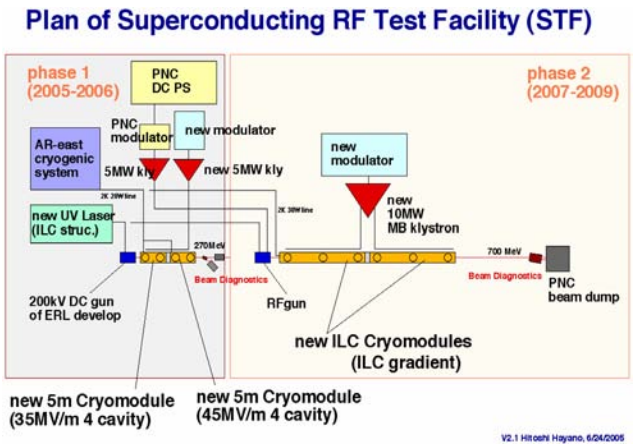

Figure 14: STF block diagram.

These three test facilities are similar in scale and the sum will be about 1% of the stage 1 linac of ILC (250GeV).

What is challenging in the ILC technology is not only the acceleration but also the luminosity issue, i.e., how to create small emittance beams, how to accelerate them without degradation of the emittance, and how to focus and keep them in collision. The ATF at KEK has proved the feasibility of creating low emittance beams for the ILC. Now ATF is going to be extended for the last item: final focus technology. As shown in Fig. 15, a final focus system will be added to the ATF extraction line. This part is called ATF2. ATF2 is one of the hot topics in this workshop and there is a dedicated session for this.

The goals of ATF2 are

- To focus the beam down to ∼35nm by using the same optics as in the ILC and to maintain the small size over a long interval of time,
- To control the beam position at the focal point to nanometer precision and to establish the bunch-by-bunch feedback system with ILC-like beam.

The total cost is estimated to be around 4M$. This will be constructed by international collaboration, hopefully by more or less equal sharing of the budget among the three regions. The installation is being planned in late 2007 and the commissioning in the beginning of 2008.

References

[1] http://www.linearcollider.org/cms/

[2] http://tesla-new.desy.de/content /index_eng.html

[3] http://ilc-dms.fnal.gov/Workgroups/SMTF/

[4] http://lcdev.kek.jp/STF/

[5] http://lcdev.kek.jp/ATF2/

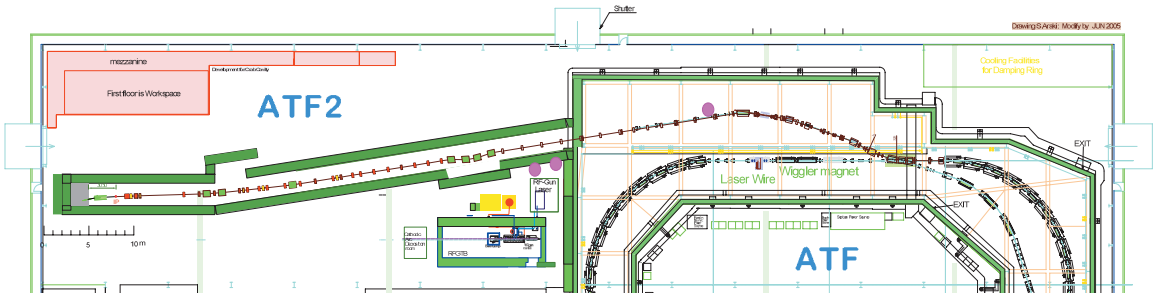

Figure 15: ATF2 beamline. The northern half of the present ATF damping ring is seen at bottom right. The extraction line is going to be extended to the west (left) for adding a final focus system. The length of the hall from left to right is about 120m.

ISSUES OF STABILITY AND GROUND MOTION IN ILC*

Andrei Seryi, Linda Hendrickson, Glen White, SLAC, Stanford, CA, USA

Abstract

Stability of International Linear Collider is determined by the stability of the site, additional noises of beamline component, energy and kicker jitter, and performance of train-to-train and intratrain feedback. Stability goals in terms of the beam jitter at the end of the linac, in BDS and at the IP are discussed in this paper, and translated to stability goals for the site and for component jitter. Present status of stability studies is reviewed and feasibility of achieving the stability goals is discussed.

BEAM JITTER IN ILC

Studies of beam stability for linear collider have long history, in terms of site stability studies, development of stable hardware and beam-based feedbacks. In particular, in 2002-2003 the Technical Review Committee performed studies and confirmed that ILC (at that time TESLA) requires the fast intra-train feedback. Without such feedback even the moderately noisy sites may result in luminosity loss. Another TRC recommendation was to make urgent studies of stability of the linac quadrupoles, located in the cryostats, since at that time there were no reliable data to quantify total motion of the beamline components [1].

Sources of beam jitter in ILC are the motion of beamline components, in the linac, in the Beam Delivery System (BDS) and in Final Doublet (FD), as well as the energy and intensity jitter, Damping Ring extraction kicker jitter and so on. The motion of beamline components in turn consists of a) site ground motion and ILC in-tunnel and near-tunnel hardware noise; b) additional noise of beamline components including amplification of floor motion by supports.

The approach to control of beam jitter in ILC with its low repetition rate of 5Hz is based on reliance on the fast IP intra-train feedback to steer the beams to collision and recover luminosity for most of the long train of 2820 bunches. The capture range of this feedback is rather large, couple of IP beam size sigmas in the horizontal plane and up to about a hundred sigmas in the vertical plane. With fast feedback, the requirements for ground motion, linac and BDS quad jitter and stability of FD has to be determined not from IP jitter, but, in particular, from diagnostic performance and emittance preservation.

Discussing the ILC jitter goals, one need to stress that the large capture range (tens of sigmas) of fast feedback does not mean that larger jitter is allowed along the machine. On the contrary, there are many reasons why the jitter should be smaller than the beam size, in particular a) to minimize beam emittance growth due to collimator wake-fields; b) to provide acceptable conditions for beam diagnostics; c) to minimize jitter effects on dispersion free steering (see e.g. [2]); etc.

In terms of the effects listed above, considered at the end of the linac at the entrance to BDS diagnostics and collimation, the edge of the comfortable range can be approximately defined as: end of the linac jitter < 50% beam sigma. In this case, for example, in the BDS diagnostic section, the effective beam size, with jitter added in quadrature, is just 10% larger than nominal. In comparison, if the jitter would be equal to the beam size, the effective size in the diagnostics section would be already 40% larger than nominal which would significantly complicate beam measurements and tuning.

In the Beam Delivery System the optics is strong, has nonlinear elements, and there are magnets which have much tighter stability tolerance than in the weak linac. One can therefore expect that BDS would contribute noticeably to the total jitter. One can allow the jitter to grow along the BDS to about approximately 100% of beam sigma (excluding FD contribution), without noticeable deterioration of performance.

The Final Doublet contributes one-to-one to the IP jitter, however its jitter is less relevant, as soon as it is taken out by fast feedback, since the beam transport from FD to IP is straightforward and nonlinear contributions due to jitter in the FD sextupoles are small. The FD jitter of the order of 100nm or somewhat more should be manageable. In this case no active stabilization of FD should be needed, while FD position monitoring would still be useful.

DISCUSSION OF ILC JITTER GOALS

The tentative stability goals suggested above for discussion are based on general common sense as well as on earlier and also recent integrated simulations for ILC. Some results of these recent simulations will be highlighted below. Note that this work is ongoing and more details may be available soon, which could be useful for clarifications of the stability requirements.

Integrated simulations of ILC, from linac entry to the IP were set up with 5Hz feedback and idealized IP feedback. Ground motion models B, C [1] and K (model for KEK site, it is close to model C in 1-10Hz, but less noisy above 20Hz [3]) were used, together with additional jitter of components and energy jitter.

The 5Hz feedback loops were cascaded and have exponential response of 36 5Hz pulses. There were 5 distributed loops in linac, each with 4X and 4Y dipole correctors, and 8 BPMs. In BDS there was one loop, with 9 BPMs and 9 dipole correctors. The IP deflection (X&Y) in 5Hz loop was not cascaded and has 6 pulse exponential response.

Additional component jitter of 25 nm in BDS (including FD) and 50 nm in linac was used in simulations. The DR extraction kicker jitter was 10% of beam sigma. The beam current jitter was 5%. The energy

jitter corresponded to 0.5% uncorrelated amplitude on each klystron, 2 degrees uncorrelated phase on each klystron, 0.5 degrees correlated phase on all klystrons. The BPM resolution was assumed to be 100 nm.

In these assumptions, the vertical jitter at the end of the linac is 1%, 33%, 61%, 70%, 72% of the beam size with ground motion B only, ground motion K only, all jitter sources and ground motion B, all jitter sources and ground motion K, all jitter sources and ground motion C. From these numbers, one can conclude that ground motion K or C is acceptable from the linac stability point of view, however the linac component vibration of 50nm is somewhat too high. One would wish it to be no more than 30nm, and in that case the ground motion and component vibration would contribute about equally to the end of the linac beam jitter.

In terms of the jitter in the BDS for ground motion K, we observe that luminosity is reduced to 17% with 5Hz feedback only or 70% with ideal intratrain. If we omit all additional jitter sources except for ground motion, these numbers become 37% or 84%. Results for gm C are similar. Luminosity reduction is attributed to effects in BDS (not FD, not linac) and is being studied further. The models C or K appear too noisy for the BDS area (this agrees with the earlier studies done for TRC [1]), and one would wish, roughly, the conditions to be a factor of three quieter (this scaling factor would be applied only to high frequency part of the spectrum in the ground motion model). From another point of view, ground motion B would be exceedingly quiet – the IP beam jitter is only about 30% with ground motion B only and one could allow a factor of three noisier conditions. The component jitter assumed for BDS in simulations (25nm) is too high, one wishes it not to exceed about 10nm.

Summarizing, the tentative goals for tunnel floor stability and additional component jitter suggested for discussion are up to ground motion K or C with additional component jitter up to 30nm in the linac and up to ground motion “B*3” or “C/3” and component jitter up to 10nm in the BDS area.

One needs to note that linac and BDS may in fact have different specs for on-the-floor noise because the noise consist of ground noise plus noise from nearby utilities, which are different in linac and BDS areas. Moreover, the BDS area may be located in a quieter place than the average linac vibration level. In particular, we believe that all sample sites considered at this moment for ILC, including the DESY site, would satisfy the suggested stability goals.

One other thing that needs to be discussed is how to divide the vibration budget. Let’s say the requirement for on-the-tunnel floor stability in linac area is ground motion C (and gm “C/3” in BDS). This motion includes natural ground motion of the site and added noise by ILC conventional facility and other nearby equipment. One can set the budget for the added noise to be ~70% of gm C and require the initial site to be also ~70% of gm C. This approach is conceivable but may show limitations in the future. One could also discuss feasibility of another approach, with initial site motion significantly quieter than ground motion C (and “C/3” in BDS), and the entire vibration budget is given to conventional facilities and other added noise.

ACHEVABILITY OF STABILITY GOALS

Let us discuss whether the stability goals, suggested above for consideration, could be achieved. As was mentioned earlier, the sample sites themselves are sufficiently stable (better or equal to C in linac and C/3 in BDS area). When the real site is chosen for ILC, the stability criteria would need to be considered again.

The biggest challenge for ILC stability is in its own noise. In terms of additional noise in the BDS area – earlier studies of FFTB quadrupole stabilities have shown that the differential motion to ground is small (~2nm at 5Hz), for the quadrupole on movers and with cooling water flow [4]. Lower frequency is relevant for the 5Hz machine (0.2-0.5Hz) but was not studied accurately. Detailed and careful design is important, but one can expect that the 10nm goal for component jitter may be achievable in the BDS area.

The 30 nm goal for linac component jitter is another challenge. Presently, there are insufficient data to determine how difficult this goal is. The measurements inside of cryostats are difficult and just being developed. Recently, stability of TTF cryostats was measured with the stretched wire technique [5] and with seismic and piezo sensors [6]. It appears from these results that the discussed stability goal is 5-10 times tighter than what was observed for vibration of quads in the cryostats. However, present observations were performed in a very noisy environment of on-surface labs.

One should also note synergy of these linac stability studies with XFEL program. The XFEL is shorter and has fewer quads than ILC linac, but focusing is stronger, there are more quadrupoles per km, and the beam jitter requirements are tighter – 10% of beam size sigma [7]. XFEL plans to achieve beam jitter goals by both using fast feedback and improving the cryomodule stability, while with 70 nm (rms) quad movement there is about 5% of beam jitter at linac end [7]. Still, the XFEL component stability goal is several times more relaxed that that of ILC. Focused engineering efforts are needed to achieve the stability of ILC linac components.

Noise of nearby utilities is important and need to be carefully minimized in ILC. Earlier studies of vibration transmission from surface, along the tunnel and between two tunnels [8] as well as developments of passive noise reduction methods [9] are applicable.

Common collider hall for two detectors was recently suggested. This is certainly more challenging for IR stability. As mentioned above, with fast feedback, the FD stability goal is about 100nm – such jitter should be achievable for single collider hall, in terms of high frequencies (several Hz) in normal operation (scenarios with parallel construction of second detector need more study). However, lower frequency of about 0.5Hz and

temperature stability may be more difficult in a common collider hall. Monitoring of FD motion will be needed to resolve its stability issues. Optical interferometers or nonmagnetic seismic sensors (pendulum based or with molecular electronic transfer [10]) been developed for earlier projects can be applicable for ILC.

ACKNOWLEDGEMENT

The authors would like to thank many colleagues who contributed to discussion and work on these issues.

SUMMARY

In this paper, we discussed the ILC stability goals and suggested for consideration by the community the tentative stability criteria, which could be summarized as up to ground motion C with additional component jitter up to 30nm in the linac and up to ground motion "C/3" or "B*3" and component jitter up to 10nm in the BDS area. The biggest challenge is in achieving the specified component jitter. The level of ongoing studies is increasing. The focused efforts should bring their results.

REFERENCES

[1] International Linear Collider Technical Review Committee, Second Report, SLAC-R-606, 2003.
[2] P.Tenenbaum, Steering Simulations Study, NLC Machine Advisory Committee, June 2003.
[3] T.Tauchi et al. Ground motion measurements at KEK, in a borehole near Higashi-Odori.
[4] M.Woods et al, FFTB stability quad.
[5] A.Bosotti et al., PAC2005.
[6] H.Brueck et al., TESLA Meeting, 03/31/2005.
[7] XFEL WG-Minutes, Oct.2003.
[8] Parsons Co./Geovision, August 2003, LCC-122.
[9] F.Asiri, NLC MAC, June 2003.
[10] PMD/eentec, www.eentec.com

Test Beams for ILC Final Focus

G. A. Blair
Dept. of Physics, Royal Holloway, Univ. of London, Egham, Surrey. TW20 0EX. UK

The International Linear Collider (ILC) will require 250 GeV-500 GeV electron and positron beams to be focused down to a few nanometers in the vertical dimension at the interaction point. This will require unprecedented specifications for the final focus region and related controls. To this end, a set of international test facilities are being planned to address key performance goals of beam delivery sub-systems. These test facilities are described and future plans outlined.

1. INTRODUCTION

The beam delivery system (BDS) is the ILC sub-system that is situated between the main linac and the detector [1]. The BDS has several roles and includes:

- a beam diagnostics section to measure accurately the beam emittance at the exit of the linac,
- a collimation section to reduce beam halo,
- tuning sections so that the beams have the right properties to be focused down to nanometer scales,
- feedback systems to ensure the particle bunches meet at the interaction point (IP),
- crab cavities to ensure that the bunches overlap fully during collision at finite crossing angle,
- upstream (of the IP) beam measurements including polairmetry and high-precision spectrometry,
- the final focus quadrupoles that focus the beams to namometre scales at the interaction point.

These critical components are being tested at international facilities, as described below. These tests, together with a planned integrated test facility by the ATF2 collaboration, will be an important component of the ILC R&D programme over the coming years.

2. TEST FACILITIES

A set of test facilities are in operation (or in advanced planning) with a view to addressing the key technological challenges of the ILC final focus system. These are now outlined in turn.

2.1. End Station A at SLAC

The End Station A (ESA) [2] at SLAC has the parameters listed in Table I. This facility is being used to address:

- Collimator wakefield measurements; the wakefields may perturb beam motion and lead to both emittance dilution and magnification of position jitter at the IP. The aim is to find optimal materials and geometry for the collimating jaws. The principle of the measurement is shown in Fig.1. 8 new collimators have recently been manufactured in the UK and have been shipped to SLAC for tests at ESA in 2006.
- Experiments T-474, T-475 for energy spectrometers. Precision energy measurements to 50-200 parts per million are needed for Higgs boson and top quark mass measurements. Beam Position Monitor (BPM) and synchrotron stripe spectrometers will both be evaluated in a common 4-magnet chicane. Initially, SLAC

Linac BPMs will be used. New electronics based on nano-BPM work at KEK is being developed by UC Berkeley.

Table I: Beam parameters of the SLAC End Station A compared to those at the ILC.

Parameter	SLAC ESA	ILC-500
Repetition Rate	10 (up to 30) Hz	5 Hz
Energy	28.5 GeV	250 GeV
e- Polarization	(85%)	>80%
Train Length	Single bunch; (up to 400 ns possible)	1 ms
Microbunch spacing	20-400 ns	337 ns
Bunches per train	1 (or 2)	2820
Bunch Charge	2.0 x 10^{10}	2.0 x 10^{10}
Energy Spread	0.15%	0.1%

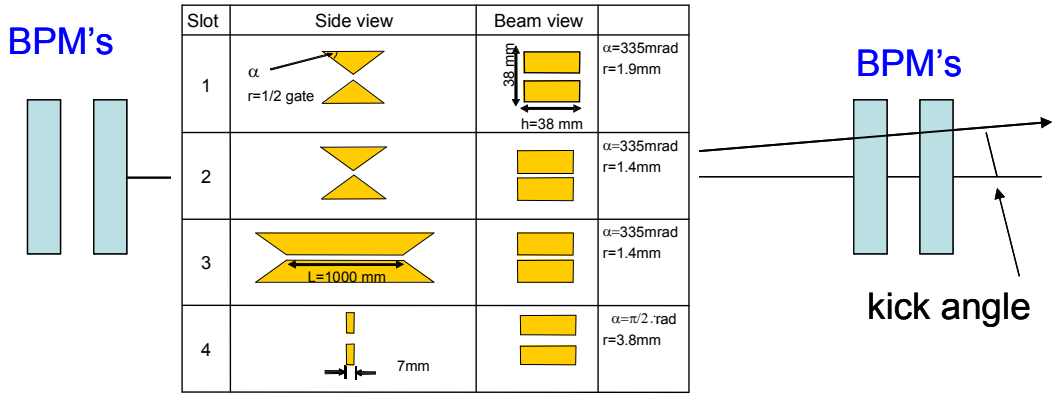

Figure 1: Principle of the collimator wake-field measurement at the SLAC ESA. A variety of collimator geometries will be tested in this way and results compared to simulations for the purposes of optimization.

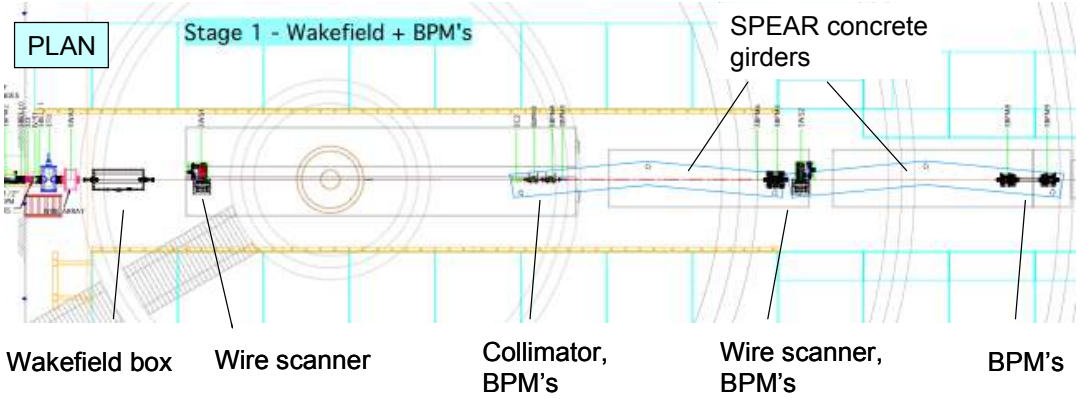

Figure 2: Plan view of the ESA layout for spectrometry and collimator wake-field experiments.

ILCAW0906

New BPMs, optimized for energy spectrometry, are being designed at University College London in collaboration with BPM experts at SLAC and KEK. A plan view of the ESA area is shown in Fig.2. Other ESA plans and/or possibilities include:

- BPM test stations.
- IP BPMs/kickers (necessary for fast inter-train and intra-train feedbacks), studies of sensitivity to backgrounds and RF pickup. Possibilities for installing a feedback system are also under investigation.
- Electromagnetic interference (EMI) impact on beam instrumentation or detector electronics, with plans to characterize EMI along ESA beam-line using antennas and fast scopes.
- Bunch length and longitudinal profile measurements; in particular: electro-optic, Smith-Purcell, coherent transition radiation, and possibly others.
- Spray beam or fixed target to mimic pairs, beamsstrahlung, disrupted beam for testing a synchrotron stripe energy spectrometer, IP BPMs, and BEAMCAL (the very low angle calorimeter).
- Interaction region mockup of the beam-line geometry at the IP within ±5 meters in *z* and ±20 cm radially.
- Single particles (electrons, photons, pions) with energies 1-25 GeV and 1 or fewer particles/bunch at 10Hz for ILC Detector tests.

2.2. PETRA

PETRA is an electron (and positron) storage ring with the beam properties listed in Table II.

Table II: Beam parameters of PETRA.

Energy (GeV)	4.5 to 12
Bunch Length σ_z (ps)	~ 100
Charge per bunch (nC)	1 to 3
Horizontal beam size σ_x (μm)	100 to 500
Vertical beam size σ_y (μm)	~ 100

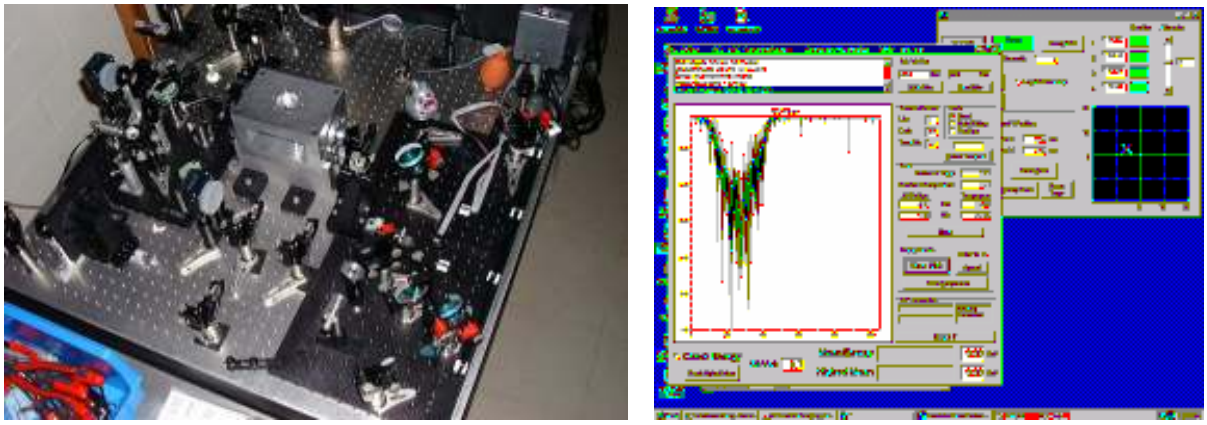

Figure 3. Left: layout of PETRA laser-wire hardware under test in the lab at RHUL before shipment to DESY. Right: a screenshot from a run in February 2005 that shows the laser-wire scan (forward) and BMP reading (rear).

The PETRA laser-wire hardware, shown in Figure 3 (left) has now been running for approximately 2 years and is routinely providing useful results as shown in Figure 3 (right). A scan takes about 30s, limited by the laser repetition frequency of 30Hz. The hardware has recently (Dec. 2005) been upgraded to enable scans in both *x* and *y* and the original Q-switched laser is being replaced with an injection-seeded system that should improve the longitudinal mode quality. Data taking with the new system is planned for spring 2006. Further details are provided in [3,4,5]

2.3. ATF

The ATF ring at KEK has the properties listed in Table III.

Table III: ATF beam parameters

Maximum energy		1.28 GeV (γ=2500)
Beam emittance	Vertical	$(1.5 \pm 0.25) \times 10^{-11}$ m rad
	Horizontal	$(1.4 \pm 0.3) \times 10^{-9}$ m rad
Bunch Length		~ 8mm (26 ps)
Single bunch population		1.2×10^{10}
Energy Spread		0.08%

The mission of the ATF/ ATF2 collaboration [6,7] is:

- ATF, to establish the technologies associated with producing the electron beams with the quality required for ILC and to provide such beams to ATF2 in a stable and reliable manner.
- ATF2, to use the beams extracted from ATF at a test final focus beam-line which is similar to that envisaged for the ILC. The goal is to demonstrate the beam focusing technologies that are consistent with ILC requirements. For this purpose, ATF2 aims to focus the beam down to a few tens of nm (rms) with a beam centroid stability within a few nm for a prolonged period of time.
- Both the ATF and ATF2, to serve the mission of providing young scientists and engineers with training opportunities of participating in R&D programs for advanced accelerator technologies.

Current ATF projects include:

- polarised positron generation R&D at the ATF extraction line (ended June 2005),
- laser wire R&D in the damping ring (Kyoto University); see below,
- high quality electron beam generation by photo-cathode RF Gun (Waseda University),
- X-Synchrotron Radiation monitor R&D (University of Tokyo),
- Optical diffraction radiation R&D (Tomusk University); see below,
- beam based alignment R&D,
- nano-BPM project of SLAC, LLNL and LBNL; see below,
- nano-BPM project of KEK; see below,

- FONT project (UK Institutes); see below,
- laser wire project at extraction line (UK Institutes); see below,
- fast kicker development project (DESY, SLAC, LLNL),
- fast ion instability research,
- multi-bunch instability study.

Some examples of these projects are now reviewed briefly.

The ATF has been host for many years to a very successful laser-wire project [8,9] located in the damping ring. This system uses a continuous wave (CW) laser combined with an high Q-factor optical cavity to increase the laser power at the IP; a cavity is required for each of the vertical and horizontal dimensions as shown in Figure 4 (Left) together with a photograph of the system in Figure 4 (right). The entire optical table is moved with high precision actuators, to provide the scanning mechanism.

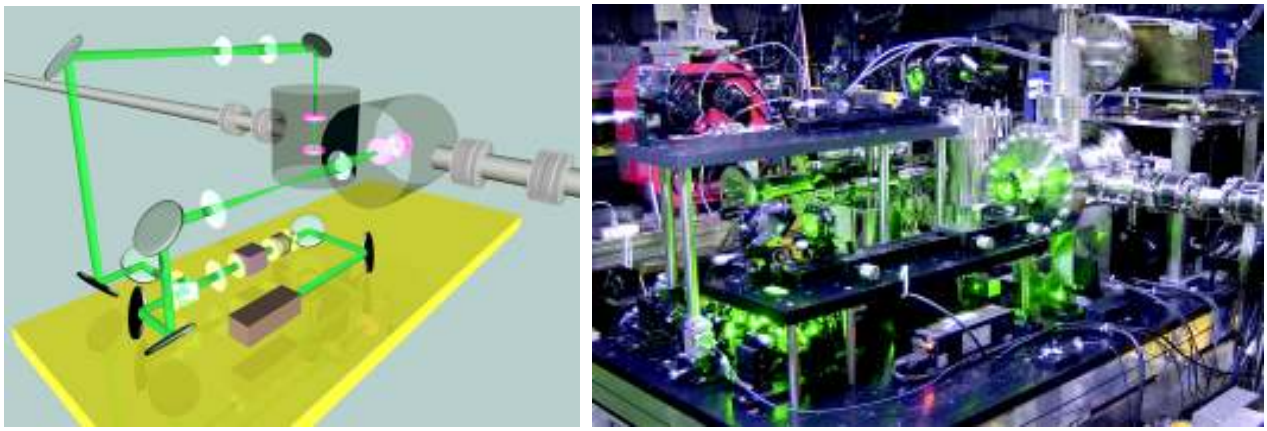

Figure 4. Left: schematic of the ATF damping ring laser-wire showing the horizontal and vertical optical cavities. Right: a photograph of the system showing the optical table that is moved by high precision actuators during a scan.

The laser used at the ATF to provide light to the optical cavities is a 300 mW 532 nm solid-state CW system and the optics is set up to provide a waist of 14.7 μm in *x* and 5.7 μm in *y*. A scan takes about 15 minutes for *x* and 6 minutes for *y*. The system has been used to show the damping mechanism taking place in the ring, using the Compton detector timing to isolate the relevant timing period from several separate scans [9].

Another laser-wire experiment has recently (Dec. 05) been installed at the ATF extraction line [4]. This aims at a single-pass device to measure micron-scale electron spot sizes, such as will be needed at the BDS (and linac) of the ILC. For such a system a high-power pulsed laser system is required, which supplies of order 10 MW (or higher) pulsed power. The technical challenges for such a system centre on the design of f/1 optics for the laser final focus system (to obtain micron-scale electron spot-sizes) and on maintaining the high-power laser [5]. It is planned to learn from the experience at the ATF extraction line laser-wire system to construct a laser-wire based emittance measurement station for the ATF2 programme.

The ATF Nano-BPM project has two 600 mm triplets of cavity BPMs. The KEK triplet is shown in Figure 5 (left) and the SLAC/LLNL triplet shown on the right. The triplets are spaced apart by about 5m in the ATF extraction line.

ILCAW0906

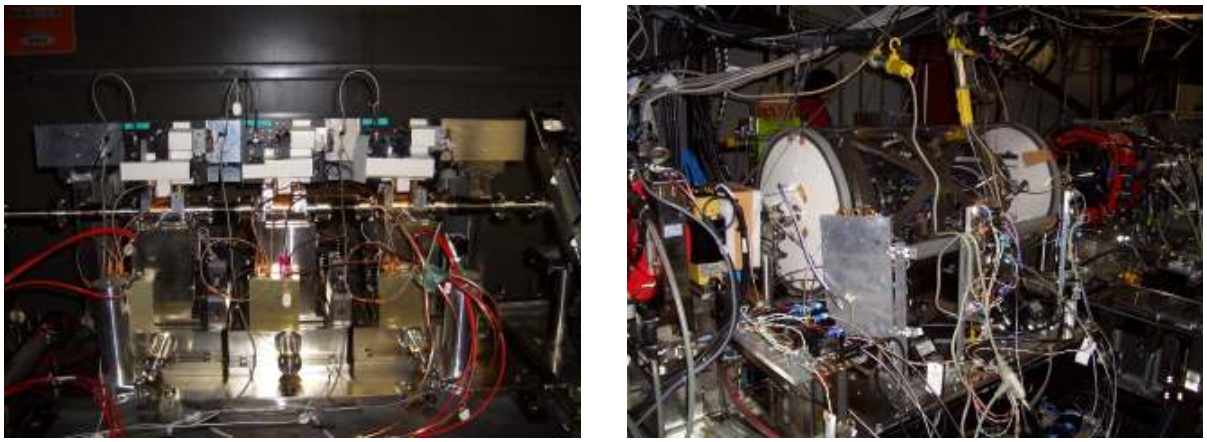

Figure 5. Left: the KEK triplet of BPMs. Right the SLAC/LLNL triplet, including the LLNL support frame.

The LLNL frame (shown in Figure 5, right) contains three BPMs made at BINP with approximately 2 cm dipole mode selective couplers. In addition the setup contains high precision movers that allow one BPM at a time to be moved. In this way the BPM phase, scale and offset as well as beam motion can be extracted by linear regression of BPM readings against mover position, together with all the other BPM readings. With one minute of data-taking using 100 pulses a rms resolution of 17 nm has been obtained. Details are described elsewhere in these proceedings.

The two independent nano-BPM systems will be coupled to an optical geodetic structure, employing a two-dimensional grid of Michelson interferometers, to explore the possibility of using active stabilization at the ILC. This project is now being set up at the ATF extraction line [10].

The development of non-invasive micron beam size diagnostics using optical diffraction radiation (ODR) has been achieved at the ATF [11]. The results for a multi-shot measurement are shown in Figure 6 (left); the periodic behavior of the ODR pattern as a function of the target position was confirmed. As shown in Figure 6 (right), single shot ODR measurements with an ICCD have been performed and the electron beam size was estimated and compared with measurements using a wire scanner

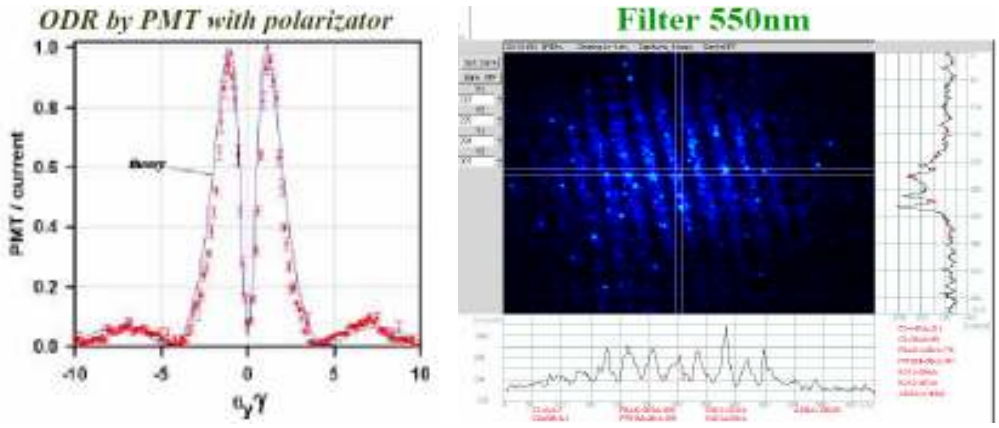

Figure 6. Left: ODR multi-shot measurement. Right: ODR interference as captured on CCD [11]

A set of projects performed within the Feedback On Nanosecond Timescales (FONT) collaboration has been based for several years at the ATF [12]. The system, shown in Figure 7 (left) has demonstrated feedback with a delay

loop, using an ultra-fast system with a total latency of 23 ns. During this project the main gain, delay loop length, and delay loop gain were varied; the system behaved as expected as shown in Figure 7 (right).

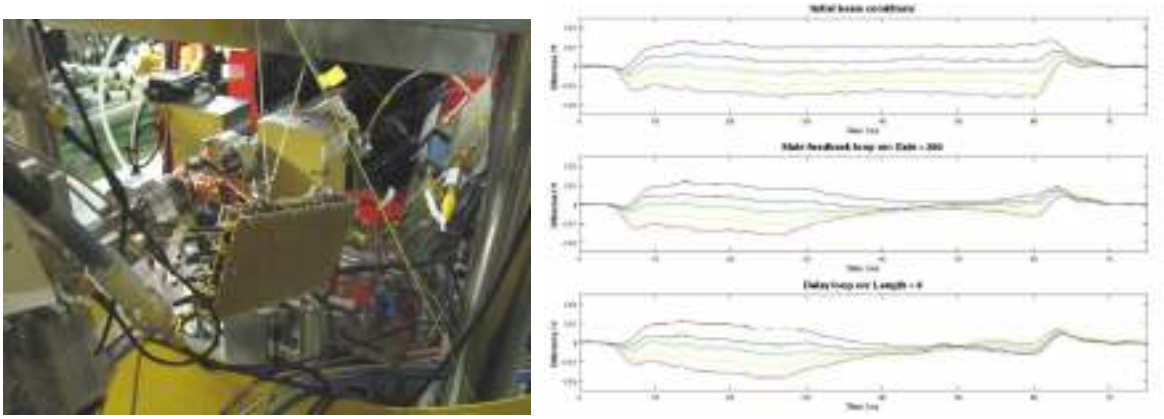

Figure 7. Left: FONT3 amplifier installed at the ATF extraction line. Right: results from FONT3 run showing the effects of feedback on the beam position.

FONT4 will use the new 1.3 GeV ATF extraction line beam that consists of 3 bunches with spacing of approximately 150ns. The project will use a modified FONT3 BPM front-end signal processor, a digital feedback system together with a modified FONT2 solid-state amplifier providing a 300 ns long output pulse, and the FEATHER adjustable-gap kicker. FONT4 is aiming for a first demonstration of feedback with ILC-like bunches with an electronics latency goal of 100 ns and the stabilisation of the 3rd bunch at the micron level. First results are expected early in 2006. An additional possibility currently under investigation is to use μm feed-forward system using BPM measurements in the damping ring to reduce the beam jitter in the ATF extraction line via a new strip line kicker.

2.4. ATF2

The main aim of ATF2 [6] is to demonstrate that nm scale electron spot-sizes can be obtained reliably and to improve on the results obtained at the FFTB [13]. This will require:

- achievement of ~37 nm electron beam size,
- demonstration of a compact final focus system based on local chromaticity correction,
- maintenance of the small beam size over extended running periods,
- control of beam position,
- demonstration of beam orbit stabilization with nm precision at the IP,
- establishment of beam jitter controlling techniques at nm level with ILC-like beam,
- development of a successful commissioning and tuning process, of relevance also to the ILC.

The ATF has achieved the necessary pm emittance and so provides the ideal source to achieve the ATF2 goals. The ATF2 proposed optics IP parameters are presented in Table IV. The ATF2 beams are therefore similar to those for the ILC in chromaticity, energy spread and aspect ratio; but differ in geometric emittance and bunch length [7]. The ATF2 goals are to have extracted beam position jitter of less than 1/3 σ_y in the first stage, decreasing to 1/20 σ_y in the final stage. The bunch structure will be 3 bunches with 150 ns spacing in the first stage, with many bunches with a few ns spacing for the final stage. The preferred ATF2 schedule aims at commissioning in February 2008.

Table IV: ATF2 proposed optics parameters in comparison with those for the ILC.

	ATF2	**ILC**
Beam Energy [GeV]	1.3	250
L* [m]	1	3.5 - 4.2
$\gamma\varepsilon_x$ [m-rad]	3.10^{-6}	$1.\ 10^{-5}$
$\gamma\varepsilon_y$ [m-rad]	3.10^{-8}	4.10^{-8}
β_x^* [mm]	4.0	21
β_y^* [mm]	0.1	0.4
η' [rad]	0.14	0.094
σ_E [%]	~0.1	~0.1
Chromaticity W_y	$\sim 10^4$	$\sim 10^4$
σ_z [mm]	8	0.3

2.5. TTF

Possibilities exist for installing beam diagnostics projects at the Tesla Test Facility (TTF) at DESY, although no candidate projects exist yet for final focus studies because the main efforts have been concentrating on developing the superconducting linac. There is a bypass line on top of the TTF undulator that could be used for new projects and a modification of the beam-line in order to use a dedicated bunch structure for experiments would be possible. There might be some restrictions arising from scheduling issues and from the beam losses (radiation protection) in that area.

2.6. CTF3

The CLIC Test Facility CTF3 aims at demonstrating the CLIC drive beam generation scheme, generating 30 GHz power for testing of the 30 GHz structures, and acting as a test bed for CLIC technology. As a part of this programme, a CLIC Experimental Area (CLEX) is planned, with construction of a new building in 2006. In this area there will be a Probe Beam Injector linac, providing beam to a two-beam test stand and to a Test Beam Line (TBL) for studies of drive beam decelerator dynamics, stability and losses.

Table V: Properties of the CTF3 Probe Beam Injector

Energy [MeV]	~ 200
Normalised rms emittance [mm mrad]	< 20π
Energy spread [%]	< ± 2
Bunch Charge [nC]	0.5 nC
Bunch spacing [ns]	0.333
Number of bunches	1 - 64
rms bunchlength [ps]	< 0.75

ILCAW0906

The TBL will not be used all the time and so the Probe Beam Injector will in principle be available to provide beam for other studies; the properties of this beam are presented in Table V. The current CTF3 schedule shows the probe beam in full use during 2006-7, so from 2008 onwards the TBL could be a new facility for beam diagnostics tests.

3. SUMMARY

Several test facilities exist world wide for ILC final focus projects, including dedicated projects at ESA at SLAC, PETRA (and possibly TTF in the future) at DESY, ATF/ATF2 at KEK and also plans at CTF3. Projects include diagnostics, feedback and nano-BPM R&D, among others. The ATF2 is an international project, ideally suited for R&D in the key final focus issues for the ILC.

Ackowledgments

Material was obtained from various sources; thanks are due specifically to M. Ross and M. Woods (SLAC), J.Urakawa (KEK), H. Weise (DESY) and H. Braun (CERN) for their input. Work supported in part by a Royal Society Joint Project with Japan, by the PPARC LC-ABD Collaboration, and by the Commission of European Communities under the 6th Framework Programme Structuring the European Research Area, contract number RIDS-011899.

References

[1] A. Seryi et al, ILC Baseline Conceptual Design (2005): http://www.linearcollider.org/wiki/doku.php?id=bcd:beam_delivery:beam_delivery_home

[2] EUROTEV Report 2005-008-1: http://www.eurotev.org/e158/e1365/e1378/e1582/EUROTeV-Report-2005-008-1.pdf

[3] J. Carter et al., “Beam Profile Measurements and Simulations of the PETRA Laser-Wire”, Proc PAC05 (2005).

[4] Laser-wire mini workshop, these proceedings.

[5] G. A.Blair “ILC Laser-Wires”, proc. Snowmass 2005.

[6] J. Urakawa, these proceedings. ATF2 Proposal, A. Griishanov *et al*., KEK-REPORT-2005-2, http:// lcdev.kek.jp/ILC-AsiaWG/WG4notes/atf2/

[7] K. Yokoya, ILC-BDIR workshop, RHUL (2005). https://ilcsupport.desy.de/cdsagenda/fullAgenda.php?ida=a0522&stylesheet=nicecompact&dl=talk&dd=

[8] Y. Honda *et al.* Nucl.Instrum.Meth.**A538:**100-115,2005.

[9] Y. Honda, talk at ILC-BDIR workshop, RHUL (2005): https://ilcsupport.desy.de/cdsagenda/fullAgenda.php?ida=a0522&stylesheet=nicecompact&dl=talk&dd=

[10] D. Urner, these proceedings.

[11] P. Karataev *et al*. , talk at ILC-BDIR workshop, RHUL (2005); EPAC-2004-THOALH02.

[12] P. Burrows, these proceedings.

[13] V. Balakin *et al*. Phys. Rev. Lett. **74**, 2479–2482 (1995)

ILCAW0906

FRONTIERS OF LIGHT SOURCES

T. Yamazaki#, Kyoto University, Gokasho, Uji, Kyoto 611-0011, Japan.

Abstract

Present status and future prospects of light sources from electron beam are briefly reviewed with emphases on free-electron lasers and light sources based on ERL (energy-recovery linac).

INTRODUCTION

Main light source from high-energy electron beam at present may be synchrotron radiation from so-called 3rd-generation electron storage rings. However, FELs (free-electron lasers) and light sources based on ERL (energy-recovery linac) are deemed to be the light sources of next generation because of their possibility of higher brightness and/or coherence, though the technologies associated with storage rings are developing steadily. In the following, present status, problems left for the future, and their prospects will be reviewed. The usual synchrotron radiation will be discussed only for the purpose of comparison.

FREE-ELECTRON LASERS

There are many types of free-electron lasers. Some of them will be reviewed and discussed in terms of not the accelerator types but the major purposes.

Short-wavelength Free-Electron Lasers

The cost for the FEL is rather high because expensive electron accelerator has to be used. Therefore, one should widen the FEL wavelength region to where conventional lasers cannot reach, though the FEL has some prominent features, e.g., high power and/or special time structure. One of the directions is in the mid or far infrared region and the other is toward shorter-wavelength region to be described below.

Figure 1 shows FEL projects in the world and in Japan in terms of the FEL wavelength (ordinate) and electron-beam energy (abscissa). The types of accelerators used are distinguished by symbols. The closed symbols mean that lasing with oscillation type was successfully achieved. The acronyms of the institutes will be described in the following when necessary. It should be noted that the values of electron energy and FEL wavelength are fairly rough averages because they are variable in FEL.

As is well known, the shorter-wavelength FEL is difficult because the gain is lower and the cavity loss increases. FELs in the region have mainly been carried out on storage rings so far (see Figure 1).

The first FEL oscillation on storage ring was achieved at LURE (France) on the storage ring ACO in visible wavelength region [1]. In 1988, the first lasing in the ultraviolet (UV) region (240 nm) was accomplished on the storage ring VEPP-3 of Budker Institute of Nuclear Physics (BINP) at Novosibirsk, Russia [2], where a

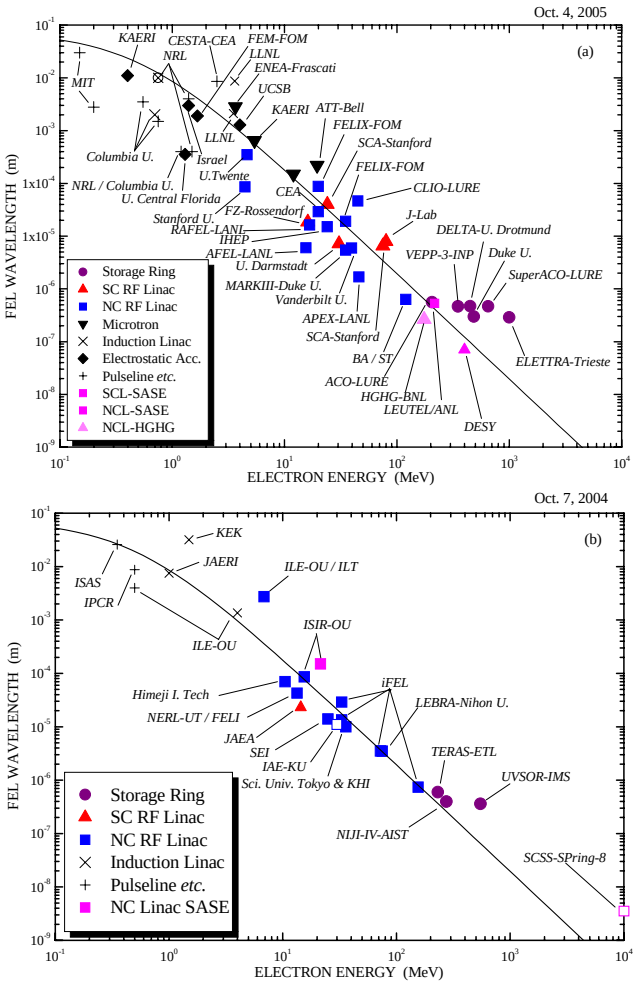

Figure 1. FEL projects in the world (a) and in Japan (b).

special long straight bypass was constructed in the ring to install a long OK (optical klystron).

In Japan, the first oscillation of FEL was achieved at the former ETL (Electrotechnical Laboratory which was reformed to AIST, National Institute of Advanced Industrial Science and Technology) on the storage ring TERAS in 1991 in the visible region (591 nm) [3]. A compact storage ring NIJI-IV was constructed in parallel at the ETL [4]. The ring is of a racetrack type with a triple-bend achromatic lattice. It was the first storage ring in the world dedicated to FEL research.

From 1993 to 1997, oscillation in the UV region was achieved consecutively on the Super-ACO of LURE, the UVSOR of IMS (Institute of Molecular Science), and the NIJI-IV. A circular-polarization undulator was used at the IMS in order mainly to avoid the mirror degradation because there is no higher-harmonic component of spontaneous emission in the centerline. With the undulator, they succeeded in lasing at 239 nm [5], slightly shorter than the record at the BINP.

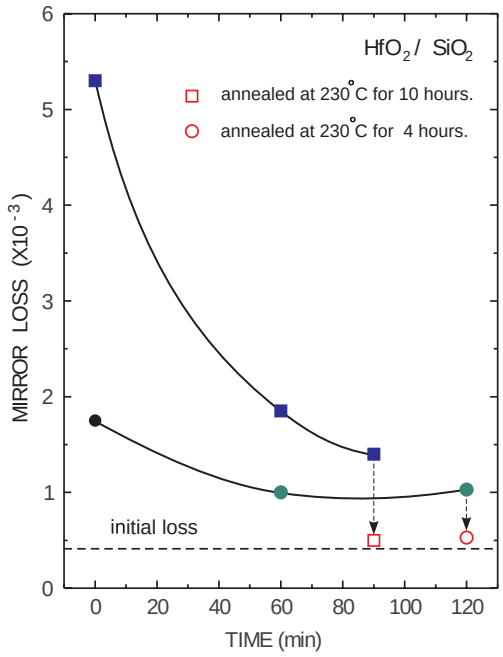

Figure 2 Recovery of degraded mirror.

Dielectric multilayer mirrors frequently used for short-wavelength FELs are seriously degraded after irradiation of UV (ultraviolet) and VUV (vacuum UV) harmonic components. Two mechanisms of degradation had been considered: (1) surface degradation; CO and/or CO_2 in the residual gas are adsorbed in the mirror surface, and then the oxygen are removed by the irradiation of UV/VUV, and island-like carbon layer remains on the surface, (2) volume degradation; some defects or color centers are generated inside the mirror. At the ETL, recovery of the degraded mirrors was successfully achieved for the first time in the world [6] by applying both an oxygen-plasma treatment which oxidized the carbon again and annealing which removed defects, as shown in Figure 2.

In 1998, lasing at wavelengths below 230 nm was achieved at the Duke University and the ETL. The shortest wavelength at the time was achieved at the end of 1998 at the ETL by the use of Al_2O_3/SiO_2 multilayer mirrors [7]. It opened the door to the oscillation of FELs in the vacuum UV (VUV) region, and oscillation in the VUV region was achieved at the Duke University (193 nm) in 1999 on a 3rd-generation storage ring ELETTRA (189 nm) at Trieste (Italy) [8], and NIJI-IV (198 nm). The Trieste FEL is the shortest wavelength of the oscillator type at present.

Lasing in the UV region was achieved with linacs also. Those are a 3rd harmonic oscillation at the Los Alamos National Laboratory (LANL), U.S.A. and lasing at 278 nm (fundamental wavelength) at the Free Electron Laser Research Institute (FELI, Japan, now iFEL of Osaka Univ.) [9], the latter of which is still the shortest FEL oscillation wavelength with linacs.

FEL oscillation in the shorter-wavelength region is quite difficult at present because there is no mirror with high reflectivity in the deep VUV region. Therefore, a scheme of self amplification of spontaneous emission (SASE) is tried in many institutes. The scheme uses a very high-energy linac and a very long undulator, and the spontaneous emission is amplified in a single pass. Typical SASE scheme is shown in Figure 3. The optical cavity is not necessary in the scheme, and there is no limit in FEL wavelength due to the cavity loss. However, the undulator should be very long and electron-beam quality should be excellent with high peak current because the FEL should be amplified in a single pass. The injector can be a RF gun or a DC gun with a buncher section. The linac is either superconducting or normal conducting. One or two bunching sections (usually chicanes as shown in Figure 3 are installed because quite high electron density is necessary and short-pulse laser is one of the merits of SASE. The shortest wavelength with the SASE lasing had been 80 nm on TESLA (TeV Energy Superconducting Linear Accelerator facility at DESY (Deutsche Elektronen-Synchrotron, Germany) [10]. They reported the successful lasing down to 32 nm recently [11]. The SASE is one of the candidates of the so-called the 4th generation light source because it has a potential of lasing at wavelengths down to 0.1 nm. There are 3 more big SASE projects in the world. They are the LCLS project in the U. S. A. which uses a part of SLAC (normal-conducting linac) [12], European X-Ray FEL Project at DESY [13] which will use a superconducting linac like the one of TESLA, and the SCSS (SPring-8 Compact SASE Source) in Japan [14]. There is a new SASE proposal of PAL (Pohang Accelerator Laboratory, Korea) which is to be built in the present accelerator site [15].

However, there are many difficult problems to be solved. The emittance of the electron beam should be quite low. It should be lower than $\lambda/(4\pi)$ which is .0008 nm·rad and the normalized emittance of 0.03 μm·rad for a 2-GeV electron beam. Another example of difficulties is the undulator magnetic-field tolerance. The tolerance of 10^{-4} for K value corresponds to vertical electron-beam misalignment of 50 μm. The most serious problem will be that the pulse-to-pulse stability is quite poor and timing jitter is very large, because the FEL starts up from noise and there is no feedback like that in the oscillation type FELs. The average bandwidth of the SASE FEL is inherently very wide from the same reason. In the TESLA

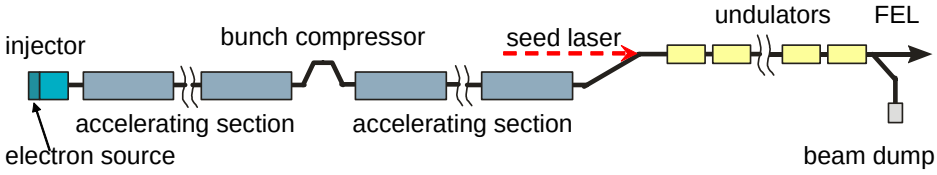

Figure 3. Typical SASE and HGHG scheme.

case, the relative bandwidth is about 2 %, while it is of the order of 10^{-4} in the storage ring FELs. Seeding by high harmonic of conventional laser is being considered to cope with the problem [16]. Finally, the number of the users' beamlines will be much smaller than that of the 3rd-generation SR sources.

Another single-pass FEL scheme is so-called high-gain harmonic generation (HGHG). The scheme is also shown in Figure 3, where a conventional laser is used as a seed and it is amplified in the undulator section. At present, there is only one HGHG FEL in operation, which is at the Brookhaven National Laboratory (BNL) of the U. S. A. They succeeded in amplifying the Ti:sapphire laser at around 265 nm (the 3rd harmonic of the seed) [17]. Though the FEL was far more stable than in the SASE scheme, it will take a long time to go down to 0.1 nm.

High Power Free-Electron Lasers

There is no objection to saying that high-power FEL is desirable.

Superconducting (SC) linac has been thought to be quite suitable for high average-power FELs because there is no RF power loss at the wall of the accelerating cavity. The first oscillation of the FEL in the world was achieved at the Stanford University with a SC linac and an undulator made of double spiral SC coils [18], and the system is still in operation with many modifications, though it is not aiming at high-power FEL. After the lasing, there had been no other SC linac FELs for a long time. At the former Japan Atomic Energy Research Institute (JAERI, now Japan Atomic Energy Agency, JAEA), research on 500-MHz SC linac had been continued for a long time, and the first oscillation at 28 μm with the system was achieved in 1998 with a macropulse peak power of 100 W which was the highest power in the world at the time [19]. Shortly after this, oscillation at 3.1 μm with 1.7-kW average power was recorded at the Thomas Jefferson National Laboratory (TJNL), U. S. A. with an L-band SC linac with a GaAS photocathode [20]. An energy-recovery linac (ERL) system, by returning the spent electron beam to the accelerating cavity in a decelerating phase and converting the beam energy to the RF power to accelerate successive electron beam, worked beautifully to enhance the power. However, the lifetime of the photocathode is rather short. The highest quasi-CW average power at the time (2.4 kW) was achieved at the JAERI in 2001 [21]. One of the salient features of the lasing was that the highest power was obtained at perfect tuning with very narrow pulse width, though it occurs with a little detuning in usual lasing owing to a lethargy effect. In 2004, the TJNL achieved the highest power of 10 kW after substantial renewal of the FEL system [22]. In order to take advantage of the high efficiency of the SC linac, JAEA is also developing the energy recovery system.

One of the problems with such a system is that the FEL bandwidth is inherently wide especially at zero detuning, though the mechanism is different from the case of SASE. Thus, application of such FELs to spectroscopy is not very advantageous. High power FELs will be used in the field of material processing, power beaming, etc. The ERL scheme as SR sources will be described later.

The FEL system with normal-conducting linac is being built at the BINP with a scheme of so-called multi-turn accelerator-recuperator (MARS) which will be described later. The 1st stage has already been working, and the average FEL power of 0.4 kW was obtained recently at wavelength region of 120-180 μm [23]. The goal is the 4-stage FEL system. There is another project at Korea Atomic Energy Research Institute (KAERI) with similar scheme but using superconducting cavities from CERN [24]. It should be noted here that there are a few FEL system based on energy-recovery electrostatic accelerators, though they are not described further in the present paper.

THz Radiation Sources

FEL wavelength is extending to longer-wavelength region also because there are few intense conventional sources in the region. Especially, the THz region of 100 μm ~ 3 mm is currently explored quite actively because it is a new region with many areas of application expected.

The only FEL system working in the THz region is that of KAERI where a FEL system based on a compact microtron powered by a magnetron and a unique electromagnet undulator is in operation. The FEL covers the wavelength from 100 μm to 1.2 mm (0.3 – 3 THz). The main applications of the FEL are THz imaging, spectroscopy for bio-medical research, and THz material study, and some results have already been demonstrated [25].

Though the THz FEL seems quite promising, there are many competitors, e.g. coherent SR and coherent transition radiation (TR) which use electron beam of very short bunch, while the FEL makes the bunching of the electron beam through interaction of electron and photon beams. Though the feasibility of generating the coherent SR had been suggested earlier, we had to wait until 1989 for the confirmation by a group of Tohoku University [26] because the measurement of the radiation in the mm (THz) wavelength region was rather difficult. The brightness of the coherent SR was as high as several orders of magnitude times that of ordinary non-coherent SR, as expected. Angular distribution of the radiation is limited in the forward cone of angle of about $1/\gamma$. Transition radiation (TR) is emitted by a uniformly moving electrons passing from one medium to another of different dielectric constant. Though usual TR is incoherent, the TR generated by a microbunched electron beam can be coherent in just the same way as the coherent SR.

Researches on application of coherent SR and TR have been made by several groups, especially for imaging, measurement of absorption coefficients, etc. [27]. Very high-power THz coherent SR has been generated at the TJNL with a quasi-CW electron beam [28].

THz radiation is also generated by conventional femtosecond lasers also, though it is neither very intense

Table 1 FEL users' facilities in the world.

Institution	Accelerator	Wave-length (μm)	Peak Power (Av. Power)	Appliations
Stanford Univ. (U.S.A.)	S. C. Linac 66 MeV, 5.6 A	3 -15 20 - 60	1.2 MW (1 W)	Solid-State Phys. Biologymedical
Univ. California Santa Barbara (U.S.A.)	Van de Graaff 5 MeV	350-2500 60 - 350 30 - 90	(～10 kW)	Semiconductor Phys.
Duke Univ. (U.S.A.)	N. C. Linac 45 MeV, 40 A	1.8 - 9.5	2 MW (3 W)	Solid-State Phys.
Vanderbilt Univ. (U.S.A.)	N. C. Linac 45 MeV, 40A	2 - 8	3 MW (6 W)	Biology-Medical Solid-State Phys.
FOM FELIX (Netherland)	N. C. Linac 45 MeV, 40 A	5 - 30 16 - 110	5 MW (0.5 W)	Atomic-Molecular Phys. Biology-Medical
LURE CLIO (France)	N. C. Linac 45 MeV, 70 A	1.8 - 17.5	10 MW (3W)	Solid-State Phys.
Los Alamos National Laboratory (U.S.A.)	N. C. Linac 15 MeV, 100 A	4 - 6	10 MW (1.5 W)	Medical
LURE Super-ACO (France)	Storage Ring 800 MeV	0.3 - 0.63	(0.3 W)	Solid-State Phys. Electronic Devices
iFEL, Osaka Univ (Japan)	N. C. Linac 33 MeV, 42 A 75 MeV, 50 A 165 MeV, 60 A 35 MeV, 40 A 25 MeV, 40 A	 5 - 22 1 - 6 0.28 - 1.2 20 - 80 50 - 100	 5 MW (2 W) 5 MW (0.5 W) 5 MW (0.5 W) 5 MW (1 W) [2 MW (1 W)]	 Solid-State Phys. Isotope Separation Medical App. Bio-Egineering New Materials
Tokyo Univ. of Science, Kawasaki Heavy Industries, Ltd. (Japan)	N. C. Linac 40 MeV, 12 A	4 - 16	30 kW (0.5 μW)	FTIR
LEBRA Nihon Univ, (Japan)	N. C. Linac 100 MeV, 35 A	1.2 ~ 6.2	2 MW (0.5 μW)	beginning (PXR)

nor monochromatic. It should be noted, however, that weak and white radiation is sometimes advantageous for some kinds of applications.

Users' Facilities

Table 1 shows the main users' facilities in the world. The first facility of this kind was constructed at the University of California, Santa Barbara (UCSB), U. S. A. with a van de Graaff electrostatic accelerator with an energy-recovering system, and then, pioneering facilities were opened at Stanford University and Vanderbilt University.

At the FELIX in Netherlands, a linac with macropulse as long as 10 μs was realized, and then, CLIO of LURE and FELI followed the scheme. The long macropulse is necessary to reach saturation in a small-gain oscillator. The macropulse length reached 24 μs at the FELI.. The FELI facility was constructed by a company of consortium style with a total budget of 860 million Japanese yen partly financed by the former MITI (now METI), and it used to be the only one users' facility in Japan. It was made over to the Osaka University, and the name of the facility is iFEL at present. The FEL is used mainly for medical and bio-engineering applications. After it, a users' facility was constructed by the Kawasaki Heavy Industries, Ltd., and it is in operation at the Tokyo University of Science. Recently, another uses' facility named LEBRA was built at the Nihon Univ., and application of the FEL has been begun.

All the facilities in Table 1 are based on linacs except those of the UCSB and Super-ACO. The storage ring Super-ACO offers the SRFEL beam to the users one day per week. Two-color (FEL and SR) experiments are now being carried out with some interesting results.

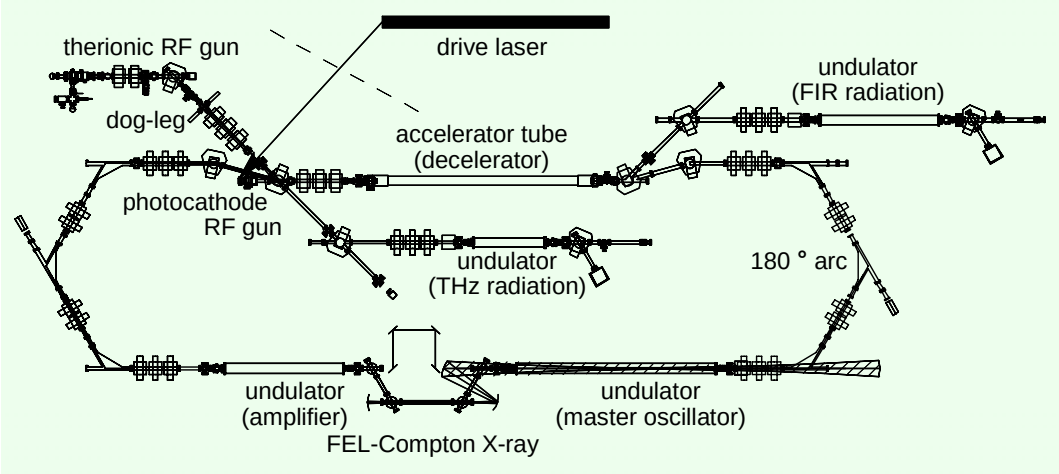

Figure 4 Schematic view of the KU-FEL.

It should be noted that the FEL for a users' facility should be flexible in terms of wavelength, intensity, pulse structure, etc. to conform with users' various requests.

Compact Facilities

Though the large-scale users' facilities are used for many purposes as described above, compact and economical FEL system is desirable if it is to be used in a small laboratory in a university or a company. If such compact FELs are realized, there will be more and more users of FELs. Such a system may be dedicated for special purposes.

At the Institute of Advanced Energy, Kyoto University (IAE/KU), a compact and economical FEL system named KU-FEL is under construction [29]. A conceptual view of the system is shown in Figure 4 together with future upgrade plans. The frequency of the system is S band (about 2856 MHz) that is the most reliable at present and moderately compact. A thermionic 4.5-cell RF gun is used as an injector, which generates the electron beam and accelerates up to about 9 MeV. The electron beam from the RF gun can be far brighter than that from conventional system of static DC gun and buncher system. The electron beam is further accelerated in the accelerator tube up to 20~40 MeV. The target FEL wavelength is in the far-infrared (FIR) region from a few μm to over 100 μm where there are few conventional lasers available.

There are two undulators in Figure 4. A MOPA (master oscillator and power amplifier) system is considered for the future in order to generate the FEL of narrow band width even at high power. Generation of quasi-monochromatic soft x-ray beam is also considered by using the FEL beam and the electron beam after the FEL system. Finally, the spent electron beam will be re-injected into the accelerator in the decelerating phase, and the electron-beam energy will be converted to the RF power to accelerate the successive electron beam. Though the energy recovery system will save the RF power to some extent, the energy efficiency will not be very high because the system is not superconducting. However, the load to shield ionizing radiation will be eased because the final energy of the electron beam thrown into the beam dump is very low. A photocathode RF gun is also considered for the future in order to accommodate the users' demands for short-pulse FEL.

Construction of the KU-FEL system began in 1995, and it is almost finished now though the progress is rather slow because of the budget problem. An S-band 4.5-cell thermionic RF gun was manufactured after a design work with a computer simulation [30]. The cutaway view of the RF gun is shown in Figure 5. Electron beam was accelerated successfully up to about 9 MeV by the RF gun with high-power RF from a klystron and a compact modulator manufactured by Nissin Electric., Co. However, there is a serious problem of backbombardment. At the IAE, the macropulse length was limited to 3 μs owing to the problem. The temperature rise of the cathode was measured quantitatively, and it was analyzed by particle simulations and heat-transfer calculation [31]. The countermeasures, e.g. external magnetic field and small-size cathode to moderate the heating were explored with some success. Recently, a method to moderate the problem by adjusting the input RF waveform is tried [32], which seems fairly promising. Furthermore, a RF gun with a triode structure is being designed with computer simulations, result of which is also quite hopeful [33].

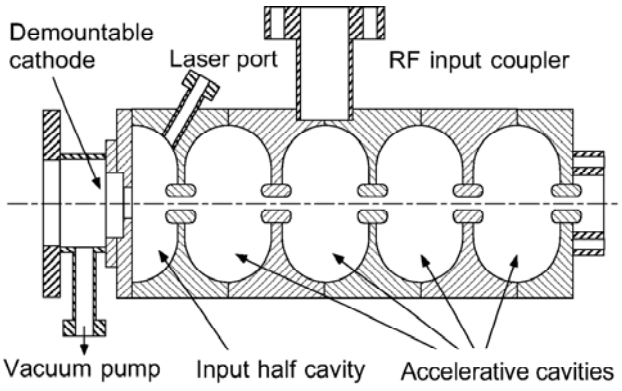

Figure 5 A 4.5-cell RF gun.

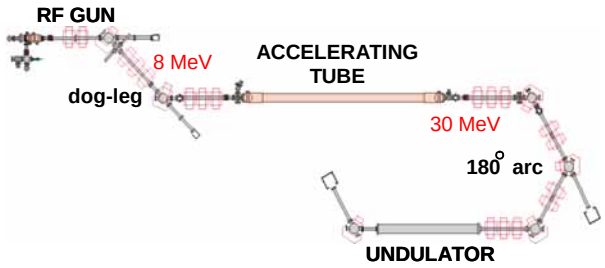

Figure 6 Present KU-FEL system.

On the other hand, a 3-meter accelerator tube was installed after the low-energy beam-transporting system, and electron beam was successfully accelerated up to around 30 MeV. The electron-beam parameters were measured and compared with the results of computer simulations [34].

The above experiments were carried out parasitically at a building of Advanced Research Center for Beam Science belonging to the Institute of Chemical Research. Though the building was a facility with complete ionizing-radiation shielding, there were several other accelerators, and the machine time for each accelerator was limited. Therefore, an old experimental hall, which used to be used for experiments of plasma physics, was renewed with adding shielding walls, which was completed in 2004, and the KU-FEL system was moved to the hall. The installation of the equipments has almost been finished, and the present layout of the system is as shown in Figure 6. The undulator and an optical cavity have been prepared also. The beam test and experiments related to FEL with the new system will be begun soon.

In the mean time, researches on linac and FEL have been conducted in various directions including the future upgrades described before. A method for measurement of electron-beam emittance and phase-space distribution has been developed by exploiting a tomography method [35]. Design of the FEL system and estimation of the FEL gain have been made using the parameters available at present [36]. Concerning the undulator, a compact staggered array undulator which is more economic and easier to manufacture than the conventional undulator was designed and the parameters were optimized [37]. A new superconducting undulator and polarization-variable undulator are being designed also.

In the future, a photocathode RF gun is considered to be used in parallel with the present thermionic one. A numerical simulation was made, and the FEL gain with the system was confirmed to be much higher than that with the present gun [38]. Design of the energy recovery system has been carried out also. A counter-reinjection scheme was found to be quite effective to enhance the efficiency [39].

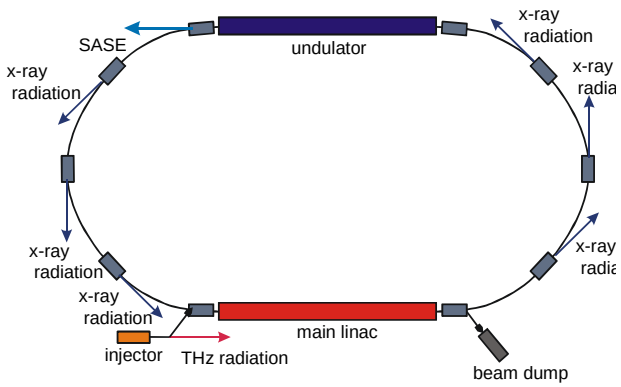

Figure 7 An example of ERL scheme.

ERL BASED SR SOURCES

Although many storage rings are constructed and the SR is supplied to many active users, like SPring-8 in Japan, there are many kinds of beam instability inherent to the storage ring and the peak beam current is low though the average current is high. The ERL SR source is regarded as a competitor of the SASE scheme for the next-generation light sources. An example of the ERL scheme is shown in Figure 7 where ERL FEL and are also included. There are many variations of the ERL scheme.

Energy Recovery Linacs

In the ERL scheme, low-energy electron beam from an injector is accelerated in the main linac and goes through a large-scale beam-transport system and returns back to the main linac in the decelerating phase, and then, it is decelerated to almost the injection energy and goes to the beam dump. In the beam-transport system, many x-ray beam lines and insertion devices are installed.

Table 2 shows the comparison of parameters of 3 types of light sources. The numbers are rough because there are many variations for each type.

Table 2 Parameters of light sources.

	storage rings	ERL (SR)	SASE
energy	2 ~ 8 Gev	1 ~ 10 GeV	1 ~ 15 GeV
micropulse width	30 ~ 100 ps	10 fs ~ 1 ps	10 fs ~ 1 ps
emittance	1 ~ 20 nm (H) 0.1 ~ 1 nm (V)	0.1 ~ 1 nm	0.02 ~ 2 nm
repetition rate	10 ~ 500 Mpps	10 ~ 1000 Mpps	10 ~500 pps
average brilliance	$0.01 \sim 10 \times 10^{20}$ ph/s/0.1%bw/mm^2/mrad^2	$10^{22} \sim 10^{23}$ ph/s/0.1%bw/mm^2/mrad^2	$10^{22} \sim 10^{26}$ ph/s/0.1%bw/mm^2/mrad^2
peak brilliance	$10^{22} \sim 10^{23}$ ph/s/0.1%bw/mm^2/mrad^2	$10^{25} \sim 10^{26}$ ph/s/0.1%bw/mm^2/mrad^2	$10^{33} \sim 10^{34}$ ph/s/0.1%bw/mm^2/mrad^2
no. of beamlines	many	many	1 ~ 10

Table 3 Comparison of light sources.

	storage rings	ERL (SR)	SASE
electron beam	now available	low emittance CSR, HOM, wake very high stability emittance growth at mergers space chare (energy gain)	very low emittance CSR, HOM, wake very high stability
undulators	now available	high precision	very high precision
radiation	now available many beamlines	high av. flux many beamlines	high peak brilliance shot-to shot instability small no. of beamlines competition with X-ray lasers
	SR + FEL compatible	ERL + SASE compatible?	

The electron beam in the case of ERL is always fresh, and there is no problem of beam instabilities inherent to the storage ring. The emittance is lowered as the electron beam is accelerated owing the adiabatic damping. The microbunch width can be quite short as in the case of SASE, which is much shorter than the bunch length of 3rd-generation light sources. The pulse repetition rate can be even higher than that of the storage ring, and it is much higher than that in the SASE. Though the peak brilliance is much lower than that of SASE, average brilliance is comparable. Number of beam lines can be as large as that of the storage ring, while the number is limited in the case of SASE. There is no problem of shot-to-shot instability which is of great problem in the case of SASE, but the stability of the storage ring SR is much superior.

Because of above attractive features of the ERL scheme, there are many proposals of the ERL scheme. The readers can visit the URL of ERL2005 Symposium for detailed description of ERL projects [40]. Examples are; upgrade of the present ring at Cornell University, U. S. A. [41], PEARL project at Brookhaven National Laboratory (BNL), U. S. A. [42], and 4GLS project of Daresbury, U. K. [43]. In Japan, there are proposals of JAEA [44] and KEK [45].

However, there are many difficult problems to be solved. There is no problem of shot-to-shot instability which is of a great problem in the case of SASE, but the stability of the storage ring SR is much superior. The ERL scheme should compete with the present 3rd-generation light source, which is different from the case of SASE. The emittance of the electron beam may be higher than that in the SASE, but it should be at least as low as the vertical emittance in the storage ring.

Many of the difficulties associated with the ERL is similar to those of the SASE, but there are some problems peculiar to the ERL scheme. For example, the merging system from the injector to the main linac is quite difficult to design when the energy gain in the main linac is very high compared to the injection energy. The difference in focussing the beams of quite different energies is also a serious problem.

It should be noted that the ERL scheme has actually been realized at only a few FEL projects.

Multi-Pass Accelerator Recuperators (MARS)

Some of the difficulties described in the previous section may be solved with the multi-pass scheme proposed by the BINP group [46]. It is basically a kind of microtron with energy-recovery. The above problem of merging system is greatly moderated since the ratio of energy gain to the injection energy is relatively small at each stage. The focussing problem is not very serious from the same reason. The main advantages of the MARS over the single-pass ERL are that it can be smaller, the total RF power is smaller, and thus, the building area and cost is lower. There is a paper concerning the comparison in these Proc. [47], and readers can refer to it.

SUMMARY

Concerning the FEL oscillators in shorter-wavelength region, there is a serious problem of optical cavity loss, though the FEL is quite stable and bandwidth is narrow. Also we have to find the attractive application areas around the shortest-wavelength region. On the other hand, IR and FIR FELs are mature, and there are many application areas. The only problem may be diffraction. There is a competition with OPO scheme in the μm region. Both large-scale users' facilities and compact systems are important. THz FEL is quite attractive, but there are many competitors. High-power FELs are and will be based on the ERL scheme.

SASE and ERL SR sources are candidates of next-generation light sources, but there are many difficulties to be overcome. Table 3 compares qualitatively the features of SR from 3rd-generation storage rings, ERLs, and SASE. Though there are many problems in common in the ERL and SASE, there are also peculiar problems of each. However, the author believes that those problems will be solved by continuing efforts of the researchers in the community.

ACKNOWLEDGMENTS

The author collected much information from many slides of many homepages.

REFERENCES

[1] M. Billardon, P. Elleaume, J.M. Ortega, C. Bazin, M. Bergher, M. Velghe, Y. Petroff, D.A.G. Deacon, K. E. Robinson, and J.M.J. Madey: Phys. Rev. Lett. **51** (1983).

[2] I. B. Drobyazko, G. N. Kulipanov, V. N. Litvinenko, I. V. Pinayev, V. M. Popik, I. G. Silvestrov, A. N. Skrinsky, A. S. Sokolov, and N. A. Vinokurov: Proc. SPIE 1133 (1989) 2.

[3] T. Yamazaki, K. Yamada, S. Sugiyama, H. Ohgaki, T. Tomimasu, T. Noguchi,T. Mikado, M. Chiwaki, and R. Suzuki: Nucl. Instrum. & Meth., **A309** (1991) 343.

[4] T. Yamazaki, K. Yamada, N. Sei, H. Ohgaki, S. Sugiyama, T. Mikado, R. Suzuki, T. Noguchi, M. Chiwaki, M. Kawai, M. Yokoyama, S. Hamada, A. Iwata, and S. Nakagawa: *Synchrotron Radiation Facilities in Asia*, (Ionics, Tokyo) (1994) 189.

[5] H. Hama, K. Kimura, M. Hosaka, J. Yamazaki, and T. Kinoshita: *Free Electron Laser and its Application in Asia*, *Proc. AFEL97* (IONICS) (1997) 17.

[6] K. Yamada, T. Yamazaki, T. Shimizu, N. Sei, and T. Mikado: Appl. Opt., **34** (1995) 4261.

[7] K. Yamada, N. Sei, T. Yamazaki, H. Ohgaki, T. Mikado, S. Sugiyama, M. Kawai, and M. Yokoyama: Jpn. J. Appl. Phys., **37** (1998) L1151; T. Yamazaki, K. Yamada, N. Sei, H. Ohgaki, V. S. Sugiyama, R. Suzuki, T. Miklado, M. Chiwaki, T. Ohdaira, and H. Toyokawa: Proceedings of AFEL'99 4th Asian Symposium on Free Electron Lasers and Korea-Russia Joint Seminar on High-Power FELs, Korea Atomic Energy Research Institute, Taejon, Korea (2000) 22.

[8] A. Gatto, J. Heber, N. Kaiser, D. Ristau, S. Günster, J. Kohlhaas, M. Marsi, M. Trovo, and R. P. Walker: Nucl. Instr. & Meth. **A483** (2002) 357.

[9] T. Tomimasu, E. Oshita, S. Okuma, K. Wakita, T. Takii, A. Koga, S. Nishimura, A. Nagai, H. Tongu, K. Wakisaka, Y. Miyauchi, K. Saeki, and A. Kobayashi: Nucl. Instr. & Meth., **A383** (1996) 337.

[10] J. Rossbach, et. al.: Nucl. Instr. & Meth., **A475** (2001) 13.

[11] S. Schreiber: Proc. 27th Intern. Conf. Free Electron Lasers, Stanford, U. S. A. (2005), *to be published.*

[12] http://www-ssrl.slac.stanford.edu/lcls/

[13] A.S.Schwarz: Proc. 26th Intern. Free Electron Laser Conf., Trieste, Italy (2004) 85.

[14] http://www-xfel.spring8.or.jp/Index.htm

[15] H. S. Kang: these Proc.

[16] M. E. Couprie: these Proc.

[17] L. H. Yu: Proc. 26th Intern. Free Electron Laser Conf., Trieste, Italy (2004) 1.

[18] D.A.G. Deacon, L.R. Elias, J.M.J. Madey, G.J. Ramian, H. A. Schwettman, and T.I. Smith: Phys. Rev. Lett., **38** (1977) 892.

[19] E. J. Minehara, M. Sugimoto, M. Sawamura, R. Nagai, N. Kikuzawa, T. Yamanouchi, and N. Nishimori: Nucl. Instr. & Meth., **A429** (1999) 9.

[20] G. R, Neil, S. Benson, G. Biallas, C. L. Bohn, D. Douglas, H. F. Dylla, R. Evans, J. Fugitt, J. Gubeli, R. Hill, K. Jordan, G. Krafft, R. Li, L. Merminga, D. Oepts, P. Piot, J. Preble, M. Shinn, T. Siggins, R. Walker, and B. Yunn: Nucl. Instr. & Meth., **A445** (2000) 192.

[21] E. J. Minehara: Nucl. Instr. & Meth., **A483** (2002) 8.

[22] S. Benson, D. Douglas, K. Beard, C. Behre, G. Biallas, J. Boyce, F. Dilla, R. Evans, A. Grippo, J. Gubeli, D. Hardy, C. Hernandez-Garcia, K. Jordan, L. Merminga, G. R. Neil, J. Preble, T. Siggins, R. Walker, G. P. Williams, B. Yunn, S. Zhang,and H. Toyokawa, Proc. 26th Intern. Free Electron Laser Conf., Trieste, Italy (2004) 229.

[23] N. A. Vinokurov: these Proc.

[24] B. C. Lee, Y. U. Jeong, S. H. Park, Y. G. Lim, and S. Miginsky: Nucl. Instr. & Meth., **A526** (2004) 106.

[25] Y. U. Jeong, H. J. Cha, S. H. Park, B. C. Lee: Proc. 26th Intern. Free Electron Laser Conf., Trieste, Italy (2004) 667; Y. U. Jeong: these Proc.

[26] T. Nakazato, M. Oyamada, N. Niimura, S. Urasawa, O. Konno, A. Kagaya, R. K ato, T. Kamiyama, Y. Torizuka, T. Nanba, Y. Kondo, Y. Shibata, K. Ishi, T. Ohsaka, M. Ikezawa, Phys. Rev. Lett. **63** (1989) 1245.

[27] *e. g.*, M. Takanaka, M. Nakamura, S. Okuda, R. Kato, T. Takahashi and S. Nam: Proc. 23rd Intern. Free Electron Laser Conf.and 8th FEL Users Workshop, Darmstadt, Germany, (2001) II-95.

[28] G. L. Carr, M. C. Martin, W. R. McKinney, K. Jordan, G. R. Neil, and G. P. Williams: Nature, **420** (2002) 153.

[29] T. Yamazaki, H. Ohgaki, K. Masuda, T. Kii, S. Amazaki, T. Horii, H. Toku, and K. Yoshikawa: Proc. 23rd Intern. Free Electron Laser Conf., and 8th FEL Users Workshop. Darumstadt, Germany, M. Brunken, H. Genz, and A. Richter, ed. (2002) II-13.

[30] Y. Yamamoto, T. Inamasu, K. Masuda, M. Sobajima, M. Ohnishi, K. Yoshikawa, H. Toku, and E. Tanabe: Nucl. Instr. & Meth., **A393** (1997) 443.

[31] T. Kii, T. Yamaguchi, R. Ikeda, Z. Dong, K. Masuda, H. Toku, K. Yoshikawa, and T. Yamazaki: Nucl. Instr. & Meth., **A475** (2001) 187; T. Kii, K. Masuda, S. Amazaki, T. Horii, H. Toku, K. Yoshikawa, H. Ohgaki, and T. Yamazaki: *ibid*., **A483** (2002) 310.

[32] T. Kii, K. Hayakawa, K. Masuda, S. Murakami, H. Ohgaki, T. Yamazaki, K. Yoshikawa, and H. Zen: Proc. 26th Intern. Free Electron Laser Conf., Trieste, Italy (2004) 443.

[33] K. Kusukame, T. Fukui, T. Kii, K. Masuda, Y. Nakai, H. Ohgaki, T. Yamazaki, K. Yoshikawa, and H. Zen: Proc. 27th Intern. Conf. Free Electron Lasers, Stanford, U. S. A. (2005), *to be published*.

[34] H. Ohgaki, S. Hayashi, A. Miyasako, T. Takamatsu, K. Masuda, T. Kii, K. Yoshikawa, and T. Yamazaki: Nucl. Instr. & Meth., **A528** (2004) 366.

[35] H. Zen, T. Fukui, T. Kii, K. Kusukame, K. Masuda, Y. Nakai, H. Ohgaki, T. Yamazaki and K. Yoshikawa: Proc. 27th Intern. Conf. Free Electron Lasers, Stanford, U. S. A. (2005), *to be published*.

[36] H. Ohgaki, I. Tometaka, K. Yamane, T. Kii, K. Masuda, K. Yoshikawa, and T. Yamazaki: Nucl. Instr. & Meth., **A507** (2003) 150.
[37] K. Masuda, J. Kitagaki, Z. Dong, T. Kii, T. Yamazaki, and K. Yoshikawa: Nucl. Instr. & Meth., **A475** (2001) 608; J. Kitagaki, K. Masuda, Z. Dong, T. Kii, T. Yamazaki, and K. Yoshikawa: *ibid*., 613.
[38] H. Ohgaki, K. Hayakawa, S. Murakami, H. Zen, T. Kii, K. Masuda, K. Yoshikawa, T. Yamazaki: Proc. 26th Intern. Free Electron Laser Conf., Trieste, Italy (2004) 454.
[39] K. Masuda, S. Matsumura, T. Kii, K. Nagasaki, H. Ohgaki, K. Yoshikawa, and T. Yamazaki: Nucl. Instr. & Meth., **A528** (2004) 134.
[40] http//www.jlab.org/interlab/calendar/archibe04/index.html
[41] http://erl.chess.cornell.edu/
[42] http://nslsweb.nsls.bnl.gov/nsls/org/PEARL/
[43] http://4gls.ac.uk/
[44] R. Hajima: these Proc.
[45] http://pfwww.kek.jp/pf-sympo/21/m04325.pdf
[46] G. N. Kulipanov, A. N. Skrinsky, and N. A. Vinokurov: J. Synchrotron Rad., 5 (1998) 176.
[47] G. N. Kulipanov, A. N. Skrinsky, and N. A. Vinokurov: these Proc.

THE "STABILIZATION OF THE FINAL FOCUS OF THE ILC" PROJECT

D. Urner, P. Coe, A. Reichold, Oxford University, UK

Abstract

We describe techniques to measure and stabilize the relative motion of two objects with respect to each. The position measurements are based on interferometry. Several potential applications at the ILC are studied

IMPORTANCE OF MOTION MEASUREMENT AND STABILIZATION AT THE ILC

Future accelerators in particular the International Linear Collider (ILC) will use nanometre sized beams. At the ILC the luminosity is crucially dependent on keeping the two last focusing elements stable with respect to each other. The StaFF experiment sets out to measure that relative motion at the nanometre level.

Interaction region

The most stringent requirements apply at the interaction region. With a horizontal spread of a few hundred nanometre and a vertical spread of a few nanometres the ILC beam will have a focal point planned to be about 3 orders of magnitude smaller than foci in current state of the art accelerators. This will give rise to new challenges some we can foresee others we cannot. An obvious challenge is that the two final focus quadrupoles have to be mechanically stable with respect to each other at nanometre levels. There are various sources of motion.

Ground motion is very serious as it is irreducible. Ground motion measurements [1] around the world agree that at frequencies above 100 Hz the integrated motion is far below 1nm. The ILC will operate with 5 pulses per second; each containing about 3000 bunches with a spacing of 300ns. The ground motion between bunches should be negligible for the final focus, however at 5 Hz the ground motion could be (depending on the site) in the micrometre region.

Vibrations from pumps and other mechanical sources can be picked up causing additional motions. In principle they can be suppressed by isolation or passive damping of the quadrupoles and/or the vibration source. In this respect it is important to design the quadrupoles such that their resonance frequencies, which would be activated by small residues of external vibrations, lie in a region where the quadrupole is naturally stiff and therefore the vibration amplitudes remain small. This means usually to stride for high frequency resonances.

The relative shift of the two quadruples between pulses has to be measured and taken into account when colliding beams. Fortunately the beam-beam feed-back system [2] should be able to take such motion into account. The idea is to measure the deflection angle of the two spent beams with a strip-line beam position monitor (BPM). This deflection depends on beam shape, bunch distortion and most importantly x and y offsets. The measured information is then used to kick the next bunches towards a better collision point. Simulations have shown that within a few hundred pulses optimal luminosities should be achieved. Very little luminosity should be lost, since wake fields will cause small luminosities in the first few bunches anyway.

A mechanical measurement of the relative position of the two quadrupoles would be very advantageous:

- Simulations of such feed-back systems are often optimistic. Less than perfect signals from the BPM's for example (which incidentally measure the centre of a hard to measure disrupted beam) might cause a slower convergence or possibly even a convergence to a non-optimal point. Both problems are much reduced, if a mechanical measurement of the quadrupoles between pulses is performed, since it allows the beam-beam feed-back system to start its luminosity optimization close to the best solution.
- It has to be expected that quite often there will be gaps in data taking of the order of minutes to hours to fix minor problems. Returning to full luminosity after such short interruptions plays an important role in achieving large integrated luminosities. Larger times between pulses mean larger potential mechanical shifts and a more difficult task for the beam-beam feed-back system. Again a measurement of the accumulated relative quadrupole shift is needed.
- During commissioning one can expect the colliding beams to be significantly distorted. This will cause worse BPM signals degrading the effectiveness of the beam-beam feed-back.
- Our ultimate measure of beam quality is the achieved instantaneous luminosity. It is the job of the beam instrumentation to help to disentangle all the relevant parameters, which lead to the observed luminosity, allowing the operators to find ways to make improvements. During commissioning progress is slowed down by low luminosity (allowing only for very crude pulse to pulse luminosity measurements), which makes the process of disentangling the system difficult. Additional measurements, particularly if measuring a parameter directly and independent of beam quality are of great help. A relative quadrupole position measurement does exactly that, and has the additional advantage, that it can be tested and fully operational before the start of beam operations.

There are two ways to make such a measurement can: with seismic sensors or interferometrically. Seismic sensors are well suited for high frequencies, but are difficult to optimise for frequencies in the 5Hz range and

are not suitable for timescales of minutes or hours. It also is very hard to make them work well in magnetic fields. Furthermore they are bulky (especially low frequency types), and space around the final focus quadrupoles, which are inside the detector is tight.

Laser interferometers do not have these difficulties; however they require one and usually several lines of sight to the measured objects. Fortunately the quadrupoles lie according to today's detector concepts in the region of the instrumented (for muon detection) return yoke. The return yokes consist of vertical mounted iron plates with (usually proportional chambers) between them. Often some of the spaces between the plates are not instrumented and can be used to view the quadrupoles from outside the detector. Another obstacle is the compensating solenoid around the quadrupole, which is usually built in several rings, allowing lines of sight between rings. Attention has to be paid to the integration of final focus optics and detector to allow for the required lines of sight for interferometer access.

The method for correlation of the position of one quadrupole to the other is first to gain the 6-d position knowledge of two platforms outside the detector (straight down below the quadrupoles) relative to the corresponding quadrupole and then measure the shift (6d again) between the platforms.

In principle one could use piezo movers to stabilize the two quadrupoles with respect to each other. This poses several problems. however. Again there is a space issue. Feedback loops with large masses tend to be non-trivial. Feedback loops sometimes introduce a common mode motion (both quadrupoles move together), which would be very undesirable. The idea is to move the beam rather than the magnet and hence allow the fast beam-beam feed-back system to start its optimization close to the optimal point.

If the quadrupoles are superconducting magnets as currently foreseen, the cold mass containing the relevant coils generating the magnetic field are inside a cryostat. This cryostat is the object that can be observed from outside. Motion between the cryostat and the cold mass should be minimized as much as possible by construction, but might have to be monitored as well. Viewing the cold mass directly from outside (using windows in the cryostat) might be optimal, but designing the necessary interferometers is a further challenge. Otherwise the information from the systems, internal and external to the cryostat must be combined.

Other critical magnets in the beam delivery region (BDR)

There are other magnets in the BDR, which have critical positioning tolerances. Beam simulations [3] shifting individual magnets found five magnets with critical tolerances below 200 nm, as shown in figure 1. Motion of these magnets has to be corrected for. Although in principle position shifts can be found with the beam, it is not exactly straightforward. Monitoring the magnet motion and then correcting the position of the magnets with a feed-back loop would be desirable. The motion of each magnet with respect to the next one can be measured and stabilized using interferometers of the type discussed below. Everything can be anchored to the final focus magnet, e.g. the critical magnets of the BDR would follow the motion of the final focus quadrupole.

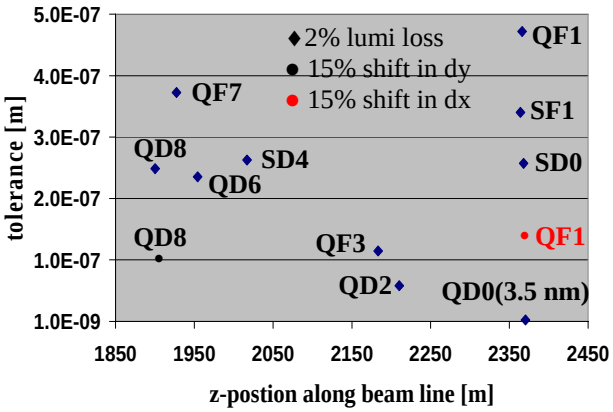

Figure 1: position tolerances of critical BDR magnets.

The upstream energy chicane is another application where laser interferometry is well suited. The current idea of the upstream energy chicane is a 4-magnet chicane as shown in fig. 2. There are two types of measurements required. One for the travel of the central BPM. The other to relate the horizontal position of the central BPM to the position of the BPMs on the left and right sides. The first task needs a distance meter with a few tens of nanometres resolution and a dynamic (travel) range of about 10mm. The second task uses straightness monitors measuring the position of an object perpendicular to its line of sight. We need to measure horizontal motion of the central BPM with respect to the side BPM's with a few tens of nanometres resolution, over a distance of roughly 25m.

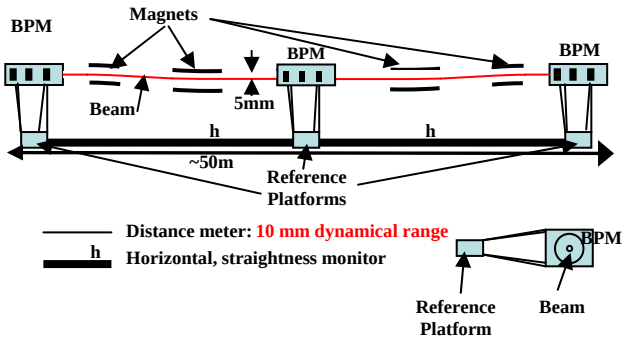

Figure 2: Upstream spectrometer layout. Above: top view. Below right: view along beam axis.

In most applications one can expect to have to measure relative motion of two objects that do not have direct line of sight between them. One has to project out first using distance meters to establish all 6 degrees of freedom of the position of a platform for each object and then using a

straightness monitor to correlate the position of the platforms.

THE DISTANCE METER

The Oxford group plans to develop and build in a first step a distance meter and as a second step a straightness monitor based on interferometers with nanometre resolution. We will concentrate on the distance meter in this paper, and how several distance meters can be employed as a network to effectively build a straightness monitor.

Concept of distance meter

A distance meter that can perform the functions as described in the section above has to be compact, has to be able to measure a relative position with at least 1000Hz. It has to be fairly cheap or at least scale well if larger numbers are built. It has to have a relative distance resolution of 1 nm between two objects that are 10m apart. To gain 6d position information (such as projecting the coordinates of a magnet out to a platform) one can use a network of distance meters. In order to determine the network geometry absolute distance measurements are required.

For our distance meter we chose a wavelength in the infrared around 1500nm. This wavelength is used in telecom applications, resulting in cheap availability of commercial components. It also allows us to share equipment with the LiCAS[4] experiment.

Figure 3 depicts a schematic drawing of how our distance meter prototype operates. Laser light is launched from a fibre and collimated by a lens. It is reflected from a retro reflector mounted on the target object. The collimation is deliberately made slightly imperfect, so that the returning light can be picked up by several optical fibres mounted close to the launch fibre. This we call the long arm. The light of the short arm is reflected at the farther end of the collimating lens (uncoated glass to air boundaries will reflect about 3-4%). The curvature of the lens has to be chosen in such a way that all the reflected light ends up in a target area around the launch fibre in which the return fibres are placed. The reflection of the nearer side of the collimating lens (left side in fig. 3) is unwanted. The glass curvature is such that only a small fraction of the reflected light is focused back to the fibre area. Furthermore antireflective coating of this side of the lens reduces the reflected light by at least two orders of magnitude. For the first prototype we did not pay enough attention to the short arm and ended up, despite antireflective coating, with similar amounts of light coupled back into the return fibres from each side of the collimating lens. Nevertheless clear interference patterns have been observed. A new prototype is under construction. A nice advantage of this setup is, that light of both arms pass through the lens and therefore, to first order, through the same material, minimizing the temperature dependence of the interferometer.

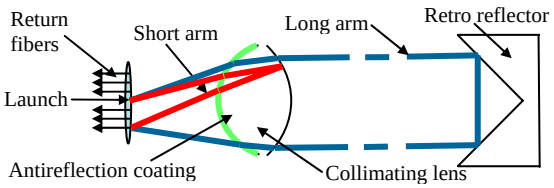

Figure 3: Concept of distance meter.

Measurement with 1nm relative resolution

We also call this the Michelson mode of our interferometer (although our interferometer has unbalanced arm lengths). Phase differences between coherent light passing through long and short arms, generate sinusoidal fringe patterns. Each return line will enable us to measure this pattern at a slightly different length difference. Hence each return line will record a different phase in the interference pattern as displayed in fig. 4a). The light intensity observed by each fibre is recorded using a photo-diode, and appropriate amplification and digitization. Length changes of the distance meter (e.g. changes of the length difference between short and long arm) will move the sampling position of each return fibre along the sinusoidal interference pattern.

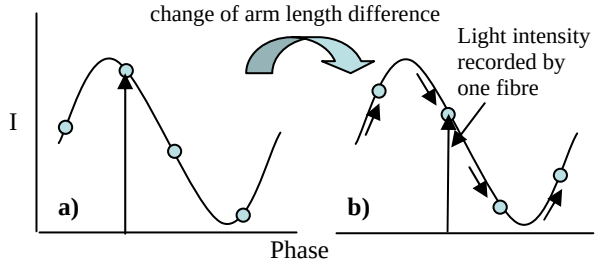

Figure 4: a) Interference pattern is recorded at four points using four readout fibres. b) A change in distance meter length will move the interference pattern changing the light intensity recorded at each point.

To reconstruct a sinusoidal function one needs at least four measurements with a established phase-spacing of 90°. Our setup will result, however, in basically random phase angles for individual returns. We are using a fibre head containing 12 fibres, and hence can chose six return lines (out of 11 possible lines) that have a nearly identical spacing of about 60°. We still have to know the phase difference between the individual return lines, which can be measured with FSI, see next section. To achieve 1nm resolution we have to measure phase shifts of 0.07% of 2π. We are planning to use the electronics developed for the LiCAS experiment, which allows for sampling rates up to 2.1MHz. We therefore easily get the statistical precision needed for measurements at 1kHz. This system will also be able to track motions of the target of up to about a meter per second.

Measurement with 1 μm Absolute Resolution (FSI).

The absolute distance will be measured using the frequency scanning interferometry technique[8]. Here only one return line is needed. For each distance measurement the laser is tuned over a large frequency range (we plan to use 1530-1560 nm) at a constant tuning speed. The detected phase for an optical path length difference between long and short arm of L and laser frequency ν is

$$\Phi = \left(\frac{2\pi}{c}\right)\nu L + \Phi_0 . \qquad (1)$$

Changing the laser frequency will generate a sequence of fringes that has to be recorded with at least four samples per fringe. The extraction of absolute distances by FSI is based on a reference interferometer with known optical path length difference R. The laser light has to be split, and the two interferometers have to be read out simultaneously. The absolute length then can be extracted from the measurement of the change in the phase ratio q:

$$q = \frac{\Delta\Phi}{\Delta\Phi_R} = \frac{L}{R} \text{ with } \Phi_R \text{ the reference phase} \qquad (2)$$

In practice reflections from other surfaces can contribute additional fringe patterns. Such additional reflections must be kept very small otherwise the Michelson mode measurement precision will be systematically. A fast Fourier transformation of the measured FSI pattern allows us to observe all fringe frequencies (corresponding to all length differences) picked up by the interferometer, as well as their strength. This will allow us to identify and eliminate unwanted reflective surfaces.

Taking a series of FSI measurements with all return lines will allow us to measure the phase shift between the different fibres. This information is needed to gain the correct phase information from our Michelson type measurement, see previous chapter.

Systematic Limits of Measurements

There are several systematic problems to be overcome if we want to achieve the stated goals. We should worry about constant tuning speed (FSI), laser frequency instabilities (Michelson), refraction effects from air, and much more. The reference interferometer is not only useful as an absolute length standard, but can also remove or at least reduce some of the systematic effects that would limit our measurement accuracy. The important feature is that it is made from materials, which expand very little with temperature. Furthermore several different materials can be combined in such a way that the active elements on each side of the interferometer behave as if one would have used a single material with a temperature coefficient of zero.

For FSI we had assumed constant frequency tuning speed, which is unfortunately not the case with current lasers. The dominant changes of the fringe frequency result from changes in the laser tuning speed. This effect can be seen in fig. 5a). Hence one can measure the change in tuning speed and correct the data of all the other interferometers accordingly. If applied to the data of the reference interferometer itself one then would expect after a Fourier transform ideally a delta function. Figure 5b) shows the Fourier spectrum of a simple reference interferometer. This picture contains several pieces of information. The area under the peak is proportional to the combined light return of the two arms. The side lopes and the peak width are artefacts from the limited (tuning range) number of fringes that are used in the Fourier transform. The background is very flat indicating that there is very little reflection from other surfaces.

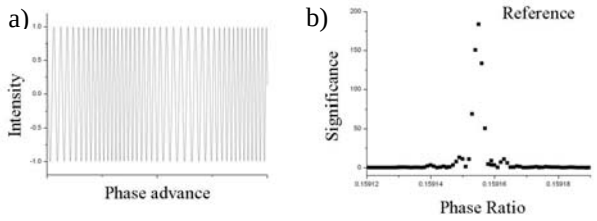

Figure 5a: beat frequency of reference interferometer. A faster tuning speed in the right centre of the plot is clearly visible. 5b: Fourier spectrum of reference interferometer data after correcting for tuning speed.

If we run our instrument in Michelson mode, we need a very stable laser frequency in the order of a few tens of kilohertz, since a frequency shift can not be distinguished from a change in distance. The best results would be obtained if we could lock the laser with a feedback loop to an absorption line. Unfortunately that is quite difficult, since there are no strong absorption lines in the 1500nm region. It can be done by frequency doubling and locking against the Rb D_1 line. An alternative solution is to equip the reference interferometer also with a multi-fibre launch head. We can then extract the frequency shifts of the laser, assuming the path length difference of the reference is stable enough over relevant time scales (seconds to minutes).

The time to take one length measurement in FSI mode is non-negligible. The observed path length difference can change enough in this time span to cause a systematically wrong FSI result. The problem is that even small changes in length are amplified due to the fact that we are only scanning over a relatively small frequency range. A fast tuning speed (about 20-40 nm/s) will reduce the problem. This requires electronics which can cope with high data rates.

Measurements with nanometre resolutions at distances of order a metre cannot be made in air, because of refraction effects. Hence we have to build a vacuum system. If one tries to establish the (relative) position of

an object to 1nm, it is not a good idea to introduce mechanical activation frequencies through the vacuum system. A single vacuum bellow can be used to decouple the vacuum system from the object; however, it will produce a 100kPa force on the object, which again is not desirable. Hence we needed to design a force-free mount using a double bellow system. Figure 6 shows the drawing of a test setup, which can measure the residual forces. We are trying to establish the force if the object is moved away from the nominal position, as it is aligned in the beamline for example.

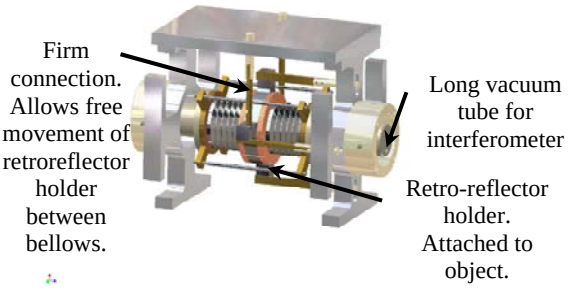

Figure 6: Test setup to measure residual force of a force-free mount system.

STAFF AT ATF (KEK)

A network of distance meters will be employed at the ATF test facility at KEK: to act as a straightness monitor, to measure the relative motion and eventually to stabilize the two existing nano-BPM [6] setups with respect to each other. Figure 7 shows schematically the proposed experiment. The two nano-BPM setups have enough redundancy to get a separate measurement of their relative position using the beam and therefore to cross-check both the StaFF measurement and validate the stabilization scheme. It will also allow us to test the behaviour of the distance meter in an accelerator environment.

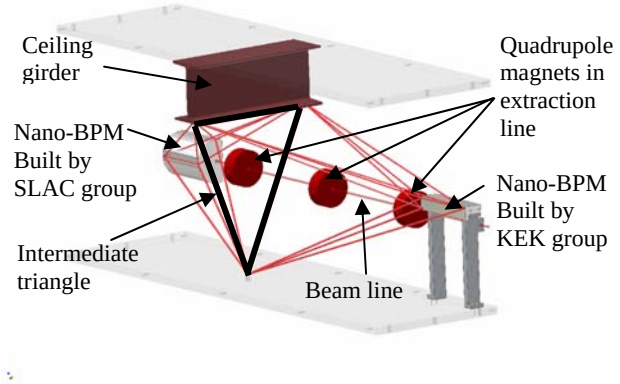

Figure 7: Planned setup of distance meter network at ATF (KEK, Japan).

Both nano-BPM setups consist of 3 individual BPMs. We will not directly measure the position of each one, but instead relate the SLAC reference frame to the KEK reference frame. The two groups have found very different solutions on how to reference the position of their individual BPMs, see fig. 8 The KEK group has built a large aluminium bar above the BPMs and anchored everything very firmly to the ground. (The ATF floor consists of 1m thick concrete slabs under the damping ring and extraction line. The position of the individual BPMs are related to the aluminium bar with a 1-d Michelson interferometer. The SLAC setup will have two frames. The inner frame built from steel is optimized to be mechanically rigid. The BPMs are mounted on this frame and can be repositioned with hexapod movers and the whole frame can be moved by steppier motors mounted in the frame legs. An outer carbon fibre frame is optimized to be thermally stable. From this frame small tubes protrude inwards almost touching the BPMs. Attached to the end of these tubes are commercial 2-dimensional interferometers. They use a grid scanning technique to relate the position of the thermal frame to the position of the BPMs.

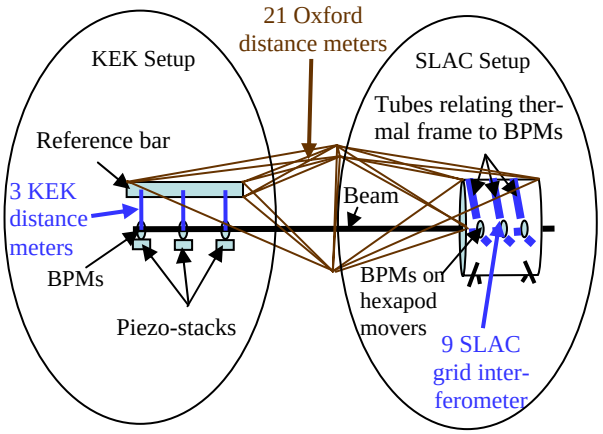

Figure 8: Schematic setup of BPMs and measurement devices.

Simulation of network.

We have simulated the behaviour of this network using the opto-geometric simulation package Simulgeo[7]. The basic idea is to constrain the 6d position of an intermediate triangle with respect to 3 nodes attached to the SLAC-BPM carbon fibre frame using 9 distance meters. Figure 9 shows the two BPMs with superimposed lines representing the distance meter vacuum system.

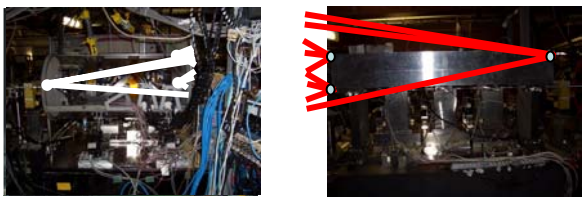

Figure 9 left: SLAC-BPM setup, right: KEK BPM setup.

We are interested mainly in the vertical displacement of the KEK-BPM with respect to the SLAC-BPM. Therefore

the intermediate triangle should be as tall as possible and hence we plan to mount one corner node on the floor and two corner nodes on the ceiling girder, see fig. 7. The geometry of the intermediate triangle is also determined by 3 internal distance meters, nine further distance meters are used to then relate the position of the KEK-BPM to the intermediate triangle. All distance meter launch heads are packaged into the 3 corner nodes of the triangle. We will use the force free mount discussed in the chapter above to attach one retro-reflector to each of the 3 measuring nodes of the BPM (in total 6 retro-reflectors for the two BPMs). The retro-reflectors need large angle coverage (about 90°) to reflect the light from all distance meter converging on them.

The simulation finds that we should be able to measure vertical shifts with a resolution of about 20nm, assuming a distance meter resolution of 1nm. It is important to pay attention to detail however. The distance meters in the corners of the triangle will not measure from a common point. In practice the distance meter launch heads will be mounted on a platform that can experience angular motion. These triangle nodes are quite complex, since each will contain 7 launch heads and one retro reflector. A motion of a few micro radians can limit the achievable resolution. It is important, therefore to minimize the distance between the optical launch points of the distance meters. The situation at the BPMs is much less critical, because of the use of a single retro-reflector for each node.

Stabilization

We intend to stabilize the KEK BPMs with respect to the SLAC BPMs. We assume that the SLAC BPMs, which are mounted very rigidly, are moving with respect to each other at a rate below our measurement resolution. The KEK BPMs are individually mounted on piezo stacks and can be moved very swiftly over small distances. We are planning to use these existing piezo movers to test our stabilization schemes. We will have to integrate three measurements: the commercial interferometers relating the SLAC BPMs to the thermal frame, our straightness monitor built from distance meters relating the SLAC thermal frame to the KEK aluminium bar and the Michelson interferometer information relating the KEK aluminium bar to the KEK BPMs. All this information has to be recorded, combined and finally a signal has to be generated that can move the KEK piezo stacks cancelling the relative vertical motion of the two BPM sets at a rate of several hundred Hertz. The movers on the SLAC system will only be used to correct large angles if motion is needed beyond the travel range of the KEK piezo stacks. For a system with so many measurements, controls and probably resonances classical feedback control based, on transfer functions, is difficult to apply and suffers from poor performance. More effective, complicated schemes are very hard to tune. Keeping the feedback systems separate is not an option, because the systems interact making tuning even harder. The situation can be improved by including the fact that we can measure resonance frequencies of the system separately, we can measure what effects actuators have on the system and we can gain knowledge about relevant disturbances. The state vector model, which is a rigorous theory, is available and more details can be found in [8]. The difficulty in practice is to find a good model for the control system.

SUMMARY

Distance monitoring at nanometre scales can be a powerful tool at several places in the beam delivery system of the ILC. We need distance meter and straightness monitors with nm resolution over 10m distances. This is a formidable challenge. We plan to build such distance meters with a fairly simple fibre coupled interferometer.

We investigate the possibility of active magnet stabilization, which would be great to have for example for critical magnets in the beamline outside the detector.

These interferometers are also an excellent tool to monitor the position of the BPM's for the upstream energy spectrometer.

REFERENCES

[1] See for example Y. Nakayama et al. "Characteristics of ground motion at KEK and Spring-8", Proceedings of EPAC 2004, Lucerne, Switzerland. V. Shiltsev, "Introduction to Ground Motion Issues in Linear Colliders", Fermilab-FN-0717, March 2002.

[2] G. White, "Feedback on nano-second timescales: Fast feedback simulations", Proceeding of the 2003 Particle Accelerator Conference, http://www.jacow.org.

[3] Private communication with J. Jones CCLRC.

[4] P. Baker et al., "Measurements of the LiCAS System", IWA A2004, CERN, Geneva 2004.

[5] J. Thiel et al., "Interferometric measurement of absolute distances of up to 40 m", Measurement 16 (1995) 1-6.

[6] M. Ross, "NanoBPM work at ATF (overview)", http://www-project.slac.stanford.edu/lc/local/nanoBPM/nanoBPM.htm

[7] Simulgeo package developed for CMS muon detector, CMS note 1998/079.

[8] T. Mattison, "Optical Interferometer Vibration Control", 2005 ILC physics and detector workshop, Snowmass, 2005, http://alcpg2005.colorado.edu:8080/alcpg2005/program/accelerator/WG4/aug24_mattison-opto-anchor.pdf

ELECTRON MICROSCOPE AS A NANO-BEAM ANALYZER

S. Isoda and H. Kurata
Institute for Chemical Research, Kyoto University, Kyoto 611-0011, Japan

Abstract

Electron microscope has already 70 years history since its invention by Ruska in 1931, and many family members have been created during the history. In particular, big efforts for improving its resolution have been continued by optimizing its optical system, using high voltage acceleration, correcting the spherical aberration, or utilizing a new microscopy like scanning transmission electron microscopy. Addition to the high resolution interests, recent researchers interests are focusing on the point analysis such as elemental and electronic states analyses at atomic scale. These efforts are reviewed in this report from our experiences accumulated in Kyoto University, and the present and future prospects are described.

INTRODUCTION

Since E. Ruska and M. Knoll have invented a transmission electron microscope (TEM) with electro-magnetic type lenses [1], TEM has developed in the past seventy years and is widely used for studying natural science because of such great advantages as high resolution and microanalysis, in particular in the field of nano-science and nano-technology currently. During those days, TEM brought various electron microscopes into being, such as reflection electron microscopy, low-energy electron microscopy, Lorentz microscopy, electron holography method, scanning electron microscopy, scanning transmission electron microscopy (STEM), scanning reflection electron microscopy, scanning Auger electron microscopy and so on [2]. However, as for the spatial resolution, TEM is superior among these microscopes and the resolution has certainly developed as shown in Fig.1. In particular, big efforts were devoted to high voltage TEMs because of their merit in short wavelength.

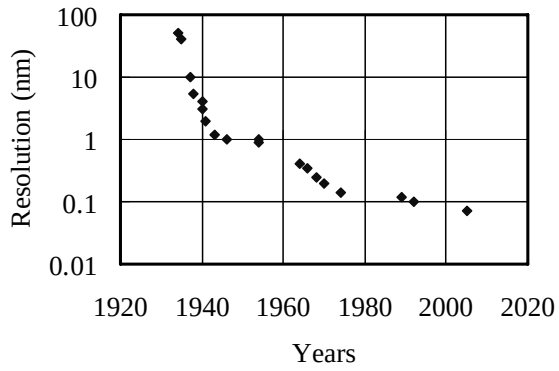

Figure 1: Development in resolution

HIGH VOLTAGE TEM

We started to build high voltage TEMs since 1957 in Kyoto University and reached now to 0.12 nm resolution with a 1000 kV TEM [3]. In this long course, we understood the importance of mechanical and electronic stabilities of the machines and overcame them successfully by using specially designed vibration-isolation systems, and high voltage and lens current controlling systems. For example, high resolution TEM image of phthlocyanine molecular crystals was firstly demonstrated by Menter in 1958 [4], later by Uyeda et al. in 1970 [5] and recently by Kobayashi et al. [6]. The images show clearly the development in resolution.

High Voltage electron microscopes were developed so as to minimize the image deterioration due to the spherical aberration which is the most important aberration in TEM imaging. However, recently, many studies to correct the spherical aberration have been done; by image processing from many images taken at different defocuses, by using thin lens or concave lens, and by adopting hexapole lens system. Among them, the hexapole lens corrector is the most promising one [7], and by utilizing this system the resolution reaches now to 0.07nm (70pm) in STEM as describe later.

ELELCTRON ENERGY-LOSS SPECTROSCOPY AND IMAGING

Recent trend of electron microscopy is strongly on nano-scale analysis of elements and electronic states instead of direct structural analysis [8]. Cathode luminescence, X-ray, Auger electron and inelastically forward scattered electron can be used as signals to analyse the local states being irradiated with incident electron beam. Among them, electron energy-loss spectroscopy (EELS) is an excellent tool to study elemental and electronic state distributions at high resolution [9]. Fig.2 shows schematically EELS measurement and its imaging, where incident electron beam is scattered elastically or inelastically with a specimen, and a magnified image is formed mainly by the elastically scattered electrons on the screen (the position a). On the other hand, the inelastically scattered electrons form a spectrum on a slit with a magnetic energy analyzer (the position b). In this case, by using an aperture, an area giving the EELS can be selected. From the spectrum, one can know inelastic events happened as single electron excitations or collective excitations, which gives us information on elements and electronic band structure of specimens. Furthermore one can observe a distribution of

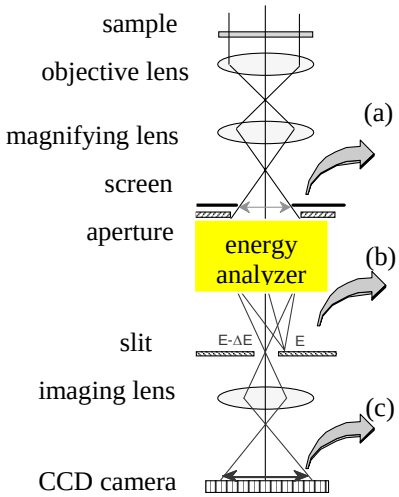

Figure 2: Illustration of EELS and its imaging system; (a) conventional imaging, (b) EELS spectrum and (c) its imaging.

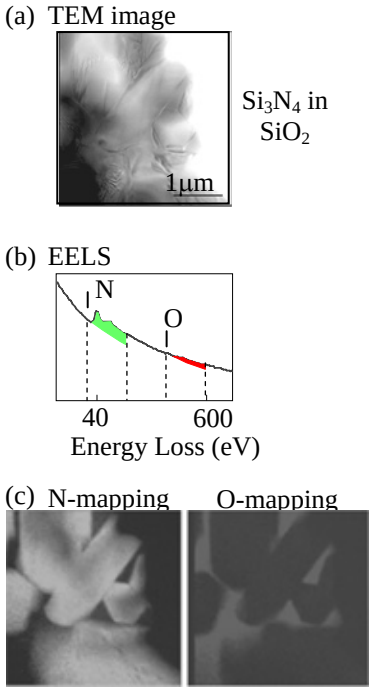

Figure 3: (a) Conventional TEM imaging, (b) EELS spectrum and (c) its imaging on distributions of N and O in Si_3N_4 in SiO_2.

these inelastic events, when electrons specified in its energy are passed with a slit and then magnified again (the position c). The respective observations are shown in Fig.3 in the case of Si_3N_4 in SiO_2. The image in (a) is a conventional TEM image, the spectrum in (b) is the EELS indicating absorption edges of K-shell excitations of N and O for example, and EELS images in (c) (often called energy-filtered images: EF-imaging) showing spatial distributions of N and O in the sample. In such a way, one can observe spatial distribution of each element separately.

Furthermore differences in chemical bonding of an element can be imaged (chemical mapping) when one uses a narrow energy slit to select a part of near edge structure just above an absorption edge [10]. The electron-energy-loss near-edge structure (ELNES) from an inner-shell excitation corresponds to the unoccupied partial density of states near the bottom of conduction band (or LUMOs), which reflects surely the chemical bonding.

The 1000kV TEM in Kyoto University was constructed to be able to observe these EELS and EF-imaging, so that the machine was named as high resolution electron spectromicroscope [3]. The TEM is the first one to fulfill both high resolution investigation and spectroscopic study as a high voltage transmission electron microscope [11].

ANOTHER IMPROVEMENT IN RESOLUTION

As shown in Fig.1, the initial improvement in resolution has been achieved by optimizing optical system in electron microscopes from 1930 to 1960, and later HV-TEMs contributed largely in the progress around 1990. However, microscopists have still a problem of spherical aberration which is the main factor to deteriorate the spatial resolution. There have been many efforts to overcome the barrier by using image processing, thin lens, concave lens and so on. Recently aberration correction method with a hexapole lens system has been proposed as a most practically one [7], in which the spherical

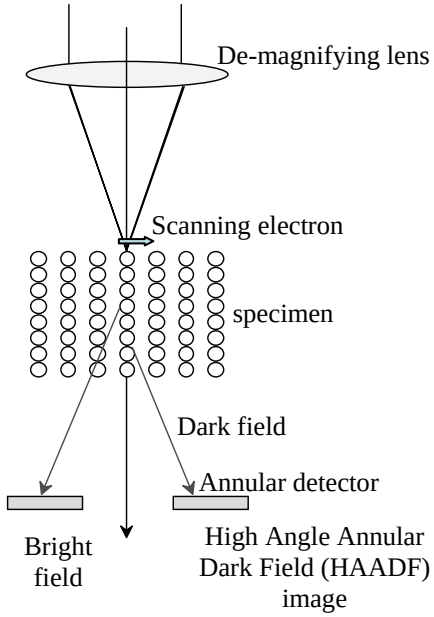

Figure 4: Schematic illustration of STEM. Electron beam is focused on a specimen, and scattered electrons are detected at central forward or at outer beam (scattered at high angles). In particular a high angle annular detector provides us a dark-field image (HAADF) at high resolution because of the incoherent scattering by phonon.

aberration can be corrected down to μm-order from mm-order in conventional EM [12].

In addition to these efforts, another microscope, that is scanning transmission electron microscope (STEM), came into existence. In particular, high angle annular dark field (HAADF) imaging is an excellent candidate for getting higher resolution, because the image is formed by incoherent phonon scattering under scanning a fine beam on a specimen as schematically illustrated in Fig.4 [8]. Consequently the resolution of image is determined only by the electron probe size. The image contrast is originated according to the atomic number, Z. However, a lens is used to de-magnify the electron beam for forming a fine probe, so that the spherical aberration is still a large problem for realizing finer beam. Therefore, a hexapole spherical aberration corrector has been successively incorporated in STEM for forming a finer beam as small as 0.07nm [13].

POINT ANALYSIS

As already mentioned, STEM is a tool not only to get high resolution images but also to obtain information on elemental and electronic states at atomic scale. Usually in STEM, an atomic scale probe is scanned over a sample surface. There are three signals for imaging; (i) directly transmitted electrons (Bright field imaging), (ii) diffracted electrons (Dark filed imaging) and (iii) scattered electron at high angle (HAADF imaging). When the incident beam is positioned at a certain point on a specimen and the directly transmitted beam is analyzed with an EELS analyzer for example, one can determine elemental and electronic states at the point by getting absorption energy values, integrated absorption intensities and fine spectral features near the absorption edges (ELNES). Fig.5 shows HAADF, Ti-map and Si map in a multilayer of Al_2O_3/TiO_2 on Si substrate. When the beam is located at a point in Si substrate, then the Si $L_{2,3}$-ELNES exhibits well that of the pure Si. Instead, the beam is located at a interfacial layer between the Si and the first Al_2O_3 layers, another ELNES is observed similarly to that of SiO_2. In such a way, the point analysis becomes very important in addition to imaging.

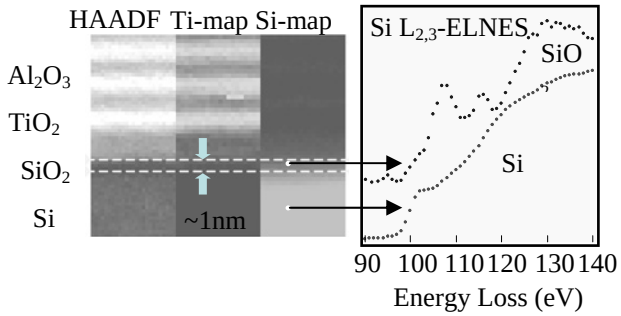

Figure 5: The left; HAADF, Ti-map and Si map in a multilayer of Al_2O_3/TiO_2 on Si substrate. The right; Si $L_{2,3}$-ELNES obtained from the two points in the left images.

ELELCTRON SOURCE

Most interesting point in STEM is to realize a real point analysis by probing a certain interesting area of the beam size. Then nano-meter or even pico-meter beam size becomes crucial in imaging and analysis in STEM, and at the same time a bright electron beam source is looked to for quick and accurate analysis.

W-wire, LaB_6-tip and field-emission gun (FEG) were normally used for the source of electron beam, and FEG is now a day frequently used as a bright and highly coherent electron source. In our group, much finer FEG is tried to fabricate for the source, where the single crystalline W-wire is prepared by thermal field treatment (Fig.6). The thermal field treatment is carried out by (i) high temperature flashing, (ii) treatment at negative voltage and (iii) treatment at positive voltage. The process can be described by surface atoms diffusion under electric gradient. When the treatment is correctly performed, then the tip of W-wire turns into a very sharp one, almost atomically sharp, and the emitted beam becomes very sharp as shown in Fig.7. In this figure, (a) shows a emission pattern from a normal tip and a widely spread emission is observed around at a center. On the other hand, (b) shows a emission pattern from a nano-tip where the emission is strictly centered a probe hole and major emission pass through the hole. The nano-tip was installed in a conventional TEM to test its performance.

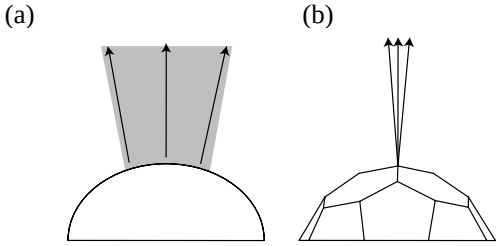

Figure 6: (a) Normal field emission gun, and (b) nano-tip gun.

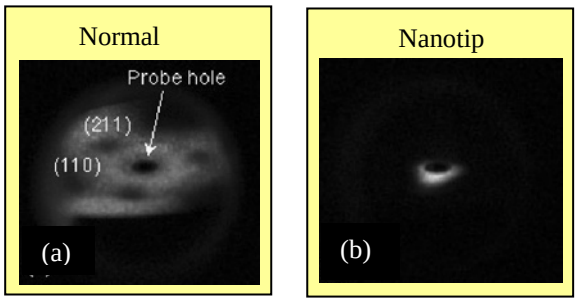

Figure 7: (a) Normal emission pattern, and (b) Nanotip pattern.

CONCLUDING REMARKS

As described above, the electron microscopes have been developed in imaging and analysis. However, it is still awaited many further developments as dedicated analytical tools. The near future prospects are the follows. Brighter and coherent electron source, higher resolution measurements, atomic scale resolution of tomography, down sizing of machines, mechanical stabilization with rigid body, and ultra fast measurements. These issues will come true soon.

REFERENCES

[1] M. Knoll and E. Ruska, Z.Phys., 78 (1932) 318.
[2] S. Amelinckx, D. van Dyck, J. van Landuyt and G. van Tendeloo, “Handbook of Microscopy”, VCH, 1997
[3] S. Isoda, S. Moriguchi, H. Kurata, T. Kobayashi and N. Uyeda; Ultramicroscopy, 39 (1991) 247.
[4] J. W.menter, Proc.Poy.Soc., A236 (1956) 119.
[5] N. Uyeda, T. Kobayashi, K. Ishizuka and Y. Fujiyoshi, Chemica Scripta, 14 (1978/79) 47.
[6] T. Kobayashi, S. Moriguchi, H. Kurata, T. Ogawa and S. Isoda; Bull.Inst.Chem.Res.,Kyoto Univ., 70 (1993) 451-461; *ibid*.,70 (1993) 462.
[7] M. Haider, U. G. Braunsha and E. Schwan, Optik, 99 (1995) 167.
[8] D. B. Williams and C. B. Carter, “Transmission Electron Microscopy”, Plenum Press, 1996.
[9] R. F. Egerton, “Electron Energy-Loss Spectroscopy in the Electron Microscope”, Plenum Press, 1996.
[10] H.Kurata, S.Isoda and T.Kobayashi; J.Electron Microsco., 45 (1996) 317.
[11] H. Kurata, S. Isoda and T. Kobayashi; Microsco. Microanaly. Microstruct., 6 (1995) 405; H. Kurata, S. Moriguchi, S. Isoda and T. Kobayashi, J.Elec.Micro., 45 (1995) 79.
[12] F. Hosokawa, T. Tomita, M. Naruse, et al., J. Elec. Micro., 52 (2003) 3.
[13] P. D. Nellist, M. F. Chisholm, N. Dellby, O. L. Krivanek, M. F. Murott, Z. S. Szilagyi, A. R. Lupini, A. Borisevich, W. H. Sides Jr., and S. J. Pennycook, Science, 1741 (2004) 305.

TeV —The Dream Energy Scale—*

Hitoshi Murayama
Department of Physics, University of California, Berkeley, CA 94720, USA
Theoretical Physics Group, Lawrence Berkeley National Laboratory, Berkeley, CA 94720, USA

Abstract

In this talk, I'd like to explain why the TeV, 1,000,000,000,00 electron volt, is a particularly interesting energy scale in physics. I being recapitulating what particle physics is all about, citing two big questions: what the Universe is made of, and Einstein's dream of unification. TeV energy appears to be relevant to both questions, suggesting rich and complex physics at this energy. I outline how two facilities, LHC and ILC, will work together with reveal what is going on at this exciting energy scale.

RECAP OF PARTICLE PHYSICS

I'd like to first recapitulate what Particle physics is all about.

When we look up the sky and think about the universe, our eyes get attracted to stars and galaxies. However, we particle physicists are a strange folk; we are interested in things we don't see.

With the advent of precision cosmology, we now have a detailed accounting of the energy budget of the universe with unprecidented certainty. What please our eyes in the night sky, stars, make up only about 0.5% of the energy budget of the universe. We don't see the remaining 99.5% of the universe; that is what we would like to understand.

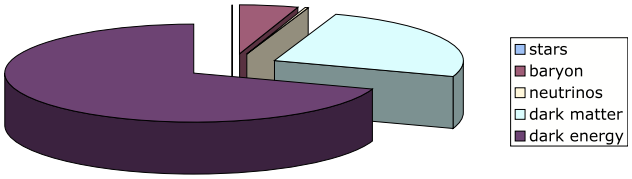

Figure 1: The energy budget of the universe, shown in a pie chart.

For many decades, we thought the neutrinos do not have mass and contribute negligibly to the energy budget; with the recent discovery that they have tiny but finite mass, they contribute somewhere between 0.1 and 1.5% of the total energy. We don't exactly know the number because we don't know their absolute masses very well. It would be very interesting to know it precisely because it affects the way the galaxies formed. It is amusing that neutrinos, ghostly elementary particles, contribute as much as all stars in the universe. We used to think that much of the universe is made of the same stuff we are made of, namely ordinary atoms composed of electrons, protons, and neutrons. However, all the atoms in the universe make up only 4.4%.

The next bigger piece of the pie is *Dark Matter*, that contributes 23% of the total energy budget of the universe. We don't know what it is. The next and the largest piece is *Dark Energy*, which gives 73%. We don't know what it is. Not only they are components which we don't know, there is also a puzzle about a component we know but doesn't appear to be there: anti-matter. When the universe started with the Big Bang, it created as much anti-matter as matter. Where did they go? Finally, there is another component which I call *Dark Field*, which permeates the universe and slows down all elementary matter particles we know from the light speed. If we estimate how much it contributes to the overall energy budget, it comes out to be 10^{62}%; clearly we are missing something here.

To understand what the universe is made of is one of the big goals of particle physics.

Another driving force behind particle physics is what some people call "Einstein's Dream." Albert Einstein asked a very simple question: is there an underlying simplicity behind vast variety of phenomena in Nature? To answer this question, he dreamed to come up with a unified description of all phenomena in the universe. It is well known that he tried to come up with such a "unified field theory," in which he tried to describe electromagnetism and his theory of gravity (general relativity) on one shot, but he failed.

Unification is actually not an exotic idea, but rather a theme that goes through the history of physics. Newton unified apples and planets. It was a revolutionary thinking back then that ordinary objects such as apples and heavenly bodies such as planets follow the same laws: a true unification. Out of this unification came the inverse-squared law of gravity and Newton's law of mechanics. Next big unification in physics is well known. Maxwell unified the theories of electricity and magnetism into a single theory of electromagnetism: Maxwell's equations. At the time of Einstein, people were studying new phenomena in atomic physics, that eventually led to the discovery of quantum mechanics. There were also scattered phenomena in nuclear physics such as α, β, and γ rays.

Einstein *reconciled* electromagnetism and mechanics in his special theory of relativity. I wouldn't say it was a unification because the special relativity does not *include* electromagnetism. He made them consistent with each other, but the theory itself does not include both. He then unified the relativity and gravity in his general theory of relativity. This theory is another true unification as it includes both gravity and mechanics in a single theory in an essen-

*This work was supported in part by the DOE under contracts DE-FG02-90ER40542 and DE-AC03-76SF00098 and in part by NSF grant PHY-0098840.

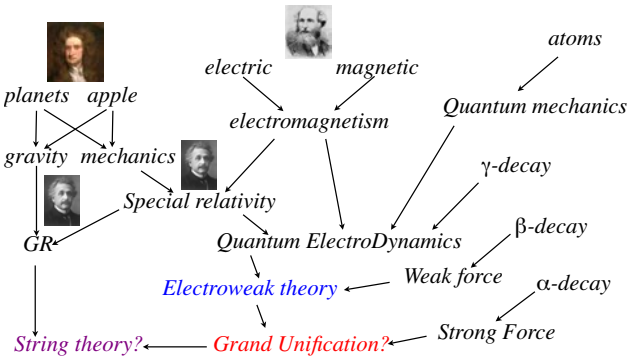

Figure 2: A brief history of unification in physics.

tial way. However, he could not achieve any further levels of unification.

Since then, there was a unification in a theory called Quantum ElectroDynamics (QED).[1] Somehow we physicists do not often talk about it, but I regard it as a remarkable unification in physics. It includes the special relativity, electromagnetism, and quantum mechanics in an essential manner and is a staggering success. It allows us to predict the strength of the magnet carried by each electron, namely the magnetic moment, down to the twelfth digit. Amazingly, it can also be measured experimentally down to the twelfth digit. They are

$$1.001\,159\,652\,154(28) \quad \text{theory} \qquad (1)$$
$$1.001\,159\,652\,188(04) \quad \text{experiment} \qquad (2)$$

in the unit of $\frac{e\hbar}{2m_e c}$. Subject to the uncertainty of the input parameter, namely the fine-structure constant, in the theoretical prediction, they completely agree with each other. It is the most accurate physical theory ever, and demonstrates the power of unification in physics.

While the γ-decay of nuclei has been understood also within the QED, other nuclear phenomena led to the discovery of two more forces in nature: β-decay caused by the weak force, and α-decay by the strong force.

We particle physicists believe that we are just about to achieve another layer of unification, between the QED and the weak force in the *electroweak theory*. Beyond it, it is still a realm of speculation. There are good reasons to think that the strong force is also unified with the electroweak forces into the so-called *grand-unified theory*. Hopefully the Einstein's general relativity will also be unified with the rest; the best contender is the superstring theory.

In this plot (Fig. 3), you see the strengths of the electromagnetism and the weak force measured at varying energies. When the particle physics started, the measurements were done way off the scale to the left of this plot, where the two forces have strengths that differ by many orders of magnitude. By an amazing insight, our predecessors had figured out that they are actually of the same origin. In-

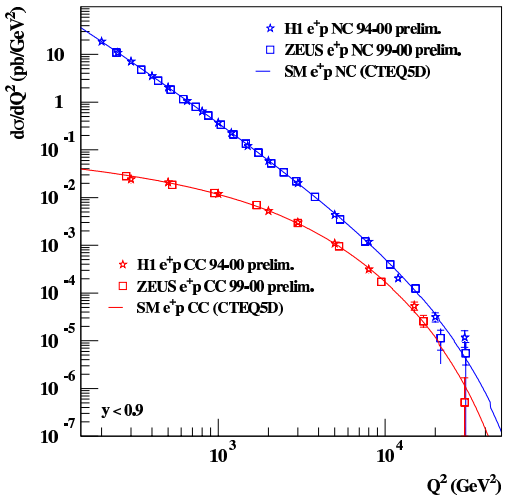

Figure 3: We are heading towards unification of the electromagnetism and the weak force.

deed, as we inched up in energy of measurements over almost a century, we now see clearly that the two forces are coming together. To see them truly unified is the long-term goal since 60's and we are clearly getting there. However, the unification is not completely until we can answer the question: *if they are unified and of the same origin, what makes them look so different from each other?* The missing link that stands in the way between us and the unification is the Dark Field.

DARK FIELD = COSMIC SUPERCONDUCTOR

As I mentioned already, Dark Field is the obstacle for the next layer of unification in physics. It is supposed to be the answer to the old puzzle in physics. Why is the weak force short-ranged?

Forces we are familiar with are long-ranged. Gravity acts on massive bodies, and is long-ranged. Otherwise Earth cannot revolve around the Sun. Electromagnetism pulls objects and opposite charges and is also long-ranged. Otherwise the compass wouldn't point north by the magnetic field of the Earth. On the other hand, the weak force pulls the electron and proton, but is *extremely* short-ranged: it goes only over 10^{-16} cm, ten billionths of the size of atoms. This is why we don't experience the weak force in our daily life. But it is crucial for our life: the Sun wouldn't burn without it!

If the weak force and the electromagnetism are unified and of the same kind, how is it possible that the weak force doesn't go very much at all? Here is the standard theory: we are swimming in the Dark Field that permeates the entire universe (Fig. 4). The Dark Field is a kind of quantum liquid. It does not disturb gravity because it does not have mass[2]. It does not disturb electromagnetism either be-

[1] Clearly, this acronym is a pun of *quod erat demonstrandum*, namely that the truth of the theory is demonstrated as in mathematical theorems.

[2] It may still have energy, which may be as large as 10^{62}% of the energy budget of the universe. Apparently it doesn't. This is still a major

cause it is electrically neutral. Both forces go a long way with light speed because they are not disturbed. But when the weak force wants to act on a distant body, the force gets bounced around by the Dark Field and it does not go very far. The force carrier of the weak force, the W-boson, therefore cannot go at light speed and is slowed down; in other words it has acquired a mass. In fact, all elementary particles we know get bounced around by the Dark Field and that is why they do not go at the speed of light. If we turn off the Dark Field now, the electrons in our body would fly apart at light speed and our body would disintegrate in a nanosecond. It is a very bizarre idea; but remember this is the *standard* theory.

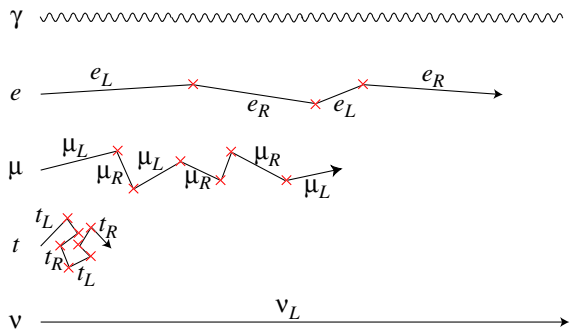

Figure 4: In the Standard model, all elementary particles we know slow down from the speed of light because they keep bumping on the Dark Field, and cannot go very far. The exceptions are photons and neutrinos, but the latter are now believed to have finite mass and we are yet to understand the mechanism.

There is a precise analogy between superconductor and the cosmic Dark Field. A superconductor is a chilled piece of metal that lets the electrical current flow with zero resistance. It is well known that a piece of superconductor floats on a piece of magnet because it does not allow magnetic field to get inside, called Meißner effect. Actually, if you look closely at the surface of a superconductor, the magnetic field gets in for a limited distance called the penetration length. In other words, the magnetic force becomes a *short-ranged* force in a superconductor. This is precisely what is going on with the weak force. We live in a cosmic superconductor.

It is truly amazing that our predecessors figured it out without ever leaving the superconductor. Imagine a physicist living in a piece of superconductor. She never could get out of it and attach electrodes to the two ends of the universe. But after careful measurements and theorizing, she figured out that the magnetic force, which she sees as a short-ranged force in her laboratory, must actually be long-ranged. She also figured that this is because there is a mysterious charged-two Dark Field in her "Universe." But she does not know that the Dark Field in her universe is made of electrons because she has a severe funding problem. She lacked funding to build a powerful particle accelerator and pump enough energy into the "empty space" to knock out electrons out of the Bose–Einstein condensate of the Cooper pairs and observe what the Dark Field is made of. This is exactly the situation we particle physicists are in right now.

mystery in particle physics.

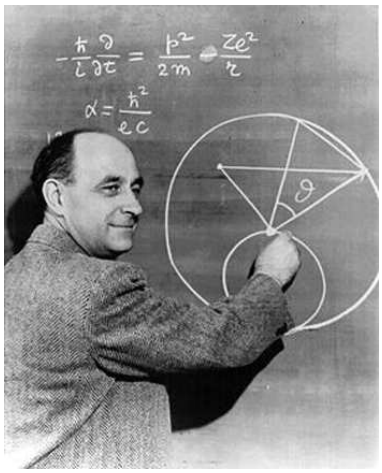

Figure 5: A nice picture of Fermi, except the definition of the fine structure constant that is wrong. What was he thinking?

We know how much energy we are supposed to pump into our "empty space" of the universe to knock out whatever that makes up the Dark Field. In fact, Enrico Fermi, back in 1933 when he wrote the first theory of weak force, knew that this is an important energy scale in physics. His theory had a dimensionful constant, $G_F \approx (0.3\text{TeV})^{-2}$, which we now call Fermi constant. Therefore, we are sure we will know what the Dark Field is made of, once we get up to the TeV energy in particle accelerators. The good news is that we are indeed getting up to the TeV.

In the case of a superconductor, you can observe the so-called "gap excitation," which is nothing but the electrons that causes the superconductivity, if enough energy is pumped in. In the same way, we should be able to observe what makes up the Dark Field of the universe by pumping enough into the empty space. It already has a name: Higgs boson. But be careful: if you name something, you get fooled that you already know it. We don't. Even though it has a name already, it doesn't mean we know what it is. We need to see it first and find out what it is. By putting all data we have right now, it is expected that the Higgs boson is basically just around the corner. It must be lighter than 260 GeV/c^2 (95% CL), while the current lower limit is 114 GeV/c^2.

This is where the Large Hadron Collider (LHC) comes in. Currently Tevatron, a proton anti-proton collider at Fermilab, runs at the center-of-momentum energy of 2 TeV. Because proton is a composite made of quarks and gluons, the actual energy used for a collision of elementary particles is typically of the order of 100–200 GeV. On the other hand, the LHC will collide beams of protons at 14 TeV, in-

creasing the typical energy of collisions beyond the TeV. The experiments at the LHC are scheduled to start in mid-2007.

Once the LHC accelerator and experiments reach their full performance, we expect the Higgs boson to be discovered for all possible values of its mass we can imagine, $100 \lesssim m_H \lesssim 600$ GeV, within a few years, if not sooner (Fig. 6).

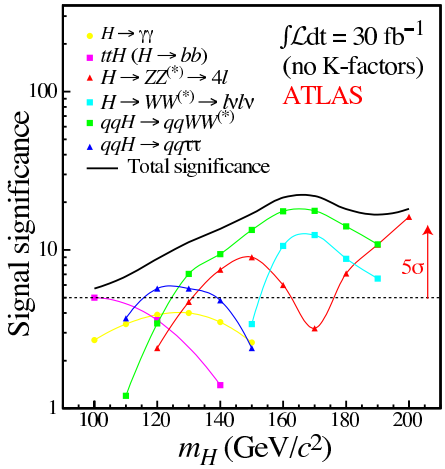

Figure 6: The robust discovery reach of the Higgs boson by the LHC experiment (ATLAS) for the most difficult range of Higgs mass. Beyond this range, the discovery becomes much easier.

But given how bizarre the idea of living in a cosmic superconductor is, we would like to be absolutely sure. Is the particle discovered *really* the particle that makes up the Dark Field? Is it really disturbing the weak force, and all elementary particles to slow them down from the light speed? To have a definite proof, we need detailed measurements of the properties of the newly discovered particle.

For this purpose, we believe we need yet another kind of experiment. Instead of colliding composite objects such as protons, we would like to collide elementary particles such as electrons and positrons to provide well-understood environment for the detailed and precise studies of the new particle. To accelerate electron beams up to the required high energies 250–500 GeV, we have to avoid the energy loss due to synchrotron radiation and hence make the accelerator linear. I couldn't believe people were seriously talking about such a machine when I've first heard about it. You need to accelerate the beam over some 15 kilometers, focus them down to a few nanometers in size, and make sure they meet head-on! It is people like you, accelerator experts, who told us that you can focus and steer the beam at this incredible level of accuracy. I am counting on you to make it happen; then we will be in business.

At an electron-positron linear collider, we can measure how the new particle interacts with other particles, proving that it can slow down (and give mass to) elementary particles exactly by the amount it should (Fig. 7). We can also prove that it is indeed condensed right here in our universe. By observing the production of this particle through the process $e^+e^- \to Z^* \to ZH$, we will be convinced that there is the three-body interaction of ZZH. We can also be sure that the new particles doesn't have spin and is parity even, namely has the quantum number of empty space, and qualifies to be filling up the universe. On the other hand, we know the Z boson has only two kinds of interaction with spinless particles: ZHH and $ZZHH$ types. The only way to have an interaction of ZZH type is by picking the four-body $Z\ ZHH$ interaction, and replace one of the H by its amount condensed right there in the laboratory of the experiment. This way, we can see that the particle we see in the apparatus indeed fills the empty space of the universe, and can even measure how much. We may even find that it does not give enough of Dark Energy, giving evidence for more of its cousins. This way, we will be confident about this bizarre picture of the empty space: a new particle makes up the Dark Field that fills the universe, slowing down the elementary particles and making them massive and short-ranged.

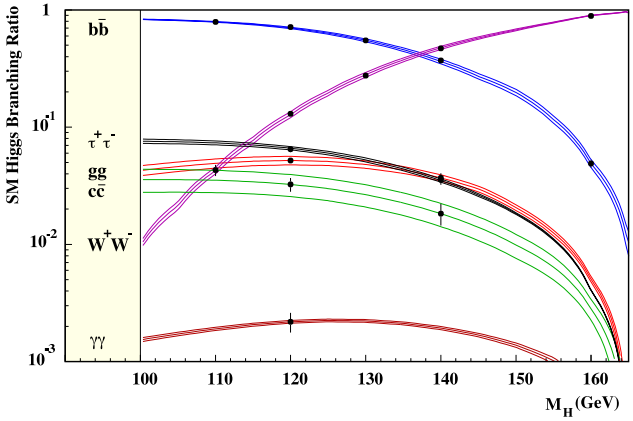

Figure 7: Measurement of Higgs coupling to various particle species at the ILC.

HIERARCHY PROBLEM

As we have seen in the previous section, we will be able to see *what* is filling up our universe, but we still don't know *why*. The question breaks down to two conceptually independent problems:

1. Why anything is filling up the universe at all,
2. Why is the scale of Dark Field ~ 0.3 TeV, much much smaller than the scale of gravity $\sim 10^{15}$ TeV.

Answers to these problems are likely be at equal to or less than TeV scale because this is the relevant energy scale of the problem.

However, there is a serious obstacle to attack these problems. It is called the "hierarchy problem."

To explain what the hierarchy problem is, let us rewind the video back to the end of the 19th century. *Once upon a*

time, there was a hierarchy problem. It was a crisis about the mass of the electron. We know like charges repel. It is hard to keep electric charge in a small pack because it repels itself. On the other hand, we know the electron is basically point-like. Our best limit that the "size" of the electron is less than something like 10^{-17} cm. The problem is that, if you want to keep the charge in such a small pack, you need a lot of energy. A naive guess is that you need at least

$$\Delta E \sim \frac{\alpha}{r_e} \sim 1\ \mathrm{GeV}\frac{10^{-17}\ \mathrm{cm}}{r_e}. \qquad (3)$$

But we know we can't afford it. The energy carried by an electron is just $E = mc^2 = 0.511$ MeV, nowhere close to what we need. In fact, the best we can do is to pack the charge down to about 10^{-13} cm, which is the so-called the classical radius of electron. In other words, the classical theory of electromagnetism breaks down around this distance scale, and we cannot discuss physics below 10^{-13} cm. We can't get started!

But we don't talk about this problem anymore, because there was a resolution. Anti-matter came to the rescue. We solved the crisis by doubling the number of particles. Here is how it works.

The electron creates a Coulomb field around itself, and it feels its own field. Namely, it repels itself (Fig. 8, top). But we discovered anti-matter. Moreover, we discovered that the world is quantum mechanical. One you have these two ingredients, there is an inevitable consequence. The "vacuum" we see isn't empty at all. It constantly creates pairs of electrons and positrons, together with a photon. Of course, energy conservation forbids it, but quantum mechanics allows us to borrow energy as long as nobody notices it. The created pair must annihilate back to the vacuum within time allowed by the uncertainty principle (Fig. 8, center). Such pairs are called "vacuum bubbles."

When you place an electron in this fluctuating vacuum, it "sees" a positron nearby. Sometimes, it decides to annihilate the positron in the bubble. Then the electron that was originally a part of the bubble now remains as a "real" particle (Fig. 8, bottom). It turns out that this process also contributes to the energy of the electron with a *negative* sign, that nearly exactly cancels the self-repelling energy we were worried about. The grand total is roughly

$$\Delta m_e c^2 \sim m_e c^2 \times \frac{\alpha}{4\pi}\log(m_e r_e). \qquad (4)$$

This is nice. First of all, the additional energy you need is proportional to the original energy (the rest energy $m_e c^2$), and we are talking about the percentage correction. Second, even if you take the smallest size imaginable, namely the Planck size $r_e \sim 10^{-33}$ cm, the size of the correction is only about 10%. Now we can get started to think about physics below 10^{-13} cm.

The problem we are facing now is very similar. The minute you think that we are swimming in the Higgs BEC, you should ask if Higgs can be contained in a small package. It turns out that the Higgs also repels itself because

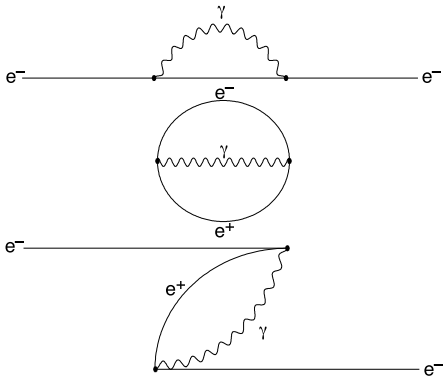

Figure 8: Top: Electron sees the Coulomb field it created itself. Center: The vacuum is full of "bubbles" in which an electron position pair is created spontaneously and annihilate back to vacuum within time allowed by the uncertainty principle. Bottom: An electron may decide to annihilate the positron in the "bubble" while the electron originally in the "bubble" remains as a real particle.

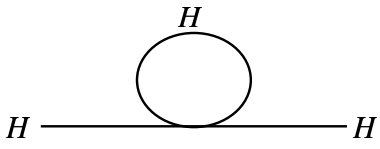

Figure 9: The self repulsion of the Higgs boson makes it hard to be contained in a small size.

of its self interaction (Fig. 9). It requires a lot of energy to contain itself. The theory breaks down again, this time around 10^{-17} cm. We are stuck. We can't get started to address the big questions. We can't "see" the interesting physics at shorter distances that answers the big questions (Fig. 10).

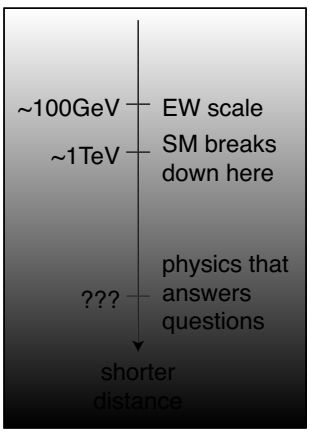

Figure 10: We would like to access physics at a short distance that answers some of the big questions. But before getting there, the standard model breaks down around TeV and everything at shorter distances is grayed out.

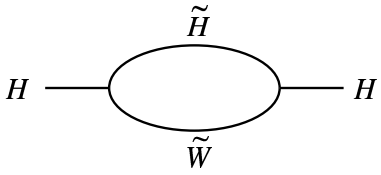

Figure 11: The supersymmetric attraction diagram cancels the Higgs self-repulsion diagram.

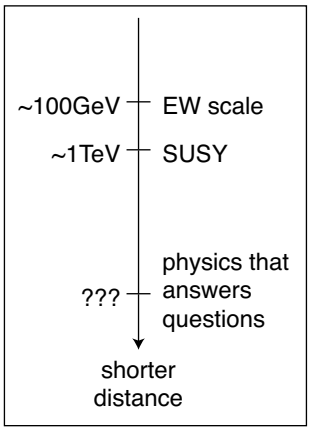

Figure 12: Once the hierarchy problem is solved, we will be allowed to talk about physics at shorter distances to address the big questions.

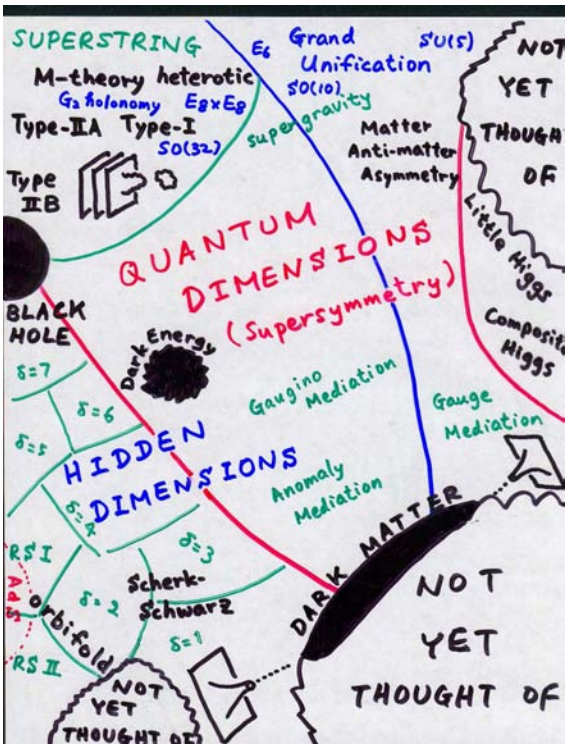

Figure 13: The landscape of theories that has many uncharted territories. The task for experiments is to zoom down to a point on this map.

One way to solve this problem is to assume that history repeats itself. We double the number of particles again. The new particles cancel the contribution from the Higgs self-repelling energy (Fig. 11). This is the idea of supersymmetry, which makes the Standard Model consistent with whatever physics there is at shorter distances. Indeed, the correction to the Higgs energy is

$$\Delta m_H^2 \sim \frac{\alpha}{4\pi} m_{SUSY}^2 \log(m_H r_H), \qquad (5)$$

where r_H is the "size" of the Higgs boson. Of course supersymmetry is not the only solution, but it is true that any solution of this kind appears at the TeV scale.

Once the hierarchy problem is solved, we can finally get started. It opens the door to the answers to the big questions (Fig. 12). The sky clears up and we can start "seeing" physics at shorter distances. An even more interesting possibility is that the solution itself provides additional probes to physics at shorter distances. We will talk about some examples soon.

For a long time, theorists, including myself, had been talking about three major directions to solve the hierarchy problem. One is supersymmetry, which I already talked about. It is the idea that the history repeats itself. Just like the anti-matter solved the crisis of the electron mass, we double the number of particles. The second direction is to learn from Cooper pairs. The Higgs condensate is a composite made of two fermions. This idea is often called technicolor. These two ideas are two-decades old, and many of you have witnessed a nearly religious war between two camps. The third direction is relatively recent: physics *ends* at TeV. TeV-scale is the ultimate scale of physics where quantum gravity manifests itself. It may be superstrings. We may produce blackholes at accelerators or by cosmic rays. This is possible if there are hidden dimensions curled up in small sizes, somewhere between 10 μm to 10^{-17} cm.

But the fact that the third direction was proposed relatively recently suggests that there are many more possibilities we theorists haven't thought of. Indeed, just the last two years have seen an outbreak of new ideas. The Higgs boson may be like pions in QCD, a pseudo-Nambu-Goldstone boson. Models based on this idea are called the "little Higgs" theories. Or maybe the Higgs boson is actually a gauge boson. Extra-dimensional components of a gauge field do not appear to have spins to a four-dimensional observer because they are spinning in extra dimensions. This idea is sometimes called Gauge-Higgs Unification. Or maybe there is no Higgs after all, and the reason why W and Z are massive is because they are Kaluza–Klein bosons, running along the extra dimension to acquire their "rest" (for a 4D observer) energies. This idea became to known as "Higgsless" theories. Most recently, I'm pushing the idea of "technicolorful supersymmetry." You see, I'm pretty ecumenical.

Clearly the landscape of theories is getting more and more complicated (Fig. 13). As the solution to the problem draws near experimentally, theorists are proposing more

possibilities. It is increasingly clear that all the theoretical possibilities we have talked about, designed the experiments around, and ran Monte Carlo on, are only a small portion of the land of all theories. There are many islands and continents already labeled on the map, but much of the land is uncharted.

The task for the future experiments is enormous: to zoom in to a point on the map most of which is still uncharted. We need to identify the physics responsible for Higgs BEC, and it is quite likely that we haven't thought of the right solution yet. We are all excited about the LHC, where we will discover particles and new phenomena that address this issue. Many possibilities will be ruled out. However, new interpretations will necessarily emerge. Then the race will be on. Theorists come up with new interpretations. Experimentalists exclude new interpretations. It will be a *long* period of elimination. As is always the case, the crucial information is in *details*. We would like to elucidate the physics by reconstructing the Lagrangian of the "true theory" term by term from measurements.


The New York Times

July 23, 2008

The Other Half of the World Discovered

Geneva, Switzerland

Figure 14: A possible headline of the claimed discovery of supersymmetry at the LHC.

Let me first emphasize that LHC will do a fantastic job to explore the TeV landscape and we all hope that it will make a major discovery. For example, the LHC will have an enormous reach for supersymmetry, an order of magnitude higher than Tevatron (Fig. 15). Once it finds superparticles, it will start all kinds of precision measurements (Fig. 16).

In this process, the absolute confidence behind our understanding is crucial, especially when we witness a major discovery. Just for the sake of discussion, let us say that supersymmetry happens to be the "true theory." It is relatively easy to reach, what I'd like to call, "New York Times-level confidence." We will see a headline like Fig. 14. But everybody in this auditorium knows that there is a long way to go from this level of confidence to the other level of confidence, which I'd like to call "Halliday–Resnik-level confidence." It will take an incredible level of confidence to put a paragraph like this one in the freshman physics textbook:

> *We have learned that all particles we observe have unique partners of different spin and statistics, called superpartners, that make our theory of elementary particles valid to small distances.*

Upon seeing this slide, one of my colleagues in Berkeley was impressed by the fact that Halliday and Resnik can turn something as exciting as the discovery of supersymmetry into something this dry and dull. Well, *that* wasn't

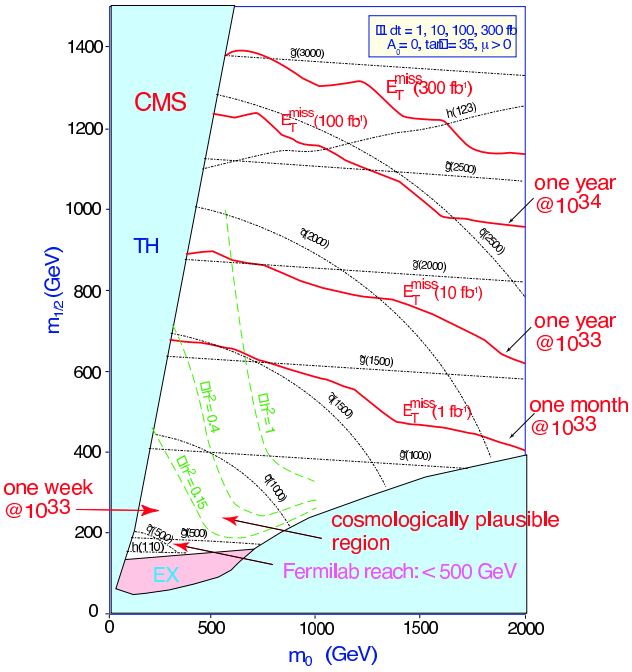

Figure 15: Discovery reach for supersymmetry at the LHC (CMS).

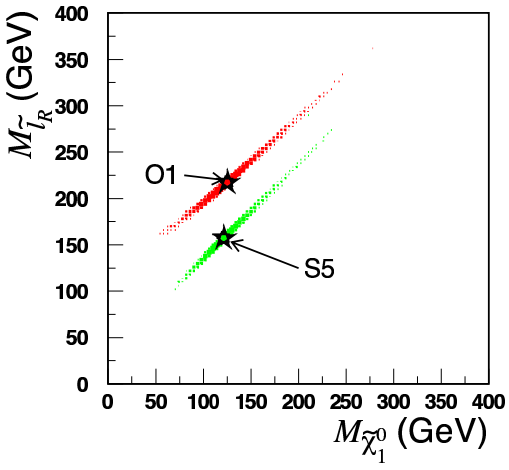

Figure 16: Precision measurement of superparticle masses at the LHC.

my point. My point is that we need to go through many detailed, precise, unambiguous measurements for us to reach this level of confidence.

The problem is that many new physics possibilities would look alike at the LHC (Fig. 17).

Again for the sake of discussion, let us say that hidden dimensions happen to be the "true theory." We will see events where the high-energy collisions on our three-dimensional sheet will produce some particles we can see and other particles that disappear into the extra dimensions, such as the graviton (Fig. 18, top). Then we find that the energy and momentum are not balanced apparently. There is clearly something exciting going on. However, such a

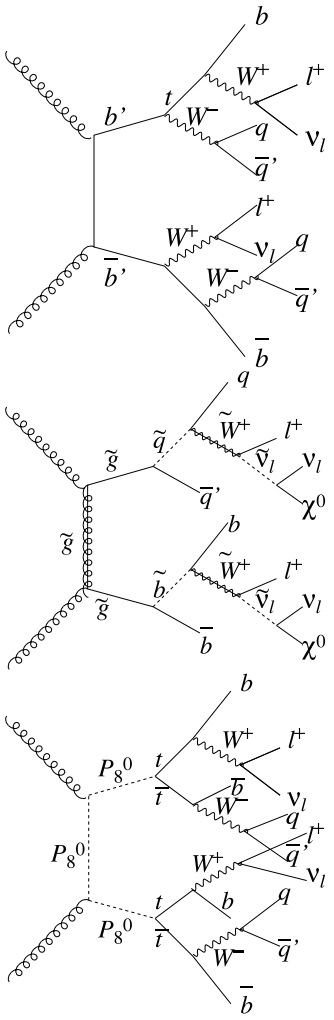

Figure 17: Many new physics looks alike. Here, signatures of fourth generation, supersymmetry, and technicolor, are all shown to give multi-jet events with missing E_T and same sign di-leptons.

discovery wouldn't establish the theory. We'd like to know how many of such extra dimensions there are, for instance. One way to address this question is to measure the rates of this kind of events at two different energies at an e^+e^- Linear Collider. The energy dependence of the rates can tell us the number of extra dimensions (Fig. 18, bottom).

Let us pick supersymmetry again. In this case, Tevatron and/or LHC will expand our sensitivity in the parameter space greatly beyond where we are, and many precise measurements will be performed at the LHC as we have seen before. However we will still like to know if the new particles truly have the same quantum numbers as the particle we already know, and their spins differ by 1/2. Again the Linear Collider can determine quantum numbers and spins, they have the correct couplings, etc (Fig. 19). This way, we will establish supersymmetry with absolute confidence.

Beyond the unification of electromagnetism and the weak force at the TeV-scale, how do we gain any information about the next layer, the grand unification? We have all seen during the conference that the strengths (gauge couplings) of three forces, $SU(3)$, $SU(2)$, and $U(1)$, appear to become equal at a very high-energy scale 10^{16} GeV, if the standard model is supersymmetric. The energy scale appears so remote that we may not gain any further information. However, if supersymmetry is discovered, and the masses of new particles are measured to a high precision by combining the data from the LHC and the LC, we will have a quantitative test of grand unification. The superpartners of the gauge bosons, gauginos, should have masses that unify at the same energy scale where the gauge couplings unify. This is a highly non-trivial test of whether forces unify. If this happens, we would definitely want to see proton decay! This is a wonderful example of how, once the hierarchy problem is solved, its solution itself will provide new probes to physics that directly address the big questions.

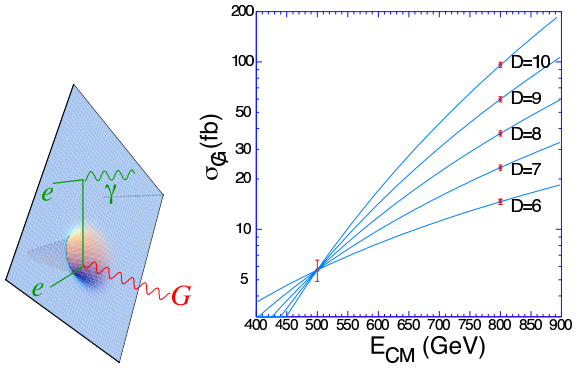

Figure 18: Top: Emission of graviton into the hidden dimensions. Bottom: The energy dependence of the rates for various number of dimensions at the ILC.

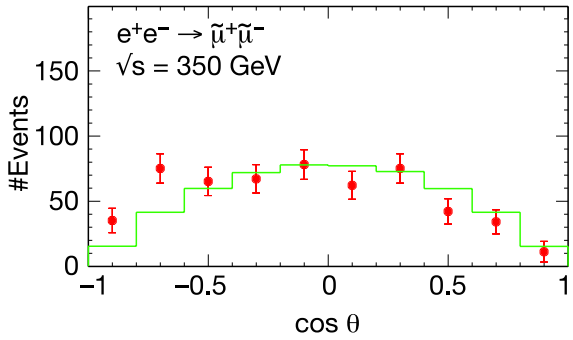

Figure 19: Test if smuon has spin zero at LC. The spin one case would show an upside down angular distribution.

DARK MATTER

The evidence for dark matter has been around for a few decades. One of the oldest is the rotation curve of the galaxy. If you measure how fast the hydrogen gas is rotating in a spiral galaxy, it is way too fast (Fig. 21). It needs to be held inside the galaxy by a gravitational pull

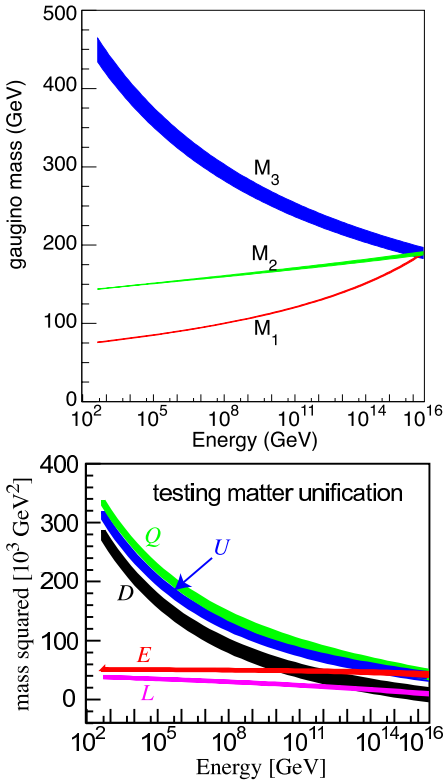

Figure 20: If supersymmetry is found, it will provide a further probe to shorter distance scale physics, such as testing grand unification using the gaugino and scalar masses.

much stronger than what is given by all the stars combined. There must be something that is not seen by light in galaxies: dark matter.

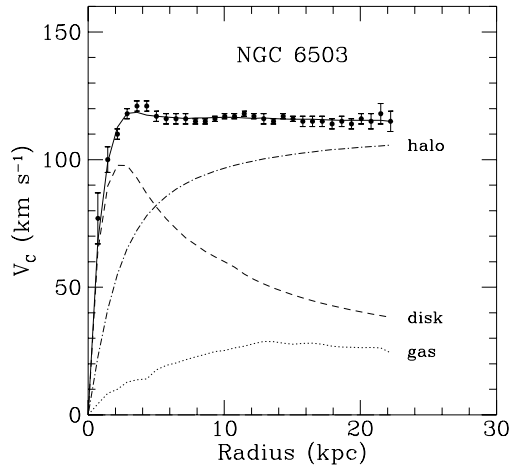

Figure 21: Rotation curve of a spiral galaxy.

Recently, the study of cosmic microwave background anisotropies by the WMAP satellite led to precise measurements of important cosmological parameters that include

$$\Omega_M h^2 = 0.135 \pm 0.009,$$
$$\Omega_b h^2 = 0.0224 \pm 0.0009.$$

These two numbers are different at the 12 σ level: $|\Omega_M - \Omega_b|h^2 = 0.113 \pm 0.009$. Namely, there is a lot more mass in the universe than all atoms combined, and hence the dark matter is *not the atoms we are made of*. It must be something else.

People have looked for dim stars or big planets that make up dark matter in the halo of our galaxy, dubbed MACHOs (Massive Compact Halo Objects). The search resulted in a strong upper limit on the halo fraction of such astronomical objects. Instead, we are led to WIMPs (Weakly Interacting Massive Particles). They are stable heavy particles produced in early Universe when the temperature was as high as their mass. As the universe cooled, the temperature was so low that they were no longer created. They started to annihilated with each other, but as the universe expands, they saw fewer and fewer or each other and beyond some point they could no longer find each other to annihilate. This way, there are left-overs from the near complete annihilation. The amount of energy density left over is

$$\Omega_M \approx 0.23 \frac{\pi\alpha^2/(\mathrm{TeV})^2}{\sigma_{ann}}. \qquad (6)$$

It is very interesting that weakly coupled (as weak as α) particle at the TeV scale provides the correct energy density to explain the Dark Matter.

A stable, weakly-coupled particle would be an excellent candidate for Dark Matter. Actually, it should be very weakly coupled because ordinary neutrinos would be too strongly coupled and are excluded by the negative search results. There are no such candidate particles in the Standard Model. The candidate most talked about is the Lightest Supersymmetric Particle (LSP), which is the superpartner of the photon or Z in most models.

To discover Dark Matter, one hopes to see the dark matter particle scattering off an ordinary atomic nucleus. A very sensitive device is placed deep underground to be shielded from cosmic-ray induced backgrounds. Then you wait, wait, and wait, until a dark matter particle leaves a little kick on one of the nuclei and hence a small (keV) amount of energy. Such experiments are called direct detection experiments. Another possibility is indirect detection experiments. For example, the dark matter particles may be trapped by the Sun, accumulate in the center over time, and start to annihilate with each other just like they used to do in Big Bang. The annihilation typically produces energetic neutrinos which exit the Sun without any problems and hit a large (*e.g.*, km^3!) neutrino detector in The Sun. Indeed, the next generation experiments will take a significant bite out of the interesting part of the parameter space. This way, we will know that Dark Matter is indeed there floating in the halo of our galaxy. On the other hand, we would also like to know what it is. For this purpose, we'd like to produce ample quantities of Dark Matter in the laboratory and study its detailed properties.

I have argued that the Dark Matter is likely be a TeV-scale electrically neutral weakly interacting particle. There are many such candidates: Lightest Supersymmetric Par-

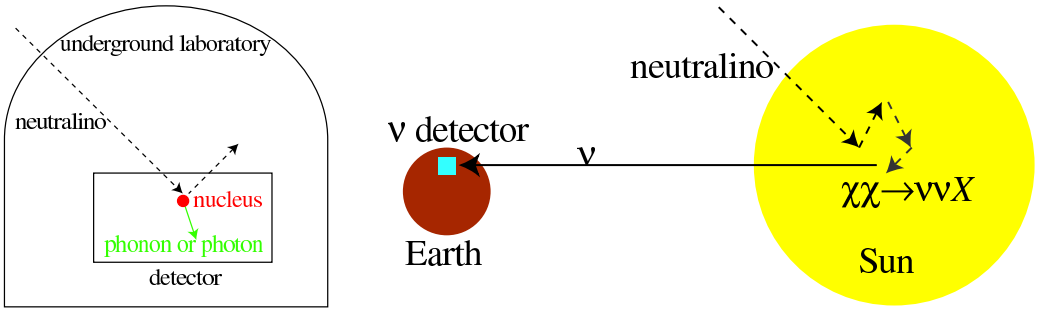

Figure 22: Direct and indirect experiments to discover dark matter.

ticle, Lightest Kaluza–Klein particle in universal extra dimension, etc. It is quite conceivable that one of those particles is stable (or long-lived enough) to be the Dark Matter. If so, it will be accessible at accelerators, such as LHC and LC.

We look for events like that in Fig. 23 in the detector. The event shows particles going towards the upper hemisphere, while very few in the lower hemisphere. Because the momentum must be conserved, the logical conclusion is that there must be invisible particle(s) produced in the particle collision that escaped the detector downwards. Once such events are seen copiously above the background expected by the known processes (*e.g.*, neutrinos), we will have high hopes that we have found dark matter particles. How do we know this is the case?

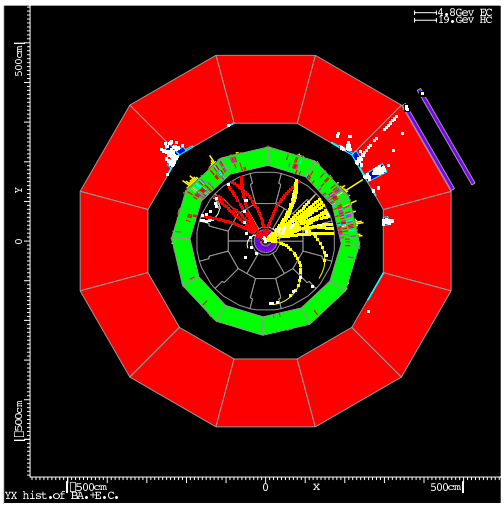

Figure 23: Events with an apparent imbalance in momenta and missing energy.

Once we find a new invisible particle, precision measurements of its mass and couplings to other particles at LHC and ILC will allow us to calculate its cosmic abundance. We can also calculate the scattering cross section of the new invisible particle on atomic nuclei. If these calculations turn to agree with data from the cosmological measurements and direct detection experiments, it would be a major triumph of modern physics. We will understand the universe all the way back to when it was only about

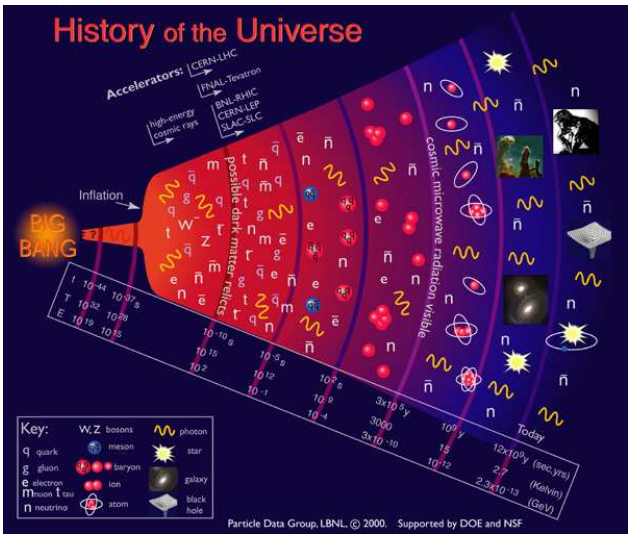

Figure 24: Schematic history of Universe. We have a pretty good grip on physics back to about a second after the Big Bang thanks to CMB and nucleosynthesis. The quark-gluon plasma is physics back at 10^{-5} sec. An agreement between accelerator-based data on Dark Matter and cosmological data would provide understanding much closer to The Beginning, back to 10^{-12} sec after the Big Bang.

10^{-12} sec old after Big Bang! (Fig. 24)

CONCLUSION

I argued that TeV scale is a focal point in physics, where much of particle physics and cosmology meet. We've been waiting to reach this energy scale for more than seven decades. The LHC will be the next major break-through at the TeV-scale, and we look forward to seeing many exciting results from the LHC. On the other hand, if the physics at the TeV scale is as rich as we currently expect, we will likely need a lot of detailed information to fully understand what is going on. The ILC will study new particles one by one, and would allow us to reconstruct the underlying Lagrangian of new phenomena. Then we will have the "Halliday–Resnik level confidence" to move on with an absolute confidence.

NANOMATERIAL AND ITS MEDICAL USE: SMART POLYMERIC MICELLES AS NANOCARRIERS FOR GENE AND DRUG DELIVERY*

K. Kataoka

Department of Materials Engineering and Center for Disease Biology and Integrative Medicine, The University of Tokyo, 7-3-1 Hongo, Bunkyo-ku, Tokyo 113-8656, Japan

Block copolymers with amphiphilic character, having a large solubility difference between hydrophilic and hydrophobic segments, are known to assemble in an aqueous milieu into polymeric micelles. These micelles have a fairly narrow size distribution and are featured by their unique core-shell architecture, where hydrophobic segments are segregated from the aqueous exterior to form inner core surrounded by a palisade of hydrophilic segments. Recently, progressive interest has been raised in the application of these block copolymer micelles as novel carrier systems in the field of drug targeting because of the high drug-loading capacity of the inner core as well as of the unique disposition characteristics in the body [1,2]. A variety of hydrophilic polymers with a flexible nature can be selected as shell-forming segments of the micelles, which assemble into the dense palisades of tethered chains to achieve effective steric stabilization propensities. Core segregation from aqueous milieu is the direct driving force for micellization and proceeds through a combination of intermolecular forces including hydrophobic interaction, electrostatic interaction, metal complexation, and hydrogen bonding of constituent block copolymers. A variety of drugs with diverse characteristics, including genes and proteins, can be incorporated into the core by engineering the structure of the core-forming segment of the block copolymer so that one can expect a sufficiently strong interaction with drug molecules. Compared to surfactant micelles, polymeric micelles are generally more stable with remarkably lowered CMC and have a slower rate of dissociation, allowing retention of loaded drugs for a longer period of time, and eventually, achieving higher accumulation of a drug into the target site. Furthermore, polymeric micelles have a size range of several tens of nanometers with a considerably narrow distribution. This feature in size is similar to that of viruses and lipoproteins, natural nanocarrier systems, and is certainly a crucial factor in determining their body disposition, especially when an Enhanced Permeation Retention effect (EPR effect) is involved. Indeed, longevity in blood circulation as well as enhanced tumour accumulation through EPR effect was observed for doxorubicin- [3], cisplatin- [4] and paclitaxel-loaded micelles [5], achieving significant tumour regression. Note that doxorubicin- and paclitaxel-loaded polymeric micelles are now in phase II and phase I clinical trials, respectively, at National Cancer Center Hospital in Tokyo.

Recently, smart polymeric micelles with core structure responding to external stimuli have successfully been prepared. Polymeric micelles from doxorubicin-conjugated block copolymer poly(ethylene glycol)-poly(aspartame hydrazine doxorubicin) [PEG-p(Asp-Hid-DOX)] were contrived to retain drugs at physiological condition, pH7.4, and release drugs as pH decreased below 6.0 corresponding to the conditions in intracellular endosomes and lysosomes, which was controlled by pH-sensitive imine bond between drugs and polymer chains [6]. The intracellular drug release profile was clearly evidenced by the laser confocal fluorescence microscopy, corresponding nicely to their impressive in vivo anticancer activity by tumour-bearing animals [7]. Physical stimuli can also be applied to tune the biological activity of polymeric micelles. In this regard, we have prepared photo-activating micelles entrapping dendrimer porphyrin in the core for the use in photodynamic therapy (PDT), which is known to be a very promising treatment of cancer and age-related macular degeneration (AMD). Dendrimer-entrapped micelle underwent appreciable cellular uptake as confirmed by laser confocal microscopy, and revealed remarkably higher PDT efficacy, evaluated from IC_{50} value under photoirradiation, compared to protophorphyrin as a control and dendrimer porphyrin itself [8]. Indeed, this micelle achieved highly improved PDT efficacy compared to commercial photosensitizer in the treatment of AMD model developed in experimental animals,

suggesting the high clinical potential of this micelle as environment-sensitive delivery system of photosensitizers for PDT [9].

Functionalization of the outer surface of the polymeric micelle to modify its physicochemical and biological properties is of great value from the standpoint of designing micellar carrier systems for receptor-mediated drug delivery. This can be accomplished in a regulated fashion by constructing the micelles from a variety of end-functionalized block copolymers. Polymeric micelles having sugars and peptides on their periphery have recently been prepared to explore their utility in the field of gene and drug delivery [10]. Furthermore, a new type of intracellular pH-sensitive polymeric micelle drug carrier whose surface was modified with folic acid for active drug delivery was prepared from an amphiphilic block copolymer, folate-poly(ethylene glycol)-poly(aspartate hydrazone doxorubicin) [Fol-PEG-P(Asp-Hyd-DOX)] [11]. Because folate-binding proteins (FBP) are selectively overexpressing in cancer cells, the folate-bound micelles can be guided to the cancer cells in the body. FBP-binding selectivity of the micelle was evaluated by surface plasmon resonance (SPR) measurements, and tetrazolium dye method (MTT assay) using human pharyngeal cancer cell (KB cell) revealed that the micelle significantly improved cell growth inhibitory activity in spite of a short exposure time due to the selective and strong interaction between folate molecules and their receptors.

The development of *in vivo* delivery systems for plasmid DNA (pDNA) and siRNA is strongly desired to increase their clinical utilities. Despite enormous efforts in this field, the rationale to design efficient delivery systems has not been obtained yet. Recently, polyplex micelles, which are formed through an electrostatic interaction between pDNA and poly(ethylene glycol) (PEG)-polycation block copolymers (e.g., PEG-poly(L-lysine) (PEG-PLL)), have received much attention due to their small size (less than 100 nm) and excellent biocompatibility [12]. We have so far demonstrated that polyplex micelles show high tolerability against serum incubation and enzymatic degradation, prolonged blood circulation after i.v. administration, and appreciably high *in vitro* and *in vivo* transfection efficacy [13]. The environment-sensitive polyplex micelles, in which the polyion complex core was stabilized through the disulfide cross-linking, was firstly developed by our group [14]. The cross-linked micelles showed the efficient DNA release responding to the reductive intra-cellular condition, while showing remarkable stability in non-reductive extra-cellular condition, achieving an appreciable *in vivo* gene transfer to liver by i.v. route [15]. Worth noting is that the cross-linked micelles maintained the physicochemical and biological properties even after the freeze-drying and rehydration processes. An A-B-C type triblock copolymer, tandemly aligning two types of polycations with different pK_a in a single polymer strand, was then developed for the construction of novel polyplex micelles, satisfying a high DNA condensing ability as well as a proton buffering activity directed to elevating gene transfection [16]. The micelle is featured by the distinctive three-layered structure where an inner polyplex layer of condensed pDNA with poly(L-lysine) (pK_a~9.4) is successively wrapped with an intermediate layer of poly[(3-morpholinopropyl)aspartamide] with a comparatively low pK_a of ~ 6.2 to provide a buffering effect and an outer PEG layer as a biocompatible palisade.

The control of the transgene expression by external physical energy, such as photo-energy, has been attracting an progressive interest in the development of synthetic gene carriers. Recently, Berg et al. have proposed a new technology named “photochemical internalization (PCI)”, in which the cytoplasmic delivery of gene carriers is enhanced by the photochemical rupture of the endosomal membrane using light and a hydrophilic photosensitizer [17]. Based on this technology, we have developed a novel ternary complex composed of a core containing the packaged DNA and an envelope of anionic dendrimer phthalocyanine as a light-responsive gene carrier [18]. The ternary complex showed more than 100-fold photochemical enhancement of the transgene expression *in vitro* with reduced photocytotoxicity. In animal experiment, subconjunctival injection of the ternary complex and the following laser application resulted in the transgene expression only in the laser-irradiated site. To our knowledge, this is the first success in the PCI-mediated gene delivery *in vivo*. Also, this paper offers new biomedical applications of dendrimers, which have attracted growing interest as materials for drug and gene delivery.

An siRNA nanocarrier formed through self-assembly of PEG-based block catiomer possessing two distinct amino groups with different pKa values in a side chain was constructed [19]. This design provided the carrier with both a sufficient siRNA complexation and a buffering capacity in the

endosomes, allowing it to exhibit remarkable gene knockdown abilities as well as a sufficient serum tolerability. Alternative approach to design nanocarriers for siRNA delivery is based on the assembly of PEG-siRNA conjugate with appropriate polycation, such as poly(lysine) [20]. Indeed, the remarkably enhanced gene silencing in hepatoma cells was achieved by PIC micelles from lactosylated-PEG-siRNA conjugate bearing acid-labile b-thiopropionate linkage. The PIC micelles with clustered lactose moieties on the periphery were successfully transported into hepatoma cells in receptor-mediated manner, releasing active siRNA molecules into cellular interior responding to pH decrease in endosomal compartment. Eventually, almost 100 times enhancement in gene silencing activity compared to the free conjugate was achieved by the use of the smart micelle systems.

REFERENCES

[1] K. Kataoka, A. Harada, and Y. Nagasaki, *Adv. Drug Deliv. Rev.* **47** (2001) 113.

[2] Y. Kakizawa and K. Kataoka, *Adv. Drug Deliv. Rev*. **54** (2002) 203.

[3] M. Yokoyama, T. Okano, Y. Sakurai, S. Fukushima, K. Okamoto, and K. Kataoka, *J. Drug Targeting* **7** (1999) 171.

[4] N. Nishiyama, S. Okazaki, H. Cabral, M. Miyamoto, Y. Kato, Y. Sugiyama, K. Nishio, Y. Matsumura, and K. Kataoka, *Cancer Research* **63** (2003) 8977.

[5] T. Hamaguchi, Y. Matsumura, M. Suzuki, K. Shimizu, R. Goda, I. Nakamura, I. Nakatomi, M. Yokoyama, K. Kataoka, and T. Kakizoe, *Br. J. Cancer* **92** (2005) 1240.

[6] Y.-S. Bae, S. Fukushima, A. Harada, and K. Kataoka, *Angew. Chem., Int'l Ed.* **42** (2003) 4640

[7] Y.-S. Bae, N. Nishiyama, S. Fukushima, H. Koyama, Y. Matsumura, and K. Kataoka, *Bioconj. Chem.* **16** (2005) 122.

[8] W.-D. Jang, N. Nishiyama, G.-D. Zhang, A. Harada, D.-L. Jiang, S. Kawauchi, Y. Morimoto, M. Kikuchi, H. Koyama, T. Aida, and K. Kataoka, *Angew. Chem., Int'l Ed.* **44** (2005) 419.

[9] R. Ideta, F. Tasaka, W.-D. Jang, N. Nishiyama, G.-D. Zhang, A. Harada, Y. Yanagi, Y. Tamaki, T. Aida, and K. Kataoka, *Nano Lett.* (2005) in press.

[10] E. Jule, Y. Nagasaki, and K. Kataoka, *Bioconjugate Chemistry* **14** (2003) 177.

[11] Y.-S. Bae, W.-D. Jang, N. Nishiyama, S. Fukushima, and K. Kataoka, *Molecular BioSystems* **1** (2005) 242.

[12] K. Itaka, K. Yamauchi, A. Harada, K. Nakamura, H. Kawaguchi, and K. Kataoka, *Biomaterialss* **24** (2003) 4495.

[13] M. Harada-Shiba, K. Yamauchi, A. Harada, K. Shimokado, and K. Kataoka, *Gene Therapy* **9** (2002) 407.

[14] K. Miyata, Y, Kakizawa, N. Nishiyama, A. Harada, Y. Yamasaki, H. Koyama, and K. Kataoka, *J. Amer. Chem. Soc.* **126** (2004) 2355.

[15] K. Miyata, Y. Kakizawa, N. Nishiyama, Y. Yamasaki, T. Watanabe, M. Kohara, and K. Kataoka, *J. Contrl. Rel.* (2005) in press.

[16] S. Fukushima, K. Miyata, N. Nishiyama, N. Kanayama, Y. Yamasaki, and K. Kataoka, *J. Amer. Chem. Soc.* **127** (2005) 2810.

[17] A. Hogset, L. Prasmickaite, T. E. Tjelle, and K. Berg, *Human Gene Therapy* **11** (2000) 869.

[18] N. Nishiyama, A. Iriyama, W.-D. Jang, K. Miyata, K. Itaka, Y. Inoue, H. Takahashi, Y. Yanagi, Y. Tamaki, H. Koyama, and K. Kataoka, *Nature Materials* (2005) in press.

[19] K. Itaka, N. Kanayama, N. Nishiyama, W.-D. Jang, Y. Yamasaki, K. Nakamura, H. Kawaguchi, and K. Kataoka, *J. Amer. Chem. Soc.* **126** (2004) 13612.

[20] M. Oishi, Y. Nagasaki, K. Itaka, N. Nishiyama, and K. Kataoka, *J. Amer. Chem. Soc.* **127** (2005) 1624.

STUDY OF CELLULAR RADIATION RESPONSE USING HEAVY-ION MICROBEAMS

Y. Kobayashi, JAEA-Takasaki, Gunma 370-1292, Japan

Abstract

At the Takasaki Ion accelerators for Advanced Radiation Application (TIARA) of JAEA-Takasaki, the innovative R&D is carried out laying emphasis on the effect of ion beams to organisms and on the effective utilization of positron emitters as a probe, in order to solve the problems related to conservation of circumstances and insurance of foods, and the promotion of new industries based on advanced techniques is also aimed.

One of the most prominent techniques we have developed is a heavy-ion microbeam, as a tool for microsurgery to analyze their normal function of various cell parts, and as a radiobiological tool to elucidate cellular radiation responses in ways that cannot be achieved using conventional broad-field exposures. We have established a single cell irradiation system, which allows selected cells to be individually hit with defined number of heavy charged particles, using a collimated heavy-ion microbeam apparatus at the TIARA in JAEA-Takasaki. Using this system, separately inoculated Chinese hamster ovary cells, confluent normal human fibroblasts, and single plant cells (tobacco protoplasts) have been irradiated. These are the first studies in which single-cell/single-particle hit effects have been investigated using a high-LET heavy ion microbeam. Furthermore, both in sparsely inoculated CHO-K1 cells and in confluent human fibroblasts, we have observed ionizing radiation-induced bystander effects, where irradiated cells emit signals resulting in damage to nearby unirradiated bystander cells.

INTRODUCTION

Environmental exposure to high-LET radiation, such as alpha particles ejected by inhaled radon and its decay products, or the space radiation to which astronauts are constantly exposed during a long-term space mission, occurs mainly at low dose and low dose-rate. At low dose and low dose-rate exposure, effects like the response of cells not directly hit by heavy charged particles may impact radiosensitivity. Even when the energetic heavy ions are used therapeutically at high dose, cells around the irradiation field may only be hit sparsely. Energetic heavy ions deposit their energy to biological organisms through highly dense ionization along the particle trajectories. By exposure of the population of cells to high-LET heavy ions at low doses, a few cells, but not the majority of cells, are actually traversed by a particle. At somewhat higher doses, the greater number of the cells receives two or more events according to the Poisson distribution of ion injections. This fluctuation of particle trajectories among individual cells thus makes the comprehension of radiological effects of heavy ions difficult. Using microbeams, we can overcome this limitation by accurately delivering a counted number of particles to each cell to study cellular radiation responses individually. A microbeam can be used for the targeted irradiation of individual cells, followed by examining the changes in the targeted cell and in their neighbouring non-traversed cells. The use of microbeam allows the direct investigation of the cell-to-cell communications, such as “bystander effects”, namely, radiation effects transmitted from hit cells to their non-hit neighbours. Furthermore, a microbeam with sufficient spatial resolution will be useful for analyzing the interaction of damages caused by separate events within an irradiated cell, the dynamics of damage repair, and the intracellular processes, including apoptosis by means of highly localized irradiation of a part of a nucleus or cytoplasm.

The earliest heavy particle microbeam experiments were performed in 1953 by Zirkle and Bloom at University of Chicago using a 2 MV Van de Graaff accelerator and micro-collimators to form a proton microbeam to study the process of cell division [1]. Then, an 11 MeV/amu proton and 22 MeV/amu deuteron microbeam was developed at Brookhaven National Laboratory using a cyclotron [2]. These earlier microbeam systems were very helpful in studying radiation effects in living systems, especially to show that damage to the cytoplasm had a very limited effect on the survival of the cell. However, all of these systems were limited at relatively high doses. To investigate the effects at lower doses, it is necessary to establish single particle irradiation technique.

Recently the need to understand the effects of low doses of radiation has led to the need to control the number of charged particles. One microbeam system designed for this purpose was installed on the horizontal beam line of the UNILAC linear accelerator at GSI-Darmstadt where ions of many elements, ranging from carbon to uranium, with energies of 1.4 MeV/amu were available [3]. Etched tracks of high-energy heavy particles were used to collimate beams. Using this system, the impact parameter dependence of the inactivation of *Bacillus subtilis* spores were measured [4]. This microbeam system was also used to investigate the effects of single particle tracks with LETs from 500 to 12,000 keV/μm on the growth and chromosome structure of mammalian cells. However, this work was later abandoned because the irradiation procedure was so time-consuming that only about 20 samples, each with approx. 20 cells, could be irradiated with single ions during 10 hours of beam time.

The next single-particle microbeam was developed at Pacific Northwest National Laboratory [5]. An

electrostatic accelerator was used to produce hydrogen and helium ions. Two sets of four adjustable knife-edges were used to construct two apertures in series to collimate microbeams. A thin plastic scintillator and photomultiplier were used to detect individual particles. Using this system, CHO-K1 cells were exposed to controlled number of 3.2 MeV a-particles and the biological responses of individual cell were quantified [6]. However, this microbeam apparatus has been removed and reinstalled at Texas A&M University.

Similar single-cell/single-particle irradiation systems have been developed at the Gray Cancer Institute (GCI) [7,8] and at Columbia University [9], where single protons and helium ions can be aimed at single cells with a few microns resolution. At GCI, Prise *et al*. demonstrated that targeting individual alpha particles to four cells within a population produced more micronucleated and apoptotic cells than expected on the basis of a direct effect only [10]. It was also reported that when a single cell within a population was targeted by an alpha particle, typically an additional 80-100 damaged cells were observed in surrounding population of about 5000 cells [11]. This bystander effect was observed when only a cell was targeted, but not when only the medium was exposed, confirming that a cell-mediated response is involved. At the microbeam facility of Columbia University, a bystander mutagenic effect has been found in non-traversed cells when a proportion of mammalian cells have suffered a precise number of nuclear traversals by alpha particles [12,13]. Furthermore, it was found that targeted cytoplasmic irradiation, of all cells within the population with alpha particles, induced mutations in mammalian cells suggesting that cytoplasm is an important target for cellular killing and mutation [14]. Recent studies with the GCI microbeam have also shown that targeting the cytoplasm induces bystander responses to the same extent as that observed from nuclear irradiation [15].

These are truly operational particle microbeams, however only protons and helium ions can be used. Therefore, we have developed a novel single-cell/single-particle irradiation system using heavy-ion microbeams for targeting cells individually with a specific numbers of heavy particles to elucidate the radiobiological effects of a single high-LET particle traversal [16].

EXPERIMENTAL SETUP

The cell irradiation system has been incorporated into the collimated heavy-ion microbeam apparatus, which was installed below a vertical beam line of the AVF cyclotron at TIARA in JAEA-Takasaki. The heavy-ion beams delivered from the AVF cyclotron are collimated with a set of apertures. Then the collimated beams are extracted into air through a microaperture on a 100 μm-thick tantalum disk perforated using an electrical discharge machining (spark erosion) method. The smallest microaperture, 5 μm in diameter, was used for cell irradiation with a precise number of 11.5 MeV/amu ^{40}Ar and 13.0 MeV/amu ^{20}Ne ions; and a microaperture of 20 μm in diameter was used for 18.3 MeV/amu ^{12}C ions irradiation.

So far, two inverted optical microscopes are in operation with this system. One of the microscopes is installed below the vertical beam line in the beam room as an ”on-line microscope” for cell targeting and for delivery of a certain number of particles. The other microscope, which is called “off-line microscope”, is used in the preparation room for cell finding prior to the irradiation and for cell revisiting and observation during post-irradiation incubation. A local-area network connects these control systems allowing the object database created at the off-line microscope to be used by the cell-targeting system.

Preparation of the microbeam target-cell dishes and the microbeam irradiation protocol used have been described elsewhere [17,18]. Figure 1 shows the procedure of targeted irradiation of cultured cell with a heavy particle microbeam. Briefly, cells grown in special dish made of ion track detector TNF-1 (modified CR-39) are positioned so that the desired portion of the cell aligns with collimator. The number of ions penetrating the sample is counted with a constant fraction discriminator coupled to a preset counter/timer. A pulse-chopper in the injection line of the cyclotron was used as fast beam switch. The gate output of the counter/timer was fed to the pulse-chopper to turn on the beam until the chosen number of ions had detected. The actual number of particle tracks that passed through cell nuclei was detected with prompt etching of the bottom of the cell dish with alkaline-ethanol solution at 37ºC for 15-30 minutes. After that, the phase-contrast microscopic image of the irradiated cells was overlaid with the image of the etched ion pits obtained at the same field of view. It is possible to revisit each irradiated cell reproducibly during post-irradiation incubation according to the object database.

RESULTS

Direct nucleus-hit effect and bystander effect on the growth of sparsely inoculated CHO-K1 cells

Chinese hamster ovary (CHO-K1) cells were individually irradiated with counted number of 11.5 MeV/amu ^{40}Ar ions (LET 1,260 keV/μm) using our heavy ion microbeam [17,18]. The actual number of particle tracks that passed through cell nuclei was detected by promptly etching the bottom of the cell dish, which was made of ion track detector TNF-1 (modified CR-39), with alkaline-ethanol solution at 37ºC for 15-30 min. Effects of direct hit of heavy ions were evaluated by scoring the number of cells in each colony < 60 hr after irradiation. We observed a reduced number of cells per colony in the direct hit cells 60 hr post irradiation. This reduction of cell number per colony was due to reproductive death of the hit cell, rather than to cell division delay caused by radiation damage. Among the irradiated cells hit in their nuclei with a single ^{40}Ar ion, their proliferation was highly suppressed, and the fraction of lost cells (detached

cells) was increased to > 40%. Morphological changes were observed in the detached cells within 12-24 hr after irradiation.

Moreover, an inhibitory effect on the non-hit cells was also observed. When the culture media but not cells were exposed, < 25 cells/colony were observed. Meanwhile, when the fraction of cells within the population was exposed, the growth of non-hit cells was suppressed (approximately 12 cells/colony). An increased yield of lost cells was also observed in this cell group. This growth inhibition in the non-hit cells in the same dish containing co-cultured hit and non-hit cells might be caused by a bystander effect. In our experiments, the cells were inoculated sparsely in the sample holder, implying the medium-mediated transmission of molecules causes this limited growth of the non-hit cells.

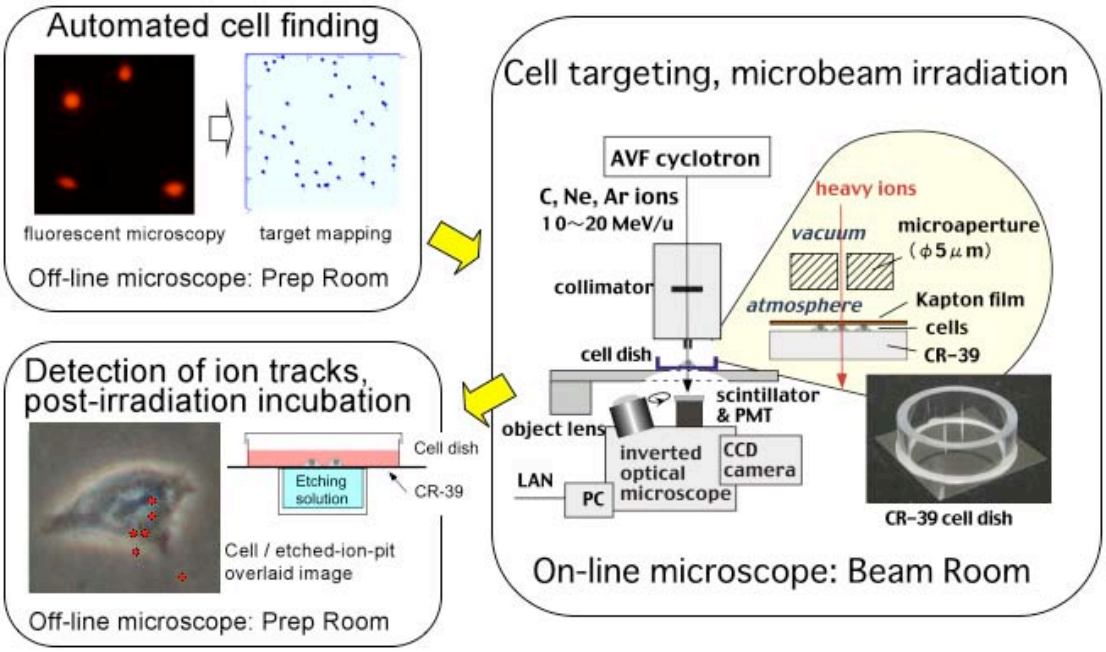

Figure 1: Procedure of targeted irradiation of cultured cells with a heavy particle microbeam. Before irradiation, positional data of the individual cells is obtained at the off-line microscope in the preparation room by microscopically searching the cell dish. Using the object database, targeting and irradiation at the on-line microscope are quickly carried out. Immediately after irradiation, the cell dish is refilled with medium, and then the bottom is etched from the opposite side of the cells to detect the accurate position of ion tracks on the cells.

Bystander effect induced by counted high-LET particles in confluent human fibroblasts

Primary human fibroblast (AG01522) cells within a confluent population were individually targeted by a high-LET heavy particle microbeam of 13.0 MeV/amu ^{20}Ne or 11.5 MeV/amu ^{40}Ar with LET values of 380 keV/μm and 1,260 keV/μm, respectively [19]. Even when only a single cell within the confluent culture was hit by one ^{20}Ne or ^{40}Ar particle, a 1.4-fold increase in micronuclei (MN) was detected demonstrating a bystander response. When the number of targeted cells increased, the number of MN biphasically increased; however, the efficiency of MN induction per targeted cell markedly decreased. When 49 cells in the culture were individually hit by 1 to 4 particles, the production of MN in the irradiated cultures were ~2-fold higher than control levels but independent of the number and LET of the particles. MN induction in the irradiated culture was partly reduced by treatment with DMSO, a scavenger of reactive oxygen species (ROS), and was almost fully suppressed by a mixture of DMSO and PMA, an inhibitor of gap junction intercellular communication (GJIC). Accordingly, both ROS and GJIC contribute to the above-mentioned bystander response and GJIC may play an essential role by mediating the passage of soluble biochemical factors from targeted cells.

However, GJIC is not always required for the induction of bystander responses. By irradiating non-confluent human fibroblast cells with a precise number of particles, the findings that targeting of a single cell led to additional 10s of cells being damaged [20] gives direct evidence of existence of non-GJIC paths and of the likelihood of medium-mediated bystander responses. To clarify the mechanisms of transduction of the bystander signal through GJIC, an irradiation method to obtain the distance distribution in the induction of MN in non-irradiated cells from irradiated cells was established [21]. Briefly, a 25-mm-diameter cell culture coverslip (NUNC 174985) was attached to the center of a 60-mm plastic dish over a 13-mm hole in bottom of the dish and sealed with white Vaseline. In the middle of the coverslip, a 1-2 mm wide adhesive tape was put on the surface to prevent cells from attaching to this “clear zone”, which split the surface of

the coverslip into two “confluent zones”. Only a fraction of the cells in the confluent zone in one side of the clear zone were irradiated. MN can only be seen in growing cells at the border between the clear zone and the confluent zone. The distributions of the distances over which the bystander effects occurs from the irradiated cells can be obtained by measurement of the distribution of MN cells in the border of the clear zone in the irradiated side. If there are still medium-mediated bystander effects, even if suppressed by inhibitors, we can observe their effect in the opposite side of the irradiated side.

Development of procedures for the irradiation of single plant cells with a heavy-particle microbeam

An ion microbeam system for irradiating single plant cells was developed to analyze the exact biological effects of heavy charged particles [22]. Tobacco BY-2 protoplasts were used as a model of single plant cells. Protoplasts were cultured with their positions fixed in thin agarose medium on a specially designed irradiation-vessel, which has a CR-39 sheet in a bottom. The colony formation rate of unirradiated protoplasts was 22.7 ± 6.7% after a month of culture. Protoplasts were irradiated with counted numbers of 18.3 MeV/amu ^{12}C ions (LET 121 keV/μm) collimated by a 20 μm diameter microaperture. After irradiation, the ion-hit positions within the protoplasts were accurately determined by etching the CR-39 sheet in 13.4 M KOH solution at 27ºC for 9 hours. In preliminary results, the colony-forming rate of tobacco protoplasts was not reduced by the irradiation of 1 to 10 ^{12}C particles per protoplast.

CONCLUSION

Single-cell/single-particle irradiation methods have been developed using collimated energetic heavy-ion microbeams. In addition, a procedure for detection of an ion-hit track within the beam time has been established. With this microbeam probe, the radiation response in individual cells irradiated with high-LET heavy particles can first be analyzed in detail by single-cell assays, and then a cytomolecular biological analysis of irradiated cells can be performed. It was realized that microbeam is of critical importance in investigating biological influences of low-dose radiations as well as in its radiological application. Furthermore, radiomicrosurgery technique using heavy-ion microbeam will be applied for the elucidation of plant functions to develop the technologies for production of safe provisions and conservation of environment with plant.

REFERENCES

1) Zirkle, R. E. and Bloom, W. (1953) Irradiation of parts of individual cells. Science, **117**, 487-493.
2) Baker, C. P., Curtis, H. J., Zeman, W., and Woodley, R. G. (1961) The design and calibration of a deuteron microbeam for biological studies. Radiat. Res., **15**, 489-495.
3) Kraske, F., Ritter, S., Scholz, M., Schneider, M., Kraft, G., Weisbrod, U. and Kankeleit, E. (1990) Direct irradiation of mammalian cells by single charged particles with a given impact parameter. Radiat. Prot. Dosimetry, **31**, 315-318.
4) Weisbrod, U., Buecker, H., Horneck, G., and Kraft, G. (1992) Heavy-ion effects on bacteria spores: The impact parameter dependence of the inactivation. Radiat. Res. **129**, 250-257.
5) Braby, L. A. and Reece, W. D. (1990) Studying low dose effects using single particle microbeam irradiation. Radiat. Prot. Dosimetry, **31**, 311-314.
6) Nelson, J. M., Brooks, A. L., Metting, N. F., Khan, M. A., Buschbom, R. L., Duncan, A., Miick, R., and Braby, L. A. (1996) Clastogenic effects of defined numbers of 3.2 MeV alpha particles on individual CHO-K1 cells. Radiat. Res., **145**, 568-574.
7) Folkard, M., Vojnovic, B., Prise, K. M., Bowey, A. G., Locke, R. J., Schettino, G., and Michael, B. D. (1997) A charged -particle microbeam: I. Development of an experimental system for targeting cells individually with counted particles. Int. J. Radiat. Biol., **72**, 375-385.
8) Folkard, M., Vojnovic, B., Hollis, K. J., Bowey, A. G., Watts, S. J., Schettino, G., Prise, K. M., and Michael, B. D. (1997) A charged -particle microbeam: II. A single-particle micro-collimation and detection system. Int. J. Radiat. Biol., **72**, 387-395.
9) Randers-Pehrson, G., Geard, C. R., Johnson, G., Elliston, C. D., and Brenner, D. J. (2001) The Columbia University single-ion microbeam. Radiat. Res., **156**, 210-214.
10) Prise, K. M., Belyakov, O. V., Folkard, M., and Michael, B. D. (1998) Studies of bystander effects in human fibroblasts using a charged particle microbeam. Int. J. Radiat. Biol., **74**, 793-798.
11) Belyakov, O. V., Malcolmson, A. M., Folkard, M., Prise, K. M., and Michael, B. D. (2001) Direct evidence for a bystander effect of ionizing radiation in primary human fibroblasts. Br. J. Cancer, **84**, 674-679.
12) Zhou, H., Randers-Pehrson, G., Waldren, C. A., Vannais, D., Hall, E. J., and Hei, T. K. (2000) Induction of a bystander mutagenic effect of alpha particles in mammalian cells. Proc. Natl. Acad. Sci. USA, **97**, 2099-2104.
13) Zhou, H., Suzuki, M., Randers-Pehrson, G., Vannais, D., Chen, G., Trosko, J. E., Waldren C. A., and Hei, T. K. (2001) Radiation risk to low fluences of α particles may be greater than we thought. Proc. Natl. Acad. Sci. USA, **98**, 14410-14415.
14) Wu, L.-J., Randers-Pehrson, G., Xu, A., Waldren, C. A., Geard, C. R., Yu, Z.-L., and Hei, T. K. (1999) Targeted cytoplasmic irradiation with alpha particles induces mutations in mammalian cells. Proc. Natl. Acad. Sci. USA, **96**, 4959-4964.

15) Shao, C., Folkard, M., Michael, B.D. and Prise, K.M. (2004) Targeted cytoplasmic irradiation induces bystander responses, Proc. Natl. Acad. Sci. USA, **101**, 13495-13500.
16) Kobayashi, Y., Funayama, T., Wada, S., Furusawa, Y., Aoki, M., Shao, C., Yokota, Y., Sakashita, T., Matsumoto, Y., Kakizaki, T., Hamada, N. (2004) Microbeams of heavy charged particles. Biol. Sci. Space, **18**(4), 235-240.
17) Kobayashi, Y., Funayama, T., Wada, S., Taguchi, M. and Watanabe, H. (2003) Irradiation of single mammalian cells with a precise number of energetic heavy ions - Applications of microbeams for studying cellular radiation response. Nucl. Instr. and Meth. in Phys. Res. B, **210**, 308-311.
18) Funayama, T., Wada, S., Kobayashi, Y. and Watanabe, H. (2005) Irradiation of mammalian cultured cells with a collimated heavy-ion microbeam. Radiation Research, **163**(2), 241-246.
19) Shao, C., Furusawa, Y., Kobayashi, Y., Funayama, T. and Wada, S. (2003) Bystander effect induced by counted high-LET particles in confluent human fibroblasts: a mechanistic study. The FASEB J., **17**, 1422-1427.
20) Shao, C., Stewart, V., Folkard, M., Michael, B. D. and Prise, K. M. (2003) Nitric oxide-mediated signaling in the bystander response of individually targeted glioma cells. Cancer Res., **63**, 8437-8442.
21) Furusawa, Y., Aoki, M., Shao, C., Kobayashi, Y., Funayama, T., Sakashita, T. and Wada, S. (2004) Development of irradiation procedure to detect distance the signal transfer of GJIC bystander effect. JAERI-Review **2004-025**, 88-90.
22) Yokota, Y., Funayama, T., Kobayashi, Y., Sakashita, T., Wada, S., Hase, Y., Shikazono, N., Tanaka, A. and Inoue, M. (2003) Development of an ion microbeam system for irradiating single plant cell[s]. Biol. Sci. Space, **17**(4), 298-301.

MICROBEAM SYSTEM FOR HEAVY IONS FROM CYCLOTRON TO IRRADIATE LIVING CELLS

W. Yokota, Y. Ohara, K. Arakawa
Japan Atomic Energy Agency, 1233 Watanuki, Takasaki, Gunma 370-1292, Japan

Abstract

The study to elucidate cellular radiation response at low dose is being carried out at the ion beam facility of Japan Atomic Energy Agency using cyclotron beams of 5 to 10 μm spot in diameter formed with a collimating microbeam system. A smaller diameter down to 1 μm has become necessary with the progress of the study. In order to realize the required beam spot size, a focusing microbeam system using a quadruplet quadrupole magnet is being developed under supporting techniques which are the existing microbeam techniques developed for the electrostatic accelerators, reduction of cyclotron beam energy spread to minimize contribution of the chromatic aberration to focusing, and stabilization of cyclotron beam. A beam spot of about 2 μm in diameter is obtained at present. The paper reports the supporting techniques, the design of the focusing microbeam system, experimental results of microbeam formation and the near future plan.

INTRODUCTION

The ion beam irradiation facility in the Takasaki site of Japan Atomic Energy Agency (JAEA) was completed in 1993. The facility, named TIARA (Takasaki Ion Accelerators for Advanced Radiation Application), is an ion accelerator complex consisting of an AVF cyclotron, a 3MV tandem accelerator, a 3MV single-ended accelerator and a 400kV ion implanter. These accelerators are dedicated to studies on biotechnology and materials science [1] such as ion beam breeding of plant, single event upset (SEU) analysis of an LSI for a spacecraft and creation of new functional materials. The elucidation of cellular radiation response at low dose [2] is one of the world-leading research promoted at TIARA. In this study, single-ion hit is an essential technique which allows targeting a nuclear or a plasmid area of a living cell with spatial accuracy of the order of micrometer. Heavy ion beams at energies above a hundred MeV having high linear energy transfer (LET) are also necessary in the study. A microbeam system of collimating method was developed and is in use since 1998 at a vertical beam line of the AVF cyclotron in order to meet these requirements [2]. It forms a 5 μm or larger beam spot using a collimating aperture of 5 μm in diameter. The mechanisms of apoptosis and bystander effect are becoming understood using this system. However, the progress of the study requires a smaller beam spot down to 1 μm and faster targeting for single-ion hit. The collimating system cannot satisfy this requirement for the reason described later. Therefore the development of a new microbeam system of focusing method was strongly desired.

We have a technical backbone for the new microbeam system development, which is two microbeam systems for the electrostatic accelerators of TIARA developed in early 1990's. One is the heavy-ion microbeam system [3] installed in the tandem accelerator beam line for analysis of SEU of semiconductor devices for space environment. The other is a light-ion microbeam system [4] installed in the single-ended accelerator beam line mainly for PIXE analysis of, for example, 2-dimensional distribution of atomic elements in a cell. Each of them focuses the beams to a spot of 1 μm diameter or smaller with a doublet quadrupole magnet lens and is equipped with a single-ion hit and scanning device to allow precise and fast hit of single ions.

The development of a new focusing microbeam system for heavy ions from the cyclotron started in 2001. The major component of the system was installed in a vertical beam line and the test operation started in 2002. At the same time, a flat-top acceleration system was designed and installed in the cyclotron in order to reduce beam energy spread which was ten times as large as that of electrostatic accelerators and subsequently obstructed focusing to 1 μm because of chromatic aberration. The stability of cyclotron magnetic field is indispensable to maintain the small beam energy spread, steady beam trajectory and many other conditions of beams. The stabilization was realized by keeping temperature of the cyclotron magnet constant, and the field strength fluctuation $\Delta B/B$ is now regulated to about 1×10^{-5}. A number of microbeam formation experiments were carried out using 260-MeV Ne beam accelerated with the flat-top system, and the diameter of around 2 μm was constantly obtained in 2005.

MIROBEAM SYSTEMS FOR ELECTROSTATIC ACCELERATORS

The heavy-ion microbeam system of the 3 MV tandem accelerator was constructed mainly for the study of microscopic mechanism of SEU in a semiconductor device, which is most serious problem for electronics systems of a spacecraft in a long space mission. The SEU depends on a hit position on the microcircuit as well as on a mass and energy of a hitting ion. A single ion must hit exactly the aimed position of the microcircuit to observe the transient charge from an SEU. For this purpose, the heavy-ion microbeam system realized focusing to less than 1 μm spot size and positioning of single ion with accuracy within ±1μm.

The light-ion microbeam system of the single-ended accelerator was constructed for local element analysis of PIXE, RBS and NRA and study on irradiation effect of local area of semiconductor devices. It can provides a minimum beam spot size of 0.25 μm diameter for H^+ and He^+. A chromatic aberration is the most dominant limiting factor at this level of the beam spot size. Therefore a combination of a Schenkel DC high voltage generator and a high resolution beam analyzing system is adopted to provide the beam energy spread $\Delta E/E \sim 1 \times 10^{-5}$ in order to reduce the contribution of the chromatic aberration.

All the beam line components of each system are mounted on a set of rigid rectangular beams welded to each other to reduce relative movement and installed on massive plinths interleaved with rubber pads to isolate the system from building vibrations. The characteristics of the mirobeam systems are listed in Table 1. The both systems are equipped with a device consisting of a beam scanner and a beam shutter. The beam scanner is a fast electrostatic deflector which allows the accurate beam positioning. The beam shutter is triggered by signals of secondary electron from the target to shut out ions to further hit the target. Figure 1 shows a schematic picture of the device and phosphor distribution in a cell measured by means of PIXE with this system.

Table 1: Design parameters of the microbeam systems of the electrostatic accelerators.

	Heavy-ion microbeam system	Light-ion microbeam system
Accelerator	3 MV tandem	3 MV single-ended
Ion	Heavy ions	Light ions
Focusing lens Pole length Bore radius	Doublet quadrupole 120 mm 10 mm	Doublet quadrupole 80 mm 10 mm
Demagnification factor: x, y	4.6, 28	12, 60
Minimum beam spot size	1.0×1 μm^2	0.25×0.25 μm^2

DESIGN OF FOCUSING MICROBEAM SYSTEM

The following problems will be arise in forming 1 μm microbeam with the collimation method using a 1 μm aperture in diameter: 1) Beam intensity is reduced by the aperture to less than a tenth of that for the present collimating system with a 5 μm aperture. 2) Considerable portion of ions are scattered by the edge of the aperture and they can hit the target only millimeters away from the aperture. 3) Targeting speed is limited to about a few hit a minute because the target needs to be mechanically moved. In the focusing microbeam system, beam intensity is reduced by a object slit of larger diameter (5 μm in our case) installed a few meter upstream of the target and beams are magnetically or electrically scanned allowing very fast single ion hit more than 100/s.

The vertical beam line was selected for the new microbeam system as in the case of the collimating system in order to reduce problems associated with cell movement by gravity and the complexity for setting target in a horizontal system. The focal point of the microbeam was set at about 1.5 m above the bottom of the sunken floor for a sufficient space to set the experimental apparatuses such as a microscope and a sample stage (Fig. 2). Consequently the length of the beam line for the focusing microbeam system was set about 5 m between the focal point and the gate valve at the end of the existing beam line. The beam optics was calculated by use of TRANSPORT taking the second order aberration into account. The main parameters decided by the design are summarized in Table 2. It should be noted that the beam energy spread $\Delta E/E$ must be less than 2×10^{-4} to reduce the contribution of chromatic aberration which determines the limit of the minimum beam size. Therefore the cyclotron had to be modified to attain the required energy spread by means described in the next section.

The schematic view of the microbeam line [5] is shown in Fig.2. A heavy-ion beam from the cyclotron is deflected by 90 degrees with a bending magnet and lead into a vertical beam line. The slit system defines the object and the divergence of beams. The micro slits to form the object of 1 μm to 150 μm are composed of two wedged shape slits that cross perpendicularly to one

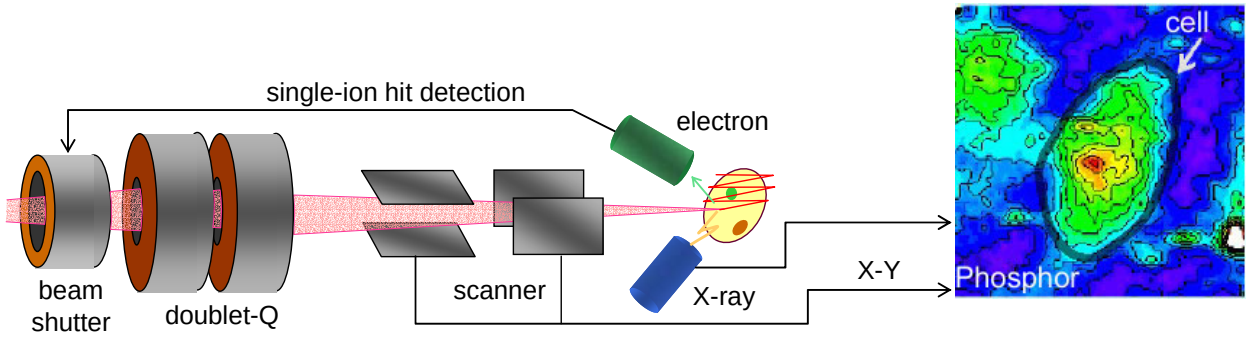

Figure 1: Schematic picture of the single-ion hit system for PIXE analysis and phosphor distribution in a cell.

another. The divergence defining slits are composed of four ordinary slit chips. The motion of each slit is remote-controlled by a stepper-motor-driven precision stage with a 0.5 μm positional resolution. In order to measure the beam profile and current passing through the slit systems, a beam monitor is installed after each slit, which consists of a beam viewer of CaF2 (Eu) scintillator and a Faraday cup mounted on a single diagnostic rod moved by a two-step pneumatic actuator. Each quadrupole magnets has a bore radius of 15 mm and mechanical pole length of 150 mm. The working distance is 300 mm resulting in the x- and the y-demagnification of 5. The assembly tolerance of 50 μm was set in manufacturing to reduce irregularities in the quadrupole field and the risk of geometrical misalignment of the magnet poles, or yokes, since there is no mechanism for adjusting relative position of each magnet. The magnet current supplies are stabilized to $\Delta I/I$ values of less than $\pm 1 \times 10^{-5}$ to maintain a stable beam sfocus. Air-core coils placed just above the first focusing element are used either to target the beam or to scan the beam over a 0.8 mm × 0.8 mm area of the sample for the most rigid beam from the cyclotron.

Table 2: Main parameters of the focusing microbeam system for the cyclotron

Ion	Heavy ions
Focusing magnet lens	Quadruplet quadrupole
Pole length	150 mm
Bore radius	15 mm
Demagnification factor: x, y	5.0, 5.0
Minimum beam spot size	1.0×1.0 μm^2
Chromatic aberration: x, y	71, 103 μm/mrad/%
Required beam energy spread	$\Delta E/E \leqq 0.02\%$

FLAT-TOP ACCELERATION SYSTEM OF CYCLOTRON

The energy spread $\Delta E/E$ of the beam accelerated by a conventional AVF cyclotron using a sinusoidal acceleration voltage wave is typically of the order of 10^{-3}. With this $\Delta E/E$ value, the minimum beam diameter obtained by focusing with a set of quadrupole magnets is limited to several μm due to contribution of the chromatic aberration. The energy spread can be reduced to the order of 10^{-4} in principle, for example, by defining the beam phase with a set of slits placed in a central region of the cyclotron. However, beam intensity enormously decreases down to impractical quantity for ion beam applications. In the flat-top acceleration method, a combination of the fundamental and the harmonic voltage wave forms homogeneous acceleration voltage as shown in Fig. 3. The energy can be reduced with this voltage without limiting usable phase width followed by large beam intensity decrease. The single-turn extraction is an indispensable condition to minimize the energy

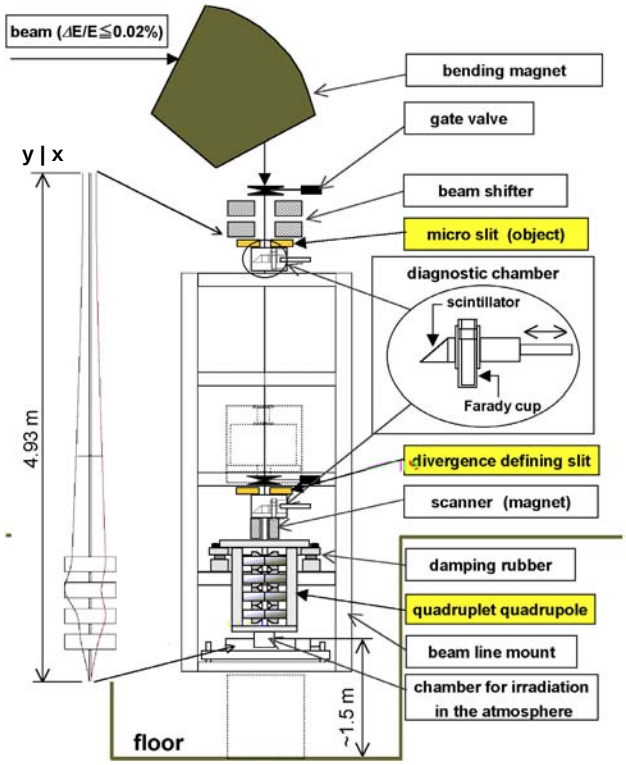

Figure 2: Schematic arrangement of the focusing microbeam line. Beam envelope is shown on the left side.

spread with this method since additional revolutions cause the increase in energy spread .

A flat-top acceleration system was first introduced to an AVF cyclotron at NAC (at the National Accelerator Center in South Africa) [6]. The NAC cyclotron is of a fixed frequency type and designed to make the single-turn extraction. On the other hand, the TIARA cyclotron [7] is of variable frequency covering 11 to 22 MHz for a wide range of energy and ion species, and beams are extracted by multi-turn extraction with the fundamental frequency alone. Therefore we can make the most of the advantage of the flat-top acceleration. The third or fifth harmonic of the fundamental frequency is generally used for the flat-top acceleration and the harmonic voltage wave is supplied by an additional resonator mounted on the fundamental wave resonator through a capacitive coupling. The amplitude of the harmonics wave, which leads to the best flat-top acceleration voltage wage, is estimated to be $1/N^2$ times the fundamental wave voltage, where N is the order of the harmonics. We selected the fifth harmonics to save output power of an amplifier. The fifth-harmonics frequency range is 55 to 110 MHz to fully cover the fundamental frequency range so as to be able to apply the flat-top acceleration to all the ion beams that can be accelerated by the TIARA cyclotron.

Figure 4 shows the beam current distributions in the beam extraction area comparing the case with and without the flat-top acceleration. They were measured with a beam current probe with a 0.5 mm thick sheet of tungsten which was scanned in the radial direction at the entrance of a pair of parallel plate electrodes, a beam extractor

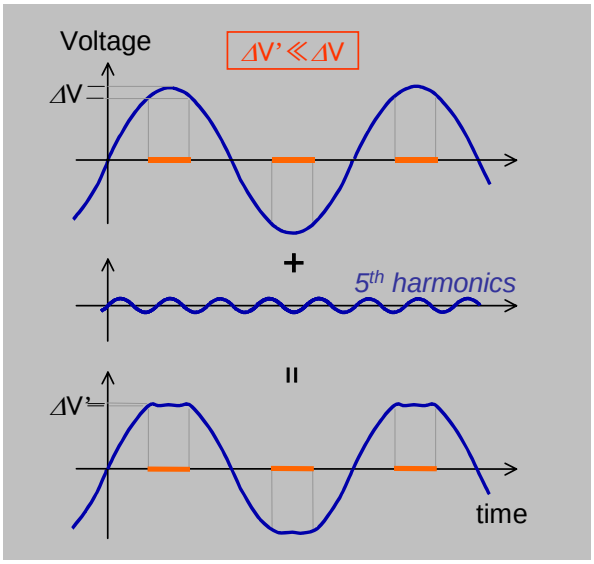

Figure 3: Flat-top acceleration voltage formed by superimposing a fifth harmonics on the fundamental voltage wave.

called 'deflector' [8]. Reduction of beam size in the radial direction by the flat-top voltage is clearly seen. Each separated peaks with the flat-top acceleration corresponds a individual turn and the outermost peak (seen at right end in Fig. 4) alone went into the deflector to be extracted by the single-turn extraction. The peaks are not separated around 50 mm of the probe position. This is due to a precessional motion of the beam revolution center. The beams of 260 MeV Ne and 45 MeV H are available with flat-top system now.

STABILIZATION OF CYCLOTRON MAGNETIC FIELD

Unstable cyclotron magnetic field causes various instabilities of accelerated ion beams. The acceleration phase drift of internal beam, change in the beam trajectory inside and outside the cyclotron, consequent beam intensity decrease due to the drop in the extraction efficiency are examples of the typical instabilities. From a historical point of view, stability of power supplies such as current supplies to the coils has been severely regulated. However, another essential factor contributing to the magnetic field instability, that is temperature of the magnet, has not been seriously taken into account. In the

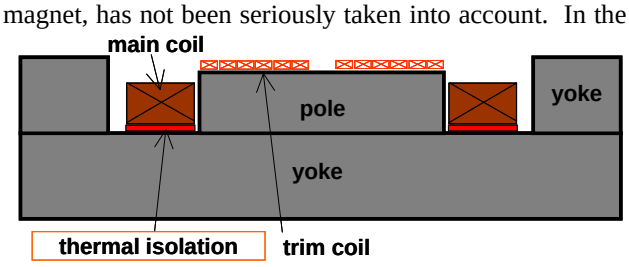

Figure 5: Arrangement of the yoke, the pole and the coils. The lower half of the cyclotron magnet is shown.

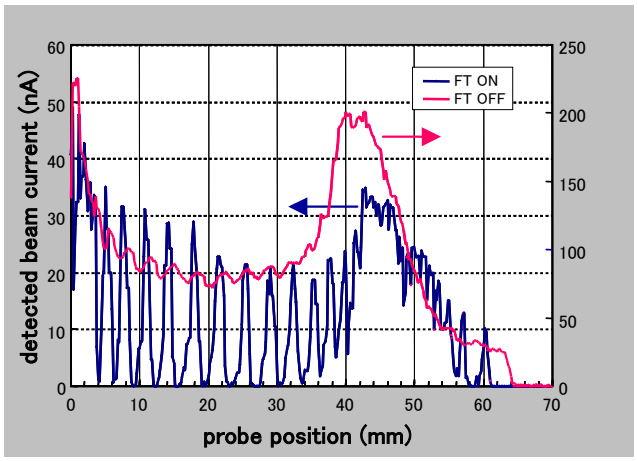

Figure 4: Turn separation of 260 MeV Ne beam measured at the entrance of the deflector electrodes comparing with and without the flat-top acceleration..

case of the TIARA cyclotron [9], we experienced a strong decrease of beam intensity for several years after it was completed. In the typical case of 195 MeV $^{36}Ar^{8+}$ acceleration at 820 A of the main coil current (1.6 T average magnetic field), beam current went down to zero in ten hours. The acceleration phase of internal beam drifted as well. We observed the temperature at 50 points of the cyclotron yoke surface and the magnetic field strength at about 800 mm radius for two years. It turned out, as a result, that the temperature of the yoke rose as high as 5ºC at the high main coil currents and it caused the change in the main magnetic field strength $\Delta B/B$ of the order of 10^{-4} resulting in the beam intensity decrease. The simulation using the thermal analysis code NASTLAN made clear the large heat conduction from the main coils to the yoke and the pole. The simulation also showed the remarkable effect of a thermal isolation between the coils and the yoke (Fig. 5). Figure 6 shows a example of calculated temperature distribution 50 hours after the cyclotron magnet is excited at the initial yoke temperature 25ºC. Without the thermal isolation (Fig. 6-a), which was the case in the original design, the heat generated by the main and the trim coils warms the whole

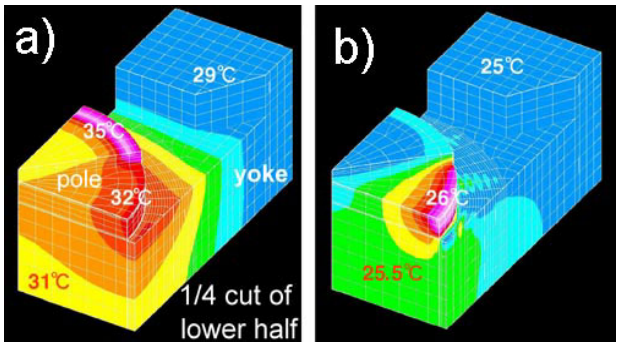

Figure 6: Simulated distribution of temperature 50 hours after magnet excitation started. A 1/4 part of the lower pole and the lower yoke is shown.

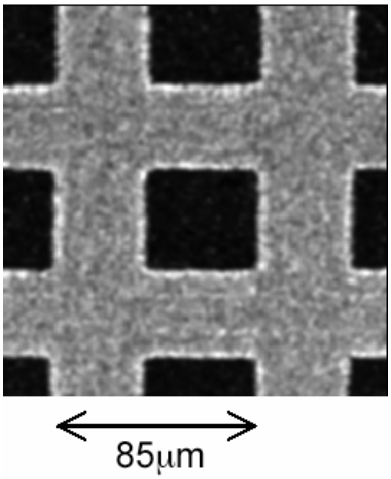

Figure 7: The secondary electron image of the copper grid. Black squares are spaces.

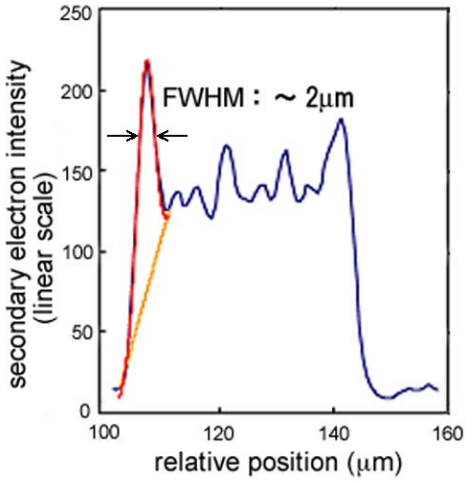

Figure 8: One dimensional distribution of secondary electron intensity across the grid. The beam spot size was estimated from a peak width at a grid edge.

magnet and the temperature considerably rises especially at a part of the yoke and the pole facing to the coils. On the other hand, with the thermal isolation (Fig. 6-b) of a plate with constant temperature of 25ºC between the yoke and the main coil, the temperature increase is reduced to less than a tenth. Taking these results into account, a water cooled plate with temperature kept at 25ºC was inserted between the main coil and the yoke, and the coil coolant temperature control was modified in order to regulate the temperature rise over the whole yoke to less than 0.5ºC. As a result, the change in the magnetic field strength $\Delta B/B$ has been reduced from 3×10^{-4} to about 1×10^{-5}, which is small enough for the steady flat-top acceleration.

MICROBEM FORMATION AND SIZE MEASUREMENT [10]

The beam of 260-MeV Ne accelerated with the flat-top acceleration system is used in the all experiments of microbeam formation. We used scintillators to observe beam spot for tuning and to measure the spot sizes in the early experiments to form microbeam. After achieving a 30 μm diameter, the beam size is measured with secondary electron image (SEM image) of a copper grid.

The microbeam is scanned two dimensionally on a copper grid at the focal point by the scanning coil magnets to measure the SEM images. The values of the scanning coil currents is used as X-Y position of the beam. The slit gaps and the quadrupole lens currents were adjusted so as to make the grid image as clear as possible under real-time observation of the image. The obtained grid image is remarkably sharp as shown in Fig. 7. The beam spot size was estimated from the width of the electron intensity peak at the grid edge (Fig. 8), and the smallest was below 2 μm. This is currently the smallest in the world for the cyclotron heavy-ion beams above a hundred MeV.

SUBJECTS AND NEAR FUTURE PLAN

The beam spot size around 2 μm was obtained using 260-MeV Ne beam in the successive five experiments carried out after November in 2004, and a 1 μm diameter is expected to be attained in next year or earlier. There are subjects to be solved before regular microbeam application will start in a few years. The trajectory and the intensity of the beam sometimes change suddenly or gradually with time. The beam spot size changed several hours after the focusing tune complete. Instability in the cyclotron magnetic field, the ion source plasma, acceleration voltage, etc. might cause the changes. Although the TIARA cyclotron is highly stabilized to $\Delta B/B\sim1\times10^{-5}$, higher stability may be required to solve the subjects by the severer yoke temperature control as well as the coil current stability of the order of 10^{-7}.

The test irradiation of the microbeam is planed to living cells in the atmosphere and to semiconductors in the atmosphere in early 2006. After achieving a 1 μm diameter, the development of a system of high speed automated cell recognition and high speed targeting will start, which will allow single-ion hits at rates higher than 100/s.

REFERENCES

[1] R. Tanaka, K. Arakawa, W. Yokota, Y. Nakamura, T. Kamiya, M. Fukuda, T. Agematsu, H. Watanabe, N. Akiyama, S. Tanaka, T. Nara, M. Hagiwara, S. Okada and M. Maruyama, Proc. 12th Int. Conf. on Cyclotron and their Applications, Berlin, Germany, edited by B. Martin and K. Ziegler (1989) 566

[2] Y. Kobayashi, “Study of cellular radiation response using heavy-ion microbeams”, this workshop

[3] T. Kamiya, N. Utsunomiya, E. Minahara, R. Tanaka and I. Ohdomari, Nucl. Instr, and Methods B64 (1992) 362

[4] T. Kamiya, T. Suda and R. Tanaka, Nucl. Instr, and Methods B104 (1995) 43
[5] M. Oikawa, T. Kamiya, M. Fukuda, S. Okumura, H. Inoue, S. Masuno, S. Umemiya, Y. Oshiyama and Y. Tairal, Nucl. Instr. Meth. B210 (2003) 54
[6] J. L. Conradie, A. H. Botha, J. J. Kritzinger, R. E. F. Fenemore, and M. J.Van Niekerk, Proceedings of the 14th International Conference on Cyclotrons and Their Applications, Cape Town, South Africa, edited by J. C.Cornell (1995) 249.
[7] M. Fukuda, S. Kurashima, S. Okumura, N. Miyawaki, T. Agematsu, Y. Nakamura, T. Nara, I. Ishibori, K. Yoshida, W. Yokota and K. Arakawa, Rev. Sci. Instr. 74 (2003) 2293
[8] S. Kurashima, N. Miyawaki, N. Miyawaki, I. Ishibori, K. Yoshida, H. Kashiwagi, M. Fukuda, T. Nara, T. Agematsu and Y. Nakamura, TIARA annual report 2004, in print
[9] S. Okumra, K. Arakawa, M. Fukuda, Y. Nakamura, W. Yokota, T. Ishimoto, S. Kurashima, I. Ishibori, T. Nara and T. Agematsu, Rev. of Sci. Instr. 76 (2005) 033301
[10] T. Satoh, M. Oikawa, T. Sakai, M. Fukuda, S. Okumura, S. Kurashima, N. Miyawaki and T. Kamiya, JAERI-Review 2004-25 (2004) 253

STABILIZATION OF STORED BEAM IN THE SPRING-8 STORAGE RING

H. Tanaka*, JASRI/SPring-8, 1-1-1, Kouto, Sayo-cho, Sayo-gun, Hyogo 679-5198, Japan

Abstract

Thorough suppression of perturbation sources has been carried out to stabilize stored beam in the SPring-8 storage ring. Consequently, quite high orbit stability: 4μm in horizontal and 1μm in vertical planes by a standard deviation was achieved without a fast orbit feedback system over a frequency region ranging from DC to 200Hz. This paper illustrates the process to achieve the present stability of the SPring-8 storage ring.

INTRODUCTION

Beam orbit stability is one of the most important issues for a light source, especially for a third-generation light source with small transverse beam sizes. In our case, the horizontal and vertical beam sizes are small, ~280 μm and several μm by a standard deviation, respectively at the source point of each standard insertion device (ID). Various efforts had thus being made to achieve good orbit stability. However, the achieved stability until the year of 2001 did not reach to a sufficient level, especially in a vertical plane because the beam orbit variation is generated by a complicated system that various kinds of perturbation sources are interrelated and widely distributed over the ring. This complex environment prevents us from finding out the main perturbation sources easily and also limits the effectiveness of countermeasures. To overcome this issue, it is essential that equipment, utility systems, beam controls, and a building structure, such all machine subsystems are re-investigated, improved and re-integrated from the total viewpoint of orbit stability. In this context, a project on beam orbit stabilization in the SPring-8 storage ring started aiming at sub-micron stability at the beginning of year 2001. Experts of all machine subsystems were gathered to form the project team for systematic and unilateral investigation of the problem. As a result of the elaborate and well-conducted investigation, the project team succeeded in reducing the orbit variation in a frequency region ranging from 1Hz to 100Hz. Activity of the project has still been playing an important role in further stabilization of the stored beam in the SPring-8 storage ring.

APPROACH TO ORBIT STABILIZATION

Our goal of the orbit stabilization is a sub-micron level. It would be impossible that such high stability can be achieved by only feedback-like system covering broad frequency-band from DC to a few hundred Hz. The Gain of such a system is generally limited at most to 20dB or so. This means that the orbit stability should be a micron level at least before introducing some feedback system. In SPring-8, we are trying to achieve the stability of a micron or less not by the feedback system but by the thorough source suppression as a first step. And then, some proper feedback correction should be installed to push the stability down to sub-micron level as a second step. This is our approach to realize the orbit stability of sub-micron level [1]. We stress here that conditioning; in other word exhaustive source suppression before installing the feedback system is the key for the ultimate stability.

STABILIZATION OF SLOW ORBIT DRIFT

Before starting the beam orbit stabilization project, our efforts were mainly focused on the source suppression of slow orbit drift.

Conservation of thermal equilibrium of magnets, girders, etc in machine tunnel

In the autumn of 1997 non-stop excitation of the main magnets between the operation cycles started to maintain thermal equilibrium of magnets, girders and power cables in the machine tunnel. This non-stop excitation effectively eliminates the slow vertical orbit drift over a few days at the beginning of each operation cycle.

Reduction of temperature variation of cooling water

From 1997 to 1998 temperature control of the cooling water system was improved to keep the temperature variation under 0.3 centigrade. The temperature variation causes the deformation of C-type bending magnets and mainly changes horizontal closed orbit distortion (COD) with a time scale from several to a few tens minutes [2].

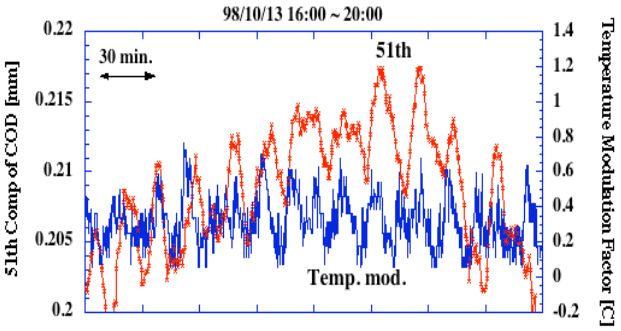

Figure 1: Correlation between the amplitude of tune harmonic of horizontal COD and temperature change of cooling water after the improvement.

By this improvement the variation of horizontal COD was suppressed in the corresponding frequency range. Figure 1 shows the correlation between the amplitude of

tanaka@spring8.or.jp

tune harmonic of horizontal COD and temperature change of cooling water after the improvement.

Improvement of COD correction system

In the autumn of 1998 the periodic COD correction started in the user operation to stabilize photon beam axes distributing over the ring [3]. The correction was performed every 5 minutes using regular horizontal and vertical steering magnets. The period was gradually shortened and it is now about 30 seconds to fix the photon axes precisely. Figure 2 shows the correction performance obtained in December 1998.

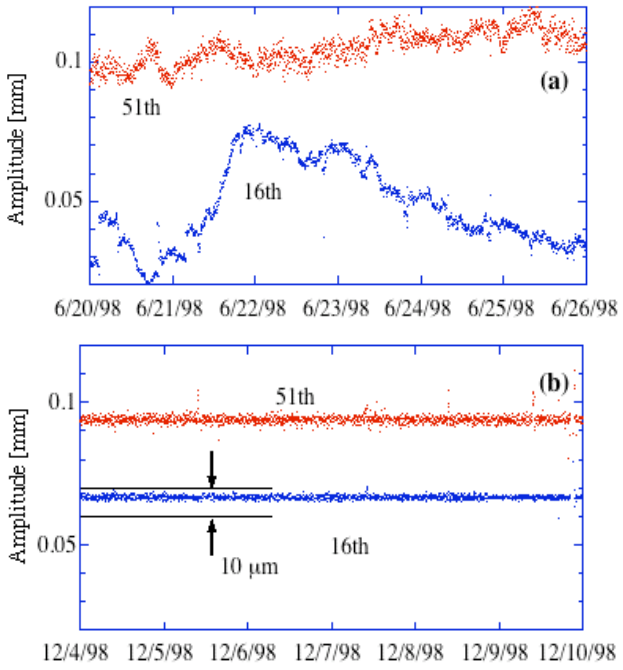

Figure 2: Horizontal (51st) and vertical (16th) tune harmonics of COD with (upper) and without (lower) periodic COD correction.

In the autumn of 1999 users found photon beam jumps correlating to the periodic correction. We thus started to improve the accuracy of the periodic COD correction. Main causes of this jump are the following two; the noise of beam position monitors (BPMs) used in the correction and a steering setting error due to limited resolution and steering magnet hysteresis. We firstly introduced averaging of several tens measured data to each BPM to improve the signal to noise ratio. By this averaging, the BPM reproducibility of a few microns was achieved [4, 5]. Continuously in the spring of 2000 we also installed hysteresis-free steering magnets of air-core type with high resolution (HPSTs) to suppress the steering setting error. The setting resolution was raised up to 0.1nrad. Owing to these improvements, the orbit jumps disappeared in the winter of 2000 as shown in Fig. 3. The number of HPSTs was increased by two steps from 12 to 48 for each plane in the autumn of 2004 to reduce the slow orbit drift over a long operation period [5].

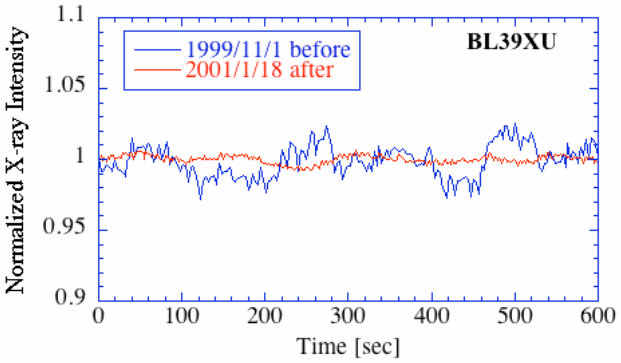

Figure 3: Variation of photon flux at BL35XU before and after improvement of the COD correction system.

Correction of interference between magnet and vacuum chamber

In the autumn of 1998 mechanical interference between one quadrupole magnet and the vacuum chamber was found by analysis of the orbit response against the step change of cooling water temperature [2]. Figure 4 shows the observed orbit response against the step change of temperature of the magnet cooling water. This interference was caused by the chamber modification to install the new beamline for experiments with GeV-photons and it was actually the source of horizontal orbit variation in combination with the temperature variation of the cooling water. To remove this source the chamber was scraped so as to generate sufficient clearance against the magnet yoke of the quadrupole in the winter of 1998. After this remedy, the unusual high sensitivity shown in Fig. 4 disappeared.

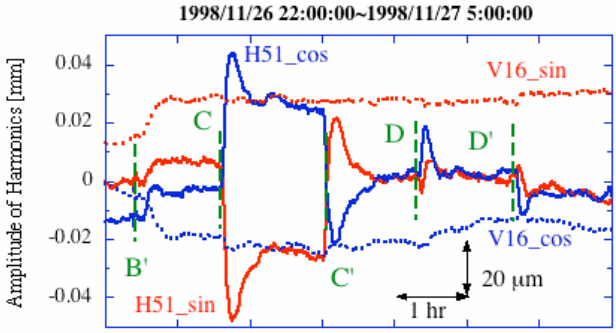

Figure 4: Observed orbit response against the step change of temperature of the magnet cooling water. The cooling water is supplied to the magnets by four cooling water loops, named by A, B, C and D. The response was measured by changing the temperature of each loop. The green perpendicular dashed lines with C and D represent the time starting step change of the temperature in zone C and D. The Green perpendicular dashed lines with B', C' and D' represent the time returning the temperature to the nominal value in the corresponding zone. This figure suggests that the sensitivity against the temperature change is markedly high in the zone C due to the interference.

Correction of circumference variation

In the summer of 2000, four magnet-free long straight sections were built in the storage ring by rearranging the magnets locally [6]. This lattice modification much increased the second order dispersion at insertion devices. Tidal movement changes the beam energy through the pseudo-periodic slow circumference variation. This energy change shifted the photon beam axes of insertion devices (IDs) installed in the linear dispersion-free straight sections due to the large second order dispersion [6]. In the winter of 2000, the correction of the circumference variation started to keep the beam energy constant and stabilize the photon beam axes along the ring. Figure 5(a) and (b) mainly show the RF frequency drifts caused by tidal movement (period ~12hr) and seasoning effect, respectively.

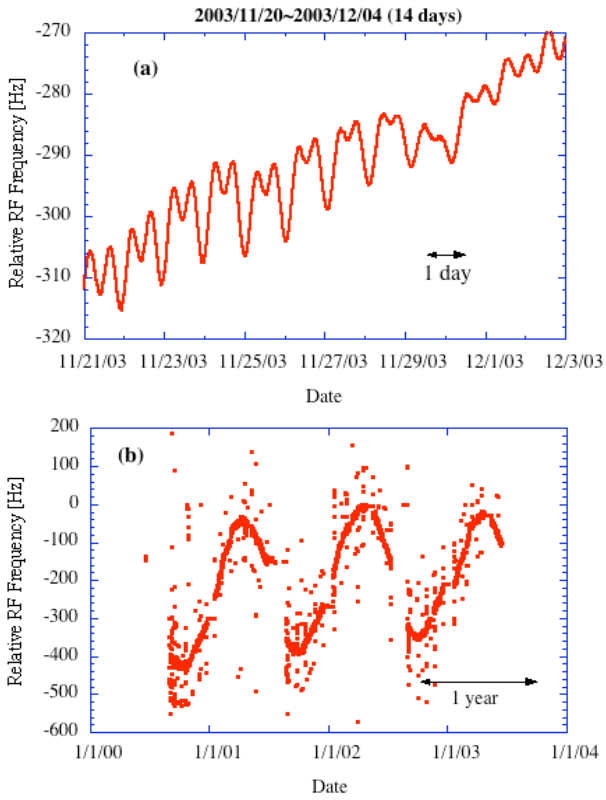

Figure 5: Observed RF frequency variation in keeping the store beam energy constant. Figure 4(a) shows the short-term change (6 days) clearly showing the circumference change by tidal movement and Figure 4(b) shows the seasoning change for about three years.

Correction of ID error field

Since the beginning of SPring-8 beam operation, we have been improving the accuracy of feed-forward correction table for gap and phase changes of each ID. Owing to this effort, here at SPring-8, the users can independently change energy and polarization of the photon beam at each beamline by changing parameters of each ID during their experiments. The orbit variation by each ID was suppressed below several microns at worst before the orbit stabilization project. However, as the number of IDs increased and various functions are equipped, the variation of ID error fields by changing their gaps or phases is one of the biggest perturbation sources during the user operation. In order to improve the accuracy of the correction table, a new scheme based on a real time synchronization-measurement system of electron and photon beam positions was developed [7]. Here, an idea of signal modulation is taken to precisely extract the orbit variation originating from the change of ID parameters [8-10]. Figure 6 shows a correction example of COD induced by a phase drive of ID23 (Apple II type undulator).

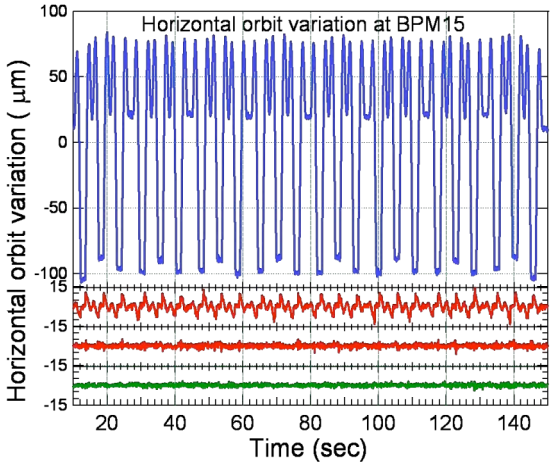

Figure 6: Correction example of COD induced by a phase drive of ID23 (Apple II type undulator installed at beamline #23 of SPring-8). The top, second, third and fourth figures show the CODs before the correction, with only the static correction, with full (static and dynamic) correction and background without the correction and phase drive, respectively.

Top-up operation

The top-up operation has been started for user-time since May 2004 [11]. This operation has an advantage on the orbit stabilization, because heat-load to vacuum components such as a crotch absorber is kept constant and consequently mechanical positions of BPMs are stabilized. Furthermore, since users can continue their experiments during the beam injection, large and coherent shifts of ID parameters, gap and phase disappear before and after the beam injection, which reduces the perturbation sources during the user time.

STABILIZATION OF FAST ORBIT VARIATION

As a result of extensive survey and study, we successfully found out the causes of the fast orbit variation and suppressed them by reducing the current ripple of quadrupole magnets [12] and suppressing the vacuum chamber vibration within the quadrupole magnets [13, 14]. The detail is described later.

Current ripple suppression of quadrupole magnet power supplies

It was known that the current ripple of quadrupole and sextupole magnets induces a vertical dipole field at around the center of the vacuum chamber [15]. This can be explained by the shape of the chamber cross-section which is symmetric vertically but asymmetric horizontally. An accurate current monitoring system with the resolution of 10^{-6} had thus been developed since January 2000 to investigate the current ripple for the power supply diagnosis and the orbit stability [16].

On the other hand, the storage ring lattice was modified in the summer of 2000 to install four magnet-free long straight sections. Before and after the modification, a load for each quadrupole power supply was changed due to decrease of the total number of the magnets. The tuned parameters of the current control module were no longer an optimum. We started to retune the parameters as well as to investigate the stability of power supplies for the quadrupole magnets (QPSs). Each QPS is composed of 12th phase (and 24th phase for only QP9) thyristor diodes and an active filter system with a reactor transformer. In the autumn of 2000 the thyristor firing-phase was retuned and phase detection circuit was modified in each QPS. By this improvement, the amplitude of the horizontal beam variation was much reduced in the frequency region ranging from DC to 10Hz as shown by the blue line in Fig. 7. Following this from January to May 2001, more accurate DCCT replaced previous one in each current stabilizing circuit to stabilize the output current.

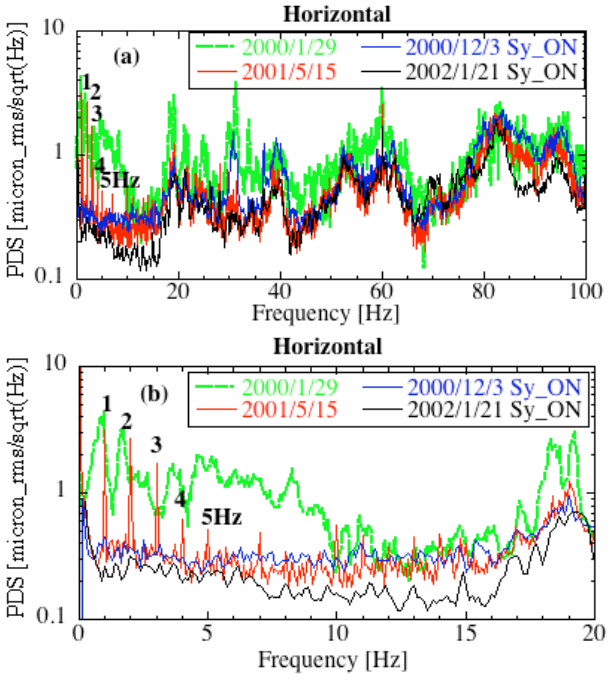

Figure 7: Change of power spectrum density of horizontal beam oscillation by improvement of magnet power-supplies. The upper (a) and lower (b) have only the difference in a horizontal scale.

However, even after this, the spikes of 1Hz and its higher harmonics were still observed in the horizontal spectrum during 1Hz pattern operation of the synchrotron as shown by the red line in Fig. 7. In order to prevent the induced noise in the AC400V input line from perturbing the output current, the thyristor phase control circuit was modified to improve its time response. As shown by the black line in Fig. 7, after this modification higher harmonics of 1Hz disappear in the horizontal spectrum even during the synchrotron operation. We see no significant change of vertical beam spectrum in this period as shown in Fig. 8. This is due to the symmetry of the vacuum chamber cross section and the current ripple mainly induces the vertical dipole field, i.e., the horizontal kick under the SPring-8 boundary condition.

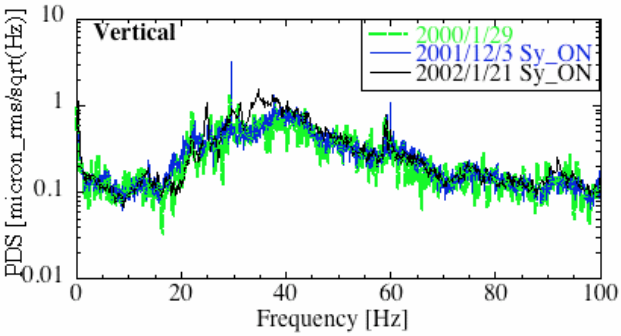

Figure 8: Change of power spectrum density of vertical beam oscillation by improvement of magnet power-supplies.

Suppression of the vacuum chamber vibration within quadrupole magnets

Through the spectrum survey of perturbation sources, we found a broad peak around 30Hz in the vertical vibration spectrum of a part of vacuum chambers, which is similar to that observed in the vertical beam spectrum. The chamber is located at the upstream of the first bending magnet in each unit cell. It is long and supported rigidly at only one side and is connected to an absorber. Owing to this mechanical structure, the chamber is easily vibrated by disturbance of the cooling water supplied to the absorber. We confirmed the clear correlation between the beam variation and the chamber vibration by the machine study in which the chamber vibration was changed by changing flow-rate of the cooling water. The correlated spectrum change was seen not only in the vertical beam spectrum but also in the horizontal one. As a result of detailed investigation of the chamber vibration, we found plural parts of the chambers excite the vertical orbit variation from 20 to 70Hz and horizontal one from 50 to 100Hz.

An ideal quadrupole field linearly depends on horizontal or vertical displacement from the field center. This means that the differential of the quadrupole filed is constant at any point. When the conductive thin and flat chamber shifts horizontally in the field, a constant vertical field change occurs in all small flat areas on the chamber,

which corresponds to just sudden excitation of a vertical dipole field through the flat chamber. Induced current in the chamber flows to cancel out this dipole and a resultant induced field kicks electron beam horizontally. In the case where real resistance is small, the induced current flows to cancel out the field change completely. The horizontal or vertical chamber shift generates an equivalent field change to that induced by the same shift of the quadrupole field center [13]. In the SPring-8 case, the chamber is made of thick aluminum and the resistance is low compared with a thin stainless steel chamber. This condition actually enhances effects of chamber vibration within the quadrupole magnets on the beam.

May 2002, to suppress the chamber vibration at the upstream of the first bending magnet in each unit cell, following three measures were taken; (1) addition of support, (2) exchange valves from grove to needle type and (3) reduction of cooling water flow-rate [13, 17]. After this, the vertical peak was drastically reduced as shown by the cyan line in Fig. 10. The horizontal beam variation was also reduced in the range from 70 to 100Hz as shown in Fig. 9. In the summer of 2002, the remained parts with the larger vibration were improved with the same manner. The orange lines in Figs. 9 and 10 show respectively the horizontal and vertical beam spectrums after the modification. We see the horizontal beam variation was suppressed in the range from 50 to 70Hz.

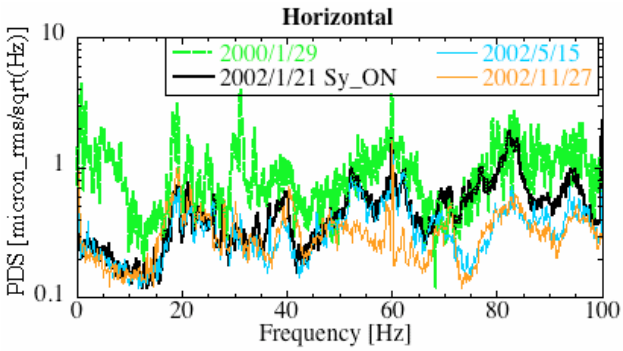

Figure 9: Change of power spectrum density of horizontal beam oscillations by suppression of vacuum chamber vibration.

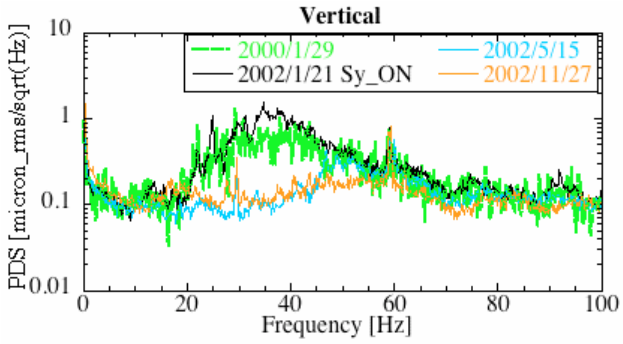

Figure 10: Change of power spectrum density of vertical beam oscillations by suppression of vacuum chamber vibration.

Figures 11 and 12 show respectively the horizontal and vertical beam orbit variations measured by the same system as used for the beam spectrum. We see that the countermeasures reduce the horizontal and vertical fast orbit variations respectively to about half and one forth.

To suppress the remaining peaks, efforts have been continued with help of 3D structure analysis. New additional supports have been added one by one by estimating the reduction effect of the support comparing the measured result with the simulation one [18].

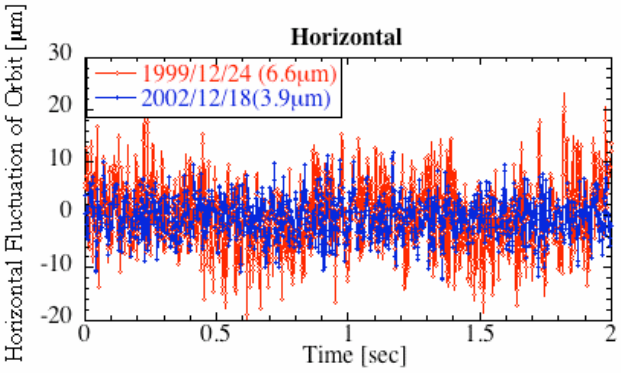

Figure 11: Comparison between horizontal beam variations before and after the countermeasures.

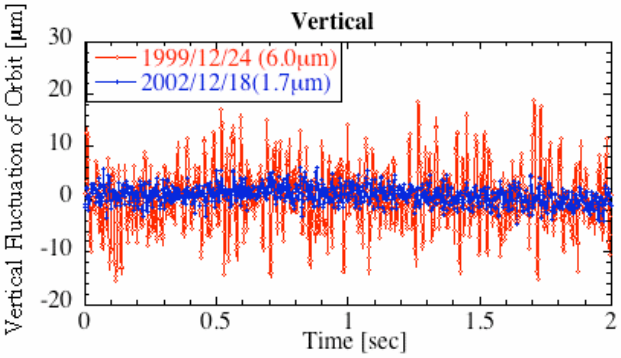

Figure 12: Comparison between vertical beam variations before and after the countermeasures.

Suppression of coherent synchrotron oscillation

As for the suppression of the fast horizontal orbit variation in dispersive sections, a coherent synchrotron oscillation at around 2kHz was corrected by the frequency modulation of the reference RF generator [19]. As shown in Fig. 13, this correction loop reduced the amplitude of the forced oscillation by 20dB and its peak disappears when the correction loop works.

Fast Orbit Correction

To achieve the fast and precise COD correction, fast sampling and low noise dedicated electronics for BPM has been developed [20]. New system will be introduced in 2007.

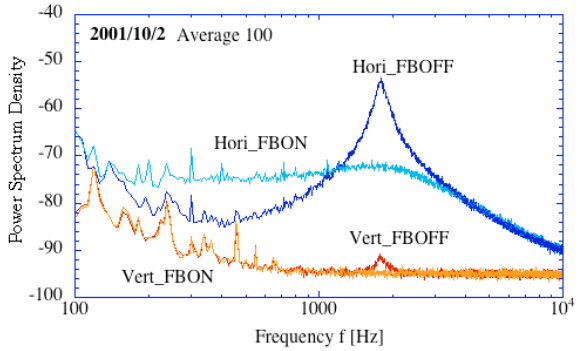

Figure 13: Measured power spectrum density of beam oscillation with and without feedback of coherent synchrotron oscillation. The characters "FBON" and "FBOFF" denote measurement with and without the feedback.

ACHIEVED BEAM ORBIT STABILITY

The present beam orbit stability is summarized [21] in Table 1. Since the vertical beam size (~5 μ m @Low emittance optics of ~3nmrad) is much smaller than the horizontal one (~280 μ m @Low emittance optics of ~3nmrad) at each standard ID source, The further orbit stability is necessary in the vertical plane for efficient use of the sharp photon beam.

Table 1: Present beam orbit stability at ID source point

	Horizontal (rms.)	Vertical (rms.)
Fast(0.1~200Hz)	~4μm	~1μm
Slow(<0.1Hz)	1~2 μm/week	2~3 μm/week

Figure 14 and 15 show the recent beam power spectra and rms. amplitudes (square root of power spectrum integrated by frequency) integrated from 200Hz to the DC direction.

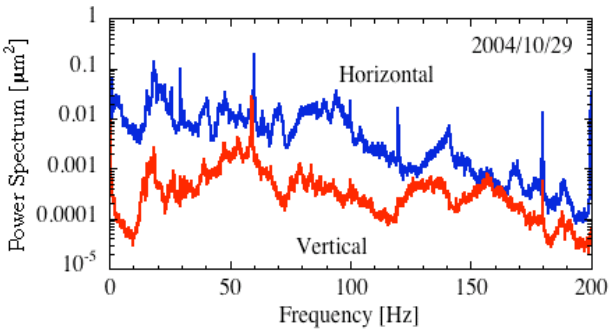

Figure 14: Power spectrum of horizontal and vertical beam oscillations.

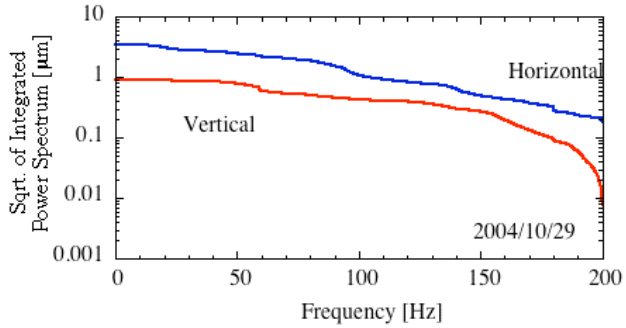

Figure 15: Rms. amplitude integrated from 200Hz to the DC direction. The data of Fig. 13 were used.

Figure 16 shows comparison between orbit drifts for decay and top-up modes introduced since May 2004. It is clear that the orbit jumps before and after the beam injection disappears due to top-up operation. Before the introduction of top-up, beam refilling is scheduled once a day for multi-bunch filling and twice a day for several bunch or hybrid (multi-bunch beam train + several single bunches). The manual orbit correction is performed at the every scheduled beam refilling.

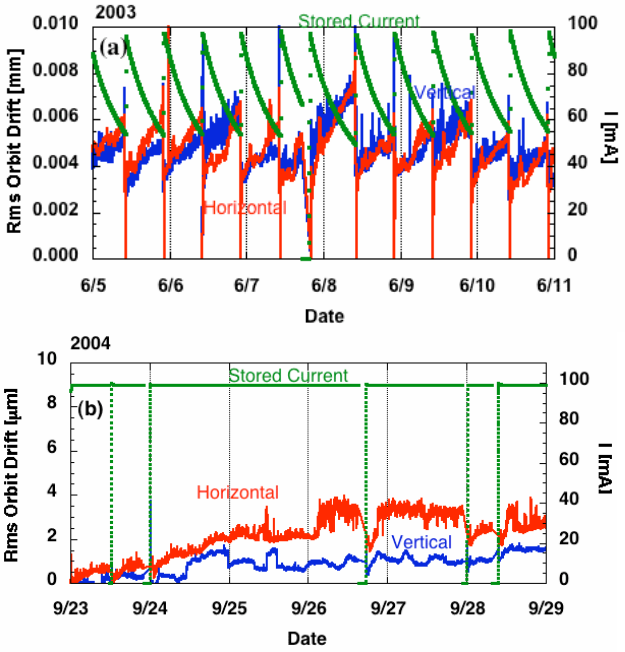

Figure 16: Comparison between orbit drifts for decay (a) and top-up modes (b).

By adjusting RF frequency the stored beam energy has been stabilized under the variation of ~2×10^{-5} in full width. Fig. 17 shows the typical energy stability for the user operation over 5 days. We see the RF frequency change, the red line in the figure reflects the tidal movement of which period is about half a day [22].

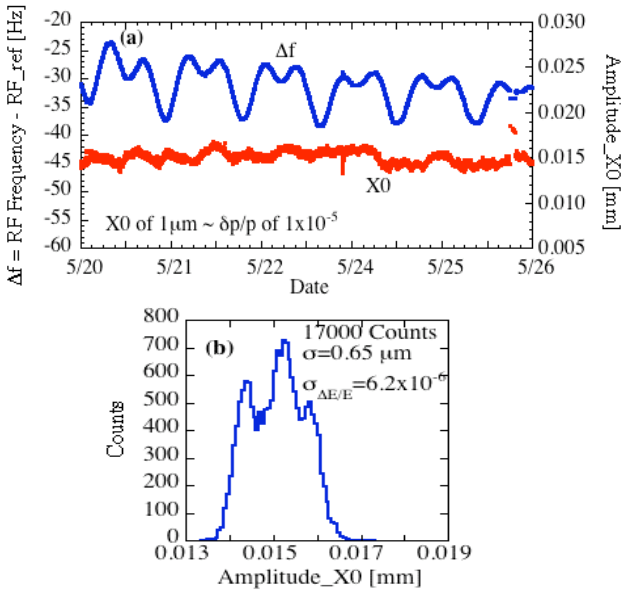

Figure 17: Typical energy stability for the user operation over 5 days. Fig. 17(a) shows changes of RF frequency and amplitude of DC component of COD measured by about 280 BPMs. The amplitude of 1 μ m corresponds to $1x10^{-5}$ by δp/p. Fig. 17(b) shows statistical distribution of the measured amplitudes of DC component in Fig. 17(a).

REFERENCES

[1] H. Tanaka, "*Orbit Stabilization at SPring-8*", presented in the 2nd International Workshop on Beam Orbit Stabilization 2002, SPring-8, Hyogo, Japan, December 2002.

[2] K. Kumagai et al., "*Beam Orbit Distortion Caused by Temperature Fluctuation of Cooling Water at SPring-8 Storage Ring*, Proc. of the 12th Symposium on Accelerator Science and Technology, Wako, 1999, p.420.

[3] H. Tanaka et al., "*Orbit Stabilization in SPring-8 Storage Ring*", Proc. of the 1999 Particle Accelerator Conference, New York City, 1999, p.2340.

[4] S. Sasaki, private communication.

[5] K. Soutome, "*Slow Orbit Correction in the SPring-8 Storage Ring*", presented in the 2nd International Workshop on Beam Orbit Stabilization 2002, SPring-8, Hyogo, Japan, December 2002.

[6] H. Tanaka et al., "*Beam Commissioning and Achieved Performance of SPring-8 Storage Ring Phase-2 Lattice with Four Magnet-Free Long Straight Sections*", Nucl. Inst. and Meth., A486, 521 (2002).

[7] T. Nakatani et al., "*Application of PC Based Off-the-Shelf Measurement System*", presented in the 4th International Workshop on Personal computers and Particle Accelerator Controls, Frascati, Italy October 2002.

[8] T. Matsushita et al., "*Analysis of the Orbit Distortion Caused by SPring-8 ID23 Using the Wavelet Transformation*", Journal of the Japanese Society for Synchrotron Radiation Research, Vol. 15, No. 5, 37 (2002). (In Japanese)

[9] H. Tanaka, et al., "*Scheme for Precise Correction of Orbit Variation Caused by Dipole Error-Field of Insertion Device*", presented in the 3rd International Workshop on Beam Orbit Stabilization2004, Hotel Kirchbül, Grindelwald, December 6-10th (2004).

[10]T. Nakatani et al, "*Scheme for Precise Correction of Orbit Variation Caused by Dipole Error-field of Insertion Device*", Rev. Sci. Instrum. Vol. 76, 055105 (2005).

[11]H. Tanaka et al., "*Top-up Operation at SPring-8 - Towards Maximizing the Potential of a 3rd Generation Light Source*", Proc. of the 9th European Particle Accel. Conf., Lucerne, 2004, p.222.

[12]H. Takebe, "*Magnet Power Supply Stabilization and Checking System Development*", presented in the 2nd International Workshop on Beam Orbit Stabilization 2002, SPring-8, Hyogo, Japan, December 2002.

[13]S. Matsui et al., "*Orbit Fluctuation of Electron Beam due to Vibration of Vacuum Chamber in Quadrupole Magnets*", Jpn. J. Appl. Phys. Vol. 42, L338 (2003).

[14]T. Nakazato et al., "*Observation of Beam Orbit Fluctuation with Forced-Vibrating Magnets and Vacuum Chambers*", Proc. of the 2nd International Workshop on Mechanical Engineering Design of Synchrotron Radiation Equipment and Instrumentation, ANL, Argonne, USA, September 2002, p.147.

[15]Takebe et al., http://sp8sun.spring8.or.jp/~takebe/mag/Chamber-Ripple/Chamber-Ripple.html

[16]Takebe et al., http://acc-web.spring8.or.jp/~takebe/mag/QP-Kaizo/mon-sys.html

[17]S. Matsui and M. Oishi, "*Orbit Fluctuation of Electron Beam due to Vibration of Vacuum Chamber in Quadrupole Magnets*", presented in the 2nd International Workshop on Beam Orbit Stabilization 2002, SPring-8, Hyogo, Japan, December 2002; http://acc-web.spring8.or.jp/~oper/iwbs2002/pdf/4-Q2-1.pdf (presentation by Matsui), http://acc-web.spring8.or.jp/~oper/iwbs2002/pdf/4-Q2.pdf (presentation by Oishi)

[18]T. Yorita, "*The optimization for the reduction of the vacuum chamber vibration via structure analysis*", presented in the 3rd International Workshop on Beam Orbit Stabilization'04, Hotel Kirchbül, Grindelwald, December 6-10th (2004).

[19]T. Ohshima and N. Kumagai, "*Suppression of Coherent Synchrotron Oscillation of the SPring-8 Storage Ring*", Proc. of the 2001 Particle Accelerator Conference, Chicago, 2001, p.1975.

[20]S. Sasaki, "*SPring-8 Closed Orbit Feedback System, A Challenge for Suppression of the Closed Orbit Vibration Down to Sub-micron Level*", presented in the 2nd International Workshop on Beam Orbit Stabilization 2002, SPring-8, Hyogo, Japan, December 2002

[21]H. Tanaka, "*Present Status of Orbit Stabilization at SPring-8*", presented in the 3rd International Workshop on Beam Orbit Stabilization'04, Hotel Kirchbül, Grindelwald, December 6-10th (2004).

[22]S. Daté and N. Kumagai, "*A Long-Term Observation of the DC Component of the Horizontal COD in the Storage Ring of SPring-8*", Nucl. Inst. and Meth. A421, 417 (1999).

Summary of Laser-wire Mini Workshop

G. A. Blair
Dept. of Physics, Royal Holloway, Univ. of London, Egham, Surrey. TW20 0EX. UK

A summary is presented of the laser-wire mini workshop held as part of Nanobeam 2005. Topics that were covered include machine optics studies of the ILC diagnostics section, simulation of laser-wires in the ILC beam delivery system, the development of pulsed laser stacking plus applications, a laser interferometer in an optical cavity, fast laser-wire scanning with electro-optics, and status reports on the ATF and PETRA laser-wire systems.

1. INTRODUCTION

The latest in a series of laser-wire (LW) mini workshops [1] was held during Nanobeam 2005. Talks were on:

- optics studies of the ILC diagnostics section (D. Angal-Kalinin),
- simulation of the LW in the ILC beam delivery system (BDS) and systematic errors (G. Blair),
- the development of pulsed laser stacking plus applications (N. Sasao),
- a laser interferometer with an optical cavity and cavity beam position monitors (BPMs) (J. Urakawa),
- fast laser-wire scanning with electro-optics (A. Bosco) [2]
- status report on the ATF laser-wire (N. Delerue) [3]
- status report on the PETRA laser-wire system (M. Price) [4].

2. SUMMARY OF PRESENTATIONS

2.1. Laser-wires in the Emittance Measurement Section of the ILC

The current proposal for the ILC emittance measurement section in the BDS has β_y ~34 m, giving σ_y ~ 0.8 μm at 500 GeV centre of mass energy, assuming the extracted emittance from the damping ring, or σ_y ~ 1.1 μm for the budgeted emittance. A LW system would thus need to be able to make an accurate measurement of ~1 μm electron spot-sizes, which is the central goal of an ongoing R&D project at the ATF extraction line [3]. However, as discussed below, the systematic errors involved in extracting the electron bunch size from the LW scan mean that larger electron sizes of order 3 μm are preferred (assuming green light), if measurement accuracies of order a few percent are needed. This would require increasing the 60m diagnostics section, shown in Figure 1, to about 480m for the damping ring emittance (i.e. ideal low-emittance transport) or about 200m for the budgeted emittance. The trade-off of diagnostics system length against the accuracy of the emittance measurement is a topic currently under study for the ILC Reference Design Report (RDR). In addition to providing a sufficiently large electron spot size, the machine optics must also enable the LW signal (Compton scattered photons and/or electrons) to be extracted cleanly. Two designs are currently being investigated, one based on a chicane [5] and another based on a dog-leg [6].

- The chicane contains many dipoles and the beam comes back on axis. The total length is 111m and the emittance growth at 500 GeV CMS is ~1% . The chromatic aberrations are negligible

- The dog-leg solution contains a few dipoles and quadrupoles. The beam is offset at the exit and the length is 122m. The emittance growth at 500 GeV CMS is ~0.16%. There are some small chromatic aberrations.

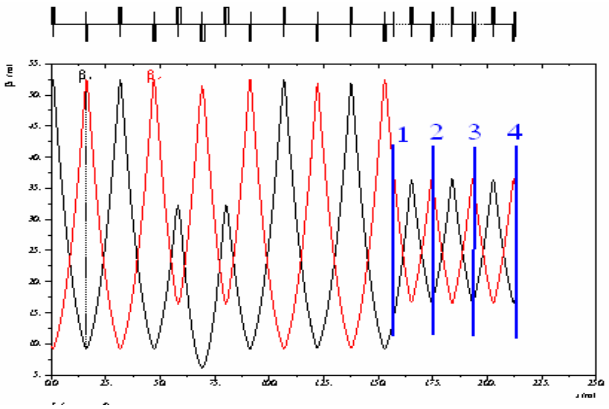

Figure 1. Proposed optics for the ILC emittance measurement section.

The chicane or dog-leg solution could be incorporated as part of a fast-extraction system for machine protection, where any significant energy offset of the beam at the exit of the linac, as measured in the chicane, could trigger a fast extraction kicker.

2.2. Laser-wire Systematic Errors and Simulation

A raw LW profile measurement, σ_m, is a convolution of the electron bunch size σ_e and the laser spot-size σ_ℓ. In the approximation of neglecting the Rayleigh range effects of the laser waist $\sigma_m^2 = \sigma_\ell^2 + \sigma_e^2$. The systematic error from the laser beam profile can then be estimated [7]: define $r \equiv \sigma_\ell / \sigma_e$ and $\delta \equiv \delta\sigma/\sigma$ with the subscripts e, m, ℓ referring to the electron bunch, the measured raw profile, and the laser spot respectively. The electron bunch error is then $\delta_e = \sqrt{\delta_m^2 (1+r^2)^2 + \delta_\ell^2 r^4}$ so $r = \sqrt{\delta_e/\delta_\ell}\left[1 + O\left((\delta_m/\delta_e)^2\right)\right]$. If δ_e <~2.5% (for a 5% emittance measurement) and $\delta_\ell \approx 0.1$, then there results the requirement that $\sigma_e >\sim 2-3\sigma_\ell$. Achieving small laser spot-sizes is therefore essential because the necessary length of the BDS diagnostics section is proportional to the β-function, which in turn is proportional to σ_e^2.

Simulations of the LW in the ILC BDS are ongoing; Figure 2 (left) shows the electron and photon distributions downstream from the LW, whose detection is needed to perform the profile scan. The photons can be extracted cleanly at a single point. Other considerations include the synchrotron radiation (SR) from the chicane and the resulting SR photon energy distribution is shown in Figure 2 (right); for a bunch of 10^{10} electrons, this would result in 1.8×10^7 GeV of SR energy per bunch, to compare with about 10^5 GeV from the LW Compton photons. This SR radiation consists of low energy photons compared to the high energy LW Compton photons; however the large amount of total SR power means that appropriate shielding in front of the LW detector will be necessary.

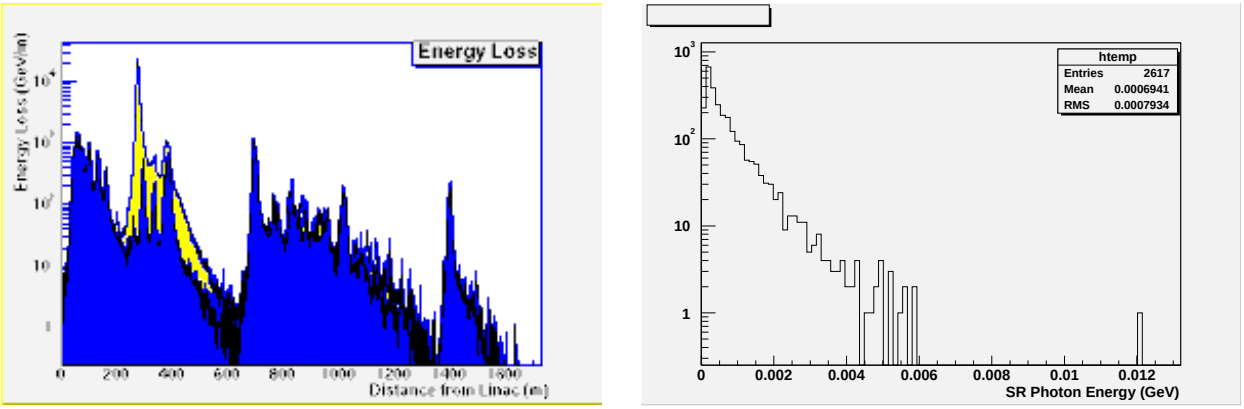

Figure 2. Left: energy escaping the beam-line downstream of the LW from the Compton scattered electrons (blue/dark grey) and photons (yellow/light grey). Right: SR radiation from the chicane; this energy will also enter the LW detector, unless appropriate shielding is included.

2.3. ATF Damping Ring Laser-wire

The LW at the ATF damping ring has been in operation for several years [8]. The system uses a CW laser amplified by an optical cavity at the LW interaction point. Two such cavities exist, one for the vertical scan and one for the horizontal. Results of these scans are shown in fig.3 (left and centre).

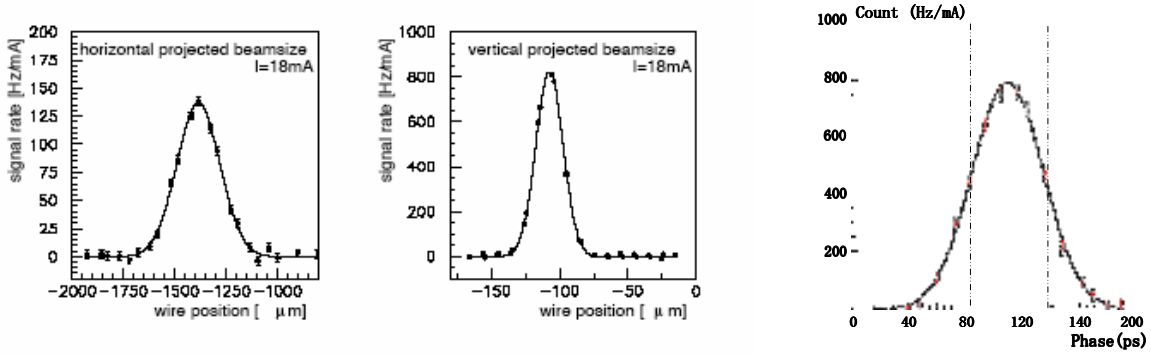

Figure 3. Left and centre: transverse LW scans at the ATF damping ring. Right: Longitudinal phase-scan.

A more recent development [9] is the measurement of the longitudinal bunch profile using a pulsed laser and accurate timing. The laser pulse width is 7 ps, which is very much less than the electron bunch length of ~28 ps. Two methods are employed:

- phase-scan method, where the laser frequency is synchronized with the e^- beam so that the relative timing (phase) is fixed. The signal is measured against the overall timing, which is varied with a trombone. Results of such a scan are shown in Figure 3 (right).
- Phase-sense method, where the laser is run freely run and, for each event, the laser-and-RF relative phase are measured.

The current laser beam waist size (w_0=10 μm) is close to the vertical e^- beam size at the ATF, so the spatial resolution must be improved. One method employed at the ATF is to use higher transverse modes of the laser as shown in Figure 4 (left and centre). A result of the scan is shown in Figure 4 (right); using this method, with the size of the central dark region of the TM01 laser waist tailored to match the beam size, the resolution was improved by a factor of about 3.

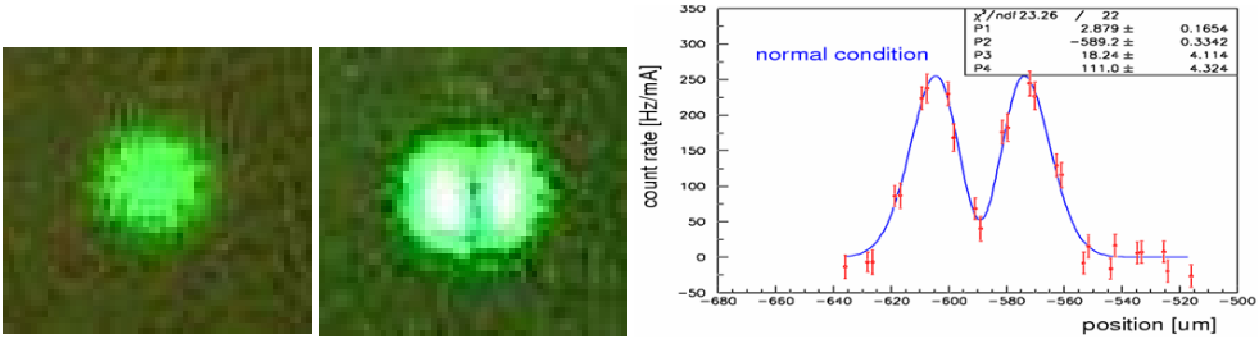

Figure 4. Left: theTEM00 used in the scans shown in Figure 3. Centre: the laser TEM01 mode. Right: profile scan using the TEM01 mode.

A new proposal [10] is to create an interferometer in an optical cavity, which could be a backup system for the Shintake monitor. In this scheme, a short laser pulse is generated by many longitudinal waves that are completely mode-locked; a 7ps pulse width requires 200 longitudinal modes in the case of a 714 MHz repetition rate. The length of the LW optical cavity has now been changed from 84cm to 42cm to match the 741 MHz mode-locked laser. The specification of the laser is 800mW, 7 ps pulse width (FWHM) and 0.4 ps (rms) timing jitter. The first step will be to confirm that interference is taking place, the second step will be to move the interference pattern by a phase shift by using a mover-table. Once these goals have been achieved, the system will be installed in the ATF damping ring. Future plans are to design the chamber, which includes the vertical 42cm optical cavity and is attached with an upstream and a downstream cavity BPM. The two BPMs can measure the beam orbit with an accuracy of a few nano-meters. The laser wavelength will be changed from 1064 nm to 532 nm (Green).

2.4. ATF Extraction Line Laser-wire

As discussed in Sec. 2.2, a key challenge for the LW is to measure electron bunch sizes of ~1 μm. This issue is being addressed head-on at the ATF extraction line where a high-power pulsed green laser light will be focused down to measure an electron bunch with $\sigma_y \sim 1$ μm. This has required the development of low f-number optics; a final focus preliminary system has been designed to be f/1.3 and a future upgrade to f/1 is planned. More details are given in [3].

2.5. PETRA Laser-wire

A high-power pulsed LW system has been in operation at the PETRA accelerator [11] and a screen-shot from a representative LW scan is shown in Fig.5 (left). The laser used is a ~5 MW Q-switched system and each entry in the plot in Fig.5 (left) is the Compton signal from a single laser shot. The scans are performed by moving the laser spot using a mirror on a piezo-driven mount. The signal fluctuations are believed to be due to the multiple longitudinal modes of the laser; an upgrade is planned to an injection-seeded Q-switched laser system which should reduce these fluctuations considerably. In addition, a vertical breadboard plus optics mounted on stepping-motor drives have been installed in the PETRA tunnel to enable both vertical and horizontal scans using the same laser system as shown in Figire 5 (right). More details of this system can be found in [4].

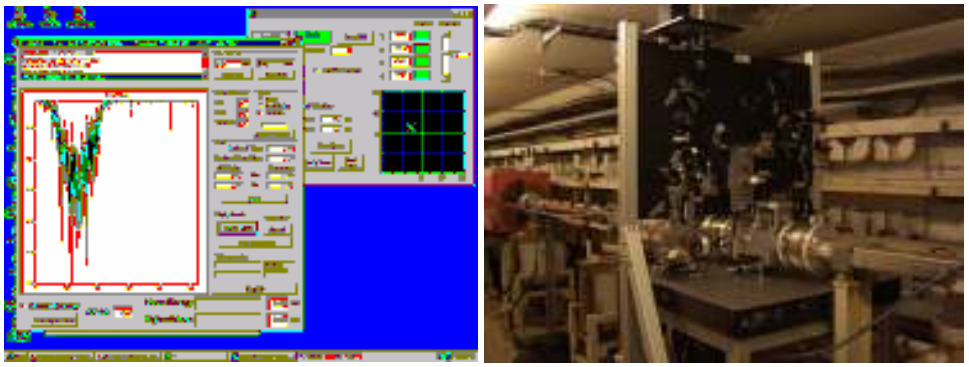

Figure 5. Left: LW scan of the vertical beam dimension at PETRA using original (horizontal) system. Right: New vertical system installed at PETRA that will allow both vertical and horizontal LW scans.

3. SUMMARY

Laser-wire R&D is ongoing at several test facilities world wide. Dedicated projects at exist at PETRA at DESY, and two projects at the ATF at KEK. LW techniques give rise to a variety of applications. The use of a LW as a beam size monitor has already been established as shown above, however there is still R&D required to produce faster monitors with better spatial resolution. An example of such R&D was presented [2] where an ultra-fast scanning system based on electro-optic crystals is being explored. Additional LW applications include X-ray sources (and many proposals exist) and also tertiary beam sources such as of positrons or neutrons. The technologies are challenging and R&D efforts have only just started.

Ackowledgments

All participants of the laser-wire mini-workshop are thanked for their contributions. Work supported in part by a Royal Society Joint Project with Japan, the Daiwa foundation, the JSPS, the PPARC LC-ABD Collaboration, and by the Commission of European Communities under the 6th Framework Programme Structuring the European Research Area, contract number RIDS-011899.

References

[1] LBBD website: http://www.pp.rhul.ac.uk/~lbbd

[2] A. Bosco *et al.*, these proceedings.

[3] N. Delerue *et al.*, these proceedings

[4] C. Driouichi *et al.*, these proceedings.

[5] M. Woodley, Snowmass 2005.

[6] D. Angal-Kalinin, Snowmass 2005.

[7] G. A. Blair, proc. Snowmass 2005.

[8] Y. Honda *et al.* Nucl.Instrum.Meth.**A538:**100-115,2005.

[9] N. Sasao, this workshop.

[10] J. Urakawa, this workshop.

[11] J. Carter *et al.*, Proc. PAC05, arXiv:physics/0508137.

SUMMARY ON BEAM DELIVERY SYSTEM DESIGN AND INTERACTION REGION

D. Angal-Kalinin, ASTeC, Daresbury Laboratory, WA4 4AD, UK

S. Kuroda, KEK, 1-1 Oho, Tsukuba-shi, Ibaraki, Japan

A. Seryi, SLAC, Stanford, CA 94309, U.S.A.

Abstract

This report summarises the session WG2a : "Beam Delivery System Design and Interaction Region" of the Nanobeams 2005 workshop. The major topic of discussion during this session was the progress on the International Linear Collider (ILC) Beam Delivery System (BDS) lattice design since the Snowmass workshop. The progress on the nonlinear collimation system for CLIC was also discussed.

INTRODUCTION

The baseline configuration recommended for the ILC has two interaction regions. One of the interaction regions (IR) has a large crossing angle (20 mrad), providing possibility of γ–γ collisions while the other IR has a very small crossing angle (2 mrad), providing advantages of almost head-on collision. The designs of both these interaction regions and the extraction lines were discussed in details during the Snowmass workshop [1,2]. This working group discussed the design progress between the Snowmass and this workshop. In particular, the design of intermediate crossing angle of 14 mrad, use of anti-DID, the civil engineering layout details to upgrade one IR to two IRs were main discussion topics. The large crossing angle needs crab cavities with very tight phase tolerances to reach the design luminosity and the status of crab cavity system design after snowmass was discussed. The high power ILC beam can be very destructive and thoughts as per how to design the fast abort system were presented. To abort the high power beam in a best possible way needs well thought scheme, which was discussed during this session.

The non-linear collimation system developed for CLIC uses skew sextupoles to blow up the vertical beam size at the spoilers, so as to guarantee collimator survival in case of beam impact. Optics of this scheme and its properties were discussed.

ILC CROSSING ANGLE

Though the large crossing angle design has an advantage of a simpler beam line and lower extraction beam loss because of independent incoming and extraction optics, this scheme requires the use of crab cavity correction, increases the synchrotron radiation emittance growth in the detector solenoid and increases photon backscattering from the forward calorimeter of the detector. To reduce these effects, 14 mrad design was discussed in details during the session [3]. A new quadrupole scheme near the interaction point has been proposed which allows a reduction of the crossing angle to 14 mrad. This design is based on the 20 mrad design and the new quadrupole scheme near the interaction point. The design maintains the advantage of separate extraction lines, a simpler optics and lower losses in the extraction line. The synchrotron radiation emittance growth in the solenoid and the photon backscattering from the forward calorimeter of the detector are reduced. With the use of the anti-DID correcting field these detector backgrounds can be as small as in the 2 mrad case. The details of the optimisation of large crossing angle IR, where specially shaped transverse field of the detector integrated dipole can be reversed and adjusted to optimise trajectories of the low energy pairs, so that their majority would be directed into the extraction exit hole [4]. Civil engineering details of upgrade path from single to two IRs with different crossing angles was discussed [5].

Revised collimation depths for the 2 mrad design were described and the immediate plan of beam loss comparison using BDSIM and DIMAD was discussed [6].

In case of large crossing angle, it is necessary to rotate the bunches using crab crossing to re-cover the loss in luminosity. The status of the crab cavity system development was discussed [7], which described the required tight phase tolerances for the ILC crab cavities and the issues for the proposed 3.9 GHz Fermilab CKM deflecting cavity.

FAST ABORT SYSTEMS

The ILC beam is potentially very destructive and a fast beam abort system is essential as part of the machine protection strategy. Kicker reference designs for the ILC with full linac aperture and limited aperture were presented [8]. It is best to design the kicker, septum, optics and physical components of both the normal and aborted beam lines as a unit, including the possibility of modifying the optics and component design on the normal beam line to reduce the difficulties of the abort system. The details described in this paper for the kicker pulse, power, aperture, efficiency and the cost optimisation provides a good guideline for the design of fast abort system.

NON-LINEAR COLLIMATION FOR CLIC

The collimation scheme for CLIC should sustain the impact of off-energy bunches and have a large chromatic bandwidth, in addition to ensuring a high collimation efficiency and tolerable wake fields. The non-linear energy collimation system for CLIC [9] use skew sextupoles to blow up the vertical beam size at the spoiler. The properties of such system are evaluated and

compared with those of the baseline linear collimation system. Two new optics designs were developed and optimised, one with a high filling factor of dipole magnets and the other without any dipoles between the two main skew sextupoles. The optics performance without dipoles is better.

REFERENCES

[1] Y. Nosochkov for the SLAC-BNL-UK-France task force, presented at the Snowmass ILC workshop 2005, Snowmass, USA (2005)
[2] Y. Nosochkov, et al, presented at the Snowmass ILC workshop 2005, Snowmass, USA (2005)
[3] Y. Nosochkov, et al, "ILC extraction line for 14 mrad crossing angle", These proceedings.
[4] A. Seryi, et al, "IR optimisation, DID and Anti-DID", These proceedings.
[5] A. Seryi, et al, "BDS civil layouts and upgrade path from single IR to two IRs", These proceedings.
[6] D. Angal-Kalinin, et al, "Update on 2 mrad crossing angle extraction line for the ILC", These proceedings.
[7] P. Goudket, et al, "Status of the crab cavity system development for the ILC", These Proceedings.
[8] T. Mattison, "Thoughts on fast beam aborts for the International Linear Collider", These Proceedings.
[9] A. Faus-Golfe, et al, "Alternative optics design : Nonlinear collimation system", These proceedings.

WORKING GROUP 2B SUMMARY: STABILISATION AND FEEDBACK

P.N. Burrows, Queen Mary, University of London, UK.

INTRODUCTION

We summarise the proceedings of Working Group 2b, dedicated to the issues of stabilisation and feedback of nanobeams. The submissions to the sessions were as follows:

- *Ground Vibration Measurements and Site Comparison*: R. Amirikas, A. Bertolini, W. Bialowons, H. Ehrlichmann.
- *Simulations of ILC intra-train feedback system and beam-delivery*: Glen White.
- *Integrated linac/BDS beam feedback system simulations*: Linda Hendrickson, Glen White.
- *Active stabilisation of a future linear collider final focus quadrupole mock-up*: C. Adloff , Y. Bastian, B. Bolzon, F. Cadoux, N.Geffroy, C. Girard, A. Jeremie, Y. Karyotakis, L.Brunetti , F. Formosa, J. Lottin.
- *Prototyping and beam tests of beam-feedback hardware for ILC collision optimisation*: G. Christian.
- *BPM support system for nanometer resolution beam monitoring*: Y. Honda.
- *Results of Optical Anchor R&D at University of British Columbia*: T. Mattison.

These can be grouped into common thematic areas:

1. Vibration measurements and site comparisons.
2. Active component stabilisation: inertial techniques, and optical interferometry.
3. Beam-based feedback systems.

These will be briefly reviewed and summarised.

1. VIBRATION MEASUREMENTS AND SITE COMPARISONS

R. Amirikas described [1] the characterisation of 18 sites around the world in terms of their ground motion properties. The effort was performed by the same team, using the same equipment and identical data analysis techniques. This provides a common framework for the accurate relative comparison between the ground-motion properties of each of the sites. Two complementary sets of instruments were deployed for this purpose: broadband seismometers which measure acceleration, and a geophone system which measures velocity. Datasets were taken continually over long periods and discrete Fourier transforms were taken to obtain the power spectrum density as a function of frequency, within the range roughly 0.01 Hz to 100 Hz. The power spectrum was then integrated above a cutoff frequency to obtain the r.m.s. vertical displacement vs. frequency. An example (from Ellerhoop, near DESY) is shown in Figure 1.

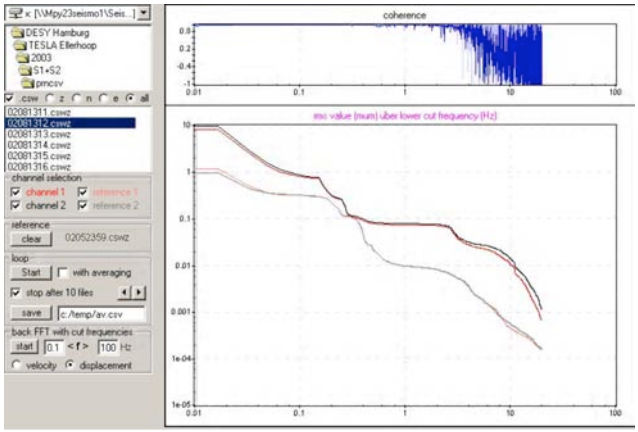

Figure 1: Example of integrated ground-motion spectrum.

Systematic study was made of the day/night and weekday/weekend difference in characteristics, as well as systematic differences between different sites, for example comparison of surface and deep sites. As expected the noisiest conditions pertain at surface sites during weekdays, and the quietest conditions at deep sites at weekends, when cultural noise sources are reduced. Under the best conditions the vertical motion can be as small as 1nm r.m.s., but the situation can be over 100 times worse at less favourable sites.

An attempt was made to develop a model of cultural noise, taking the following into account:

- Mechanical model of the ground in response to road and rail traffic.
- Numbers of vehicles and their damper characteristics.
- Unevenness of the street/tracks and distance of these sources form the site.
- Soil parameters.

The results are impressive at the qualitative level (Figure 2). This activity is ongoing and will provide vital input to the International electron-positron Linear Collider (ILC) site characterisation and selection process.

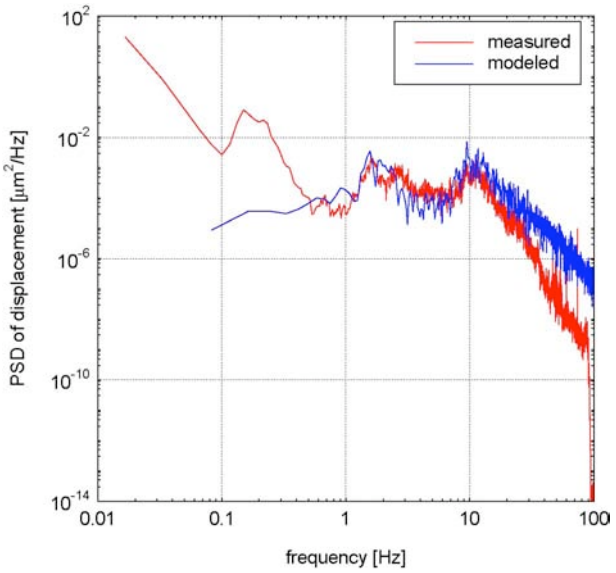

Figure 2: Example of modelling of cultural noise [1].

2. ACTIVE COMPONENT STABILISATION

INERTIAL STABILISATION

B. Bolzon described the active stabilisation programme that is being pursued at Annecy [2]. This ambitious effort comprises:

- Measurement of sensor characteristics, ground vibrations and structural vibrational modes of test objects.
- A modal analysis and interpretation of the structural properties in terms of a model of the object's internal vibrational characteristics.
- Understanding of the dynamic response of the test object to externally driven vibrations.
- Modification of the dynamic response properties via optimised design.
- Application of feedback to damp the object vibrations.

The obvious potential applications of such techniques are to active stabilisation of critical components of accelerator systems, for example the stabilisation of the relative vertical positions of the final-focus magnets in the electron and positron beamlines of the ILC final-focus system.

A system comprising a cantilevered metal beam has been studied in some detail [2], Figure 3. Resonances induced by excitation of the beam have been studied in a modal analysis using finite-element analysis techniques. A dynamics response model was constructed and yields impressive agreement with the data, Figure 4. It was attempted to damp some of the resonant frequencies using piezo actuators in a feedback loop; 6 frequencies could be rejected.

The next step is to develop a model of the ILC final-focus quadrupole design, perform a modal analysis of the resonant frequencies and propose improvements in the design in order to reduce the vibrational tendencies. Since the ILC quadrupoles will likely be mechanically complex superconducting magnets, comprising a cold mass, cryostat, associated supports, beampipe, flanges, pipes, bellows etc. this could prove a challenging enterprise.

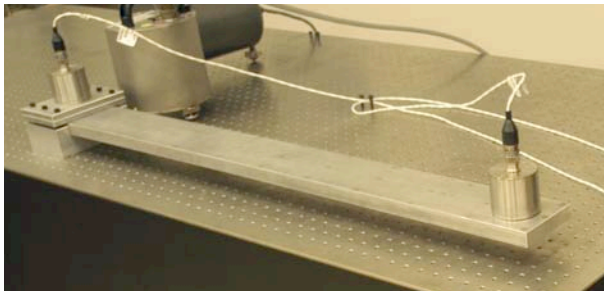

Figure 3: Cantilevered beam test system for active stabilisation studies [2].

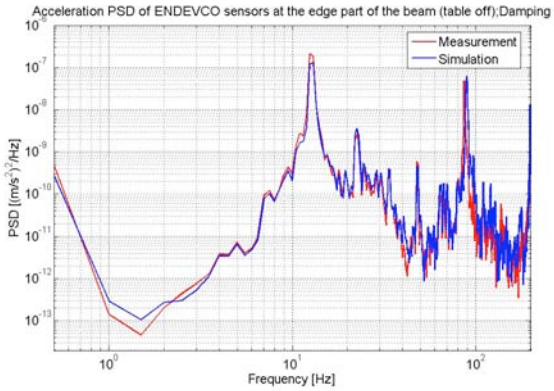

Figure 4: Dynamic response of cantilevered beam: comparison of data and simulation [2].

OPTICAL INTERFEROMETRY

T. Mattison described [3] an alternative scheme for possible stabilisation of the ILC final-focus quadrupoles. This is based upon optical interferometry. The concept involves monitoring of a Michelson interference pattern between laser beams reflected from the quadrupoles on the electron and positron beam sides of the final focus, Figure 5. In principle actuators can be used in a feedback loop to compensate for the relative motion.

At Nanobeams 2002 Mattison reported stabilisation of an interferometer mirror on the ground to sub-nanometre

accuracy [3]. A 10kg test mass was stabilised to the level of 5nm (on the ground) and about 1nm (on an isolated table). A number of problems have since been addressed and a better understanding gained of the performance and limitations of this test system. However, the performance of the feedback is comparable with that reported in 2002. This is believed to be due to noise caused by the 'push-back' of the actuators on the reference mirror via the external mechanical frame [3]. This illustrates the difficulty of implementing a mechanical feedback system for even very simple objects in a controlled environment. Such objects and environments are considerably simpler than the final quadrupole magnets and their engineering environment in the ILC final focus.

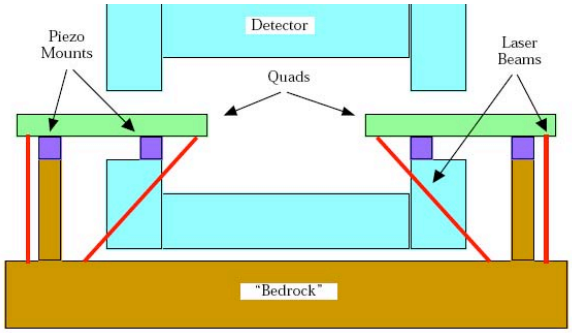

Figure 5: Optical anchor stabilisation concept [3].

Y. Honda described a stabilisation scheme for the KEK cavity 'nanoBPM' system [4]. The design is illustrated in Figure 6. An optical interferometer distance meter monitors the vertical displacement of each of the three BPMs with respect to a rigid reference bar. Stiff movers based on elastic hinges driven by piezo actuators provide the motion correction. The system is being assembled and commissioned and results can be expected at future Nanobeam conferences.

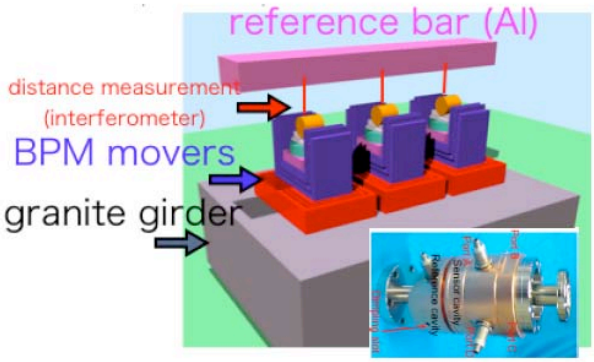

Figure 6: KEK cavity nanoBPM stabilisation concept [4].

3. BEAM-BASED FEEDBACK SYSTEMS

A number of fast beam-based feedback systems are required at the ILC. At the interaction point (IP) a very fast system, operating on nanosecond timescales within each bunchtrain, is required to compensate for residual vibration-induced jitter on the final-focus magnets by steering the electron and positron beams into collision. A pulse-to-pulse feedback system is envisaged for optimising the luminosity on timescales corresponding to 5 Hz. Slower feedbacks, operating in the 0.1 – 1 Hz range, will control the beam orbit through the Linacs and Beam Delivery System (BDS).

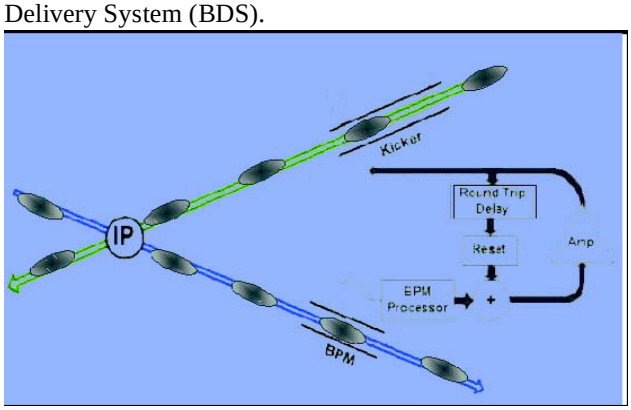

Figure 7: Schematic of IP intra-train feedback system for an interaction region with a crossing angle. The deflection of the outgoing beam is registered in a BPM and a correcting kick applied to the incoming other beam.

The key components of each such system are beam position monitors (BPMs) for registering the beam orbit; fast signal processors to translate the raw BPM pickoff signals into a normalised position output; feedback circuits, including delay loops, for applying gain and taking account of system latency; amplifiers to provide the required output drive signals; and kickers for applying the position (or angle) correction to the beam. A schematic of the IP intra-train feedback is shown in Figure 7, for the case in which the electron and positron beams cross with a small angle.

SIMULATIONS

G. White reported on simulations of the intra-train feedback performance, as well as on the work of L.Hendrickson on the linac and BDS 5Hz orbit feedbacks [5]. The long-term aim of this programme is the development of a dynamic integrated beam transport/feedback simulation for the whole ILC from the damping-rings to the IP, including the effects of ground motion and wakefields. Simulation of the process of beam-based alignment of the BDS quadrupole and higher-order magnets has also started [5].

The most critical correction is in the vertical axis at the IP, where the 5nm-sized electron and positron beams must be steered into collision. Figure 8 shows the performance of the IP intra-train position and angle feedback system in restoring near-nominal design luminosity within the first 100 bunch crossings.

FONT HARDWARE PROTOTYPES

Feedback On Nanosecond Timescales (FONT) is a collaboration between UK academic groups (Oxford, Daresbury) and the ILC Group at SLAC with the purpose of prototyping and testing IP feedback components. Two rounds of earlier tests have taken place (FONT1, FONT2) with the 65 MeV electron beam at the NLC Test Accelerator (NLCTA) at SLAC. At NLCTA the train length was c. 170ns, and an ILC-like intra-train feedback system was demonstrated with a latency of 54ns and a correction ratio of 14/1.

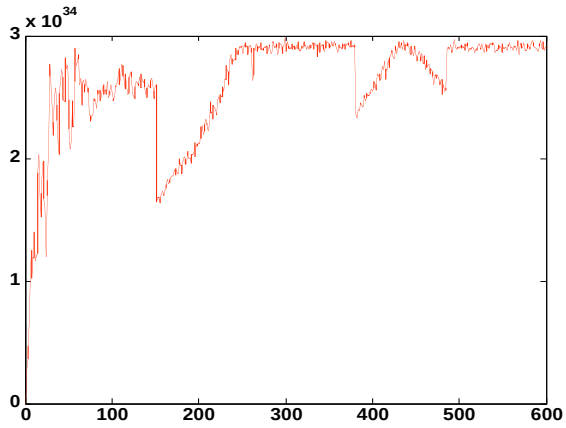

Figure 8: ILC intra-train feedback recovery of luminosity [5].

G. Christian reported [6] on beam tests of the latest prototype, FONT3, which we operate at the Accelerator Test Facility extraction line at KEK. The current bunchtrain comprises up to 20 electron bunches separated by 2.8ns with a beam energy of c. 1.3 GeV. The total train length of 56ns presents a severe challenge for an intra-train feedback system.

A schematic of the experimental configuration in the ATF beamline is illustrated in Figure 9. The layout is functionally equivalent to the ILC intra-train feedback system. An upstream dipole corrector magnet can be used to steer the beam so as to introduce a controllable vertical position offset in stripline BPM ML11X. A signal processor and a feedback circuit provide a correction signal to drive the adjustable-gap stripline kicker so as to steer the beam back into nominal vertical position. BPMs ML12X and ML13X serve as independent witnesses of the beam position. The experimental setup in the extraction line is illustrated in Figure 10. The amplifier power and BPM resolution are the same as those required for the IP feedback system at the ILC.

The system performance with beam is illustrated in Figure 11 [6]. A total latency for correction of 23ns was achieved, with c. 10ns being due to speed-of-light signal propagation delays. Although the FONT3 analogue technology could be deployed at ILC, the longer bunch interval and large number of bunches allow for a digital approach to signal processing, and hence the implementation of more sophisticated feedback algorithms.

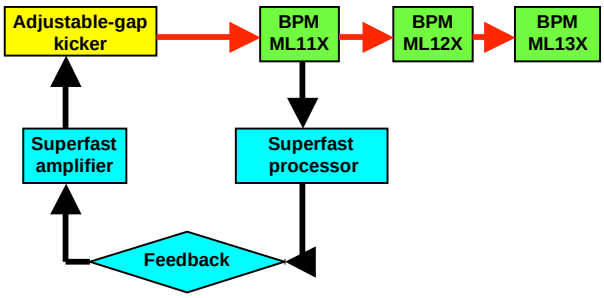

Figure 9: Schematic of the ATF beamline showing location of the kicker, BPMs and feedback system.

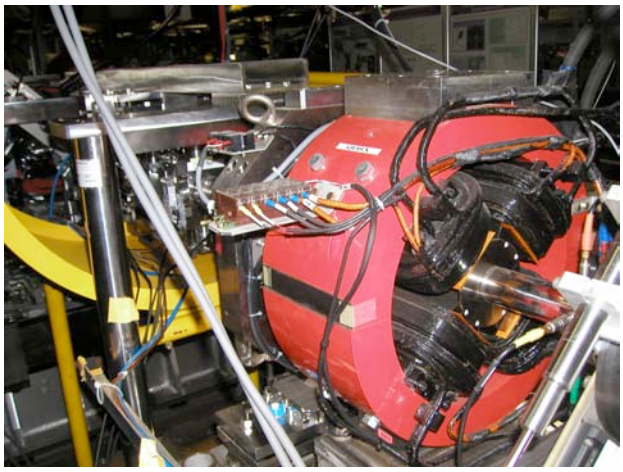

Figure 10: ATF beamline showing the kicker (left) and BPM (right) [6].

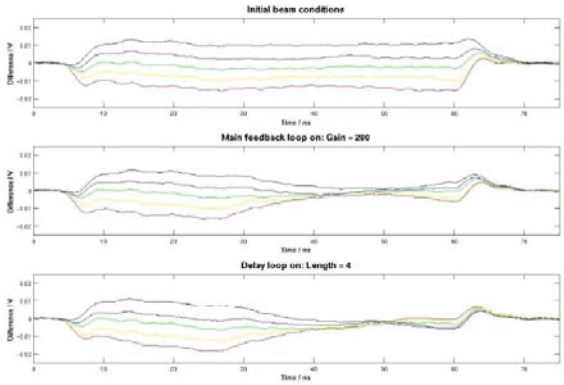

Figure 11: FONT3 feedback system performance [6].

Hence a digital feedback system approach is being pursued for ILC. The first prototype, FONT4, will comprise:

- A front-end BPM processor similar to that for FONT3 described here.
- A fast analogue-to-digital converter to digitise the baseband processor output.
- A field programmable gate array (FPGA) device for algorithm deployment.
- A fast digital-to-analogue converter to drive the kicker amplifier.
- A kicker amplifier comprising a modified version of the FONT2 amplifier.

The system design is in progress and first tests in the ATF beamline are planned for Spring 2006. The latency target is c. 100ns. This is designed to match both the ILC requirement and the planned initial beam structure at ATF of 3 bunches extracted from the damping ring with a time separation of c. 150ns. This will allow a limited test involving measurement of the first bunch, correction of the second, and delay-loop correction of the third. Eventually it may be possible to extract a longer train of at least 20 bunches with nominal ILC spacing, which would allow more extended feedback algorithm development.

REFERENCES

[1] R. Amirikas: these proceedings.
[2] B. Bolzon: these proceedings.
[3] T. Mattison: these proceedings.
[4] Y. Honda: these proceedings.
[5] G. White: these proceedings.
[6] G. Christian: these proceedings.

Summary of Working Group 2c: Future R&D Plans

Frank Zimmermann, CERN, Geneva, Switzerland;
Masao Kuriki, KEK, Tsukuba, Japan;
Marc Ross, SLAC, Stanford, USA

Abstract

We summarize the presentations and discussions of the working group 2c at the Nanobeam 2005 workshop, which was devoted to 'Future R&D Plans'. The latter are naturally centered around the ATF/ATF2 programme.

1 INTRODUCTION

The Working Group 2c addressed future R&D plans. In total 19 talks were given in this group, a large part of which related to the ATF/ATF2 project.

Specifically, the working-group schedule included the following presentations and agenda items, listed in chronological order:

- ATF2 Project by A. Seryi of SLAC [1];
- ATF Damping-Ring Performance by S. Kuroda of KEK [2];
- ATF2 Commissioning by T. Okugi of KEK [3];
- ATF International Collaboration, including a discussion of recent results and future plans, by J. Urakawa of KEK [4];
- ATF2 Budget and International Contribution by T. Tauchi of KEK [5];
- Discussion of ATF/ATF2;
- ILC R&D in Japan by K. Yokoya of KEK [6];
- CLIC R&D by F. Zimmermann of CERN [7];
- Status of Laser Fringe Beam Profile Monitor (Shintake Monitor) by T. Suehara of the University of Tokyo [8];
- Electron Beam Probe Beam Size Monitor by T. Yaskina of BINP [9];
- Photon Colliders by T. Takahashi of Hiroshima University [10];
- High Power Lasers for the Photon Collider by J. Gronberg of LLNL [11];
- Cavity BPM R&D at ATF by S. Walston of LLNL [12];
- Q BPM and IP-BPM at ATF2 by Y. Honda of KEK [13];
- Polarized Positron Source Based on Compton Scattering by J. Urakawa of KEK [14];
- Progress on the Development of an Upstream Spectrometer for the ILC by M. Slater of Cambridge (UK) [15];
- The SLAC End Station A Linear Collider Test Beam by M. Hildreth of U. de Notre Dame du Lac [16].

The working-group 2c summary talk at Nanobeam'05 was given by Marc Ross of SLAC. The following write up includes and extends his presentation.

2 ILC R&D

K. Yokoya reviewed the R&D efforts for the International Linear Collider (ILC) [6]. These address energy issues, luminosity issues, civil engineering and site study. Regarding energy, different versions of TESLA-type cavities are being developed and tested. Gradients of about 50 MV/m were reached in single cells. Four 9-cell cavities, so-called ICHIRO, have been fabricated in Japan. The goal of the new Japanese test facility STF is to construct a full linac unit by Asian/Japanese industry for an accurate cost estimate, as well as to build up the expertise for mass production. The R&D at ATF/ATF2 focuses on the luminosity-related issues. In addition to stabilization, nanometre beam-position monitoring, novel diagnostics tools, extreme beam-size measurements, and various beam dynamics issues, also fast kicker magnets are studied, and tested, at the ATF facility, e.g., ones providing a maximum 80 μrad with a full time width of 4 ns. The ATF2 related R&D will focus on the reduction of the final extracted emittance from 4.5 pm to 3 pm (ATF2 goal), the suppression of the beam jitter from 0.4 σ to 0.05 σ (ATF2 goal), via correction of 2nd order dispersion and longitudinal feedback, and implementation of new kickers which can generate an ILC-type bunch structure (either long flattop kicker or series of fast stripline kickers). Some other R&D for ILC is performed at KEKB, such as positron target tests and electron-cloud studies.

3 CLIC R&D

F. Zimmermann reviewed the R&D efforts for the Compact Linear Collider (CLIC) [7]. These concentrate on the so-called R1 and R2 feasibility issues identified by the second ILC Technical Review Committee. More than half of these issues are addressed by the CLIC Test Facility no. 3

(CTF-3), almost all the remaining ones investigated in the framework of EUROTEV. Related to nano-beams are the beam dynamics and design studies of the CLIC beam delivery system and damping ring. The latter aims to produce a beam of unprecedentedly small emittance operating in a novel regime of strong intrabeam scattering. The beam delivery studies focus on shortening the system and improving the machine protection. A promising candidate optics is based on nonlinear collimation employing skew sextupoles, which was presented by A. Faus-Golfe in another session of this workshop. New simulation and design tools are also being deployed, such as PLACET, MAD-X and PTC. A BINP-CERN collaboration has conceived an improved wiggler technology for the CLIC damping ring based on Nb_3Sn superconductor, realizing a high wiggler peak field of 2.5 T together with a short period of 45 mm. Assuming these wiggler parameters, in simulations the emittances produced by the CLIC damping ring are smaller than the target values, even taking into account the effect of intrabeam scattering. Other ongoing damping-ring studies include tuning simulations, tune scans with imperfections, as well as studies of electron-cloud and ion effects. CERN contributions to ATF/ATF2 were presented, which include hardware (active stabilization table, transformer BPMs) and manpower (1 man year). In the US, CLIC R&D has recently been strengthened, by the newly established US Multi-TeV Linear Collider collaboration (MTLC). CLIC has a strong interest in testing, at the ATF, various aspects of a polarized positron source based on Compton scattering.

4 R&D SUPPORT FOR ILC AND CLIC

ATF/ATF2 will remain the focus of emittance 'nano' R&D for future linear collider projects, such as the ILC and CLIC.

The ATF offers a combination of attractive and unique features, which render it the ideal site for low-emittance R&D:

- the ATF damping ring produces the smallest, most available and stablest beam in the world;
- it already serves as a testbed for cavity BPM's with nanometre resolution;
- many kinds of laser wires already are — or will soon be — disponible at this facility, e.g., cw laser wires, 01 mode wires, high-power pulsed laser wires, and a Shintake monitor based on laser interference; the Shintake monitor is now being upgraded to half the wavelength previously used at the FFTB, and with a dedicated fringe phase detection and control (at the FFTB the fringe phase vibration was of order 22 nm, which is clearly unacceptable for ATF2); in addition two types of background-resistant gamma detectors are being developed to cope with the large beam-gas bremsstrahlung background, either multi-material Cherenkov chambers or multi-layer inorganic scintillators; the reduction of large-amplitude beam halo by collimation may also be necessary [8]; Figure 1 illustrates the need for a shorter Shintake-monitor laser wavelength at ATF2 compared with FFTB;
- fast feedback is operational at the ATF; various incarnations of the FEATHER and FONT feedback architectures have been tested;
- stabilization of the ATF beam has been a primary emphasis over the last decade; various noise sources related to cooling, air conditioning, and power converters, were identified and mitigated; all optical cells are mounted on special tables which are aligned relative to each other by a laser tracker system; the BPM resolution was continually improved by upgrading the electronics; a double kicker system minimizes the effect of kicker jitter; and in ATF2 the active-stabilization table from CERN will be installed for suppressing magnet and monitor vibrations in the critical region around the focal point;
- novel diagnostics devices are foreseen, such as an electron beam probe for measuring beam tilts, bunch length and beam size;
- numerous beam dynamics questions have been and are being explored experimentally at the ATF, e.g., the effects of Touschek, intrabeam and gas scattering, the dynamic aperture, impact of the wiggler and its nonlinear fields, the fast beam-ion instability, etc.

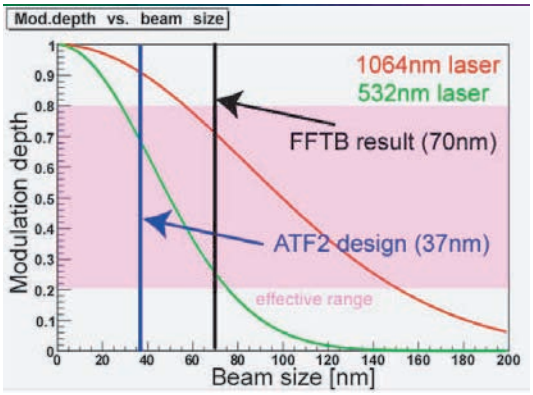

Figure 1: Modulation depth of Shintake-monitor signal as a function of rms beam size for two different laser wavelengths; the target values for ATF2 and FFTB are also indicated [8].

The mission of ATF/ATF2 is twofold, namely (1) to develop technology for the future linear colliders, and (2) to provide a real-life experience to young scientists as well as reviving interest in more experienced staff. The ATF is presently training 20 graduate and post-doctoral students, about half of which come from outside Japan.

5 ATF STATUS AND NEAR-TERM R&D

S. Kuroda reviewed the ATF damping-ring performance [2]. The vertical-horizontal emittance ratio after damping is smaller than 0.5%, a vertical emittance increase is seen along a bunch train and it might be caused by the fast beam-ion instability, in particular since an effect of beam scrubbing has been observed. It was pointed out that at a charge of 10^{10} electrons per bunch the vertical emittance in the extraction line is more than 4 times larger than the emittance measured in the damping ring, possibly due to nonlinear fields in septum or kicker magnets. The discrepancy between ring and extraction line increases with the bunch charge, which could imply that wake fields also contribute. Wiggler studies revealed a reduction in the damping time consistent with prediction in the longitudinal plane, but somewhat smaller than predicted in the two transverse planes. The transverse emittances were slightly reduced by the wiggler. No strong effect of nonlinear wiggler fields on the dynamic aperture has been seen. Longitudinal coupled-bunch oscillations are observed.

In the ATF extraction line, beam tails were measured by T. Suehara using wire scanners. The non-Gaussian tails were found to decrease with the 4th power of amplitude, as shown in Fig. 2. An inverse third power dependence had been expected on theoretical grounds from gas scattering [17]. The tails adversely affect beam position and beam-size measurements.

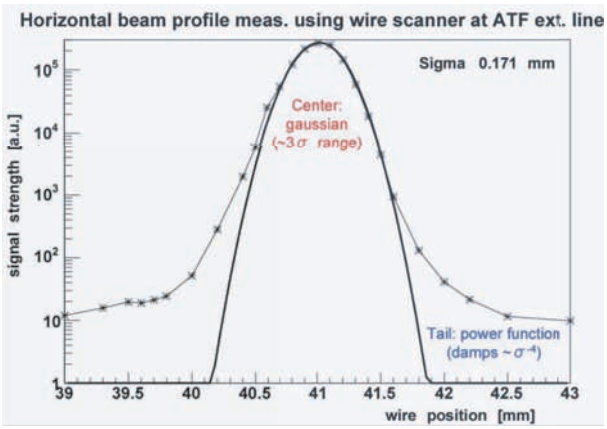

Figure 2: Beam tails measured in the ATF extraction line using a conventional wire scanner [8].

The near-term plan foresees the following developments and studies at the ATF:

- demonstration of C-band cavity BPMs with a resolution below 10 nm;
- laser wire measurements for a beam size of less than 1 μm;
- fast digital-feedback stabilization, with ILC bunch-to-bunch latency and high precision; the analog feedback system which was already studied would be suitable for CLIC;
- optical anchor measuring relative motion of 10 nm over a distance of 5 m, and a "straightness monitor" [18];
- electron-probe devices, sensitive to beam tilts at the level of a few mrads;
- the further improved use of optical diffraction radiation for beam diagnostics;
- 'damping' monitors [19];
- beam dynamics issues, including the demonstration of a stable 1-pm beam emittance and studies of the fast beam-ion instability.

These items constitute a full programme for a facility which operates less than 2000 hours a year. The structures and procedures of the ATF/ATF2 collaboration were newly re-organized to handle the growth in projects and participants [4].

Laser-particle beam physics is a rich field for investigations. Available high laser power and the ATF beam brightness combine to allow for the production of polarized photons and positrons, for neutrons, and other specialized beams. The applications of the ATF results in this domain extend far beyond high-energy physics. Of particular interest and charm is the combined rf/laser instrumentation, for example the dual meaning and dual use of the word 'cavity' (for beam-rf or for laser).

6 ATF2

The ATF2 project within the ATF collaboration covers almost all nano-issues for the ILC and for CLIC, in particular the emittance preservation from the damping ring to the IP. The only topics not addressed are the superconducting linac for the ILC, the bunch compressor and short-bunch phenomena. The latter two topics were, and are, extensively studied at the CLIC Test Facilities 2 and 3, respectively, and they will also be at SLAC ESA. For the present CLIC design, the superconducting linac is not an issue.

The ATF2 aims producing beam sizes well below those achieved at the SLAC Final Focus Test Beam (FFTB). This is made possible by a different final-focus optics (Raimondi-Seryi type instead of conventional), by a different beam source (ATF damping ring), different ways of beam handling (e.g., double-kicker compensation and fast feedback), and aggressive stabilization. New issues may be discovered as this facility enters into a new regime. The ATF/ATF2 complex can produce and study beams with bunch spacings representive for either ILC or for CLIC. ATF2 is organized from the start as an international project with large participation from the Americas and Europe. The ATF budget with contributions from three continents was discussed by T. Tauchi [5].

Some important technical questions were raised in the presentation by A. Seryi, namely the finalization of the ATF2 layout, the design of the ATF2 final doublet (conventional, permanent magnet, or superconducting, e.g., using BNL technology), and the test of tail-folding octupoles at the ATF2 [1]. In particular, he mentioned the prospect of testing the stability of the final-quadrupole magnetic field center at the nm level using the beam and the option of tuning the final focus with corrector coils in the final doublet instead of with magnet movers.

ATF2 commissioning strategies are being developed. T. Okugi discussed orbit tuning using only cavity BPMs, beam-size tuning with a scan of the final focal length, position scans for the Shintake monitor, and the further plan. He highlighted the necessity of optics changes when measuring the beam size with different devices (carbon wire scanner, Mitsuhashi/Naito monitor, or Shintake monitor) which are located at different longitudinal positions, so as to move the beam waist to the monitor in question. Figure 3 shows the beam size as a function of longitudinal position with and without adjustment of the final-doublet fields.

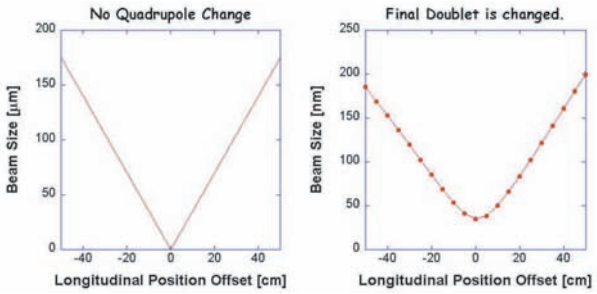

Figure 3: Beam size as a function of longitudinal position with final doublet held constant (left) and when the final doublet is changed to make the focal point coincide with each longitudinal position (right) [3].

The ATF nano-beam can be used to check nano-metre stabilization over macroscopic distances. Two different stabilization systems were compared at the workshop: STAFF was presented by D. Urner of Oxford in the plenary session; its application to ATF, illustrated in Fig. 4, links two different sets of three cavity BPMs [18]. The other is a geodetic network surrounding the beamline systems ('nanoGrid') [12]. A broad range of applications are expected, including alignment.

7 OTHER NANO-TEST BEAMS

Other nano-beam facilities include End Station A (ESA), CTF-3, CESR, TTF, and STF. The beam produced in ESA more closely resembles the short ILC or CLIC bunches. The rms bunch length in ESA can be made as small as 0.1 mm compared with 8 mm at the ATF. Figure 5 shows a simulation of bunch compression for the ESA experiment, resulting in an rms bunch length of about 100 μm [16].

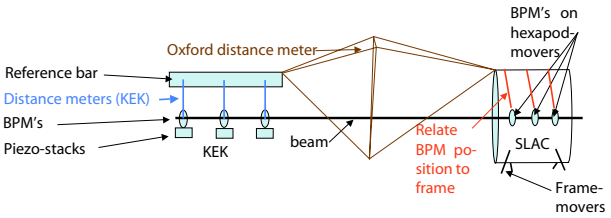

Figure 4: Active stabilization of ATF rf BPMs based on STAFF developments [18].

The ESA beam energy is 30 GeV, in contrast with the ATF-energy of 1.3 GeV. A plethora of experiments are foreseen. For example, ESA allows for system integration, robustness tests (exposure to beam tails), and rapid testing of rf BPM designs. The ESA and ATF programmes nicely complement each other. The ESA start up is scheduled for January 2006.

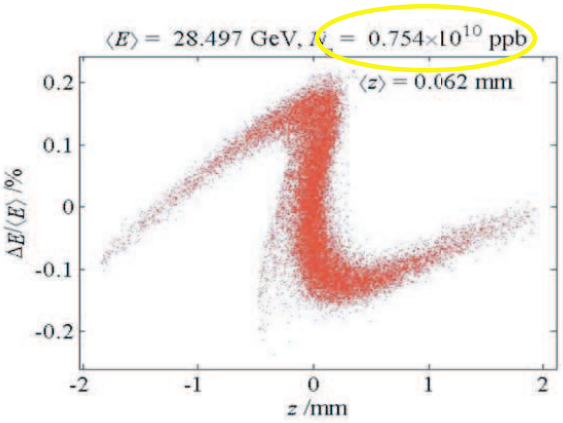

Figure 5: Simulated electron-bunch phase space after bunch compression for the ESA experiment (Paul Emma) [13].

The ILC requires a measurement of the beam energy with a precision better than 10^{-4}. M. Slater presented the plan for installing an energy spectrometer, based on a set of precision dipoles and precision rf BPMs [15]. The concept is similar to the spectrometer employed at LEP. Optimized rf BPMs designed specifically for the spectrometer will be manufactured and installed at the SLAC ESA. The BPM design makes use of the experience with rf BPMs and with their noise limitations gained at the ATF [15].

CTF-3 is designed to demonstrate the drive-beam generation via bunch frequency multiplication using a delay line and a combiner ring, deceleration and power extraction, as well as the generation of the CLIC design gradient over the design pulse length. The CTF-3 facility allows for studies of bunch compression and coherent synchrotron radiation.

CESR and TTF are different from the above in that they are not dedicated to nanostudies, but must provide beam to

users. Also STF is not primarily conceived as a nano-beam facility.

8 CAVITY BPMS

Recent nano-BPM measurements at the ATF demonstrated a resolution of 23.6 nm over half an hour. The resolution was inferred by comparing readings from a set of three BPMs (inner BPMs vs. the average of the two outer ones). Figure 6 shows the result obtained by S. Walston [12].

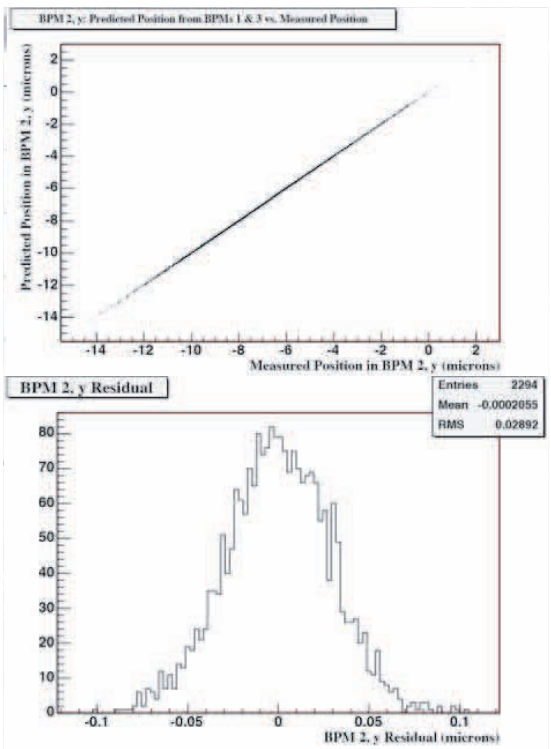

Figure 6: ATF nano-BPM resolution inferred from a set of 3 BPMs mounted in a row [12]; center position predicted from outer BPMs vs. the reading of the inner BPM (top) and a histogram of the resolution so obtained (bottom).

The next stage will be higher-order mode s.c. rf cavity BPMs. An attempt at TTF in November 2005 has achieved only 3-micron resolution, whereas nm resolution had been expected. The result suggests that many coupled cavities complicate this type of measurement.

A cavity-BPM frequency around 7 GHz with a 14-mm gap is optimum for the ATF bunch length. For shorter bunches small cavities and higher frequencies are favored, as is illustrated in Fig. 7.

9 TRANSFORMER BPMS

The CLIC study develops a different BPM for the CLIC main linac, namely one of transformer type [7]. Figure 8 illustrates the operating principle of a precision transformer BPM.

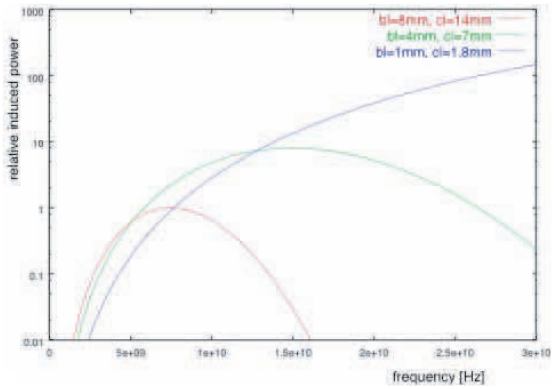

Figure 7: Relative power as a function of frequency for three different combinations of bunch length and cavity length [13].

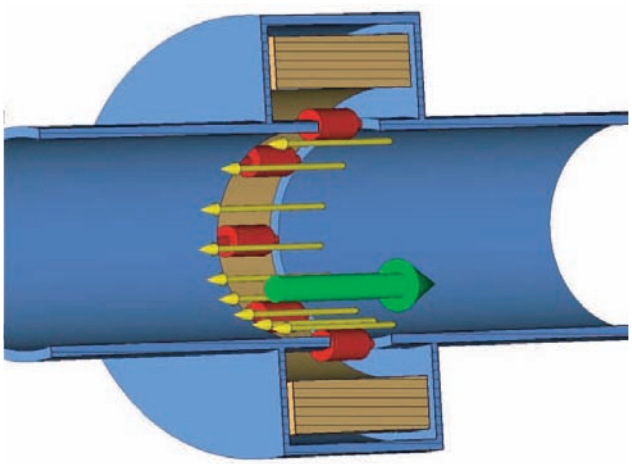

Figure 8: Operating principle of precision transformer beam-position monitor [20].

The starting point of the BPM design is a similar monitor, already used at CTF-3, with a larger aperture [21]. The transformer BPM development is performed in the framework of, and supported by, the EuroTEV. Two or three prototype monitors could be deployed at ATF2.

The advantages of the transformer BPMs, as compared with cavity BPMs, are that they function for arbitrary bunch spacing, have a large frequency bandwidth (almost 6 decades) and a simple readout electronics, and that they are insensitive to spray from lost beam particles.

10 NANOBPM R&D SPINOFF

The future R&D will certainly include the consolidation of the HEP accelerator applications, in particular of very large projects. There is an inter-related expansion in other fields, like FELs, Compton sources, and Compton-based polarized positron sources. Novel tools are needed to extend accelerator systems to the nanometre region. These new

tools can be tested at ATF/ATF2 and ESA. The available beam operations time is fully subscribed. The workshop indicated a strong demand for additional facilities. Many 10 nm resolution cavity BPMs at ATF2 will open up a new window into the nano-world. There will be a total of about 50 such BPMs at ATF/ATF2. The ATF2 represents the first large-scale application of precise single-pass measurement devices. Beam angle and tilt will also be monitored. Collective effects in the ring as well as ones during and after beam extraction will be investigated. Thermal and electromagnetic interaction of the beam and beam diagnostics with the enviroment are another point of interest. The ATF cavity BPMs were originally built for jitter tracking.

The tuning and stability requirements for SASE FEL operation are very similar to those for a future linear collider. Valuable experience is gained at the TESLA Test Facility working on FEL-light saturation at 30 nm wavelength. Integration with the photon beam through an external reference is needed [19].

At the ATF and in ESA, novel BPM systems can be tested which will support major advances at all types of facilities.

11 BEAM SIZE MONITORS

Beam size measurements in the sub-micron region remain challenging. A 700-m long insertion may be required for the ILC laser wire. The use of the 01 laser mode may help. This procedure was already successfully tested at the ATF. The fringe switching is cumbersome, however. Strategies for improving power and signal will help, but a breakthrough performance would be nice.

The electron wire developed at BINP is based on a 90-degree interaction of the beam with a 200-kW electron beam, which acts as a time-resolved 'field' sensor [9]. Two such devices are in operation at BINP. Figures 9 and 10 show the sensitivity of the electron wire to vertical beam offsets and tilts, respectively.

12 POLARIZED POSITRON SOURCE BASED ON LASER-COMPTON SCATTERING

J. Urakawa reviewed the past experiments, design and further R&D for a polarized positron source based on laser-Compton scattering. The Compton source would provide a positron beam with high polarization, unlike a conventional source. Also, different from an undulator source, the laser-based source does not require a full-energy high-intensity low-emittance electron beam, and it keeps the operation of the main linacs decoupled from the positron source. This strategy incorporates the lessons learnt at SLC, where operators needed to constantly tune the positron lines and the main linac to counteract negative feedbacks and instability. It should also greatly improve the uptime of the accelerator complex. The operation, the energy choice, the commissioning, the development, and the electron-positron arms

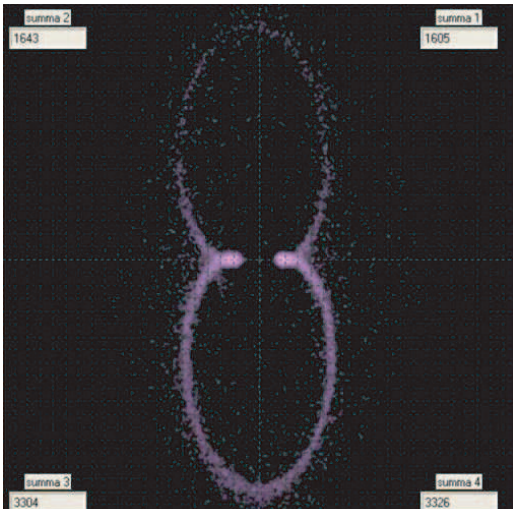

Figure 9: Example of electron-wire measurement for a 30-μm vertical bunch displacement [9].

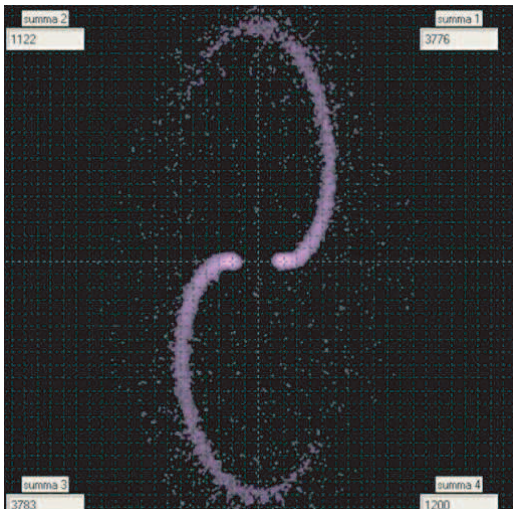

Figure 10: Example of electron-wire measurement for a 17-mrad bunch tilt [9].

are all kept independent, which makes it easy to run the collider at lower energy, e.g., at the Z resonance.

A proof-of-principle experiment has been ongoing for several years at the ATF, where both polarized positrons and polarized electrons were produced. At the same time polarimetry and beam diagnostics have been refined. A special Compton 'tri-chamber' was constructed and operated for the electron-laser collisions. The polarimetry at the ATF is based on a sequence of bremsstrahlung, Compton scattering, and pair creation, in a lead target, magnetized iron and CO_2 Cherenkov counter, respectively. The ATF experiment was highly successful, culminating in the first ever production of a high-intensity short pulse of polarized positrons, with a measured polarization of about 80%. This result demonstrated the efficient propagation of the

polarization from laser photons via gamma rays to polarized electron-positron pairs. Polarimetry for gamma rays, positrons and electrons was established along the way.

A conceptual design of a polarized positron source based on Compton scattering for the ILC was submitted to Snowmass 2005. The Snowmass proposal showed that a Compton source is a viable option for a cold collider, with a new and improved design, making full use of the low repetition rate. The main novelties with respect to the earlier GLC/NLC design are the storage of electrons in a Compton ring, the recycling of the laser pulse stacked in an optical cavity (simultaneously serving as Compton collision chamber) which is installed in the Compton ring, and the accumulation of positrons produced from subsequent electron-laser collisions in the main damping ring. The overall layout of such a facility is sketched in Fig. 11. Two laser options are being considered, based on CO_2 or YAG, respectively. For the ILC, one laser feeds 30 optical cavities in a daisy chain. For CLIC a single optical cavity suffices. For ILC the main 5-GeV positron accelerator before accumulation is superconducting, for CLIC it can be normal-conducting. Stacking in the damping ring was simulated and proved feasible. Designs for the two alternative laser systems also exist.

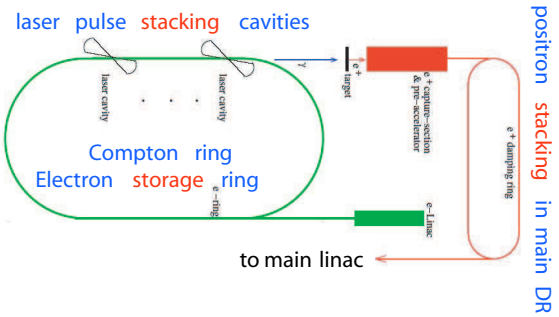

Figure 11: Conceptual layout of a polarized positron source for ILC based on laser-Compton scattering [14].

After the successful completion of the first R&D stage (ATF proof-of-principle experiment), present R&D focuses on the conceptual design, mainly using simulation programmes, and on component development with experimental validation. Several pertinent hardware installations are foreseen at the ATF in 2006 and 2007. These offer a lot of synergy with beam diagnostics upgrades, e.g., laser wire. A detailed proposal for a CLIC polarized positron source based on Compton scattering is in preparation.

13 PHOTON COLLIDERS

T. Takahashi addressed technological issues related to the interaction region and to the laser for photon colliders [10]. An example is the laser pulse stacking cavity, whose technical aspects are similar to those of the Compton-based positron source. Critical points are the stability of the optical cavity, cavity losses, and wavefront quality, for high power and large scale. Constructing of a prototype stacking cavity at ATF2 is planned. The ATF2 may then serve as a testbed for the photon collider conversion point. J. Gronberg reviewed the status of the laser technology [11]. He drew the optimistic conclusion that the basic technologies needed for the photon-collider laser have been developed, but he cautioned that the LLNL high average-power MERCURY laser produces single pulses at 10 Hz and a redesign of this laser for linear-collider needs will be required. One problem to be solved for linear-collider applications is the so-called amplified spontaneous emission.

14 EPILOGUE

By bringing together different communities, the Nanobeam workshop matched well the long-standing ATF tradition of coupling R&D efforts related to a linear collider with others, e.g., ones for medical applications.

15 REFERENCES

[1] A. Seryi, "ATF2 Project," these proceedings (2005).

[2] S. Kuroda, "ATF DR Performance," these proceedings (2005).

[3] T. Okugi, "Beam Instrumentation Devices for ATF2 Commissioning," these proceedings (2005).

[4] J. Urakawa, "ATF International Collaboration," these proceedings (2005).

[5] T. Tauchi, "ATF2 Budget and International Contribution," these proceedings (2005).

[6] K. Yokoya, "ILC R&D Plan in Asia," these proceedings (2005).

[7] F. Zimmermann, H. Braun, L. Soby, "CLIC R&D," these proceedings (2005).

[8] T. Suehara et al, "Status of Shintake Monitor for ATF2," these proceedings (2005).

[9] T.A. Yaskina et al, "Possible Applications of Electron Beam Probe for ILC Beam Diagnostic System," these proceedings (2005).

[10] T. Takahashi, "Photon Colliders," these proceedings (2005).

[11] J. Gronberg, "High Power Lasers for the Photon Collider," these proceedings (2005).

[12] S. Walston, "Cavity BPM R&D at ATF," these proceedings (2005).

[13] Y. Honda, "ATF/ATF2 Cavity-BPMs," these proceedings (2005).

[14] J. Urakawa, "Polarized Positron Source based on Compton Scattering," these proceedings (2005).

[15] M.W. Slater, "Progress on the Development of an Upstream Spectrometer for the ILC," these proceedings (2005).

[16] M. Hildreth, "The SLAC End Staion A Test Beam Program," these proceedings (2005).

[17] T. Raubenheimer, "Emittance Growth due to Beam Gas Scattering," KEK-92-7 (1992).

[18] D. Urner, "The Stabilization of the Final Focus of the ILC Project," these proceedings (2005).

[19] M. Ross, "Future R&D Plans - Working Group 2c," presentation at Nanobeam'05.

[20] Web site:
https://cern-eurotev-wp5.web.cern.ch/CERN-EUROTeV-WP5/

[21] M. Gasior, "An Inductive Pick-Up for Beam Position and Current Measurement," CERN-AB-2004-053-BDI, CLIC Note 572, presented at DIPAC 2003 (2003).

SUMMARY OF WORKING GROUP 2D

- FINAL FOCUS Q-MAGNET-

M.Kumada, NIRS, Chiba, Japan,

B.Parker, BNL, Upton, NY, USA

F.Kircher, CEN Saclay, Gif sur Yvette, Cedex, France

Abstract

This report is a summary of seven speakers of the session WG2d of "final focus Q-magnet" of BDS&FFIR of Linear collider in the international workshop of NANOBEAM2005. Details of each presentation are in the reference, which is in the proceedings.

BNL ACTIVITY

Extensive activity on a various kind of compact superconducting magnet and R&D activities regarding various kind of ILC compact superconducting final focus magnets[1]. This is based on a direct winding technique. The QD0 quadrupole, the final focus magnet closest to the Interaction Point (IP) for the ILC 20 mr crossing angle layout, provides strong focusing yet be adjustable to accommodate collision energy changes for energy scans and low energy calibration running. It must also be compact to allow disrupted beam and Beamstrahlung coming from the IP to pass outside into an independent instrumented beam line that leads to a high-power beam absorber. In designing QD0 they take advantage of BNL experience making direct wind superconducting magnets. It was presented test results for a QD0 magnetic test prototype and introduce a new shielded magnet design, to replace the previous side-by-side design concept, that greatly simplifies the field correction scheme and holds promise of working for crossing angles as small as 14 mr.
Then Animesh Jain described about Vibration Measurements in a RHIC Quadrupole at Cryogenic Temperatures. Compact superconducting quadrupoles are being considered for use in the final focus region of the ILC. One of the concerns in using superconducting magnets is the influence of the cryogen flow on the vibration characteristics. Since very little is known about vibration of superconducting magnets at nanometer levels, as a first step, a project was undertaken at BNL to measure the vibrations in a spare RHIC quadrupole under cryogenic conditions. Given the constraints of cryogenic operation, and limited space available, it was decided to use a commercially available dual head laser doppler vibrometer for this work. The performance of the laser vibrometer was tested in a series of room temperature tests and compared with results from Mark L4 geophones. The laser system was then used to measure the vibration of the cold mass of the quadrupole with respect to the outside warm enclosure. These measurements were carried out with the cold mass at room temperature, as well as at cryogenic temperatures. The measurement set up and the results obtained were described in detail.

LESSON FROM KEKB IR EXPERIENCE

K. Tsuchiya of KEK commented from his experience at KEKB IR[2] . He made emphasis that The goal of the interaction region (IR) design for ILC is to deliver the highest possible stable luminosity to the experimental facility with minimum background noise. In order to reach this goal, a number of design iteration of each part will be required, and also the information from other IR design will be helpful to accelerate the design process. He made an introduction of the KEKB-IR system . for example, he pointed out that making actively shielded magnets can be challenging and it is important to do 3D calculations and not just depend upon 2D estimations. Also it good to make and test a prototype. Brett Parker also commented that dipoles are harder than quadrupole due to slower external field fall off..

SACLAY APPROACH

Saclay approach is to use Nb_3Sn from their long experience in this field to make very strong field gradient in addition to compactness[3]. F.Kircher presented his rich experience in LHC , TESLA TDR and ILC new design. In the example of the 56 mm bore LHC Qudadrupole magnet, the field gradient is 211 T/m and peak filed is 8.3 T with external solenoid field. Detail 3D calculation with solenoid was shown. He concluded:

1 –LHC present IR quads have proved their feasibility:
215 T/m in _70 mm, NbTi@ 1.9 K
2 –Using Nb3Sn at4 .5 K and so me improvement in the
Mechanical support can almost certainly enable to
reach250 T/m in _70 mm or 210 T/m in _90 mm.
But this is still to be proved
3 –Higher r performances will l need developments
and/or
New design. Is the small quantity of magnets needed?

Justify such an effort**?**
4 –More results on Nb3Sn magnets are expected within Few years. This experience will be useful for ILC
5 –Our first main goal must be to define the parameters

These magnets in a reasonable range. Follow up oft he Expected progress for the LHC upgrade and development tof HTS conductors will enable us to make technical choices within few years with more information.

HIGH GRADIENT PERMANENT QUADRUPOLE MAGENT[4]

Mihra presented recent result of the high gradient permanent project of Kyoto University/NIRS/KEK collaboration. He started reviewing pros and cons as ;

(i) Pros,

•No vibration source (power cable, cooling water, or He pipe, etc...)

•Edge of effective length equals to L* (Super-Q needs 20cm more space for thermal shield)

• Small size and light weight

• Strong field gradient

• Less power consumption

(ii) Cons,

•Temperature dependency (It can be compensated with temperature compensation alloys.)

•Radiation damage

He then presented the structure, magnetic measurements and shimming technique and remodeling of the developed discretely adjusted permanent quadrupole. Finally the report of demagnetization upto 4 T external field was reported.

EXOTIC HIGH T_C MATERIAL

Kumada presented a high-Tc oxide bulk superconductors (QMG) which have high current capacity up to several 10^4 A/cm^2 at 77K we introduce development for the materials and their applications. This is developed by Morita of Nippon Steel Corporation. The QMG eddy magnet is one of the important applications. QMG eddy magnet consists of eddy shape and planar superconducting QMG coils. These coils are stacked and connected in series by solder. They fabricated eight-layer QMG eddy magnets that have 11 turn and cross section of 1.0 x 2.1 mm and diameter of 74mm.

•

REFERENCES

[1] B.Parker and A.Jain, This proceedings
[2] K.Tsuchiya, This proceedings.
[3] F.Kircher, This proceedings.
[4] T.Mihara, This proceedings.
[5] M.Kumada, This proceedings.

SUMMARY OF WORKING GROUP 3A: LOW EMITTANCE SOURCES

J. E. Clendenin, SLAC, Menlo Park, CA 94025, U.S.A.
J. W. Lewellen, ANL, Argonne, IL 60439, U.S.A.
K. Masuda, Institute of Advanced Energy, Kyoto University, Kyoto 611-0011, Japan
F. Stephan, DESY, 15738 Zeuthen, Germany

Abstract

We summarize the main issues and conclusions of the working group devoted to low emittance sources.

INJECTOR OVERVIEWS, PHOTOCATHODE DRIVE LASER, MODELING

Overview of Photo Injectors

Experimental and design data for 15 different photo injector projects that includes DC and NC and SC RF photo cathode guns producing from 1 pC to 10 nC bunches with time structure from single bunches at 10 Hz to cw beams and emittances ranging from 0.1 to 11 mm-mrad are summarized.[1] Simulations predict very good performance by all three basic photo injector types (plus hybrids). Experimental progress has been made for each of the major subsystems—gun, laser, diagnostics—and on measured beam quality, although the challenge to "Get 1 μm @ 1 nC" announced by P. O'Shea at the 1999 ICFA workshop at UCLA has not yet been reached. Methods to reach this goal are defined.

Besides the known methods to produce low emittance beams from the three basic photo injectors, new ideas include the generation of bunches that at the cathode have either a pancake shape with a half-sphere transverse profile or a cigar shape with a parabolic longitudinal profile. These are shapes that can evolve into an ellipsoidal distribution in space which results in linear space charge forces and low emittance. A second new idea is to generate the bunch not from a conventional cathode at all, but from cold atoms trapped in an inhomogeneous B field.

In the future, as progress is made toward emittances that approach the limit set by the thermal emittance, it will become increasingly important to understand better the emission process itself.

UV Pulse Shaping

To achieve a low emittance, a flat or top hat pulse shape, spatially and temporally, is desired. Spatial shaping of uv pulses directly using a deformable mirror (DM) is compared with a micro lens array (MLA).[2] DM is superior with respect to wave length limit, achievement of ideal profile and pointing adjustability, but at present is significantly more expensive. With an electron profile monitor and a feedback algorithm both methods can be used to correct for inhomogenities in the distribution of QE on the cathode surface.

Temporal shaping of uv pulses can be performed with a spatial light monitor (SLM). Two types are discussed. An acousto-optic SLM such as the Dazzler is able to modify spectral phase and amplitude. It is generally more versatile than a fused-silica SLM although it is more expensive.

Finally, ellipsoidal shapes can be produced by simultaneous use of DM plus an optical fibre bundle. However, this technique is limited to cathodes that can be illuminated from their back surface.

Multiscale Methodology

A wavelet-based solver for the 3D-Poisson equation was developed to account for multi-scale dynamics in multi-particle simulation codes.[3] It initially was included in an N-body PIC code and tested with an IMPACT-T simulation to reconstruct in detail the charge distribution of a 1-nC bunch from the FermiLab NICADD photo injector both before and after compression. Initial results show a 15-20% increase in speed while the number of data sets is reduced by 1/10.

PHOTOCATHODE MATERIALS, POLARIZED ELECTRONS, THERMAL EMITTANCE

Thermal Emittance of Cs_2Te

As the techniques for producing lower emittance sources continue to progress, the limit set by the thermal emittance, ε_{th}, becomes more important. Recently ε_{th} for Cs_2Te cathodes was measured for the first time in the operating conditions of an RF gun using the scanning slit method.[4] For this experiment, ASTRA simulations were used to confirm that space charge and RF contributions to the total emittance from the 3 pC, 3 ps bunch produced by the 1.6-cell RF L-band gun would be a small perturbation. ε_{th} is derived from the slope of the measured emittance as a function of laser rms spot size, σ, at the cathode. The result averaged over x and y for two cathodes is a normalized rms emittance of ε_{th} = 1.1 mm-mrad per mm σ, corresponding to an average kinetic energy of ~1 eV at the cathode surface..

Polarized Photocathodes

To generate highly polarized beams, many types of photocathodes based on GaAs have been tried, including single strained-layer GaAs and both unstrained and strained superlattice structures. The best choice today is

the strained GaAs-GaAsP superlattice, which yields an electron polarization of 90% with a QE of 0.5% using laser excitation of visible wavelength.[5] A second critical factor for polarized sources is dark current, which must be maintained below an average of ~10 nA. Extensive testing of electrode materials for DC guns has led to the finding that the best choice is Mo for the cathode, Ti for the anode. With proper cleaning, this combination results in only 1 nA average peak current at 130 MV/m after high-voltage processing.

Polarized RF Gun

GaAs photocathodes have not yet been successfully used in RF guns. The principal problems are recognized to be back bombardment of the cathode by field-emitted electrons and the required vacuum of better than 10^{-11} Torr.[6] It should be possible to significantly reduce field emission. A single S-band cavity carefully manufactured and cleaned has been processed to a peak surface field of 140 MV/m with a peak current of <25 pA, which for the ILC duty factor corresponds to an average current of <1 pA! The vacuum of a NC RF gun can be improved by surrounding the gun in a UHV system and then pumping through Z slots or multiple small holes (a sieve) in the outer cylinder. Further improvement in the conductance between the cathode and the pumping system is possible using RF gun designs that have a more open structure, such as PWT or HOM designs. The latter, combined with a sieve, results in at least a factor 20 improvement in the conductance compared with conventional RF gun vacuum systems. This results in an expected pressure at the cathode of $<10^{-11}$ Torr after RF processing if the outgassing rate is reduced to that of well-baked Cu.

LOW EMITTANCE ELECTRON GUNS

SC RF Guns

The status of SC RF guns is reviewed.[7] The guns being developed range from hybrids in which the cathode is NC, to all-Nb SC cavities. Cathode materials that are being studied include Cs_2Te, Pb and CsKSb/diamond as well as Nb. Emittance compensation for SC RF guns is a problem. An interesting emittance-compensation possibility for a multi-cell gun is to operate one of the cells in a magnetically focusing RF mode.

Ultra-Low Emittance,Ultra-Short Bunch Length

RF guns are routinely selected as the electron source for low emittance beams. A 1.6-cell S-band RF gun with a Cu cathode has been used to generate an ultra-low emittance bunch.[8] With a flat top laser pulse of 9 ps and a charge of 1 nC, an emittance of 1.2 mm-mrad was measured. When running at a reduced charge of 0.17 nC and after passing through a phase-optimized accelerating section, a pulse length of 98 fs was obtained.

Thermionic RF Gun With Independently Tunable Cells

A thermionic RF gun is described that has independently tunable cells.[9] By tuning the cells for velocity bunching, external bunching stages can be eliminated, resulting in a very simple configuration. This type of gun is being developed for a coherent THz SR source, but should be of interest for any application requiring high current.

DC thermionic gun for SCSS

To avoid the dark currents associated with an RF gun and also the non-linear space charge field associated with pulsed charge extraction, a pulsed thermionic gun is being developed for SCSS in which a 2-ns pulse is selected downstream from the 1 μs pulse produced by a 500 kV gun.[10] The normalized emittance at the cathode is measured to be 1.1 mm-mrad. The CeB_6 cathode using a graphite heater can produce current densities >40 A/cm^2. The theoretical thermal emittance for this cathode is 0.4 mm-mrad.

REFERENCES

[1] F. Stephan, “Status and Perspectives of Photo Injector Developments for High Brightness Beams,” to be published in the proceedings of the workshop “The Physics and Applications of High Brightness Electron Beams”, Erice, October 2005.

[2] H. Tomizawa, “Adaptive Laser Shaping or Homogenizing System for Both Spatial and Temporal Profiles of a Highly Stabilized UV-Laser Light Source for a Photo-Cathode RF Gun,” these proceedings.

[3] B. Terzić, “Applying Multiscale Methodology to Beam Simulations,” these proceedings.

[4] T. Nakanishi, “Superlattice NEA Photocathode and Gun Technology Developed for High Polarization and Low Emittance Electron Beam,” these proceedings.

[5] V. Miltchev, “Measurements of Thermal Emittance for Cesium Telluride Photocathodes at PITZ,” these proceedings.

[6] J. E. Clendenin, “RF Guns for Generation of Polarized Electron Beams,” these proceedings.

[7] J. Teichert, “Status and Future Prospects of SRF Gun Developments,” these proceedings.

[8] J. Yang, “Ultra-Low Emittance and Ultrashort Bunch Electron Sources,” these proceedings.

[9] H. Hama, “Design Study on an Independently Tunable-Cells Thermionic RF Gun,” these proceedings.

[10] T. Shintake, “Experiences of HV Pulse Thermionic Gun,” these proceedings.

SUMMARY OF WORKING GROUP 3B:FEL-RADIATION SOURCES

H. Ohgaki, IAE, Kyoto University, Kyoto, 611-0011, Japan
M.E. Couprie, CEA, DSM/SPAM, 91 191 Gif-sur-Yvette, France
G. Kulipanov, Budker Institute of Nuclear Physics, 63090, Novosibirsk, Russia

Abstract

We summary the several issues on the working group devoted to FEL-Radiation Sources which are deeply relayed on the generation and application of the electron beams with very small emittances both in transverse and longitudinal directions. The working group consists of "ERL & New SR sources", "Oscillator FELs", "Single Pass FELs" session, and "Beam Diagnostics & Stabilization".

INTRODUCTION

The electron beam with a small emittance both in transverse and longitudinal directions is an essential for generation of free-electron laser (FEL) and synchrotron radiation (SR) to explore the frontier science. In terms on the transverse coherence, the diffraction limit, $\Delta x \Delta x' - \varepsilon = \lambda/2\pi$, is the upper limit for third generation SR sources. So the beam emittance of 'nano' to 'sub-nano' m-radian is required in the X-ray region. By using such small size electron beam, the beam stabilization issues become a challenging issue on the 3rd generation SR sources. To obtain a further intense radiation, FELs have been developed and already generated diffraction limit radiations from VUV to FIR region using linacs and SR rings. In the X-ray region, several FEL projects have already been started for construction. In terms of the longitudinal coherence, Fourier limit, $\Delta\omega\Delta t$ - 1, is upper limit and obviously SRs from undulators are far from this limit, because a typical bunch length in 3rd generation SR sources are -10 ps. Energy Recovery Linac (ERL) has been proposed to generate a fully spatially coherent radiation in X-ray region as a 4th generation SR source.

In working group 3b, we focused on the topics on "ERL & New SR sources", "Oscillator FELs", "Single Pass FELs" session, and "Beam Diagnostics & Stabilization". A characteristics of the different sources presented in this working group is shown in Table 1. More detailed description is presented in the following sections.

Table 1 Charateristics of the different sources presented in the working group WG3-b.

Topics	Institution	
ERL and New Sources on SR Ring	JAEA + KEK	6 GeV ERL
	BINP	4 passes MARS
	UVSOR-II	Bunch slicing, THz, CHG
	LNS	Isochronous THz ring
Oscillator FELs	BINP	0.12-0.18 mm, 70 ps, 0.04 mJ, 0.4 kW Imaging, FIR ablation
	JAEA	16-23 μm, 2.34 kW, 255 fs Prevention of cold working cracking
	ISIR	Improvement of L-band linac fs pulse radiolysis
	NIJI-IV	IR and VUV PEEM application
Single Pass FELs	LCLS	X-FEL: 230 fs, 1-15 angstrom, 0.8-0.06x10^{33} ph/sec/mm^2/mrad^2/0.1%, 14.3-4.5 GeV, 1.2 mm-mrad
	SCSS	X-FEL: 1 angstrom, 8 GeV, C-band Linac
	PAL	X-FEL: 3(1) angstrom, 3.7 GeV
	ARC-EN-CIEL	Seeding and Harmonic Generation

ERL & NEW SR SOURCES

One of the most prominent candidates for the next generation light source is Energy-Recovery Linac(ERL), because it will deliver a short wavelength, short pulse duration and high brilliance radiation to many experimental stations simultaneously. Moreover ERL has a potential for reducing the radiation hazard and high average current, compare to SR rings.

A talk entitled "Energy-Recovery Linacs: overview and present status in JAEA-ERL" is presented by R. Hajima (JAEA)[1]. The overview is based on the long experience in their 17 MeV ERL machine. The upgrade plan in JAEA ERL facility is also presented. JAEA ERL will be operated with 83.3 MHz (present 10.4 MHz) with average current of 40 mA (present current of 5.2 mA). To drive such high power beam, the 2.5 MeV injector and its' rf power sources will be upgraded. The future plan (a prototype ERL light source machine), which is announced to be a collaborative work between JAEA and KEK, is also presented. The tentative machine parameters are:

GUN: photo-cathode DC gun, 200-500 kV, 100 mA,
Injector:(1-cell or 2-cell) x 4 cavities, 240 kW,
Main Accelerator: 100-200 MeV,
Refrigerator: 200 W@2 K, 200 W@77 K.

Table.2 Comparison of parameters of SR sources MARS (Ie=2.5 mA) and Spring-8 (Ie=100 mA)

		Number of beam-lines	Brightness (ph/sec/mm^2 /sr) $\Delta\lambda/\lambda=10^{-3}$	Flux (ph/sec) $\Delta\lambda/\lambda=10^{-3}$
MARS	U,Nu-10^2	48	10^{22}	4.6×10^{13}
	U,Nu-10^3	12	10^{23}	4.6×10^{14}
	U,Nu-10^4	4	10^{24}	4.6×10^{15}
Spring -8	Bending	23	10^{16}	10^{15}
	U,Nu-130	34	3×10^{20}	2×10^{15}
	U,Nu-780	4	10^{21}	1.2×10^{16}

U:Undulator, Nu:number of period

A talk entitled “Comparison of one pass(ERL) and multi pass accelerators-recuperators(MARS) as coherent X-ray sources” is presented by G. Kulipanov(BINP)[2]. The advantage of multi pass configuration with fully spatially coherent beam is clearly shown by comparison of SPring-8 and MARS (Table.2).

The argument also refers to the single pass scheme, ERL, and concluded that the MARS has significantly less expensive RF system. A 6 GeV, 4 turns MARS design is shown as a realistic comparison. The design machine has a cascade injection system to prevent large energy difference between accelerating beam and decelerating beam in single turn ERL.

There also two other talks related on the new radiation source with short electron bunch in circulator machine. A talk entitled “Development of new radiation sources at UVSOR-II” is presented by M. Katoh(UVSOR)[3]. The upgraded SR source UVSOR-II has a modified Chassman-Green lattice and realizes an emittance of a few tens nano-meter radian. By using the low emittance electron beam short wavelength FEL experiments have been performed. Under the condition of a low momentum compaction factor to shorten the electron bunches coherent THz radiation has been observed in UVSOR-II. The bunch slicing method developed in LBNL[4] has been also applied to UVSOR-II.

A talk entitled “LNS Isochronous THz Ring project” is presented by H. Hama(LNS, Tohoku U.)[5]. An isochronous lattice has been designed to keep a femto-second pulse duration of the electron beam generated by a thermionic RF gun. Calculation of the beam dynamics in the lattice clearly shows that there are two origins of the bunch lengthening in the storage ring. One is due to the energy spread of the electron beam and the other, which is much serious, is due to the betatron oscillation in the arc section of the ring. Choosing an optimized phase advance in the arc section, however, the bunch lengthening can be suppressed.

OSCILLATOR FELS

FELs, fully spatially coherent radiation sources covering a spectral range from VUV to FIR have already been generated by using linacs and storage rings with oscillator configurations. For far IR, microtrons and Van de Graff are also used. Obviously, the high power FELs are challenging topics and kW-class FELs have been generated by using ERL. A talk entitled “Status and future of Novosibirsk high power FEL, based on one pass and four passes accelerator-recuperator” is presented by N. Vinokurov(BINP)[6]. The FEL driven by one pass 12 MeV accelerator-recuperator has already been applied for THz imaging, high power density experiments, and ultra-soft laser ablation of DNA. The FEL main parameters are

Wavelength: 120-170 μm,
Average Power: 400 W,
Minimum relative linewidth: 3×10^{-3} (FWHM).

The electron energy will be enhanced to be 40 MeV by using the four pass accelerator-recuperator and the FEL with average power of 10 kW will be generated from 3 to 20 μm in wavelength.

A talk entitled “The JAEA Superconducting RF Linac Driver for Free-Electron Lasers” is presented by E. Minehara(JAEA)[7]. A 2 kW average power FEL of 16-23 μm in wavelength has been generated by 16.5 MeV JAEA ERL. The cryostat system has been developed and realizes the continuous ‘Zero-Boil off’ operation from 2001. The upgrade plan of the injector system for a 10 kW FEL also presented. The high power FEL applications, e.g. prevention of cold-worked stress corrosion cracking and decommissioning of the nuclear power plant, are shown.

A talk entitled “Renewal of the L-band electron linac at ISIR, Osaka University for advanced quantum beam sciences” is presented by G. Isoyama(ISIR, Osaka U.)[8]. In ISIR the pulse radiolysis in the time range down to femto-seconds and development of a far-infrared FEL are driven by an L-band linac which has been constructed in 1978. Since an extremely high stabilized electron beam is required for the magnetic pulse compression, renewal of the L-band linac has been performed in 2002. To stabilize the electron beam a klystron and power supply, RF power supplies for sub-harmonic bunchers, and DC power supplies for almost all the magnets have been replaced. The cooling water system with temperature variation within 0.03 degree for RF cavities and the air conditioner with temperature variation within 0.3 degree in the short term and -1 degree in the long term are introduced. As the result the beam stability without the long-term drift of 0.34 % and long-term drift of 0.08% / 10 min have been achieved at the experimental room.

A talk entitled “Present status in AIST FEL” is presented by N. Sei(AIST)[9]. Storage ring FELs have a potential for oscillating in VUV region for their high energy electron beams with low emittances. They also have an advantage in a narrow line-width. In AIST, storage ring (NIJI-IV) FEL has been developed to explore a short wavelength (<190 nm) region. They have also

been developed IR FEL in storage ring. As an example of FEL Application the photo-electron emission microscopy has been developed with the DUV/VUV FELs.

SINGLE PASS FELS

Extremely high brilliant radiation in hard X-ray region has strongly been desired. A fully spatially coherent X-ray beam can be generated by a single pass FEL with the electron energy in several GeV, emittance of -1 mm mrad, and peak current of -kA. Several X-FEL projects have been started for constructions. A talk entitled "Present Status of LCLS" presented by M. Reichanadter (SLAC) [10] is one of approved project. The total estimated cost is $315M including engineering, design, procurements, construction, and installation. The LCLS design parameters are listed below.

Fundamental FEL wavelength: 1.5 -15 angstrom
Electron Beam Energy: 14.3-4.5 GeV
Normalized Slice Emittance: 1.2 mm-mrad
Peak Current: 3.4 kA
Bunch Length: 230 fs (FWHM)
Relative Slice Energy Spread: < 0.01%
Peak Brightness: $0.8\text{-}0.06\text{x}10^{33}$ ph/sec/mm^2/mrad^2/0.1%

The existing SLAC linac will be extended and used for the LCLS driver linac. The injector section consists of 1.2 MeV photocathode RF gun, following L0 linacs (135 MeV), and matching section for the existing linac. The undulator section is expandable to at least six hard X-ray FEL undulators. The project has already started main tunneling, excavation on SLAC site. The injector and the bunch compressor(BC-1) will be installed in July 2006 shutdown. The first FEL will be coming at July 2008.

The other approved project on X-FEL is introduced by T. Shintake(RIKEN/Spring-8)[11]. The title is "Status of X-FEL in RIKEN/SPring-8". A 1 angstrom X-ray FEL program driven by 8-GeV C-band linac has been approved. A 250 MeV test accelerator is under construction to generate 60 nm FEL. The first light will be coming in Nov. 2005. The linac consists of thermionic DC gun, C-band linac, and in-vacuum undulator to provide stable and reliable FELs at the SPring-8 site. The CeB_6 cathode is adopted for thermionic DC gun to generate small emittance electron beam (1 A, 1.1 πmm-mrad at gun) without dark current. The in-vacuum undulator with nominal gap of 3.5 mm is used. To guarantee the high precision alignment a stable support system using Cordiereite Ceramic and a laser alignment system have been developed. The construction of the final system will be started from 2006 and commissioning will be started from 2010.

In Korea an X-FEL project has also been planned. H. S. Kang (PAL) presented "Issues in PAL XFEL Project"[12]. The existing injector linac for PLS will be extended to accelerate electron beam up to 3.7 GeV to generate a 0.3 nm X-ray FEL. The 3.7 GeV electron beam has larger divergence than the 0.3 nm radiation beam so that the transverse higher modes can have comparatively larger growth rates, which may result in poor transverse coherency. However, a simulation study shows that both the transverse coherence and the saturation length are satisfactory with the uncorrelated energy spread of 1 MeV. In order to put the system into PLS site in-vacuum undulator with minimum gap of 4 mm will be used. To reduce the undulator wake field effect, Al coating and low charge option (0.5 nC) is being considered. The third harmonics could be used for a 0.1 nm X-ray FEL.

The other topic related on the single pass FELs is high harmonics with seeding laser. The talk entitled "Seeding with High Harmonics in gas" is presented by M. E. Couprie(CEA)[13]. The seeding FEL can reduce the fluctuation of self-amplified spontaneous emission FELs because it originates from the shot noise. The seeding also reduces the FEL saturation length (resulting in compactness) and improves coherence. However, an available seeding source is strictly limited, i.e. YAG, Ti-Sa and their harmonics in crystals. On the other hand, high harmonic generation in gas with the tera-watt laser has good potential for seeding source in terms of spatial and temporal coherency, tuneability, and power. Demonstration experiments at SCSS prototype and SPARC have been prepared. An application to the ARC-EN-CIEL phase 2 is also planned.

BEAM DIAGNOSTICS & STABILIZATION

In the 3rd generation SR sources, the beam emittance of nano m-radian has already been available. By using such small size electron beam, beam stabilization issues, e.g. orbit stabilities in both transverse and longitudinal spaces, are the most crucial topics in a SR facility. The beam stabilization issues in SPring-8, one of the most advanced 3rd generation SR facility, are reported from S. Sasaki(Spring-8/JASRI) as "BPM related issues on orbit stabilization in SPring-8 storage ring"[14]. The measured orbit resolutions exhibit -15 $\mu m_{pk\text{-}pk}$ in horizontal plane and -10 $\mu m_{pk\text{-}pk}$ in vertical plane by using the position readout circuit whose position resolution is -1 $\mu m_{pk\text{-}pk}$ in SPrimg-8. In order to achieve the sub–μm resolution, the stable beam, which is free from the mechanical vibration in the BPM chamber for instance, is required for orbit measurement. T. Nakamura(Spring-8/JASRI) also report "The residual beam motion driven by the noise at a transverse feedback"[15]. Since the noise and/or resolution of a BPM system propagate through the feedback line and drive kickers in a transverse feedback system, a betatron motion is excited in the circulating beam. This effect is serious at bunch-by-bunch feedback because of its wide-band performance. This phenomenon is analyzed and a high resolution BPM is developed to reduce the amplitude of the motion to be less than micro meters for the SPring-8.

As is shown in above report, a high resolution beam monitor system (BPM) is also important issue to stabilize the electron beam. H. Sakai(ISSP, U. Tokyo) introduce "Present stratus of Fresnel Zone Plate monitor at KEK-ATF damping ring"[16]. The monitor based on an X-ray imaging optics with two Fresnel Zone Plates by using synchrotron radiation from a bending magnet. The

expected spatial resolution is less than 1 μm. A mechanical shutter has been installed in the monitor system to suppress the unexpected 100 Hz vibration which has been observed in the KEK-ATF damping ring. By applying this mechanical shutter with the short opening time, the time resolution can be achieved less than 1ms on beam profiling.

The beam stabilization is not only important issue in SR rings, but also important issue in linacs especially for operating the SR/FEL user-facility and generation of X-FELs. “Stability in SPring-8 injector Linac” is presented by H. Hanaki(Spring-8/JASRI)[17]. To achieve the beam energy stability of less than 0.03% rms in Spring-8 injector linac, 1) stabilization of RF amplitude and RF phase, 2) reduction of beam loading fluctuation, 3) compensation of uncontrollable energy variation, and 4) reduction residual beam position and energy drift are performed. Stabilization of RF related parameters are mainly secured by improvements in the air conditioning system and the water cooling system. Installation of the new timing system which synchronizes the linac RF with the ring RF reduces of beam loading fluctuation. Introduction of the conventional energy compression system compensates the uncontrollable energy variation. Installation of the feedback system based on the BPM data at the beam transport lines reduces residual beam position and energy drift. Consequently, the beam energy stability of 0.02% rms and the beam position stability of 30 μm rms have been achieved.

To improve the beam quality, beam diagnostics are important. H. Zen(Kyoto U.) presents “Issues on the transverse phase space tomography”[18]. The low energy tail of the beam, which is typically seen in thermionic RF gun, enlarges the reconstructed image because the transfer matrix used in the tomography is mono-energetic one. On the other hand, the energy spread of the beam is not serious for the reconstruction.

CONCLUSION

Nanobeams, the electron beam with a small emittance both in transverse and longitudinal directions, are required for the generation of high brightness (fully spatially coherence) radiation sources in wide spectral range from the THz to the X-ray region. By using nanobeams, the beam stabilization and diagnostics issues become a challenging issue on the 3rd generation SR sources, and also in X-FELs and ERLs. X-FELs and ERL radiation sources will be realized in near future by developments in the nanobeam generation including the low emittance electron source. Moreover, interdisciplinary cooperation with the International Linear Collider program and high intensity lasers will promise great leaps in the developments in the nanobeam generations and applications because there are many common technologies and problems behind them.

REFERENCES

[1] R. Hajima, “Energy-Recovery Linacs: overview and present status in JAEA-ERL”, in these proceedings.
[2] G. Kulipanov “Comparison of one pass(ERL) and multi pass accelerators-recuperators(MARS) as coherent X-ray sources” , in these proceedings.
[3] M. Katoh, “Development of new radiation sources at UVSOR-II”, in these proceedings.
[4] R.W. Schoenlein et al., “Generation of Femtosecond Pulses of Synchrotron Radiation”, Science 287, 2237 (2000).
[5] H. Hama, “LNS Isochronous THz Ring project”, in these proceedings.
[6] N. Vinokurov, “Status and future of Novosibirsk high power FEL, based on one pass and four passes accelerator-recuperator”, in these proceedings.
[7] E. Minehara, “The JAEA Superconducting RF Linac Driver for Free-Electron Lasers”, in these proceedings.
[8] G. Isoyama, “Renewal of the L-band electron linac at ISIR, Osaka University for advanced quantum beam sciences”, in these proceedings.
[9] N. Sei, “Present status in AIST FEL”, in these proceedings.
[10] M. Reichanadter, “Present Status of LCLS”, in these proceedings.
[11] T. Shintake, “Status of X-FEL in RIKEN/SPring-8”, in these proceedings.
[12] H. S. Kang, “Issues in PAL XFEL Project”, in these proceedings.
[13] M. E. Couprie, “Seeding with High Harmonics in gas”, in these proceedings.
[14] S. Sasaki, “BPM related issues on orbit stabilization in SPring-8 storage ring”, in these proceedings.
[15] T. Nakamura, “The residual beam motion driven by the noise at a transverse feedback”, in these proceedings.
[16] H. Sakai, “Present stratus of Fresnel Zone Plate monitor at KEK-ATF damping ring”, in these proceedings.
[17] H. Hanaki, “Stability in SPring-8 injector Linac”, in these proceedings.
[18] H. Zen, “Issues on the transverse phase space tomography”, in these proceedings.

SUMMARY OF WG3C1, LEPTON BEAM

Young Uk Jeong

KAERI, Daejon, Korea

Abstract

During the workshop, lepton beam, which means electron and photon beam, had been discussed at a working of WG3c1. There had been five presentations which cover wide range of light spectrum from gamma ray to far infrared radiation generated by high quality electron beams. The discussions showed that the advanced radiation technology can play important role as a tool for next-generation science and technology. The titles and speakers of the presentations are listed in the Table 1.

WG3C: Lepton (Electron & Photon) Beam

- γ-ray : 2.4 GeV photon by Compton scattering of 6 GeV Spring-8 beam and 351 nm Ar+ laser beam *(N. Muramatsu, Osaka Univ.)*
- X-ray :
  - Hard X-ray (~50 keV) compact Compton scattering source *(F. Sakamoto, Univ. of Tokyo)*
  - Calculation for coherent Attosecond X-ray generation by nonlinear Compton scattering *(K. Lee, KAERI)*
  - Monochromatic X-ray (4~35 keV) by parametric X-ray generation for imaging application *(Y. Hayakawa, LEBRA)*
- IR : Intense light of 0.8~6 μm radiation from a S-band linac FEL *(Y. Hayakawa, BEBRA)*
- FIR (THz) : High power THz of 100~1200 μm radiation from a Microtron FEL *(Y. Jeong, KAERI)*

Table 1: Summary of the WG3C1, lepton beam.

GAMMA-RAY

Generation of high energy photon beam by Compton scattering of SPring-8 beam and UV laser beam was presented by N. Muramatsu from Osaka University [1]. By using the 8-GeV Spring-8 electron beam and 351 nm Ar^+ laser beam, γ-ray having the maximum energy of 2.4 GeV was generated and characterized. The photon energy was measured by detecting the direction of recoil electrons. The measured γ-ray spatial and energy distribution is shown in Fig. 1 with the parameters of the laser and electron beam. The linear component of the polarization of the γ-ray is approximately 95% at the maximum energy.

The purpose of the γ-ray is to produce various hadrons and to probe interactions at quark-nuclear scale. The photon beam was used to produce hadrons of Pentaquark. The maximum photon energy was extended to 3 GeV by using a 257 nm laser. Discussions had been devoted to generate photon beam having higher intensity and energy.

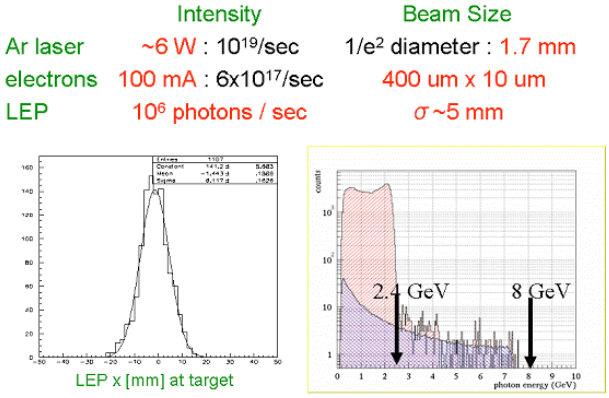

Figure 1: Measured spatial and energy distribution of the high energy photon beam. Characteristics of the electron, laser, and generated photon beam are listed in the upper part of the results.

X-RAY

There were three presentations on generation and application of X-rays. Development and application of Compton scattering hard X-ray based on X-band electron linear accelerator was presented by F. Sakamoto from University of Tokyo [2]. The main idea of their system is to produce dual-energy monochromatic hard X-ray by using a compact X-band accelerator and two Q-switched Nd:YAG lasers. The interaction scheme is also Compton-back scattering between the electron and laser beams. The main parameters of the system are listed in the Table 2.

Performance of compact hard X-ray source

Electron beam	
	Frequency : 11.424 GHz (X-band)
	Electron gun : 3.5-cell thermionic RF-gun
	Energy : 56 MeV (MAX)
	Charge : 20 pC/bunch
	Micropulse duration : ~ psec
	Multi-bunch : 10^4 bunches/RF pulse
	RF pulse length : 1 usec, 50 MW
Laser	
	Q-switch Nd:YAG laser: 1064 nm, 2J/10ns, 10 pps
X-ray	
	Energy :56 keV (MAX)
	Intensity :10^8 photons/sec

Table 2: Main parameters of the compact hard X-ray source.

The proposed system is shown in Fig. 2. The typical electron energy is 35 MeV with a bunch charge of 20 pC. The repetition rate of the macropulse beam is 10-50 Hz. Laser beams having different colour of 1064 and 532 nm are injected to the electron beam for generating 20 and 40 keV X-rays. The beam line for the experiment of a RF gun was constructed and RF aging of the RF gun was being performed. They expected to start the generation of the hard X-ray during 2006.

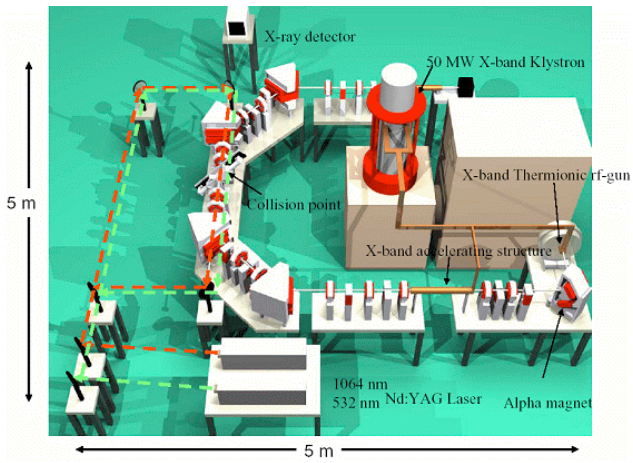

Figure 2: Schematic layout of a compact Compton scattering hard X-ray source based on an X-band linac.

Generation of ultrashort radiation pulse has been attracted much interesting because it could be a unique tool to investigate ultra-fast dynamics in nature, such as motions of electrons in atoms or nucleons in atomic nuclei. K. Lee from KAERI proposed a scheme to produce coherently enhanced attosecond X-ray by nonlinear Compton scattering [3]. Originally he proposed a nonlinear Thomson scattering to use an extremely thin film much less than a micrometer for the attosecond X-ray generation [4]. However the prepulse of femtosecond laser beam easily can destroy the thin film. The required contrast ratio of the femtosecond laser beam is 10^{10} and it is too high to reach.

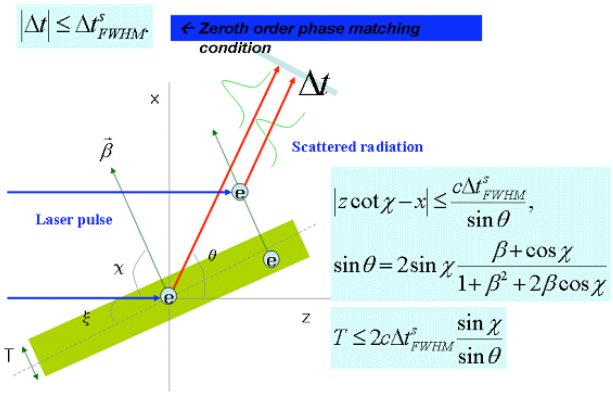

Figure 3: Geometric condition for producing coherent attosecond X-ray pulse by nonlinear Compton scattering.

To solve the problem, the thin film is substituted by electron bunch having duration of several tens or hundreds nanometers. Modulated electron beam by FEL interaction can be used for the thin electron bunches. The calculation results are shown in Fig. 4 for practical electron beam conditions. The effect of the beam parameters on the harmonic spectrum was discussed. Including the finite focal size of the laser pulse, a few 10 TW was estimated to be required to demonstrate the coherent nonlinear Thomson scattering.

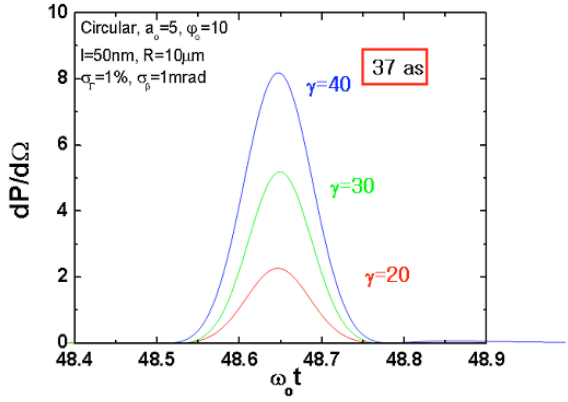

Figure 4: Calculated attosecond X-ray pulse by the intense laser of tens femtoseconds and the electron beam having the practical parameter of energy spread and emittance.

S-band electron linac	
Max. energy	125 MeV
	100MeV(typ.)
Beam intensity	100 mA
Duration	20 μs
Repetition	12.5 Hz
	2Hz (typ.)
Average current	25 μA
ΔE/E	~ 1%
Emittance	~15π mm mrad

Table 3: Main parameters of the S-band electron linac in Nihon University.

Y. Hayakawa from Nihon University presented activities on monochromatic X-ray and IR by a S-band linac based system [5]. The main parameters of the accelerator are listed in Table 3. They produced high energy photon by the scheme of parametric generation and filtered by a second crystal for monochromatic X-ray. The scheme and parameters for the X-ray generation is shown in Fig. 5. The monochromatic X-ray of 6 to 20 keV was generated and used for X-ray imaging and the experiments of X-ray absorption fine structure (XAFS) for various samples. The preliminary experiments suggest

that applications of the monochromatic X-ray such as imaging and XAFS measurement are promising.

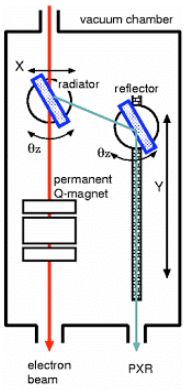

PXR generator	
Electron energy	100 MeV
Average current	5 μA
Target crystal	Si perfect crystal
X-ray energy	
Si(111)	4 ~ 20 keV
Si(220)	6.4 ~ 34 keV
X-ray beam size	98mm in diameter @extraction port

Figure 7: Measured polarization of the THz FEL beam by using a metal-wire polarizer having 20 μm spacing.

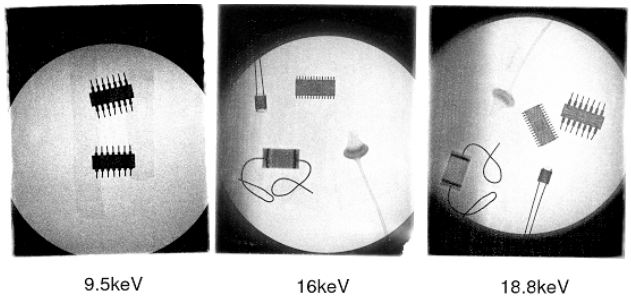

Figure 8: X-ray imaging of electric devices for different X-ray energies of 9.5, 16 and 18.8 keV.

INFRARED

The S-band linac in Nihon University is used as a driver for an infrared (IR) free electron laser (FEL). The FEL operates in near IR range of 0.8 to 6 μm.

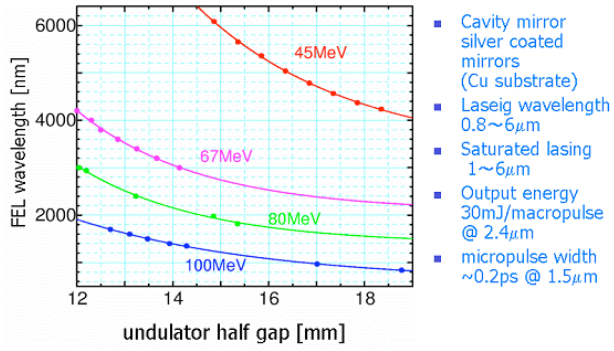

Figure 9: Operating wavelength range of the Nihon University FEL depending on undulator gap and main parameters of the FEL beam.

Figure 9 shows the operating wavelength range of the FEL depending on undulator gap and main parameters of the FEL beam. The femtosecond FEL beam was used for drilling holes on a human tooth. Due to the ablation effect by the ultrashort IR beam, they could make quite small holes on the tooth. The wavelength range of the FEL was extended to 371 nm by HGHG (high gain higher harmonics) process. Dynamic tuning of the RF phase to match the cavity detuning length showed the increased power of the FEL beam up to two times.

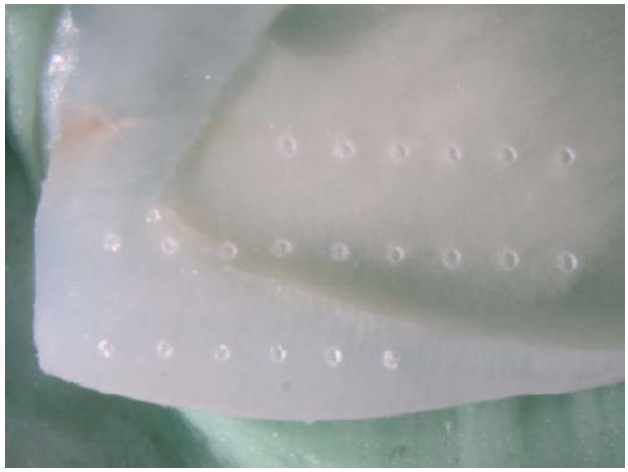

Figure 10: Holes on a human tooth drilled by ultrashort IR FEL beam of 2.94 μm [6].

FAR INFRARED

Y. U. Jeong from KAERI presented on a far infrared (FIR) or terahertz (THz) FEL driven by a compact classical microtron as shown in Fig. 11 [7]. The FEL operates in the wavelength range of 100–1200 μm, which corresponds to 0.3–3 THz. The peak power of the FEL micropulse having 30 ps pulse duration is 1 kW and the pulse energy of the 3-μs-FEL-macropulse is approximately 0.3 mJ. The main application of the FEL is THz imaging and spectroscopy for bio-medical research and THz material study [8].

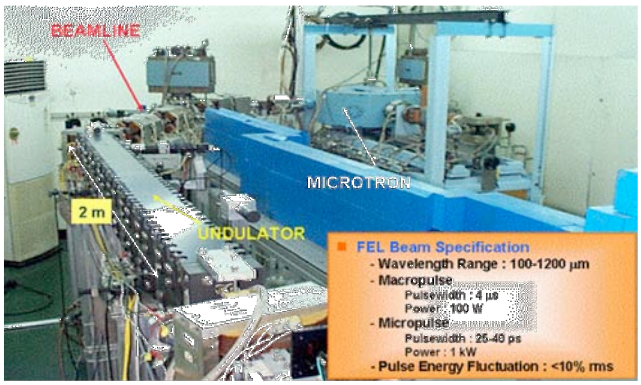

Figure 11: Photograph and specifications of the KAERI compact THz FEL.

Y. U. Jeong tested the FEL for transmitted imaging of bio-samples. Figure 12 shows transmitted THz imaging of living-condition bio species by using the FEL light. The THz frequency of the imaging is 3 THz. We could get

transmitted THz imaging of the bio-samples, even the image is not so clear. The results show the high power THz source can be used for an advanced imaging application like mammography.

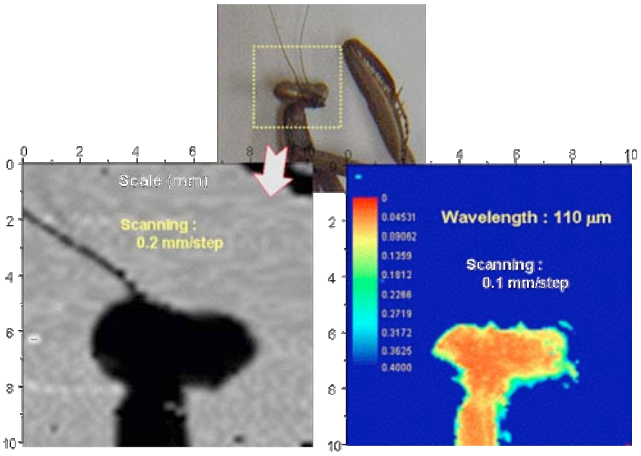

Figure 12: Transmitted THz imaging of the head part of a mantis. The sample was also killed just before the measurement.

REFERENCES

[1] N. Muramatsu, 'High energy beam of laser-electron photons at Spring-8 LEPS experiment', NANOBEAM 2005, Oct. 2005, Kyoto, Japan.
[2] F. Sakamoto, 'Development and application of Compton scattering hard X-ray source based on X-band electron linear accelerator', NANOBEAM 2005, Oct. 2005, Kyoto, Japan.
[3] K. Lee, 'Coherently enhanced attosecond X-ray generation by nonlinear Compton scattering', NANOBEAM 2005, Oct. 2005, Kyoto, Japan.
[4] K. Lee *et al.*, Phys. Plasma **12**, 043107 (2005).
[5] Y. Hayakawa, 'Tunable and monochromatic light sources at LEBRA in Nihon University', NANOBEAM 2005, Oct. 2005, Kyoto, Japan.
[6] T. Sakae *et al*., International Journal of Oral-Medical Science, Vol. 4 (2005) 8.
[7] Y. U. Jeong, 'THz radiation in KAERI', NANOBEAM 2005, Oct. 2005, Kyoto, Japan.
[8] Y.U. Jeong, et al., Nucl. Instr. and Meth. A 543 (2005) 90.

SUMMARY OF WORKING GROUP 3C-2: ION BEAM

H. Hanaki, JASRI/Spring-8, Hyogo 679-5198, Japan

Abstract

This working group was intended to treat generation of high quality ion beams and their applications. Important techniques for the beam cooling, present status of ion storage rings and projects ongoing are summarized.

INTRODUCTION

Importance of high-intensity or high-quality ion beams is recently growing especially in practical applications such as the heavy-ion therapy or the microbeam probe, as well as the experimental physics. In addition, analysis of the dynamics of molecular ion reactions utilizing heavy-ion storage rings has been successful during the last decade. Because of this situation, the working group 3C-2 (Ion Beam) was thus formed to discuss about generation of high quality ion beams and their applications.

In this working group, four facilities (KEK, NIRS, Kyoto Univ. and MPI-K) provided presentations regarding ion storage rings and electron coolers. Principal specifications of the presented storage rings are summarized in Table 1 for reader's convenience. The electron coolers developed by BINP (Novosibirsk) and their important technologies were also introduced.

Summarizing this working group, the author will mainly focus on the electron cooling, which is one of the key technique to enhance the ion beam quality.

TECHNIQUES FOR BEAM COOLING

The following eight techniques for cooler were presented or referred in this workshop:

Adiabatic Expansion [1,2]

Electron coolers are generally equipped with solenoid coils which guide an electron beam from a cathode to a collector via a cooling section. If the solenoidal field strengths gradually decrease along the trajectories of the electrons extracted from the cathode, the electron beam diameter transversely expand; the transverse electron temperature is thus reduced due to this adiabatic expansion. The ratio R of the magnetic field in gun region to that in cooling section determines the transverse electron temperature T_e as $T_e = T_{cath}/R$, where T_{cath} is the cathode temperature.

KEK equipped their electron coolers with superconducting solenoids to enhance the magnetic fields around an electron gun; the magnetic ratio R of 100 was achieved. Then the electron transverse temperature was consequently reduced to about 1 meV.

Laser Cooling [4,5,9]

The conventional cooling method reduced the temperature of stored ions to a few kelvins in the longitudinal direction and a few hundred kelvins in the transverse direction, whereas the laser cooling technique has been expected to realize ultracold ions of a few millikelvins.

The laser cooling in ion storage rings has been extensively studied, however, only the longitudinal cooling was successful because a laser beam has to be injected along the ion beam trajectories. To realize the 3D laser cooling, the coupling resonance method was proposed. S-LSR, a compact ion storage ring at Kyoto University, is going to try the coupling resonance method with the aim of exploring the lowest temperature limit of ion beams such as the crystalline beam.

Photocathode Electron Gun [7,10]

Developed The photocathode material GaAs can be formed on a substrate by the appropriate process so as to have the negative electron affinity (NEA). The NEA-GaAs photocathode has the following advantages: The quantum efficiency is essentially much higher than those of metal cathodes. The energy distribution of the free electrons ejected from a cathode can be narrower than cases of metal cathodes when the laser wavelength is optimized.

The storage ring TSR at MPI-K in Heidelberg

Table1: Principal specifications of ion storage rings presented in the workshop

	KEK [1,2]		NIRS	Kyoto U.	MPI-K
	TARN-II*	ESR**	HIMAC [3,4]	S-LSR [5,6]	CSR [7,8]
Type of bend#	Mag	ES	Mag	Mag + ES	ES
Circumference	78 m	8.1 m	129.6 m	22.5 m	33.9 m
Ion species	light ion	heavy ion	heavy ion	p, C^{6+} / Mg^{+}	u =1~100
Energy	10 MeV	20 keV/q	6~55 MeV/u	7, 24 MeV/ 35 keV	20~300 keV/q
Electron cooling					
Energy	20 keV	1~100 keV	3~30 keV	1~5 keV	6~165 keV
Current	0.4 A max.	2 mA	2 A max.	0.4 A max.	4.2 mA max.
Cooling†	AE	AE	AE	AE / LC	AE + PC + CT
Expansion factor	1~100	10~100	1~10	1~3	20 / 90

Note * This machine was shutdown in 1999. ** ESR: Electrostatic Storage Ring
Mag: Magnetic bend, ES: Electrostatic bend
† AE: Adiabatic expansion, LC: Laser cooling, PC: Photocathode, CT: Cryogenic temperature

accomplished the longitudinal electron temperature of 0.02 meV and the transverse one of 0.5 meV, combining the adiabatic expansion and a cryogenic photocathode at 90 K when irradiated by laser lights. The storage ring CSR in construction will employ the same cryogenic photocathode.

Cryogenic Storage Ring [7,8]

The whole of vacuum chambers of the CSR (MPI-K) will be cooled down to a temperature of around 2 K; the following benefits will be obtained: Extremely low rest-gas pressures leading to the long storage time and drastic reduction of the blackbody radiations which excite the rotational states of the stored molecular ions. The latter is expected to realize the rotational ground state of molecule.

Hollow Electron Beam [11,12]

BINP developed a novel electron gun which ejects a beam with a variable profile. The beam profile, the transverse charge distribution, can be controlled continuously from a solid beam to a hollow beam by adjusting a voltage applied to the control electrode between a Pierce electrode and an anode. An optimised electron beam profile, which has the low electron density in the center, decreases the recombination and enables uniform cooling of ions with various betatron amplitudes. This technique was employed by the recent projects, CSR at IMP (Lanzhou, China) and LEIR at CERN.

Electron Beam Recuperation [11-13]

When a beam collector of the electron cooler has the potential slightly higher than the potential of a cathode electrode, the most part of the electron beam can be recuperated. Secondary electrons emitted from the cathode are accelerated and go back toward the cathode. If the toriod section between the collector and a cooling section would have magnetic bends, the backward electrons would be deflected there to the opposite side with respect to the deflection of the foregoing electron beams and then lost. BINP has chosen electrostatic bending system in the toroid sections, which deflects the backward electrons to the same side, to avoid the loss of the secondary electrons. The secondary electrons hence run along the trajectory oscillating between the cathode and the collector, and are finally absorbed by the collector.

Canceling Transverse Magnetic Fields in Cooling Solenoid [11,12]

The transverse components of the solenoid fields in the cooling section degrade the maximum cooling rate. The cooling solenoid developed by BINP is composed of tiltable coil elements called pancake. The residual transverse magnetic fields are minimized by adjusting mechanically the tilt of each coil.

Cyclotron Charging System [11,13]

BNP proposed a novel idea for charging the high voltage terminal of an electrostatic accelerator for the beam cooling. That is the cyclotron charging system, which ejects energetic H^- ions to the terminal to charge it. Comparing to the conventional mechanical charging system such as pelletron, the proposed system is expected to have the higher terminal voltage stability and the faster charging speed. A turbine power generator driven by SF^6 gases will be mounted on the terminal to supply electric powers to an electron gun and so on.

EXPERIMENTS AND EXPERIENCES AT COOLER RINGS

TARN-II and Electrostatic Storage Ring at KEK [1,2]

TARN-II, a conventional magnetic storage ring, had been operated from 1989 to 1999. It was equipped with the electron cooler holding the superconducting adiabatic expansion system mentioned above. The electron temperatures were measured by observing the dissociative recombination of $^4HeH^+$ molecule. A minimum transverse temperature of electrons was about 1 meV.

An electrostatic storage ring was also constructed to store heavy ions for atomic and molecular physics experiments. The storage ring has twofold symmetry holding two straight sections; the one is equipped with an electron cooler which is mainly used as a thick electron target. They observed that the lifetime of stored proton beams was almost doubled when cooling electrons were injected. This was a clear evidence of the electron cooling in the transverse direction.

HIMAC at NIRS [3,4]

An electron cooler was installed in HIMAC aiming at the followings: enhancement of the beam intensity, development of a microbeam probe, etc. In their experiment of cool-stacking injection of Ar^{18+} at 6 MeV/u, the transverse coherent instability was observed when the electron and ion densities were high. This phenomenon was well explained by a simulation including the coherent interaction between electron and ion. The instability was damped by employing the transverse RF heating which decreases the peak density of the stored beam because the coherent interactions depend on the ion density. They also found that minimum values of products of the beam cross sections and bunch lengths were almost constant for both of the coasting and bunching beams. That is, a minimum transverse beam size at any bunch length is determined by the maximum particle density.

PROJECTS ONGOING

S-LSR at Kyoto University [5,6,14]

The storage ring S-LSR has been developed as a compact and high performance injector for a medical heavy ion synchrotron. Now S-LSR is in commissioning.

S-LSR has the following features: The lattice of S-LSR has six-fold symmetry to enable the crystalline mode where betatron phase advance per period is less than 90 both in horizontal and vertical directions. The laser beam

will cool down Mg^+ (35 keV) ions to form the crystalline beam. An electron cooler is also installed to cool down a proton beam (7 MeV) or laser-produced C^{6+} (24 MeV) ions. Bending magnet chambers hold electrostatic deflectors inside to avoid the shearing force heating.

Recent status of the S-LSR commissioning with proton beams was as follows: A maximum stored current was 300 μA. The momentum spreads, which were measured by the Shottky spectrum monitor installed, were 1.1% at 300 μA and 0.6% at 100 μA. The lifetime was 550 seconds. Beam monitors (DCCT, Schottky monitor, profile monitor, ESBPM), which were carefully designed to fit the small storage ring, were examined to function without problems. The measurement and correction of COD using the ESBPM's was also successful.

CSR at MPI-K [7,8,10]

Construction of the cryogenic electrostatic storage ring, CSR, is now in progress. This storage ring was designed mainly for studying atomic and molecular physics. It will be possible to store slow beams of molecular ions in a wide mass range up to bio-molecules. The energy range of the stored ions is foreseen to be adjustable from 20 to 300 keV per charge.

An electron cooler employing the cryogenic photocathode mentioned above will be installed and be also used as cold electron targets. The ring will be operated at cryogenic temperature to achieve the rotational ground state of stored ions.

Other features as follows: The lattice of the ring has four-fold symmetry. Electrostatic cylindrical deflectors at the four corners have grounded electrodes at both ends of the deflector plates to reduce the fringing fields. These electrodes and trimming of the deflector-plate lengths resulted in precise adjustment of the actual deflection angle.

Their recent status reported at the workshop was that the storage of 300 keV proton beams was successful.

Electron Coolers Developed by BINP [11-13]

BINP has recently developed three electron coolers, EC-35 and EC-300 for CSR at IMP (Lanzhou, China), and EC-40 for LEIR at CERN. These electron coolers employed the following new technologies mentioned above: the hollow electron beam formation, the combination of magnetic and electrostatic bends, and the mechanically adjustable sectioned solenoids.

They are also proposing 2 MeV and 8 MeV electron coolers to new projects at COSY (Research Center, Jülich) and HESR (GSI), respectively. Both the electron coolers will employ the novel idea under studying: the cyclotron charging system to charge their high voltage terminals equipped with electron guns. A cooling section of the 8 MeV electron cooler will be 30-m long and hold the superconducting pancake solenoids.

REFERENCES

[1] T. Tanabe, “Electron beam cooling at a magnetic storage ring, TARN-II, and an electrostatic storage ring”, in these proceedings.
[2] T. Tanabe et al., “An electrostatic storage ring with a merging electron beam device at KEK”, NIM **A532** (2004) 105.
[3] T. Uesugi, et al., “Electron beam cooling and beam instability issues in HIMAC synchrotron”, in these proceedings.
[4] N.Noda et al., “Electron cooling of bunched ion beam at NIRS-HIMAC”, NIM **A532** (2004) 129.
[5] T. Shirai et al., “Lattice design and cooling simulation at S-LSR”, in these proceedings.
[6] A. Noda et al., “Ion beam cooling at S-LSR”, NIM **A532** (2004) 150.
[7] H. Fadil et al.,“Lattice and Electron Cooler design of the Heidelberg CSR”, in these proceedings.
[8] R. von Hahn et al., “CSR – A cryogenic storage ring at MPI-K”, EPAC 2004, Lucerne, Switzerland.
[9] Y. Yuri et al., “Generating ultralow-emittance ion beams in a storage ring”, Phys. Rev. Lett. **93**-20 (2004) 204801.
[10] D. A. Orlov et al., “Photocathodes as electron sources for high resolution merged beam experiments”, J. Phys., Conf. Series **4** (2005) 290.
[11] V. Vostrikov et al., “Recent projects of BINP electron cooling group”, in these proceeding.
[12] E. Behtenev et al., “Commission of electron cooler EC-300 for HIRFL-CSR”, RuPAC 2004, Dubna.
[13] A. Bubley et al., “Budker INP proposals for HESR and COSY electron cooler system”, COOL 2005, Galena, USA.
[14] S. Fujimoto et al., “Beam monitoring system and orbit correction in S-LSR”, in these proceedings.

SUMMARY FOR THE WG4: PHYSICS WITH HIGH INTENSITY LASERS

T. Takahashi*, Graduate School of Advanced Sciences of Matter, Hiroshima University, Higashi-Hiroshima, 739-8530, Japan

Abstract

There are many physics opportunities in laser-beam interactions and innovations in the laser- and the beam technologies expand them or even open new window in the field. Therefore, physics with high intense lasers is an attractive application of nanobeam technologies. The topics in the working group 4 covers fundamental physics based on technique related with nanobeam development aiming to encourage communication between physics and accelerator communities. Due to the limited time for the preparation, we did not try comprehensive coverage of the field but invited topics which are planed near future or can be studied at the ILC test facilities.

OVERVIEW

Laser-beam interactions are used in many fields of the nanobeam technologies such as, the laser wire, Shintake monitor, the RF gun, the laser cooling , polarized positron sources and photon colliders, etc. The usage covers all aspects of nanobeam technologies; i.e., beam monitors, sources and improvement of beam quality.

Interactions between electromagnetic field (lasers) and beams are fundamental physics which is well described by the Quantum Electro-Dynamics(QED) (and is why it can be used for beam technologies). However, there sill are topics to be studied as fundamental physics. One is the case that the laser field become very strong. In this case, we have to consider the laser field as a strong electromagnetic field or, quantum mechanically, an intense coherent state which could trigger higher order effects. The other case is that interactions of electromagnetic field with matters leads or enhances new phenomena. In any case, they require high intense laser field and/or high quality laser beams. In addition, high quality and well controlled electron beams are essential for some application. Therefore, technologies for the nanobeam development can be applied directly to the physics being an additional motivation of the nanobeams.

The purpose of the session is to encourage communication between nanobeam community and physics community, particularly, those who want to use nanobeam related technologies but not familiar with them. In the session, we had four talks and two of them (Homma and Takahashi) was related with the first one and other two(Yoshimura and Sakabe) can be categorized in the later case .

CONTRIBUTIONS

#tohru-takahashi @ hiroshima-u.ac.jp

Exploring High Energy Frontier by High Quality Laser

Yoshimura discussed a new possibility to enhance phenomena beyond the Standard Model such as lepton non-conservation in an atomic system with lasers [1].

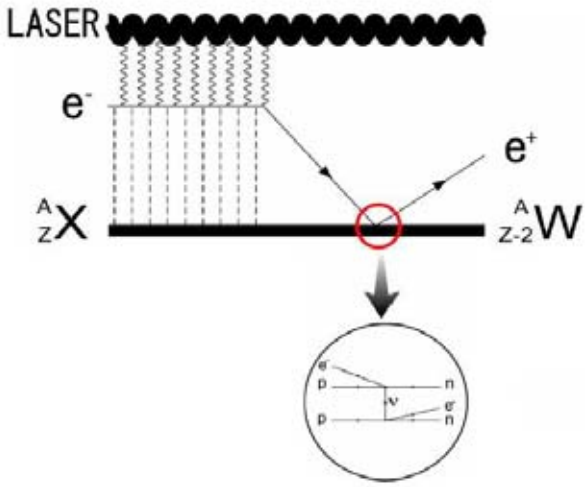

Figure 1: Schematic view of Laser assisted lepton non-conservation process in an atomic system.

The principle of the idea is illustrated in figure 1 for the case of a lepton number non-conservation process. An electron in the atomic state $^{A}_{Z}X$ is exited to a higher level by absorbing a laser photon and then decays into a lower level. If one consider two level states irradiated by a continuous laser, the electron and the laser system makes a Rabi oscillation with a definite frequency. However, if the higher level electron decays to a state other than the original lower state indicated by an arrow in figure 1, the laser can be regarded as a trigger for the process and if the process is the one beyond the standard model, it is possible to explore new physics via this scheme. Yoshimura pointed out that the reason of the enhancement of the rare process can be attributed to the compression of the electron cloud due to electron oscillation in the laser field and named it PHoton IRrAdiated Compression (PHIRAC)[2]. The enhancement factor Q can be expressed as;

$$Q \approx 1.6\times 10^{6}\tau\left(\frac{P}{\mathrm{W/mm^2}}\right)\left(\frac{\omega_0}{\mathrm{eV}}\right)\left(10^{-9}\frac{\omega_0}{\Delta E}\right),$$

where $P, \omega_0, \Delta E$ are power, energy, and width of the incident laser. τ is ratio of the wave function and is $\tau \approx 1/m^6$ with m being principal quantum number. Therefore, the laser power as well as quality (width) of

the laser is crucial to obtain high enhancement factor.

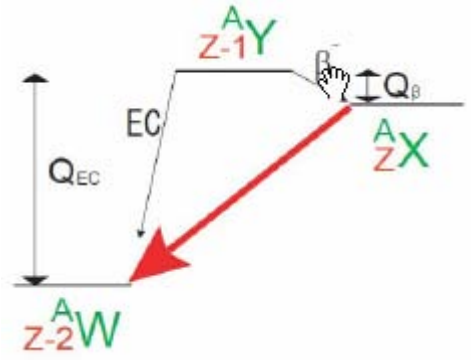

Figure 2: Level scheme of related three adjacent nuclei of the mass number A and the atomic number Z.

The principle of the PHIRAC can be tested by observing the enhancement of the electron capture from the intermediate state ${}^{A}_{Z-1}Y$ (see figure 2).

Energetic ion generation by Coulomb-explosion of cluster molecules with an intense femtosecond laser

Sakabe reported the experiments on the energetic ion generation using femtosecond a laser and atomic clusters. The idea is that if atoms are ionized within a very short period by a femtosecond laser pulse. All electrons in atoms in a cluster are expelled leaving highly positively charged ions. So that energetic ions will come out due to strong repulsive force between ions and is called the Coulomb Explosion. Sakabe and his colleagues performed an experiment with T6 laser facility at the Institute of Laser Engineering in Osaka University which provided laser pulses of 10^{16} W/cm^2 [3]. Figure 4 shows the energy of the ions as a function of the back-pressure of the hydrogen gas jets (corresponding to the cluster density).

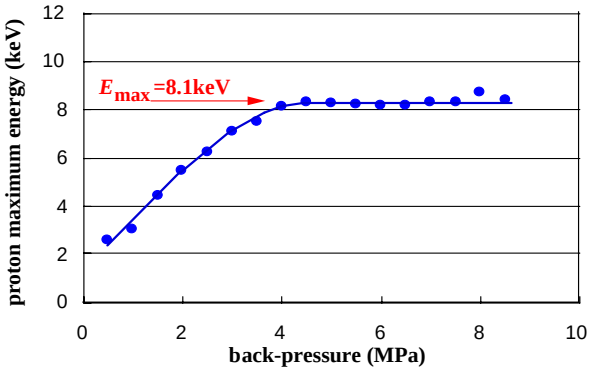

Fig. 4 Proton energy as a function of the backpressure.

Observed maximum energy of the protons from the Coulomb explosion was 8.1keV which showed good agreement with model calculation and an extrapolation from 3D-PIC simulations.

A question arose in the summary session regarding use of expelled electrons for new kind of electron source. According to Sakabe, laser produced electrons can be a new electron source. It is unnecessary to use the cluster target for the electron source. Ions are generated by Coulomb-explosion, but electrons are just ionized and accelerated by a laser pulse. For electron generation, simply, for example, thin foil target or gas target may be available.

Study of virtual vacuum polarizations in a strong electromagnetic field

Homma discussed on possibility of observing QCD effect in the vacuum polarization in strong laser field. In the presence of the intense laser field, the diffraction index of the vacuum may be changed via the virtual polarization. If the effect is large enough it can be observed as a change of threshold of the Chrenkov radiation in the laser field. However, if we consider such effect by the QED, it may require Peta Watt laser colliding with the 45 GeV electron to change diffraction index $O(10^{-10})$. Homma pointed out that it may be possible that QCD vacuum contribution enhance deviation of the index to observable level.

He showed the results of the experiment of the interaction of intense laser and the 40 MeV electrons. The experiment originally aimed to measure the spectrum of scattered photons off the electron for the purpose of femrosecond X ray generation by Compton Scattering. However, if the change of the diffraction index manifested in the process, it may appear as extra photon yield in visible light region.

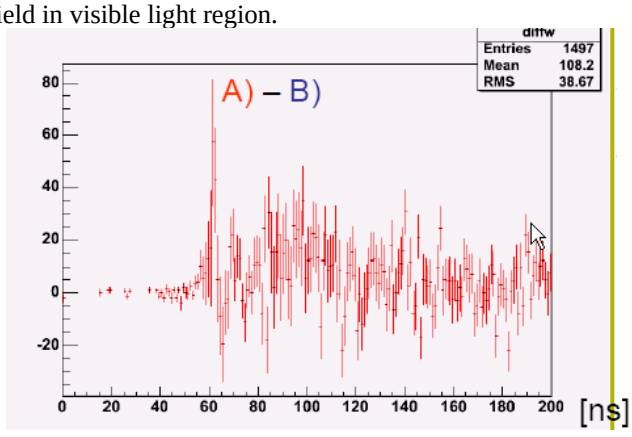

Fi.g 5 Timing distribution of visible photons

Figure 5 shows timing distribution of observed photon after choosing visible light. An excess counts (about two standard deviations) was observed around the time of 60 ns which corresponds the time when laser and electron pulse overlapped. The statistical significance may not be enough to confirm the excess, thus other experiments for the confirmation is awaited. Particularly, an electron facility with more intense lasers is favourable.

Laser Facility at ATF2

Takahashi introduced a plan to construct a laser facility at the ATF2. First, he introduced resent results of nonlinear Compton experiments, performed at the T6 laser facility at the ILE-Osaka (which is the same as introduced by Sakabe)[4]. The experiment was the collision of intense laser pulse of 4×10^{15}W/cm^2 with the wave length of 800nm and the electron of 10 keV. In this energy region, a nonlinear effect in Compton scattering could manifest as an appearance of scattered lights in the second harmonic region, i.e., wave length around ≤ 400nm.

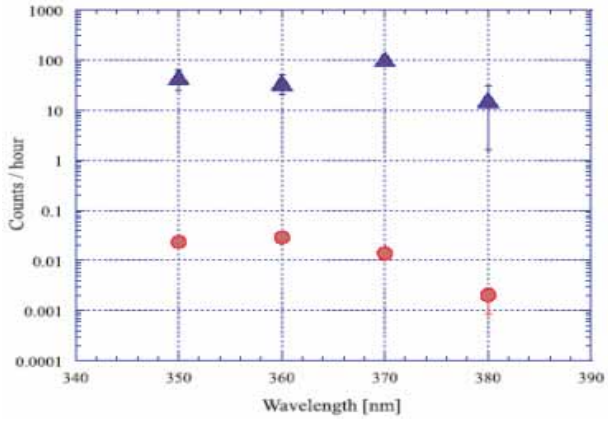

Figure 5: Number of photons observed as a function of wave length. Triangles are for experimental observation while circles are for simulation based on a nonlinear effect in Compton scattering.

Their result is shown in figure 6. The experimental observation is about 3 orders of magnitude of higher than the expectation of simple non-linear effect in Compton scattering. They examined their results in term of, experimental errors, self-focusing of the lasers in the electron beam, the interaction of lasers and residual gasses, nonlinear scattering between lasers and material around the interaction points, etc. According to their investigation, none of above effects could explain observed excess in the 2nd harmonic region. It is left as open question and another experiments are necessary.

SUMMARY

The laser and nanobeam technologies for physics in the energy frontier, such as the ILC, can also be applicable for other field of fundamental physics. A high quality laser itself may open new feasibility to explore physics beyond the Standard Model in low energy experiments. The interaction between the intense laser field and the electron beam still have open question to be explored. For this purpose, it is strongly desirable to construct facility of high quality electron beam such as ATF2 with TW or PW laser systems available.

The author would like to thank speakers for the working group 4 for valuable contribution. They all prepared their talks in very short term. He also thank organizers of the workshop for allowing us to cut in this session and for excellent organization.

REFERENCES

[1] M. Ikeda, I. Nakano, M. Sakuda, R. Tanaka, M. Yoshimura, “New method of enhancing lepton number nonconservation”, hep-ph /0506062 v2.
[2] M. Yoshimura, “Photon Irradiated Compression as a Tool of Investigating Fundamental Physics beyond Standard Model”, hep-ph/0507248
[3] S. Sakabe, et al., Phys. Rev. A 69, 023203(2004)
[4] M. Iinuma, K. Matsukado. I. Endo, S. Sakabe, T. Takahashi, T, Tauchi, Phys. Lett. A346/4 (2005) 255-260

LASER WIRE LOCATION IN ILC DIAGNOSTICS SECTION AND TUNE-UP EXTRACTION

D. Angal-Kalinin, ASTeC, Daresbury Laboratory, WA4 4AD, UK
M. Woodley, SLAC, Stanford, CA 94309, U.S.A.

Abstract

In the International Linear Collider (ILC), the luminosity will depend on maintaining the small emittance delivered by the damping rings. It is proposed to use laserwires for measuring the beam sizes in the Beam Delivery System (BDS) for emittance diagnostics and coupling correction. The accuracy of the beam size measurement depends on the beam size at the laserwire location. A proposed dipole chicane or a bend design located after the emittance measurement section will detect off-energy bunches coming from the upstream accelerator. These insertions will also help to extract the laserwire signals from the emittance measurement section. This paper discusses the design issues and implications for the overall BDS design.

INTRODUCTION

In the present baseline layout recommended for the ILC [1], coupling correction and emittance measurement sections are located at the beginning of the BDS. The proposed scheme at the time of Snowmass [2] assumed detection of off-energy bunches at the energy-spoiler located around 600 m downstream and thus the abort system would allow many bunches to pass through the BDS. The spoilers can only survive up to 2 full-charge bunches at 500 GeV CM and only 1 bunch at 1 TeV CM [3]. Thus, care must be taken in the design not to pass more than 1-2 bunches to the spoilers. It was proposed during Snowmass discussions to design a chicane to detect the energy errors as close as possible to the abort system in order to allow only a few bunches to reach the spoiler. Chicanes and other bending systems located at the exit of the emittance diagnostic section have been studied. In addition, these systems must provide the necessary clearance for extracting and detecting the laserwire compton photons. Thus the bend magnets must be designed to allow these photons to pass through, and the details of the synchrotron radiation spectrum need to be considered for the overall system design.

In the present emittance measurement section design, the vertical beam sizes at the laserwire locations can be less than 1 μm. With the present laserwire size, beams of this size can be measured with at best 10% accuracy [4]. To increase the measurement accuracy to 1% will require increasing the beam sizes at the laserwire locations to at least 3 μm. This will necessitate a significant increase in the length of this section. Various optics solutions, as well as improvements to the laserwire system, are being considered [5]. Detailed performance studies are required to define the required measurement accuracy.

DETECTION OF OFF-ENERGY BEAMS

Detection of off-energy bunches requires some dispersion in the design. In order to keep the increase in the horizontal emittance due to synchrotron radiation in the dipoles to a minimum, very soft bends are required at 1 TeV CM. In both the chicane and the bend designs presented below, the optical functions and the parameters given in Table 1 are used. In order to be able to measure the energy spread in these designs, the chromatic beam size should be, at most, of the order of the geometric size. Choosing a horizontal dispersion value of 20 mm and β_x of 5 m as shown in Table 1 can meet these requirements. However if, as discussions within the BDS working group indicate, the precise measurement of the energy spread is not required at this location, the optics can be relaxed. The energy spread measurements can then be done further downstream at the location of the energy spectrometer.

Table 1: Parameters used for energy detection

		@500 GeV CM	@1 TeV CM
Emittance -*x*		2.044×10^{-11} m.rad	1.022×10^{-11} m.rad
Energy spread		0.06%	0.03%
At the centre of chicane/ bend	β_x	5 m	5 m
	η_x	20 mm	20 mm
	$\sigma_{x\beta}$	10 μm	7 μm
	$\sigma_{x\eta}$	12 μm	6 μm

Dipole chicane design

A dipole chicane as shown in Figure 1 uses a string of positive and negative dipoles to provide a closed bump for all beam energies. The beam returns exactly to it's original line. This design gives more flexibility in the general layout. As there are no quadrupoles in this design, the chromaticity is zero at the end of the chicane. Both BMP dipoles suggested by B. Parker for the US-cold option studies [6] and TESLA TDR C-type dipoles [7] have been considered for this chicane.

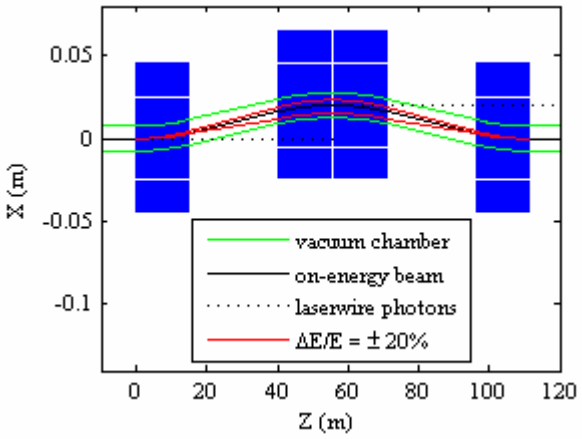

Figure 1: Dipole chicane for detection of off-energy beams and also for laserwire photon detection

The length of the chicane is 111 m with BMP magnets (as shown) and 122 m with TESLA TDR magnets. The emittance increase due to synchrotron radiation at 1 TeV CM is 1% in both designs. Given a vacuum chamber diameter of 15 mm, clearance of 12.5 mm will be available for the laserwire detectors.

Bend design

In the bend design, all dipoles deflect the beam in the same direction and the beam ends up going in a different direction. It restricts the flexibility of the overall BDS layout, e.g. if in the future it becomes necessary to extend the BDS upstream to include, for example, more stages of collimation, the bend in this design will not be suitable. In the present bend design, the beam centre is offset at the end by 6 cm. This design uses fewer dipoles and includes quadrupoles. The emittance increase due to synchrotron radiation is 0.16% at 1 TeV CM. As quadrupoles are used in this design, the chromaticity is not zero at the exit, though the values are negligible and should not cause any deterioration in the Final Focus optics. The optical functions for this design are shown in Figure 2. It is possible in this design to increase the clearance for the laserwire detector by moving it away from the first set of dipoles for emittance measurement and from the second set of dipoles for energy spread measurements as shown in Figure 3.

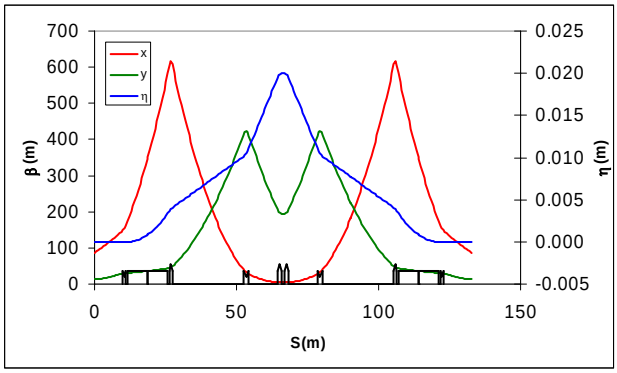

Figure 2: Optics of the bend design

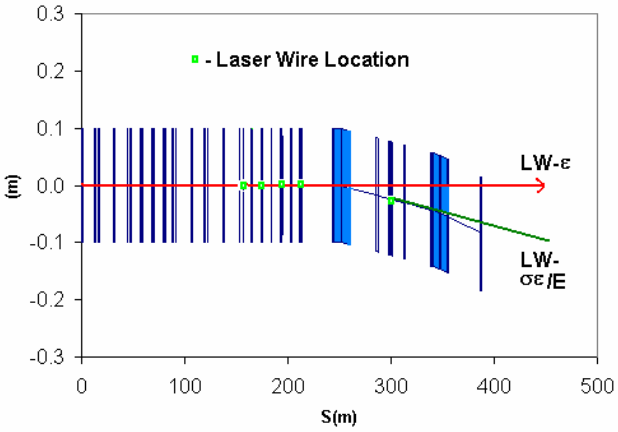

Figure 3: Schematic of coupling correction and emittance measurement section with bend design at the end.

In order to extract the laserwire signal from the emittance measurement section, a sufficient clearance can be obtained as the beam line is bent from the laserwire axis.

FAST EXTRACTION AND TUNE-UP DESIGN

The fast extraction line will also serve as a tune-up line during commissioning or tune-up mode. The design needs to abort the beam for energy errors exceeding ±1.5% and for beams with betatron errors coming from the linac. For off-energy bunch detection, the abort trigger will be the signal from a Machine Protection System (MPS) beam position monitor (BPM) at a point of nonzero dispersion, e.g. in the centre of the chicane. For detecting betatron errors, the abort signal will be taken from BPMs in the upstream skew correction and emittance diagnostic section where the phase advances between BPMs are ideal and $\beta_{x,y}$ are large. The proximity of the abort kickers to these BPMs, the kicker rise time, and the processing time required will determine the number of bunches that will pass to the downstream systems. One idea [6] is to detect the first bad bunch and then wait until after the subsequent bunch to fire the kickers, allowing 2 bunches to get through. This will give the abort electronics more time to think and the kicker specifications will be more reasonable for 300 nsec bunch spacing. The NLC tune-up extraction line was designed for ±20% energy acceptance [2], whereas the TESLA FEXL design was for -5% to -1.5% in emergency extraction mode and -5% to +0.5% in commissioning mode [8]. In tuning or commissioning mode, DC dipole magnets will be powered to divert the beam for extraction. The design philosophy as described in [9] will be used to design this part of the line. The optics of the extraction line will then be designed, and rastering will be used, to assure the survivability of the dump window.

INCREASE IN EMITTANCE DIAGNOSTIC SECTION LENGTH

For the present optics of the emittance measurement section, Table 2 gives beam sizes under different conditions. The "worst-case scenario" occurs when the damping ring extracted emittance (2.0×10^{-8} m.rad normalised) is transported without dilution to the end of the main linac during 1 TeV CM operation. This is improbable; the budgeted emittance, resulting from Low Emittance Transport (LET) simulations through the main linac, is 3.4×10^{-8} m.rad normalised [10]. The total length of the present emittance measurement section is 60 m.

Table 2: Beam parameters and beam sizes at laserwires

	@500 GeV CM	**@1 TeV CM**
β_y at laserwire (m)	34	34
DR ε_y (m.rad)	2.044×10^{-14}	1.022×10^{-14}
σ_y minimum (μm)	0.83	0.589
Budgeted ε_y (m.rad)	6.95×10^{-14}	3.47×10^{-14}
σ_y budgeted (μm)	1.54	1.1

Studies indicate [5] that to achieve 3 μm vertical beam sizes at the laserwires under "worst case" conditions, the length of this section would need to be increased to 680 m, assuming the ideal 45° phase advance between

laserwires. This can be reduced to 480 m if the phase advance is increased to 135° between the wires. These numbers can be further decreased to 400 m (45°) and 280 m (135°) assuming the budgeted emittances. The minimum length required for this section would then be 280 m (from 60 m). Clearly some tradeoffs must be made between system length, emittance measurement accuracy, and laserwire technology and cost. Detailed performance studies are required to decide whether a 10% emittance measurement accuracy will be good enough, or if laserwire R&D can provide better accuracy with the present optics.

CONCLUSIONS

This paper discusses the issues related to detection of off-energy bunches entering the beam delivery system. Two possible designs viz. dipole chicane and a bend design have been discussed. The design of the emittance measurement section followed by energy diagnostics and fast extraction needs to be worked out in detail. Using the dipoles for energy detection allows for extraction and detection of the laserwire signals from the upstream emittance measurement section. To measure the beam sizes with 1% accuracy, the present status of laserwire technology requires significant increase in the length of the emittance measurement section.

REFERENCES

[1] A. Seryi et al, “WG4 summary”, First ILC workshop, KEK, November 2004.
[2] M. Woodley, “ILC strawman design: beam switchyard, tune up dump, diagnostics”, BDIR workshop, June 2005.
[3] L. Keller, Private communication.
[4] G. Blair, “Simulation of ILC laserwire”, These proceedings.
[5] M. Woodley, “BSY emittance diagnostics section”, SLAC BDIR Meeting, September 2005. http://www-project.slac.stanford.edu/lc/bdir/Meetings/beamdelivery/2005-09-27/index.htm
[6] B. Parker, Private communication.
[7] TESLA TDR, DESY 2001-011, 2001.
[8] O. Napoly et al, “Emergency extraction high-energy beam line for TESLA”, TESLA 2001-13, 2001.
[9] T. Mattison, “Thoughts on fast beam aborts for ILC”, These proceedings.
[10] P. Tenenbaum, Private communication.

CLOSING REMARKS FOR NANOBEAM2005*

Junji Urakawa
High Energy Accelerator Research Organization(KEK), 1-1 Oho, Tsukuba-shi, Ibaraki, Japan

On behalf of the organizing committee of the workshop, I would like to address some closing remarks to all the participants. This second workshop was successfully realized at Uji City in Kyoto by the local organizing committee (see the web site of http://wwwal.kuicr.kyoto-u.ac.jp/NanoBM). Uji City is famous because of the Byodo-in Temple, which appears on the web site of the Nanobeam2005 workshop, and also on the reverse side of the Japanese 10 Yen coin.

It is a great pleasure for me to inform you that the Budker Institute of Nuclear Physics has accepted to be the host for the 3rd Nanobeam Workshop in May 2008. I am extremely happy to announce that the total number of the participants to the 2nd Nanobeam Workshop in Kyoto was 104 (63 from Japan, 15 from United States, 7 from United Kingdom, 7 from Germany, 4 from Russia, 3 from France, 3 from Korea, 1 from Switzerland and 1 from Spain) and that there were 9 working groups with a lot of fruitful discussions in each working group. The members of the local organizing committee (LOC) and the conveners of the working groups had prepared hard before the start of this workshop as well as during the workshop. We should acknowledge their great efforts and all the preparatory work. Especially, we have to acknowledge the following persons: Secretaries (Yagi-san and Mori-san) for their kind hospitality, Tongu-san for the nice preparation of coffee etc., and the students of Kyoto University for helping the LOC.

This workshop was sponsored by the 21st Century Center of Excellence, Center for Diversity and Universality in Physics at Kyoto University and it has been supported financially by a Grant-In-Aid for Creative Scientific Research of JSPS (KAKENHI 17GS0210) and by the UK-Japan Collaboration (Japan-United Kingdom Research Cooperative Program Joint Project). The Nanobeam2005 was jointly hosted by three institutes: Institute for Chemical Research, Kyoto University, High Energy Accelerator Research Organization (KEK) and Yukawa Institute for Theoretical Physics. Also, it was approved as the 36th ICFA Advanced Beam Dynamics Workshop.

Thank you for your nice contribution.

*LASER INTERFEROMETER WITH OPTICAL CAVITY AND CAVITY BPMS**

Junji Urakawa for ATF2 project
High Energy Accelerator Research Organization(KEK), 1-1 Oho, Tsukuba-shi, Ibaraki, Japan

Abstract

We are planning the construction of ATF2 final focus beam line and propose the new laser interferometer with optical cavity and cavity nano-BPMs. The design value of final focus beam size is 37 nm and we have to confirm this value even if orbit jittering within a few 100 nm in σ exists. This proposed beam size monitor measures number of γ photons and beam orbit within the resolution of several nm bunch-by-bunch. We have a possibility to reconstruct the data which will be measured together with orbits data bunch-by-bunch in order to obtain the value of the visibility.

1 OUTLINE OF ATF2 PROJECT

The ATF2 design and schedule for ATF2 hardware development address two major goals, namely achieving a 37nm beam size (goal A) and nanometer control of beam position (goal B). The ATF has the high quality beams required to achieve these goals – it has successfully produced beams with the lowest emittance ever achieved, in both single and multi-bunch modes, which are very similar to those for ILC. Further hardware and diagnostics must be developed and the extracted beam quality improved for ATF2 [1].

The ATF2 final focus design is based on the recently proposed compact final focus optics with local chromaticity correction, which now serves as the basic for the ILC FF design.

In addition to the final focus proper, the ATF2 design includes an extended new diagnostics section, that would allow coupling correction of the beam and accurate measurements of its properties.

To fully realize the ATF2 program and fulfill both goals A and B, a number of hardware developments and other improvements are needed to the ATF damping ring and extraction system.

For goal A, an interferometer-based beam size monitor (BSM) will be installed at the IP. The laser interference monitor uses the interaction of the beam with laser interference fringe, and observes the gamma-ray modulation by scanning the beam. This monitor was already demonstrated while detecting a 60 nm beam size in the FFTB experiment [2]. The laser will operate with higher modes than those used for the FFTB measurements. To measure the beam orbit and maintain the beam size with feedback, the beam line magnets will be equipped with 100nm resolution cavity-BPMs and will be placed on movers. Tuning methods will be established based on BSMs as well as BPMs. To achieve the goal B, a set of precision “nano-BPMs” will be installed at the IP. A set of BPMs with a resolution of better than 2nm are now being developed by the Japan-US-UK group. The possibility of combining the two goals, with both the BSM at the IP and nano-BPMs nearby to achieve both the small beam size and nanometer stability, is under investigation.

The beam quality must also be improved for ATF2. The present normalized emittance in the ATF extraction line is estimated to be $4.8\text{x}10^{-8}$ m, three times larger than that in the damping ring. The emittance can be reduced to the nominal value of $3\text{x}10^{-8}$ m by correcting the x-y coupling. The jitter must be reduced to about 30% of the beam size for goal A, and 5% for goal B. The vertical beam jitter in the ATF extraction line is now typically about 30% of the beam size (up to 100% on a time scale of several minutes), which is much larger than the 10% beam jitter observed in the damping ring. The slow jitter in the extraction line is believed to come from the magnet system in the damping ring and the extraction line, which may be improved by an upgraded double-kicker scheme together with an additional feed-forward system [3]. This is expected to reduce the jitter to the same level as in the damping ring.

The beam stability can be further improved with a new 300 ns kicker which will make it possible to extract a train of 3 bunches separated by 150 ns. A fast feedback system being developed by UK and KEK groups, will be used to further stabilize the third bunch. The nano-BPM system will be able to verify the performance of the fast feedback system at the nanometer level. Further beam jitter control at the nanometer level with an ILC-type beam will require a very fast kicker with less than a ns rise time and stable pulse height. This will make it possible to extract an ILC-type train, i.e. 60 bunches with about 300ns separation at 5Hz [4]. These developments may evolve over several years and continue during ILC construction.

The BSM proposed in this paper is a new laser interferometer consisting of an optical cavity and cavity nano-BPMs which are stiffly fixed to the vacuum chamber for the optical cavity at the upstream and the downstream side of the IP. It is a back-up for the interferometer-based beam size monitor in case the vertical orbit jitter of the electron beam cannot be reduced to less than about 50 nm at the IP due to the floor vibration, mainly in the vertical direction.

2 LASER INTERFEROMETER WITH OPTICAL CAVITY

Figure 1 shows the concept of the proposed BSM which comprises two highly reflective spherical mirrors separated by a distance of 42 cm. We are developing a 42 cm Fabry-Perot optical cavity with high finesse of more than 6000. At present, 100 μm waist size at the center of the cavity and a factor 1000 enhancement are achieved. The cavity will be installed in a 50-MeV small linac for

*junji.urakawa@kek.jp

the study of X-ray generation by inverse-Compton scattering during this year [5]. The design specification of this optical cavity for the ATF2 project is as follows:
Laser wavelength 1064 nm or 532 nm,
Enhancement factor more than 3000,
Laser pulse width 7 psec(FWHM),
Waist size at the center of the cavity 20 μm in σ,
Repetition rate of mode-lock laser 714MHz,
Power of the laser 12W.

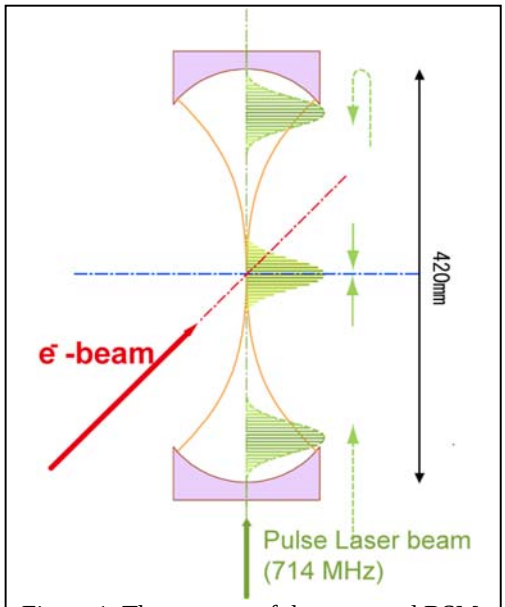

Figure 1. The concept of the proposed BSM

We can calculate number of γ photons generated by inverse-Compton scattering between interfering laser pulses and the electron beam assuming perfect resonance of the optical cavity, perfect interference of two laser pulses in the optical cavity, perfect collision with electron beam in the case of several electron beam sizes (30nm, 50nm, 100nm, 200nm) and the colliding position displacement due to the electron orbit jitter. In the case of the design beam parameters, the number of γ photons is expected to be more than 100 per collision. The collision timing control within 0.1 psec in σ is very challenging and the transverse position control within 100 nm in σ is also challenging. However, we optimistically believe that the accurate adjustment of the optical cavity system is feasible, because the frequencies of the mode-lock laser and of the damping ring RF are the same and the accurate mover table for the optical cavity system was already developed [6]. So, we have to consider the transverse beam orbit jitter (especially vertical). Then, we need two nano-BPMs with the resolution of nanometer level to evaluate the number of γ. There is a possibility to reconstruct the data which will be produced by the inverse Compton scattering in the interference of two laser pulses with the optical cavity and two cavity BPMs. In section 5 we discuss the relationship between the beam orbit jitter and the beam size measured, for this BSM.

3 BEAM SIZE MONITORS IN BD (BEAM DELIVERY)

A gamma-ray detector placed downstream of the scanner detects gamma rays from beam-wire interaction. Downstream of the main damping ring, the beam size becomes very small (around 100x10 μm), while the bunch charge remains the same. Since the carbon wire cannot withstand the condition in such a high density beam, a laser wire scanner is used there as a non-breakable wire. The laser wire is produced in the optical cavity, which is kept on resonance by a piezo-mirror control. The laser wire chamber consists of vertical laser wires and cavity BPMs on both sides, as shown in Fig. 2. The wire is moved together with the chamber within the stretching limit of the bellows. The mover resolution is 0.5μm. Since the yield of the generated gamma-ray is much less than the carbon wire, the scanning time will be much longer, like 1 or 2 minutes for one profile. The gamma-ray detector is the same as that of the carbon wires [7]. On the other hand, we also have the possibility of a different laser wire using high power pulsed laser system like SLC laser wire[8] for fast scanning.

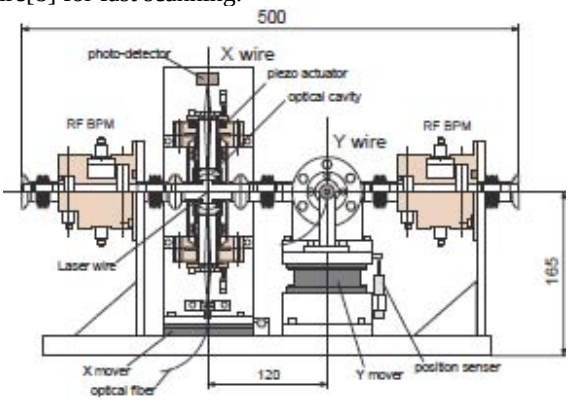

Figure 2. Laser wire scanner.

4 NANO-BPM AT ATF2

The beam position monitors (BPM), which measure the transverse positions of the beam centroid with the resolution of 2 nm in σ, should be developed, especially for the BPMs in the interaction region of ILC. The capability requirements for the BPM at ILC include: a single pass measurement, high resolution, and high accuracy. The cavity BPM technology is applied for these high resolution and high accuracy BPMs. We are going to develop cavity BPMs with a resolution of 0.1 μm over a measurement range of +/-100μm and with a resolution of 2 nm over a measurement range of +/-2μm.

Cavity BPM in BD (Beam Delivery)

For BPMs in the BD area, a mechanical short term stability of a few nm or better in any time scale is required during operation. The cavity BPMs based on a cylindrical microwave cavity have a much more rigid structure. Consequently, a superior long-term mechanical stability is expected, and the cavity BPMs are considered to be suited for deployment in this area. Their resolution is 0.1 μm over a measurement range of +/-100μm. The absolute accuracy is 10μm. Since the sensor cavity and its outer surface have a concentric, cylindrical shape, their centers

can be determined within a few μm.

Temperature control is essential for maintaining the mechanical stability. The BPM temperature is affected by the ambient temperature. An electrical temperature controller with a +/-0.1degree accuracy is installed in the BPM body. Drifts of the BPM offset due to common mode contaminations are suppressed by employing the slot magnetic coupling and the external suppressor circuit using two port combiner. The frequency of the difference mode in the sensor cavity is chosen to be 6.5 GHz, since it has no relation to any accelerator frequency [9].

5 RELATIONSHIP BETWEEN BEAM SIZE AND ORBIT JITTER

We started the development of the Nano BPM which has about 2 nm resolution and so far confirmed 17 nm resolution for the existing cavity BPMs. A new design of the nanometre cavity BPM is under consideration and the prototype will be manufactured soon. The total length of the new laser interferometer including the optical cavity chamber and two cavity BPMs is less than 600 mm. So, center-to-center length of the two cavity BPMs is less than 500 mm. If we assume that the angle jitter stability of the beam is less than 2 μrad [3], the vertical displacement of the electron beam during the passage through the laser waist at the IP is much less than 1 nm for an rms waist size of 20 μm at the center of the cavity. The Rayleigh length of the laser is more than 5 mm vertically and the rms horizontal electron beam size 3 μm at the IP. We can calculate the yield of γ photons per collision with a vertical position offset assuming several electron vertical beam sizes (30nm, 50nm, 100nm, 200nm) and obtain the visibility by combining the data from the measured γ yield with the simultaneous data from the two nano BPMs. Figure 3 shows the calculated results assuming a Gaussian distribution for both the electron beam and the laser pulse. For this calculation we computed the overlap integral neglecting the hourglass effect, because of the laser pulse length of 10 psec (FWHM) and 20 μm waist size at the IP. Also, we included the interference effect of two laser pulses by averaging the square of the time-dependent electric field. Then, this calculation has been done considering only electron beam vertical offsets and displayed in Fig. 3 is the yield of γ photons per collision with a photon energy larger than 4 MeV. We have to consider as well the effects of background, change of horizontal beam size and the horizontal beam orbit jitter. The prototype of this monitor system is under construction.

Acknowledgements

The authors would like to thank Professors Y.Totsuka, F.Takasaki, Y.Kamiya, K.Yokoya, S.Kurokawa, and A.Enomoto for their encouragement. All members of KEK-ATF group and international collaborators for this research program are acknowledged. We also thank Professor E.Paterson of SLAC for supporting the ATF project as an international collaboration. The present research has been financially supported by a Grant-In-Aid for Creative Scientific Research of JSPS (KAKENHI 17GS0210) and by UK-Japan Collaboration (Japan-United Kingdom Research Cooperative Program Joint Project from 2005 to 2006).

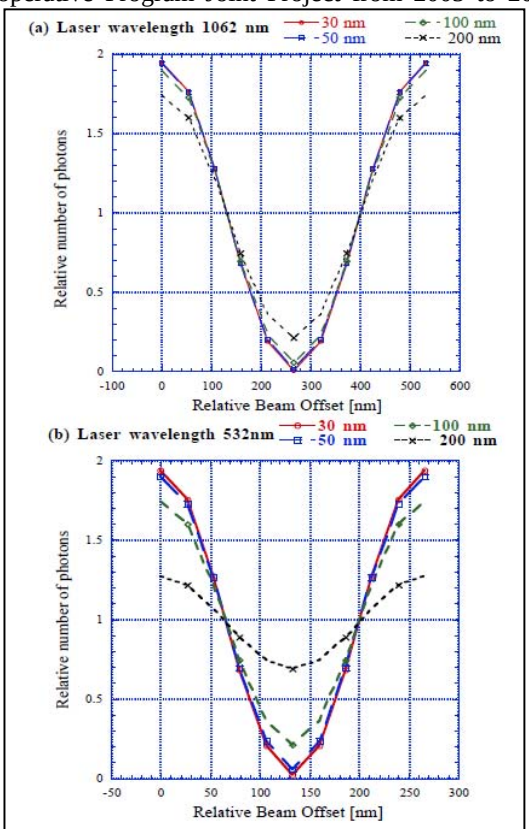

Figure 3. The calculated results of number of photons : (a) For 1062 nm, vertical axis normalized to 150 counts. (b) For 532 nm, normalized to 90 counts. Vertical electron beam sizes are 30 nm, 50 nm, 100 nm and 200 nm with the horizontal beam size of 3 μm.

6 REFERENCES

[1] ATF2 Proposal, Volume 1, CERN-AB-2005-035, CLIC note 636, DESY 05-148, ILC-Asia-2005-22, JAI-2005-002, KEK Report 2005-2, SLAC-R-771, UT-ICEPP 05-02 (2005)
[2] V. Balakin et al.,. Physical Review Letters, Vol.74, No.13, pp2479-2482 (1995).
[3] T. Imai et al., KEK-Preprint-2002-16 and P. Burrows et al., EUROTEV-REPORT-2005-003-1
[4] T. Naito, private communication (2005).
[5] K. Sakaue et al., private communication (2005).
[6] H. Sakai et al., Jpn. J. Appl. Phys Vol.41 (2002) 6398
[7] Y.Honda et al., Physical Review Letters, Vol.92, No.5, 054602-1 (2004).
[8] M.Ross, LINAC96, Proc., p.308., G.Blair, Private communication and Proc. of this workshop.
[9] Y.Honda et al., private communication (2005).

Ultrafast laser-wire scanning with Electro-Optics

A. Bosco, G.A.. Blair, G. Boorman, C. Driouichi, M. Price
Dept. of Physics, Royal Holloway, Univ. of London, Egham, Surrey. TW20 0EX. UK

The possibility is presented of using electro-optics techniques to increase laser-wire scanning rates for intra-train scanning at the international linear collider (ILC). The requirements include the preservation of the laser beam mode quality and the ability to work with laser beam powers of order 10 MW. The first ideas of a possible device configuration are presented together with a survey of EO materials and first experimental results using linear prisms.

1. INTRODUCTION

The Laser-wire (LW) is a very important tool for non-invasive electron beam profile measurements. The LW works by scanning a focussed laser beam across an electron (or positron) beam. The number of Compton-scattered photons as a function of laser spot position then provides information on the bunch transverse profile. In recent years many issues relating to these devices have been tackled and partially solved. For instance, much effort has been spent improving their resolution by focussing the laser beam down to a waist comparable with the electron beam size while maintaining a sufficient scanning range of approximately 5 times the size of the bunch [1, 2].

Another important issue related to a real-time LW monitor is the scanning speed. So far, two different scanning techniques have been considered; moving the entire LW optical system [1] and deflecting the laser beam with piezo-driven mirros [2]. Piezo driven mirrors preserve the beam quality but their speed is limited by the load (scanning mirror) attached to the piezo driver. The first idea to improve the scanning speed was to use acousto-optic devices, whose time response could be as fast as 500 ns [3]; however their major limitations are a very low damage threshold and a low diffraction efficiency (< 40%) , which dramatically affects the beam quality. Electro-optic (EO) techniques may be the key for reaching scanning rates of ~100 kHz, such as are needed for scanning bunches within an ILC train.

2. ELECTRO-OPTIC EFFECT

Consider the parameters of the ILC [4], with trains of about 2800 electron bunches spaced by 337 ns, giving a bunch repetition rate of ~3 MHz. A scanner capable of running at a rate of ~100 kHz would then provide information about the particle beam size in about one hundred different positions along the train. Such high frequencies might be reached by exploiting the EO effect, where a refractive index change is induced by an applied electric field:

$$\Delta n = \frac{1}{2} n^3 \, \vec{\vec{r}} \bullet \vec{E}$$

where n is the linear refractive index, $\vec{E}$ is the E-field vector and $\vec{\vec{r}}$ is the EO tensor, whose form and magnitude depends on the material. This refractive index modulation will change the refraction direction through an interface between the EO medium and the output (linear) medium.

Although being very fast, the EO refractive index change remains relatively small ($\Delta n \sim 10^{-5}$ with E = 1kV/cm). Moreover, the transverse dimension of the EO crystal, defining its optical aperture, should be sufficient to accommodate larger laser spot sizes both to enable working with lower laser intensities and to focus the beam down to a smaller waist. On the other hand, the applied E-field is inversely dependent on the thickness of the crystal so that the

thicker the crystal, the higher must be the applied voltage. A set of test facilities are in operation (or in advanced planning) with a view to addressing the key technological challenges fast LW scanning. These are now outlined in turn.

2.1. Material

A survey and analysis of EO materials available on the market is presented here. The chosen material should be easily available, with a relatively high nonlinear EO coefficient and, most of all, possess a very high optically induced damage threshold. A list of EO crystals is given in Table. I.

Table I: A list of EO crystals with properties relevant to Ultra-fast LW scanning

Material	EO coefficient [pm/V]	Linear refr. ind.	$\Delta n = 0.5 n_3 r_{ij} E_j$ (E=2.5kV/cm)	Damage Threshold [MW/cm^2]
$KNbO_3$	$r_{42} = 380$	$n_2 = 2.28$	4.5 X 10^{-4} (E_y)	350 (10ns)
$LiNbO_3$	$r_{33} = 30$	$n_3 = 2.15$	3.73 X 10^{-5} (E_z)	200 (10ns)
$LiTaO_3$	$r_{33} = 32$	$n_3 = 2.19$	4.2 X 10^{-5} (E_z)	500 (10ns)
SBN75	$r_{33} = 1340$	$n_3 = 2.27$	1.96 X 10^{-3} (E_z)	-
$KTiOAsO_4$	$r_{33} = 40$	$n_3 = 1.86$	3.11 X 10^{-5} (E_z)	10^4 (100ps) 10^3 (8ns)
$KTiOPO_4$	$r_{33} = 35$	$n_3 = 1.90$	3 X 10^{-5} (E_z)	500 (20ns)

At first sight, it seems that the SBN75 would be the best choice; nevertheless, it has a very low damage threshold due to a strong photorefractive effect. For the same reason, $LiTaO_3$, $KNbO_3$ and also $LiNbO_3$ (LNB) cannot be used. For high power application the best candidate is $KTiOAsO_4$ (KTA). Nevertheless, we decided to start our experimental investigation using LNB since it is a material that is readily available and, by doping it with magnesium, its photorefractive properties can be strongly reduced. According to Tab.1, both LNB and KTA would experience a similar refractive index change under the same E-field. In Tab. 1 Δn has been calculated for an electric field of 1 kV across a thickness of 4 mm (2.5 kV/cm); a variation of refractive index of approximately 4×10^{-5} is predicted.

2.2. Configuration

According to Snell's law, the variation of refractive index corresponds to a variation $\Delta\theta$ of the output direction that is linear in Δn. Moreover, for output angles close to the normal direction, this $\Delta\theta$ is equal to Δn. Such a tiny refractive index modulation would then give $\Delta\theta$ as small as 40 μ rad. The chosen configuration for the scanning device is a prism shaped EO crystal as shown in fig. 1. In this case, Δn would apply to both input and output refractions giving a total deflection $\Delta\theta = k \cdot \Delta n$, where the coefficient *k* depends on the prism angle α and increases rapidly when approaching total internal reflection. However the prism also acts as a focussing lens in the horizontal direction, turning the circular beam into an elliptical beam, and this effect also becomes stronger close to total internal reflection. A compromise between beam quality and prism steering efficiency must therefore be found.

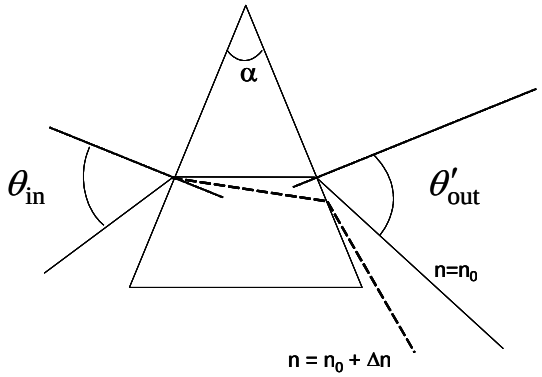

Fig. 1. Electro-optic prism. The dashed line represent the beam path when the refractive index is changed

Maintaining the output direction θ' at around 65°, it is possible to have an acceptable (or at least correctable) beam ellipticity. If the prism is embedded in a medium with intermediate refractive index, as shown in fig. 2, there are two refractions: prism-medium and medium-air which together may increase the *k* coefficient by about a factor of 4. The resulting deflection ($\approx 150\,\mu$rad) is still fairly small; focussing the beam with a 250 mm lens results in a total scan range $\Delta = f\Delta\theta$ of approximately 35 μ m, which is comparable with the waist dimension. The proposed solution for increasing the angular deflection is to use additional linear prisms to amplify the change of output angle from the nonlinear one.

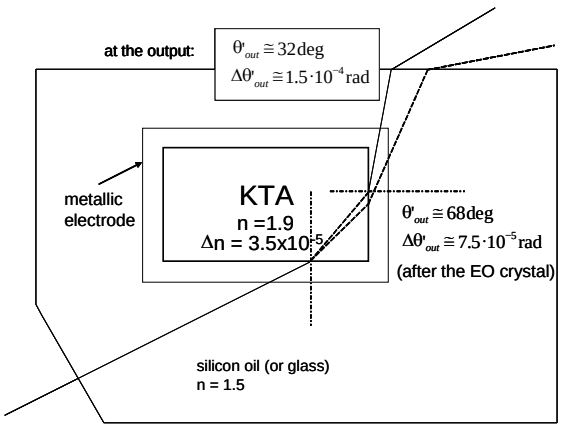

Fig. 2. EO prism embedded in an intermediate medium. The deflection is increased by the second interface

2.3. Experimental Studies

A study has begun at RHUL of the effect of a prism on light deflection and the resulting introduced ellipticity. The experimental setup is sketched in Fig. 3. A mirror mounted on a rotary stage with 500 μrad sensitivity simulates the effect of the EO prism. A focussing lens with focal length of 250 mm transforms the deflection into a translation of the focal point according to $\Delta = f\,\Delta\theta$, which is measured by a CCD camera plus a ×7 magnification system.

The position of the focus and the beam ellipticity were then measured as a function of angle of incidence. Without a prism the beam is circular (ω_x = 33 μm, ω_y = 26 μm) and a translation of 250 μm was obtained. Using a prism with an output angle of 61°, the translation increases to 410 μm but the beam become elliptical (ω_x = 60 μm, ω_y = 30 μm).

Going to an output angle of 71° the beam shift at the focus increases to about 600 μm but the beam distortion become very large (ω_x = 85 μm, ω_y = 30 μm).

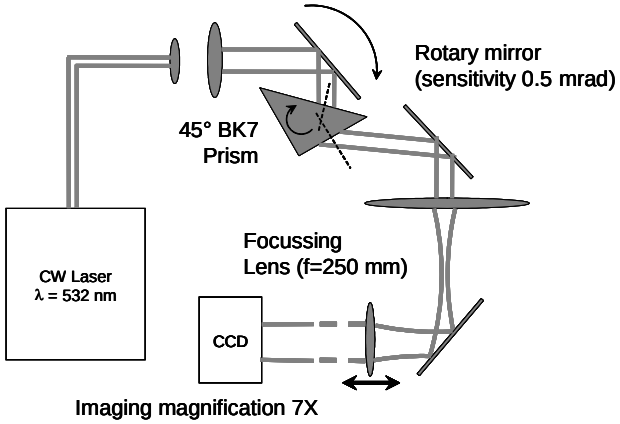

Fig. 3 Experimental set-up for measurements of prism-induced laser beam properties.

3. CONCLUSION

As expected, the use of prisms to change the beam direction affects the beam quality. Nevertheless, it may be possible to correct this ellipticity, for instance by using an (oppositely) elliptical incident beam. A second possibility is to increase the driving voltage in order to increase the EO deflection and work far from the critical angle. This would of course decrease the speed of the device, but it would still be faster than the piezo-scanners.

Ackowledgments

Work supported in part by a Royal Society Joint Project with Japan, by the PPARC LC-ABD Collaboration, and by the Commission of European Communities under the 6th Framework Programme Structuring the European Research Area, contract number RIDS-011899.

References

[1] Y. Honda *et al.* Nucl.Instrum.Meth.**A538:**100-115,2005.

[2] J. Carter et al., "Beam Profile Measurements and Simulations of the PETRA Laser-Wire", Proc PAC05 (2005).

[3] T. Kamps *et al*, Proc. PAC03 (2003).

[4] ILC Baseline Conceptual Design (2006).: http://www.linearcollider.org/

Status of the ATF extraction line laser-wire.

Nicolas Delerue, Fred Gannaway, David Howell
John Adams Institute at the University of Oxford,
Keble Road, OX1 3RH, Oxford, United Kingdom

Grahame Blair, Gary Boorman, Chafik Driouichi
John Adams Institute at Royal Holloway, University of London,
Egham, Surrey TW20 0EX, United Kingdom

Stewart Boogert
Department of Physics & Astronomy, University College London,
Gower Street, London, WC1E 6BT United Kingdom

Alexander Aryshev, Pavel Karataev, Nobuhiro Terunuma, Junji Urakawa
KEK, 1-1 Oho, 305-0801 Tsukuba Science City, Japan

Axel Brachmann, Joe Frisch, Marc Ross
SLAC, 2575 Sand Hill Road, Menlo Park, CA 94025, USA

December 2005

A new laser-wire is being installed in the extraction line of the ATF at KEK. This device aims at demonstrating that laser-wires can be used to measure micrometre scale beam size.

1 Overview of the ATF extraction line laser-wire

The Accelerator Test Facility (ATF) at KEK offers a very low emittance micrometre sized beam of 1.28 GeV electrons close from the conditions expected at the International Linear Collider (ILC). The ATF should soon be able to provide a bunch spacing similar to that of the ILC. This accelerator being a test facility it is possible to have dedicated machine time with custom beam optics for our tests. This make the ATF an ideal place to test a new beam diagnostic device such as a laser-wire to measure micrometre sized beams.

For this laser-wire installation KEK has provided a high power green laser that can deliver up to 1 GW at 532nm (this laser was previously used by the polarised positron experiment).

2 Laser system

A mode-locked seed laser (Nd:VAN) produced by Time-Bandwidth (GE-100-XHP series) is used to deliver a 600mW train of light pulses with a wavelength of 1064 nm and a repetition rate of 357 MHz. The Nd:VAN crystal is diode pumped and a semiconductor saturable absorber (SESAM)[1, 2] is used to start and stabilise the pulse forming process. The SESAM mirror forms one end of the laser cavity. It is mounted on a translation stage so that the length of the cavity can be adjusted by a picomotor and a piezo-electric crystal to cancel the effects caused by changes in ambient conditions. A photo-diode is used to monitor the output of the cavity. A timing stabiliser (Time Bandwidth CLX-1100)[3, 4] is used to phase-lock the signal from the photo-diode to the ATF 357 MHz RF signal (This is achieved by adjusting the cavity length).

The pulse train produced by the seed laser is injected in a regenerative amplifier custom-built by Positive Light (model RGN). This system amplifies one of the nanoJoule seed pulses to approximately 600 milliJoules. A Faraday isolator is used to prevent reflected pulses damaging the seed laser. Two Pockels cells are used to select the pulse that will be amplified. The first Pockels cell is located before the Faraday isolator, it is used to chop the end of the pulse. The second Pockels cell is located inside the amplifying cavity. When this second Pockels cell is deactivated the pulses do not reach the amplifying rod in the cavity. When this Pockels cell is switched on, it will trap one pulse inside the cavity. This pulse is reflected through an Nd:YAG amplifying rod and bounces back and forth in the cavity. After a number of pulse round trips in the cavity (usually 10-15) a third Pockels cell is switched on, this changes the polarisation of the pulse inside the cavity and this pulse is extracted by a polariser making a 45 degrees angle with the beam trajectory.

After extraction the pulse passes a second Faraday isolator that protects the cavity. It is then transmitted through a spatial filter and then through 2 Nd:YAG linear amplifier that amplify the pulse by a factor of 10 each, bringing it to more than 600 mJ. Before the exit of the laser system a KD*P crystal doubles the frequency of the laser pulse, bringing its wavelength to 532 nm with an efficiency close to 50% at full power. At this stage the pulses have a length of 200-300 ps.

The timing of the Pockels cells is critical to ensure that one and only one pulse is amplified and to improve the contrast ratio of the pulse by removing any pre and post pulses. This timing is controlled by a signal and delay generator (SDG-II from Positive Light). A photo-diode monitors the signal in the amplifying cavity. A second photo-diode, located after the spatial filter, monitors the signal extracted from the cavity. These two photo-diodes are used to tune the timing of the 3 Pockels cells and thus improve the extracted signal.

The amplifying rod located inside the cavity and the two linear amplifiers are optically pumped by flash lamps. The signal used to trigger the flash is taken from the ATF extraction kicker charge signal. The kicker fire signal is used to trigger the SDG and thus the amplified laser pulse.

3 Laser delivery optics and focusing lens

The laser system described above is located on top of the ATF shielding. A set of mirrors are used to bring the laser light from the output of the amplifier to the focusing light. The total length travelled by the light is of the order of 10 meters. A scanning system and diagnostic tools such as photo-diodes and camera will be installed along this path.

A F#/2 lens will be used to focus the laser light onto a very small spot[5]. This lens is made of 3 elements: the first element has an aspheric surface and a spheric one. The second element has two spheric surfaces. The last element is flat and is used as a window to allow the laser light to enter the beam pipe. All these element are made of top-quality fused silica.

Beam dynamics and mechanical considerations require the inner side of the window to be more than 20 mm away from the IP which must be roughly in the centre of the beam pipe, in our design this inner surface of the window is 24 mm away from the IP. The window has a thickness of 12.7 mm. The position of the two other elements is constrained by mechanical and cost consideration: to allow the sealing of the window these two elements must be more than 14 mm away from the window but they must be kept as close as possible to the window to limit their size (and hence their cost). In our design one of these elements is located 18 mm away from the window and has a thickness of 5.3 mm. The second element (aspheric) is located 2 mm further away and has a thickness of 7 mm. The layout of this lens is shown in figure 1.

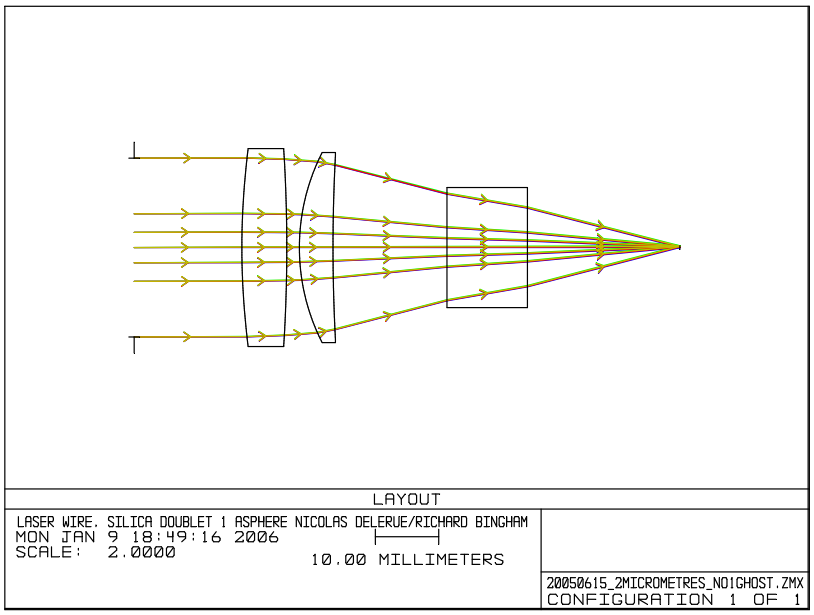

Figure 1: Layout of the F#/2 lens designed for the ATF extraction line laser-wire

The shape of these elements has been optimised using the Optical Design Software ZEMAX[6] to focus the beam to a spot size as close as possible from the diffraction limit as shown in figure 2. As the laser beam will be scanning the electron beam, the optimisation has been done for 4 different tilt angles: 0 degree (no tilt), 0.1 degree, 0.2 degree and 0.3 degree and one of the goals of the optimisation was to keep the size of the laser spot in each of these configurations a identical as possible as can be seen in figure 2.

The optimisation process has also been used to reduce the aberrations. The figure 3 shows the aberrations of the final design.

Care has been taken to minimise the effect of possible ghosts reflections of the focus in the glass elements. No single bounce ghost remains in the lens but one second order ghost with a radius of 250μm remains as shown in figure 4. As a very low reflectivity coating is being used for the lens, calculations[7] have shown that this ghost should not be an issue.

This F#/2 lens will later be replaced by a F#/1 lens that is currently being designed.

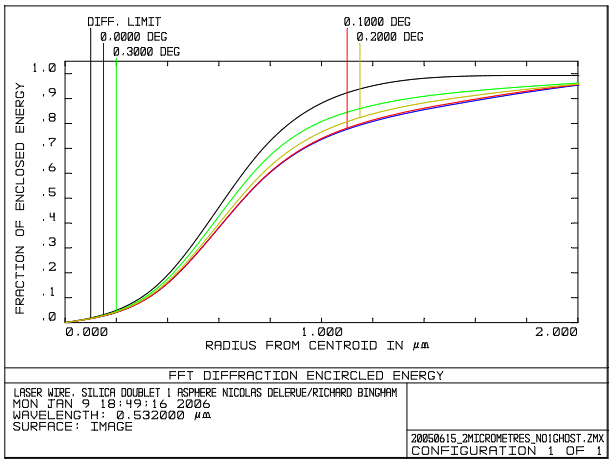

Figure 2: Fraction of enclosed energy in a given circle as a function of the radius of this circle from the centre of the beam spot. The upper (black) line shows the diffraction limit, the 4 other lines show the real value when the incoming laser beam has a tilt of 0 degree (blue), 0.1 degree (red), 0.2 degrees (yellow) and 0.3 degrees (green).

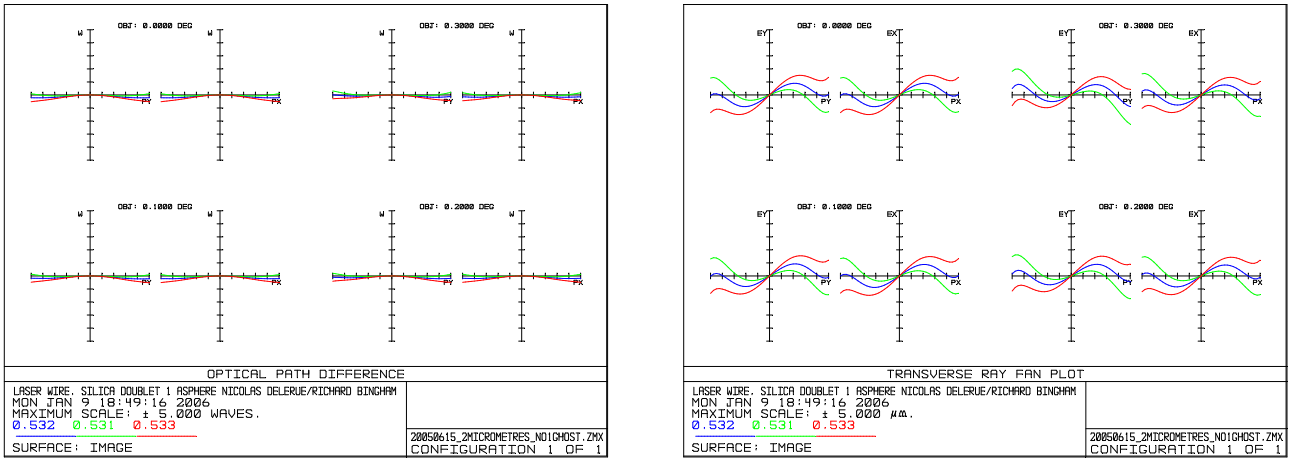

Figure 3: Aberrations of the F#/2 lens designed for the ATF extraction line laser-wire: Optical path difference on the left and transverse ray fan on the right. On each figure the 4 pairs of plots correspond to the 4 possible laser beam tilt (0.0, 0.1, 0.2 and 0.3 degrees) for vertical rays (left plot) and horizontal rays (right plot), the three rays in each plot correspond to the 3 different wavelengths studied: 531nm (green), 532nm (blue) and 533nm (red). Each plot give the aberration (vertical axis) as a function of the position of the ray (horizontal axis). The horizontal axis is normalised to the size of the lens: a ray on the edge of the lens will be on the edge of the plot whereas a central ray will be in the centre of the plot. The scale of the vertical axis is 5 waves for the OPD plot and $5\mu m$ for the transverse ray fan plot.

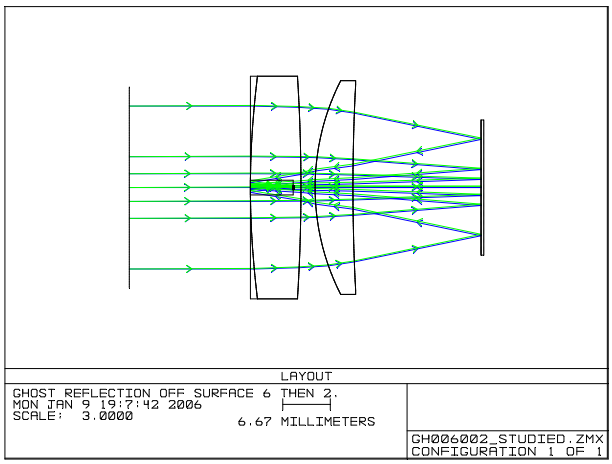

Figure 4: Ghost in the lens. This ghost reflection of the lens focus is formed by a reflection on the outer surface of the vacuum window and on the aspherical surface.

4 Interaction chamber

The interaction chamber[8] in which the collisions between the laser photons and the electrons will take place has been manufactured in Oxford and is now installed at KEK.

Photographs of this chamber are shown in figure 5 and drawings are shown in figure 6. The chamber has two ports on which a flange with a window can be mounted. These windows, made of fused silica, are used to allow the laser light to enter the ultra high vacuum of the beam pipe . The tight sealing of the glass on the stainless steel flange is achieved thanks to a novel indium seal designed specially for this purpose. The aperture of these windows is wide enough to allow the use of an F#/1 lens. Two other ports of the chamber are used to connect the chamber to the accelerator beam pipe. The chamber has 6 other ports on which diagnostics tools such as a wire-scanner, a screen or a knife edge can be installed.

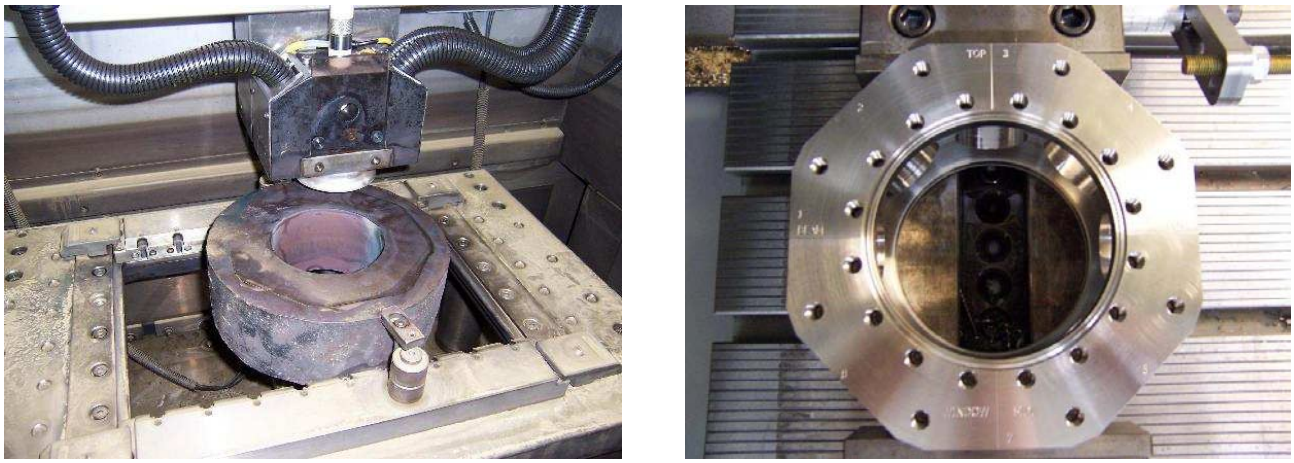

Figure 5: Raw block of stainless steel used to build the interaction chamber before processing (left) and the same after processing, the finished interaction chamber (right).

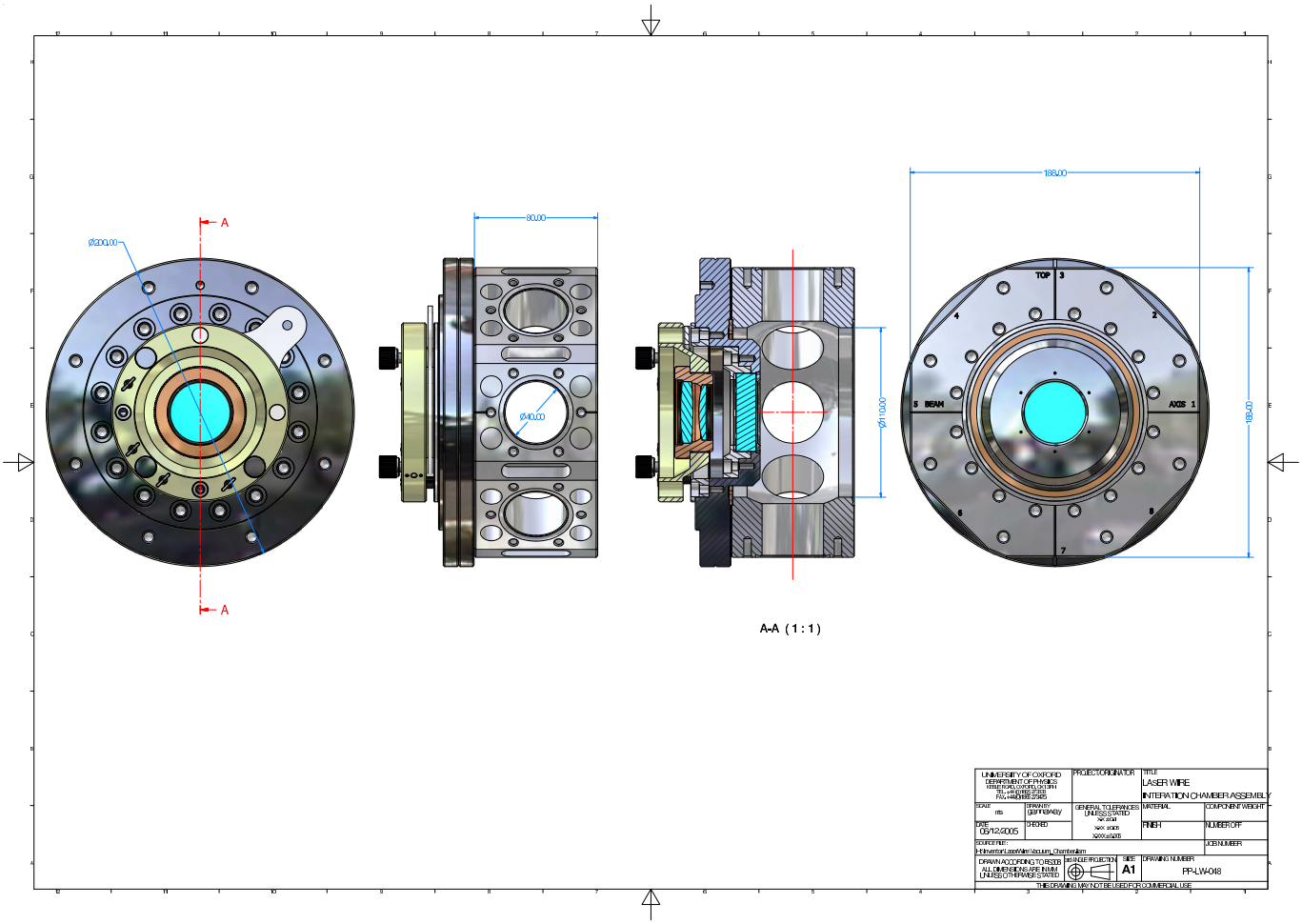

Figure 6: Drawings of the ATF extraction line laser-wire interaction chamber. In the leftmost and rightmost drawings the electron beam direction is in the plan of the paper and the laser beam direction is perpendicular to the paper's plan. In the two inner drawings the laser beam is in the plan of the paper and the electron beam is perpendicular to the plan of the paper.

5 Conclusion

The ATF extraction line laser-wire will allow us to demonstrate that laser-wires can be used to measure the very small beams produced in the ILC linac. In the near future we hope that our laser-wire will be an important diagnostic tool at the ATF2.

6 Acknowledgements

We would like to thank the ATF group at KEK for their kind support and their availability to our requests.

Work supported in part by the Daiwa Anglo-Japanese Foudation, The Royal Society, the PPARC LC-ABD Collaboration, and by the Commission of European Communities under the 6th Framework Programme Structuring the European Research Area, contract number RIDS-011899.

References

[1] B. G. Kim, E. Garmire, S. G. Hummel, and P. D. Dapkus. Nonlinear Bragg reflector based on saturable absorption. *Appl. Phys. Lett.*, 54p1095–1097, (1989).

[2] U. Keller, D. A. B. Miller, G. D. Boyd, T. H. Chiu, J. F. Ferguson, and M. T. Asom. Solid-state low-loss intracavity saturable absorber for Nd:YLF lasers: an antiresonant semiconductor Fabry - Perot saturable absorber. *Optics Lett.*, 17p505–507, (1992).

[3] M.J.W. Rodwell, D.M. Bloom, and K.J. Weingarten. Subpicosecond laser liming stabilization. *IEEE Journal of Quantum Electronics*, 25p817–827, (1989).

[4] D.R. Walker, D.W. Crust, W.E. Sleat, and W. Sibbett. Reduction of phase noise in passively mode-locked lasers. *IEEE Journal of Quantum Electronics*, 28p289–296, (1992).

[5] Nicolas Delerue. Laser optics for the ATF laser-wire. *BDIR Workshop, https://ilcsupport.desy.de/cdsagenda/fullAgenda.php?ida=a0522&stylesheet=nicecompact&dl=talk*, (June 2005).

[6] Zemax Development Corporation. Zemax optical design Program. *http://www.zemax.com*, (2005).

[7] Nicolas Delerue. Thermal effects on the laser-wire lens. *http://www-pnp.physics.ox.ac.uk/ delerue/laserwire/lensDesign/thermalEffects.ps*, (2005).

[8] David Howell. ATF extraction line laser-wire infrastructure plans. *BDIR Workshop, https://ilcsupport.desy.de/cdsagenda/fullAgenda.php?ida=a0522&stylesheet=nicecompact&dl=talk*, (June 2005).

A two-dimensional Laser-wire Beam Profile Measurement System at PETRA

Chafik Driouichi, Grahame Blair, Gary Boorman, Alessio Bosco, Mike Price, Stewart Boogert
John Adams Institute at Royal Holloway, University of London
Egham, Surrey TW20 0EX, UK

Nicolas Delerue, Fred Gannaway, David Howell
John Adams Institute at the University of Oxford
Keble Road, OX1 3RH, Oxford, UK

Alexander Aryshev, Pavel Karatev, Nobuhiro Terunuma, Junji Urakawa
KEK, 1-1 Oho, 305-0801 Tsukuba Science City, Japan

Axel Brachmann, Joe Frisch, Marc Ross
SLAC, 2575 Sand Hill Road, Menlo Park, CA 94024, USA

The transverse beam profile at the PETRA positron storage ring will be measured using a two-dimensional laser-based beam profile monitor. Such a device, newly installed, uses a finely focused laser beam to scan across the charged particle beam. The flux of the compton scattered photon varies with the position of the laser beam, thus establishing the transverse beam profile. In this paper, aspects related to the laserwire setup, such as the focusing optics, both pre- and post-interaction point diagnostics optics, scanning optics, and ghost analysis are described in detail.

1 Introduction

Precision beam diagnostics for position and beam profile are vital to achieve high performance at a TeV energy lepton collider, such as the International Linear Collider [1]. The high brightness of the lepton beams is well beyond the threshold density for single pulse melting of any material used for conventional wire scanners, thus making their use ineffective. A laser-based profile monitor, in contrast, uses a finely focused laser beam to scan across the lepton beam. The evaluation of the Compton scattered photon flux as a function of the laser beam position yields the transverse lepton beam profile. A two-dimensional laserwire device is being built and is planned to be installed at the PETRA positron storage ring. This paper describes different aspects related to the development of such a laser-wire profile monitor.

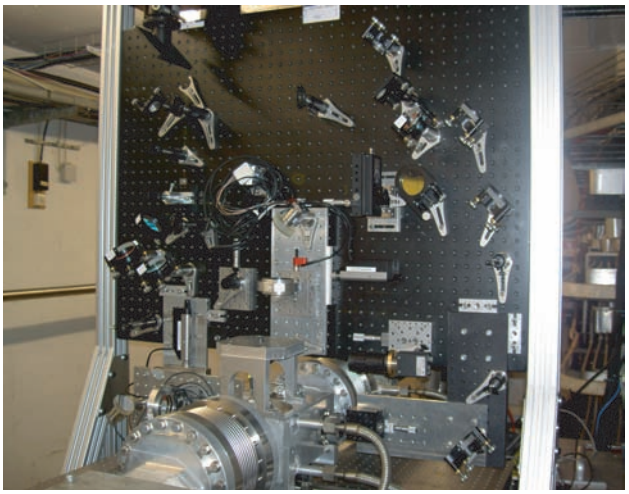

Figure 1. Picture of the laserwire breadboard installed at the PETRA positron storage ring.

2 Experimental Setup

The experimental setup is mainly divided into two areas, the laser hut where both the laser system and the DAQ hardware are installed, and the PETRA accelerator tunnel where the laserwire breadboard setup is installed. Figure 1 shows a picture of the laserwire setup installed at the PETRA positron storage ring. The laser beam, after being expanded by a variable beam expander (1:8), is transported using a matched Gaussian relay made of two $f = 5$ m lenses over a distance of 20 m from the laser via an access pipe into the tunnel housing the accelerator [2]. The beam is then picked up at the entrance of the laserwire breadboard by a 50 mm mirror. Height adjustment and correction for lateral shifts are corrected by combining two other mirrors. The beam is then deflected selectively by a piezo-driven scanner for either a vertical (SV) or horizontal (SH) scan of the electron beam.

3 Focusing lens

The laser beam is focused using a plano-convex lens with a focal lens of 250 mm. Figure 2 shows a ZEMAX [3] simulation of the waist of a high quality mode laser beam at the focus as a function of different input waists at the en-

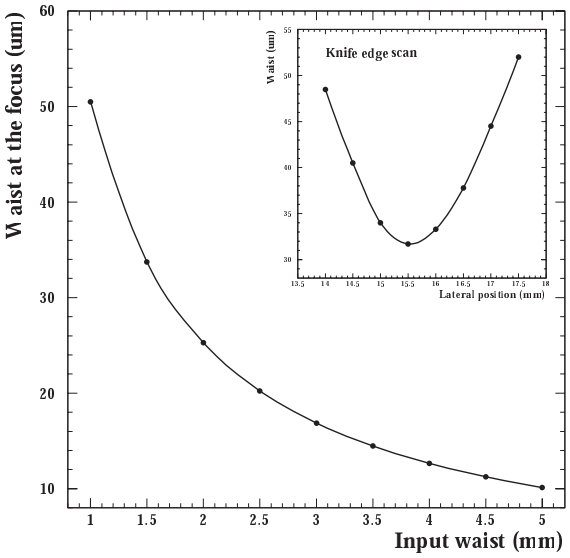

Figure 2. ZEMAX simulation of the variation of the beam waist at the focus as a function of the beam radius at the entrance of the focusing lens. The knife edge scan measurement is shown on the top right.

trance of the focusing lens. For a fixed input laser beam waist of 3 mm, the waist at the focus is $\omega_f \simeq 17\ \mu$m and the rayleigh range $z_f = 1350\ \mu$m. Such a choice is a compromise between having a fine focus at the interaction point to scan across the charged particle beam and a long enough rayleigh range.

The characterization of the focusing lens in real life was done by expanding the output beam of a He-Ne laser to have a waist of 3 mm. The waist at the focus was determined using a knife edge scan (Fig. 1, top right) and was around 17 μm, in complete agreement with the ZEMAX simulation. This measurement was also cross checked using a WinCAM and beam profiler and all results agreed.

4 Diagnostics:

The diagnostics section is divided into a pre- and post-interaction point diagnostics. The pre-IP diagnostics consists of imaging the interaction point (IP) for both horizontal and vertical dimensions into individual CCD cameras. For each dimension, an appropriate cubic beam sampler reflects a small fraction of the beam towards a ten time beam expander in front of a CCD camera. Figure 3 shows a schematic drawing of the diagnostics section. The post-IP diagnostics consists of imaging the waist at the focus using a plano-convex lens with a focal length f of 125 mm into a CCD camera. The distance p between the imaging lens and the interaction point and the distance q between the

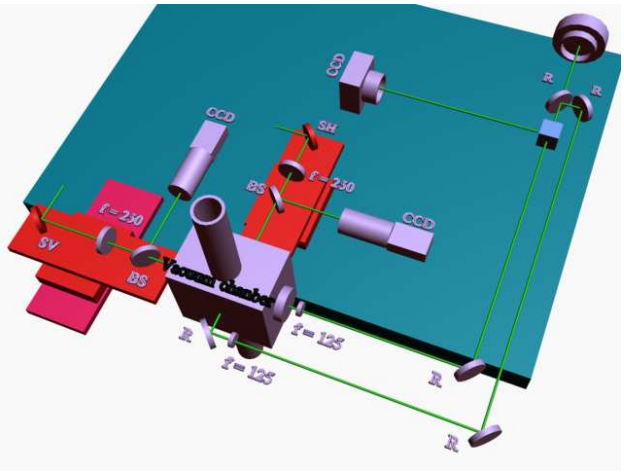

Figure 3. Schematic of the imaging section of the laserwire setup for both vertical and horizontal dimensions. SR and SH are the piezo scanners for horizontal and vertical dimensions, R is for high reflective mirrors

imaging lens and the CCD camera are set precisely to have almost the same magnification used for the pre-IP imaging system.

Table 1 shows measurements of the beam waist at the interaction point, at the pre-IP and post-IP. The input laser beam at the entrance of the focusing lens was set to 3 mm. Once the magnification of the beam waist at the post-IP is measured, it is enough to rely on the post-IP diagnostics system. The pre-IP section can be disposed of, thus reducing the cost of the laserwire setup.

	IP	pre-IP	post-IP
Vertical	17.37	17.5	16.5
Horizontal	16.78	17.23	16.44

Table 1. Measurements of the beam waist at the IP. pre-IP and post-IP.

5 Scanner

A piezo-driven platform with an attached 50 mm high reflective mirror has been used to scan the laser beam across the charged particle beam. The platform is driven by two pairs of piezo actuators, each controlled as a unit in push/pull mode when supplied by a voltage. The tilt range is 2 mrad. The load frequency depends on the load on the piezo platform. Simulation showed that with a load equivalent to a 50 mm mirror on the platform, the maximum loaded frequency necessary to have a scan range of 2 mrad is around 400 Hz. Figure 4 shows the achieved laser beam deflection as a function of the voltage supplied to the piezo scanner.

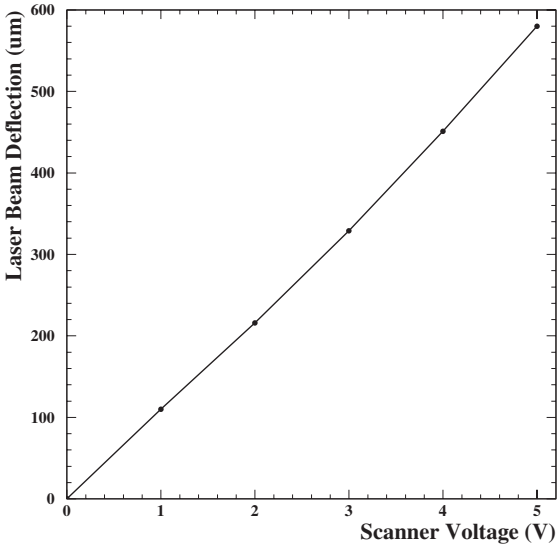

Figure 4. Dependence of the travel range as a function of the voltage supplied to the piezo scanner.

A scan range of 580 μm, corresponding to a voltage supply of 5V to the piezo scanner, was measured on the CCD camera. This limit is set by the aperture of the chip on the CCD camera.

6 Ghost analysis

A ghost analysis using the ZEMAX program revealed the existence of several ghosts, of which the most critical are those hitting the viewport of the vacuum chamber. These ghosts originate from the imaging lenses for the port-IP diagnostics situated just behind the viewports. Figure 5 indicates, in arrows pointing from right to left, the location of such ghosts. These were confirmed by looking at the back reflection of imaging lenses. Placing a 1 to 1000 neutral filter in front the imaging lenses reduces the ghosts encircled energy to a safe level.

7 Conclusion and outlook

A two-dimensional laserwire profile monitor is been built and installed at the PETRA positron storage ring in December 2005 and is ready for operation. Both horizontal (x) and vertical (y) electron beam sizes will be determined by scanning a finely focused across the charged particle beam using a piezo-driven mirror. A new injection seeded laser with a good mode quality will allow the determination of the transverse beam profile with a high accuracy.

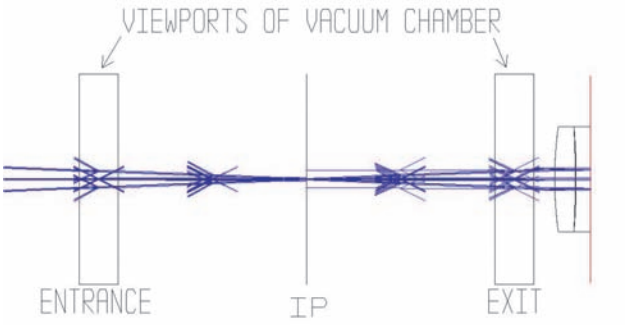

Figure 5. ZEMAX simulation of the location of the ghosts (arrows from right to left) hitting the viewports of the vacuum chamber.

8 Acknowledgements

We would like to thank the DESY MDI group for their support. This work is supported in part by The Royal Society, the PPARC LC-ABD Collaboration, and by the Commission of European Communities under the 6th Framework Programme Structuring the European Research Area, contract number RIDS-011899.

References

1. International Linear Collider *http://www.linearcollider.org*,
2. K. Balewski et al, "Beam Profile Measurements at PETRA with the Laserwire Compton Scattering Monitor", EPAC-2004-THPLT026, DESY-M-04-03D, October 2004.
3. ZEMAX optical design program *http://www.zemax.com*,

Alternative Optics Design: Nonlinear Collimation System

A. Faus-Golfe,IFIC-Valencia;
D. Schulte, F Zimmermann, CERN, Geneva, Switzerland;
J. Resta-Lopez CERN/IFIC; T. Asaka CERN/SPring-8;

Abstract

The collimation system of a Linear Collider must serve multiple purposes and fulfill a number of constraints. In particular, we require that the collimation system should sustain the impact of off-energy bunches and have a large chromatic bandwidth, in addition to ensuring a high collimation efficiency and tolerable wake fields. We describe the design of a nonlinear energy collimation system for CLIC at 3 TeV, in which skew sextupoles are used to blow up the vertical beam size at the spoiler, so as to guarantee collimator survival in case of beam impact. Its properties, like chromatic bandwidth and collimation survival, are evaluated and compared with those of the baseline linear collimation system.

INTRODUCTION

The collimation system of a Linear Collider (LC) should (1) reduce the background in the detector by removing particles at large betatron amplitudes or energy offsets, which otherwise would be lost generating muons near the Interaction Point (IP) or emit synchrotron radiation (SR) photons in the final doublet; (2) withstand the impact of a full bunch train in case of machine failure, and (3) not produce intolerable wake fields that might degrade the orbit stability or dilute the emittance.

The basic layout of a nonlinear collimation system is illustrated in Fig. 1. The purpose of the first nonlinear element is to blow up beam sizes and particle amplitudes, so that the collimator jaw can be placed further away from the nominal beam orbit (reducing the wake fields) and the beam density is decreased (for collimator survival). A second nonlinear element downstream of the spoiler, and π from the first nonlinear element, cancels all aberrations induced by the former.

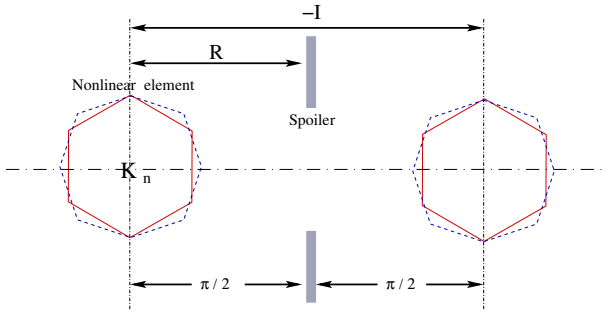

Figure 1: Schematic of a nonlinear collimation system.

At each nonlinear element a particle suffers deflections $\Delta q_i' = -\partial H_n/\partial q_i$, where H_n is the Hamiltonian of the multipole. As was pointed in Ref. [1], higher-order multipoles (decapoles, dodecapoles, etc.) are not useful, because they do not penetrate to the small distances necessary. Skew sextupoles and octupoles could be used.

Different types of nonlinear collimation systems for future linear colliders have been described in the literature [1, 2, 3, 4]:

- For the NLC, in [1] a scheme with skew-sextupole pairs for nonlinear betatron collimation in the vertical plane has been proposed.
- Subsequently, in [2], a halo reduction method with the addition of "tail-folding" octupoles ('Chebyshev arrangement of octupoles') in the NLC final focus system is presented (see also [5] for an earlier study with only 1 octupole in front of the final doublet).
- For the TESLA post-linac collimation system a magnetic energy spoiler (MES) has been suggested [3]. An octupole is placed at a high dispersion point between a pair of skew sextupoles (at $\pi/2$ phase advance from the octupole). The skew sextupoles are separated by a optical transfer matrix $-I$. The result is a significant increase in the vertical beam size at a downstream momentum spoiler.

A characteristic feature of all these systems is that they separate between energy and betatron collimation, and typically employ the nonlinear elements only in one or the other half.

A nonlinear collimation system for CLIC with three skew sextupoles was explored in [4]. It contains a single vertical spoiler which collimates in the horizontal and vertical betatron amplitude at both betatron phases as well as in energy. The scheme is illustrated in Fig. 2. More details of this system can be found in Ref. [4].

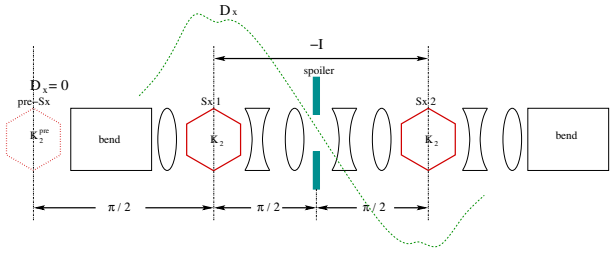

Figure 2: Schematic of a nonlinear collimation system for CLIC [4].

NONLINEAR ENERGY COLLIMATION FOR LINEAR COLLIDERS USING PAIR OF SKEW SEXTUPOLES

In this section we describe a nonlinear energy collimation system based on the layout of [4]. We have refined the equations describing the energy collimation for two different beam momentum distributions.

The integrated sextupole strength K_s can be expressed in terms of the sextupole length l_s, the pole-tip field B_T, the magnetic rigidity $(B\rho)$, and sextupole aperture a_s as

$$K_s = \frac{2B_T l_s}{(B\rho)a_s^2} \ . \tag{1}$$

The sextupole at a location with horizontal dispersion $D_{x,\mathrm{sext}}$ deflects a passing particle by

$$\begin{aligned} \Delta x' &= K_s(D_{x,\mathrm{sext}}\delta + x)y \ , & (2)\\ \Delta y' &= -\frac{1}{2}K_s(y^2 - x^2 \\ &\quad -D_{x,\mathrm{sext}}^2\delta^2 - 2D_{x,\mathrm{sext}}\delta x) \ , & (3) \end{aligned}$$

with δ the relative momentum offset.

The position at the downstream spoiler is obtained from

$$\begin{aligned} x_{\mathrm{sp}} &= x_{0,\mathrm{sp}} + R_{12}\Delta x' \ , & (4)\\ y_{\mathrm{sp}} &= y_{0,\mathrm{sp}} + R_{34}\Delta y' \ , & (5) \end{aligned}$$

where $x_{0,\mathrm{sp}} = x_{\beta,\mathrm{sp}} + D_{x,\mathrm{sp}}\delta$ and $y_{0,\mathrm{sp}} = y_{\beta,\mathrm{sp}}$ are the horizontal and vertical position of the particle at the spoiler without the sextupole, written in terms of the betatronic parts, $x_{\beta,\mathrm{sp}}$ and $y_{\beta,\mathrm{sp}}$, and the horizontal dispersion at the spoiler, $D_{x,\mathrm{sp}}$. For flat beams, such as in the case of CLIC, $x_\beta >> y_\beta$. R_{12} and R_{34} at the optical transport matrix elements between the skew sextupole and the spoiler.

The transversal root mean squared beam sizes at the spoiler are given by the expressions

$$\begin{aligned} \sigma_x &= \sqrt{\langle x_{\mathrm{sp}}^2\rangle - \langle x_{\mathrm{sp}}\rangle^2} \ , & (6)\\ \sigma_y &= \sqrt{\langle y_{\mathrm{sp}}^2\rangle - \langle y_{\mathrm{sp}}\rangle^2} \ . & (7) \end{aligned}$$

The horizontal mean squared position of particles at the spoiler is given by

$$\begin{aligned} \langle x_{\mathrm{sp}}^2\rangle &= \langle (x_{\beta,\mathrm{sp}} + D_{x,\mathrm{sp}}\delta \\ &\quad + R_{12}K_s\left(D_{x,\mathrm{sext}}\delta + x_{\beta,\mathrm{sext}}\right)y_{\beta,\mathrm{sext}})^2\rangle \\ &\simeq \langle (D_{x,\mathrm{sp}}\delta + R_{12}K_s D_{x,\mathrm{sext}}\delta y_{\beta,\mathrm{sext}})^2\rangle \ , & (8) \end{aligned}$$

and the average horizontal beam offset by

$$\langle x_{\mathrm{sp}}\rangle = D_{x,\mathrm{sp}}\langle\delta\rangle \ . \tag{9}$$

In the approximation we assume that x_β and y_β are small compared with $D_x\delta$ both at the spoiler and at the sextupole.

In a similar way, the vertical mean squared position at the spoiler is

$$\begin{aligned} \langle y_{\mathrm{sp}}^2\rangle &= \langle (y_{\beta,\mathrm{sp}} - \frac{1}{2}R_{34}K_s(y_{\beta,\mathrm{sp}}^2 - x_{\beta,\mathrm{sp}}^2 \\ &\quad -D_{x,\mathrm{sext}}^2\delta^2 - 2D_{x,\mathrm{sext}}\delta x_{\beta,\mathrm{sext}}))^2\rangle \\ &\simeq \frac{1}{4}R_{34}^2K_s^2D_{x,\mathrm{sext}}^4\langle\delta^4\rangle \ , & (10) \end{aligned}$$

and the average vertical offset

$$\begin{aligned} \langle y_{\mathrm{sp}}\rangle &= \langle (y_{\beta,\mathrm{sp}} - \frac{1}{2}R_{34}K_s(y_{\beta,\mathrm{sp}}^2 - x_{\beta,\mathrm{sp}}^2 \\ &\quad -D_{x,\mathrm{sext}}^2\delta^2 - 2D_{x,\mathrm{sext}}\delta x_{\beta,\mathrm{sext}}))\rangle \\ &\simeq \frac{1}{2}R_{34}K_sD_{x,\mathrm{sext}}^2\langle\delta^2\rangle \ . & (11) \end{aligned}$$

From Eqs. (6), (7), (8), (9), (10) and (11), considering a *Gaussian momentum distribution*:

$$P(\delta) = \frac{1}{\sqrt{2\pi}\sigma_\delta}e^{-1/2\left(\frac{\delta+\delta_0}{\sigma_\delta}\right)^2} \ , \tag{12}$$

with a width σ_δ and with an average momentum offset δ_0, the transverse beam sizes at the spoiler take the form:

$$\begin{aligned} \sigma_x &\simeq (D_{x,\mathrm{sp}}^2\sigma_\delta^2 + R_{12}^2K_s^2 \\ &\quad D_{x,\mathrm{sext}}^2(\delta_0^2 + \sigma_\delta^2)\beta_{y,\mathrm{sext}}\epsilon_y)^{1/2} \ , & (13)\\ \sigma_y &\simeq (\frac{1}{2}R_{34}^2K_s^2D_{x,\mathrm{sext}}^4(\sigma_\delta^4 + 2\delta_0^2\sigma_\delta^2))^{1/2} \ . & (14) \end{aligned}$$

On the other hand, if we consider the case of a *uniform flat momentum distribution*:

$$P(\delta) = \begin{cases} 0 & \text{for} \quad \delta < -\frac{\delta_{\mathrm{flat}}}{2} + \delta_0 \\ \frac{1}{\delta_{\mathrm{flat}}} & \text{for} \quad -\frac{\delta_{\mathrm{flat}}}{2} + \delta_0 < \delta < \frac{\delta_{\mathrm{flat}}}{2} + \delta_0 \\ 0 & \text{for} \quad \delta > \frac{\delta_{\mathrm{flat}}}{2} + \delta_0 \ , \end{cases} \tag{15}$$

with a full width δ_{flat} and an average momentum offset δ_0, the transverse beam sizes at the spoiler take the form:

$$\begin{aligned} \sigma_x &\simeq \left(D_{x,\mathrm{sp}}^2\frac{\delta_{\mathrm{flat}}^2}{12} + R_{12}^2K_s^2 \right. \\ &\quad \left. D_{x\mathrm{sext}}^2\left(\frac{\delta_{\mathrm{flat}}^2}{12} + \delta_0^2\right)\beta_{y,\mathrm{sext}}\epsilon_y\right)^{1/2} \ , & (16)\\ \sigma_y &\simeq \left(\frac{1}{4}R_{34}^2K_s^2D_{x,\mathrm{sext}}^4 \right. \\ &\quad \left. \left(\frac{\delta_{\mathrm{flat}}^4}{180} + \frac{1}{3}\delta_{\mathrm{flat}}^2\delta_0^2\right)\right)^{1/2} \ . & (17) \end{aligned}$$

For spoiler survival, a minimum beam size $\sigma_{r,\min}$ is required so that $\sigma_y\sigma_x \geq \sigma_{r,\min}^2$.

We can perform the energy collimation with a vertical or horizontal spoiler, using either the nonlinear second order vertical dispersion or the linear horizontal dispersion at the location of the spoiler. Alternatively, we can also use a spoiler for both planes with properly chosen horizontal and vertical gap sizes, so that the collimation occurs at the same momentum offset in the two planes.

If we employ a vertical spoiler, the nonlinear terms in the sextupolar deflection also yields a weak collimation for horizontal or vertical betatron amplitudes, at a collimation depth in units of σ_x or σ_y respectively of

$$n_x = \frac{D_{x,\mathrm{sext}}\Delta}{\sqrt{\epsilon_x \beta_{x,\mathrm{sext}}}}\,, \quad (18)$$

$$n_y = \frac{D_{x,\mathrm{sext}}\Delta}{\sqrt{\epsilon_y \beta_{y,\mathrm{sext}}}}\,, \quad (19)$$

where Δ is the energy collimation depth in units of δ. We can solve these equations for the beta functions at the sextupole and match for meaningful values of n_x and n_y. This was the approach chosen in [4], which tended to introduce large chromaticity.

Additionally, we can collimate in the other betatron phase, using the linear optics. Denoting the horizontal and vertical spoiler half gaps by a_x and a_y, respectively, and assuming that the vertical gap is adjusted for collimation at the same offset Δ as the horizontal one, instead of (18) and (19) we would get (dependent on the plane of linear collimation)

$$n_x^{(2)} = \frac{a_x}{\sqrt{\epsilon_x \beta_{x,\mathrm{sp}}}} \simeq \frac{D_{x,\mathrm{sp}}\Delta}{\sqrt{\epsilon_x \beta_{x,\mathrm{sp}}}}\,, \quad (20)$$

$$n_y^{(2)} = \frac{a_y}{\sqrt{\epsilon_y \beta_{y,\mathrm{sp}}}} \simeq \frac{1}{2}\frac{|R_{34}K_s|D_{x,\mathrm{sp}}^2\Delta^2}{\sqrt{\epsilon_y \beta_{y,\mathrm{sp}}}}\,, \quad (21)$$

where a_x and a_y are the half gap at the spoiler, and the super-index (2) refers to the orthogonal betatron phase, considering that the spoiler and the skew sextupole are placed roughly 90 degrees out of phase. These equations can be matched for the beta functions at the spoiler.

In principle, by combining Eqs. (18), (19), (20) and (21), we could collimate in both betatron phases and in energy using a single spoiler. If we opt for nonlinear betatron collimation , the other phase could also be collimated by installing a "pre" skew sextupole with a phase advance of about $\pi/2$ in front of the first skew sextupole, as proposed in [4].

The achievable value of the dispersion $D_{x,\mathrm{sext}}$ is limited by the emittance growth $\Delta(\gamma\epsilon_x)$ due to synchrotron radiation in the dipole magnets. The latter restricts the value

$$\Delta(\gamma\epsilon_x) \approx (4\times 10^{-8}\ \mathrm{m}^2\ \mathrm{GeV}^{-6})E^6 I_5 < f\epsilon_x \quad (22)$$

to a fraction f of the initial emittance. Here I_5 is the radiation integral [6], $I_5 = \sum_i L_i < \mathcal{H} > /|\rho_i|^3$, the sum runs over all bending magnets, with bending radius ρ_i, length L_i, and the "curly $\mathcal{H}$" function as defined by Sands [7].

NON LINEAR ENERGY COLLIMATION SYSTEM FOR CLIC USING PAIR OF SKEW SEXTUPOLES

Optics Design

Two new optics designs for nonlinear energy collimation at CLIC were developed and optimized. The main changes with respect to the previous nonlinear collimation optics [4] are:

- The collimation is performed only in energy. The sole purpose of the first skew sextupole is to the increase vertical spot size at the spoiler. A horizontal spoiler and the linear horizontal optics are used for the energy collimation.
- We have increased the overall fraction of the system occupied by bends and decreased the bending angle until the effect of synchrotron radiation became reasonably small.
- We kept the beta functions as regular as possible to avoid need of a dedicated chromatic correction inside the collimation system.

One of the two new optics features no dipoles between the two main skew sextupoles, the other has a high filling factor of dipole magnets. Both optics are displayed in Fig.3.

The beta functions are kept approximately constant along the line, which results in negligible chromatic emittance growth. The dispersion at the first main skew sextupole and the skew-sextupole strength are chosen so as to guarantee spoiler survival in case of a full beam impact. Notice that in the case with high filling factor of dipole magnets there is no change of sign in the dispersion function. The length of the two systems was reduced to the minimum value for which emittance growth due to synchrotron radiation does not yet affect the collider performance. The bending angles were adjusted accordingly. Beam, collimation and optics parameters of CLIC at 3 TeV are listed in Table 1for the two optics. In the calculation of the collimation and beam parameters we have considered a *uniform flat momentum distribution*. The minimum beam size required for spoiler survival is about $\sigma_{r,\min} \approx 120\ \mu$m (allowing for carbon or beryllium as spoiler material) [8]. A value of $I_5 = 10^{-19}$ m corresponds to $\Delta(\gamma\epsilon_x) \approx 0.046\ \mu$m for CLIC at 3 TeV or to about 7% emittance growth, but chromatic effects may further increase the luminosity degradation due to synchrotron radiation. The value $I_5 = 10^{-19}$ m has been taken as constraint for the dispersion function and dipole angle in the optics design.

Tracking studies

Multiparticle tracking studies were done using an initial distribution of 10000 particles with 1% full width energy spread for a flat square energy distribution, δ_{flat}. Different average energy offsets δ_0 for such a particle distribution were further considered. The tracking along the two optical systems of Fig. 3, from the entrance to the spoiler location, was done using the code `MAD` [9]. The simulated horizontal and vertical rms beam sizes at the spoiler were calculated from the tracking result as a function of the skew sextupole strength and δ_0, and compared with the analytical expressions (16) and (17), which represent a first order calculation). A good agreement was obtained for the vertical case,

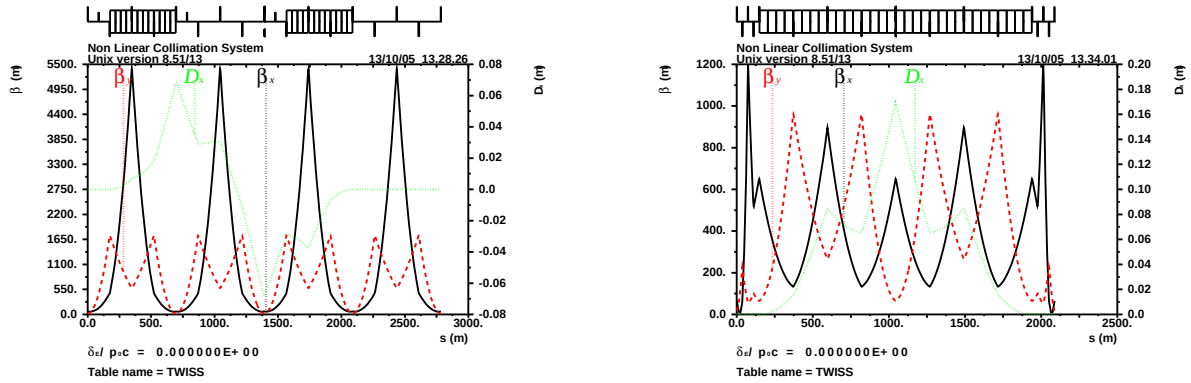

Figure 3: Optics of the new nonlinear energy collimation system without (left) and with bends between the skew sextupoles (right).

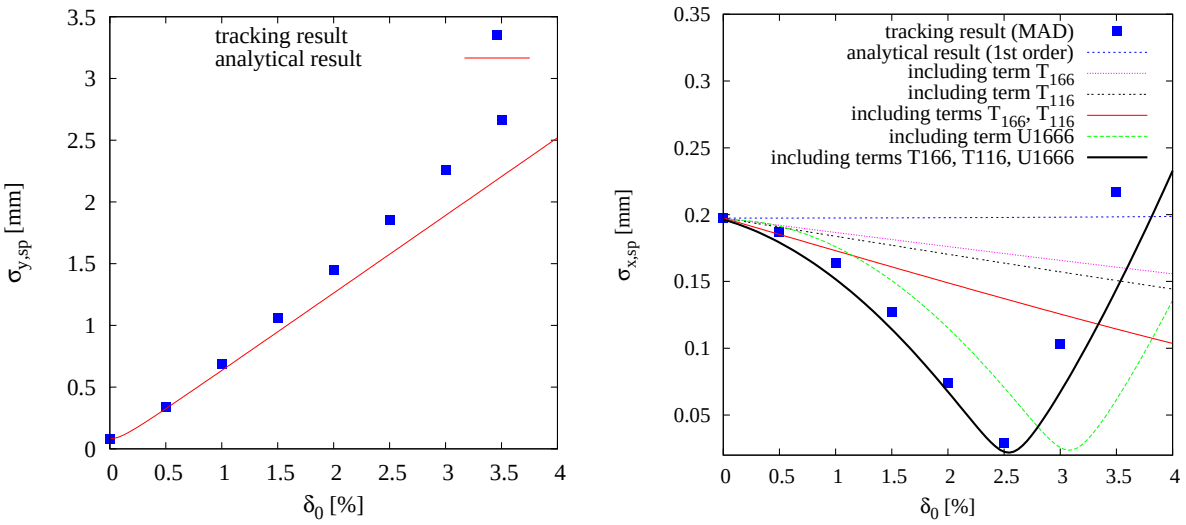

Figure 4: Vertical (left) and horizontal rms beam size (right) as a function of the average energy offset δ_0, for the optics solution of Fig. 3 (left).

Table 1: Beam, optics and collimation parameters for the two new nonlinear energy collimation systems without and with bends between the skew sextupoles.

variable	symbol	w/o bends	w bends	units
beam energy	E	1.5	1.5	TeV
rms momentum spread	σ_ϵ	2.8×10^{-3}	2.8×10^{-3}	
hor. geom. emittance	ϵ_x	0.23	0.23	pm
vert. geom. emittance	ϵ_y	6.8	6.8	fm
full width	$\delta_{\rm flat}$	0.01	0.01	
total length	l_t	2784.0	2088.0	m
cell length	l_c	170.0	220.0	m
dipole angle	θ_b	0.00008	0.00014	rad
skew sextupole pole tip field	B_T	1.4	1.4	T
skew sextupole aperture	a_s	4	4	mm
skew sextupole length	l_s	3	3	m
skew sextupole strength	K_s	104.3	104.3	m^{-2}
hor. beta function at entrance	β_x^0	65.0	650.0	m
ver. beta function at entrance	β_y^0	18.0	65.0	m
hor. phase advance from sext. to spo.	μ_x	0.322	0.250	2π
ver. phase advance from sext. to spo.	μ_y	0.293	0.500	2π
transport matrix from sext. to spo.	R_{12}	86.6	763.2	m
transport matrix from sext. to spo.	R_{34}	87.4	131.5	m
hor. dispersion function at sext.	$D_{x,\rm sext}$	0.049	0.085	m
hor. dispersion function at spo.	$D_{x,\rm sp}$	-0.068	0.170	m
synchrotron integral	I_5	2.9×10^{-21}	1.0×10^{-20}	m
spoiler survival size	$\sigma_{r,\rm sp}$	126.4	424.7	μm
energy collimation depth	Δ	0.013	0.013	
hor. spoiler half gap	$a_{x,\rm sp}$	0.089	2.206	mm
ver. spoiler half gap	$a_{y,\rm sp}$	1.835	8.343	mm

as is illustrated in Figs. 4 and 5 (left pictures). However, an analytical description including second and third order transport coefficients is necessary to reproduce the trend of the simulations for the horizontal case, shown in the right pictures of Figs. 4 and 5.

For the optics solution of Fig. 3 (left), the horizontal rms beam size decreases for values $\delta_0 < 2.5\%$ (see right picture of Fig. 4). For higher average energy offsets, the horizontal beam size increases steeply. Figure 6 (right picture) illustrates how the horizontal particle distribution with $\delta_0 = 1\%$ shrinks at the spoiler position due to the effect of the skew sextupole. On the other hand, for the optics solution of Fig. 3 (right), the horizontal rms beam size increases smoothly as a function of δ_0; see Figs. 5 and 7. This behavior is desired to increase the probability of spoiler survival.

In order to study the luminosity performance of the two optics solutions for nonlinear collimation, we tracked a distribution of 40000 particles with 1% full width energy spread from the entrance of the collimation system to the interaction point. The corresponding optics are displayed in Figs. 8. The cases with and without synchrotron radiation have been considered in these simulations. The luminosity has been computed by the beam-beam interaction code `GUINEA-PIG` [10]. This program performs detailed simulations of the beam-beam interactions at the IP, including the hourglass effect, the pinch effect, beamstrahlung and e^+e^- production. In Fig. 9 we present the simulated luminosity as a function of the skew sextupole strength for the two optics solutions of Fig. 3. The luminosity for either optics drops with the excitation of the skew sextupoles. The decrease for optics without bends between the skew sextupoles is moderate; on the other hand, for the optics with high filling factor of bends between the skew sextupoles the luminosity drops dramatically, losing almost two orders of magnitude for $K_s = 104\ \mathrm{m}^{-2}$ with respect to the value of luminosity for $K_s = 0\ \mathrm{m}^{-2}$. For comparison, the linear baseline CLIC collimation system provides a luminosity of $L_{w/oSR} = 10.714 \times 10^{34}\ \mathrm{cm}^{-2}\mathrm{s}^{-1}$ and $L_{wSR} = 7.441 \times 10^{34}\ \mathrm{cm}^{-2}\mathrm{s}^{-1}$ calculated using the codes `MAD` [9] and `GUINEA-PIG` [10], from [11].

OUTLOOK

Two new optics designs for the CLIC nonlinear energy collimation were developed and optimized, one with a high filling factor of dipole magnets, the other without any dipoles between the two main skew sextupoles. The beta functions are kept approximately constant along the line, which results in negligible chromatic emittance growth. The dispersion at the first main skew sextupole and

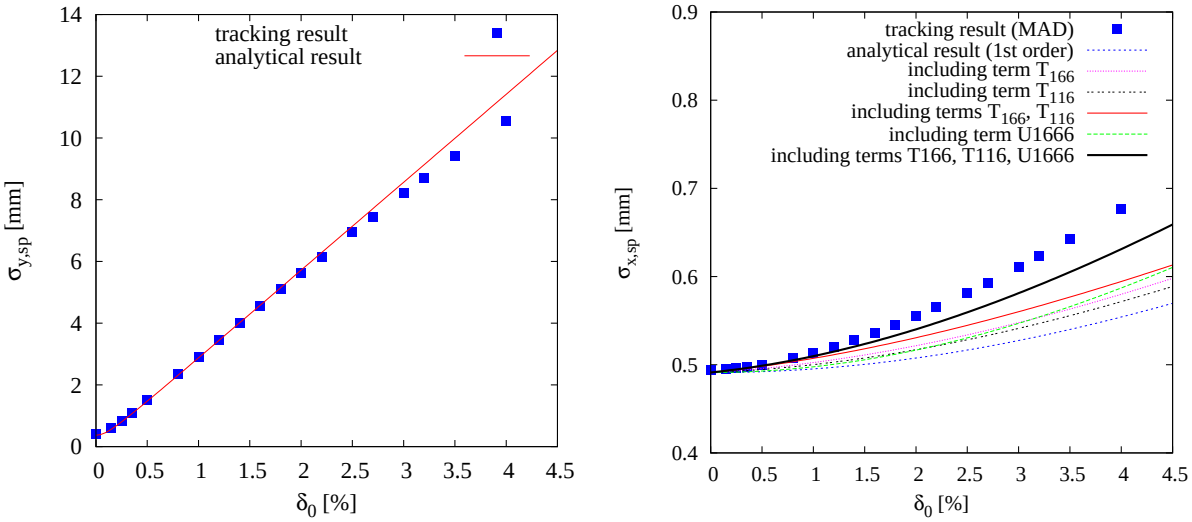

Figure 5: Vertical (left) and horizontal rms beam size (right) as a function of the average energy offset δ_0, for the optics solution of Fig. 3 (right).

the skew-sextupole strength are chosen so as to guarantee spoiler survival in case of a full beam impact.The length of the two systems was reduced to the minimum value for which emittance growth due to synchrotron radiation does not yet affect the collider performance.The bending angles were adjusted accordingly.

The chromatic behavior of the optics was characterized, and the simulated horizontal and vertical rms beam sizes at the spoiler as a function of the skew sextupole strength were compared with analytical expressions. A good agreement was obtained after accounting for second and third order expansion coefficients of the optical transport.

For zero skew sextupole strength, the luminosity for both new optics exceeds that of the CLIC baseline linear collimation system. However, the luminosity for either optics drops with the excitation of the skew sextupoles. The better performance is obtained for the optics without any dipoles between the skew sextupoles. It has, therefore, been chosen as a reference for future improvements.

Fortunately, it was realized that the skew sextupole strengths can be set to much lower values than previously assumed, if a maximum beam density for spoiler survival is required only for an off-momentum beam, and not for the nominal one. This is illustrated in Fig. 10. The survival limit corresponds to a density of about 50×10^9 mm^{-2} per bunch.

ACKNOWLEDGEMENT

This work is supported by the Commission of the European Communities under the 6^{th} Framework Programme "Structuring the Eurpean Research Area", contract number RIDS-011899.

REFERENCES

[1] L. Merminga, J. Irwin, R. H. Helm and R. D. Ruth, "Collimation systems for a TeV linear collider," Part. Accel. 48, 85 (1994) and SLAC-PUB-5165 Rev. may 1994.

[2] R. Brinkmann, P. Raimondi and A. Seryi, "Halo reduction By Means of Non Linear Optical Elements in the NLC Final Focus System," PAC2001, Chicago (2001).

[3] R. Brinkmann, N.j. Walker and G. Blair, "The TESLA Postlinac Collimation System," TESLA-01-12 (2001).

[4] A. Faus-Golfe and F. Zimmermann, "A Nonlinear Collimation System for CLIC," EPAC 2002 Paris (2002).

[5] K. Thompson, R. Pitthan, F. Zimmermann, et al., NLC Collimation Meetings, in particular 22.05.98, 29.05.98, and 31.08.98.; see web site: *http://www-project.slac.stanford.edu/lc/bdir/meetings_collimation.asp*

[6] R. Helm, M. Lee, P. Morton and M. Sands, "Evaluation of Synchrotron Radiation Integrals," SLAC-PUB-1193 (1973).

[7] M. Sands, "The Physics of Electron Storage Rings," SLAC-121 (1970).

[8] S. Fartoukh, et al., "Heat Deposition by Transient Beam Passage in Spoilers," CERN-SL-2001-012 AP (2001)and CLIC Note 477.

[9] H. Grote and F.C. Iselin, "The MAD program (Methodical Accelerator Design) version 8.16," User's reference manual, CERN/SL/90-13(AP) (1995).

[10] D. Schulte, Ph.D. thesis, University of Hamburg, TESLA-97-08(AP) (1996).

[11] T. Asaka and J. Resta Lopez, "Characterization and Performance of the CLIC Beam delivery Sysytem with SAD, MAD and Placet", CARE/ELAN Document 2005-011 (2005).

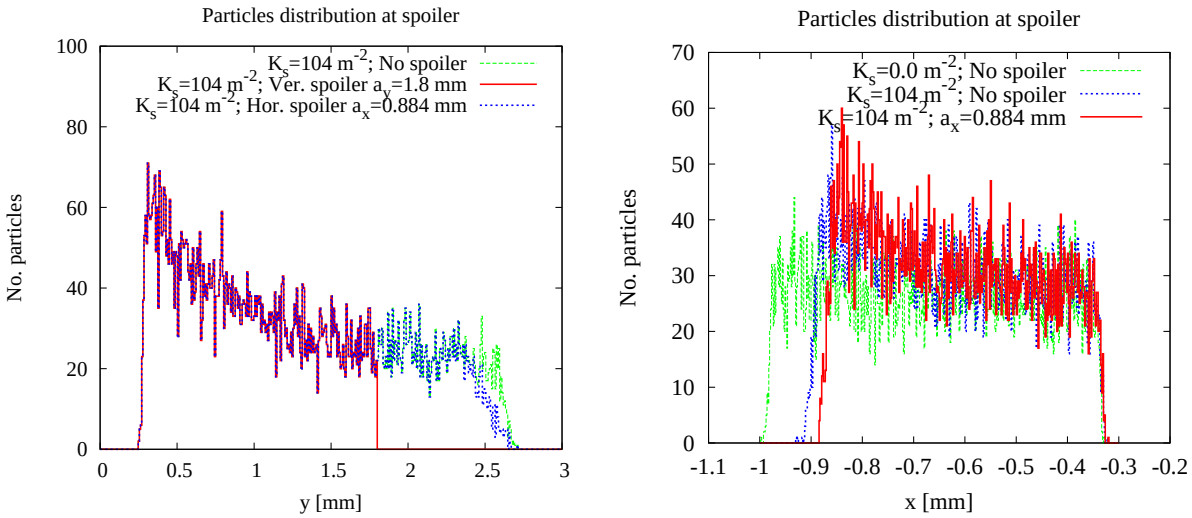

Figure 6: Vertical (left) and horizontal particle distribution (right) with an average energy offset of 1% at the spoiler, for the optics solution of Fig. 3 (left), considering various skew-sextupole strengths and collimator settings.

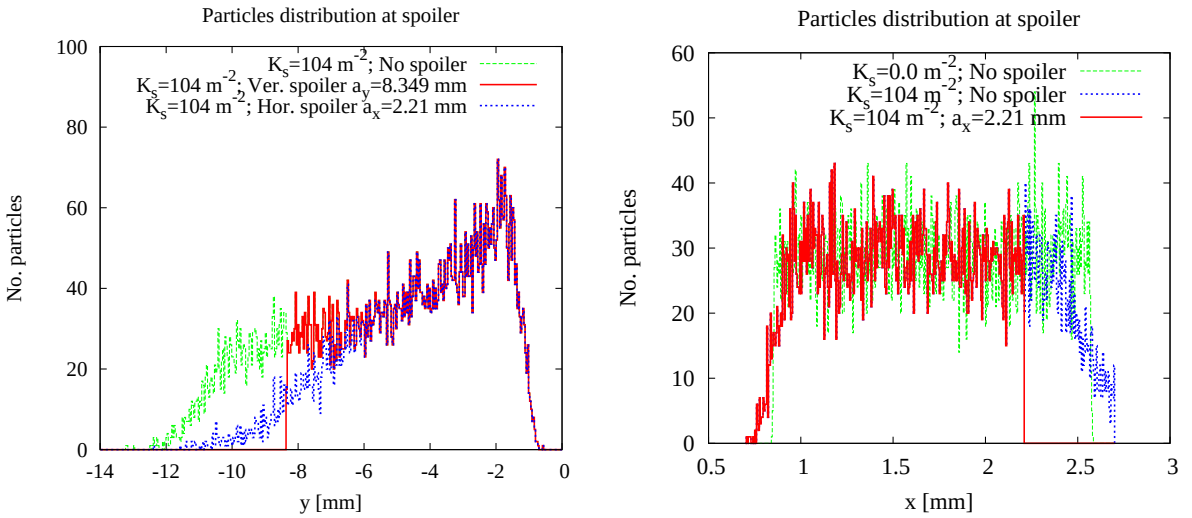

Figure 7: Vertical (left) and horizontal particle distribution (right) with an average energy offset of 1% at the spoiler, for the optics solution of Fig. 3 (right), considering various skew-sextupole strengths and collimator settings.

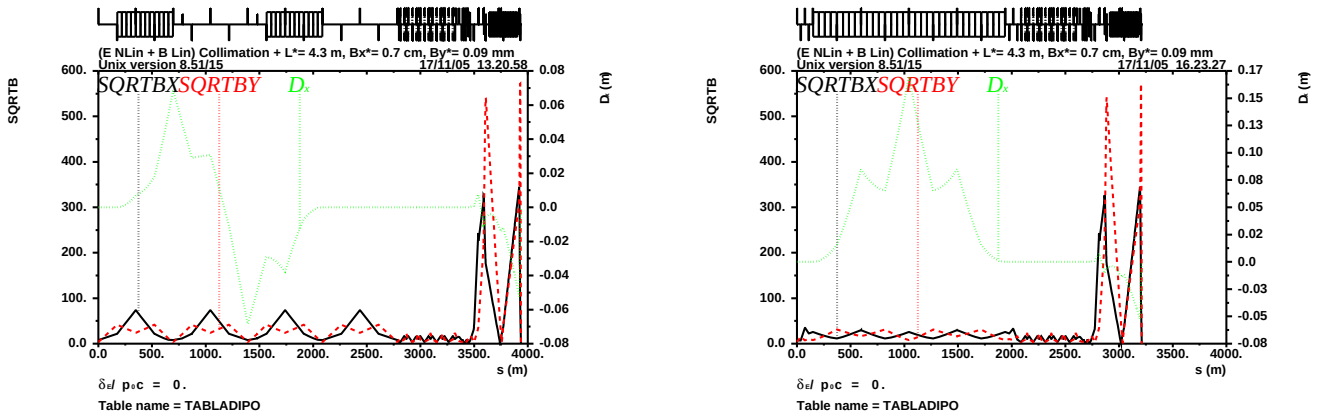

Figure 8: Optics of the complete CLIC beam delivery system with nonlinear energy collimation using a pair of skew sextupoles from Fig. 3. Both optics, without and with bends between the skew sextupoles, were designed using the code MAD.

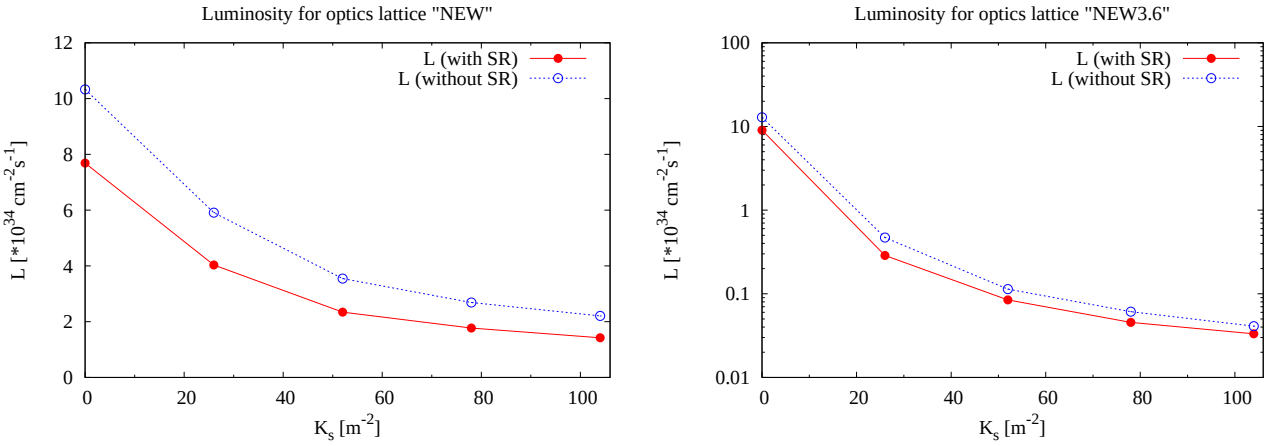

Figure 9: Luminosity as a function of the integrated skew sextupole strength, for the two optics solutions of Figs. 3 or 8. The two curves refer to MAD simulations with and without synchrotron radiation. The luminosity was computed by GUINEA-PIG.

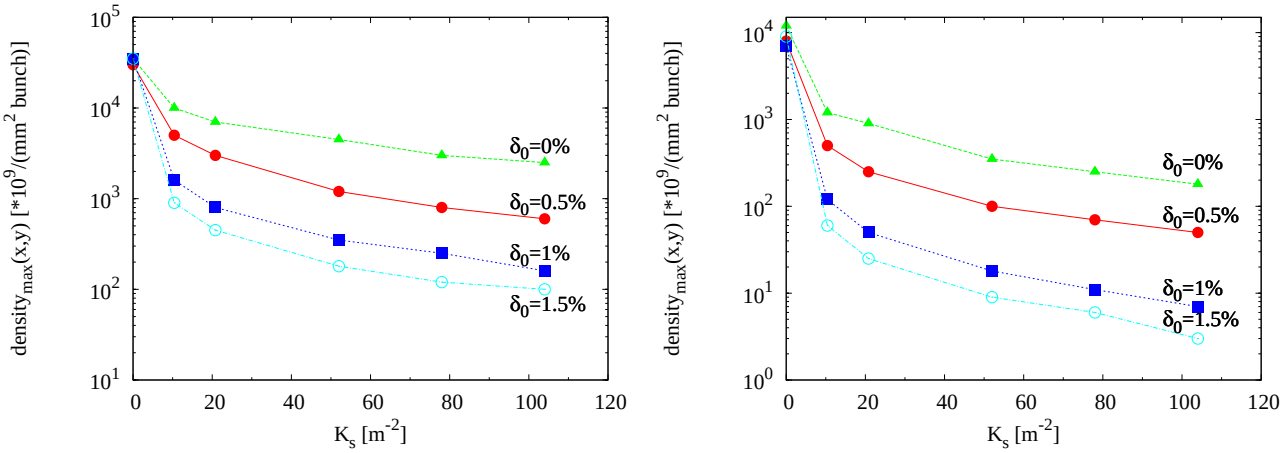

Figure 10: Peak density at the spoiler as a function of the skew sextupole strength for the two optics solutions of Fig. 3.

ILC EXTRACTION LINE FOR 14 MRAD CROSSING ANGLE*

Y. Nosochkov†, T. Markiewicz, T. Maruyama, A. Seryi, SLAC, Menlo Park, CA 94025, USA
B. Parker, BNL, Upton, NY 11973, USA

Abstract

The earlier studies of the ILC extraction line for 20 mrad and 2 mrad crossing angle options [1]-[5] showed that the 20 mrad design has an advantage of a simpler beamline and lower extraction beam loss because of the independent incoming and extraction optics. However, the large 20 mrad crossing angle requires the use of a crab cavity correction, increases synchrotron radiation emittance growth in the solenoid, and increases photon backscattering from the forward calorimeter of the detector. To reduce these effects, an attempt has been made to minimize the crossing angle while keeping the extraction and incoming lines separate. A new quadrupole scheme near the interaction point has been proposed which allows a reduction of the crossing angle to 14 mrad [6]. The optics design and results of tracking and background simulations for the 14 mrad extraction line are presented.

INTRODUCTION

Preliminary designs of the ILC extraction line for 20 mrad and 2 mrad crossing angles have been developed [1]-[5]. In both designs, the extraction line must transport up to 18.1 MW of the primary disrupted beam and the beamstrahlung (BS) photons to a common or separate dumps without excessive loss on the extraction magnets. These designs also include the dedicated optics for energy and polarization diagnostics.

Comparison of the two designs shows that the 20 mrad option has an advantage of a simpler beamline and lower extraction beam loss because of the independent incoming and extraction optics. However, the disadvantages of the large crossing angle are the stronger dependence of luminosity on a crab cavity correction, the higher synchrotron radiation (SR) emittance growth in the detector solenoid, and the increased photon backscattering from the forward calorimeter of the detector. To reduce these effects, an attempt has been made to minimize the crossing angle while keeping the extraction and incoming lines separate. A new quadrupole scheme near the interaction point (IP) has been proposed which allows a reduction of the crossing angle to 14 mrad [6]. Below, we present the optics design and the results of particle tracking and detector background simulations for the proposed 14 mrad extraction line.

* Work supported by the Department of Energy Contract DE-AC02-76SF00515.

† yuri@slac.stanford.edu

OPTICS

The proposed 14 mrad extraction optics is similar to the 20 mrad design [4] with a few differences described below. In both designs, the extraction optics is separate from the incoming optics, and the primary disrupted e^+/e and BS photons travel through the same extraction magnets to one shared dump. In the 20 mrad design, the first incoming and extraction quadrupoles are placed at the same distance, s = 3.51 m after the IP. This is based on the superconducting (SC) compact quadrupole design [7] which makes it possible to have side-by-side quadrupoles in the independent cryostats with a small 70 mm horizontal separation between the beams. However, further reduction of the separation and the crossing angle is not recommended in this option since it would be technically risky and would increase the remnant field outside of the quadrupole on the other beam axis.

To achieve a smaller crossing angle, it was proposed to move the first extraction quadrupole farther from the IP and behind the first incoming quadrupole QD0 [6]. In this case, the separation between the QD0 and the extraction beam pipe can be reduced for the smaller 14 mrad crossing angle. The schematic of the 14 mrad crossing with the nearest to IP incoming and extraction magnets is shown in Fig. 1, where the first extraction quadrupole QDEX1A is placed 6 m after the IP and 0.29 m behind the QD0. As shown in Fig. 2, the QD0 and the extraction pipe are placed in the same cryostat. In this scheme, the QD0 and QDEX1A quadrupoles are actively self-shielded which practically eliminates the remnant field outside of the quadrupole on the other beam axis [6].

One disadvantage of this solution is that the extraction focusing starts later after the IP which tends to increase the beam size in the extraction quadrupoles. However, in this design it was possible to sufficiently increase the gradient of the QDEX1A quadrupole [6] and, therefore, reduce the effect of the missing focusing near the IP.

The lattice functions in the 14 mrad extraction line are shown in Fig.3, where the IP is at $s = 0$ and the dump is at 400 m. As in the 20 mrad design, the optics consists of the initial DFDF quadrupole system, followed by the two vertical chicanes for energy and polarization diagnostics, and a long drift with three collimators before the dump.

In this optics, the first three extraction quadrupoles are superconducting and are placed between s = 6 m and 11.5 m from IP. They are followed by the dedicated 4 m drift to provide more transverse space for the crab cavity placed on the incoming line at this location. And the warm extraction magnets start at s = 15.5 m. The diagnostic energy and polarization chicanes create local bumps of the

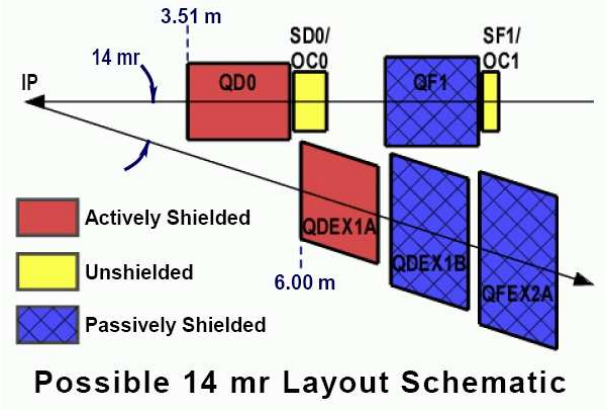

Figure 1: Schematic of the 14 mrad crossing with the incoming and extraction magnets on one side of the IP.

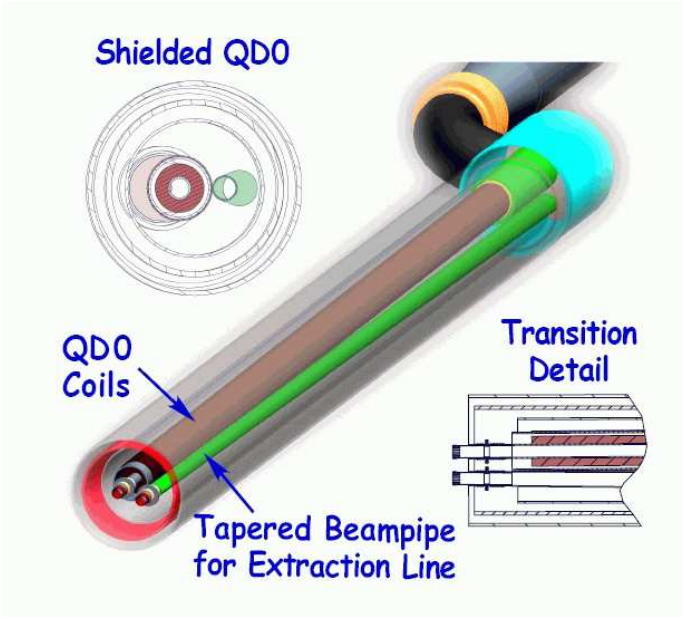

Figure 2: Design drawing of the nearest to IP incoming quadrupole QD0 and the extraction beam pipe in one cryostat.

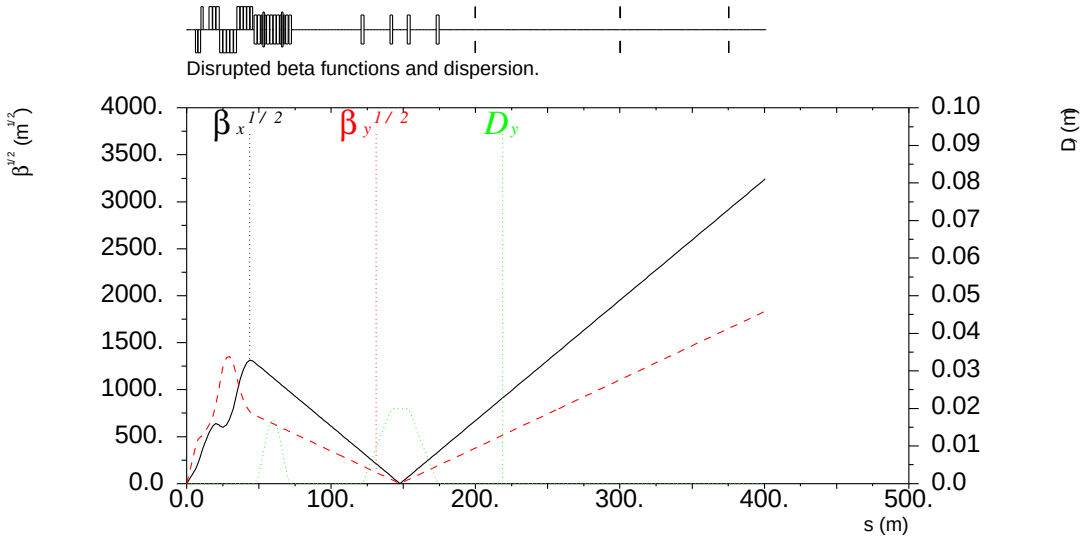

Figure 3: Disrupted beta functions and vertical dispersion in the 14 mrad extraction line. IP is at s = 0.

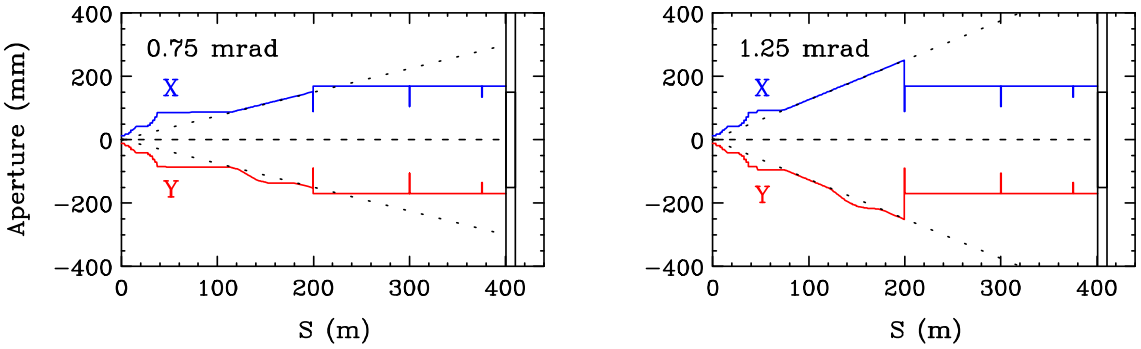

Figure 4: Two models of extraction aperture providing acceptance for the BS photons with the maximum IP angle of 0.75 mrad (left) and 1.25 mrad (right). The dotted lines show the 0.75 mrad and 1.25 mrad angles. Three collimators at s $>$ 200 m limit the beam size to 15 cm radius of the dump window.

vertical orbit and vertical dispersion with 1.7 cm and 2 cm peak values, respectively. The optics provides the 2nd focal point at the center of the polarimeter chicane at s 148 m to attain the required $<$ 100 m RMS beam size for the Compton polarimeter. The horizontal angular transformation term $R_{22} =$ 0.503 from IP to the 2nd focus is made close to one of the optimum values (0.5) for the polarization measurement. The diagnostic scheme for the 14 mrad extraction is the same as for the 20 mrad design which is described in detail in [3, 8].

In addition to the primary disrupted electron and BS photon beams, the extraction dump must also accept the full power of undisrupted beam if there is no collision at the IP. However, without the disruption, the beam size at the end of the last extraction magnet is too small for the dump window. The final 226 m drift is included to naturally increase the undisrupted beam size in order to avoid damage to the window. However, this long drift also increases the larger sizes of the disrupted electron and BS photon beams. In order to fit the disrupted beam sizes to the specified 15 cm radius of the dump window [9], three round collimators are placed at s 200 m, 300 m and 375 m.

The extraction apertures are made sufficiently large to avoid excessive power loss on the extraction magnets. Because of the large energy spread in the disrupted beam, most of the losses occur in the very low energy tail due to overfocusing in the quadrupoles. For the ILC nominal and high luminosity beam parameter options [10, 11], the size of the quadrupole aperture in the beginning of the extraction line is dominated by the electron beam size. But in the region of chicane bends farther from the IP the photon aperture becomes dominant. Because photons follow the straight lines, the full photon beam size can be rather large far from IP. In the 14 mrad design, we studied two models for the photon aperture in the magnets. In the first model, the magnet apertures were set to accept the photons with the maximum angle of 1.25 mrad at IP. This angle corresponds to the maximum photon angle for the ILC nominal and high luminosity options as will be shown below. Therefore, the photons will not be lost on magnets in this case. However, there will be photon losses on the three final collimators which have smaller apertures to limit the beam size at the dump window. In the second model, the magnet apertures were set to accept the photons with a smaller maximum angle of 0.75 mrad at IP. The latter has an advantage of smaller and more practical apertures in the magnets far from IP compared to the 1.25 mrad model. Also, the 0.75 mrad photon aperture is favored for the diagnostics [8]. However, both electron and BS photon losses will increase in the bend region in this option. Fig. 4 shows the schematic of these two aperture models. Note that the difference between the models is in the region from s 45 m to 200 m.

Parameters of the 14 mrad extraction quadrupoles are listed in Table 1 for 1 TeV center of mass (CM) energy, where L, B′ and R are the length, gradient and aperture radius, respectively. The chicane bends are 2 m long with 0.8339 T field at 1 TeV CM. At 0.5 TeV CM, the magnet field is two times lower.

Table 1: Quadrupole parameters at 1 TeV CM.

Name	L [m]	B′ [T/m]	R [mm]
QDEX1A	1.6407	-83.333	18
QDEX1B	1.6407	-50.000	24
QFEX2A	1.6187	+40.000	30
QFEX2B,2C,2D	2.1431	+23.809	42
QDEX3A,3B	2.1058	-23.809	42
QDEX3C	2.1058	-21.739	46
QDEX3D	2.1058	-19.231	52
QDEX3E	2.1058	-16.129	62
QFEX4A	1.9448	+14.084	71
QFEX4B,4C,4D,4E	1.9448	+11.765	85

PARTICLE TRACKING

Simulation of beam transport from the IP to the dump was performed using the DIMAD code [12]. Beam distributions of up to $3.5 \cdot 10^7$ disrupted e^+ and e at the IP were generated using the GUINEA–PIG code [13] for the ILC nominal and high luminosity (high-L) options of beam

Table 2: Disrupted beam parameters at the IP for various ILC beam options.

CM energy	Luminosity [10^{38}] [m ^{2}s ^{1}]	Beam power [MW]	Δy offset [nm]	Primary electrons			BS photons	
				E_{min}/E_0 [%]	X'_{max} [rad]	Y'_{max} [rad]	X'_{max} [rad]	Y'_{max} [rad]
0.5 TeV nominal (c11)	2.03	11.3	0	36	529	253	369	212
			200	36	474	674	366	537
0.5 TeV high-L (c15)	4.92	11.3	0	17	1271	431	723	320
			120	17	1280	1415	782	1232
1.0 TeV nominal (c21)	2.81	18.1	0	20	496	159	271	148
			100	19	423	566	279	408
1.0 TeV high-L (c25)	7.81	18.1	0	6.3	2014	489	937	296
			80	6.2	1731	1592	974	1200
1.0 TeV high-L (c26)	5.72	21.7	0	15	661	249	338	170
			100	14	598	696	376	585
1.0 TeV high-L (c27)	4.64	18.1	0	15	597	236	546	159
			100	14	537	691	342	532

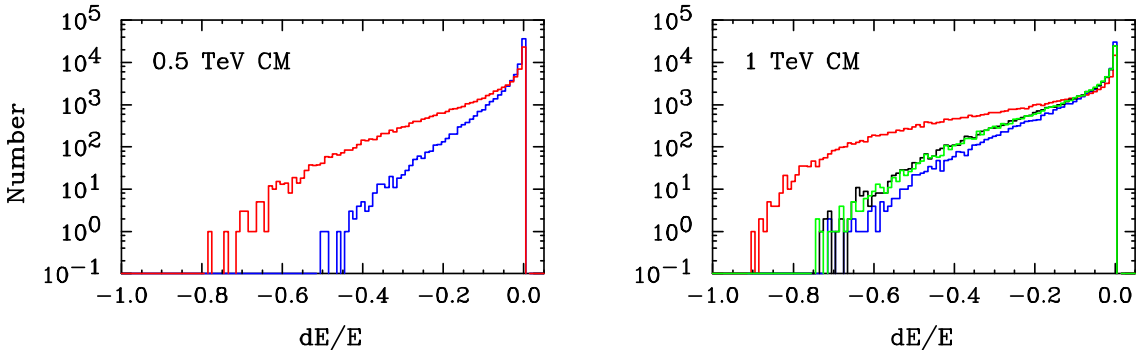

Figure 5: Disrupted energy distribution at IP for the ILC beam options: left figure - c11 (blue), c15 (red); right figure - c21 (blue), c25 (red), c26 (black), c27 (green).

parameters [10] and for the two alternative 1 TeV CM high-L options [11]. Distributions of the BS photons were also generated for each option, but with a lower statistics. In addition, two cases were considered: 1) ideal beam collisions, and 2) collisions with a large vertical beam-to-beam offset Δy which increases the vertical divergence in both the primary and BS photon beams. The value of Δy was selected to maximize this divergence. Summary of the disrupted beam parameters in these options is presented in Table 2. The lowest relative energy E_{min}/E_0 and maximum IP angles in the beam are the critical parameters affecting the loss of primary e^+/e and BS photons. Note that the angular and energy spread in the high-L options (c15, c25) are large compared to the other options. The two alternative high-L options (c26, c27) are designed to reduce the energy spread, but at the cost of somewhat lower luminosity. One can see that at the ideal collisions the disrupted beam size is large in the horizontal plane, but the vertical size can dominate at a large Δy offset. The low energy tail increases with the beam energy and luminosity. The disrupted energy distributions for the 0.5 TeV CM and 1 TeV CM options are shown in Fig. 5.

As mentioned earlier, the dump must accept the full power of undisrupted beam. Table 3 shows the x and y RMS sizes of the undisrupted primary beam at the dump at s 400 m. Note that at 0.5 TeV CM the SR effect on the beam size is rather small, but at 1 TeV CM it increases the vertical size more than a factor of 2. At 0.5 TeV CM, the undisrupted beam size satisfies the requirement of x $y >$ 1.7 mm^2 for a long term survival of the dump window [9]. However, a significantly larger size ($\sim$70 mm^2) is required

Table 3: Undisrupted beam size at dump for various ILC beam options.

CM energy	x [mm]	y [mm]	x y [mm^2]
0.5 TeV nominal (c11)	3.97	0.43	1.71
0.5 TeV high-L (c15)	5.75	0.52	2.97
1.0 TeV nominal (c21)	2.35	0.78	1.84
1.0 TeV high-L (c25)	4.06	0.79	3.21
1.0 TeV high-L (c26)	2.35	0.75	1.77
1.0 TeV high-L (c27)	2.77	0.75	2.06

Table 4: Disrupted beam power loss in the extraction line for 0.75 mrad photon aperture model.

CM energy	Δy offset [nm]	Total electron loss (kW)				Total BS photon loss (kW)				Electron loss on SC quads [kW]
		Prior to collim.	Collimators			Prior to collim.	Collimators			
			1	2	3		1	2	3	
0.5 TeV nominal (c11)	0	0	0	1.4	0.77	0	0	0.002	0	0
	200	0.0009	3.8	25	2.7	0	0.09	13	0	0
0.5 TeV high-L (c15)	0	2.0	39	230	46	0	1.8	28	0	0.002
	120	15.5	477	584	53	0.48	136	195	0	0
1.0 TeV nominal (c21)	0	0.25	0.46	0.39	0	0	0	0	0	0
	100	2.3	1.1	14	2.1	0	0	0.17	0	0
1.0 TeV high-L (c25)	0	105	32	376	60	0.013	1.2	7.2	0	0.55
	80	256	587	1404	69	0.99	47	276	0	0.58
1.0 TeV high-L (c26)	0	1.8	1.5	1.4	1.4	0	0	0	0	0
	100	10.2	4.2	203	17	0	0.07	2.1	0	0
1.0 TeV high-L (c27)	0	1.3	0.84	0.94	0.15	0	0	0.003	0	0
	100	6.7	4.3	119	8.4	0	0.04	0.90	0	0

Table 5: Disrupted beam power loss in the extraction line for 1.25 mrad photon aperture model.

CM energy	Δy offset [nm]	Total electron loss (kW)				Total BS photon loss (kW)				Electron loss on SC quads [kW]
		Prior to collim.	Collimators			Prior to collim.	Collimators			
			1	2	3		1	2	3	
0.5 TeV nominal (c11)	0	0	0	1.4	0.77	0	0	0.002	0	0
	200	0.0004	3.8	25	2.7	0	0.09	13	0	0
0.5 TeV high-L (c15)	0	1.3	40	230	46	0	1.8	28	0	0.002
	120	5.2	493	585	52	0	137	195	0	0
1.0 TeV nominal (c21)	0	0.11	0.62	0.39	0	0	0	0	0	0
	100	1.4	1.7	14	2.5	0	0	0.17	0	0
1.0 TeV high-L (c25)	0	80	55	377	60	0	1.2	7.2	0	0.55
	80	213	633	1405	67	0	48	276	0	0.58
1.0 TeV high-L (c26)	0	0.93	2.9	1.4	1.4	0	0	0	0	0
	100	6.4	7.2	203	17	0	0.07	2.1	0	0
1.0 TeV high-L (c27)	0	0.66	1.3	0.94	0.15	0	0	0.003	0	0
	100	4.1	6.9	119	8.8	0	0.04	0.90	0	0

to prevent the water boiling in the dump vessel [9]. We consider that a further increase of beam size can be achieved by using a rastering system in front of the dump for sweeping the bunches over a wider area on the dump window. The additional benefit of the rastering system is that the length of the final drift could be significantly reduced, and the dump moved from 400 m after the IP to about 250-300 m. For the same size of the dump window, the closer position of the dump would also naturally open up the apertures of the final collimators and, therefore, reduce the collimator loss. Note that the dump cannot be placed closer than 250 m to IP because of the required minimum separation of 3.5 m between the dump and the incoming beamline.

Summary of the beam loss in the extraction magnets and collimators is presented in Tables 4 and 5 for the 0.75 mrad and 1.25 mrad photon aperture models. The detailed distributions of the primary beam loss in the region of the extraction magnets (prior to collimators) are shown in Fig. 6–16. Note that no losses were observed in the magnet region for the 0.5 TeV CM nominal option (c11) with $\Delta y = 0$. The detector solenoid is not included in the calculation, but the earlier studies [3] showed that it has a small effect on beam loss if the orbit from the solenoid is corrected.

The tracking shows that the most loss in the extraction magnets comes from the lowest energy particles in the primary beam. Typically, the electrons with relative energy of $> 40\%$ will survive in the magnet region regardless of the IP angles. But in the final three collimators with smaller apertures, the losses are due to both the low energy and the large IP angle.

The last column in Tables 4 and 5 shows the primary loss on the SC quadrupoles. It is critical that this loss does not exceed the level of a few Watts. The nominal and the two alternative high-L options did not produce any SC loss

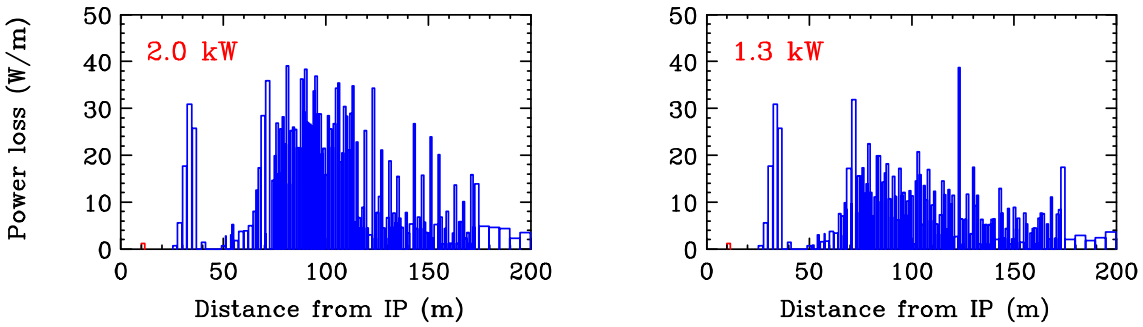

Figure 6: Primary beam loss for 0.5 TeV CM high-L option (c15), $\Delta y = 0$, and 0.75 mrad (left) and 1.25 mrad (right) photon aperture.

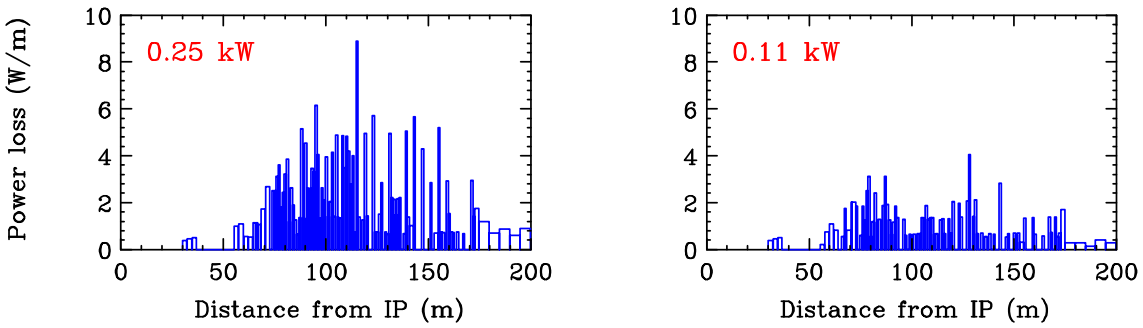

Figure 7: Primary beam loss for 1.0 TeV CM nominal option (c21), $\Delta y = 0$, and 0.75 mrad (left) and 1.25 mrad (right) photon aperture.

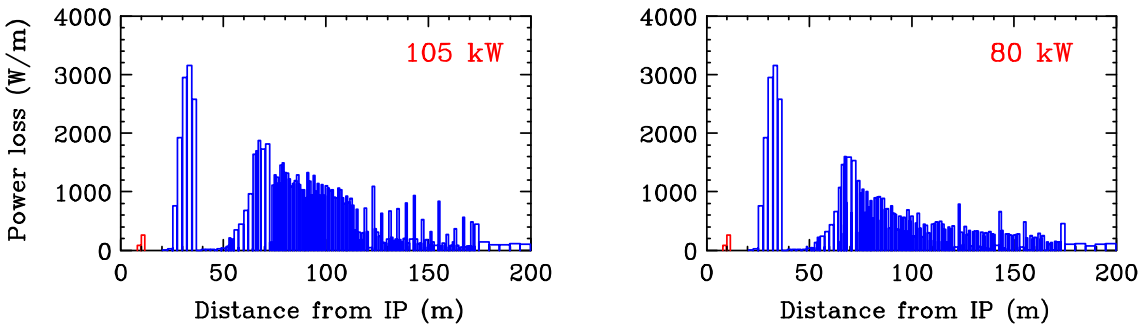

Figure 8: Primary beam loss for 1.0 TeV CM high-L option (c25), $\Delta y = 0$, and 0.75 mrad (left) and 1.25 mrad (right) photon aperture.

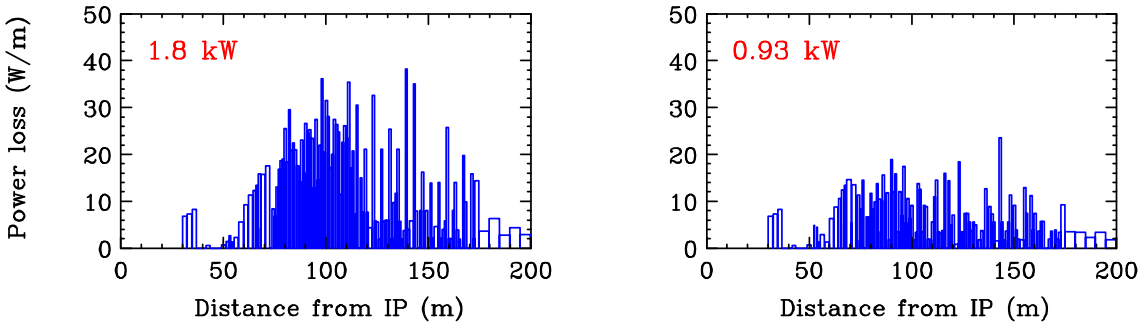

Figure 9: Primary beam loss for 1.0 TeV CM high-L option (c26), $\Delta y = 0$, and 0.75 mrad (left) and 1.25 mrad (right) photon aperture.

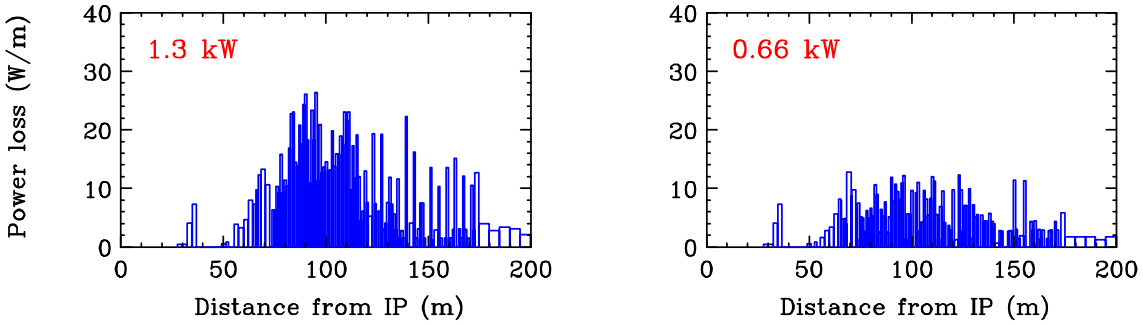

Figure 10: Primary beam loss for 1.0 TeV CM high-L option (c27), $\Delta y = 0$, and 0.75 mrad (left) and 1.25 mrad (right) photon aperture.

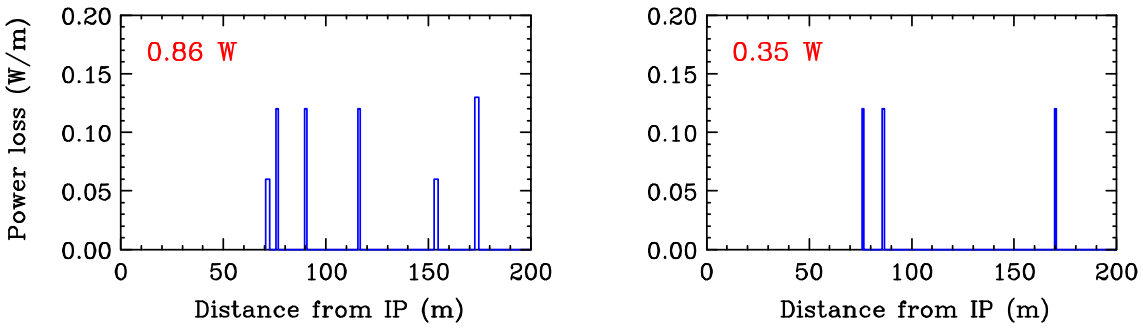

Figure 11: Primary beam loss for 0.5 TeV CM nominal option (c11), $\Delta y = 200$ nm, and 0.75 mrad (left) and 1.25 mrad (right) photon aperture.

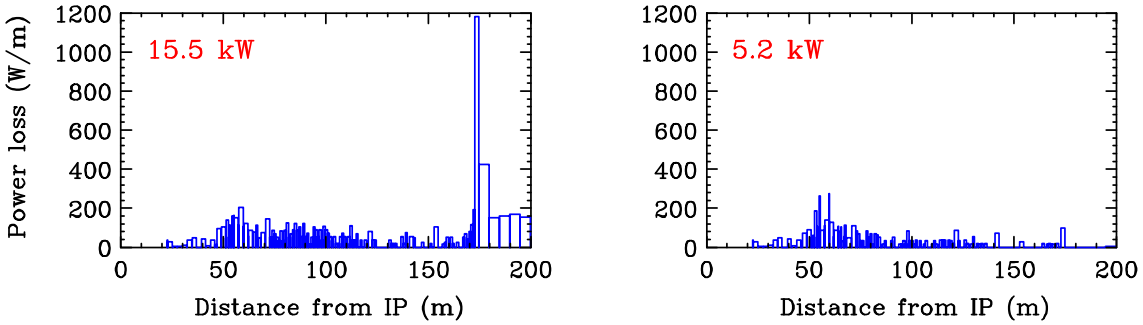

Figure 12: Primary beam loss for 0.5 TeV CM high-L option (c15), $\Delta y = 120$ nm, and 0.75 mrad (left) and 1.25 mrad (right) photon aperture.

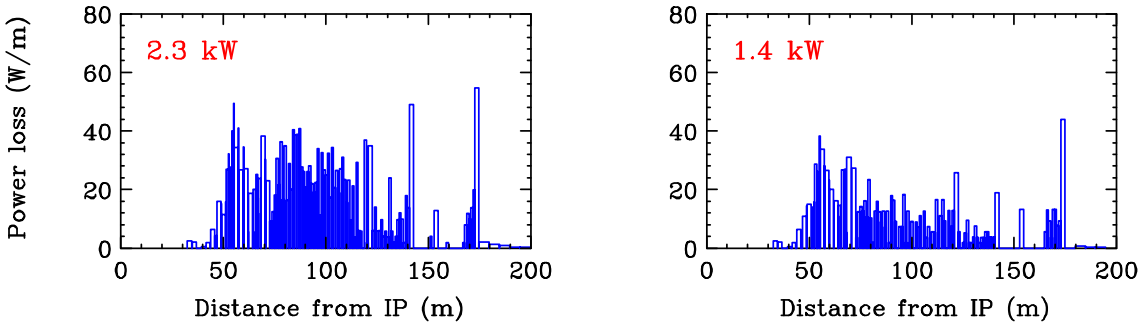

Figure 13: Primary beam loss for 1.0 TeV CM nominal option (c21), $\Delta y = 100$ nm, and 0.75 mrad (left) and 1.25 mrad (right) photon aperture.

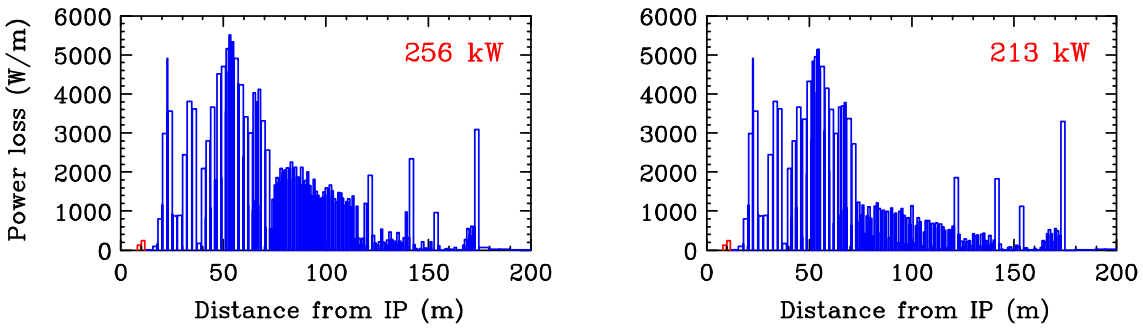

Figure 14: Primary beam loss for 1.0 TeV CM high-L option (c25), $\Delta y = 80$ nm, and 0.75 mrad (left) and 1.25 mrad (right) photon aperture.

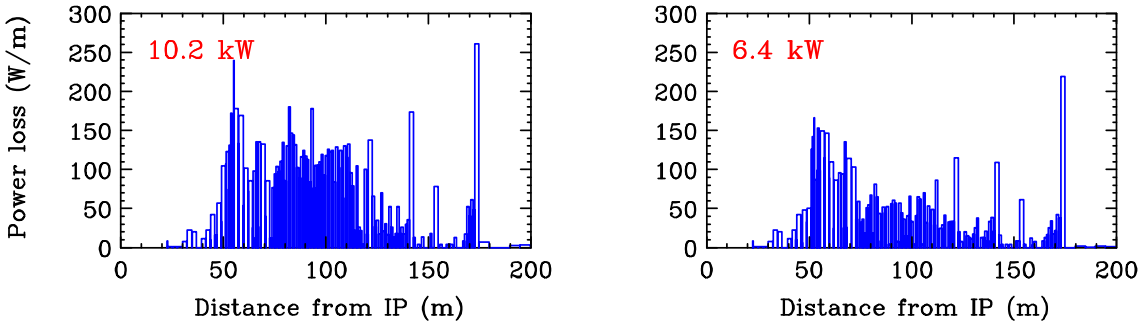

Figure 15: Primary beam loss for 1.0 TeV CM high-L option (c26), $\Delta y = 100$ nm, and 0.75 mrad (left) and 1.25 mrad (right) photon aperture.

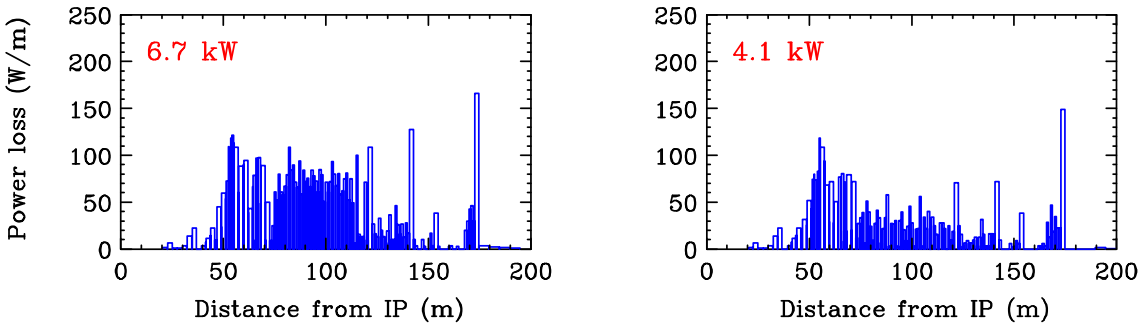

Figure 16: Primary beam loss for 1.0 TeV CM high-L option (c27), $\Delta y = 100$ nm, and 0.75 mrad (left) and 1.25 mrad (right) photon aperture.

in the tracking. In the 1 TeV CM high-L option (c25) the loss on the SC quads is very large and is clearly unacceptable. This option also creates an excessive loss in the downstream warm magnets. This is because of the significant beam power in the low energy tail in this option. In the 0.5 TeV CM high-L option (c15), the primary loss on the SC quads is within 2 W which may be acceptable if the additional losses from secondary particles are minor.

Comparison of the Tables 4 and 5 shows that the primary beam loss on magnets (prior to collimators) is typically a factor of 1.5-2 higher in the 0.75 mrad aperture model due to the smaller aperture in the chicane region. Consequently, the primary loss on the 1st collimator at s 200 m is lower in the 0.75 mrad model since some of the large amplitude particles are lost earlier than in 1.25 mrad model. For both models, the primary loss in the warm magnets is below 1 W in the 0.5 TeV CM nominal option, and below 10 W/m and 60 W/m in the 1 TeV CM nominal option for $\Delta y = 0$ and 100 nm offsets, respectively. In the high-L options, excluding the 1 TeV CM option (c25), the primary loss density is below 40 W/m and 300 W/m for zero and non-zero offsets, respectively. This loss level is considered tolerable for the conventional magnets. One exception is a spike of $\sim$2.4 kW loss in the last polarimeter bend at s 175 m in the 0.5 TeV CM high-L option with $\Delta y = 120$ nm for 0.75 mrad aperture model as shown in Fig. 12. This loss can be reduced by including a protection collimator in front of this bend, however the collimation effects on the diagnostics would have to be checked.

By design, there is no BS photon loss in the extraction quadrupoles for all the nominal and high-L options and for both the 1.25 and 0.75 mrad aperture models. There is also

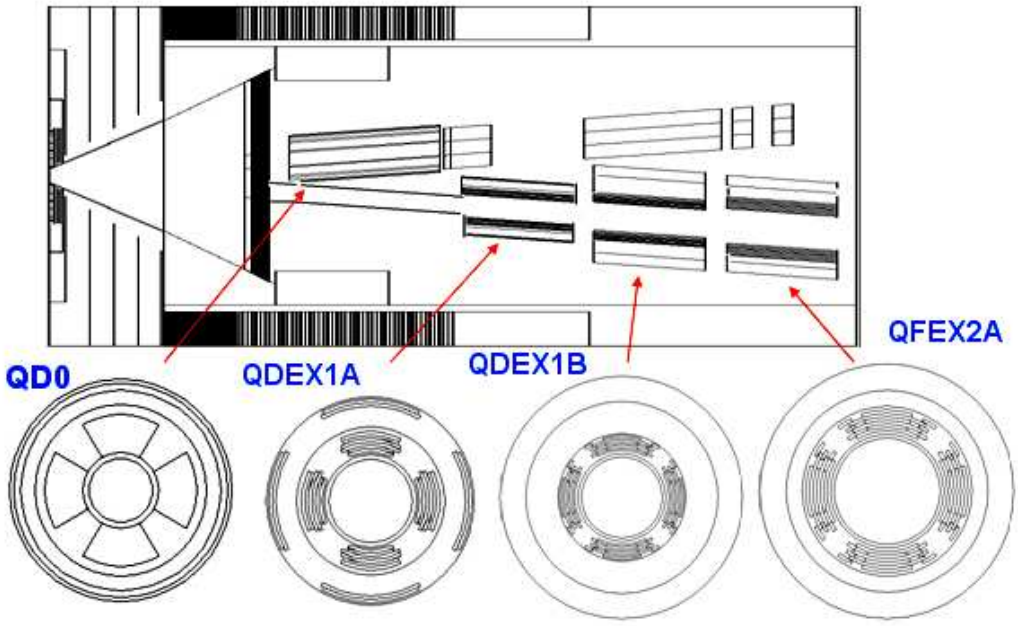

Figure 17: GEANT geometry model used in the background calculation. Top - horizontal view of the nearest to IP incoming and extraction magnets, bottom - cross-sections of the SC quadrupoles.

no BS photon loss in the diagnostic chicanes for the 1.25 mrad aperture model. But there is some photon loss in the chicanes for the 0.75 mrad model in the high-L options (c15 and c25) with large Δy offset, however it is much smaller than the primary electron loss.

The losses of primary electrons and BS photons on the three final collimators are very similar in the 0.75 mrad and 1.25 mrad aperture models. The total collimator loss is moderate in the nominal luminosity options (c11 and c21) and in the alternative 1 TeV CM high-L options (c26 and c27), especially under ideal conditions with $\Delta y = 0$. But the collimator loss is rather high in the 0.5 and 1 TeV high-L options (c15 and c25) due to the large IP divergence for both the disrupted electrons and BS photons. In option (c15) the total collimator loss is 0.35 MW and 1.5 MW for $\Delta y = 0$ and 120 nm, respectively. And in option (c25) it is 0.5 MW and 2.4 MW for $\Delta y = 0$ and 80 nm. Since the collimator loss at $\Delta y = 0$ is dominated by the large horizontal IP angles, one possible way to reduce it is to increase the horizontal size of the dump window and, proportionally, the aperture of the collimators. In this case, the remaining high loss at large Δy should not significantly increase the cumulative loss since the collisions with large offset should be rare. As mentioned earlier, the use of the rastering system could allow to move the dump 100-150 m closer to the IP which would naturally increase the collimator apertures and reduce the collimator loss. In the present setting, the losses are not evenly distributed on the three collimators. With further optimization of the apertures and s-positions of the collimators, and possible enlargement of the dump window size, the maximum loss in the collimators could be further reduced.

Based on these calculations, we conclude that the level of beam loss is acceptable in the nominal options (c11, c21) and 1 TeV CM alternative high-L options (c26, c27). The beam loss is unacceptable in the 1 TeV high-L option (c25), therefore this parameter set should be excluded from consideration. The 0.5 TeV CM high-L option (c15) is tentatively acceptable assuming enlargement of the size of the dump window and the collimator apertures, and with an additional protection collimator at the last bend. The other choice would be to create an alternative 0.5 TeV CM high-L option with reduced IP divergence. Finally, comparison of the two aperture models shows that the increase of beam loss in the extraction magnets due to the reduced aperture in the 0.75 mrad model is acceptable. Because this model also satisfies the diagnostic aperture specifications and significantly reduces the bend apertures, we consider it the preferred model.

DETECTOR BACKGROUND

The incoming and extraction magnets within approximately 20 m of IP were modeled in the GEANT 3 code, and the detector background from the incoherently produced e^+e pairs was calculated for the SiD detector. Figure 17 shows the GEANT geometry model used in the calculation. The materials and geometries of the self-shielded magnets are represented in the model. The detector and masking scheme are described in [14]. The VXD layers are at the radial and longitudinal positions of r = 1.4, 2.6, 3.7, 4.8, 6.0 cm and |z| = 6.25 cm. The e^+e pairs were generated using the GUINEA–PIG code [13] for the ILC 0.5 TeV nominal beam parameters.

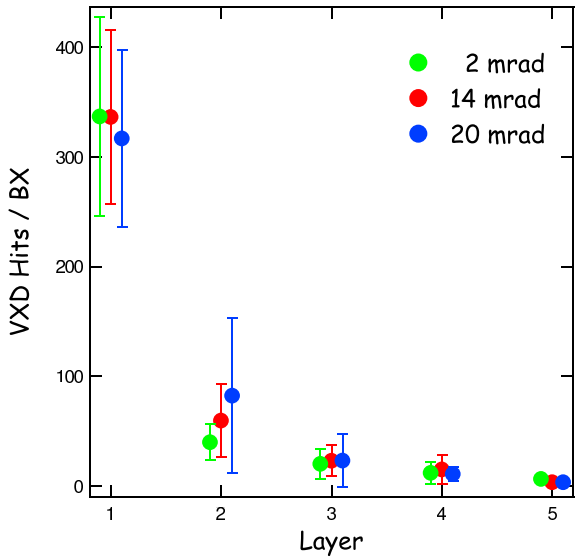

Figure 18: Calculated number of charge particle hits per bunch crossing in the vertex detector layers for the 2 mrad, 14 mrad, and 20 mrad crossing angle schemes.

Figure 18 compares the calculated number of charge particle hits per bunch crossing in the vertex detector layers for the 2 mrad [5], 14 mrad, and 20 mrad [4] crossing angle schemes. The average and RMS values are calculated from 20 statistically independent bunches. Since the majority of VXD hits are due to the low energy e^+/e directly hitting the VXD layers, and the contribution from the secondary e^+/e backscattered from the very forward calorimeter (BeamCal) is small, the number of VXD hits is not very dependent on the crossing angle. There is, however, about 30% of bunch-to-bunch fluctuation, but the crossing angle dependence is certainly smaller than this fluctuation. For 20 mrad crossing, a detector-integrated-dipole (DID) field is proposed for compensation of the detector solenoid field on the incoming beam orbit [15]. The DID field, however, increases the effect on the extraction beam. One advantage of the smaller 14 mrad angle is that the effects of synchrotron radiation, detector solenoid and DID field are reduced compared to 20 mrad crossing. On the other hand, one can reverse the DID field to correct the extraction beam rather than the incoming beam (anti-DID). In this case, the field strength of the anti-DID is optimized in order to maximize the number of pairs into the extraction hole. The number of charge particle hits in the VXD detector was calculated using the DID and anti-DID options, but the DID field dependence was found negligible.

When e^+e pairs hit BeamCal, secondary photons are generated, which will form a secondary background in the VXD and silicon trackers. The secondary photon production is proportional to the amount of energy deposited in BeamCal. This energy is highly dependent on the crossing angle and the radius of the beam holes in BeamCal. Furthermore, this energy is also dependent on the DID field for the 14 mrad and 20 mrad crossing angles. Figure 19

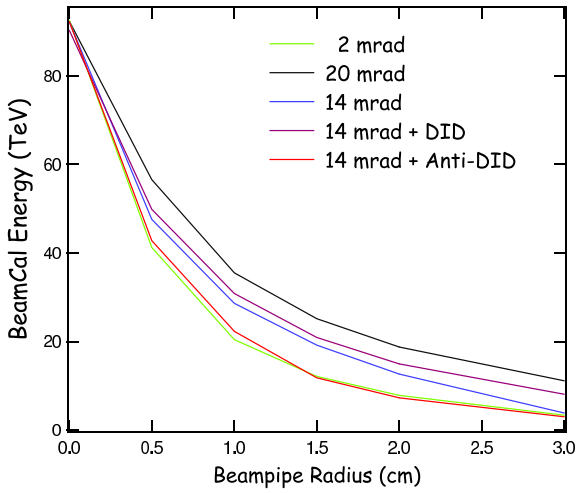

Figure 19: Total energy in BeamCal as a function of the extraction beam hole radius.

shows the total energy in BeamCal as a function of the extraction beam hole radius. There is only one beam hole for the 2 mrad crossing scheme, while the radius of the incoming beam hole is fixed to 1 cm for the 14 mrad and 20 mrad crossing schemes. Without the DID field, the energy for 14 mrad angle is about 25% smaller than that for 20 mrad at r = 1.5 cm used in the detector background calculations. With the anti-DID field, the energy for 14 mrad angle is reduced and becomes comparable to that for 2 mrad. The number of secondary photons in the silicon tracker is 1800 per bunch crossing for the 14 mrad crossing, and this number decreases to 800 with the anti-DID, which is comparable to 700 for the 2 mrad scheme.

CONCLUSION

The presented design of the ILC 14 mrad extraction line is based on the 20 mrad design and the new quadrupole scheme near the IP. Compared to the 2 mrad design, the 14 mrad option maintains the advantages of the separate extraction beamline, a simpler optics and lower beam loss as in the 20 mrad design. However, it also reduces the negative effects of the large crossing angle. With the smaller 14 mrad angle, the luminosity dependence on the crab cavity correction is reduced. Additionally, the SR emittance growth in the solenoid and the photon backscattering from the forward calorimeter of the detector are reduced. With the use of the anti-DID correcting field these detector backgrounds can be as small as in the 2 mrad design. The tracking simulations showed that the losses of primary electrons and BS photons are acceptable in the considered nominal and high-L options except the 1 TeV CM high-L option (c25) which should be excluded from consideration. Further optimization and enlargement of aperture of the final collimators and the dump window are considered for the reduction of beam loss on the collimators in the 0.5 TeV CM high-L option (c15).

REFERENCES

[1] Y. Nosochkov, *et al.*, SLAC–PUB–11363 (2005), presented at the LCWS 2005, Stanford, CA, USA (2005).

[2] R. Appleby, *et al.*, SLAC–PUB–11372 (2005), presented at the LCWS 2005, Stanford, CA, USA (2005).

[3] Y. Nosochkov, *et al.*, SLAC–PUB–11205 (2005), presented at the PAC 2005, Knoxville, TN, USA (2005).

[4] Y. Nosochkov, *et al.*, presented at the Snowmass ILC Workshop 2005, Snowmass, CO, USA (2005), http://alcpg2005.colorado.edu:8080/alcpg2005/program/accelerator/WG4/aug17_nosochkov_extraction20mrad.pdf .

[5] Y. Nosochkov for the SLAC-BNL-UK-France Task Force, presented at the Snowmass ILC Workshop 2005, Snowmass, CO, USA (2005), http://alcpg2005.colorado.edu:8080/alcpg2005/program/accelerator/WG4/aug17_nosochkov_extraction2mrad.pdf .

[6] B. Parker, "Recent Progress Designing Compact Superconducting Final Focus Magnets for the ILC," these proceedings.

[7] B. Parker, *et al.*, "Compact Superconducting Final Focus Magnet Options for the ILC," presented at the PAC 2005, Knoxville, TN, USA (2005).

[8] K.C. Moffeit, *et al.*, SLAC–PUB–11322 (2005), presented at the LCWS 2005, Stanford, CA, USA (2005).

[9] D. Walz, presented at the Snowmass ILC Workshop 2005, Snowmass, CO, USA (2005), http://alcpg2005.colorado.edu:8080/alcpg2005/program/accelerator/WG4/aug17_beam_dump_d_walz.pdf .

[10] T. Raubenheimer, http://www-project.slac.stanford.edu/ilc/acceldev/beamparameters.html (February 28, 2005).

[11] A. Seryi, presented at the Snowmass ILC Workshop 2005, Snowmass, CO, USA (2005), http://alcpg2005.colorado.edu:8080/alcpg2005/program/accelerator/GG1/aug17_seryi_high_lumi_pars.ppt .

[12] http://www.slac.stanford.edu/accel/ilc/codes/dimad/ .

[13] D. Schulte, "Beam-Beam Simulations with GUINEA–PIG," ICAP98, Monterey, CA, USA (1998).

[14] T.W. Markiewicz and T. Maruyama, SLAC-PUB-10465, presented at the 5th International Workshop on Electron-Electron Interactions at TeV Energies, Santa Cruz, CA, USA (2004).

[15] B. Parker and A. Seryi, SLAC–PUB–11038 (2005).

IR OPTIMIZATION, DID AND ANTI-DID*

Andrei Seryi, Takashi Maruyama, SLAC, Stanford, CA, USA
Brett Parker, BNL, Upton, NY 11973, USA.

Abstract

In this paper, we discuss optimization of the larger crossing angle Interaction Region of the Linear Collider, where specially shaped transverse field of the Detector Integrated Dipole can be reversed and adjusted to optimize trajectories of the low energy pairs, so that their majority would be directed into the extraction exit hole. This decreases the backscattering and makes background in 14mrad IR to be similar to background in 2mrad IR.

INTRODUCTION

In the machines with crossing angle, the detector solenoid field results in a deviation of the vertical trajectory and in a small vertical angle at the IP (about 100 μrad for crossing angle of 20mrad). This angle is anti-symmetrical for e+e- machines and does not affect the luminosity. The vertical angle at the IP also causes rotation of the spin by about a degree resulting in a misalignment of the spin orientation at the IP with respect to the upstream polarimeter. The Detector Integrated Dipole (DID) is a pair of coils wound on the detector solenoid which creates sine-like transverse field, giving the possibility to adjust the beam trajectories near the interaction region [1]. The DID was originally suggested as a way to compensate the vertical angle at the IP, as illustrated in Fig.1, and avoid spin misalignment.

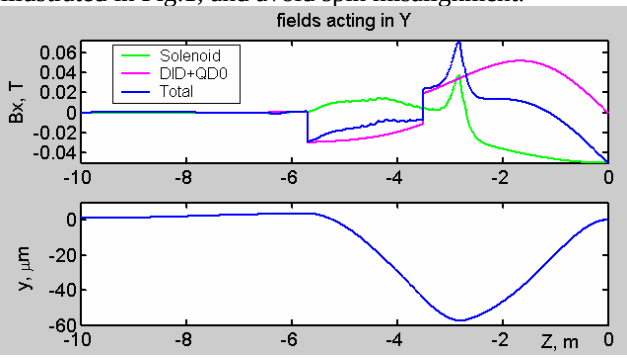

Figure 1: Compensation of the incoming beam vertical angle at the IP with DID and dipole corrector of the QD0 quadrupole. Field acting in Y (top) and vertical trajectory (bottom). SiD detector, crossing angle 20mrad, IP at z=0.

The DID field creates U-like distortion of the central field line of the detector solenoid, and compensation of the vertical angle of the incoming beam is in fact equivalent to aligning the field line, effectively, with the incoming beam. This increases the transverse field seen by the outgoing beam, in particular the beamstrahlung pairs. The high energy pairs continue along the initial direction of the beam, while the low energy pairs spiral around the field line and disperse, as shown in Figs.2-3.

*Work supported by US DOE, contract number DE-AC02-76SF00515

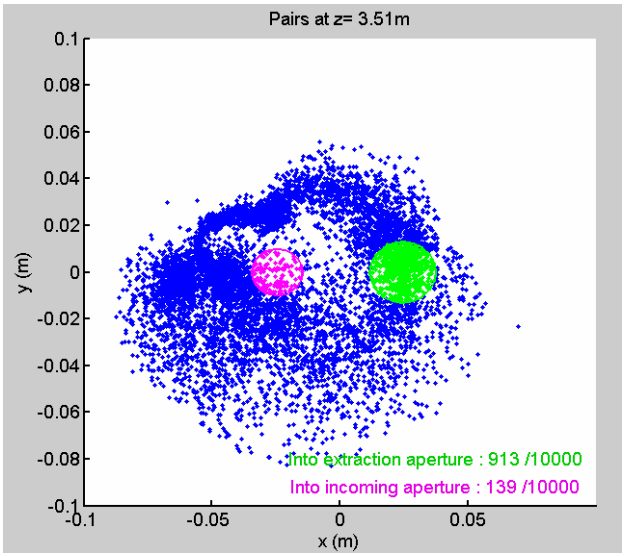

Figure 2: Distribution of pairs at 3.5m from IP in SiD detector when DID is used to compensate the vertical IP angle of the incoming beam. The incoming and outgoing apertures are shown by magenta and green colors.

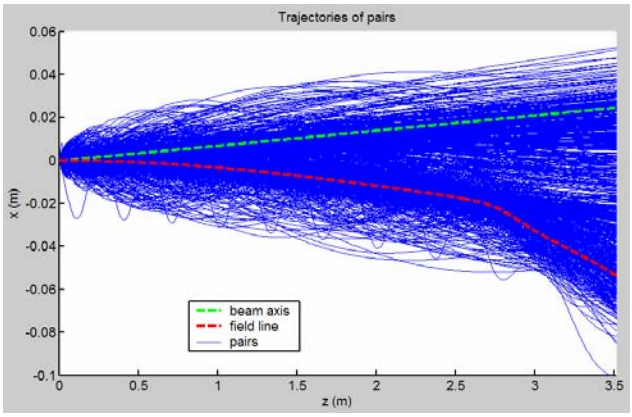

Figure 3: Trajectories of pairs coming from the IP in SiD detector when DID is used to compensate the vertical IP angle of the incoming beam. The high energy pairs follow the beam axis (green dashed line) while the low energy pairs spiral around the field line (red dashed line).

Large spread of the pairs on the face of BEAMCAL resulted in backscattering and increase of background photon hits in TPC (Time Projection Chamber). The number of photon hits in TPC increased several times and the effect was especially dramatic when the outgoing aperture was not optimized [2].

The technology of compact direct wind SC magnets allows reducing the crossing angle to 14mrad [3]. With reduced crossing angle, the synchrotron radiation (SR) effects significantly decreased ($\Delta\sigma_{sr}\sim\theta_c^{5/2}$), simplifying use of reversed DID (anti-DID) described below.

ANTI-DID

While the normal polarity of DID allows to compensate locally the effect of crossing the solenoid field for the incoming beam, the anti-DID (reversed polarity) allows to effectively zero the crossing angle for the outgoing beam (and pairs) – the U shaped distortion of the field lines is adjusted to guide the low energy pairs to the extraction aperture as shown in Fig.4.

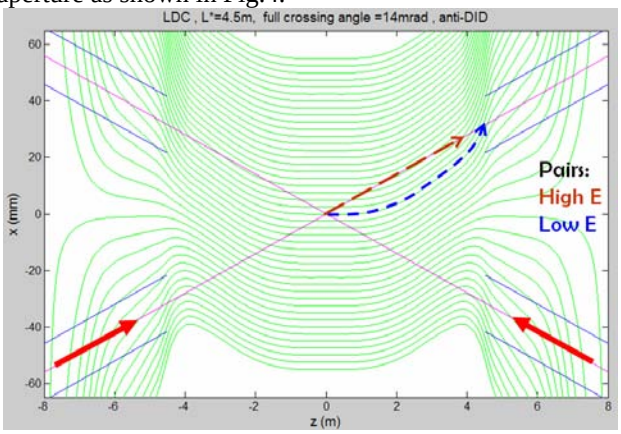

Figure 4: Field lines in LDC detector with anti-DID. The anti-DID field shape has flattened central region, to ease TPC calibration. The total crossing angle is 14mrad.

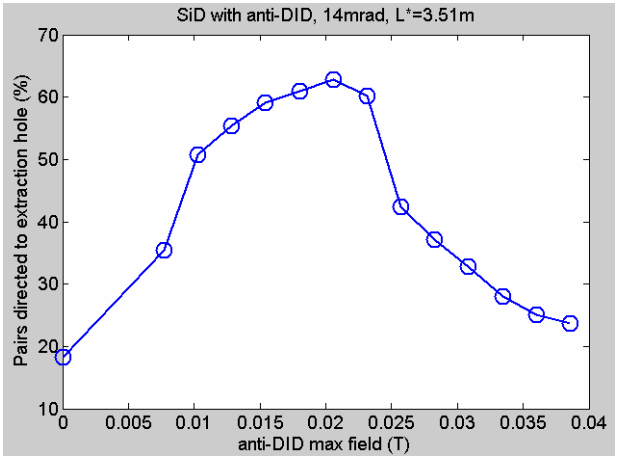

Figure 5: Fraction of pairs directed into extraction aperture in SiD versus anti-DID maximum field.

Figs.5-7 give quantitative results of tracking of beamstrahlung pairs in realistic solenoid field of SiD detector taking into account the anti-DID field. The shape of anti-DID field was obtained earlier, in simulations with 2D and 3D magnetic models [1]. The pairs were obtained from beam-beam simulations by Guinea-Pig program [3].

Fig.5 shows the fraction of pairs entering the extraction aperture versus maximum field of anti-DID. Fig.6 and Fig.7 corresponds to the optimal strength of anti-DID and show distribution of pairs 3.5m from the IP and trajectories of the pairs along the SiD detector. One can see that more than 60% of the pairs can be directed into the extraction aperture.

Similar optimization, as for SiD, can be done for other two detectors, GLD and LDC. In this optimization, we used real solenoid field maps, and the shape of anti-DID field used for GLD and LDC was specifically optimized for these larger detectors with TPC (see below). We used ILC final focus optics with different L* (distance between IP and first quadrupole of FD): L*=3.51m for SiD and L*=4.51m for GLD and LDC. The Final Doublet was properly overlapped with the solenoid field.

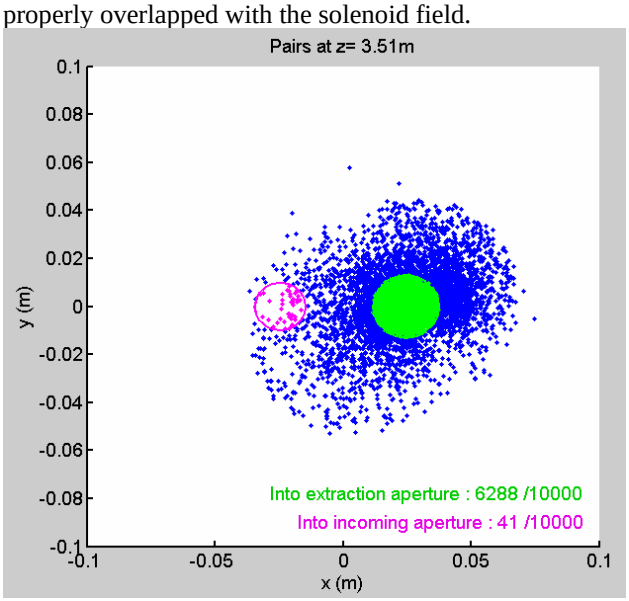

Figure 6: Distribution of pairs at 3.5m from IP in SiD detector when anti-DID is adjusted to direct pairs to the extraction hole. The incoming and outgoing apertures are shown by magenta and green colors.

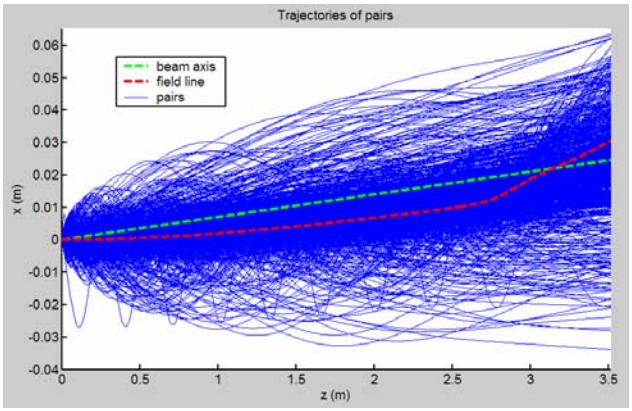

Figure 7: Trajectories of pairs in SiD with anti-DID.

	B_t,Gs	θ_{IP} , μr	$\Delta\sigma_{sr}$, nm	L , %	P_{ex}, %
SiD	205	-102	0.32	99.8	63
GLD	236	-96	0.65	>99	51
LDC	235	-122	1.01	98	49
LDC	354	-138	1.67	95	62

Table 1: Maximum field of anti-DID B_t, angle of the incoming beam at the IP θ_{IP}, SR beam size growth $\Delta\sigma_{sr}$ (to be added to σ_{y0}=5nm in quadratures), luminosity L taking into account SR effects, fraction of pairs P_{ex} directed to extraction aperture. Total crossing angle is 14mrad.

The results of these optimizations are summarized in the Table 1 in terms of the optimal field of anti-DID,

number of pairs at extraction aperture, SR beam size growth and its effect on the luminosity. The vertical angle of the incoming beam at the IP (which is now left uncorrected) is also shown in this table.

One can see that in all cases one can direct more than half of the pairs into the extraction aperture. In LDC detector, with its 4Tesla field, the optimal anti-DID would increase SR effects noticeably and could result in loss of 5% of luminosity. Decreasing the anti-DID strength by one third from the optimum could reduce the effect on the luminosity to 2% while still directing about 50% of pairs into the extraction aperture.

As clear from the above figures, the anti-DID increases the transverse field seen by the incoming beam and increases SR effects. Comparing the angle of incoming beam at the IP without and with anti-DID, one can find that the anti-DID increases the effective crossing angle for the incoming beam by 40-50%. If the total crossing angle is 14mrad, the effective crossing angle for the incoming beam is still about twenty mrad.

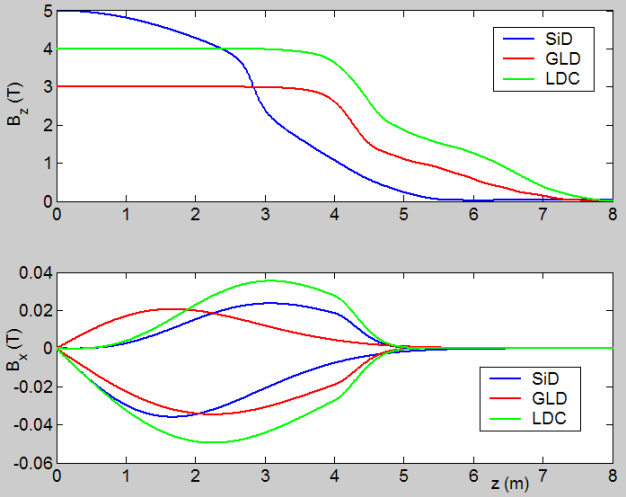

Figure 8: Top plot: detector fields. Bottom plot: field of anti-DID (positive curves) in comparison with DID (negative curves) for 14mrad crossing angles. The DID field corresponds to earlier results, where flattening of the field in the central region was not yet implemented.

Finally, one need to note that the strength of anti-DID in comparison with DID is smaller by 30-40%, as illustrated in Fig.8 where the anti-DID fields are shown.

Vertical angle at the IP with anti-DID

With anti-DID, it is naturally to leave the vertical angle at the IP uncorrected and to zero only the IP position, using dipole corrector in FD. The trajectory in this case would look like the one shown in Fig.9. (The angle at the exit from the detector will be zeroed by correctors at the entrance of the extraction line).

The vertical angle at the IP still can be compensated, if needed for polarization, less locally, using dipole fields in the Final Doublet correctors. One can consider zeroing only the vertical angle but allowing offset of the IP position; zeroing both the vertical angle and IP position.

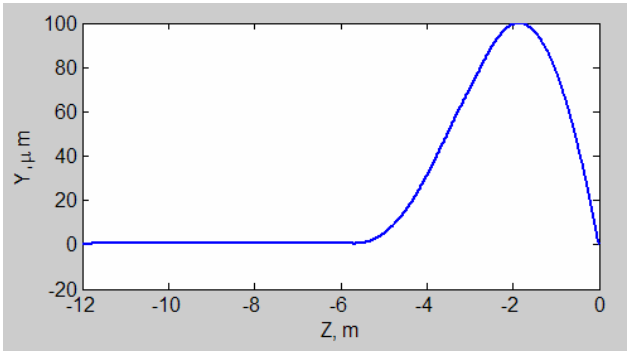

Figure 9: Vertical trajectory of the incoming beam in SiD with anti-DID and crossing angle 14mrad. IP is at z=0.

Although further optimization may be possible, analysis of SR effects shows that in anti-DID case, for present parameters and for considered detector models it is not practical to zero both IP angle and position. Due to non-local character of correction the deviation of the orbit and SR effects become large and luminosity loss even for SiD would be about 40%, and larger for other detectors.

Another option, to zero only the angle, may however be feasible (illustrated in Fig.10). The vertical orbit deviation is increased but SR effects are tolerable. In the SiD detector with anti-DID and 14mrad crossing angle the SR results in $\Delta\sigma_{sr}$ =1.2nm and the loss of luminosity due to SR is about 2.8% (the loss in GLD or LDC can be estimated as 2-6% knowing the uncorrected angle at the IP from Table.1). It is also clear from Fig.10 that for the two beams to collide, the incoming vertical orbits of the two beams should be shifted.

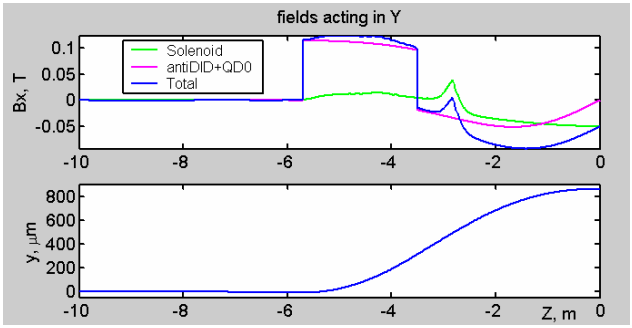

Figure 10: Fields acting in Y and vertical trajectory in SiD with anti-DID when dipole correctors in FD were adjusted to zero the IP angle. Shown for crossing angle of 20mrad and for anti-DID stronger than the optimum.

So, it is in principle possible to use anti-DID and simultaneously zero the IP angle to align the spin in parallel to the upstream polarimeter. However, the necessity to zero (or even to reduce) the vertical IP angle is being reevaluated [4] and may not be necessary.

Indeed, the procedure of setting the IP beam polarization would involve maximization of polarization at the upstream polarimeter (which can be done with accuracy θ_P =25mrad rms for spin angle misalignment [5]) and taking into account that the IP polarization will be smaller by a known amount due to vertical angle at the IP. The spin precession due to finite vertical angle at the IP is

$\theta_S = \gamma\ \theta_{IP}$ (g/2-1) = θ_{IP} E (GeV) / 0.44065. The maximum practical angle from Table.1 is θ_{IP} =122μrad which for the spin angle gives θ_S =69mrad (and does not depend on energy, since for fixed detector field θ_{IP} ~1/E). The polarization behaves as cosine of the angles $\cos(\theta_P+\theta_S)$ and thus it does not allow full factorization of the effects of the angles at the IP and at the upstream polarimeter. In the assumption that $\theta_P<\theta_S$ and that the beam orbit angle at the IP can be measured with precision better than about 10μrad, the precision of polarization knowledge at the IP with respect to measurement at the upstream polarimeter is dominated by the spin misalignment at the polarimeter and could be expressed as $\mathrm{rms}(\theta_P)*\theta_S$. This gives about 0.17% rms for the polarization precision which is better than the target goal of 0.25%.

Moreover, when the vertical IP angle is not corrected, one can still tilt the beam orbit in the downstream polarimeter (where the SR beam emittance increase does not matter, in contrary to the upstream polarimeter) to match the IP angle.

These considerations suggest that while it is possible to zero or decrease the vertical angle at the IP, this may not be necessary, since polarization precision goals can be met.

Anti-DID and TPC Operation

Let us discuss compatibility of DID (or anti-DID) transverse field with Time Projection Chamber operation. Traditionally, TPC specify requirements for field uniformity with certain high precision. However, precise 3D field maps are used in tracking reconstructions anyway. Therefore, providing 3D map of solenoid field with DID (for several settings) would solve this particular TPC-DID concern. However, there is another issue related to TPC track-based calibration. It was suggested by Dan Peterson [6] that uniform magnetic field is required in some region about half-a-meter around the IP in order to perform a track-based calibration the magnetic field. Such uniform field region would allow isolating the effects of the field distortions on track trajectories from the effects of field distortions on the drift path. It was suggested [6] that the uniformity requirement is $dB/B < 4*10^{-4}$ for $|z| <$ 50 cm, while the uniformity is less important at larger z – the current DID design field of 0.07T at $|z|$= 2.2m (in LDC at 20mrad) would be acceptable. Details of TPC operations and specifics of the field-map requirements due to the anti-DID will be discussed in details in upcoming notes [7].

To address the above challenge, we suggested to modify the design of DID coils and construct the field using two coils, a shorter and a longer one. The 3D models of the coils were created, with the same radius of 3.5m and with pattern length of 1.5m and 3m, as illustrated in Fig.11. The resulting field was used in the optimization.

In the field calculation the effect of detector iron was neglected (we checked earlier that this is a reasonable approximation) but eventually the iron should be included in detailed simulations. The “short” and “long” DID coils were combined and the currents were adjusted to flatten the field in the center. It was found that in order to flatten the field, the current ratio for the short/long coils should be equal to -1.245, and both currents need to be increased 2.5 times to have the same max field for the combined DID as for single coil.

With combined DID coil, reduction of the field in the central region ($|z| < 0.5$m) was found to be about 65 times with respect to the single long DID, as illustrated in Fig.12. Such modification of the DID field shape should ease TPC calibration. The DID field shape used in this paper for GLD and LDC was similar to the one shown in Fig.12, but had sharper decay after $|z|>5$m due to effect of the iron of the detector yoke (shown in Fig.8).

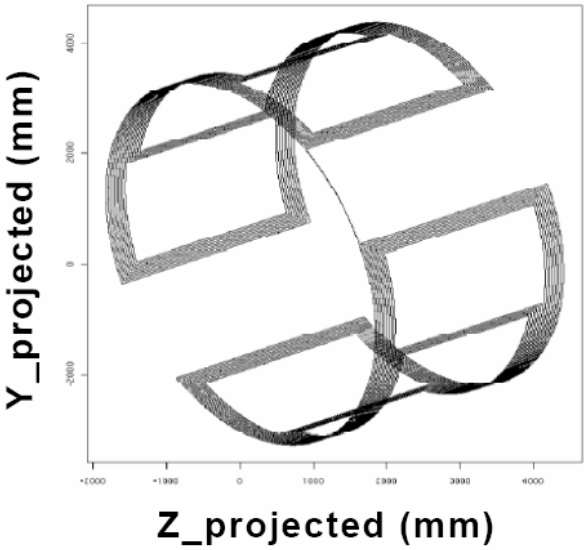

Figure 11: 3D model of a longer DID coil. Coil radius is R=3.5m, length 3m, effective magnetic length 3.97m. The shorter DID coil had the same radius and length of 1.5m.

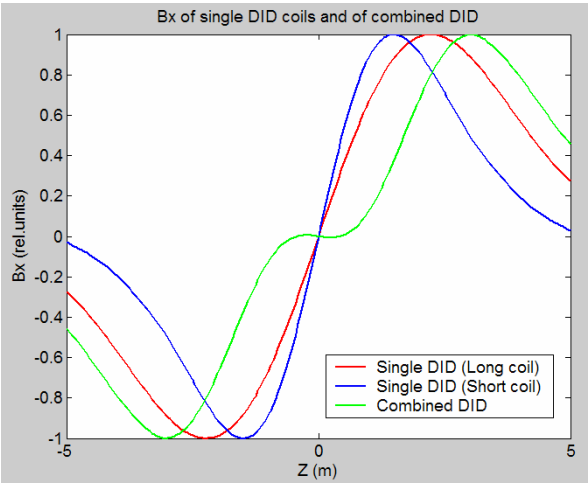

Figure 12: Field of the shorter (1.5m pattern length) and longer (3m) DID coils and the field of the combined DID coil optimized for detectors with TPC.

Background in SiD with Anti-DID

GEANT model of SiD with 14mrad IR was created [8], as illustrated in Fig.13.

Background calculations include counting hits in the vertex detector (VXD) and in the tracker. The ILC 500GeV CM nominal beam parameters were used in background calculations. The 14mrad IR calculations were also compared with 20mrad and 2mrad IR for SiD.

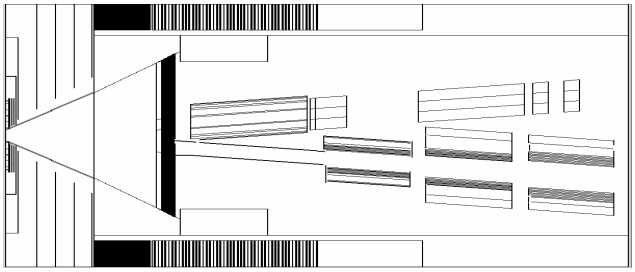

Figure 13: GEANT model of SiD with 14mrad crossing angle, with Final Doublet and extraction quadrupoles.

14mrad	14mrad+DID	14mrad+anti-DID	2mrad
1800	1900	830	720

Table 2: Number of photons going into SiD tracker per bunch crossing.

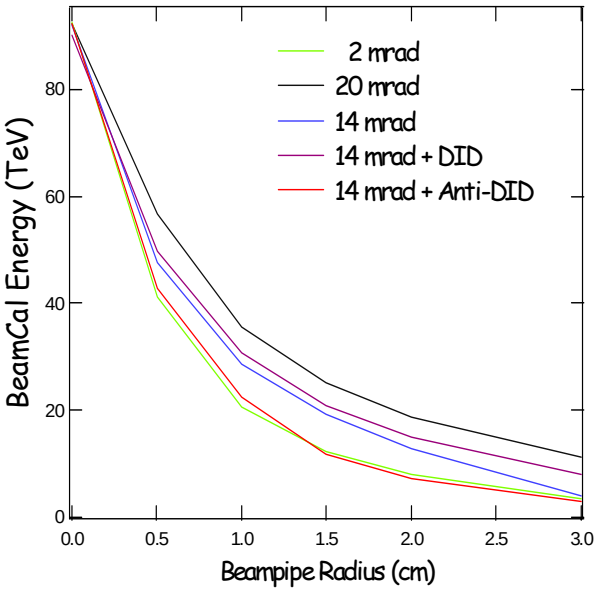

Figure 14: Total energy of beamstrahlung pairs hitting BEAMCAL versus radius, SiD with different crossing angle and with DID or anti-DID.

It was found that DID or anti-DID field settings have almost no effect on VXD hits. However, the total energy of pairs hitting into BEAMCAL was found to be smaller in 14 mrad crossing in comparison with 20mrad IR. It was found that the anti-DID can further reduce the energy to the 2 mrad crossing angle level, as illustrated in Fig.14. The number of secondary photons generated in BEAMCAL and going to the tracker is also smaller in 14mrad with anti-DID, and is about the same as in 2mrad, as shown in Table.2. Therefore, with anti-DID the background in 14mrad IR can be similar as in 2mrad IR. Similar optimizations and background calculations should be done for GLD and LDC detectors.

Application to 20mrad, to e-e- and $\gamma\gamma$

Scaling the results of the Table.1 to 20mrad crossing angle, one can easily see that the anti-DID can work fine for SiD and also for GLD with reduced anti-DID field, while it may be problematic for LCD with its large 4Tesla detector solenoid. However, the concept presented in this paper certainly can be further optimized. In particular, optimization of the anti-DID field shape and also of the way to make the dipole corrections in FD can be considered and may result in improved applicability of anti-DID for 20mrad for all considered detectors.

Finally, in the cases of e-e- or $\gamma\gamma$ collisions the vertical trajectories are symmetrical and the vertical angle must be compensated, either with DID (as in Fig.1) or with FD only (as in Fig.10). In the latter case the anti-DID could be applied to improve background.

SUMMARY

Application of anti-DID was considered for SiD, GLD and LDC for intermediate crossing angle 14 mrad. With optimized anti-DID strength, the number of pairs directed to extraction aperture is more than 50%. The maximum field of the optimal anti-DID is about 0.6 of DID. With anti-DID, the IP angle still can be zeroed or decreased, with less local correction, however, compensation of the vertical angle appears not necessary as the polarization precision goals can be met. The modified DID with flattened field in the central region was suggested for GLD and LDC, to ease TPC calibration. Background simulations with anti-DID show that photon flux toward tracker region is decreased and is same as in 2mrad IR.

ACKNOWLEDGEMENT

Authors would like to thank Dan Peterson, Ken Moffeit, Klaus Moenig, Mike Woods, Philip Bambade, Ron Settles and Witold Kozanecki for useful discussions.

REFERENCES

[1] B. Parker, A. Seryi, Phys. Rev. ST Accel. Beams 8, 041001 (2005).
[2] K. Buesser, Pair Backgrounds, Snowmass 2005.
[3] D. Schulte, Guinea-Pig program.
[4] P. Bambade, K. Moenig, K. Moffeit, M. Woods, H. Yamamoto et al., private communication, November 2005.
[5] K. Moffeit, M. Woods, private communication, November 2005.
[6] D. Peterson in his private communication to W. Kozanecki, August 2005.
[7] D. Peterson, R. Settles, W. Wiedenmann, LC Notes in preparation.
[8] Y. Nosochkov, T. Maruyama, et al., in these proceedings, Nanobeam 2005.

STATUS OF THE CRAB CAVITY SYSTEM DEVELOPMENT FOR THE ILC

P. Goudket, L. Ma, A. Kalinin, C. Beard

ASTeC, Daresbury Laboratory, Warrington, Cheshire, WA4 4AD, UK

G. Burt, A. Dexter

Microwave Research Group, Lancaster University, Lancashire, LA1 4YW, UK

Abstract

The crab cavity project covers all aspects of the development of the crab cavity system for the ILC. Main issues are the phase control tolerances, which are very tight in order to achieve acceptable luminosity losses, integration into the beam delivery system, and extraction of undesirable modes from the cavity. Differential phase jitter is found to be the tightest phase control requirement (0.066° at 3.9GHz), and will require the development of a high precision control system. The integration of the cavity into the BDS should not pose any particular problems in the case of a 20mrad crossing angle solution, space constraints may present challenges for much smaller crossing angles. The cavity should be placed as close as possible to the final focusing doublet. The crab cavity should be superconducting in order to minimise phase noise. Extraction of the lower order mode is an issue that must be addressed.

INTRODUCTION

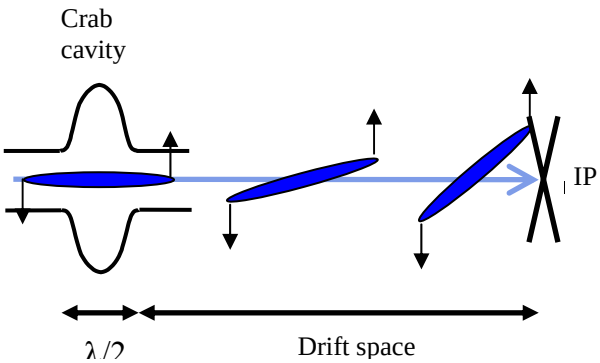

Figure 1: Bunch rotation due to a crab cavity

A possible design of the ILC is to have a crossing angle between the electron and positron lines [1]. A consequence of having a crossing angle is the reduction in luminosity due to the geometry of the collision. Such a loss in luminosity can be recovered by rotating both bunches prior to collision. One method of achieving this rotation is to use a crab cavity. A crab cavity is a RF cavity that uses the first dipole mode for its operation instead of the accelerating monopole mode. The dipole mode has zero longitudinal electric field and a large transverse magnetic field along its beam axis. The action of this magnetic field provides a Lorentz force perpendicular to both the magnetic field and the velocity of the bunch.

If the phase of the RF is timed so that the centre of the bunch passes through the cavity when the magnetic field is zero then the head and tail of the bunch will experience equal and opposite Lorentz forces, causing the bunch to appear as if it has rotated, as shown in Figure 1.

PHASE TOLERANCES

The very high luminosity of the ILC can only be preserved if the bunches collide in optimal conditions. The crab cavities provide transverse kick to the bunches, that could, if uncontrolled, cause the bunches to miss or collide partially. We can consider two main mechanisms for errors in the crab kick. The first potential cause of error being in amplitude of the kick received, leading to over- or under-rotation of the bunches. The second source of error would be in the phasing of the cavities, where we will distinguish between cavity-to-beam errors and cavity-to-cavity errors.

Amplitude tolerance

If a bunch receives a kick greater than the nominal kick, the transverse displacement of the particles at the IP will also be too large and the bunch will be over-rotated. Likewise, the bunch would be under-rotated if it received a kick less than the nominal kick. This could occur because of errors in the voltage of the cavity.

Calculations of the voltage stability required to achieve luminosity losses not exceeding 2%, using nominal 1TeV ILC beam parameters, indicate that the stability required is within 3.7% of the nominal voltage [2].

Cavity-to-beam phase tolerance

If a bunch arrives early or late compared to the nominal bunch arriving at a phase such that it receives no kick in its centre of mass, the bunch would receive a net transverse momentum. If the voltages are correct and the phase error small, the bunch would still have achieved the desired rotation at the IP but would have drifted transversely away from the $x=0$ position.

Should the error be caused by a phase difference between the beam and the cavities, where both cavities resonated at the same phase, both sets of bunches would receive the same amount of transverse kick in the same

direction. The result of this is that the collision between the bunches would still occur with little loss of luminosity, albeit at a location offset from the nominal collision point. To avoid losing 2% of luminosity, the cavity-to-beam phase offset only needs to be less than 15° [2], which is easily achievable.

Cavity-to-cavity phase jitter tolerance

Should there be a phase error between the cavities, however, the bunches would receive different amounts of transverse kick and the bunches could easily begin to collide partially or miss each other entirely.

A crab cavity rotates a bunch by producing a transverse deflection that varies with time. The amount each particle is deflected at the IP is

$$x_{offset} = \frac{c\theta_r}{\omega}\sin(\Delta\varphi) \qquad (1)$$

where Δφ is the phase at the centre of the cavity. The two sets of crab cavities should be in phase with each other and the centre of each bunch should reach the centre of the cavity at zero phase.

If one of the cavities is out of phase, the bunch will be deflected as can be seen in equation (1). This causes a loss in luminosity as the electron and positron bunches do not completely overlap.

For a 2% luminosity loss, the phase jitter tolerance is 0.066° at a cavity frequency of 3.9GHz and a 20mrad crossing angle.

BEAM DYNAMICS CONSIDERATIONS

The optics of the beam delivery system has been investigated with regards to the optimal location of the crab cavities. The final focusing quadrupole doublet can have a great effect on the transverse displacement of particles at the IP due to their focusing effect. As crab cavities provide a momentum kick to the particles, that is only converted to transverse displacement after a length of drift space, the location of the cavities has a significant effect on the rotation achieved with a given voltage in the cavities.

It was found that the optimal realistic location for the crab cavities in the 20mrad crossing would be as close as possible to the final focusing quadrupoles, as this configuration most reduces the focusing effect of the quadrupole QF1. The voltage required for a 10mrad crab rotation of the bunch at 1TeV was calculated at this position to be 6.1MV at 3.9GHz. The voltage required is inversely proportional to cavity frequency.

The relationship between the transverse kick and the position at the IP was calculated in [3] to be proportional to the ratio of the square root of the β_x at the crab cavity location and at the IP. Figure 2 shows the beta-functions for the ILC BDS, confirming the optimal location of the crab cavity close to the final doublet.

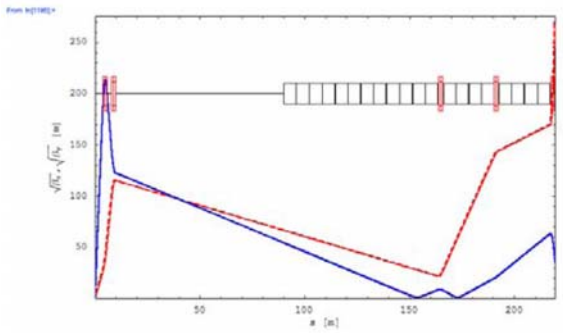

Figure 2: β_x (red), β_y (blue) for the 20mrad ILC BDS

The position for the 2mrad case has yet to be fully studied, however it is likely to be much further upstream.

RF DESIGN ISSUES

As has been previously mentioned, the crab cavity system has a very tight phase jitter tolerance, as a result of this the cavity design chosen must be very phase stable. It is well known that it is easier to stabilise the phase of a continuous RF system rather than a pulsed one. However, as the energy of the beam is very high, a large transverse voltage is required to rotate the bunch requiring a lot of energy to be stored in the cavities. If a normal conducting cavity is used, the energy would have to be spread over several cavities to avoid overheating, hence a superconducting cavity would be preferred.

One problem associated with cavities operating in the dipole mode is the presence of a trapped lower order mode (LOM). Most accelerating cavities operate in the fundamental mode of the cavity, however in a dipole cavity the fundamental accelerating mode is unwanted and, because the resonant frequency of this mode is far below the cut-off frequency of the beam-pipe, the fundamental mode does not couple strongly to traditional higher order mode (HOM) couplers. In order to remove this mode from the cavity special LOM couplers must be designed that penetrate further into the cavity than HOM couplers. Another problem is that the dipole mode has two polarisations that are resonant at the same frequency in axially symmetric cavities. To avoid exciting the unwanted polarisation the resonant frequencies of the two polarisations must be separated by making the cavity asymmetric.

A superconducting dipole cavity is currently under development at Fermilab as a bunch separator, which could be used for the ILC crab cavity with some modifications [4, 5]. The cavity, known as the CKM cavity, is a 13-cell cavity that operates at 3.9GHz and has a beampipe diameter of 3.0cm. The separation of modes in the dipole passband is quite tight using a 13 cell cavity, hence for the ILC it may be preferred to use fewer cells per cavity. At an operating gradient of 6MV/m, four 9-cell versions of this cavity could be used on each side of the interaction region to rotate the bunch on the ILC (with 1TeV CM). This would require an active cavity length of

2m, and a total length of 4-5m for the crab system (including couplers, gate valves, pumping ports and all other elements of a cavity system), however this can be split into several shorter sections if required.

Recent results by A. Drozhdin [6] suggest that a beam clearance of at least 15mm should be observed to avoid photons hitting the cavity. The LOM couplers currently designed for the CKM cavity penetrate to 13mm from the beam-pipe centre. In order to have the LOM coupler to be 15mm from the centre of the beam-pipe, the aperture of the end-cells must have a larger radius than the current design. The effect of having a larger aperture is that the cavity R/Q may drop, however design work is underway to reduce this effect.

CONCLUSION

The phase and amplitude stability of the ILC crab cavities have been studied. The phase jitter tolerances of the crab cavity are tight, however a significant effort is dedicated to solving the stability issue. It should be noted that phase stability better than that required of the ILC crab cavity has previously been demonstrated on accelerating cavities [7]. The crab cavity is likely to be placed near the final focus for the 20mrad crossing angle and is likely to be between 4-5m long.

The Fermilab 3.9GHz CKM cavity design is being evaluated for use as the ILC crab cavity. The current design has 13 cells per cavity, however for the ILC fewer cells per cavity would probably be a better choice. Current problems are the end-cell aperture size and the LOM coupler, which are being studied at the Cockcroft Institute and Fermilab.

ACKNOWLEDGEMENTS

We would like to thank Deepa Angal-Kalinin for her contribution and for presenting the work at the Nanobeam Workshop. We would also like to thank A. Seryi, A. Drozhdin, C. Adolphsen and L. Bellantoni for their helpful input.

REFERENCES

[1] WG4 Summary, First ILC Workshop, KEK, 2004, http://lcdev.kek.jp/ILCWS/Talks/15ple-4-WG4_summary.pdf

[2] G. Burt, Crab Cavity Errors, Crab Cavity Videoconference, April 2005, http://www.astec.ac.uk/rf/PDFs/crab/talk_02.pdf

[3] P. Goudket, G. Burt, Snowmass Workshop 2005, http://alcpg2005.colorado.edu:8080/alcpg2005/program/accelerator/WG4/aug18_burt_Crabsnow.ppt

[4] M. McAshan, R. Wanzenberg, RF Design of a Transverse Mode Cavity for Kaon Separation, Fermilab-TM-2144 May 2001

[5] L. Bellantoni, Snowmass Workshop 2005, http://alcpg2005.colorado.edu:8080/alcpg2005/program/accelerator/WG4/aug18_CRAB_intro_bellantoni.pdf

[6] A. Drozhdin, http://www-project.slac.stanford.edu/lc/bdir/Meetings/beamdelivery/2005-09-27/summary.htm

[7] M. Liepe, Pushing Q_L, Proc. ERL 2005 Workshop, March 2005

UPDATE ON 2 MRAD CROSSING ANGLE EXTRACTION LINE FOR THE ILC

D. Angal-Kalinin, F. Jackson, ASTeC, Daresbury Laboratory, UK

R. Appleby, The University of Manchester and the Cockcroft Institute, UK

P. Bambade, O. Dadoun, B. Mouton, LAL, Orsay, France

G. Blair, J. Carter, RHUL, University of London, UK

A. Drozhdin, FNAL, USA

O. Napoly, J. Payet, CEA, Saclay, France

B. Parker, BNL, USA

A. Seryi, Y. Nosochkov, C. Spencer, SLAC, Stanford, U.S.A.

Abstract

The complete optics design 2 mrad crossing angle IR and extraction line design was presented at the Snowmass. Following the discussions at the Snowmass and also to optimise the design further, some new updates have been made. This paper describes the current design status and ongoing and planned work by the "2 mrad task force".

OPTICS DESIGN OF 2 MRAD

The complete optics design of the 2 mrad extraction line including beam diagnostics chicanes was presented at Snowmass [1]. The design of the final doublet is of particular importance in this scheme, as it is shared by both the incoming and the extracted beams. The final quadrupole "QD0" is a large bore superconducting magnet with a radius of 35mm. In the present design, a gradient of 180 T/m in the presence of detector solenoid field has been considered assuming NbTi technology. The outgoing beam passes off-axis in this magnet and hence receives a large dipole kick. The QF1 magnet is a normal conducting magnet with bore radius of 10 mm in the snowmass design. The outgoing beam passes through the pocket region of this magnet and experiences off-axis field. The magnet design of QF1 gives the details of this pocket field. The effect of these pocket multipoles is then incorporated in the tracking studies to see their effect on the outgoing beam. The sextupoles placed close to the final doublet for correcting the chromaticity are also large bore superconducting magnets to accommodate the outgoing beam.

The length of the extraction line is about 700m between the interaction point and the beam dump. The optics consists of a vertical chicane for collimation, a vertical chicane for energy spectrometer and a vertical polarimetry chicane. The beam is allowed to grow through long drifts before reaching the dump window. There are no extraction line sextupoles in this optics as this reduces the second order geometric aberrations and gives a smaller geometric beam size at the secondary focus of the polarimeter.

The charged particle beam losses have been computed using STRUCT, TURTLE and DIMAD for this line. The worse case beam loss scenario for the TeV machine occurs when the beams are vertically offset by 100nm at the IP. The losses are distributed along the line and sum to around 250 kW for the TeV machine nominal parameters.

COLLIMATION DEPTHS

The collimation depths are computed by considering the synchrotron radiation fan produced in the final doublet. The location of the limiting aperture, size of the aperture and centering of this mask; around the detector or around the QD0 axis decide the collimation depths for the 2 mrad configuration. For the Snowmass, the Beamcal aperture was assumed to be 15mm and it was centred around QD0. The resulting collimation depths were $8.6\sigma_x$ x $54.5\sigma_y$ as shown in figure 1a. The aperture assumed by the detector people was 12 mm and the mask was centred around the detector axis. The re-evaluation for this configuration increased the collimation depths to $10.5\sigma_x$ x $66.8\sigma_y$ as shown in figure 1b. The synchrotron radiation fan distance of closest approach to beamcal increases, which relaxes the collimation depth despite the narrow aperture.

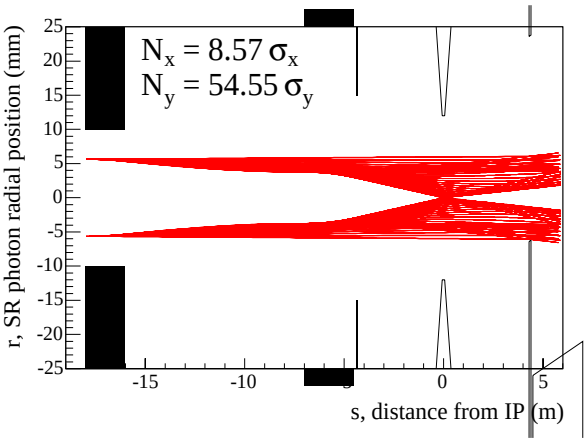

Figure 1a : Collimation depths presented at Snowmass

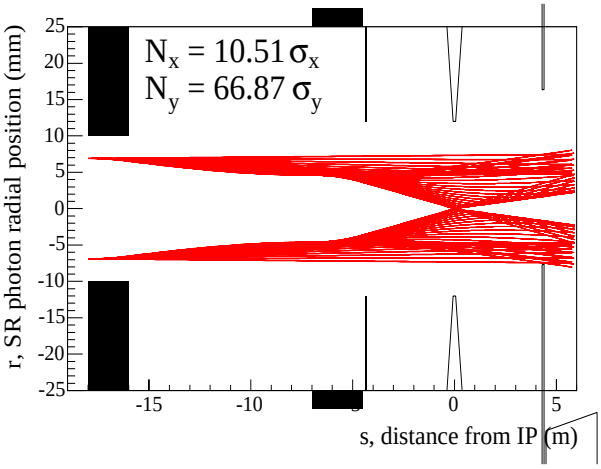

Figure 1 b : Revised collimation depths after Snowmass

Enlarged aperture QF1

The large beam halo size and the associated synchrotron radiation photons generate photo-electrons in the pockets of QF1 [2]. Though this effect need more detailed studies to investigate whether they cause any problem at the IP, the most obvious solution would be to increase the aperture of this quadrupole. Increasing the QF1 aperture also increases acceptance for the incoming beam halo, since the horizontal beam size is quite large (1 σ_x of the order of 1mm) at the QF1 entrance. It was suggested during Snowmass to increase the radius of this quadrupole from 10mm to 15mm. The new magnet design with 15mm radius was provided [3]. The multipole components for this new design were incorporated into the optics of the extraction line. The comparison of beam envelope for 10mm and 15 mm QF1 radius is shown in Figure 2. The beam size slightly reduces for 15mm radius QF1 multipoles, due to the different multipole content of the field in the pocket region. The effect on losses in the downstream extraction line is being investigated for this design.

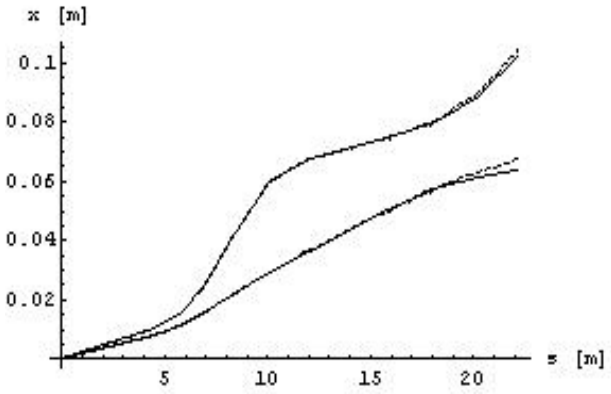

Figure 2 : The horizontal beam size in the final doublet, for a 10mm QF1 (dashed line) and a 15mm QF1 (solid line)

POWER LOSS COMPUTATIONS

To minimise the losses on the collimators and magnets, the optics design will be further optimised. As a first step to do this, the computation of both integrated beam loss (in Watts) and distributed loss (in Watts/meter) is currently being estimated using STRUCT, TURTLE and BDSIM. This will be done for all the parameter sets, including the new high luminosity parameter sets [4] and for a range of IP conditions.

SUMMARY AND PLANS

This paper gives an update on the 2 mrad extraction line design since Snowmass. The ongoing work is focussed on the power losses along the extraction line and final doublet design. The team is using BDSIM to look at the backgrounds from charged particles losses along the extraction line, which will create a series of kW level sources and study secondary particle production resulting in the undesirable detector backgrounds. Using Nb_3Sn technology, it will be possible to increase the strength of the QD0 to 250 T/m in the presence of the detector field. This will reduce the length of QD0 reducing the losses in the extraction line. An analytical study of the final doublet parameter space would allow better insight into the choice and optimisation of the key parameters.

REFERENCES

[1] Y. Nosochkov for 2 mrad task force, " Extraction line optics for 2 mrad crossing angle", presented at Snowmass, August 2005.
[2] J. Carter, "Halo collimation depth using BDSIM", presented at Snowmass, August 2005.
[3] C. Spencer, private communication.
[4] A. Seryi, "Alternative 1 TeV high luminosity parameters", presented at Snowmass, August 2005

THOUGHTS ON FAST BEAM ABORTS FOR THE INTERNATIONAL LINEAR COLLIDER

T.Mattison
Dept. of Physics & Astronomy, University of British Columbia, Vancouver BC V6T 1Z1 CANADA

Abstract

The ILC beam is potentially very destructive, and a fast beam abort system is useful as part of the machine-protection strategy. Scaling laws for kicker pulse power and length optimization are presented. Kicker reference designs for the ILC with full linac aperture, and limited aperture, are presented. Power levels are of order 10^8 W for 100 nsec filling times, and length scales are of order 100 m. Design issues for beam transport to a dump are considered. Separation of the beams at the defining obstruction and energy bandwidth force either a long drift after the septum bend or long quads with large apertures for dispersion control.

1 MACHINE PROTECTION ISSUES

The International Linear Collider (ILC) bunch energy is of order kiloJoules, and the bunch train energy is megaJoules. The average beam power is of of order 10 megaWatts, and the train power is gigaWatts. These magnitudes are sufficient to destroy machine components, and make even a dedicated beam dump difficult to design. The obvious limiting apertures are the background collimators in the beam delivery system, but there are others, like the transition between the large aperture of the linac and the small aperture of the positron production undulator.

The beam emittance is very small, so the surface power density is very high. The thermal expansion from dE/dx energy loss in solid material can exceed the tensile strength of the surrounding unheated material and fracture it, particularly if repeated beam impacts cause fatigue. With nominal ILC beam delivery system parameters, the fracture limit is typically a few bunches. Some experiments at SLAC with micron beams and thin targets produced clean holes rather than fractures, but such holes could negate the effectiveness of spoilers or collimators.

There are 3 basic defense strategies against damage by the beam: prevention, diversion, and passive protection. Prevention means that the beam is not injected unless it is known that it will not do any damage. Diversion means re-directing the beam to someplace where it will not do damage. Passive protection means designing limiting apertures so they minimize damage to other components. Prevention requires monitoring systems to predict problems. If problems can only be detected after the beam is injected, it is still possible to use diversion. But if the detection mechanism involves seeing beam loss, there may still be some damage. Passive protection is the simplest in operation, since it requires neither monitoring nor action on the beam. But one must anticipate all loss scenarios (or add more protection as new scenarios are discovered).

Passive protection was the primary strategy for the SLAC Linear Collider (SLC), which had much lower bunch and train energies and much higher emittances. The cooling of the passive protection collimators was ususally not sufficient to absorb the total beam power, so the pulse rate was lowered or stopped when beam losses were detected. Since there were only 3 bunches with short spacing in the linac, diversion was not an option for the SLC.

For the ILC, it is difficult to make "survivable" passive protection apertures for the beam deliver system that would not be damaged by the beam. But it would still be wise to design "consumable" passive protection apertures, in the same sense that if a circuit breaker is not feasible, a fuse should be used instead. Prevention will likely be a large part of the strategy, but prevention won't be perfect: not all problems will be detected, and some will develop after injection into the linac has started.

The time-structure of the warm ILC design was unfavorable for diversion schemes, so the collimation system emphasized renewable or consumable apertures. The cold ILC time structure is compatible with detecting problems and diverting the beam within a few bunches, so the TESLA design included a fast-abort kicker between the end of the linac and the beam-delivery collimators. A "pilot" bunch of low charge and/or higher emittance so it is below the single bunch damage threshold, with a substantial delay before the rest of the bunches, has been suggested to improve the effectiveness of diversion.

The role of a fast-abort system is to minimize damage to the downstream passive protection apertures from inefficiencies of the prevention system. The elements of a fast-abort system are monitors for abnormal conditions, a fast kicker device and associated pulsed power supply, and a region where the normal and extracted beam lines are in a single, probably wider, beam pipe. Conceivably, the aborted beam could be absorbed at the end of the wide pipe. If this is not possible, the wide pipe ends in a "fork" collimator, followed by a DC septum magnet with very different fields in the normal and aborted-beam paths. After this is a beam line ending in a beam dump. The dump line may need to have large apertures and deal with a wide energy range. The normal and aborted beam lines are close together for some distance, and mechanical interferences between the beam lines are significant. It is best to design the kicker, septum, optics, and physical components of both beam lines as a unit, including the possibility of modifying the optics and component design on the

normal beam line to reduce the difficulties of the abort system.

2 KICKER ENERGY AND POWER

The magnetic field of the kicker contains stored energy which depends on the beam energy, the required kick magnitude, the drift length, and the kicker aperture and length. Supplying the energy quickly requires peak power which grows inversely with the required filling time, and can be rather large.

For a kicker with uniform magnetic field B in Tesla and length K in meters, for beam energy E in GeV, the total kick angle is

$$\theta = BK\ (299.97\ \text{MeV})/\text{E} = 1.200\times10^{-3}\,BK\ (250\ \text{GeV})/\text{E}$$

The displacement after the kicker plus drift distance D is $\Delta = (K/2 + D)\theta$. If the kicker is fraction f of a total kicker + drift length ℓ, the kicker length is $K = f\ell$ and the displacement is $\Delta = (1 - f/2)\ell\theta$. The magnetic energy stored in the kicker aperture is $U = B^2 Kwh/2\mu_0$, where w and h are the (uniform) width and height of the kicker aperture.

Combining these results, we find

$$U = \frac{1}{2\mu_0}\left(\frac{1}{1.200\times10^{-3}}\right)^2\left(\frac{E}{250\ \text{GeV}}\right)^2\left(\frac{\Delta}{\ell(1-f/2)f\ell}\right)^2 \ell fwh$$

in Joules for E in GeV and Δ, w and ℓ in meters. We can rewrite this as

$$U = \frac{1}{2\mu_0}\left(\frac{1}{1.200\times10^{-3}}\right)^2\left(\frac{1}{250}\right)^2 \frac{E^2\Delta^2 wh}{\ell^3}\frac{1}{f(1-f/2)^2}.$$

To minimize the kicker stored energy, we set the derivative of the denominator of the last factor to zero, so $(1-f/2)^2 + 2f(1-f/2)(-1/2) = 0$. This has solution $f = 2/3$, meaning that the kickers should fill 2/3 of the space before the septum. At the minimum, the final factor has value $\frac{1}{f(1-f/2)^2} = \frac{1}{(2/3)(1/3)^2} = \frac{9}{4}$. The stored energy for the optimal f = 2/3 filling factor is $U = u\frac{E^2\Delta^2 wh}{\ell^3}$ where we have defined the numerical factor

$$u = \frac{1}{2\mu_0}\left(\frac{1}{1.2\times10^{-3}}\right)^2\left(\frac{1}{250}\right)^2\frac{9}{4} = 9.95\times10^6.$$

There will be energy stored in magnetic return flux and in electric fields, so we define η as the ratio of magnetic energy in the kicker aperture to total energy stored in the kicker fields. The power required to supply the required energy to the kicker in time t is $P = u\frac{E^2\Delta^2 wh}{\eta\ell^3 t}$. Using $E = 500$ GeV, the ILC main linac aperture of 0.07 m for $w = h = \Delta$, a kicker plus drift length $\ell = 100$ m, the magnetic energy stored in the kicker aperture would be about 60 Joules. If the kicker filling time is 100 nanoseconds (compared to the 300 nanoseconds between bunches), and $\eta = 1$, the peak power is 600 MW!

3 KICKER APERTURE

The beam displacement at the septum Δ is determined by the requirement that the dump line full aperture A_{dump} and the normal beam full aperture A_{norm} are separated by the physical thickness of the septum and associated beam pipe walls s, as shown in Figure 1. The distance between the centers of the full apertures is then $\Delta = (A_{norm} + A_{dump})/2 + s$.

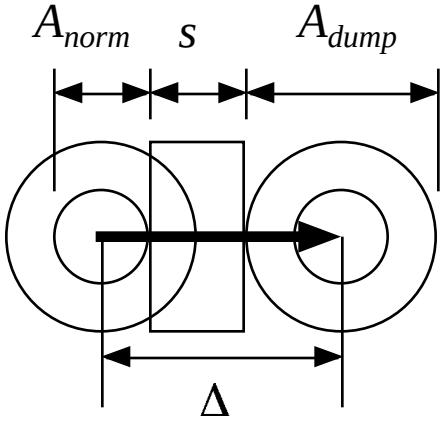

Figure 1: Beam envelopes at septum

The kicker width w must be large enough for the abnormal beam at the entrance, the displaced abnormal beam at the exit, and the normal beam at the exit. If the kicker field is uniform, and the kicker fills the optimum 2/3 of the space, then the beam displacement at the end of the kicker is $\Delta/2$. Then the required width is

$$w = \frac{A_{dump}}{2} + \max\left(\frac{3A_{norm} + A_{dump}}{4} + \frac{s}{2}, \frac{A_{dump}}{2}\right).$$

If both the normal beam and the dumped beam require the same aperture, we have $\Delta = A_{dump} + s$ and $w = 3A_{dump}/2 + s/2$. This is a factor of at least 1.5 in the stored energy and power compared to the simple scaling formula, and even more if the septum thickness is significant compared to the aperture. If the normal beam aperture is negligible compared to the dump beam aperture, $\Delta = A_{dump}/2 + s$ and $w = \max(A_{dump}, 3A_{dump}/4 + s/2)$. For $s < A_{dump}/2$, this is just $w = A_{dump}$. For a negligible septum thickness, this will give a factor of 4 less stored energy and power than the simple scaling formula (because the beam displacement is half as large).

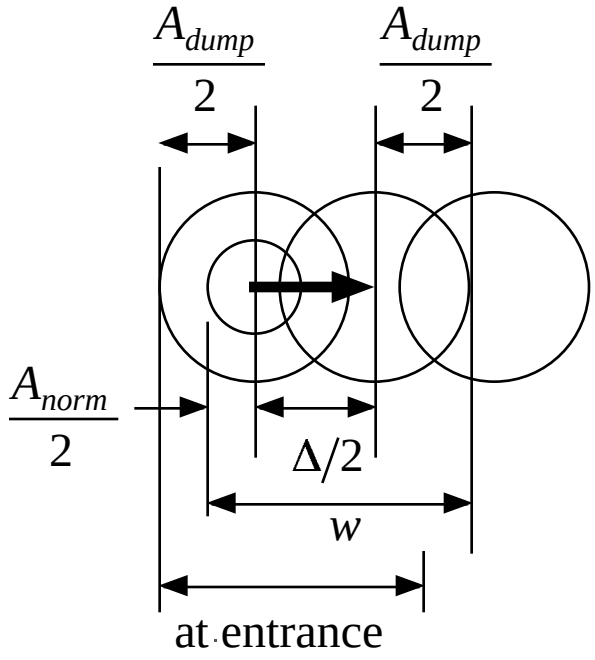

Figure 2: Beam envelopes setting kicker aperture

4 KICKER EFFICIENCY

The kicker efficiency is defined here as the ratio of the total energy stored in the kicker, including stray magnetic field and internal or external capacitive energy, to the energy stored in the magnetic and electric fields inside the aperture, weighted by their effect on the beam.

If the kicker uses parallel strip electrodes and a ferrite flux return, there is negligible magnetic energy in the return flux, so the magnetic efficiency is essentially 1 (there can still be inefficiency due to capacitive energy). If no ferrite flux return is used, and the strips are far from any conducting walls, the energy in the return magnetic flux is typically comparable to the magnetic energy in the beam aperture, so the magnetic efficiency is about 0.5. If the strips are confined in a closely-fitting conducting pipe, similar to a stripline beam position monitor, the return flux must go through the small gap between the strips and the wall. The magnetic field strength and thus magnetic energy in this region is high, but it does not contribute to deflecting the beam. The magnetic efficiency of such a structure is substantially less than 1.

The kicker structure also has capacitance, from conductor to conductor, and from conductor to enclosure. Energy is stored in the kicker capacitance. The capacitance combined with the inductance determines an impedance. If the kicker is terminated by a resistor that matches its impedance, then it turns out that the electrical energy stored in the capacitance is equal to the magnetic energy stored in the inductance. This statement is independent of the capacitance, because adding capacitance lowers the impedance, which lowers the voltage required to get the same current to get the same kick, and the stored electrical energy is the same.

If the kicker structure is a uniform cross section in vacuum, with no external capacitance or ferrite flux return then it is a $v = c$ transmission line. For a $v = c$ transmission line terminated in its characteristic impedance, the electric and magnetic kicks for a $v = c$ beam are equal. If the electrical pulse direction is opposite to the beam direction, the kicks add. While there is electric field energy, it contributes to kicking the beam, so it does not reduce the efficiency. But if the electrical pulse direction is the same as the beam direction, the kicks cancel, so the efficiency is zero.

The impedance is of order 377 Ohms for isolated strips in vacuum with a square aspect ratio, which is inconveniently high unless the pulser is mounted directly on the kicker. Capacitance can be added to lower the impedance. One way of doing this is to increase the strip to ground capacitance by bringing the walls of the enclosure close to the strips. The structure is still a $v = c$ transmission line, and the electric field between the strips still contributes as much to kicking the beam as the magnetic field. But the structure is not very efficient. There is a lot of energy in the electric field of the capacitance between the strips and the walls, and in the magnetic return flux in the same region.

Another way of lowering the impedance is to add external capacitance, perhaps distributed along the strips. This reduces the electrical wave propagation velocity below $v = c$. We also reduce the electric kick relative to the magnetic kick. The energy stored in this capacitance remains equal to the energy stored in the inductance, if we keep the kicker terminated in its characteristic impedance.

A kicker can in principle be run as a “short circuit” rather than being terminated. If we think of the kicker as a transmission line, then we get a reflection from the short circuit that doubles the current and cancels the voltage. This doubles the magnetic field for a given pulser power, but also doubles the filling time, since the current pulse wavefront must propagate down and back inside the kicker.

For a $v = c$ transmission line kicker (of any impedance and efficiency), short-circuiting gives no efficiency advantage relative to termination, because the backward wave does not give a net kick to the beam.

But for a capacitively-loaded kicker, where the electric kick is less of a help, we can get an effective doubling of the efficiency. We get the same kick if we run at 1/2 the pulser current and voltage (1/4 the power) for twice as long a pulse, for a net factor of 2 less pulse energy. This makes sense, because we have the same magnetic field energy, but no electric field energy stored in the kicker.

If we want to keep the risetime the same rather than having it double when we short-circuit the kicker, we could cut the kicker in half and feed the halves in parallel with identical 1/4 power pulses, which would not need to be double-length. Or, we could reduce the kicker loading

capacitance by a factor of 4, reducing the filling time back to the original terminated value. This would increase the impedance by a factor of 2, so we would be back to the original terminated voltage value, but at half current and thus half power. In either case, we get a factor of 2 less total stored energy for a shorted kicker.

However, we must deal somehow with the reflection from the shorted kicker back at the pulser. The simplest solution is to drive the kicker through a series-termination resistor right at the pulser that matches the kicker and cable impedance. This absorbs the reflection and allows the kicker to still be driven through long cables. However, it reduces the cable voltage to half of the pulser voltage, and the cable power to half of the pulser power. So series-termination cancels out the apparent efficiency advantage of shorting the kicker!

A shorted ferrite kicker with no termination either at the pulser or at the kicker would have an efficiency of 1. A terminated ferrite kicker would have an efficiency of 0.5 (whether the termination is at the pulser or after the kicker) due to energy stored in capacitance (independent of the amount of capacitance). Removing the ferrite costs another factor of order 0.5 in efficiency due to stray magnetic flux energy if the strips are isolated from the walls, worse if the strips are close to the wall (as in a 50-Ohm $v = c$ structure, even including the electric kick enhancement).

5 KICKER COST OPTIMIZATION

There is a tradeoff between length and pulser power, both of which will be significant cost drivers. The total cost can be written $C = C_L \ell + C_P P$ where C_L is the cost per meter of tunnel (including the kicker and vacuum system), and C_P is the cost per Watt of peak power. We can then write $C = C_L \ell + C_P u \frac{E^2 \Delta^2 wh}{\eta \ell^3 t}$. The length that minimizes the cost is the solution of

$$C_L - 3C_P u \frac{E^2 \Delta^2 wh}{\eta t} \ell^{-4} = 0, \qquad \text{or} \qquad \ell = \sqrt[4]{\frac{3C_P u E^2 \Delta^2 wh}{C_L \eta t}}.$$

We can also write this as $\ell = \sqrt[4]{\Delta^2 wh}\, \frac{\sqrt{E}}{\sqrt[4]{t}} \sqrt[4]{\frac{C_P}{C_L}} \sqrt[4]{3u}$. The factor $\Delta^2 wh$ scales roughly as the fourth power of the aperture a, so we can write $\ell = a \frac{\sqrt{E}}{\sqrt[4]{\eta t}} \sqrt[4]{\frac{C_P}{C_L}} \sqrt[4]{3u}$.

The cost-optimum length is proportional the square-root of beam energy, roughly proportional to the aperture, inversely with the fourth root of the product of the required risetime and the kicker structure efficiency, times the fourth root of the ratio of the cost per Watt and the cost per meter. It would take a factor of 16 change in the cost ratio, the required risetime, or the kicker structure efficiency to change the optimum length by a factor of 2. But changes in aperture show up directly in length.

At the minimum, the total cost over total length is

$$C_L + C_P u \frac{E^2 \Delta^2 wh}{\eta t} \left(\sqrt[4]{\frac{3C_P u E^2 \Delta^2 wh}{C_L \eta t}} \right)^{-4} = C_L + \frac{C_L}{3}.$$

So the cost-optimum solution is to spend three times as much money on length as on power. Also, the total cost at the optimum will simply be proportional to the length.

If the system length is set arbitrarily rather than by cost optimization, the system cost will be larger. If the length is twice the optimum, the length-dependent cost is doubled, from 3/4 to 6/4, and the power-dependent cost is reduced from 1/4 to 1/32, so the total cost is 53% higher than optimal. But if the length is half the optimum, while the length cost goes from 3/4 to 3/8, the power cost goes up a factor of 8, from 1/4 to 2, more than doubling the total cost compared to the optimum. This may be an underestimate, because the cost per length of the kicker structure may no longer be small compared to the cost per length of tunnel, since we are putting 8 times the power into 1/2 the length compared to the cost-optimal solution. So the cost risk of allocating too little space for a kicker is higher than the cost risk of allocating too much.

6 REFERENCE KICKER DESIGNS

We calculated from the simple scaling formula that to cover the full linac aperture at 500 GeV with 100 ns filling time and 100 meters is available for the kicker plus drift required of order 600 MW of peak power (and realistically several times that). A large thyratron tube can supply of order 50 MW, while a FET can only supply of order 10 kW. So the scale is a dozen large thyratrons or thousands of FETs to drive the kickers. A 50 ohm cable operated at 25 kV into a matched load supplies 12.5 MW. It would take about 50 such cables to supply 600 MW.

A full millisecond at 600 MW is 600 kiloJoules, compared to the 60 Joules of stored energy in the kicker aperture magnetic field. Presumably it is possible to send a signal upstream to another mechanism that can stop the beam. If the upstream mechanism is 15 km away, then the beam will stop in 100 microseconds, and after only 60 kiloJoules.

We assume the apertures are $A_{dump} = 70$ mm, $h = 70$ mm, and $A_{norm} = 20$ mm, and the septum plus beampipe allowance is $s = 20$ mm, giving a displacement at the septum of $\Delta = 65$ mm, and kicker width $w = 77.5$ mm. We allocate $K = 100$ m for the kicker, implying $\ell = 150$ m for the kicker plus drift. The magnetic energy in the kicker aperture is $U = 9.95 \times 10^6 E^2 \Delta^2 wh / \ell^3$. At $E = 500$ GeV this is $U = 16.9$ Joules. We multiply by 2 for return-flux energy, and by 2 for capacitive energy, or $U = 67.6$ Joules. For a 100 ns filling time, the required power is 676 MW. Using 50 ohm cables running at 25 kV, this would require 54 cables, or about 1 cable every 2 meters.

Since there are inefficiencies at the ends of the kickers it is preferable to have units that are several meters long, so we assume 25 kickers each 4 meters long and fed by 2 cables. Since this is only 50 cables not 54, we raise the power per cable by 8% (4% in voltage, or 26 kV). The cable current is then 520 Amps, so the kicker current is 1040 Amps. The total magnetic energy of each kicker unit is 16.9 x 2/25 = 1.35 Joule, so the inductance is 2.6 μH per unit. To match to a 25 ohm source impedance, the loading capacitance must be 4 nF. The total power per magnet is 27 MW, which would be supplied by one thyratron, for a total of 25 thyratrons.

If the incoming beam aperture is only 20 mm, and we need to deflect all of it past a septum plus beampipe thickness of 20 mm, and the nominal beam aperture is 20 mm, the required deflection is $\Delta = 40$ mm. The kicker width must be at least $w = 40$ mm to allow for the full incoming aperture plus deflection inside the kicker. The kicker height is $h = 20$ mm. If we assume 100 meters of kicker and 50 meters of drift, at 500 GeV beam energy the stored magnetic energy is only 0.94 Joules. Multiply by 2 for return flux and 2 for capacitive energy, and it's 3.8 Joules. For a 100 nsec filling time, it's 38 MW. So we would need only 3 cables, and only one thyratron.

This power is so low that it feels like we are wasting length. Let's squeeze it down to 75 meters (50 m of kicker and 25 m of drift). Then the power after fudge factors is 300 MW. This is about 24 cables, or about 1 cable per 2 meters. If we make 2 meter magnet units, for a total of 25 magnets with 1 cable per magnet, we need to run at 24.5 kV. We could probably drive 4 or 5 magnets per thyratron, using only 5 or 6 thyratrons total. But we might want to use more thyratrons so the loss of kick if a thyratron fails to fire would be smaller.

7 SEPTUM AND DUMP LINE DESIGN

The above analysis assumed there were no quadrupoles between the kicker and the septum. Any quadrupole between the kicker and septum will presumably be centered on the undeflected beam, and needs to have large enough aperture for both normal and deflected beams. Defocusing quads enhance the kick, and focusing quads tend to cancel the kick (and thus should be avoided). The kick enhancement from a defocusing quad is maximized if it is halfway between the center of the kicker string and the fork collimator. For the optimal 2/3 filling factor, this is exactly at the end of the kicker string.

The fork collimator defines the junction between separate pipes for the normal and aborted beam and the single pipe containing both. If the abort kicker fires at the wrong time, at the wrong amplitude, or if the beam orbit or energy error is larger than anticipated, the beam will hit the fork collimator. The fork collimator protects the septum bend and the component on the normal beamline that the septum is diverting the beam around.

A septum bend magnet is normally a either current-sheet septum (with a thin conductor and no flux return on the undeflected-beam side), or a Lambertson bend (with a channel through one pole tip for the undeflected beam). The field is limited to about 10 kG, because the field grows rapidly in the undeflected beam region if the septum magnets saturate. At the practical current density limit for conventional water cooling of 80 amps per square mm, a 10 kG current sheet septum requires a septum coil thickness of about 10 mm. At 500 GeV beam energy, a minimum of 60 meters of 10 kG bend are required to produce 1 meter of physical separation, or about 20 meters for 10 cm of separation.

The dump line probably needs to safely propagate the beam even if there is a large energy error. The septum and kicker introduce dispersion, which needs to be contained and reversed by quadrupoles, then cancelled by other bends. As will be seen below, it easier to control the dispersion if we use a small septum bend angle and a long drift downstream of it. So there is little to be gained by using a strong septum field, which means the septum magnet should be relatively straightforward to build.

We must specify the fractional energy range δ over which we must cleanly transport the beam to the dump. We identify the machine components on the normal beam line that are being diverted around, and the distance X the beam must be physically displaced to accomplish this. The aperture of the entry to the dump line needs to be $\pm X\delta$, and the dump line will require a focusing quad with this aperture to control the dispersion. For a magnetic field B in Tesla and length L in meters, for beam energy E in GeV, the deflection angle is $\theta = BL\,(299.97\text{ MeV})/E$. The focal length F in meters of a quad with pole-tip field of $1\ T$, bore radius R, and length L at 500 GeV is $F = R/(0.6\times10^{-3}L)$. If the focal length equals the distance S from the center of the septum bend to the quad, the dispersion from the septum will change from linearly increasing to constant. If the quad strength is doubled, the dispersion will focus down to zero at distance S downstream, and another bend magnet there can cancel the dispersion derivative. Setting $F = S/2$ and $R = \delta X$, we find the quad length $L = (3.33\times10^{3}\ \text{m}^2)X\delta/S$. If the septum is 100 meters upstream of a 0.3 meter wide machine component on the normal beam line, and we need acceptance for a 20% off-energy beam, we need a dispersion-control quad that is 2 meters long with pole-tip radius of 60 mm and pole-tip field of 10 kG at 500 GeV. This is a rather large quadrupole, dimensionally similar to an e^+e^- storage ring low-beta quad, although it need not be of similar quality. If the distance from the septum to the obstacle is reduced by a factor of 2, the aperture goes down a factor of 2, but the length grows a factor of 2. Several quads of this scale would be used to propagate the dumped beam to a DC bend that cancels the dispersion. A few sextupoles would be required to make the cancellation reasonably achromatic.

If the actual energy error is larger than the design energy error, the beam would hit the first dispersion-control quad. A protection collimator (which may need periodic replacement) should be placed upstream. After the dispersion is cancelled, the dump line apertures might be made smaller. The limit would probably be set by the incoming beam position and angle errors, and kicker amplitude variations, either from pulse to pulse, or within a pulse.

The abort beam dump must be able to handle a significant fraction of the total bunch train at the local energy. Presumably a clone of the final extracted beam dump would be satisfactory as an abort dump. It may be possible to economize in some ways due to lower beam energy, lower bunch train length and lower average power (enforced by limiting extraction from the damping ring).

8 CONCLUSIONS

The ILC beam is potentially very destructive, and a fast beam abort system is useful as part of the machine-protection strategy. One application is to minimize damage to background collimators in the beam delivery system. The components of a fast beam abort system are sensors, a fast kicker and pulsed power supply, a drift region ending in a fork collimator, a DC septum bend magnet, more drift, a beam dump line with dispersion control defined by the energy error bandwidth, and a beam dump. The required kicker pulse power scales as $P = u\frac{E^2\Delta^2 wh}{\eta \ell^3 t}$. The kicker magnets should fill 2/3 of the distance before the septum magnet. There is a steep tradeoff between length and power, and the cost optimum length is $\ell = \sqrt[4]{\frac{3C_P u E^2 \Delta^2 wh}{C_L \eta t}}$. At the optimum, 3/4 of the cost is length (tunnel, vacuum, kicker), and 1/4 is pulsed power.

A reference design for a 20 mm normal aperture, 70 mm error aperture, and 100 nsec filling time is 25 vacuum stripline kickers each 70 mm high, 77.5 mm wide, and 4 meters long, followed by 50 meters of drift before the septum magnet. Each kicker has external loading capacitance and termination and is fed a 26 kV pulse from its own thyratron by 2 cables of 50 Ohm impedance. If the error aperture is only 20 mm instead of 70 mm, the 25 kickers can be 40 mm wide, 20 mm, and 2 meters long. They would be driven by 1 cable per magnet at 24.5 kV, and one thyratron could drive several magnets.

The separation of the beams at the defining obstacle, and the energy bandwidth required for energy errors, determines the aperture required for the dispersion control quadrupoles of the dump line. The required quad length of depends on the separation, the bandwidth, and the distance from the magnetic center of the septum: $L \propto X\delta/S$. If the energy bandwidth requirement is 20%, and the septum is required to produce a 0.3 m separation after 100 m, we need dispersion-control quads that are 2 meters long with pole-tip radius of 60 mm and pole-tip field of 10 kG at 500 GeV.

ACKNOWLEDGEMENTS

This work is supported by the Canadian National Science and Engineering Research Council (NSERC).

GROUND MOTION & COMPARISON OF VARIOUS SITES

R. Amirikas, A. Bertolini, W. Bialowons, H. Ehrlichmann *, Deutsches Elektronen-Synchrotron
DESY, 22603 Hamburg, Germany

Abstract

The study of ground motion and its impact on the International Linear Collider (ILC), where e^+ e^- beams of the order of nanometers must collide with high luminosities, may not be negligible. All sources of vibration, including ground motion, can cause the beams to simply miss each other at the interaction region (IR).

In this paper, we describe a program of site characterization and comparison, via measurement of ground motion spectra, using inertial broadband seismometers. The emphasis is on using the same equipment and data analysis techniques as applied to all the sites studied. Our database of ground motion measurements for each site is available to the scientific community.

INTRODUCTION

It is envisaged that ILC will collide nanometer-size e^+ e^- beams at a center-of-mass energy of 500 GeV, and possibly, up to 1 TeV, at a high luminosity (a few times 10^{34} cm^{-2} s^{-1}). Maintaining such beams in collision could be a major challenge and requires a detailed study of sources of degradation of machine parameters.

The influence of ground motion on the performance of the collider is not negligible. It can cause colliding beam offset in the IP region and beam emittance growth. It is imperative to understand the influence of ground motion, specific to each site, with respect to geological conditions and human activity, commonly known as 'cultural noise'.

A program of site characterization has been initiated in DESY where different sites have been studied using the same equipment and data analysis tools. Therefore, this database of accumulated measurements can be used for site comparison. The sites studied comprise high energy laboratories, synchrotron light sources and reference sites.

Reference sites chosen in this study are situated at geologically stable and remote locations. Reference sites facilitate a comparison base for 'noisier' sites with high cultural noise content.

Moreover, each site is studied in different locations, such as, tunnel vs. surface, inside vs. outside a building etc. to get a better impression of the cultural noise situation. The measurement period is for 24 hours, or, in the majority of the cases, one week, so that variation with respect to day and night, weekday and weekend is apparent.

GROUND MOTION MEASUREMENTS

Güralp Broadband Digital Output Seismometers

Ground motion measurements are undertaken using state-of-the-art Güralp triaxial feedback seismic sensors [1]. There are three CMG-3TDs and two CMG-6TDs in our possession for this purpose. These seismometers can measure a frequency range of up to 80 Hz. They are hermetically sealed devices which produce a digitized voltage that is proportional to the velocity measured in each axis (east-west, north-south and vertical). They contain an inverted pendulum for the two horizontal axes, and a leaf-spring for the vertical axis. A feedback loop with a force transducer compensates the ground acceleration acting on a seismic mass. The feedback current is proportional to the ground acceleration, which is internally integrated, and therefore, is proportional to the ground velocity.

This voltage is then digitized with an internal 24 bit digitizer, without amplifier, with 200 Hz sampling rate, and is linked to a notebook/PC via serial data cables. The software used for data acquisition, is called 'SCREAM' from Güralp Systems Ltd by which, continuous velocity signal of all three components is digitized and stored in one minute files. The output voltage to ground velocity calibration is flat over the operating frequency range of the seismometers, and the resolution of the instrument is about 0.4 nm/s/bit, for all frequencies, which is sufficient to measure ground motion at quiet sites. The system is supplied with GPS antennas which can keep their internal clocks synchronized with satellite-based UTC time signals in order to provide a time reference signal with the data. It should be emphasized that seismometers measure absolute motion, since measurements are relative to an inertial frame. This is the preferred method over differential methods in which relative motions are measured.

ANALYSIS OF DATA

Power Spectral Density

The power spectral density (PSD) of a noise signal is defined as [2]:

$$S_x(f) = 2\lim_{T\to\infty}\frac{1}{T}\left[X(f)\right]^2 \qquad (1)$$

* corresponding author: heiko.ehrlichmann@desy.de

$X(f)$ is the Fourier transform of the noise signal defined as:

$$X(f) = \int_{-T/2}^{T/2} x(t) e^{-2\pi i f t}\, dt \qquad (2)$$

The factor of 2 in (1) is because only positive values of frequency, f, have been used in the definition of the PSD.

Since, one cannot perform an infinite measurement in time, discrete Fourier transform is used where integrals are replaced by sums.

The sampling rate selected for a seismometer defines the upper frequency limit of the resultant data. In our case, 200 samples per second correspond to an upper frequency limit of 100 Hz (Nyquist criterion).

The dimension of the PSD is 'power' per unit frequency band, e.g., $(\mu m/s)^2/Hz$ for the PSD of velocity. Since displacement and velocity are related via $v = dx/dt$, their Fourier harmonics are related as follows:

$$V(f) = -2\pi i f\, X(f) \qquad (3)$$

As the magnitude of the displacement experienced in a given frequency band is more informative, one can calculate displacement PSD defined as:

$$S_x(f) = \frac{S_v(f)}{4\pi^2 f^2} \qquad (4)$$

Equation (4) is used to extract displacement PSD from the measured velocity PSD with a unit of $(\mu m)^2/Hz$. It is customary to average a number of spectra in order to smooth out single event noise so that real features of the spectra are clearly visible. We have adopted the practice of taking average spectra every 15 minutes or longer depending on the analysis concerned. In most cases, no windowing is applied to the Fourier transform.

Average displacement PSDs of various sites are shown in Fig. 1.

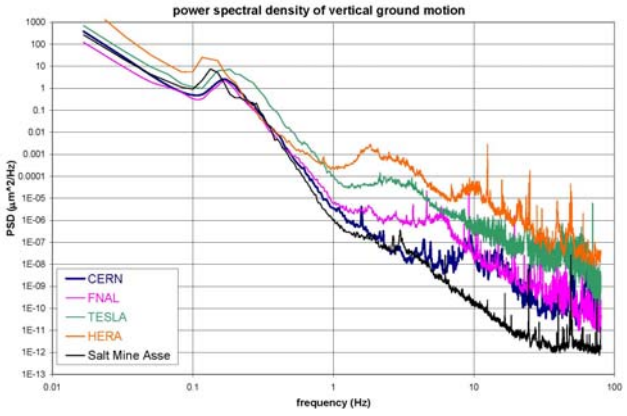

Figure 1: Average displacement PSDs for various sites, including a reference site (rock salt mine Asse in Germany)

Using displacement PSD, one can calculate total root mean square (rms) displacement over the whole frequency range (or in any frequency band desired, such as (f_1, f_2)). This is achieved by integrating the displacement PSD (e.g. in vertical direction, z) and taking the square root:

$$z_{rms}(f_1, f_2) = \sqrt{\int_{f_1}^{f_2} S_x(f)\, df} \qquad (5)$$

Integrated PSD spectra, calculated from the spectra in Fig. 1, are shown in Fig. 2. Our cut frequency value is usually at f > 1 Hz, as cultural noise is dominant at this frequency range and is uncorrelated. This region is therefore, of interest for ILC site comparison.

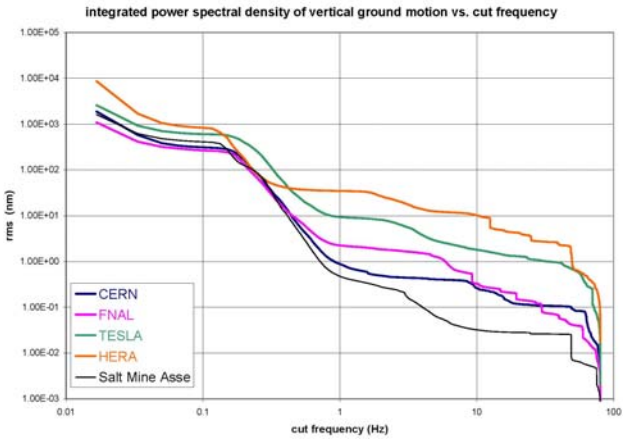

Figure 2: Integrated PSDs as obtained from Fig. 1

GROUND MOTION SPECTRA

Ground motion can be divided into two categories: slow motion, at f < 1 Hz, is referred to 'slow ground motion'. For example, microseismic peak at 1/7Hz (frequency range of 0.1 to 0.25 Hz), is caused by the coastal waves and can even be seen in the center of the continents. It is clearly visible in all the PSD spectra shown in Fig.1. The general shape of the PSDs follows $1/f^4$ behavior which is a random walk noise trend. This region of the seismic spectrum can also be affected by atmospheric changes.

On the other hand, f > 1 Hz, where 'cultural noise' prevails, is referred to 'fast ground motion' [3]. In this region, the shape of the PSDs can change drastically from site to site, as seen from Figs 1 and 2. One can clearly see the deviation from $1/f^4$ behavior of HERA spectrum compared with rock salt mine Asse in Germany. On the other hand, the spectrum measured at CERN has much smaller amplitude at f > 1 Hz. Fermi laboratory and the proposed TESLA IR, measured in Ellerhoop, 17 km northwest of Hamburg, Germany, fall between the HERA and CERN maxima and minima respectively. Cultural noise stems mainly from human activities in the vicinity or at a site. Comparison of measured ground motion

spectra at several sites, including DESY, with a simple ground mechanical model confirms an earlier, independent conclusion, based on the extensive measurements, that traffic (both road and railway) might be the main source of cultural noise [4].

CHARACTERIZATION OF SITES

All sites have been measured with the same equipment and data analysis techniques. This facilitates comparison between sites. In many cases, simultaneous measurements with more than one seismometer, placed at a distance from each other, provides better information on the sources of ground vibration as this method of measurement, provides correlation information of the seismic signals [5, 6].

In most cases, data is taken for a long period, one week or longer which includes weekends. An example of rms spectrum of vertical displacement (in nm) versus time, in calendar days, at a cut frequency of f > 1 Hz, is shown in Fig. 3 for the HERA tunnel. The two peaks at lower amplitude (right most corner of the figure) highlight reduction of cultural noise during weekends compared with weekdays. In addition, day and night variations are also clear.

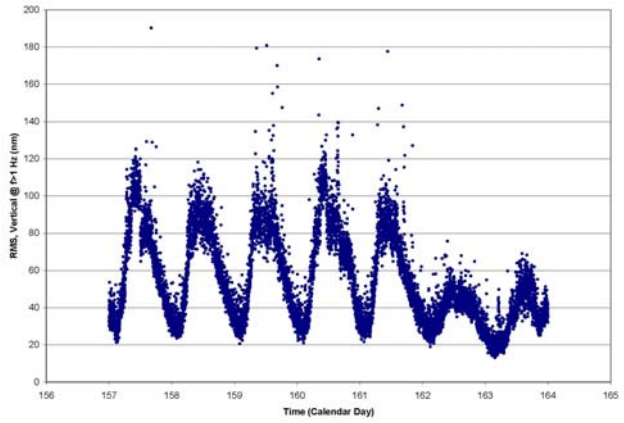

Figure 3: Weekday and weekend variation of ground vibrations (vertical direction) as experienced in the HERA tunnel. Weekend peaks with reduced amplitude are seen on the right.

Histograms of rms values, for a complete measurement period, (for vertical motion, in most cases) are one way to characterize a site as ‘quiet’ or ‘noisy’ as shown in Figs. 4 and 5.

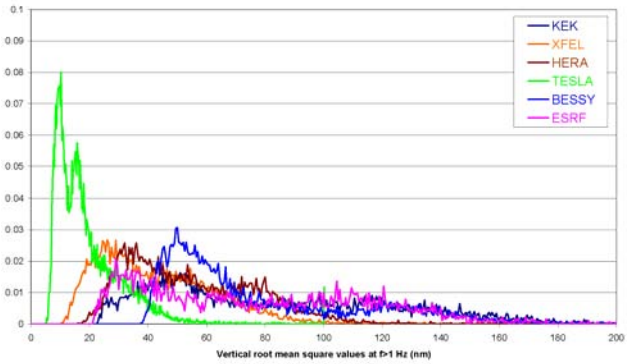

Figure 4: Vertical rms distributions of ‘noisy’ sites as defined in the text

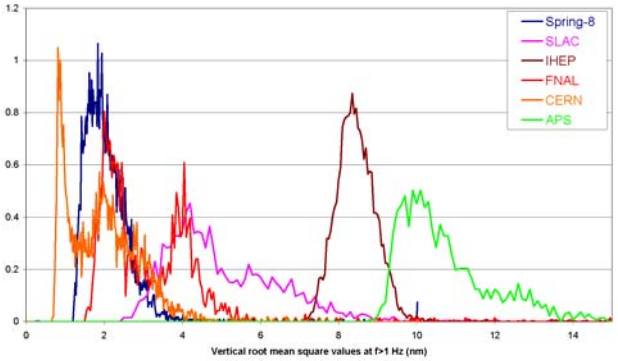

Figure 5: Vertical rms distributions of ‘quiet’ sites

The shape of the distributions differs from site to site, as many spectra have two maxima, signifying day and night variations of cultural noise. In these figures, rms distributions with vertical motion of less than 15 nm are classified as ‘quiet’, and the rest as ‘noisy’.

Another method which does not rely on Fourier transform is the numerical calculation of displacement maxima and minima, after seismometer calibration values have been applied, for the one minute raw data files. In this method, numerically integrated ground velocities (within 1 s time window) are binned into peak-to-peak histograms, as shown in Figs 6 and 7.

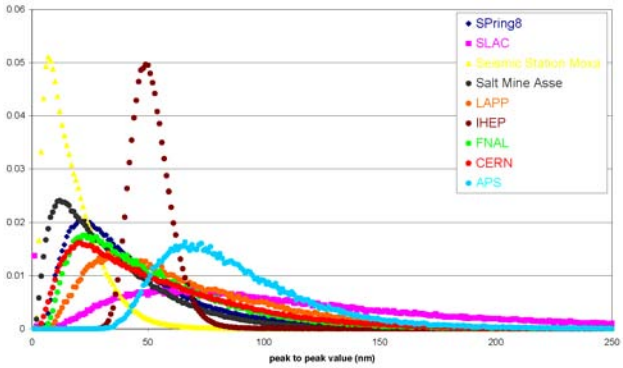

Figure 6: Normalized displacement peak-to-peak histograms of vertical motion for ‘quiet’ sites

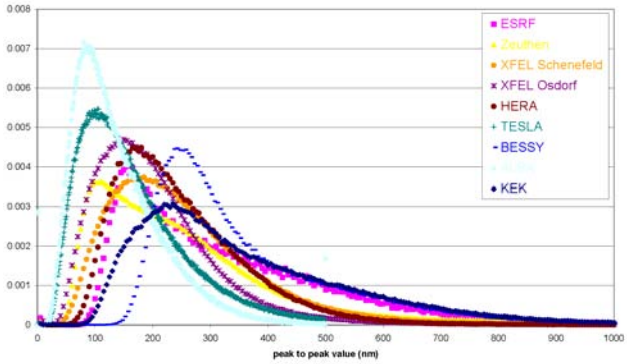

Figure 7: Normalized displacement peak-to-peak histograms of vertical motion for 'noisy'sites

This method is an independent way to characterize a site. As it can be seen in the figures above, maxima, full width at half maxima (FWHM) and the shapes of the histograms differ from site to site. Peak-to-peak values are essentially the worst case scenario for ground vibrations for a specific site. Peak-to-peak calculation is sensitive to short bursts in the 1 minute raw data files, for example when a train passes nearby a site, a short time duration burst can be seen in the raw displacement/velocity data. Short duration 'events' as such, influence the peak-to-peak values. While on the contrary, rms calculation is not greatly influenced by these 'events'. However, short burst 'events' are ever present in each site with different magnitude and frequency, depending on each site studied, and may not be ignored in site comparison and characterization program.

Similar to the rms distributions shown above, the maximum value and the spread at FWHM indicate the number and strength of cultural noise sources [5, 6]. For example, the peak-to-peak distribution of IHEP (Beijing) is almost a Gaussian with a very small spread (please see Table 1), which indicates relative weakness of the sources of cultural noise and their variation, as seen in the peak-to-peak amplitude and FWHM respectively, compared with APS (Argonne), for instance.

In Table 1, we have summarized our compiled database of site measurements [7]:

Pk-Pk_{Max} (left most column), is the maximum peak-to-peak values (in nm), for vertical displacement, and their corresponding FWHM. The third and fourth columns from the left are the average rms values for a complete measurement period, at f > 1 Hz frequency cut, and the corresponding standard deviation (SD) in nm. In this analysis, a cut of 5% to the highest rms values, in 1 minute data files, is applied.

The last two columns on the right are the average rms values, of vertical displacement at f > 1 Hz, for a snapshot period of one hour corresponding to quiet conditions, uaually around midnight, and noisy conditions, usually around midday.

These values are complementary to average rms values for the whole measurement period.

For site comparison and characterization purposes, this database provides a reliable means of site evaluation to the scientific community [7].

SUMMARY

We have measured ground motion spectra, for various sites, some, which are potential sites for the ILC. In this project, we have used the same equipment and analysis techniques to facilitate site comparison. Our database is available to anyone interested in pursuing research on ground motion issues for accelerator stabilization.

Table 1: Site comparison

	Site Location	Pk-Pk_{Max} (nm)	FWHM (nm)	RMS (nm)	SD (nm)	Quiest RMS	Noisy RMS
1	ALBA Cerdanyola	87	125	18.3	9.5	9.1	42.0
2	APS Argonne	68	56	10.5	1.0	9.8	11.0
3	BESSY Berlin	245	160	72.8	28.1	53.1	140.7
4	CERN Geneva	21	53	1.8	0.9	0.9	2.8
5	DESY TESLA	104	160	17.4	8.4	9.3	35.9
6	DESY HERA	170	200	51.8	18.9	34.8	77.0
7	DESY XFEL Schenefeld	180	245	38.7	16.6	35.1	70.0
8	DESY XFEL Osdorf	150	195	28.9	11.9	19.5	48.4
9	DESY Zeuthen	105	235	64.0	40.4	88.5	75.6
10	ESRF Grenoble	155	175	71.6	34.9	40.2	137.2
11	FNAL Batavia	23	49	2.9	0.9	2.2	4.0
12	IHEP Beijing	49	18	8.4	0.5	8.1	9.0
13	KEK Tsukuba	170	210	78.0	36.0	38.0	125.1
14	LAPP Annecy	35	59	3.3	1.6	1.9	7.0
15	Salt Mine Asse	12	35	0.5	0.1	0.5	0.7
16	Seismic Station Moxa	7	17	0.6	0.1	0.5	0.9
17	SLAC Menlo Park	60	105	4.8	1.2	4.1	7.4
18	Spring-8 Harima	22	40	2.0	0.4	1.8	2.5

ACKNOWLEDGEMENTS

This work is in part supported by the Commission of the European Communities under the 6th Framework Program 'Structuring the European Research Area', contract number RIDS-011899. We acknowledge the assistance of numerous persons in all the sites we have visited and the persons who have provided IT support.

REFERENCES

[1] Güralp Systems Ltd, http://www.guralp.net/
[2] D. Holder, "Basics of Site Vibration Measurements as Applied to Accelerator Design", Daresbury Laboratory, AP-BU-rpt-001, Jan. 2000.
[3] A. Seyi, "Ground Motion Models for Future Linear Colliders", EPAC 2000 (Vienna, Austria), SLAC-PUB-8487, June 2000.
[4] J. Grabe, and T. Bierer, "Measurements and Numerical Analysis of Ground Vibrations at DESY-Hamburg", in Proceed. of Structural Dynamics-**EURODYN 2005**, C. Soize & G. I. Schuëller (editors), Millpress, Rotterdam , p. 635-640.
[5] W. Bialowons and H. Ehrlichmann, "Ground Vibration Measurements at the Proposed ALBA Site in Barcelona", TESLA Report 2005-10, March 2005.
[6] W. Bialowons and H. Ehrlichmann, "Ground Vibration Measurements at the European XFEL Site in Hamburg", in preparation.
[7] DESY's recently upgraded homepage on ground vibrations: http://vibration.desy.de

MODELLING OF SIMPLE CASES IN VIEW OF ACTIVE STABILISATION FOR A FUTURE LINEAR COLLIDER

B.Bolzon*, N.Geffroy#, C.Adloff, Y.Bastian, F.Cadoux, C.Girard, A.Jeremie, Y.Karyotakis,
LAPP-IN2P3-CNRS, Laboratoire d'Annecy-le-Vieux de Physique des Particules, BP110,
F-74941 Annecy-le-Vieux, France
L.Brunetti§, J.Lottin, LISTIC, Laboratoire d'Informatique, Systèmes, Traitement de l'Information et de la Connaissance, Université de Savoie, BP806, F-74016 Annecy-le-Vieux, France
F.Formosa, LMECA, Laboratoire de Mécanique Appliquée, Université de Savoie, BP806,
F-74016 Annecy-le-Vieux, France

Abstract

Final focus magnet stabilisation is an important issue when working with nanometre size beams. The present study focuses on mechanical stabilisation. As a first step, the case of a 1m free-fixed aluminium beam placed on a table with active stabilisation has been studied. This work describes three aspects, namely, sensors and actuators to measure and compensate ground motion, mechanical simulations and a feedback loop.

Measurements done with low frequency velocity sensors (down to 0.1Hz) in our Annecy lab during office hours show that the displacement RMS on the active table is 1nm at 4Hz compared to 10nm without active stabilisation.

Simulations of the dynamic response of the beam have been compared to measurements done with accelerometers placed on the clamping and on the free end of the aluminium beam. The results are in good agreement. We are therefore able to predict by simulation the response of a structure subjected to an external excitation.

A first sketch of a feedback loop to compensate specific vibrations has also been developed and allows the simultaneous elimination of several resonance peaks on a reduced-size mock-up. This algorithm will be applied to stabilise a larger mock-up, leading to more realistic experimental conditions. In future tests, the active table will globally stabilise in a range of frequencies from 0.5Hz to 50Hz whereas the feedback loop will compensate single strong resonances.

INTRODUCTION

Final focus magnet stabilisation is an important issue when working with nanometre size beams. Depending on the frequency range needed, this stabilisation can be achieved either by active mechanical stabilisation or by active beam based feedback. We are considering the requirements for mechanical stabilisation of the final focus magnet. This note describes the recent results obtained on the test benches installed in Annecy [1]. The study covers three main aspects: simulation, measurement and feedback loop. Simulation is important to understand the system to be stabilised, and gives a powerful tool to design a final focusing element with the best characteristics for vibration rejection. To get the know-how required for such a project, the first step is to study a simple case and compare measurements with simulation before moving on to more realistic and complicated systems.

SETUP DESCRIPTION

Mechanical hardware

We are using a rectangular aluminium beam, 110cm long, 10cm wide and 2cm thick in a free-fixed configuration. The final focus magnet will be close to, or even inside the experiment so that it has to be cantilevered from outside the experiment. Our experimental setup is shown in fig. 1.

Are shown on figure 1 an active TMC table that has been made available by the CERN CLIC team, the aluminium beam clamped on one side, the Endevco sensors, one on the clamping, the other on the beam end, a Güralp geophone and a DAQ running product sofware from Brüel&Kjaer. The TMC table is composed of honeycomb material passively damping the frequencies under 230Hz.

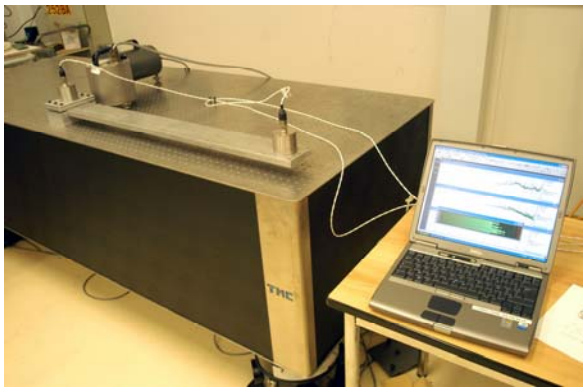

Figure 1: test bench including active table, free-fixed beam, accelerometers, geophones and DAQ running Pulse software.

*Benoit.Bolzon@lapp.in2p3.fr
#Nicolas.Geffroy@lapp.in2p3.fr
§Laurent.Brunetti@univ-savoie.fr

The active Stacis2000 feet have geophones measuring the table displacements, and piezoelectric actuators compensating the movements driven by a controller. This table has been used by the CERN-CLIC team to stabilise the top of a CLIC quadrupole model to the nanometre level [2].

Sensor description

The sensors used for this study are of two types. On the aluminium beam are placed two Endevco Model 86 piezoelectric accelerometers. In addition, a Güralp CMG-40T has been placed on the table as a reference. The characteristics of the sensors are given in table 1.

Table 1: Sensor characteristics.

Sensors	**Calibration for 1V**	**Frequency range**	**Type**
Güralp CMG-40T	±12.5mm/s	0.033-50Hz	Pick-up coil
Endevco 86	0.1g	0.01-100Hz	Piezoelectric

The first step was to characterise the sensors. Ground motion measurements were performed, since it is an important component of the excitation of the aluminium beam on the table. Figure 2 shows the coherence between two identical sensors, placed side by side on the ground, measuring ground motion. The coherence has been determined following equation (1) (more details can be found in ref [3]).

$$C(f) = \frac{\left|\Re e(\langle \tilde{v}_1(f)\tilde{v}_2^*(f)\rangle)\right|}{\sqrt{\left|\langle \tilde{v}_1^*(f)\rangle\langle \tilde{v}_2^*(f)\rangle\right|}} \quad (1)$$

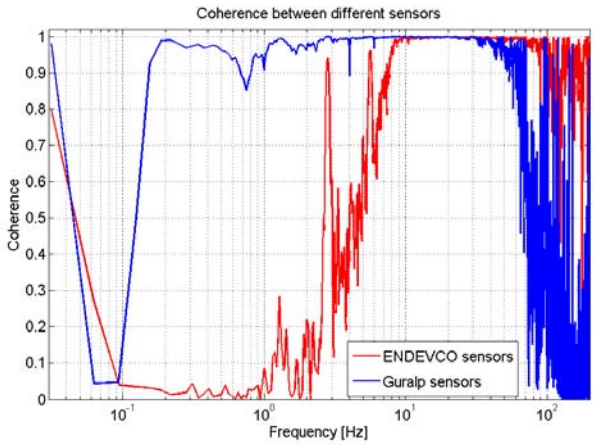

Figure 2: Coherence between two identical sensors. The red curve shows the result for two Endevco accelerometers, and the blue curve for two Güralp sensors.

where v_1 and v_2 are the sensor outputs, $\tilde{v}_1$ and $\tilde{v}_2^*$ the discrete Fourier transforms, * indicating the complex conjugate. The ENDEVCO accelerometers show a drop in coherence below 7 Hz. At low frequencies, the ground motion has a very low acceleration amplitude, and is below the accelerometer resolution. On the other hand, the Güralp sensors measure the ground motion velocity. The amplitude of this signal is sufficiently high to be above this sensor's resolution.

The sensor resolutions have been determined following equation (2) and are shown in figure 3.

$$PSD_c(f) = (1 - C(f))\sqrt{PSD_1(f)PSD_2(f)} \quad (2)$$

PSD_c is the Integrated Corrected Difference, the PSD_1 and PSD_2 respectively the Power Spectral Density of the

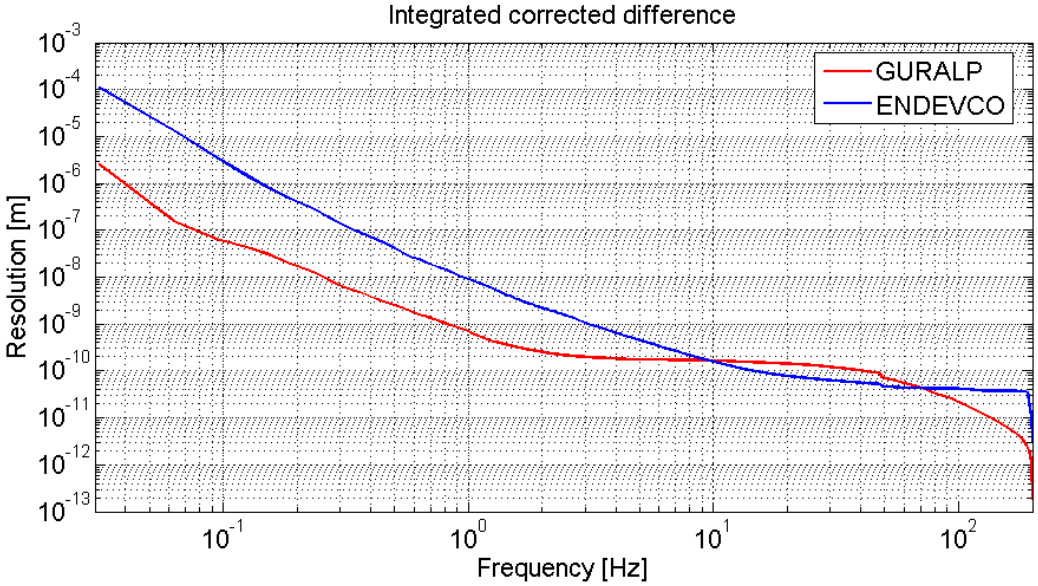

Figure 3: Sensor resolution for the Endevco accelerometers and the Güralp geophones.

first and second sensor used for the study, and C(*f*) the coherence between the two sensors

Notice that above 1 Hz, the Güralp sensors can measure below the nanometre.

The displacement RMS of the ground measured by the Güralp sensor on top of the table has been measured and determined following equation (3).

$$RMS(f) = \sqrt{\sum_{f}^{f_{max}} PSD(f)df} \qquad (3)$$

Figure 4 shows the measurement with the feedback loop of the active table turned on, and the feedback loop turned off. For comparison, at 4 Hz, the displacement on top of the table is 10nm, whereas when the feedback loop is on, this displacement is reduced to 1nm. These measurements reproduce the results shown in [2].

FINITE ELEMENT SIMULATION

The numerical part of this study is performed with the finite element code SAMCEF. Thanks to this software it is possible to perform not only modal analysis, but also dynamic response predictions.

Modal analysis

The aim of this simulation is to obtain the different eigenfrequencies and the corresponding mode shapes of a given structure. In our case the structure is a free-fixed beam made of aluminium, whose geometrical characteristics are the following:

length = 1000 mm
width = 100 mm
thickness = 20 mm

The parameters used in the finite element model, are listed below:

E = 74000 MPa	(Young modulus)
ν = 0.3	(Poisson's ratio)
$\boldsymbol{\rho}$ = 2825 kg/m^3	(density)

At last, given that thickness is a small dimension compared with the others, we opted for a meshing composed of shell finite elements. Then SAMCEF can solve the eigenvalue problem and compute the eigenfrequencies and their corresponding vibration modes. Note that the analyzed structure is assumed to be without damping. The computed eigenfrequencies, are listed in table 2. The measurements were done with a smart hammer set-up by Bruel&Kjaer. Figure 5 shows the difference between measurements and calculations.

Moreover, the first and the third mode shapes are shown on figures 6 and 7:

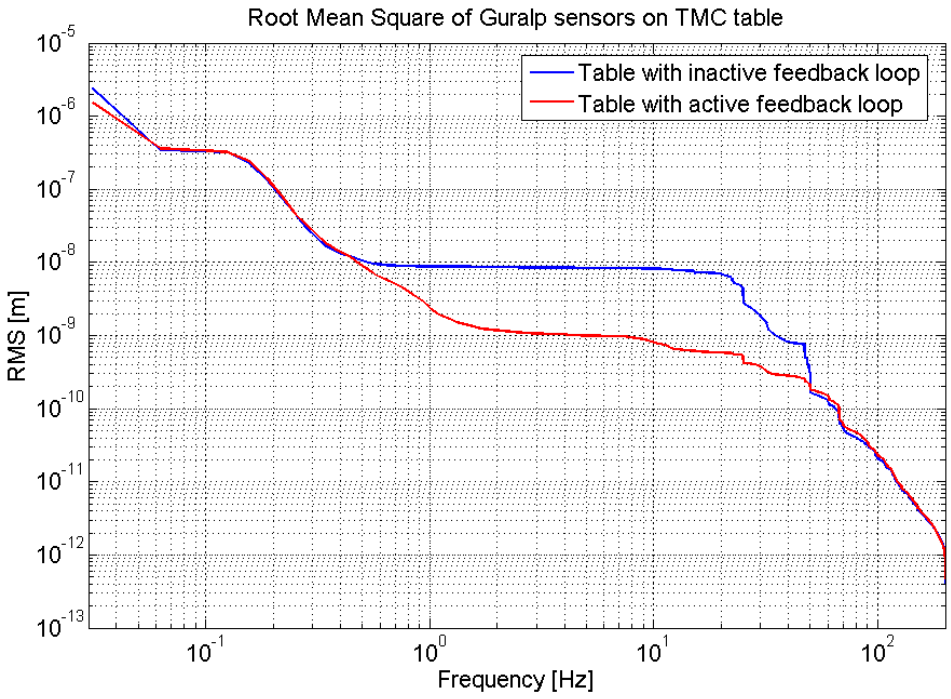

Figure 4: Displacement RMS of the ground measured by the Güralp sensor on top of the table. The two curves show the result for a measurement on the inactive table and on the active table.

Table 2: Measured and calculated eigenfrequencies of the free-fixed aluminium beam.

	1	2	3	4	5	6
Mode description	Z - Flexion	Y - Flexion	Z - Flexion	Z - Flexion	Torsion	Y - Flexion
Experimental frequencies	16 Hz	72 Hz	97 Hz	269 Hz	281 Hz	428 Hz
Numerical frequencies	16 Hz	74 Hz	102 Hz	286 Hz	302 Hz	456 Hz

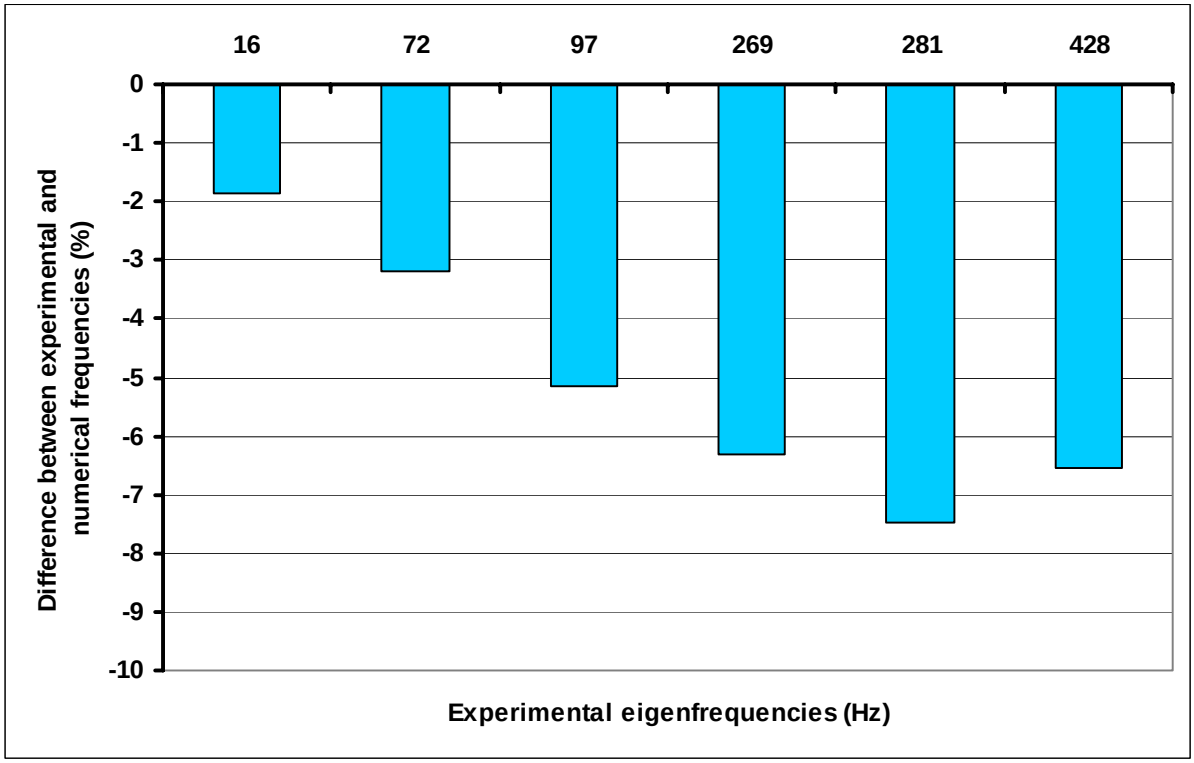

Figure 5: Comparison bar graph of measured and calculated frequencies.

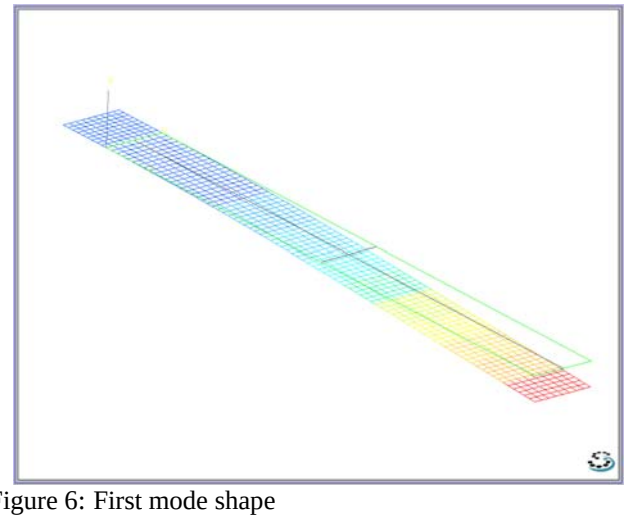

Figure 6: First mode shape

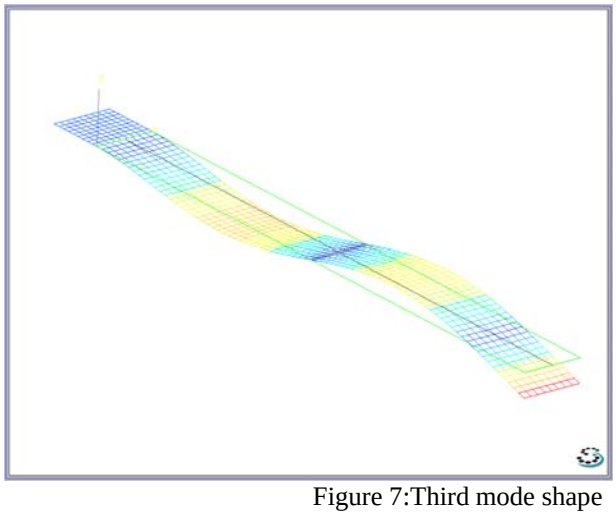

Figure 7:Third mode shape

Note that, in order to obtain better results in terms of frequency, the simulation should include the model of the clamping system, which does not ideally clamp the different degrees of freedom of the structure. As a result, the modelled beam is stiffer than the experimental one. In addition, damping is not taken into account in the model for this calculation. These are the reasons why the computed frequencies are higher than the experimental ones.

Dynamic response

This kind of simulation is used to get the structural response (in acceleration, velocity or displacement terms) under an external perturbation. In the case of this study, the excitation is the ground acceleration as a function of time. The results are obtained from the computation of the fundamental equations of motion. In order to solve the system made of differential equations, SAMCEF uses the implicit iterative scheme of Newmark. Finally the results are, for instance, accelerations or displacements along the structure, as a function of time.

The model used to perform this simulation is the same as for modal analysis, except that it is now possible to introduce structural damping. An ad doc value of 0.1% of damping was introduced for the first two modes.

The aim of this simulation is to compare the numerical prediction of the motion of the free beam extremity with the experimental one. The latter is measured with the Endevco accelerometer. Therefore, a lumped mass of 830g, located at the beam's edge, is introduced in the model to simulate the accelerometer when computing the dynamic response.

The results of the simulation are given in figure 8. Acceleration of the clamping system as measured, (red curve), and acceleration of the free extremity of the beam (black curve) as computed, are superimposed in order to compare their amplitudes. The duration of the analysis is 8 seconds (X-axis), whereas the acceleration scale is 10^{-3} $m.s^{-2}$ (Y-axis).

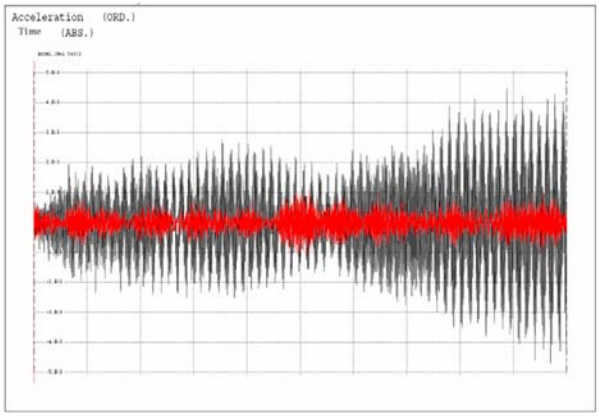

Figure 8: Acceleration calculated on the free-end of the beam (black curve) when excited by the acceleration on the clamping measured by an accelerometer (red curve).

Note that measured and calculated accelerations correspond to the vertical Z-axis component. Thus only Z-flexion modes are excited. Moreover, acceleration is amplified along the fixed-free beam. The same conclusion could be made for velocity and displacement along the structure.

Finally, the next step consists in the comparison between the numerical predictions (previous results) with the experimental dynamic response.

COMPARISON BETWEEN VIBRATION MEASUREMENTS AND SIMULATION

The measurements are compared to finite element analysis. This will enable us to build mechanical models of our accelerator components and ultimately help in the design of the accelerator parts by optimizing the component, but also by optimizing the actuator, support and sensor position.

Dynamic response of the free-fixed beam

The accelerometer placed on the free extremity of the beam, measures the dynamic response (cf. test bench shown on Figure 1).

Peaks at 13Hz and 90Hz, shown on figure 9, correspond to the first two Z-flexion modes. That is why acceleration is greatly amplified along the structure.

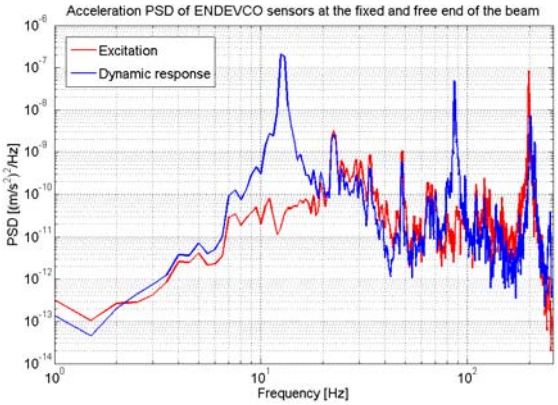

Figure 9: Red curve gives the excitation on the clamping and the blue curve shows the dynamic response.

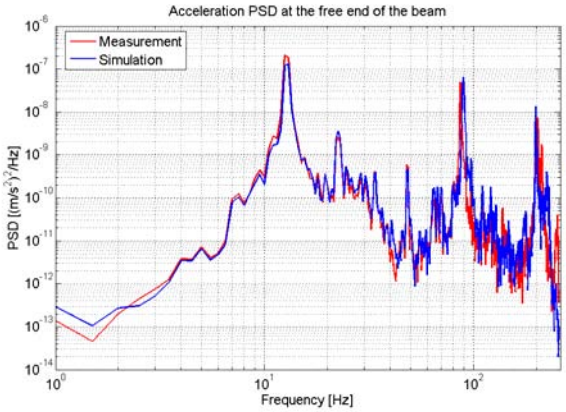

Figure 10: Measurement and simulation result on the free end of the beam using the input shown in figure 9.

Figure 10 shows the measurement obtained at the free end of the beam and the result of the simulation using as input the excitation as shown in figure 9. Stiffness has been adjusted, and some damping of 0.1% has been included. The agreement is impressive.

Influence of boundary conditions

Another possibility to damp vibrations of a structure is to add boundary conditions. Typically in the case of a fixed-free beam, it consists in blocking degrees of freedom, for instance in the middle of the beam.

The hereafter results show how to damp Z-flexion modes. The main hypothesis is that the amplitude of the excitation decreases as its frequency increases.

Then, the principle is to block Z-displacements of a beam section, by adding a new support, in order to have a "fixed-simple supported-free" beam. Therefore the Z-flexion eigenfrequencies are shifted to higher values than for a fixed-free beam (cf table 3 and Figure 11).

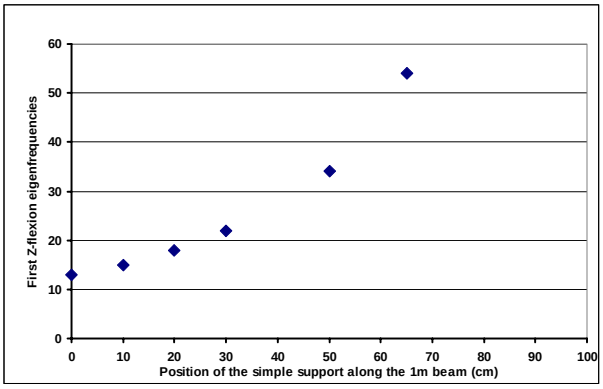

Figure 11: First eigenfrequencies for different distances between the clamping and the extra support.

Comparisons between simulations and measurements have been done for two distances of the support: 20cm and 50cm (cf. figure 12). Results of the simulation are in good agreement with measurements.

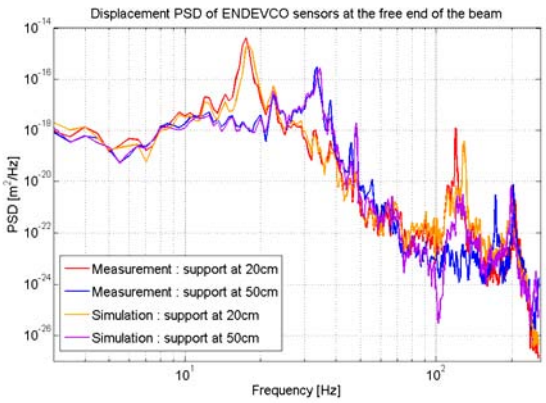

Figure 12: Displacement PSD of the free end.

It is also very interesting to display the results of the dynamic response of the new beam for the different positions of the support. Figures 13 and 14 show the displacement PSD for measurement and simulation respectively. For both cases, figures show an increase of amplitude for the first resonance peak of each configuration, especially when the support is located at 30cm, and not a reduction as expected. The explanation is the following. The excitation spectrum does not decrease uniformly when the frequency increases (cf. red curve on figure 15). Therefore the excitation peak at 22.5 Hz in the above spectrum excites any structure whose eigenfrequency is around 22.5 Hz. That is exactly the case of the beam with the support at 30cm, but not for the 20cm configuration, since its first eigenfrequency is equal to 18 Hz (cf. table 3). Consequently at 22.5 Hz, the response of the beam is more amplified when the support is fixed at 30cm than at 20cm.

The opposite comment could be made for the peaks at 18 Hz.

Note that these results are explained thanks to the simulation. For this given excitation spectrum (which does not decrease uniformly with frequency), the conclusion could be that, according to figure 13, a beam with no additional support is a better option than with additional support at 30cm, but would not be as efficient as a beam with additional support at 50cm.

In a general way, the best option is to prevent modes to be excited, by shifting them. Obviously, the excitation spectrum must be well known…

Table 3: First Z-flexion eigenfrequencies.

Localization of the simple support along the 1m beam	no additional support	10cm	20cm	30cm	50cm	65cm
First Z-flexion eigenfrequencies	13 Hz	15 Hz	18 Hz	22 Hz	34 Hz	54 Hz

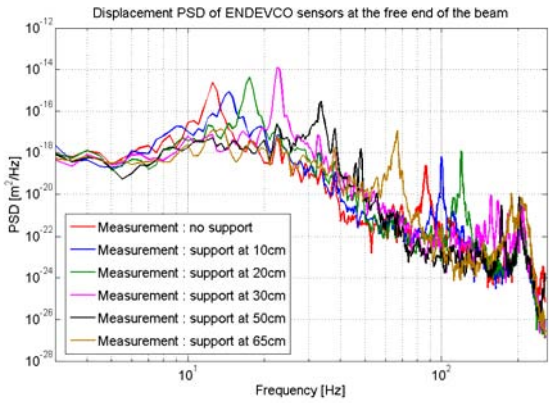

Figure 13: Displacement PSD (measurement).

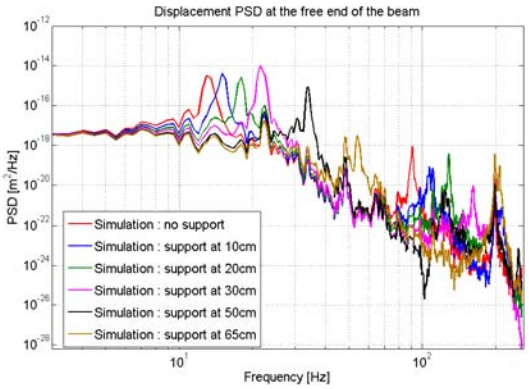

Figure 14: Displacement PSD (simulation).

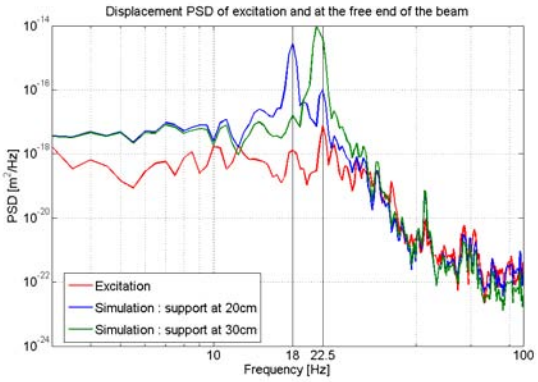

Figure 15: Displacement PSD (excitation and response).

VIBRATION REJECTION

Context

The aim of this study is to evaluate the performances of a new algorithm for disturbance rejection. In order to facilitate the analysis, a reduced-size mock-up is used. It should be noticed that due to limitations of PZT actuator capability and of PZT sensor sensitivity, performances are not as good as expected for the future linear collider. However it is possible to analyze the robustness of the algorithm with respect to model mismatch, to evaluate the computational burden and to get an idea of appropriate sampling rate since the frequency ranges are almost equivalent [4],[5].

Principle

The following reasonable assumptions are made to simplify the design of the control loop:

- main effort is devoted to peaks that appear in the spectral decomposition of the measured signal. These peaks either correspond to resonant modes of the mechanical structure or to particularly amplified modes of the disturbances
- for these peaks, the amplitudes of external disturbances are constant or at least slowly varying with respect to the dynamics of the system/controller
- the peak amplitudes are independent with respect to each other
- the dynamical behaviour of the system is not well known for these particular frequencies

The goal is to create an excitation signal with appropriate amplitude and phase such that the combination of excitation and disturbances is null at the sensor location.

In order to simplify the control scheme synthesis, instead of dealing with amplitude and phase, a decomposition on the (sine, cosine) basis is used. The main advantage is that the rejection problem becomes a linear one [6].

Since resonant peaks are independent, it is possible to treat them separately, and then to add all the contributions in order to get the excitation signal.

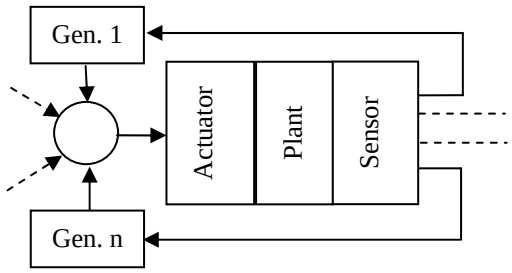

Figure 16. Principle of vibration rejection.

First all interesting frequencies are obtained by means of a Fourier analysis of the measured signal. Since it was shown by simulation tests that the algorithm is very sensitive to frequency deviation, an on-line procedure will be introduced to adjust these frequency parameters. Two methods are investigated: one of them is based on recursive least mean squares while the other deals with the PLL principle [7].

For each frequency under consideration, the problem consists in controlling a two-input two-output coupled system.

Since for each frequency, the disturbance is supposed to have constant characteristics, the control scheme is based on Proportional-Integral (PI) control loop. This means that control inputs, namely sine and cosine amplitudes of excitation signal, converge to constant value corresponding to the null values of sine and cosine amplitudes of output signal.

Because of coupling effects between both inputs and outputs, a simple PI scheme is not suitable. Introducing state spaces approach, it is possible to get the expected results through static state feedback.

The main functions of the control scheme, whose roles are explained later on, are shown in the following figure.

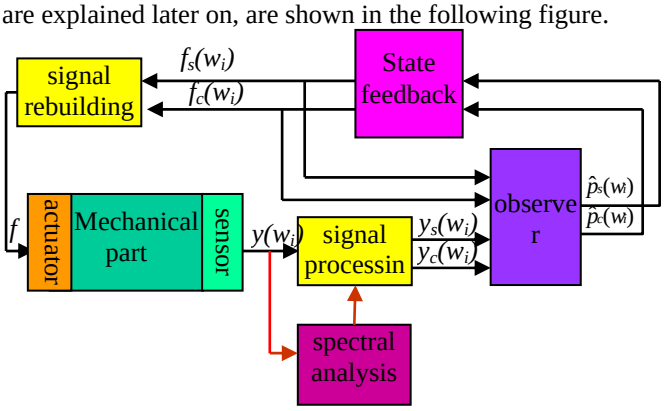

Figure 17. Organization of the algorithm.

A narrow band digital filter whose frequency bandwidth is centred at the considered frequency is used to clean the signal in the vicinity of the frequency.

Then the sine and cosine components are computed by minimizing a least squares criterion. Since this optimization problem is linear with respect to parameters, computations are fast.

The main block of the algorithm is an observer whose role is to estimate the amplitudes (as sine and cosine components) of a virtual disturbance acting on an arbitrary but well defined location in the plant, and creating the same effect on the output as the actual but unknown disturbance.

By means of a predetermined state feedback matrix gain, it is possible to compute the sine and cosine components of the control signal, on the basis of estimated virtual disturbance and matrix gain derived from transfers between virtual disturbance and output on the one hand and control input and output on the other hand.

Knowing sine and cosine components of the control signal for the frequency under consideration, it is easy to build the real-time corresponding contribution.

All these blocks are duplicated as many times as there are peaks to attenuate. Each block parameters are tuned according to the corresponding frequency. All the contributions are summed up in order to create the control signal which feeds the actuator.

Experimental setup

To test this rejection algorithm, a reduced-size mock-up is used (Fig. 18).

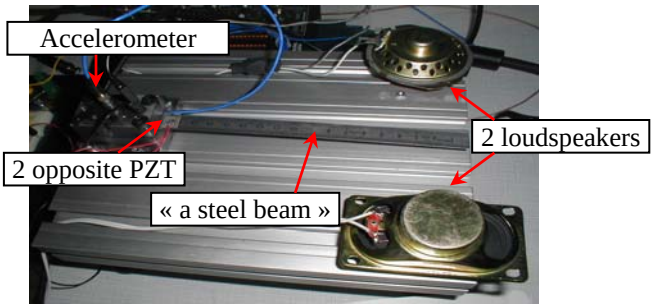

Figure 18. Mock up.

It is composed of:

- a steel beam
- two small loudspeakers as disturbance generators
- one PZT ceramic glued on one side of the beam is used as an actuator, (Fig. 19)
- another collocated PZT ceramic glued on the opposite side is used as a sensor.

Besides, a PC with Matlab software is used to prepare the control algorithm, by means of Simulink and XPC target toolboxes. The final program is downloaded to another PC which is connected to the plant via a National Instruments data acquisition board.

The small size of this experimental set-up induces higher frequency range, and consequently higher sampling rate. This is why, XPC target is used instead of Real Time Windows Target. However the feasibility of the procedure with this mock-up guarantees efficiency when dealing with larger sizes of plants. The actual dimensions were chosen because of easy use of PZT ceramics in the corresponding frequency range.

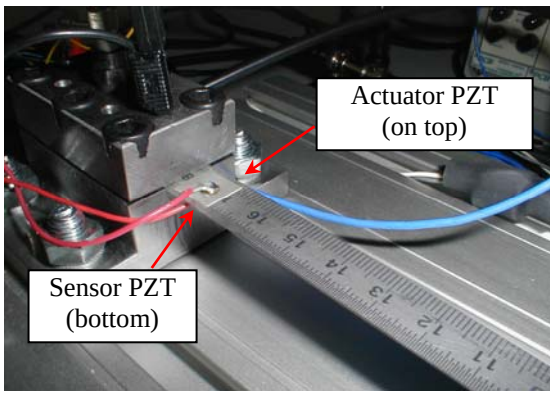

Figure 19. PZT used as actuator. Another PZT on the opposite side is used as sensor.

Results

Each loudspeaker is fed with a sinusoidal input. A rough harmonic analysis of the system output reveals six resonant modes in the frequency range under consideration: 13, 26, 28, 39, 67 and 82.5 Hz. The corresponding amplitudes are shown in figure 20. One could expect that some of the amplified frequencies come from harmonic components of the excitation inputs created by loudspeakers.

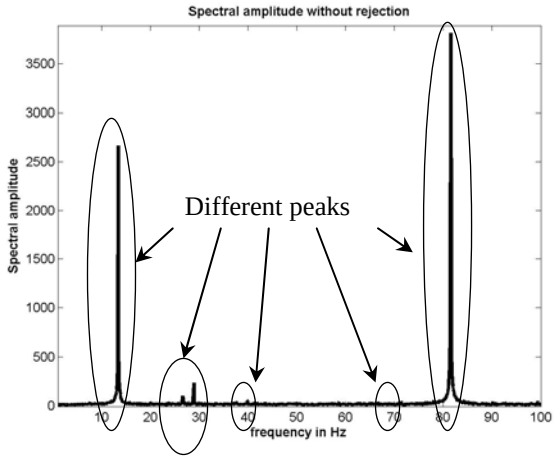

Figure 20. Frequency spectrum before rejection.

Then six parallel algorithms are activated to elaborate the six contributions of the control signal. When feeding the system PZT actuator with this disturbance, the new spectral decomposition shown in figure 21 is obtained. Note the difference of scale compared to figure 20.

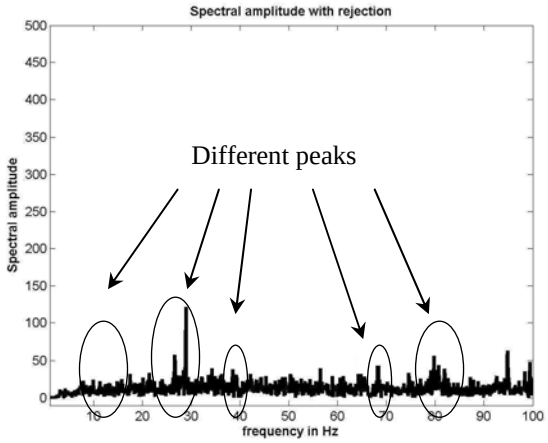

Figure 21. Frequency spectrum after rejection.

To get this result, the required excitation of the PZT actuator has to be as in the following figure.

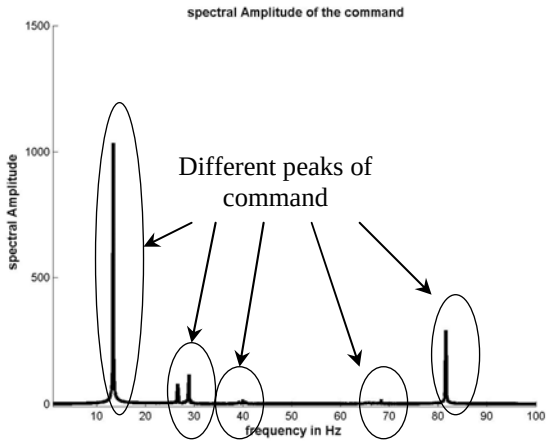

Figure 22. Frequency spectrum of the required PZT command.

Though not perfect, the result is fairly good:

- peaks are reduced
- no other peak is created

Since the amplitudes are not null, it is necessary to investigate and find some explanations. One of these could be a mismatch between frequencies used in sinusoidal signal generators and actual disturbance frequencies. This is due to quantification of the spectrum, which is related to the sampling rate.

CONCLUSION AND FUTURE PROSPECTS

The first step towards a feasibility analysis is to study the three major aspects of active stabilization separately. The velocity sensors that have been characterized on our mock-ups can measure ground motion down to 0.1Hz. The active stabilization table used in this study reduces ground motion from 10nm at 4 Hz to 1nm.

The mechanical modeling gives information about optimal location of sensors and actuators, as well as expected values of eigenmodes that must be considered first by the rejection system and is a powerful tool for further design of test benches and final focus quadrupole.

The six parallel algorithms of the feedback loop reduce considerably the resonance peaks of the reduced-size mock-up while not creating new resonance peaks. More investigation is however needed. This algorithm will be applied to stabilise a larger mock-up, leading to more realistic experimental conditions. In future tests, the active table will globally stabilise in a range of frequencies from 0.5Hz to 50Hz whereas the feedback loop will compensate single strong resonances.

A new mock-up is currently being developed that will have a geometry closer to a final focus quadrupole. Simulation will be used to simulate the whole system: the feedback loop, the sensors, the actuators and their most efficient location. Measurements will be done to validate the whole system in view of active stabilisation for a future linear collider.

REFERENCES

[1] C. Adloff, B. Bolzon, F. Cadoux, N. Geffroy, S. Géneté, C. Girard, A. Jeremie, Y. Karyotakis, L. Brunetti, J. Lottin, “Vibration stabilization for the final focus magnet of a future linear collider”, Proceedings REM 2005, Annecy-le-Vieux, July 2005.

[2] S. Redaelli, R. Assmann, W. Coosemans, G. Guignard, D. Schulte, I. Wilson and F. Zimmermann, “CLIC magnet stabilization studies,” Proceedings of LINAC2004 TUP88, August 2004, pp. 483–485.

[3] S. Redaelli, “Stabilization of Nanometre-size Particle Beams in the Final Focus System of the Compact Linear Collider (CLIC),” PhD Thesis, Université de Lausanne, 2003, 194 pages, also as CERN-AB-2004-025.

[4] J. Lottin, M. Corduneanu, “Vibration Reduction of magnet quadrupole for beam positioning within a CLIC system”, IMAACA’2004, Gênes, October 2004.

[5] J. Lottin, F. Formosa, V. Cozma, “Experimental evaluation of a new active vibration algorithm”, World IFAC Congress, Praha, July 2005.

[6] M. Bodson and S.C. Douglas, "Adaptive Algorithms for the Rejection of Sinusoidal Disturbances with Unknown Frequency"

[7] B. Wu and M. Bodson, “Multi-channel active noise control for periodic sources-indirect approach".

Prototyping and beam tests of beam-feedback hardware for ILC collision optimisation

R. Barlow, M. Dufau, A. Kalinin
Daresbury Laboratory
G. Myatt, C. Perry
Oxford University
P. Burrows, G. Christian, C. Clarke, H. Dabiri-Khah,
A. Hartin, S. Molloy, C. Swinson, G. White
Queen Mary, University of London
C. Adolphsen, R. Arnold, J. Frisch, L. Hendrickson, K. Jobe,
T. Markiewicz, D. McCormick, J. Nelson, M. Ross, A. Seryi, S. Smith,
T. Smith, M. Woodley, M. Woods
Stanford Linear Accelerator Center

20 October 2005

Abstract

The small vertical spot size at the International Linear Collider (ILC) will make the luminosity very sensitive to ground motion and facilities noise. Three generations of prototype feedback system have been developed and tested to correct for the relative beam misalignment caused by this. These systems were based on fast analogue beam position monitor (BPM) processors aimed at correcting the beam within the short ($\sim$ 270 ns) bunch crossing of the warm (X-band) machine. Future generations of feedback prototype will be aimed towards the cold (superconducting) ILC design, where a much longer bunch train of $\sim$ 1 ms would allow the use of a digital processor to employ more sophisticated feedback algorithms. Details and results from the first three prototype systems are discussed and the development of a digital feedback processor for future tests is described. Plans to irradiate a BPM with background particles, of similar flux to that expected in the ILC interaction region, are also discussed.

Introduction

The Interaction Point (IP) feedback system is recognised to be the last line of defence against relative beam misalignment at the International Linear Collider (ILC). To reach the luminosity required for precision physics at the ILC the colliding beams will need to be focused down to a few nanometres vertical spot size at the IP. This makes the beam position at the IP very susceptible to ground motion and facilities noise, and hence the luminosity would be very much reduced if uncorrected.

Fortunately, the electromagnetic effects of the colliding bunches missing one another provides valuable information on their relative misalignment at the IP. A displaced bunch arriving at the IP will see the opposite charge distribution of the opposing bunch and will be deflected towards the opposing bunch. From measuring the resulting change in angle, the initial spatial offset between the two bunches can be calculated, and so this information can be used to correct the position of later bunches prior to arrival at the IP.

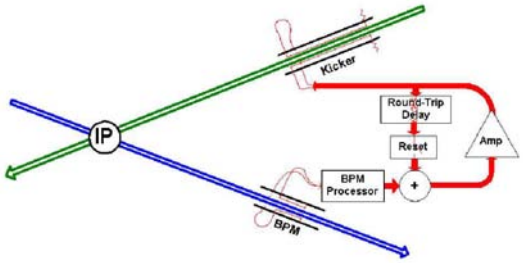

Figure 1: The IP Feedback System

A schematic for the IP feedback system is shown in Fig. 1 [1]. A beam position monitor (BPM) is used downstream of the IP in either the positron or electron extraction line, to measure the magnitude of the beam-beam kick at the IP, which in turn gives information on the relative offset of the two bunches. This information is then processed by a super-fast BPM processor and passed on to a fast amplifier used to drive a fast rise-time kicker to correct the vertical position of the incoming bunch train into the IR. To ensure that a significant proportion of the luminosity is not lost, the time taken to correct the beam, or system latency, including the delay in the electronics, signal propagation time in the cables and time-of-flight between the kicker and BPM, must be significantly shorter than the time-of-flight of the train itself.

One further feature of such a system is the inclusion of a round-trip delay loop, without which the system would not work. Without the delay loop, after one complete latency period the beam would move back to its original position as the processor would measure a zero position offset at the BPM, which would take take one further latency period to re-correct. In this way the system would oscillate between corrected and uncorrected position settings. The inclusion of the delay loop prevents this from occurring by adding in the drive signal from previous latency periods into subsequent periods, with the provision that the delay loop propagation time must be matched to the system latency.

Several prototype systems have so far been demonstrated at the NLC Test Accelerator (NLCTA) and the Accelerator Test Facility (ATF) at KEK. These experiments have been dubbed Feedback On Nanosecond Timescales (FONT). A detailed de-

scription of the feedback system setup for FONT3 at the ATF is given later.

The first three generations of prototype feedback systems were geared towards the more challenging requirements of the 'warm-LC' design. In this scenario the time structure of 192 bunches, separated by 1.4 ns, requires a very low latency feedback system to avoid significant luminosity loss. In order to correct the beam within a reasonable portion of bunch-train there is not the opportunity to employ sophisticated algorithms or include information from other upstream beam feedbacks, and the only feasible solution is to use analogue electronic processing.

In the wake of the ITRP decision in 2004, the ILC IP feedback system can now be designed solely to the requirements of the 'cold' machine. In this design, the ∼1ms train, with ∼300ns bunch spacing, allows the latency requirements to be greatly relaxed with respect to the warm machine. A longer latency is ideally suited to digital processing techniques which would support the use of more sophisticated algorithms to recover an even greater proportion of the luminosity. A very low latency feedback system may, however, still be suitable for CLIC.

One further aspect of study related to the FONT project is that of BPM performance in a high e^+e^- pair background flux. It is intended to study this in a test beam at End Station A (ESA) at SLAC, to understand the effects of pair flux on the BPM signal noise and to verify the long-term stability and performance of the BPM.

Summary of FONT Analogue Systems

The first two prototype feedback experiments, FONT1 and FONT2, were installed at the NLCTA with a 65 MeV beam, 170 ns train length, and 87 ps bunch spacing. FONT1 [2], which ran in 2001 and 2002, was the first demonstration of such a closed-loop system and achieved a latency of 67 ns. This system gave a 10:1 beam position correction ratio, in that the system could make a correction down to a factor ten times smaller than the original beam offset. FONT2 [3], in 2003 and 2004, was an improved demonstration with a latency of 54 ns. This system employed logarithmic amplifiers for real-time charge normalisation, a beam-flattener to straighten the train profile, and the three-stage tube amplifier of FONT1 was upgraded to a more compact solid state amplifier.

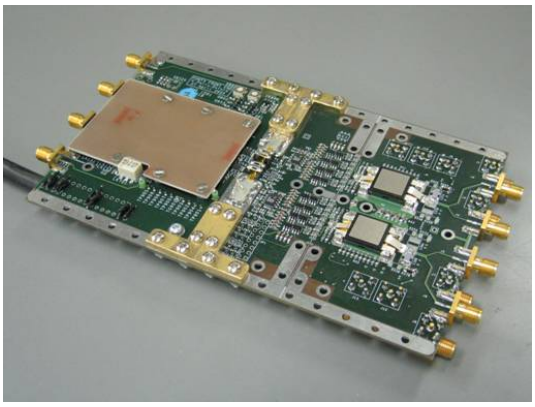

Figure 2: FONT3 solid-state amplifier with integrated feedback

The third generation experiment, FONT3 [4] in 2004 and 2005, was installed at the ATF, to take advantage of the low emittance beam extracted from the ATF

damping ring, with a beam energy of 1.3 GeV, a train length of 56 ns, and a bunch spacing of 2.8 ns. The aim of FONT3 was to provide an ultra-fast demonstration of feedback with a latency goal of 20 ns. This system used three stripline BPMs in the ATF extraction line, the FEATHER adjustable gap kicker, and a new high-power solid-state amplifier with integrated feedback circuit, Fig 2, providing approximately the same drive power as would be required at the ILC. Fig. 3 shows a schematic of the experimental arrangement of the components on the extraction line. The BPM ML11X, downstream of the kicker, is the feedback BPM which passes the signal to the super-fast BPM processor and amplifier. ML12X and ML13X are two witness BPMs.

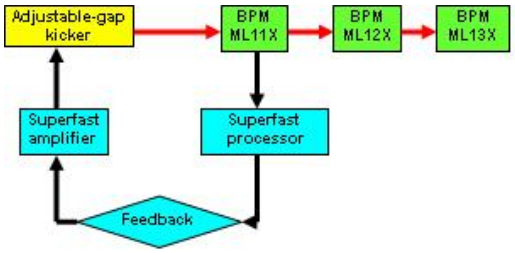

Figure 3: FONT3 schematic

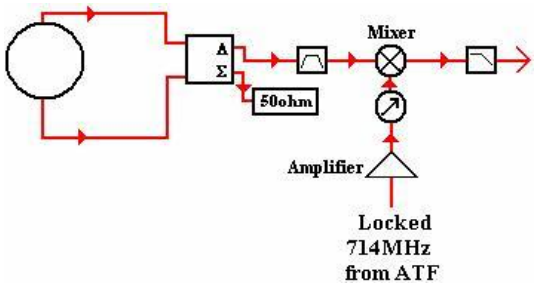

Figure 4: FONT3 processor schematic

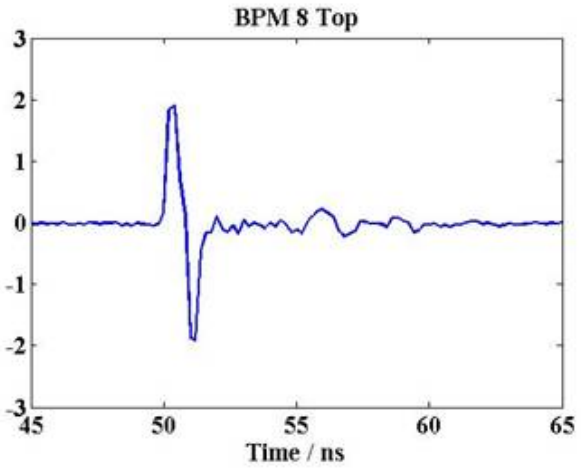

Figure 5: Raw output from top BPM stripline

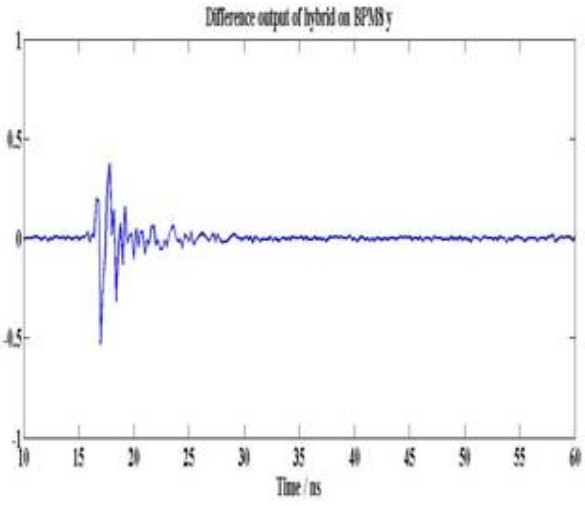

Figure 6: Output from the hybrid device

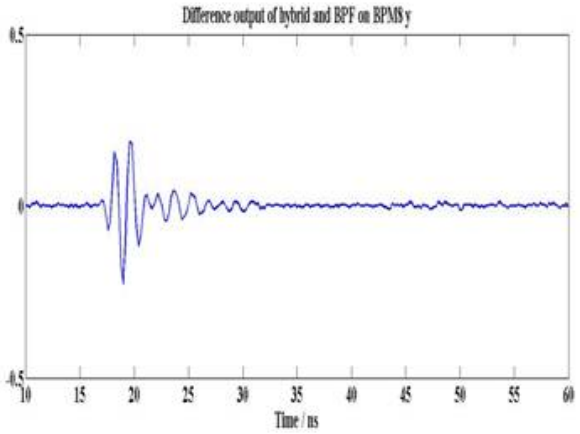

Figure 7: Output from the band pass filter

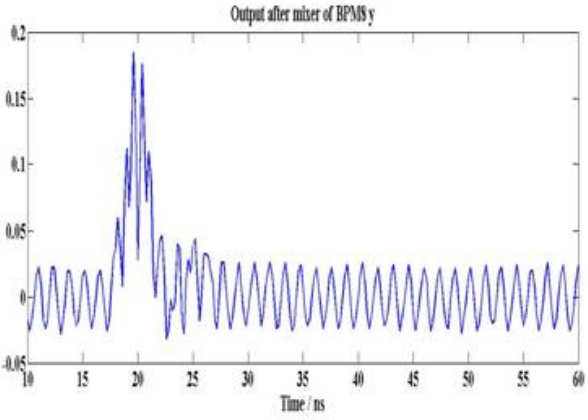

Figure 8: Output from the mixer

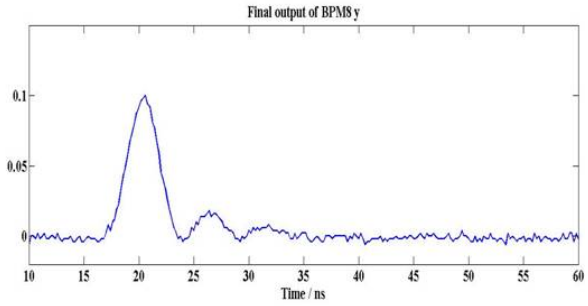

Figure 9: Output from the low pass filter

The latency budget of 20 ns for the FONT3 system was chosen so as to allow two complete latency periods and most of the third period to be seen, to demonstrate the operation of the delay loop. The irreducible latency was estimated to be 10 ns, composed of the 4 ns time-of-flight of the beam from the kicker to the BPM and a 6 ns signal propagation time in the cables. The remaining 10 ns for the electronics was apportioned equally between the BPM processor and amplifier, at 5 ns each.

Fig. 4 shows a schematic of the BPM processor, and Figs. 5–9 show the signals at various stages of processing for single bunch data in December 2004, which were used to demonstrate that the operation of the processor was as expected. The raw signals from the BPM striplines comprise of two delta function impulses separated by twice the length of the strips (12 cm for the ATF extraction line BPMs), as shown in Fig. 5. The top and bottom signals are then subtracted using a hybrid device, Fig. 6, the sum output of which is terminated to a 50 ohm impedance, as with a latency goal of 20 ns there is not enough time to normalise by the charge. The difference signal is then band-pass filtered using a 3 pole Bessel filter centred on 714 MHz, Fig. 7. This signal is then mixed with a 714 MHz local oscillator signal locked to the ATF, Fig. 8, to bring the signal to baseband, and then low-pass filtered using a 3 pole Chebyshev filter with 170 MHz cutoff, to remove the high frequency component produced by the mixer, Fig. 9.

Figs. 10–16 show some results for the latency, calibration, and resolution of the BPM processor for 20 bunch data in March 2005. The latency of the processor was

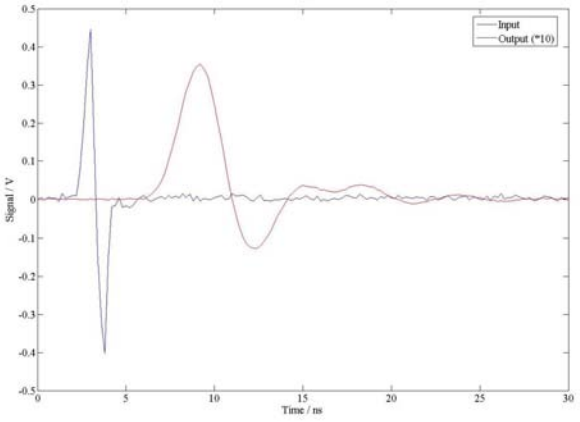

Figure 10: Latency of the BPM Processor. Raw BPM signal (blue), processor output (red).

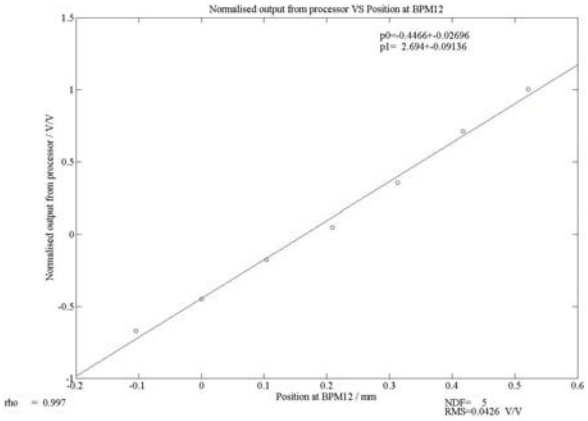

Figure 12: Calibration of BPM12

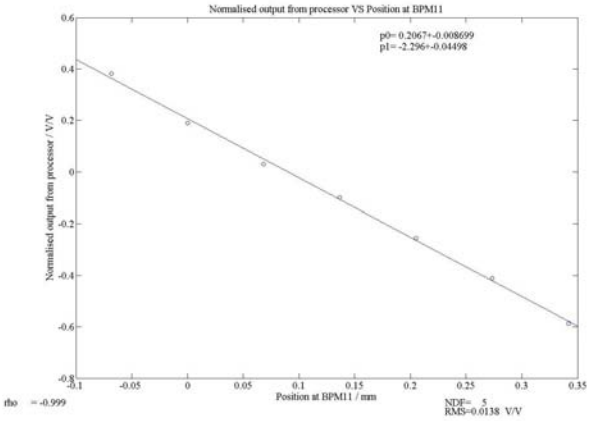

Figure 11: Calibration of BPM11

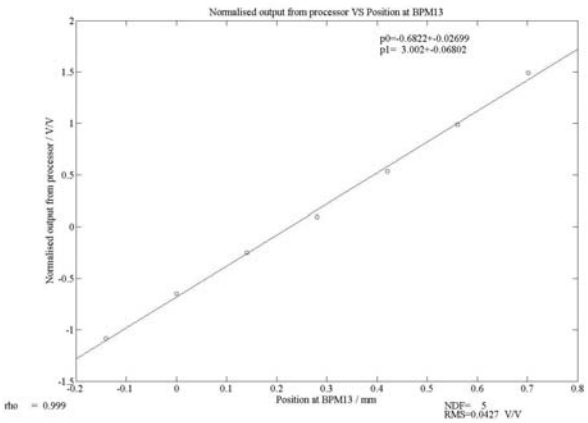

Figure 13: Calibration of BPM13

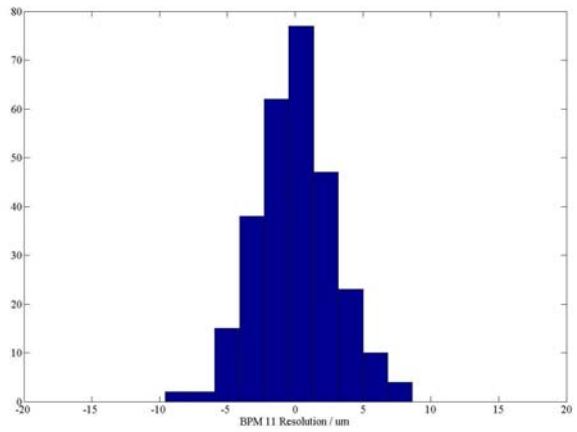

Figure 14: Resolution measurement for BPM11

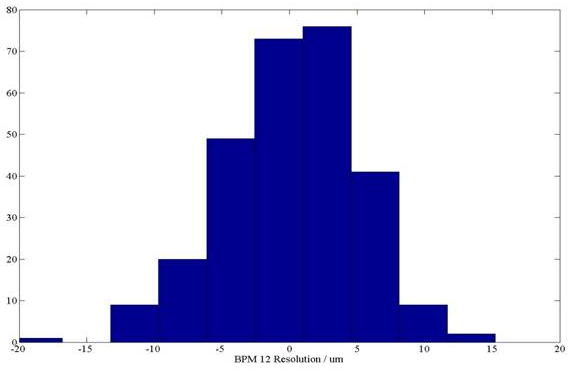

Figure 15: Resolution measurement for BPM12

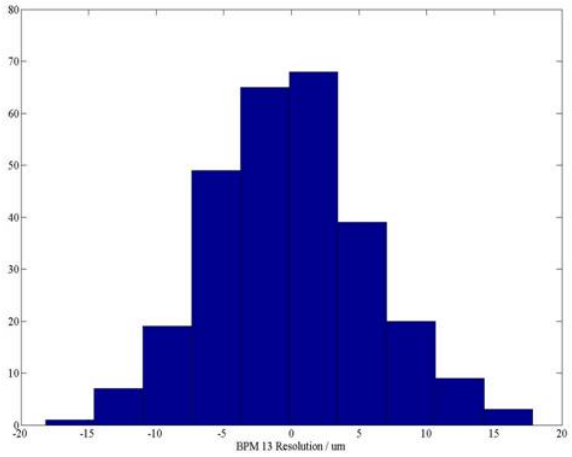

Figure 16: Resolution measurement for BPM13

measured to be 4.3 ns, by measuring the difference in the time of arrival between the peak of the raw stripline signal and the 1/e point of the processor output pulse. The processors were calibrated by moving the beam to seven known positions using the ATF orbit BPMs, and fitting to the output of the processors. The calibration data for the three BPMs are shown in Figs. 11–13, and a good fit to the data can be seen in each case. The resolution of the BPM processors was measured to be between 3 and 5 microns. Figs. 14–16 show the distribution of residuals of the measured position in each BPM compared with that predicted from the other two BPMs for 240 pulses.

Figs. 17–19 show the results of the closed loop feedback system. In each case the top plot shows the beam position output of the BPM processor with the feedback and delay loops turned off, for the beam at five different position settings, averaged over 40 pulses per position setting. The maximum

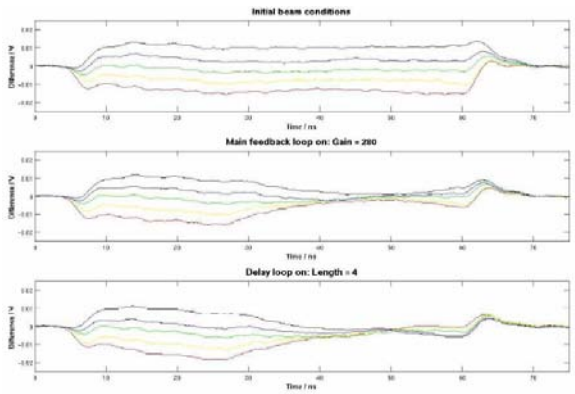

Figure 17: Operation of the feedback system with nominal gain setting

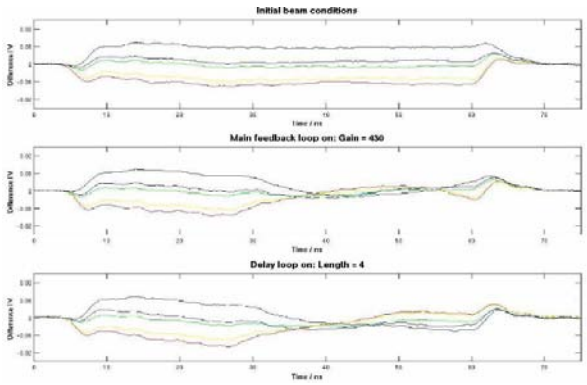

Figure 18: Operation of the feedback system with high gain setting

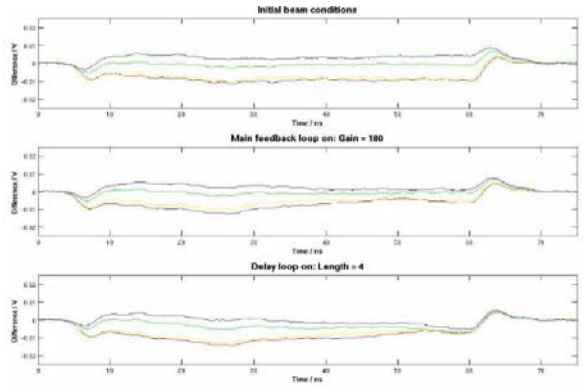

Figure 19: Operation of the feedback system with low gain setting

excursion of the beam between position settings is ∼200 μm vertically. The 56 ns train duration is clearly visible in the plot. The middle plot in Fig. 17 shows the same five position settings but with the feedback loop switched on with a nominal feedback gain setting of '280', see [5]. The beam positions look similar to those of the plot above for the first ∼20 ns, which corresponds to the first latency period. After which the feedback system begins to work and the beam positions converge towards zero, although it is not until about 50 ns that the beam position is fully corrected. The system latency can be estimated from this plot to be ∼ 23 ns. After the second latency period the beam begins to return to its initial displacement in the absence of the delay loop. With the nominal delay loop gain and nominal delay loop length setting of '4', Fig. 17 lower plot, it can be seen that a different behaviour occurs, instead of remaining corrected for the third latency period the beam positions appear to cross over the axis. This is understood to be the effect of using too high a gain in the delay loop.

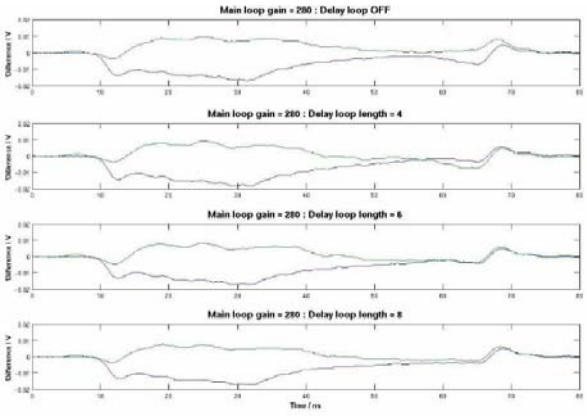

Figure 20: Variation of delay loop length on the feedback operation

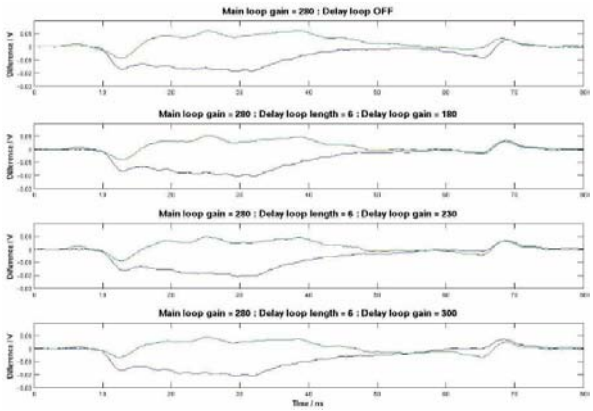

Figure 21: Variation of delay loop gain on the feedback operation

The three parameters which could be used to optimise the feedback system performance were the main feedback loop gain, delay loop length and delay loop gain. Figs. 18 and 19 show the effect of using too high and too low main loop gain respectively. In Fig. 18 the higher gain causes the beam positions to converge faster to zero but also to overshoot zero within the second latency period. This is exacerbated by turning on the delay loop with unoptimised settings. Using too low a main loop gain results in the system never being able to correct the beam to zero. With the inclusion of the delay loop eventually the positions converge to zero, but only at the end of the third latency period.

Figs. 20 and 21 show the variation of delay loop length and gain for just the two outer most beam initial beam positions, with a main loop delay setting of 280. In Fig. 20 a delay loop length setting of '6' appears to be optimal, as the effect of having a shorter or longer delay loop is to over or under correct the beam respectively. Fig. 21 shows the effect of varying the delay loop gain for with the delay loop length held constant at setting '6'. In this case it appears that the best correction is given by using a delay loop gain of '180', as higher gains appear to over-correct the beam. Although the results are understood and it was verified that the system behaves as expected, unfortunately, due to time constraints, it was not possible to fully optimise all three parameters for the feedback system.

Development of Digital Feedback Processor and Beam Tests

The next generation of prototype feedback system, FONT4, will be a first step towards demonstrating a representative IP feedback system for the 'cold' ILC. This system will be tested at the ATF and its future upgrade ATF2 [6], where the installation of a new fast extraction kicker will give an ILC-like time structure to the beam in the extraction line, with ∼150 ns bunch spacing, initially with 3 bunches per train and later up to 20 bunches. FONT4 will employ a digital processor which will support the use of more sophisticated algorithms than an analogue system, which will eventually be used to incorporate information from other upstream feedback systems and beam monitors.

A modified FONT3 front-end BPM processor will be used to supply the digital processor with the analogue position (and possibly charge) inputs. These modifications will consist of changing the filtering in an attempt to broaden the output pulse of the processor to aid sampling by an ADC, at the expense of increasing the

latency. The system will also consist of a modified FONT2 solid-state amplifier with 300 ns output pulse, and the FEATHER adjustable-gap kicker will be used as for FONT3. Fig. 22 shows a sketch of the proposed layout for the digital processor board. The proposed solution is centred around the use of a Field Programmable Gate Array (FPGA), of which the Xilinx Virtex 4 has been selected, with AD6675 ADCs and AD9744 DACs. The FPGA will take a clock signal derived from the ATF timing system. On-board ROM and RAM will be provided for memory storage and retrieval, and three different interfaces, JTAG, serial, and USB, are being considered for interfacing with the device for programming and delivering output data for monitoring.

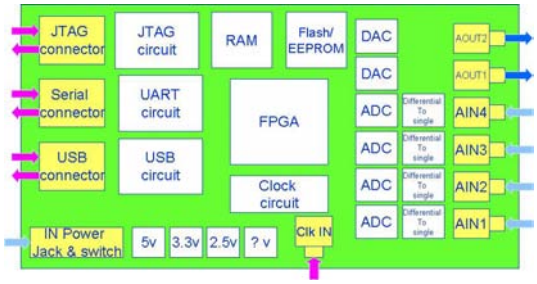

Figure 22: Schematic of FONT4 digital processor board

The aim of FONT4 is to provide stabilisation of the third bunch at the micron level, which is a future requirement for ATF2. To achieve this the latency budget (see Table 1) has been set at just shorter than than the bunch spacing. The irreducible latency of 22 ns derives from a 7 ns time-of-flight delay from the kicker to the feedback BPM, assuming a 2 m lever-arm, and a signal propagation time of 15 ns due to cable delays. The latency budget for the modified analogue processor is 10 ns, the amplifier 40 ns, and the digital processor ∼68 ns, based on ∼40 ns for ADCs and DACs, 3 ns for FPGA input/output, and 25 ns for the FPGA processing, assuming 8 clock cycles. This gives an total latency of ∼118 ns from the electronics and an overall latency of ∼140 ns. Currently the design of the digital board is underway using Mentor Graphics software and the development of the FPGA programming has begun using Xilinx ISE foundation software.

One further important area of work for the IP feedback system is to characterise the system performance in the e^+e^- pair and photon backgrounds expected in the ILC interaction region (IR). Studies have been made of the pair flux incident upon the strips of the feedback BPM in a GEANT model of the IR, for both the 2mrad and 20 mrad crossing angle designs [7]. One aim of these studies is to optimise the layout of the IR, and such parameters as the position of the BPM and the first quadrupole, QFEX1, in the extraction line, L*, and the detector magnetic field, have been varied.

The effect on the number of hits on the BPMs as a function of azimuthal angle around the beampipe and as a function of the different proposed machine parameter sets has also been studied. Fig. 23 shows that with certain parameter sets, especially the high luminosity schemes with large crossing angle, up to 10^4–10^5 low energy pairs may be hitting the strips. This is a possible problem for the BPM performance as it estimated that for every charge absorbed or knocked out from a stripline, a 1 pm error in resolution may be observed [8].

It is necessary, therefore, to characterise

Time of flight: kicker to BPM	7 ns
Signal propagation delay: BPM to kicker	15 ns
Irreducible Latency	22 ns
BPM analogue processor	10 ns
Digital processor	∼68 ns
Amplifier	40 ns
Electronics Latency	∼118 ns
Total Latency	∼140 ns

Table 1: Latency budget for FONT4

the performance of a stripline BPM in a background similar to that expected in the ILC IR, to study the noise on the BPM signals and ascertain the long-term survivability and performance. It is also planned to undertake electromagnetic modelling of the BPM stripline to gain theoretical understanding of the predicted degradation of performance in the pair background.

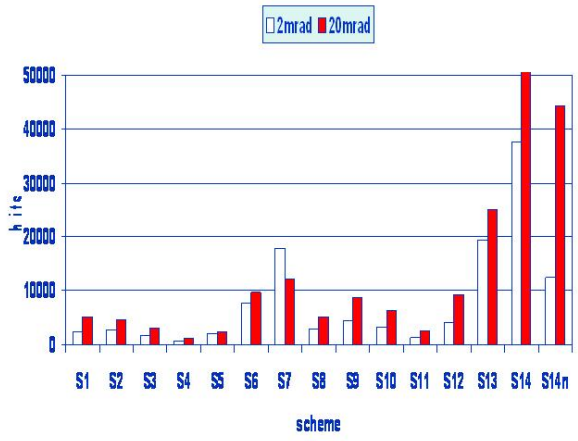

Figure 23: Number of hits at feedback BPM for different proposed machine parameter schemes

It is planned to study these effects in a test beam at End Station A at SLAC, as part of Stage 2 of the planned ILC beam tests, starting in the summer of 2006 [9]. The plan is to create the pair background by firing the 30 GeV beam into a fixed target radiator situated in the Beam Switchyard (BSY) to reproduce the primary flux of pairs which go on to scatter off material in the IR in the GEANT model. A further option is to build a mechanical mock-up of the material, i.e. masks, in the forward region of the IR, to realistically simulate the production of secondary and tertiary electrons and positrons which go on to hit the BPM itself.

Two options for the radiator have been suggested, a thick target and a thin target. The purpose of the thin target is to add a radiative tail to the beam to simulate the low energy background. This is envisioned to be 5–10 % X_o of carbon and would be placed in the A-line near to the BPM under test. The function of the thick target is to create a spray beam of low energy electrons at the entrance to the A-line, and would most likely re-use an existing 40 % X_o Beryllium target in the BSY, see [10]. This option would give greater control over the flux and energy of the electrons in the spray beam. One could also think of using a combination of both the thick and thin tar-

gets to create the required flux to simulate the ILC IR.

Fig. 24 shows a sketch of the proposed layout of the test beamline at ESA, for stage 1 and stage 2. In stage 2 the FONT BPM will be located in the IR mock-up region upstream of the SLD R-20 module. A detector will be required to monitor the flux in the spray beam, and for this a Cherenkov detector upstream of the BPM has been proposed. Figs. 25 and 26 show the results of simulations using GEANT for the thick target. Fig. 25 shows the beam energy distribution after the Be target. A small peak can be seen at the initial beam energy of 30 GeV as well as a larger peak at low energies. The flux of these particles accepted into the A-line as a function of the A-line momentum setting is shown in Fig. 26, for a range in initial beam energies between 7 and 30 GeV. It can be seen that two variables can be used to create the desired flux of low energy pairs, the beam energy and the A-line momentum setting.

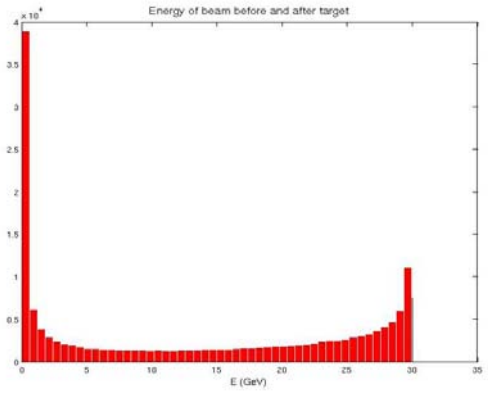

Figure 25: Energy distribution of spray beam after Be target in BSY

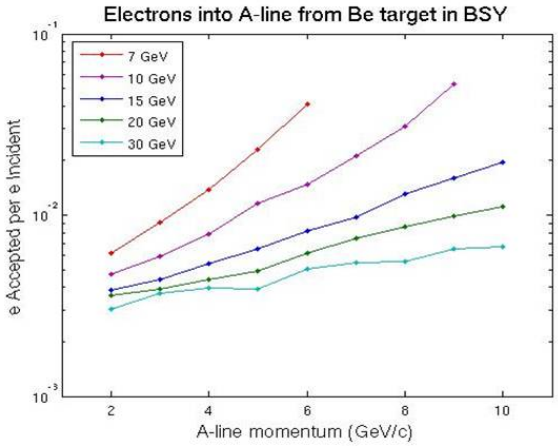

Figure 26: Flux of electrons accepted into the A-line as a function of momentum setting

Summary and Future Prospects

A demonstration of ultra-fast beam feedback system with delay loop, FONT3, has been made at the ATF, with a measured latency of 23 ns. The main loop gain, delay loop length, and delay loop gain were varied, and the system was shown to behave as expected.

Development is underway for the next generation of prototype feedback system, FONT4, which will be designed for the cold ILC parameters and tested with an ILC-like beam at the ATF and ATF2. First tests of a modified front-end processor will be made in December 2005, with tests of the digital processor in spring 2006, and the complete system with amplifier and kicker in summer 2006. In addition beam tests of BPM long-term performance and survivability in a pair background will begin at ESA in summer 2006.

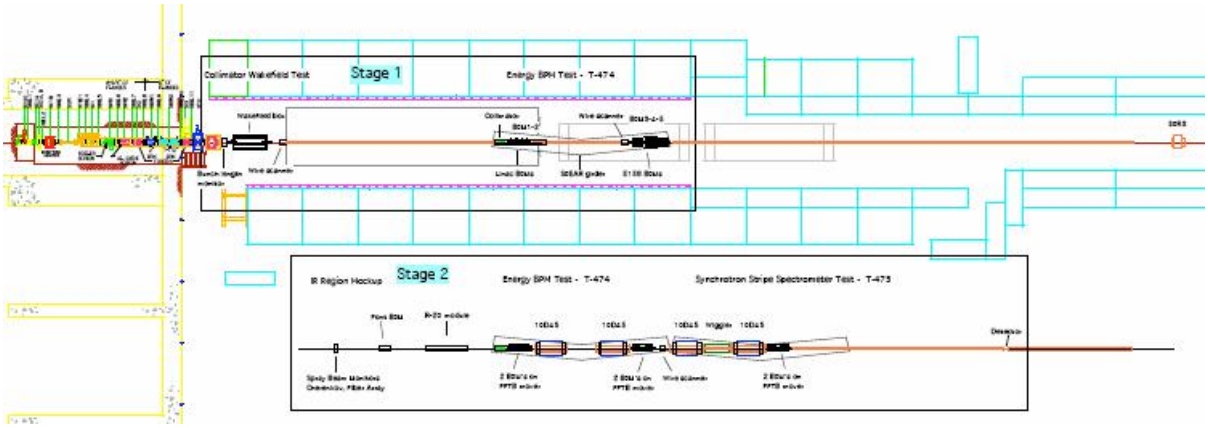

Figure 24: Proposed layout for stage 1 and stage 2 of the ILC beam tests at SLAC ESA

Acknowledgements

We thank the technical staff of SLAC and KEK accelerator departments for their operational support for this work.

This work is supported by the Commission of the European Communities under the 6th Framework Programme "Structuring the European Research Area", contract number RIDS-011899.

References

[1] S. Smith, *Design of an ILC Intrapulse Feedback System*, March 2001, Linear Collider Collaboration Tech Notes LCC-0056 03/01

[2] P. Burrows, *Feedback on Nanosecond Timescales (FONT): Results from the First Beam Tests at the NLCTA at SLAC*, Proceedings of PAC, Portland, Oregon, May 2003, p.687

[3] P. Burrows *et al*, *Nanosecond-timescale Intra-bunch-train Feedback for the Linear Collider: Results of the FONT2 Run*, Proceeding of EPAC, Lucerne, July 2004, p.785

[4] P. Burrows *et al*, *Tests of the FONT3 Linear Collider Intra-train Beam Feedback System at the ATF*, Proceeding of PAC, Knoxville, Tennessee, May 2005, p.1359

[5] S. Molloy, *A Fast Feedback System Designed to Maintain Luminosity at a Linear Collider*, PhD Thesis, Queen Mary, University of London, in preparation

[6] ATF2 Collaboration, *ATF2 Proposal*, August 2005, http://lcdev.kek.jp/ILC-AsiaWG/WG4notes/atf2/proposal/public/ATF2proposal1.pdf

[7] A. Hartin, *Feedback BPM background environment and BDS design*, Talk given at Snowmass, August 2005, http://alcpg2005.colorado.edu:8080/alcpg2005/program/accelerator/WG4/aug18_hartin_fbk_bpm.ppt

[8] S. Smith, Private Communication.

[9] M. Woods *et al*, *A Test Facility for the International Linear Collider, at SLAC End Station A for Prototypes of Beam Delivery and IR Components*, May 2005, SLAC-PUB-11180

[10] R. Arnold and T. Fieguth, *Spray Electron Beam for Tests of Linear Collider Forward Calorimeter Detectors in SLAC End Station A*, June 2004, IPBI-TN-2004-5

BPM support system for nanometer resolution beam monitoring

Y.Honda

2005/10/20

Abstract

Mover and stabilization system for the high resolution cavity BPM experiment at the ATF was described.

1 Introduction

In order to demonstrate an ultra-high resolution cavity BPM, we have developed a rigid mover system to support three BPMs.

2 Mover system

To align all the three BPMs precisely on a given beam orbit, the support system has to have an alignment mechanism for at least four directions (horizontal, vertical, yaw, pitch). At the same time, the system should be as stiff as possible not to excite an internal vibration. Well isolated four axes elastic hinge mechanism driven by piezo actuators was designed for the support.

3 Active stabilization

An active stabilization system was implemented for the most important direction, vertical. The relative displacement of the three BPM is important for our case. An aluminum bar was placed above the mover as a reference object. Each BPM's position with respect to the bar was monitored by an optical interferometer. The active mover which was driven by a fast piezo controled the vertical position of the BPM in a closed loop using the interferometer signal.

4 Present status

So far the resolution of our cavity BPM seemed to be limited by the performance of the cavity itself, not by the mechanical stability of the support system.

OPTICAL ANCHOR R&D AT UNIVERSITY OF BRITISH COLUMBIA

T.Mattison, A.Turner, M.L'Heureux, R.Greenall, M.Wong, M.Chen
Dept. of Physics & Astronomy, University of British Columbia, Vancouver BC V6T 1Z1 CANADA

Abstract

The Optical Anchor concept uses laser interferometry to measure the position of an object and a piezoelectric actuator to correct its position. Methods for retaining sub-nanometer interferometer accuracy when measuring moving objects are presented. Limitations of filtered-PID feedback control for our 10 kg test platform are explained, and state-vector formalism for optimal control is introduced. Methods for determining the parameters of the state-vector model and calculating the optimal gains are presented. They are applied to data from piezo-mirrors and the 10 kg platform, and used for both simulated and actual control. For piezo-mirrors, performance is excellent in simulation and experiment (0.08 nm RMS). For the platform, the state-estimator give 0.15 nm RMS residuals, and control performance is 5.8 nm RMS with the automatically-generated model parameters and gains. This is nearly as good as our best manually tuned filtered proportional-integral-derivative (PID) control, but is still disappointing. The performance is equally disappointing in simulation, therefore it must be due to a property captured in the system model, rather than a disagreement between the model and reality. Several simple mass-and-spring simulations are used to show that placement of the piezo and mirrors relative to the platform can be critically important for good control. The disappointing control performance with the platform may be due to vibrations of the interferometer reference mirror.

1 INTRODUCTION

The beam spot of a TeV-scale linear collider is of order 1 nanometer vertically. If the final quadrupoles vibrate by a comparable amount, the luminosity will be greatly reduced. The "Optical Anchor" concept uses laser interferometry to measure the positions of the quads with respect to an external reference, and piezoelectric actuators to correct their positions. At the University of British Columbia (UBC) we use a Michelson interferometer with an end mirror on a piezo to develop interferometer calibration and reconstruction methods and feedback control. We have also built a test platform with an interferometer mirror, piezo actuator, and variable mass and spring constant for more realistic feedback tests with a mass of 10 kg or more.

At Nanobeam 2002, we reported[1] interferometer position accuracy of 0.01 nm, estimated from residuals of the fit to the array of 6 photodiodes in the interference fringes. However, resolution degraded to several percent of the motion amplitude for moving objects. We also reported filtered proportional-integral-derivative (PID) control of a piezo-mirror to 0.06 nm RMS. For the 10-kg platform, results were disappointing. With the platform not isolated from the ground, the result was 5 nm RMS with feedback on vs. 90 nm RMS with feedback off.

2 INTERFEROMETER IMPROVEMENTS

The classical Michelson configuration is shown in Figure 1. The HeNe laser light goes through a beam splitter, down two perpendicular arms with end mirrors, and back to the beam splitter which recombines the beams on a linear photodiode array. Interference fringes form if the mirrors are adjusted so the two beams hit the photodiode array at a slightly different angles. The fringe pattern shifts if an interferometer mirror changes position. Fitting the photodiode signals allows the motion to be measured. The wavelength of HeNe light is 632 nm, so one milliradian of phase is 0.1 nm, or 0.05 nm of mirror motion. To calibrate, a piezo slowly moves one of the mirrors while we rapidly digitize the photodiodes. Plotting photodiode voltage vs. piezo setting gives an offset sinusoid with wiggles due to mirror vibration.

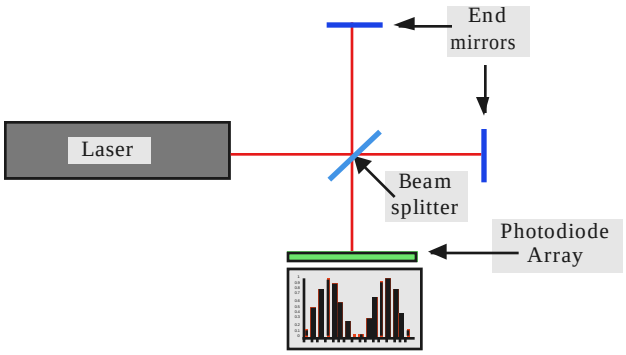

Figure 1: Michelson Interferometer

In our previous calibration algorithm, the signals were modeled with $V_{ik} = A_k + B_k \sin(\psi_k + \phi_i)$, where V_{ik} is the voltage of photodiode k at piezo setting i, the A_k, B_k and ψ_k parameters are calibration constants for photodiode k, and the ϕ_i parameter is the phase at piezo setting i. The maximum and minimum voltages from each photodiode were used to estimate A_k, B_k, then these were used to estimate ψ_k via

$$\psi_k = \psi_{k-1} + \left\langle \sin^{-1}\frac{V_k - A_k}{B_k} - \sin^{-1}\frac{V_{k-1} - A_{k-1}}{B_{k-1}} \right\rangle$$

These estimated constants were used to fit for ϕ_i for each

piezo setting i. Then the data from each photodiode V_{ik} as a function of ϕ_i were fit for A_k, B_k and ψ_k. The ϕ_i were then recalculated, and used to refit A_k, B_k and ψ_k. Further iterations produced very small changes. Figure 2 shows the measured and fit V_{ik} as a function of ϕ_i for one photodiode, and the difference between them multiplied by 1000. The residuals are rather small, although there are hints of a systematic trend.

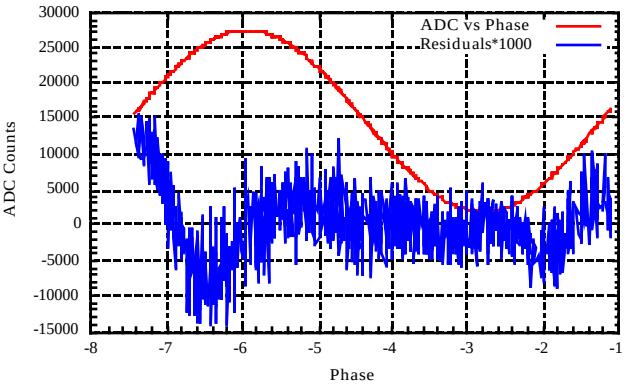

Figure 2: Previous Calibration Residuals

Our previous interferometer position reconstruction algorithm was to measure the photodiode voltages V_k and fit for ϕ and C in $V_k = (1+C)[A_k + B_k \sin(\psi_k + \phi)]$, where C is the relative laser intensity. Initially, A_k, B_k and ψ_k were held constant, but it was found that adjusting A_k by a very small fraction of the residual of V_k after each measure and fit cycle greatly reduced the residuals. The interferometer resolution calculated from the residuals was as low as 0.01 nm.

However the fit residuals degraded substantially if the interferometer was measuring large rapid motions. This was initially blamed on amplifier time constants. Reducing the integration time constant and using faster op-amps resulted in less improvement than expected. It was eventually discovered that the light falling on nominally insensitive parts of the photodiode array still produced a signal, but with a very long time constant. These regions were masked off with black tape.

Studies of calibration data with fast piezo motion were undertaken to measure the remaining time constants. It was discovered instead that the fringe spacing changed as the fringe pattern shifted. These spacing shifts are probably due to the mirror tilting as it translates. Studies of calibration constant drift over many hours also showed slow drifts in fringe spacing, as well as slow changes in A_k, B_k that are probably due to laser steering drift.

These effects were incorporated into the signal model used for reconstruction. The photodiode data is fit for ϕ and ϕ' in $V_k = (1 + C + kC')[A_k + B_k \sin(\psi_k + \phi + k\phi')]$. The ϕ' fit parameter represents a phase-gradient across the photodiode array, and compensates for mirror tilt during calibration and measurement, and non-simultaneous photodiode measurements. This results in residuals and thus resolution with greatly reduced dependence on motion. The values of A_k, C, C' are adjusted by a small fraction of the residuals after each fit to account calibration systematics and for laser intensity and steering changes, but the changes are now very small.

Recently, we have built a piezo-mirror with a range of many wavelengths (the previous one shifted the fringes only about one cycle). This made it clear that the systematic residuals visible in Figure 2 were periodic in ϕ. Studies of the calibration fitting algorithm (which alternates between finding A_k, B_k, ψ_k with ϕ_i fixed, and finding ϕ_i with A_k, B_k, ψ_k fixed) with simulated data showed that while the parameters stopped changing significantly after very few iterations, they did not actually converge to the true solution! The resulting calibration constants gave reconstructed positions with sinusoidal systematic deviations at harmonics of the light wavelength.

The ideal solution to this problem would be to fit the V_{ik} calibration data to A_k, B_k, ψ_k and ϕ_i simultaneously instead of alternating. This would make it impractical to have hundreds to thousands of ϕ_i, and using fewer ϕ_i would increase the statistical error of the calibration. A successful compromise is to retain the alternating rather than simultaneous fits but use a better signal model:

$V_{ik} = A_k + B_k \sin(\psi_k + \phi_i + k\phi_i' + P_k \sin\phi_i + Q_k \cos\phi_i)$.

The P_k, Q_k parameters absorb any sinusoidal distortion of the ϕ_i reconstruction scale. After the first few iterations they become statistically consistent with zero, because the right solution for the A_k, B_k, ψ_k parameters is found. Figure 3 shows the resulting calibration fit residuals for all 6 photodiodes. The random electronic noise is somewhat higher than in Figure 2 due to the electronics changes mentioned above, but now there is no significant systematic trend.

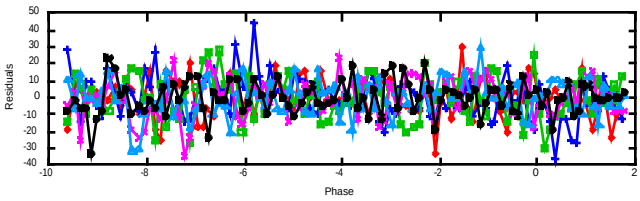

Figure 3: New calibration fit residuals

The software infrastructure for interferometry has been completely rewritten since Nanobeam 2002. We have written a generic Linux driver module framework to allow us to migrate between Linux kernel versions with minimal changes elsewhere. Inside the framework we have implemented a driver for our Keithley KPCI-3108 card which gives access to all of its functionality including interrupts. The driver also contains specialized code for the

interferometer, PID feedback, and state-vector feedback. The driver functions are accessed from user programs in the C language with command-line arguments. There are tcl/tk/BLT graphical interfaces to both the general KPCI-3108 functions, and the specialized interferometer and feedback functions.

In addition, we have developed a simpler interferometer reconstruction method, requiring only two photodiode signals and a DSP, and requiring no explicit controlled calibration step[2]. Basically, plotting one photodiode signal against another (ideally about 90° away in phase) gives an ellipse, and simple transformations turn it into a circle. A single inverse-tangent function then gives the interferometer phase. Methods were developed to determine the ellipse center, height, width, and slant from the data stream. The methods require initial motions large enough to trace out the ellipse, but they can be random rather than controlled.

3 LIMITATIONS OF PID CONTROL

A piezo mounted between a mass and a spring, with its length controlled by the motion of the mass, can be used to artificially raise or lower the oscillation frequency, or to damp the motion. Changing the piezo length proportional to the error in the mass position (proportional or P-gain) changes the resonant frequency. To raise the resonant frequency by a factor of K, the P-gain must be $(K+1)^2$. The mass can be placed at a desired location by changing the piezo length according to the time-integral of the error in the mass location (integral or I-gain). Changing the piezo length according to the velocity (derivative or D-gain) can damp the motion. The canonical "Optical Anchor" could be implemented by a combination of large P-gain to artificially stiffen the support, D-gain to critically damp it, and I-gain to maintain precise alignment.

As we reported at Nanobeam 2002[1], PID feedback worked well to control an interferometer mirror mounted directly on a piezo (0.07 nm), but our experiments with the 10 kg platform were disappointing (5.0 nm). It was not possible to apply sufficient gain to do much more than damp the fundamental vibration mode without making the system unstable. Notch-filters at oscillation frequencies only allowed minor gain increases. However, it was possible to use narrow band filters for feedback control of disturbances from coherent man-made vibrations, even above the fundamental mode.

The control theory literature contains many equivalent criteria for determining if a system will be stable, but most require either algebraic expressions rather than measurements, or are complicated statements about the topology of a graph of the measurements. Our stability criterion, which can be applied directly to a measured transfer function, is that the amplitude of total transfer function (product of "plant" and "controller" transfer functions) must be less than 1 at any frequency where the phase of the total transfer function is $180^{\circ} + n \times 360^{\circ}$.

Figure 4 shows (in green) the measured "plant" transfer function for the 10-kg platform[2]. It has a large fundamental resonance, plus several other resonances with amplitudes of order one, with the usual phase-shift of 180° per resonance. Also shown (in magenta) are the transfer functions of the empirically optimized PID controller, and (in glue) its product with the "plant" function. At points A and D, the phase of the product is very close to a dangerous value and the product amplitude is greater than 1, so the controller is predicted to be at the edge of stability (which was the case). At point C the amplitude is above 1 but the phase is safe. At points B and E the phase is dangerous but the amplitude is safely less than 1. The predicted closed-loop feedback response is shown in red.

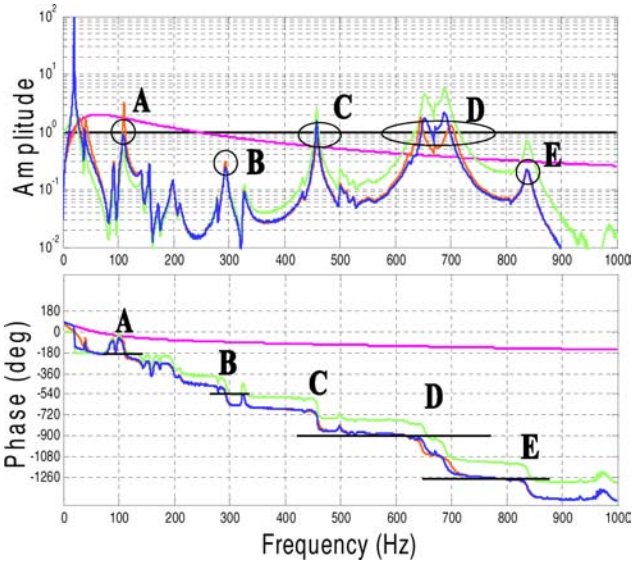

Figure 4: Response of 10-kg platform

The optical anchor requires high feedback gain to be effective. A controller with high gain from 0 to somewhat below the first parasitic resonance, and a sharp cutoff at higher frequencies, is the conservative strategy. This is stable, and controls actively at low frequency, but does nothing at high frequency. The gain is limited by the sharpness of the cutoff, because this increases the phase-shift below the cutoff, which eventually makes the fundamental mode unstable. Reducing the gain at parasitic resonance frequencies with notch-filters is an appealing strategy, but these also introduce phase shifts that can lead to instability, and tuning such a system manually is difficult.

4 STATE VECTOR CONTROL

The "state-vector" approach to control theory can circumvent some of these problems. It offers not just guaranteed stability but "optimal" control of linear systems, even with multiple resonances. Complex cases usually

require digital computation inside the feedback loop, but the interferometer reconstruction requires this already. The calculations are simple linear algebra with minimal branching, but do require model and gain constants. Gains are pre-calculated from a model of the system and disturbances, and a choice of what to optimize.

The "state vector" x_i is the set of numbers required to describe the system at time t_i. For N masses coupled by springs in 1 dimension, the state vector could be the N positions and N velocities. The state vector could instead be the sine and cosine amplitudes of the N normal modes. It can also contain things like setpoints, variables needed to compute filtered signals, or non-random environmental disturbances. The "control variable" u_i is the control that is applied at time t_i. The "free evolution matrix" A describes the change in the state vector during a single time step in the absence of control or disturbance. The "drive vector" B describes the effect of the control variable on the state vector in a single time step. The state x_{i+1} at time t_{i+1} can be calculated via $x_{i+1} = Ax_i + Bu_i$. The goal is to compute the control variable u_i such that the state x_i is driven toward the desired value.

"Optimal control" here means that we minimize the sum over time of a quadratic form $V = \sum_i (x_i^T Q x_i + R u_i^2)$, where Q is the "state penalty matrix" that specifies the importance of controlling different combinations of the state vector elements, and R is the "control penalty" that specifies the cost of control.

The "observation vector" C relates the "measurement" y_i to the state via $y_i = Cx_i$. We estimate all the elements of the state vector from a sequence of measurements y_i, which need not correspond to any single element of the state vector. The measurement has "variance" (noise) S, and the estimated state has a covariance matrix, which gets smaller as measurements are added. The state vector also has a "disturbance covariance matrix" T, which describes how random environmental effects change the state, relative to free evolution plus control of the state.

The A matrix and B and C vectors are constants describing the dynamics of the system and the measurement. The measurement variance S and the disturbance covariance matrix T are constants describing noise and the environment. The state penalty matrix Q and the control penalty R are constants chosen by the feedback designer.

The optimal "control gain vector" G can be calculated from A, B, Q, R and the optimal "estimator gain vector" K can be calculated from A, C, S, T. The estimator gains are independent of the control gains and can be calculated separately. There are well-established methods to do the gain calculations, which are numerically intensive but only need to be done once, outside the feedback loop. It is easy to derive recursively the solutions for finite time horizons, and these typically converge to asymptotic values. The asymptotic solution is often called the LQG regulator (for Linear systems with Quadratic state and control penalties and Gaussian disturbances and measurement errors). The asymptotic solutions can be found directly by solving a matrix Riccati equation using eigenvector techniques. The commercial program Matlab and its Control Theory Toolbox are commonly used for this.

The calculated control gains are guaranteed to be stable (provided Q, A and B obey a few simple constraints), and optimal (using the definition implicit in the Q matrix and R), for the system defined by A and B. The estimator gains essentially give a running fit for the state, and are guaranteed to produce stable results provided all state elements have some distinguishable effect on the measurement. In the literature, the control and estimator gain are often called K and L respectively, rather than G and K. Our notation recognizes that the state estimator component of the algorithm is a Kalman filter.

If the goal specified by Q and the system specified by A and B are incompatible, the calculated gains may be unreasonably high, but they should always give stable control, at least in a numerical simulation. High gains may be unstable in practice, because A and B are only an approximation of the real system. High gains may be unusable in practice due to control range limits or cost. It is always possible to reduce the control gains by increasing the value of R, but this compromises the quality of control. It may be possible to reduce the control gains by re-defining Q so the feedback is no longer trying to control the less relevant elements of the state vector.

It is useful to carefully analyze the disturbances to the system. If the disturbances are not random, they can be built into the state vector. The estimator gain calculation will determine how to measure them in the data stream, and the control gain calculation will determine how to optimally correct them. The disturbance covariance also determines the gains of the Kalman filter state estimator. If the assumed disturbance covariance for some mode is large, the estimator gain for the mode will be large. If that mode really does suffer large disturbances, this is good, because the mode estimator will converge quickly to the right value for the disturbance, and the mode controller will take the action that most rapidly damps that mode. But high estimator gains increase the response to sensor noise, which causes noise in the calculation of the control variable. Also, if the state vector model is incomplete, then the system response to control commands deviates from expectation, which the estimator gains attribute to external disturbances of other modes. The feedback then tries to correct the non-existent disturbances, which can cause further deviations from expectation, and ultimately to instability.

Inside the feedback loop, the calculations are simple. The state vector x is initialized to an arbitrary estimate, and the control variable u is initialized to zero. On each iteration, the state estimate is evolved by $x = Ax + Bu$, the measurement residual is calculated by $\Delta y = y - Cx$,

the state estimate is updated by $x = x + K\Delta y$, the control variable is calculated by $u = Gx$, and the control is applied to the real system.

There are several reasons why state-vector control can be superior to classical control. Since the system model ideally contains all the modes, and applies different gains optimized to control each mode, the stability constraints in classical control are automatically satisfied. It provides a definite prescription for the "optimal" gains, so there is no uncertainty about whether further tuning could improve performance. The estimated state is updated directly as control is applied, as well as from the measurement, so there is no phase shift. The state estimator is constructed with disturbance and noise information not normally used in classical control theory, in a way that has the optimal signal to noise ratio, and has higher gain at frequencies where disturbances are larger. This minimized the introduction of sensor noise into the control variable. Finally, state-vector methods are easily extended to multiple sensors, multiple actuators, and multiple degrees of freedom.

5 DETERMINING STATE VECTOR MODEL PARAMETERS

Since the feedback loop calculations are simple and the gain calculations are at least a solved problem, the most challenging task is to determine the matrices and vectors describing the system dynamics, disturbances, and noise. This is known in the literature as "system identification".

In principle, a finite-element calculation with knowledge of the shape, density, elasticity, and damping of all the material objects in the system could be used to calculate the A matrix and B vector, but this is unlikely to be practical, and would need to be repeated any time the configuration is changed. And even with a perfect simulation, we would still need to do measurements on the real system to determine the environmental disturbances. An experimental procedure to measure all the required information on the real system is preferred.

Our procedure for finding the state vector control parameters has several steps. First, we calibrate the interferometer as described in Section 2. Next, we acquire a data file of the system response to square-wave excitation by the piezo. We use the square-wave file to determine the internal modes of the system, their excitation by the piezo, and the piezo calibration. Then we acquire a data file of system response to environmental disturbances. We use this file to determine the frequencies of large coherent external vibration sources, and the disturbance covariance of the internal and external vibration modes. Then we calculate the control and estimator gains, with user input for the state and control penalties. These gains are then downloaded to the feedback interrupt handler, along with parameters for performing an experiment.

Our convention is that x, y, and u have units of interferometer radians. One unit of control u changes the DC position element of x and the asymptotic interferometer reading y by one radian of phase. The elements of the drive, measurement, control-gain, and estimator-gain vectors are all of order one in this convention.

We use the piezo increment as the control variable u, rather than the absolute piezo setting. This somewhat simplifies the construction of A and B, and also means that the control penalty R applies to piezo changes rather than the absolute piezo setting. The feedback interrupt handler code integrates u and converts it to an absolute DAC setting for the piezo.

We use a mixed modal representation for the state vector x. The first element of x is the feedback setpoint. It has no free evolution, so the first row of A is zero except for a 1 on the diagonal. It is not driven by the piezo, so the first element of B is zero. The second element of x is the DC component of the interferometer reading. This also has no free evolution, so the second row of A is also zero except for a 1 on the diagonal. The DC component is driven by the piezo, so the second element of B is the interferometer phase change per control step, which is 1 by definition in our normalization. The next few elements of x are decaying exponentials for piezo creep (if necessary), with A elements on the diagonal which are slightly less than 1, and elements of B containing the relative initial creep amplitude. The next 2N elements of x are the in-phase and out-of-phase components of damped sinusoidal vibration modes. For each mode, there is a 2x2 block on the diagonal of A derived from the frequency and damping, and 2 elements of B for the initial relative amplitudes. The next M elements of x are used for fast initial transients (if necessary). Their elements in B are simply the difference between the measured response to a normalized control step and the interferometer measurement as predicted by all the other terms. They have 0 on the diagonal and 1 next to the diagonal in A, which shifts the transient by 1 element per time step.

The interferometer signal is modeled as the sum of the asymptotic position of the piezo, any exponential piezo creep, the damped sinusoidal vibrations, and any initial transients. So the elements of the observation vector C are 1 for the DC component, the exponential-creeps, the N in-phase damped sinusoids, and the first transient element. The C elements are zero for the setpoint, the N out-of-phase components of the sinusoidal vibrations, and all but the first of the M transients.

To determine the parameters, we apply a low frequency large-amplitude square-wave to the piezo, and measure the interferometer response with a high sampling rate. The result is a square wave with transient vibrations and random environmental disturbances superposed. We average the waveform over many cycles to reduce the effect of measurement noise and random disturbances, then write the result to a data file. If the first half of the period is added to the second half, the transients from the edges cancel, and the deviation from flatness is a measure of the remaining disturbances. This is useful as an on-line diag-

nostic for whether enough cycles have been averaged. Figure 5 shows square-wave data from the 10-kg platform.

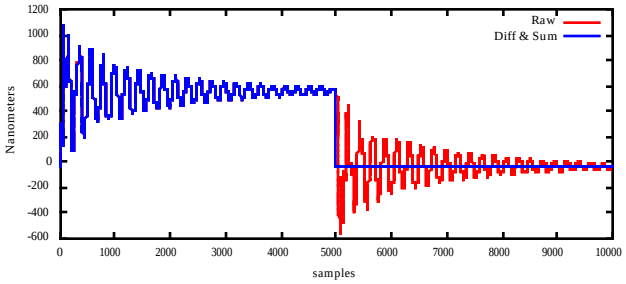

Figure 5: Square-wave response of platform

The time-averaged cycle is then fit to an offset square wave (plus exponential terms for piezo creep). The amplitude of the square wave in radians divided by the DAC increment used to produce it is noted for later use in the feedback interrupt handler. The parameters of the exponential creep terms are used to calculate the corresponding elements of A and B. The residuals from this fit are used to determine the frequency, damping, amplitude and phase of damped sinusoidal vibrations. The second half of the residuals are of opposite sign, and are subtracted from the first half to double the signal to background ratio. The first half is also added to the second to cancel the transient, as a measure of the disturbance background.

Figure 6 shows the Fourier spectrum of the residual signal (red) and background (green). Several broad peaks are visible in the signal spectrum, and the background is much lower and flatter. A much richer and easier to analyze signal spectrum (blue) is produced if the residuals are multiplied by a Hann window function $1-\cos(2\pi t/t_w)$ where the width t_w is half the square-wave period. The frequency resolution is improved by zero-padding the signal by a factor of 4 before the transform. Local minima in the amplitude are replaced by the mean of the neighboring amplitudes in 4 passes, to avoid finding false peaks.

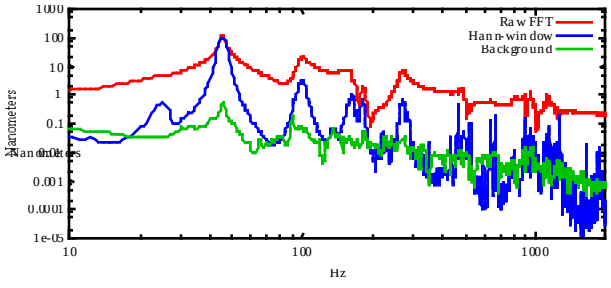

Figure 6: Spectrum of residuals and background

Peaks are found where the amplitude falls by a specified percentage within a specified frequency range. The peaks are sorted by amplitude, and the frequency, amplitude, and phase of peaks are noted.

The time-domain residuals are then fitted by as $a\exp(-|bt|)\cos(2\pi ft+\phi)$ using $[1-\cos(2\pi t/t_w)]^{-1/2}$ for errors to match the Hann window weighting. It is critical to have a good initial estimate of f and ϕ from the Fourier transform, and fit first for just a,b, then float ϕ, and finally float f. The absolute value in the damping term avoids pathological fits when fitting marginal signals. The largest amplitude peak is done first, and if the fit succeeds, the function is subtracted before the next largest peak is fit.

The sum of the fits is then Fourier transformed with the same padding, windowing, and minimum-filling as the residuals. For each peak, if the amplitudes the two spectra disagree, or the fitted frequency is inconsistent with the peak frequency, the fit is rejected. The sum of the accepted fits is then subtracted from the input in the time domain, and this is also Fourier transformed with the same padding, windowing, and minimum-filling.

Figure 7 shows the input spectrum (red), the peaks found (blue), the sum of accepted fits (green), and the residuals after subtracting the accepted fits (magenta). Most of the fits agree very well and are accepted. In this example, the fit is rejected for some peaks around 160 Hz.

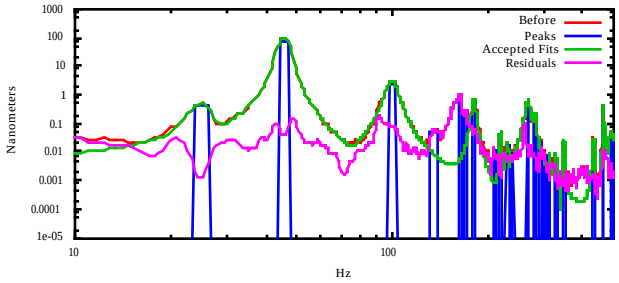

Figure 7: Peaks and residuals with full window

Because the Hann window attenuates signals at early times, this algorithm is inefficient at finding modes that damp out quickly, even if their initial amplitude is large. So the process is repeated using a shorter Hann window that focuses on early times. Figure 8 is the analog of Figure 7 for this window. A peak near 150 Hz, and several higher frequency peaks not apparent in the long-window spectrum, are accepted in this pass.

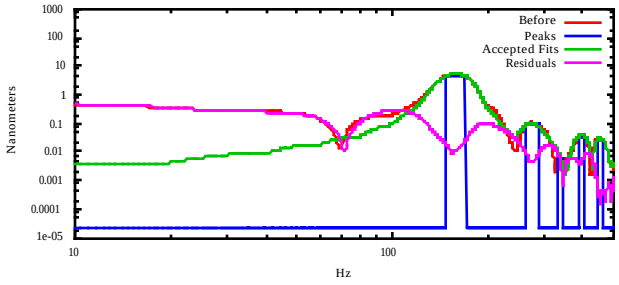

Figure 8: Peaks and residuals with short window

Figure 9 compares the un-windowed spectrum of the raw transients and the sum of accepted mode fits from both windows. It shows that nearly all of the transient power has been attributed to modes. The most significant

residual power is near 150 Hz. There appears to be both fast-damping and slow-damping resonances near this frequency, and the fast-damping one interfered with accepting the fit for the slow-damping one. This might be improved by repeating the full-window peak search after the short-window search.

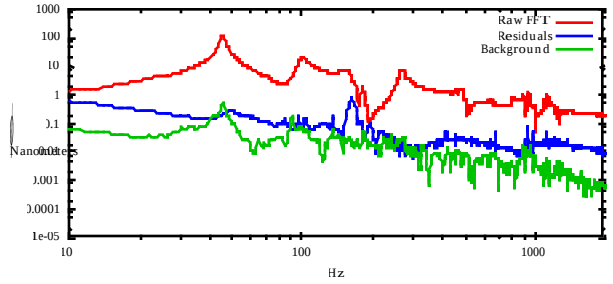

Figure 9: Transient spectrum, residuals, and background

The elements of the 2x2 block of A for each mode are calculated from the frequency and damping (f and b) parameters of the mode fits. The corresponding 2 elements of B for each mode are calculated from the amplitude and phase (a and ϕ) parameters, with a simple correction for the fact that transients do not necessarily completely damp out during the half-cycle of square-wave that is analyzed.

After subtracting all the accepted damped sinusoid fits from the square-wave fit residuals, the first M elements of the residuals are used as the transient amplitudes in B.

The environmental disturbances are determined by acquiring a data file with a fixed piezo setting, and Fourier-

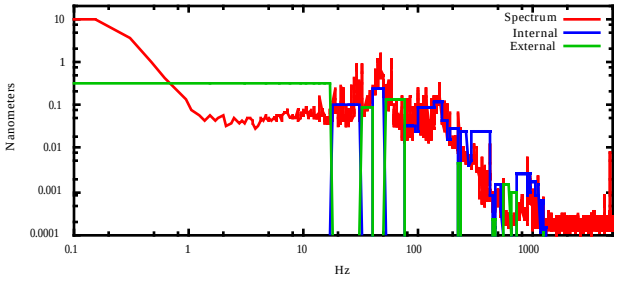

Figure 10: Disturbance spectrum

transforming it, as shown in Figure 10. There are large motions at low frequency (which are probably due to air currents in the interferometer light paths rather than actual platform motion). There is a flat noise floor above 1 kHz due to sensor noise (using a longer file would lower the noise floor). The fundamental resonance of the 10-kg platform is clearly visible. Many of the modes found in the square-wave analysis are not prominent here, because they are not strongly excited by external disturbances.

There are also many narrow peaks at other frequencies due to coherent external disturbances. The user can add band boundary markers to the output from the mode-fitting program to bracket external disturbance peaks that do not correspond to internal modes.

The disturbance covariance is calculated by a simple program using this spectrum, plus the output from the mode-fitting program. Frequency bands are defined for "internal" modes using the frequencies and widths of the mode-fits. "External" mode bands are defined in any the gaps between them, and by any user band boundaries inserted above. The disturbance covariance for a mode is the sum of squared FFT amplitudes in its frequency band, times the frequency width of the band. For the external modes, the mean frequency in the band (weighted by the squared amplitude) is also calculated. Figure 10 shows the resulting internal (blue) and external (green) band boundaries and the square root of the disturbance covariance values for the 10-kg platform.

The disturbance calculation program adds the external modes to the state vector model. The A matrix block for an external mode uses the power-weighted mean frequency, and the damping calculated from the frequency width. Such modes are not driven by the piezo, so their drive-vector B elements are zero. Finally, the disturbance covariances for all the internal and external modes are added to the output.

The next step is controller and estimator gain calculation. The Q matrix is constructed to minimize the square of deviation between the setpoint and the predicted interferometer measurement, plus a user parameter (which can be zero) times the sum of the squares of the out-of-phase mode elements in the state vector. The control penalty R and signal error S is also set by the user. Rather than using Matlab to solve the Riccati equation, we use our own program, which does direct forward iteration for the estimator gains and backward iteration for the control gains. It makes plots we use to check the convergence, which typically requires about as many cycles as it takes the actual feedback to control the motion from an arbitrary initial state. It also produces plots from a simulation of the system dynamics, the disturbances, the state estimator, and the state controller. And it makes a text file containing the system description, controller gains, and estimator gains.

The information from this file is then downloaded to the feedback interrupt handler, along with the interferometer calibration parameters, and the parameters for a feedback experiment. Many variables about each time step of the state during the experiment are transmitted back to the user process for analysis.

The set of acquisition and analysis programs for all these steps are in the C language and have tcl/tk/BLT graphical interfaces. They run on the Linux PC along with the data acquisition and feedback interrupt handler. The same programs have been used to determine the parameters and perform experiments with the 10-kg platform, and two different piezo-mirror combinations. These systems have rather different mode structures and disturbances, but essentially only user-parameter changes are required for the different cases.

6 STATE VECTOR FEEDBACK RESULTS

Figure 11 shows the results from a simulated feedback experiment using the model of one of the piezo-mirrors. The state-estimator was run on simulated disturbances and noise with no control for 10000 cycles (1 second), then the controller was turned on for 10000 cycles. The estimator residual (difference between the measurement and that predicted by the state estimator) was dominated by sensor noise. After control was turned on, the measurement was forced to essentially zero, with only a slightly larger estimator residual. The integrated piezo setting (with a minus sign) looks very similar to the position "measurement," since the controller is moving the piezo to cancel out the disturbances.

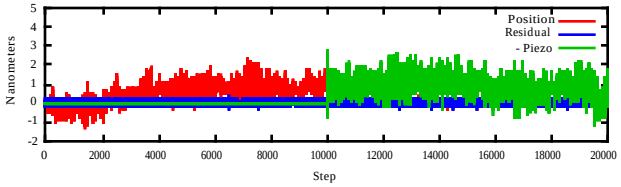

Figure 11: Mirror feedback simulation

Figure 12 shows the corresponding frequency spectrum. The predicted control is nearly perfect, and is non-zero only because of the non-zero value of the out-of-phase state penalty in Q. The residuals are much smaller, with a notch at the fundamental resonance (because it has a high estimator gain). The system performance with feedback is essentially as good as the estimator performance.

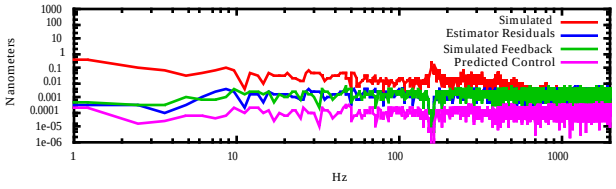

Figure 12: Mirror feedback simulation spectrum

Figures 13 and 14 show the same type of experiment performed on the real piezo-mirror system. The basic behavior of very small estimator residuals and good control is reproduced. In this case the estimator residuals degrade perceptibly when control is turned on, presumably because the system model is not perfect. The frequency spectrum shows that the disturbances are somewhat lower in the real data, but the quality of control is similar, essentially the same as the estimator residual spectrum.

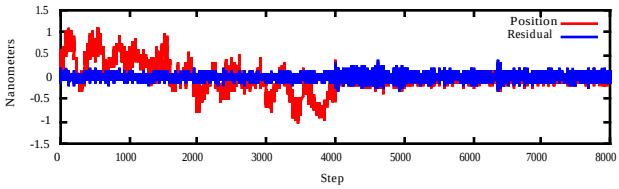

Figure 13: Mirror feedback data

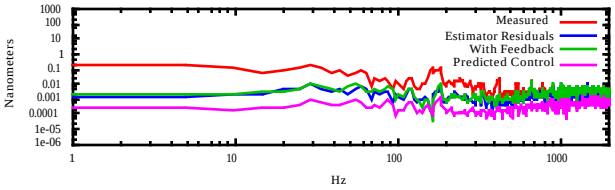

Figure 14: Mirror feedback data spectrum

Figure 15 shows the ratio of the spectra with feedback on and off, for both simulated and actual data. The agreement is excellent. There is an overall reduction in RMS motion by a factor of 6.14 in data (to 0.070 nm) and 7.25 (to 0.080 nm) in simulation. There is a deep dip at the fundamental resonance, low frequencies were attenuated by a factor of 10 to 100, and motion at essentially all frequencies below 1000 Hz is improved, although at higher frequencies there is some degradation.

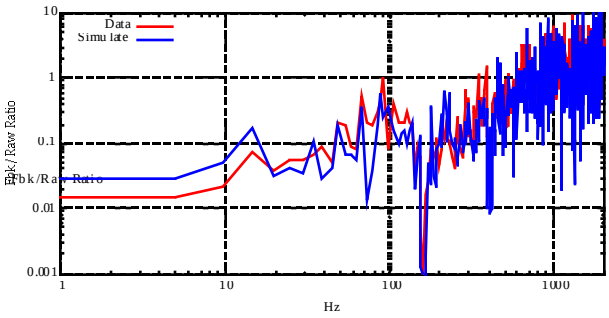

Figure 15: Mirror feedback attenuation comparison

The piezo-mirror system is nearly ideal mechanically, and similar performance can be achieved by manual optimization of PID feedback. The notable point is that we have achieved that performance with an automated technique that can be applied to more complex systems.

The control and estimator gains were calculated, with the same small out-of-phase and zero control penalties used above, for the measured model of the 10-kg test platform. While these gains were stable in simulation, they caused the piezo motion with control on to be substantially larger than the platform motion with control off. This was perhaps not surprising, because the platform response is much less ideal than the piezo-mirror.

The same gains were unstable on the real 10-kg platform, presumably because the model was imperfect. It was necessary to increase the control penalty to $R = 5$ and the out-of-phase penalty to $Q' = 5$ to get gains that were stable on the real platform. In simulation, these new gains made the piezo motion with control on comparable to the platform motion with control off, but did not greatly degrade the overall quality of control.

Figure 16 shows the spectra for the real platform of the measured position with feedback off (red), the estimator residuals (blue), the predicted position with feedback on (magenta), and measured position with feedback on (green). The measured position is indistinguishable from the predicted position. The estimator residual is very

much smaller than the disturbance level, in fact the RMS is only 0.015 nm. However control is disappointing, with only the fundamental peak and very low frequencies improving.

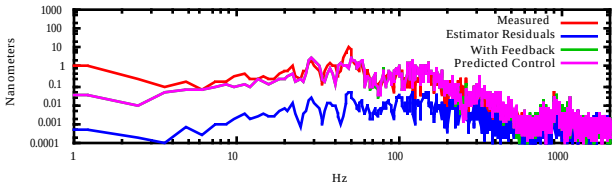

Figure 16: Real platform spectra

Figure 17 shows the spectra for the simulation of the platform. The features are similar: the estimator residuals are good, the state-estimator prediction matches the simulated position, but the control only improves the fundamental resonance and low frequencies.

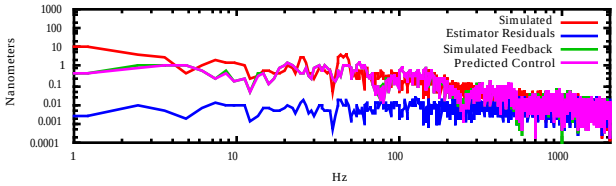

Figure 17: Simulated platform spectra

Figure 18 shows the ratio of feedback on to feedback off for both data and simulation of the 10 kg platform. The agreement is reasonably good, but apart from damping the fundamental resonance, there is not much suppression, except at low frequency.

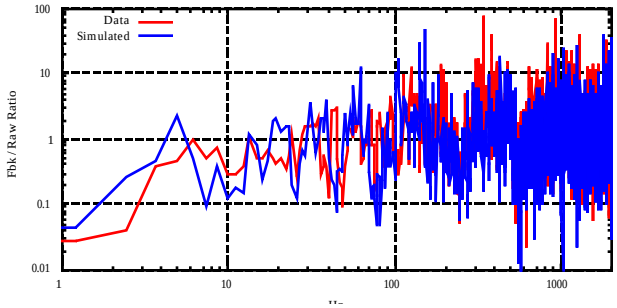

Figure 18: Feedback On/Off ratio
for real and simulated platform

Turning on feedback reduced the RMS of the interferometer measurement to 5.8 nm, which is nearly as good as the 5.0 nm reported at Nanobeam 2002. That result was based on laborious manual tuning of PID gains, notch filters to suppress oscillations, and narrow-band feedback on coherent disturbances. The present result is from a largely automated procedure, with the goal of seeing how well such a procedure could work. Some improvement might be expected if the mode finding could be improved to find the remaining peak in Figure 9, which might allow the R and Q' values to be reduced, increasing the controller gains. The previous result was achieved on a background RMS of 90 nm, vs. 9.2 nm for the present result, so the previous result had a larger attenuation factor. However, most of the previous background was from large coherent disturbances at about 20 and 30 Hz, which had narrow-band feedback applied to them manually. If those coherent disturbances existed in the present data, the procedure would probably have created external modes at those frequencies and controlled them away automatically.

7 UNDERSTANDING THE RESULTS

The difference between the excellent feedback results for the piezo-mirror and the disappointing results for the 10-kg platform reported at Nanobeam 2002 was blamed on the more complicated mode structure of the platform. We had hoped that state-vector control, given a model of all the modes, would be able to do better. While we did find that the nearly automated procedure of determining the system parameters and gains produced stable feedback with performance comparable to manually tuned filtered-PID, the performance was not substantially better. For the nearly ideal piezo-mirror case, this was perhaps not surprising. But it was puzzling for the 10-kg platform.

The fact that the estimator residuals for the 10-kg platform (0.15 nm) were much smaller than the RMS motion suggests that the feedback does understand and measure the dynamics quite well. But even with the high gains produced by the small out-of-phase penalty and zero control-penalty (which is unstable on the real platform but stable in simulation), the predicted control was much worse than the estimator residuals, rather than much better than the estimator residuals as it was for the piezo-mirror. In the simulation, nothing can be blamed on an imperfect model, since the exact same model was used for the gain calculation and the simulation. It must be that something in the model forced the gain calculation to choose low gains that give poor control.

Simulation of a multiple-mode mechanical system in Figure 19 shed some light on the issues. The system was 10 masses and springs in series, with a piezo between the last mass and its spring, and another piezo between the spring at the other end and the "ground." The A matrix and B vector were constructed for this system. Then optimal control gains were calculated for each piezo (used separately) to control the position of the "payload" mass farthest from the ground, with a small additional penalty on its velocity, and zero penalty for the position or velocity of the other masses. A feedback simulation with no external disturbances then used the gains and the "true" positions and velocities of the masses.

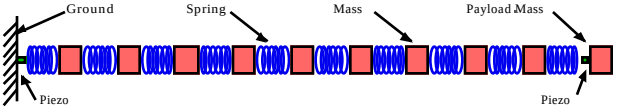

Figure 19: Mass and spring model for simulations

Figure 20 shows the motion of the payload mass from an initial displacement of 1 unit for the cases of no control, control using the piezo closest to the payload, and control using the piezo closest to the ground. For no-control, the mass initially moves back toward zero with some damped ringing, but later sees the reflection of the mechanical wave from the ground-end of the chain. Gains for the payload piezo are reasonable and give very fast control with no ringing (although the piezo continues to move afterward, to keep the motion of the other masses in the chain from moving the payload mass). Gains for the ground piezo with $R = 0$ are physically impractical and give strange simulated performance: initially the mass follows the no-control trajectory, but before the speed-of-sound transit time from the ground piezo, the mass jumps to zero and stays there (with some very high frequency ringing). Recalculating with $R = 10^{-6}$ gives low gains, and the simulation follows the no-control trajectory including the ringing, except the ground-piezo "eats" the mechanical wave so there is no large "reflection" of the payload mass.

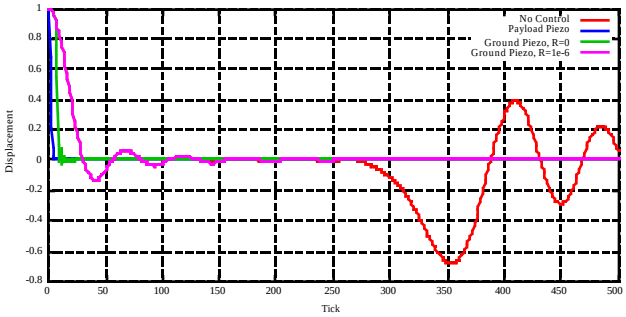

Figure 20: Simulated control of mass chain

State-vector methods give excellent control if the piezo is right next to the payload. So the existence of 10 strong resonances is not sufficient to prevent a feedback from performing well (although one suspects that manually tuning a filtered-PID feedback would be very hard in this case). But optimal state-vector control gives either impracticably high gains and unphysical performance ($R = 0$) or low gains and disappointing performance ($R = 10^{-6}$) if the piezo is mechanically far from the payload. Apparently a perfect model of the 10 resonances and theoretically optimal gain calculation is not sufficient to guarantee good performance if the piezo is in the wrong place.

Figure 21 shows the 10-kg test platform. The piezo is in the metal cylinder to the right of the inverted-U spring and below the eyebolts and tensioning springs. The piezo was mounted directly to the test platform, rather than being far away, so it is closer to the good topology than the bad topology of the mass-chain simulation.

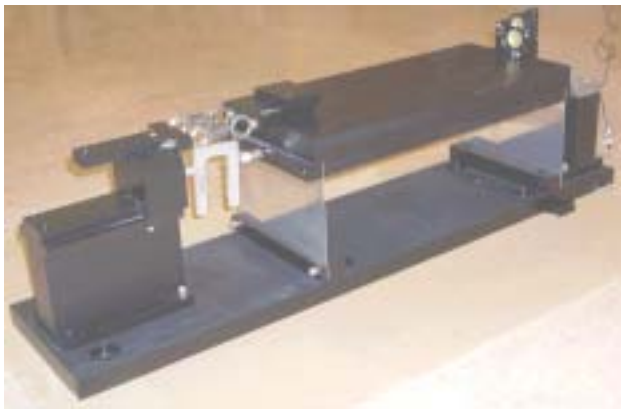

Figure 21: 10-kg test platform, piezo and springs

Figure 22 shows the other end of the test platform, where the signal mirror (left) and reference mirror (right) are mounted. The signal mirror is on a mount which may not track the platform motion exactly.

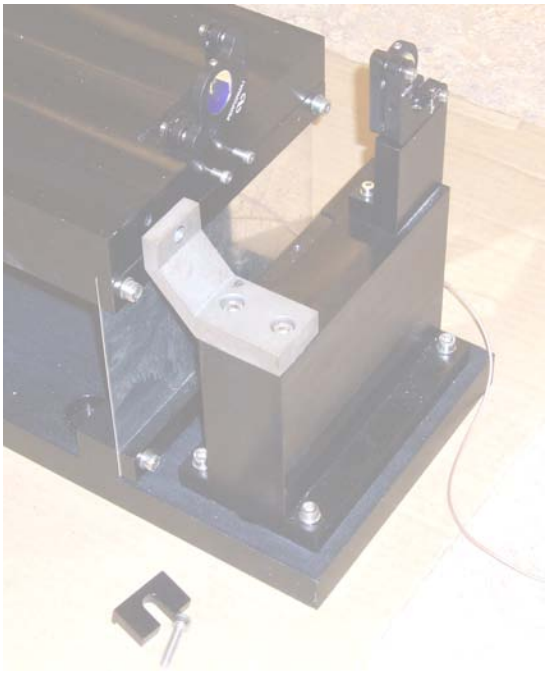

Figure 22: Mirror end of 10-kg platform

Figure 23 shows a model intended to simulate motion of the signal mirror relative to the platform. A low mass "signal mirror" is connected by a spring to the payload mass at the end of the chain. Gains were calculated to control the position of the mirror.

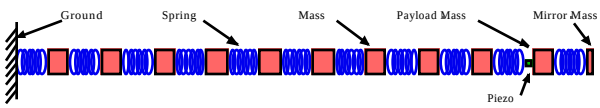

Figure 23: Model with signal mirror

Figure 24 shows the payload (magenta) and mirror (green) motions from an initial offset of 1 with control, and the no-control (red) and control-on-payload (blue) motions for reference. The mirror is controlled nearly as well as the payload was without the mirror. The payload mass undergoes some fast transients when controlling on the mirror, but they settle down rapidly. So vibrations of the interferometer signal-mirror do not seem to be a good candidate for the platform problem.

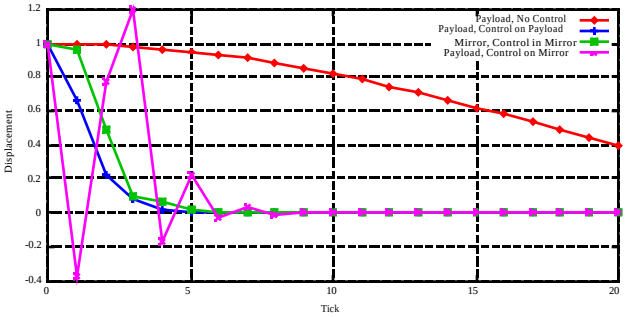

Figure 24: Signal mirror simulation results

However, as visible in Figure 22, the interferometer reference mirror is mounted to a post on the same baseplate that holds the piezo mount post. It is known that many of the platform resonances are due to flexing of the supports. So it is likely that there is some motion transmitted to the reference mirror mount when the piezo moves. Figure 25 shows a model with a low mass "reference mirror" connected to the mass closest to the ground by a spring. Gains were calculated to control the payload position minus the reference-mirror position, using the payload piezo.

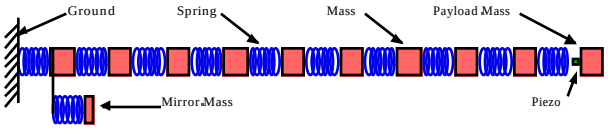

Figure 25: Model with reference mirror

Figure 26 shows the motion of the payload (green) and mirror (blue), the payload-mirror difference (magneta and plotted with an offset), and for reference the payload motion with no control from Figure 20 (red). Initially, the algorithm moves the payload rapidly toward zero. But this launches a wave down the chain, which would soon move the reference-mirror away from zero. To prevent this, the algorithm pulls the payload partly back toward 1, which launches a wave of opposite polarity. It then wiggles the payload such that its motion matches the reference-mirror motion as soon as it starts. In fact, it succeeds in making the two motions rather similar, but does not make either one much smaller! The damping time scale for the difference is comparable to the mechanical transit time of the chain.

The algorithm is trying to keep two mechanically separate objects (the payload and the reference-mirror) moving synchronously, using a single piezo that has an immediate effect on one object but a weak and delayed effect on the other object. Understandably, this is hard to do, even though it has a perfect model of the system dynamics and no noise or disturbances. We know from the other simulations that there are reasonable gains that can relocate the payload very quickly using this piezo. But in this topology, trying to do so causes delayed reactions of the reference-mirror. Presumably trying to make the payload motion match them would require more piezo motions, which would cause still more reference-mirror reactions, and unstable motion. The optimal solution in this case seems to be, not to try too hard.

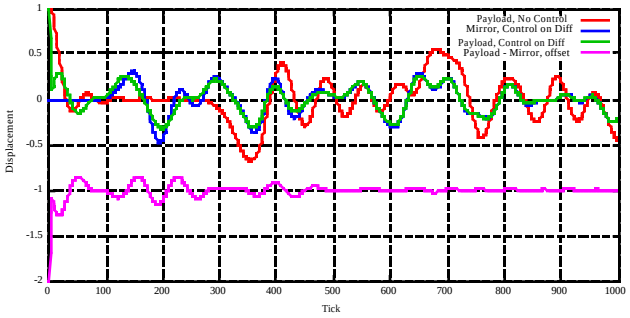

Figure 26: Reference mirror simulation results

Vibrations of the reference mirror induced by the piezo are therefore a good candidate for why the 10-kg platform is hard to control, even with state-vector methods with knowledge of many modes, even when the state-estimator is able to predict the platform motion to a fraction of a nanometer. The measurements used to create the state-vector model include any reference mirror motion, so even the simulation could be hard to control.

8 CONCLUSIONS

Masking regions of the interferometer photodiode array that had slow response, speeding up the electronics, and introducing a phase-gradient (mirror-tilt) parameter into the interferometer fits has reduced the degradation in resolution when measuring moving objects, and reduced the need to slowly adjust the calibration constants. A sinusoidal distortion of reconstructed interferometer positions due to subtle convergence problems in the calibration fits has been found, and fixed by introducing distortion parameters into the fit.

The reason that the 10-kg test platform filtered-PID gain parameters needed to be low for stability has been explained by a criterion easily applicable to simple experimental measurements. The multiple strong resonances of the platform made it hard to apply high broadband gain. State-vector control methods were described that should be better adapted to such complex systems.

Automated methods to determine the parameters of a state-vector model, and calculate the optimal gains, were developed. They were used on a piezo-mirror and gave

RMS control of 0.070 nm, comparable to manually optimized filtered-PID, and in agreement with simulation.

The methods were also applied to the 10-kg platform. The initially calculated control gains were unstable on the real system, but increasing the R and Q' values produced gains that were stable on the real platform. The feedback controlled the platform with RMS of 5.8 nm, comparable to manually optimized filtered-PID, but disappointingly not better either. The calculated control gains were relatively low, and the predicted performance was equally poor in simulation. Even the somewhat higher gains that were stable in the simulation gave poor performance. However the state-estimator was able to predict future position measurements on the real platform with a 0.15 nm RMS, suggesting that the measurement noise, disturbance model, and system model were not the cause of the poor performance.

Simulations of state-vector control of mass-spring systems with multiple modes show that if the piezo connected directly to the payload mass, the calculated control is excellent. If the piezo is far from the payload mass, the calculated optimal control is not much better than passive damping. However, the topology of the 10-kg platform does not appear to be this unfavorable. A simulation with vibrations of the interferometer signal-mirror did not show dramatic degradation of control. But a simulation with a reference-mirror mechanically distant from the payload mass gave low optimal gains and poor control performance, qualitatively similar to the 10-kg platform performance.

9 ACKNOWLEDGEMENTS

In addition to the authors, UBC Physics students Travis Downs, Parry Fung, Jason Thompson, and Ken Yau did important early work on the optical anchor program. This work is supported by the Canadian National Science and Engineering Research Council (NSERC).

---

1 T. Mattison et al, "Vibration Control Feedback R&D at University of British Columbia" in Proceedings of the 26th Advanced ICFA Beam Dynamics Workshop on Nanometer Size Colliding Beams (Nanobeam 2002), Lausanne CH, Sept. 2-6, 2002, ed. R.Assmann, F.Zimmerman.

2 R.Greenall, "Nanovibration Control," M.Sc. thesis, University of British Columbia, June 2004.

ATF INTERNATIONAL COLLABORATION *

Junji Urakawa for the ATF International Collaboration
High Energy Accelerator Research Organization(KEK), 1-1 Oho, Tsukuba-shi, Ibaraki, Japan

Abstract

The KEK Accelerator Test Facility (ATF) is a 1.3GeV storage ring capable of producing ultra-low emittance electron beams and has a beam extraction line for ILC (International Linear Collider) R&D. The ATF has proven to be an ideal place for researches with small and stable beams. $2x10^{10}$ single bunch and 20, 3, or 2 bunch-train with 2.8nsec, 154nsec or 308nsec bunch spacing, respectively, have been extracted to develop Nano-Cavity BPM's, Nano Beam Orbit handling technique, Optical Diffraction Radiation (ODR) monitor, a precision multi-bunch laser-based beam profile monitor and polarized positron beam generation via backward-Compton scattering by the international collaboration [1].

This report is a selection from the document of ATF MoU (Memorandum of Understanding for the ATF) and a short description of ATF2 project under the ATF International Collaboration.

1 INTRODUCTION

We have established an International Collaboration of ATF (including ATF2 project) with many institutes and it was launched on Aug. 1st 2005. Now several additional institutes are preparing to join into this collaboration.

The International Collaboration of ATF is based on the Memorandum of Understanding (MoU) which defines the organization of the international collaboration to carry out the research programs at ATF and its extension ATF2, so as to maximally contribute to the world design and development efforts in the areas of particle sources, damping rings, beam focusing and beam instrumentation towards the International Linear Collider (ILC) project. We are adding the MoU, the chart of the organization and related material into new ATF Homepage (http://atf.kek.jp/).

As evident from this MoU, the construction and operation of ATF2 will be executed in the framework of the International Collaboration of ATF. The management of activities of ATF2 will be carried out under the supervising bodies as described in the section 3.

We described the simplified explanation of the ATF MoU and additional decisions after the 1st ICB (International Collaboration Board) meeting in the following sub-sections.

2 MISSION of ATF/ATF2

ATF is to establish the technologies associated with producing the electron beams with the quality required for ILC and to provide such beams to ATF2 in a stable and reliable manner.

ATF2 is effectively to use the beams extracted from ATF at a test final focus beamline which is similar to what is envisaged at ILC. The goal is to demonstrate the beam focusing technologies that are consistent with ILC requirements. For this purpose, ATF2 aims to focus the beam down to a few tens of nm (rms) with a beam centroid stability within a few nm for a prolonged period of time.

Both the ATF and ATF2 is to serve the mission of providing the young scientists and engineers with training opportunities of participating in R&D programs for advanced accelerator technologies.

3 ORGANIZATION of ATF/ATF2

To execute the scientific programs at ATF/ATF2, the following bodies were instituted:
- International Collaboration Board (ICB)
- Technical Board (TB)
- Spokesperson (SP) with his/her Deputies
- System/Group Coordinators (SGCs)

3-1 International Collaboration Board (ICB)

The International Collaboration Board (ICB) is the decision making body for executive matters related to the ATF collaboration. Each collaborating institute can delegate one member to the ICB. In addition, the ICB is joined by the three GDE Regional Directors, who represent Asian, North American and European regions. One of the members of the ICB is to serve as the ICB Chair. The nomination of the ICB Chair is done through mutual voting by all of the ICB members.

According to the 1st ICB meeting at Snowmass 2005, an ICB meeting will be held approximately once per year. Research programs and near term schedules of the machine operation will be posted to the ATF homepage, usually for the upcoming two weeks. If some collaborators have a need to change the schedule, SP or deputies have to coordinate it.

3-2 Technical Board (TB)

The TB consists of approximately 4~5 members from each of the Asian, North American and European regions. The members of the ATF Technical Board (TB) are nominated and appointed by the ICB. The TB serves the following tasks:

- At the request of ICB, assist the Spokesperson in formulating the ATF Annual Activity Plan, which outlines the activity plans of ATF/ATF2 including the budget and beam time allocation for each Japanese fiscal year.
- Assist the ICB in assessing the scientific progress that is being made by the ATF collaboration.

The SP has three Deputies and serves as the TB Chair for efficient management. Usually schedule of ATF machine operation is divided to two blocks of operating

*junji.urakawa@kek.jp

time per year with about four months summer long shutdown. One block is from mid. of Oct. to Dec, and the other is from mid. of Jan. to mid. of June. Since there are many collaborators, we propose two meetings of TB per year in Dec. and May for review and recommendation of the research programs at ATF.

3-3 Spokesperson (SP)

The SP serves the following tasks:

- Direct and coordinate the work required at ATF/ATF2 in accordance with the ATF Annual Activity Plan.
- Report the progress made by the collaboration to the ICB and the director of KEK.
- Report the matters related to KEK budget and KEK properties to the director of KEK.

To carry out these tasks, the SP will

- Appoint, with an approval of ICB, up to three Deputies to assist his/her tasks in the areas of
  - Beam operation,
  - Hardware maintenance, and
  - Design, construction and commissioning of ATF2.
- Appoint, with an approval of ICB, the System/Group Coordinators (SGCs) on critical ATF/ATF2 subsystems and study programs.
- Organize a "Coordination Group" with the Deputies and System/Group Coordinators for coordinating the details of the operation and development at ATF/ATF2 on a daily (during the beam operation period) or weekly (during the maintenance and construction period) basis.

The report and the discussion are usually carried out through the ATF Homepage (http://atf.kek.jp/) with members of ICB, TB and SGCs.

3-4 System/Group Coordinators (SGCs)

- The System/Group Coordinators were appointed by the Spokesperson with an approval of ICB.
- The appointment of the System/Group Coordinators was made in a manner consistent with the ATF Annual Activity Plan.
- The System/Group Coordinators coordinate the tasks charged to the assigned Systems or Groups, and assist the Spokespersons and the Deputies coordinate the ATF/ATF2 research programs.

In case of small study groups with less than 5 members, the Spokesperson or the Deputies may assume the role of its Coordinator on an acting basis.

Simplified organization chart is shown in Fig.1.

3-5 Execution of Research Programs at ATF/ATF2

The ATF Spokesperson (SP) supervises the construction and operation programs of ATF/ATF2 in accordance with the ATF Annual Activity Plan, as approved by the ICB. The ATF SP can delegate part of his/her tasks to the Deputies and System/Group Coordinators, as deemed appropriate. The planning and execution of the construction and operation programs of ATF/ATF2 must be conducted in a manner consistent with the Japanese laws, KEK internal regulations and other rules applicable in case of activities by non-KEK members of the collaboration. Details of the group structures are to be formulated in ways optimized in accordance with the technical nature of each program in question, e.g.. activities such as design, simulation, testing, construction, commissioning, operation, and investigation.

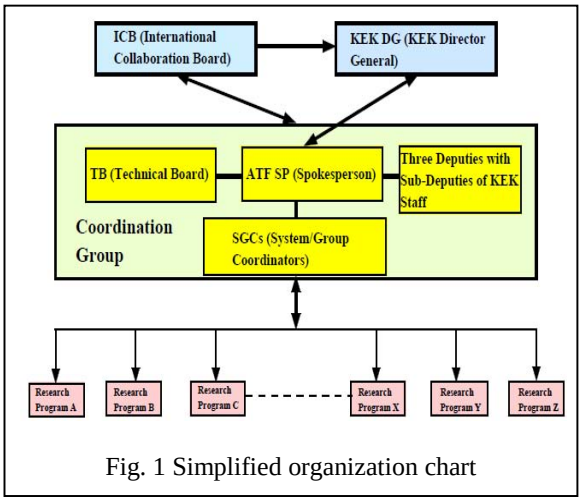

Fig. 1 Simplified organization chart

Additional agreements concerning the matters related to execution of non-KEK budget, management of non-KEK properties at the premise of ATF, together with handling of KEK properties at the premises outside KEK, are to be individually dealt with in Annexes attached to the ATF MoU.

The detailed coordination of beam time allocation will be done by the Coordination Group.

An institute who has not signed on the ATF MoU may participate in part of the research programs at ATF, with an authorization of the ATF SP, in as much as the proposed activity is:

- within the ATF Annual Activity Plan,
- under the consent by the relevant the Deputies or System/Group Coordinators, and
- promptly reported to the ICB.

Should a conflict of interests occur among the members or Work Groups within the collaboration, the Spokesperson will make the best efforts to resolve it in an amicable manner. When a suitable resolution cannot be reached, the Spokesperson will bring the matter to the ICB for further negotiation towards a resolution.

3-6 Membership of the Collaboration

Membership of new institutes for the ATF collaboration is subject to approval of the ICB. Institutes who desire to join the ATF collaboration shall submit a

proposal to the Spokesperson, who will relay the matter to ICB.

Withdrawal of a member institute from the ATF collaboration is subject to acknowledgement by the ICB. Institutes who desire to withdraw from the ATF collaboration shall submit a notification to the Spokesperson, who will relay the matter to ICB.

4 New Proposal + Present Research Program

There are several R&D proposals to the ATF international collaboration. We are expecting the approval of following research programs with related institutes.

StaFF : Stabilization of the Final Focus of the ILC
CSR(Coherent Synchrotron Radiation) Study in Damping Ring
Positron Generation based on Laser Compton Scattering in Damping Ring
Gamma-Gamma Collider Study

We are going to research and develop following items at ATF.

Laser wire R&D in Damping Ring
High quality electron beam generation by photo-cathode RF Gun
X-ray SR(Synchrotron Radiation) Monitor R&D
ODR(Optical Diffraction Radiation) monitor R&D
Beam Based Alignment R&D
Nano-BPM project of SLAC, LLNL, LBNL and UK
Nano-BPM project of KEK, PAL, SLAC and UK
FONT(Feedback On Nanosecond Timescales) R&D
Laser Wire R&D at EXT
Fast Kicker Development project
Fast Ion Instability Study
Multi-bunch Instability Study

Especially, we explain the details on R&D for Cavity BPM and ATF2.

Cavity BPM at BDIR (Beam Delivery &Interaction Region) For BPMs in the BDIR area, a mechanical stability of 1 μm or better in any time scale is required during operation. The Cavity BPMs based on a microwave cylindrical cavity have a much more rigid structure than other BPMs. Consequently, a superior long-term mechanical stability is expected, and the Cavity BPMs are considered to be suited for deployment in this area. Their resolution is 0.1 μm over a measurement range of +/-50μm. The absolute accuracy is 10μm. Since the sensor cavity and its outer surface has a concentric, cylindrical shape, their centers can be determined within a few μm. The installation into the quadrupole magnet, as shown in Fig. 2, and the calibration of the BPM center to the magnetic center is done to an accuracy of 10 μm. The singing wire method determines the magnetic center, and an external coordinate machine correlates it to the BPM outer surface, which is the reference surface of the BPM.

Temperature control is essential for maintaining the mechanical stability. The BPM temperature is affected by the ambient temperature and heat from the quadrupole magnet. An electrical temperature controller with a +/-0.1degree accuracy is installed in the BPM body. Drifts of the BPM offset due to common mode contaminations are suppressed by employing the slot magnetic coupling and the external suppressor circuit using two port combiner. The frequency of the difference mode in the sensor cavity is chosen to be 6.5 GHz, since it has no relation to any accelerator frequency.

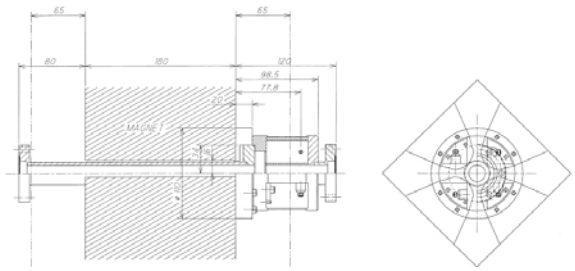

Fig. 2 Installation of Cavity BPM into the Q-magnet

This allows one to avoid interference into the circuit. The detection circuit consists of a synchronous phase detector with the reference cavity pickup, a pulse stretching amplifier, a diode amplitude detector, a pulse amplifier and a 16 bit track-hold ADC.

ATF2 project

ATF2 aims to focus the beam down to a few tens of nm(rms) with a beam centroid stability within a few nm for a prolonged period of time. Detail report of the ATF2 is given in [2]. Development of above monitors and beam tuning method will be established during the experiments of ATF2 project. Both the ATF and ATF2 will be managed to serve the mission of providing the young scientists and engineers with training opportunities in R&D programs for advanced accelerator technologies.

Acknowledgements

The authors would like to thank Professors Y.Totsuka, F.Takasaki, Y.Kamiya, K.Yokoya, S.Kurokawa, and A.Enomoto for their encouragement. All members of KEK-ATF group and international collaborators for these research programs are acknowledged. We also thank Professor E.Paterson of SLAC for supporting the ATF project as an international collaboration.

5 REFERENCES

[1] J.Urakawa, Results from DR and Instrumentation Test Facilities, PAC2005
[2] ATF2 Proposal, Volume 1, CERN-AB-2005-035, CLIC note 636, DESY 05-148, ILC-Asia-2005-22, JAI-2005-002, KEK Report 2005-2, SLAC-R-771, UT-ICEPP 05-02 (2005)

CLIC R&D

F. Zimmermann, H. Braun, L. Soby
CERN, Geneva, Switzerland

Abstract

We review the focus and schedule of R&D for the Compact Linear Collider (CLIC), recent developments on the CLIC beam delivery system and damping rings, and CERN/CLIC contributions to ATF/ATF-2.

1 INTRODUCTION

The Compact Linear Collider (CLIC) [1] is the only known cost-effective scheme which can extend the energy of an electron-positron linear collider to the multi-TeV energy range. The CLIC technology is not completely mature yet, and it still requires challenging R&D. However, numerous promising results have already been obtained at the CLIC Test Facility 2 (CTF-2) and in the £rst stages of the new CLIC Test Facility 3 (CTF-3). The remaining feasibility issues have been clearly identi£ed by the International Linear Collider Technical Review Committee (ILC-TRC) [2]. A multilateral collaboration has been established, addressing all CLIC speci£c feasibility issues before the year 2010. Technology-independent feasibility issues are studied in the framework of EUROTeV and in close collaboration with the ILC.

2 GENERAL CLIC R&D FOCUS AND R&D SCHEDULE

A concise history of CLIC as well as its near-term future are shown in Fig. 1. From 1995 onwards, CTF-2 demonstrated the two-beam acceleration. In 2002 it generated an rf gradient of 190 MV/m. The CLIC physics report was published in 2003 [3]. In 2004 the CLIC R&D schedule was accelerated, in order to obtain answers to all ILC-TRC feasibility questions by 2009 [2]. It is foreseen to produce a preliminary cost estimate in 2008.

The key issues related to the CLIC technology were identi£ed by the 2nd ILC Technical Review Committee (TRC) in 2003. They are grouped in different categories, the most important ones being so-called ‘R1’ items (feasibility) and the next ones the ‘R2’ items (design £nalization). Speci£cally, the R1 (feasibility) items for CLIC are

1.1: test of damped accelerating structure at the design gradient and pulse length;

1.2: validation of drive beam generation scheme with fully loaded linac operation; and

1.3: design and test of damped ON/OFF power extraction structure.

The R2 (design £nalization) items comprise

2.1: developments of structures with hard breaking materials (W, Mo);

2.2: validation of stability and losses of drive-beam decelerator, and design of machine protection system;

2.3: test of relevant linac sub-unit with beam;

2.4: validation of drive beam 40 MW, 937-MHz multibeam klystron with long rf pulse;

2.5: effects of coherent synchrotron radiation in bunch compressors;

2.6: design of an extraction line for 3 TeV centre of mass.

The items 1.1–1.3 and 2.1–2.3 are all addressed by CTF-3, a schematic of which is shown in Fig. 2. The last two items, 2.5 and 2.6 are covered by EUROTeV. For the last point, 2.4, a feasibility study was done. It would now need an industrial development. This point is not thought to be critical, as the drive-beam parameters can be adapted to other klystron power levels, if needed.

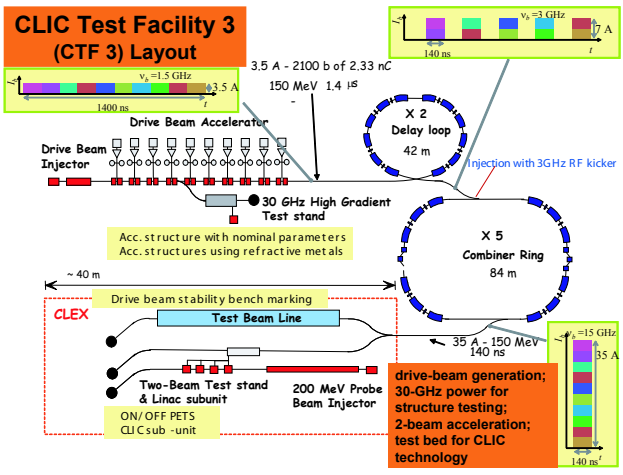

Figure 2: Schematic of the CLIC Test Facility 3 with some further details.

Figure 3 presents the CTF-3 schedule, together with the date of the expected demonstration for the various R1 and R2 items. The complete demonstration is foreseen by 2009, in accordance with the overall CLIC time schedule, but results for the most critical (R1) items will be obtained already one or two years earlier.

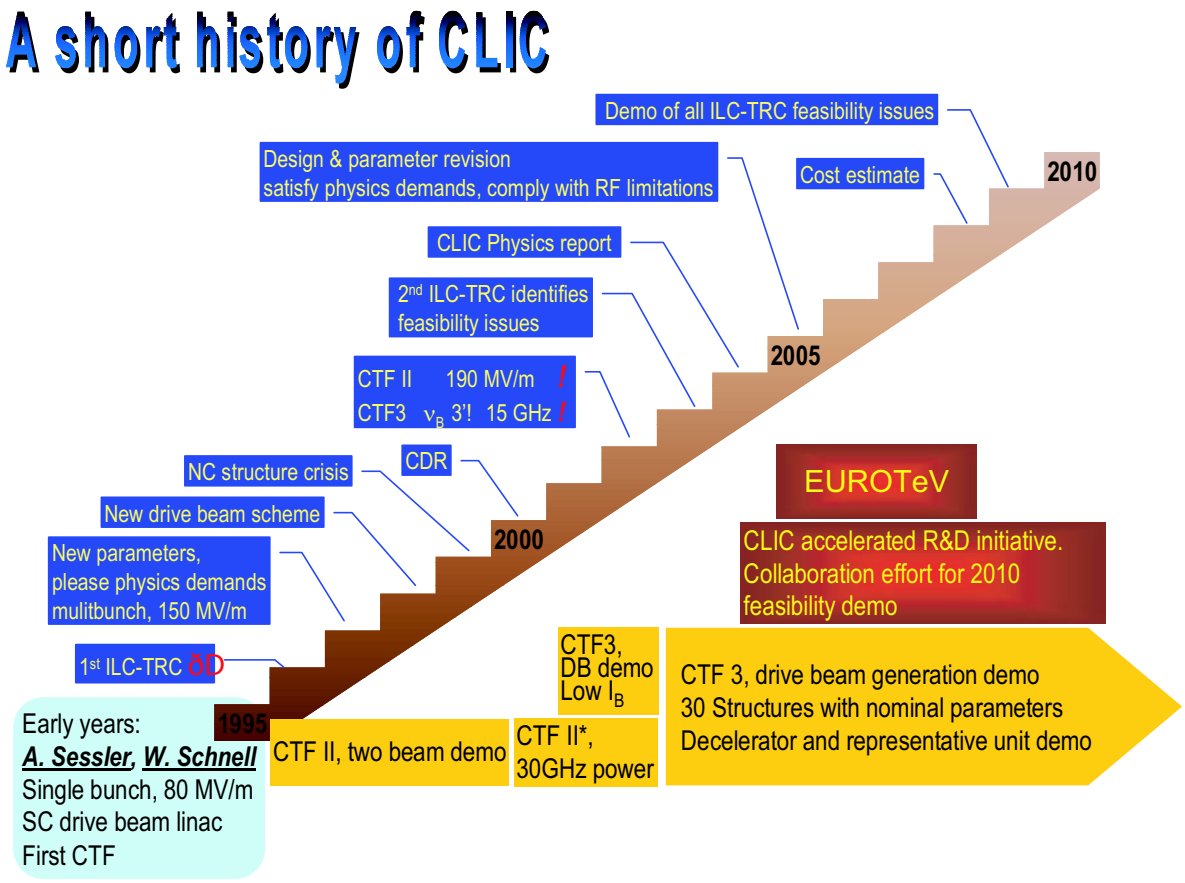

Figure 1: A short history of CLIC [4].

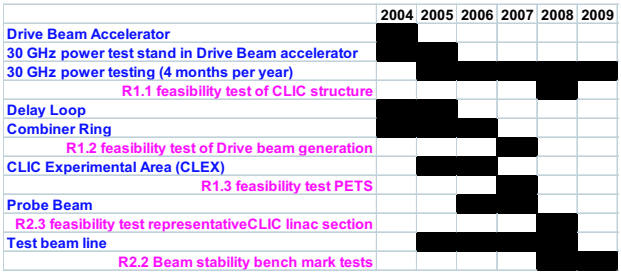

Figure 3: CTF-3 schedule.

3 R&D FOR BEAM DELIVERY SYSTEM

Recent effort for the beam delivery system (BDS) was devoted to cross-benchmarking of various simulation codes, such as MAD-X, SAD, PLACET, and PT [5], and to the design optimization of the alternative nonlinear collimation system [6], in particular to assessing its performance and to comparing the latter with the linear baseline system [7].

The further plans for BDS development foresee

- to automate the £nal-focus matching;
- to add nonlinear matching to MAD-X/PTC;
- to improve the BDS chromatic bandwidth;
- to modify, e.g., shorten the linear and nonlinear collimation systems;
- to possibly design a new £nal-focus optics from scratch;
- to design an extraction line for 3-TeV centre-of-mass energy and to assess its performance;
- to study the collimation ef£ciency;
- to survey wake £elds in the BDS;
- to reconsider and streamline machine protection;
- to investigate and perhaps incorporate octupole tail folding; and
- to continue the CLIC stabilization study at Annecy [8].

As an example, chromatic aberrations are studied by means of tracking matched phase-space ellipses at 1σ amplitude for different values of momentum deviations. Figure 4 shows a typical result from PLACET. The red line

represents the position of the beam centroid predicted from a third order Taylor expansion:

$$x_c(\delta) \approx R_{16}\delta + T_{166}\delta^2 + U_{1666}\delta^3 , \quad (1)$$
$$x'_c(\delta) \approx R_{26}\delta + T_{266}\delta^2 + U_{2666}\delta^3 . \quad (2)$$

It is apparent that for a momentum deviation of $\delta = -0.4\%$ the third order expansion no longer is a good approxmation and that in addition the ellipse gets strongly distorted.

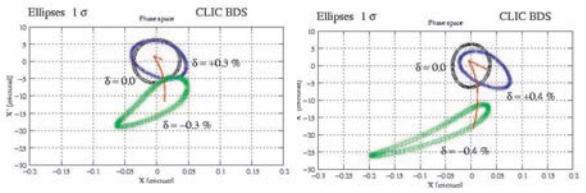

Figure 4: Chromatic effects in the CLIC BDS revealed by tracking phase-space ellipses at momentum deviations equal to 0, -0.3% and $+0.3\%$ (left), and 0, -0.4% and $+0.4\%$ (right) [5]; the PLACET code was used.

To review and organize the CLIC BDS studies a "CLIC BDS Day" was organized on 22 November 2005. The presentations on various topics can be found on the CLIC BDS Day web site [9].

4 R&D FOR DAMPING RINGS

A collaboration between CERN and the Budker Institute for Nuclear Physics (BINP) has identi£ed the most suitable wiggler technology and optimized the wiggler parameters for the CLIC damping ring [10]. A superconducting wiggler has many advantages compared with a permanent magnet one, in particular, it can yield a higher £eld amplitude (shortening the damping time, which scales with the inverse square of the £eld), a lower period length (resulting in emittance reduction; the equilibrium emittance scales with the square of the wiggler period), and it allows for easy tuning of the magnetic £eld (intrabeam scattering depends on the beam intensity). The wiggler always increases the energy spread and the longitudinal emittance. Superconductors based on Nb_3Sn technology can sustain signi£cantly higher £elds and current densities than the more conventional NbTi magnets. Some 10-T Nb_3Sn wigglers were already built at BINP; one was installed in the SPring-8 light source. The wiggler peak £eld and wiggler period were optimized, by minimizing the equilibrium emittances as a function of these two parameters. The equilibrium emittances are determined by the interplay of radiation damping, intrabeam scattering, and, to a lesser extent, quantum excitation. They are computed using an iterative self-consistent algorithm [12]. The optimum peak £eld for CLIC was found to be 2.5 T and the optimum period 45 mm. The wiggler pole gap is 20 mm, with a beam aperture of 12 mm, and a transverse £eld quality of 10^{-4} at ± 1 cm transverse distance from the center. Magnetic £eld calculations were performed by the MERMAID code.

Other CLIC damping-ring R&D comprises an assessment of the ring performance with wiggler-£eld errors and beam-based corrections [13]. Typical errors considered are quadrupole misalignments of 90 μm, sextupole misalignments of 40 μm, quadrupole and dipole rolls of 100 μrad, and 2 μm BPM resolution.

The simulation with the BETA code [11] models the beam-based correction of x-y closed orbit cross-talk, emittance coupling, and dispersion. The £nal vertical emittance with errors and after correction stays below the CLIC target value, while the dynamic aperture is decreased by 10–20% with respect to the error-free case.

The dynamic aperture of the CLIC damping ring was studied independently as part of the CERN-BINP collaboration using the programme Acceleratricum [14]. Figure 5 shows the horizontal and vertical on-momentum dynamic aperture as a function of the horizontal and vertical tune for the ideal optics. Figure 6 presents the same 2-D scan obtained after introducing a 5% beta beat. Evidently, the beta beat gives rise to unstable regions as well as to new non-systematic resonances.

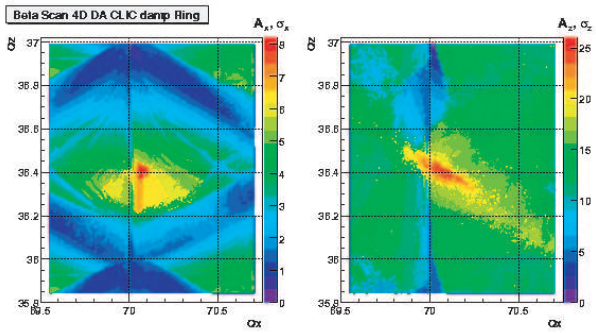

Figure 5: Tune scan of the horizontal (left) and vertical dynamic aperture (right) for the ideal optics; the colour code indicates the dynamic aperture in units of the rms beam size [14].

Another area of CLIC damping-ring R&D concerns the studies of electron cloud and ion effects. The focus here is on the use of realistic wiggler £elds, the benchmarking of electron-cloud simulations with data from DAFNE, CERN SPS, KEK B factory, RHIC, Tevatron etc., and the benchmarking of ion simulations at the KEK Accelerator Test Facility (ATF) and KEKB.

5 CERN CONTRIBUTIONS AND PLANS FOR ATF/ATF-2

The CLIC Team at CERN proposes contributions to the following four groups of "studies" at ATF-2 [15]:

- Development of the commissioning strategy. A corresponding section was already written for the ATF-2

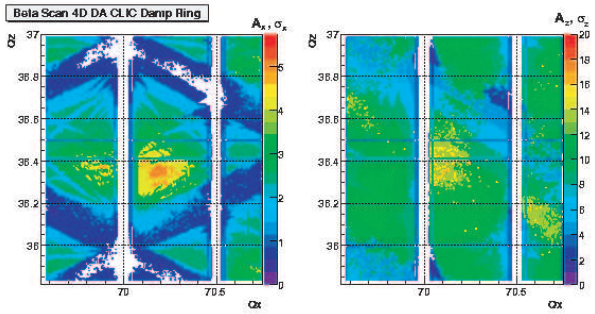

Figure 6: Tune scan of the horizontal (left) and vertical dynamic aperture (right) for an optics with 5% beta beating; the colour code indicates the dynamic aperture in units of the rms beam size [14].

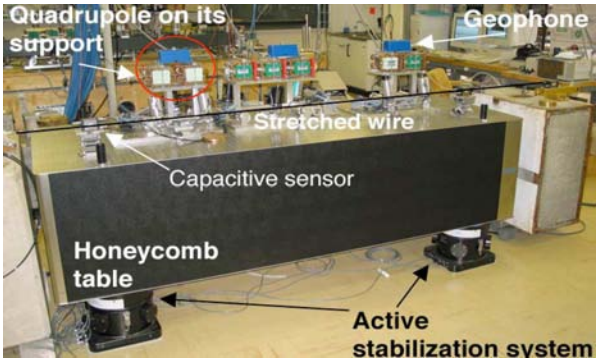

Figure 7: Resonance-free honeycomb table mounted on the active stabilization system in the CLIC stabilization test stand [19].

design report, Volume 1 [15] (*1 person month*);

- Investigation of optimum beam-based alignment procedures, e.g., as in [16], with pertinent speci£cation of the BPM ranges (*3 person months*);
- Simulations of IP tuning and the determination of maximum tuning knob ranges, e.g., in the spirit of [17] (*4 person months*);
- Survey of relevant collective effects in ATF-2 and the ATF extraction line, in particular wake £elds, e.g., as in [18] (*1 person month*);
- Participation in commissioning activities (*3 person months*).

In total, the manpower for the proposed study contributions sums up to 1 person year.

In addition, the following hardware contributions are offered:

- An active stabilization table including stabilizing feet (STACIS2000 system from TMC), shown in Fig. 7. The table is a honeycomb support structure with length 2.4 m, width 0.8 m, and height 0.8 m. The manufacturer guaranteed the absence of any structural resonances below 230 Hz. The stabilizing feet are equipped with integrated geophones for measuring ground vibrations, rubber pads for passive damping, and piezoelectric movers for active damping of load vibrations induced from the ground. The stabilized table was successfully used for the CERN stability study [19]. Presently it is on loan at LAPP (Annecy). The table would be available from the middle of 2006. The best use of this table for ATF-2 needs to be identi£ed. One possibility may be to stabilize the £nal quadrupoles and the IP monitors. *The value of this table is about 100,000 CHF, or 8.72 MYen.*
- Three high-precision transformer BPMs. The projected spatial BPM resolution is 100 nm and the time resolution 15 ns. The BPM aperture is 4 mm in the original design, but it can be enlarged to 6 mm, so as to alleviate concerns about aperture restrictions in ATF-2. These BPMs would be available at the end of 2007. *The development cost for these BPMs is about 160,000 CHF, or 13.95 MYen, plus manpower; they are co-£nanced by the EU via EUROTeV [20].*

Table 1: Characteristics of EUROTeV transformer BPM.

aperture	4 (6) mm
resolution	100 nm (CMMR $>$ 92 dB)
absolute precision	10 μm
rise time	$<$ 15 ns
dynamic range	$\pm$1.5 mm
linearity error	$<$ 1%
24-h stability	1 μm
vibrations	$<$ 100 nm
low-frequency cutoff	100 kHz
high-freqency cutoff	30 MHz
bake-out temperature	150°
operating temperature	20° C
vacuum	10^{-9} Torr

We now discuss the transformer BPMs in some more detail, namely we present the deliverables of the EUROTeV project, schedule, operating principle, design idea, and a comparison of beam parameters [21].

The deliverables of this EUROTeV work package include the design and construction of the monitor with characteristics as speci£ed in Table 1, the design and construction of a high resolution (100 nm) mechnically stable test bench, the development of the front-end electronics, a report on the bench measurements, and a report on beam tests with three BPMs on separate supports. Figure 8 presents the schedule of the BPM project.

Figure 9 illustrates the operating principle of the precision transformer BPM. The distribution of image current around the beam pipe re¤ects the beam position. At the

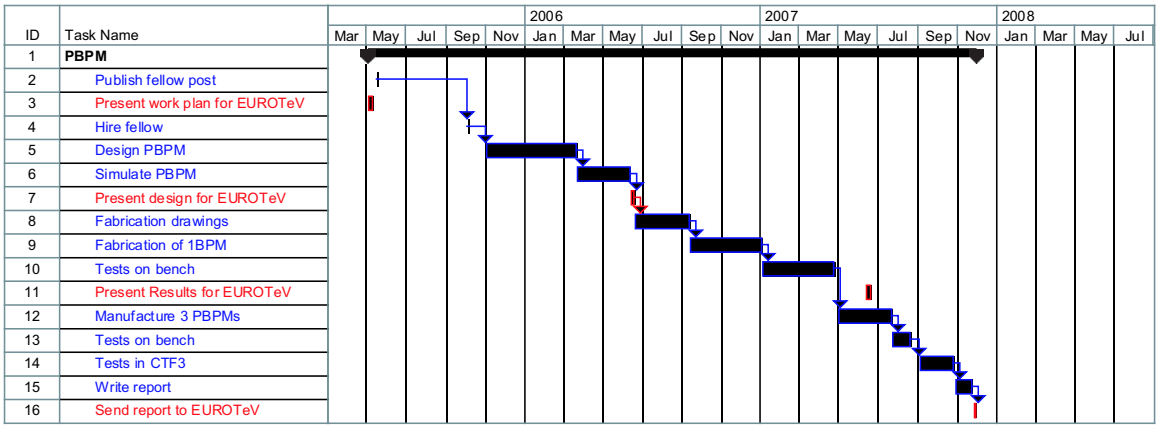

Figure 8: Schedule of transformer BPM project in EUROTeV [21].

monitor, the image current is forced to pass through 4 or 8 resistors. The intensity signal is proportional to the sum over all resistor voltages. The position dependent signal is proportional to the difference of the voltage at opposite resistors.

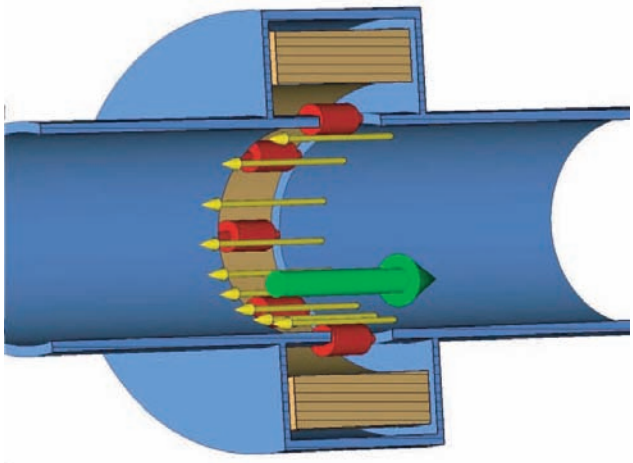

Figure 9: Operating principle of precision beam position monitor [21].

The starting point of the BPM design is a similar monitor, used at CTF-3, with a 40-mm aperture [22]. Figure 10 shows a photo of the components, and Fig. 11 the £nal assembly. The goal of the EUROTeV work package is to reduce the size of the BPM by a factor of 10 and to improve its resolution accordingly, from a few microns to 100 nm.

Table 2 compares beam parameers for various facilities and projects at which the transformer BPM could be deployed.

It was commented that with 4 mm aperture the resolution should be much better than 100 nm (rf BPMs reach 2 nm with 6 mm aperture) [23], and, conversely, that for 100 nm resolution one could have a much larger aperture than 4 mm (e.g., > 20 mm for C-band rf BPMs) [23]. However,

Figure 10: Components of 40-mm transformer BPM [22].

Table 2: Beam parameters for various test facilities and projects at which precision transformer BPMs could be used. The acronym 'ILC' refers to the International Linear Collider.

	ATF-2	ILC	CLIC
energy	1.3 GeV	variable	variable
repetition rate	0.7 Hz	5 Hz	150 Hz
beam pulse length		950 μs	58 ns
bunch spacing	2.8 ns (154 ns)	337 ns	267 ps
charge per bunch	5×10^9	2×10^{10}	2.56×10^9
no. of bunches	1–20	2820	220
peak current		3220 A	4023 A
(LP 10 MHz)		(0.2 A)	
current / pulse		9.5 mA	1.5 A

the CLIC BPMs are not rf BPMs, but transformer BPMs. The existing 40-mm aperture transformer BPMs have a resolution of less than 5 μm at 3 A and of less than 50 μm at 0.3 A mean current pulse. They are in use at CTF-3.

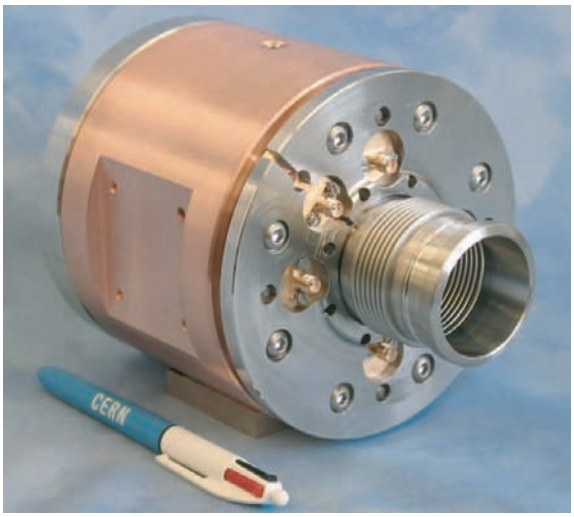

Figure 11: Final assembly of 40-mm transformer BPM [22].

The advantages of the transformer BPMs compared with, e.g., rf BPMs, are that they function for arbitrary bunch spacing, have a large frequency bandwidth (almost 6 decades) and a simple readout electronics, and that they are insensitive to spray from lost beam particles.

The EUROTeV packages leave some ¤exibility. For example, it would be possible to increase the BPM aperture to 6 mm. Concerning the ATF/ATF-2 application, information is needed on the desirable aperture, the surrounding beam pipe, the ¤ange sizes, and the type of ¤anges.

6 POLARIZED POSITRON SOURCE

At CERN there is a great interest to participate in further ATF experimental studies related to a polarized positron source based on laser-Compton scattering.

Figure 12 shows a schematic layout of a polarized source for CLIC, with laser-Compton scattering in a dedicated Compton ring. A similar source was earlier proposed for the ILC by J. Urakawa, E. Bulyak, P. Gladkikh, K. Moenig and others [24]. The ILC proposal foresees a Compton ring with 30 interaction points between the electron beam and the laser beam, and stacking of the produced positrons in the main ILC damping ring. As shown, for CLIC a simpler scheme is possible. Since 100 times less charge is required per pulse, the positrons can be produced using a single laser-beam interaction point. Also, unlike for the ILC, the positrons are stacked in a dedicated compact predamping ring.

7 US MTLC COLLABORATION

Recently, a Multi TeV Linear Collider (MTLC) Collaboration was launched by the U.S. Department of Energy [25]. Noting that in the past, the US DOE has supported extensive research on high-gradient acceleration and high-

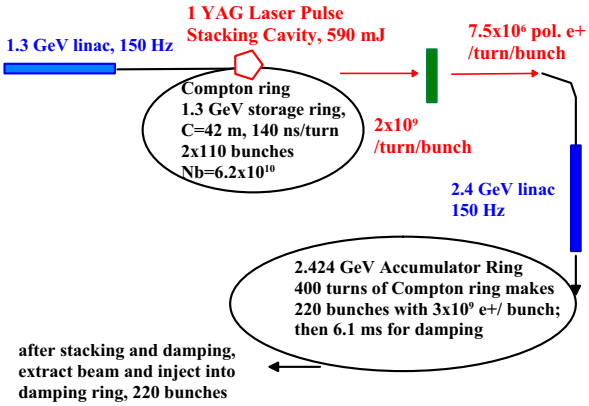

Figure 12: Schematic layout of CLIC polarized positron source.

power generation at DOE laboratories, universities and small businesses, the DOE now expresses the wish to focus this work on developing a technology path towards a cost-effective electron-positron linear collider. The DOE has asked the directors of SLAC and FNAL to organize a US collaboration for this purpose. The MTLC collaboration comprises US national laboratories, universities, and small businesses. It will collaborate with CERN on the CLIC two-beam approach. Ron Ruth has been selected to lead this effort.

8 SUMMARY

The aim of the CLIC R&D is demonstrating CLIC feasibility by 2010, i.e., at a time when £rst results from the LHC become available.

The centrepiece of the CLIC R&D is CTF-3, which addresses all critical issues realted to 30-GHz technology, drive-beam generation, drive beam dynamics, and two-beam acceleration with CLIC design pulse length and gradient.

The CLIC stability study demonstrated that colliding nanobeams are feasible with regard to ground motion and stabilization; open issues, like support resonances and sensors, are presently addressed by LAPP in Annecy.

In 2004/05, the beam-delivery work concentrated on nonlinear collimation and code benchmarking. Further optimization of the BDS optical properties and a comprehensive performance evaluation now are in progress. Extraction-line studies have also started, in Uppsala.

Recently signi£cant progress was made on the CLIC damping rings by a CERN-BINP collaboration. With a new s.c. wiggler, the CLIC target emittances are reached, even taking into account intrabeam scattering and alignment errors. Prototyping a s.c. CLIC wiggler unit is under discussion.

Other damping-ring studies for CLIC concern instabilities, intrabeam scattering, electron cloud and ion effects.

ATF and ATF-2 are important cornerstones of the CLIC

R&D for beam-delivery system and damping rings. CERN has signed the ATF-2 memorandum of understanding.

Studies of polarized positron production based on Compton scattering at ATF would be of great interest for CLIC.

It is worth emphasizing that the CLIC studies proceed in a fruitful collaboration with ILC. Figure 13, from Barry Barish, illustrates the impact of LHC physics results and CLIC R&D on the ILC design effort.

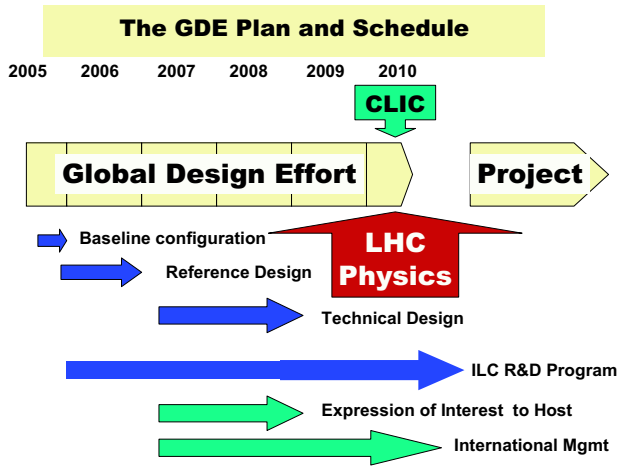

Figure 13: Plan of the ILC Global Design Effort including the impact of LHC physics and CLIC R&D (from Barry Barish) [26].

9 REFERENCES

[1] The CLIC Study Team, "A 3 TeV e+e- Linear Collider Based on CLIC Technology," CERN 2000-008 (2000).

[2] International Linear Collider Technical Review Committee, "ILC-TRC," G. Loew et al, web site *http://www.slac.stanford.edu/xorg/ilc-trc/2002/* (2002).

[3] CLIC Physics Study Group, "Physics at the CLIC Multi-TeV Linear Collider," edited by M. Battaglia, A. de Roeck, J. Ellis, and D. Schulte, CERN-2004-005 (2004).

[4] H. Braun, "CLIC", 8th ICFA Seminar on "Future Perspectives in High Energy Physics," Daegu, Korea, 28 September – 1 October 2005, web site *http://chep.knu.ac.kr/ICFA-Seminar/* (2005).

[5] T. Asaka, J. Resta Lopez, "Characterization and Performance of the CLIC Beam Delivery System with SAD, MAD and PLACET," CLIC Note 637 (2005).

[6] A. Faus-Golfe, F. Zimmermann, "A Nonlinear Collimation System for CLIC," EPAC'02 Paris (2002).

[7] A. Faus-Golfe et al, "Alternative Design for Collimation System," Proc. Nanobeam'05 (2005).

[8] B. Bolzon et al, "Active Stabilization of a Future Linear Collider Final Focus Quadrupole Mock-Up," Proc. Nanobeam'05 (2005).

[9] Web site of the CLIC BDS Day: *http://ab-clic-bdsday.web.cern.ch/ab-clic-bdsday*

[10] M. Korostelev, E. Levichev, P. Vobly, "Progress with Damping Wiggler Design," CLIC Seminar 16.09.2005, web site *http://ab-abp-clic-dr.web.cern.ch/ab-abp-clic-dr/talks.htm* (2005).

[11] J. Payet, "BETA User's Guide," DSM/DAPNIA/SEA.

[12] M. Korostelev, F. Zimmermann, "Optimization of CLIC Damping Ring Design Parameters," EPAC'02 Paris (2002).

[13] M. Korostelev, "CLIC Damping Ring Design," PhD thesis to be published (2005).

[14] E. Levichev, P. Piminov, "Dynamic Aperture of CLIC Damping Ring," Draft CLIC Note, September'05 (2005).

[15] ATF2 Collaboration (B. Grishanov et al.), ATF2 Proposal, Volume 1, SLAC-R-771, CERN-AB-2005-035, CLIC-Note-636, DESY-05-148, ILC-ASIA-2005-22, KEK-Report-2005-2 (2005).

[16] T. Raubenheimer, D. Schulte, "The Ballistic Alignment Method," PAC99, New York (1999).

[17] F. Zimmermann, "Magnet Alignment Tolerances in the SLC Final Focus System Determined by Lie Algebra Techniques," Nucl. Instr. Meth. A364, 231 (1995).

[18] F. Zimmermann, K.L.F. Bane, C.K. Ng, "Collimator Wake Fields in the SLC Final Focus," EPAC96, Sitges (1996).

[19] R. Assmann, W. Coosemans, G. Guignard, N. Leros, S. Redaelli, D. Schulte, I. Wilson, F. Zimmermann, "The CLIC Stability Study on the Feasibility of Colliding High Energy Nanobeams," Proc. Nanobeam'02, CERN-Proceedings-2003-001, p. 87 (2003).

[20] Web site *www.eurotev.org*

[21] Web site: *https://cern-eurotev-wp5.web.cern.ch/CERN-EUROTeV-WP5/*

[22] M. Gasior, "An Inductive Pick-Up for Beam Position and Current Measurement," CERN-AB-2004-053-BDI, CLIC Note 572, presented at DIPAC 2003 (2003).

[23] T. Tauchi, private communication (2005).

[24] S. Araki et al, "Design of a Polarized Positron Source Bsaed on Laser Compton Scattering," KEK-PREPRINT-2005-60, CLIC-Note-639, LAL 05-94 (2005).

[25] P. Debenham, slides presented at US Workshop on 'High Gradient Research for MTLC', SLAC, 11–12 July, 2005 (2005).

[26] B. Barish, "Report from GDE Director," 8th ICFA Seminar on "Future Perspectives in High Energy Physics," Daegu, Korea, 28 September – 1 October 2005, web site *http://chep.knu.ac.kr/ICFA-Seminar/* (2005).

*POLARIZED POSITRON SOURCE BASED ON COMPTON SCATTERING**

Junji Urakawa for the Compton Posipol Project
High Energy Accelerator Research Organization(KEK), 1-1 Oho, Tsukuba-shi, Ibaraki, Japan

Abstract

The KEK Accelerator Test Facility (ATF) is getting an opportunity for the demonstration of the scheme of Compton based positron source for ILC. We describe outline of proposed scheme and recent consideration for operational reliability and flexibility.

1 Introduction

The Compton scheme can generate the high intensity positron beam which meets the ILC(International Linear Collider) requirements with enough margin. In contrast to the undulator scheme, the Compton scheme has advantages as follows: [1]

1. It is a completely independent system from the electron arm. It avoids complex interference between two arms that is important feature especially for the commissioning.
2. Because of the independency, there is much flexibility to change the beam structure, intensity, etc.
3. The performance can be much improved by introducing some new technology, e.g. more powerful laser system, more precise high-gain optical cavity, etc. These improvement can be made after enough confirmation of the new technology in the laboratory without any risk.
4. Because the operation is completely independent from the electron linac, there is no limitation at the lower energy operation. The collision at the energy from 5 GeV up to 250 GeV (500GeV eventually) can be easily made without any cost.
5. The injection scheme is totally different from that of the undulator scheme. Any fast kicker, which is one of the most difficult device in ILC injector, is not necessary.
6. It can generate the polarized positron. The polarization depends on the laser helicity which can be switched pulse by pulse. This polarization switching is very important for the physics experiment. It is hard to switch pulse by pulse the polarization in the undulator scheme which is requiring an extra section to implement the switching.

Addition to these advantage, the critical elements of the Compton scheme can be demonstrated prior to the real construction and partly demonstrated already. Then the Compton system can be developped step by step. This feature is remarkable in contrast to the undulator because the undulator scheme is hard to demonstrate with a reasonable scale prior to the construction. Even though it features these advantages compared to the undulator scheme, the Compton scheme is still in an initial stage to develop the real ILC positron source because a high current electron beam needs to be produced and a complicated high power laser scheme is needed. However, this concept is so attractive that the collaborating groups at several laboratories keep their aggressive R&D efforts towards a well matured design based on the Laser Compton scheme.

There are several important components and technologies for the Compton scheme. Among them, a couple of essential components were already demonstrated in KEK-ATF as follows: [2]

1. High gain laser cavity
2. The Compton scattering to yield enough gamma rays,

that means the proof of principle of Compton scheme, is reasonably confirmed.

There are several issues to be studied for the Compton scheme as follows,

1. High power CO_2 or YAG laser system.
2. Controlling the chain of the laser cavities.
3. High current Compton Ring.
4. Positron beam stacking into the main DR(Damping Ring).
5. Availability.

2 Outline of Polarized Positron Source based on Compton Scattering

The Compton based polarized positron source consists of (1) an electron linac which is the injector of the Compton ring, (2) an electron storage ring named Compton ring, (3) a laser which sends laser beam to pulse stacking cavities, (4) laser pulse stacking cavities which are installed in a straight section of the Compton ring, (5) conversion target and capture section (6) positron injector linac, and (7) a damping ring.

Now two versions of design are under consideration. One uses CO_2 laser and the other uses YAG laser. The former is called CO_2-version, and the later is called YAG-version. In the following description, the number corresponding to CO_2-version is firstly shown in each statement, then that of the YAG-version is shown in parentheses.

Compton ring is a high current electron storage ring. The energy of the ring is 4.1 GeV (1.3 GeV). The ring has long straight section in which 30 laser stacking cavities are installed. The circumference of the ring is 649.2 m (276.7m). Two trains are (one train is) circulating in the ring. In both CO_2- and YAG-versions a train consists of 280 bunches with bunch to bunch spacing of 3.077 nsec, and the bunch population is 6.2×10^{10}. An electron linac with an energy of 4.1 GeV (1.3 GeV) is employed to inject electron to the Compton ring. The linac does not need to be a high current one, because electron population loss due to Compton scattering is negligible. The collisions of electrons circulating in the Compton ring and photons stored in laser stacking cavities create polarized γ-rays. In one turn of the Compton ring, 280 x2 (280) γ -ray bunches are created. Polarized positrons are created from those γ -rays on thin

*junji.urakawa@kek.jp

(~$0.5X_0$ Radiation length) target, then positrons in the high energy side of the spectrum are collected in the capture section.

Each laser stacking cavity stores a photon bunch with an energy of 210 mJ (600 mJ). The laser stacking cavity is designed to have an enhancement factor of 100. Thus, each bunch of laser beam delivered from a laser should have energy of 2.1 mJ (6.0 mJ). The laser operates at 100 Hz and each pulse of laser contains $3.6x10^4$ ($2.9x10^4$) bunches with bunch-to-bunch spacing of 3.077 nsec. The duration of the laser pulse is 110μs (90μs). Single laser provides laser beam to 30 stacking cavities in daisy chain. The laser operates at 100Hz, thus laser cavities are filled by photons every 10ms.

Then positron injector linac accelerates positrons up to 5 GeV. A cold linac is employed. The linac is almost identical to the main linac, except that the injector operate at 100 Hz. Since the linac operates 100 Hz, necessary cooling power is 4 times larger than that of main linac. However, the excess of total cooling power of the collider is not significant. After acceleration, positrons are sent to the damping ring. In the Compton scheme the damping ring has two functions: stacking and damping. Actually, main damping ring itself is the ideal choice of stacking ring, because it can store full number of positron bunches, it can be designed to have short damping time of ~10 msec, and it has large longitudinal bucket area. The circumference of the damping ring is chosen to be 3247 m (2767 m), which is 5 times (10 times) larger than that of the Compton ring.

The procedure of collision in the Compton ring and positron stacking in the damping ring is as follows. The collisions with laser photons make negligible loss of electron population in the Compton ring, however collisions give rise to bunch lengthening. Due to bunch lengthening, number of γ-rays created by collisions decrease as a function of turn number. Therefore number of γ-rays becomes practically zero, if laser photons always exist in cavities. Pulsed mode operation is applied to cure this problem. Laser cavities are filled by photons only in 110μs (90μs). This corresponds to 50 (100) turns of the Compton ring. Then laser is turned off for ~9.9ms of cooling time. In the cooling time, bunch length becomes shorter and goes back to primary length. Average number of γ-rays per turn is $1.8x10^{10}$/bunch ($1.4x10^{10}$/bunch) in the energy range of 23-29 MeV. Then, the average time which corresponds to the cooling time of the Compton ring is ~9.9ms and the longitudinal phase space occupied by injected positrons is damped to the size which is small enough to accept the next injection. Since the laser operates at 100 Hz, next injection starts at this timing. This alternate cycle of injection and damp is repeated 10 times. Therefore, 100 times of stacking in each bucket are made in total. At this moment, the damping ring still has 100ms which is enough to make the emittance of positron beam fully damped. The simulation shows that the average stacking loss is 18%. Therefore total number of stacked positrons in the damping ring is $2.0x10^{10}$/bunch ($1.6x10^{10}$/bunch). [3]

3 R&D Plans

Regarding to "High current Compton Ring" and "Positron beam stacking into the main DR", since we have developed full beam tracking simulation code, research of the realistic values on beam parameters will be finished until Sep. of 2006. Then, parameters on laser systems and laser cavity will be revised. On the other hand, we already started the design of the double chain of the laser cavities and the installation will be planned at ATF. Hopefully, test of laser focus to 5μm will be established at the center point in the cavity within a few years and we will install the double chain of the laser cavities in ATF damping ring in the future and generate a huge amount of γ ray for the demonstration of the availability. In this case we will use the high quality YAG laser system. Another challenge of our scheme is the necessity of high power and high quality laser. We have to develop long laser pulse amplification system using commercial available components. YAG flash lamp or solid state amplifiers are applicable for this R&D. Study using high power laser for photo-cathode RF gun is on going and the future R&D is under consideration. Essential hardware R&D's are almost on schedule and the results will be demonstrated within three years.

4 Change and Prospect of R&D's

We are considering the enhancement factor of about 3000 of optical cavity system based on recent discussion and R&D's. If the enhancement more than 1000 with small waist size at the center of the optical cavity will be demonstrated at ATF, we have to change our scheme of the laser system for the polarized positron source based on Compton scattering as follows:

5 sets of independent optical cavity system will be installed into the straight section of the Compton ring, which mean 1.26J/laser pulse of CO_2-version (3.6J/laser pulse of YAG-version) with the assumption of the 3000 enhancement factor. In this case we have to check nonlinear Compton scattering effect [4] and 0.42mJ (1.2mJ) laser pulse train with 100μs duration is injected into the optical cavity. Single laser pulse train is divided into 5 ways for 5 sets of independent optical cavity system. Then, we need 2.1mJ (6mJ) laser pulse train generation. This new laser system gives us operational reliability and flexibility on the operation of the optical cavity.

On the other hand, we are going to design the Compton ring with low momentum compaction factor which will be controlled in the range of $2x10^{-4}$ to 0 by changing the value of negative dispersion [5]. The fine tuning of the ring parameters (especially nonlinear terms in the orbit compaction and the implementation of the RF-phase manipulation) will improve the performance up to the ideal model.

Acknowledgements

The authors would like to thank Professors Y.Totsuka, F.Takasaki, Y.Kamiya, K.Yokoya, S.Kurokawa, and A.Enomoto for their encouragement. All members of KEK-ATF group and international collaborators for this research program are acknowledged. We also thank Professor E.Paterson of SLAC and Frank Zimmermann of CERN for supporting the ATF project as an international collaboration. The present research has been financially supported by a Grant-In-Aid for Creative Scientific Research of JSPS (KAKENHI 17GS0210) and UK-Japan Collaboration (Japan-United Kingdom Research Cooperative Program Joint Project from 2005 to 2006).

5 REFERENCES

[1] Sakae Araki et al., Alternative Recommendation for ILC Positron Source Based on Laser Compton Scattering, Submitted to 2nd ILC Workshop at Snowmass, page 39 (2005).

[2] J.Urakawa, Results from DR and Instrumentation Test Facilities, PAC2005.

[3] Sakae Araki et al., Conceptual Design of a Polarised Positron Source Based on Laser Compton Scattering (A Proposal Submitted to Snowmass 2005), KEK Preprint 2005-60, physics/0509016, CARE/ELAND Document-2005-013, CLIC Note 639, LAL 05-94, page 39 (2005).

[4] M.Babzien et al., Quadrupole radiation in Thomson scattering of laser and relativistic electron beams Phys. Rev. Lett. accepted. (2005)

[5] Eugene Bulyak and Peter Gladkikh, private communication.

PHOTON COLLIDERS

T. Takahashi*, Graduate School of Advanced Sciences of Matter, Hiroshima University, Higashi-Hiroshima, 739-8530, Japan.

Abstract

Physics in the photon collider option expands opportunities at the ILC. It is important for the ILC program to keep the expendabilities and to explore feasibility of the option both in physics and technological aspects. In this talk, we present principle of the photon colliders as well as technological issues. In particular, the focus is put on the issue related with the interaction region and the laser technology.

INTRODUCTION

If we switch the positron beam of the ILC e^+e^- collider to the electron beam, two electron beams are brought to the interaction region of the ILC and both beams are expected to be ~90% polarized. The idea of photon collider is to convert the electron beams to the photon beams by backward Compton scattering a few mm before the interaction points.

Physics opportunities and technical feasibility has been studied and recent progress was summarized in [1,2]. Since the start up of the ILC project, intensive discussion on the interaction region of the ILC has been made and is in progress. As the photon collider need to modify the interaction region to construct the conversion point from the electron to the photon beam, keeping compatibility of the interaction region is an important issue for the photon collider. Particularly, since the photon collider needs larger beam crossing angle than e^+e^- collider to extract spent (e^-) beam from the interaction point, the issue on the beam crossing angle is one of the most important and it is also related with the number of interaction points at the ILC.

In this talk, the principle and general property of the photon collider is introduced and then issues, status and prospects were reviewed.

PHOTON COLLIDERS

In photon colliders, photon beams are generated by the backward Compton scattering of electron and laser beams just before the interaction point. The maximum energy of the generated photon is expressed as;

$$E_\gamma^{\max} = \frac{x}{x+1} E_e \qquad (1)$$

Here, x is a kinematical parameter of the Compton scattering defined as

$$x = \frac{4\omega_L E_e}{m^2 c^4} \cos^2(\theta/2) \qquad (2)$$

where E_e, ω_L, and θ the electron energy, laser photon energy and angle between the electron beam and the laser beam. A calculated photon energy spectrum generated by the backward Compton scattering is shown in figure 1.

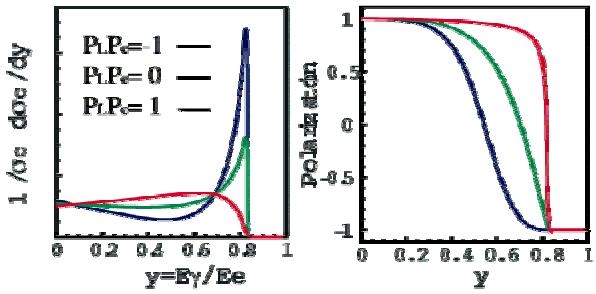

Figure 1: Calculated photon energy and polarization as a function of photon energy for various combination of laser and electron polarization.

As seen from the figure, the energy distribution of the photons depends on the polarization of the electrons and the laser beam, i.e., one can obtain a broad energy distribution or peaked distribution by controlling the polarization. Usually, x in equation (2) is restricted to be smaller than $2+2\sqrt{2} \approx 4.83$ to avoid pair creation process by the collision of the Compton photon and the laser photon, corresponding to the maximum photon energy of about 80% of the electron energy.

With typical parameters of the photon collider, the average number of Compton interactions for an electron in a laser pulse is assumed to be 1 which corresponds to the conversion efficiency, $k \approx 0.63$. In most cases, we are interested in the high energy part of the spectrum and if we take high energy part of the spectrum, the effective conversion efficiency k' can be regarded as $k' \approx 0.3$. Therefore, the high energy part of luminosity of the photon collider is expressed approximately as $L_{\gamma\gamma} \approx 0.1 L_{ee}$, where L_{ee} is the geometric luminosity of e^-e^- collisions. It should be noted that the geometric luminosity can be higher than the same as the e^+e^- collider. Since the effect of the beam-beam interaction is less serious than e^+e^- interaction, the geometric luminosity is possibly higher that the e^+e^- collision. With a photon collider parameter based on the ILC, the geometric luminosity is $5.9\times10^{34}\mathrm{cm}^{-2}\mathrm{s}^{-1}$, while it is $1.6\times10^{34}\mathrm{cm}^{-2}\mathrm{s}^{-1}$ for e^+e^- collider.

Precise estimation of the luminosity spectrum can be performed using numerical simulation assuming the ILC nominal beam emittance but smaller beam size at the interaction point and the laser beam. The results of a simulation is shown in figure 2.

*tohru-takahashi @ hroshima-u.ac.jp

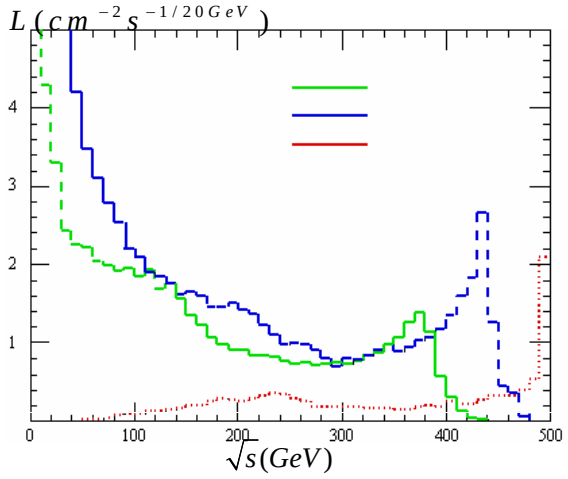

Figure 2: Luminosity spectra for γγ(sloid), eγ(dashed), and e^-e^- collisions based on the ILC nominal emittace.

We have γγ, eγ, and e^-e^- interaction simultaneously and low energy interaction caused by beamstrahlung photons.

ISSUES FOR PHOTON COLLIDERS

There are two aspects in technologies for the photon colliders. One is for beam parameters such as the beam emittance, the final focus optics and the beam crossing angle. These issues are, in other word, to find a way to accommodate options with e^+e^- operation of the ILC. The second is the laser technology as we have to bring high power laser pulses into the interaction region with the repetition rate of 3000×5 per second. The laser technologies were reviewed by elsewhere in this workshop[3].

The beam parameters for several proposal for the photon collider options are summarized in table 1.

Table 1: Parameters for photon coliders

		ILC optimisti	ILC w/ e+e-	NLC γγ	e+e-
f_{rep}	Hz	5	5	120	5
n_b		2820	2820	95	2820
σ_x^*/σ_y^*	nm	88/4.3	175/4.3	166/3.0	553/5
β_x^*/β_y^*	mm	1.5/0.3	1.5/0.3	4/0.08	11/0.4
$\varepsilon_{xn}/\varepsilon_{yn}$	μm rad	2.5/0.03	10/0.03	3.6/0.071	10/0.03
L_{geom}^{ee}	$cm^{-2}s^{-1}$	11.8×10^{34}	5.9×10^{34}	4.0×10^{34}	1.6×10^{34}

In the table, the column of "ILC optimistic" is a set of parameters which tried to maximize the luminosity. It assumes a modification of the dumpling ring of the ILC. The "ILC e^+e^-" parameters are the same as the e^+e^- operation except for the horizontal β function at the interaction point. For references, parameter sets for the TESLA photon collider and current ILC e^+e^- parameters are shown in the table.

The beam crossing angle at the interaction point is one of the most important issue to accommodate photon colliders. The situation is illustrated in figure 3.

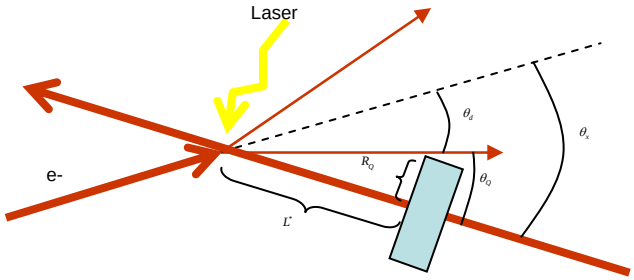

Figure 3: Schematic of beam crossing angle and disruption angle.

The electron beam after passing through an intense laser pulse has large energy spread from the original beam energy down to as low as about 5 GeV. Therefore the outgoing electron beam will have a large disruption angle due to the strong beam-beam interaction at the interaction point. According to the beam simulation by CAIN[4], the low energy electrons have the disruption angle θ_d of about 10 mr. Since these disrupted beam should not hit the final focus magnet which will be placed at L^* from the interaction point, we have to set a finite beam crossing angle $\theta_x = \theta_d + \theta_Q$, where θ_Q is the solid angle of the final focus magnet. The beam disruption angle can be estimated by the laser-Compton and the beam-beam simulation, however, the angle θ_Q depends on the L^* (and therefore the final focus beam optics) as well as physical dimension of the final focus magnet.

There is an idea to set beam crossing angle at 20 mr using a superconducting magnet with $L^* = 3.8$m [5]. However, detail simulation for the beam interaction and the study of the final focus optics to achieve enough luminosity for the photon collider is required. Seryi studied geometric luminosity including chromo-geometric aberration as shown in figure 3[6].

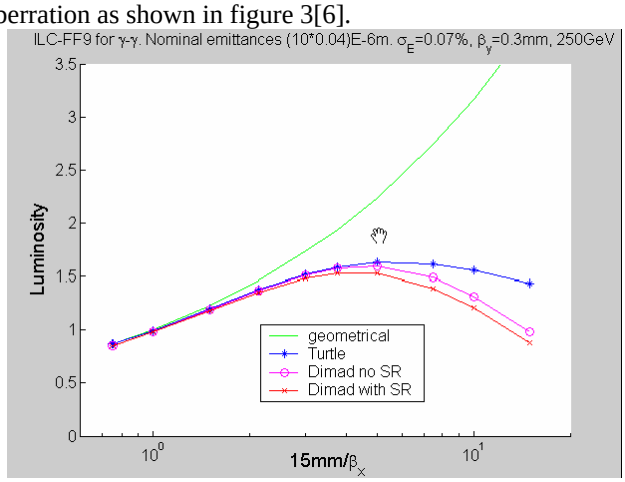

Figure 3: Geometric luminosity as a function of horizontal β function with the ILC nominal emittance.

It is seen that, with the ILC nominal emittance, the optimal horizontal β function is 3 mm rather than 1.5 mm which is used in table 1. So that the effective beam size is

larger than those assumed in the previous study, resulting in the smaller disruption angle. The price to pay for this case is that the geometric luminosity is somewhat smaller, $2.7\times10^{34}\,\mathrm{cm^{-2}s^{-1}}$ while it is $5.9\times10^{34}\,\mathrm{cm^{-2}s^{-1}}$. Therefore it is important to keep investigating feasibility of smaller horizontal emittance such as shown in table 1 as the ILC optimistic. An discussion on modification of the dumping ring for smaller emittance was found tin the Snowmass workshop but the feasibility was not conclusive at that time[7].

LASERS

The ILC accelerate 5 bunch trains in a second and each train consists of about 3000 electron bunches of 337 ns separation in time. Laser pulses for the photon conversion have to be synchronized with the electron bunches and each pulse should have O(5J/pulse) to achieve high conversion efficiency. The cost for the high power laser is roughly proportional to the cost for the pumping laser, and therefore the pumping power to amplify 3000 pulses in 1 ms. Thus, if we assume to obtain enough laser power directly from laser amplifiers, the cost for the laser system may beyond tolerable level.

A way out is to amplify the laser power outside of the laser system using an optical resonator, i.e., pulse stacking cavity. For example, in case that 100 of laser pulses can be stacked in right phase, the power of a laser pulse will be 100 timeslarger than those at the laser system. In other word, the output power from the laser system can be reduced to 1/100. In the real system, each laser pulse have to be synchronized with the electron bunches of 337 ns (about 100 m) separation and optical components must be placed outside of the detector, it is necessary to construct the cavity of 100 m circumference. A schematic of a pulse tacking cavity for the photon collider is shown in figure 4.

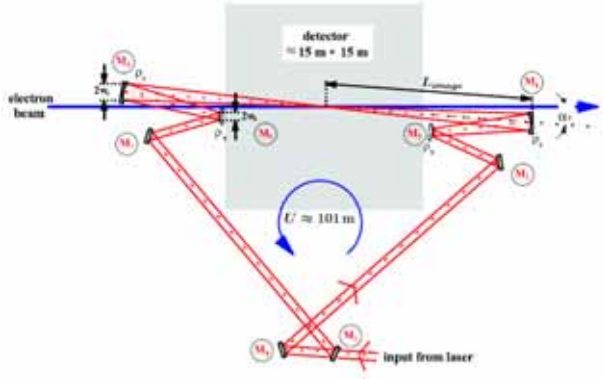

Figure 4: Schematic of a laser pulse stacking cavity for the photon collider[8].

The performance of the cavity requires;

- Stability of the cavity: To keep the Q factor of the cavity, the cavity length has to be kept at very high accuracy. It requires a feedback system to control position of the optical components. In addition keeping distance between the focal point and the final focus mirror is crucial to maintain the laser spot size at the conversion point.
- Cavity losses. The optics in the system retain >99.7% of the laser power in each round trip. This requires the development of high efficiency coating which can survive the high fluence.
- Wavefront quality. Wavefront distortions will accumulate as the pulse travels through the system. This will limit the size of the beam focus at the interaction point. This can quickly degrade the laser intensity at the focus and reduce the backscattering rate. An adaptive optics system has to be implemented to compensate the distortions.

Systems have been created that can do any of these thing individually but a system that does all simultaneously for high power/large scale cavity is unprecedented. The power buildup cavity is popular for the CW laser and power buildup factor of 10^5 is reported and large scale cavity has been developed for the gravitational experiment. The pulse stacking cavities, on the other hand, are not popular as for the CW lasers. A cavity for the laser-wire system for the ATF has been reported[9], however, feasibility of large scale cavity is yet to be studied.

In order to demonstrate feasibility of the cavity, constructing a prototype at the ATF2 is discussed[10]. Once the ATF2 achieves its primary goal, its focus point can be a suitable site to test laser-electron beam collision.

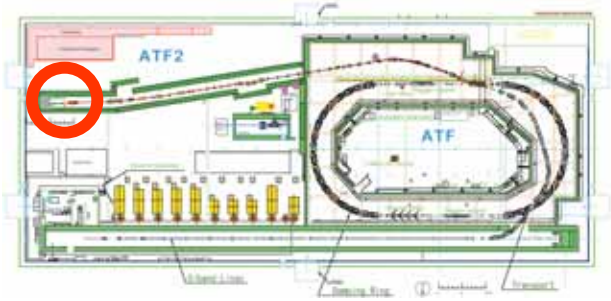

Figure 5: Layout of the ATF2. The possible site for the laser test is indicated by the red circle.

The scope of the plan include high intensity γ ray facility, study of fundamental interaction between a high intense laser and the electron as well as test bed for the photon collider conversion point.

SUMMARY

The photon collider will add attractive physics opportunities to the ILC program and its possibility has to be kept. However, to keep the possibility, the interaction points and the detector has to be made compatible with e^+e^- mode. It requires careful decision of the beam crossing angle, design of the detector and the final focus system. It is also preferable to explore possibility to improve horizontal emittance of the electron beam. There have been discussions on these issues since the start up of the ILC program. The author think that we do not find any show-stopper for the compatibility through we do not

reach agreeable design of the option. We hope to find the reasonable answer by efforts in next a few year.

This talk is based on many discussions in the ILC the Machine Detector Interface working group and photon collider working group. The author would like to thank all member of the working group.

REFERENCES

[1] "Proc. International Workshop on High Energy Photon Colliders", Nucle. Instr. and Meth. 472A (2001)
[2] B.Badelek et.al., Int. J of Mod. Phys. A19 5091 (2004).
[3] G. Groberg, in this proceedings.
[4] K. Yokoya, http://www-acc-theory.kek.jp/members/cain/default.html.
[5] B. Perkar, 2005 International Linear Collider Physics and Detector Workshop and second ILC Accelerator Workshop, Snowmass, Aspen, August 2005.
[6] A. Seryi, 2005 International Linear Collider Physics and Detector Workshop and second ILC Accelerator Workshop, Snowmass, Aspen, August 2005.
[7] A. Wolski, 2005 International Linear Collider Physics and Detector Workshop and second ILC Accelerator Workshop, Snowmass, Aspen, August 2005.
[8] G. Klemz, K. Monig, I. Will, "Design study of an optical cavity for a future photon-collider at ILC", physics/0507078.
[9] Y. Honda, LCWS05, Stanford, March 2005.
[10] "ATF2 Proposal", KEK Report 2005-2

High Power Lasers for the Photon Collider

J. Gronberg*, LLNL, Livermore, CA 94550, USA

Abstract

The photon collider experiment at the International Linear Collider will require enormous average laser power. The MERCURY laser, being developed for a inertial fusion energy application, has the potential to provide sufficient laser power to realize the experiment. In this paper we report on the technical advances in laser technology that will enable this experiment.

THE PHOTON COLLIDER LASER REQUIREMENTS

The basic design and calculations for a photon collider have been previously reported [1, 2]. In short, each electron bunch must intersect a laser pulse of several Joules flash energy in order to convert most of the electron beam energy into high energy photons through Compton backscattering. As the International Linear Collider (ILC) produces 28200 electron bunches per second in its two beams this implies a total average power for the laser of around 100 kWatts. This would be prohibitively expensive for an experiment but the possibility exists to reuse much of the laser power leading to a reduction in the laser plant required.

During the Compton backscattering most of the photons in the laser pulse are undisturbed. Only one in 10^9 of the photons are lost. This opens the possibility to reuse the laser energy by recirculating the laser pulse in a ring cavity. A design for such a cavity has been developed [3, 4] and from that a set of laser requirements can be deduced.

To build up a 5 Joule pulse circulating in the cavity the laser must provide a pulse of 40 mJoules, given a conservative estimate of 125 for the quality factor of the cavity. The recirculation time in the cavity is set by the electron bunch spacing to 337ns. Laser pulses must be provided before the arrival of the first electron bunch in order to build the recirculating pulse up to it's full value. This implies a need for 1000+2820 = 3820 laser pulses per train. At the train repetition rate of 5Hz this leads to the average power requirement of 764W. This is a significant amount of laser power compared to currently existing lasers. Especially when the pulse must be compressed to the ns time scale and high wavefront quality is desired so that it can be focused to a small spot.

* This work was performed under the auspices of the U.S. Department of Energy by the University of California, Lawrence Livermore National Laboratory under Contract No. W-7405-Eng-48

Facility	Flash Energy
Janus	100J
Shiva	10KJ
Nova	30KJ
NIF	1.8MJ

Table 1: The progress of increasing flash energy of lasers fielded by LLNL

THE HISTORY OF HIGH POWER LASER DEVELOPMENT AT LLNL

The Lawrence Livermore National Laboratory (LLNL) has been developing laser systems with increasing flash energy for several decades. This program is driven by the desire to create laser initiated fusion in the laboratory. As shown in Table 1, the flash laser energy has progressed over the years and will culminate with the National Ignition Facility (NIF) at 1.8MJ. However, these lasers are all limited in their repetition rate, and can fire only once every 8 hours. Even for the NIF this leads to an average power of only 55 Watts.

A laser that could serve as the basis for fusion power generation would need to be able to run at a much higher repetition rate. The Inertial Fusion Energy (IFE) program has been working on new laser technologies to support that goal. The MERCURY laser [5] is a first step toward a high average power laser for the IFE application. Its parameters are detailed in Table 2. The design average power of 1kW makes this technology a viable option for driving the laser cavity.

KEY TECHNICAL DEVELOPMENTS IN LASER TECHNOLOGY

The high peak power lasers that have been developed have a number of drawbacks for reaching high average power. Amplifier crystals driven by flashlamps tend to be very inefficient in converting electrical power into laser en-

Parameter:	
Flash Energy	100J
Repetition Rate	10Hz
Average Power	1KW
Pulse Length	3-10 ns
Efficiency	10%
Wavelength	1 micron

Table 2: Design parameters of the MERCURY laser.

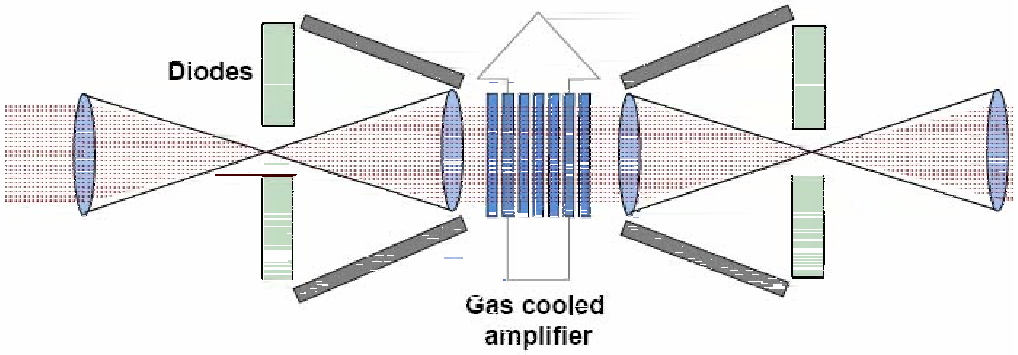

Figure 1: The basic geometry of the MERCURY amplifier head. The diode arrays shine on the face of the amplifier crystals, in the same direction as the laser pulse. Helium cooling flow is transverse to the direction of the laser beam.

ergy. Also most amplifier crystals dissipate a large amount of heat which then distorts the amplifier medium. Typical systems allow 8 hours between shots so that the crystal can come to thermal equilibrium. The MERCURY laser employs three technologies to avoid these problems, as shown in Figure 1.

Diode Pumping

Laser diode arrays can produce power matched to the absorbtion line of the amplifier medium. This allows a system to achieve an electrical power to laser power efficiency of 10%. LLNL has been developing diode technology and has reached a cost of $5/Watt of peak diode power. Accelerated lifetime testing has shown no significant degradation in diode operation for 10^8 shots. This would be the equivalent of two years running at the ILC.

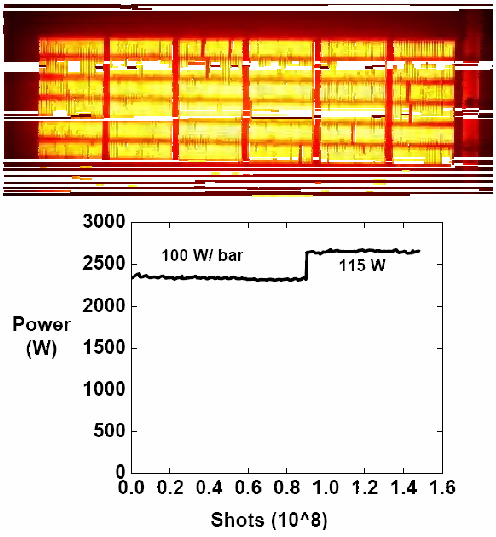

Figure 2: A diode array in operation with lifetime data shown below.

Amplifiers

The MERCURY laser uses a Ytterbium:Strontium-FluorAppetite crystal as it's amplifying medium. This amplifier has a long upper-state lifetime and a low quantum defect. The long upper-state lifetime allows the crystals to be charged over a longer period of time reducing the peak diode power required. This is a direct cost savings to the system since the diode cost is the primary cost driver. The low quantum defect reduces the amount of power dissipated in the crystal which reduces the cooling requirements.

The procedure for growing, cutting and polishing the amplifier crystals has been refined over the past several years. Overall yields for the crystals have grown to 60%. Magneto-rheological finishing of the amplifier surface has been employed to bring the surface flatness of the crystals down to 0.1 of a wavelength. This is important since the power extraction efficiency and the ability to focus the amplified laser pulse to a small spot is adversely affected by wavefront distortions.

Helium Gas Cooling

Heat deposition in the crystals causes a change in index of refraction which can lead to wavefront distortion. The MERCURY removes heat from the amplifier crystal through sub-sonic helium gas flow across the face of the crystals. The heat flow through the crystal to the helium is along the direction of the laser pulse thus minimizing the distortions. This is a marked improvement versus edge cooled crystals. The total distortion due to heat flow in the wavefront has been measured to be 1.1 wavelength for one amplifier head and 2.6 wavelengths for the second head. The distortion pattern varies smoothly over the face of the crystal and is stable versus time. It is expected to be removed by a correcting optic during normal operations.

ADAPTING MERCURY TECHNOLOGY TO ILC

The basic MERCURY laser is designed to produce a single laser pulse of 100J with a repetition rate of 10 Hz. In recent tests the MERCURY achieved stable operation at 10Hz with a 55J pulse energy for 8 hours, as shown in Figure 3. This is an average power of 550W and is within a factor of two of the cavity laser requirement of 764W. The single pulse nature of the MERCURY architecture needs to be modified to support the laser pulse train that the cavity needs. However, all of the basic technology can be reused to create that laser architecture. The MERCURY is designed to put a single low power pulse through the amplifiers multiple times until it has been amplified enough to extract all of the stored energy. For our application, a low power pilot train of laser pulses would be amplified in the laser medium with the diodes in continuous operation to replace the energy lost and maintain the amplification. This will require close attention to the design to prevent amplified spontaneous emmission from damaging the laser. However, there is no obvious reason why this configuration would not be achievable [6].

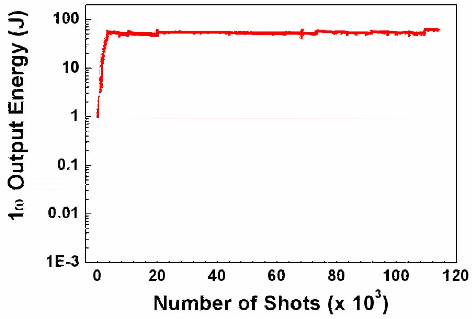

Figure 3: A 8 hour run of the MERCURY laser at 10Hz and 55J per pulse.

CONCLUSION

Recent advances in long upper state lifetime amplifier crystals combined with the continued fall in the cost of diodes has made high average power lasers feasible. The existing MERCURY laser has achieved the average power performance necessary to drive a recirculating cavity for a photon collider experiment. Modifications to the laser architecture could convert the single shot MERCURY into a laser capable of producing the train of low energy laser pulses required by the photon collider laser cavity.

ACKNOWLEDGMENTS

The laser technology reported in this paper is the work of the Inertial Fusion Energy group at LLNL. The author is grateful for their support in developing laser technology for the photon collider application.

REFERENCES

[1] I. Ginzburg, G. Kotkin, V.Serbo and V. Telnov, *Pizma ZhETF* **34** (1981) 514; *JETP Lett.* **34** (1982) 491 (Preprint INF 81-50, Novosibirsk (1981) in English).

[2] V. Telnov, *Nucl. Instr. and Meth.* **A 355** (1995) 3.

[3] I. Will, T. Quast, H. Redlin and W. Sander, "A Laser System For The TESLA Photon Collider Based On An External Ring Resonator", *Nucl. Instrum. Meth.* A **472** (2001) 79.

[4] G. Klemz, K. Monig, I. Will, "Design study of an optical cavity for a future photon-collider at ILC", submitted to NIM A.

[5] L. Hackel, *et al.*, *UCRL-TB-136126-01-20*

[6] B. Stuart, LLNL, private communications.

Progress on the Development of an Upstream Spectrometer for the ILC

M. W. Slater,

Department of Physics, High Energy Physics, Cavendish Laboratory, J. J. Thompson Avenue, Cambridge, CB3 0HE, England

Abstract

One of the primary goals of the International Linear Collider (ILC) physics programme is to make a precise measurement of the top quark mass to better than 40 MeV. Obtaining this level of experimental error would make the top quark mass a precision constraint on the Standard Model. In order to acheive this mass resolution, the incoming beam energy upstream of the ILC interaction point must be known to better than 10^{-4}. Two spectrometer designs incorporating very low emittance growth have been proposed to perform this measurement. Both require a beam position resolution and stability of $\sim$ 100 nm. This report provides details of the requirements placed on an upstream spectrometer and summarises current progress in demonstrating the feasability of these requirements.

INTRODUCTION

To fully exploit the physics potential of the ILC, accurate determination of the beam energy is essential to provide control over the collision energy $\sqrt{s}$ at the Interaction Point (IP) [1]. The benefit of such a determination of $\sqrt{s}$ has already been demonstrated at such facilities as the Large Electron Positron Collider (LEP) at CERN. In this case, a technique based on the resonance depolarisation of the orbiting lepton beams measured the collision energy at LEP to an accuracy of $1.4 \;\; 10^{-5}$ [2], thus allowing a determination of the Z^0 mass to $2\ \mathrm{MeV}$ or 23 ppm [3].

For LEP2, three independent methods were used to verify the calibration of the energy measurement. One of the methods employed was a spectrometer consisting of two sets of BPM triplets placed in the beamline either side of a dipole magnet with a well determined magnetic field. By measuring the deflection of the particle beam through this dipole magnet, the average beam energy could be determined over many turns of the accelerator to an overall accuracy of $\sim 1.2 \;\; 10^{-4}$ [4]. Using the spectrometer in combination with other techniques for energy determination, the LEP2 collaborations were able to measure the W mass with an accuracy of $50\ \mathrm{MeV}$ [5].

The high precision measurements that are hoped to be made at the ILC will require a knowledge of the beam energy to a similar or better level than that acheived at LEP. The principal method of measuring the incoming energy that has been proposed is to use a magnetic spectrometer upstream of the IP, similar to that used at LEP. The performance of this spectrometer system would have to be considerably greater than that used at LEP however, as the technique of averaging over many turns would not be available in a linear style accelerator. This report will outline the requirements of such a system and the current designs under consideration. It will also summarise the current progress that has been made and future tests that are planned.

PHYSICS MOTIVATION

A precise knowledge of the collision energy at the ILC is essential for two types of physics analysis. The first of these is the determination of a final state cross section with respect to $\sqrt{s}$. Accurate measurement of this dependence at threshold allows particle masses to be determined (*e.g.* $\mathrm{m_t}$). The second type of analysis to benefit from accurate measurements of the collision energy is the reconstruction of particle resonances. With accurate knowledge of the incoming beam energy, kinematical constraints can be applied that can improve the mass resolution.

One of the main goals of the ILC is to make detailed threshold scans of top quark production (see Fig. 1) and from this, make accurate measurements of the top quark mass. A precise measurement of $\mathrm{m_t}$ has a significant impact on current Standard Model (SM) and Super Symmetric predictions. If an overall mass resolution of $\mathrm{m_t}$ $100\ \mathrm{MeV}$ can be achieved, stringent consistency checks can be made on a range of models. By obtaining an accumulated luminosity of $10\ \mathrm{fb}^{-1}$ at energies around the $\mathrm{t\bar{t}}$ threshold ($\sqrt{s} \sim 350\ \mathrm{GeV}$), a statistical error of $\sim$ $40\ \mathrm{MeV}$ is possible. Combining this with a theoretical error that is predicted to be of a similar magnitude, the overall uncertainty on the beam energy must be $\sim 10^{-4}$ or 100 ppm to achieve the desired accuracy.

Another example of an analysis that would benefit from a precise beam energy measurement is the reconstruction of particle resonances, an example of which is the determination of the mass of the SM Higgs Boson by direct reconstruction of the Higgs-strahlung process $e^+e^- \rightarrow HZ$. Using a similar technique to that employed at LEP to measure the W mass, an uncertainty of the beam energy translates directly into an error on the Higgs mass. A precision of of 10^{-4} would provide an error of $12\ \mathrm{MeV}$ on the Higgs mass.

SPECTROMETER REQUIREMENTS

There are several considerations to take into account for any proposed spectrometer design:

Minimal Emittance Growth
A maganetic spectrometer will by necessity have to bend the incoming beam through a minimum of three magnets in order to measure the energy of the beam

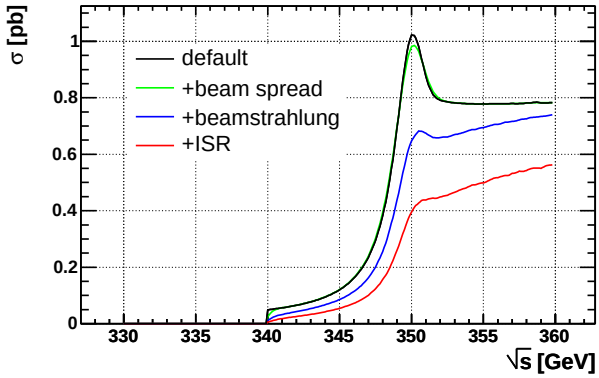

Figure 1: A plot showing the predicted $t\bar{t}$ threshold after applying different corrections.

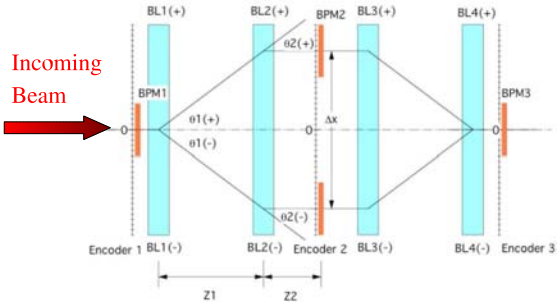

Figure 2: A design for the ILC spectrometer based on the production of a pure displacement in the beam through two magnets. Measurement of this displacement would allow a determination of the beam energy.

and then return it to the nominal trajectory. It is beneficial to have these bends as large as possible in order to maximise the achievable resolution. However, these magnet bends will produce synchrotron radiation and consequently, emittance growth. This growth in emittance would have a defocusing effect on the beam with a consequent reduction in luminosity. A compromise between the emittance growth and the achievable resolution of the spectrometer must be found.

Physical Space Available
One of the variables on which the energy resolution of a spectrometer depends on is the length of the spectrometer arms. The larger the length of these arms, the greater the change in position at different energies and consequently, the better the energy resolution for a given accuracy in the beam position measurement. However, there is limited space available in the ILC beamline and this constraint must be taken into account when designing the beam optics for the spectrometer.

Beam Position Monitors
An essential part of the spectrometer is the high resolution Beam Position Monitors (BPMs) that will measure the position of the beam before and after the magnet bends. It is proposed to use cavity BPMs for this purpose which rely on the production of resonant electromagnetic fields by the passing of the bunch train. These fields are proportional to the charge of the bunch, the bunch offset and the obliquity of the bunch. Using appropriately designed electronics, all these beam characteristics can be extracted to a very high degree of accuracy. The achievable resolution and stability of the BPMs and electronics will be a significant factor when designing the spectrometer.

ILC Bunch Train
The ILC bunch train is likely to consist of $\sim$ 2000 bunches with a bunch spacing of either 337 ns or 150 ns. At this frequency, the BPMs will require a relatively fast decay time and have a resonant frequency specifically designed to be a harmonic of the repetition frequency. In addition, the analysis methods used to extract the position information from the BPMs will need to be robust enough to handle overlap between the BPM response to each bunch crossing.

SPECTROMETER DESIGNS

There are two favoured designs for the spectrometer currently under investigation, both of which have advantages and disadvantages [6]. The first relies on the measurement of a pure displacement of the beam due to the magnet bends and the other on the measurement of a change in angle of the beam through the magnets.

Displacement Design

The spectrometer design based on pure displacement design contains four precision magnets, two before and two after a measurement station [1] (see Fig. 2). A measurement station is also required before the chicane to record the initial beam position and a final BPM station after the chicane to ensure the beam has returned to the correct trajectory. The two pairs of precision magnets would be designed to only displace the beam off axis and consequently, this displacement would be proportional to the energy of the beam. The central measurement station would measure this displacement and, after proper calibration, this would be used to calculate the beam energy. The main advantage to this spectrometer design is that only a change is displacement is produced and so the analysis methods would not have to deal with significant tilt signals. Additionally, fewer measurement stations are required for this design than the Angle Design. The significant disadvantage however, is that all four magnets must be measured precisely in order to

[1] A measurement station would consist of a minimum of two actual BPMs. More BPMs would provide greater redundancy and a consequent improvement in resolution

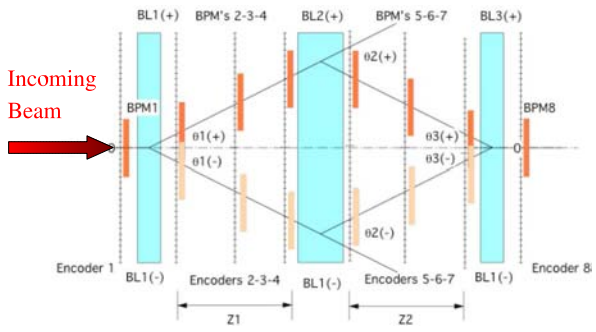

Figure 3: A design for the ILC spectrometer based on the change of the beam angle as it passes through two magnets. Measurement of this angle would allow a determination of the beam energy.

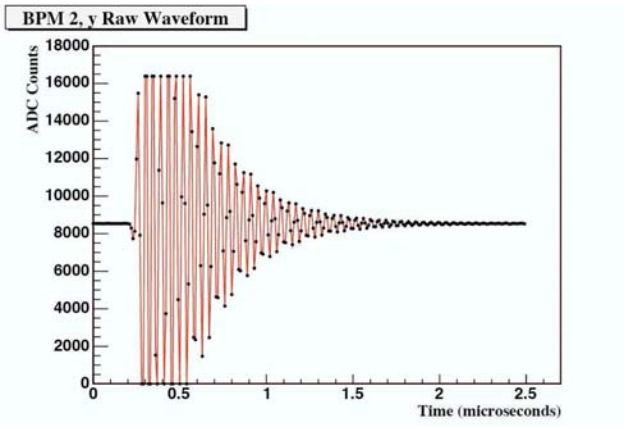

Figure 4: An example of a digitised waveform produced by one of the BINP designed BPMs. Saturation of the digitisers can be seen at the beginning of the waveform.

give the required accuracy in the beam energy measurement.

Angle Design

The Angle Design contains a central precision magnet that bends the beam through an angle θ (see Fig. 3). The incoming trajectory would be recorded with a minimum of two measurement stations (though three is favoured) spread over the length of the spectrometer arm. A similar set of measurement stations positioned after the central magnet would record the out-going beam trajectory. Magnets before and after the measurement stations bend the beam off axis and back on axis respectively. The princpal advantage of this design is that only a single precision bend is required [2] rather than the four needed by the dsiplacement design. However, a minimum of four BPM stations are required to accurately measure the incoming and outgoing trajectories and the analysis methods must also deal with significant (and changeable) tilt signals.

Required Spectrometer Parameters

The achievable resolution of any given spectrometer design can be computed as a function of the following parameters:

Accuracy of the integrated magnetic field

Number of Beam Position Monitors (BPMs) per measurement station

The length of the spectrometer arm and bending angle (Angle Design)

The beam offset from the nominal orbit (Displacement Design)

BPM Resolution

[2] Studies have shown that two magnets will be required to perform the single bend while minimising the emmitance growth

Assuming that the magnetic field can be measured to an accuracy of $\sim 2 \quad 10^{-5}$, there are three BPMs per measurement station and there is ~ 50 m of available space within the beamline, the BPM resolutions required for various parameter sets can be computed [1]:

Offset 5 mm - $_{\mathrm{BPM}} \simeq 200$ nm

Bending Angle 1 mrad - $_{\mathrm{BPM}} \simeq 500$ nm

Bending Angle 0.1 mrad - $_{\mathrm{BPM}} \simeq 100$ nm

Another important factor affecting the spectrometer is that of stability. It would be impractical to interrupt the ILC data-taking to recalibrate the BPMs more than once every few hours and so the BPMs must be stable up to the above resolution levels over the course of this time.

CURRENT PROGRESS

Significant progress has been made in demonstrating the feasability of using cavity BPMs in a future ILC spectrometer [7]. The majority of the work so far has been carried out using the Accelerator Test Facility (ATF) at KEK in Japan. At the ATF, two BPM triplets are available for testing: One set designed at BINP, the other at KEK. The BINP BPMs are mounted on hexapod movers and housed in a purpose built space frame whereas the KEK BPMs are individually mounted on piezo flexure movers. For each machine pulse of the ATF, an extracted bunch is passed down the extraction line and through the BPMs. The resultant resonant electromagnetic fields induced within the cavities are coupled out using waveguides, and sent through dual stage downmix electronics before being digitised and stored (see Fig. 4).

Two parameters require extraction from the digitised waveforms in order to determine the position of the beam as it passed through the cavity. First, the Amplitude of the waveform, which is proportional to the beam offset and the

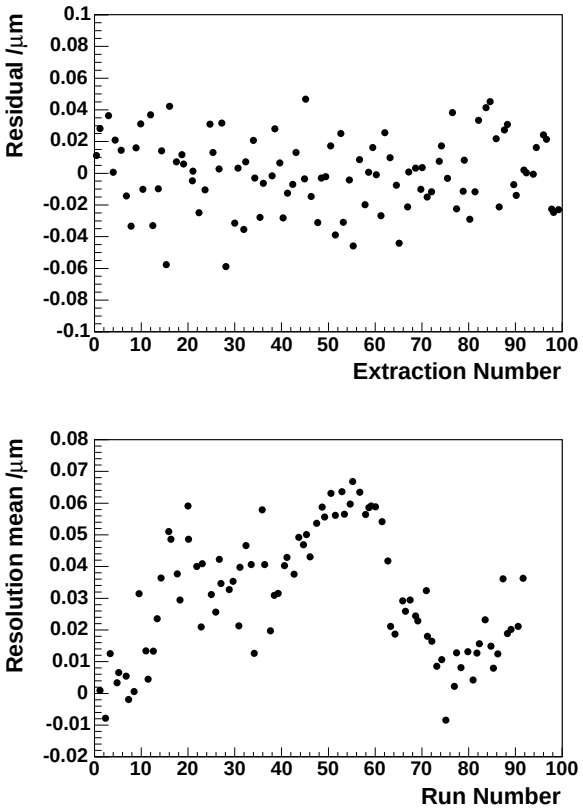

Figure 5: (a) The residual between the predicted and measured positions of the Y orientation in the second BPM over the course of ∼minute, (b) the variation of the mean residual in the second BPM's Y orientation over the course of ∼hours.

bunch charge and second the phase, which is required to separate the position and tilt signals. A reference cavity is also required, in addition to the position cavities, to remove the bunch charge and the phase offset from the parameters determined from the position cavities.

Two methods have been developed to extract the required parameters from the digitised waveform. The first is an additional level of downconversion from 25 MHz to DC performed in software. A filter is then applied to isolate the required signal and the amplitude and phase is extracted. The second method is based on fitting the digitised waveform with an exponentially decaying sine wave. From this, the amplitude and phase are determined directly. Detailed information on these analysis methods can be found in reference [7].

BPM Resolution

The resolution of a BPM could be determined by calculating the RMS of the residual between the measured position of the central BPM and that predicted by the two spectator BPMs. The prediction was made by determining a set of constants that related the spectator BPM position data to the measured BPM position data through matrix inversion. Using the positions calculated from both the fitting and digital downconversion methods, a resolution for a single BPM of ~ 20 nm has been measured (see Fig. 5a).

BPM Stability

The stability of the BPM system was found by using a similar method to that used to find the resolution. The constants that predicted the position of the beam in the central BPM from the two spectator BPMs were determined using 100 pulses of data (~ 1 minute). These constants were then used to compute the residuals for the remaining data in sets of 100 pulses. The stability of these constants provides a measure of the stability of the system and so the variation of the mean value for this residual gives an indication of the stability of the BPMs. Using this method, a variation of ~ 40 nm over periods of both minutes and hours was seen (see Fig. 5b).

Prototype BPM Designs

In addition to the tests carried out at KEK, two prototype BPMs are being designed specifically for the ILC spectrometer (see Fig. 6). One is a cylindrical cavity while the other is rectangular but both are based on current technologies that have already been shown to give a high resolution (e.g. the BINP BPMs tested at KEK). The rectangular cavity, though more difficult and expensive to produce, would allow excellent isolation of the two resonant field orientations. Both prototypes have rectangular waveguides and coupling slots to suppress the monopole mode. For safety and to give higher flexibility to the, as yet, undetermined ILC optics, a 30 mm beam pipe diameter has been used. A frequency of 2.8 GHz has been chosen for the cavities to fit into a well explored frequency range and again allow for a change in beam pipe diameter. The coupling strength has been set to allow several oscillations between bunches. The cavities have also been designed with symmetric outputs that would be combined in a hybrid before being transferred through the mix down electronics.

Current Baseline Spectrometer Design

The current baseline design for the spectrometer at the ILC is based on the displacement design described above (see Fig. 7) [8] [9]. The spectrometer is to be located in the collimation and final focus region, ~ 900 m upstream of the IP with ~ 55 m of beamline space available (see Fig. 8). A 5 mm offset is to be produced using 6 m long magnets and 3 measurement stations through the chicane. A minimum of 3 BPMs will be used for each measurement station. To measure the energy to the level of 10^{-4}, the determination of this offset must be to within 500 nm. This will correspond to an individual BPM resolution of ~ 200 nm. After reoptimising the optics, the impact of this proposed

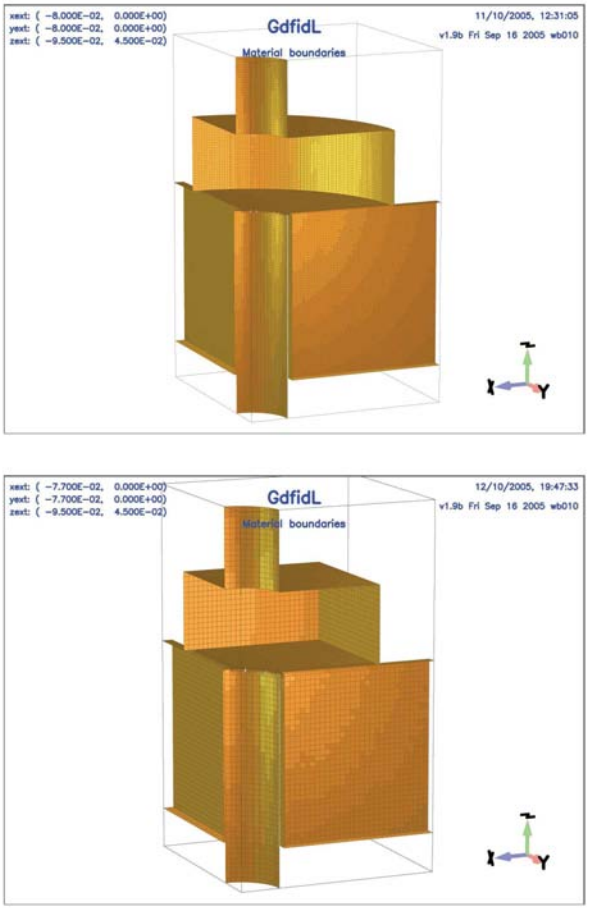

Figure 6: Diagrams showing the current protoype designs for the cavity BPMs to be used at the ILC spectrometer: (a) a cylindrical cavity and (b) a rectangular cavity.

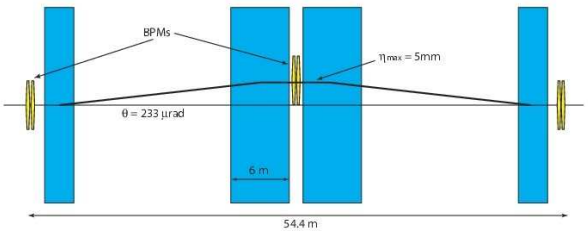

Figure 7: A schematic showing the baseline spectrometer design, based on a measurment of a pure displacement of the beam through the chicane.

chicane on the emittance and dispersion was found to be minimal.

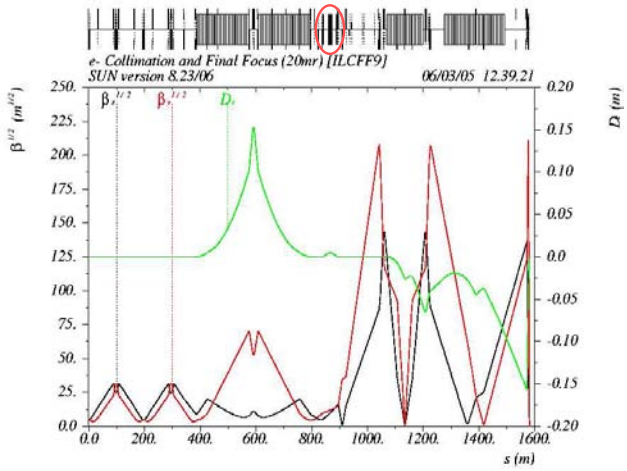

Figure 8: A plot showing the dispersion and emittance through the current optics of the ILC final focus region. The red elipse shows the proposed location of the spectrometer.

FUTURE TESTS

Further Work at the ATF

Several experiments are planned for 2006 to further test, not only the performance of cavity BPMs in a spectrometer environment, but also chicane design as a whole. These tests are to carried out at both the ATF at KEK and End Station A at SLAC.

Improving BPM Resolution and Stability

Using data taken in May 2005 it was possible to predict the achieveable resolution and, from these studies, propose possible changes in the electronics and beam conditions to improve the resolution of the BINP BPMs.

Centring the BPMs
By examining the contributions to the resolution limits, it was found that the optimum waveform size was between 5000 and 10000 counts (see Fig. 9) which corresponds to the signal being on the verge of saturating the digitisation electronics. By steering down the BPMs to this level, an improvement in resolution should be seen. Steering down in the horizontal direction will also reduce the affect of coupling between the two orientations.

Increasing the Bunch Charge and Shortening the Bunch Length
Both of these changes should effectively improve the loss factor of the cavities and consequently improve the signal to noise ratio.

Decreasing the Attenuation in the Reference Cavity
The reference cavity was found to have the most significant contribution to the noise due to it being

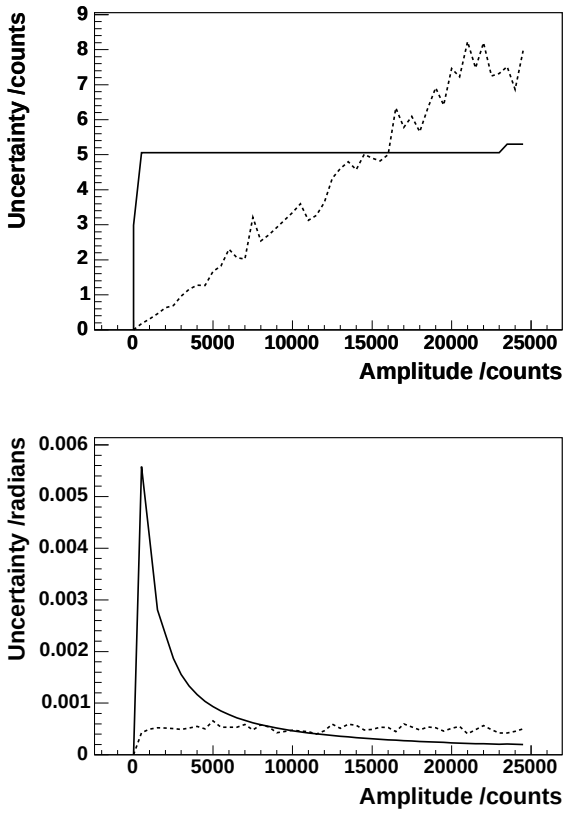

Figure 9: Plots showing the uncertainty in (top) amplitude and (bottom) phase determination as a function of amplitude using simulated waveform data for the vertical channel of the second BINP BPM. The solid line indicates the contribution from thermal noise and the dashed line is the contribution from phase noise.

weighted by magnitude of the vertical signal. To improve the signal to noise ratio in this cavity, it is proposed to reduce the attentuation in the electronics.

Decreasing Phase Noise
Though the thermal noise can not be reduced significantly, it is hoped that the phase noise present in the local oscillators can be lowered to some degree.

Linking the KEK BPMs and BINP BPMs

During the upcoming run in December, it is hoped that the KEK BPMs downstream of the BINP triplet will be analysed to a similar level as the BINP BPMs. After this has been done, the magnets between the two sets of BPMs will be turned off and the response of all the BPMs investigated by scanning the beam in both the horizontal and vertical directions. It is hoped that direct proportionality will be observed between the two sets of BPMs. After completing this initial test, one of the dipole magnets between the BPMs will be switched on forming a basic magnetic spectrometer chicane. Using this, it is hoped that a approximate energy measurement can be made.

Chicane Tests at End Station A

Commissioning is going to start in January for full chicane tests at End Station A (ESA) in SLAC. The tests are planned in two stages [10]: the first will include testing (similar to that done at the ATF) of two BPM doublets mounted on a girder in the beamline. This is scheduled to be carried out in February. The second stage, to be carried out during the summer of 2006 will involve the mounting of two additional BPM doublets on a second girder and the installation of magnets and movers. This will form a fully functioning spectrometer chicane. The stability and resolution of the different chicane designs can then be tested and compared. For more information, see reference [10].

CONCLUSIONS

In order to complete the proposed physics programme at the ILC, the incoming beam energy must be measured to an accuracy of 10^{-4}. It has been proposed to use a magnetic spectrometer to make this measurement. There are several design constraints imposed on such a device however, including minimising emitance growth, fitting into the beamline space available and bunch by bunch analysis of the ILC bunch train. Two designs for the spectrometer are currently under discussion: one measuring a change in displacement of the beam and the other, a change in angle. Both of these designs will require high precision measurements of the beam position to an accuracy of a few hundred nanometres.

Work has been carried out at the ATF in Japan to show the feasability of using cavity BPMs for the spectrometer. At present, a resolution of $\sim 20\ \mathrm{nm}$ has been demonstrated with a stability of $\sim 40\ \mathrm{nm}$ over periods of both minutes and hours. BPM prototypes have been designed specifically for the spectrometer based on this work. Further work is planned at both the ATF and ESA at SLAC to investigate the full spectrometer chicane design as well as attempting to improve the BPM resolution.

ACKNOWLEDGEMENTS

The author would like to acknowledge significant contributions from members of the following institutions: Budker Institute of Nuclear Physics (BINP), Deutsches Elektronen Synchrotron (DESY), KEK, Laurence Berkeley National Laborotory (LBNL), Laurence Livermore National Laborotory (LLNL), Queen Mary College London (QMUL), Stanford Linear Accelerator Centre (SLAC), University of Cambridge, University College London (UCL) and Universit de Notre Dame du Lac. The author would also like to thank the Particle Physics and Astronomy Research Council (PPARC) and EuroTeV for providing financial support for this work.

REFERENCES

[1] V. N. Duginov *et al.*, LC-DET-2004-031

[2] R. Assmann *et al.*, Eur. Phys. J. C **6** (1999) 187.

[3] ALEPH, DELPHI, L3, OPAL Collaborations, the LEP Electroweak Working Group, the SLD Electroweak and Heavy Flavours Group arXiv:hep-ex/0509008.

[4] R. Assmann *et al.* [LEP Energy Working Group], Eur. Phys. J. C **39** (2005) 253 [arXiv:hep-ex/0410026].

[5] G. Abbiendi *et al.* [OPAL Collaboration], arXiv:hep-ex/0508060.

[6] M. Hildreth, Talk given at 2005 MDI workshop, SLAC, http://www-conf.slac.stanford.edu/mdi/talks/Energy/spect_talk_Hildreth.ppt

[7] S. Walston, Proceedings for talk given at 2005 Nanobeams Conference, Kyoto, http://atfweb.kek.jp/nanobeam/files/proc//proc-WG2c-20.pdf

[8] D. Miller, Talk given at 2005 BDIR workshop, RHUL, https://ilcsupport.desy.de/cdsagenda/askArchive.php?base=agenda&categ=a0522&id=a0522s27t1/moreinfo

[9] M. Hildreth, Talk given at ATF mini-workshop in May 2005, KEK, http://acfahep.kek.jp/subg/ir/nanoBPM/nano.project/third/talks/hildreth.pdf

[10] M. Hildreth, Talk given at 2005 Nanobeams Conference, Kyoto, http://atfweb.kek.jp/nanobeam/files/presen//presen-WG2c-15.ppt

A TEST FACILITY FOR THE INTERNATIONAL LINEAR COLLIDER AT SLAC END STATION A FOR PROTOTYPES OF BEAM DELIVERY AND IR COMPONENTS*

M. D. Hildreth†, University of Notre Dame
R. Erickson, J. Frisch, C. Hast, R.K. Jobe, L. Keller, T. Markiewicz,
T. Maruyama, D. McCormick, J. Nelson, T. Nelson, N. Phinney, T. Raubenheimer,
M. Ross, A. Seryi, S. Smith, Z. Szalata, P. Tenenbaum, M. Woodley, M. Woods, SLAC
D. Angal-Kalinin, C. Beard, C. Densham, J. Greenhalgh, F. Jackson, A. Kalinin, CCLRC
F. Zimmermann, CERN
I. Zagorodnov, DESY
Y. Sugimoto, KEK
S. Walston, LLNL
J. Smith, D. Burton, R. Tucker, N. Shales, Lancaster University
R. Barlow, A. Mercer, G. Kurevlev, Manchester University
P. Burrows, G. Christian, C. Clarke, A. Hartin, S. Molloy, G. White, QMUL, London
W. Mueller, T. Weiland, TEMF TU Darmstadt
N. Watson, University of Birmingham
D. Bailey, D. Cussans, University of Bristol
Y. Kolomensky, University of California, Berkeley
M. Slater, M. Thomson, D. Ward, University of Cambridge
S. Boogert, A. Liapine, S. Malton, D.J. Miller, M. Wing, UCL, London
R. Arnold, University of Massachusetts, Amherst
N. Sinev, E. Torrence, University of Oregon

Abstract

The SLAC Linac can deliver damped bunches with ILC parameters for bunch charge and bunch length to End Station A. A 10Hz beam at 28.5 GeV energy can be delivered there, parasitic with PEP-II operation. We plan to use this facility to test prototype components of the Beam Delivery System and Interaction Region. We discuss our plans for this ILC Test Facility and preparations for carrying out experiments related to collimator wakefields and energy spectrometers. We also plan an interaction region mockup to investigate effects from backgrounds and beam-induced electromagnetic interference[1].

INTRODUCTION AND OVERVIEW

The International Linear Collider (ILC) is envisioned to be the next frontier accelerator facility for particle physics after the LHC begins operation, providing exceptional resolving power and precision for exploring the TeV energy scale. New discoveries are expected in one or more exciting areas: Higgs and the explanation of particle masses, supersymmetry, dark matter, extra dimensions, unification of fundamental forces. The luminosity at this facility will be a factor 1000 greater than that achieved at LEP and 10,000 times greater than achieved at the SLC.

In SLACs End Station A (ESA), we are planning to test prototype components of the Beam Delivery System (BDS) and Interaction Region (IR). This program [2] involves both machine and detector physicists, reflecting the close connections between the accelerator and experiment. Primary areas of study are collimation, backgrounds and precision energy measurements. The ESA experimental program includes many of the critical beam tests [3] discussed for the BDS at the 2004 KEK ILC Workshop. It also plays an important role for the test beam program considered by the Worldwide Study on Detector test beams [4].

BEAM SETUP TO ESA

The ESA beam tests are planned to run parasitically with PEP-II with single damped bunches at 10Hz, beam energy of 28.5 GeV and bunch charge of $2x10^{10}$ electrons.

The long (5mm rms) bunch length out of the damping ring can be compressed in the Ring-to-Linac transfer line and in the 24.5-degree A-line bend from the Linac to ESA to achieve ~300μm bunch length in the end station. A simulation with LiTrack [5] gives the results in Fig. 1 for the energy spread and bunch length in ESA. Transverse beam sizes for the tests planned are expected to be 100-200 μm rms.

COLLIMATOR WAKEFIELDS

At the ILC, collimators are required to remove halo

*Work supported in part by U.S. Department of Energy contract DE-AC02-76SF00515, by the Commission of European Communities under the 6th Framework Programme contract number RIDS-011899, and by the Research Corporation.
†mikeh@undhep.hep.nd.edu

particles (having large amplitudes relative to the ideal orbit) to minimize damage to beam line elements and particle detectors and to achieve tolerable background levels. Short-range transverse wakefields excited by these collimators may perturb beam motion and lead to both emittance dilution and amplification of position jitter at the IP.

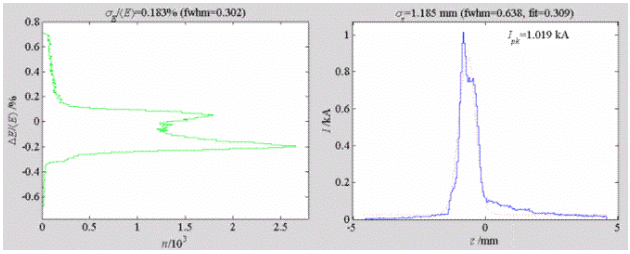

Figure 1. End Station A beam parameters

The goal of these tests [6] is to find optimal materials and geometry for the collimator jaws to minimize wakefield effects while achieving the required performance for halo removal. The collimators will be rectangular in transverse section with a shallow longitudinal taper, long relative to the ~300μm ILC bunch length. To optimize their design, accurate modeling of wakefield effects for short bunches is needed, including the non-linear near-wall region which has implications for machine protection. However, calculating the impedance for such an insertion using analytic methods is difficult, even for an idealized design without real engineering features such as contact fingers. Similarly, tools such as MAFIA have problems in this regime due to grid dispersive effects.

The ESA beam tests will allow further progress with both analytic calculations and development of state-of-the art 3-d electromagnetic modeling methods [7]. Earlier measurements [8] have already enabled significant development of analytic calculations, but the typical consistency with data is only within a factor 2-3. The ILC design goal is agreement at the 10% level [9].

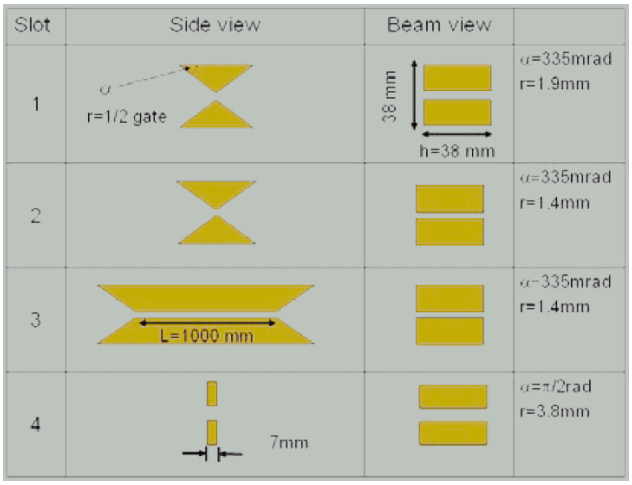

Figure 2. Collimator insertions planned for a first set of measurements.

Initial ESA measurements will measure resistive wakes in copper and study two-step tapers. Two sets of four collimator insertions will be used, and Fig. 2 shows the first set of four collimator insertions we plan to install in the Collimator Wakefield Box [10]. Collimator 1 is the same as used in a recent measurement [8], and is essential for commissioning and control of systematics. Two collimator sandwiches are available, each holding four collimator insertions. Future plans could include investigations of different grades of copper, aluminium, and iron for resistive wakefields, and optimised tapers, as proposed in [7].

ENERGY SPECTROMETERS

At the ILC, beam energy measurements with an accuracy of 100-200 parts per million (ppm) are needed for the determination of particle masses, including the top quark and Higgs boson. Energy measurements both upstream and downstream of the collision point are foreseen by two different techniques to provide redundancy and reliability of the results [11]. Upstream, a LEP-style beam position monitor (BPM) spectrometer is envisioned to measure the deflection of the beam through a dipole field. Downstream of the IP, an SLC-style spectrometer is planned to detect stripes of synchrotron radiation (SR) produced as the beam passes through a string of dipole magnets.

In the proposed ESA tests, we plan to implement the BPM measurement and the synchrotron stripe technique in the same chicane (Figs. 3 and 4), which will have the same 5mm dispersion at mid-chicane and similar dipole fields (~1 kG) as the currently designed upstream ILC energy chicane. It should be possible to measure beam offset with the BPMs at the same time as measuring the synchrotron light position, so beam energy determined from the two techniques can be compared directly. Knowing the ∫Bdl of the magnets and the chicane geometry, together with the position of the offset beam in the BPMs and the horizontal offset of the synchrotron light swath, the beam energy can be determined and compared with that delivered by the SLAC A-line bend magents. To study systematics of the measurements we can dither the beam energy or trajectory at the end of the Linac, as well as change the beam trajectory in the ESA chicane.

BPM Energy Spectrometer

The BPM spectrometer tests [5], will use existing rf cavity BPMs (at least for the first stage), but will upgrade the BPM processing electronics. The overall goal for system (mechanical and electrical) stability is ~500 nm, corresponding to 100 ppm energy precision over a one hour time scale. One hour is a possible calibration timescale where one reverses polarity of the chicane and moves the BPMs at mid-chicane by 10mm on precision movers. We are also investigating possibilities for a stretched wire or laser interferometer system to monitor

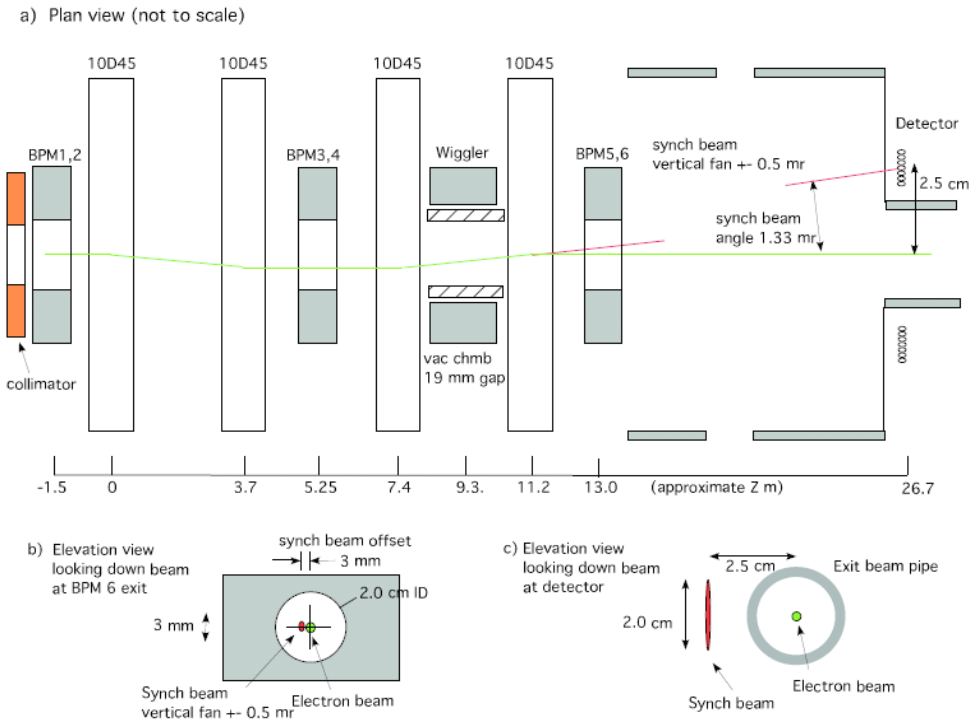

Figure 3. Chicane for BPM and SR stripe energy spectrometer measurements.

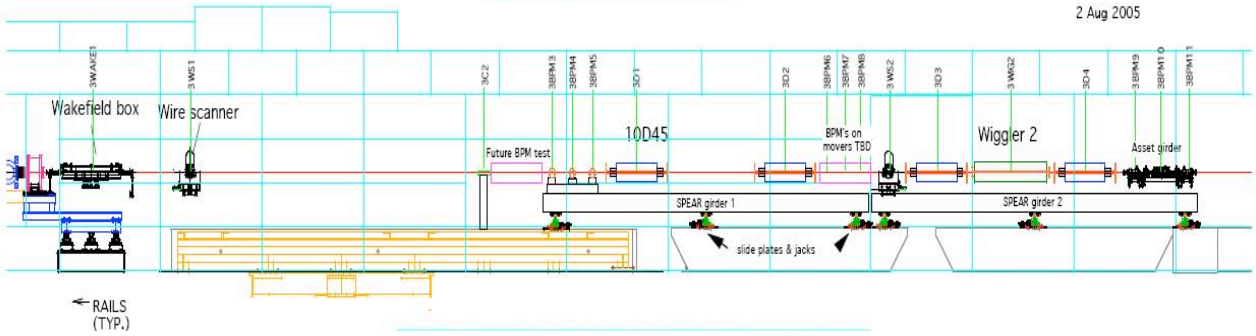

Figure 4. Elevation view of final End Station A configuration, showing locations of chicane elements.

mechanical stability of the support girder. A 6-axis moveable stage would allow us to gauge the effects of beam tilts on the BPM measurements by observing any measurement bias as a function of overall BPM rotation. We also plan temperature sensors along the girder to study temperature sensitivity of mechanical motion and electronics drifts.

SR Stripe Energy Spectrometer

The SR stripe energy spectrometer [6] must make precise measurements of the centroid and shape of the SR stripe. A vertical SR stripe will be generated by a wiggler in the third leg of the chicane. (The ILC chicane will have wigglers in both the first and third legs; an additional wiggler in the first chicane leg in the ESA setup is a possible upgrade option.) We are planning to test a detector array with 100μm quartz fibers read out by a multi-anode PMT that senses Cherenkov light produced by secondary electrons generated by SR photon interactions in the fibers and the upstream window/radiator. The beam test will validate Monte Carlo simulations of the Cherenkov light production and detection efficiency. We will study backgrounds and cross-talk and compare energy measurements (energy jitter and absolute energy scale) with the BPM spectrometer and existing A-line diagnostics.

OTHER STUDIES: IP BPMS, EMI

We want to demonstrate that the fast IP BPMs and kickers, located within 4 meters of the IP, can work to the required precision in the presence of the intense beam-beam interaction. We are studying simulating aspects of the beam-beam interaction with either a 5 radiation length fixed target or a spray beam to mimic a high flux of low energy pairs. This system has been identified as one of the highest risks to delivering design luminosities for both the warm and cold LC designs, in part because of the difficulty of simulating the collision environment in a test beam. We also plan to make measurements to quantify beam-induced electromagnetic interference (EMI) along

the beamline and near features such as toroids, BPMs, and bellows. We plan to measure the EMI frequency spectrum and its dependence on bunch charge and bunch length.

REFERENCES

[1] This submission is largely identical to M. Woods *et al.*, SLAC-PUB-11180, Proceedings of PAC05, Knoxville, TN, May 16-20, 2005.

[*2*] Website for SLACs ILC program in End Station A, wwwproject.slac.stanford.edu/ilc/testfac/ESA/ESA.html.

[3] M. Woods and S. Kuroda, Critical Beam Tests for the Beam Delivery System, http://lcdev.kek.jp/ILCWS/Talks/14wg419-CriticalBeamTests2.pdf.

[4] Worldwide LC Test Beam Working Group, Report on Worldwide Linear Collider Test Beam Effort, http://wwwlc.fnal.gov/lc testbeams/tbpage.html.

[5] P. Emma and K. Bane, LITrack: A Fast Longitudinal Phase Space Tracking Code with Graphical User Interface, SLACPUB-11035 (2005), contributed to PAC-05.

[6] See Projects link at website in [2].

[7] I. Zagorodnov and T.Weiland, A Conformal Scheme for Wake Field Calculation, Proc. EPAC-02 (2002); I. Zagorodnov, T. Weiland, and K. Bane, Calculation of Collimator Wakefields, SLAC-PUB-9727, Proc. PAC-03 (2003).

[8] P. Tenenbaum and D. Onoprienko, Direct Measurement of the Resistive Wakefield in Tapered Collimators, SLAC-PUB10578, Proc. EPAC-04 (2004).

[9] Sec. 7.3.9, G. Loew et al., ILC-TRC 2nd Report (2003).

[10] P. Tenenbaum et al., An Apparatus for the Direct Measurement of Collimator Transverse Wakefields, SLAC-PUB8137, Proc. PAC-99 (1999).

[11] D. Cinabro, E. Torrence and M. Woods, Status of Linear Collider Beam Instrumentation Design, ALCPG IPBI-TN-2003-1, 2003. http://www.slac.stanford.edu/xorg/lcd/ipbi/notes/white.pdf

STATUS OF SHINTAKE-MONITOR (LASER FRINGE BEAM SIZE MONITOR) FOR ATF2

T.Suehara#, T.Sanuki, The Univ. of Tokyo, Tokyo, Japan
T.Tauchi, Y.Honda, T.Kume, KEK, Ibaraki, Japan

Abstract

Shintake-monitor[1][2] is an electron beam size monitor that is the most realistic solution to measure sub-micron beam size now.

We are planning to measure 37nm ATF2[3] beam size by this Shintake-monitor. It has already measured 70nm FFTB beam size, but we need some upgrade to use it in ATF2.

We will describe current status of Shintake-monitor for ATF2, and discuss about the upgrade plans, schedule, etc.

OVERVIEW OF SHINTAKE-MONITOR

Fig. 1 shows a schematic of Shintake-monitor. Photon beam from YAG Laser is split and go across the focal point of electron beam line from opposite direction to make interference fringe pattern. Photons in the fringe interact with electron beam by inverse Compton scattering process.

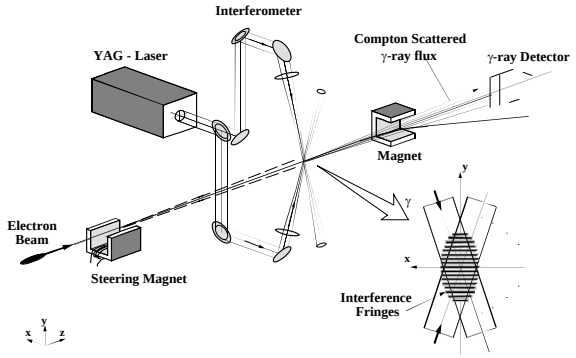

Fig.1 : Schematic of Shintake-monitor

The fringe pattern behaves as a kind of modulation of photon density, so number of scattered photons can modulate by changing phase of the laser fringe on IP.

Depth of the modulation of Compton photon density ($\Delta N/N_0$) depends on electron beam size by,

$$\frac{\Delta N}{N_0} = \exp\left(-\frac{(2k_0\sigma_y)^2}{2}\right) \quad (1)$$

(k_0 : laser wavenumber, σ_y : y axis of beam size)

So, we can obtain electron beam size by measuring this modulation depth with a gamma-ray monitor located downstream of the IP.

Shintake-monitor in FFTB & ATF2

Shintake-monitor has been operated at FFTB experiment from 1992 to 1997. They successfully measured 70 nm beam size, that is close to the designed beam size (60 nm). Fig. 2 shows a typical modulation pattern obtained in the FFTB Shintake-monitor.

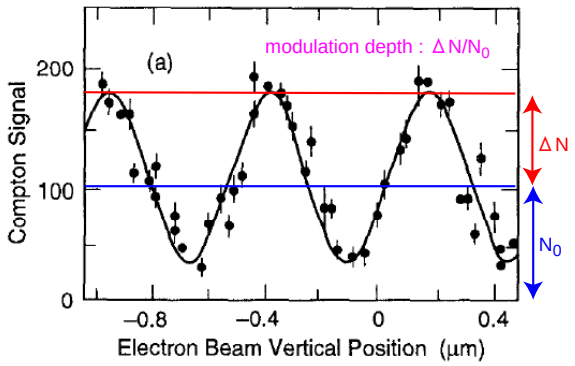

Fig.2 : Typical modulation pattern at FFTB

Because of some different conditions of FFTB and ATF2 experiment, the Shintake-monitor of ATF2 must have some different characteristics from that of FFTB.

Fig. 3 shows major difference between FFTB and ATF2. We will discuss about the upgrade plans below.

Measurement error of Shintake-monitor

We estimate some error elements of Shintake-monitor.

- Statistics of background photons
  There are background photons from beam line. The amount of background is difficult to estimate. This background can be subtracted by laser-off pulse, but statistical fluctuation may increase measurement error.
- Statistics of signal photons
  Signal (Compton) photons also fluctuate by statistics. We estimated 0.6% modulation error 1300 photons, that is ideal photon number for single bunch, 45 points measurement, assuming 1 minute measurement time.
- Laser fringe instability and imperfect fringe contrast
  Both elements lower modulation depth and

	FFTB	ATF2 (plan)
period	1992 - 1997	2007-
beam energy	50 GeV	1.3 GeV
beam size @ IP	70 nm (meas.)	37 nm (plan)
rep. rate	30 Hz	1.5 – 3 Hz
laser wavelength	1064 nm	532 nm
# of signal γ	4300	2600
Compton photon energy max.	15 GeV (1/3 of beam)	29 MeV (1/40 of beam)

Fig.3 : Comparison between FFTB and ATF2

increase measurement error. We have to estimate or measure this fringe instability and fringe contrast to subtract contributions for measurement error by these elements.

- Efficiency for conversion, photon counting etc.
  These elements cause detector-oriented error. We will find optimised detector conditions to decrease measurement error.

UPGRADE PLANS

We are planning to improve following elements of Shintake monitor for ATF2.

Wavelength change

ATF2 design beam size is 37 nm, that is about twice smaller than FFTB. If we will choose 1064 nm laser wavelength for ATF2 Shintake-monitor, that is the same as FFTB, observed signal modulation will be larger than 90% (without background). In this high-modulation area, change of modulation depth by beam size change is relatively small, that causes poor beam size resolution. Optimum modulation depth is around 50% (We assume "effective modulation depth" for 20~80%, See Fig. 4).

For 37 nm ATF2 beam size, we plan to use 532 nm (YAG 2nd) instead of 1064 nm. With 532 nm laser, modulation depth will be around 68%, that is within

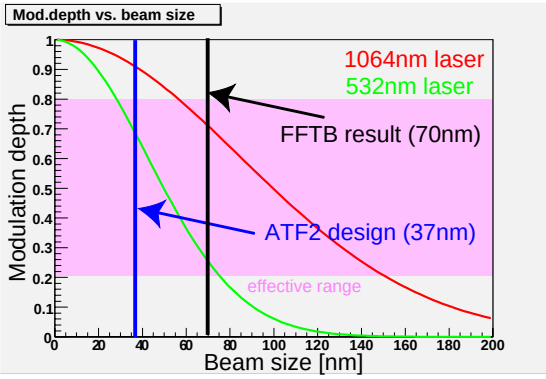

Fig.4 : Modulation depth and beam size

"effective" area. We have to put SHG optics in the laser, and replace mirrors and lenses.

Fringe phase detection & control

Instability of the phase of the laser fringe lowers the modulation depth and limited resolution of beam size. In FFTB fringe stability was measured to be around 22 nm (σ) in 25 sec window[4]. (See Fig. 5)

We plan to detect this phase drift and control it if possible. We are trying to detect it using a field lens to magnify the fringe. Detailed set up is under discussion.

Gamma detector

Gamma detector is one of major R&D issues in ATF2 Shintake-monitor.

Background of gamma detector will be very heavy because of its low signal energy (about 29MeV) and high background energy (up to 1.3GeV).

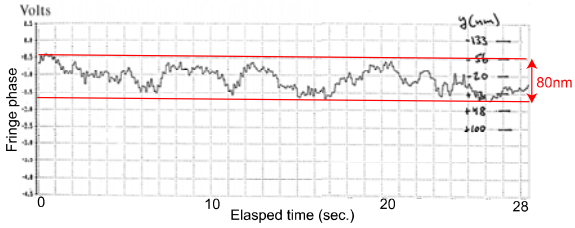

Fig.5 Typical fringe vibration in 25 sec window at FFTB

We think of 4 background sources.

i. Synchrotron radiation
   This is major background at FFTB experiment, but at ATF2, critical energy at bending magnet (assuming 1 Tesla) is about 1 keV. As a result, synchrotron photons can be easily stopped by beam pipe.
ii. Scattering with residual gas
   Because ATF2 beam line is relatively short (~50m), number of photons of this background is negligibly small.
iii. Beam halo scattering with beam pipe by bremsstrahlung
   This is the major background in ATF2. It has large energy up to beam energy (1.3GeV), and large number of photons created without halo-cut components. We have analysed it in detail below.
iv. Particles from beam dump
   This may also be large background, but it can be eliminated by geometry, if we put the detector behind the beam dump.

Since i.,ii.,iv. background can be suppressed, we focus on iii.

Charge distribution of beam halo

To estimate strength of bremsstrahlung background, we measured charge distribution of electron beam of ATF extraction line using wire scanners this summer.

Wire scanners are designed to measure charge distribution around beam center, but it can measure also that of beam halo (~10 σ) by increasing the voltage of PMT power supply.

Fig. 6 shows measured charge distribution. To cover over 10^3 dynamic range, we use several PMT voltage values for one scan. The graphs show that the charge distribution is well described by a gaussian around beam center (< 3 σ), but the tail distribution (> 3 σ) behaves as power function ($\sim\sigma^{-4}$). We decide σ (beam size) by gaussian fitting of beam center (inside ~±3σ).

Fig. 7 shows dependence of the halo distribution by beam size. By this data, charge of halo depends on number of σ rather than absolute distance from beam center. No specific difference was observed between horizontal and vertical distribution.

As a result, we estimate the number of electrons outside 3 σ assuming σ^{-4} distribution (Fig. 8).

Beam size and aperture of ATF2 beam line

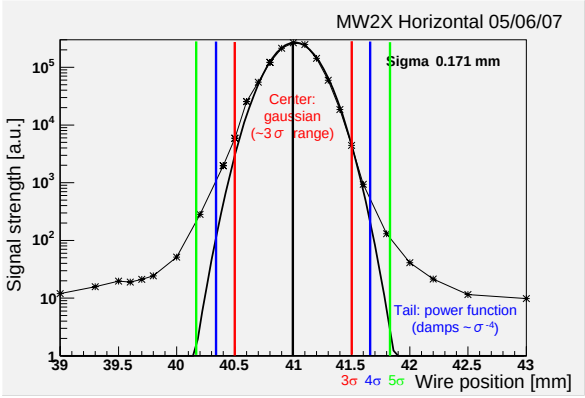

Fig.6 Charge distribution of electron beam.
~3σ center is gaussian, while tail is like power function

In present specification, the smallest aperture size on ATF2 beam line is 20mm ϕ (C-band cavity-BPM beside all quadrupoles). The largest beam size before IP is about 3mm σ (horizontal, around QF1). Then beam pipe is at about 3.3 σ of the beam around BPM of QF1. QF1 is on the final straight section to IP, so most of bremsstrahlung photons created on QF1 will go to the gamma detector through IP.

If we will use S-band cavity-BPM instead of C-band for QF1, the aperture size can be expanded to 40mm ϕ (Y. Honda, WG4 meeting 2005/11/02), that is 6.6 σ of the beam.

S/N ratio

For modulation measurement in reasonable time, at least 1:1 S/N ratio is required. Number of signal photons is order 10^4 by present specification (8ns, 200mJ laser focused to 100μm radius, 10^{10} electrons per bunch).

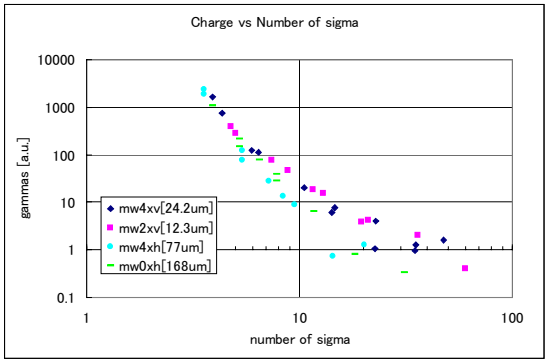

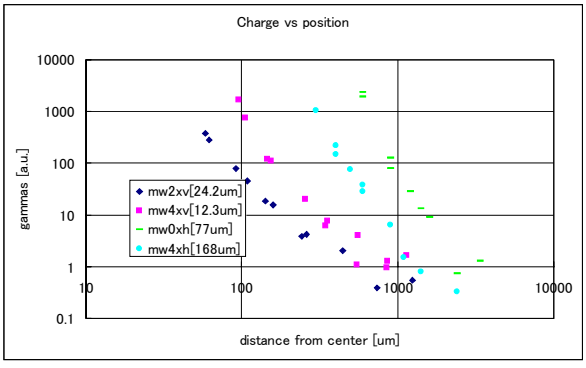

Fig.7 Charge of beam halo with various beam parameters

According to Fig 8., number of electrons hitting the beam pipe around QF1, most of which become background photons, must be larger than 10^7, 3 order larger than signal (in even 40mm ϕ set up). Apparently we need countermeasures.

- Collimators
  Some collimators (for both horizontal and vertical) are indispensable. At least the number of sigma of collimator aperture must be smaller than 6.6σ for horizontal, and 25σ (QD0 aperture) for vertical.
- Octapole magnets
  Some octapoles on proper position and strength can help focusing beam halo.
- Laser upgrade
  To increase the number of signal photons, laser upgrade is the most straightforward way. Pulse length of Shintake laser (8 to 10 ns) is too long, wasting power. Laser of 100ps pulse length with same power per bunch increases signal strength about 100 times.

Combining these countermeasures, we must get to 1:1 S/N ratio (or better, of course) somehow to obtain beam size by Shintake-monitor.

STATUS

Optical table

FFTB Shintake-monitor has been transported from SLAC to Japan (The Univ. of Tokyo, Hongo campus) this summer. We have checked the major components, and tested mirror actuators and their driver modules. Mirrors, beam splitters, lenses, etc. has been replaced for 532 nm laser. Laser axis alignment is now going on.

Control system

FFTB control system is over 10 years old. It's difficult to maintenance and modify because it's programmed in ROM in the VME CPUs and ROM programming device is no more available.

We decided to replace control software with a new VME CPU. Some modules (ADC etc.) and mirror

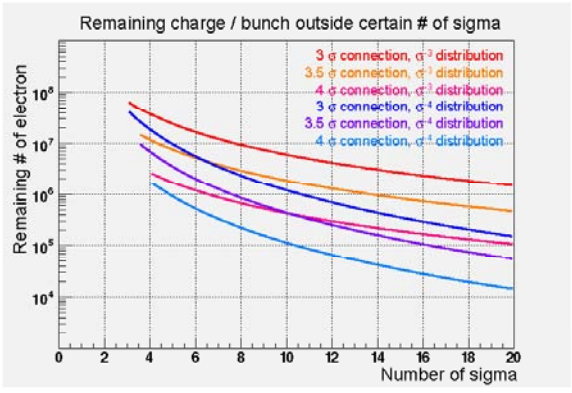

Fig.8 Estimated charge distribution of beam halo

actuator drivers (mentioned before) are also usable by new system.

FFTB laser system

Laser system used in FFTB was also transported. It's Nd:YAG(1st) laser that can expose 600mJ/pulse 1064nm 10pps pulse light. To use it in ATF2 we need additional SHG crystal to convert wavelength to 532nm.

The operation test of the laser by manufacturer (Spectra-Physics co.) was finished, it emitted about 510mJ/pulse light. Order of SHG crystal was also finished, and we are waiting for arrival (Dec05).

Gamma detector

For gamma detector, as discussed before, background suppression is very difficult and important. We have 2 ideas of gamma detector now.

First is multi material cherenkov detector. It stands for thin lead absorber proceeding with 2 layer cherenkov material. Gamma ray interacts with absorber and created charged particles go through 2 cherenkov material.

First layer is the gas cherenkov with the threshold energy of higher than 30 MeV, which only counts background brems. signal.

Second layer is with the threshold energy of less than 30 MeV, which counts both Compton and background signal.

Brems. background can be subtracted by forward gas cherenkov signal.

This method is seemed to be relatively insensitive to background statistics, because subtraction of high energy background have done by signal of particles which pass following (signal) cherenkov without conversion, so it is not influenced by conversion statistics.

The problem of this detector is low signal strength because of using low refractive index gas cherenkov detector. So, this detector will be appropriate if background rate is high.

Second concept is multi layer inorganic scintillator. It use shower scale difference for energy separation.

Low energy signal gamma creates EM shower in the scintillator, but it stops before reaching right part of the layer. On the other hand, high energy background gamma creates bigger EM shower that reaches further than signal. We can use right part of the layer as background subtraction.

This detector has simple structure and easy to make and operate. It have sufficient signal strength because of large number of photons created in scintillator, but it's influenced by fluctuation of shower development.

We are studying these 2 detector concepts using Monte-Carlo simulation (Geant4) now.

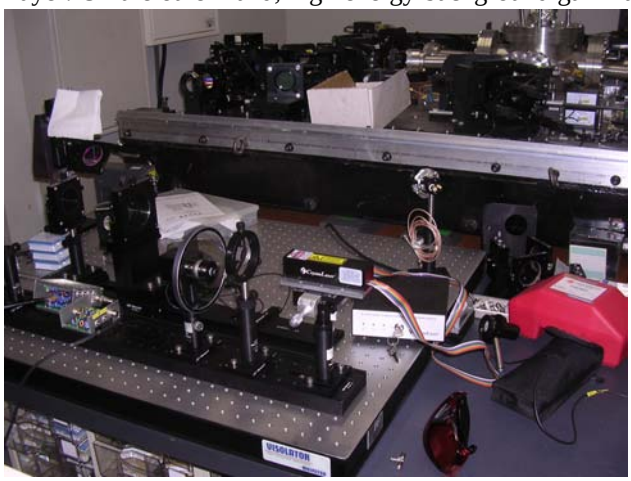

Fig.9 Shintake-monitor and laser injection optics

SUMMARY AND PROSPECTS

We plan to install Shintake-monitor in ATF2 IP and measure 37nm ATF2 beam size with it. We will upgrade Shintake-monitor by wavelength change (1064 nm to 532 nm), laser fringe detection, control, scan, development of background resistive gamma detector, etc.

Status of Shintake-monitor is as follows,

- Shipping from SLAC was finished.
- Check of actuators and sensors are going on.
- System test will be performed using low power cw. 532nm laser.
- There are some ideas for fringe monitoring.
- Control system will be totally replaced.
- Testing of FFTB laser was finished, we are waiting the arrival of SHG crystal for the laser.
- We have 2 ideas (scintillator model, Cherenkov model) for gamma detector. Simulation study is going on.

Shintake-monitor study and upgrade at The Univ. of Tokyo will be finished by fiscal year 2006 and will be transported to ATF2 beam line by summer 2007.

REFERENCES

[1] T. Shintake, "Proposal of Nano-meter Beam Size Monitor for e+e- Linear Collider", Nucl. Inst. Meth. A311 (1992) 453

[2] 新竹積, "極微のビームサイズを測る", 日本物理学会誌, Vol.53 No.5 (1998) 333

[3] ATF2 Collaboration, "ATF2 Proposal", KEK Report 2005-2

[4] M.Woods et al., "Stability and modulation depth of Interference Fringes of the FFTB BSM", FFTB note 98-02

Possible applications of electron beam probe for ILC beam diagnostic system.

T.A. Yaskina, P.V. Logachev, D.A. Malutin, A.A. Starostenko.
Budker Institute of Nuclear Physics, Novosibirsk, Russia

Abstract

Low energy and low current precise electron beam can be used as nondestructive diagnostic tool for high energy beams with very high power density. This method can be used as an online diagnostic of main beam parameters at different places, during normal operation of Linear Collider. The analysis of different electron beam probe applications for ILC beam diagnostic system is presented in this paper.

1 GENERAL PRINCIPLES OF THE ELECTRON BEAM PROBE

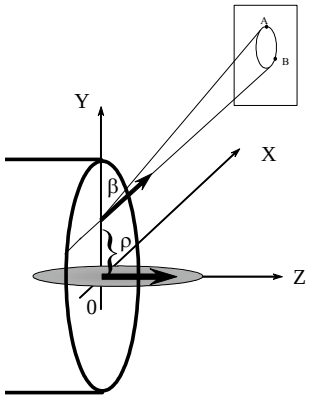

Fig. 1 ***The basis idea of electron beam probe***

The main idea of the electron beam probe (EBP) is based on an interaction of the thin low-energy electron beam with electro-magnetic fields of investigated intensive high-energy bunch. The deflection of low-energy electrons in the fields permits to define different parameters of it such as longitudinal density, displacement of relativistic bunch and its tilting.

We used to inject the probe beam across the path of relativistic bunch. This type of an electron beam probe is suitable for both circular and linear accelerators.

The based model is following. The thin probe beam moves along X axis that is orthogonal to the direction of the relativistic bunch motion (Z axis), with offset parameters ρ (see Fig.1). The density of testing beam is uniform along X axis, beam diameter is d.

This problem has several types of solution.

1) The transverse sizes of the both beams are much less than the offset parameter.

Let the center of the relativistic bunch is located at the origin at time t=0, and at the same moment every testing beam particle is corresponded to the certain x - coordinate. Then the total deflecting angle in Y direction for every testing beam electron under the influence of the electric field of the relativistic bunch can be expressed as (in assuming of small deflection):

$$\theta_y(x) = \frac{2\rho r_e}{\beta}\int_{-\infty}^{+\infty}\frac{n(z)dz}{\rho^2+(x+\beta z)^2}$$

The expression for the deflecting angle of the particle in Z direction due to magnetic field can be written in the similar way:

$$\theta_z(x) = 2r_e\int_{-\infty}^{+\infty}\frac{(x+\beta z)n(z)dz}{\rho^2+(x+\beta z)^2}$$

Here r_e is classical electron radius, $\beta = v_t/c$ is relative velocity of the probe beam, n(z) is the relativistic bunch linear density along Z axis.

As the result, the deflected probe beam traces the closed curve on the screen. Analysis of the distribution of charge density on the screen allows restoring the dependencies of deflecting angles and then the longitudinal density of tested bunch. This solution and experimental results are given in [1,2,3].

2) The other possibility is using electron beam probe as BPM. One can define the vertical displacement of relativistic bunch mass center and bunch tilting if the transverse size of probe beam is much more than the characteristic size of tested bunch. In this case thin relativistic bunch passing through the probe beam cuts it into two parts (see Fig. 2).

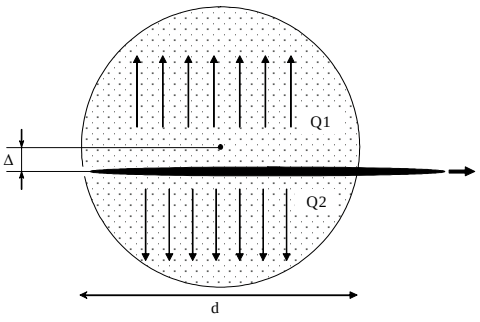

Fig. 2 ***The definition of relativistic bunch vertical displacement***

Each parts of the probe beam traces its own curve on the screen (see Fig. 3a).

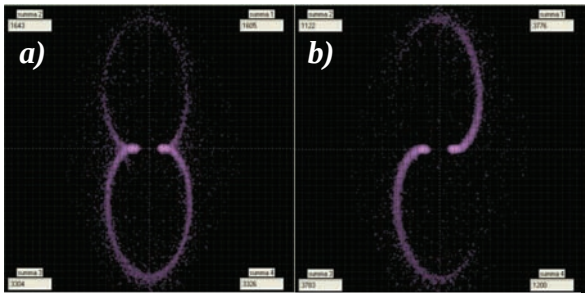

Fig. 3 ***The simulation of charge distribution on the screen for: a) bunch displacement 30 μm, b) bunch tilting 17 mrad. The transverse bunch size is about 7 μm.***

The small displacement of main bunch relative to the center of the probe beam can be defined as:

$$\Delta = \frac{\pi d}{8}\frac{Q_1 - Q_2}{Q_1 + Q_2}$$

where Q_1 and Q_2 are the total charges of the upper and down curves correspondingly, d – diameter of the probe beam.

The same mode of probe beam operations allows defining the bunch tilting (see Fig. 3b). Moreover, the method allows investigating also the more complicated bunch shape such as banana-like.

2 SIMULATION RESULTS

Simulations presented here were performed for relativistic bunch with radial and longitudinal Gauss distributions. The bunch parameters coincide with typical ILC bunch parameters after dumping ring: 26 ps bunch duration, 7 μm bunch transverse size (the smaller transverse bunch dimension was chosen), 10^{10} electron per bunch, 1.28 GeV bunch energy. The longitudinal charge distribution, position of beam center mass and transverse sigma in each section was specified.

The probe beam had uniform distribution in the transverse section, beam energy is 100 keV, transverse energy is 0.1 keV, transverse size is 100 μm at the gun exit and 200 μm in the interaction region. The maximum deflection angle of probe beam is about 40 mrad.

In the ideal case the interaction of the probe beam and the tested bunch results in symmetrical image on the screen. A small bunch displacement or its tilting leads to violation of this symmetry (see fig. 3).

In order to measure the bunch displacement in Y-direction the simulated image on the screen was split into two parts: the first part with y>0 and the second – with y<0. Q_1 is the number of electrons in the part 1of the screen, Q_2 – in the part 2. Finally the value $\Delta_d = \frac{Q_2 - Q_1}{Q_2 + Q_1}$ was calculated. On the fig. 4 the dependence of Δ_d on the fixed vertical displacement δy is shown (here error bars show the statistical error defined as $\frac{1}{\sqrt{N_e}}$, N_e=50000 is the number of electrons in the probe beam).

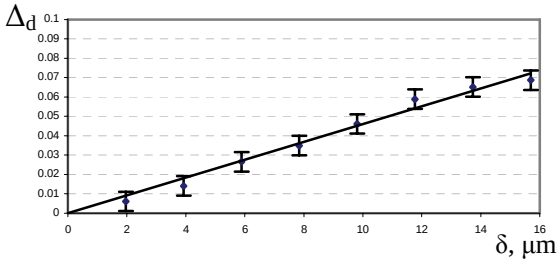

Fig. 4 ***The dependence of the measured value Δ_d on the fixed vertical displacement δy of the relativistic bunch.***

To measure the bunch tilting in Y-direction the simulated image should be split into four parts: 1-(x>0,y>0), 2-(x<0,y>0), 3-(x<0,y<0), 4-(x>0,y<0). Q_1 is the number of electrons in the part 1 of the screen, Q_2 – in part 2 and so on. This method allows estimating the banana-like bunch shape. For example, such investigations were performed for NLC bunch parameters. Results the simulations are presented on the fig. 5, 6. The probe beam energy is 200 keV, transverse size at the gun exit is 100 μm.

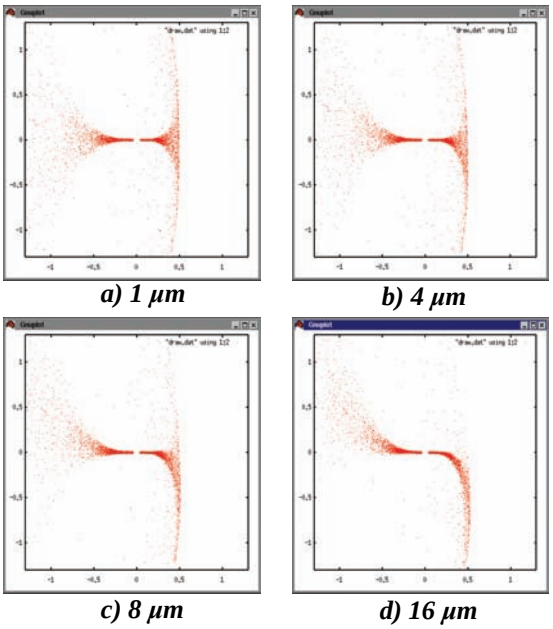

a) 1 μm ***b) 4 μm***

c) 8 μm ***d) 16 μm***

Fig. 5 ***Results of the simulations for the different bunch tilting: a) 1 μm, b) 4 μm, c) 8 μm, d) 16 μm.***

Fig.5 represents four pictures with different bunch tilting amplitudes: 1 μm, 4 μm, 8 μm, 16 μm. Tilting amplitude 1 μm means that the bunch head (at 1 sigma longitudinal) displaced 1 μm up and the tail (at – 1 sigma longitudinal) displaced 1 μm down.

Fig. 6 shows the image asymmetry dependencies on the bunch tilting amplitude: $\Delta_1 = \frac{Q_4 - Q_1}{Q_4 + Q_1}, \Delta_2 = \frac{Q_2 - Q_3}{Q_2 + Q_3}$. Here statistical error is the same with N_e=5000.

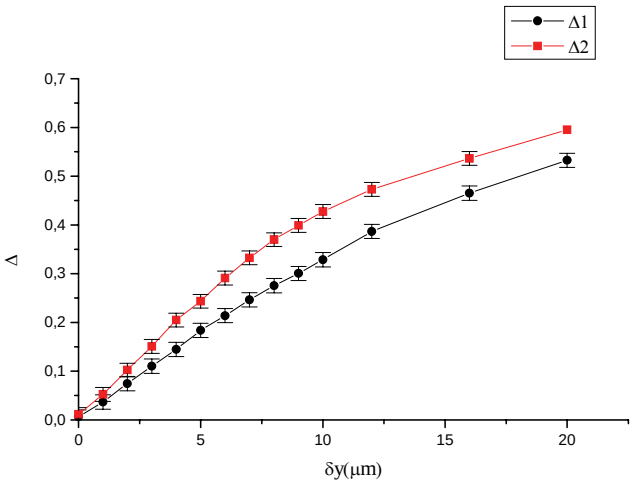

Fig. 6 ***The image asymmetry dependencies (defined above) upon the bunch tilting amplitude***

Using this method for ATF bunch is suitable with the decreasing the probe beam transverse size.

To estimate the simple bunch tilting the value $\Delta_a = \frac{Q_1 Q_3}{Q_2 Q_4}$ can be used, which has the faster growth in comparison with Δ_1, Δ_2 used for estimation of NLC bunch tilting. The dependence is shown on the fig. 7. The image asymmetry becomes clearly seen already for angles in several mrads (here error bars show the same statistical error as for fig. 4).

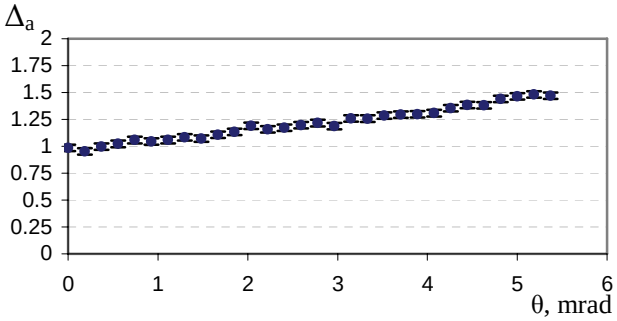

3 PERSPECTIVES

At present time the electron beam probe successfully works on the complex VEPP-5 and VEPP-4, BINP. However, implementation of the EBP for ILC or ATF2 bunch monitoring poses several serious problems in realization this method in practice.

To increase the method precision the transverse beam size and transverse energy should be decreased. Other problem is a time resolution of this method. The time resolution is limited by the probe beam vertical position instabilities. The investigations on the electron gun and EBP optics improvements are being carried out at present time.

To register the result of the interaction the probe beam and relativistic bunch the Micro Channel Plate (MCP) is used. To avoid the MCP saturation the thing strip is used. The change of the MCP parameters with time requires its regular calibration. The calibration program already has been written.

4 CONCLUSION

Here we present several useful qualities of the method:

1.The ability of measurement not only longitudinal distribution of beam density, but also the transverse position of its center of mass and its tilting with good precision.

2.The testing beam has practically no influence on the relativistic bunch, so its parameters don't get worse.

The simulation results show that Electron Beam Probe can be used as beam position monitor in ILC initial part.

5 REFERENCES

1. Physics and Technology of Linear Accelerator System. Proceedings of the 2002 Joint USPAS-CAS-Japan-Russia Accelerator School.

2. P.V. Logachov et al. Non-destructive diagnostic tool for monitoring of longitudinal charge distribution in a single ultrarelativistic electron bunch. PAC-99.

3. A.A. Starostenko. Non-destructive single pass bunch length monitor: experiments at VEPP-5 preinjector electron linac. EPAC-2000.

4. P.V. Logatchov et al. Non-destructive single pass monitor of longitudinal charge distribution. HEACC-2001.

LAWRENCE
LIVERMORE
NATIONAL
LABORATORY

UCRL-CONF-216283

Performance of a Nanometer Resolution Beam Position Monitor System

Vladimir Vogel, Mark Slater, David Ward, Hitoshi Hayano, Yosuke Honda, Nobuhiro Terunuma, Junji Urakawa, Yury Kolomensky, Toyoko Orimoto, Carl Chung, Pete Fitsos, Jeff Gronberg, Sean Walston, Glen White, Joe Frisch, Justin May, Douglas McCormick, Marc Ross, Steve Smith, Tonee Smith, Stewart Boogert, Alexey Lyapin, Stephen Malton, David Miller

October 18, 2005

Nanobeam 2005
Kyoto, Japan
October 17, 2005 through October 21, 2005

Disclaimer

Performance of a Nanometer Resolution BPM System

Vladimir Vogel
DESY, Hamburg, Germany

Hitoshi Hayano, Yosuke Honda, Nobuhiro Terunuma, Junji Urakawa
KEK, Tsukuba-shi, Ibaraki-ken, Japan

Yury Kolomensky, Toyoko Orimoto
Lawrence Berkeley National Laboratory, Berkeley, California, USA

Carl Chung, Pete Fitsos, Jeff Gronberg, Sean Walston
Lawrence Livermore National Laboratory, Livermore, California, USA

Glen White
Queen Mary College, London, UK and Stanford Linear Accelerator Center, Menlo Park, California, USA

Joe Frisch, Justin May, Douglas McCormick, Marc Ross, Steve Smith, Tonee Smith
Stanford Linear Accelerator Center, Menlo Park, California, USA

Mark Slater, David Ward
University of Cambridge, Cambridge, UK

Stewart Boogert, Alexey Lyapin, Stephen Malton, David Miller
University College, London, UK

(Dated: November 2, 2005)

International Linear Collider (ILC) interaction region beam sizes and component position stability requirements will be as small as a few nanometers. It is important to the ongoing ILC design effort to demonstrate that these tolerances can be achieved – ideally using beam-based stability measurements. It has been estimated that an RF cavity BPM with modern waveform processing could provide a position measurement resolution of less than one nanometer. Such a system could form the basis of the desired beam-based stability measurement, as well as be used for other specialized purposes. We have developed a high resolution RF cavity BPM and associated electronics. A triplet comprised of these BPMs has been installed in the extraction line of the KEK Accelerator Test Facility (ATF) for testing with its ultra-low emittance beam. The three BPMs are rigidly mounted inside an alignment frame on six variable-length struts which can be used to move the BPMs in position and angle. We have developed novel methods for extracting the position and tilt information from the BPM signals including a robust calibration algorithm which is immune to beam jitter. To date, we have been able to demonstrate a resolution of approximately 20 nm over a dynamic range of ± 20 μm. We report on the progress of these ongoing tests.

I. INTRODUCTION

The design for the International Linear Collider (ILC) calls for beams which are focused down to a few nanometers at the interaction point. This poses unique engineering challenges which must be overcome. To wit, final focus components must be effectively stabilized at the nanometer level.

Some years ago, LINX was proposed as a new facility at SLAC to support engineering studies of, among other things, stabilization techniques for beamline components [1]. One goal was to demonstrate nanometer stability of colliding beams. Located in the SLD collider hall, LINX was to reuse much of the existing hardware of the SLC and SLD. During the Nanobeam 2002 Workshop in Lausanne, Switzerland in September of that year, it was suggested that nanometer resolution beam position monitors (BPMs) could verify the nanometer level vibration stability without the LINX beam-beam collision project. The intent of our experiment is to understand the limits of BPM performance and to evaluate their role in overcoming some of the thorny engineering issues the interaction region of the ILC presents.

The intrinsic resolution of a BPM is limited by the signal to noise ratio of the system: The signal voltage of the BPM is determined by the beam's energy loss to the antisymmetric transverse magnetic TM_{110} mode (discussed in some detail in section II) and by the external coupling of the waveguide; the overall noise of the system comes from thermal noise as well as contamination from the symmetric transverse magnetic TM_{010} mode (again, see section II) . It has been estimated that an RF cavity BPM along with state-of-the-art waveform processing could have a resolution below one nanometer [4].

With sufficient resolution, other beam-diagnostic measurements are also feasible. For example, a finite-length bunch having either a non-zero angle of obliquity or angle of attack (relative to the orientation of the cavity) produces a signal – hereafter referred to simply as "tilt" – which is in quadrature to the position signal produced by a simple displacement of a very short bunch. It is therefore possible to independently measure both the position and tilt of the beam by using in-phase/quadrature-phase (I/Q) demodulation of the signal from the cavity BPM: The conversion from I and Q to position and tilt is a simple rotation.

This paper describes the NanoBPM experiment and discusses recent progress in the collaboration's efforts to develop nanometer resolution cavity BPMs.

II. THEORY OF CAVITY BPMS

When a bunch transits a cavity, the field of the bunch excites the eigenmodes of the electromagnetic fields within the cavity. For the case of a cavity in the shape of a right circular cylinder (ignoring the effects of the beam pipe openings), the frequencies of the eigenmodes naturally depend on the length L and radius R of the cavity. For cavities with $L < 2.03R$, which is the case here, the first transverse magnetic (TM) mode is the fundamental oscillation of the cavity [5].

For beams near the center of the cavity, the TM_{010} or monopole mode has the highest excitation of all the modes, is symmetric, and is proportional to the charge of the bunch. The explicit expressions for the fields of the TM_{010} mode are

$$E_z = CJ_0\left(\frac{j_{01}r}{R}\right)e^{i\omega_{010}t} \quad (1)$$

$$H_r = 0 \quad (2)$$

$$H_\phi = -iC\frac{\omega_{010}\epsilon_0 R}{j_{01}}J_0'\left(\frac{j_{01}r}{R}\right)e^{i\omega_{010}t}. \quad (3)$$

where C is proportional to the amplitude of the oscillation, J_m is a Bessel function of the first kind of order m, and j_{mn} is the nth root of the equation $J_m(j) = 0$; $j_{01} = 2.405$ [6]. These fields are illustrated in Figure 1.

The TM_{110} or dipole mode, however, is antisymmetric and its amplitude has a strong dependence on the transverse offset of the beam relative to the electrical center of the cavity; the power thus has a quadratic dependence on the offset. The phase depends on the direction of the offset. The explicit expressions for the fields of the TM_{110} mode are

$$E_z = CJ_1\left(\frac{j_{11}r}{R}\right)\cos(\phi)e^{i\omega_{110}t} \quad (4)$$

$$H_r = -iC\frac{\omega_{110}\epsilon_0 R^2}{j_{11}^2 r}J_1\left(\frac{j_{11}r}{R}\right)\sin(\phi)e^{i\omega_{110}t} \quad (5)$$

$$H_\phi = -iC\frac{\omega_{110}\epsilon_0 R}{j_{11}}J_1'\left(\frac{j_{11}r}{R}\right)\cos(\phi)e^{i\omega_{110}t} \quad (6)$$

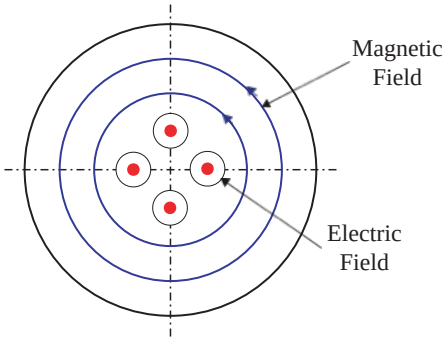

FIG. 1: The fields of the TM_{010} or monopole mode. The amplitude of the monopole mode is proportional to the bunch charge.

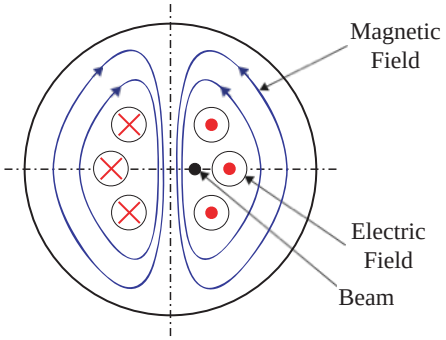

FIG. 2: The fields of the TM_{110} or dipole mode. The amplitude of the dipole mode has a strong dependence on offset of the beam relative to the electrical center of the cavity.

where $j_{11} = 3.832$ [6]. These fields are illustrated in Figure 2.

Physical cavities have finite values for the quality factor $\mathcal{Q}$: They dissipate energy in the cavity walls as well as in any dielectric in the cavity. Each of the cavity's resonant frequencies is therefore not simply a single frequency but rather is smeared out, and appreciable excitations can occur over a narrow band of frequencies around the eigenfrequency. The monopole mode can therefore have a finite tail at the dipole mode frequency, as illustrated in Figure 3. These components cannot be simply filtered out.

III. EXPERIMENTAL SETUP

This experiment employed three identical cavity BPMs designed at Budker Institute of Nuclear Physics (BINP) [7]. The resonant frequency of the dipole TM_{110} mode was 6426 MHz. The dipole mode – whose amplitude is comparatively small when the beam passes near the electrical center of the cavity – was selectively coupled out by two orthogonal slots – one each for x and y –

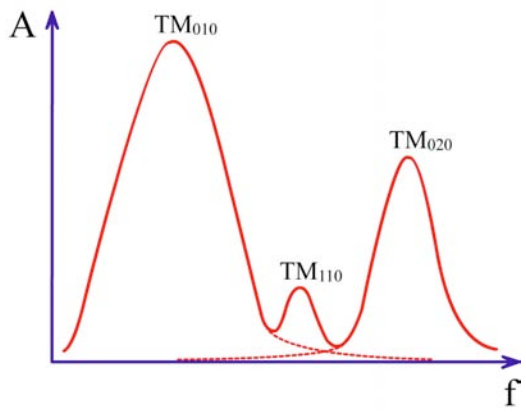

FIG. 3: The the first two monopole modes surround the (usually) much smaller amplitude dipole mode, and because of the finite $\mathcal{Q}$ of the cavity, have components at the dipole mode frequency.

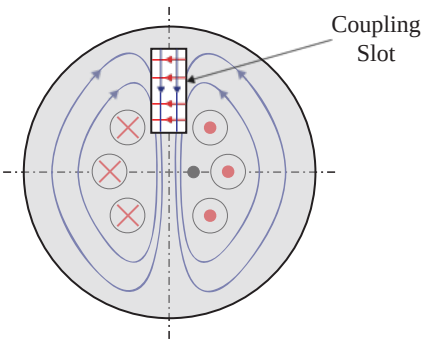

FIG. 4: The dipole mode was selectively coupled out by means of two long, narrow, radial slots on one face of the cavity. The electric field vector points circumferencially across the slot while the magnetic field vector points radially. (The slot shown is not to scale and is for illustrative purposes.) The cavities had two orthogonal slots corresponding to x and y.

which exploited the difference in the field structure of the monopole and dipole modes to reject the monopole mode – and in particular the side bands which reside at or near the dipole mode frequency. This is illustrated in Figure 4. A quarter view of the material boundaries of the BINP BPM cavities is shown in Figure 5.

To the three directional cavities must be added a fourth "reference" cavity whose monopole TM_{010} mode had a resonant frequency of 6426 MHz. The signal from this cavity was used to normalize the amplitudes of the signals from the three directional cavities to remove the effects of variations in the bunch charge; it also provided a single reference for comparing the phases of the signals from the three directional cavities. The signal from the reference cavity was also split with one part being passed through a crystal detector; this information was used to determine the time the bunch transited the apparatus.

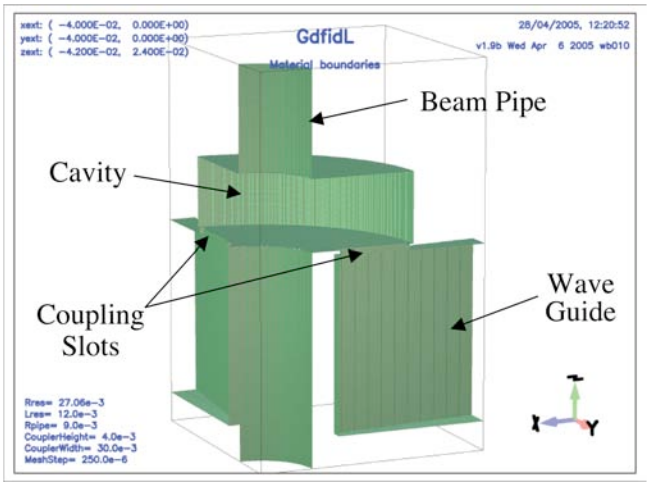

FIG. 5: A quarter view of the inside surface of a BINP BPM.

The three directional BPMs were located in the ATF extraction line and were rigidly mounted inside an alignment frame consisting of a steel space frame which was designed and built at LLNL. The entire alignment frame assembly was suspended by four variable length motorized legs and a non-motorized variable length center strut which allowed the alignment frame to be moved in x, y, yaw, pitch, and roll. Pure y, and yaw motion were possible; x motion included a small amount of roll while pitch necessarily changed the z position slightly. The physical layout of the experiment is illustrated in Figure 6. The Livermore space frame, before the BPMs were mounted inside, is shown in Figure 7. The reference cavity was not contained in the alignment frame, but was located a few centimeters downstream from the third directional BPM.

Each individual BPM was rigidly mounted on six variable length struts which allowed it to be moved by small amounts in x, y, z, yaw, pitch, and roll. The mounting scheme for a single BPM is illustrated in Figure 8. The structure of the hexapod struts is inherently stiff, and coupled with the rigidity of the Livermore space frame allowed rigid-body motion of the three BPMs. A strut is pictured in Figure 9.

Single bunch extractions from the ATF ring were used for all of our tests. Each ATF extraction contained between 6 and 7×10^9 e^- at an energy of 1.28 GeV. The machine repetition rate was ~ 1 Hz.

The electronics used to process the raw signals from the BPMs may be summarized as follows:

1. Bandpass filter, 6426 MHz with 225 MHz bandwidth: Removed of out-of-band signals, most notably monopole mode which due to imperfect coupling slots may not be completely rejected

2. Amplifier, 20 dB gain

3. Mixer, 5950 MHz LO: Mix down to 476 MHz

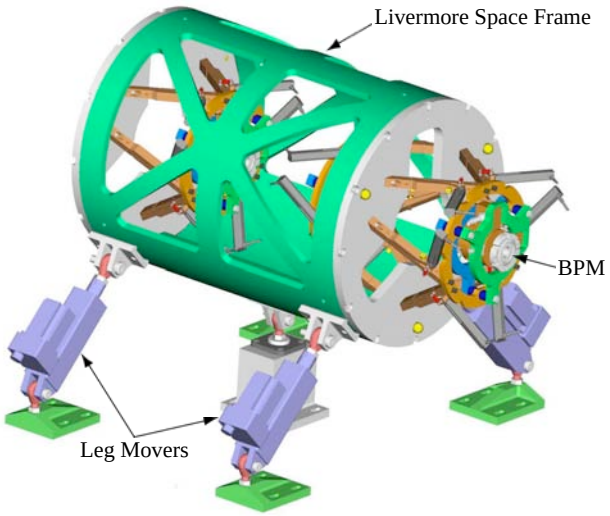

FIG. 6: The Livermore space frame served as the mounting platform for the three BINP BPMs.

FIG. 7: The Livermore space frame held the entire three-BPM assembly rigid. The first vibrational mode was at 200 Hz.

4. Lowpass filter, 700 MHz cutoff: Removed residual LO signal

5. Amplifier, 20 dB gain

6. Bandpass filter, 476 MHz with 20 MHz bandwidth: Removed out-of-band noise which could be aliased into the signal band

7. Mixer, 456 MHz LO: Mix down to 26 MHz

8. Lowpass filter, 30 MHz cutoff: Removed residual LO signal

9. Amplifier, 16 dB

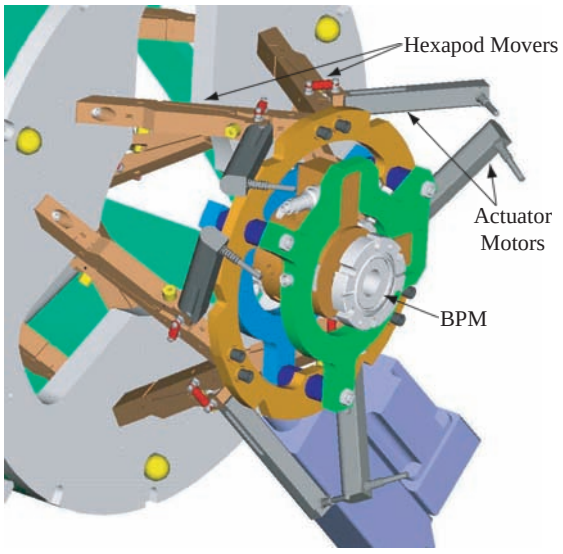

FIG. 8: The BPMs are mounted on hexapod strut movers.

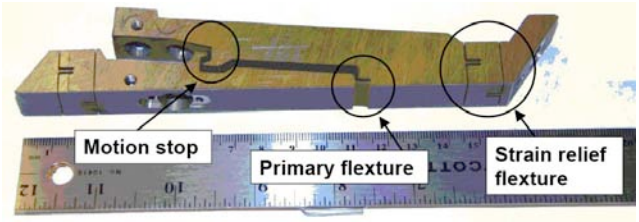

FIG. 9: Each hexapod strut employs a flexure with approximately a 12 to 1 mechanical advantage, i.e. a change in the gap results in a 1/12 change in length of the strut.

10. Lowpass filter, 30 MHz cutoff: Removed out-of-band noise which could be aliased into the signal band

11. Digitizer, 14 bit, 100 Megasamples per second

This is diagrammed in Figure 10.

IV. WAVEFORM PROCESSING

In order to tease out the skein of beam position and trajectory from the raw BPM signals, precise determinations of the amplitudes and phases of the digitized waveforms were needed. A representative raw waveform is illustrated in Figure 11.

The process began by determining the decay rate Γ_i and the frequency ω_i for each of the six channels i as well as for the reference cavity signal. Each of the seven digitized waveforms were initially fitted with the equation

$$V = V_0 + Ae^{-\Gamma(t-t_0)}sin[\omega(t-t_0)+\varphi], \qquad (7)$$

where the values of A, Γ, ω, and φ were all considered as parameters to be determined by the fit. The pedestal

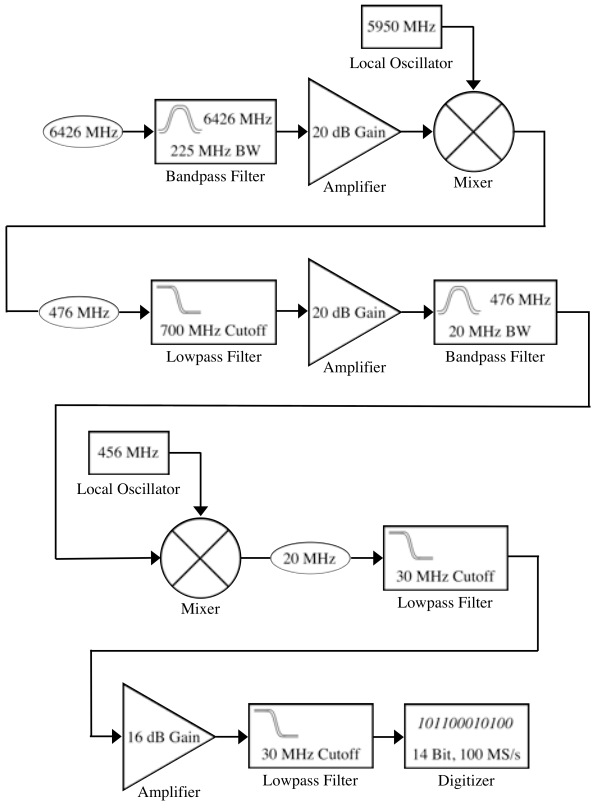

FIG. 10: The electronics used to process the signals from each channel.

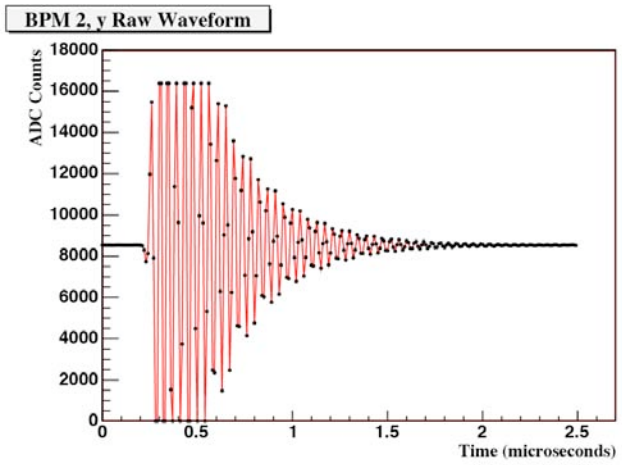

FIG. 11: An example of a raw waveform – this one happens to be from BPM 2, y. Note that in this case the samples between 0.3 μs and 0.6 μs are saturated.

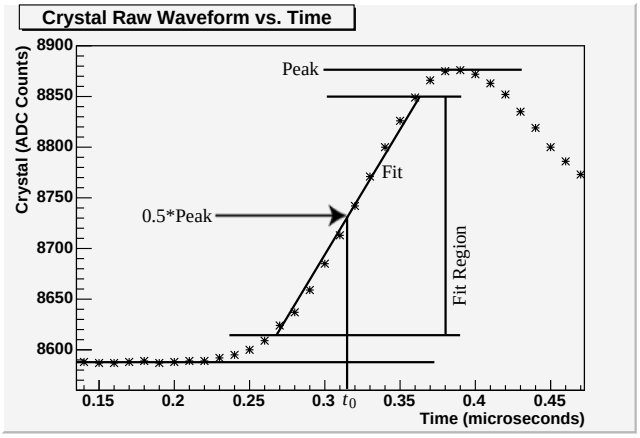

FIG. 12: The value for t_0 was determined on an event by event basis by fitting the rise of the signal from the crystal detector, and defining t_0 to be at the midpoint of the rise, i.e. the time corresponding to when the signal is 0.5 times the value at the peak. So that only the linear portion of the waveform is used, the top and bottom of the rise are excluded from the fit.

value for the ADC, V_0, was taken as the mean value for the first 20 or so samples in the waveform which occurred before the bunch transited the cavity. The value for t_0 was determined by fitting the midpoint of the rise of the signal from the crystal detector, as shown in Figure 12. All waveforms were fitted using only samples taken after the waveform was no longer saturated, or after 60 μs, whichever was later, with the latter criterion being employed to allow any monopole mode which had leaked through to decay away.

The decay rates Γ and the frequencies ω should not vary from event to event as these quantities are properties of the cavities themselves (a rather small variation on long time scales might be expected due to temperature variations of the cavities). For the six directional BPM channels, the Γ_i and ω_i were determined by taking the median value of the distribution of events with large amplitudes, typically defined as those events where the BPM has been moved a relatively large amount in such a way as to produce a large signal in channel i. For the special case of the reference cavity, the decay rate $\Gamma_{\rm Ref}$ and the frequency $\omega_{\rm Ref}$ were determined by simply taking the median over all events.

Once all the decay rates Γ and frequencies ω had been determined, one of two methods were employed for the final determination of the amplitudes A and phases φ: Fitting, or digital down-conversion. Each method will be discussed in some detail below.

The quantities I_i and Q_i were then calculated by normalizing each amplitude A_i and phase φ_i to the the reference cavity amplitude $A_{\rm Ref}$ and phase $\varphi_{\rm Ref}$,

$$I_i = \frac{A_i}{A_{\rm Ref}} cos(\varphi_i - \varphi_{\rm Ref}) \quad (8)$$

$$Q_i = \frac{A_i}{A_{\rm Ref}} sin(\varphi_i - \varphi_{\rm Ref}). \quad (9)$$

The position and tilt signals , P_i and T_i respectively, were

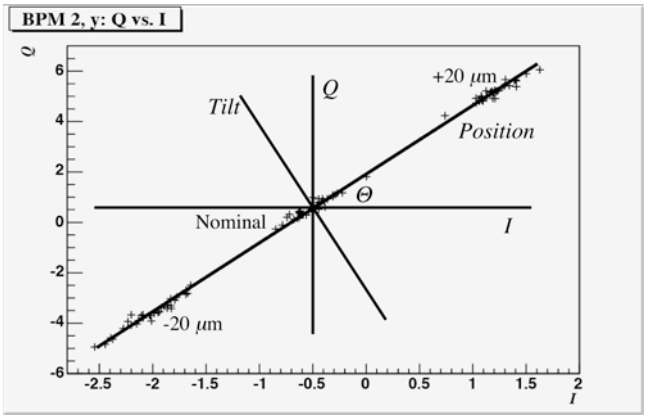

FIG. 13: Q plotted against I (in this case for BPM 2, y). The three clusters of points each contain 32 beam pulses corresponding to three different y positions for BPM 2: The nominal position, and $\pm$ 20 μm. The IQ-phase Θ is the angle between the the I-Q basis and the *Position*-*Tilt* basis. The point spread in each cluster is due to beam jitter. The center cluster, which corresponds to the nominal y position of BPM 2, is not located at $(0, 0)$ owing to a small amount of residual y tilt and y offset for BPM 2.

then a rotation from I_i and Q_i,

$$\begin{pmatrix} P_i \\ T_i \end{pmatrix} = \begin{pmatrix} \cos\Theta_i & \sin\Theta_i \\ -\sin\Theta_i & \cos\Theta_i \end{pmatrix} \begin{pmatrix} I_i \\ Q_i \end{pmatrix}. \quad (10)$$

where Θ_i was the IQ-phase for channel i. This is illustrated graphically in Figure 13. The quantities x, x', y, and y' were then proportional to the quantities P and T:

$$x_n \text{ or } y_n = s_i P_i \quad (11)$$
$$x'_n \text{ or } y'_n = s'_i T_i \quad (12)$$

where each of the six different channels i corresponded to x or y for BPM 1, 2, or 3, and where s_i and s'_i were the position and tilt scales respectively.

A. Fitting

In the fitting algorithm, the waveforms from each of the channels i as well as the reference cavity waveform were simply fitted a second time using equation 7; this time, however, only the amplitude A and phase φ were considered as parameters to be determined by the fit.

B. Digital Down-Conversion

In the digital down-conversion (DDC) algorithm, the raw waveform was first multiplied by a local oscillator (LO) of the same frequency ω to yield a zero intermediate frequency (IF) – denoted U, the real and imaginary parts

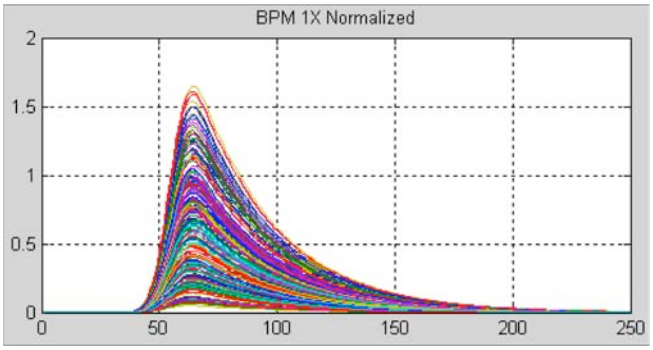

FIG. 14: Demodulated waveforms from BPM 1, x for a data set. Each colored line represents a seperate ATF extraction and has been normalized by the corresponding amplitude of the reference cavity. In the plot, the x axis refers to the sample number.

of which were

$$\Re U = (V - V_0) \times \cos(\omega t) \quad (13)$$
$$\Im U = (V - V_0) \times \sin(\omega t). \quad (14)$$

The real and imaginary parts of each IF were then multiplied by a 39 coefficient, symmetric, finite impulse response (FIR), low-pass filter with 2.5 MHz 3 dB bandwidth,

$$\begin{pmatrix} D_1 \\ D_2 \\ \vdots \\ D_{249} \\ D_{250} \end{pmatrix} = \quad (15)$$
$$\begin{pmatrix} 0 & \cdots & 0 & U_1 & U_2 & \cdots & U_{20} \\ 0 & \cdots & U_1 & U_2 & U_3 & \cdots & U_{21} \\ \vdots & \vdots & \vdots & \vdots & \vdots & \vdots & \vdots \\ U_{229} & \cdots & U_{248} & U_{249} & U_{250} & 0 & \cdots \\ U_{230} & \cdots & U_{249} & U_{250} & 0 & 0 & \cdots \end{pmatrix} \begin{pmatrix} F_1 \\ \vdots \\ F_{39} \end{pmatrix}$$

where here the subscripts on U and D indicate sample number, F denotes the filter vector, and D the demodulated waveform. A series of demodulated waveforms are illustrated in Figure 14.

The amplitude for each channel was defined at a particular time selected to be near the peak of the waveform. If, however, the amplitude could not be evaluated there due to electronic saturation, the amplitude and phase were evaluated at the first non-saturated time and their value at the nominal time was determined by extrapolation using the measured decay constant and frequency.

V. CALIBRATION

To get x, x', y, and y' from the the raw BPM signals, several parameters had to be known a priori: The IQ-phase Θ had to be known to determine the position P and

tilt T from I and Q for each channel; because P and T had arbitrary units, the position scales s and tilt scales s' had therefore be known to determine x and y in μm and x' and y' in μrad. The calibration procedure described here determined the IQ-phase Θ_i, and the position and tilt scales s_i and s'_i respectively for both the x and y channels of each of the three BPMs in a manner which eliminated the effects of beam jitter.

A. IQ-Phase Determination

For a given transverse direction, x or y, the value of I or Q in any one BPM should be related by a linear equation to the values of I and Q in the other two BPMs since the 1.28 GeV beam travels through the three BPMs in a very nearly straight line:

$$I_i = a_{ij}I_j + b_{ij}Q_j + a_{ik}I_k + b_{ik}Q_k + c_i \quad (16)$$
$$Q_i = f_{ij}I_j + g_{ij}Q_j + f_{ik}I_k + g_{ik}Q_k + h_i \quad (17)$$

where $i, j, k = 1, 2, 3$ and $i \neq j \neq k$. We desired to find the values of the coefficients a, b and c, and f, g and h which would allow us to predict I and Q in one BPM from the values of I and Q in the other two. Repeated application of the above two equations (denoted by ellipses below) for many ATF extractions yielded a set of simultaneous equations which could be expressed in terms of a single matrix equation $\mathbf{b} = \mathbf{A}\mathbf{x}$, where $\mathbf{x}$ was a column vector comprised of the coefficients a, b and c, or f, g and h, $\mathbf{b}$ was a column vector of the measured values for either I or Q from a given BPM, and $\mathbf{A}$ was the matrix of Is and Qs from the other two BPMs. The matrix also contained a column of ones which allowed for a constant term. Each row of $\mathbf{A}$ and $\mathbf{b}$ corresponded to a single ATF extraction:

$$\begin{pmatrix} I_i \\ \vdots \end{pmatrix} = \begin{pmatrix} I_j & Q_j & I_k & Q_k & 1 \\ \vdots & \vdots & \vdots & \vdots & \vdots \end{pmatrix} \begin{pmatrix} a_{ij} \\ b_{ij} \\ a_{ik} \\ b_{ik} \\ c_i \end{pmatrix} \quad (18)$$

$$\begin{pmatrix} Q_i \\ \vdots \end{pmatrix} = \begin{pmatrix} I_j & Q_j & I_k & Q_k & 1 \\ \vdots & \vdots & \vdots & \vdots & \vdots \end{pmatrix} \begin{pmatrix} f_{ij} \\ g_{ij} \\ f_{ik} \\ g_{ik} \\ h_i \end{pmatrix} \quad (19)$$

Once $\mathbf{A}$ and $\mathbf{b}$ were known, the question became how to find the optimal solution to the equation for the coefficients a, b, and c and f, g, and h in $\mathbf{x}$. We chose the method of singular value decomposition (SVD) to invert the non-square and possibly singular $m \times n$ matrix $\mathbf{A}$ to yield the matrix $\mathbf{A}^+$: This method has the property that the solution $\mathbf{x} = \mathbf{A}^+\mathbf{b}$ minimizes the magnitude $|\mathbf{A}\mathbf{x} - \mathbf{b}|$ [8].

Once these coefficients were known, I and Q in one BPM could be predicted from the values of I and Q from the other BPMs for any ATF extraction. This is illustrated in Figure 15. Events where BPM i had been moved were then considered, and ΔI_i and ΔQ_i were defined as the difference between the predicted and measured values for I_i and Q_i respectively: Then

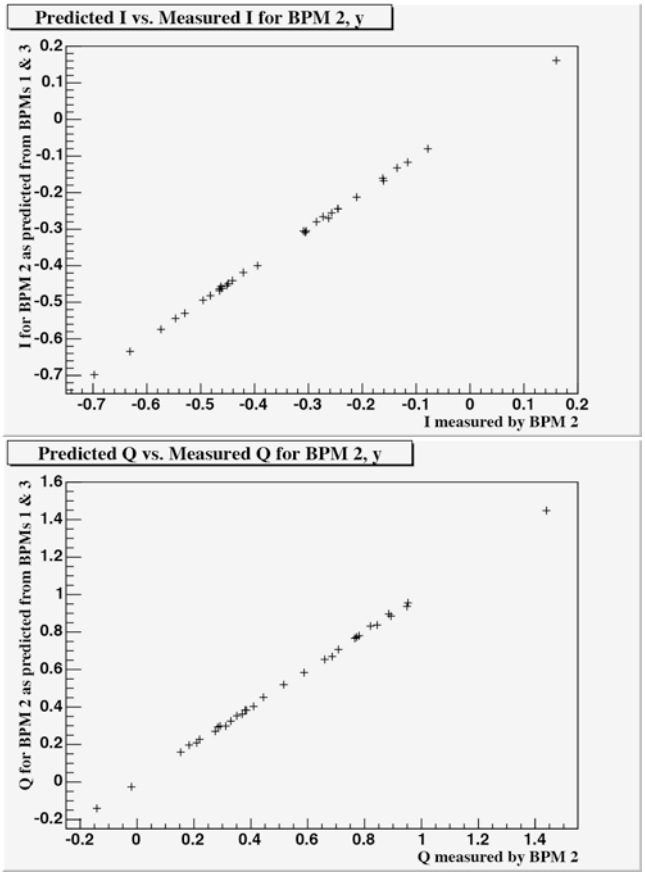

FIG. 15: Calculated values of I (top) and Q (bottom) plotted against the respective measured values (in this case for BPM 2, y). Only ATF extractions with all BPMs in their nominal positions were used in the regressions. Note that the calculated values are highly correlated with the measured values.

$$\Delta I_i = I_i - (a_{ij}I_j + b_{ij}Q_j + a_{ik}I_k + b_{ik}Q_k + c_i) \quad (20)$$
$$\Delta Q_i = Q_i - (f_{ij}I_j + g_{ij}Q_{lj} + f_{ik}I_k + g_{ik}Q_k + h_i) \quad (21)$$

and any significant deviation from zero of ΔI_i and ΔQ_i was attributed to the change in position of BPM i. For pure translations of BPM i, the values of ΔI_i and ΔQ_i lay along a straight line, as illustrated in Figure 16. ΔQ_i could then be regressed against ΔI_i,

$$\begin{pmatrix} \Delta Q_i \\ \vdots \end{pmatrix} = \begin{pmatrix} \Delta I_i & 1 \\ \vdots & \vdots \end{pmatrix} \begin{pmatrix} A_i \\ B_i \end{pmatrix} \quad (22)$$

and the IQ-phase was the arctangent of the slope A_i,

$$\Theta_i = \arctan(A_i). \quad (23)$$

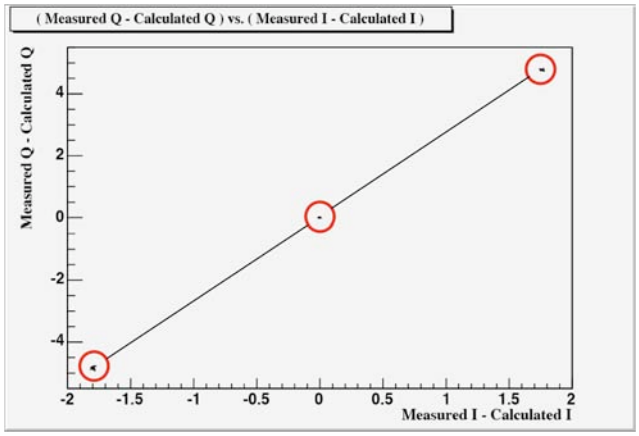

FIG. 16: ΔQ plotted against ΔI (in this case for BPM 2, y). Each of the three tiny blobs (inside the red circles) actually contains 32 ATF extractions.

B. Position Scales

The determination of the position scales s_i began by noting that the trajectory of the beam between BPMs 1 and 2 was the same as that between 2 and 3, irrespective of how the BPMs had been moved. The electrical centers of BPMs 1 and 3, in their nominal positions, were used to define a coordinate axis, and BPM 2 was allowed to have a residual offset with respect to this axis. This is shown schematically in Figure 17, and may be written mathematically as

$$\frac{(m_2 + x_2 + s_2P_2) - (m_1 + s_1P_1)}{z_{12}} = \frac{(m_3 + s_3P_3) - (m_2 + x_2 + s_2P_2)}{z_{23}} \quad (24)$$

where m_n denotes the amount BPM n has been moved away from it's nominal position, and where x_2 denotes the offset of BPM 2 relative to the axis defined by the electrical centers of BPMs 1 and 3. The BPMs were moved one at a time, resulting in four different linearly independent configurations:

$$m_1 = m_2 = m_3 = 0, \quad (25)$$
$$m_1 \neq 0,\ m_2 = m_3 = 0, \quad (26)$$
$$m_2 \neq 0,\ m_1 = m_3 = 0, \quad (27)$$
$$m_3 \neq 0,\ m_1 = m_2 = 0. \quad (28)$$

Repeated application of equation 24 over multiple ATF extractions with the four configurations noted in equations 25 through 28 yielded the matrix equation

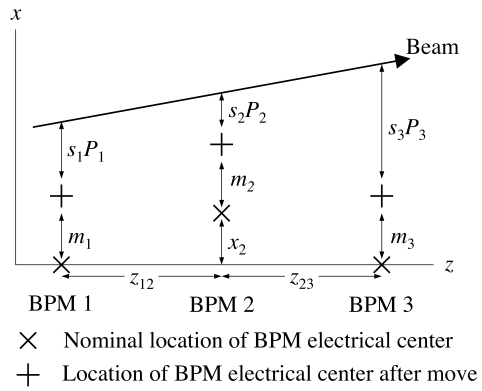

FIG. 17: The nominal positions of the electrical centers of BPMs 1 and 3 define the coordinate system, and BPM 2 is allowed to have a relative offset: These are denoted above with a $\times$. Each BPMs is then moved in turn away from its nominal position by known a amount m_n. The new position for the electrical center of the BPM is denoted by a $+$. The quantity z_{mn} is the distance between BPMs along the beamline.

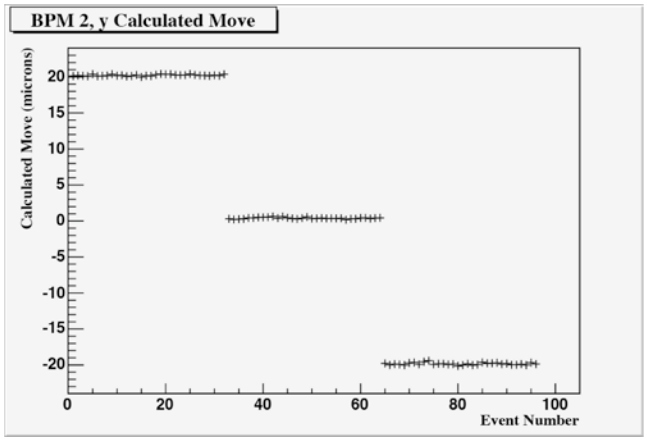

FIG. 18: Once x_2 and s_n had been determined, the amount by which any BPM had been moved could be calculated as a means of verifying the calibration. This plot shows the calculated move for the 96 events over which BPM 2, y was being moved, and clearly shows the pattern used: Nominal location plus 20 μm, nominal location, and nominal location minus 20 μm.

$$\begin{pmatrix} \frac{m_1}{z_{12}} - \frac{m_2}{z_{12}+z_{23}} + \frac{m_3}{z_{23}} \\ \vdots \end{pmatrix} = \begin{pmatrix} \frac{1}{z_{12}+z_{23}} & \frac{-P_1}{z_{12}} & \frac{P_2}{z_{12}+z_{23}} & \frac{-P_3}{z_{23}} \\ \vdots & \vdots & \vdots & \vdots \end{pmatrix} \begin{pmatrix} x_2 \\ s_1 \\ s_2 \\ s_3 \end{pmatrix} \quad (29)$$

The result of inverting this matrix using the technique of singular value decomposition allowed x_2 and s_n to be determined.

The calibration could be verified by using x_2 and s_n

to calculate the amount each BPM had supposedly been moved, and this result compared to the amount the BPM was actually moved. This comparison is shown in Figure 18.

C. Tilt Scales

In one respect, the tilt signals were more difficult to calibrate because there was no way to separate the contribution to the tilt signal due to the angle of obliquity of the beam from that due to the angle of attack of the bunch (both relative to the orientation of the cavity). However, the trajectory of the beam could be independently determined from its positions registered in the other two BPMs, and this in turn could be related to the angle of obliquity by a constant θ_{0i} which was the nominal orientation of the cavity relative to the electrical centers of the other two BPMs. The average angle of attack over a series of ATF extractions was assumed to be nearly constant, or in any case fluctuations in the average were assumed to be small compared to the other terms, most notably the tilt t_i of the BPM as applied by the movers. For a given BPM, the trajectory of the beam as determined from the position signals in the other two BPMs was taken as equal to the sum of θ_{0i}, the angle of applied tilt of the BPM t_i, and the scaled tilt signal $s_i'T_i$ (neglecting the bunch's angle of attack). This is illustrated schematically in Figure 19, and may be written mathematically as

$$\frac{x_k - x_j}{z_{jk}} = s_i'T_i + \theta_{0i} + t_i \tag{30}$$

As with the position calibration, the BPMs were moved one at a time, resulting in four different configurations:

$$t_1 = t_2 = t_3 = 0, \tag{31}$$
$$t_1 \neq 0,\ t_2 = t_3 = 0, \tag{32}$$
$$t_2 \neq 0,\ t_1 = t_3 = 0, \tag{33}$$
$$t_3 \neq 0,\ t_1 = t_2 = 0. \tag{34}$$

Repeated application of equation 30 over multiple ATF extractions with the four configurations noted in equations 31 through 34 yields the matrix equation

$$\begin{pmatrix} \frac{x_k - x_j}{z_{jk}} - t_i \\ \vdots \end{pmatrix} = \begin{pmatrix} T_i & 1 \\ \vdots & \vdots \end{pmatrix} \begin{pmatrix} s_i' \\ \theta_{0i} \end{pmatrix}. \tag{35}$$

The matrix may be inverted using the technique of singular value decomposition to determine s_i' and θ_i. Unlike the position calibration procedure, the tilt calibrations of the separate BPMs are uncoupled.

The calibration could be verified by using θ_{0i} and s_i' to calculate the amount each BPM had supposedly been tilted, and this result could then be compared with the amount the BPM was actually tilted. This comparison is shown in Figure 20.

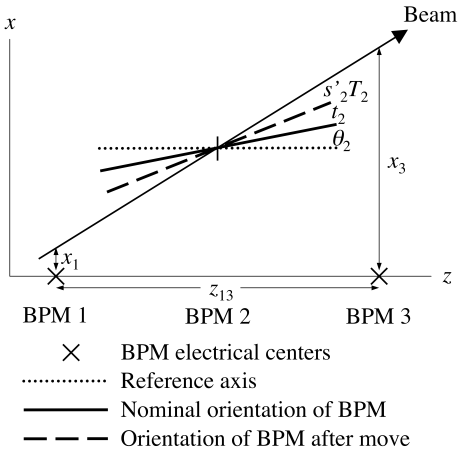

FIG. 19: When calibrating the tilt scales s_i' for a given BPM, the electrical centers of the other two BPMs define the coordinate system. The beam's trajectory is determined relative to this coordinate system by the position signals in those two BPMs. The nominal orientation of the BPM in question relative to this coordinate system θ_i, the applied tilt t_i, and the scaled tilt signal $s_i'T_i$, added together, should equal the beam trajectory, as illustrated.

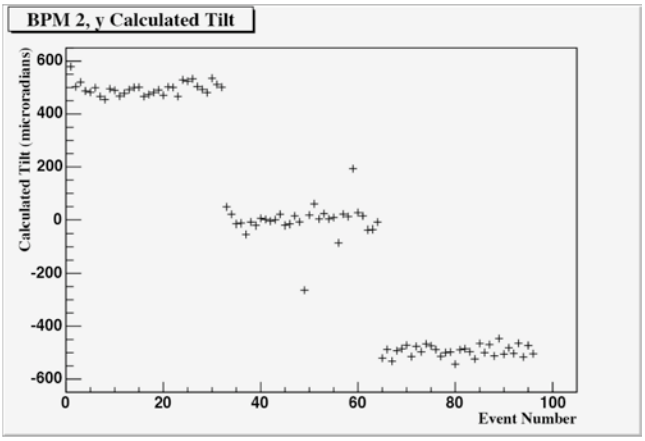

FIG. 20: Once θ_{0i} and s_i' have been determined, the amount by which the BPM has been tilted may be calculated as a means of verifying the calibration. This plot shows the calculated tilts for the 96 events over which BPM 2, y was being tilted, and clearly shows the pattern used: Nominal orientation plus 500 μradians, nominal orientation, and nominal orientation minus 500 μradians. Deviations from the applied tilts may be attributed to jitter in the bunch's angle of attack.

VI. BPM RESOLUTION

BPM resolution was determined by measuring the residual – that is the difference between the predicted position, as calculated from the beam's position in the other two BPMs, and the measured position of the beam in the BPM in question. This is illustrated in figure 21.

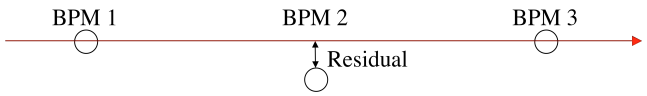

FIG. 21: The residual is the difference between the position of the beam measured by a given BPM and the position predicted from the other two BPMs. In this illustration, the circles represent the location of the beam measured by each BPM; the red line represents the beam's trajectory. In this case, the beam's trajectory is defined by it's position in BPMs 1 and 3, and the residual is relative to the measured position in BPM 2.

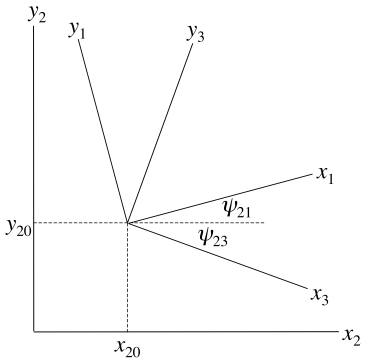

FIG. 22: Let the axis defined by the electrical centers of BPMs 1 and 3 be the origin in the xy planes of all three BPMs: The coordinates associated with BPM 2 are then translated by an offset (x_{20}, y_{20}). Further, let the orientation of the x and y axes of BPM 2 define the principle axes of the coordinate system: The orientations of the BPMs 1 and 3 will then be rotated relative to BPM 2 by angles ψ_{21} and ψ_{23}, respectively.

The resolution was then proportional to the width of the distribution of the residuals over many ATF extractions.

Because the ATF damping ring involves bends and kickers which operate in the xz plane, the transverse stability of the beam was significantly worse in the x direction. The electronics used to process the BPM signals were thus attenuated in channels corresponding to the x direction so that the electronics would not be overwhelmed by the large signals which were possible. The longest lever arm for constraining the beam's trajectory was that between BPMs 1 and 3. These two facts conspired to make BPM 2, y the channel of choice for measuring the resolution.

In the right coordinate system, as detailed in Figure 22, the y position of the beam in BPM 2 could be related in a straight-forward way to the x and y positions of the beam in BPMs 1 and 3 by the equation

$$\begin{aligned} y_2 &= y_{20} + \frac{z_{12}}{z_{13}}\left[-\sin(\psi_{21})x_1 + \cos(\psi_{21})y_1\right] \\ &\quad + \frac{z_{23}}{z_{13}}\left[-\sin(\psi_{23})x_3 + \cos(\psi_{23})y_3\right]. \end{aligned} \quad (36)$$

where y_{20} was the y offset of BPM 2 from the axis defined by the electrical centers of BPMs 1 and 3, ψ_{21} and ψ_{23} were the rotations about the z axis of BPMs 1 and 3 relative to BPM 2, and where z_{mn} was the distance along z between BPMs m and n.

To the degree that the coupling slots for x and y were not orthogonal ($\beta - \alpha \neq 0$ in Figure 37d), x_2 was correlated with y_2. To see this, consider the limiting case where the x and y coupling slots are parallel to each other (i.e. $\beta - \alpha = 90°$); then $x_2 = y_2$ and the parameters associated with the other two BPMs become irrelevant. It was therefore important to exclude x_2 from the regression because its inclusion could artificially reduce the measured resolution. In any case, x_2 was unnecessary because its value was constrained by x_1 and x_3.

Equation 36 may be written simply as

$$y_2 = a_2 + b_{21}x_1 + c_{21}y_1 + b_{23}x_3 + c_{23}y_3. \quad (37)$$

Repeated application of equation 37 over many ATF extractions yielded the matrix equation

$$\begin{pmatrix} y_2 \\ \vdots \end{pmatrix} = \begin{pmatrix} 1 & x_1 & x_3 & y_1 & y_3 \\ \vdots & \vdots & \vdots & \vdots & \vdots \end{pmatrix} \begin{pmatrix} a_2 \\ b_{21} \\ b_{23} \\ c_{21} \\ c_{23}- \end{pmatrix}. \quad (38)$$

Taking for y_2 the measured values, the coefficients a, b, and c were determined by inverting the matrix using the method of singular value decomposition. These coefficients could be determined using either the entire data sample for a run period or a subset of the data. Once the coefficients had been determined, the residual was calculated as

$$\delta y_2 = y_2 - (a_2 + b_{21}x_1 + c_{21}y_1 + b_{23}x_3 + c_{23}y_3) \quad (39)$$

Other terms could be added to equation 37 to include additional parameters in the determination of y_2. Such parameters could include x'_1, y'_1, x'_3, and y'_3. Other possible parameters included beam energy or BPM temperature – indeed any parameter which could be correlated with y_2.

The resolution R_{2y} was then calculated by dividing the standard deviation of the residual distribution by a geometric weight factor,

$$R_{2y} = \frac{\sqrt{\langle(\delta y_2)^2\rangle - \langle\delta y_2\rangle^2}}{\sqrt{\left(\frac{1}{2}\right)^2 + 1^2 + \left(\frac{1}{2}\right)^2}} \quad (40)$$

VII. RESULTS

We present here the results from two data sets, the first taken on the evening of 11 March, 2005, and the second taken during the day on 27 May, 2005.

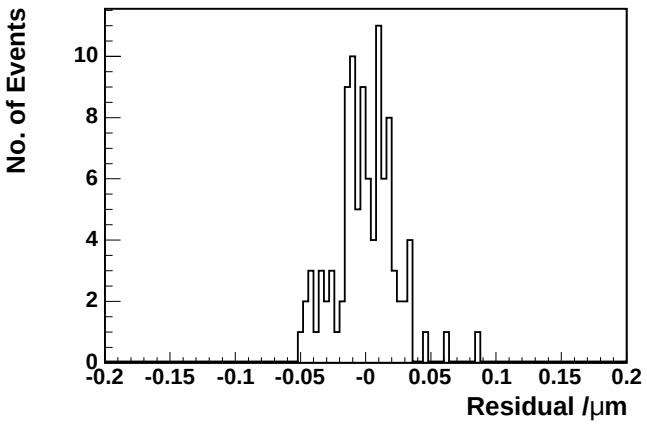

FIG. 23: The residuals δy_2 for 100 ATF extractions from 27 May 2005. This data was analyzed using the fitting algorithm.

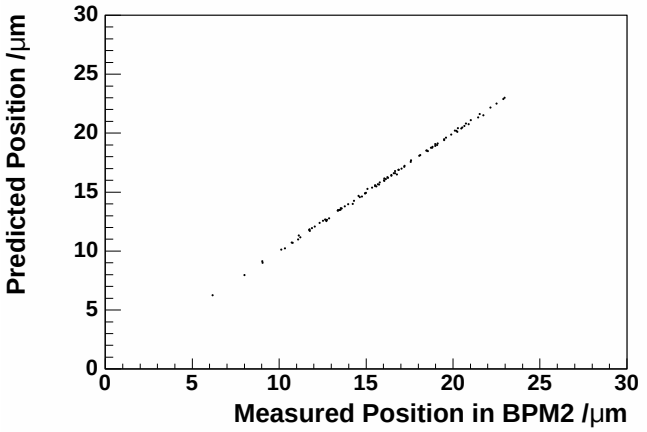

FIG. 24: The beam position at BPM 2 as predicted by BPMs 1 and 3 vs. the measured position in BPM 2 for 100 ATF extractions from 27 May 2005. This data was analyzed using the fitting algorithm.

A. Resolution on Short Time Scales

Figure 23 shows the distribution of the residuals for 100 ATF extractions from 27 May, 2005. This small data set spanning a period of roughly a minute and a half yielded among the best resolutions achieved to date using the fitting algorithm:

$$R_{2y} = \frac{23.1 \text{ nm}}{\sqrt{3/2}} = 18.9 \text{ nm}. \quad (41)$$

Figure 24 shows the correlation between the predicted position and the measured position, the difference of which is the residual.

Figure 25 shows the residuals plotted against beam position in BPM 2, y for 100 ATF extractions from 27 May, 2005. This small data set spanning a period of roughly a minute and a half yielded among the best resolutions achieved to date using the digital down-conversion (DDC) algorithm. The calculation of the residual in this case added additional terms for x'_1, y'_1, x'_3, and y'_3 to equations 37 through 39:

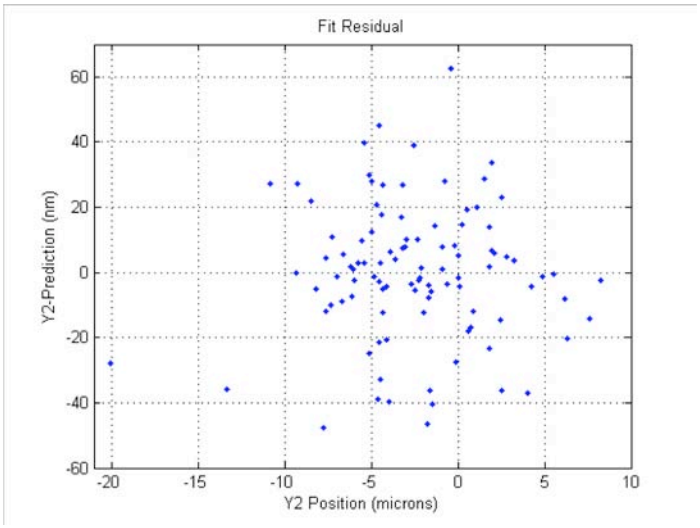

FIG. 25: The residual δy_2 for BPM 2 vs. the position in BPM 2, y for 100 ATF extractions from 27 May 2005. This data was analyzed using the digital down-conversion (DDC) algorithm, and the calculation of the predicted position included terms for x'_1, y'_1, x'_3, and y'_3.

$$R_{2y} = \frac{20.8 \text{ nm}}{\sqrt{3/2}} = 17.0 \text{ nm}. \quad (42)$$

Figure 26 shows the correlation between the predicted position and the measured position, the difference of which is the residual.

B. Resolution over Longer Time Scales

Figure 27 shows the distribution of the residuals δy_2 for 800 ATF extractions from 27 May 2005. This data set was analyzed using the digital down-conversion algorithm and the calculation of the residual in this case added additional terms for x'_1, y'_1, x'_3, and y'_3 to equations 37 through 39. The data here covered a roughly 10 minute time period and demonstrated that high resolution was achievable over longer time periods as well. The distribution in Figure 27 yielded a resolution of

$$R_{2y} = \frac{29.4 \text{ nm}}{\sqrt{3/2}} = 24.0 \text{ nm}. \quad (43)$$

Plotting the residual against time showed that the fluctuations in the residual remained fairly constant across

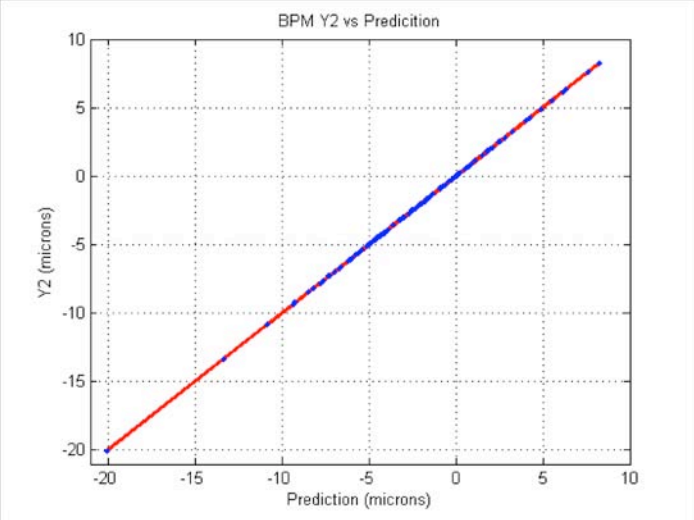

FIG. 26: The measured position vs. the predicted position for BPM 2 for 100 ATF extractions from 27 May 2005. This data was analyzed using the digital down-conversion (DDC) algorithm, and the calculation of the predicted position included terms for x'_1, y'_1, x'_3, and y'_3.

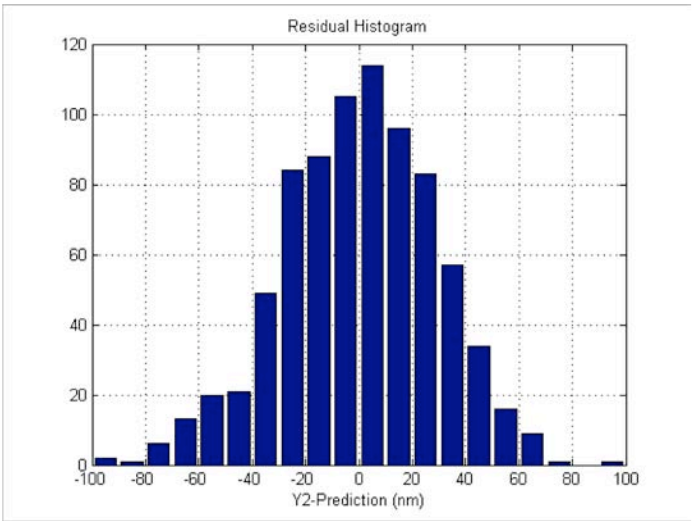

FIG. 27: The residual δy_2 for 800 ATF extractions from 27 May 2005. This data was analyzed using the digital down-conversion (DDC) algorithm, and the calculation of the predicted position included terms for x'_1, y'_1, x'_3, and y'_3.

the entire time span – note the lack of structure in Figure 28. This was in sharp contrast to the obvious structure which appeared when the beam position was plotted against time, as shown in Figure 29: The beam clearly drifted over the period of data taking. But despite movements of the beam, the residual remained stable.

Figure 30 shows the distribution of the residuals δy_2 for 2300 ATF extractions from the evening of 11 March 2005. Four events were removed on account of having a low

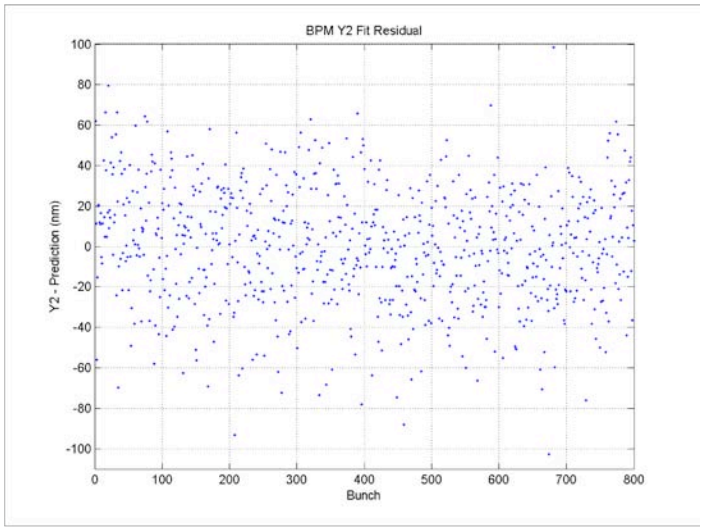

FIG. 28: The residual for BPM 2 vs. the event number (equivalent to time) for 800 ATF extractions from 27 May 2005. This data was analyzed using the digital down-conversion (DDC) algorithm, and the calculation of the predicted position included terms for x'_1, y'_1, x'_3, and y'_3. The lack of structure here demonstrates the stability of the experiment.

reference cavity amplitude and a further two flier events were removed for a total of 2294 events. This data set covered a much longer time period of order half an hour and demonstrated that high resolution was achievable over very long time periods as well. The distribution in Figure 30 yields a resolution of

$$R_{2y} = \frac{28.9 \text{ nm}}{\sqrt{3/2}} = 23.6 \text{ nm}. \quad (44)$$

Figure 31 shows the correlation between the predicted position and the measured position, the difference of which is the residual. Plotting the residual against time showed that the fluctuations in the residual remained fairly constant across the entire time span – note the lack of structure in Figure 32. This was in sharp contrast to the obvious structure which appeared when the beam position was plotted against time, as shown in Figure 33: The beam clearly drifted over the period of data taking. But despite movements of the beam, the residual remained stable.

VIII. OTHER EFFECTS

A. t_0 Reference Point

Nominally, the parameter t_0 was calculated by fitting the rise of the signal from the crystal detector, and defining t_0 to be at the midpoint of the rise, i.e. the time corresponding to when the signal was 0.5 times the value at the peak. This was detailed in Figure 12. However, the

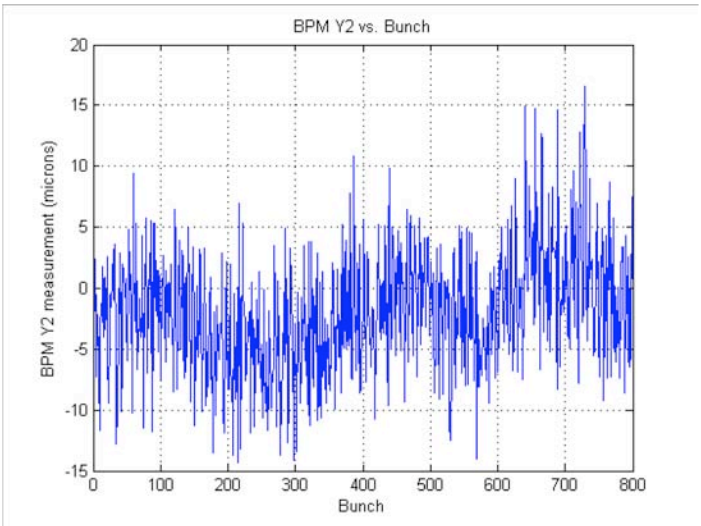

FIG. 29: The beam position measured in BPM 2 vs. the event number (equivalent to time) for 800 ATF extractions from 27 May 2005. This data was analyzed using the digital down-conversion (DDC) algorithm, and the calculation of the predicted position included terms for x'_1, y'_1, x'_3, and y'_3. The structure shown here illustrates the beam drifts which occurred during the period of data taking.

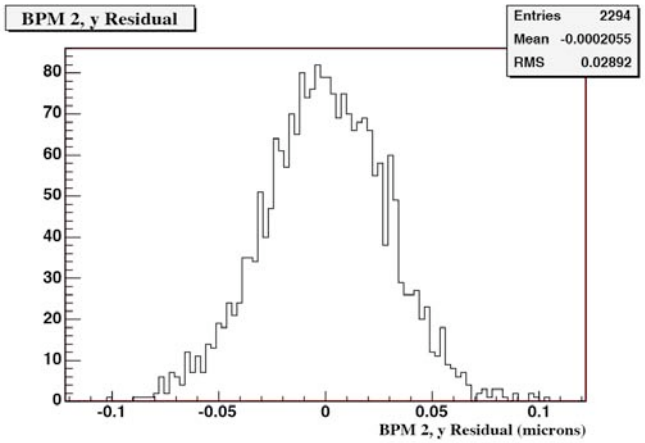

FIG. 30: The residuals δy_2 for 2300 ATF extractions from a period spanning approximately half an hour on the evening of 11 March 2005. Four events were removed on account of low reference cavity amplitude, which usually signifies either a missing bunch or at least a very low current bunch, and a further two flier events were removed for a total of 2294 events. The coefficients used to calculate the residuals were determined from the entire data set less the low reference cavity amplitude events.

seven channels did not have precisely the same resonant frequencies, which fact could introduce phase errors – most notably between the reference cavity and the other channels. By varying the fraction of the peak of the crystal detector signal used as the reference point at which t_0 was defined, we could study it's effect on the resolution and thereby hope to minimize any adverse effect on resolution. Figure 34 shows how the standard deviation of the residuals – which is proportional to the resolution – is effected by varying the t_0 reference point in the data for 2300 ATF extractions taken on the evening of 11 March 2005. Defining t_0 to be at 0.6 of the peak of the crystal detector signal improved the resolution only minimally: R_{2y} goes to 23.52 nm from 23.60 nm.

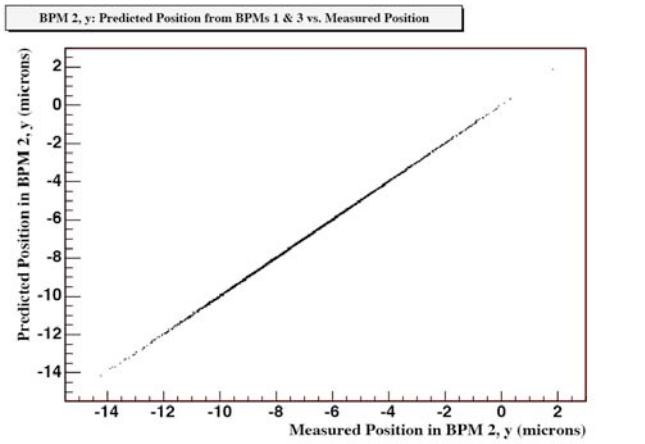

FIG. 31: The beam position at BPM 2 as predicted by BPMs 1 and 3 vs. the measured position in BPM 2 for 2300 ATF extractions from the evening of 11 March 2005. Four events were removed on account of low reference cavity amplitude, which usually signifies either a missing bunch or at least a very low current bunch, and a further two flier events were removed for a total of 2294 events. The coefficients used to calculate the position at BPM 2 from the positions in BPMs 1 and 3 were determined from the entire data set.

B. Magnetic Fields

A magnetic field having an x component (in the coordinates of the beam) will cause the beam to assume a curved trajectory in the yz-plane as it passes through the three BPMs. If the sagitta is constant, the measurement of the resolution is unaffected and is taken into account by the constant term y_{20} in equation 36. However, the presence of such a magnetic field can have an effect on the measured resolution in two ways: Changes in either the beam's energy or the strength of the magnetic field will cause changes in the radius of the curvature of the beam's trajectory and thus to the sagitta. The sagitta δ may be calculated as

$$R(cm) = \frac{1}{c \times 10^{-17}} \times \frac{p(\mathrm{GeV}/c)}{B_\perp(\mathrm{gauss})}, \quad (45)$$

$$\sin\theta = \frac{L}{2R}, \quad (46)$$

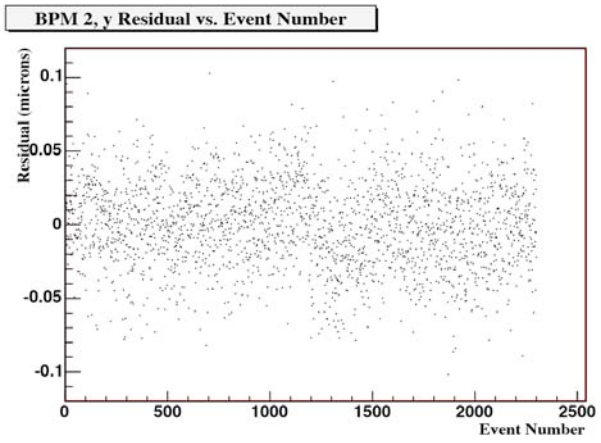

FIG. 32: The residual for BPM 2 vs. the event number (equivalent to time) for the 2300 ATF extractions from the evening of 11 March 2005. Four events were removed on account of low reference cavity amplitude, which usually signifies either a missing bunch or at least a very low current bunch, and a further two flier events were removed. The lack of structure here demonstrates the stability of the experiment.

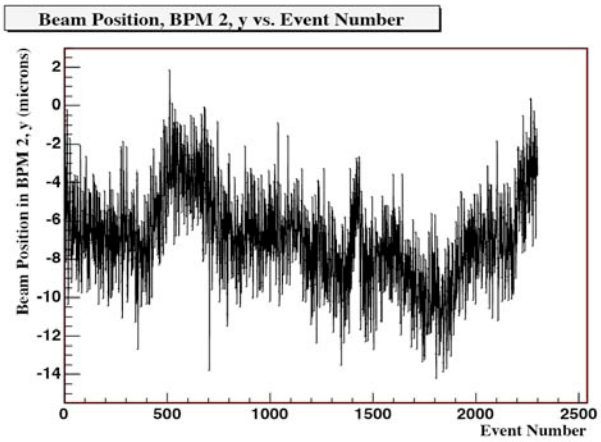

FIG. 33: The beam position measured in BPM 2 vs. the event number (equivalent to time) for the 2300 ATF extractions from the evening of 11 March 2005. Four events were removed on account of low reference cavity amplitude, which usually signifies either a missing bunch or at least a very low current bunch, and a further two flier events were removed. The structure shown here illustrates the beam drifts which occurred during the period of data taking.

$$z = \frac{L}{2\tan\theta}, \quad (47)$$

$$\delta = R - z. \quad (48)$$

and is shown schematically in Figure 35.

The earth's magnetic field at the ATF on 11 March 2005 was determined to have a total intensity of 46,430.02 nT, changing by -14.22 nT per year [12]. For

$$p = 1.28\,\mathrm{GeV}/c,$$

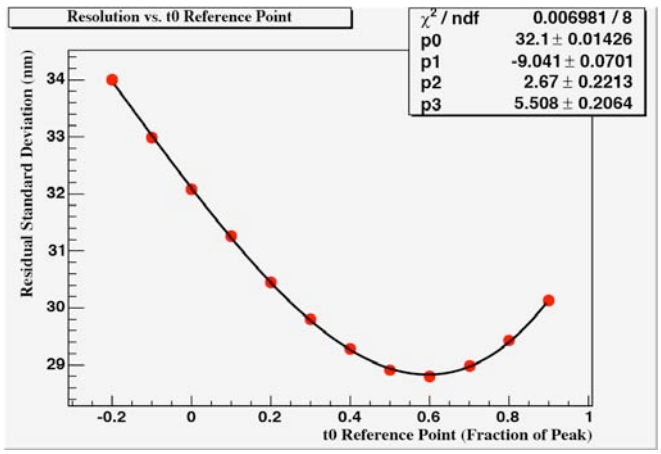

FIG. 34: The standard deviation of the residuals (proportional to the resolution) is plotted against the fraction of the peak of the crystal detector signal used as the reference point at which t_0 is defined; i.e. the number 0.5 in Figure 12 is varied to determine how the resolution changes. This data fits to a third-order polynomial of the form $y = \sum_n p_n x^n$ with the coefficients shown, and the minimum is at 0.596.

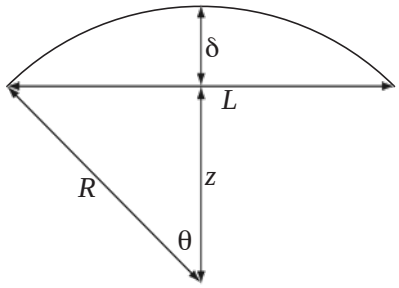

FIG. 35: The sagita of the beam due to a magnetic field orthogonal to the beam.

$$L = 60\,\mathrm{cm},$$
$$B_\oplus = .46430\,\mathrm{gauss},$$

the radius of curvature of the trajectory R and sagitta δ were

$$R = 3.33 \times 10^6\,\mathrm{cm}$$
$$\delta = 489\,\mathrm{nm}$$

The stability of the beam energy was investigated by using the measured position of the beam from the 52 BPMs in the ATF arcs:

$$\frac{\Delta E}{E} = \frac{1}{N} \sum_{\mathrm{ATF\ BPMs}} \frac{x_i - \langle x_i \rangle}{\eta_i}, \quad (49)$$

where η_i was the design dispersion for BPM i and $\langle x_i \rangle$ for a given event was calculated from the average position in

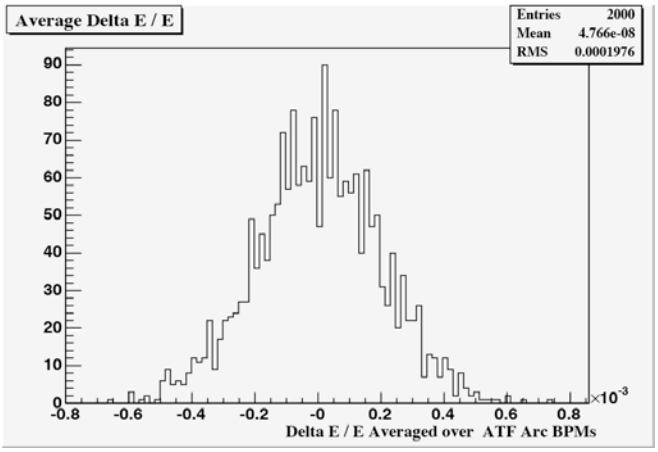

FIG. 36: Estimate of the fractional variation in the beam energy. The average is taken over the 52 BPMs in the ATF arcs.

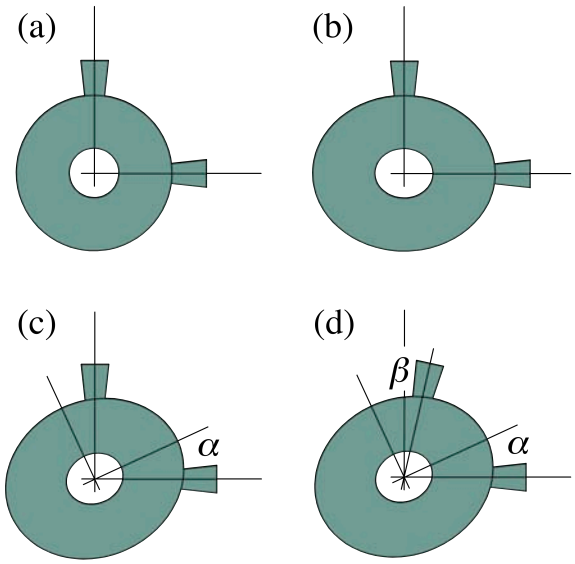

FIG. 37: (a) A perfectly circular cavity with the wave guides at right angles. (b) An elliptical cavity with the semi-major and semi-minor axes aligned with the wave guides. (c) An elliptical cavity with the semi-major and semi-minor axes rotated by an angle α relative to the wave guides. (d) An elliptical cavity with the semi-major and semi-minor axes rotated by an angle α relative to the x-wave guide and by an angle β relative to the y-wave guide.

BPM i of 40 events surrounding the event in question:

$$\langle x_i \rangle \;=\; \frac{1}{40} \sum_{n=\text{event}-20}^{\text{event}+20} x_{in}. \qquad (50)$$

The distribution in Figure 36 is in excellent agreement with the design energy stability of the ATF.

The stability of the beam energy and the fluctuations of the earth's magnetic field had the following affects on the sagitta and by extension the measured resolution of the BPMs:

$$\frac{\Delta p}{p} = .0002 \;\rightarrow\; \Delta\delta = 0.07\,\text{nm}$$
$$\frac{\Delta B}{B} = \frac{14}{46430} \;\rightarrow\; \Delta\delta < 0.15\,\text{nm}$$

The figure for $\Delta B/B$ should be considered as an upper limit as the worst-case scenario was assumed – namely that the orientation of the earth's magnetic field was perpendicular to the beam.

C. Temperature

Five temperature sensors, distributed among the mounting rings and the hexapod strut movers, were associated with each BPM. The data from these sensors was read out on a run by run (as opposed to an event by event) basis. No correlation was seen between this data and the residual δy_2 and no improvement in the residual was found when this data was added as an additional parameter to equations 38 and 39.

D. Cross Talk

If the BPMs are not perfectly machined but rather the cavities have a degree of eccentricity, excitations of the cavities' antisymmetric modes in the x direction may become coupled with those in the y direction. In a perfectly round cavity, as shown in Figure 37 (a), the x and y antisymmetric modes are degenerate:

$$X \;=\; X_0 + A_x e^{-\Gamma(t-t_0)} \sin\left[\omega(t-t_0)+\varphi_x\right], \qquad (51)$$
$$Y \;=\; Y_0 + A_y e^{-\Gamma(t-t_0)} \sin\left[\omega(t-t_0)+\varphi_y\right], \qquad (52)$$

where X_0 and Y_0 are the pedestal values for the signals from the x and y channels, respectively. If the cavity has a non-zero eccentricity, as shown in Figure 37 (b), but the waveguides are aligned with the semi-major and semi-minor axes, the x and y antisymmetric modes become non-degenerate:

$$X \;=\; X_0 + A_x e^{-\Gamma_x(t-t_0)} \sin\left[\omega_x(t-t_0)+\varphi_x\right], \qquad (53)$$
$$Y \;=\; Y_0 + A_y e^{-\Gamma_y(t-t_0)} \sin\left[\omega_y(t-t_0)+\varphi_y\right]. \qquad (54)$$

If, however, the waveguides are not aligned with the semi-major and semi-minor axes, as shown in Figure 37 (c), the antisymmetric modes of x and y can mix:

$$X \;=\; X_0 + \cos(\alpha) A_x e^{-\Gamma_x(t-t_0)} \sin\left[\omega_x(t-t_0)+\varphi_{xx}\right] + \sin(\alpha) A_y e^{-\Gamma_{xy}(t-t_0)} \sin\left[\omega_y(t-t_0)+\varphi_{xy}\right], \qquad (55)$$
$$Y \;=\; Y_0 - \sin(\alpha) A_x e^{-\Gamma_x(t-t_0)} \sin\left[\omega_x(t-t_0)+\varphi_{yx}\right] + \cos(\alpha) A_y e^{-\Gamma_y(t-t_0)} \sin\left[\omega_y(t-t_0)+\varphi_{yy}\right]. \qquad (56)$$

The situation is only slightly more complex if the waveguides are not perfectly orthogonal to each other, as shown

in Figure 37 (d),:

$$X = X_0 + \cos(\alpha)A_x e^{-\Gamma_x(t-t_0)}\sin\left[\omega_x(t-t_0)+\varphi_{xx}\right] + \sin(\alpha)A_y e^{-\Gamma_y(t-t_0)}\sin\left[\omega_y(t-t_0)+\varphi_{xy}\right], \quad (57)$$

$$Y = Y_0 - \sin(\beta)A_x e^{-\Gamma_x(t-t_0)}\sin\left[\omega_x(t-t_0)+\varphi_{yx}\right] + \cos(\beta)A_y e^{-\Gamma_y(t-t_0)}\sin\left[\omega_y(t-t_0)+\varphi_{yy}\right]. \quad (58)$$

We explicitly looked for cross talk between the x and y modes by trying to fit the raw waveforms to an equation of the form of equations 57 and 58 (see Figure 37d). To date, no conclusive evidence of crosstalk has been found.

IX. BPM OUTPUT SIGNALS AND RESOLUTION

A. Energy in a Cavity

The exchange of energy between the beam and the cavity depends entirely on the geometry of the cavity and the properties of the bunch rather than on the cavity material. It can be characterized by the normalized shunt impedance

$$\frac{R}{\mathcal{Q}} = \frac{V^2}{\omega U}, \quad (59)$$

where V is the integral of E_z in the cavity along the beam trajectory, ω is the resonant frequency, and U is the energy stored in the cavity, all calculated for the mode of interest of the cavity – usually the TM_{110} mode whose excitation depends on the beam's trajectory. The shunt impedance is a function of the beam's trajectory because the voltage V excited in the cavity is proportional to the transverse offset of the beam relative to the electrical center of the cavity.

The energy left in the cavity after a short bunch of charge q passes through it can be calculated as [9]

$$W = \frac{\omega}{4}\frac{R}{\mathcal{Q}}q^2. \quad (60)$$

and is proportional to the square of the beam offset. By comparison, a gaussian distributed bunch of length σ leaves less energy in the cavity when σ is comparable to or larger than the wavelength of the dipole mode oscillations. This fact leads to a modification of equation 60, [7]

$$W = \frac{\omega}{4}\frac{R}{\mathcal{Q}}q^2 e^{-\frac{\omega^2\sigma^2}{c^2}}, \quad (61)$$

where c is the speed of the light (we assume the bunch to be relativistic).

The external quality factor of the cavity describes the strength of the cavity coupling to the outer network, and may be expressed as

$$\mathcal{Q}_{\rm ext} = \frac{\omega U}{\overline{P}_{\rm out}}. \quad (62)$$

Only a portion of the energy in equation 61 proportional to $1/\mathcal{Q}_{\rm ext}$ will be coupled out of the cavity. The output power coming from the cavity just after the excitation is

$$P_{\rm out} = \frac{\omega^2}{4\mathcal{Q}_{\rm ext}}\frac{R}{\mathcal{Q}}q^2 e^{-\frac{\omega^2\sigma^2}{c^2}}, \quad (63)$$

assuming a small change in $P_{\rm out}$ over a cycle.

The voltage in an output line with impedance Z is

$$V_{\rm out} = \sqrt{P_{\rm out}Z} = \frac{\omega}{2}\sqrt{\frac{Z}{\mathcal{Q}_{\rm ext}}\frac{R}{\mathcal{Q}}}e^{-\frac{\omega^2\sigma^2}{2c^2}}q. \quad (64)$$

As the energy stored in the cavity decays, the output power also decays. It is important to include here both the power going into the output network as well as the power dissipated in the cavity walls. The latter term depends on the wall material and is described by the internal quality factor $\mathcal{Q}_0$. The decay is exponential with a decay constant τ which may be written as

$$\tau = \frac{2\mathcal{Q}_L}{\omega} \quad (65)$$

where

$$\frac{1}{\mathcal{Q}_L} = \frac{1}{\mathcal{Q}_0} + \frac{1}{\mathcal{Q}_{\rm ext}}. \quad (66)$$

and where the internal quality factor is

$$\mathcal{Q}_0 = \frac{\omega U}{\overline{P}_{\rm diss}}. \quad (67)$$

Most of the energy stored in the cavity decays over this time period. By the same reasoning, most of the energy coupled out of the cavity is also contained in the same time period. We can determine this energy by integrating the output power,

$$W_{\rm out} = \int_0^\tau P_{\rm out}e^{-\frac{t}{\tau}}dt = P_{\rm out}\tau\left(1-\frac{1}{e}\right). \quad (68)$$

In order to get a realistic estimation of the cavity output, the BPMs were simulated using electromagnetic fields simulation code GdfidL [10]. Basic cavity parameters like resonant frequencies and shunt impedances needed for the calculation of the output power were estimated. The results are listed in Table I.

The output energy, equation 68, normalized by the beam offset and the bunch charge is also known as the loss factor. This value charecterizes the sensitivity of the system for a given geometry and material of the cavity. The loss factor for the BINP cavities was extracted from the measured data: The cavities were calibrated such that a beam offset x for a bunch with a charge q corresponded to a known voltage V_x at the output of the downconversion electronics. The loss factor was then given by

$$k_{\rm loss} = \left(\frac{V_x}{x}\right)^2\frac{\tau}{GZq^2}, \quad (69)$$

Parameter	TM_{010}	TM_{110}
Resonant frequency, GHz	4.4	6.4
Shunt impedance, Ω	106	1.24 @ 1 mm
Inernal quality factor	8390	9810
External quality factor	$\rightarrow \infty$	25970
$P_{\rm out}$, 8 mm long bunch, $W\ mm^{-2}\ C^{-2}$	-	$6.12{\cdot}10^{16}$
$W_{\rm out}$ over decay time τ, $J\ mm^{-2}\ C^{-2}$	-	$1.23{\cdot}10^{9}$

TABLE I: Simulated parameters of the BINP BPMs

where G was the gain of the electronics and Z was the coaxial line impedance – 50 Ω in our case.

The calculation of the loss factor included only signals caused by the position of the beam in the cavity, and excluded signals from any tilt that the beam may have had. This also removed a feature in which the loss factor could appear to tend towards infinity at small offsets; the residual signal from the beam tilt would be divided by zero position. The position signal was proportional to the amplitude of the rotated in-phase component of the waveform. As the magnitude of the signal remained constant under this rotation, the voltage due to the beam position was related to the total signal by

$$V_x = \frac{I\,\cos\Theta + Q\,\sin\Theta}{\sqrt{(I^2+Q^2)}}\,V_{\rm RMS}. \qquad (70)$$

The loss factor was normalised by the charge of each bunch as determined by the amplitude of the monopole mode signal in the reference cavity. This was calibrated from the ATF bunch charge data included in runs from 1st-3rd June. (As the ATF current monitor data was not thought to be synchronised with the BPMs' data, the average amplitude over each 100 pulses was used.)

The gain in each channel was measured by feeding a local oscillator signal of a well known level into the electronics in place of the BPM output. The frequency of the signal was adjusted to match that of the cavity, in order to pass correctly through the filters and mixers. Given a power input of −76 dBm, the amplitude of the digitised signal was measured to determine the gain. As the power meter could not measure a value this low, the power was measured at a higher value, and reduced by a known amount using attenuators before being passed to the electronics. Results are shown in Table III.

The resulting loss factors for all 6 BPM channels are shown in Fig 38 and Table II. The results were close to $1.23 \cdot 10^9\ J\,C^{-2}\,mm^{-2}$ predicted by the theory (another estimation done by Zenghai Li of SLAC predicted $1.37 \cdot 10^{10}\ J\,C^{-2}\,mm^{-2}$) but some differed by a factor of 3 from the prediction. This could be explained by a shorter real length of the bunch than the 8 mm used for the estimations.

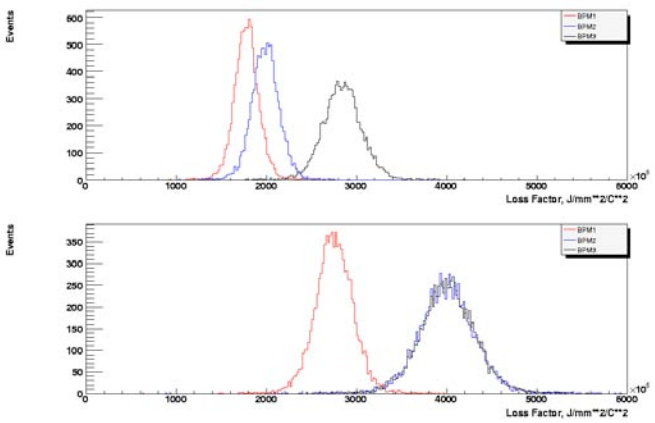

FIG. 38: Measured loss factors in the x (top) and y (bottom) directions from the data measured on 27/05/05. See Table II for explicit values.

B. Noise in the system

Two sources of noise were found to be limiting the achiveable BPM resolution, thermal/electronic noise and phase noise. Both were analysed and measured allowing their affect on the BPM resolution to be predicted and improvements proposed.

1. *Thermal and Electronic Noise Figure*

The signal processing electronics both amplified and contributed to the thermal noise present in the output of the BPMs. This noise could be seen in the recorded waveforms as random voltage variations around the pedestal value, as shown in Figure 39, top plot. The power spectrum of this noise, shown in Figure 39, bottom plot, was found to be flat with an increase over a 20 MHz bandwidth around the final mixdown frequency. This corresponded to the tightest bandpass filter present in the signal processing electronics.

The thermal noise power P of a system is given by

$$P \;=\; kT\Delta f \qquad (71)$$

where k is Boltzmann's constant, T is the operating temperature, and Δf is the noise bandwidth. Assuming an operating temperature of 293 K and a bandwidth of 20 MHz (defined by the tightest filter in the system) gave a thermal noise power at the BPM output of −100.9 dBm.

		1	2	3
BINP	x	1.78	1.99	2.84
$x10^9\ J\,C^{-2}\,mm^{-2}$	y	2.75	4.00	4.01

TABLE II: Measured loss factors for the BINP cavities.

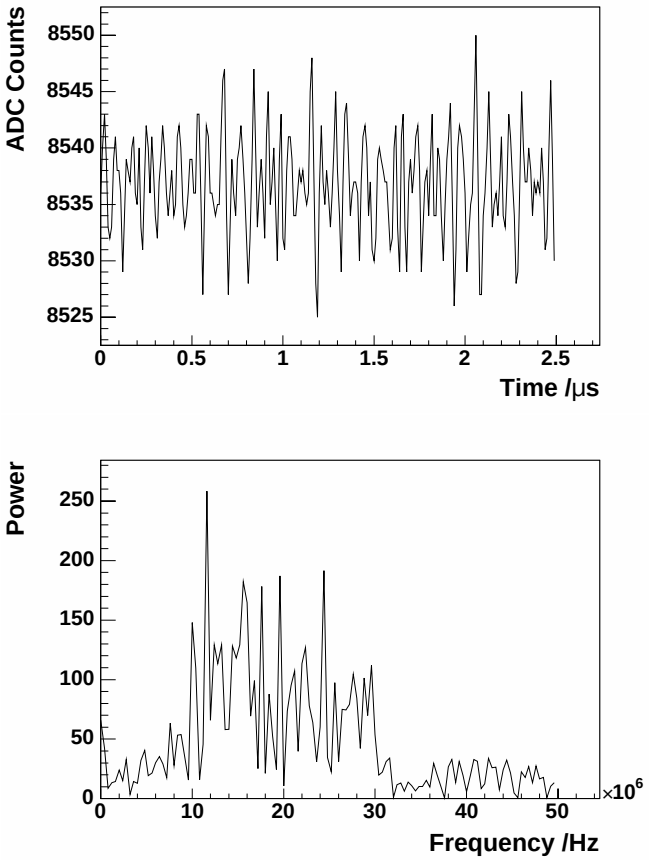

FIG. 39: Plots showing the noise at the digitiser without any signal (top) and the Fast Fourier Transform of that noise (bottom).

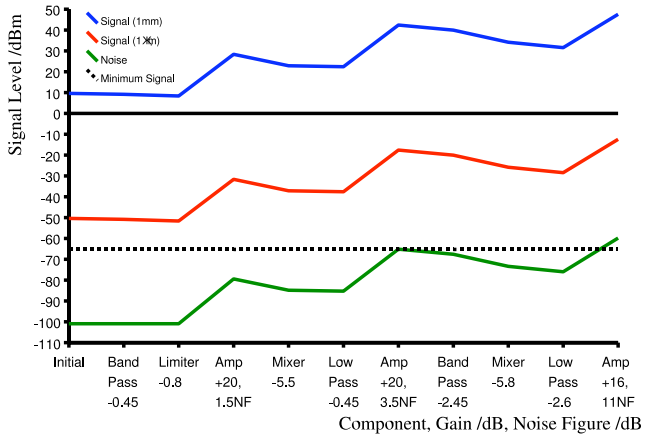

FIG. 40: Graph indicating the theoretical signal level at each component of the electronics.

Channel	Gain, dB	σ of ADC counts	Noise Figure, dB	Phase Noise, mrad
Reference	43.2	4.7	5.9	2.3
BPM 1, x	43.1	3.8	4.1	2.7
BPM 1, y	43.4	4.2	4.7	2.6
BPM 2, x	43.6	3.8	3.6	2.5
BPM 2, y	42.8	3.8	4.4	2.4
BPM 3, x	43.3	4.5	5.4	2.2
BPM 3, y	44.9	4.1	3.0	3.1

TABLE III: Table showing the measured gains, amplitude noise and noise figures for each BPM channel.

Introducing this value – along with the cavity parameters from the GdfidL simulation – into equation 63 and solving it against the shunt impedance resulted in a resolution for the BPM system of about 1 nm, assuming ideal electronics.

The additional noise introduced into the system by the electronics could be predicted using the specifications of the particular components and applying Friis's formula for noise in a cascaded system [11]:

$$F = F_1 + \frac{F_2 - 1}{G_1} + \frac{F_3 - 1}{G_1\, G_2} + ... \qquad (72)$$

where F was the total noise factor of the circuit, F_N was the noise factor of component N and G_N was the gain of component N (all dimensionless ratios). The theoretical signal diagram is shown in Figure 40. Using Friis's formula, the theoretical gain of each separate signal channel was computed to be 39.0 dB with a noise figure of 3.1 dB.

The actual gain for each channel was measured by passing a known signal through the electronics and recording the output power (see Table III). The noise figures for each channel were measured by analyzing waveforms that contained only thermal noise – no signal from a bunch transiting the cavity was present: The pedestal value was found by taking the mean of all 250 sample values, and the voltage noise was taken as the standard deviation. The voltage noise over 50 pulses (measured in ADC counts) was then averaged and converted to a power P using the formula

$$P = 10\,\mathrm{dBm} \times \log_{10}\left(\frac{\mathrm{V}^2/\mathrm{Z}}{1\,\mathrm{mW}}\right) \qquad (73)$$

where V was the voltage measured at the ADCs and Z was the impedance (50 Ω). By combining this with the measured gains and the theoretical level of thermal noise, the noise figures for each channel were found. These are listed in Table III.

2. *Phase noise figure*

Contributions to the phase noise came from both the local oscillators used down-convert the signal as well as from the digitizer. To quantify the level of this noise

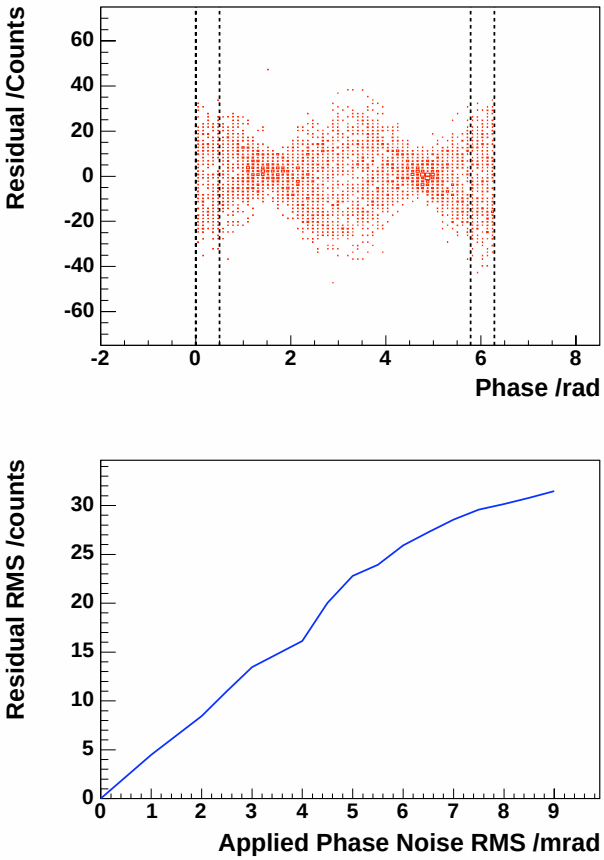

FIG. 41: Plot showing the variation of residual versus phase of the test tone.

present, a tone at the BPM frequency was applied to the electronics and the resultant waveforms recorded at the ADCs were fitted with a sine function

$$V = A\sin(\omega t + \varphi). \quad (74)$$

The residual between this fit and the data was plotted against phase $(\omega t + \varphi)$ between 0 and 2π. A "bow-tie" effect, which can be seen in Figure 41, was interpreted as being due to phase noise in the system. At points where the slope of the sine wave was large ($\varphi = 0,\ \pi,\ 2\pi$), the residual was also large; at points were the slope of the sine wave was small ($\varphi = \pi/2,\ 3\pi/2$), the residual was small. This was as expected since the residual due to the phase noise was predicted to be proportional to the gradient of the waveform.

To estimate the phase noise present in each channel, simulated sine waves

$$V = A\sin(\omega t + \varphi). \quad (75)$$

were generated and added to the thermal noise data (i.e., no signal present from a bunch transiting the cavity) used in Section IX B 1. The amplitude of the generated wave was set at the same value as that from the test-tone data. Phase noise was applied to these simulated pulses by adding a random gaussian component to the phase,

$$V = A\sin(\omega t + \varphi + \sigma_\varphi). \quad (76)$$

Performing the same sine wave fit to these generated pulses as was carried out on the data produced similar "bow-tie" style plots as seen in Figure 41, top plot. The magnitude of the bow-tie effect was found to be proportional to the phase noise applied, disappearing completely if the phase nosie was removed altogether. To quantify the size of the bow-tie, the standard deviation of the residual for phase between $0 \rightarrow 0.5$ and $2\pi - 0.5 \rightarrow 2\pi$ was measured. By generating bow-tie plots for a range of values of phase noise, the correlation between phase noise and bow-tie size could be plotted, as shown in Figure 41, bottom plot. Using this relation, the size of the bow-tie in the data could be measured and the corresponding amount of phase noise found. This procedure was performed for all the channels and the amount of phase noise found in each is shown in Table III.

C. Predicting the Resolution

To predict the achievable resolution in a specific BPM channel with the level of noise as measured in Section IX B, the response of the fitting algorithm needed to be systematically analysed to determine the uncertainties in the fitted parameters. To accomplish this, simulated BPM responses to ATF extractions – modeled as exponentially decaying sine waves (see equation 7) – were generated for a range of amplitudes. The frequencies and decay constants as measured from data were used for the appropriate channel being simulated. The parameter t_0 was fixed. If a particular sample value was greater than the ADC maximum (16384 counts) or less than the ADC minimum (0 counts), the sample value was fixed at these limits, thus modeling the saturation seen in actual data. Phase and Thermal noise appropriate to each particular channel were also applied.

The simulated pulses were generated with amplitudes ranging between 0 and 25000 counts and then analysed using the fitting algorithm in the same way as the actual data. For each amplitude value, fifty simulated BPM signals were generated and analyzed, and the standard deviation of the fitted amplitude and phase were found. The dependence of these fitted values on the amplitude of the BPM signal is shown in Figures 42 and 43. A fourth order polynomial was used to fit to the amplitude curve in Figures 42 and an inverse dependence was used for the phase curve in Figure 43. Using these parameterizations, the uncertainty on the fitted amplitude and phase could be predicted given the amplitude of the waveform.

The position of the beam was calculated by normalizing both the amplitude and phase by the reference cavity and then performing an additional rotation given by the

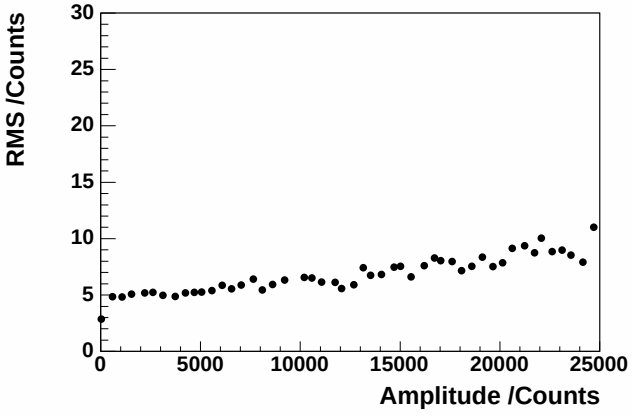

FIG. 42: Plot showing the variation with amplitude of the amplitude RMS.

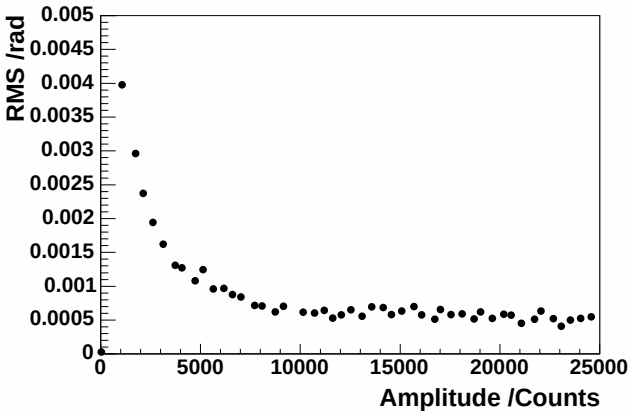

FIG. 43: Plot showing the variation with amplitude of the phase RMS.

IQ-phase, as ordinarily (described in Section IV, equations 8-11). This could be be rewritten in the following form:

$$y_i = s_i \frac{A_i}{A_{\mathrm{Ref}}} \cos(\varphi_i - \varphi_{\mathrm{Ref}} - \Theta_i) \qquad (77)$$

where y was the position, s the scale factor, A was the waveform amplitude, A_{Ref} was the reference amplitude, φ was the phase of the waveform, φ_{Ref} was the reference phase, and Θ was the rotation relating position and tilt to I and Q (see equation 10). Assuming the uncertainties were uncorrelated, the uncertainty on the position was given by:

$$\sigma_{y_i}^2 = \left(\sigma_{s_i}\frac{\partial y_i}{\partial s_i}\right)^2 + \left(\sigma_{A_i}\frac{\partial y_i}{\partial A_i}\right)^2 + \left(\sigma_{A_{\mathrm{Ref}}}\frac{\partial y_i}{\partial A_{\mathrm{Ref}}}\right)^2 + \left(\sigma_{\varphi_i}\frac{\partial y_i}{\partial \varphi_i}\right)^2 + \left(\sigma_{\varphi_{\mathrm{Ref}}}\frac{\partial y_i}{\partial \varphi_{\mathrm{Ref}}}\right)^2 + \left(\sigma_{\Theta_i}\frac{\partial y_i}{\partial \Theta_i}\right)^2 \qquad (78)$$

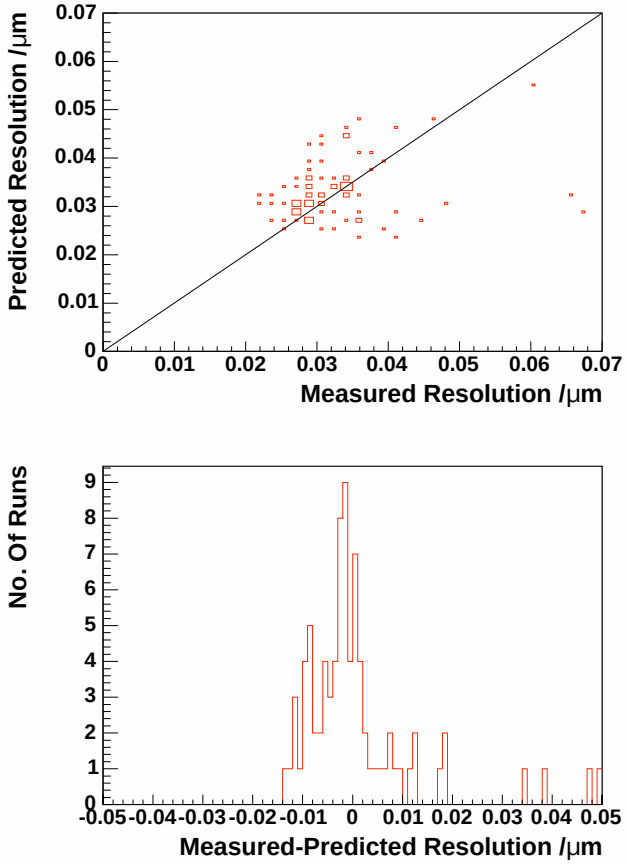

FIG. 44: Plots showing the predicted vs. measured resolutions (top) and the difference between the predicted resolution and the measured resolution (bottom).

The uncertainties associated with the determination of the IQ-phase Θ_i and scale factor s_i were assumed to be negligable, i.e. $\sigma_{s_i} = \sigma_{\Theta_i} \approx 0$.

The amplitude A_i and phase $(\varphi_i - \varphi_{\mathrm{Ref}} - \Theta)$ were computed by taking the mean of the set of BPM signals under study, and the resolution of a single BPM channel in isolation was computed using equation 78. The overall resolution was then calculated by summing in quadrature the resolutions for each individual channel, using the weights given by the result of the singular value decomposition (see Section VI, equation 38). This gave a prediction that could be directly compared to the measured resolution obtained using the method described in Section VI.

Using data taken on 27 May 2005 from a 2 hour run, the resolution was predicted for each set of 100 recorded ATF extractions. Each result was then compared with the measured resolution for the same 100 ATF extraction dataset. Significant correlation was found between the two (see Figure 44) indicating that the level of noise measured in Section IX B limits the achievable resolution of the BPMs.

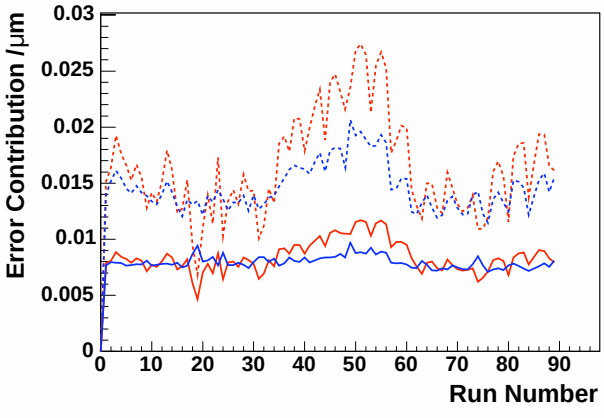

FIG. 45: Plots showing the relative contributions to the BPM resolution between the Amplitude (red) and Phase (blue) determination for the reference (dashed) and directional (solid) channels.

X. PROPOSED CHANGES TO IMPROVE RESOLUTION

Using the methods described in Section IX C, the dominant contributions to the resolution limit could be found and from this, possible ways to improve this limit. Initially, the resolution prediction (as given by equation 78) was broken down into four contributions, these being uncertainties in the determination of the amplitude and phase for both the reference cavity and the channel under study (y_2 was used throughout). The four contributions to the uncertainty are plotted in Figure 45, and show that the dominant contribution arises from the uncertainty in the determination of the reference cavity parameters. This was primarily as a result of the large weighting factor given by the y amplitude.

Additional information was provided by splitting up each contribution into the respective components due to phase and thermal noise, as shown in Figure 46. In the amplitude range of the y channel under study – typically between 10000 and 20000 ADC counts, neither source of noise was particularly dominant. However, for the amplitude range of the reference cavity – typically 3000 - 4000 counts, the thermal noise was dominant; particularly noteworthy was its contribution to the uncertainty in the waveform's phase φ_{Ref} as shown in Figure 46, bottom plot.

After examination of this data, the following proposals are suggested to try to improve the resolution of the BPMs:

- Increasing the gain in the electronics associated with the reference cavity would improve its signal to noise ratio.

- Reducing the attenuation between the reference cavity and its electronics would also improve the signal to noise ratio.

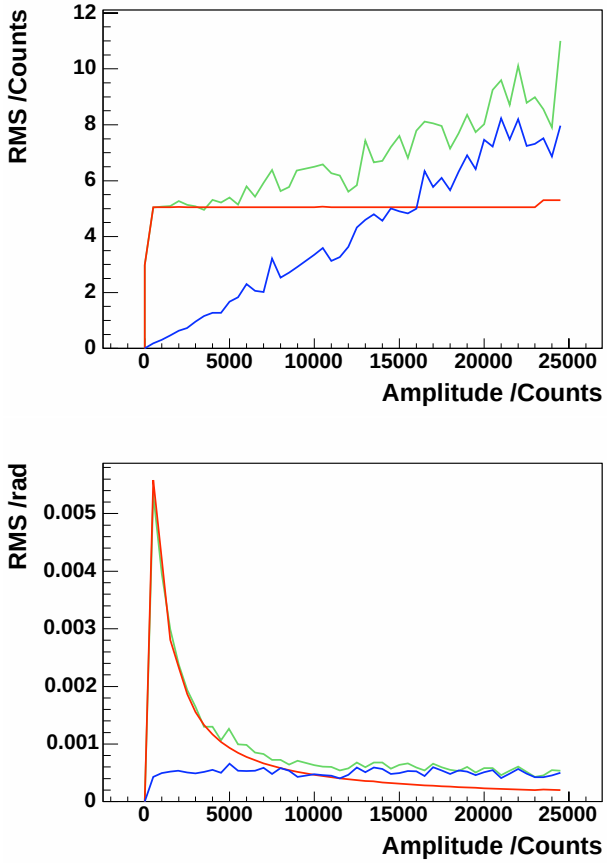

FIG. 46: Plots showing the contributions to the overall error in Amplitude determination (top) and Phase determination (bottom) from Thermal noise (red) and Phase Noise (blue) for the $y2$ channel. Similar plots were found for the reference channel.

- Better centering the BPMs on the beam in all directions will reduce the effects of the reference cavity noise. Because the term $\partial y_i/\partial A_{\mathrm{Ref}}$ in equation 78 is proportional to the y amplitude, reducing this weighting factor should improve the resolution. It should be possible to reduce the y amplitude to ~ 5000 counts giving an improvement in resolution of $\sim 30\%$.

- Increasing the bunch charge should increase the reference cavity amplitude and should decrease the error in the parameter determination for it. The minimum error possible from the reference cavity is at ~ 5000 counts. This should also improve the signal to noise in the directional cavities as well.

- Addressing the local oscillators used in the down-mix of the BPM signals may go some way in reducing the phase noise.

- Shortening the bunch length will increase the loss factor and improve the resolution.

XI. CONCLUSIONS

To date, we have demonstrated a resolution of less than 20 nm over short time periods spanning a minute or two, and a resolution of only slightly more than 20 nm over time periods spanning as long as half an hour. This resolution attains using two different analysis algorithms and is repeatable across multiple data sets.

Our plans for trying to improve on this resolution begin with improving the signal to noise in, most notably, the reference cavity, which may be accomplished by a combination of increasing the reference cavity gain and reducing the attenuation. Furthermore, better centering the directional BPMs on the beam will decrease the effects of this reference cavity noise on the resolution. Increasing the bunch charge will also have a positive effect on resolution by improving the signal to noise ratio in both the directional cavities as well as the reference cavity. Our resolution is also being limited by phase noise, and the local oscillators used in the down-mix of the BPM signals will have to be addressed. A higher loss factor (i.e. more power coupled out) would also go some length in improving the resolution, and one method for achieving this would be to shorten the bunches. The original 1 nm theoretical resolution prediction was based on the loss factor for a δ-function bunch, but the reality at ATF is a bunch which is approximately 1 cm long. There is clearly still room for improvement.

[1] Draft letter of intent for the LINX test facility at SLAC. http://www-project.slac.stanford.edu/lc/linx/papers/LINX_07-15-01.pdf.

[2] Tor Raubenheimer. Discussion of nanobeam summaries and areas for future collaboration. In *Web Proceedings of the 26th Advanced ICFA Beam Dynamics Workshop on Nanometre-Size Colliding Beams (Nanobeam 2002)*, Lausanne, Switzerland, 2002. ICFA. http://icfa-nanobeam.web.cern.ch/icfa-nanobeam/slides/raubenheimer_Nanobeams_summary_09-02.pdf.

[3] Steve Smith. Private communication.

[4] Zenghai Li, Stephen R. Smith, Takashi Naito, and Jeffrey Rifkin. Cavity BPM with dipole-mode selective coupler. In *Proceedings of the 2003 Particle Accelerator Conference*, Portland, OR, 2003. IEEE.

[5] J. D. Jackson. *Classical Electrodynamics, Second Edition.* John Wiley and Sons, New York, 1975.

[6] Milton Abramowitz and Irene A. Stegun. *Handbook of Mathematical Functions.* Dover Publications, Inc., New York, 1965.

[7] V.Balakin et al. Discussion of nanobeam summaries and areas for future collaboration. http://www.vlepp.serpukhov.su/engl/bnl/bpm.html.

[8] David J. Jackson, Dong Su, and Fred J. Wickens. Internal alignment of the SLD vertex detector using a matrix singular value decomposition technique. *Nucl. Instrum. Meth.*, A491:351–365, 2002. SLAC-PUB-9092.

[9] Alexey Lyapin. *Strahllagemonitor fuer das TESLA-Energiespektrometer.* Dissertation, TU-Berlin, Berlin, 2003.

[10] The GdfidL electromagnetic field simulator. http://www.gdfidl.de.

[11] Devendra K. Misra. *Radio-Frequency and Microwave Communication Circuits, 2nd Ed.,.* John Wiley and Sons, New York, 2004.

[12] The latitude and longitude of the ATF were determined with a handheld GPS receiver. The earth's magnetic field and the rate of change of the field for that location for the date 11 March 2005 were then found on the website of the National Geophysical Data Center (NGDC) of the NOAA Satellite and Information Service: http://www.ngdc.noaa.gov/seg/geomag/jsp/struts/calcPointIGRF.

This work was performed under the auspices of the U.S. Department of Energy by University of California, Lawrence Livermore National Laboratory under contract No. W-7405-Eng-48.

ATF/ATF2 Cavity-BPMs

Y.Honda

2005/10/19

Abstract

Development studies of cavity BPM at the ATF was listed up in this talk.

1 Introduction

We have been testing (or planning to test) cavity BPMs in the extraction line of the ATF. Many of the cavity parameters, such as frequency, are naturally determined from the characteristics of the beam in the line. Experiments are underway with two types of existing cavity BPM. Other two types are newly designed for future uses in the ATF2 experiment.

2 Existing Cavity BPMs in ATF

Two sets of triplet BPM have been installed in the beam line. Although both system proved the position resolution better than 100 nm, there turned out to be some problems in the signal properties. We have learned a lot from these works and understood the BPMs well by now.

3 Status of ATF2 Q-magnet BPM development

In the ATF2 beam line, the main beam orbit monitor will consist of cavity BPMs attached on each quadrupole magnet. We have modified the designs of existing cavities for this application. The first prototype model has just completed.

4 Status of ATF2 IP-BPM development

In order to measure the beam fluctuation at the focal point of ATF2 beam line, we have designed a special cavity BPM. The electrical design work has just completed. We are going to make a prototype model soon.

5 Summary

We listed up works related to cavity BPM development at ATF.

RECENT PROGRESS DESIGNING COMPACT SUPERCONDUCTING FINAL FOCUS MAGNETS FOR THE ILC*

B. Parker#, BNL, Upton, NY 11790, U.S.A.

Abstract

QD0, the final focus (FF) magnet closest to the interaction point (IP) for the ILC 20 mr crossing angle layout, must provide strong focusing yet be adjustable to accommodate collision energy changes for energy scans and low energy calibration running. But it must be compact to allow disrupted beam and Beamstrahlung coming from the IP to pass outside into an independent instrumented beam line to a high-power beam absorber. The QD0 design builds upon BNL experience making direct wind superconducting magnets. We present test results for a QD0 magnetic test prototype and introduce a new shielded magnet design, to replace the previous side-by-side design concept, that greatly simplifies the field correction scheme and holds promise of working for crossing angles as small as 14 mr.

PROGRESS BEFORE SNOWMASS'05

An initial compact superconducting magnet design for a 20 mr crossing angle configuration for the NLC FF was developed shortly after Snowmass'02[1-4]. The design drew upon direct wind magnet experience the HERA-II and BEPC-II Luminosity upgrades[5,6]. Field strengths of the compact superconducting magnets are adjustable to accommodate energy and optics changes and the magnets fit within the original NLC permanent magnet solution space envelope.

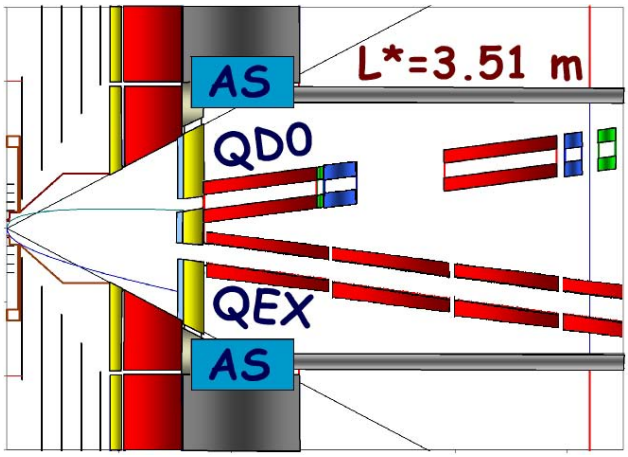

Figure 1. Plan View Schematic of Side-by-Side IR Layout (Obsolete). Disrupted beam from IP goes outside QD0 into the extraction line.

*This manuscript has been authored by Brookhaven Science Associates, LLC under Contract No. DE-AC02-98CH1-886 with the U.S. Department of Energy. The United States Government retains, and the publisher, by accepting article for publication, acknowledges, a world-wide license to publish or reproduce published form of this manuscript, or allow others to do so, for the United states Government purposes.

#parker@bnl.gov

The initial direct wind design was limited in that the inner coil layers used single-strand superconducting wire rather than seven-strand round cable used for the main HERA-II and BEPC-II magnets since we hade never wound such small bend radius patterns before. with But seven-strand cable has an advantage that less dead space is taken up by insulation and other materials so a higher effective engineering current density is possible with cable than single-strand coil windings.

Thanks to recent direct wind research and development, we now wind much tighter bend radius coil patterns using seven-strand cable[7,8]. This advance, along with a change from 4.5°K supercritical liquid He to 1.9°K superfluid He-II cooling, makes the side-by-side magnet scheme, shown in Figures 1 and 2 viable. Here the incoming and extraction beamline magnets start at the same L* and the required superconducting coil thicknesses are thin enough that the cold masses can be housed in separate cryostats. While starting the extraction beam line close to the IP is helpful in maximizing extraction line acceptance, the main benefit of the side-by-side configuration is for the extraction line where it permits local compensation of the external field generated outside QD0.

We wound and tested a short QD0 prototype, QT, in order to demonstrate that we could meet the ILC QD0

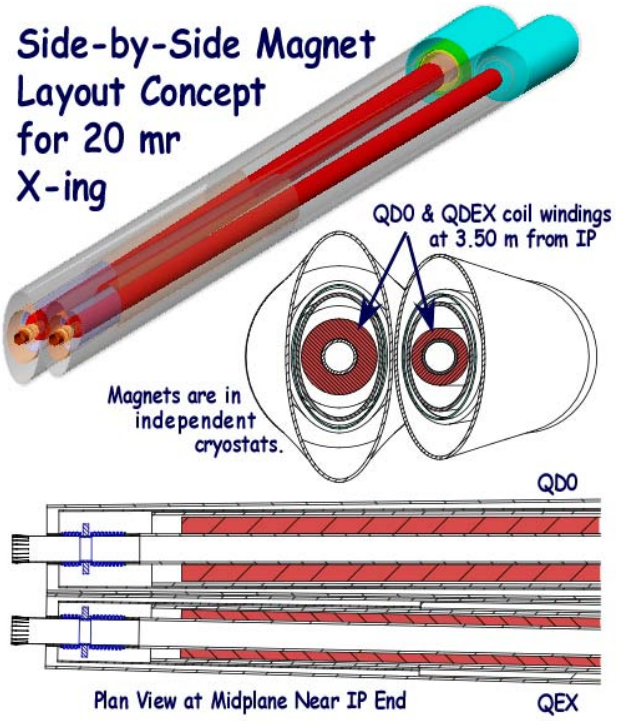

Figure 2. The Side-by-Side Magnet Concept for 20 mr Crossing Angle (Obsolete). Same L for extraction line enables partial compensation of QD0 external field.*

Figure 3. Winding the Short QD0 Magnetic Test Prototype, QT, and CAD Model of Final Six Layer Quadrupole Coil Pattern. QT production is complete along with warm field harmonic measurements. Quench testing was performed in an existing BNL dewar at 4.3 to 3.0° K temperature, 1 to 10 A/s ramp rates and solenoidal background fields up to 6 T.

design requirements of 20 mm clear full aperture and 140 T/m operating gradient in the presence of a 3 T solenoidal background field. Figure 3 shows the start of QT coil winding along with full final coil structure. QT was produced in three winding steps as Serpentine style dual-layer coil sets A, B and C, for a total of six cable layers[8]. Before winding was complete warm magnetic measurements were performed and the results were used to make minor pattern corrections to the final coil set C.

The chosen 380 mm QT coil length is a compromise between it being long enough to accurately measure central "body" harmonics separately from the field harmonic contribution of each end and it being short enough to fit inside an existing laboratory dewar test setup with an 8 T solenoid. We powered QT in the presence of a background solenoidal field to simulate the impact of the detector solenoid on QD0 performance both in terms of total field on the conductor and the extra internal coil forces due to field interactions at the coil ends.

QT field measurement results are summarized in Table 1. During QT production we learned to wind even tighter bend radius patterns which let us fit more turns. We were also able to slightly decrease interlayer radial spacing for a net 7% increase in transfer function.

Table 1. QT Measured Integral Field Quality. Harmonics are expressed in "units," a part in ten-thousand, at a reference radius of 5 mm. Numbering convention: N=3 is sextupole. Values less than 0.01 omitted. ILC QD0 design goal has all harmonics less than 10 units at this radius.

Harmonic Number	Coils A+B+C	
	Normal	Skew
T.F. (T/m/kA)	210.7	--
3	0.19	0.43
4	-0.03	1.49
5	-0.20	0.18
6	0.17	0.09
10	-0.26	0.01

Even though ILC field uniformity requirements for QD0 are fairly loose, 0.1% at 5 mm reference radius which corresponds to 10 units in Table 1, the QT coil radius is five times smaller than that of HERA-II for which we had experience. Thus we were interested to see what level of uniformity could reasonably be achieved by adjusting the winding pattern of the last coil set.

Based upon warm measurements done after coil set B was wound, without final tuning we would have expected to see some harmonics as large as 3 units. But with the exception of the skew-octupole, the correction made with coil set C brought all integral harmonics to well below 1 unit; for the skew-octupole a wrong sign correction was input and the harmonic error that should have ended up below 1 unit instead increased to 1.5 units. As expected with Serpentine style coil patterns, the measured integral harmonics tracked the central "body harmonics" very well[9]. Since QT is one-sixth QD0's length, it has greater end harmonic sensitivity than QD0. So we anticipate no real difficulty in producing FF magnets that meet the 10 unit ILC QD0 field requirements.

Figures 5 and 6 show QT being prepared for cold

Figure 5. Completed QT Prototype Being Prepared for Vertical Cold Testing. During production we learned to decrease turn spacing and bend radius for a 7% transfer function gain.

testing by adding voltage tap and spot heater diagnostics and attaching QT's leads to current lead feedthroughs. QT was tested with a background field solenoid housed inside in a small laboratory test dewar. The solenoidal field profile is plotted in Figure 6. Testing was performed for various temperature (4.2 to 3.0 ° K), ramp rate (1 to 10 A/s) and background field (0 to 6 T) combinations.

QT reached conductor short sample after a single training quench. At 10 A/s ramp rate QT quenched close to 85% (six-sevenths) of short sample due to well known lack of current sharing with center conductor. The 6-around-1 cable used for QT is not intended for fast ramping since the central conductor "drops out" due to its not being transposed with the outer 6 conductors. Slow ramp rate quench results are summarized in Table 2. QD0 is specified to reach 140 T/m in a 3 T background field when cooled to 1.9 °K and QT exceeded this gradient by 13% at 3 T while at an elevated operating temperature of 4.3 °K. QT almost reached operating gradient in a 4 T, background field at 4.22 °K.

To test at lower temperature we lowered the helium dewar pressure via vacuum pumping. Unfortunately such pumping causes the helium level inside the dewar to drop significantly. Because QT had to be "long" to make accurate body harmonic measurements (enough straight section length to get harmonics of the central 254 mm via subtraction of rotating coil readings at two positions) the helium level fell below the current leads around 2.5 °K. The lowest test temperature we took quench data with simple pumping setup, i.e. no λ-plate, was 3.0 °K. In order to avoid running at excessively high current we increased background field to 6 T. Such an increased background field still gives large Lorentz forces in the coil ends but lets us remain below dangerous current

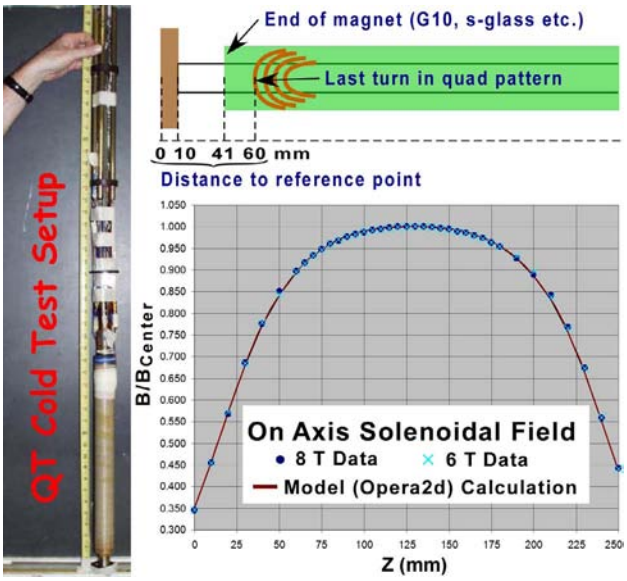

Figure 6. Quench Testing with an Existing Small Dewar and 8 T Solenoid. Solenoid field distribution was modeled and compared to measured (on-axis) data. Off-axis behavior (Bz, Br) was then calculated to determine high field points in the QT prototype during testing.

Table 2. Summary of Slow Ramp Quench Results (i.e. less than 10 A/s where current sharing of central conductor is not a significant issue). Note: ILC QD0 operational target is 140 T/m gradient in presence of 3 T solenoidal background field while cooled with superfluid He-II @ 1.9°K. These data scale to 232 T/m under proposed ILC operating conditions for operation at 60% short sample.

Background Solenoid (T)	Temp (°K)	Gradient (T/m)
3	4.30	158
4	4.22	139
5	4.22	134
6	3.00	137

levels where quench protection is an issue. At 3.0 °K and 6 T background, QT reached 137 T/m. When this result is scaled to 1.9 °K and 3 T background field QT should reach 232 T/m (1100 A). So the nominal working point is at 60% of predicted short sample. In future work we plan to test a shorter ILC prototype that should enable data acquisition at lower temperature with the same test setup.

DEVELOPMENTS AFTER SNOWMASS'05

The proceeding discussion summarizes the compact superconducting magnet design status just before the Snowmass'05 meeting. During Snowmass many issues were discussed and in particular the detector groups wanted to know what the minimum crossing angle is for which the compact superconducting could still be used to retain the main advantages of the 20 mr layout, i.e. truly independent incoming and extraction beamlines for which upstream and downstream beam diagnostic sections could be provided. Referring to the side-by-side configuration shown in Figure 2, one approach to reducing the beamline separation is to eliminate space for the double cryostat and put both cold masses in a common cryostat. But the mutual external fields present at both beamlines increases very rapidly with decreasing separation. This forces us to use stronger correction coil windings which then generate their own stronger external fields which have to be compensated. The "cross talk" between the two beamlines increases dramatically with reduced separation and optimization of the correction/compensation scheme becomes more difficult.

It is interesting to consider what occurs when the first extraction line magnet, labeled QDEX in Figure 2, is replaced by a bare beam pipe. The external field generated by QDEX is gone but so is the opportunity for local compensation of QD0's external field unless we add an active shield coil.

As outlined in Figure 7 and shown implemented, for realistic QD0 coil parameters in Figure 8, active shielding can have minimal impact on QD0 performance when the average inner and outer coil radii, a_1 and a_2, are

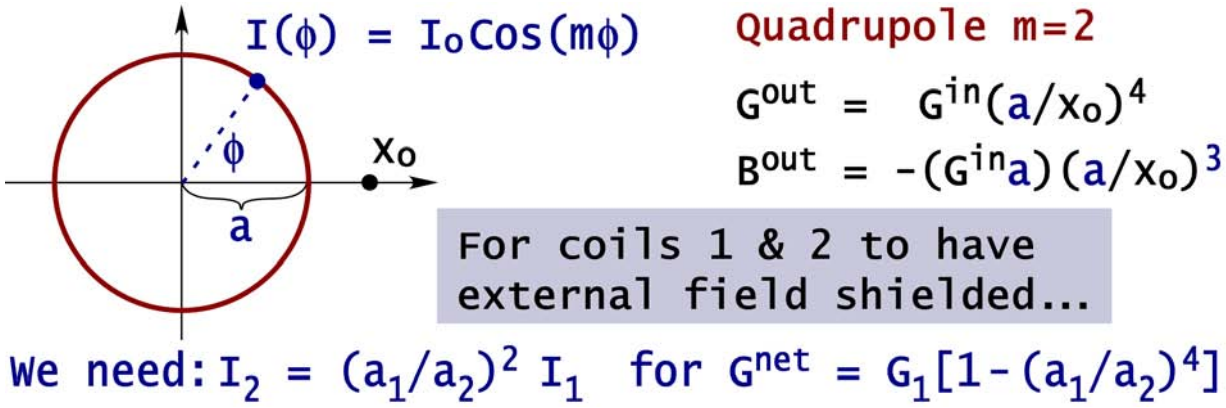

Figure 7. Criteria for Field Cancellation at Point X_o Outside Two Concentric Nested Current Distributions. The case of quadrupole external field shielding is emphasized. For a pure quadrupole its external field can be eliminated while retaining a significant net inside gradient, G^{net}, thanks to the forth power scaling with average coil radius.

sufficiently different. Our proposed QD0 active shield design brings only a 5% increase in excitation current.

With reduced external field we can place the extraction beam pipe close to the outer shield. In Figure 9 we plot the external field seen by extracted beam with this new solution as a function of distance to the IP, Z_{IP}, for QD0 L* of 3.51 m but now done for a 14 mr crossing angle. Near the middle of QD0 the cancellation is nearly perfect while at each end there is a small residual field. The 2D approximation outlined above breaks down near the coil ends and the IP end separation is smallest yielding the largest residual field there.

We manufactured a shield coil for the QT prototype with the coil layout shown in Figure 10 that could just fit inside our test solenoid in order to test the active shielding

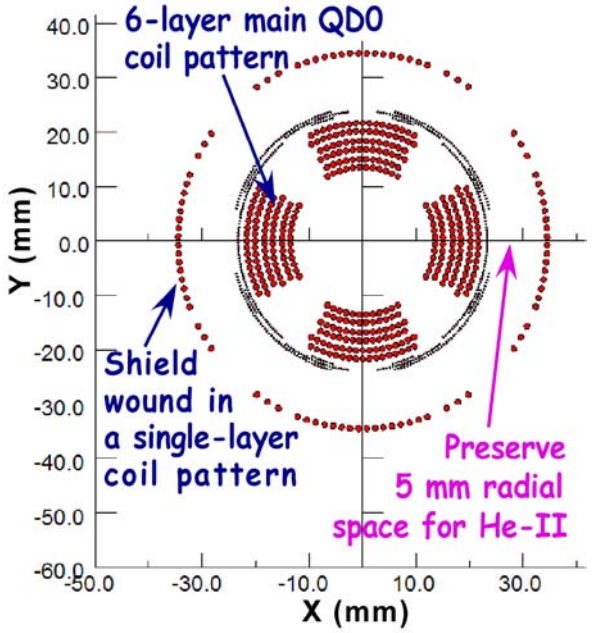

Figure 8. Actively Shielded QD0 Design Compatible with 14 mr Crossing Angle. The inner and outer coils are wound on separate support tubes (not shown) with 5 mm space left inside the outer support tube for He-II cooling. Running both coils at ≈700 A gives 148 T/m from the inner coil and -8 T/m from outer for 140 T/m net gradient.

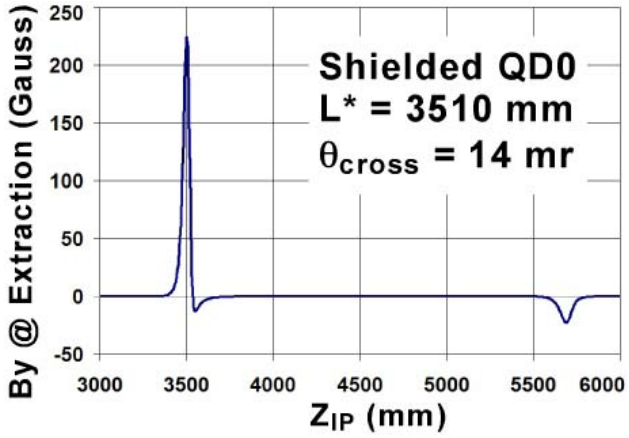

Figure 9. Field Seen Outside an Actively Shielded QD0 Magnet at Extraction Beamline.

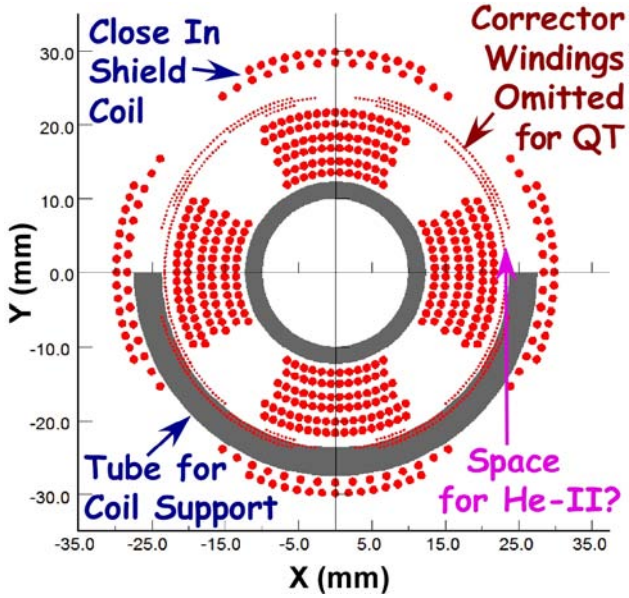

Figure 10. Shield Coil Design for QT, the QD0 Magnetic Prototype. For 748 A, G_{in} is 157.5 T/m while G_{outer} is -17.5 T/m for net 140 T/m gradient. There is limited space for He-II between QD0 and the support tube that is produced by omitting the QD0 correction coil windings.

Figure 11. Production of QT Two-Layer Active Shield.

concept. Because this QT shield coil is pulled closer in, a greater number of shield turns are required.

Both layers of the QT shield coil are pictured during winding in Figure 11 and assembled with the original QT prototype in Figure 12. Due to the short time span between the end of Snowmass'05 and the present Nanobeam'05 conference, we produced the shield coil support tube using existing stock with wall thickness about 1 mm thicker than desired. The correction windings shown in Figure 10 were omitted in order to provide some space for helium cooling and not to delay production.

This QT active shield coil illustrates issues that arise with bringing the shield closer in to QD0 than the amount budgeted in Figure 8 (i.e. if one tries to reduce the crossing angle below 14 mr). An obvious impact of pulling the closer in similar to the QT shield design is that the current now has to rise to 748 A in order to reach 140 T/m which is a 13% increase compared to a bare QD0. The associated reduction in operating margin is troubling but is not the most important impact.

In Figure 10 we see that the space available for direct He-II cooling of such an inner coil package is quite tight. While superfluid helium can penetrate small gaps, the amount of heat that can be removed through a long cooling section depends critically on available space. Since QD0's beam related energy deposition occurs primarily on its innermost structure, the annular space available for He-II in contact with the inner coils determines the temperature profile along QD0's length.

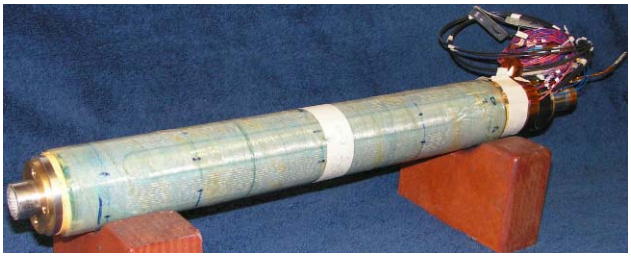

Figure 12. QT Magnet Installed Inside its Two-Layer Active Shield.

The outer radius shown in Figure 8 of the 14 mr crossing angle compatible shield coil is only a few millimeters larger than that shown for QT in Figure 10 but includes 5 mm space inner helium cooling while QT has essentially none. Some of the outer radial space that could have been gained by pulling the QT shield closer in was instead lost due to doubling the shield coil thickness.

However even with its tight design space constraints, the shield coil was quite successful in reducing the QT external field. Magnetic measurements made with a rotating coil parallel to the QT axis and almost touching the shield coil outer surface show that the integrated external field is reduced by a factor of 22 when the QT and shield coils are powered in series. This result gives us confidence that active shielding should work very well for the proposed 14 mr crossing angle shield configuration. The field at the shield coil is already smaller and the cancellation is not as delicate as for QT. For QD0 we foresee providing a small trim current across the shield coil for fine tuning capability, but our QT active shielding test result suggests that this precaution may not really be necessary. We will make further tests when a full length actively shielded QD0 prototype is finally produced.

Figure 13 shows one possible realization of an actively shielded QD0 for 14 mr crossing with a tapered extraction beam pipe almost touching the shield coil at the IP end. Note that here the QD0 coils and the extraction line beam pipe share a common He-II volume in a cold mass and are supported in a single cryostat. Important features, such as the IP end warm-to-cold beam pipe transition and connection to a helium supply line with control valves and current leads, are shown but may be modified as the design matures.

Preliminary designs have been worked out for all the compact superconducting magnets needed to implement the 14 mr crossing angle IR. A schematic representation of the compact superconducting magnets on one side of the IR for 14 mr crossing angle and L* of 3.51 m is shown in Figure 14. Note that with the proposed scheme the first extraction line magnet, QDEX1A, starts past QD0 at 6 m. The actively shielded coil layout for QDEX1A is shown in Figure 15. It is important that the stray field from QDEX1A seen at the incoming beam

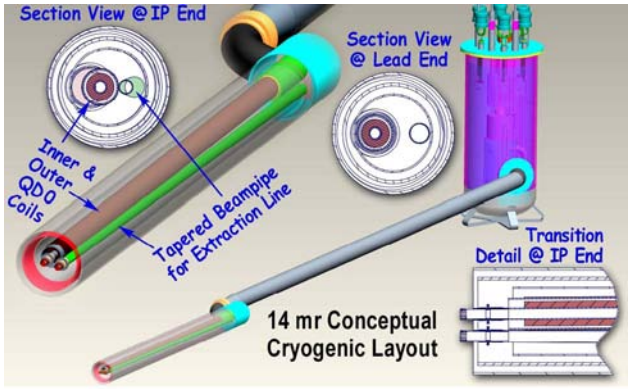

Figure 13. CAD Schematic of QD0 Cryogenic Assembly. Tapered extraction line beam pipe is along side QD0 and shares a common He-II volume inside a common cryostat.

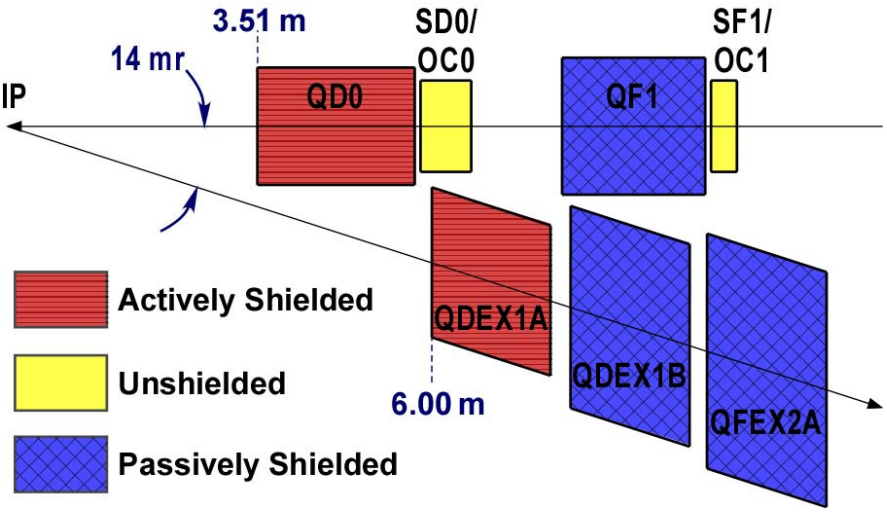

Figure 14. Schematic Representation of the Compact Superconducting Magnets on One Side of the IP (Plan View). Note that distances are compressed along the incoming beamline and this has the effect of distorting the apparent shape of magnets that are not parallel to this direction. Sizes shown for the various magnet boxes are intended to give a comparative indication of the various magnets' sizes. Coding is as indicated: actively shielded (red with horizontal banding), unshielded (plain yellow) and passively shielded (blue hatched). Passive shielding is used for magnets well outside the detector solenoid where they have thin magnetic yokes that reduce their external fields. Unshielded magnets are either weak correction coils or have sufficiently high multipolarity that their external fields die off rapidly.

location be small since too large a field, even with a zero net integral, could cause too much synchrotron radiation and impact luminosity by spoiling the beam's emmitance. Fortunately even though QDEX1A has a larger average coil radius than QD0, so its fringe field ought to extend further out, it is weaker than QD0 and the beam separation is greater at QDEX1A, so residual stray field seen by the incoming beam, shown in Figure 16, is small.

With direct wind magnet production it is natural to co-wind different magnet coils in concentric layers (instead of longitudinal segmentation). For instance by making an octupole magnet, such as OC0, longer we can achieve its required integrated field strength with fewer coil layers and the resulting coil package is itself more efficient because the average coil radius is smaller. Thus we can combine the original space allocation for the SD0 sextupole with OC0 and co-wind them in the pattern shown in Figure 17.

The octupole, being the higher multipolarity, is most favorably wound first on the support tube since this dramatically reduces its field strength at the conductor inner surface. But then the sextupole radial start point goes outward and for a fixed number of coil layers the sextupole ends up being weaker. However, since the sextupole is now longer, the required integrated field strength is still attained without increasing the excitation

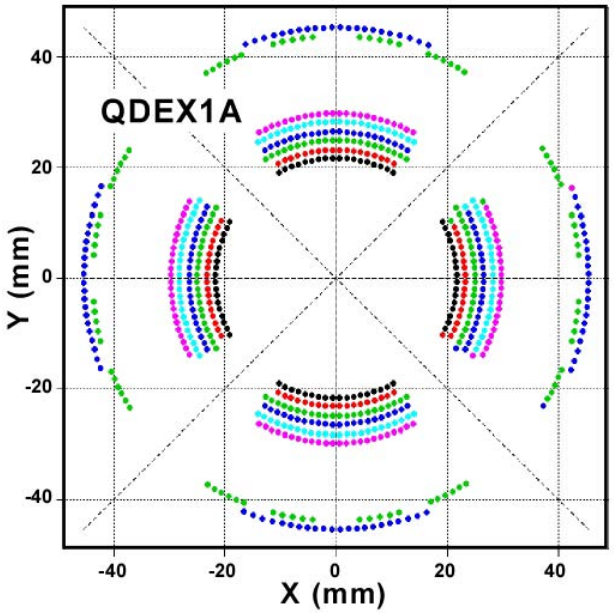

Figure 15. Actively Shielded QDEX1A Design for 14 mr Crossing Angle. Inner and outer coils are wound on separate support tubes. For 730 A, G_{in} is 93.8 T/m while G_{outer} is -10.5 T/m for net 83.3 T/m gradient.

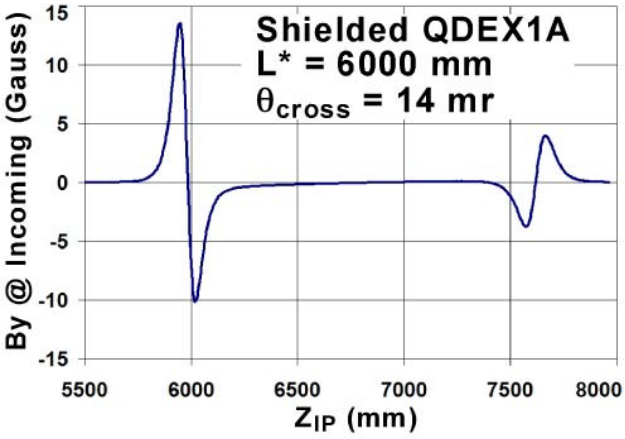

Figure 16. Stray Field Seen Outside QDEX1A at the Incoming Beamline. Stray field at the incoming beam location is more critical there than at the extraction line; so we seek to reduce it as much as possible, both in an integral sense and locally, to avoid large field excursions.

Table 3. Parameter Summary for the SD0, OC0 and Correction Windings in Their Common Coil Package.

Design of 6-Oct-2005	L_tot (mm)	T.F @ cent -	I.T.F -	L_mag (mm)	I_op (A)	B or Gradient	Units	B @ 10 mm (T)	Ext' @ 85 mm	|B| @ 85 mm (Gauss)
octupole	716 + 20	1.901E+03	1.346E+03	708.0	79	1.50E+05	T/m^3	0.150	3.10E-06	0.5
sextupole	716 + 20	8.462E+00	5.923E+00	700.0	709	6.00E+03	T/m^2	0.600	1.34E-02	81
skew sextupole	716 + 20	3.814E+00	2.651E+00	695.2	79	3.00E+02	T/m^2	0.030	4.07E-02	12
dipole (hor)	716 + 20	1.165E-03	7.610E-04	653.0	86	1.00E-01	T	0.100	9.31E+02	93
dipole (vert)	716 + 20	7.681E-04	4.997E-04	650.6	91	7.00E-02	T	0.070	9.74E+02	68

current. One consequence of co-winding different multipolarity coils with the same pattern length is that they naturally end up with different magnetic lengths. In Table 3 OC0 and SD0 show the same 716 mm coil pattern length but their respective magnetic lengths, 708 and 700 mm, differ.

The additional corrector windings shown in Figure 17, and parameterized in Table 3, are:

- skew-sextupole (specified to have 5% of main sextupole integrated strength for generating an effective sextupole field rotation)
- dipole and skew-dipole windings (used to shift the magnetic center).

These correction coil windings are useful because the SD0/OC0 package is wound on a continuation of the QD0 coil support tube and it is not practical to move or rotate this package independently inside a cryostat.

In order to compare the stray field generated by these elements at the extraction beamline, we display in the last column of Table 3 the field contribution from each one when operated at maximum specified operating current and at the minimum beam separation. We see that even though the dipole and skew-dipole corrector fields are much weaker than the sextupole at the 10 mm beam pipe inner radius, if these correctors were to be run up to full current they would contribute almost as much as the sextupole to the external field seen at the extraction line because their external fields fall of much more slowly (combination of larger average radius and dipole's $1/r^2$ dependence compared to sextupole's $1/r^4$). But note that even though the octupole field magnitude, is one-quarter the sextupole field inside at 10 mm radius, the octupole contribution is negligible at the extraction beamline (octupole has smaller coil radius and $1/r^5$ dependence). Finally the skew-sextupole is 5% of the main sextupole inside the aperture but 15% of the main sextuple outside (skew-sextupole radius is larger and same r-dependence).

The SD1/OC1 coil package has the same coil cross section as SD0/OC0 but its stray field seen at the extraction line will be much smaller because:

- the beamline separation at SD1/OC1 is greater,
- and the passive shielding keeping QFEX2A stray field from the incoming beamline also works to keep SD1/OC1 stray field from reaching the extraction line.

Magnets which are beyond QDEX1A are comfortably outside the experimental detector solenoid where we can switch from active shielding via reverse polarity coils to passive shielding with magnetic materials. Unlike active shielding which reduces magnetic strength, passive shielding adds to the strength and works for all the field multipolarities that are present (i.e. on correction coils as along with the main magnets).

The cross section of a passively shielded magnet, QF1, is shown in Figure 18. For passive shielding we use a magnetic yoke shell that is placed at large enough radius

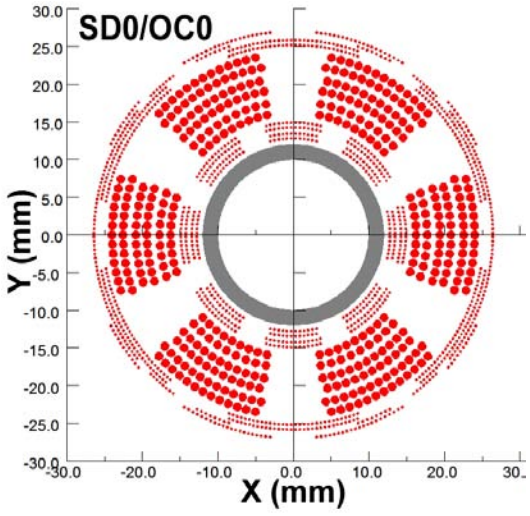

Figure 17. SD0/OC0 Common Coil Package. The SD0 (sextupole) and OC0 (octupole) coils are co-wound on a support tube and have the same physical length. First OC0 is wound with 4 layers of single stand wire followed by 6 cable layers for SD0. Atop this are skew-sextupole, dipole and skew-dipole correction coil windings.

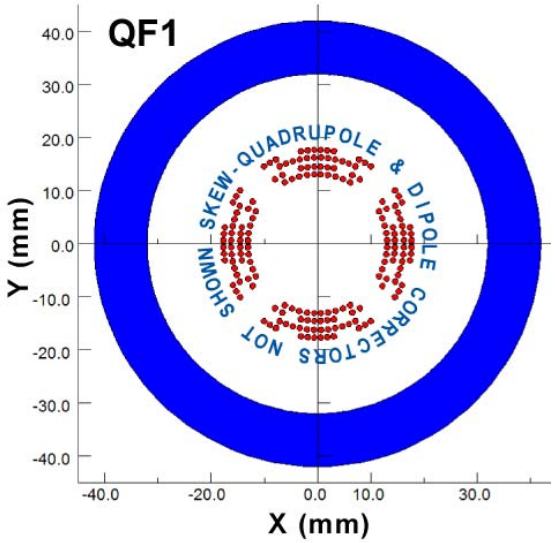

Figure 18. A Passively Shielded QF1 Magnet that is Suitable for 80 T/m Operation. A thin cold magnetic yoke surrounds the QF1 coil (both containing stray field and increasing transfer function). This design has space inside the yoke for He-II cooling in contact with the inner coil

Table 4. Incoming Beamline Magnet Package Summary.

Package Name	Multipole Type	Shield	Winding Type	Total # Layers
QD0	Main Quadrupole	Yes	Cable	6
	Dipole	No	Wire	1
	Skew-Dipole	No	Wire	1
	Skew-Quadrupole	No	Wire	1
	Shield Quadrupole	—	Cable	1
SD0	Octupole	No	Wire	4
	Sextupole	No	Cable	6
	Skew-Sextupole	No	Wire	2
	Dipole	No	Wire	1
	Skew-Dipole	No	Wire	1
QF1	Quadrupole	Yes	Cable	4
	Dipole	Yes	Wire	1
	Skew-Dipole	Yes	Wire	1
	Skew-Quadrupole	Yes	Wire	1
	Magnetic Yoke	—	—	1
SF1	Octupole	No	Wire	4
	Sextupole	No	Cable	6
	Skew-Sextupole	No	Wire	2
	Dipole	No	Wire	1
	Skew-Dipole	No	Wire	1

Table 5. Extraction Beamline Magnet Package Summary.

Package Name	Multipole Type	Shield	Winding Type	Total # Layers
QDEX1A	Main Quadrupole	Yes	Cable	6
	Dipole	No	Wire	1
	Skew-Dipole	No	Wire	1
	Skew-Quadrupole	No	Wire	1
	Shield Quadrupole	—	Cable	2
QDEX1B	Quadrupole	Yes	Cable	6
	Dipole	Yes	Wire	1
	Skew-Dipole	Yes	Wire	1
	Skew-Quadrupole	Yes	Wire	1
	Magnetic Yoke	—	—	1
QFEX2A	Quadrupole	Yes	Cable	6
	Dipole	Yes	Wire	1
	Skew-Dipole	Yes	Wire	1
	Skew-Quadrupole	Yes	Wire	1
	Magnetic Yoke	—	—	1

to remain unsaturated. With the shell being at large radius it has only minimal impact on field quality and has little sensitivity to relative centering errors between the coils and shield. Note it is still important to provide space for He-II cooling in direct contact with the coil surface inside the passive shielding shell.

Since QF1 is not impacted by the detector solenoid field, has a lower operating gradient of 80 T/m and passive shielding that boosts its gradient, its conductor requirements are greatly relaxed compared to QD0 and is wound with fewer cable layers. QF1 will still have the same compliment of skew-quadrupole, dipole and skew-dipole correction coils (not shown in Figure 18) as QD0. For QF1 its passive shielding has two additional benefits:

- external fields generated by the correctors are also shielded from the extraction beamline
- and the shield prevents outside stray fields from reaching the incoming beamline.

For completeness the designs for the remaining passively shielded extraction line magnets are shown in Figure 19. Summaries for all the coil packages are given in Tables 4 and 5. The extraction line QDEX1B and QFEX2A magnets are similar to QF1; however, in order to reduce energy loss due to disrupted beam coming from the IP their apertures must be increased. Given the tight transverse separation between the incoming and extraction beamlines, shown in Figure 14 and the need not to saturate the QDEX1B and QFEX2A magnetic yokes (avoid higher external field from saturated yokes), the

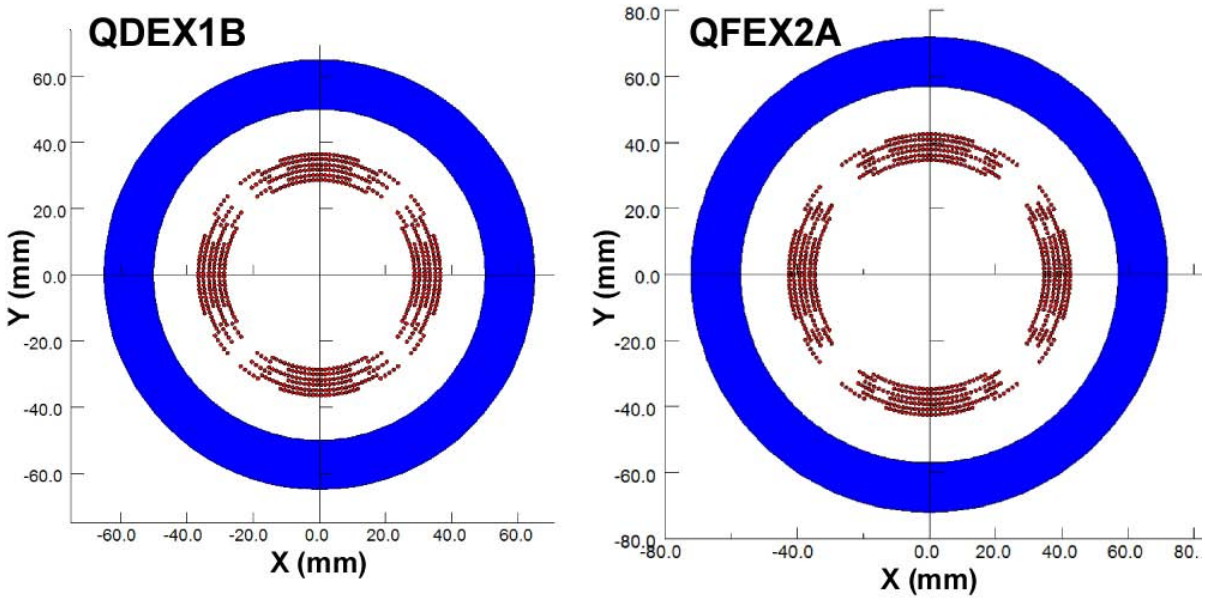

Figure 19. Passively Shielded Designs for the Final Two Extraction Line Superconducting Magnets QDEX1B and QFEX2A. As we go further from the IP the extraction line aperture must grow in order to keep energy deposition manageable and therefore the quadrupole field strength drops from 50 T/m for QDEX1B to 40 T/m for QFEX2A.

Table 6. Coil Package Physical Parameters for the 14 mr Crossing Angle Layout. L_{pat} is the coil pattern length, R_{apt} the beampipe inner radius (half-aperture) and R_{outer} the outer package radius (for coil or yoke as appropriate).

Package Name	L_{pat} (mm)	R_{apt} (mm)	R_{outer} (mm)
QD0	2220	10	36
SD0	716	10	28
QF1	2020	10	42
SF1	366	10	28
QDEX1A	1674	18	46
QDEX1B	1680	24	62
QFEX2A	1686	30	72

QDEX1B and QFEX2A magnetic fields at their inner apertures are set to be less than 1.2 T.

Relevant physical parameters of the coil package and yoke sizes used for the 14 mr layout are given in Table 6. Note that these data are useful for deriving a lower limit for the crossing angle with the present design even if L* were to be increased by 1 m from 3.51 to 4.51 m. With the present 14 mr layout, the QF1 and QDEX1B yokes are close to touching at 7.9 m with (7900*0.014–42–62) or 6.6 mm. With L* increased to 4.51 m, we find that it would take a crossing angle of 12.4 mr to maintain this same spacing at the new 8.9 m location and this crossing angle is more than the value of 11 mr estimated from simple L* scaling (i.e. 3.51/4.51*14 mr).

SUMMARY

We have shown how to use BNL direct wind coil production techniques, originally developed for the HERA-II and BEPC-II Luminosity Upgrades, for making compact superconducting ILC FF magnets compatible with L* of 3.51 m and 14 mr total crossing angle. Some critical milestones were:

- learning to wind small bend radius cable coil patterns on small diameter coil support tubes (increased engineering current density)
- adoption of He-II cooling (better performance)
- and the development of active and passive external field shielding configurations (to eliminate beamline magnet field cross talk).

A short actively shielded QD0 prototype, QT, was produced and tested and QT performance exceeded ILC field quality and quench performance requirements. Even with the somewhat compromised shield design that had to be adopted to fit test dewar space limits, the QT active shield performed very well and reduced QT's integrated external field on contact by 22 fold.

In future work we will integrate heating elements directly into the body of a test coil prototype in order to directly measure the energy required to quench compact superconducting magnets under ILC operating conditions. With preliminary coil and yoke dimensions now in hand we are proceeding with a cryogenic design that integrates the 14 mr layout magnets in a common cryostat. Finally we plan to produce a full length prototype to be housed and supported in a full cryostat in order to be able to investigate vibration and active stabilization issues.

REFERENCES

[1] B. Parker, "Superconducting Magnet Issues," ICFA Beam Dynamics Workshop on Nanometer-Size Colliding Beams, Nanobeam 2002, Lausanne Switzerland, September 2002, http://www.bnl.gov/magnets/Staff/Parker/ParkerNano2002Talk.pdf.

[2] B. Parker, "Superconducting Final Focus Magnet Issues," NLC US Machine Advisory Meeting, November 20002, SLAC, Palo Alto, CA, USA, http://www.bnl.gov/magnets/Staff/Parker/ParkerMAC7NovTalk.pdf.

[3] B. Parker, "The Compact Superconducting Final Focus Doublet Option," American Linear Collider Workshop, Cornel University, Ithaca, NY, USA, July 2003.

[4] B. Parker, "A review of the BNL Direct-Wind Superconducting IR magnet Experience," 30th Advanced ICFA Beam Dynamics Workshop on High Luminosity e^+e^- Collisions, Palo Alto, CA, USA, October 2003 http://www-conf.slac.stanford.edu/icfa03/pres/MOP03.pdf and http://www-conf.slac.stanford.edu/icfa03/pres/MOP03.mov

[5] P. Wanderer, *et.al.*, "Completion of Superconducting Magnet Production at BNL for the HERA Luminosity Upgrade," 17th International Conference on Magnet Technology, MT-17, Geneva, Switzerland, September 2001, http://www.bnl.gov/magnets/magnet_files/Publications/BNL-71432-2003-CP.pdf.

[6] B. Parker, "The Serpentine Coil Design for BEPC-II Superconducting IR Magnets," Mini-Workshop on BEPC-II IR Design, IHEP, Beijing, P. R. China, January 2004, http://www.bnl.gov/magnets/Staff/Parker/serpentine_review.pdf.

[7] B. Parker, "Technology Development for Linear Collider Final Focus Quadrupoles with Small-Aperture High-Gradient Superconducting Coils," BNL LDRD Project Number **LDRD-03-014**, 2003.

[8] B. Parker, *et.al.*, "Compact Superconducting Final Focus Magnet Options for the ILC," 2005 Particle Accelerator Conference, PAC'05, Knoxville, Tennessee, USA, May 2005, http://accelconf.web.cern.ch/AccelConf/p05/PAPERS/RPPP017.PDF

[9] B. Parker and J. Escallier, "Serpentine Coil Topology for BNL Direct Wind Superconducting Magnets," 2005 Particle Accelerator Conference, PAC'05, Knoxville, Tennessee, USA, May 2005, http://accelconf.web.cern.ch/AccelConf/p05/PAPERS/TOAA010.PDF.

DEVELOPMENT OF FINAL FOCUS PERMANENT MAGNET

T. Mihara, Y. Iwashita, Kyoto ICR, Uji, Kyoto
Masayuki Kumada, NIRS, Chiba-shi
Cherrill M. Spencer, SLAC, Menlo Park, California

Abstract

A superstrong permanent magnet quadrupole (PMQ) is one of the candidates for the final focus lens for the International Linear Collider (ILC). Our prototype PMQ can produce variable strengths from 3.5T to 24.2T in 1.4T steps. The magnetic center of the PMQ must not move more than a few microns during a 20% strength change of final quad in ILC. Measured tens of microns of center movements are effectively suppressed by shimming magnet rings with thin films.

Outgoing beam line goes very nearby the incoming beam line around final quad in some crossing angles. We suggest designs of PMQ not to interrupt the outgoing beam line for each crossing angles.

Renewal plan of our prototype PMQ and rotating coil system is also shown.

INTRODUCTION

Strength variable permanent magnet quadrupole (iPMQ) is one of the candidate for final quad of ILC. Its good for its small size and light weight (our PMQ weighs about 100kg with 40cm x 40cm x 23cm), Less power consumption, No vibration source (power cable, cooling water, or He pipe, etc…), Edge of effective length equals to L* (Super-conducting quadrupole needs 20cm more space for thermal shield).

We achieved a 120T/m iPMQ, its strength is adjusted by 7T/m step.

PERMANENT MAGNET QUADRUPOLE

We fabricated a strength-variable permanent magnet quadrupole as a candidate for the final quad in a linear collider. The PMQ is composed of an inner ring and four outer rings [1]. (see Fig. 1 and table 1 for its dimensions and parameters.)

Only the outer rings are rotated in order to change the integrated gradient. The fixed inner ring suppresses any errors caused by rotation of outer rings. Outer rings are rotated just 90^{o} to switch the phase of that section's quadrupole (from focus to defocus and vice versa). Therefore, this PMQ with four outer rings can produce a series of 16 integrated gradients from 3.7T to 24.2 T in 1.4 T steps. Integrated gradient is proportional to "Switched on" length (SWL), the summation of outer rings lengths which are at the "strong" phase[2].

The inner ring is directly supported by stainless steel (SS) end plates that are fixed on the magnet base block. Each outer ring is supported in a ball bearing that is fitted into a SS ring support plate. Each outer ring has a spur gear that is rotated (4 DC motors with worm gears move the spur gears). These four plates are secured on the SS base block.

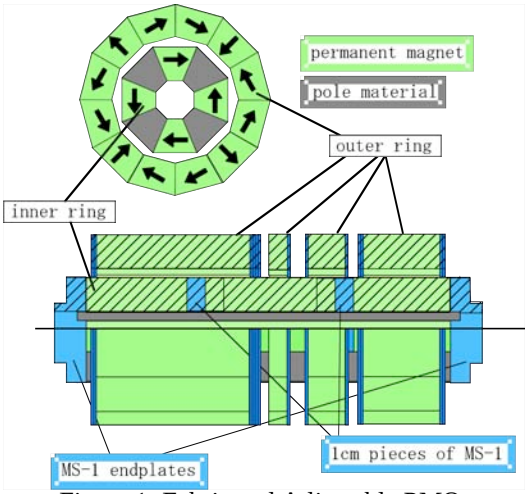

Figure 1: Fabricated Adjustable PMQ.

Table 1: scale and performance of the PMQ

Bore radius	1cm
Inner ring radii	In 1cm out 3cm
Outer ring radii	In 3.3cm out 5cm
Outer ring section lengths	1cm, 2cm, 4cm, 8cm
Physical length	23cm
Pole material	Permendur
Magnet material(inner ring)	NEOMAX38AH
Magnet material(outer ring)	NEOMAX44H
Integrated gradient(strongest)	24.2T (120T/m)
Integrated gradient(weakest)	3.7T (1.8T)
Int. gradient step size	1.4T

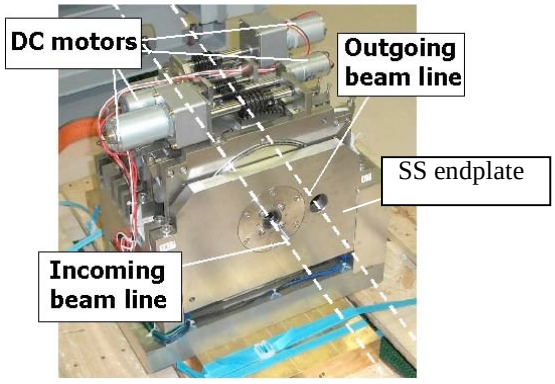

Figure 2: Fabricated adjustable PMQ.

POLE ANGLE ADJUSTMENT

It is necessary to adjust the stopping angle of each outer ring precisely because the skew angle of the ILC's final quad's field must be less than a few μrad. The procedure for adjusting the stop angles and the results follow.

The stopper block fixed on the spur gear comes in contact with the stopper lever which is fixed on the ring support plate, and the rotation stops. Therefore, the rotation stop angle of an outer ring is controllable by the stopper lever position, it can be fine-tuned by turning the appropriate thrust screw (see Fig. 3).

If the phase of the inner ring's quad equals that of the outer ring, the quadrupole strength should be maximum. We tuned the stopper by turning the screw, checking the integrated strength by a rotating coil measurement system, and searched for the best position.

It is thought that the angle that gives the maximum (minimum) value of the magnetic field is the correct stop ping angle (skew=0). The screw proceeds 1mm a turn, and the stopper lever moves a few hundred microns. A turn of screw corresponds to about 30μrad on the figure 4. Skew angle can be suppressed to less than 30μrad [3].

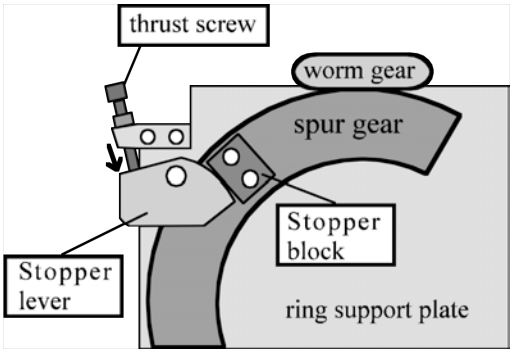

Figure 3. Gear stopper adjustment Stop angle on each side can be adjusted by the screw.

MAGNETIC CENTER ADJUSTMENT

ILC requires the final quad's placement to be correct to within a few microns. Which means the magnetic center of the PMQ must move less than a few microns when an outer ring is rotated to change its strength.

When the PMQ was first assembled and measured we observed that its magnetic center position, defined by X and Y coordinates quoted relative to the axis of the rotating measuring coil, moved by several tens of microns when measured at different strengths. (see Fig. 4)

There are two scenario that could produce the center movement. First is that the magnetic center axis of the individual outer ring does not coincide with this rotation axes. Second is that the rotation axis of an outer ring is shifted from that of the inner ring.

The inner ring is fixed directly to the SS base in our PMQ, and each outer ring is supported by a bearing fitted

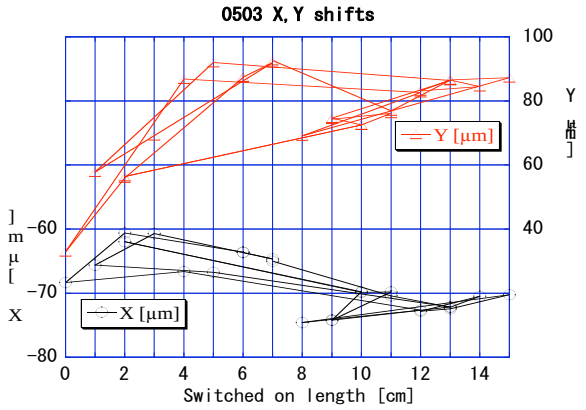

Figure 4: Center position of PMQ at different strengths. Lines between points shows history of measurements.

in that ring's support plate. Each plate with an outer ring is put on the SS base block, and fixed with screws.

It is possible to shift an outer ring by placing a shim between a ring support plate and the SS base block where the outer ring is supported. (see Fig.5) We put different thicknesses of shims between the SS base block and the 4 outer ring cases, thus moving each outer ring, one at a time, and measured the movement of the magnetic center. Shimming can only lift up or move an outer ring in the –X direction, therefore we could not adjust the center in the -Y direction or +X direction. Grinding the SS frame or SS base would make it possible to adjust all outer rings

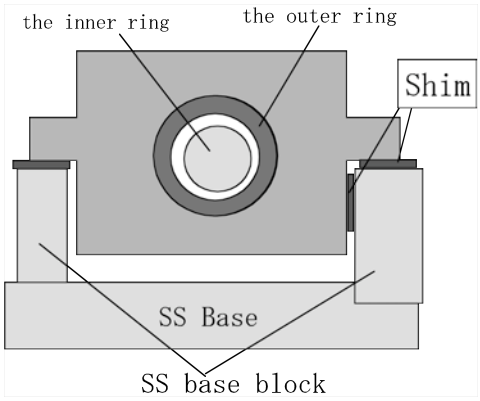

Figure 5. Sketch of PMQ showing shim placement

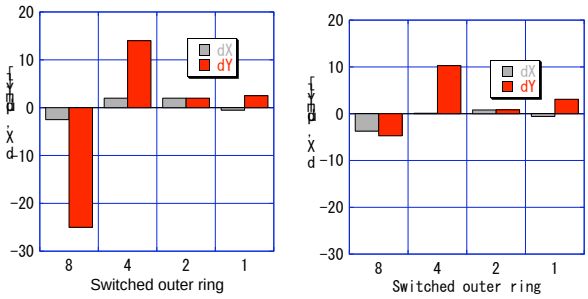

Figure 6. Center Movement affected by shimming. Left: Before shimming. Right: 8cm ring lifted up by 76μm. "8" means 8cm long outer ring.

and shift the center in any direction.

Lifting the 8cm outer ring up by 51μm reduced the center movement from 30μm to 10μm when the strength was changed by about 45% (see Fig.6 left). Fig. 6 right shows a example of shimming by lifting and horizontal displacement. The 8cm outer ring is lifted up by 76μm and 4cm outer ring is moved to –x direction by 51μm. Then the Y-magnetic center shift when 8cm is rotated becomes < 5μm and the X-shift of 4cm outer ring becomes < 1μm.

PMQ FOR CROSSING ANGLES

Outgoing beam line goes nearby (several centimetres) the incoming beam line if crossing angle is 2mrad of 20mrad (not zero). Thus PMQ must be designed not to interrupt the outgoing beam line L* is about 3~5m. IF 2mrad and L*=5, outgoing beam pipe exist 10mm from incoming beam pipe.

We suggest designs of PMQ for each crossing angles (see Fig. 7). Arrowed block shows the magnet block magnetization direction. Not arrowed shows magnetic pole. A designed Field strength is shown on Table 2.

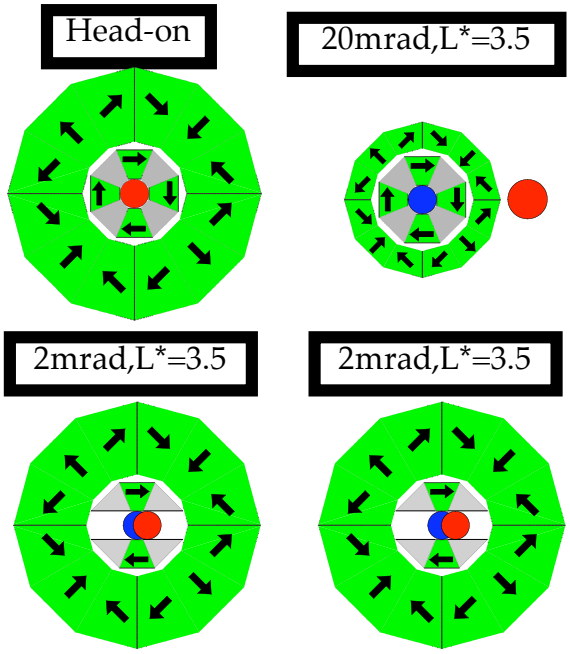

Figure 7. Varieties of PMQ for crossing angles

Table 2 Field gradient of PMQs with 20mm bore.

	head on	2mrad	20mrad
Outer diam	180mm	180mm	100mm
Grad	180T/m	130T/m	120T/m

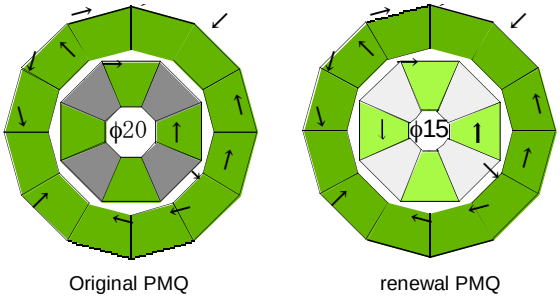

Figure 7. renewal plan of PMQ

SUMMARY AND FUTURE PLAN

The PMQ's field quality is moderately good and it was not affected by changing integrated strength or shimming.

The magnetic center axes of the outer rings are adjusted by using 25.4 μm shims. The center movement caused by rotation of the 8 cm outer ring was successfully reduced from some tens of microns to 5μm in Y coord by lifting it up by 76μm. The effect of the 4cm outer ring on the X coord could also be reduced by moving it in the –X direction by 51μm.

Because the shimming worked very well in some cases, an automated shimming mechanism should be incorporated in a future design. Particularly, fine adjustments in both polarities are important.

We are also preparing a rotating coil with ϕ13mm quarts rod (see figure 8). Quarts rod has small thermal expansion rate, thus the thermal instability of measurement by coil expansion is small.

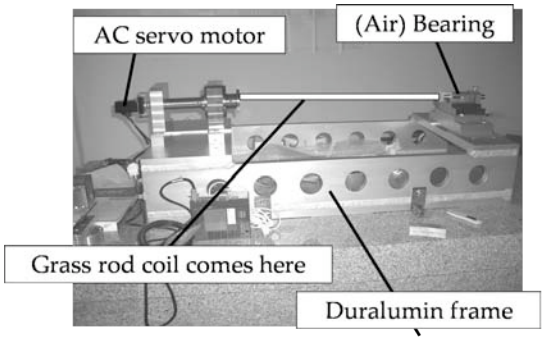

Figure 8. Rotating coil system with a quarts rod.

REFERENCES

[1] T. Mihara, Y. Iwashita, M. Kumada, C. M. Spencer, E. Antokhin," Super Strong Permanent Magnet Quadrupole for a Linear Collider," *IEEE trans. Appl. Supercond.* Vol.14, No.2, pp 469-472, June 2004.

[2] T. Mihara , Y. Iwashita, M.Kumada, C.M.Spencer "Superstrong Adjustable Permanent Magnet for a Linear Collider Final Focus" 12th Linear Accelerator Conference, Lubeck, Germany, August 16-20, 2004. SLAC-PUB-10878.

[3] T. Mihara , Y. Iwashita, M.Kumada, C.M.Spencer "Field Quality and Magnetic Center Stability Achieved in a Variable Permanent Magnet Quadrupole for the ILC", Particle accelerator conference, Knoxville, Tennessee, U.S.A., May 16-20,

VIBRATION MEASUREMENTS IN A RHIC QUADRUPOLE AT CRYOGENIC TEMPERATURES*

Animesh Jain#, Sevan Aydin, Ping He, Michael Anerella, George Ganetis, Michael Harrison, Brett Parker and Stephen Plate
Brookhaven National Laboratory, Upton, NY 11973-5000, U.S.A.

Abstract

One of the concerns in using compact superconducting magnets in the final focus region of the ILC is the influence of the cryogen flow on the vibration characteristics. As a first step towards characterizing such motion at nanometer levels, a project was undertaken at BNL to measure the vibrations in a spare RHIC quadrupole under cryogenic conditions. Given the constraints of cryogenic operation, and limited space available, it was decided to use a dual head laser Doppler vibrometer for this work. The performance of the laser vibrometer was tested in a series of room temperature tests and compared with results from Mark L4 geophones. The laser system was then used to measure the vibration of the cold mass of the quadrupole with respect to the outside warm enclosure. These measurements were carried out both with and without the flow of cold helium through the magnet. The results indicate only a minor increase in motion in the horizontal direction (where the cold mass is relatively free to move).

INTRODUCTION

Compact superconducting quadrupoles are being considered for use in the final focus region of the International Linear Collider (ILC) [1]. These magnets must meet stringent requirements of the stability of the magnetic field center at nanometer level. One of the concerns in using superconducting magnets is the influence of the cryogen flow on the vibration characteristics of the magnets. Since very little is known about vibration of superconducting magnets at nanometer levels, as a first step, a project was undertaken at BNL to measure the vibrations under cryogenic conditions in a spare arc quadrupole built for the Relativistic Heavy Ion Collider (RHIC) [2]. The cross section of the magnet cold mass in its cryostat is shown in Fig. 1. The cold mass is supported by vertical posts, but is not constrained in the horizontal direction. Even though this magnet is not designed to minimize vibrations, and has a construction very different from that foreseen for the ILC, the present exercise has proved beneficial in developing suitable vibration measurement techniques.

* This work was supported by the U.S. Department of Energy under contract number DE-AC02-98CH10886. This manuscript has been authored by Brookhaven Science Associates, LLC under Contract No. DE-AC02-98CH1-886 with the U.S. Department of Energy. The United States Government retains, and the publisher, by accepting the article for publication, acknowledges, a worldwide license to publish or reproduce the published form of this manuscript, or allow others to do so, for the United States Government purposes.

#jain@bnl.gov

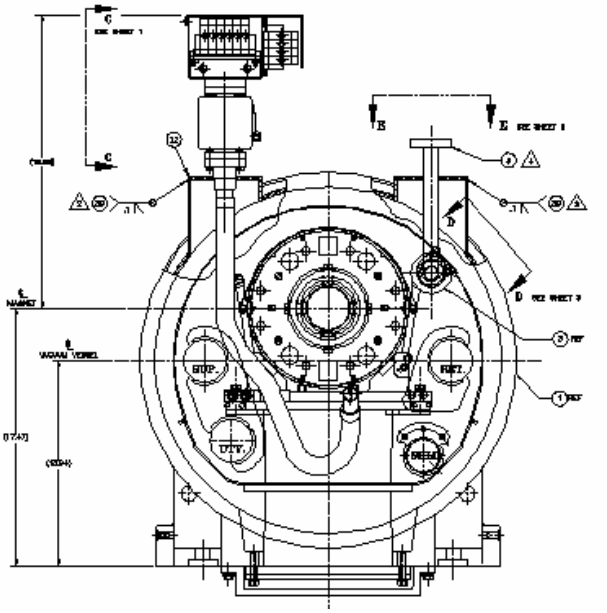

Fig. 1 Cross section of a RHIC quadrupole cold mass in its cryostat.

Given the constraints of cryogenic operation, and limited space available, it was decided to use a commercially available dual head laser Doppler vibrometer for this work. The performance of the laser vibrometer was tested in a series of room temperature tests and compared with the results from geophones. The laser system was then used to measure the vibration of the cold mass of the quadrupole with respect to the outside warm enclosure. These measurements were carried out both with and without the flow of cold helium through the magnet. The results indicate only a minor increase in motion in the horizontal direction (where the cold mass is relatively free to move).

MEASUREMENT TECHNIQUE

Geophones with suitable characteristics provide a reliable means to measure vibrations. However, nearly all such instruments are very bulky and cannot work at cryogenic temperatures. Furthermore, these cannot work in the presence of magnetic field. Given the constraints of cryogenic operation, and limited space available, it was decided to employ an optical interferometric technique to measure the vibration in this work. Even though the magnet was not powered in the present tests, the optical techniques employed can be used even in the presence of a magnetic field. After a careful review of the commercially available laser systems, a dual fiber-optic

head laser Doppler vibrometer model OFV-552 with a model OFV-5000 controller from PolyTec Inc.[3] was selected for this work. The performance of the laser vibrometer was tested in a series of room temperature tests and compared with results from Mark L4 geophones [4]. It was clear from these preliminary tests that the motion of the laser head itself could be a serious limitation to the accuracy of the results. The choice of a dual head laser system allows more reliable differential measurements between two objects provided the motions of the two arms of the laser interferometer can be kept the same. The laser system was used to measure the vibration of the cold mass of the quadrupole with respect to the outside warm enclosure. These measurements were carried out both with and without the flow of cold helium through the magnet while the cold mass was maintained at or near 4.5 K. A comparison of the vibration spectra with and without helium flow reveals any significant increase in the vibration as a result of cryogen flow.

All measurements were carried out with the laser vibrometer set to the most sensitive range of 1 mm/s per Volt. The analog output from the OFV-5000 controller was amplified (20X to 500X) and recorded using a 16-bit ADC at a rate of 1600 Hz for a period of 143.5 seconds. The data were Fourier analyzed in blocks of 32K points (0.05 Hz resolution) or 16K points (0.1 Hz resolution) with a Hanning window and 50% overlap between successive data blocks. Each run of 143.5 seconds thus provides many power spectra, which were averaged.

LASER SYSTEM PERFORMANCE TESTS

The first performance test carried out was a measurement of the intrinsic noise in the system. For this test, both the beams of the laser system were terminated with a small mirror. Neglecting any small motion of the mirrors themselves, the laser vibrometer output is expected to be ideally zero. The measured power spectrum is shown in Fig. 2. The noise is less than 1 nm/√Hz for all frequencies above 2 Hz. A few isolated peaks are seen at higher frequencies, but the total RMS motion for any peak is below 1 nm. The total integrated noise is ~2 nm for frequencies above 1 Hz, and is below

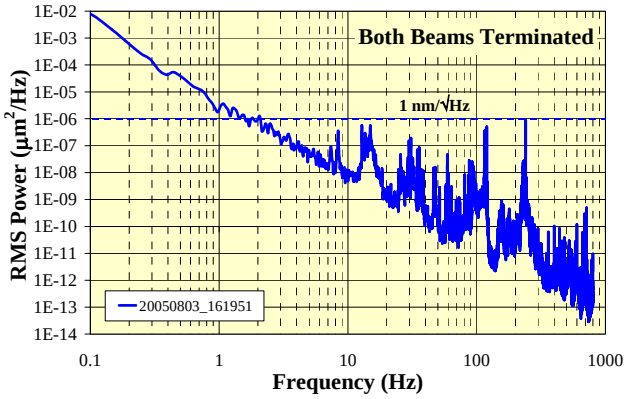

Fig. 2 Intrinsic noise of the laser system, as measured by terminating both beams with a small mirror.

1 nm for frequencies above 10 Hz. These noise figures are well below the typical motion of the magnet on our test stand. It should be noted that the mirrors are perhaps not entirely vibration free at sub-nanometer level. So, some of the high frequency peaks may even be due to mirror motion.

The performance of the laser system was studied next in the single beam mode using a specially built laser head holder and comparing results with the geophone data. For these tests, the reference laser beam was terminated with a mirror. The measurement beam head was mounted in a specially built holder placed on a table, as shown in Fig. 3. The laser beam was used to measure the motion of a large granite table. One geophone was used to independently measure the motion of the granite table, and another geophone was used to measure the motion of the laser holder itself. In the single beam mode, the measurements are sensitive to the motion of the laser head. The output from the laser vibrometer is expected to match the relative motion of the granite table and the laser holder, as deduced from the data from the two geophones.

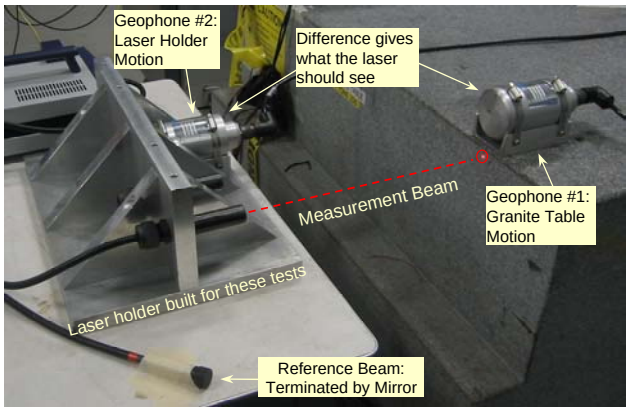

Fig. 3 Measurement set up for performance test of the laser system used in the single beam mode.

Fig. 4 shows the results of the single beam measurements. It can be seen that the power spectrum of the laser signal matches very well with that derived from

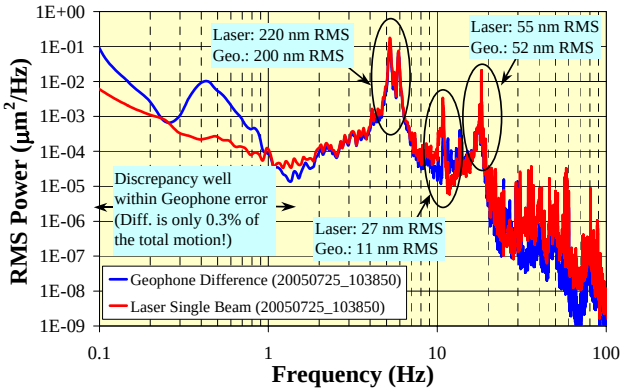

Fig. 4 Comparison of the power spectra measured by the laser system in the single beam mode with that expected from a difference of the two geophone signals.

the two geophone signals. The total RMS motions at the prominent peaks are indicated in Fig. 4. At frequencies below 1 Hz, both the granite table and the laser holder have correlated motions. The difference is only a small fraction of the total power. The geophone subtraction is not very accurate in this case due to limited calibration accuracy, as well as drop off of the geophone sensitivity below the 1 Hz resonance frequency.

In the single beam performance test described above, the total motion of the laser holder with respect to the object being measured (the granite table) was more than 200 nm RMS integrated above 1 Hz. If the dual beam mode is used to measure the relative motion of two objects that have nearly identical motion, it is expected that the motion of the laser holder itself with respect to the object will not affect the measurements. However, in practice, the effect of laser holder motion may not be completely eliminated. In order to test the performance of the laser system in the dual beam mode, we mounted both laser heads on the specially built holder and measured the relative motion of two spots near each other on the side of the large granite table, as shown in Fig. 5. Under the assumption that the relative motion of the two laser heads is negligible, and the assumption that the relative motion of the two spots on the granite table is negligible, the dual beam data should essentially give zero motion.

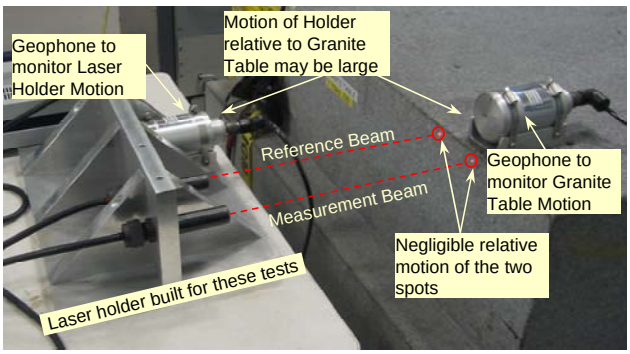

Fig. 5 Measurement set up for performance test of the laser system used in the dual beam mode.

Fig. 6 shows the power spectra for the relative motion of the laser holder with respect to the granite table (derived from geophones data) and the relative motion of the two spots measured with the laser in the dual beam mode. It can be seen that several of the prominent peaks in the geophones data are also present in the dual beam spectrum. However, the amplitudes are suppressed by a factor of 10 or more. The total motion, integrated over 1 Hz and above, is 220 nm RMS for the holder relative to the granite table, and is 17 nm RMS for the dual beam data. These results show that while there is a significant suppression of the laser holder motion in the dual beam mode, it is still desirable to keep the holder motion as small as possible. There is also a peak (~10 nm RMS) at 10.6 Hz, which is not suppressed at all in the laser dual beam data. This motion is entirely from the laser holder, since it is seen in the geophone data on the holder, but is absent from the geophone data on the granite table.

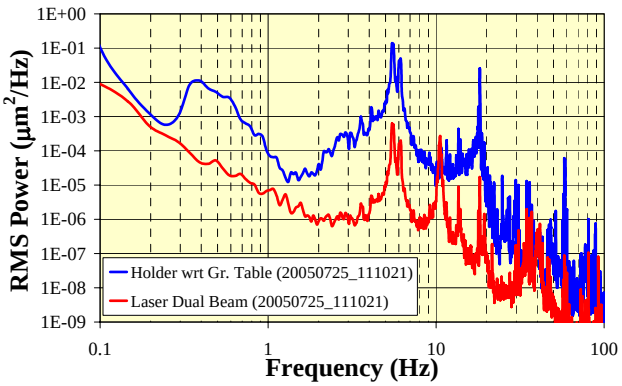

Fig. 6 Demonstration of the suppression of the laser holder motion in the dual beam data.

RHIC QUADRUPOLE TEST SET UP

The RHIC quadrupoles are assembled along with a corrector package and either a sextupole or a trim quadrupole in a single cold mass assembly, referred to as a CQS assembly [2]. For the purpose of these tests, we have used a spare RHIC CQS assembly in a cryostat. Viewports needed to shine the laser beam on the cold mass were installed in large bellows that were used to connect the cryostat to the cryogenic system of the test stand. In order to minimize transmission of high frequency vibrations from the test stand to the magnet, the magnet was mounted on isolation mounts with a resonance frequency of 3-4 Hz, as shown in Fig. 7. These mounts worked well in initial warm tests when the magnet was not hooked up to the cryogenic system. However, the bellows proved to be stiff enough to couple test stand motion to the magnet and the isolation mounts were not very effective once the bellows were in place.

For measurements of the horizontal motion, a holder for the laser heads was built and installed on the test stand, as shown in Fig. 7. The holder has platforms for geophones

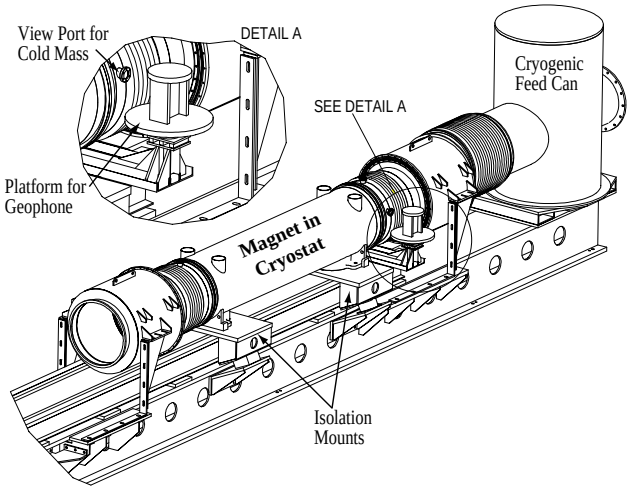

Fig. 7 RHIC quadrupole on the cold test stand and the laser holder for measurements of the horizontal motion.

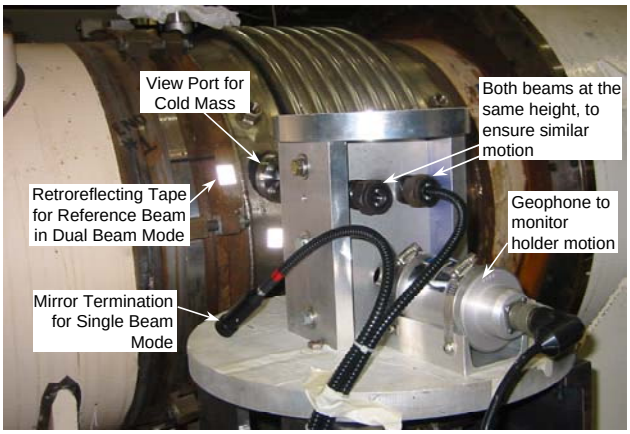

Fig. 8 Set up for the measurement of the horizontal motion of the RHIC quadrupole cold mass.

that were used to monitor the motion of the holder itself. The two laser heads were mounted at the same height, as shown in Fig. 8, to ensure negligible relative motion of the two arms, even though the motion of the holder itself (~300 nm RMS, integrated above 1 Hz) was not very small. The suppression of the laser holder motion in the dual beam mode was verified once again by carrying out measurements on an aluminum plate clamped to the view port. The relative motion of the plate and the laser holder was ~250 nm RMS, integrated above 1 Hz, as measured using the single beam mode. In the dual beam mode, the relative motion of the two adjacent spots on the aluminum plate was measured to be ~40 nm RMS, integrated above 1 Hz. It should be noted that at least some part of this motion might indeed be true relative motion of the .two adjacent spots on the aluminum plate. In any case, this "background" was well below the actual relative motion of the cold mass and the cryostat.

A slightly different holder design was used for measuring the vertical motion. The laser beam entered through a view port at the top of the bellows on the end opposite to the horizontal set up (the end away from the cryogenic feed can). The laser heads were attached to holders mounted on sturdy aluminum frames mounted to the test stand, as shown in Fig. 9. A geophone was used to monitor the vertical motion of the holder itself, which

Fig. 9 Set up for the measurement of the vertical motion of the RHIC quadrupole cold mass.

was ~250 nm RMS, integrated above 1 Hz. The performance of the laser system was also checked for this configuration by shining the laser beam on an aluminum plate attached to the viewport, as in the case of the horizontal motion. The relative motion of the plate and holder was measured to be ~200 nm RMS, integrated above 1 Hz, using the single beam mode. In the dual beam mode measurement, the relative motion of the two adjacent spots on the aluminum plate was ~45 nm RMS, integrated above 1 Hz. This is comparable to what was obtained for the horizontal set up.

MEASUREMENT PLAN AND ANALYSIS

The magnet was hooked up to the cryogenic system and cooled down to 4.5 K. Measurements of the horizontal and the vertical cold mass motion were first made in both the single beam and the dual beam modes with the cryogens flowing. Three independent sets of data were acquired in each case at a scan rate of 1600 Hz for a duration of 143.5 seconds. Analysis was done in block sizes of 16K data points (~0.1 Hz resolution), with 8K overlap. All the power spectra obtained in this way (27 subsets per run, 81 spectra total) were then averaged for better statistics. The total RMS motion above a certain frequency, *f*, was obtained by integrating the power spectra from *f* to infinity, and taking the squre root of the integral. We will refer to the plots of such RMS motion as a function of frequency as the *integrated spectra*. A set of three measurements was then made with the cryogen flow stopped and a wait of about 30 minutes. Finally, the cryogen flow was resumed, and the measurements were repeated in order to unambiguously correlate any changes in the spectra to the presence of cryogen flow.

RESULTS

The integrated spectra for the horizontal motion in the single beam mode are shown in Fig. 10. These spectra represent the motion of the cold mass with respect to the laser holder. The RMS motion above 1 Hz is rather large, over 400 nm, with a dominant peak around 30 Hz. The single beam measurements are sensitive to the motion of

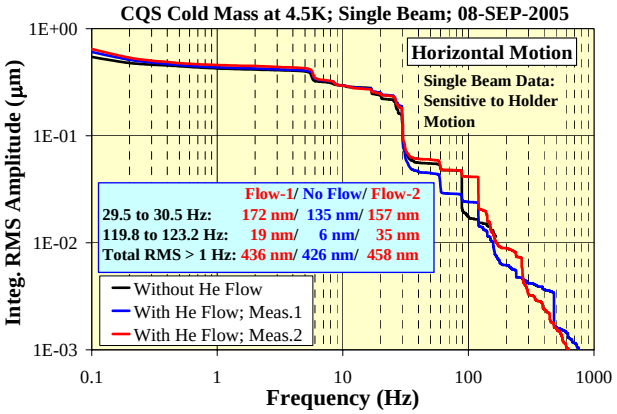

Fig. 10 Integrated spectra for the horizontal motion, as measured in the single beam mode.

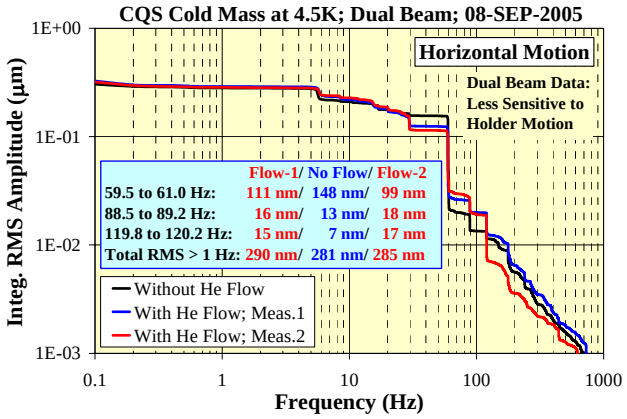

Fig. 11 Integrated spectra for the horizontal motion, as measured in the dual beam mode.

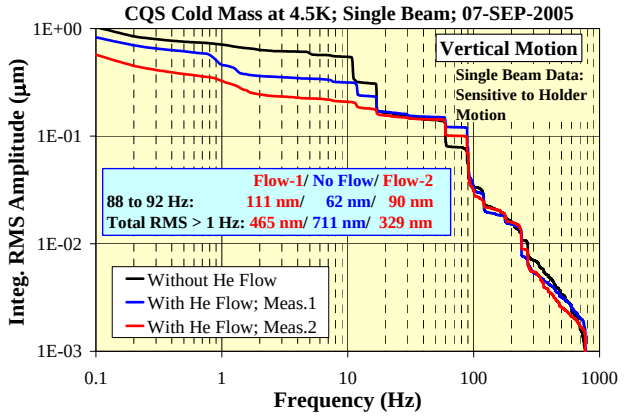

Fig. 12 Integrated spectra for the vertical motion, as measured in the single beam mode.

the laser holder itself, which was ~300 nm RMS integrated above 1 Hz. The RMS motions for some of the dominant peaks in the spectra are also tabulated in Fig. 10. A comparison of the spectra for the cases of with and without helium flow shows only a minor increase (less than 30 nm) for the 120 Hz peak. The overall motion above 1 Hz is also slightly less without helium flow.

The integrated spectra for the horizontal motion measured in the dual beam mode are shown in Fig. 11. These spectra represent the motion of the cold mass relative to the cryostat (strictly speaking, relative to the body of the bellows, which are attached to the cryostat). The dual beam measurements are relatively insensitive to the holder motion, but are sensitive to the cryostat motion. The RMS motion above 1 Hz is ~290 nm in this case, and is significantly lower than in the single beam mode. The 30 Hz motion is much lower than the single beam case, but the 60 Hz motion is much larger. This indicates that the 30 Hz signal in the single beam mode is perhaps dominated by the holder motion, whereas the 60 Hz motion in the dual beam mode is dominated by the cryostat motion. The data from the geophones, taken concurrently with the laser vibrometer data, also confirm this. As in the case of the single beam data, the dual beam data also show that there is no significant increase in the RMS motion above 1 Hz. The increase in motion at 120 Hz due to helium flow is more consistent in the dual beam data, and is ~10 nm. There is also an increase of less than 10 nm at 90 Hz.

Fig. 12 shows the integrated spectra for the vertical motion of the cold mass relative to the laser holder, measured using the single beam mode. Surprisingly, the total motion above 1 Hz is much more in the case of no helium flow, as compared to the two measurements with helium flow. The increased motion for the no helium flow case largely arises from two strong peaks at ~11 Hz and ~17 Hz. An examination of the geophone data for the laser holder and the cryostat shows that the 11 Hz peak is almost entirely from the magnet motion, whereas the 17 Hz peak comes partly from the holder motion and partly from the magnet motion. The motion at these frequencies was found to vary a lot with time. For example, these peaks are almost nonexistent in the measurements after the helium flow was resumed (red curve in Fig. 12). If we ignore these peaks, then the only prominent peaks remaining are at ~60 Hz and ~90 Hz. The motion at 60 Hz is insensitive to helium flow, but the 90 Hz motion is clearly less with the helium flow stopped.

The integrated spectra for the vertical motion measured in the dual beam mode are shown in Fig. 13. The large step in the single beam spectrum at ~11 Hz is practically non-existent in the dual beam data, and the step at ~17 Hz is also much smaller. The dual beam spectra are mostly independent of helium flow, except for a slightly larger motion at 60 Hz in the case of no helium flow.

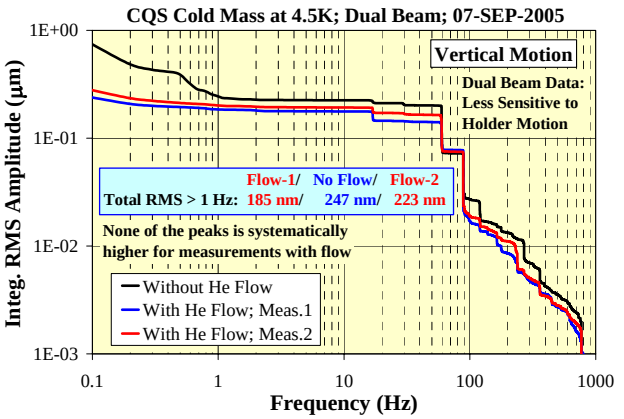

Fig. 13 Integrated spectra for the vertical motion, as measured in the dual beam mode.

In view of the large run-to-run variations in the amount of motion at 11 Hz and 17 Hz, the measurements of vertical motion were repeated on the next day. However, only one set of measurements was made with the helium flowing, instead of two. Figs. 14 and 15 show the integrated spectra in the single and the dual beam modes respectively. The single beam spectrum measured with the helium flowing shows significant motion at 7.5 Hz, 11 Hz and 17 Hz. However, the spectrum without helium flow is now relatively clean, except for a small step at

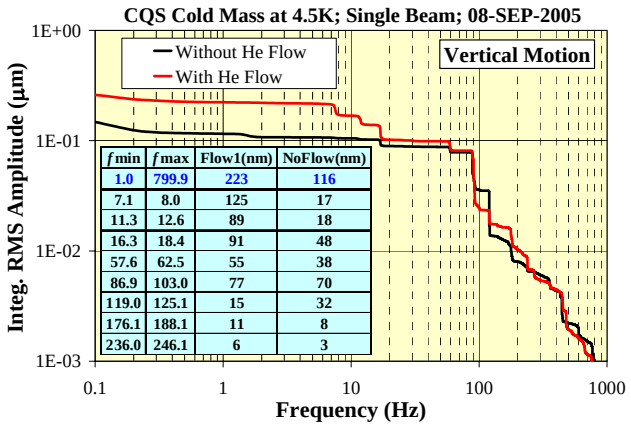

fmin	fmax	Flow1(nm)	NoFlow(nm)
1.0	799.9	223	116
7.1	8.0	125	17
11.3	12.6	89	18
16.3	18.4	91	48
57.6	62.5	55	38
86.9	103.0	77	70
119.0	125.1	15	32
176.1	188.1	11	8
236.0	246.1	6	3

Fig. 14 Integrated power spectra for the vertical motion, as measured in the single beam mode on a different day.

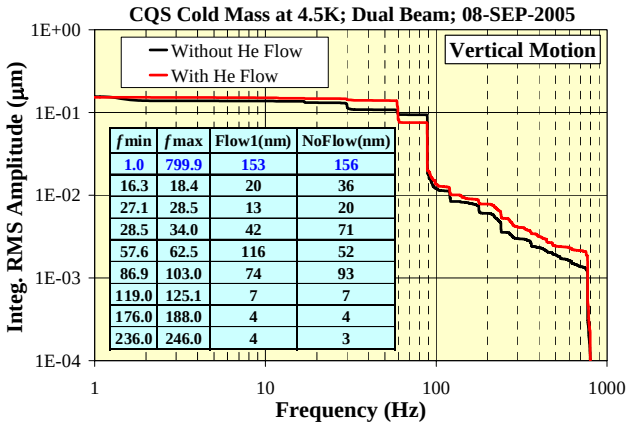

fmin	fmax	Flow1(nm)	NoFlow(nm)
1.0	799.9	153	156
16.3	18.4	20	36
27.1	28.5	13	20
28.5	34.0	42	71
57.6	62.5	116	52
86.9	103.0	74	93
119.0	125.1	7	7
176.0	188.0	4	4
236.0	246.0	4	3

Fig. 15 Integrated power spectra for the vertical motion, as measured in the dual beam mode on a different day.

17 Hz. These results are in sharp contrast to the single beam data taken on the previous day, shown in Fig. 12. On the other hand, the dual beam data in Fig. 15 show very little overall difference with and without helium flow. This is generally consistent with the results on the previous day (Fig. 13), except at 60 Hz. The 60 Hz motion was slightly less with helium flow on the previous day, but is more on the next day. Thus, the influence of helium flow on the vertical motion could not be established unambiguously in this study. Further data, perhaps with multiple cycles of measurements with and without helium flow, are needed to further resolve this.

CONCLUSIONS

The vibrations in a superconducting RHIC quadrupole have been measured with and without helium flow in order to investigate the effect of cryogen flow on the magnet stability. Performance of a laser Doppler vibrometer used for these measurements was studied in detail, and was shown to be satisfactory. For the horizontal motion, where the magnet is relatively free to move, the flow of helium increases the motion at a few frequencies by ~10-30 nm. For the vertical direction, where the magnet is supported by insulating posts, no conclusive evidence of either an increase or a reduction in the motion with helium flow could be established in the single beam data. For the dual beam measurements, which provide the relative motion of the cold mass with respect to the cryostat, no systematic increase in the vertical motion was observed with helium flow, except for a significant increase at 60 Hz in some runs. Further measurements are needed to help resolve the issue of vertical motion with better certainty. Finally, the absolute motion of the magnet is rather large, which limits the sensitivity and accuracy of these measurements. It will be desirable to carry out similar studies in magnets that are better stabilized. Despite the limitations of this study, these results appear quite encouraging for the use of superconducting technology for the quadrupoles in the final focus region of the ILC.

ACKNOWLEDGMENT

We thank J. Frisch, T. Himel, T. Markiewicz and A. Seryi of SLAC for many useful discussions and suggestions. The expert help from R. Ceruti, J. Cintorino, T. Dilgen, G. Herbst, P. Kovach and W. Mc Keon of BNL in setting up and carrying out these measurements is gratefully acknowledged. We also thank J. Danieli of PolyTec, Inc. for his help in carrying out preliminary evaluations of the laser Doppler vibrometer system.

REFERENCES

[1] Brett Parker, “Recent Progress Designing Compact Superconducting Final Focus Magnets for the ILC,” Paper WG2d-01 at Nanobeam 2005 (this workshop); http://wwwal.kuicr.kyoto-u.ac.jp/NanoBM.

[2] M. Anerella, et al., “The RHIC Magnet System,” Nucl. Instrum. Meth. A499 (2-3), pp. 280-315 (2003).

[3] PolyTec Inc. http://www.polytec.com.

[4] Geophone: model L-4, 1 Hz resonant frequency, from Sercel, Inc.; http://www.sercel.com.

DEVELOPMENT OF ADAPTIVE OPTICAL SYSTEM OF BOTH SPATIAL AND TEMPORAL BEAM SHAPING FOR UV-LASER PULASE

H. Tomizawa, H. Dewa, T. Taniuchi, A. Mizuno, T. Asaka, K. Yanagida, S. Suzuki, T. Kobayashi, H. Hanaki, Accelerator Division, Japan Synchrotron Radiation Research Institute (SPring-8)
Kouto, Mikazuki-cho, Sayo-gun, Hyogo 679-5198, Japan
F. Matsui, Creative & Advanced Research Department, Industrial Technology Center of Fukui Prefecture61 Kawaiwashitsuka-cho, Fukui City 910-0102, Japan

ABSTRACT

We have been developing a stable and highly qualified UV-laser pulse as a light source of an rf gun for an injector candidate of future light sources. The CPA (chirped pulse amplification) Ti:Sapphire laser system is operated at a repetition rate of 10 Hz. At the third-harmonic generation (central wavelength: 263 nm), the laser pulse energy after a 45-cm silica rod is up to 850 mJ/pulse. In its present status, the laser's pulse energy stability has been improved down to 0.2~0.3 % at the fundamental and 0.7~1.4% (rms; 10pps; 33,818 shots) at the third-harmonic generation, respectively. This stability has been held for one month continuously, 24 hours a day. The improvements we had passively implemented were to stabilize the laser system as well as the environmental conditions. We introduced a humidity-control system kept at 50~60% in a clean room to reduce damage to the optics. In addition, we prepared a deformable mirror for spatial shaping and a spatial light modulator based on fused-silica plates for temporal shaping. We are applying both of the adaptive optics to automatic optimization of the electron beam bunch to produce lower emittance with the feedback routine. After the improvements, we can now freely form any arbitrary laser intensity distribution on the surface of the cathode. A fiber bundle was used to passively shape the laser spatial and temporal profile for the backward cathode illumination. The profile was spatially shaped into a perfectly homogeneous one with a 90-cm long fiber bundle. This shaping technique is based in practice on pulse stacking with 1,300 different optical paths. The 80-fs laser is shaped as a quasi-Gaussian profile with a pulse duration of 16 ps (FWHM). Combining with the computer-aided deformable mirror, the fiber bundle laser homogenizer can realize the ideal ellipsoidal laser profile to suppress emittance growing due to the space charge effect.

INTRODUCTION

We have been developing a photo-cathode rf gun [1] as a highly qualified electron beam source to achieve future X-ray light sources (ERL (Energy Recovery Linac), FEL (Free Electron Laser), Compton back scattering, etc.) since 1996 in a test facility at the SPring-8 site. Future X-ray light sources will require an electron beam source with a low emittance of ~1π mm•mrad at a charge of more than 1 nC/bunch. Our development of this type of gun is oriented toward a long-lived stable system for user experiments. It is necessary for the copper cathode of an rf gun to have less damage illuminated by an UV-laser pulse with the pulse width of ~10 ps and the photon energy of ~4 eV.

When we started the construction of a test facility, there were two issues concerning the laser light source. One was the energy stability of the UV-laser light source. Generally, the stabilization of the system should be controlled first passively and then actively. However, we completed only the passive stabilization as for the laser system. The other was the spatial and temporal laser profiles. The quality of the laser beam is essential to the stabilization and the generation of a low-emittance electron beam.

The optimal spatial and temporal profiles of a shot-by-shot single laser pulse are essential in order to suppress the emittance growth of the electron beam emitted from a photo-cathode rf gun. This laser-shaping project has proceeded in two steps since the beginning in 2002. Specifically, higher stability of the pulse energy was required and homogeneous Silk-hat (cylindrical flattop) with spatial and rectangular temporal profiles of the UV-laser light source must have been generated.

In the first spatial shaping test run, we shaped the laser spatial profiles with the use of a microlens array. Consequently, the horizontal emittance was significantly improved from 6 to 2 π mm•mrad at a beam charge of 0.1 nC/bunch. The experimental data obtained represented a new record for the minimum emittance of an electron beam from a single-cell-cavity rf gun [2].

In the next test run, we applied both types of adaptive optics to automatically shape the spatial and temporal UV-laser profiles with a feedback routine simultaneously. We prepared a deformable mirror for spatial shaping and a spatial light modulator based on fused-silica plates for temporal shaping. Both adaptive optical elements were installed in the system.

We are also developing optical shaping and transport system of backward illumination system for transparent diamond cathode for industrial application with Hamamatsu Photonics K.K. We are responsible to develop Fourth harmonics generation (FHG: 197 nm) of

Ti:Sapphire laser as a light source for diamond cathode and its shaping techniques. The fiber bundle is a useful system to shape both spatial and temporal profiles. It is also ideal user-friendly laser transport from laser light source to the cathode. The operating wavelength of this fiber bundle (Ceram Optec Industries, Inc.) was tested between 197 and 1100 nm. At present, our developing FHG oscillates with pulse energy of 20 μJ/pulse after pulse shaping.

The development processes of our beam quality control systems are reviewed in the remainder of this paper.

LASER STATUS UNDER ENVIROMETAL CONTROL

Configuration of CPA - Ti: Sa Laser System

The UV-laser light source for the rf gun consists of a mirror-dispersion-controlled Ti: Sapphire laser oscillator (Femtolasers Produktions GmbH) operated at a repetition rate of 89.25 MHz, a chirped pulse amplification system (Thales Lasers Co., Ltd.) operated at a repetition rate of 10 Hz, and a third harmonic generator system. The fundamental laser oscillates at a central wavelength of 790 nm with a spectral bandwidth (FWHM (full-width at half maximum)) of 40~50 nm. This spectral bandwidth has a strong influence on the pulse duration after the compressor. If the BBO crystal thickness is not matched with the laser pulse duration, the laser spatial profile becomes worse (see the original worse laser profiles on the left-hand side in figure 5 and 7). The laser spatial profile at the optimized condition is homogeneous as shown on the left-hand side in Figure 1.

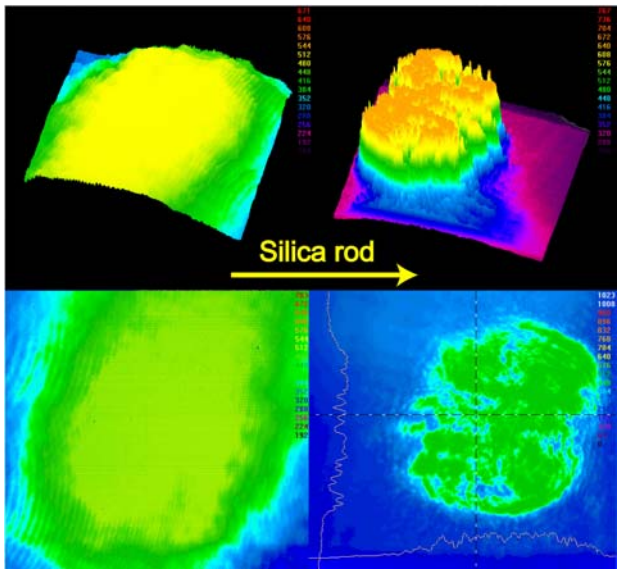

Figure 1: THG profiles before and after silica rod as a UV-pulse stretcher

In the following amplification system, the laser pulse is amplified up to 30 mJ/pulse after the multi-pass amplifier. And then, it is compressed down to 80 fs at the compressor to generate THG at the central wavelength of 263 nm. This UV-laser pulse is sent through a 45-cm silica rod. This silica rod is used as a UV-pulse stretcher from 80 fs to 10-ps region. The laser pulse energy through the silica rod is 850 μJ/pulse at maximum. Note that, its output pulse energy and pulse duration depend on the laser fluence at the entrance of the silica rod. It can stretch the pulse to 11-ps long at a fluence of 1.8 mJ/cm^2. However, due to the nonlinear process in the first few millimeters, some hot spot structures appear on the laser spatial profile (see on the right-hand side in figure 1). This nonlinear process is essential to broaden the spectral bandwidth. The spectral-broadened laser pulse is stretched with the dispersion of silica rod.

The best short-term pulse energy stability (rms) of the original laser system was 2% for the fundamental and 3% for the THG. However, the original THG stability was getting worse down to 10% (rms) in a few days after the best tuning. This original system could not keep the laser spatial profile homogeneous for long periods of operation, mainly due to tiny damage on dichromatic mirrors, mismatching between the compressed pulse duration and THG (BBO) crystal thickness, and misalignments in the compressor and THG sections.

Environmental control system for the laser

In principle, we planned only passive stabilization of the system. We considered environmental controls in the clean room to reduce optical damage accidents and constructed a new humidity-controlled clean room in 2003. Then we re-installed the total laser system in this room in 2004. The relative humidity of this new clean room at room temperature is in a region of 50~60% with a stability less than 2% (p-p).The temperature was kept constant at 21 ℃ (±0.3 ℃) on the laser table. Also, the laser pumping sources are stabilized with a temperature-controlled base plate. As a result, the short pulse energy stability of laser has been improved, with a reduction to 0.7~1.4% (rms; 10 pps; 33818 shots) at the THG (263 nm). This stability was held for one month continuously without any significant tuning since last 6 months. In this improvement we just passively stabilized the system.

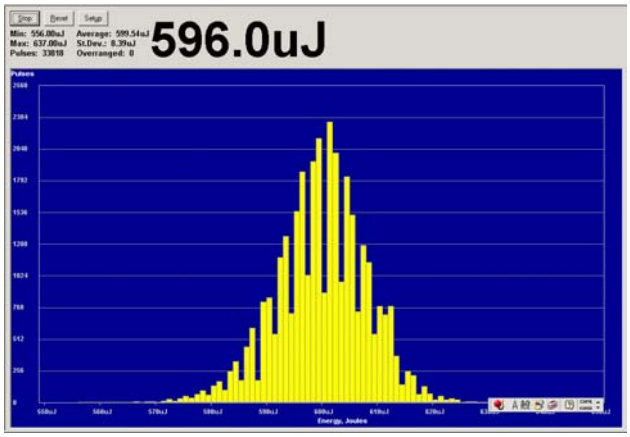

Figure 2: THG rms stability of 1.4 % for 33818 shots

At the present state of development, long-term stability within two months depends only on the stability

of mode locking at the oscillator laser. The continuous operation more than two months is limited by the lifetime of the flash lamp for the amplifiers. If the oscillator is stable without out-of-mode locking, the overall laser system can be stable for long-term operation with short pulse energy stability as mentioned above.

TESTED OPTICAL ELEMENTS FOR LASER-PROFILE SHAPING

Microlens array as a spatial homogenizer

We applied several microlens arrays (a single lens array) as a homogenizer for the first test run [2]. This microlens array is a collection of small hexagonal convex lenses with a pitch of 250 μm. The transmission of this optical array is about 80% in the ultraviolet region. This makes it possible to shape any laser spatial profile as a Silk-hat (cylindrical flattop) by combining with a convex lens. The main difficulty in utilizing this optical system is the manner in which the homogenized laser profile transports toward the cathode surface while focusing.

Deformable mirror and SLM as a 3D-shaping

Consequently, we used a deformable mirror (left upper in Figure 3) as a spatial shaper for the second test run. This deformable mirror consists of an aluminum-coated, multilayer silicon nitride membrane and 59 small hexagonal mirror-actuators behind the reflective membrane with a center-to-center distance between the actuators of 1.75 mm. The outermost layer of the reflective membrane is protected with an MgF_2 coating to keep reflectivity at about 70% in the ultraviolet region. Adjusting the voltages between the control electrodes on the boundary actuators performs fine adjustment of each mirror-actuator. The adjustable region of the control voltages is between 0 and 250 V with a step of 1 V. This makes it possible to shape any laser spatial profile with a total forming possibility of 250^{59}($\sim 10^{141}$). However, such a high adjustability makes manual as well as simple algorithm adjustment impossible. Thus, this spatial shaping method needs a sophisticated algorithm. One concept for a sophisticated program based on this genetic algorithm for a deformable mirror has been developed through a joint project [3].

To control the temporal parameters of the laser pulses, we are preparing a programmable pulse shaping system in the fundamental wavelength region using a spatial light modulator (SLM) based on fused-silica plates (Cyber Laser Inc.: right in Figure 3). The temporal profile is measured with a streak camera. We applied a simulated annealing algorithm to find optimal solution of each angle of fused-silica plates. Through the optimization of phase spectrum with changing angles of the plates, the SLM optimize the laser pulse shape.

We installed a deformable mirror and an SLM while developing a sophisticated program to examine the spatial and temporal shaping ability of inhomogeneous original UV-laser profiles.

Figure 3: Adaptive-optics complex for shaping both spatial and temporal laser profiles

Silica fiber bundle as a spatial homogenizer and pulse shaper

The fiber bundle is a practical system to shape both spatial and temporal profiles during laser pulse transportation. This method has big disadvantage to make ideal laser spot size on the cathode in realistic working distance for conventional cathode illumination. Therefore, we proposed this technique for just backward cathode illumination system. The fiber bundle with a diameter of 8 mm is a collection of 1300 small fiber strands with fused end (see in Figure 4).

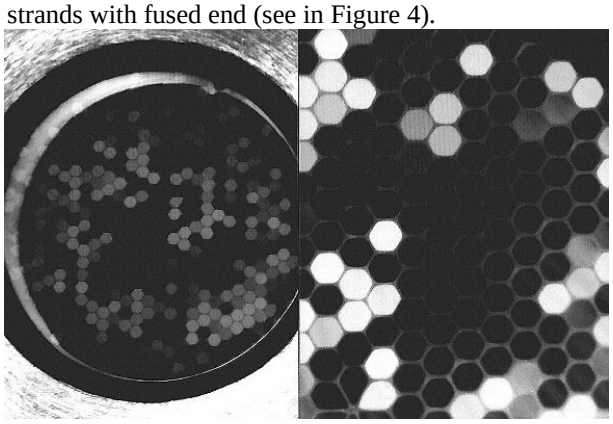

Figure 4: The fused surface structure of fiber bundle

EXPERIMENTAL RESULTS FOR SPATIAL SHAPING

Results and effects of spatial shaping with microlens array (in first test run)

The laser spatial profile without homogenization is shown on the left-hand side in Figure 5. The profile was spatially shaped by a microlens array as a quasi-Silk-hat profile (see the right-hand side of Figure 5). These profiles were measured with a laser beam profiler (Spiricon Inc., LBA300-PC). By spatially homogenizing, the emittance improved from 3.3 to 2.3 π mm•mrad at a beam charge of 0.1 nC/bunch. While it was not perfectly Silk-hat-shaped, laser profile was greatly improved.

However, many small spikes (hot spots) appear on the homogenized laser profile. Such spikes can be suppressed, if a double microlens array installed in the confocal configuration.

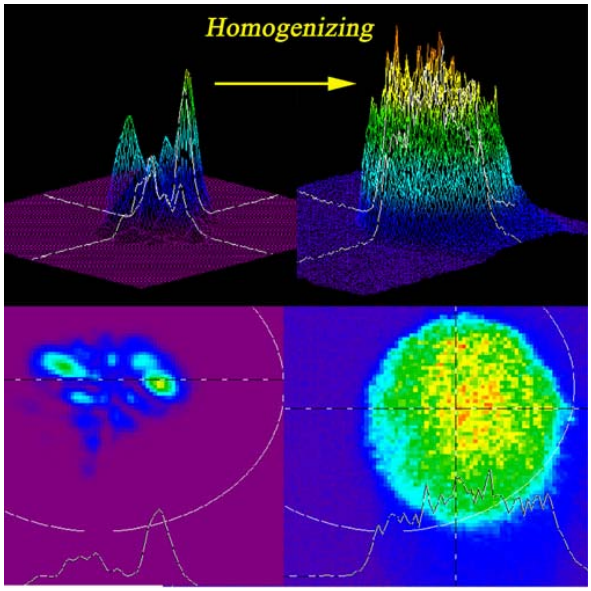

Figure 5: Homogenization results with microlens array

Result of spatial shaping with deformable mirror (in second test run)

Table 1: Set parameters and usages for fitting function to evaluate spatial profile optimization

Fitting function parameters for flattop shaping	
Beam Centre	Minimize differences from initial centre position (x, y)
THF [4]	Maximize Top Hat Factor (0~ 1) (Flattop: THF=1.0; Gaussian: THF=0.5)
Effective Area	Maximize integrated energy within set circle area
Effective Diameter	Minimize differences from diameter of set circle
Flatness	Minimize standard deviation divided by the average in a flattop area
Peak-to-peak	Minimize differences between max. and min. in a flattop area
Beam Diameter	Minimize differences from set diameter
Hot Spot (max.)	Minimize max. in a flattop area
Dark Spot (min.)	Maximize min. in a flattop area

The laser spatial profile was automatically optimized with self-developed genetic algorithms for a deformable mirror. We measured the profile with a laser profile monitor (Spiricon, Inc.: LBA300-PC) whose analyzing program can provide many parameters of beam profiles. We chose useful parameters to evaluate flattop profiles and made a fitting function for the developed genetic algorithm to optimize the profile toward an ideal flattop. These parameters for flattop shaping and their meaning are shown in Table 1. The value of this fitting function is returned as feedback to control the deformable mirror with the genetic algorithm.

As a result, the laser profile on the cathode surface was spatially shaped as a quasi-flattop profile (right-hand side of Figure 6). The laser spatial profile was drastically improved by this shaping technique. Note that, this shaping was successful thanks to our long-term stable UV-laser light source: This shaping technique is far from shot-by-shot beam quality control. It takes 2 hours to optimize the laser profiles.

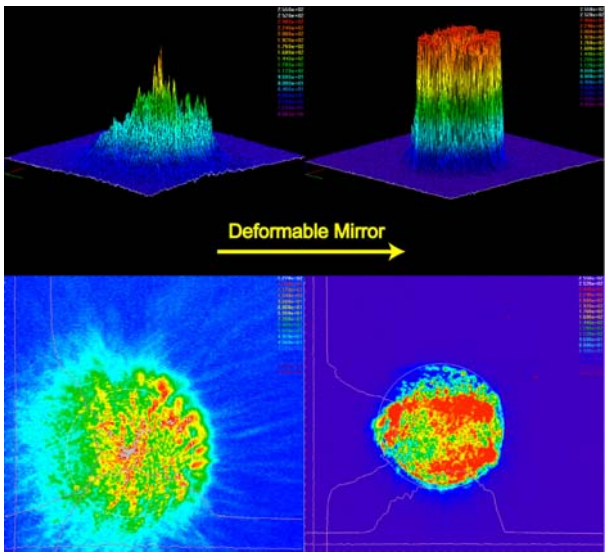

Figure 6: Spatial shaping result with a deformable mirror

Result of spatial and temporal shaping with fiber bundle for backward illumination

The laser spatial and temporal profile was shaped passively for the backward cathode illumination with a fiber bundle. The profile was spatially shaped with a 90-cm long fiber bundle as a perfectly homogeneous profile (see Figure 7).

This shaping technique is based on practically pulse stacking with 1300 different optical paths. The 80-fs laser is shaped as a homogenized profile with pulse duration of 16 ps (FWHM). This 16-ps pulse shape does not change down to the input laser pulse energy of 60 nJ/pulse (see Figure 8). This indicated that this pulse shaping (or stretching) is not base on nonlinear effect like silica rod. The pulse duration mainly depends on the length of the fiber bundle and mapping its fiber strands.

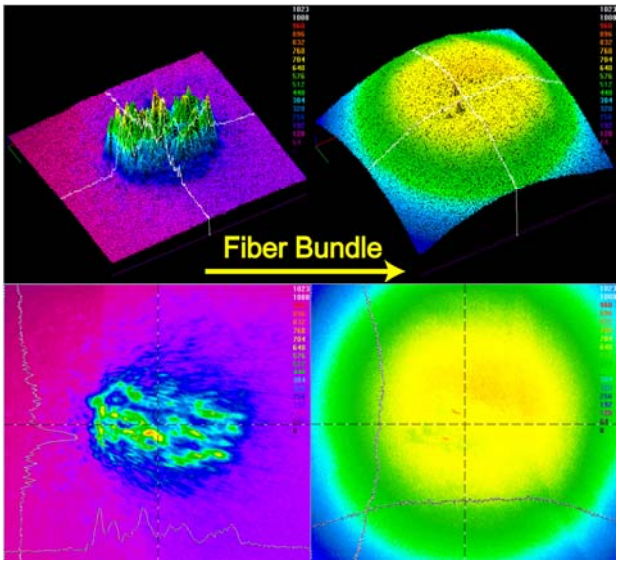

Figure 7: Homogenization results with fiber bundle

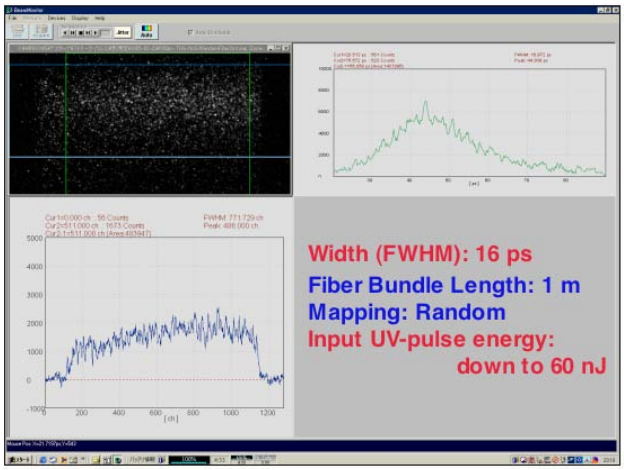

Figure 8: Pulse shaping results with fiber bundle

FUTURE PLANS AND DISCUSSION

Comparing the results of the spatial profiles among the different tested optical elements shown in Figures 5-7, we can see each of methods were successful. Especially, it seems to be no difficulty to generate Flattop or homogeneous profiles. However, recently another more ideal 3D-shape was proposed [5]. The proposed 3D-shape is an ellipsoidal with the equivalent fluence along the temporal axis. In this case, the microlens array or deformable mirror cannot realize this ellipsoidal. In the paper [5] pulse stacker is proposed for this solution. It makes possible to realize ellipsoidal beam pulse. However, it is not simple to adjust. The method with a fiber bundle is one of the solutions to avoid difficulty of adjustment of different optical paths. For shaping as ellipsoidal profile, it is necessary to combine the method with some adaptive optics to control the laser spatial distributions (see Figure 9). Automatic optimization with a deformable mirror can be helpful with genetic algorisms, if the ideal profile is within its searching area. Considering the response time of photocathode and reliable adjustability of optics, we do not have clear solution to generate this ideal ellipsoidal pulse.

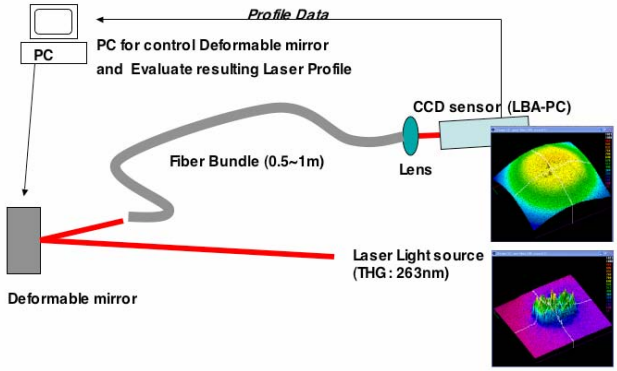

Figure 9: Closed control system for fiber bundle with computer-aided deformable mirror

For the shot-by-shot optimization of each laser pulse profiles, the laser system should be passively stabilized by environmental controls. At present, 1-hour pulse energy stability of the THG has been improved to 0.7~1.4%. This stability is sufficient for shot-by-shot automatic optimization with adaptive optics. For the test of long-term mode-locking stability, a new oscillator laser (Femtosource Synergy; Femtolasers Produktions GmbH) has been installed in our system since April 2005. As we tested, its mode-locking has been kept stable with the locked repetition rate of 89.25 MHz for one month. We are expecting that its stability be kept more than three months. Also, we are preparing the feedback system to control long-term drift due to the lifetime of the flash lamp.

In the future, we are applying the both adaptive optics to automatically optimize the electron beam bunch for lower emitance with a feedback routine. With this procedure, ideal electron beam profiles can be generated with compensation for some of the optical distortions and the inhomogeneous distribution of the quantum efficiency on the cathode surface. However, the phenomena related to laser incident on the cathode must be very important to make clear and should be carefully studied together with cathode surface physics.

ACKNOWLEDGEMENTS

Many companies have contributed towards the developing and understanding of long-term stability issues in our laser system and its reliable pulse shaping: All stuffs of Femtolasers Produktions GmbH, H. Jousselin (THALES LASER Co., Ltd.), K. Takasago (Cyber-Laser Inc.). Their contributions are gratefully acknowledged. The part of this work on developing spatial light modulator and FHG was supported by Advanced Compact Accelerator Development Project in Japan.

REFERENCES

[1] T. Taniuchi et al., Proc. of 18th. Int. Free Electron Laser Conf., Vol. 2, 137, Rome, 1996.
[2] H. Tomizawa et al., Proceedings of the 2002 European Particle Accelerator Conference, 1819, Paris, July 2002.
[3] T. Itatani, AIST Today, p. 18, April 2003.
[4] Operator's Manual, Model LBA PC Series, Version 2.50, Spiricon, Inc.: chapter 6.19 "Top Hat Factor."
[5] C. Limborg et al., Proc. of workshop ERL2005, March 2005, Newport News, to be published in NIM A.

APPLYING MULTISCALE METHODOLOGY TO BEAM SIMULATIONS *

B. Terzić†, Northern Illinois University, DeKalb, IL 60115, USA
I. V. Pogorelov, Lawrence Berkeley National Laboratory, Berkeley, CA 94720, USA

Abstract

We report on a successful implementation of a wavelet-based Poisson solver for use in 3D particle-in-cell (PIC) simulations. The solver harnesses advantages afforded by the wavelet formulation, such as sparsity of operators and data sets, existence of effective preconditioners, and the ability simultaneously to remove numerical noise and further compress relevant data sets. Having tested our method as a stand-alone solver on two model problems, we merged it into IMPACT-T to obtain a fully functional serial PIC code. We present and discuss preliminary results of application of the new code to the modeling of the Fermilab/NICADD and AES/JLab photoinjectors.

INTRODUCTION AND MOTIVATION

PIC simulations are widely used in large-scale computational modeling in application fields as diverse as accelerator physics, galactic dynamics, plasma physics, and solid state device design. The PIC method [1] models the multiparticle dynamics of the system by tracking a set of tracer particles that sample the initial phase-space distribution function of the system. In quasi-static approximation, where the dynamics is modeled as the solution of the Vlasov-Poisson system of equations, the efficiency of the self-consistent inter-particle force calculation can be increased significantly by depositing the charge/mass distribution onto a computational grid, and solving the field equation on the grid. In accelerator physics applications, it is important that the on-grid Poisson solver used in PIC modeling be able to satisfy the following requirements:

1. account for *multiscale dynamics*, because even the fluctuations on smallest scales can lead to global instabilities and fine-scale structure formation, as exemplified by halo formation and microbunching instability observed in beam dynamics experiments [2, 3],

2. *minimize the numerical noise* due to the fact that the number of particles used to sample the phase-space distribution function in the N-body simulation is several orders of magnitude smaller than the number of particles in the physical system which is being modeled, and

3. be as *efficient* as possible in terms of computational speed and storage requirements, without compromising accuracy.

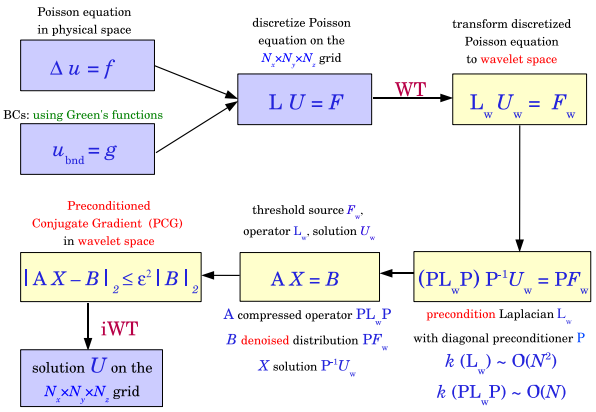

Figure 1: Flow-chart outline of the wavelet-based Poisson solver using (constrained) preconditioned conjugate gradient (PCG) method. The gray boxes represent the wavelet space; the physical space is in white. Constraining the PCG method is applied in the bottom middle box.

DESCRIPTION OF THE SOLVER

We have built on earlier work of Beylkin and co-workers [4, 5, 6] to design and implement an iterative algorithm for solving the Poisson equation in three dimensions on the grid, subject to general (inhomogeneous) Dirichlet boundary conditions. A combination of three circumstances makes iterative solver particularly attractive in the current setting: Firstly, the Laplacian operator remains sparse in a wide variety of wavelet bases. Secondly, preconditioners for the Laplacian exist that are effectively diagonal in a wavelet basis. Finally, the fact that the Poisson equation has to be solved repeatedly, with the source term not changing significantly from one timestep to the next, simplifies to some extent the choice of the initial approximation (one can, *e.g.*, use the potential computed on the previous timestep as the initial approximation for the present-time potential).

The flow chart in Figure 1 provides a summary of the algorithm. One begins by introducing a rectangular computational grid that envelopes tightly the density distribution, and whose boundaries may or may not coincide with the physical boundaries of the system on which the boundary conditions are specified. After computing the potential on the surface of the computational grid, one performs a

* Work of B.T. is supported by Air Force contract FA9471-040C-0199. Work of I.V.P. is supported by the U.S. Department of Energy contract DE-AC03-76SF00098.
† bterzic@nicadd.niu.edu

Fast Discrete Wavelet Transform (FDWT) [7] on the source term and the Laplacian operator, solves the Poisson equation in the wavelet space, and performs the inverse FDWT to recover the on-grid potential in the physical (configuration) space. We now proceed to describe the boundary condition implementation in one important special case, and present the basic details of the preconditioned conjugate gradient (PCG) algorithm that forms the core of our solver.

Implementation of Boundary Conditions

A (Dirichlet) boundary condition often encountered in practice with beam dynamics simulations is that of the zero potential on the walls of an infinite pipe of rectangular cross-section, with open BCs in the longitudinal (z) direction. The Green's function for such BCs is analytically known, so that the corresponding potential can be found by solving the set of equations

$$\rho^{lm}(z) = \frac{4}{ab}\int_0^a\int_0^b \rho(x,y,z)\sin(\alpha_l x)\sin(\beta_m y)dydx, \tag{1}$$

$$\frac{\partial^2\phi^{lm}(z)}{\partial z^2} \quad {}^{2}_{lm}\phi^{lm}(z) = \quad \frac{\rho^{lm}(z)}{{}_0}, \tag{2}$$

$$\phi(x,y,z) = \sum_{l=1}^{N_x}\sum_{l=1}^{N_x}\phi^{lm}(z)\sin(\alpha_l x)\sin(\beta_m y), \tag{3}$$

where ρ is the charge distribution, ϕ is the potential, $\alpha_l = l \ /a$, $\beta_m = m \ /b$, ${}^{2}_{lm} = \alpha_l^2 + \beta_m^2$, ${}_0$ is the permittivity of vacuum and the geometry of the pipe is given by $0 \quad x \quad a$ and $0 \quad y \quad b$ [8, 9]. Eq. (3) is evaluated only on the surface of the computational grid, and for the predefined number of expansion coefficients N_x and N_y.

Preconditioned Conjugate Gradient

The 3D Laplacian is a sparse, positive definite operator. The same holds true of the wavelet-decomposed Laplacian, assuming that one applies to it a thresholding procedure whereby all coefficients with magnitudes below a user-specified threshold are set equal to zero. In this setting, a conjugate gradient (CG) algorithm [10] provides an efficient way to invert the operator, the convergence rate depending on the condition number κ [10] as

$$\left|U \quad U^i\right|_2 \quad \left(\frac{\sqrt{\kappa} \quad 1}{\sqrt{\kappa}+1}\right)^i |U|_2 \,. \tag{4}$$

A major advantage of working in a wavelet basis is the existence of a diagonal preconditioner (first reported in [4] for the case of periodic BCs) that lowers κ from $O(N^2)$ to $O(N)$. Our preconditioned conjugate gradient (PCG) algorithm is a combination of the operator formulation of the CG method with a wavelet-basis preconditioner.

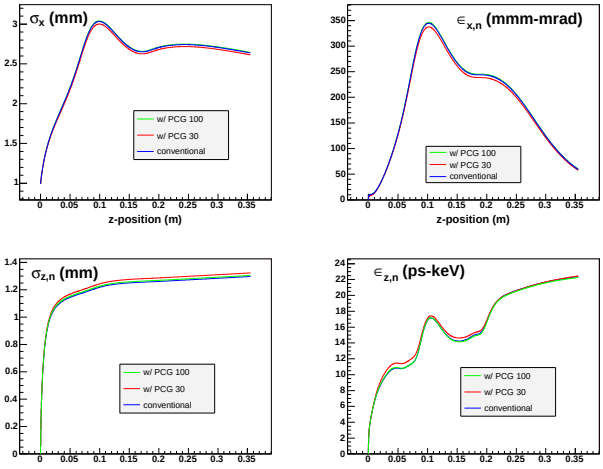

Figure 2: Comparison of conventional IMPACT-T (blue lines), IMPACT-T with PCG and $N_x = N_y = 30$ expansion coefficients (red lines) and IMPACT-T with PCG and with $N_x = N_y = 100$ expansion coefficients (green lines) for the Fermilab/NICADD photoinjector (bunch charge of 1 nC).

Denoising by Wavelet Thresholding

The thresholding operation performed both on operators and potential/density data sets is the simplest possible way to effect simultaneous compression and denoising. After transforming the noisy charge distribution into wavelet space, the signal (physical component) is generally represented by a smaller number of large coefficients, while the numerical noise is largely mapped to many small wavelet coefficients. Wavelet thresholding is a process whereby the contribution of the wavelet coefficients deemed to represent noise is eliminated. Simply, the wavelet coefficients whose magnitudes are below a certain noise threshold T are set to zero. The noise threshold T must be chosen carefully, avoiding two extremal perils: on one end, over-smoothing the distribution in case the threshold T is overestimated, and on the other, not removing enough unphysical small-scale oscillations due to noise in case it is underestimated. Correctly gauging the threshold T requires a thorough and systematic investigation of the nature of numerical noise in particle-in-cell simulations, which is currently underway.

Virtually all studies of efficient wavelet-based denoising discussed in literature has been on data sets contaminated by gaussian noise. Our preliminary results indicate that the noise in PIC simulations is poissonian, which appreciably reduces effectiveness of denoising by simple wavelet thresholding. We are presently working on augmenting the simple wavelet thresholding with data transformations which would enable more clear delineation of noise and signal.

The details of this important aspect of the algorithm will be reported in a future publication.

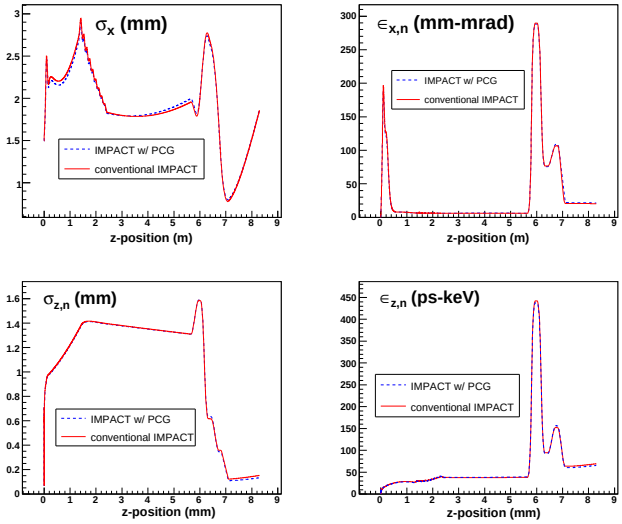

Figure 3: Comparison of conventional IMPACT-T (solid red lines), IMPACT-T with PCG and $N_x = N_y = 30$ expansion coefficients (dashed blue lines) for the Fermilab/NICADD photoinjector with a bunch compressor at $z = 5.65$ (bunch charge of 1 nC).

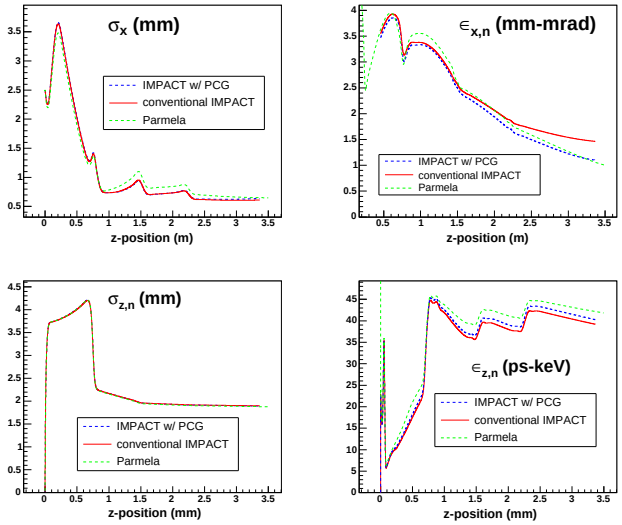

Figure 4: Comparison of conventional IMPACT-T (solid red lines), IMPACT-T with PCG and $N_x = N_y = 30$ expansion coefficients (dashed blue lines) and Parmela (dashed green lines) for the AES/JLab low-charge photoinjector (bunch charge of 133 pC).

PHOTOINJECTOR SIMULATIONS

Having tested the solver in the stand-alone mode on two three-dimensional test density distributions, one mimicking a charged particle beam and the other a galaxy [14], we have merged it into the IMPACT-T [8, 9] PIC code (replacing IMPACT-T's standard Poisson solver based on the use of Green's functions and the FFTs). Figures 2, 3 and 4 present the results of simulations performed using IMPACT-T with the "native" solver and IMPACT-T with the new PCG solver. Figure 2 shows a standard set of rms diagnostics computed in a 200000-particle simulation of the Fermilab/NICADD photoinjector when electron transverse distribution is highly non-uniform. In this case, only true 3D algorithms, such as the one we discuss here, should be used. Figure 3 shows the same set of rms diagnostics for the Fermilab/NICADD photoinjector with uniform distribution and a bunch compressor; it is evident that when the effects of space charge are amplified by bunch compression, the agreement between the two codes is exceptional. Figure 4 shows the same set of rms diagnostics as in Figures 2 and 3 for the AES/JLab photoinjector [11] for a uniform transverse distribution. The agreement among the results is clearly quite good. Going beyond the rms characterization of dynamics, Figure 4 illustrates the level of agreement in resolving the fine-scale structure of the charge density distribution; the latter was computed in simulations of the AES/JLab photoinjector performed with 200000 simulation particles with non-uniform transverse initial distribution. As for the computational efficiency of the new solver, in serial simulations, IMPACT-T with PCG is about 20% *faster* than the conventional IMPACT-T (the exact ratio depending on the total simulation length).

CONCLUSIONS

A new, wavelet-based 3D solver for the Poisson equation subject to general (inhomogeneous) Dirichlet boundary conditions has been implemented and successfully integrated into IMPACT-T. The solver is based on the operator formulation of the preconditioned conjugate gradient method. It takes full advantage of sparsity of wavelet-decomposed and compressed operators and data sets, existence of efficient (diagonal) preconditioners in wavelet bases, and recursive nature of the PIC method. Compact (compressed) representation of the charge distribution and potential afforded by wavelet thresholding can be used for efficient storage of the time-dependent density and potential. This should facilitate notoriously difficult simulations such as the influence of coherent synchrotron radiation in magnetic bends and halo formation. The former requires integration over the history of the density to evaluate the retarded potential [12], and the latter involves integrating a large population of test particles in the time-dependent potential to provide a statistically meaningful population of the tails of the distribution [13].

The new solver has been tested using standard IMPACT-T simulation results as a benchmark, and subsequently used in modeling the Fermilab/NICADD and AES/JLab photoinjectors. To our knowledge, work reported here and in [14] constitutes the first application of a three-dimensional wavelet-based multiscale methodology to beam dynamics simulations.

REFERENCES

[1] R. Hockney and J. Eastwood, "Computer Simulations Using Particles", Institute of Physics Publishing, London (1988).

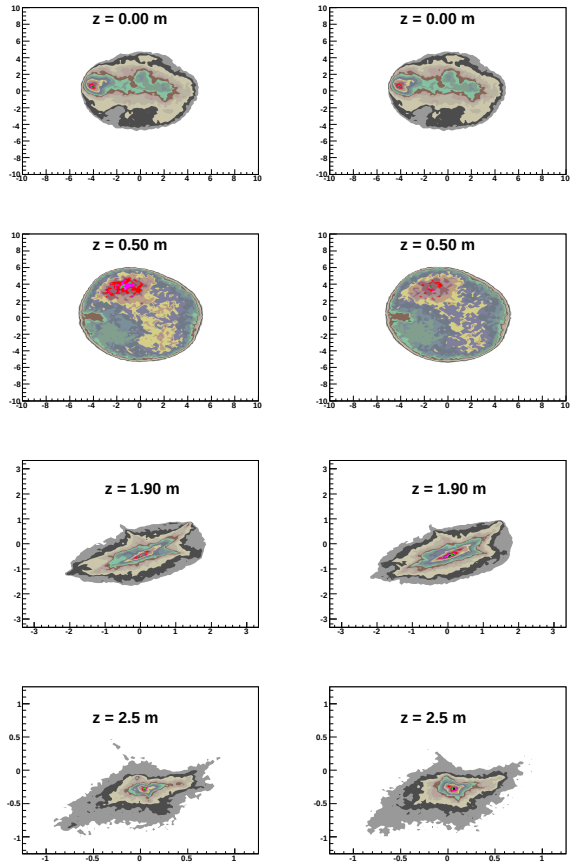

Figure 5: Comparison of IMPACT-T (left column) and IMPACT-T with PCG (right column) for transverse distributions at different z-locations along the AES/JLab low-charge photoinjector (bunch charge of 133 pC).

[2] C. L. Bohn and I. V. Sideris, Phys. Rev. Lett., 89 (2003), 214802.

[3] J. Qiang, R. D. Ryne and I. Hofmann, Phys. Rev. Lett., 92 (2004), 174801.

[4] G. Beylkin, In "Wavelets: Mathematics and Applications", eds. J. Benedetto and M. Frazier, CRC Press LLC, Boca Raton, Florida, 1993.

[5] A. Averbuch, G. Beylkin, R. Coifman, P. Fischer and M. Israeli, http://www.cs.tau.ac.il/∼amir1/PS/poisson.pdf

[6] A. Averbuch, G. Beylkin, R. Coifman, P. Fischer, M. Israeli, In "Signal and Image Representation in Combined Spaces", eds. Y. Zeevi and R. Coifman, Academic Press, San Diego, 1998.

[7] I. Daubechies, "Ten Lectures on Wavelets", SIAM, Philadelphia, 1992.

[8] J. Qiang, R. D. Ryne, S. Habib and V. Decyk, J. Comp. Phys., 163 (2000), 434.

[9] J. Qiang and R. D. Ryne, Comp. Phys. Comm., 138 (2001), 18.

[10] G. H. Golub and C. F. Van Loan, "Matrix Computation", The Johns Hopkins Press, Baltimore and London (1996).

[11] A. Todd et al., In Proc. 2003 Part. Accel. Conf., IEEE Cat. No. 03CH37423, 977 (2003).

[12] C. L. Bohn, AIP Conference Proceedings, 647 (2002), 81

[13] I. V. Sideris and C. L. Bohn, Phys. Rev. ST Accel. Beams 7 (2004), 104202

[14] B. Terzić and I. V. Pogorelov, Ann. of New York Acad. of Sci., 1045 (2005), 55.

SUPERLATTICE NEA PHOTOCATHODE AND GUN TECHNOLOGY DEVELOPED FOR HIGH POLARIZATION AND LOW EMITTANCE ELECTRON BEAM

Tsutomu Nakanishi*, Department of Physics, Nagoya University, Nagoya 464-8602, Japan

Abstract

The performance required for PES (Polarized Electron Source) is dependent on variety of accelerators and physics experiments. Usually following items are included; 1) high polarization, 2) high quantum efficiency, 3) high peak current for a pulse beam, 4) high average current for a CW beam, 5) sub-nanosecond multi-bunch structure for a future ILC (international linear collider) beam, 6) long cathode-lifetime and 7) low beam emittance. Here, technologies developed to improve these performances are briefly reviewed. In addition, further applications of NEA-GaAs photocathode gun, such as ERL (Energy Recovery Linac) or SPLEEM (Spin Polarized Low Energy Electron Microscopy) are discussed.

1. INTRODUCTION

Nowadays, polarized electron beam has been widely used for various spin physics experiments at many electron accelerator laboratories, and the GaAs-PES is considered as an unique solution to satisfy requirement of high energy accelerators. It is based on a combination of two physical mechanisms, a) polarization mechanism; optical pumping of VB (Valence Band) electrons by circular photons to CB (Conduction Band) and b) emission mechanism; NEA (Negative Electron Affinity) surface enables the CB electrons to tunnel into vacuum through a thin potential-barrier, as shown in Fig. 1, where the GaAs-GaAsP strained superlattice is used as a photo-cathode.

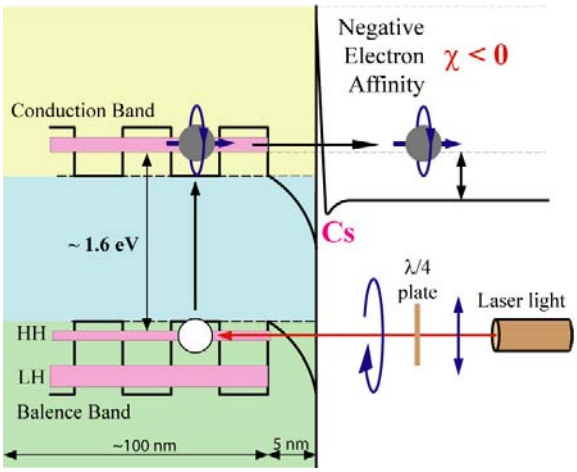

Fig. 1: Polarization and emission mechanisms of GaAs-PES with superlattice photocathode

* nakanisi@spin.phys.nagoya-u.ac.jp

A GaAs type photo-emitter consists of a thin crystal layer (thickness ≈100nm) with special microstructure and a thin NEA surface layer (thickness ≈5nm). Various physical processes in both layers affect on to PES performances. In fact, various procedures which can control these phenomena to make fit to our purpose have been developed so far, and following performances were achieved; (1) high polarization ≥85% with high QE (Quantum Efficiency) ≥0.5%, (2) high peak current (≥ 10A), (3) high average current for ERL(≥ 0.5mA), (5) long lifetime (≥several weeks) and (6) sub-ns multi-bunch beam for ILC.

However, more PES R/D works are still required to achieve better performances for future PES applications. For example, it is not yet successful to produce a ultra-short pulse beam with high charge (10ps, @1nC/bunch) or a low emittance beam with high charge (for example, $\leq 1 \times 10^{-6}$μm/mm-radius @1nC/bunch). In this report, successful achievements are briefly summarized and further problems are discussed.

2. HIGH POLARIZATION PHOTOCATHODE

In order to produce the highest polarized electrons, degeneracy between heavy-hole and light-hole band of semiconductor must be removed, and the laser wavelength must be tuned to the band-gap energy (≈1.5eV at room temperature) so that only the heavy-hole band can be excited. The strained GaAs layer [1] or InGaAs-AlGaAs superlattice [2] has provided such highly polarized (≥80%) electron beam for the current electron accelerators. The GaAs-GaAsP superlattice photocathode has been also developed from 2000 at Nagoya [3][4][5], and high polarization (≥85%) and high QE (≥0.5%) are simultaneously obtained at 780nm laser wavelength

3. LIFE TIME PROBLEM OF NEA PHOTOEMITTER

For the reliable PES operation, NEA-surface-state must be kept in good condition for long time. The electron affinity of bulk GaAs crystal is positive ($\chi \approx 4.0$eV), and two techniques are used to pull down the vacuum energy level so that χ becomes negative; (1) heavily p-doping bends the surface band level downward by 0.5eV, and (2) Cs and oxygen deposition to GaAs surface enable to form the Ga(+)-Cs(−) dipole layer. Then electron affinity of surface state changes from positive ($\chi \approx 3.5$eV) to negative ($\chi \approx -0.3$eV). In fact, the NEA state is realized by a few mono-layers of Ga(+)-Cs(-) dipoles at surface, it is easily destroyed by (1) adsorption of impurity atoms

and (2) back-bombardment of positive ions produced by collision of electron beam itself with residual gas molecules, as shown in Fig. 3. For higher average current machine like ERL, the damage due to ion back-bombardment becomes dominant and determines the lifetime. However, it is remarked that this damage can be recovered by making refresh surface and reactivating by Cs and oxygen.

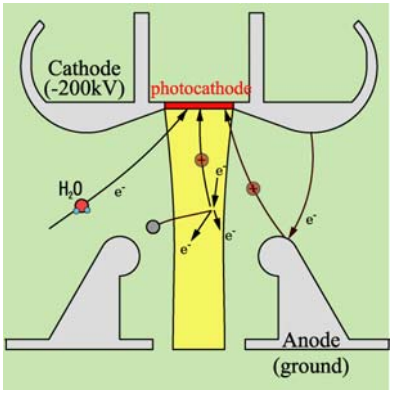

Fig. 2: Degradation of NEA surface caused by various processes

The solution for this NEA problem is unique, keeping the photocathode in extremely good UHV (Ultra-High-Vacuum) chamber, where the vacuum pressure is as good as 10^{-11}–10^{-12} torr. In addition, gas molecules, ions and X rays produced by the field emission dark current between HV electrodes must be also negligibly small (total dark current ≤10nA). The dark current problem is described later in section 6.

4. SURFACE-CHARGE-LIMIT EFFECT

It becomes well known that the maximum limit of current density emitted from NEA-GaAs surface is determined not by space-charge limit effect, but by so called SCL (Surface-Charge-Limit) effect. The tunnelling probability for CB electrons through NEA-surface-barrier into vacuum is usually not higher than 10−20%, and a sizable number of electrons are temporary trapped in the band bending (BB) region. This surface-charge causes temporal decrease of the BB magnitude, and it results in decrease of electron current amplitude. This degraded BB magnitude comes back soon to the initial magnitude, since the trapped electrons annihilate by recombination with the VB holes. The SCL effect becomes significant if the accumulation rate of surface-charge becomes faster than the annihilation rate, because the decrease of BB magnitude is maintained for long time. Such phenomena can be observed clearly in multi-bunch beam generation (for ILC) as shown in Fig. 4(a), where the second-bunch charge is much smaller than that of the first bunch [6].

Two kinds of solution were found to relax the SCL effect. One is to make the BB region narrower by heavily p-doping ($\geq 10^{19}$/cc) so that the VB-holes can recombine faster with surface CB electrons. Another is to use the NEA photocathode with superlattice structure such as GaAs-GaAsP combination.

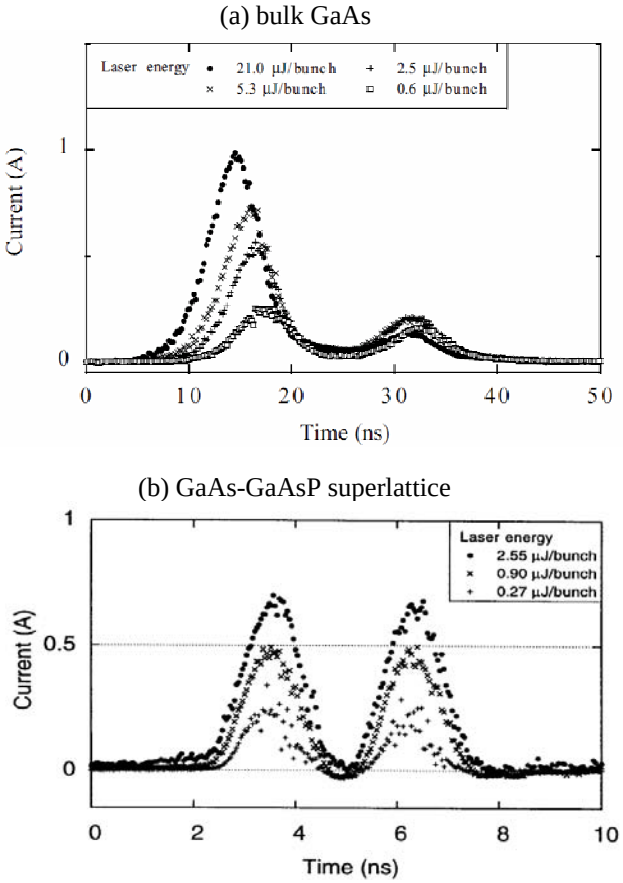

Fig. 4: Time profile of double-bunch electron beam produced by two different photocathodes

For the superlattice structure, the energy level of CB-electrons in GaAs layer shifts upward and that of VB-holes shifts downward in comparison with the original CB and VB energy levels of bulk GaAs. The former CB level shift can increase the escape probability into vacuum and decrease the surface-charge accumulation rate and the latter VB level shift can increase the recombination rate with holes, as shown in Fig. 5.

Our data of Fig. 4(b) shows the SCL effect can be overcome for **ILC** condition which corresponds to peak current density of $\approx 10^5 A/m^2$, but SCL problem will revival if the peak current density exceeds this value.

The decrease of BB magnitude could be observed by another approach using core-level photoelectron spectroscopy in combination with synchrotron radiation and a laser at Okazaki. In this case, the surface photo-voltage (SPV) can be estimated by the energy shift of the As-3d or Ga-3d core-level photoelectron spectra, and the shifts for GaAs-GaAsP superlattice are much smaller than those for bulk-GaAs. The time dependence of SPV were also observed and it shows that the SPV decays much faster for superlattice than for bulk-GaAs. It again demonstrated the advantage of superlattice photocathode [7].

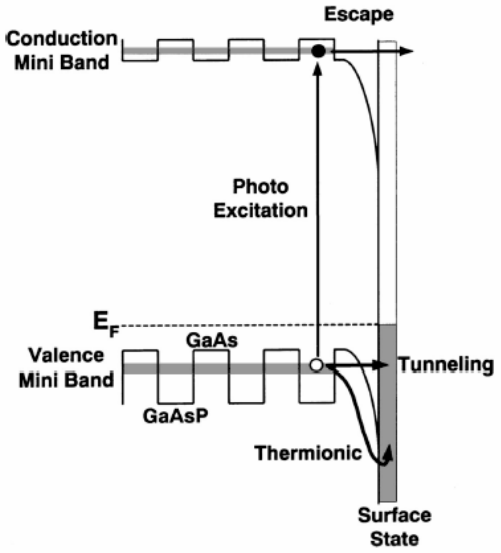

Fig. 5: Tunnelling of CB electrons into vacuum and recombination of trapped electrons with VB holes at BB region in superlattice photocathode

5. LOW EMITTANCE BEAM BY NEA-PHOTOEMITTER

The thermal emittance (ε_{th}) is defined as the mean transverse momentum of electrons emitted from the cathode surface multiplied by source radius. Although it is not easy to measure ε_{th}, Heidelberg group measured the mean transverse energy (MTE) as a function of mean longitudinal energy (MLE) for electrons emitted from NEA-GaAs surface [8], as shown in Fig. 6.

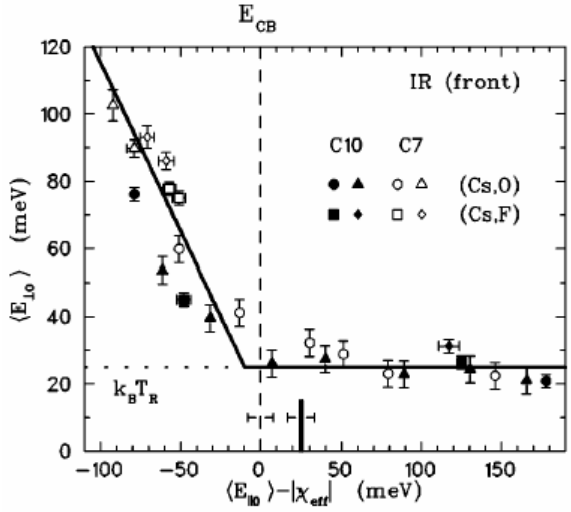

Fig. 6: Mean transverse energy as a function of longitudinal energy of emitted electrons from the NEA-GaAs photocathode (from Heidelberg data)

This data shows clearly that the MTE is nearly constant (≈25meV, similar to the lattice temperature) for a very small numbers of hot (higher energy) electrons which undergo no scattering in BB region. On the other hand, the MTE becomes slightly higher for a large number of low-energy electrons that undergo the scatterings in BB region but finally can escape into vacuum through the NEA surface. Using this MTE value, the ε_{th} can is estimated to be 0.1×10^{-6}m/mm-radius by a formula (r/2) $\times\sqrt{}$ (kTe/mc^2). This emittance value is really small, compared with those of other electron sources with metal or Cs-Te cathode, and demonstrated that the NEA-cathode will be useful to produce the low emittance beam.

However, the overall source-emittance depends also on the space charge effect inside the gun chamber, the sufficiently high field gradient is required for the gun to keep the small value of ε_{th}.

6. REDUCTION OF DARK CURRENT OF HIGH-GRADIENT ELECTRODE

In order to obtain the small source-emittance by reducing the space charge effect, high gradient field must be applied to cathode surface. On the other hand, the dark current between the electrodes must be still low level (below 10nA) for such high field gradient (≥3.0MV/m) to preserve the quality of NEA surface. The properties of dark currents from SUS (stainless steel), Cu, Mo and Ti electrodes were studied at KEK by changing gap-separation and applied voltage [9][10].

The result shows Mo and Ti are much better materials than stainless-steel or copper. In general, dark current consists of two components; (1) primary field emission current from cathode described by Fowler-Nordheim formula and (2) enhanced current initiated by anode bombardment of primary electrons. The primary field emission can be separated from total dark current by using its gap-separation dependence, and it is confirmed that Mo is favourable material for cathode due to low field emission, and Ti is same for anode due to small enhancement effect. In Fig. 7, the behaviour of dark current from Mo-cathode and Ti-anode is shown in comparison with those of Ti-Ti and Mo-Mo electrodes, where the highest field cathode area is 7mm2. The dark current is suppressed below 1nA level up to 130MV/m for the Mo-Ti electrode and this information seems useful for design of high field gradient gun.

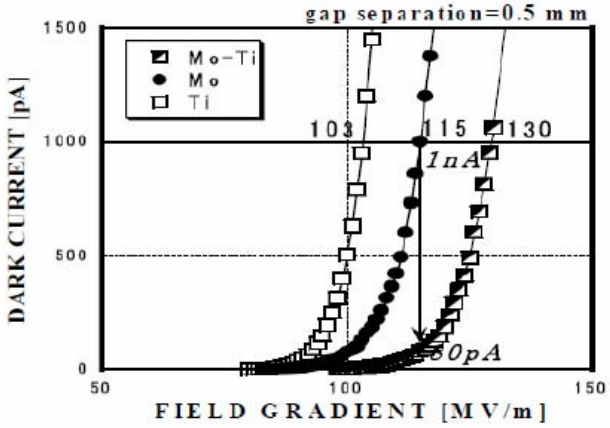

Fig. 7: Comparison of dark-currents from Ti-Ti, Mo-Mo, and Mo-Ti electrodes.

7. HIGH-GRADIENT POLARIZED/UNPOLARIZED DC-GUN

As a proto-type gun to obtain the small source-emittance, a 200keV polarized gun with cathode surface voltage of 3.0MV/m (cf. 1.8MV/m for SLC gun [11]) has been developed at Nagoya. The gun system consists of three chambers (gun, activation and loading) and a cathode pad is transferred using by two load-lock systems, as shown in Fig. 8 [12].

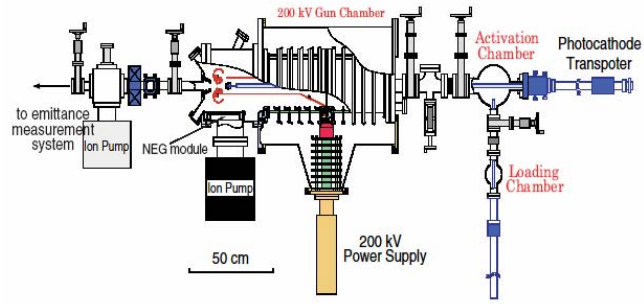

Fig. 8: A schematic view of 200keV polarized electron gun assembly

The loading chamber has a function of atomic hydrogen cleaning of GaAs surface. The dark current could be suppressed below 1nA at the bias voltage of 200kV, by using the clean stainless-steel electrodes. The normalized source-emittance of this gun is simulated to be 13×10^{-6} m for following conditions; laser irradiated photocathode diameter of 18mm, bunch-charge of 5nC and bunch width of 0.7ns by using GPT (General Particle Tracer) code [13]. This performance satisfies the ILC emittance requirement.

Although it is not the polarized gun, a more ambitious high gradient DC-gun with NEA-GaAs photocathode having a bias voltage more than 500kV is considered to be necessary for future ERL projects and its design work is started at Cornell-JLAB, JAEA-KEK-Nagoya etc. The source-emittance of ERL is an order of 0.1×10^{-6} m for average beam current more than 1mA.

8. MICROMETER- OR NANOMETER-SIZED POLARIZED BEAM FOR ELECTRON MICROSCOPE

The LEEM (low energy electron microscopy) apparatus has been making an important role for real-time observation of surface metallic-film-formation with space-resolution of 10nm. E. Bauer group made the pioneer works in this field, and they developed also SPLEEM (spin LEEM) to observe magnetic domain formation using the NEA-GaAs photo-emitter [14]. However, the brightness of present PES is not enough for the real-time SPLEEM observation. The main reason is that laser spot size at photocathode can not be smaller than 100μm due to present geometry of optical lens system.

In order to overcome this limitation, a pyramidal shaped GaAs photo-emitter shown in Fig. 9 was developed at Nagoya [15]. The high field gradient due to sharp tip radius (≈25nm) enables field emission of CB electrons through poor NEA or slightly positive electron affinity (PEA) GaAs surface.

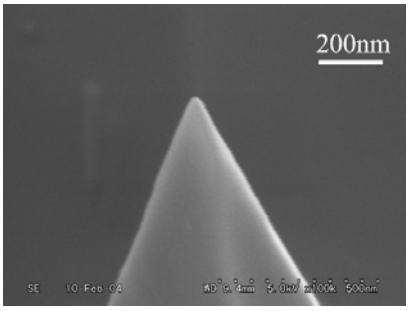

Fig.9: Pyramidal shaped GaAs fabricated by anisotropic wet etching in H_3PO_4 solutions

In fact, the extracted current shows Fowler-Nordheim behaviour and the observed polarization degree is similar to that of bulk-GaAs for band gap energy excitation, but slightly higher for higher photon energy region (≥1.6eV) where field emission mechanism becomes dominant, as shown in Fig. 10. The field gradient of GaAs-head was estimated to be 2.9MV/m for this experiment.

The problem of this naïve tip-GaAs photocathode is that the current/tip is limited below 0.1μA due to melt-down of the tip-head by self Joule-heating. Further improvement is required and new method must be also pursued to overcome this difficulty.

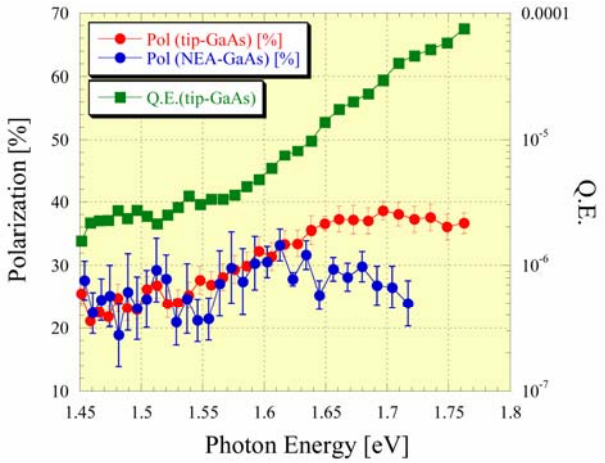

Fig.10: Polarization and quantum efficiency spectra for pyramidal shaped GaAs compared with polarization data of standard NEA-GaAs photocathode

9. CONCLUSIONS

Various special technologies have been developed to obtain the best performances of polarized NEA-GaAs photo-emitter, such as polarization, QE, NEA-lifetime, resistance against surface-charge effect and source-emittance. In parallel, the deep understandings for the complex physical phenomena arise inside and surface region of NEA cathode have been accumulated. At moment, R/D of polarized electron gun-system that can

produce low emittance beam with current density of an order of $10^5 A/m^2$ is urgently required from ILC, ERL and SPLEEM, where current limit phenomena due to not only space charge, but also surface charge become dominant. Therefore it must be remarked that the efforts to find the best solution against surface charge limit effect is still challenging and must be continued.

The author thanks to S. Okumi, M. Yamamoto, M. Kuwahara, N. Yamamoto of Nagoya University, F. Furuta, H. Matsumoto, M. Yoshioka of KEK and K. Togawa of RIKEN for PES collaboration works. This work is partially supported by Grants-in-Aid (Nos. 15204019) from the Ministry of Education, Science and Technology.

REFERENCES

[1] T. Nakanishi et al., Phys. Lett. A158 (1991) 345
[2] S. Nakamura et al, N.I.M. A411 (1998) 93
[3] T. Nakanishi et al., N.I.M. A455 (2000) 109
[4] T. Saka et al., Surface Science 454-456 (2000) 1042
[5] T. Nishitani et al., Journal of Applied Physics 97 (2005), 094907
[6] K. Togawa et al. N.I.M. A414 (1998) 431
[7] S. Tanaka et al., Journal of Applied Physics 95 (2004) 551
[8] S. Pastuszka et al., Journal of Applied Physics, 88 (2000) 6788
[9] C. Suzuki et al., N.I.M. A462 (2001) 337
[10] F. Furuta et al., N.I.M. A538（2005）33
[11] R. Alley et al., N.I.M. A365 (1995) 1
[12] T. Nakanishi et al., “Polarized Electron Source”, in “JLC-1”, KEK-Report 97-1(1997)
[13] M. Yamamoto, private communication
[14] K. L. Man et al., Phys. Rev. B67 (2003) 184402
[15] M. Kuwahara et al., to be submitted for J. of Japanese Applied Physics

RF GUNS FOR GENERATION OF POLARIZED ELECTRON BEAMS*

J. E. Clendenin#, A. Brachmann, D. H. Dowell, E. L. Garwin, K. Ioakeimidi, R. E. Kirby,
T. Maruyama, C. Y. Prescott, SLAC, Menlo Park, CA 94025, U.S.A.
R. Prepost, U. Wisconsin, Madison, WI 53706, U.S.A.

Abstract

Several accelerators, including the SLC, JLAB, Mainz, Bates/MIT, and Bonn have successfully operated for medium and high energy physics experiments using polarized electron beams generated by dc-biased guns employing GaAs photocathodes. Since these guns have all used a bias on the order of 100 kV, the longitudinal emittance of the extracted bunch is rather poor. Downstream rf bunching systems increase the transverse emittance. An rf gun with a GaAs photocathode would eliminate the need for separate rf bunchers, resulting in a simpler injection system. In addition, the thermal emittance of GaAs-type cathodes is significantly lower than for other photocathode materials. The environmental requirements for operating activated GaAs photocathodes cannot be met by rf guns as currently designed and operated. These requirements, including limits on vacuum and electron back bombardment, are discussed in some detail. Modifications to actual and proposed rf gun designs that would allow these requirements to be met are presented.

INTRODUCTION

Polarized electron beams have become a mainstay for much of accelerator-based medium- and high-energy physics. The most widely used technique for producing polarized electrons for accelerators is photoemission from an activated GaAs film using a dc-biased gun. However, because of the extremely high vacuum required for these photocathodes, extraction energies have generally been limited to about 100 kV to avoid high voltage breakdown. The Stanford Linear Collider (SLC) polarized electron source operated successfully from 1991 through 1998 with a cathode bias of 120 kV dc. A source more recently developed at Nagoya operates in the laboratory at 200 kV dc, while the JLAB FEL source, which utilizes a GaAs cathode for production of an unpolarized cw electron beam, operates at 350 kV dc. The principal limitation of the dc-biased source is the low energy of the electrons in the gun and in transit to the injector accelerator section. For the SLC source, the space charge forces were reduced by keeping the bunch radius and bunch length at the cathode relatively large. After extraction from the gun, the bunch was passed through an rf bunching system to reduce the bunch length for injection into a single S-band bucket, which meanwhile resulted in approximately an order of magnitude increase in the transverse emittance.

*Work supported by Department of Energy contracts DE-AC02-76SF00515 (SLAC) and DE-AC02-76ER00881 (UW).
#clen@slac.stanford.edu

A polarized rf gun, i.e., an rf gun with a GaAs photocathode, should produce a low emittance short-bunch polarized electron beam eliminating the need for rf or magnetic bunchers. While an e^+e^- collider such as the ILC requires a much lower transverse normalized emittance at the IP than can be generated by rf guns as presently developed, the transport and acceleration systems between the injector and damping ring could be significantly simplified and operated more reliably using an rf gun. In addition, for certain types of FEL linacs, the emittance of the source is critical. The transverse normalized thermal emittance of GaAs cathodes has been shown to be on the order of 0.1 μm compared to 0.6 μm for metal cathodes.

A test at the CLIC Test Facility (CTF) using an unactivated GaAs cathode prepared at SLAC demonstrated that a highly doped GaAs cathode has no obvious negative effect on the operation of a high-field S-band gun.[1] An activated GaAs cathode was not tested. Separately, an S-band rf gun was specifically developed at BINP to accommodate an activated GaAs cathode. The NEA cathode was shown to have a normal lifetime in the gun prior to the application of rf power. However, with rf power on, the QE lifetime was only a few rf pulses.[2]

Since simulations indicate that ion back bombardment should not be a problem for an rf gun,[3] the two most obvious factors contributing to the BINP result are vacuum and back bombardment of the cathode by electrons. For a typical rf gun design, the vacuum in the gun is maintained by an ion pump (IP) attached to the waveguide near the rf input coupler. The pressure as read at the IP is typically mid to high 10^{-10} Torr with rf off, rising to low 10^{-9} Torr with full rf. The pressure at the cathode itself is significantly higher.

The BINP group eventually concluded that back bombardment of the cathode by electrons was the chief culprit.[4] A runaway condition is readily established since the secondary electron coefficient for NEA GaAs is very high.

REDUCTION OF FIELD EMISSION

Field emission (FE) electrons from the cathode and/or the backplane of the cathode cell that do not exit the cell before the rf phase reverses, present one problem. In fact the rf joint made by the cathode holder is a classic source of rf breakdown for high power rf guns. Two other potential significant sources are the irises and the rf input coupler. Mitigation measures for each of these FE sources exist. For the cathode holder, the holder surface can be in the same plane as the GaAs emitting surface. The outer diameter of the holder might be made quite large so that the rf seal is in a lower field region.

To reduce field and secondary electron emission from a disk, the iris diameter can be made larger without decreasing the shunt impedance.[5]

The rf input coupler is a potential source of FE. For the BNL 1.6-cell gun design, θ coupling was used to minimize the dipole mode. If dual rf feed is used, the dipole mode is not generated, so z coupling can be used. Z coupling results in significantly lower surface temperatures and in addition is easier to fabricate.[5] Alternatively, one can use a co-axial feed.

Despite the design changes discussed above, it would still be desirable to decrease the peak fields. For a given gun design, the path of FE electrons may be simulated to determine if there is a range of peak field values for which the electrons are unlikely to hit the GaAs cathode, e.g., see Fig. 1. Careful simulation studies are underway to better understand the secondary electron emission effects in an rf gun.[6]

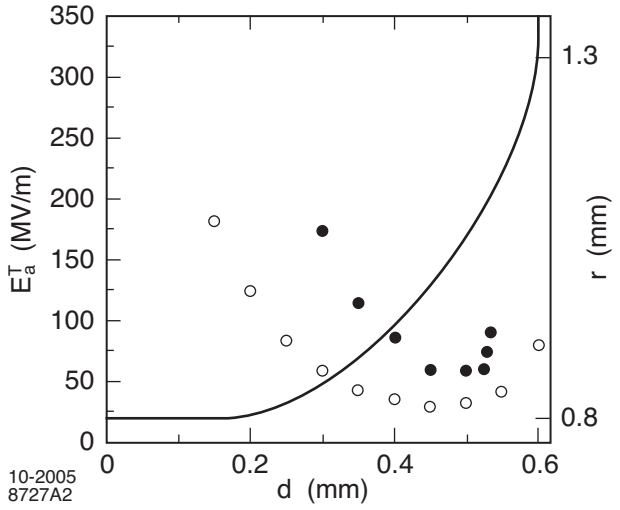

Figure 1: Threshold peak axial field, E_a^T, for electrons emitted from the first iris at an annular distance r from the cell axis (d from the center plane of the disk) in an S-band rf gun to reach the cathode surface: open and closed circles are data points for 0 and 90° rf phase at emission respectively; the solid line represents the iris profile in the r-d plane. (Data from ref. [8].)

A polarized rf gun must include a high-quality cathode preparation chamber and load-lock for introducing the activated cathode into the rf chamber. The gun can be baked and then rf processed using a *dummy* cathode prior to inserting the activated cathode. Extensive rf processing will be needed both to reduce the dark current and to regain the original vacuum. Tests at KEK have demonstrated that if proper attention is paid to the fabrication and assembly of a Cu S-band rf cavity, it can be rf processed to a peak surface field of 140 MV/m (limited by the available rf power) and with a corresponding peak dark current of <25 pA.[7] For an L-band rf gun, the peak surface field will be < 60 MV/m.

ACHIEVEMENT OF ADEQUATE VACUUM

Charged particles that hit the walls of the rf gun desorb molecules that raise the pressure in the gun. These molecules can drift to the cathode surface where they can be adsorbed, decreasing the QE. For dc-biased guns, residual pressures for oxidizers such as H_2O, CO_2, and O_2 must be kept $<10^{-12}$ Torr. Residual pressures of some gas species, such as H_2 and CO, are not as critical. To achieve the desired pressure, two things are necessary. First the gun must be fabricated and assembled so as to minimize the number of molecules available for desorption. HIP Cu can be used to minimize gasses in the grain boundaries. Lubricant-free single-crystal diamond machining along with simple alcohol and distilled water rinsing can be used to minimize residual molecular layers. Brazed joints must avoid virtual leaks. A high temperature bake is necessary to drive gases from the walls. All assembly must be done in at least a class 100 clean room to avoid contamination by dust. Following these procedures one can expect at least an order of magnitude decrease in the outgassing rate in the gun. The base pressure should not change significantly during rf processing other than during rf breakdown.[7] The high temperature bake will assure that the pressure at the cathode is dominated by H_2.

In addition to the BNL 1.6-cell gun design, there are at least 2 other rf gun designs that might prove advantageous for operation with GaAs. Any of these designs can be scaled to L-band. In the plane wave transformer (PWT) design, the disks are suspended inside a larger radius cylindrical tank. The side-coupled rf is transformed from a TEM-like mode at large radius to a TM-like mode on axis. The open structure would appear to lend itself to efficient pumping of the cathode. For an integrated function design (e.g., 7-10 cells), a lower accelerating gradient can be used without a significant increase in the transverse emittance.

Recently an HOM TM012 single-cell design has been proposed.[9] This design eliminates the intermediate disk of the 1.6-cell gun, but if the radius and length of the cell are appropriately chosen, the accelerating field on axis is essentially equivalent. For equal peak accelerating field the radius of the HOM cell is about twice that of a standard TM010 cell (see Fig. 2), while the shunt impedance is significantly lower requiring a higher total rf power. By altering the radius of the outer cylinder as a function of axial distance, the required rf power can be reduced to about twice that of the 1.6-cell gun.[10]

Both the PWT and HOM designs have a significantly larger radius than the BNL 1.6-cell gun. The larger surface area increases the gas load in the gun.

There are a number of techniques for improving the pumping that should work for any of the 3 gun designs discussed here. The most obvious idea is to increase the number of pumping ports and to include NEG pumping. A variation on this theme is to immerse all or a fraction of the outer cylinder in a UHV system and pump either through a large number of z-slots as for the AFEL[11] or

through an even larger number of small holes.[12] Thus the pumping speed through the outer cylinder can be increased by an order of magnitude, so that including a massive array of NEG pumps in the surrounding vacuum chamber will account for a factor of 10 improvement in the vacuum.

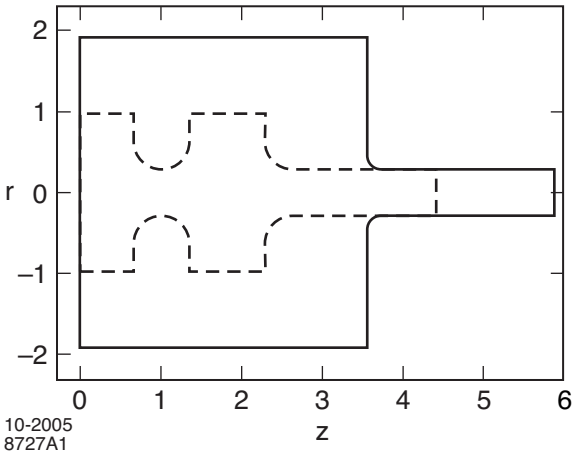

Figure 2: Cross section of the HOM TM012 rf gun (solid line) superimposed on standard 1.6 cell TM010 gun (dotted line), where the units for r and z are the same. (Similar to ref. [9].)

An additional decrease in the pressure could be achieved by operating the gun at 20 K, which would lower the vapor pressures for most of the residual gases to the order of 10^{-10} Torr.[13]

A typical 1.6-cell S-band gun operates at 8×10^{-10} Torr at the ion pump corresponding to an outgassing rate of $\sim1.2\times10^{-11}$ Torr-l/s cm^{-2} for Cu. Under these conditions, the pressure difference at the cathode is estimated to be $\Delta P_0=2\times10^{-9}$ Torr. NEG pumping through extra slots or a sieve would drop the differential at least a factor of 3. For the PWT design with a sieve at cell 5, the pressure difference is $\Delta P_0/7$, while for the HOM it is $\Delta P_0/20$ due to the absence of any internal disk. With careful preparation the outgassing rate for Cu can be reduced by an order of magnitude. Thus a pressure of 10^{-11} Torr or better at the cathode is feasible with either the HOM or PWT design. A summary of the estimated conductances and the resulting pressure differentials for 2 assumed outgassing rates is presented in Table 1. The pressure at the cathode is given by adding the pressure at the pump (which depends primarily on the size and type of pump) to the pressure differential in the table. Since the surface area and the conductance both scale approximately inversely with the resonant frequency, to first order the results in the table should be independent of the resonant frequency of an rf gun.

Table 1: Conductance and pressure differential at cathode for various S-band gun designs with 2 assumed outgassing rates for Cu.

Gun Design	**Conductance**	**ΔP (Torr) for:**	
	(l/s)	**10^{-11} Torr-l/s cm^{-2}**	**10^{-12} Torr-l/s cm^{-2}**
BNL 1.6-cell SB with conventional pumping	3.7	1.6×10^{-9}	1.6×10^{-10}
with sieve	12	5×10^{-10}	5×10^{-11}
PWT (2/2+7 to 10 cells)	28	2×10^{-10}	2×10^{-11}
PWT (1.5 cells)	50	1.2×10^{-10}	1.2×10^{-11}
HOM	75	8×10^{-11}	8×10^{-12}

THERMAL EMITTANCE

The uncorrelated or "thermal" emittance of a given cathode material determines the lower limit of the normalized transverse emittance that can be generated using a given cathode material and beam radius. The thermal emittance for a Cu photocathode has been measured for a low charge (2 pC), short (<5 ps FWHM) pulse by varying the spot size of the UV laser on the cathode. A normalized rms emittance ($\varepsilon_{n,rms}$) of about 0.6 μm for a hard edge radius of 1 mm was found.[14] By contrast, polarized electrons from an activated GaAs-type photocathode originate from near the conduction band minimum where they arrive at the surface fully thermalized. Thus the uncorrelated energy at the cathode surface should correspond to the crystal lattice temperature, or about 25 meV for room temperature, which corresponds to $\varepsilon_{n,rms}$ = 0.1 μm per mm radius.[15] The thermal emittance of GaAs has been measured using the method of adiabatic expansion of the beam in an axial magnetic field, $B_{//}$.[16] An important advantage of this method is that it is independent of charge. Under conditions in which $E_\perp/B_{//}$ is an adiabatic invariant, $B_{//}$ is decreased as the beam drifts to a retarding-potential detector, in which case transverse energy, $E_\perp$, is transferred to longitudinal energy, $E_{//}$. By measuring $\langle E_{//} \rangle$ at the detector as a function of the ratio of original and reduced $B_{//}$, the value of $\langle E_\perp \rangle$ at the cathode surface can be calculated. In an additional important refinement, the experimental apparatus allowed the vacuum level and thus the value of $E_{//}$ at the surface to be controlled. The overall result was a measured value of

$\langle E_{\perp} \rangle$ ~ 25 meV, but only if the electron affinity is maintained zero or positive. The corresponding emittance is 0.1 μm per mm radius.

CONCLUSION

The prospects for successfully operating an rf gun with an activated GaAs photocathode have been discussed. Achieving the required vacuum will require new fabrication and pumping techniques. Reducing the dark current to a level that will protect the cathode from runaway secondary electron effects is a serious challenge, but there is experimental evidence that dramatic reductions are possible. A successful GaAs photocathode rf gun promises low transverse and longitudinal emittances for a polarized electron beam.

REFERENCES

[1] K. Aulenbacher et al., CLIC Note 303 and NLC Note 20 (1996).
[2] A. Aleksandrov et al., EPAC98, p. 1450.
[3] J. W. Lewellen, PRST-AB 5, 020101 (2002); R. P. Fliller III et al., "Progress on Using NEA Cathodes in an RF Gun," contributed to PAC05.
[4] N. Dikansky et al., EPAC00, p. 1645.
[5] L. Xiao et al., "Dual Feed RF Gun Design for the LCLS," contributed to PAC05.
[6] J.H. Han et al., PRST-AB 8, 033501 (2005).
[7] H. Matsumoto, Linac96, p. 626.
[8] Y. Luo et al., PAC03, p. 2126.
[9] J. Lewellen, PRST-AB 4, 040101 (2001).
[10] J. Lewellen, Linac02, p. 671.
[11] R. Sheffield, PAC93, p. 2970.
[12] D. Yu et al., PAC03, p. 2129.
[13] R. P. Fliller III et al., "Progress on Using NEA Cathodes in an RF Gun," contributed to PAC05.
[14] E. S. Graves et al., PAC01, p. 2227.
[15] J. E. Clendenin et al., NIM A455, 198 (2000).
[16] S. Pastuszka et al., JAP 88, 6788 (2000).

STATUS AND FUTURE PROSPECTS OF SRF GUN DEVELOPMENTS

Jochen Teichert#, for the Rossendorf SRF gun collaboration
Forschungszentrum Rossendorf
01314 Dresden, Germany

Abstract

While the concepts of DC and normal-conducting photo-injectors are well proofed, the SRF gun development still possesses a high risk. Challenges are the thermal and contaminant isolation needed between the cathode and superconducting cavity, the choice of the right photocathode and its life time, the difficulty of coupling high-average power into the gun, and beam excitation of higher order cavity modes. But in combination with SRF linacs, the SRF guns are the best solution for high current and CW operation. Thus, several R&D projects of SRF gun have been launched. The talk will give an overview of the history and progress of the SRF gun development. In more detail the technical concept, performance, and status of the Rossendorf superconducting RF gun project, a collaboration of BESSY, DESY, MBI and FZR, will be presented.

MOTIVATION FOR SRF GUN DEVELOPMENT

Most of the proposed electron accelerator projects for FELs, ERLs, or 4th generation light sources require electron beams with an unprecedented combination of high-brightness, low emittance and high average current. In all of the projects photo-injectors will be applied. At present, two types of photo-injectors are in operation at linear accelerators: DC photo-injectors and radio-frequency (RF) photo injectors. In photo-injectors the electron bunches are produced by laser pulses hitting a photo cathode. This allows to generate high brightness, short electron bunches of a few ps length and bunch charges up to some nC direct at the cathode.

In order to preserve the short bunches and prevent a transverse emittance growth due to space charge forces, a strong acceleration field is needed near the photo cathode. In a DC photo-injector the extraction of the electrons from the photo cathode happens in a high electric DC field [1]. The present DC gun of the Jefferson Lab FEL operates at 350 kV [2]. A cesiated GaAs photo cathode is used, which is illuminated by a frequency-doubled, mode-locked Nd:YLF laser beam. In continuous wave (CW) operation, this gun delivers 74.85 MHz pulses at over 9 mA average current, corresponding to 135 pC per bunch. An upgrade of the DC gun for 500 kV and 100 mA average current together with a new closely coupled SRF booster cryomodule is being realized [3,4]. For the Daresbury ERL test facility a DC gun similar to the JLab 350 kV injector will be installed [5]. The DC photo gun is suitable for the production of high average current electron beams. But the comparably low acceleration field strength at the cathode limits the bunch charge and a medium transverse emittance can be obtained only.

RF photo-injectors can produce electron beams with low emittance at high bunch charges. Here the photo cathode is placed inside a RF cavity. The high RF accelerating field at the cathode retains the small longitudinal emittance and prevents an increase of the transverse emittance. The first RF photo-injector experiment was carried out at LANL in 1985 [6]. Steady improvements of gun design, lasers and photo cathodes have increased the average current and improved the beam quality. The understanding of emittance compensation in RF photo-injectors [7], its implementation [8] and shaping of the drive laser pulse [9] have further reduced the transverse emittance to about 1 mm mrad at 1 nC bunch charge [9,10]. A problem of RF photo-injectors is the RF power dissipation in the copper cavities. Therefore the RF must be pulsed with typical duty factors between 0.1% and 1%. The Boeing gun [11,12] designed in 1992 and operated at 25% duty factor and a macropulse current of 132 mA, is still the RF photo-injector with the highest average current. At present, a CW mode normal-conducting RF photo-injector for 100 mA is under development within a collaboration of LANL and Advanced Energy Systems (AES) [13]. The CW mode operation causes serious cooling problems. Therefore the field gradient is low (e.g. 7 MV/m in the LANL/AES project) with negative consequences on the transverse emittance. On the other side, there are strong efforts to reduce the transverse emittance below 1 mm mrad [14].

The advantages of both types of photo-injectors can be combined in superconducting RF (SRF) photo-injectors in which a superconducting niobium cavity is used instead of a normal-conducting Cu cavity. Superconducting cavities with low RF losses allow CW mode operation with high average currents. Similar to normal conducting RF (NCRF) guns, SRF photo-injectors can produce electron bunches with low emittance and high charge since a high accelerating field strength at the cathodes should be possible. For example, the upgraded version of the 1.3 GHz NCRF gun of the PITZ test facility will have an electric field of 60 MV/m at the cathode [14]. In superconducting acceleration cavities of TESLA type, peak fields of 50 MV/m (25 MV/m acceleration gradient) are standard with the usual chemical polishing procedure [15] and 35 MV/m (70 MV/m peak field) recently has been obtained by electro-polishing [16].

In addition to the much higher complexity of the SRF

#j.teichert@fz-rossendorf.de

photo gun, there are several new unsolved problems and risks: i) the design, construction and preparation of the superconducting cavity with its specific geometry; ii) the choice of the photo cathode type (normal-conducting or superconducting etc.) and its operation at cryogenic temperature; iii) degradation of the superconducting cavity during operation due to pollution from the photo cathode; iv) the emittance compensation scheme replacing the magnetic solenoid field applied in NCRF guns.

.

HISTORY

The use of a superconducting resonator in a RF photo-injector was proposed at the University of Wuppertal [17] and a first experimental set-up was installed [18, 19]. Whereas Piel et al. [17] suggested a reentrant shape cavity, the experiments by Michalke [19] were carried out with a 3 MHz elliptical half cell of niobium. A drawing of the cavity with RF input coupler, band pass filter and photo cathode is shown in Fig. 1. The cathode stem was also made of niobium and was cooled down in order to be superconducting. The quarter wave band pass filter prevented RF power losses through the coaxial gap between cavity and cathode stem. For photo emission a Cs_3Sb layer was used. It was irradiated with a 543 nm, 0.5 W laser. Photoemission could be obtained at 4.5 K but the gradient achieved in the cavity was too low to produce an electron beam.

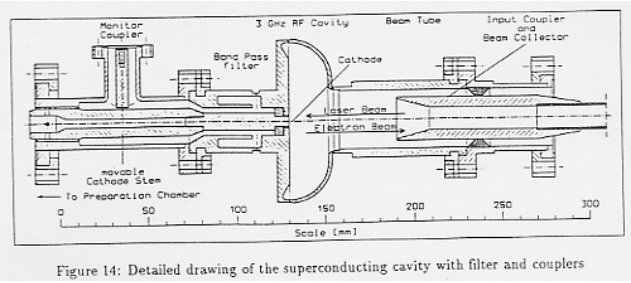

Figure 14: Detailed drawing of the superconducting cavity with filter and couplers

Fig. 1: Drawing of the Wuppertal SRF gun cavity with band filter and cathode stem [19].

Later, at the FZ Rossendorf a SRF photo-injector project was launched [20, 21]. The cavity was a 1.3 GHz TESLA type half cell closed by a shallow cone with an opening for the cathode and an additional superconducting choke flange filter [22]. A photograph of the Nb cavity is shown in Fig. 2. Similar to the Wuppertal solution, the filter was necessary because the coaxial gap between cavity and photocathode acts as a RF gain. But a normal-conducting photocathode with a Cs_2Te photo layer was used. A special support structure insulated the cathode thermally and electrically from the surrounding cavity and held it at liquid nitrogen temperature. The components are shown schematically in Fig. 3. The Cs_2Te photocathode could be moved with a manipulator from the preparation chamber into the cavity. The cavity was mounted in a test cryostat. An RF system, a CW driver laser with 262 nm wave length and 1 W power, a diagnostic beam line and control system were installed. Photo cathodes were prepared in an attached preparation system. After several tests, the gun was cooled down to 4.2 K and was in operation during a period of seven weeks (approximately five hours per day) [23].

Fig. 4 shows the measurement of the quality factor of the cavity in dependence on the peak electric field strength. The maximum field strength of 22 MV/m is limited by field emission. The insignificant difference of Q-values with and without cathode shows the good performance of the choke filter. Fig. 5 presents the cathode emission and accelerated (dump) current together with the corresponding electron energy as a function of the laser phase. For a phase window of 60° complete transmission was obtained. The energy has its maximum value at 0° and decreases for higher phase values.


Fig. 2: Photograph of the Rossendorf half-cell cavity.

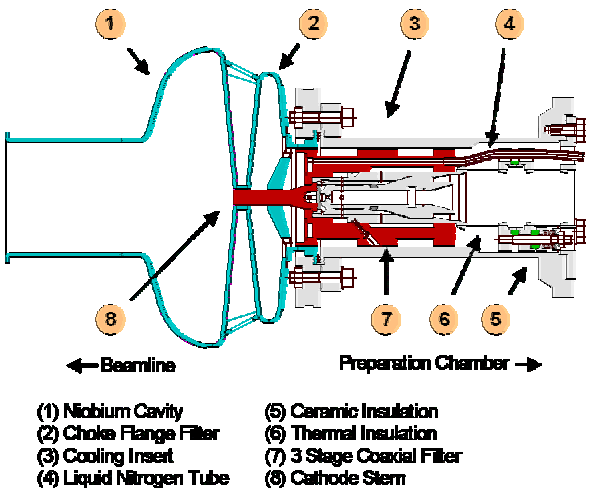

Fig. 3: Schematic drawing of the Rossendorf SRF gun arrangement with cavity, choke filter, cathode and cooler.

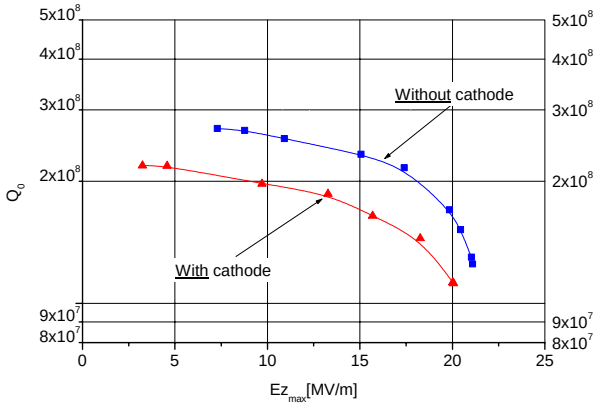

Fig. 4: Measured quality factor versus cavity field strength of the Rossendorf half-cell cavity.

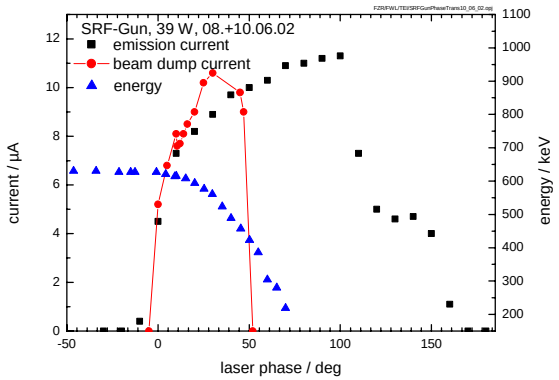

Fig. 5: Measurement of the emission current, accelerated current and energy as function of laser phase for the Rossendorf half-cell SRF gun.

During the whole period of operation, no changes of the quality factor of $Q = 2.5\times10^8$ of the cavity were measured. The electron energy was 900 keV and the maximum bunch charge obtained was 20 pC, which corresponds to an average current of 520 µA in the cw mode. It was limited by average power and repetition rate of the laser and by the small quantum efficiency of the photo cathode. Due to the long drift space after the gun and the arrangement of optical elements, the transverse emittance could only be measured for bunch charges between 1 and 4 pC. The normalized rms values were between 1 and 2.5 mm×mrad.

Nearly at the same time SRF gun research projects began at Brookhaven and Peking University. The Beijing project is ongoing and will be described later. BNL developed in collaboration with Advanced Energy Systems (AES) an “all-niobium” SRF photo gun [24, 25].

The cavity was a 1.3 GHz elliptical half cell terminated by an end wall. RF drive coupler and pick-up were both at the beam line end of the cavity. HOM couplers and tuner were not installed for this proof-of-principle experiment. In the gun, the niobium of the cavity end wall itself was used as the photo emitter. Fig. 6 shows a photograph of the cavity. Studies were carried out to improve the quantum efficiency (Q.E.) of niobium by different ways of surface treatment, high intensity UV laser cleaning and utilizing the Schottky effect [25]. An improvement of the Q.E. from about $2\text{x}10^{-7}$ to $5\text{x}10^{-5}$ could be reached. The still comparably low Q.E. and the maximum laser power density, coming from the Kapitza conductivity limit of about 1 W/cm^2 [26] provides a limit of the maximum average current. Advantages of this gun concept are the durability and simple regeneration of niobium by laser cleaning. But more important is that a Q-value degradation of the cavity by particles from the photocathode can be excluded. The cavity was cooled down to 4 K to measure frequency and Q-value. Recently, photo has been investigated emission in the gun at 4 K [27].

Fig. 6: Photograph of the AES/BNL all-niobium gun cavity [24].

REVIEW OF CURRENT SRF GUN PROJECTS

Peking University DC-SRF Photo-Injector

A DC-SC photo-injector has been designed and installed at the Peking University Accelerator Facility, Beijing [28,29,30]. The photocathode is outside the cavity with a DC voltage extraction gap and Pierce shaped electrodes. The superconducting cavity has 1+½ cells and operates at a frequency of 1.3 GHz. The DC accelerating gap and the half cell geometry have been optimized by computer simulation and beam parameters have been calculated. Fig. 7 shows the layout of the gun. The injector is designed to operate in CW mode and high average current. The motivation for the design is mainly to avoid the difficulties connected with a photocathode inside the superconducting cavities. Especially, RF losses due the photocathode, dark current initiated by the RF field, electron emission inside the cavity by reflected laser

light can be prevented and the immigration of particles from the photocathode into the cavity can be considerably reduced. The price is a loss in beam quality due to the comparably weak accelerating field in the DC gap. The photo cathodes are made of Cs_2Te and a laser with 262 nm wavelength and 81.25 MHz pulse repetition rate is used. Photo cathodes have been prepared in a chamber connected with the gun. The Helium bath cryostat will operate at 2 K. The gun is equipped with a coaxial input coupler and a 5 kW solid state power amplifier exists. All components are installed and were tested, a cool-down to 4 K was carried out. In 2005 electron beam could be produced and parameters were measured [30].

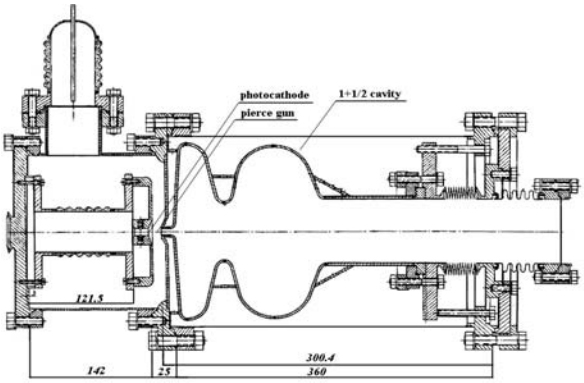

Fig. 7: Schematic picture of the Peking University DC-SRF photo injector [29].

Rossendorf 3+1/2 Cell SRF Photo-Injector

In the research center Rossendorf (FZR) a superconducting RF photo-injector (SRF gun) with a 3 ½-cell niobium cavity is under development and will be installed at the ELBE electron accelerator [32]. This gun will allow for continuous wave operation with a final electron energy of 9.5 MeV up to an average current of 1 mA. The goal of this project, carried out in a collaboration of BESSY, DESY, MBI and FZR, is to build a fully functioning superconducting photo-injector. Beside the significant beam quality improvement expected for the ELBE accelerator, the operation at ELBE will allow long term studies of important issues of SRF injectors like low-temperature operation and lifetime of photo cathodes, or cavity quality degradation. Because of its attractiveness, the capability for the future applications in FEL light sources and energy recovery linacs will be demonstrated. Therefore the SRF gun will be operated in three modes: the standard ELBE FEL mode with 77 pC and 13 MHz pulse repetition, the high charge mode for neutron physics at ELBE and ERL studies (1 nC, 1 MHz), and the BESSY FEL mode (2.5 nC, 1 kHz). A UV driver laser system for these three operation modes is under development. Beam parameter studies will be performed with a new diagnostic beam line [33]. The ELBE mode is determined by the existing and constructed far infrared FELs which need 13 MHz bunch repetition rate, as well as the maximum average current of the ELBE accelerator. For this mode the new gun will improve the beam quality essentially in comparison to the existing thermionic injector at ELBE (about 8 mm mrad normalized transverse emittance at 77 pC). The high charge mode is impossible with the existing injector, but it is essential for neutron physics experiments at ELBE where time-of-flight measurements require 1 ns pulse spacing without average current reduction. At the same time, 1 nC is a typical bunch charge for new FEL projects and state-of-the-art NCRF photo injectors (e.g. the EUROFEL project at DESY) where the beam parameter should be measured and compared. For the soft x-ray BESSY FEL project [34] a bunch charge of 2.5 nC is envisaged and the SRF gun will be evaluated with respect to future application.

The SRF gun cavity consists of three full cells, a specially designed half-cell and the choke filter. The three full cells have TESLA shapes [35]. The back wall of the half-cell has a slightly conical shape and a centered hole for the photocathode. The photocathode consists of a normal-conducting copper stem with a Cs_2Te layer. A circular vacuum gap prevents the heat transport from the photocathode to the cavity. Therefore the heat loaded in the cathode does not burden the helium bath. On the other hand, to prevent RF power losses through the coaxial line formed by this geometry, an additional superconducting niobium choke filter is attached. The cavity has an RF power coupler, two higher-order mode couplers and a pick-up adopted from the TESLA cavity [35], and one extra pick-up especially for the cathode half-cell.

Fig. 8: Photograph of the Rossendorf 3+1/2 cell cavity.

The production of two Nb cavities by ACCEL, with RRR 300 and 40 respectively, was finished in March 2005. Fig. 9 shows a photograph of the cavity. In Fig. 10 the design of the cryomodule is shown. It consists of a stainless steel vessel of about 1.2 m length. Below the He port a heater pot exists. From there the He flows through the two-phase supply tube and the chimney into the He tank. The heaters are installed for He level control and balances the variable dynamic load of the cavity. The 80 K shielding is performed with liquid nitrogen. Liquid N_2 is also used in the cathode cooling system. The liquid N_2

tank in the upper part of the module must be refilled after about 5 h from an outside dewar. The cavities are passively shielded against ambient magnetic fields by means of a cylindrically shaped mu-metal sheet, closed at both sides, which is placed between the 80 K shield and the vacuum vessel. The 10 kW CW main power coupler is completely adopted from the ELBE accelerator module. Two tuners will be installed, one for the half-cell and one for the three TESLA cells. Like in the ELBE module, the tuners are dual spindle-lever systems. Modifications were necessary due to different tuning ranges and the available place, since both tuners are at the cathode end of the cavity. Specific features of the tuners are that the lever bearing points are flexible connects without any rotational parts and that the use of two levers ensures a force-free spindle bearing point. The drive motors and the low-vibration gears are outside the vacuum vessel. From outside it is also possible to move the cathode cooling system which allows adjustment of the cathode with respect to the cavity. The helium tank with the cavity is supported by thin titanium spokes. In the beam line tube, the cathode exchange tube, the RF coupler, and in the tuner shafts thin-walled stainless-steel bellows are integrated to lower the heat transport.

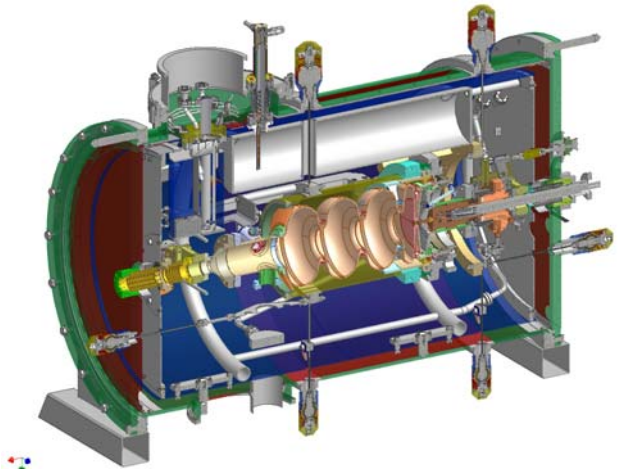

Fig. 9: Design of the cryomodule of the Rossendorf 3+1/2 cell SRF gun.

The further time schedule of the project is to finish the installation of the gun in autumn 2006, and to generate the first beam in 2007.

SRF Split Photo-Injector

The basic idea of the SRF split photo injector consists in splitting the combination of RF field and magnetic solenoid field which is usual in NCRF photo-injectors. The solenoid is placed downstream, as shown in Fig. 11, where it does not disturb the superconducting cavity [36, 37]. In the injector a 1.3 GHz 1.6 cell Nb cavity is used. The full cell shape is similar to a TESLA inner cell [35], while the first cell is longer than a half cell in order to compensate for phase slippage. A coaxial input coupler has been considered as in the normal conducting TESLA gun design, in order to avoid any asymmetry in the accelerating field and transverse RF kicks. The solenoid is located 36 cm downstream from the cathode producing a 0.3 T maximum field on the axis. In the gun design the electrons will be accelerated up to 6.5 MeV, and a RF peak field of 60 MV/m is assumed. The maximum field at the cathode will have the same value of 60 MV/m. With HOMDYM simulation [38], it was shown that the emittance compensation process works with an emittance minimum at about 3.3 m downstream, where the beam is injected in the first accelerator module. The final transverse emittance is less than 1 mm mrad for 1 nC bunch charge and a 19.8 ps long, flat-top laser pulse.

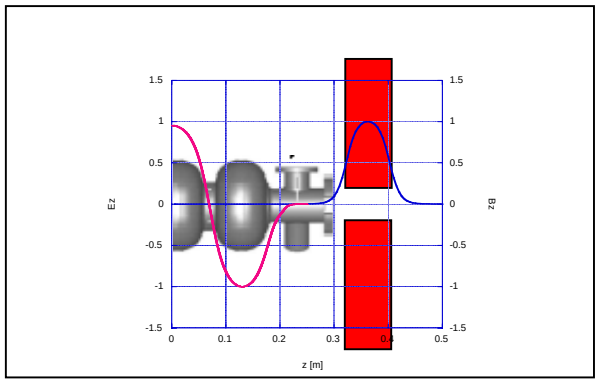

Fig. 10: Design of the SRF split injector [51].

AES/BNL Hgh-Current SRF Photo-Injector

For the ERL test ring at Brookhaven National Laboratory [39] a SRF gun is being developed by the company AES [40]. The aim of this development is a photo-injector delivering 0.5 A average current. This high current requires a considerably different design than the other SRF gun projects.

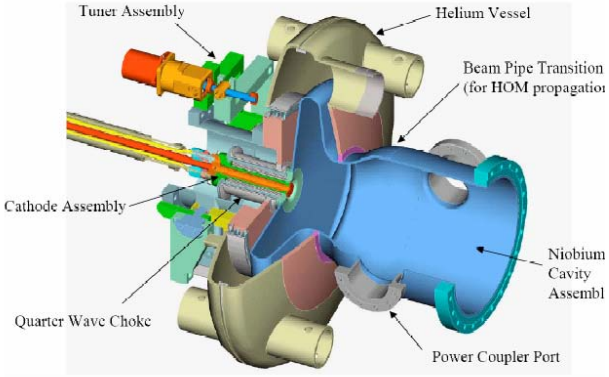

Fig. 11: Design of the AES/BNL half-cell cavity for the high current SRF gun [51].

A lower RF frequency was chosen (703.75 MHz to be compatible with the RHIC RF system) and only a half-cell cavity. The cavity will be equipped with two main power couplers, each of 1 MW. The cathode concept is similar to the Rossendorf approach, i. e. the photo cathode is normal conducting, thermally isolated from the cavity and cooled by liquid nitrogen. A quarter wave choke joint prevents the RF power leakage. Delivery to BNL is planned for early 2007.

DISCUSSION OF CRITICAL TOPICS

Photocathodes

Table 1 lists the photo cathodes which are used or planned to be used in the running SRF gun projects described above. Additionally, information on metal and GaAs photo cathodes are shown which are applied in NCRF and DC photo-injectors. Three crucial factors determine the choice: prevention of cavity contamination using superconducting metallic cathodes; high quantum efficiency and long life time are obtained with Cs_2Te cathodes; and for the high-current project the antimonides which are sensitive for green laser light, and the diamond SE amplifier are considered.

Photoemission studies of the superconducting metals Nb (T_c=9.3 K) and Pb (T_c=7.2 K) have been carried out by Smedley at BNL [41, 42]. The quantum efficiency measurements of Nb are related to the "all-niobium" gun. Especially, the improvement of the Q.E. by laser cleaning has been studied. At 248 nm the Q.E. of the niobium was increased from $2x10^{-7}$ up to $5x10^{-5}$. Recent photo emission measurements in the gun itself at 4.5 K provides Q.E. values of $2x10^{-6}$ at 266 nm and $3x10^{-5}$ at 248 nm [27]. Very promising are the results for lead. After laser cleaning of arc deposited Pb layers, Q.E. values of $2.7x10^{-3}$ at 213 nm and $5.4x10^{-3}$ at 193 nm were obtained. Thus, the BNL half-cell cavity has been modified with a lead plug [43] and for the split photo-injector (s. sec. 3.3) a lead photo cathode is considered.

Cs_2Te photo cathodes are widely used in NCRF photo-injectors [14]. They possess high quantum efficiency, have long lifetime, and are relatively robust. Laser systems for these cathodes with 262 nm wave length with suitable parameters are available. After insertion of a new photocathode in NCRF photo-injectors, RF conditioning is necessary to obtain stable operation at the desired high field gradient. The RF conditioning reduces field emission, dark current and the probability for RF discharges. The effect seems to be caused by outgasing, surface cleaning and smoothening. RF discharges during conditioning or operation can destroy the surface of the photocathode [44]. Further reasons for a destroyed cathode surface could be laser ablation, thermal stress and ion back bombardment. Similar effects can also be expected for photocathodes in SRF guns. But the consequences are much more serious because particles produced by these effects at the photocathode can move inside the cavity and contaminate its surface. That can course a steady decrease of the cavity's quality factor and maximum acceleration gradient and perhaps limit the operation time of the cavity. In the experiments performed up to now [19, 23] such cavity degradation was not observed. The recurring photocathode exchange can also produce particles. Cavity pollution is regarded as the greatest risk for SRC guns and systematic studies for high gradients and high average currents over long operation periods are still outstanding.

For very high currents the quantum efficiency of the semiconductor photo cathodes is not sufficient. A diamond secondary electron amplifier has been proposed at BNL [45, 46], which could emit about a factor of 100 more electrons. In the device the electron bunches are produced in two steps. In the first step, a conventional photo cathode (CsK_2Sb) is illuminated with a laser pulse. The electrons produced are accelerated in a DC field of about 10 kV. In the second step the electrons hit the diamond window on the backside and produce a large number of secondary electrons. These electrons penetrate through the diamond and leave it at the front side, where the RF field is applied. The H-terminated front side of the

material		Q.E. range	laser wavelength	vacuum requirem.	fabrication	type	use
metal	Al, Cu, Mo	0.02-0.06 %	262 nm	10^{-7} Torr	-	NC	-
	Nb	0.005 %	248 nm	10^{-7} Torr	easy	SC	no polution
	Pb	0.15 %	213 nm	10^{-7} Torr	easy	SC	no polution
Semi-cond.	GaAs(Cs)	1-5 %	532 nm	10^{-10} Torr	moderate	NC	-
	CsK_2Sb	10-14 %	532 nm	10^{-10} Torr	difficult	NC cooled	high current
	Cs_2Te	10-14 %	262 nm	10^{-9} Torr	moderate	NC cooled	medium current
						outside cavity	no polution
SE ampl.	diamond	~1000 %	532 nm	10^{-7} Torr	difficult		highest current

Table 1: Summary of photo cathodes in SRF photo-injector projects

diamond has a negative electron affinity.

Emittance Compensation for SRF Guns

NCRF photo-injectors use a magnetic solenoid field for emittance compensation. This method was proposed by Carlsten [7]. The growth of the transverse emittance caused by space charge in the gun can be compensated by means of the magnetic field. In most cases two solenoids are placed around the RF cavity of the gun. The main solenoid produces the compensation field. The second is needed to have a vanishing field at the cathode itself. To place a solenoid around a SRF gun is not only a technical problem. The critical field strength B_c = 200 mT of Nb is one limit. But the most critical point is the magnetic field limitation during cooldown. Niobium is a soft type II superconductor, but with flux pinning for weak DC fields. The magnetic field causes a residual resistance of $R_{res,mag}$ = 3.5 nΩ/μT [35], that mean less than 1 μT is required during cooldown to get the high quality factor.

The first idea was therefore to place the solenoid downstream. That such an arrangement works was shown in simulation for the SRF split photo-injector by Ferrario [37] and by Marhauser [47]. The second method is to abandon an external magnetic focusing field and to use the RF in the SRF gun for focusing as proposed by Janssen and Volkov [48]. Here, the shape of the cavity around the cathode opening together with a withdrawn cathode causes a focusing effect. Additionally, the cathode can have a concave shape. The RF focusing will be applied in the Rossendorf SRF photo-injector project. The electric field distribution in dependence on the cathode position for the 3+1/2 cell cavity is shown in Fig. 11. From ASTRA simulation the best cathode position was found to be 2.5 mm. Recently, it was suggested to apply an additional RF frequency to the SRF gun cavity which corresponds to a higher order transverse electric mode [49, 50]. For the Rossendorf gun frequencies of 3802 MHz or 3952 MHz are proposed. The TE mode forms a longitudinal magnetic field in the cavity similar to a solenoid field. It could be demonstrated by simulation that a significant improvement of the transverse emittance can be obtained for suitable magnetic field strength.

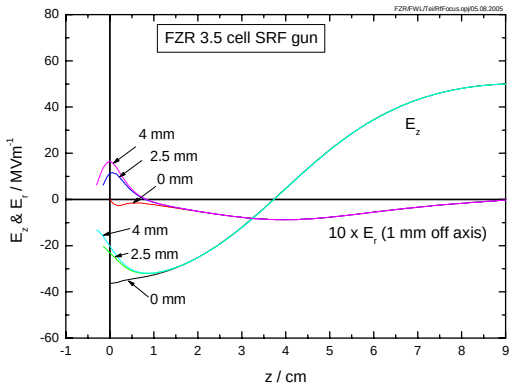

Fig. 12: Axial and radial electric field profile for RF focusing in the Rossendorf 3+1/2 cell SRF gun.

SUMMARY OF SRF PHOTO-INJECTOR PROJECTS

A summary of past und current SRF photo-injector projects is given in Table 2. After the phase of feasibility studies, the new projects at Rossendorf and Brookhaven are intended for operation at accelerators. This is also true for the next DC-SRF gun which will be developed at Peking University [31]. But SRF photo-injectors are still in the research and development phase. Also hopeful approaches are found experimental proofs and long-term tests are outstanding.

Place	Type	Cavity	Cathode	Current	Remarks	Status	References
Wuppertal Univ.	SC cathode	½	Cs_3Sb	-	feasibility demonstration	-	17-19
FZ Rossendorf	NC cathode	½	Cs_2Te	40 μA	feasibility demonstration	-	20-23
FZ Rossendorf	NC cathode	3 ½	Cs_2Te	1 mA	low emittance	cavity ready	32,33
Peking Univ.	DC-SRF NC cathode	1 ½	Cs_2Te	~1 mA	no cathode in cavity	beam experiments	28-31
Brookhaven AES/BNL	All Niobium	½	Nb	μA	no contamination	-	24-27
Brookhaven AES/BNL	NC cathode	½	CsKSb& diamond	500 mA	highest current	design finished	39,40,45,46
INFN Frascati	SC cathode	1 ½	Pb	1 mA	low emittance no contamination	design	37,38

Table 2: Past and current SRF photo-injector projects.

ACKNOWLEDGEMENT

We acknowledge the support of European Community-Research Infrastructure Activity under the FP6 "Structuring the European Research Area" programme (CARE, contract number RII3-CT-2003-506395) and the support of the German Federal Ministry of Education and Research grant 05 ES4BR1/8.

REFERENCES

[1] C.K. Sinclair, R.H. Miller, IEEE Trans. Nucl. Sci. NS-28 (1981) 2649.
[2] C.H.G. Hernandez-Garcia et al., Proc. of the 2004 FEL Conference, Trieste, Italy, 2004, p. 558.
[3] C.K. Sinclair, Nucl. Instr. and Meth. A 318 (1992) 410.
[4] A. Todd, Nucl. Instr. and Meth. A 557 (2006) 36.
[5] C. Gerth, F.E. Hannon, Proc. of the EPAC, Lucerne, Switzerland, 2004, p. 437.
[6] J.S. Fraser, et al., PAC'87, Washington DC, USA, March 16-19, 1987, p. 1705.
[7] B.E. Carlsten, Part. Accel. 49 (1995) 27.
[8] D. Engwall, et al., PAC'97, Vancouver, Canada, May 12-16, 1997, p. 2693.
[9] Y. Yang, et al., J. Appl. Phys. 92 (2002) 1608.
[10] P.G. O'Shea, L. Spenzouris, Proc. of the VIII Advanced Accelerator Concepts Workshop, Baltimore,USA, July 1998.C.K. Sinclair, R.H. Miller, IEEE Trans. Nucl. Sci. NS-28 (1981) 2649.
[11]D.H. Dowell, et al., Nucl. Instr. and Meth. A 356 (1995) 167.
[12] D.H. Dowell, et al., Appl. Phys. Lett. 63 (1993) 2035.
[13] S. Kurennoy, et al., Proc. of the 2002 FEL Conference, Argonne, USA, September 9-13, 2002, p. II-53.
[14] A. Oppelt, et al., Proc. of the 2005 FEL Conference, Stanford, USA, 2005, p. 564.
[15] L. Lilje, Proc. 11th SRF Workshop, Travemuende, Germany, 2003.
[16] L. Lilje, Proc. of the EPAC, Lucerne, Switzerland, 2004, p. 129.
[17] H. Piel et al., FEL'88, Jerusalem, Israel, 1988.
[18] A. Michalke, et al., EPAC'92, Berlin, Germany, March 24-28, 1992, p. 762.
[19] A. Michalke, *Photocathodes inside a Super-conducting Cavity*, PhD thesis, University of Wuppertal, 1993, WUB-DIS 92-5.
[20] D. Janssen et.al., PAC'97, Vancouver, Canada, May 12-16, 1997.
[21] P. vom Stein, *Hochfrequenz Elektroneninjektoren für cw-Beschleuniger*, PhD thesis, Dresden University of Technology , 1998, Report FZR-227.
[22]E. Barthels, et al., Nucl. Instr. and Meth. A445 (2000) 408.
[23] D. Janssen, et al., Nucl. Instr. and Meth. A507 (2003) 314.
[24]H. Bluem, et al., EPAC'00, Vienna, Austria, 2000, p. 1639.
[25] T. Srinivasan-Rao, et al., PAC'03, Portland, USA, May 12-16, 2003.
[26]M.D. Cole, et al., LINAC'00, Monterey, USA, Aug. 21-25, 2000.
[27]T. Rao, et al., Proc. of the PAC, Knoxville, USA, 2005, p. 2556.
[28]K. Zhao, et al., Nucl. Instr. and Meth. A475 (2001) 564.
[29]B.C. Zhang, et al., SRF'01, Tsukuba, Japan, Sept. 6-11, 2001.
[30]J.K. Hao, et al., SRF'01, Tsukuba, Japan, Sept. 6-11, 2001.
[31]G. Wang, et al., Proc. of the 2005 FEL Conference, Stanford, USA, 2005, p. 161.
[32]J. Teichert, et al., Proc. of the 2005 FEL Conference, Stanford, USA, 2005, p. 534.
[33]T. Kamps, et al., Proc. of the 2005 FEL Conference, Stanford, USA, 2005, p. 530.
[34]www.bessy.de, BESSY FEL, Technical Design Report, March 2004.
[35]B. Aune, et al., Phys. Rev. Special Topics, 3(2000) 092001.
[36]M. Ferrario, et al., Proc. of the EPAC, Lucerne, Switzerland, 2004, p. 402.
[37]M. Ferrario, et al., Nucl. Instr. and Meth. A557 (2006) 98.
[38]M. Ferrario, et al., "HOMDYN study for the LCLS Photoinjector", in *The Physics of High Brightness Beams*, 534, World Scientific, 2000.
[39] I. Ben-Zvi, et al., Nucl. Instr. and Meth. A557 (2006) 28.
[40]A. Todd, et al., Nucl. Instr. and Meth. A557 (2006) 36.
[41]J. Smedley, et al., Proc. of the EPAC, Lucerne, Switzerland, 2004, p. 1126.
[42]J. Smedley, et al., Proc. of the PAC, Knoxville, USA, 2005, p. 2598.
[43]P. Kneisel, et al., Proc. of the PAC, Knoxville, USA, 2005, p. 2956.
[44]T. Kobayashi, et al., J. Nucl. Sci. Technol. 39 (2002) 6.
[45]T. Rao, et al., AIP Conf. Proc. 737 (2004) 178.
[46]X. Chang, et al., Proc. of the PAC, Knoxville, USA, 2005, p. 2711.
[47]F. Marhauser, Proc. of the EPAC, Lucerne, Switzerland, 2004, p. 315.
[48]D. Janssen, V. Volkov, Nucl. Instr. and Meth. A452 (2000) 34.
[49]K. Floettmann, D. Janssen, V. Volkov, Phys. Rev. ST Accel. Beams 7 (2004) 099901.
[50]D. Janssen, V. Volkov, Proc. of the EPAC, Lucerne, Switzerland, 2004, p. 330.
[51]conferences.jlab.org/ERL/2005/program.html.

ULTRA-LOW EMITTANCE AND ULTRASHORT BUNCH ELECTRON SOURCE

Jinfeng Yang#

The Institute of Scientific and Industrial Research, Osaka University,
8-1 Mihogaoka, Ibaraki, Osaka 567-0047, Japan

Abstract

In the paper, an ultra-low emittance electron source and a femtosecond electron source based on photocathode rf guns are reported. The ultra-low emittance electron beam was generated with a technique of laser pulse shaping. The normalized transverse rms emittance at 1 nC was obtained to be 1.2 mm-mrad for the square pulse shape with pulse length of 9 ps FWHM. The emittance growth due to space charge and RF effects in the RF gun was experimentally investigated. The emittance was measured as a function of the electron bunch charge and the laser pulse length.

To generate a femtosecond electron beam, a magnetic compressor with second-order momentum dispersion compensation was used to rotating the bunch in longitudinal phase space. A single electron bunch with rms bunch length of 98 fs was observed for a 32 MeV electron beam at charge of 0.17 nC. The effect of space charge on the bunch compression was investigated experimentally.

INTRODUCTION

High-brightness electron sources, producing short, intense, low-emittance electron bunches, are key elements for new developments in accelerator physics. The ultra-low emittance electron sources are essential for future high-energy electron-positron colliders [1], laser or plasma wake-field acceleration [2], and new femtosecond x-ray free electron lasers (FELs) based on self-amplified spontaneous emission (SASE), such as the x-ray FEL project at Deutsches Elektronen-Synchrotron (DESY) [3], and the Linac Coherent Light Source (LCLS) [4]. The x-ray FEL project at LCLS will use an electron beam with a normalized emittance of ~1 mm-mrad at bunch charge of 1 nC to reach saturation in a single pass at 1.5 angstrom.

Ultrashort electron bunches, of the order of 100 fs, are essential to produce ultrashort x-ray FEL [5] and to reveal the hidden dynamics of intricate molecular and atomic processes through experimentation such as time-resolved electron diffraction [6] and femtochemistry [7].

To meet these requirements, laser-driven photocathode rf guns have been studied [8-10]. The electrons with a low space charge induced emittance are emitted from the photocathode surface by a strong rf electric field. However, the emittance growth in the rf gun occurs close to the cathode surface due to the defocusing space charge force, i.e. where the beam is not yet relativistic. The minimization of the defocusing space charge force is required in order to obtain the minimum expected emittance. Moreover, the reduction of nonlinear space charge effect is needed, because it causes a distortion to the phase space during acceleration and cannot be removed in the emittance compensation scheme. From theoretical studies, a technique of shaping temporal charge density distribution of electrons, i.e. a uniform temporal electron bunch, reduces the defocusing space charge force. It can be also tailed to behave like a linear space charge field, resulting in emittance compensation.

The rf gun generates short electron bunches with short laser pulses, such as a few picoseconds electron bunch with transverse emittance of a few mm-mrad. It allows us to compress the bunch into femtosecond by using magnetic bunch compressors.

In this paper, both an ultra-low emittance electron source and an ultrashort bunch electron source based on photocathode rf guns were reported. A technique of shaping temporal laser pulse was used to generate the ultra-low emittance electron beam. The emittance growth in the rf gun with Gaussian and square temporal laser pulse shaping was studied experimentally. In the ultrashort bunch electron source, a compensation technique of nonlinear effects in magnetic fields was used to generate a femtosecond electron beam by re-phasing the linac away from the zero-crossing of the rf (i.e. away from the linear slope) to produce a nonlinear energy correlation along the bunch length.

ULTRA-LOW EIMTTANCE ELECTRON SOURCE

In the source, a S-band (2856 MHz) photocathode rf gun (BNL gun-IV, produced by Sumitomo Heavy Industries (SHI) [9, 10]) was used. At the exit of the rf gun, a solenoid magnet was mounted for space-charge emittance compensation, as shown in Fig. 1. The electron beam produced from the rf gun was accelerated with a 70 cm long standing-wave linear accelerator (linac) located downstream of the solenoid magnet at a position of 1.2 m from the cathode (see Fig. 1). The input rf peak power of both the rf gun and the linac was 7.5 MW that was produced with a 15 MW Klystron. The peak on-axis electric fields in the rf gun and the linac were 100 and 25 MV/m, respectively. The operating repetition rate was 10 Hz. The accelerated beam energy was 14 MeV (4 MeV at the gun exit). To measure the beam transverse emittance, we used a standard quadrupole scan technique whereby the beam size was measured on a screen downstream of a

#yang@sanken.osaka-u.ac.jp

quadrupole magnet which was varied so that the beam passed through a waist at the screen. The beam size at each quadrupole setting was measured by averaging 16 different images. The fluctuation of the beam size was 4-5%. The limitation on the beam size measurement was <68 μm using the beam imaging technique.

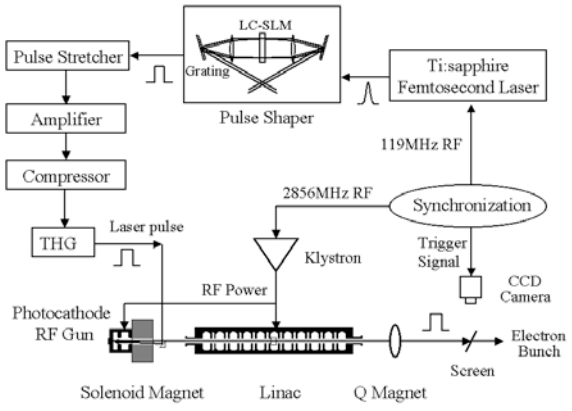

Fig. 1: Experimental arrangement of ultra-low emittance electron source, see in ref. 11 for details.

A laser [11], used to drive the rf gun, was consisted of a femtosecond Ti:Sapphire laser oscillator, a temporal pulse shaper, a pulse stretcher, an amplifier, a pulse compressor and a frequency converter. The oscillator, which was passively mode-locked at a frequency of 119 MHz (the 24th sub-harmonic of the accelerating rf), generated a 50 fs long laser pulse with a central wavelength of 800 nm and a spectral width of 15 nm FWHM for pulse shaping.

The temporal pulse shaper was accomplished through a technique of frequency-domain pulse shaping. The spectrum of the incident femtosecond laser pulse was dispersed in space between a pair of diffraction gratings separated by a pair of lenses (see Fig. 1). A spatially resolved phase mask, which was located at dispersion plane, modified the Fourier transform of the incident pulse with computer control to produce a desired shape. The gratings with a groove number of 2400 lines/mm were used and the diffraction angle from the gratings was 73.7°. A computer-addressable liquid-crystal spatial light modulator (LC-SLM) with 128 pixels was used as the phase mask. The resolution of the phase shift on LC-SLM was near 0.01π. The pulse shaper was located between the oscillator and the pulse stretcher to reduce the possibility of damage on the optics. The transmission of the laser power through the pulse shaper was about 60%. The incident laser pulse was shaped into a square-shaped pulse with phase-only filter by a numerical calculation, based generally on the intensity profile and the phase characteristics of the incident laser spectrum. To reduce the distortion and ripple on the temporal distribution of the shaped laser pulse, we reconstructed the pulse shape again by re-calculations using the shaped pulse spectra after the amplifier and the frequency conversion process.

By using a square temporal laser pulse shape with a pulse length of 9 ps FWHM, a lowest normalized rms emittance of 1.2 πmm-mrad at 1 nC was obtained. Figure 2 gives the normalized rms horizontal emittance measured as a function of the bunch charge for the Gaussian and square temporal pulse shapes with a pulse length of 9 ps FWHM. The measured data was fit as a function of

$$\varepsilon = \sqrt{(a'Q)^2 + b'^2}\ , \qquad (1)$$

where a' is a fitting parameter referred to space charge force, and b' in πmm-mrad is a zero charge emittance. The fits yield a'=0.92±0.05 and b'=0.81±0.03 for the square pulse shape, while a'=1.85±0.13 and b'=0.83±0.05 for the Gaussian pulse shape. It is found that the square pulse shape reduced the space charge force of about 50% comparing with the Gaussian pulse shape.

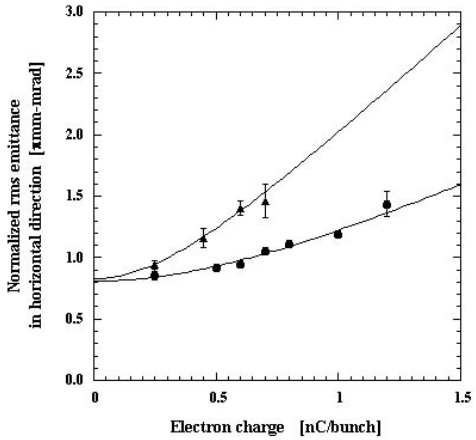

Fig. 2: The emittance versus bunch charge for the Gaussian (triangle) and square (dot) pulse shapes at a pulse length of 9 ps FWHM, see in ref. 11 for details.

ULTRASHORT BUNCH ELECTRON SOURCE

The same type rf gun was used in this source. The gun was driven by an all solid-state LD-pumped Nd:YLF picosecond laser. The electron beam produced by the RF gun was accelerated with a 2 m long S-band travelling-wave linear accelerator, as shown in Fig. 3. The linac was located at a distance of 1.2m from the cathode surface. The energy of the electron pulse was also modulated by adjusted the RF phase for bunch compression, as described below. The operating temperatures of the RF gun and the linac were 32°C and 30°C, respectively. The temperature fluctuation of both the RF gun and the linac were within 0.1°C.

The magnetic bunch compressor, as shown in Fig. 3, was constructed with two 45°-bending magnets and four quadrupole magnets (two pairs), which provides the necessary path length dependence on energy. The picosecond electron bunch, which was produced in the linac with an energy-phase correlation, was compressed into femtosecond by rotating the bunch in the longitudinal phase space distribution. In order to obtain a short bunch length, all magnets were carefully installed with the minimum lattice error to reduce the aberrations in the phase space distribution. The inside two quadrupole magnets had equal magnetic fields, while the outside

quadrupole magnets had equal magnetic fields. The dispersion function is symmetric on the midplane of the compressor. However, during the compression, higher-order momentum dispersion, especially the second-order dispersion, causes a nonlinear deformation of the longitudinal phase space, which increases the final bunch length. To reduce the nonlinear effects, we used the curvature of the rf waveform in the linac. By re-phasing the linac away from the zero-crossing of the rf (i.e. away from the linear slope), a nonlinear energy correlation along the bunch length can be introduced. The correlation can offset the effects of the nonlinear path length in the magnetic compression by optimizing the magnetic fields of four quadrupole magnets.

Figure 4 gives a temporal distribution of the electron bunch at charge of 0.17 nC obtained by measuring Cherenkov radiation emitted from the electron bunch in air at the exit of the compressor with a femtosecond streak camera. The rms bunch length was obtained to be 98 fs by fitting the bunch shape to a Gaussian distribution. In the measurement, the linac was re-phased at 94° off crest of the rf waveform, which was the optimum phase for the shortest bunch length. The rf phase of the gun was fixed at 30° off zero-crossing rf phase to produce a low-emittance beam.

The dependence of the rms compressed bunch length on the bunch charge was measured. It is found that the bunch length increase, which is independent on the bunch charge, is negligible in the compression. The bunch length increase due to the space charge effect is very close to the analytical expression of $Q^{2/3}$, where Q is the bunch charge. However, the final compressed bunch length is also determined with the longitudinal emittance of the initial beam. The space charge effect in the rf gun causes the longitudinal emittance growth, resulting in the bunch length increase.

REFERENCES

[1] F. Richard et al., "TESLA, The Superconducting Electron-Positron Linear Collider with an Integrated X-Ray Laser Laboratory, Technical Design Report", DESY Report No. DESY2001-011, ISBN 3-935702-00-0, 2001.

[2] C. Joshi and T. Katsouleas, Phys. Today, 56, 47 (2003).

[3] V. Ayvazyan et al., Phys. Rev. Lett. 88, 104802 (2002).

[4] M. Cornacchia et al., "Linac Coherent Light Source (LCLS) Design Study Report", Stanford University-University of California Report No. SLAC-R-521/UC-414, revised 1998.

[5] L. Bentson {\it et al.}, Nucl. Instrum. Methods Phys. Res. Sect. A 507, 205 (2003).

[6] B. J. Siwick {\it et al.}, Science {\bf 302}, 1382(2003).

[7] A. H. Zewail, Science {\bf 242}, 1645(1988).

[8] K.-J. Kim, Nucl. Instr. Meth. A**275** (2000) 201.

[9] J. Yang, et al., Nucl. Instrum. Meth. Phys. Res. Sect. A **491** (2002), 15-22.

[10] J. Yang, et al., Jpn. J. Appl. Phys., **44**, 8702-8707(2005).

[11] J. Yang, et al., J. Appl. Phys., **92** (2002), 1608-1612.

[12] J. Yang et al., Nucl. Instrum. Meth. Phys. Res. Sect. A **556**, 52-56(2006).

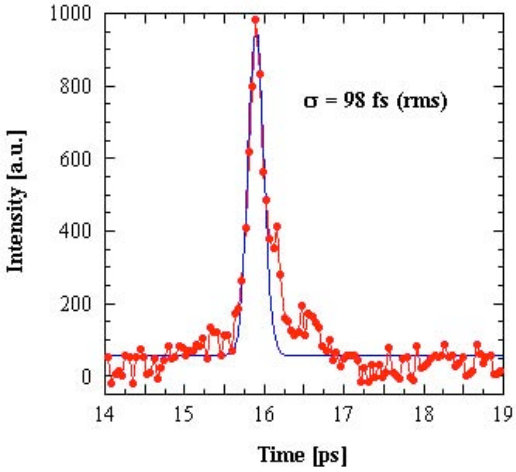

Fig. 4: The temporal distribution of 98 fs-bunch measured by the streak camera at 0.17 nC, see in ref. [12] for details.

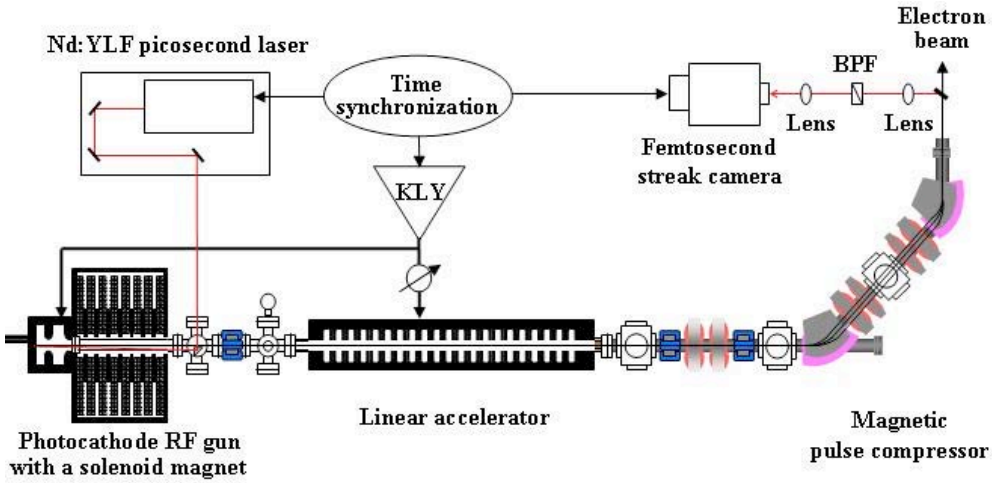

Fig. 3: Schematic diagram of ultrashort bunch electron source.

DESIGN STUDY ON AN INDEPENDENTLY-TUNABLE-CELLS THERMIONIC RF GUN

H. Hama#, T. Tanaka, F. Hinode, M. Kawai, Laboratory of Nuclear Science, Graduate School of Science, Tohoku University, 1-2-1 Mikamine, Taihaku-ku, Sendai 982-0826, Japan

Abstract

Characteristics of a thermionic RF gun have been studied by a 3-D simulation code developed using an FDTD (Finite Difference Time Domain) method as a Maxwell's equations solver [1]. The gun is consists of two independent power feeding cavities, so that we call it "independently-tunable-cells (ITC)"-RF gun. The first cell is the cathode cell and the second one is an accelerating cell. The ITC gun can be operated at various modes of different RF-power ratio and phase between two cavities. Simulation study shows a velocity-bunching like effect may be occurred in the gun, so that the short pulse beam from the thermionic RF gun is a better candidate to produce the coherent THz synchrotron radiation. Expected bunch length with a total charge of ~ 20 pC (1 % energy width from the top energy) is around 200 fs (fwhm). Even the beam energy extracted from the gun is varied by which the input powers are changed, almost same shape of the longitudinal phase space can be produced by tuning the phase.

INTRODUCTION

In these years, light sources of a wavelength region shorter than mm but longer than 100 μm, so-called THz light, are rapidly developed worldwide, because the THz light is another transparent electromagnetic wave, so that many applications are considered worldwide [2].

There have been several ways to produce the sub-THz light so far, such as a backward wave oscillator (BWO) tube, but the power is not high. Recently the THz light production using conventional lasers and non-linear crystal is developed. In this case, the power is also low but a frequency resolution is very much better.

The most promising high power broadband THz light may be coherent synchrotron radiation emitted from the extremely short electron bunch. Linac-based far-IR FELs are also candidate of the narrowband source. However the THz region has characteristics between light and microwave, an optical oscillator has to be carefully designed by considering waveguide mode, and then the instantaneous gain is normally decreased so that very high power is not expected.

Photo injectors using RF guns have been already well-developed as high brilliant electron sources. Meanwhile thermionic RF guns have not been studied so much. However those are also expected to have potential ability to create high-brightness and short-pulse beams [3]. In addition, whole system of the thermionic RF gun is simple, compact and low-cost than that of a photo-cathode RF gun, which is very attractive feature. This paper describes the results of simulations for the thermionic ITC-RF gun. A similar concept for the RF gun has already proposed by Lewellen [4].

Conventional way to compress the bunch length from the thermionic RF gun is employing an α-magnet [2]. Though the α-magnet is apparently working skilful manipulation of longitudinal phase space, it would be a bit annoyance when the beam kinetic energy is higher, because the magnetic device is getting bigger.

Beside the problem of back-bombardment [5], there is a specific feature in the longitudinal dynamics in thermionic RF guns. At the beginning of the beam extraction, a head of the electrons from the cathode is followed immediately by the electrons just behind, which is extracted by the higher electric field than that at the head of the beam train. Thus later electrons would get kinetic momentum or velocity faster than the head of the electrons. Consequently the electrons are expected to be concentrated into the head of the beam train under proper conditions such as the gun geometry and the velocity gain. This velocity-bunching-like phenomenon has already known by developers of the thermionic RF guns [2]. According to our simulation study so far, this velocity-bunched peak at the head of the beam train might possibly reach to a pulse width of ~ 200 fs with a couple of tens pC.

Table 1: Target parameters of the ITC-RF gun

RF freqency	2,856 MHz (S-band)
Material of cathode	LaB_6
Emission current density	~100 A /cm^2
Cathode radius	2 ~ 4 mm
Number of cells	2
Feeding total power	~ 5 MW
Total energy gain	~ 1.5 MeV
Bunch length (rms)	~ 100 fs
Bunch charge	~ a several ten pC
$\varepsilon_{norm.\ rms}$	< 2 π mm mrad
Δp/p	< 1 %

If the velocity-bunching-like effect occurred at the beginning of rising up of the longitudinal electric field is intentionally enhanced, the sub-picosecond beam would be obtained. In order to carefully design the ITC-RF gun, we have used the FDTD method that includes certain boundary condition and also space charge (wake-field) effect. The biggest disadvantage of this 3D simulation is the accuracy, because a very large memory area is required if one wants a general accuracy equivalent to 2-D axis-symmetrical geometry. However overall characteristics of the extracted beam can be predicted

#hama@lns.tohoku.ac.jp

because of no obvious inconsistency in solving the Maxwell's equations.

A ring type coherent terahertz (THz) radiation source is our final target by producing very short bunches from the ITC-RF gun [6]. In order to realize the THz ring project, required performance of the ITC-RF gun and other important parameters are listed on Table 1.

STRUCTURE OF THE ITC-RF GUN

The ITC-RF Gun has been designed so as to vary the relative phase and the amplitudes of RF field in each cell, independently. So far, the simulation can optimise the gun geometry and other parameters, but there has been no confidence whether the gun has been actually working with same parameter as the simulation, because errors of the fabrication, the power feed and the mode purity are not difficult to be confirmed experimentally.

The RF powers are fed separately into each cell. We performed a basic design of the ITC-RF gun by using a code SUPERFISH. The kinetic energy gain in the 1-st cell has to be reduced to less than ~ 0.5 MeV to enhance the velocity-bunching effect at the entrance of the 2-nd cell. Furthermore the length of the 1-st cell (from the cathode to the end of 1-st cell) is very important for the velocity-bunching. Finally we decided to control the power and phase of the RF for each cell independently to compensate fabrication errors and other error sources. In order to obtain, therefore, almost no RF coupling between two cells, a diameter of the connection beam duct has become to be 7 mm.

Result of the calculation of the longitudinal electric field for each cell using SUPERFISH is shown in Fig. 1.

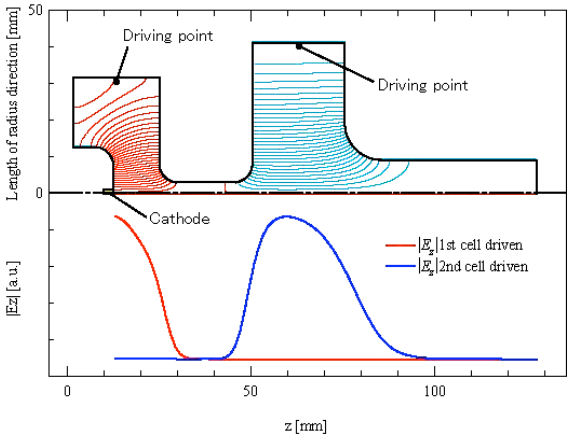

Figure 1: Calculated electric field lines and longitudinal electric field strengths along the beam axis are shown. The red line is results by excitation of the 1st cell, and the blue line indicates the case of the 2nd cell excitation.

THE FDTD SIMULATION

FDTD 3-D simulation

Definition of a 3-D cubic grid (Lee cell) is shown in Fig. 2.

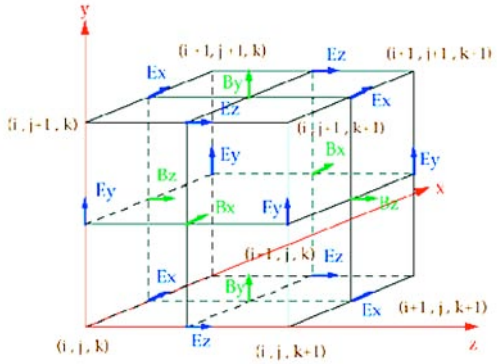

Figure 2: A 3-D cubic and locations of E and B representatives for the FDTD method. Symbols i, j and k are used to identify the grid number.

A leap-frog algorism gives a solution of the time dependent Maxwell's equation as (for example, a solution of E_x)

$$E_x^{n+1}\left(i+\frac{1}{2},j,k\right)=E_x^{n}\left(i+\frac{1}{2},j,k\right)$$
$$+c^2\,\Delta t\left[\frac{B_z^{n+\frac{1}{2}}\left(i+\frac{1}{2},j+\frac{1}{2},k\right)-B_z^{n+\frac{1}{2}}\left(i+\frac{1}{2},j-\frac{1}{2},k\right)}{\Delta y}-\frac{B_y^{n+\frac{1}{2}}\left(i+\frac{1}{2},j,k+\frac{1}{2}\right)-B_y^{n+\frac{1}{2}}\left(i+\frac{1}{2},j,k-\frac{1}{2}\right)}{\Delta z}\right]$$
$$-\frac{\Delta t}{\varepsilon_0}J_x^{n+\frac{1}{2}}\left(i+\frac{1}{2},j,k\right)$$
, (1)

where *n* is the step number, so that n+1/2 means the calculated result for the magnetic field at after 1/2-step. The location indicated by i, j and k are indicated by Fig. 2.

Results of the simulation for the ITC-RF gun

A snap shot of the beam acceleration in the gun shows in Fig. 3. In the simulation, the maximum strength of the electric field on the cathode is 25 MV/m, which was determined so as to the bunch head gets into the acceleration field of the 2nd cell just after 0.5 RF cycle passed.

Phase between two cells was decided to be p at the moment and the peak electric field in the 2nd cell has been ~ 45 MeV to obtain an approximately linear dependence of the exit time on the gained energy in the ITC gun.

In order to clarify the velocity-bunching in the ITC-RF gun, the particle distributions along the axis during the acceleration are shown in Fig. 3.

Projected spectra on the time axis and the energy axis are shown in Fig. 4. Both have spike structure at the heads of the bunch. For the time spectrun, the shape peak FWHM is approximately 200 fs, and that for the energy spectrum peak is ~ 0.3 % and the mean energy of the peak is around 1.26 MeV. This energy would be thought to be still dangerous for the space charge force, but actually there is not much charge in the peak (~ 20 pC). It is a rather suitable energy to manipulate the longitudinal phase apace.

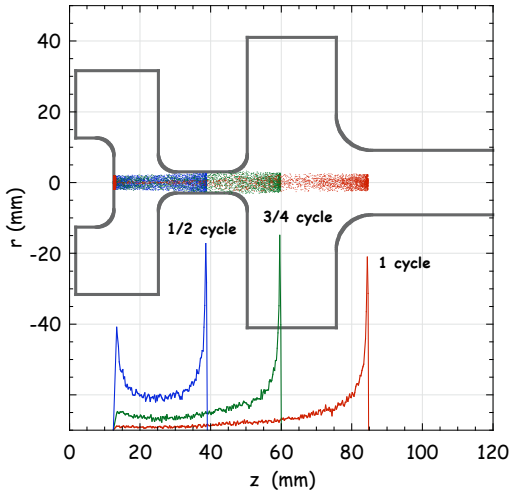

Figure 3: Three snap shots at after 0.5 rf-cycle, 0.75 rf-cycle and 1.0 rf-cycle. Longitudinal distributions for each identical time are also shown in lower part of the figure.

However we are not going to use a-magnet to get further shorter bunch because the energy spread grows. Consequently we use just the energy slit at the dispersive space placed just in front of the accelerating structure. In this case, the stability of the ITC-RF gun is very important because only the 0.3 % energy width from the top will be used. Since the mean energy of the peak structure is 1.26 MeV, if we want to reduce a energy fluctuation less than 1 %, the energy gain stability of ~ 40 eV is required.

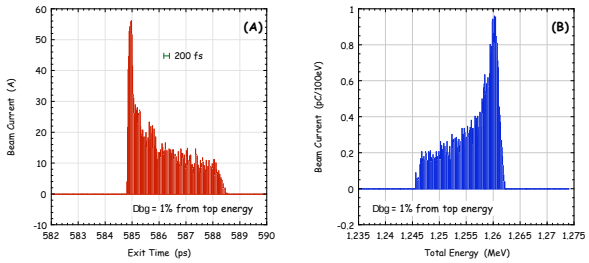

Figure 4: A final time distribution (A) and an energy spectrum (B). Both spectra were cut from 1 % energy width from the top energy. The acceleration field gradients are 25 MV/m on the cathode and 45 MV/m for the maxmum in the 2nd cell.

Transverse emittance is also derived from the FDTD simulation for various emission current density of the cathode. By using a following equation,

$$e_x = bg\sqrt{\langle x^2\rangle\langle x\phi^2\rangle - \langle x x\phi\rangle^2} \qquad (2)$$

The normalized emittance is estimated. Note the value is not elliptical area surrounding particles.

Here we cut the beam for the energy width of 1 % from the top energy, which is same condition indicated as Fig. 4. It should be noted that the normalized emittance is not much changed as increasing the beam current, staying around 1.2 p mm mrad. This may be because of relatively low charge inside the peak. After exiting the gun, beam will be transported in to the energy filter line consisted of two bending magnets and some quads. The length from the gun exit to a first accelerating structure will be 50 cm, so that actual emittance may be a bit spread. However the normalized emittance around 1.2 p mm mrad is pretty acceptable.

SUMMARY

Simulation study of an Independently-Tunable-Cells (ITC) RF gun using a thermionic cathode is discussed. The present target benchmark of the beam properties of which the time duration is a couple of hundred fs with several ten pC charge may be possible.

The FDTD simulation, which has been developed by our group shows of which a time duration of 1ps from the top of the bunch contains 30 pC.

One of the biggest technical issues is probably the cathode assembly, because we are going to a single crystal of LaB_6 that requires a very high temperature for stable operation. In order to heat up the cathode, a heater electrode is normally used. However it is difficult to keep thermal contact with a heater and the crystal. A method of laser-assisted heating is one of promising techniques. Another issue may be the energy filter to cut the bunch of only a part of 5 keV or less. Stability of the whole system and precise evaluation for designing the dispersive arc are necessary.

At the moment, we have not finished appropriate optimization for the designing the ITC-RF gun. Shape of the gun is possibly slightly changed. However we won't use a photo-cathode because it would be a very expensive system and not suitable for our THz project of which the multi-bunch beam is preferable and it may be satisfied by a relatively low charge in a bunch [6].

REFERENCES

[1] H. Hama, et al., Nucl. Instr. and Meth. A 528 (2004) 371.
[2] "Opportunities in THz Science", Report of a DOE-NSF-NIH Workshop held February 12 – 14, 2004, Arlington, VA, M. S. Sherwin, C. A. Schmuttenmaer, and P. H. Bucksbaum, Editors.
[3] J.W. Lewellen, Proc. of the 2003 Particle Accelerator Conf., Portland, Oregon, pp. 2035.
[4] C.B. McKee and J.M.J. Madey, Nucl. Instr. and Meth. A 296 (1990) 716.
[5] H.A. Enge, Rev. Sci. Instr. 34 (1963) 385; M. Borland, Ph.D. Thesis, Stanford University, 1991.
[6] H. Hama, "Dream of Isochronous Ring Again", will be published in Proc. 27th. Int. FEL Conf, Stanford, CA, Aug, 2005.

Energy-Recovery Linacs: Overview and Present Status in JAEA ERL

R. Hajima , M. Sawamura, R. Nagai, N. Kikuzawa,
N. Nishimori, H. Iijima, T. Nishitani, E.J. Minehara
Japan Atomic Energy Agency, Tokai, Ibaraki 319-1195, Japan

Abstract

In Japan Atomic Energy Agency (JAEA), we are developing an energy-recovery linac (ERL) for a high-power free-electron laser (FEL) and future X-ray light sources. The ERL was completed in 2002 by remodeling the original superconducting accelerator and commissioned to FEL experiments. In this paper, we summerize recent research activities at JAEA-ERL.

INTRODUCTION

Two national institutes for atomic energy research in Japan, Japan Atomic Energy Research Institute (JAERI) and Japan Nuclear Cycle Development Institute (JNC), were merged into a new research institute, Japan Atomic Energy Agency (JAEA), at October 2005. A research program of energy-recovery linacs (ERL), which had been conducted at JAERI, was succeeded wholly by JAEA. In this paper, we present our research activities on energy-recovery linacs for high-power FEL and future X-ray light sources.

R&D FOR A HIGH-POWER FEL

After the successful achievement of FEL lasing in kilowatt level, in 2000[1], we started the development of an energy-recovery linacs to demonstrate higher FEL power, 5-10 kW. It is considered that same-cell energy-recovery in a superconducting linac is the only practical solution to put such a high-power FEL in work efficiently[2]. Hence, we decided to remodel the superconducting accelerator into an energy-recovery linac (ERL)[3]. The original linac was shut down in the spring of 2001, and the ERL was completed after a half-year construction period. We demonstrated first energy-recovery operation at 19 February, 2002, and first FEL lasing at 14 August, 2002 [4][5].

The injector of energy-recovery linacs was further modified to increase the beam current. This injector upgrade was completed by October 2005, and we can now accelerate an electron beam of 10 mA, doubled value of the original one. FEL lasing with 10 mA beam current was obtained at 2 December 2005.

Injector RF Sources

Increasing the injector beam current is an essential path to enlarge the FEL power by taking full advantage of the energy-recovery. In the original configuration without energy-recovery, the linac was operated at 5 mA injector beam current. Two single-cell cavities of the injector were driven by 6 kW solid state amplifier for each, which is enough power for 5 mA injection. The solid state amplifier has been replaced by an IOT-klystrode of 50 kW, which enables one to inject a 40 mA beam into the ERL. The IOT is designed for CW operation as well as pulsed operation, while the original amplifier allowed only pulsed operation with small duty-cycle such as 1 ms 10Hz. We also installed a similar IOT system for 5-cell main modules, which allows future long-pulse operation.

Gun Grid Pulser

The electron gun is equipped with a thermionic cathode and operated at 230 kV DC voltage. A train of electron bunch is generated by grid pulser. In the original configuration, the gun was designed to produce 0.5 nC electron bunches at 10.4 MHz repetition, that is 5 mA. We developed a new grid pulser working at 20.8 MHz, doubled repetition of the original one, and a 10 mA beam is now available [6]. The new grid pulser is designed at Budker Institute of Nuclear Physics and can be operated in CW-mode as well as pulse-mode.

We measured electron beam properties with the new grid pulser and confirmed that it keeps similar performance to the original one. The pulse width and the normalized rms emittance at the gun are 590 ps (FWHM) and 20 πmm-mrad, respectively.

As presented above, the injection cavities are ready for 40 mA beam, which requires 83 MHz operation of the grid pulser. Design of a grid pulser for the higher repetition rate, 41.5 MHz and 83 MHz, remains a future task.

RF low-level controllers

In a superconducting accelerator, an RF low-level controller is one of the key components for achieving good stability. The original linac was equipped with a low-level controller, which kept phase flatness at ± 1 degree within a 1 ms macropulse. After the remodeling into the ERL, however, we found that the stability of the low-level controller was insufficient to extract the full performance of the ERL. Since the controller had no special function to compensate temperature drift, we could hardly obtain long-time stability against the change of room temperature.

The low-level controller was replaced by new one. The new system is based on phase and amplitude control of the

e-mail: hajima.ryoichi@jaea.go.jp

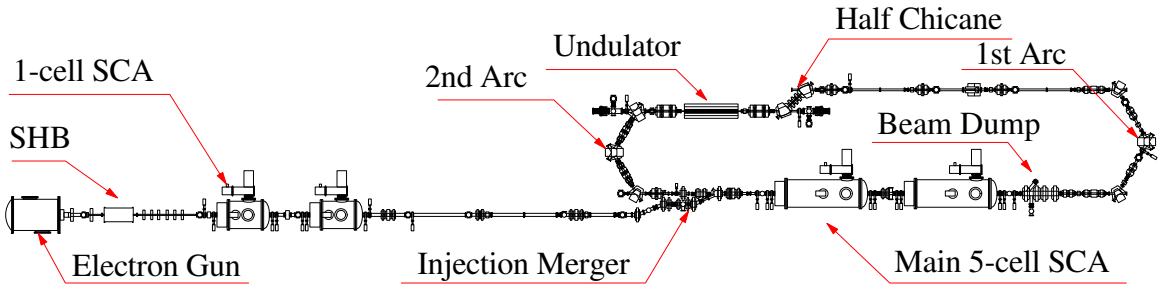

Figure 1: The layout of JAEA Energy-Recovery Linac. An electron bunch generated by 230 kV electron gun is accelerated to 2.5 MeV and injected into the energy-recovery loop. The electron bunch is accelerated to 17 MeV by main superconducting cavities and transported to the FEL undulator. The electron bunch is, then, reinjected to the main cavities and decelerated down to 2.5 MeV and collected by a beam dump. All the superconducting cavities are driven at 499.8 MHz.

cavity RF field coupled with a tuner controller, which is same as the original system. In the design of the new low-level controller, we introduced the following functions for the better stability: the feedback gain and bandwidth can be varied during operation to obtain good flatness of RF phase and amplitude within a macropulse, all the circuits are contained in boxes with temperature stabilization.

The original controller was placed at the operation room, and the feedback loop involved 50-m long cables to connect the controller and the RF cavity. We found that large temperature drift was caused by this long cables. The new controller is installed just beside the cavity to make the cable length as short as possible. Furthermore the cables between the controller and the cavities are contained in a temperature-controlled pipe to suppress the temperature drift.

After these upgrade, the accuracy and stability of accelerating RF has been greatly improved. The flatness of RF phase and amplitude within a 1 ms macropulse are 0.20 deg. and 0.013% for the old system, 0.06 deg. and 0.013% for the new system, where all the values are RMS. Phase and amplitude fluctuation for 5 minutes in the new system are measured as 0.15 deg. and 0.015%, respectively. In this measurement, mechanical vibration of the cavity due to the refrigerator is the dominant source of the fluctuation.

Operation Control System

The operation control system of JAEA-ERL has also been upgraded. The old system based on CAMAC and PC-9801 with Windows-95 became obsolete and difficult to maintain and make further extension. We have developed a new system consisting of CAMAC and local controllers working with -ITRON [7], which are robust hardware without mechanical component such as hard-disc drives. Console applications for the operation are written by JAVA and CORBA, modern software independent of platform. We have also prepared data-logging and database services using WEB and MySQL.

FEL Transport Line

A laser-beam transport line has been built to deliver FEL pulses to an experiment room. We have installed an optical-beam expander, which consists of two elliptic mirrors, at the end of FEL optical cavity to convert a diverging beam from a center-hole at a FEL cavity mirror into a parallel beam. The expanded beam is transported to the experimental room through a 24 m-long evacuated pipe.

R&D FOR FUTURE X-RAY LIGHT SOURCES

The same-cell energy-recovery is also a break-through technology for future X-ray light sources [8]. Since an electron bunch in an ERL travels a recirculation loop only once, it is free from emittance growth by quantum excitation, which is a critical issue in storage rings. The ERL light sources are, thus, expected to produce coherent X-rays via diffraction-limited electron beams. We can also produce a femto-second electron bunch in an ERL, which is quite useful to explore ultrafast X-ray science. We are proposing a 5-6 GeV ERL as a forth generation X-ray light source, where coherent and femto-second X-rays are available[5].

Since the performance of an ERL light source is restricted by performance of its electron gun, we are focusing our R&D efforts on the development of an electron gun for small-emittance and high-average current. In order to fulfill the diffraction limited condition at hard X-ray region, an electron beam having normalized emittance of 0.1 mm-mrad is required. We consider the combination of a DC gun and a photo-cathode with negative electron affinity (NEA) surface is the solution to produce such a small emittance beam. In JAEA-ERL group, we are developing super-lattice GaAs photo-cathode, which is suitable to generate small emittance and high average current beams[9]. A 250-kV, 50 mA DC gun for testing the photo-cathode is also under construction[10].

SUMMARY

An energy-recovery linac has been developed for a 5-10kW free-electron laser at JAEA. We have upgraded major components of the ERL, RF low-level controller, injector RF sources, operation control system, a gun grid pulser, for stable operation of the ERL and high-power FEL demonstration. The upgrade has been completed, and the FEL is now routinely operated. Another research program has been organized for a future ERL light source, which involves the development of a photo-cathode DC gun for a small-emittance and high-average current beam.

REFERENCES

[1] N. Nishimori et al., Nucl. Instr. Meth. **A475** (2001) 266–269.

[2] G.R. Neil and L. Merminga, Rev. Mod. Phys. **74**, 685 (2002).

[3] R. Hajima et al., Nucl. Instr. and Meth. **A445** (2000) 384–388; T. Shizuma et al., Nucl. Instr. and Meth. **A475** (2001) 569–573; R. Hajima et al., Proc. EPAC-2000, 1033–1035; T. Shizuma et al., Proc. EPAC-2000, 1074–1076.

[4] R. Hajima et al., Nucl. Instr. and Meth. **A507** (2003) 115–119.

[5] E.J. Minehara, Nucl. Instr. and Meth. **A557** (2005) 16–22.

[6] N. Nishimori et al., "20.8MHz Electron Gun System for an Energy Recovery Linac FEL at JAERI", Proc. APAC-2004.

[7] N. Kikuzawa, "Control system upgrade of JAERI ERL-FEL", Proc. FEL-2003.

[8] Sol M. Gruner et al., Rev. Sci. Instr. **73** (2002) 1402.

[9] T. Rao et al., Nucl. Instr. and Meth. **A557** (2005) 124–130.

[10] T. Nishitani et al., "The Development of the JAERI 200keV Electron Gun with an NEA-GaAs Photocathode", Proc. FEL-2004.

COMPARISON OF SINGLE-PASS (ERL) AND A MULTI-PASS (MARS) ACCELERATOR - RECUPERATORS AS A COHERENT X-RAY SOURCES

G.Kulipanov, A. Skrinsky, N. Vinokurov, Budker Institute of Nuclear Physics, 630090, Novosibirsk, Russia

Abstract

One of prospective types of accelerators for the fourth generation x-ray sources are accelerators-recuperators. The simplest one is energy recovery linac (ERL), having one orbit. The multiturn accelerator-recuperator has significantly less expensive RF system. It is therefore very attractive option for the future x-ray sources. The comparison of these two accelerators is performed in this paper.

INTRODUCTION

Development of the synchrotron radiation (SR) sources over the last 30 years was aimed at achieving various purposes. The basic tasks were: increase- of the spectral brightness, an increase in the energy of generated quanta, the use of intrinsic properties of synchrotron radiation as the polarization, time structure, coherence, etc. It was also important that each source of synchrotron radiation was simultaneously used for a great number of experimental groups from various fields of science.

The SR sources of the 3rd generation available and those under construction (ESRF, APS, Spring-8, SLS, DIAMOND, SOLEIL, etc.) are the efficient factories for generation of the new knowledge, new technologies and new materials. In the last decade, there were active discussions on the development of SR sources of the 4th generation. The world's physical community worked out the requirements to these sources (see Table 1) and suggested several ways for the development of such sources.

Table 1: List of requirements for fourth generation of the X-ray sources

full spatial coherence;

as high as possible temporal coherence ($\Delta\lambda/\lambda < 10^{-4}$) without additional monochromatization;

the averaged brightness of the source has to exceed 10^{23}–10^{24} photons·s^{-1}mm^{-2}mrad^{-2} (0.1 % bandwidth)$^{-1}$;

the photon flux of the fourth generation source must be on level of 3rd generation SR sources;

the high peak brightness of order 10^{33} photons s^{-1}mm^{-2}mrad^{-2} (0.1 % bandwidth)$^{-1}$ is important for some experiments;

electron bunch length up to 1 ps and using a specialized technique X-ray pulses smaller than 100 fs;

high long-term stability; generation linear, left-right circular polarized radiation with fast switching type and sign polarization; constant heat load on chambers and optics;

serving multi-user community.

It is worth mentioning that due to the purposeful work of the accelerator physicists the brightness of new SR sources was improved by three orders of magnitude each decade. Therefore, for the last 30 years the brightness of X-ray SR sources has been increased by the factor of a billion.

Nevertheless, at the modern sources, the flux of coherent quanta is only 10^{-3} of the total flux. Therefore, in spite of the successful demonstration of the X-ray holography, it did not become the efficient technique for structural studies of the real objects having mostly noncrystalline structures. Even for the crystalline structures, the speckle-spectroscopy is very important and it is accessible only in coherent light.

Therefore, of all the requirements to SR sources of the 4th generation, obtaining of the fully spatially coherent flux of quanta keeping the same flux of quanta provided with a source of the 3rd generation is the most important. Also, a possibility of using the undulator radiation with a monochromaticity of 10^{-3}÷10^{-4} without using of monochromators, which, as a rule, spoil the beam spatial coherence, is of great importance.

Realization of a fully spatial coherent source is possible in case of a shift from the electron storage rings to accelerators with energy recovery, which was first discussed in August, 1997 at SRI-97 [1] then in July, 1999 at ICFA Meeting in APS [2]. After that, the idea of using the accelerators-recuperators was actively discussed in many conferences and laboratories [3, 4, 5]. However, in practice, all the projects assume the use of a single-turn version (ERL) (Fig.1a) compared to our first proposal of 1997 to use a multi-turn accelerator-recuperator (MARS) (Fig.1b)

The purpose of this report is comparison of the ERL and MARS based radiation sources from the viewpoint of their realization in practice.

WHY THE 4TH GENERATION SR SOURCES SHOULD USE THE ACCELERATORS-RECUPERATORS?

All the requirements to X-ray radiation sources of the 4th generation cannot be satisfied with the use of only one kind of a source. The high peak brightness and femtosecond duration of radiation pulses can be attained at the linac based SASE FEL with a high pulse current (I_p >1 kA). All the remaining requirements are easier and cheaper realized with the use of radiation from the long undulators installed at the accelerator-recuperator. For generation of a fully spatially coherent undulator radiation with a radiation wavelength λ, it is necessary to reduce the electron beam emittance down to it diffraction limit

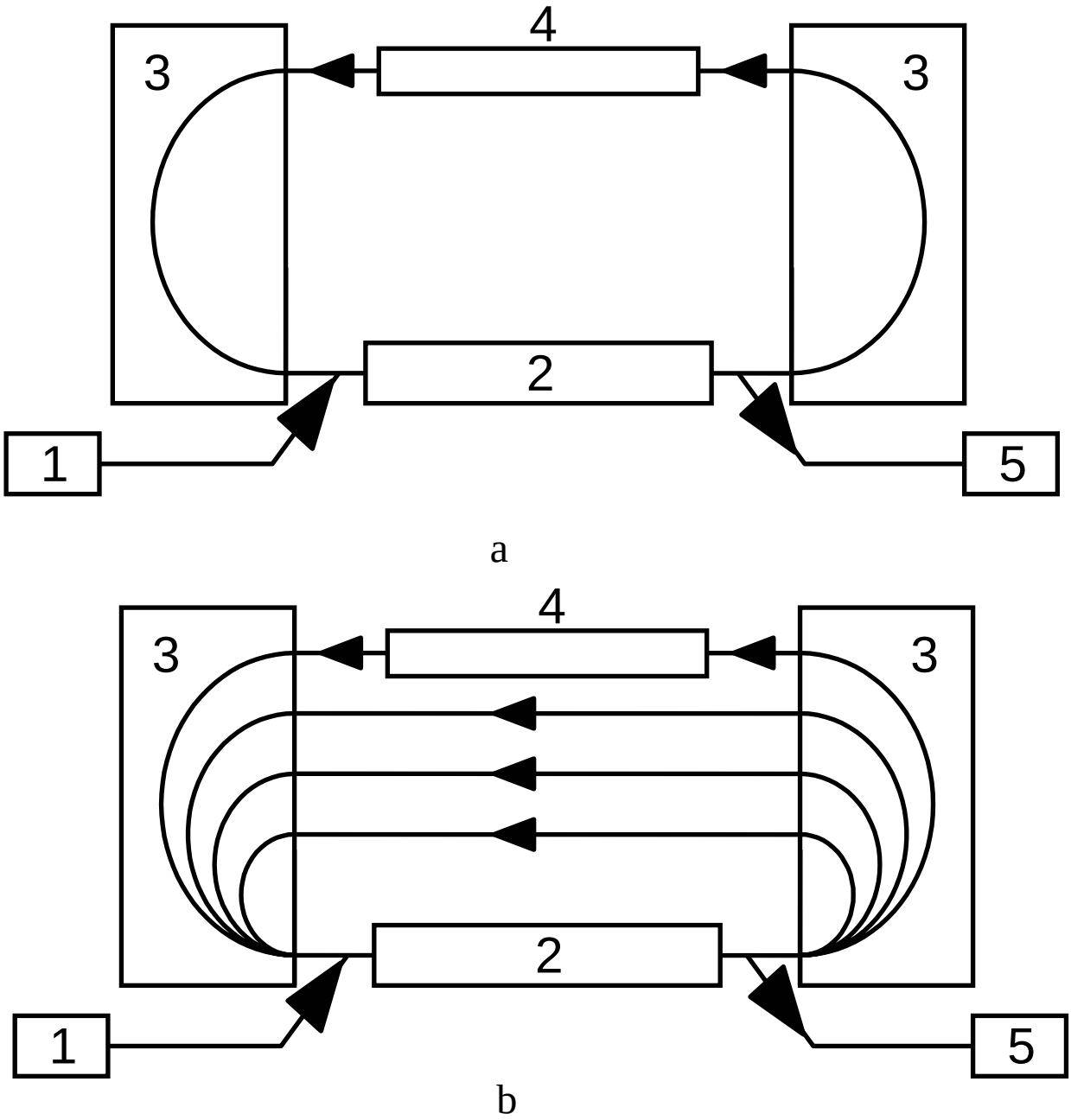

Figure 1: Scheme of the x-ray source based on accelerator – recuperator. a – single-pass, b – four-pass. 1 – injector, 2 – accelerating structure, 3 – bending magnets, 4 – undulators, 5 – beam dump.

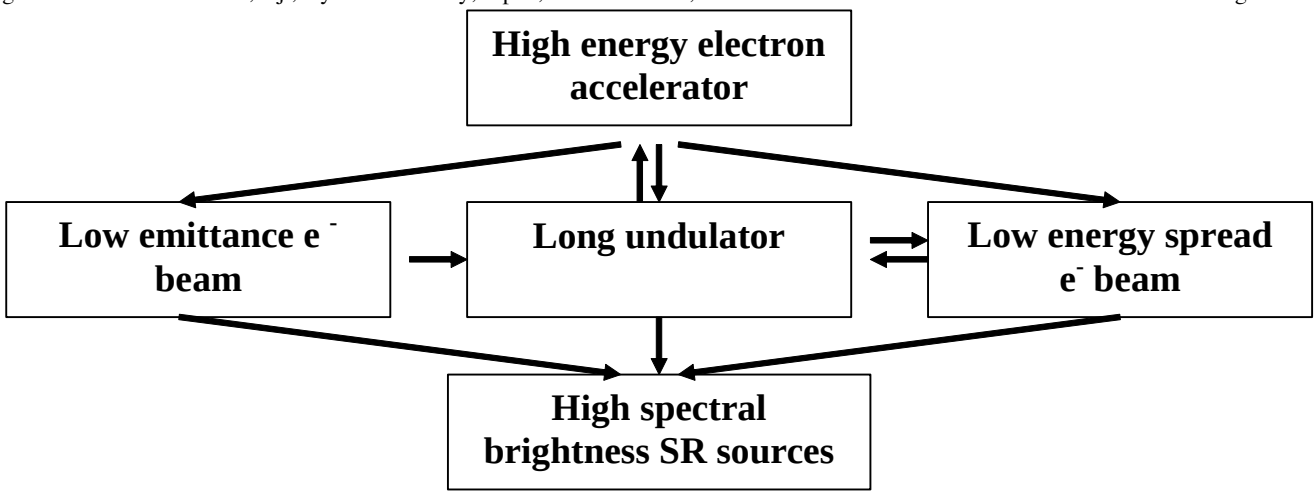

1980	$\varepsilon \sim 10^3$ nmrad	$N_u \sim 10$	$\sigma_E/E \sim 10^{-3}$
1990	$\varepsilon \sim 10^2$ nmrad	$N_u \sim 10^2$	$\sigma_E/E \sim 10^{-3}$
2000	$\varepsilon \sim 1$ nmrad	$N_u \sim 10^3$	$\sigma_E/E \sim 10^{-3}$
2010 (the aim)	$\varepsilon \sim 10^{-2}$ nmrad	$N_u \sim 10^4$	$\sigma_E/E \sim 10^{-4}$

Figure 2: Main ways of creation of fourth generation x-ray sources.

$$\varepsilon_{x,z} < \frac{\lambda}{4\pi} \approx 10^{-11}\, m \cdot rad \qquad (\lambda \sim 1\text{Å}).$$

Monochromaticity of the undulator radiation is determined by the number of undulator periods and the beam energy spread $\frac{\Delta\lambda}{\lambda} \approx \frac{1}{N_u}$ for $N_u < \frac{1}{2\pi}\left(\frac{\sigma_E}{E}\right)^{-1}$. If the electron beam energy spread is $\left(\frac{\sigma_E}{E}\right) < 10^{-4}$, one can have undulator radiation with a monochromaticity of $\Delta\lambda/\lambda \sim 10^{-3} \div 10^{-4}$.

In the storage rings, the beam emittance and energy spread are determined by equilibrium between the radiation damping ($\tau_r \sim 10^{-2} \div 10^{-1}$ sec) and two basic diffusion processes: quantum fluctuations of synchrotron radiation and intrabeam scattering. The analysis shows that in practice, there is no real solutions how to reduce the beam emittance in the storage ring $\varepsilon_{x,z} < 10^{-10}$ m·rad and an energy spread $\sigma_E/E < 10^{-3}$ (see Fig.2).

Both in the accelerators-recuperators and linacs, the normalized emittance εn can be kept the same during acceleration. Having a good injector with $\varepsilon_n < 10^{-7}$ m·rad, due to adiabatic damping at an energy E > 5 GeV the beam emittance $\varepsilon_{x,z} \sim 10^{-11}$ m·rad and energy spread $\sigma_E/E < 10^{-4}$ can be obtained. In the accelerators-recuperators, the time of acceleration is shorter compared to the time of radiation damping in the electron storage rings ($\sim 10^3 \div 10^4$ times) and because of this fact, the diffusion processes cannot spoil the electron beam emittance and its energy spread. Therefore, for experimentalists the accelerator-recuperator based source is similar to the source based on the electron storage ring with the only difference that in the accelerator-recuperator every time it is used a new electron beam with small emittance ($\varepsilon_{x,z} \sim 10^{-11}$ m·rad) and energy spread ($\sigma_E/E \sim 10^{-4}$).

Therefore, on the one hand, accelerators-recuperators have advantages of the electron storage rings as a high reactive power in a beam (~ GW) and the absence of radiation safety problems. On the other hand, accelerators-recuperators incorporate advantages of linear accelerators as a possibility to obtain electron beams with the ultimately small emittance and energy spread.

TECHNICAL SOLUTIONS FOR REALIZATION OF THE 4TH GENERATION SR SOURCES ON THE BASE OF ACCELERATORS-RECUPERATORS

Development of accelerators-recuperators for various purposes (FEL, SR sources, electron cooling) have been discussed in detail at the Conference ERL-2005 [6]. Independently of the posed tasks, many accelerator-recuperator systems can technically be realized. Therefore, at present, it more reasonable to compare parameters, realizeability and costs of the 4th generation SR sources either on the base of a single-turn (ERL) or multi-turn (MARS) accelerator-recuperator.

a. Basic overall dimensions

As an example, compare the single-turn and 4-turn accelerators-recuperators (see Fig. 3) at an energy of 6 GeV whose value was chosen for the task of obtaining the first harmonics of undulator radiation with $\lambda \sim 1$Å. We will use for estimation the superconducting TESLA

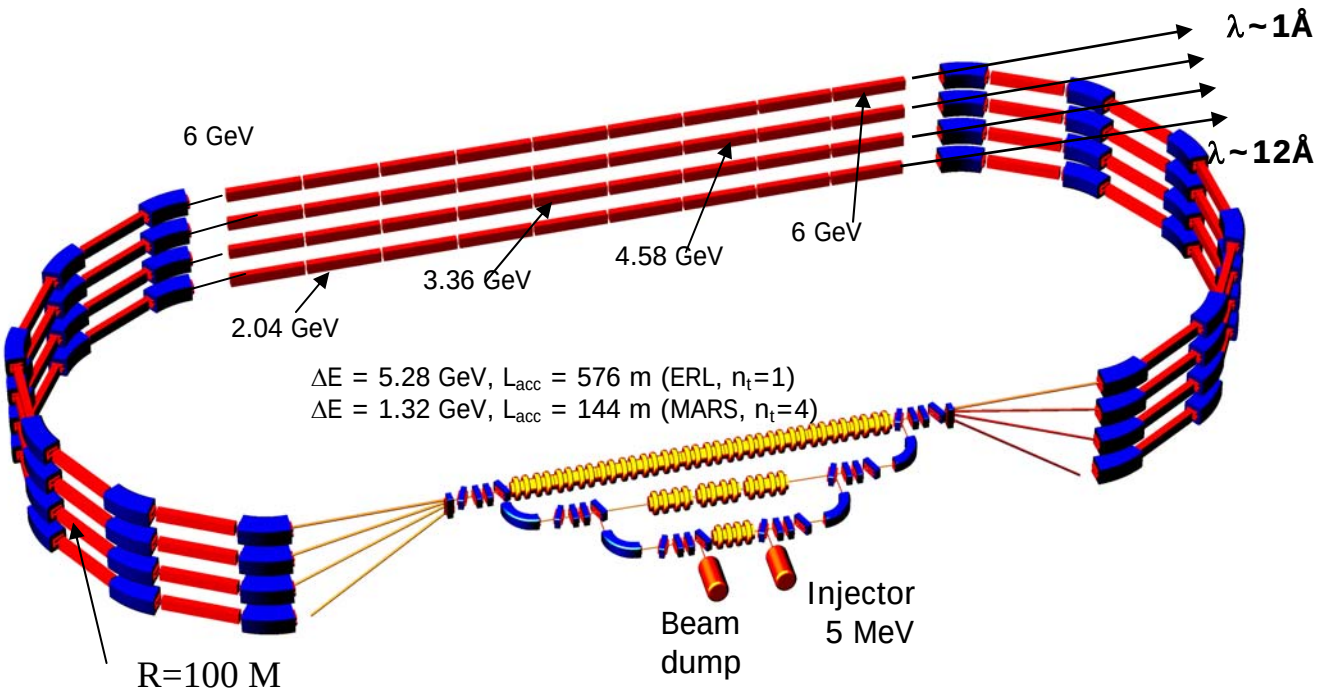

Figure 3: Basic overall dimensions ERL and MARS at E_{max} = 6 GeV.

module (L = 12 m, f_{RF} = 1.3 GHz, ΔE = 110 MeV as the accelerating gradient in cells of 15 MeV/m), the total length of a structure is L_{acc} is about 150 m for n_t = 4 and about 600 m for n_t = 1 (n_t is the number of turns). Therefore, let us choose the section lengths to be L_{sect} = 200 m for n_t = 4 and L_{sect} = 650 m for n_t = 1. The arcs radii should be of R>100 m to prevent the beam emittance degradation by the quantum fluctuations of synchrotron radiation [1].

b. Photoinjector

The normalized emittance of $\varepsilon_n < 10^{-7}$ m·rad can be obtained for the bunch of electrons with a charge of Q = 7.7 · 10^{-12} C and duration of τ_{pulse} = 14 ps. With an increase in charge, the beam emittance increases proportionally.

For a single-turn accelerator-recuperator, the injection current is the same as that in the accelerating structure I_{inj} = $Q \cdot f_{RF}$ ~ 10 mA.

In the accelerators-recuperators with several turns it is preferable to prevent short-range interaction of bunches from different turns in the accelerating straight-line section. The right choice of the turn lengths and n_t-times less injection frequency can provide it. But the beam average current is nt-times less in this case

$$I_{inj} = Q\frac{f_{RF}}{n_t}.$$

Therefore, for n_t = 4, the injector current and consequently currents of individual tracks can be I_{inj} = 2.5 mA.

c. Cascade injection

Both for the single-turn and multi-turn accelerators-recuperators it is reasonable to use our proposal [2] of the cascade injection (see Fig.4), which enables injection of electrons into all the accelerating structures with energies of no less than- $E_{max}/10$ (E_{max} is the maximum energy of electrons traveling in the accelerating structure) thereby simplifying the problem of focusing particles of different energies, which are traveling simultaneously in the accelerating structure. On the other hand, it allows the use of injector with E < 10 MeV thus decreasing the radiation background during the beam drop in the dump and removes practically the problem of the induced radiation. In addition, the cost of the injector and its RF generator is substantially reduced.

d. Main accelerating structure

The number of accelerating modules (ΔE = 110 MeV) for a single-turn accelerator-recuperator is n_{mod} = 48, for a 4-turn accelerator n_{mod} = 12. By several estimates, the cost of each module (accelerating structure, cryostat and relevant cryogenic equipment, RF generator) can vary from 5 to 9 M$; the power consumption of an individual module is ranging from ~0.6 to 0.9 MW. If we take the mean values for n_t = 1, the cost of an accelerating structure is 336 M$ and power consumption is 36 MW. For n_t = 4, the cost of an accelerating structure is 84 M$ and power consumption – 9 MW.

e. Magnetovacuum system

Taking into account that the accelerators-recuperators are the single-pass systems, the gap for bending magnets

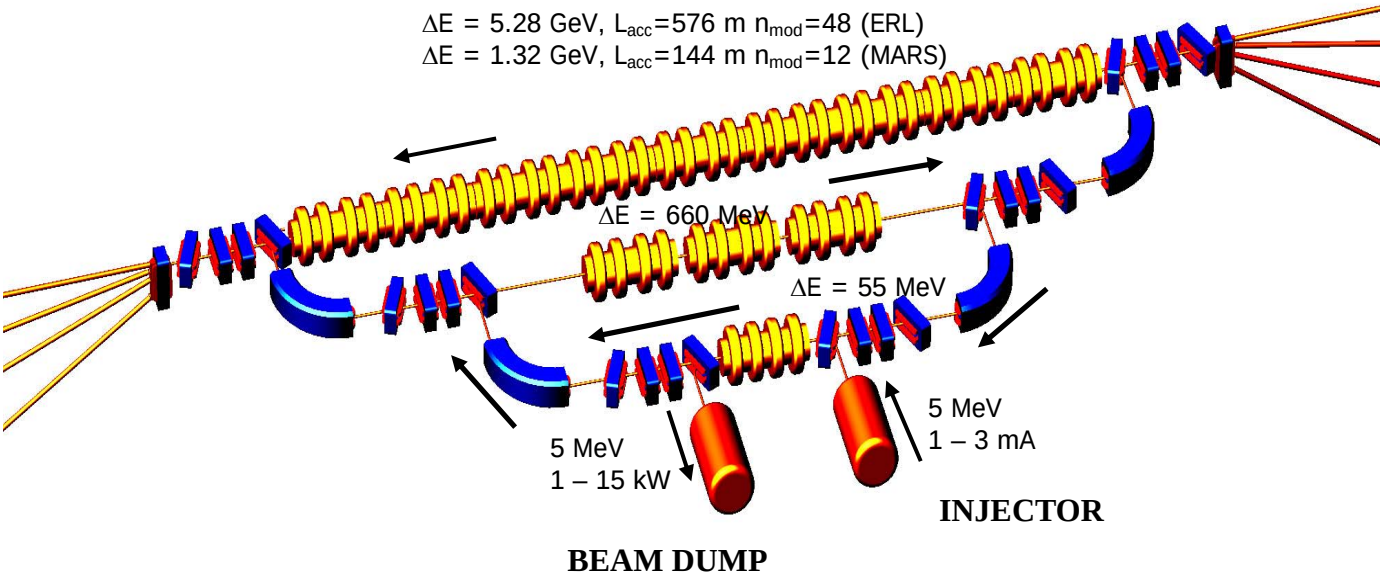

Figure 4: Cascade scheme of injection.

can be taken to be 1cm, the incircle diameter in quadrupoles – 1.5 cm, and in sextupoles – 2 cm. Thereby the overall dimensions, weight, power supply and the cost of the magnetic system are reduced substantially. With an account for the fact that in the single-pass system it is enough to have vacuum of $10^{-7} \div 10^{-8}$ Torr, the vacuum system seems to be rather simple. Rough estimations have shown that the cost of a turn (magnetic structure components with power supply system, vacuum system, diagnostics) could be of 30 M$ and power consumption ~2.5 MW.

For four turns, the cost is 120 M$ and power consumption P ~ 5 MW.

Table 2: Power consumption and cost for ERL and MARS

COMPARISON ERL AND MARS

Comparing SR sources based on a single-turn (ERL) and a 4-turn (MARS) accelerators-recuperators it is worth mentioning that:

in both versions one can have the same parameters of the sources satisfying the main requirements to the 4th generation SR sources.

the cost of many systems (building, photoinjector, beamline) are the same both for ERL and MARS;

the difference in the power consumption and cost is substantial for the magnetovacuum and RF accelerating systems of ERL and MARS.

	RF system		Magnetovacuum system		Total	
	Power MW	Cost M$	Power MW	Cost M$	Power MW	Cost M$
$n_t = 1$	36	336	2.5	30	38.5	336
$n_t = 4$	9	84	5	120	14	204

f. Undulators

In order to achieve the full spatial coherence of the source and keep at the same time the photon flux on the level of the 3rd generation sources, we suggest to use the current value of 10 mA for a single-turn accelerator and 2.5 mA for the four-turn accelerator. In this case, we solve the problem of a full spatial coherence for the sources and the 10-100 times decrease in the current value compared to that of the 3rd generation SR sources is compensated by the use of radiation only from three types of undulators (but not from bending magnets) ($N_{u1} = 10^2$, $N_{u2} = 10^3$, $N_{u3} = 10^4$). The version suggested for some ERL projects [6] of using current values of up to 100 mA for keeping the photon flux seems to be far from optimum since with such an increase in current, the brightness is not increasing and sometimes even decreases.

CONCLUSION

At present, the projects of the 4th generation SR sources on the basis of accelerators-recuperators are considered at Daresbury Laboratory, Jefferson Laboratory, Cornell University, LBL, KEK, Erlangen University, Brookhaven National Laboratory. The accelerating schemes and most of systems , which make the basis of the projects, have already been tested in many laboratories (Jefferson Laboratory, DESY, MAMI, LEP, Budker INP, KEK, MAX). There are no any essential physical problems in the development of the 4th generation SR sources on the base of accelerators-recuperators. The main problem is the cost of the project and its maintenance. Therefore, orientation toward the multi-turn accelerators-recuperators (MARS), which enable a substantial reduction in the power consumption and the cost of accelerating systems compared to those of

ERL (for our example, 14 MW instead of 38.5 MW and 204 M$ instead of 336 M$) seems to be rather pragmatic. A rough estimation has shown that in practice, the total cost of the multi-turn accelerator based project is the same as the cost of the available SR source of the 3rd generation (ESRF, APS, Spring-8).

It is quite probable that in some cases, a multi-turn accelerator-recuperator can be used for improving the brightness and for obtaining the fully spatially coherent source at the upgrade of the available SR sources of the 2nd and 3rd generations. In this case, the existing storage ring with the available generation systems, beamlines, etc. can be used as the last track.

REFERENCES

[1] Kulipanov G.N., Skrinsky A.N., Vinokurov N.A. MARS – recirculator-based diffraction- limited X-ray source. – Novosibirsk, 1997. – 10 p. – (Budker INP preprint; No 97-103). Kulipanov G.N., Skrinsky A.N., Vinokurov N.A. Synchrotron light sources and recent development of accelerator technology // J. of synchrotron radiation. – 1998. – V. 5, pt. 3. – P. 176-178. – (Proceedings of the SRI-97).

[2] Kulipanov G.N., Skrinsky A.N., Vinokurov N.A. Presentation of MARS source on ICFA workshop on future light sources, ANL, USA, 1999.

[3] Gruner S., Bilderback D., Tigner M. Synchrotron Radiation Sources of the Future: White paper. – Cornell: Cornell university, 2000. – (Cornell university technical report)

[4] Kulipanov G., Skrinsky A., Vinokurov N. Energy recirculation linac: an alternative light source concept // International workshop ERLSYN 2002: Energy recovery linacs as drivers for advanced light sources, Erlangen, Germany, May 31 and June 1, 2002: Proceedings. – Erlangen, 2002. – P. 1-26.

[5] Kulipanov G.N., Gavrilov N.G., Gorniker E.I. e. a. Status of MARS-L project of high power FEL and prototype of a diffraction limited X-ray source // International workshop ERLSYN 2002: Energy recovery linacs as drivers for advanced light sources, Erlangen, Germany, May 31 and June 1, 2002: Proceedings. – Erlangen, 2002. – P.245-262.

[6] Proceedings of the ERL-2005 (to be published in NIM).

STATUS AND FUTURE OF NOVOSIBIRSK HIGH POWER FEL, BASED ON ONE PASS AND FOUR PASSES ACCELERATOR-RECUPERATOR*

N.G. Gavrilov, D.A. Kayran, B.A. Knyazev, E.I. Kolobanov, V.V. Kotenkov, V.V. Kubarev, G.N. Kulipanov, A.N. Matveenko, L.E. Medvedev, S.V. Miginsky, L.A. Mironenko, A.D. Oreshkov, V.K. Ovchar, V.M. Popik, T.V. Salikova, S.S. Serednyakov, A.N. Skrinsky, O.A. Shevchenko, M.A. Scheglov, V.G. Tcheskidov, N.A. Vinokurov#, Budker INP, Novosibirsk, Russia

Abstract

The first stage of Novosibirsk high power free electron laser (FEL) was commissioned in 2003. It is based on the normal conducting CW energy recovery linac. Now the FEL provides electromagnetic radiation in the wavelength range 120 - 230 micron. The average power is 400 W. The status, first experiments and prospects are discussed.

INTRODUCTION

A new source of terahertz radiation was commissioned recently in Novosibirsk. [1]. It is CW FEL based on an accelerator–recuperator, or an energy recovery linac (ERL). It differs from the earlier ERL-based FELs [2, 3] in the low frequency non-superconducting RF cavities and longer wavelength operation range. Full-scale Novosibirsk free electron laser is to be based on the four-orbit 40 MeV electron accelerator-recuperator (see Fig. 1). It is to generate radiation in the range from 5 micrometer to 0.2 mm [4, 5].

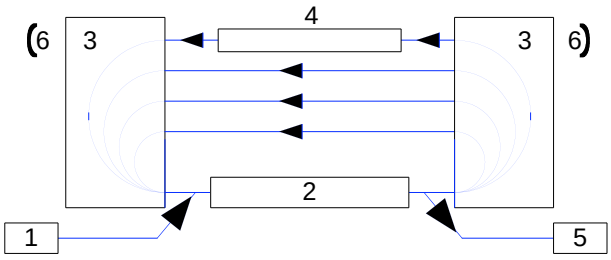

Figure 1: Scheme of the accelerator-recuperator based FEL. 1 - injector, 2 - accelerating RF structure, 3 - 180-degree bends, 4 – undulator, 5 – beam dump, 6 – mirrors of the optical resonator.

ACCELERATOR-RECUPERATOR

The first stage of the machine contains a full-scale RF system, but has only one orbit. Layout of the accelerator–recuperator is shown in Fig. 2. The 2 MeV electron beam from an injector passes through the accelerating structure, acquiring the 12 MeV energy, and comes to the FEL, installed in the straight section. After interaction with radiation in the FEL the beam passes once more through the accelerating structure, returning the power, and comes to the beam dump at the injection energy. Main parameters of the accelerator are listed in Table 1.

Table 1: Accelerator parameters (first stage)

RF frequency, MHz	180
Number of RF cavities	16
Amplitude of accelerating voltage at one cavity, MV	0.7
Injection energy, MeV	2
Final electron energy, MeV	12
Maximum bunch repetition rate, MHz	22.5
Maximum average current, mA	20
Beam emitance, mm·mrad	2
Final electron energy spread, FWHM, %	0.2
Final electron bunch length, ns	0.1
Final peak electron current, A	10

The electron source is the 300 keV DC gun with gridded cathode. Recently we changed the cathode-grid unit to the new one, and the charge per bunch increased to 1.5 nC.

FEL

The FEL is installed in a long straight section of a single-orbit accelerator-recuperator. It consists of two undulators, a magnetic buncher, two mirrors of the optical resonator, and an outcoupling system. Both electromagnetic planar undulators are identical. The length of an undulator is 4 m, period is 120 mm, the gap is 80 mm, and deflection parameter K is up to 1.2. One can use one or both undulators with or without a magnetic buncher. The buncher is simply a three-pole electromagnetic wiggler. It is necessary to optimize the relative phasing of undulators and is used now at low longitudinal dispersion $N_d < 1$.

Both laser resonator mirrors are identical, spherical, 15 m curvature radius, made of the gold-plated copper, and water-cooled [6]. In the center of each mirror there is a hole. It serves for mirror alignment (using the He-Ne laser beam) and output of small amount of radiation. The distance between mirrors is 26.6 m. The forward mirror

* Work supported by the Siberian Branch of Russian Academy of Science under the integration grant #174.
#vinokurov@inp.nsk.su

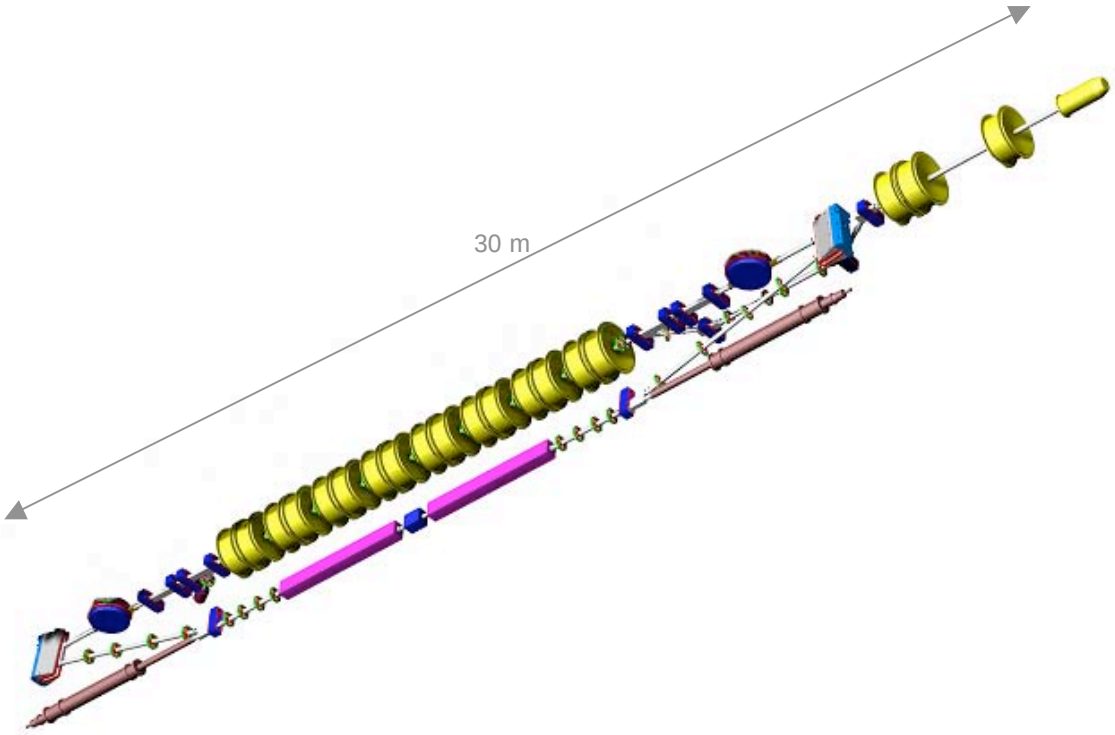

Figure 2: Scheme of the first stage of the Novosibirsk terahertz FEL. The loop lies in the vertical plain.

has the hole with the diameter 3.5 mm, and the rear one - with the diameter 8 mm. The calculated transparency of the mirror with the 8-mm hole, at the wavelength 150 micron, is 1.5%. At this wavelength the measured round-trip loss are near 7%. The output radiation pass through two windows, which separated the FEL and accelerator vacuum from the atmosphere. After the forward mirror the additional iris and the normal-incidence quartz mirror are installed. After the rear one there is a diamond window, tilted at the Brewster angle.

For FEL operation we used both undulators. Beam average current was typically 8 mA at the repetition rate 5.6 MHz, which is the round-trip frequency of the optical resonator and 32-th subharmonics of the RF frequency $f_0 \approx 180$ MHz.

RADIATION STUDY

The first measurements of radiation parameters were reported before [1].

Instead of the fine tuning of the optical resonator length we tuned the RF frequency. The tuning curve is shown in Fig. 3. The preliminary simulation results [7] demonstrate a reasonable agreement with measured data. The experimental curve is wider, which may be explained by the shortening of the optical resonator due to mirror heating.

The average radiation power, passed through the hole at the rear mirror, was about 400 W. Taking into account the 7% loss, one get approximately 2 kW of power, extracted from the electron beam.

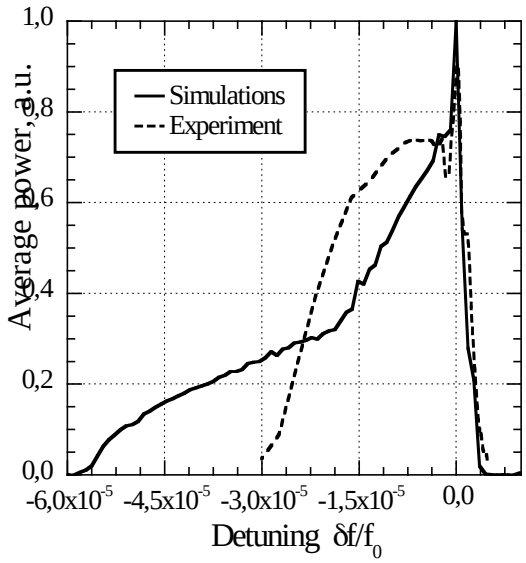

Figure 3: Dependence of the average power on the RF frequency detuning.

The electron beam power was 100 kW. Therefore an electron efficiency is about 2%. The typical radiation parameters are listed in Table 2.

Table 2: The radiation parameters

Wavelength, mm	0.12...0.18
Minimum relative linewidth, FWHM	0.003
Pulse length, FWHM, ns	0.05
Peak power, MW	1
Repetition rate, MHz	11.2
Average power, kW	0.4

To demonstrate the capabilities of our terahertz radiation source we made a hole in a plexiglas (PMMA) cube (see Fig. 4). Using the short-focusing mirror the CW breakdown in air was achieved (see Fig. 5).

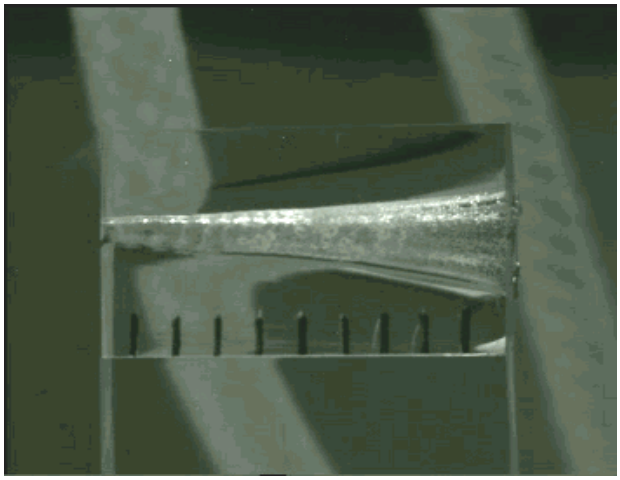

Figure 4: The conic hole in the PMMA cube, done with the terahertz radiation ablation. One division is 5 mm.

To transmit the radiation from the rear mirror hole to user stations, the beamline from the accelerator hall to the user hall was built. It comprises of one spherical mirror and 5 flat mirrors inside the stainless steel tubes. Now the beamline is filled by nitrogen. It is separated from the accelerator vacuum by the diamond window, and from the air by the polyethylene window. The beamline was commissioned successfully, and some preliminary optical measurements and experiments were done.

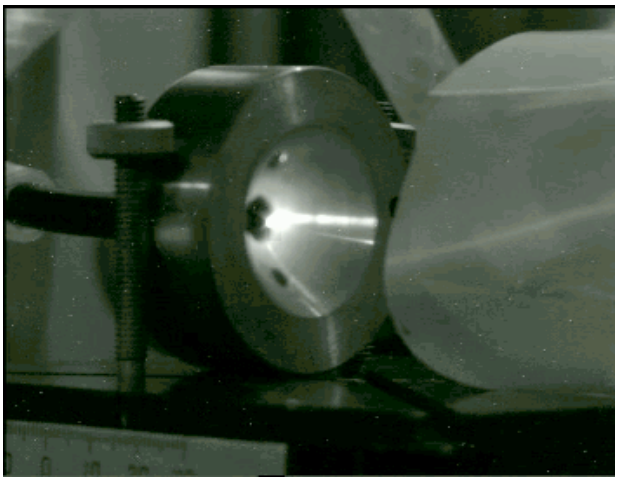

Figure 5: The CW discharge in the focus of the parabolic mirror.

In particular, the terahertz ablation of DNA and other biologically relevant molecules was performed [8]. It was shown, that transfer from surface occurred without molecular destruction.

FURTHER DEVELOPMENTS

We plan to increase further the output power. The electron gun upgrade for the increase of the average current up to 0.1 A is in progress.

The mechanical design of the second stage of the FEL is finished. The second stage scheme is shown in Fig. 6. New orbits lie in the horizontal plane. New FELs are installed at the second (20 MeV) and the fourth (40 MeV) orbits. The manufacturing of FEL components is under way.

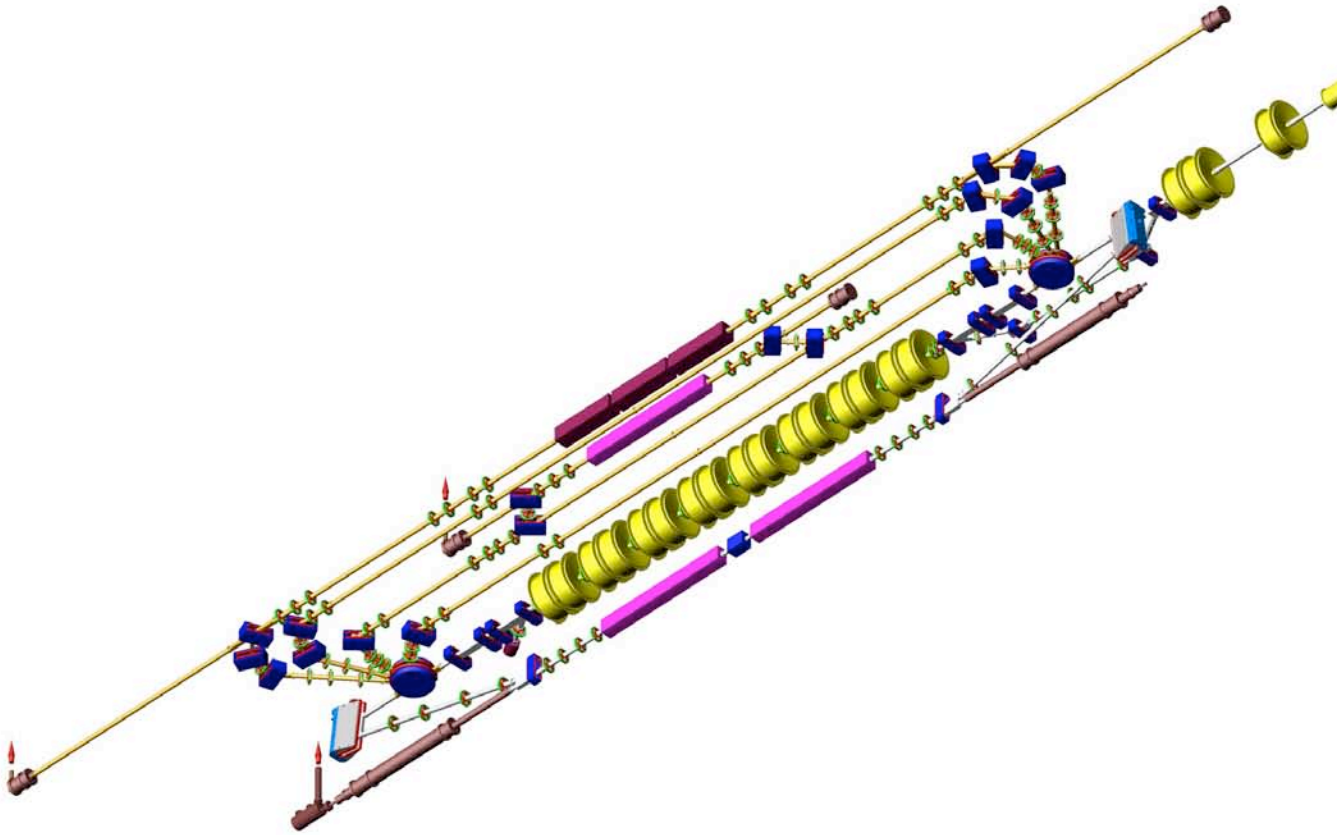

Figure 6: Scheme of the second stage of the Novosibirsk terahertz FEL. The terahertz FEL orbit lies in the vertical plain. Other four orbits lie in the horizontal one.

REFERENCES

[1] E. A. Antokhin et al. NIM A528 (2004) p.15-18.
[2] G.R. Neil et al. Phys. Rev. Lett. 84 (2000), p. 662.
[3] E.J. Minehara. NIM A483, p. 8, 2002.
[4] N.G. Gavrilov et al. IEEE J. Quantum Electron., QE-27, p. 2626, 1991.
[5] V.P.Bolotin et al. Proc. of FEL-2000, Durham, USA, p. II-37 (2000).
[6] Kubarev V.V., Persov B.Z., Vinokurov N.A., Davidov A.V. NIM A528 (2004), No. ½, p. 199-202.
[7] O.A. Shevchenko, A.V. Kuzmin, N.A. Vinokurov. NIM A543 (2005), No. 1, p. 114-117.
[8] A. K. Petrov et al., Russian Dokl. Acad. Nauk, v. 404 (2005), No. 5, p. 1 – 3.

The JAEA Superconducting RF Linac Driven Free-Electron Lasers

Eisuke J. Minehara and Nobuyuki Nishimori

Energy Recovery Linac Development Group, Advanced Photon Source Development Unit,
Quantum Beam Science Directorate, Japan Atomic Energy Agency (JAEA)
2-4 Shirakata shirane, Tokai, Naka, Ibaraki 319-1195 JAPAN,
E-mail:minehara.eisuke@jaea.go.jp

ABSTRACT

The JAEA Energy Recovery Linac (ERL) Development Group at Tokai, Ibaraki, Japan has successfully developed one of the most advanced and newest accelerator technologies named "superconducting ERLs" and some applications in near future using the ERLs. In the text, the current operation and high power JAEA ERL-FEL 10kW upgrading program, ERL light source design studies, preventing the stainless-steel cold-worked stress-corrosion cracking failures and decommissioning of nuclear power plants in nuclear energy industries were reported and discussed briefly as a typical application of the ERL-FELs.

Keywords: Superconducting Energy Recovery Linac (ERL), Free Electron Laser (FEL), Light Sources, Application, Nuclear Energy Industry, Cold Worked Stress Corrosion Cracking (CWSCC) Failure Prevention

1. INTRODUCTION

In the early stage of the JAEA high power energy recovery linac free-electron laser (ERL-EL) program in 1987 Japanese fiscal year (JFY), we had decided our three steps strategy of the FEL development program in the following. The Japanese fiscal year (JFY) starts from 1st April, and ends at 31st March, all 4 digit numbers in the text express years in JFY. The first step from 1989 to 1995 is to build the most powerful super-conducting linac FEL driver without energy recovery linac geometry (ERL) [1, 2]. The second one from 1996 to 2000 is to build the most powerful FEL lasing without ERL [3]. Because we had expected the more serious difficulties in the ERL technologies than the 2K cryogenic problems, and we could not find another funding to build the ERL, we therefore decided to postpone the ERL construction after our lasing the Japan Atomic Energy Agency (JAEA) non-ERL FEL in the second one. The third one from 2001 to 2005 is to build the most efficient FEL lasing using the ERL technology and every assignment of the third one is under development right now. During the third one, we have started large-scaled FEL applications in nuclear energy industries and others. The next one is to develop and build a huge fourth generation ERL light source facility, this is a conceptual design work and key components developmental ones. In the following sections, we introduce you some details of our existing facilities and developmental works and explained our achievements over these steps and future plans.

2. PAST AND PRESENT ACTIVITIES OF JAEA ERL

In the first step, we had built the non-ERL superconducting radio frequency (RF) linac FEL driver to demonstrate some higher electron beam power from 80kW to 100kW in quasi-continuous wave (CW) mode successfully. In order to keep cool and to use four 500MHz superconducting RF cavities, we have designed four zero-boil off cryostats with a 10K / 50K two stage Gifford-McMahon (GM) refrigerator of He gas heat-shield cooling and a 4K Joule-Thomson (JT)-GM 3 stage refrigerator of liquid He re-condensing inside the liquid He containers. The non-ERL JAEA FEL driver had been constructed in the old experimental hall of the 250 kV thermionic electron gun, 8 refrigerator compressors, large and small RF amplifiers and others, and in the old main accelerator vault of 2 main superconducting accelerator (SCA) modules, an electron energy analyzer, 14m long optical resonator hybrid undulator and beam line, respectively. The non-ERL driver had been modified to add an ERL capability in the third step in the JAEA FEL building in 2001.

Secondly, we tried to perform the most powerful FEL lasing using the non-ERL driver from 1996 to 2001. We could successfully demonstrate the world strongest FEL lasing twice, the first record of 0.1kW in the end of 1997 and the second one of 2.34 kW in the end of 1999[4]. During the final stage of the second record, we successfully found the new lasing mode to realize the a few hundreds femtosecond of 3.4 cycles, high conversion efficiency of 6-9% from the beam power to FEL light one, one GW peak power and over 2kW high average power [5,6]. These performance parameters were typically obtained in the electron energy of 16.5MeV, bunch charge of 510pC, bunch length of 2.5-5ps, bunch repetition of 10.4125MHz, wavelength of 22.4micron and quasi CW mode.

Thirdly, we have tried to realize the most efficient FEL lasing up to a 10 kW class or larger one constructing the super-conducting energy recovery linac-based free-electron laser (ERL-FEL) [7]. The JAEA ERL-FEL was naturally extended to the current configuration from the old one. The new JAEA ERL-FEL has the capability of about 8 times larger electron beam power than the old one, and was fitted into the existing JAEA FEL building interior. In the new FEL, there are the 250kV electron gun in the starting position, then sub-harmonic buncher (SHB), solenoid lens beam transport line, capture section of the first superconducting single-cell cavity, pre-accelerator of the single one, staircase-structured merging system of low and high energy electron beams, two main superconducting RF 5 cell cavities, east and west arcs of the achromatic and isochronous 180 degree bending magnet systems, an optical resonator, a hybrid undulator and a beam dump after one and half turns of the beam recirculation. All of the design parameters of the 10kW ERL were not realized because of the shortage of construction budgets. From 2001 to 2002, we modified the non-ERL FEL to re-construct the new ERL-FEL with the same current and electron energy, and the same beam power.

3. UPGRADING EXISTING FEL

In the periods from 2003 to 2005, the upgrading of ERL injector from the original parameters of 0.5nC x 10.4125MHz = about 5mA to 40mA has been tried to realizing higher repetition from 10.4125 to 41.65 MHz, and larger charge from 0.5nC to 1nC. Right now, we plan to run our grid-pulsar in 20.825MHz repetition x 1nC charge=20mA, or in 41.65MHz x 1nC = 40mA. As the grid-pulsar has had larger time jitter in 41.65MHz, we could

properly run the pulsar in 20.825MHz or slower one with 0.5nC or 1nC right now. Radio frequency amplifiers for the injector were replaced from 2 quasi CW 6kW solid state amplifiers to true CW 50kW inductive output tube (IOT) based amplifiers. Two 50kW RF main amplifiers for exciting two 500MHz superconducting 5cell cavity accelerators were upgraded from quasi CW 50kW to true CW 50kW ones without increasing RF power because both of them were designed to excite fully re-circulated and decelerated electron beams in ERL configuration. As explained above, typical electron beam power of 17MeV and 40mA case are 680kW and the FEL light power about 10kW.

4. REFRIGERATOR AND CRYOGENIC OPERATION OF JAEA SCA

The JAEA stand-alone and zero-boil-off cryostat was designed to work as a liquid He container cooled two kinds of cooling refrigerators, in short, a very big Dewar with two small refrigerators. The cryostat has the two refrigerators of 10K / 50K GM and 4K JT-GM ones in the back of the cryostat and duplex heat shields inside the cryostat vacuum vessel. Resultantly, we could minimize stand-by losses of the cryostat to cut off about 90% of the conductive heat invasion from outside in comparison with a liquefier-based conventional cryostat used currently world.

5. EASINESS IN MAINTENANCE AND OPERATION

Non-stop cryogenic operation from the program start to the end or no warm-up operation except for the final shut-down of the whole facility is only possible in the JAEA stand-alone and zero-boil-off superconducting RF linac based systems because cold maintenance to replace a non-stop and over a few years-long operated refrigerator with the new one is easily done within a 15 minutes, and pre- and post maintenance procedures of the cold maintenance for a few hours just before and after the maintenance. Except for the cold maintenance, and unscheduled power failures like a lightning induced failure, as we have had no liquid Helium loss or evaporation over these 4 years, we plan to continue the non-stop operation over 30 years or longer. No regulation of domestic pressure vessel code has been required to perform the cold maintenance. Major advantageous points of the cold maintenance or non-stop operation are summarized as follows.

The first point is no requirement of a time-consuming and difficult RF conditioning after the first conditioning just before the first beam. The second one is no expected deterioration of cryogenic and low temperature components, conditioning related devices and vacuum components because the system was frozen and kept cold and fresh around 4K and other very low temperatures over several tens years. The third is that we can always keep the whole system ready to fire. Cryogenic failure statistics of the continuous zero-boil off operation over 1year typically shows the cryogenic operation of 355 days, maintenance stop of 3 days, unscheduled one of 3 days, and scheduled one of 2 days in 1997. These 3 year statistics typically shows the cryogenic operation of 22360 hours, maintenance stop of 5.6 hours, unscheduled one of 5.2 hours, and scheduled one of 1.2 hours from 2001 to 2003.

Open problem of the non-stop operation is how to minimize running cost of electricity consumption during the idling operation, national holidays, and relatively long vacation.

6 COMBINATION BETWEEN ZERO-BOIL-OFF CRYOSTAT AND LARGE SCALE 2K AND 4K

EXTERNAL LIQUEFIERS

As we have successfully demonstrated our easy maintenance and non-stop operability of the JAEA zero-boil off cryostat over a few tens of years, then we hope to build very large cooling power 2k and 4K refrigerator systems for future JAEA ERLs using our zero-boil off cryostat technologies.

. Conventional large liquid He liquefiers have intrinsically better wall-plug efficiency to cool the cavities down to very low temperature than the zero-boil off cryostat and integrated refrigerators system. We need another independent group of about 10 or 20 night watchmen to run the large liquefier for 3 terms per year of 3 months-long continuous operation and one month-long maintenance under a severe regulation of Japanese domestic pressure vessel code. We plan to avoid these time-consuming domestic rules in a legal way and to shorten the required administrative procedures processing times introducing a so-called Japanese structure reform and free-trade zone policy in cooperating with Ibaraki Prefecture Office and METI (Japanese Ministry of Economy Trade and Industry). We hope to combine these two different cryogenic systems into one hybrid system and to keep cool using the zero-boil off systems' small refrigerator during idling without any RF excitation, and using the large liquefier during high power RF excitation and beam operation. The hybrid system can minimize the electricity consumption and probability of vacuum leak failures in the hybrid cryogenics, and therefore we can economically run our cryogenic system continuously cool without stopping and warming up to the program end over a few tens of years.

7 RRENT ACTIVITIES

Current activities itemized here are to upgrade from the over 2kW to 10kW class lasing in the following. First; the DC gun current capacity is to increase from 5mA to 50mA under commissioning. Second, capture section and pre-accelerator RF amplifiers are upgraded from 6kW to 50kW. Third, main RF amplifiers will be upgraded from the solid state quasi-CW one to IOT true CW one. Fourth, low level amplitude and phase control circuits are upgraded to reproduce their accuracy and tolerance better than 0.1 % and 0.1 degree over a very long period, respectively. Fifth, a PC-based control system is upgraded to ensure reliable and high level control capability using iTRON OS. Sixth, beam monitors will be upgraded to replace the old destructive monitors with non-destructive ones. Seventh, a timing cable network is upgraded to replace the old higher temperature coefficient and non-temperature stabilized one with low temperature coefficient and temperature stabilized one. Eighth, FEL optical transport system was redesigned and was installed to the FEL accelerator vault and the experimental hall. All of these activities will be finalized to realize the designed goal within a year.

8 JAEA ERL FUTURE PLANS AND PROGRAMS

We already explained the 3 chronological steps and next ones of the JAEA superconducting non ERL- and true ERL- FEL developmental activities. Our activities will be divided into 2 directions of high power ERL-FEL applications and ERL-light sources near future. These two programs have been already proposed to MEXT (Japanese Ministry of Education, Culture, Sports, Science and Technology) and the ERL light source one has been accepted to review as one candidate of the most important and basic technology targets next 10years in the 3rd science and technology promotion committee of MEXT. In the preparatory discussions between JAEA and MEXT officers, we proposed some conceptual design and site candidate to

construct the future ERL light source in Japan.

9 NUCLEAR ENERGY INDUSTRY APPLICATIONS

As explained in the future plans and programs, we have recently developed a few high power ERL-FEL applications in nuclear energy industries, for examples, prevention of cold-worked stress-corrosion cracking failures, very narrow width drilling and cutting and very thin depth peeling using non-thermal ultra-fast lasers like JAEA ERL-FELs and decommissioning of the nuclear power plants.

A 10 kW class high power industrial ERL-FEL which can be tuned to maximize transmission rate at around a fiber-transmittable wavelength of 1.3-1.5 micron and at around water transmittable wavelength centered around 0.5 micron will be very useful to transmit their power to a pin-pointed position in a distant area from the FEL. The FEL will be widely used in the many factories like a shipyard, automobile factory, civil engineering, nuclear power plant and so on. A few FEL application examples will cover the application of non-thermal peeling, cutting, and drilling to decommission the nuclear power plants, and to prevent stress-corrosion cracking failures in the nuclear energy industry. As a very thin cutting width has been thought to realize a so-called radio-isotope (RI) contamination-free decommissioning, we plan to use a water-jet guiding of FEL light for non-thermal peeling, cutting, and drilling in decommissioning the nuclear power plants. And we also have successfully demonstrated to prevent cold worked stress-corrosion cracking (CWSCC) failures of the vital components like reactor container vessel shroud and re-circulating pump piping in the nuclear power plant. The CWSCC failures have frequently happened in boiling water reactor (BWR) shroud and other components Japan, Europe, and other countries. A proof of principle CWSCC test experiments was performed to show to prevent the CWSCC failures of the low-carbon stainless-steel.

10 SUMMARIES

We reported briefly here the past and present activities and future programs in the JAEA ERL-FEL group in the followings. First, the developmental and operational issues of the past and present JAEA non-ERL and ERL FELs were explained, especially on the cryogenics. Secondly, the JAEA 10kW class upgrading program has been designed to increase the beam power from about 80kW to 800kW, and a current status of the program was explained briefly. Thirdly, preliminary and preparatory results of the JAEA ERL-FELs' applications in nuclear energy industries were briefly reported that the first proof of principle experiments successfully could prevent the CWSCC failures in small scaled low-carbon stainless steel pieces and nuclear reactor decommissioning was planned using non-thermal laser drilling, cutting and peeling using ultra-fast JAEA FEL pulses, respectively. Fourthly, preparatory paper works, proposals, and conceptual design activities of the JAEA ERL light source development were reported and discussed briefly.

ACKNOWLEDGEMENTS

In connection with the high repetition-rate thermionic gun pulsar development, we would like to express our thanks to Drs. Kulipanov, Vinokurov, and Kupaer of Budker Institute of Nuclear Physics, Siberria, Russia for their kind cooperation with our usage and improvement of the gun pulsar

REFERENCES

[1] M.Ohkubo et. al., Nucl. Instrum. Methods A296

(1990)270.

[2] M.Sawamura et. al. , Nucl. Instrum. Methods A318 (1992)127.

[3] E.J.Minehara et al., Nucl. Instrum. Methods A445, 183 (2000).

[4] N.Nishimori et al., Phys.Rev. Lett. 86, 5707 (2001).

[5] T. Yamauchi, et al., Jpn. J. Appl. Phys. 41 (2002) 6360-6363.

[6] E.J.Minehara, Nucl. Instrum. and Meth. A483 (2002) 8-13.

[7] R. Hajima, et al., Nucl. Instrum. Meth. A507 (2003) 115-119.

6

RENEWAL OF THE L-BAND ELECTRON LINAC AT ISIR, OSAKA UNIVERSITY FOR ADVANCED QUANTUM BEAM SCIENCES *

G. Isoyama, R. Kato, S. Kashiwagi,
Institute of Scientific and Industrial Research, Osaka University, Osaka 567-0047, Japan.

Abstract

The L-band linac at the Institute of Scientific and Industrial Research (ISIR), Osaka University has been renewed and upgraded for higher stability and higher reproducibility of operation modes as well as easy operation. Almost all the power supplies and peripheral facilities are replaced with new ones and a computer control system is newly introduced. The remodelling is successful. Beam intensity fluctuations in the transient mode, which is most frequently used in experiments, are reduced to one-tenth of the previous value before renewal.

INTRODUCTION

The 40 MeV, L-band linac at the Radiation Laboratory of the Nanoscience and Nanotechnology Center attached to the Institute of Scientific and Industrial Research (ISIR), Osaka University is used for radiation chemistry and materials science by means of pulse radiolysis in the time range down to 100 fs and also for development of an infrared free electron laser (FEL) [1] and basic study of Self-Amplified Spontaneous Emission (SASE) in the far-infrared region [2]. A schematic drawing of the L-band linac and the FEL system is shown in Fig. 1. The linac was designed and constructed to produce a high-intensity single-bunch beam. Unlike the majority of electron linacs with the RF frequency of 2.856 GHz in the S-band, the L-band linac operates at the RF frequency of 1.3 GHz. The linac consists of a pre-buncher, a buncher, and a 3 m log accelerating tube, all of which are of the travelling wave type, as well as the sub-harmonic buncher for single-bunch operation. The linac has been upgraded sometimes for higher performance since it was constructed. The construction of the linac began in 1975 and was completed in 1978. At that time, the linac was powered by a 20 MW klystron and the sub-harmonic buncher (SHB) was a single 6^{th} sub-harmonic cavity of 216 MHz. In 1981, a 5 MW klystron was added for the pre-buncher and the buncher, and the original klystron was used exclusively for the accelerating tube. Two 12^{th} sub-harmonic cavities of 108 MHz were added to the 216 MHz cavity for the sub-harmonic buncher and a single bunch beam with charge 67 nC was accelerated using the three stage SHB system in 1984. The electron gun cathode and its grid-pulser were upgraded in 2001, which resulted in 91 nC in the single bunch at maximum.

We had an opportunity to remodel the L-band linac extensively for promoting basic study of nanotechnology when the Radiation Laboratory, which had been a facility directly attached to ISIR, was reorganized in 2002 to be a part of a newly founded facility, the Nanoscience and Nanotechnology Center. The situation before remodelling was follows. As the general background, the trend of experiments was moving from simple irradiation experiments towards experiments requiring higher stability, such as laser synchronised pulse radiolysis, FEL, and coherent radiation. Production and application of an ultra-short pulse electron beam down to 100 fs are extensively studied. The magnetic compression method is used for producing such a short pulse and hence extremely high stability is required in operation of the linac. We conducted study on stability of the linac; the phase and the power of RF fed to the pre-buncher, which affect the accelerating beam significantly, were measured together with environmental variables influential to them, such as the voltage and the frequency of the AC power line, temperatures of the accelerator components, room temperatures, and temperature of cooling water, to find decisive parameters to the instability[3]. The objective of the remodelling was the pursuit of higher stability and reproducibility of operation of the linac as well as its easy operation for advanced studies of beam science and technology. Policies of the remodelling are as follows:

- Basic components are unchanged, such as an electron gun, accelerating structures, and bending magnets.
- A computer control system is newly introduced.
- Almost all the power supplies for the linac and beam lines are replaced with new ones and auxiliary facilities such as the cooling water system and an air conditioner were renewed.

We will report details of the remodelling and re-commissioning of the linac. An earlier report on the remodelling is given in ref. [4].

RF SYSTEM

Renewed components in the RF system are a klystron and its pulse modulator, the power transmission system from the klystron to the accelerating structures, three RF amplifies for the SHB system.

Klystron and Modulator

The former 1.3 GHz RF system consisted of a 20 MW klystron (Thomson) for the accelerating tube and a 5 MW klystron (Toshiba) for the pre-buncher and the buncher. In the new system, a single 30 MW klystron (Thales) is used and the RF power is divided into three for the pre-buncher, the buncher, and the accelerating tube. The new klystron has two operation modes; the normal mode with the peak power of 30 MW and the pulse duration of 4 μs for usual operation and the long pulse mode with 25 MW and 8 μs for FEL.

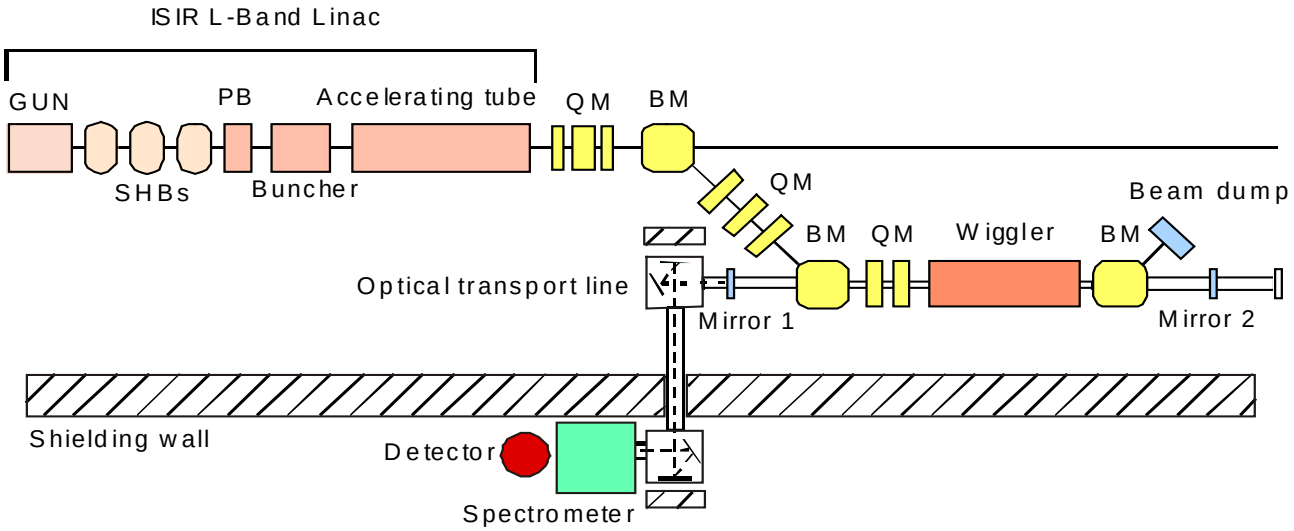

Figure 1: Schematic drawing of the L-band linac and the far-infrared FEL system.

A pulse modulator is made for the new klystron. It can provide square pulses with the maximum voltage of 295 kV and the maximum current of 275 A with the pulse duration of 4 μs and the repetition rate of 60 pulses per second (pps) in the normal mode, while the pulse duration is extended to 8 μs in the long pulse mode but the repetition rate is reduced to 30 pps.

Square pulses are produced with a pulse-forming network (PFN) and a thyratron switch. The PFN had 20 capacitance-inductance stages in total for the long pulse mode, but the first 10 stages are disconnected from the remainder and the short PFN is used for the normal mode. Inductances of 16 stages out of 20 are equipped with motor driven mechanism for adjusting inductance. The operation modes are changed with a manual switch in the pulse modulator, while inductances of the 16 stages in PFN is automatically adjusted, or remotely adjustable if necessary. The high voltage circuits including PFN are installed in a doubly shielded case to reduce electromagnetic noises coming outside.

The high-voltage power supply for PFN is a high-frequency switching power supply using IGBTs. The charging voltage of the PFN is controlled primarily by the number of charging pulses and then precisely by reducing the pulse duration gradually when the voltage is approaching the target value.

Stability of this power supply is crucial for stable operation of the linac. If the voltage applied to the klystron changes slightly, the power and the phase of output RF are affected significantly. Pulse-to-pulse fluctuations of the pulse amplitude results in fast energy fluctuations of the accelerated electron beam, while the undulation of the flat top of square pulses deteriorates the energy uniformity of the electron beam in the long pulse mode, which is important for FEL. The klystron modulator was designed and fabricated to realize the pulse amplitude fluctuation of 0.05 % (0.1 %) and the flat top undulation of 0.1 % (0.2%) as a goal, where the values in the parentheses are guarantees of its manufacturer. The pulse amplitude fluctuation is measured to be ~0.1 %, which is the limit of our measuring instrument, and the flat top undulation to be 0.12 % over 8 μs. Both of them are close to the design goals.

Power Transmission System

The power transmission system delivers 1.3 GHz RF power from the klystron on the first basement to the linac on the second basement. The system consists of various components such as wave-guides, power splitters, phase shifters, and variable attenuators and it is assembled on a frame right above the linac. The system is filled with the high pressure SF_6 gas against discharge. The power transmission system is rearranged for the single klystron. A power splitter and a variable attenuator are newly made for the buncher and prebuncher line. The phase shifter for the buncher is modified for the computer control system. A phase shifter and a variable attenuator for the pre-buncher are replaced with new ones for computer control.

RF Power Amplifiers for the SHB System

Three independent power amplifiers provided RF pulses with the peak power 20 kW and the duration 20 μs to two 108 MHz cavities and a 216 MHz cavity of the SHB system. Since an RF amplifier with vacuum tubes is suitable for an application with the high peak power but the low average power, these amplifiers are not replaced with new ones but remodelled largely. The amplifier is composed of two panels; one contains the vacuum tube assembly and the other contains DC power supplies and control circuits. The DC power supplies and control circuits are replaced with new ones, but the vacuum tube assembly remains as it is, though it is overhauled completely and some parts are replaced. To improve

stability of the linac, a feedback control of phase is newly introduced in the amplifier. The pulse duration is extended from 20 μs up to 100 μs in the new system, because the pulse duration of 20 μs is not long enough to fill the RF power in the 108 MHz cavity with the quality factor Q = 4400.

DC POWER SUPPLIES

Fifty eight DC power supplies out of 62 in total are replaced with new ones; 6 for bending magnets, 20 for quadrupoles, 24 for steering coils, and 8 for Helmholtz coils. In the system before remodelling, the DC power supplies were controlled with potentiometers and monitored with digital panel meters, and hence it is not suitable for the computer control system. The DC power supplies for steering coils were unipolar power supplies and polarity switches were used for changing directions of deflection. Since these power supplies were outdated and had no digital interfaces, most of them are replaced with new DC power supplies equipped with a computer interface. Bipolar power supplies for the steering coils are adopted for easy and fine operation. The new DC power supplies are of the switching regular type and hence they are compact.

The RS-485 serial interface is used for the computer interface of the power supplies so that wiring for the computer control is easy and simple. Up to 32 devices can be controlled with a single RS-485 line by connecting them serially. The 58 new power supplies are installed in 6 racks and each rack is connected to an RS-485 controller in a PLC. Four DC power supplies left unchanged are relatively large power supplies for some Helmhotz coils.

At this opportunity to renew the system, all the wires connecting the DC power supplies with the magnets and the coils are renewed.

TIMING SYSTEM

Three RF signals of 1.3 GHz, 216 MHz, and 108 MHz frequencies and several timing signals are necessary for operation of the linac and for experiments. The timing system producing such signals is a key component for stable operation of the linac and for higher time resolution in pulse radiolysis experiments. Relative phases of the three RF signals have to be kept constant, so that the three RF signals are generated with a single master oscillator. Various timing signals with delays in the time range from tens of microseconds to a fraction of a millisecond must be synchronized with the main acceleration frequency, 1.3 GHz, though the repetition rate of the timing signals are only 60 pps at most. The timing signals are, therefore, generated with the same master oscillator.

In order to enhance stability of the linac, the timing system is replaced with new one. In the new timing system, a rubidium atomic clock producing 10 MHz RF signal with the fractional stability of 10^{-15} in the long term is used as a time base for a frequency synthesizer, which is used as a master oscillator for directly generating the acceleration frequency of 1.3 GHz. The 1.3 GHz signal is directly counted to produce 6^{th} and 12^{th} sub-harmonic signals of 216 MHz and 108 MHz for the SHB system, a 16^{th} sub-harmonic signal of 81 MHz for the laser system used in laser-synchronised pulse radiolysis, and a 48^{th} sub-harmonic signal of 27 MHz for the clock signal of the timing system.

The linac must be operated synchronously with the AC line frequency, which is 60 Hz in the western half of Japan including Osaka, and the maximum repetition rate of the linac operation is also 60 Hz, so that the start signal is made from the AC line frequency using a present counter and then it is synchronised with the clock signal. To make an arbitrary delayed timing signal, the start signal is sent to a standard digital delay generator with a timing jitter of ~50 ps and it produces a preset delayed signal. This delayed signal is used for producing a gate signal to slice out one of the clock pulses. Thus, any timing signal can be made in an interval of 37 ns and the timing jitter of the delayed signal is determined by stability of the clock, which is expected to be as short as 1 ps.

This timing system is configured with commercially available components and devices, such as standard NIM logic modules and digital delay generators, except for the frequency divider, and it is flexible for future expansion and improvement.

CONTROL SYSTEM

The linac was operated with the analogue control system consisting of remote control boxes with potentiometers and analogue meters, though some of them were later replaced with digital meters, and only expert operators could operate it. Owing to the reorganization of the Radiation Laboratory, a skilled operator of the linac is available only in the daytime, so that users of the linac have to operate it by themselves at night. In order to make routine operation of the linac possible by an unskilled operator and to realize precise reproducibility of operation, a computer control system is newly introduced.

The new control system is based on personal computers (PCs) and programmable logic controllers (PLCs), which are widely used for control systems of accelerators, because they are reliable and cost-effective. The PCs and the PLCs are connected with networks. The PCs are used for operator terminals, while the PLCs control various devices directly. The PLCs and their wiring terminals are installed in device control stations (DCSs) and all the devices of the linac except for those connected with GPIB are wired to the DCSs. The DCSs are placed at various places to form a distributed control system; three DCSs are in the control room and four in the linac room. In addition to these DCSs, the klystron modulator and the SHB amplifiers, which are newly made or largely remodelled, have their own PLCs for internal control and a network board is added to each PLC, so that they can directly join the control network.

We have chosen FL-net (network for factory automation using Ethernet) as the network connecting these DCSs and the newly made large devices. FL-net is an open PLC network for factory automation using the same hardware for Ethernet. PLCs communicate each other with a data area or common memory shared imaginarily by network members. Data in the common memory is automatically copied in every 10 ms through the network. On the other hand, PCs communicate each other with Ethernet. In order to connect these two networks, one of the PCs equipped with both FL-net and Ethernet works as a gateway server (GW-SRV). It converts data in the common memory in FL-net to the form accessible to the other PCs and vice versa, and also works as a data based server.

The most difficult point to introduce the computer control system is that controlled devices had no computer interfaces. As described earlier, we order or select newly made devices with computer interfaces, such as the klystron modulator and the DC power supplies, but there are many other components without computer interfaces left unchanged and they are modified one by one to be equipped with computer interfaces. A variable transformer of the gun HV power supply is replaced with an automatic voltage regulator with the variable output and GPIB interface, a synchronous motor for adjusting the gun heater voltage is replaced with a pulse motor, which is easier to connect with a PLC, and some DC power supplies left unchanged are controlled with analogue signals.

The linac can be started up or shut down by a single click of a button on a computer screen.

FACILITIES

Cooling Water System

The cooling water system provides cooling water for the accelerator and peripheral components. The original system provided temperature-regulated water within $\pm 0.1^{o}$C for the SHB cavities, the pre-buncher, the buncher, the accelerating tube, and the klystron, and non-temperature-regulated water cooled with a cooling tower for coils and magnets. Since stability of the linac is very sensitive to the temperature of the RF cavities and the RF structures, a new cooling water system with higher temperature stability is introduced. The new system has a two-stage temperature control; temperature stability in the first stage is $\pm 0.1^{o}$C and it is $\pm 0.03^{o}$C in the second stage. Cooling water regulated in the first stage is used for the klystron and the RF components of the power transmission system, which are not extremely sensitive to temperature. The cooling water whose temperature is controlled in the first stage is sent to the second stage for higher temperature stability and it is used for the SHB cavities and the accelerating structures of the linac. The coils and magnets are still cooled with water coming directly from a cooling tower.

Air Conditioner for Klystron Room

The former air conditioner for the klystron room was renewed two year before the remodelling. The periodical temperature variation ran up to 3^{o}C at the klystron, because the air conditioner controlled the temperature by on-off switching of a refrigerator or a heater. The ceiling of the room is 5 m high, so that the air circulation made by the air conditioner was not sufficient, resulting in the larger temperature variation at the klystron.

In the previous study on stability of the linac, it turned out that the temperature variation of the klystron was the source of the phase drift of the 1.3 GHz RF for accelerating the electron beam [3]. A new air conditioner of the so-called inverter type, which is able to control the cooling or heating power continuously, is added on the ceiling. When the existing air conditioner is used as a n air circulator together with the new air conditioner, the temperature variation is reduced to 0.3^{o}C in the short time and the room temperature is regulated within 1^{o}C in the long run.

Automatic Voltage Regulator

In the previous study on stability of the linac, it is also found that the AC line voltage affects the output power of the klystron. The pulse modulator for the klystron receives the 3 phase 200 V AC power. The line voltage varies typically by 4 volts in the short time and by 6 volts in a day. In order to reduce the voltage variation, an automatic voltage regulator (AVR) is inserted in the AC line for the pulse modulator. The AVR can reduce the variation of its output voltage within 0.5 % or 1 V for AC 200 V with the response time of 30 ms for the input voltage change of $\pm$15 % and the output load change of 0 ~ 100 %.

CONSTRUCTION AND COMMISSIONING

The renewal of the linac began at the end of 2002, when its budget was approved in the revised budget of the government in the fiscal year 2001. The linac was shut down for remodelling in October 2002, because several essential components for linac operation were taken to factories for remodelling. Newly made and remodelled devices and instruments were delivered from January to March 2003. They were installed as they came in. The last arriving device was the computer control system. Its installation and adjustment began in April 2003 and were completed in July 2003. Meantime, all the components and devices were tested and problems were fixed one by one by the end of September 2003. The commissioning of the linac began in October 2003, though some problems were still left unsolved.

A serous problem was discharge in the RF power transmission system. To find a location of discharge, the power transmission line was broken up. Traces of discharge were found not only in newly made components but also in an old component; two 90^{o}twist wave-guides for the buncher and a power splitter for the pre-buncher

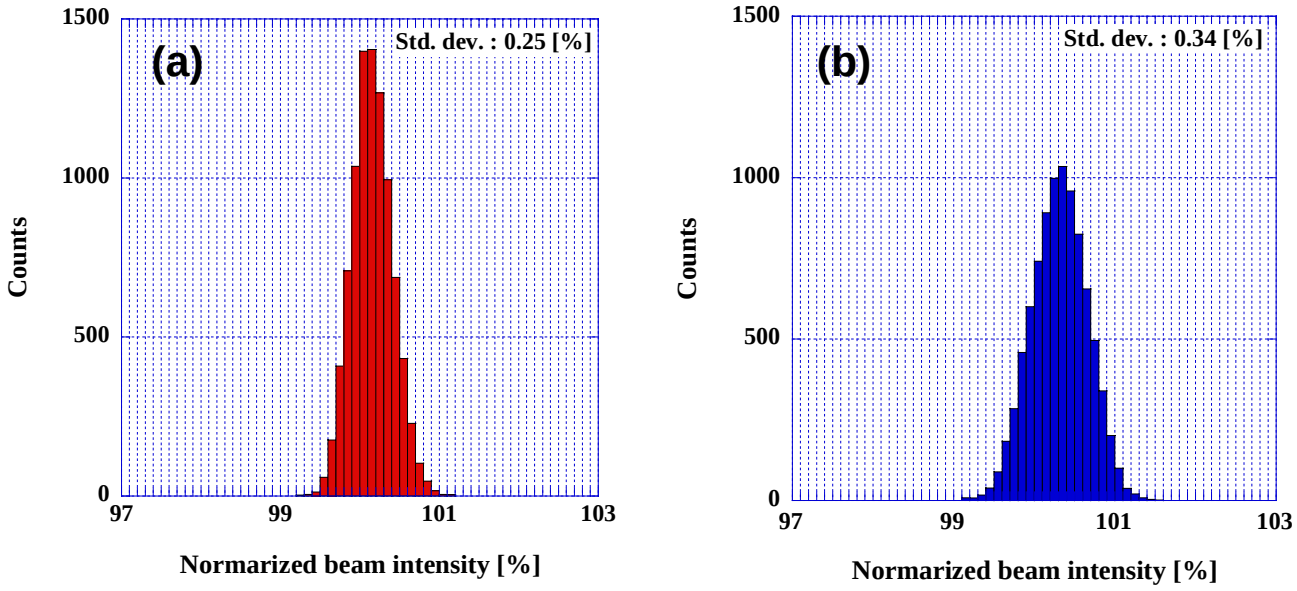

Figure 2: Histograms of beam intensities measured with beam current monitors (BCM) for the short time (a) at the exite of the accelerating tube and (b) at the beam port in the second measurement room. The beam line from the linac is bent by 90^{o} to the second measurement room.

out of new components, and the phase shifter for the buncher out of old components. The three new components were modified to cope with the problem by their manufacturer, and the old phase shifter was replaced with new one.

Another serious problem was weak discharge in the power transmission line or fine and random fluctuations of the 1.3 GHz RF power. All the components, including the accelerating tube were suspected and tested to identify a source of the problem for half a year, but in vain. We almost gave up trying to solve it, but the problem suddenly disappeared when the new timing system began to operate late. It was concluded that the source of the problem was the previous RF mater oscillator, though it had been working well till the shutdown of the linac for the remodelling. Thus the commissioning was completed in the summer of 2003.

Stability of the beam accelerated with the linac was studied in the transient mode, in which the SHB system is not used and an electron beam with the pulse duration of approximately 5 ns is accelerated. Beam intensities were measured as a function of time for an hour or so with beam current monitors of the transformer type at the exit of the accelerating tube and at the beam port in the second measurement room. The beam line from the linac is bent by 90^{o} to the second measurement room, so that the beam intensity is sensitive to the energy fluctuation of the electron beam. The measured intensity changes have two components; fast and random fluctuations, and a slow drift for long time. Fig. 2 shows histograms of beam intensities measured for the short time at the exit of the accelerating tube (a) and at the second measurement room (b). The standard deviations of the histograms are 0.25 % for (a) and 0.34 % for (b), which are approximately one tenth of the intensity fluctuations before remodelling. The long term drifts are 0.04 % in 10 min at the exit of the linac and 0.08 % in 10 min in the second measurement room.

The renewal of the L-band linac was successful. The main objectives of the remodelling have been achieved; Easy operation and high reproducibility of operation modes, and higher stability. The formal joint use began in October 2004.

REFERENCES

[1] R. Kato, S. Kondo, T. Igo, T. Okita, T. Konishi, S. Suemine, S. Okuda and G. Isoyama, Nucl. Instr. Meth. **A445** (2000) 169.

[2] R. Kato, M. Fujimoto, T. Igo, S. Isaka, T. Onishi, S. Furukawa, S. Okuda, S. Suemine, G. Isoyama, Nucl. Instr. Meth. **A507** (2003) 409.

[3] R. Kato, S. Isaka, H. Sakaki, S. Kashiwagi, G. Isoyama, Nucl. Instr. Meth. **A528** (2004) 244.

[4] G. Isoyama, Y. Honda, S. Kashiwagi, R. Kato, T. Kozawa, S. Seki, S. Suemine, S. Tagawa, T. Yamamoto, Y. Yoshida, “Upgrade of the L-band linac at ISIR, Osaka University for higer operational stability”, APAC 2004, Gyeongju, Korea, 2004, p. 237.

PRESENT STATUS IN AIST FEL

N Sei#, K. Yamada, H. Ogawa, M. Yasumoto, Research Institute of Instrumentation Frontier, National Institute of Advanced Industrial Science and Technology, 1-1-1 Umezono, Tsukuba, Ibaraki 305-8568, Japan

Abstract

A lot of efforts to oscillations and applications of free electron lasers (FELs) in a wide wavelength region have made in Advanced Industrial Science and Technology (AIST). FEL oscillations in the DUV and VUV regions have been achieved with a compact storage ring NIJI-IV. The short-wavelength FELs are used as an intense light source for real-time surface observation with the photoelectron emission microscopy (PEEM). FEL oscillations in the IR region have been also planed. A 3.6-m optical klystron, ETLOK-III, for developing IR FELs has been installed in one of the straight sections of the NIJI-IV. In addition, a new linear accelerator will be installed in AIST, and some plans to obtain intensive light sources are proposed.

INTRODUCTION

After studies of visible FEL oscillations with storage ring TERAS [1], FEL oscillations from the visible to the VUV have been developed with a compact storage ring NIJI-IV in AIST. The NIJI-IV dedicated to FEL oscillations was constructed in 1990. After a 6.3 m optical klystron ETLOK-II had been installed in the NIJI-IV in 1992, the first lasing was achieved at wavelengths of 595 and 488 nm in the same year [2]. Improvements of the electron-beam qualities in the NIJI-IV have been advanced for shortening FEL wavelength, and the first lasing in the UV region was accomplished at 350 nm in 1994. The wavelength of 212 nm, at which an FEL oscillation was achieve with the NIJI-IV, was the record for the shortest wavelength of FELs in 1998 [3]. The wavelength of the NIJI-IV FELs was down to 198 nm in 2003, and the NIJI-IV FEL reached to the VUV region [4]. FEL experiments with using low-loss cavity mirrors optimized around 195 nm are being carried out now.

Application experiments with using DUV and VUV FELs are also being developed [5]. Because the work function of transition-metals lays around 5 eV, FELs with the wavelength around 200 nm are suitable as an intense light source to observe chemical reactions which are occurred on the surface of the transition-metals. We observed a Palladium surface, where CO and O_2 gasses were introduced with various conditions, in combination with PEEM.

In order to realize storage ring FEL oscillations in the IR region, we developed an optical klystron ETLOK-III [6] and installed in a long straight section of the NIJI-IV in 2004. Spectra of spontaneous emission from the ETLOK-III with deep modulations have already been

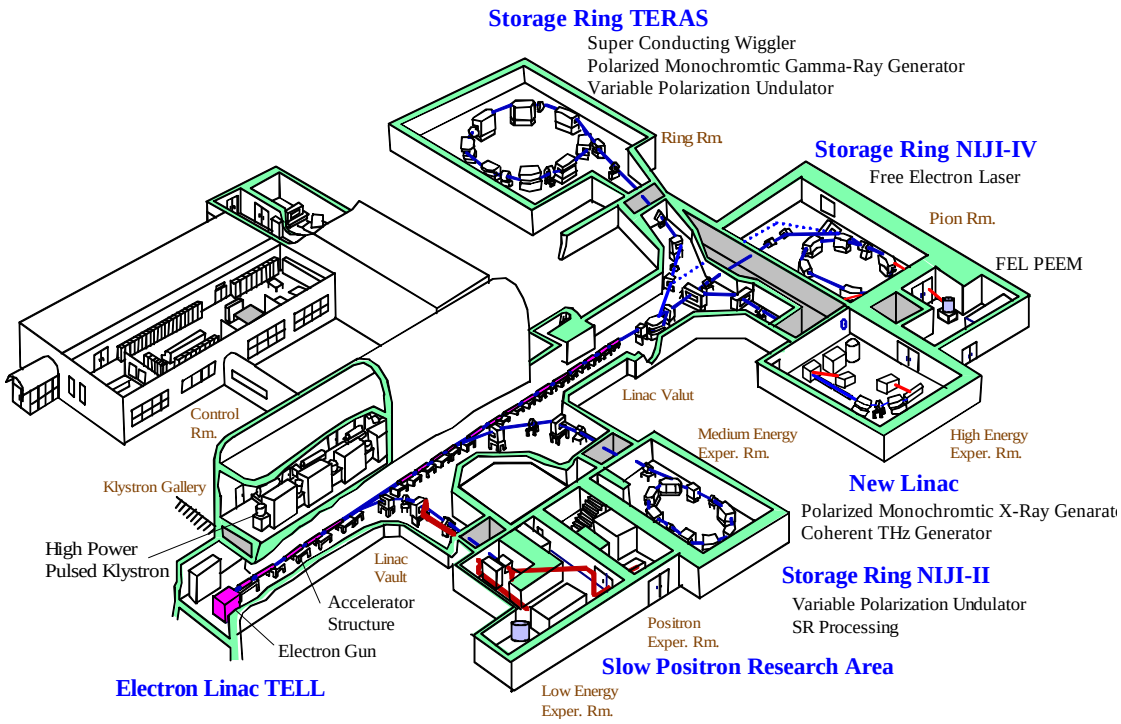

Fig. 1. Electron accelerator facility in AIST

observed in the visible and near-IR regions. FEL gain would be enough high to realize oscillations in those regions.

Moreover, a linear accelerator is moved in AIST as Fig. 1 shows. The linear accelerator has been developed for hard X-ray generation by laser Compton backscattering, so that it has the electron beam of high qualities [7]. The electron beam whose pulse length is short with 3 ps is suitable for coherent radiation, and the electron beam which has large electron charge is also suitable for FEL oscillation. We plan to develop intensive light source in the terahertz region.

In this article, recent results of the NIJI-IV FEL experiments and plans of new light source with the Linac will be described.

SHORT-WAVELENGTH FEL EXPERIMENTS

Replacing vacuum chambers in the NIJI-IV to low-impedance-type ones in 2002, microwave instability was suppressed under the electron-beam current of about 15 mA [4]. Bunch length in an electron bunch was gently increased up to the threshold current because of the potential well distortion. At the electron-beam energy of 340 MeV where FEL experiments were carried out, the natural bunch length was about 43 ps and the bunch length at the threshold current was about 64 ps. The electron beam whose peak current was over 10 A could be obtained with the NIJI-IV. Though the maximum FEL gain estimated from the electron-beam qualities was 8% or more at the wavelength of 200 nm, we could not obtain such the high FEL gain due to demagnetization of the magnets in the ETLOK-II. The effective FEL gain was evaluated to be about 3.4% by observing the bunch length with and without the FEL oscillations. The original cavity loss composed two Al_2O_3/SiO_2 multilayer mirrors, which was used for the FEL oscillations in AIST for the first time, was only 1% around 200 nm. The NIJI-IV FELs were achieved to oscillate in a wavelength range from 205 to 198 nm in 2003, and then they reached in the VUV region [4]. The maximum average FEL power was measured to be 0.5 mW per one port at 202 nm. Though we could not obtain FEL micropulses whose power was stable, we could obtain FEL micropulses whose pulse width and line width were stable. This fact suggested that the FEL oscillation continued in spite of the change of the FEL power. The pulse width and line width of the FEL micropulse considered with resolutions of the measurement system were 6 ps and 0.06 nm, respectively.

For developing new applications, FEL oscillations around 195 nm and below were tried with using two kinds of low-loss Al_2O_3/SiO_2 multilayer mirrors. They were manufactured with ion beam sputtering technique. The original cavity losses of those two kinds of mirrors were 2.6% and 1.9% at a minimum-loss wavelength of 195 nm, respectively. However, the losses rapidly increased up to 4.2% with 58 mA-h exposure and 8.0% with 23 mA-h exposure, and the minimum-loss wavelength was shifted

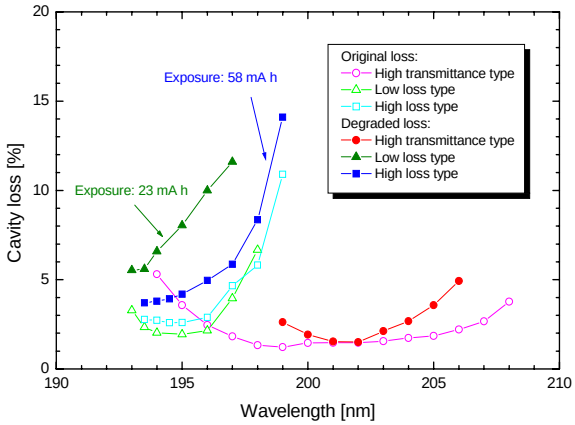

Fig. 2. Cavity losses as a function of wavelength. Triangle and quadrangle represent low original-loss type and high original-loss type, respectively. For the reference, the cavity loss of the mirrors for FELs around 200 nm is shown by circle.

to a shorter wavelength by exposure to the optical klystron radiation as shown in Fig. 2. The mirrors which had the lower loss before the exposure were more sensitive in degradation due to the exposure. It is known that mirror degradation includes both surface and volume degradations [8]. The latter type is instantaneously caused by the exposure to the optical klystron radiation, and saturates at relatively low level. The cavity loss at an optimum wavelength hardly increases even if the exposure increases. Then, the cavity loss after exposure was at least 3.7% in the FEL experiments. This value was almost equal to the maximum FEL gain obtained with the NIJI-IV FEL system around 195 nm, so that we have not realized FEL oscillations. It would be necessary for the lasing to develop low original-loss mirrors which sufficiently suppress the volume degradation.

Though the average power of the NIJI-IV FEL is 1 mW or less in the DUV and VUV regions, the line width is rather narrow, about 3×10^{-4}. The NIJI-IV FEL is suitable to investigate resonances closed in a narrow band and to obtain high spatial resolution in surface observation. We have considered that the NIJI-IV FEL can be applied as a light source of PEEM experiments, and we have developed real-time observation of physical and chemical reactions generated on surface of the transition-metals [5]. The FEL-PEEM system can monitor a dynamic change with video-camera time resolution of 33 ms, and the spatial resolution of this system is evaluated to be about 300 nm. Recently, we tried to observe a Palladium surface, where CO and O_2 gasses were introduced with various conditions, with the FEL-PEEM system. As Fig. 3 shows, it could be observed that adsorption and desorption of the gases on the Palladium surface were generated optionally with the changes of the gas pressure and the temperature of the surface. These experiments will clear up the physical conditions for the catalytic CO oxidation on Palladium surface. We also plan application experiments

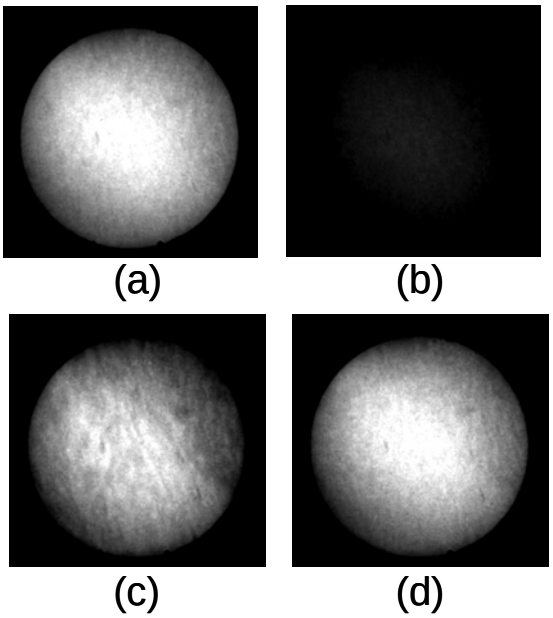

Fig. 3. A series of snapshots for PEEM images on a Pd(111) surface at 340K. After cleaning (a), a CO-adsorbed surface exposed to 2×10^{-5} Pa CO (b), and surface reaction of CO and O_2 (c)-(d) with 8×10^{-5} Pa O_2 exposure. The stored beam current was between 10 and 8.5 mA. PEEM image size is 200 μm in diameter.

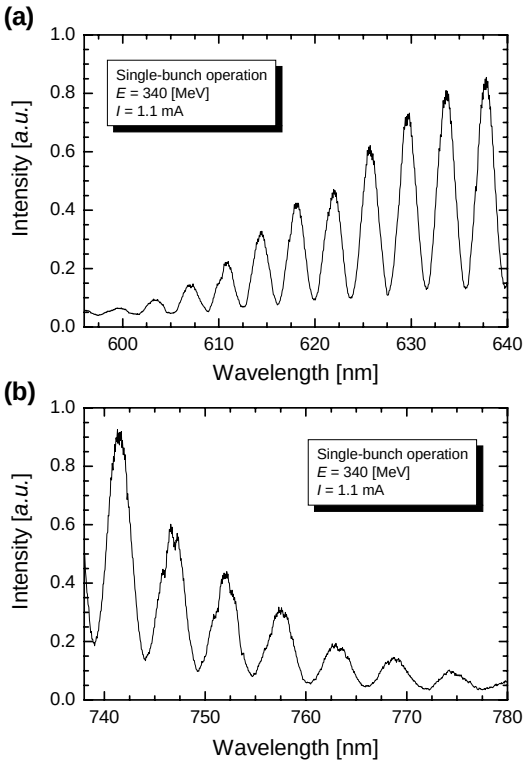

Fig. 4. Measured spectrum of the spontaneous emission from the ETLOK-III: (a) the end of the short wavelength and (b) the end of the long wavelength. The gaps of the undulator section and the dispersive section are 125 and 160 mm, respectively.

to analyze protein structure by using characteristics of storage ring FELs in future.

LONG-WAVELENGTH FEL PRELIMINARY EXPERIMENTS

Many FEL facilities have been constructed and FELs have been used for various applications in the middle-IR region where there are few kinds of useful light sources. Most of those FEL facilities use a linear accelerator as an accelerator device. Typical pulse width of the linear accelerator FEL micropulse is from 0.5 to 5 ps due to the property of the linear accelerator electron beam. Many applications which use the characteristic of the short pulse have been carried out. However, typical line width of the linear accelerator FEL is over 10^{-3} because of the short pulse. The linear accelerator FEL is too wide to apply to some experiment, such as near-field IR microspectroscopy. On the other hand, the typical line width of a storage ring FEL is about 10^{-4}, and it can be used as well as synchrotron radiation passed through a monochromator. Photon flux of the storage ring FEL at a wavelength of 10 μm is about 10^{17} /s for the average power of 1 mW. This photon flux is far larger than that of IR beam lines set in conventional storage rings.

Paying attention to this fact, we have advanced the development of the storage ring FEL in the IR region [6]. An optical klystron for the IR FEL, ETLOK-III, has been installed in one of the long straight sections of the NIJI-IV. The ETLOK-III has two 1.4 m undulator sections and a 72 cm dispersive section. The gap of the undulator sections can be changed between 36 and 150 mm. The maximum *K* value is measured to be 10.4. The gap of the dispersive section can be changed between 36 and 188 mm. Because the magnets in the dispersive section are inserted between two tables which fix the magnets of the undulator sections, the gap of the dispersive section cannot be opened from the gap of the undulator section over 38 mm. The dispersive section is so long that the electron beam with comparatively low energy meanders greatly in it. The electron beam passes in magnetic field of the dispersive section which is not uniform in the horizontal direction. Then, the electron beam is kicked in the dispersive section and comes off the center axis of the ETLOK-III. The kick force becomes stronger as the gap of the dispersive section becomes smaller. At present, the electron beam can be stored in the NIJI-IV by closing the dispersive gap down to 80 mm. In order to cancel the kick force, we attached 5 mm iron plates to shunt magnetic field of the both end magnets in the dispersive section with 3 mm thickness coils. The plate can be moved from the level of the dispersive magnet to 44 mm on the side of the dispersive magnet. We have not carried out experiments to estimate effect of the plates to the electron beam yet. They will be carried out next year.

Spectra of the fundamental and the third harmonics of the spontaneous emissions from the ETLOK-III were

measured in the visible and near-IR regions. As Fig. 4 shows, the spectrum of the fundamental of the spontaneous emission has good modulation. The energy spread evaluated from this spectrum was $2.7\pm0.2\times10^{-4}$, which was close to the natural energy spread of 2.6×10^{-4}. The maximum FEL gain is estimated to be over 2% at the electron-beam current of 15 mA in those regions. The maximum FEL gain for the third harmonics would be over 6% in the visible region due to rather large N_d, which is a number of periods of the FEL wavelength passing over an electron in the dispersive section. Because high-reflection mirrors of 99.8% or more are available in the visible and near-IR regions, it will be easy to realize FEL oscillations in those regions if we install mirror chambers in the long-wavelength optical cavity. This installation will be carried out after next year.

LINAC-BASED LIGHT SOURCE

An S-band linear accelerator is moved from Sumitomo Heavy Industries Ltd. to AIST at present. This linear accelerator was developed so as to generate intense hard X-ray via laser Compton scattering between high-intensity electron beam and high-power laser beam with short pulse width of 150 fs [7]. The linear accelerator has a photocathode RF gun, so that high electron-bunch charge of 1 nC or more can be accelerated. We plan that the electron-bunch charge will be increased up to 5nC using the high quantum efficiency photocathode. This photocathode RF gun realizes a small normalized emittance of about 3π mm-mrad. The electron beam is accelerated up to about 40 MeV with two 1.5 m accelerator structures. Bunch length of the electron beam is compressed to about 3 ps in ordinary operation by bending magnets, and it can be compressed down to 1 ps. The outline of the linear accelerator is shown in Fig. 5.

Using the characteristics of the short pulse length and high electron-bunch charge, we plan to generate intense coherent radiation in a sub-mm wavelength region. If the pulse width of the electron bunch can be compressed to 0.5 ps, spectrum of the coherent radiation from the bending magnet will have a peak at a wavelength around 0.5 mm. The expected peak intensity is estimated to be about 1 mW per cm^{-1}. Because the spectra peak of the coherent radiation is gently, this light source will be able to be applied in a wavelength range of 0.2-1 mm. Moreover, we have a plan that a variably-polarizing undulator will be installed in this S-band linear accelerator system and FELs will be oscillated with the undulator in a wavelength range of 0.1-0.3 mm in future. We will also study to develop applications with two colour imaging in which a hard X-ray beam via laser Compton scattering and intense sub-mm beam are used at the same time.

CONCLUSIONS

We have developed oscillations and applications of FELs with the compact storage ring NIJI-IV from the visible to the VUV region. Extension of FEL oscillations

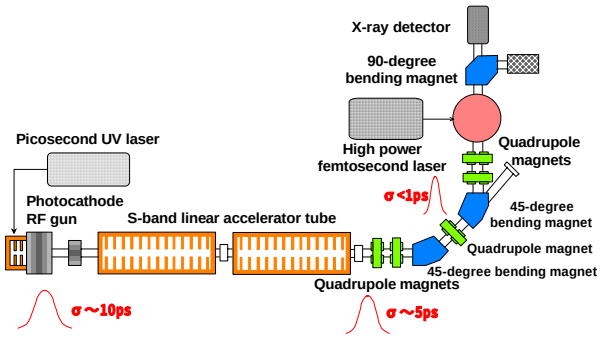

Fig. 5. Schematic of X-ray generation system with an S-band linear accelerator.

to the shorter-wavelength region could not be achieved, but the FEL-PEEM measurements were advanced. We could observe that adsorption and desorption of the CO and O_2 gases on the Palladium surface depend on the changes of the gas pressure and the temperature of the surface. Development of storage ring FELs in the IR region has been also advanced with the NIJI-IV. Spectra of the spontaneous emission from the ETLOK-III were measured below the near-IR region. The maximum FEL gain estimated from the spectra was over 2% and it would be easy to realize FEL oscillations. We can also expect FEL oscillations with using the third harmonics. Moreover, we plan to develop intense light sources in a sub-mm wavelength region with the moved linear accelerator. Studies for imaging techniques with using a hard X-ray beam via laser Compton scattering and intense sub-mm beam will be advanced.

ACKNOWLEDGEMENTS

This work was supported by the Budget for Nuclear Research of the Ministry of Education, Culture, Sports, Science and Technology of Japan.

REFERENCES

[1] T. Yamazaki *et al.*, Nucl. Inst. and Meth. **A309** (1991) 343.
[2] T. Yamazaki *et al.*, Nucl. Inst. and Meth. **A331** (1992) 27.
[3] K. Yamada *et al.*, Nucl. Inst. and Meth. **A429** (1999) 159.
[4] K. Yamada *et al.*, Nucl. Inst. and Meth. **A528** (2004) 268.
[5] K. Yamada *et al.*, *Proc. 26th Free Electron Lasers Conf., Trieste, 2002, pp.311-313.*
[6] N. Sei *et al.*: Jpn. J. Appl. Phys. **41** (2002), 1595.
[7] F. Sakai *et al.*: Jpn. J. Appl. Phys. **41** (2002), 1589.
[8] K. Yamada *et al.*, Nucl. Inst. and Meth. **A393** (1997) 44.

Physics Issues in PAL XFEL Project*

H. S. Kang†
Pohang Accelerator Laboratory, POSTECH, Pohang, Kyungbuk, 790-784 KOREA

Abstract

Pohang Accelerator Laboratory has a plan of X-ray FEL project which aims at achieving hard x-ray SASE radiation of 0.3 nm with 3.7 GeV electron beam. This PAL-XFEL will utilize the existing 2.5 GeV injection linac to the storage ring by upgrading its energy up to 3.7 GeV and using in-vacuum undulator with 4-mm gap. It will have two beamlines that cover both soft X-ray and hard X-ray. The low electron beam energy and small gap undulator cast a few difficult physics issues such as wake field in small gap undulator, micro-bunching instability, and transverse coherence, etc. The related physics study now underway will be described shortly as well as the overall description of the project.

INTRODUCTION

Pohang Accelerator Laboratory (PAL) has a plan to build a x-ray FEL called PAL-XFEL based on SASE (self amplified spontaneous emission) scheme. PAL-XFEL will utilize the existing 2.5 GeV electron linac and upgrade its energy and performance. The linac is currently used for the injection to the 2.5 GeV storage ring of Pohang Light Source (PLS). PAL-XFEL will cover from the soft x-ray radiation to the hard x-ray of 0.3 nm by upgrading the linac energy to at least 3.7 GeV.[1]

Fundamental parameters of PAL-XFEL is listed in Table 1. PAL-XFEL is aiming at achieving hard X-ray laser with a relatively low energy electron beam. To obtain 0.3 nm radiation with 3.7 GeV beam, the undulator period should be small, giving rise to the undulator gap of 4 mm, which is available only in in-vacuum undulator. Therefore, PAL-XFEL will adopt in-vacuum undulator. As shown in Table 1, each undulator segment is 4.5 m long. Between segments, a 0.5-m space is reserved for diagnostic equipments and a quadrupole for the beam focusing. The full undulator length would be 80 – 100 m to take care of possible errors.

SASE FEL is quite a scientific challenge as is well known; the generation of extremely low emittance beam through a photo-cathode RF gun, bunch compressing to an extremely short length, maintaining the low emittance to the end of the linac, and keeping the beam orbit as straight as possible in the undulator. PAL-XFEL adds a few more scientific difficulties. This is easily understood by comparing PAL-XFEL with another machine under construction, LCLS (Linac Coherent Light Source) [2], which uses 14.45 GeV electron beam that is four times bigger energy to obtain 0.15 nm radiation that is only half of the PAL-XFEL radiation. In other words, PAL-XFEL is going to achieve hard X-ray laser with a relatively low energy electron beam.

Table 1: Parameters of PAL-XFEL

Beam Parameters	**Value**	**Unit**
Electron energy	3.7	GeV
Peak current	3	kA
Normalized slice emittance	1	mm mrad
RMS slice energy spread	0.01 %	
Full bunch length	270	fs
Undulator Parameters		
Undulator period	1.5	cm
Segment length	4.5	m
Full undulator length	80 - 100	m
Undulator parameter, K	1.49	
Undulator gap	4	mm
FEL Parameters		
Radiation wavelength	3	Å
FEL parameter, ρ	5.7×10^{-4}	
Peak brightness	5×10^{31}	*
Peak coherent power	1	GW
Pules repetition rate (Max.)	60	Hz
1D gain length	1.2	m
Saturation length, L_{sat}	60	m

* photon/(sec mm^2 mrad^2 0.1%BW)

The condition of transverse overlap between photon beam and electro beam requires higher electron beam energy. The 3.7 GeV electron beam, relatively low energy, has larger divergence than the 3 $\mathring{A}$ radiation beam. Even more, if the uncorrelated energy spread becomes relatively large, the transverse coherence becomes even worse. Laser beam heating to reduce the micro-bunching instability induces an increase of the uncorrelated energy spread during the bunching process in bunch compressors. With a relatively low beam energy of 3.7 GeV and a relatively large uncorrelated energy spread, transverse higher modes can have comparatively large growth rates, which may result in poor transverse coherency. The computer simulation with GENESIS code [3] has been done to see whether the transverse coherence is still preserved or not in SASE process with the low energy electron beam.

There has been continuous skepticism about the use of in-vacuum undulator in SASE FEL, because its small gap is expected to cause some amount of wake field, bigger than that of an out-vacuum undulator.

* Work supported by Korean Ministry of Science and Technology
† hskang@postech.ac.kr

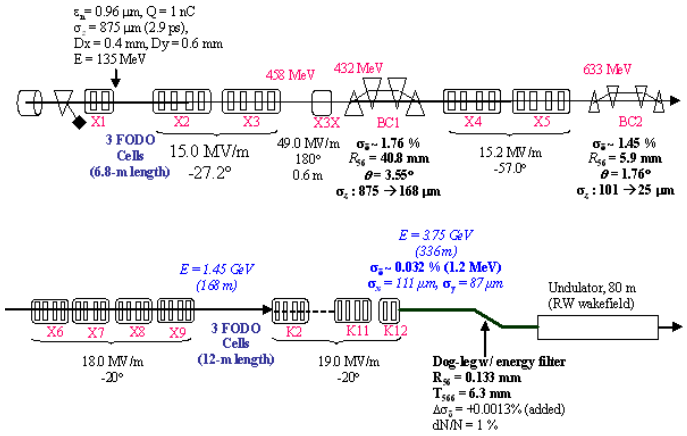

Figure 1: Layout of the PAL-XFEL injector and linac

MICRO-BUNCHING INSTABILITY AND TRANSVERSE COHERENCE

Linac is composed of two sets of bunch compressors, one X-band accelerating section that is needed to compensate non-linearities, and conventional S-band accelerating columns (see Fig. 1). In the current design, the 1st bunch compressor (BC1) is located at the point of 430 MeV and the 2nd one (BC2) is located at 630 MeV. The X-band structure is located just before BC1. BC1 compresses the 10 ps injector output to around 200 μm and BC2 compresses it further to 80 μm.

Small density modulations from the photocathode RF-gun can be significantly amplified by the coherent synchrotron radiation (CSR) in bunch compressors, which results in a micro-bunching instability. The CSR instability is easy to develop for very cold beams [4, 5, 6]. However, the growth rate of the micro-bunching instability can be remarkably reduced by increasing the uncorrelated energy spread [7]. Figure 2 shows the CSR micro-bunching instability gain at BC1 and BC2 with the uncorrelated energy spread of 1.0×10^{-5} and 1.0×10^{-4}.

To reduce the micro-bunching instability, a laser heater will be introduced just after the 135 MeV injector (see Fig. 3). If the uncorrelated energy spread of 25 keV is added by a laser heater, the uncorrelated energy spread grows to 1 MeV at the undulator entrance.

However, how big can the uncorrelated energy spread be increased? Figure 4 shows the saturation length as a function of the uncorrelated energy spread using Ming Xie's fitting formula[8]. In general, the uncorrelated energy spread should be smaller than the FEL parameter of 5.7×10^{-4} (see Table 1). Allowing a 15% increase of the saturation length, the tolerable uncorrelated energy spread at the undulator entrance is about 2.7×10^{-4} in Fig. 4, which corresponds to 1.0 MeV. Figure 5 shows the radiation power of PAL-XFEL calculated with GENESIS code assuming the uncorrelated energy spread of 1 MeV and 2 MeV, respectively. In case of 1 MeV the saturation length is around 60 m, which includes the diagnostic space. If the uncorrelated

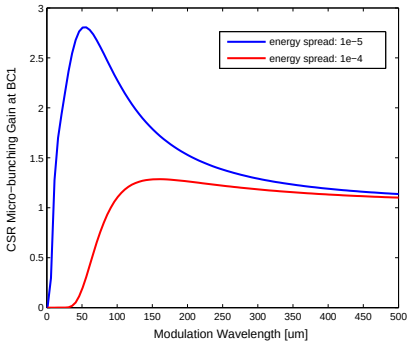

(a)

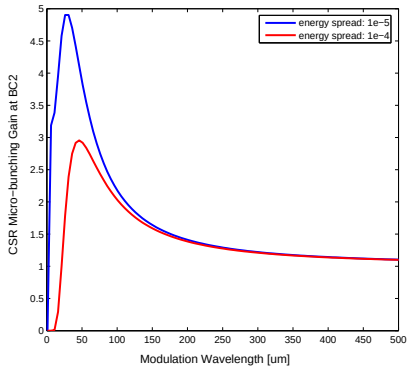

(b)

Figure 2: CSR micro-bunching instability gain at BC1 (a) at BC2 (b).

energy spread is increased to 2 MeV, the radiation power does not saturate as shown in Fig. 5(b).

It is obvious that transverse coherence depends on the energy spread. The growth rate of transverse higher order mode could be relatively high, which degrades the transverse coherency.

Full transverse coherence in SASE process requires the dominance of the fundamental mode (E_{00}). The numerical

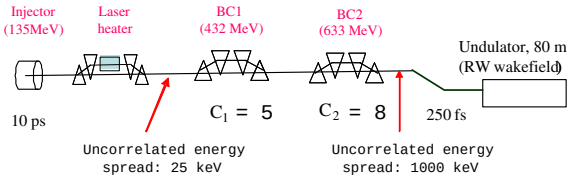

Figure 3: Layout of bunch compressors of PAL-XFEL.

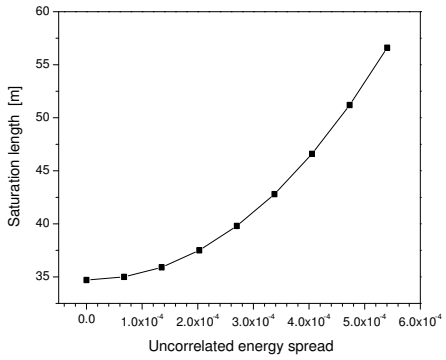

Figure 4: Saturation length as a function of the uncorrelated energy spread at the undulator entrance.

simulation study confirmed that the transverse coherence of SASE FEL reaches over 90% [9]. The fundamental mode should be most enhanced before the saturation while the higher order modes(E_{01}, E_{10}) should die out. The growth rate of E_{01} and E_{10} mode should be much smaller than that of E_{00}, which depends on undulator and electron beam parameters [10]. However, if the uncorrelated energy spread is increased in order to reduce the micro-bunching instability, the saturation length increases also (see Fig. 5) as well as the growth rate of transverse higher order mode could be relatively high, which degrades the transverse coherency. In this case, transverse higher order modes do not vanish.

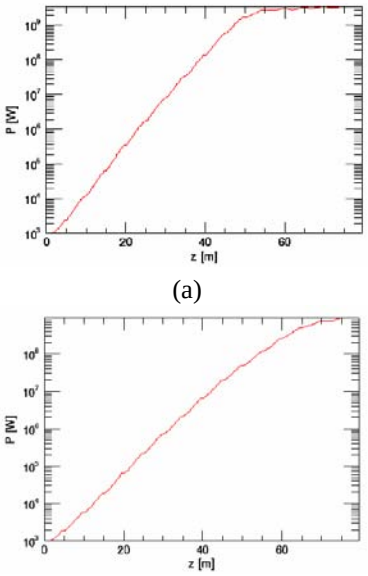

Figure 5: Power gain of PAL-XFEL with 3.7-GeV beam. The uncorrelated energy spread is 1 MeV (a) and 2 MeV(b).

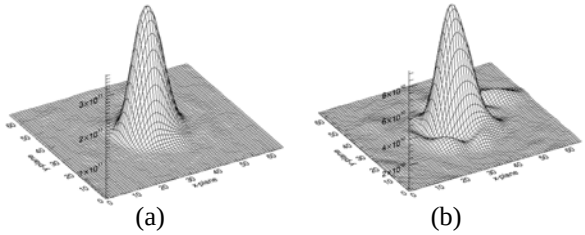

Figure 6: Radiation profile at z=80 m. The uncorrelated energy spread is 1 MeV (a) and 2 MeV(b).

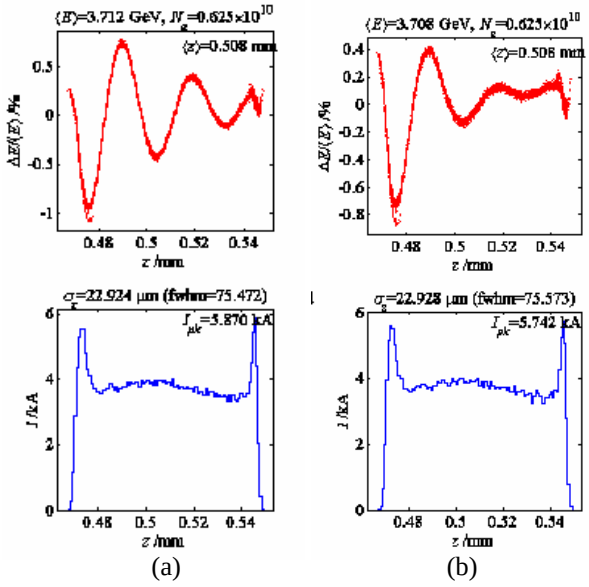

Figure 7: Energy spread along the bunch due to wake in undulator chamber with the gap of 4 mm at the end of 80-m long undulator. The chamber material is Copper (a) and Aluminum (b), respectively.

In case of full transverse coherence, the radiation beam has a profile of pure gaussian. The radiation beam profile at 80 m of the undulator is shown in Fig. 6. The uncorrelated energy spread is assumed 1 MeV and 2 MeV, respectively. In case of 1 MeV the transverse coherence looks good while in case of 2 MeV it looks poor.

The lower is the electron beam energy, the smaller is the tolerance of uncorrelated energy spread to get full transverse coherence. This is contradictory to the energy spread requirement of micro-bunching instability. Considering the increase of saturation length as shown in Fig. 5, the uncorrelated energy spread should kept below 1 MeV.

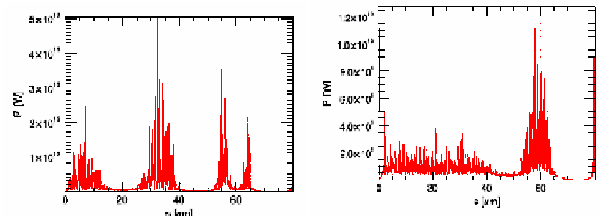

(a) (b)

Figure 8: The radiation output obtained by Genesis time-dependent simulation of PAL-XFEL assuming an uniform longitudinal distribution of electron beam. The chamber material is Copper (a) and Aluminum (b), respectively.

WAKEFIELD

The undulator wake field causes the energy spread along the many slices in the bunch. Some slices may have bigger or lower energy shift and radiate out of the target frequency eventually reducing the output power. The rms of the energy spread at the end of the undulator is given by

$$\delta_E = \frac{e^2 N L (W_z)_{rms}}{E}, \qquad (1)$$

where N is the number of particles in the bunch, L the length of the undulator, $(W_z)_{rms}$ the rms of the wake field with respect to its mean value. The undulator gap is a factor determining $(W_z)_{rms}$. Another shortcoming of low energy machine is that it makes the energy spread δ_E bigger for the same amount of $(W_z)_{rms}$. We will overcome this difficulty by using longer bunches, which lowers the wake field. For a Gaussian distribution, $(W_z)_{rms}$ has the dependence of

$$(W_z)_{rms} \propto \frac{1}{a(\sigma_z)^{3/2}}. \qquad (2)$$

The PAL-XFEL undulator gap of 4 mm is not so small, comparing it with the 5 mm chamber gap of LCLS. On the other hand, we will use bunch length longer than that of LCLS. Then, δ_E^{PAL} is as low as δ_E^{LCLS}. Furthermore, the parallel plate geometry of the undulator helps reduce the wake field effect further including the AC-conductivity effect [11].

Figure 7 shows the energy spread along the bunch at the end of 80-m long undulator due to wake in undulator chamber with the gap of 4 mm. The chamber material is assumed Copper and Aluminum, respectively. The Al case (Fig. 7.(b)) shows the smaller energy spread than Cu and a flat region near the tail of the bunch. Thus, it is clear that Al material is better than Cu. Al coating in undulator chamber is being considered to reduce the AC conductivity effect.

Figure 8 shows the radiation output obtained by Genesis time-dependent simulation of PAL-XFEL assuming an uniform longitudinal distribution of electron beam. The radiation output shows a few spikes along the bunch where the electron energy increases by the wake as shown in Fig. 7 for both Copper and Aluminum chamber. It looks like that energy loss by synchrotron radiation in undulator is balanced by energy increase in undulator due to wakefield in undulator chamber. In the simulation the horn shape can be seen in the real electron beam distribution like Fig.7 is not included. In order to confirm the wakefield effect accurately, the real electron beam distribution should be used in the simulation.

SUMMARY

Design of PAL-XFEL is underway to generate the hard x-ray radiation of 0.3 nm with the 3.7 GeV beam and in-vacuum undulator with 4-mm gap. Linac has been designed to compress the bunch to a very short length and to keep the emittance below 1 mm-mrad at the end of the linac. Physics issues such as wake field in small gap undulator, micro-bunching instability, and transverse coherence are described shortly. Transverse coherence of 0.3 nm radiation was studied with GENESIS code changing the uncorrelated energy spread which is necessary to reduce the micro-bunching instability. With the uncorrelated energy spread of 1 MeV both the transverse coherence and the saturation length are satisfactory. Undulator wake field effect is not so serious as one might consider. Simulation shows that the radiation power grows well exponentially and the saturation reaches at $Z = 60$ m. The radiation profile is satisfactory even with including the wake field effect.

REFERENCES

[1] I. S. Ko et al., in Proceedings of 2005 FEL conference.

[2] Linac Coherent Light Source (LCLS) Conceptual Design Report, SLAC-R-593, (2002).

[3] S. Reiche, Nucl. Instr. and Meth. A, 429 (1999) 242.

[4] S. Heifets et al., SLAC-PUB-9165, 2002.

[5] E. L. Saldin et al., FEL-2001, Darmstadt, Germany, 2001.

[6] Z. Huang and K.-J. Kim, Phys. Rev. ST AB, 5 (2002) 074401.

[7] Z. Huang et al., Phys. Rev. ST AB, 7 (2004) 074401.

[8] M. Xie, in Proceedings of the 1995 Particle Accelerator Conference, Dallas, TX, 1995 (IEEE, Piscataway, NJ, 1995), p. 183.

[9] Vinit kumar et al., Nucl. Instr. and Meth. A, 445 (2000) 77.

[10] M. Xie, Nucl. Instr. and Meth. A, 445 (2000) 67.

[11] K. L. F. Bane and G. Stupakov, SLAC-PUB-10707, LCLS-TN-04-11 (2004).

SEEDING FEL WITH HIGH HARMONICS IN GAS

M.E. Couprie, G. Lambert, M. Labat, M. Bougeard, W. Boutu, P. Breger, B. Carré, D. Garzella, H. Merdji, P. Monchicourt, P. Salières, CEA, DSM/SPAM, 91 191 Gif-sur-Yvette, France, D. Nutarelli LAC Univ. Paris –Sud 91 405 Orsay France
T. Hara, H. Kitamura, T. Shintake, SPring-8/RIKEN Harima Institute, Hyogo 679-5148, Japan
L. Giannessi, SPARC, ENEA, Frascati.

Abstract

Short wavelength Free Electron Lasers (FEL) usually operate in the single pass mode. Besides the Self Amplified Spontaneous Emission (SASE) configuration, seeding and High Harmonic Generation schemes have proven to be effective in the output radiation quality. We present here two tests experiment where the seed source is based on the High Harmonics produced in rare Gases (HHG), which appear to be very efficient and high quality light sources in the VUV-soft X ray domain. These tests experiments are planned both on the SCSS (SPring-8 Compact Sase Source) prototype in Japan and on SPARC (Sorgente Pulsata e Amplificata di Radiazione Coerente) in Italy. Characteristics of these FELs and implementation of the seeding experiment are described. Expected performances are then given.

FEL CONFIGURATIONS

Different configurations are usually employed for FEL sources. The most common one remains the FEL oscillator, where multi passes of the light starting from the spontaneous emission to the laser one allow multiple interaction with the FEL gain system to occur. This is used in the Infrared FEL user sources, or generally in storage ring or LINAC based LELs in the UV, near VUV. FEL gain does not need to be very high and accelerator requirements are reasonable. When a short wavelength FEL is required, lack of good reflective optics prevents the use of the oscillator configuration. In the SASE configuration, the spontaneous emission emitted in the beginning of the undulator leads to the bunching of the electron beam and to the coherent emission at the end of the insertion device, after an exponential growth of the intensity. In this case, the accelerator performances should fulfil the best qualities achievable in terms of low emittance, high brightness electron beam, short pulse. Besides, the emission between the different trains of bunches is not correlated, leading to a spiking spectral and temporal distribution, and strong intensity fluctuations. SASE has been recently observed down to 30 nm on the VUV-FEL in DESY [1]. In the Coherent High Harmonic (CHG) [2] and Seeding configuration, an external laser source is injected, providing an efficient bunching of the electron beam, which can then radiate coherently in the following sections of undulator. CHG has also been observed on Storage Rings, either with the injection of a Nd-Yag and its harmonics on ACO [3], Super-ACO [4], or with the FEL oscillator itself in DUKE [5] and ELETTRA [6].

In the High Gain Harmonic Generation (HGHG) [7], a first undulator is adjusted on the seed wavelength, whereas the second undulator is tuned on a harmonic (third or fifth typically), for shorter radiation to be produced. The harmonics intensity follows also an exponential growth of the intensity. In High Gain regime, Non Linear Harmonics are also produced, both on the SASE and CHG case. Implemented at Brookhaven National Laboratory [8] on a LINAC based FEL, the second undulator radiation tuned to the thirds harmonic of the Ti:Sa laser seed is produced. The saturation length is reduced with respect to the SASE case, leading to a more compact system. The intensity fluctuations are clearly damped down to 1 %, and the spectral and temporal distributions exhibit a smooth shape, free from the spiking structure of SASE. Tuneability can be obtained by combining a chirp on both electron beam and laser pulse [9]. The coherent third harmonic radiated by the second undulator has been used for angle-resolved photo-ionisation at 80 nm [10]. In the so-called “cascading scheme” [11], the produced radiation of the HGHG can be further injected in a second set of undulators whereas the electron bunch is slightly delayed so that the radiation interacts in a fresh part of the electron bunch, for which the energy spread has not been heated by the previous light–electron interaction. Such a scheme provides a significant shortening of the wavelength of the exit radiation. As a consequence, the seeded and HGHG configuration presents several advantages with respect to SASE case, such as the improvement of the longitudinal coherence, the reduction of the saturation length and the compactness of the device, the damping of the intensity fluctuations, and a straightforward synchronisation with an external laser source for pump-probe two-colour experiments. Nevertheless, the limitations for going towards the X-ray range comes from the wavelength of the seed laser, restricted to UV for commercial tuneable laser sources, after crystal multiplication. It has then been proposed to inject High Harmonics produced in Gas, allowing to shorten significantly the wavelength of the input seed [12]. It has been decided to perform the experiment on the SCSS prototype [13] with a seeding at 60 nm in the frame of a French Japanese collaborations, and on SPARC in Italy with a seeding between 260 and 89 nm in the frame of the EUROFEL design studies European Contract [14]. These demonstration experiments are a required step for the progress of the ARC-EN-CIEL (Accelerator Radiation Centre for Enhanced Coherent Extended Light) proposed fourth generation light source in France [15], where injection of

HHG has been considered from the beginning. Such a light seed is proposed for the BATES project [16], it has been recently adopted for the 4GLS VUV FEL [17], and is considered for SPARXINO [18], an extension of SPARC towards shorter wavelengths.

Other schemes of seeding have also been proposed, such as self-seeding where the radiation from a first undulator is spectrally cleaned by a monochromator, before being amplified in a second undulator [19]. Intra-cavity harmonic generation combined with a micro-undulator has also been proposed in Frascati [20]. Regenerative type FEL is also considered at 4GLS [21]. Super-radiant regime with a laser seed injection occurring for particular potential depth (depending on the laser intensities) versus the slippage length can also lead to sharp and short wavelength harmonic radiation after several cascades where the optical pulse slips ovcr the electron bunch and keeps increasing [22, 23].

HIGH HARMONICS IN GAS

The harmonic generation in gas results from the strong nonlinear polarisation induced on the rare gases atoms, such as Ar, Xe, Ne and He, by the focused intense electromagnetic field E_{Laser} of a "pump" laser. The three-step semi-classical model describes the radiation process (see fig.1) [24]. The external laser field strength being comparable to the internal static field V_c of the atom in the interaction region close to laser focus, atoms ionize by tunnelling of the electrons. The ejected free electrons, far from the core, are then accelerated in the external laser field and gain in kinetic energy E_C. Those which are driven back close to the core can either be scattered or recombine to the ground state emitting a burst of XUV photons every half-optical cycle.

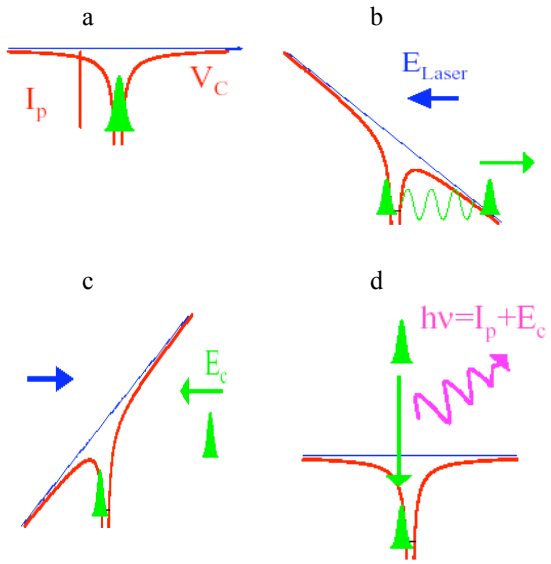

Fig.1: Three-step semi-classical model: a) initial state of the gas atom b) electron tunnelling c) gain of kinetic energy E_C d) electron absorption and photon emission.. I_P is the gas medium ionization potential.

A typical spectrum of harmonics generation in gas (see fig.2) consists of a train of XUV bursts, superposition of the high order odd harmonics, separated by twice the fundamental energy. Even if the conversion rate of this technique is relatively weak (10^{-4}-10^{-7}), the characteristic distribution of intensities is almost constant with harmonic order into the "plateau" region. For higher orders, the conversion rate and consequently the intensities decrease rapidly in a zone called "cut-off" region. The cut-off energy E_{cutoff} giving the upper spectral limit is : $\mathbf{E_{cutoff} = I_P + 3.2\,U_P}$ with I_P the gas medium ionization potential, U_p the ponderomotive potential ($\mathbf{U_P \propto I_{pump}\,\lambda^2_{pump}}$, with I_{pump} the focused intensity, λ_{pump} the wavelength of the pump and 3.2 the maximum of kinetic energy which can be reached by the electron). Light gases such as Ne and He present a high ionization potential, allowing short wavelength to be radiated. The conversion efficiency is lower.

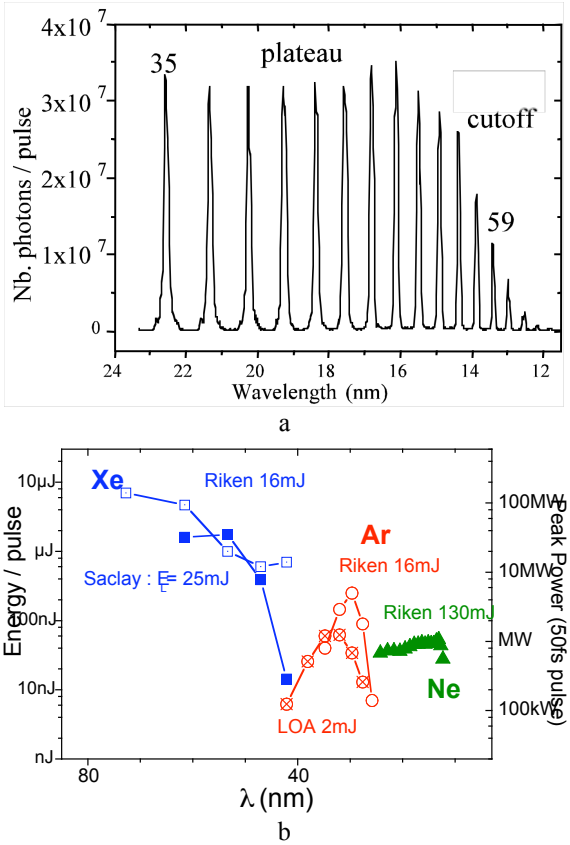

Fig.2 : a) Typical harmonics spectrum produced in a Neon jet. b) performances of the harmonics produced in gases .

Moreover, the radiation spectrum is completely tuneable in the VUV-XUV region by means of frequency-mixing techniques applied on the pump laser or modification of the chirp of the laser source [25]. High order harmonics are linearly polarized sources between 100 and 3 nm (12-400 eV) [26]. They present a high degree of temporal [27] and spatial [28] coherence. The harmonic radiation is emitted in the axis of the laser propagation with a small divergence (1 to 10 mrad). More precisely, the harmonics

waist w_{oha}, divergence div_{ha} and M2 factor $M2_{ha}$ are related to the laser's one ($w_{ola,}$, div_{las}, $M2_{las}$) according to :

$w_{ohar}=w_{olas}q^{-1/2}$, $div_{har}=div_{las}q$, $M2_{har}=M2_{las}q^{1/2}$ where (2q+1) is the harmonic number.

The temporal pulse distribution presents a femtosecond train (less than 100 fs) with attosecond pulses [29], at a relatively high repetition rate (up to few KHz).

High Harmonics produced in gases are very attractive sources for seeding at low wavelength. Indeed, they have already been successfully employed for amplification in a collisionally pumped neonlike gallium plasma X-ray amplifier [30] and in an optical field ionized plasma [31] at 33 nm.

CHARACTERISTICS OF THE SCSS PROTOTYPE AND SPARC

Table 1: Electron beam and undulator characteristics for the SCSS prototype and SPARC.

Projects	SCSS PI	SPARC
Electron Beam Characteristics		
Energy E (GeV)	0.25	0.17-0.21
energy spread σ_γ	0.0002	0.002
Slice energy spread	4e-5	5e-4
bunch charge Q (nC)	0.2	1
normalised slice emittance ε (π.mm.mrad)	1	1
Bunch length (fs FWHM)	500	6000
peak current I_P (kA)	0.2	0.15
Undulators Characteristics (Modulator/radiator)		
Resonant wavelength λ_R (nm)	60	160
undulator period λ_U (mm)	15	28
deflection parameter K	1.39	1.22
periods/section N_P	300	77
number of sections N_S	2	6
Gap (mm)	3.7	14
betatron function β_x , β_y (m)	4.7; 0.5	3 (average) ($\beta_x = \beta_y$)

Beam and undulator characteristics for SCSS prototype, and for SPARC are given in Table 1. The SCSS prototype is based on 2 C-Band Linear Accelerator sections allowing high accelerating gradients, a thermionic gun with a CeB6 cathode. In vacuum narrow gap undulators have been chosen, resulting in a compact device. The prototype is presently assembled, and first beam tests have been started in mid-November 2005. The 8 GeV SCSS facility will start construction, for planned operation in 2010. A 150 MeV advanced photo-injector is under construction in the Frascati INFN national laboratories for the SPARC project. Two main issues are investigated: optimum working point for high brightness photo-injectors and RF bunch compression technique. The system consists in a 1.6 cell RF gun operated at S-band (2.856 Ghz) and high peak field on the cathode (120MeV/m) with incorporated photo-cathode, generating a 6 MeV beam. The beam is then focused and matched into 3 accelerating sections, increasing the beam energy up to 150-200 MeV.

SEEDING IMPLEMENTATION ON SCSS PROTOTYPE AND SPARC

Characteristics of the Ti-Sa laser system and the seeding chambers are detailed in Table 2. The Ti-Sa laser will be aligned on the magnetic axis of the undulator sections. The harmonics being collinear to the Ti-Sa laser, they should then properly interact with the electron beam. An advanced system is planned on the SCSS prototype with a He-Ne alignment with iris attached to the Beam Position Monitors [32]. The chamber and optics design should take into account the best interaction in the modulator, but also geometrical constraints related to infrastructure and radiation safety (such as having a hole for light in the shielding 1 m above the electron beam level). The implementation of the chambers is shown in fig. 3.

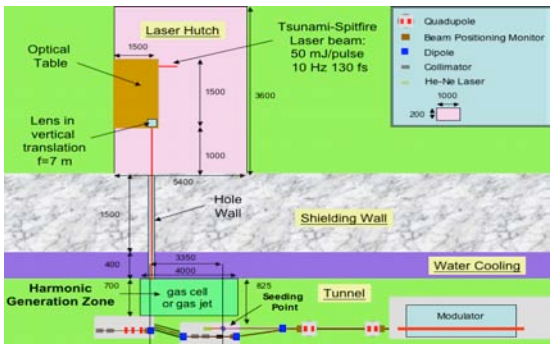

a

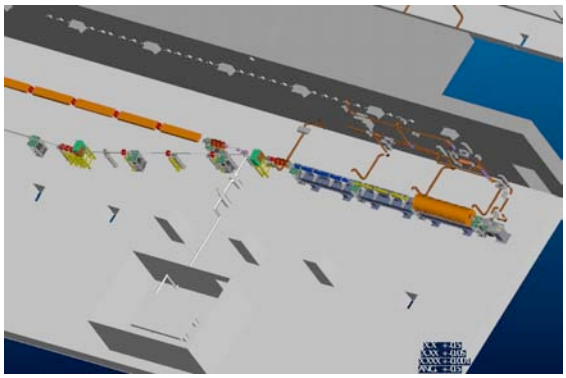

b

Fig. 3 : Implementation of the chambers for seeding on the SCSS prototype (a) and on SPARC (b)

The harmonics in gas are generated in a first chamber, with a gas jet (SPARC case) or gas cell (SCSS prototype), followed by a second chamber where a telescope composed of two spherical mirrors allows the proper focusing of the light in the first modulator, in order to have a proper interaction with the e-beam. It additionally

contributes to the spectral selection and removal of the infra-red Ti:Sa laser for the diagnostics. Mirrors are installed with the holders fixed to remote controlled under-vacuum stepping motors, providing translations and tilts for further precise adjustment of the focusing point. The drawings of the chambers from CATIA software are illustrated in fig. 4 in the case of SCSS (a), and SPARC (b). A detailed top view of the SCSS drawing for the second chamber containing the periscope composed of the two reflective concave spherical mirrors (SM_1 and SM_2) is seen in fig. 4c. The HHG are introduced in the undulator thanks to a periscope consisting of two 45° planar mirrors. The mirrors are chosen according to the given spectral range of the HHG to be injected. Additional spectral selection, allowing the removal of the Infra red Ti-Sa laser is provided by the help of specific filters. In principle, the rejection of the infrared does not seem to be essential for the FEL process since the gain spectral width is narrow. It will nevertheless be checked experimentally. Implemented diagnostics will monitor the HHG intensity, spot size and central position. Cameras visualize inside the different chambers.

Table 2 : Seeding characteristics for SCSS prototype and SPARC

	SCSS P1	SPARC
Laser characteristics: Ti-Sa laser		
Energy/pulse (mJ)	50	2.5
Pulse duration (fs)	130	100
Repetition rate (Hz)	10	10
Focus lens (m)	7	2
M2	1.5	1.5
HHG		
number	3 to 13	3 to 9
Wavelength (nm)	266-60	266-89
Energy (µJ)	1	1
Spot diameter (µm) at focus	250	250
Mirror characteristics		
Type/ 0°Reflectivity (%)	SiC : 35 (0°), 20 (p, 45°), 50 (s, 45°) Multilayers 50	Metallic mirror Multilayers (95)
Radius of curvature (m)	0.25/0.5	0.3/0.4
Infrared rejection filter		
Filter type	Al, Sn	Bandpass filter
Rejection level	10^{-4}	10^{-4}
Diagnostics	Microchannel plate (Hamamatsu)	Photodiode Det710 Thorlabs ; Photomultiplier R8486-R759 Hamamatsu

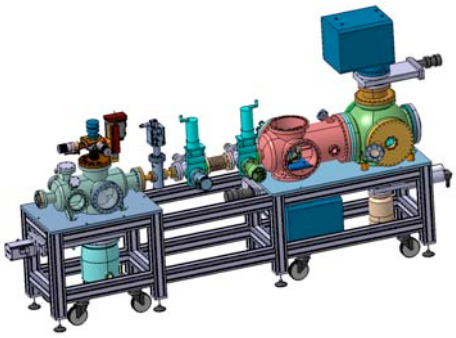

a

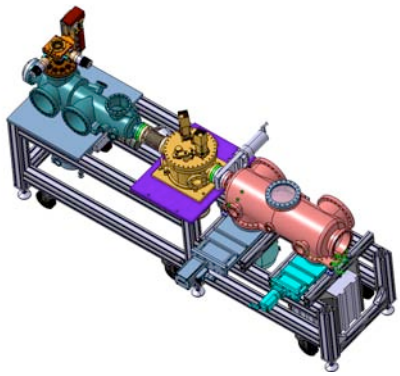

b

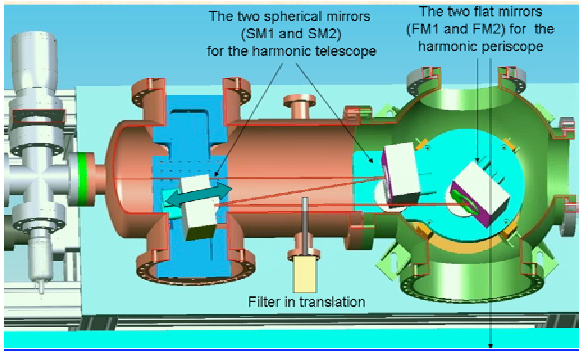

c

Figure 4 a: CATIA software 3D drawing view of seeding chambers a) general view for SCSS, b) for SPARC, c) detailed view of the second SCSS chamber for spectral selection and beam shaping.

SEEDING EXPECTED PERFORMANCES

The transport of the infra-red laser and on the gas high harmonics in the UV and VUV has been calculated in the frame of Gaussian optics, taking into account a purely non Gaussian mode (M2 factor of 1.5 for the infra-red, and 3 for HHG) [13]. Apart from avoiding optical damage (a threshold of 100 mJ. cm^{-2} has been taken) and self phase modulation of the powerful Ti-Sa laser, calculation allow to determine the conversion rate of the harmonics in gas and the transverse overlap with the electron beam. An example is shown in the SCCS prototype case, in fig. 5.

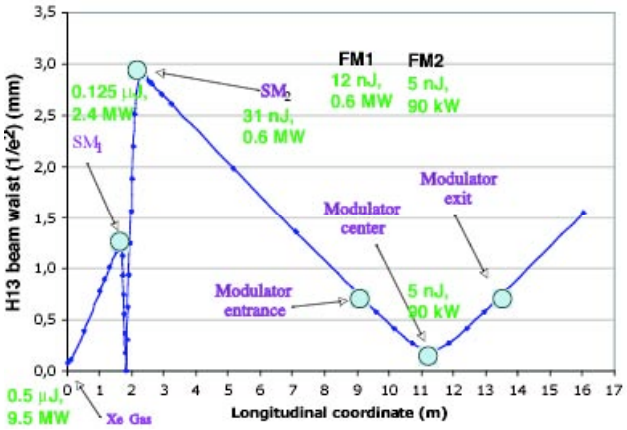

a

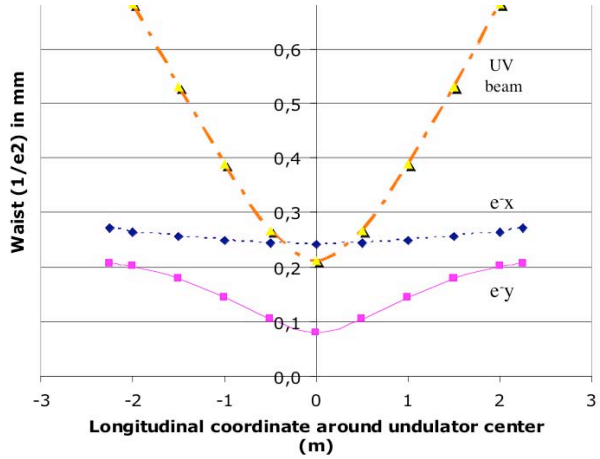

b

Figure 5:a) Longitudinal evolution of the beam radius size (waist in $1/e^2$) and corresponding peak power. b) overlap of the HHG beam sizes (Wp) with the electron beam (horzontal size Wex and vertical size Wey), as a function of the longitudinal coordinate.

The quasi Gaussian beam analysis has been applied also for the evaluation of a generalised Filling Factor, following the Colson-Elleaume analysis, taking into account the wiggling of the electrons in the undulator field [33]. This corrected filling factor has been applied as a reduction term in the gain in the PERSEO [34] simulations. Good agreement was found with the GENESIS simulations [35].
The seeding with HHG allows the gain length to be reduced from 10 to 5 m. This is illustrated for example in the SCSS prototype case in fig. 6.

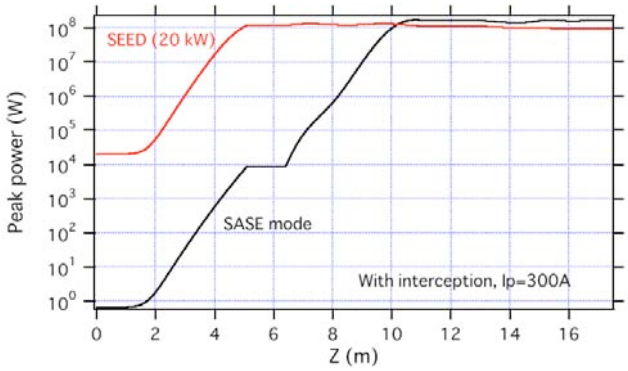

Figure 6: Comparison between SASE and Seeding HGHG configuration with 20 kW of seed in the case of the SCSS prototype.

The evolution of the peak powers of the fundamental and of the third and fifth non linear harmonics inside the radiator, at three different peak currents (100 A, 200 A and 300 A) is illustrated in fig. 7 in the SCSS prototype case. Fig.8 shows the expected characteristics in the case of SPARC. Here, we can also expect to test the cascading configuration with different adjustments of the undulator sections. Moreover, super-radiance effects are foreseen to be studied [22, 23].

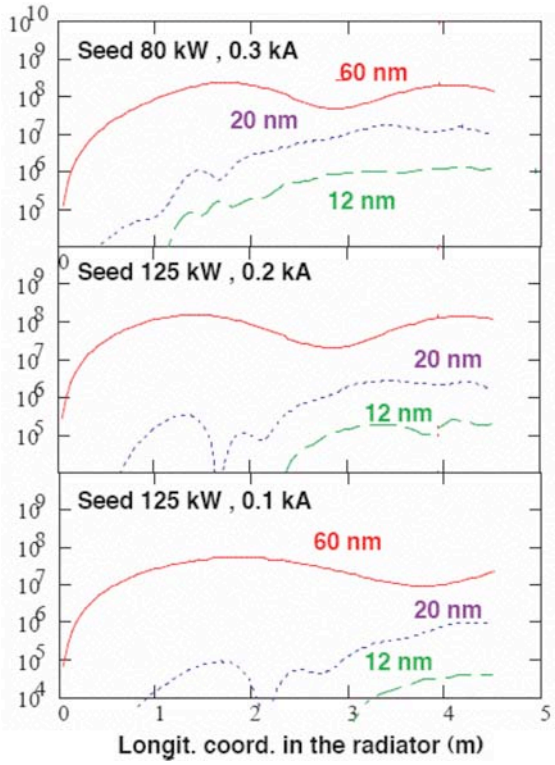

a)

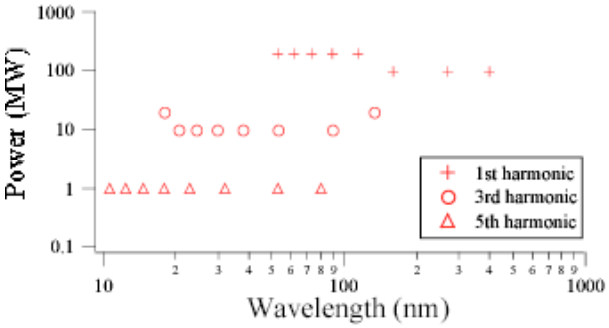

b

Figure 7: Intensity on the fundamental radiation and on the harmonics, versus the longitudinal coordinate a) for different peak current in the SCSS prototype case for a seed at 60 nm b) for different wavelengths, for a peak current of 0.3 kW. Perseo simulation taking into account the generalized filling factor.

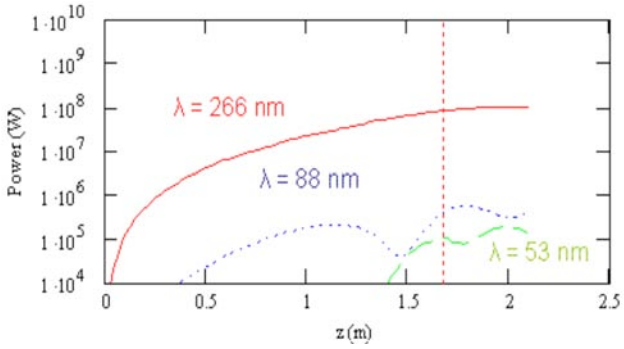

Figure 8: Output power of the fundamental radiation and of the third and fifth harmonics, versus the longitudinal coordinate in the SPARC prototype. Perseo simulation taking into account the filling factor. The seed is at λ=266 nm, for a peak power of 63 kW.

CONCLUSION

Harmonic Generation appears to be a very promising scheme for Free Electron Laser sources. Sometimes called “the second generation FEL”, they will afford higher performances in terms of coherence, stability and synchronization for users, while keeping a shorter saturation length. Seeding with High Harmonic in gases is under progress and potentially offers the path towards the generation of VUV-soft X ray coherent light injection in a FEL undulator for light application and high harmonics production.

REFERENCES

[1] S. Schreiber « First lasing at 32 nm of the VUV-FEL at DESY », Proceed. FEL Conf. 2005, Stanford, August 21-26, to be published in JACoW

[2] N. A. Vinokurov and A. N. Skrinski Preprint INP 77-88 Novosibirsk (1978) ;
R. Coisson and F. De Martini Free Electron Generators of Coherent Radiation, in Phys. Quantum Electron. vol 8-9 (Addison-Wesley, Reading; MA) 1982, 939
Ortéga et al, J. Quantum Electron. 21 (1985) 909
R. Coïsson "Perspectives of Production of Coherent VUV with Transverse Optical Klystrons" Nucl. Instr. Meth. 208 (1983) 185-188

[3] J.M. Ortega, B. Girard, Y. Lapierre, C. Bazin, M. Billardon, P. Elleaume, M. Bergher, M. Velghe and Y. Petroff "Optical frequency multiplication by an optical klystron on the ACO Storage Ring", Nucl. Instrum. Meth. A237 (1985) 268-272

[4] R. Prazeres, J.M. Ortega, C. Bazin, M. Bergher, M. Billardon, M.E. Couprie, H. Fang; M. Velghe and Y. Petroff "First Production of Vacuum-Ultraviolet Coherent Light by Frequency Multiplication in a relativistic Electron Beam" *Europhys. Lett.*, **4** (7), pp 817-822 (1987)
R.Prazeres et al *Phys. Rev. Lett.* **78**(11), 2124-2127 (1997)

[5] V. Litvinenko, Nucl. Instr. and Meth. A 507, 265 (2003)

[6] G. De Ninno, M. B. Danailov, B. Diviacco, M. Ferianis, M. Trov`o, L. Giannessi « Coherent harmonic generation using the ELETTRA storage ring optical klystron » JACoW *Proceedings of the 2004 FEL Conference, 237-240* 237

[7] L. H. Yu, I. Ben-Zvi, Nucl. Inst. Meth. A**393** (1997) 96

[8] L.-H. Yu et al Science 289, 2000, 032

[9] T. Shaftan and L. H. Yu, Phys. Rev. E71, 046501 (2005)

[10] W. Li and A. G. Suits, “Superexcited state dynamics probed with an extreme-ultraviolet free electron laser”, Phys. Rev. Lett. (2003).

[11] L. H. Yu et al Nucl. Instr. Meth. Phys. Res. A 393, 96 (1997). BNL-63639

[12] D. Garzella et al., Nucl. Inst. Meth. A 527 (2004)

[13] G.Lambert et al. "Seeding High Gain Harmonic Generation with laser harmonics produced in gases" Proceedings FEL 2004, 155-158, Trieste, Italy, 29 August-3 September 2004. G. Lambert et al., Proceed. FEL Conf. 2005, Stanford, August 21-26, to be published in JACoW

[14] L. Giannessi et al., « seeding @ sparc » TDR, L. Giannessi et al. Proceed. FEL Conf. 2005, Stanford, August 21-26, to be published in JACoW

[15] *The ARC-EN-CIEL FEL proposal,* G. Lambert, B. Carré, M. E. Couprie, M. Desmons, O. Chubar, B. Gilquin, D. Garzella, M. Jablonka, M. labat, A. Loulergue, J. R. Marquès, J. M. Ortega, F. Méot, P. Monot, A. Mosnier, L.Nahon, A. Rousse, Conf SPIE, San Diego, Aug. 2005

[16] MIT-BATES proposal: http://mitbates.mit.edu/xfel/

[17] www.4gls.ac.uk

[18] « Status of the SPARX FEL project », D.Alesini et al, Proceed. FEL Conf. 2005, Stanford, August 21-26, to be published in JACoW

[19]J. Feldhaus et al, Opt Commun 140, 341 (1997)
[20] A. Renieri Proceed. FEL Conf. 2005, Stanford, August 21-26, to be published in JACoW
[21] N. Thompson et al, « A VUV FEL for 4GLS : Design concept and simulations results » Proceed. FEL Conf. 2005, Stanford, August 21-26, to be published in JACoW
[22] L. Giannessi, P. Musumeci, and S. Spampinati, J. of Appl. Phys., 98, 043110 (2005).
[23]T. Watanabe et al., Proceed. FEL Conf. 2005, Stanford, August 21-26, to be published in JACoW
[24]P. B. Corkum, Phys. Rev. Lett. **71** (1993) 1994-1997, M. Lewenstein et al., Phys. Rev. A **49** (1994) 2117.
[25]H. Eichmann et al., Phys. Rev. A **51** (1995) R3414, K. Midorikawa, Phys. Rev. Lett. 82 (1999) 1422.
[26]P. Salières et al, Adv. At., Mol., Opt. Phys. **41** (1999) 83.
[27] P. Salières et al., Science **292** (2001) 902. E. J. Takahashi et al., Appl. Phys. Lett. 84, 4 (2004)
Opt. Lett 27, 1920 (2002), Phys. Rev. A 68, 023808 (2003)
Y. Tamaki et al., JJAP 40, L1154 (2001).
[28]L. Le Déroff et al., Phys. Rev. A **61** (2000) 043802.
[29]Y. Mairesse et al, Science 302, 1540
[30]T. Ditmire et al., Phys. Rev. A 51 (6), 1995, R4337
[31]Ph. Zeitoun, G. Faivre, S. Sebban, T. Mocek, A. Hallou, M. Fajardo, D. Aubert, Ph. Balcou, F. Burgy, D. Douillet, S. Kazamias, G. de Lacheze-Murel, T. Lefrou, S. le Pape, P. Mercre, H. Merdji, A. S. Morlens, J. P. Rousseau, C. Valentin A high-intensity highly coherent soft X-ray femtosecond laser seeded by a high harmonic beam *Nature* 431, 426-429 (23 Sep 2004) Letters to Nature
[32]SCSS CDR, www-xfel.spring8.or.jp/scss/
[33]Colson Elleaume in Appl. Phys. B 29, 101-109 (1982),
[34]Perseo by Luca Giannessi on www.perseo.enea.it
[35]GENESIS, S. Reiche, NIM A 429, (1999) 243.

BPM related issues on orbit stabilization in SPring-8 storage ring

S. Sasaki, SPring-8/JASRI, Kouto 1-1-1, Sayo-cho, Sayo-gun, Hyogo, 679-5165 Japan

Abstract

Orbit stabilization is the key factor to the third generation synchrotoron light source storage rings. Position data taken with beam position monitors are used to stabilize the orbit, however, the orbit motion itself affects the orbit measurement. This situation is described for the case of SPring-8 storage ring.

INTRODUCTION

Stable orbits are essential requirement for light source storage rings to make use of the full potential of the synchrotron light sources, especially for third generation light sources like the SPring-8 storage ring. The orbit in an electron storage ring for a light source is stabilized by utilizing the beam position data taken with beam position monitors (BPM), and by applying the correction to corrector magnets according to the BPM data.

The performance of BPM is crucial for the orbit stability. The performance includes the resolution, stability; the stability here means the low sensitivity to the stored beam current, the filling pattern, and ambient temperature change, as well as being free from long term drifts.

A BPM system consists of the pickups, usually button pickups, attached to the vacuum chamber, the signal processing electronics circuits, the interface to the control system, and the cables properly connect the components. The signal electronics circuits bear an most important roll to the performance of BPM.

On the other hand, the orbit must be stable to obtain the best performance of BPM. Even if the signal processing electronics circuits reaches very high resolution and high stability, actually measured position show sometimes the resolution and/or stability much worse than expected from the performance of the electronics.

The situation will be described in this paper, taking the SPring-8 storage ring case as an example.

RELATION BETWEEN THE BPM SIGNAL AND THE BEAM POSITION

Let us consider a difference over sum case. Beam positions are obtained from the signal amplitude as

$$x = \frac{1}{S_x}\frac{A_1 - A_2 - A_3 + A_4}{\sum A_i}, \qquad (1)$$

$$y = \frac{1}{S_y}\frac{A_1 + A_2 - A_3 - A_4}{\sum A_i}, \qquad (2)$$

where x, and y are beam positions in the horizontal and vertical direction, A_1, A_2, A_3, and A_4 are the signal amplitudes of corresponding pickups, and the geometry is something like described in figure 1.

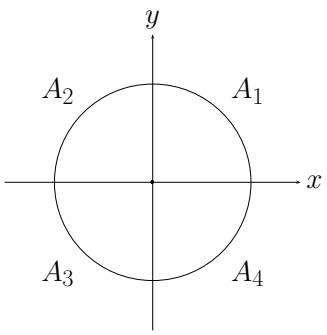

Figure 1: Geometry of pickups and corresponding signal amplitudes.

When the position error is estimated in the vicinity of the center, ($A_1 = A_2 = A_3 = A_4 = A$), the error propagation from the signal amplitude error to the position error shows

$$\delta x \text{ or } y|_{A_1=A_2=A_3=A_4} = \frac{1}{2}\frac{1}{S_{x \text{ or } y}}\frac{\delta A}{A}, \qquad (3)$$

where δA is the signal amplitude error. The position error is determined by the relative amplitude error through the coefficient called sensitivity $S_{x \text{ or } y}$.

The value of $1/S_{x \text{ or } y}$ is the same order of the vacuum chamber aperture, and order of 10 mm for most of electron storage rings. Hence achieving a sub-μm resolution requires the relative amplitude error of 10^{-4} to 10^{-5}. The stability in the same order is required to make the best use of the resolution performance.

A common way to release the stability requirement is multiplexing the signal and processing the signal through one route. Only the stability during the period of switching 4 signals is required. Unstableness with longer time constant than the switching period is canceled out. The SPring-8 storage ring BPM electronics applies multiplexing method. However, multiplexing method is affected by some spectral components of the beam motion. [1]

HISTORY OF REPEATABILITY IMPROVEMENT OF SPRING-8 STORAGE RING BPM

We present the history of change of stability related values of SPring-8 storage ring. We employed the root mean squared (rms) values of differences of positions between two consecutive measurements with the data size of more

than 100 as an estimate of repeatability. Typical interval of two consecutive position measurement is about 20 to 30 s; the rms values include not only the BPM resolution but also the movement of the beam.

Differences according to the Optics Change

Figure 2 shows the change of the repeatability according to the change of the optics.

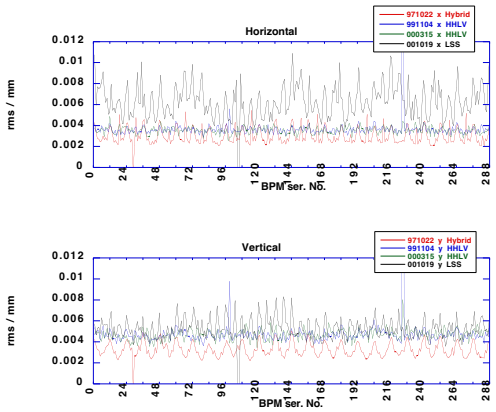

Figure 2: Differences of repeatability according to the optics change. Horizontal axes: serial No. of BPM, 288 BPMs cover whole the ring, Vertical axes: rms of difference of 2 consecutive measurements. Upper plot: horizontal direction, Lower plot: vertical direction. 971022 x/y Hybrid: hybrid optics, 991104 x/y HHLV, 000315 x/y HHLV: high horizontal and low vertical optics, 001019 x/y LSS: optics fitted for long straight sections.

The SPring-8 storage ring was first designed to be operated an optics called hybrid optics, in which the beta function took large and small values every other cell at the straight sections for insertion devices.

Then the optics was changed to HHLV which stood for High Horizontal and Low Vertical beta functions. In the HHLV optics all the straight sections had the same beta functions with large values in the horizontal direction and small values in the vertical direction.

During the summer shutdown in 2000, the magnet arrangement was largely modified and 4 magnet free long straight sections with 30-m length were installed in the storage ring. The optics was expressed as LSS (Long Straight Section).

The repeatability changed according to the optics change from Hybrid to LSS, where the LSS was worst in the three kinds of the optics.

One of the causes of this change was that the orbit stability was different for the different optics; each optics had different sensitivity to the driving factor of the beam motion, e.g. ripples of the magnet power supply, girder vibrations, etc. The measured repeatability was affected by the orbit motions.

Dependence on the Number of Averaging

Because the repeatability got worse, data taking and processing method was modified in the BPM electronics and the data taking system. The amplitude signals were converted to digital values through ADCs (analogue to digital converter). The AD converted values were stored and averaged in the ADC board.

Figure 3 shows the effect of the averaging.

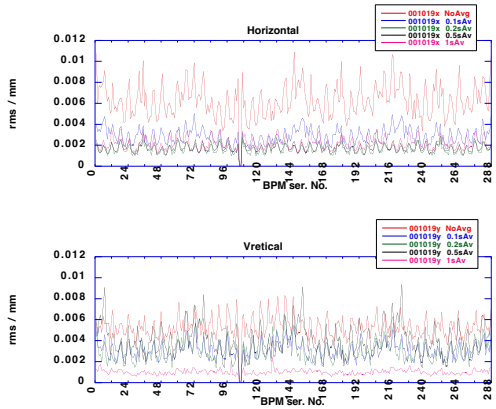

Figure 3: Average number dependence of repeatability. Horizontal axes: serial No. of BPM, Vertical axes: rms of difference of 2 consecutive measurements. Upper plot: horizontal direction, Lower plot: vertical direction. 001019x/y NoAvg: data without averaging. 001019x/y 0.1sAv: data with number of average of 10, since the data taking interval is 10 ms, the averaging effect is expressed in the unit of time. 001019x/y 0.2sAv: data with number of average of 20. 001019x/y 0.5sAv: data with number of average of 50. 001019x/y 1sAv: data with number of average of 100.

The data for averaging were taken each 10 ms because of a hardware limitation. The difference of the averaging condition is indicated by the time for integration, not by the number of data for averaging.

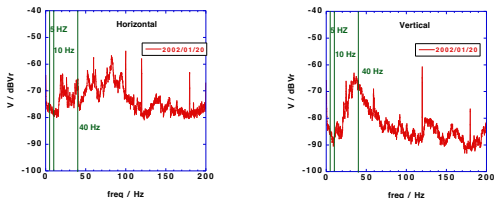

Figure 4: Spectra of beam movement. Horizontal axes: frequency in Hz. Vertical axes: power spectrum in dBVr unit, not converted to position unit. The conversion factors are approximately 2.2 mm / V, 1.4 mm / V. Vertical lines indicate the effective cutoff frequencies of low pass filters composed of simple averaging. 40 Hz: without averaging, intrinsic filter cutoff in the ADC. 10 Hz: the number of average of 10. 5 Hz: the number of average of 20.

Figure 3 indicates that effect of the averaging is different

in the horizontal and vertical direction. It suggests that the effect of increasing the number of averaging does not come from statistical effect only; the effect of changing the number of averaging corresponds to the change of the sensitivity to the beam motion spectral components. Changing the number of average changes the effective cut off frequency of a low pass filter composed of the averaging process.

An example of spectra of the beam motion is exhibited in figure 4. The spectra of horizontal and vertical directions are different. This supports the effect of changing the number averaging corresponds to the change of the effective cutoff frequency of the low pass filter.

Repeatability data recently taken are shown in figure 5. The repeatability is well in the sub-μ range. All these data were taken with the number of average of 25, (0.25 sec). Figure 6 shows the improvement of stability of beam motion. As a result of the efforts that reduces the influence of the sources of beam motion and reduces the sensitivity of the BPM measurement to the beam motion, the beam became much stable and the obtained BPM repeatability became better than before.

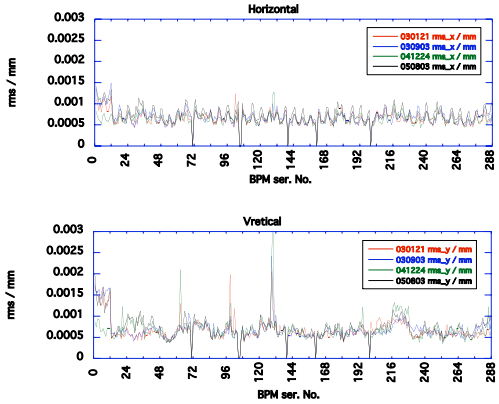

Figure 5: Recently taken repeatability data. Horizontal axes: serial No. of BPM, Vertical axes: rms of difference of 2 consecutive measurements. Upper plot: horizontal direction, Lower plot: vertical direction. All the data taken with the number of average of 25. 030121: data taken on the date of Jan. 21, 2003. 030901: data taken on the date of Sep. 1, 2003. 041224: data taken on the date of Dec. 24, 2004. 050803: data taken on the date of Aug. 3, 2005.

NEW ELECTRONICS

New signal processing electronics circuits for SPring-8 storage ring BPM are under construction to improve the performance of BPM; faster measurement with the same level of resolution as presently used one or better resolution with the same level of measurement time. The present system has been used since the beginning of the commissioning of the storage ring. The design of the circuit was optimized to small signals so that the orbit could be measured with the small amount of the stored electrons at the commissioning stage. Larger signals than the one corresponding the 1-mA stored current, are attenuated before input to the RF amplifier stage. Therefore the signal to noise ratio (S/N) cannot be improved for the larger stored current than 1 mA in spite of the increase of the signal strength.

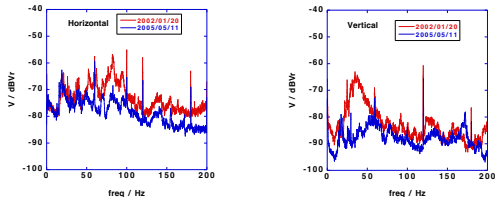

Figure 6: Spectra of beam movement. Horizontal axes: frequency in Hz. Vertical axes: power spectrum in dBVr unit, not converted to position unit. The conversion factors are approximately 2.2 mm / V, 1.4 mm / V. 2002/01/20: data taken on the date of Jan. 20, 2002. 2005/05/11: data taken on the date of May 11, 2005.

The design of the new circuits is optimized to 100-mA stored current. The typical signal strength of the 100-mA stored current at the circuit input is -20 dBm for the single 508.58 MHz spectral component. The frequency of 508.58 MHz is the acceleration RF frequency of the storage ring and also the detection frequency of the BPM signal processing circuits.

The target resolution is in the sub-μm range, and the stability must be in the same range. A multiplexing method was employed to fulfill the stability condition, [2] an ambient temperature stabilization is planned also.

One of features of the new circuit is that the intermediate frequency(IF) signal is sampled with 16-bit 2MSPS ADC to achieve a good linearity. Most of the non-linearity of the present circuit is comes from the demodulation stage, which is realized by an rms-dc conversion method. Since the non-linearity is the dominant factor of the stored current or signal strength dependence of the measured position data, improvement of the stored current dependence is expected by the IF sampling method. Figure 7 shows a simplified block diagram of one set of the new circuit. The detection RF is 508.58 MHz as described above, and it is converted to 250-kHz IF.

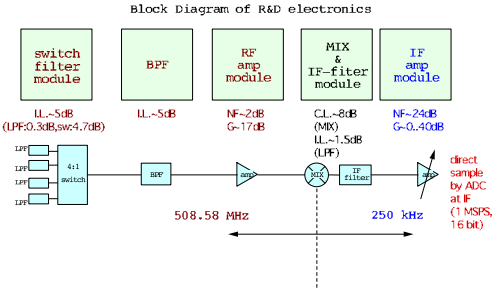

Figure 7: A simplified block diagram of the new electronics.

An example of data taken with a prototype of the new circuits is shown in figure 8. Data taken from two kinds of signal sources are compared: one is a signal generator with continuous wave (CW) output and the other is the beam signal. The signal generator output was divided to four and input to the circuit and processed. The processed signals were converted to the beam position equivalent data.

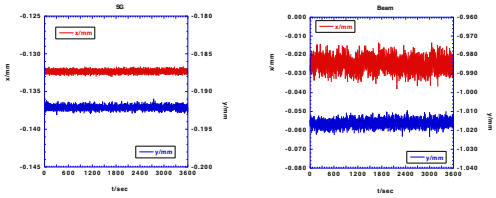

Figure 8: An example of the position data taken with the prototype of the new electronics circuits. Horizontal axes: time in second unit. Vertical axes: position in mm unit. Left plot: signal source is a signal generator. Right plot: signal source is the beam.

The data taken with the signal generator shows that the resolutions of 1 μm$_{pk-pk}$ in both horizontal and vertical direction are expected. However, data taken with actual beams shows resolution of 15 μm$_{pk-pk}$ in horizontal direction and 10 μm$_{pk-pk}$ in vertical direction, which are more than ten times worse than expected from the signal generator data. The discrepancy is due, at least partially, to the motion of the beam. Realization of the full performance of BPM system requires the separation of the effect of the beam motion to the position measurement.

SUMMARY

Beam position measurements are affected by the movement of the beam. It is important to separate the effect of the beam movement from the intrinsic error of the beam position measurement system. In the case of applying the BPM data to orbit feedback, the importance of the separation is obvious because harmfully large movement of the beam will be driven by applying the feedback based on the falsely measured data affected by the beam motion.

REFERENCES

[1] T. Straumann. ”Dynamic X-Y Crosstalk / Aliasing Errors of Multiplexing BPMs”, DIPAC 2003, Mainz, May 2003, p181.

[2] T. Fujita, S. Sasaki, M. Shoji and T. Takashima. ”A Problem in RF Switches of Multiplexing BPM System”, DIPAC 2005, Lyon, June 2005.

RESIDUAL BEAM MOTION DRIVEN BY THE NOISE AT TRANSVERSE FEEDBACK

T. Nakamura, JASRI/SPring-8, Sayo-cho, Hyogo, Japan

Abstract

The analysis on excitation of beam motion by noise of transverse feedback systems is performed. The result shows that high resolution beam position monitors of micro meter resolution for a single passage of bunches is required to reduce the amplitude of this motion to acceptable level, sub-micro meters for recent high brightness storage rings.

INTRODUCTION

Bunch-by-bunch feedback systems are widely used at storage rings to suppress beam instabilities. The most of recent systems employ digital feedback processors and the schematic diagram of the digital transverse bunch-by-bunch feedback system at the SPring-8 storage ring [1,2] is shown in Fig. 1. The positions of bunches are detected by a beam position monitor (BPM), and turn-by-turn and bunch-by-bunch position data are stored and processed by a digital feedback processor [3] to produce kick to damp betatron oscillation of bunches. For bunch-by-bunch feedback systems, the required bandwidth is more than one half of the bunch rate. In SPring-8 case, the bunch rate is 508.6MHz and the bandwidth of the feedback is more than 254MHz and noise caused by such wide bandwidth degrade the position resolution of BPMs. In the following, we analyze of the effect of this finite resolution of BPMs on the feedback.

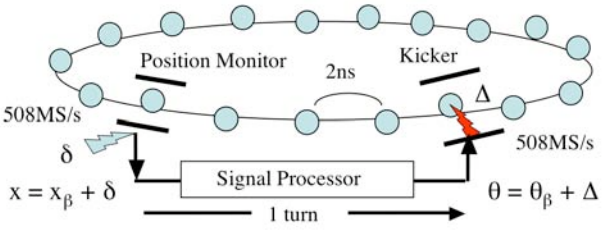

Figure 1: Schematic diagram of a bunch-by-bunch feedback system. Bunch rate and bunch spacing of the SPring-8 storage ring are 508MHz and 2ns. The bunch-by-bunch, turn-by-turn position data are stored and processed by a signal processor to produce a signal for kicker. The noise at a beam position monitor excites a feedback system and produce unwanted kick on a beam.

BUNCH-BY-BUNCH FEEDBACK

The required kick at n-th turn to damp the oscillation is

$$\theta_n = -\frac{2T_0}{\tau_{FB}} x'_n \qquad (1)$$

where T_0 and τ_{FB} are the revolution period of a ring and the feedback damping time, and x'_n is the angle of the beam at n-th turn. To produce x'_n from turn-by-turn position data of bunches, x_{n-k} (k=1,2,...), FIR filters are used in digital feedback processors.

FIR filter

A FIR filter is a one of digital filters and has the form of

$$y_n = \sum_{k=1}^{M} a_k x_{n-k} \qquad (2)$$

where x_n are the data of n-th sampling and y_n is the n-th output of the filter, and M is the number of taps.

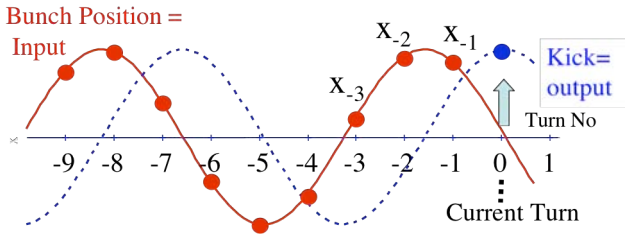

Figure 2: Turn-by-turn bunch positions (solid line) for the input data to FIR filter and required output of FIR filter (dashed line) to damp betatron oscillation shown in Eq. 3.

As shown in Fig.2, the required FIR filter for feedback systems is

$$-\beta x'_n = \sum_{k=1}^{M} a_k x_{n-k} \qquad (3)$$

where β is the beta function at the BPM and used for the normalization of the FIR filter. As shown in Fig. 2, the frequency dependence of the FIR filter should be

$$\sum_{k=1}^{N} a_k e^{-ik\phi} = e^{-i\frac{\pi}{2}} \qquad (4)$$

to fulfill the requirement of Eq. 3 where ϕ is the target betatron phase advance per turn. From Eq. 1 and Eq. 3, the kick can be expressed as

$$\theta_n = \frac{2T_0}{\tau_{FB}} \frac{1}{\beta} \sum_{k=1}^{M} a_k x_{n-k} \,. \qquad (5)$$

In this paper, we do not show the detail of methods to make such filters that fulfill Eq. 3. One of methods is shown in Ref. [1,2].

Position Error by Noise

To analyze the effect of the noise, we will apply similar discussion on radiation excitation.

We assume that the position error by noise, δ_n, is random:

$$\langle \delta_k \delta_{k'} \rangle = \delta_{kk'} \langle \delta^2 \rangle, \quad \langle \delta_k \rangle = 0 \quad . \qquad (6)$$

Using the position data with noise, $x_k + \delta_k$, the kick by feedback shown by Eq. 5, is

$$\theta_n = \frac{2T_0}{\tau_{FB}\beta}\sum_{k=1}^{M} a_k\left(x_{n-k} + \delta_{n-k}\right) = -\frac{2T_0}{\tau_{FB}}\left(x'_n + \frac{1}{\beta}\Delta_n\right) \quad (7)$$

where we set

$$\Delta_n = -\sum_{k=0}^{M} a_k \delta_{n-k}\,. \quad (8)$$

We assume that the angle of a beam has a format the neighbourhood of (n-N)-th turn:

$$x'_{n'} = A\cos n'\phi \quad (n' \sim n - N) \quad . \quad (9)$$

This evolves to n-th turn with the kick in Eq. 7 as

$$x'_n = A\cos n\phi + \sum_{k<n}^{n-N} \theta_k \cos(n-k)\phi \quad . \quad (10)$$

This can also be expressed as

$$x'_n = \left(A + \Delta A(n)\right)\cos\left(n\phi + \psi(n)\right) \quad . \quad (11)$$

where θ_k is the stochastic, and ΔA and ψ are the functions of θ_k, so that those are also stochastic. Using Eq. 7 for θ_k, the second term of the r.h.s. of Eq. 10 is

$$\sum_{k\le n}^{N} \theta_k \cos(n-k)\phi = -\sum_{k\le n}^{N} \frac{2T_0}{\tau_{FB}}\left(x'_k + \frac{1}{\beta}\Delta_k\right)\cos(n-k)\phi \quad (12)$$

We assume that the evolution of the amplitude is small during one period of betatron oscillation and we can use the approximation of $x'(k) \cong A\cos k\phi$ in r.h.s. of Eq. 12 and we have

$$\sum_{k\le n}^{N} \theta_k \cos(n-k)\phi = -\frac{2T_0}{\tau_{FB}}\sum_{k\le n}^{N}\left(A\cos k\phi\cos(n-k)\phi + \frac{1}{\beta}\Delta_k\cos(n-k)\phi\right) = -\frac{2T_0}{\tau_{FB}}\left(\frac{1}{2}NA\cos n\phi + \frac{1}{\beta}\sum_{k\le n}^{N}\Delta_k\cos(n-k)\phi\right) \quad (13)$$

where we also used the approximation:

$$\sum_{k\le n}^{N}\cos^2 k\phi \cong \frac{1}{2}N \text{ and } \sum_{k\le n}^{N}\cos k\phi\sin k\phi \cong 0$$

assuming that N is much larger than the fractional tune of the betatron oscillation.

Then from Eq. 10 and Eq. 13, we have

$$x'_n = \left(1 - \frac{T_0}{\tau_{FB}}NA\right)\cos n\phi - \frac{2T_0}{\tau_{FB}}\frac{1}{\beta}\sum_{k\le n}^{N}\Delta_k\cos(n-k)\phi \quad (14)$$

The first term of r.h.s. of Eq. 14 shows the damping and second term shows the effect of the noise.

Taking the ensemble average of x'^2_n in Eq. 14, we have

$$\left\langle x'^2_n\right\rangle = A^2\left(1 - \frac{T_0}{\tau_{FB}}N\right)^2\cos^2 n\phi + \left(\frac{2T_0}{\tau_{FB}}\right)^2\frac{1}{\beta^2}\sum_{k\le n}^{N}\sum_{k'\le n}^{N}\left\langle\Delta_k\Delta_{k'}\right\rangle\cos(n-k)\phi\cos(n-k')\phi = A^2\left(1 - \frac{T_0}{\tau_{FB}}N\right)^2\cos^2 n\phi + \left(\frac{2T_0}{\tau_{FB}}\right)^2\frac{1}{\beta^2}I_n \quad (16)$$

where

$$I_n = \sum_{k\le n}^{N}\sum_{k'\le n}^{N}\left\langle\Delta_k\Delta_{k'}\right\rangle\cos(n-k)\phi\cos(n-k')\phi \quad (17)$$

and we used $\left\langle\Delta_k\right\rangle = -\sum_{i=0}^{M} a_i\left\langle\delta_{k-i}\right\rangle = 0$.

Then we have, with Eq. 4 and Eq. 6,

$$I_n = \sum_{k\le n}^{N}\sum_{k'\le n i=0}^{N}\sum_{i'=0}^{M}\sum^{M} a_i a_{i'}\left\langle\delta_{k-i}\delta_{k'-i'}\right\rangle\cos(n-k)\phi\cos(n-k')\phi$$
$$= \sum_{k\le n}^{N}\sum_{k'\le n i=0}^{N}\sum_{i'=0}^{M}\sum^{M} a_i a_{i'}\left\langle\delta^2\right\rangle\delta_{k-i,k'-i'}\cos(n-k)\phi\cos(n-k')\phi$$
$$= \sum_{k\le n i=0}^{N}\sum_{i'=0}^{M}\sum^{M} a_i a_{i'}\left\langle\delta^2\right\rangle\cos(n-k)\phi\cos(n-k+i-i')\phi$$
$$= \left\langle\delta^2\right\rangle\sum_{k\le n i=0}^{N}\sum_{i'=0}^{M}\sum^{M} a_i a_{i'}\frac{1}{2}\left\{\cos 2(n-k)\phi + \cos(i-i')\phi\right\}$$
$$\cong \frac{1}{2}N\left\langle\delta^2\right\rangle\sum_{i=0}^{M}\sum_{i'=0}^{M} a_i a_{i'}\cos(i-i')\phi$$
$$= \frac{1}{2}N\left\langle\delta^2\right\rangle\left(\sum_{i=0}^{M} a_i\cos i\phi\sum_{i'=0}^{M} a_{i'}\cos i'\phi + \sum_{i=0}^{M} a_i\sin i\phi\sum_{i'=0}^{M} a_{i'}\sin i'\phi\right)$$
$$= \frac{1}{2}N\left\langle\delta^2\right\rangle\left\{\left(\sum_{i=0}^{M} a_i\cos i\phi\right)^2 + \left(\sum_{i=0}^{M} a_i\sin i\phi\right)^2\right\}$$
$$= \frac{1}{2}N\left\langle\delta^2\right\rangle\left|\sum_{k=0}^{M} a_k e^{ik\phi}\right|^2 = \frac{1}{2}N\left\langle\delta^2\right\rangle\,. \quad (18)$$

where we used $\left|\sum_{k=0}^{M} a_k e^{ik\phi}\right|^2 = 1$ with Eq. 4

Now we have

$$\left\langle x'^2_n\right\rangle = A^2\left(1 - \frac{T_0}{\tau_{FB}}N\right)^2\cos^2 n\phi + \left(\frac{2T_0}{\tau_{FB}}\right)^2\frac{1}{\beta^2}\frac{1}{2}N\left\langle\delta^2\right\rangle \quad .(19)$$

Using Eq. 11, we have

$$\left\langle\left(A + \Delta A\right)^2\right\rangle\cos^2\left(n\phi + \psi\right) = A^2\left(1 - \frac{T_0}{\tau_{FB}}N\right)^2\cos^2 n\phi + \left(\frac{2T_0}{\tau_{FB}}\right)^2\frac{1}{\beta^2}\frac{1}{2}N\left\langle\delta^2\right\rangle. \quad (20)$$

We take a time average for several oscillation period and we have

$$\frac{1}{2}\left\langle \left(A+\Delta A\right)^2 \right\rangle = \frac{1}{2}A^2\left(1-\frac{T_0}{\tau_{FB}}N\right)^2 + \left(\frac{2T_0}{\tau_{FB}}\right)^2 \frac{1}{2\beta^2}N\left\langle \delta^2 \right\rangle$$

$$\cong \frac{1}{2}A^2 - \frac{1}{2}A^2\frac{2T_0}{\tau_{FB}}N + \left(\frac{2T_0}{\tau_{FB}}\right)^2 \frac{1}{\beta^2}\frac{1}{2}N\left\langle \delta^2 \right\rangle \qquad (21)$$

with the assumption, $\frac{T_0}{\tau_{FB}}N << 1$.

Then the evolution of the amplitude of the betatron oscillation is

$$\left\langle \frac{d\left(A^2\right)}{dt} \right\rangle = \frac{\left\langle \left(A+\Delta A\right)^2 \right\rangle - A^2}{NT_0} =$$

$$-\frac{2}{\tau_{FB}}A^2 + \left(\frac{2T_0}{\tau_{FB}}\right)^2 \frac{1}{\beta^2 T_0}\left\langle \delta^2 \right\rangle . \qquad (22)$$

If we include radiation damping or growth by instabilities, the equation is

$$\left\langle \frac{d\left(A^2\right)}{dt} \right\rangle = -\frac{2}{\tau}A^2 + \left(\frac{2T_0}{\tau_{FB}}\right)^2 \frac{1}{\beta^2 T_0}\left\langle \delta^2 \right\rangle \qquad (23)$$

where τ is the total damping time with feedback, radiation damping and growth by instabilities. We treat A as definite value at n-N turn. However, as we see, the value A evolves stochastically with ΔA and become stochastic after many damping time. At the equilibrium, the value of Eq. 23 should be 0 and we have expectation value:

$$\left\langle A^2 \right\rangle = \frac{2\tau T_0}{{\tau_{FB}}^2}\frac{1}{\beta^2}\left\langle \delta^2 \right\rangle \qquad (24)$$

or

$$\sigma_{x'}{}^2 = \frac{1}{2}\left\langle A^2 \right\rangle = \frac{\tau T_0}{{\tau_{FB}}^2}\frac{1}{\beta^2}\left\langle \delta^2 \right\rangle \qquad (25)$$

for r.m.s. of divergence of the beam at the feedback and

$$\sigma_x = \frac{\sqrt{\tau T_0}}{\tau_{FB}}\sigma_\delta \qquad (26)$$

for r.m.s. of beam size where $\sigma_\delta = \sqrt{\left\langle \delta^2 \right\rangle}$ is the resolution of the BPM in r.m.s.

SPring-8 CASE

We will apply the result to the SPring-8 storage ring. The parameters of the SPring-8 storage ring are listed in Table 1.

Table 1: Parameters of the SPring-8 storage ring

parameter	symbol	value	unit
Revolution Period	T_0	4.79	μs
Bunch rate / RF acc. freq	f_{RF}	508.58	MHz
Beam size at feedback	σ_H/σ_V	301 / 6	μm
Average Current	I	100	mA

From Eq. 26, we have to reduce total damping time, τ, by feedback to be much faster than growth time of instabilities to keep σ_x small, and we set τ_{FB} ~ 0.5ms. With this damping time, Eq. 26 shows $\sigma_x = 0.1\sigma_\delta$. A Monte-Carlo simulation confirms this relation.

The residual amplitude of the betatron oscillation should be reduced to one tenth of the beam size. The beam size at the feedback is 6μm hence required resolution of a BPM, σ_δ, is 6μm.

The button type BPM of SPring-8 for correction of slow beam motion is 0.5μm with bandwidth ~1kHz. Scaling of the resolution to bandwidth, B is $\sqrt{B}$ and the expected resolution at B ~ 250MHz that required for the feedback is 250μm. This value is 50 times larger than required.

We developed a new shorted-stripline type BPM for the SPring-8 feedback [4] that produces tens times higher signal than button types, and its position resolution is 5μs r.m.s. for a single passage of a bunch with 0.24nC charge. Also we use 12-bit ADCs for the front-end of our feedback processor to achieve sub mm resolution with dynamic range of 0.5mm that is required to control the turbulence on the stored beam produced at injection.

CONCLUSION

We derived a formula for the amplitude of residual motion excited by a feedback driven by a noise at beam position detection. The result shows that the special high-resolution beam position monitors are required to suppress the amplitude of these motions to nano meter region.

REFERENCES

[1] T. Nakamura, S. Date, K. Kobayashi and T. Ohshima, "Transverse Bunch-by-bunch Feedback System for the SPring-8 Storage Ring", EPAC'04, Lucerne, July 2004, p. 2649, http://www.jacow.org.

[2] T. Nakamura, "High Precision Transverse Bunch-by-Bunch Feedback System with FPGA and High Resolution ADC", J. Particle Accelerator Society of Japan, Vol.1, No.3, 2004.(in Japanese)

[3] T. Nakamura and K. Kobayashi "FPGA Based Bunch-by-bunch Feedback Signal Processor", ICALEPCS'05, Geneva, Oct. 2005, PO2.022-2, http://www.jacow.org or http://icalepcs2005.web.cern.ch

[4] T. Nakamura, "Beam Position Monitor and Kicker for the SPring-8 Transverse Bunch-by-bunch Feedback", DIPAC'05, Lyon, June 2005, p. 302, http://www.jacow.org.

Recent Status of Fresnel Zone Plate monitor at KEK-ATF damping ring

Hiroshi Sakai*[A)], Norio Nakamura[A)], Hitoshi Hayano[B)], Toshiya Muto[B)]
[A)] ISSP, University of Tokyo, 5-1-5 Kashiwanoha, Kashiwa, Chiba, 277-8581
[B)] KEK, 1-1 , Oho, Tsukuba, Ibaraki, 305-0801

Abstract

We present the recent progress of the FZP (Fresnel Zone Plate) beam profile monitor constructed at KEK-ATF damping ring. This monitor is based on an X-ray imaging optics with two FZPs [1]. In this monitor, the transverse electron beam image at bending magnet is twenty-times magnified by the two FZPs and detected on an X-ray CCD camera. The expected spatial resolution is less than 1 m. Recently, we install the new mechanical shutter in order to avoid the unexpected 100Hz vibration. By applying this shutter, the shutter opening time was reduced less than 1ms and the 100Hz vibration could be neglected on the beam profile measurement. In this paper, we report the new shutter performance and the measurement results of beam profile by the improved FZP beam profile monitor.

INTRODUCTION

The Accelerator Test Facility(ATF) was built at High Energy Accelerator Reseach Organization (KEK) in order to develop the key techniques of ultra-low emittance beam generation and manupulation. The ATF consists of 1.28GeV S-band electron linac, a damping ring and extraction line. A low emittance beam is generated in the ATF damping ring where the natural horizontal emittance is designed to 1.1 10 [9]m·rad. The target value of the vertical emittance is 1.1 10 [11]m·rad. The typical beam sizes are less than 50 m horizontally and less than 10 m vertically. Our monitor (called as FZP monitor) is aimed to develop for measuring such a small beam sizes and beam profiles

Fig.1 shows the setup of the FZP monitor. This monitor is based on an X-ray imaging optics with two Fresnel Zone Plates (FZPs) by using the synchrotron radiation (SR) from the bending magnet. To avoid the large diffraction limit from the visible light, X-ray SR (3.235keV) is selected by Si monochromator. The transverse electron beam image at bending magnet is 20-times magnified by the two FZPs (shown in Fig.1 as 'CZP' and 'MZP'). and detected on X-ray CCD camera. Thanks to the small diffraction limit of SR in the X-ray regime and the large magnification (M=20) of two FZPs, the expected spatial resolution is less than 1 m in R.M.S. [2].

We briefly summarize the history of FZP monitor before describing the recent progress of FZP monitor. The FZP monitor was installed in 2002 and could measure the clear beam profile with less than 10 m vertical beam size [1]. After installing the new monochromator which was made in order to suppress the angle drift of the Si cristal, the vertical position drift of the beam image on CCD was much reduced by a factor of about 100 and was stabilized with a few m level for a long time [3]. We repaired the two FZP folders so that the FZPs could be removed up from the optical path in the vacuum. This improvement allowed us to perform more precise beam-based alignment by detecting the X-ray SR light on X-ray CCD camera directly. As a result, the aberration effects of FZPs became negligible small for the beam profile measurement[3]. Furthermore, an X-ray pinhole mask was installed to reduce the background component of the transmitted X-rays. Finally the beam profile with 50 m horizontal beam size and 7 m vertical beam size was stably obtained in 2004 [4].

Receltly, we found the unknown 100Hz oscillation of beam positon. This amplitude is large as 5-6 m in R.M.S. and is not negligible small compared with the vertical beam size. Unfortunately the previous shutter opeing time of X-CCD camera is at least 20ms, then the measured vertical beam size on X-CCD camera was enlarged by the superposition of this oscillation effect. We emphasize that this 100Hz oscillation is not concerned with the mechanical vibration of FZP monitor beam line[4]. But we now do not find the source of 100Hz vibration. To neglect this 100Hz vibration, we newly install the mechanical shutter which has the shutter opening time with less than 1ms. In this paper, we present the result of the beam profile measurement with this newly installed shutter.

MEASUREMENT OF THE BEAM PROFILE

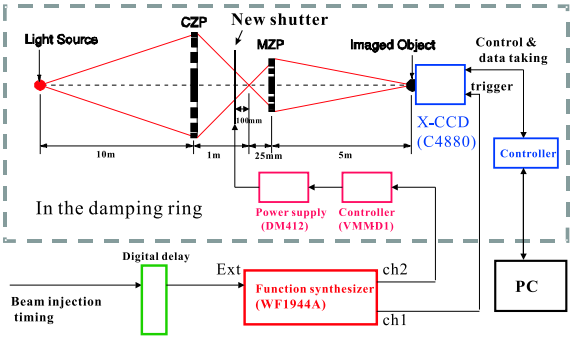

Figure 2: The block diagram of FZP monitor

We install the new mechanical shutter in ATF damping ring and measure the beam profile. Fig.2 shows the block diaglam of FZP monitor. In order to shorten the shutter opening time of the mechanical shutter, the small aperture of the mechanical shutter is needed. Then we apply the

* E-mail: hrsakai@issp.u-tokyo.ac.jp

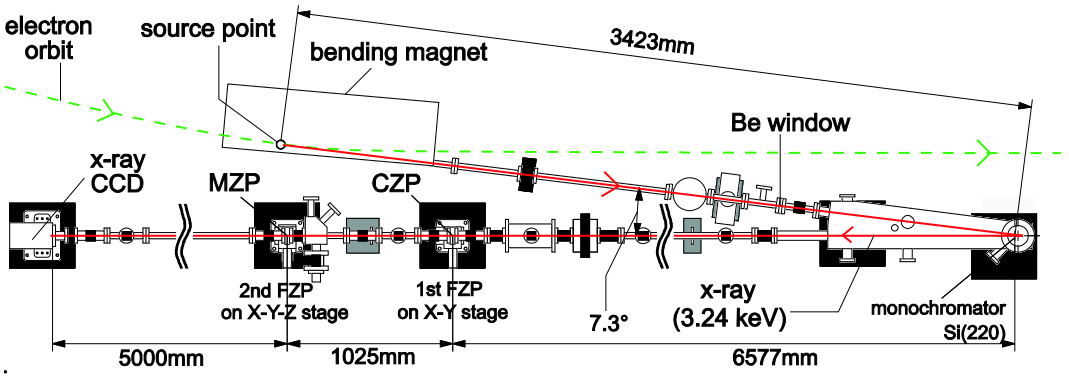

Figure 1: Setup of FZP monitor

mechanical shutter with 1mm diameter aperture which is smaller than the previous shutter aperture (5mmϕ) set in front of the X-ray CCD camera. Furthermore the mechanical shutter is installed near the first focal point of X-ray SR not to scrape off the transverse beam profile. The trigger timing is synchronized with the beam injection timing of damping ring and is divided with shutter trigger and CCD trigger timing. The shutter opening time is controlled by changing the trigger TTL pulse width. The minimum shutter opening time is almost 1ms, which is enough small to neglect the 100Hz oscillation.

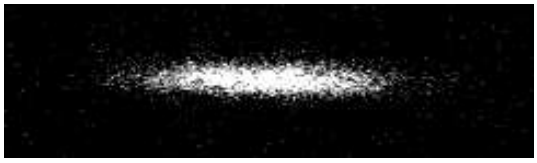

Figure 3: The measured beam profile by using newly installed mechanical shutter

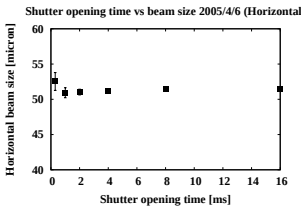

Figure 4: The shutter opening time vs horizontal beam sizes

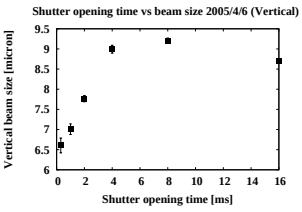

Figure 5: The shutter opening time vs vertical beam sizes

Fig.3 shows the measured beam profile by using newly installed mechanical shutter. The shutter opening time is 1ms. The clear beam profile is obtained. We also measure the beam profile by chainging the shutter opening time of the new mechanical shutter. Fig.4,Fig.5 show the change of the horizontal and vertical beam sizes corresponding to the shutter opening time, respectively. The horizontal beam size does not depend on the shutter opeining time. On the other hand, we find the enhancement of the vertical beam size as the TTL pulse width of trigger timing is enlarged. To confirm that this enhancement will depend on the 100Hz oscillation, we measure the center position of the obtained beam profile by chainging the shutter trigger timing with fixed 1ms shutter opening time. Fig6,Fig.7 show the results of the horizontal and vertical center position changes corresponding to the beam tirigger timing, respectively. The 100Hz oscillation of the center position is observed as shown in Fig.6 and Fig.7 by applying the sinusoidal fitting with 100Hz frequency. These amplitudes are 10 m horizontally and 5.5 m vertically. The beam size enhancement as shown in Fig.4,Fig.5 are explained by these 100Hz oscillation.

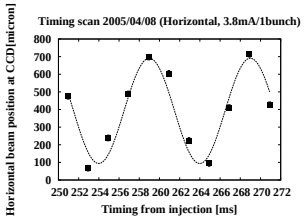

Figure 6: trigger timing vs the center of horizontal beam profiles

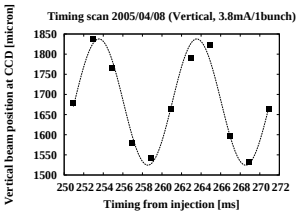

Figure 7: trigger timing vs the center of vertical beam profiles

In order to validate these measured beam size with 1ms shutter opeing time, we compare with the calculation by using the optics of the ATF damping ring with including the intra beam scattering effect. Fig.8 and Fig.9 show the comparisons of the measured horizontal and vertical beam size (boxs) and the calculation (lines), respectively. The horizontal axis shows the beam current of damping ring and vertical axis is the measured and calculated beam sizes. These measurement are agree well with the calculation assuming the betatron coupling is 0.3$\sim$0.6%. We note that the measured energy spread as shown in Fig.10 also agree well with the calculation with same assumption.

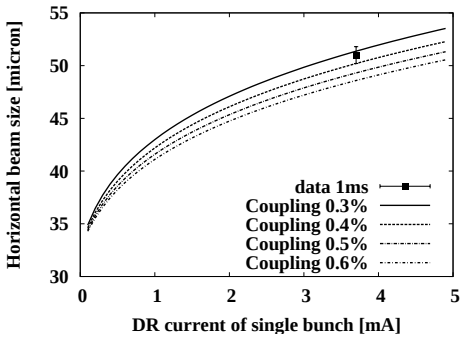

Figure 8: The comparison between the measured horizontal beam size and calculation

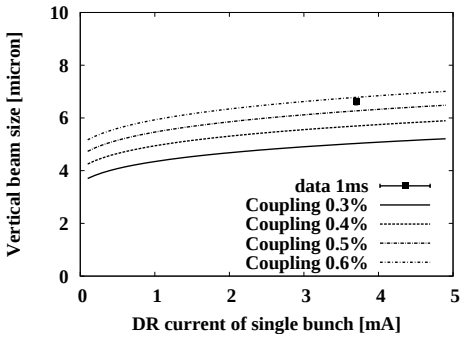

Figure 9: The comparison between the measured vertical beam size and calculation

MEASUREMENT OF THE DAMPING TIME

FZP monitor is suitable to measure the damping time because of the large dynamic range of this monitor. Futhremore the impoved time resolution by newly installed mechanical shutter allows us to measure the damping time presicely. In this year, the beam operation with wiggler was started. It is important to measure the effect by applying the wiggler magnet. Then we measure the damping time with/without wiggler magnet precisely[5]. Fig.11 is the measurement of the vertical damping time with/without wiggler magnet. The horizontal axis shows the elasped time from the beam injection into damping ring. The vertical axis is the measure beam size by FZP monitor. By fitting the damping effect to Fig.11, We obtained that the vertical damping time without wiggler magnet is $(30.9 \quad 0.6)$ms and with wiggler magnet is $(20.7 \quad 0.8)$ms. The effect of wiggler magnet to the damping time was measured. The design values of the damping time with/without wiggler magnet is 21.1ms、28.5ms, respectively. These values agree well with the damping time measurments.

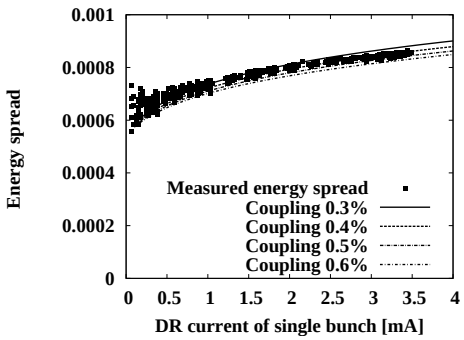

Figure 10: The comparison between the measured momentum spread and calculation

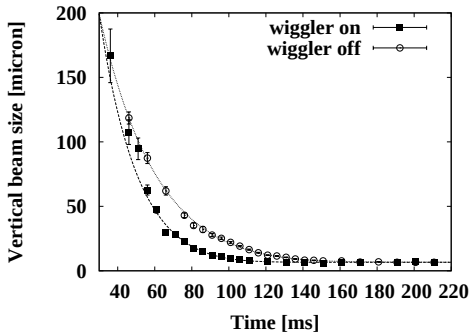

Figure 11: The results of the measured vertical damping time.

SUMMARY

We install the new mechanical shutter and measure the beam profile by using this shutter. The unexpected 100Hz beam oscillation can be removed by this mechanial shutter with 1ms shutter opening time. After that we can perform the precise measurment of the beam profile. The three measured values, which are horizontal and vertical beam size meaured by FZP monitor and the momentum spread, agree well with the calculation by the optics of ATF damping ring by assuming that the betatron-coupling is $0.3\sim0.6\%$. The damping time with/without wiggler magnet in the ATF damping ring are also measured by this monitor. The measured damping time are agree well with the calculation of the beam dynamics by usnig ATF damping ring optics.

REFERENCES

[1] K.Iida, et. al., NIM A506 (2003) 41-49

[2] T.Muto, et. al.,"Performance evaluation of a beam profile monitor using Fresnel Zone Plates", Proc. of the 2nd Annual Meeting of Particle Accelerator Society of Japan And 30th Linear Accelerator Meeting in Japan, Tosu, (2005)

[3] T.Muto, et. al., Proc. of the 14th Symposium on Accelerator Science and Technology, Tsukuba, 2003, p476

[4] N.Nakamura, et. al., Proc. of EPAC04, Lucerne, 2004, p2353.

[5] T.Naito, et. al., Proc. of PAC05, Knoxville, 2005, p2809.

ISSUES ON THE TRANSVERSE PHASE SPACE TOMOGRAPHY

H. Zen#, H. Ohgaki, K. Masuda, T. Fukui, K. Kusukame, Y. Nakai, T. Kii, T. Yamazaki,
K. Yoshikawa, Institute of Advanced Energy, Kyoto Univ., Gokasho, Uji, Kyoto 611-0011, Japan.

Abstract

Effects of energy distribution and space charge of objective beams on the transverse phase space tomography have been evaluated by numerical calculations. As the result, an acceptable error, less than 15 %, in the emittance is derived from the reconstructed transverse phase space image when the energy spread is less than 15 % for a beam with a rectangle-shaped energy distribution. However, for the energy distribution which has a low energy tail, a severely distorted image is reconstructed. To reconstruct a reasonable image with the tailed beam, a 70 % energy cut-off with respect to the peak energy is applicable.

In terms of space charge effect, reconstructed phase space image is much distorted with higher peak current beam.

INTRODUCTION

To generate a high quality electron beam, 'Nanobeam', beam emittance measurement is a very important issue. Transverse phase space tomography [1] using a quadrupole magnet and a beam profile monitor is very useful for emittance measurements especially for non-Gaussian beams, since this method directly gives transverse phase space distributions. Therefore, many measurements have been carried out by this method [2].

We have applied the method to diagnose the beam from our FEL driver Linac and thermionic rf gun [3]. However, we could not obtain reliable results due to noisy reconstructed images. One can obviously see that in the transfer matrix for the quadrupole magnet in the tomographic method, the matrix components depend on the particle energy and the space charge force. Thus, the energy distribution and the space charge force of the objective beam distort the reconstructed phase space distribution, since the method assumes a mono-energetic beam without space charge force in reconstructing the phase space distribution. For practical application to a beam with a considerable energy spread by a thermionic rf gun, evaluation of the effect of energy distribution is indispensable. And for practical application to a low energy beam with a high peak current by a photo-cathode rf gun, evaluation of the effect of space charge force is indispensable. In this paper, we evaluated the effects of the energy distribution and the space charge force of this method by simulation. Firstly we evaluated the effect of the energy spread of the beam with a rectangle-shaped energy distribution with Gaussian distribution in transverse phase space. Secondly we evaluated the effect of a low energy tail, because a thermionic rf gun inherently produces a low energy tailed beam. Finally we evaluated the effect of space charge force with mono-energetic beam.

E-mail: heishun@iae.kyoto-u.ac.jp

CRITICAL ISSUE

As shown in Eq. 1, the rotation angle θ and magnification rate A are described by transfer matrix of the quadrupole magnet and the free space assuming the measurement system shown in Fig.1. In Eq. 1, x_0, x_0' are transverse phase space parameters at the entrance of the quadrupole magnet, x is rotated image at the beam profile monitor, B_x is the gradient of the magnetic field in quadrupole magnet, Z is the length of the quadrupole magnet, E is the kinetic energy of the electron, and L is the distance between the quadrupole magnet and the beam profile monitor.

We reconstruct a phase space distribution at the entrance of the quadrupole magnet by using the tomographic technique from the measured spatial distributions of beams with many different quadrupole magnet strengths at the profile monitor. However, the rotation angle θ and magnification rate A depend on the energy of the particle. Therefore, different energy particle can not be reconstructed correctly, because we assume a mono-energy beam for reconstruction. Moreover, the transfer matrix neglects the space charge force of the beam. Therefore space charge force causes errors if it cannot be neglected.

$$x = A\left(x_0 \cos\theta + x_0' \sin\theta\right) \quad , \quad k^2 = \frac{e}{m_0\left(E/m_0c^2 + 1\right)\beta c} B_x$$
$$\theta = \tan^{-1}\left(\frac{\frac{1}{k}\sin kZ + L\cos kZ}{\cos kZ - kL\sin kZ}\right) \qquad (1)$$
$$A = \sqrt{(\cos kZ - kL\sin kZ)^2 + (\frac{1}{k}\sin kZ + L\cos kZ)^2}$$

SIMULATION

We have simulated the transverse phase space tomography procedure with our experimental setup, which consists of a quadrupole magnet and a beam profile monitor as shown in Fig. 1. In this simulation, 39 spatial projections at the profile monitor with different strength of quadrupole magnet are calculated by PARMELA code [4]. Then we reconstruct the initial phase space distributions by using the Ordered Subsets – Expectation Maximization algorithm [5]. It has been already studied that the 39 projections are enough for tomographic technique [2].

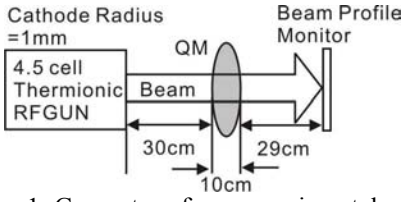

Figure 1: Geometry of our experimental setup.

RESULTS AND EVALUATION

Gaussian beams with rectangle-shaped energy distribution

Gaussian beams with rectangle-shaped energy distributions (Fig. 2(a)) with different energy spreads up to 15% were calculated to evaluate the effect of the energy spread of the beam. The unnormalized emittance of the initial phase space distribution is 1.5π mm mrad (Fig. 2(b)).

In Fig. 3, the reconstructed phase space distributions with energy spread of 0%, 5%, 10%, and 15% are shown. During the beam transfer calculations, the space charge effects are turned off. As shown in Fig.3 the reconstructed images are almost identical to the initial one. Figure 4 shows the ratios of the unnormalized emittances of the reconstructed images to that of the initial image. As shown in Fig.4, the ratio can be expressed by a parabolic function of the energy spread of the initial beam. However, the errors of emittances are acceptably low as less than 15 % when the energy spread is less than 15 %.

Low energy tailed beam

To evaluate the effect of the low energy tail, we use the PARMELA calculation which simulates the 4.5-cell thermionic RF gun, which is employed in our linac, as the initial beam distribution. The energy and phase space distributions at the entrance of the quadrupole magnet given by PARMELA code are shown in Fig. 5. The energy distribution of the beam consists of the main component and low energy tail (Fig 5(a)), and the phase space distribution is strongly correlated with energy distribution (Fig. 5(b)).

Initial phase space distribution and reconstructed phase space distribution by tomographic method are shown in Fig. 6 (a) and (b), respectively. One can see a noisy reconstructed image. The unnormalized emittance calculated from the initial phase space distribution is 1.0π mm mrad and that from the reconstructed phase space distribution is 2.7π mm mrad.

As shown in previous section, the error from main component should not be large when the energy spread is small enough. In this calculation 0.5 % (FWHM) energy spread for the main peak is used. Therefore, the noise in the reconstructed image is originated from low energy particles.

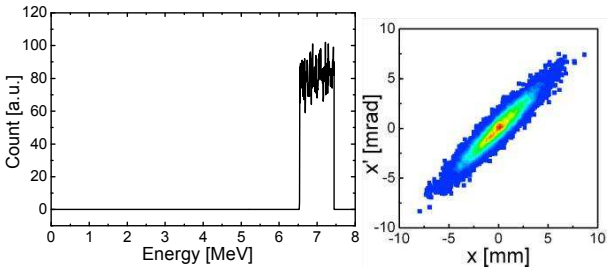

Figure 2: Gaussian beam with rectangle-shaped energy distribution, (a) Example of energy spectrum (FWHM = 10 %), (b) Phase space distribution (Gaussian, $\varepsilon = 1.5\pi$ mm mrad)

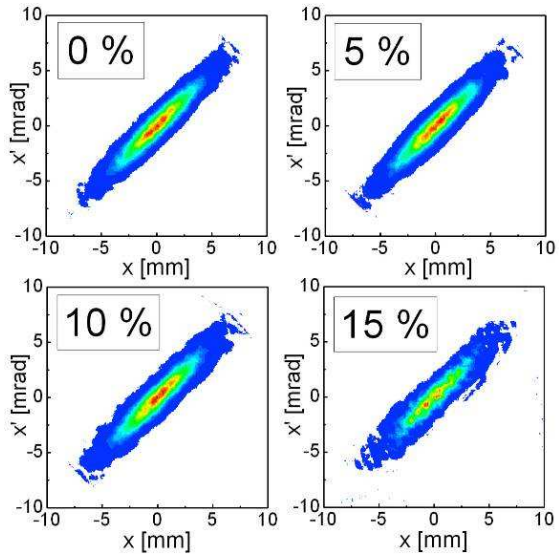

Figure 3: Reconstructed phase space distributions of Gaussian beam with rectangle-shaped energy distribution for different energy spread, upper left: mono energy, upper right: 5 %, lower left: 10 %, lower right: 15 %.

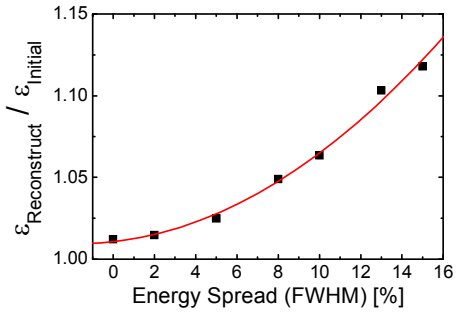

Figure 4: The ratios of the unnormalized emittances from the reconstructed phase space of Gaussian beams with rectangle-shaped energy distributions to that from the initial one. The red line is the fitted curve by parabolic function.

To clarify the contribution of low energy particles to the noise on reconstructed image we cut the particles whose energy is lower than cut-off energy ($E_{cut\text{-}off}$).

In the case of $E_{cut\text{-}off} / E_{peak}$ = 90 % (E_{peak} is peak energy of the beam), the initial and reconstructed phase space distributions are shown in Fig. 7. For the equivalent comparison, the energy filtering also applied to the initial distribution. As is shown in Fig.7(b), the noises in the reconstructed image are dramatically reduced by the energy filtering. By the energy filtering, the unnormalized emittance of the initial beam is 0.43π mm mrad and that of reconstructed image is 0.52π mm mrad. For practical use, we have to cut the low energy tail of the objective beam by using an energy filtering section, such as a bending and a slit.

To evaluate the tolerable cut-off energy of the tomographic method, the beams of different cut-off energies are also simulated. The results of emittance calculation from the reconstructed phase space distributions are plotted in Fig.8 as the function of cut-off energy. As shown in Fig. 8, the energy filtering method can be validated for the electron beams whose cut-off energies are higher than 50 %. We found, however, that the reconstructed image is still noisy with the 50 % cut-off energy (see Fig. 9).

Since that, we cannot evaluate the accuracy of the phase space measurement only by comparison of emittance, but also by reconstructed image itself. In the medical computed tomography field, the normalized mean square error (NMSE ξ) defined as Eq. 2 is commonly used as the criterion of the accuracy of the reconstructed image [6]. Therefore, we introduce this criterion to evaluate accuracy of this method.

$$\xi = \frac{\sum_{i=1}^{M}\sum_{j=1}^{N}(y_{ij} - s_{ij})^2}{\sum_{i=1}^{M}\sum_{j=1}^{N} s_{ij}^2} \qquad (2)$$

, where y_{ij} are signals on the reconstructed phase space, s_{ij} are signals on the initial phase space, and M, N is pixel numbers.

Calculated results of ξ of the beams with different cut-off energies are shown in Fig. 10. As is shown in Fig. 10, the ξ is constant at $E_{cut\text{-}off} / E_{peak} \geq 70$ % and about 6 %. As shown in Fig. 11, initial phase space distribution and the reconstructed phase space distribution are almost identical as the ξ indicates. The emittances are almost the same, too.

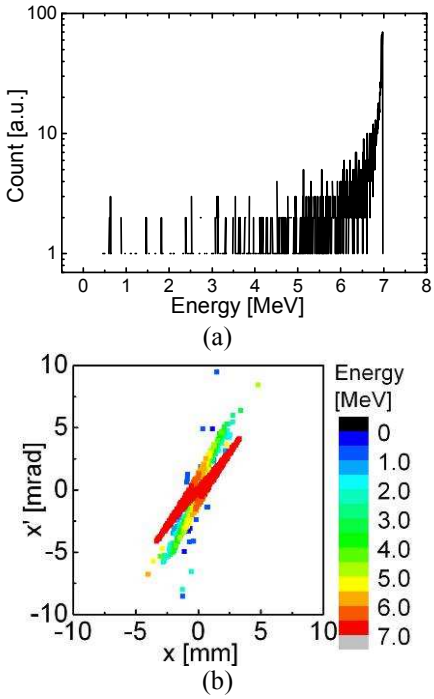

Figure 5: Low energy tailed beam from PARMELA at the entrance of the quadrupole magnet, (a) energy spectrum (FWHM = 0.5 % with tail), (b) phase space distribution (ε = 1.0π mm mrad), strongly correlated with energy distribution (the colors indicate the energy level).

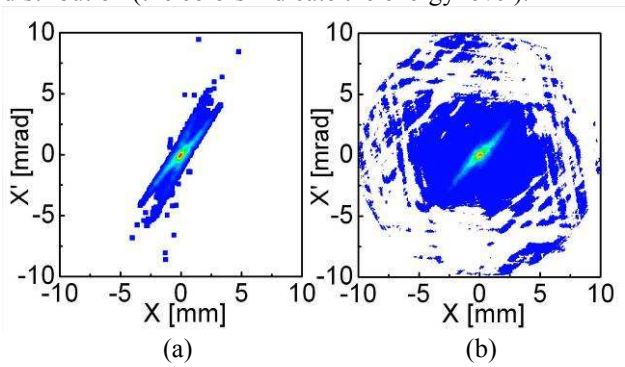

Figure 6: Phase space distributions of the realistic beam, (a) initial (ε = 1.0π mm mrad), (b) reconstructed (ε = 2.7π mm mrad)

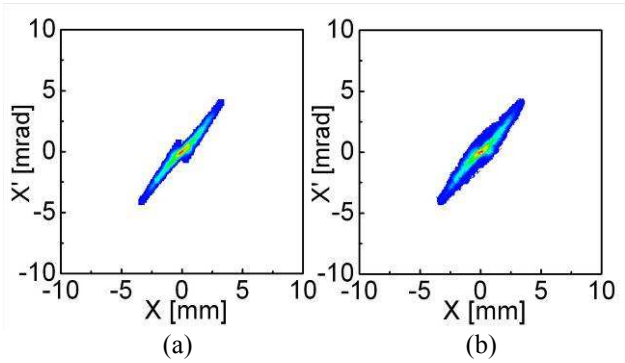

Figure 7: Phase space distributions of the realistic beam in the case of $E_{cut\text{-}off} / E_{peak}$ = 90 %, (a) initial (ε = 0.43π mm mrad), (b) reconstructed (ε = 0.52π mm mrad).

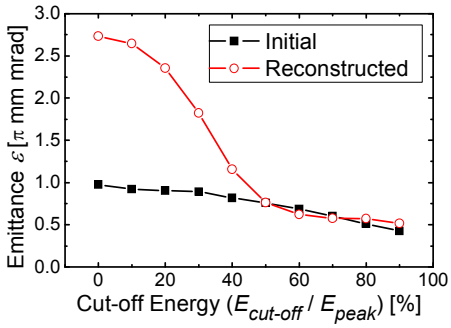

Figure 8: Calculated emittances as the function of cut-off energy ($E_{cut\text{-}off}$ / E_{peak} ≥ 50 % looks enough for emittance measurement).

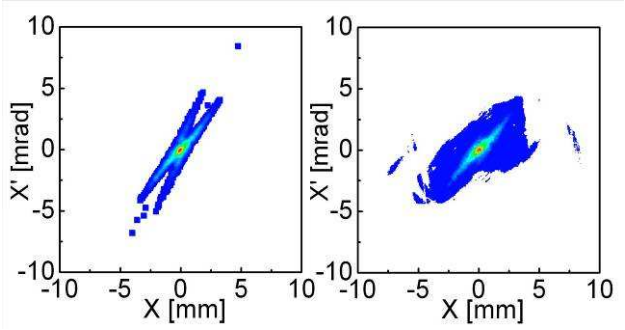

Figure 9: Phase space distributions of the realistic beam in the case of $E_{cut\text{-}off}$ / E_{peak} = 50 %, (a) initial (ε = 0.76π mm mrad), (b) reconstructed (ε = 0.76π mm mrad).

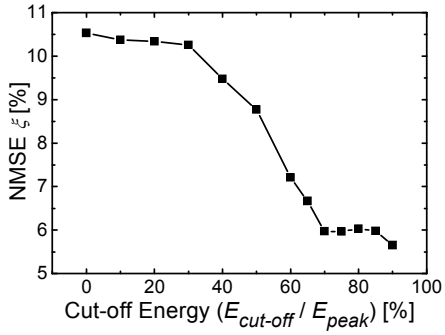

Figure 10: Normalized mean square errors of the realistic beam as the function of cut-off energy ($E_{cut\text{-}off}$ / E_{peak} ≥ 70 % looks enough).

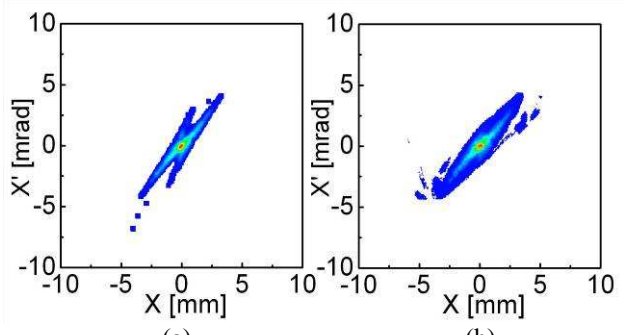

Figure 11: Phase space distributions of the realistic beam in the case of $E_{cut\text{-}off}$ / E_{peak} = 70 %, (a) initial (ε = 0.60π mm mrad), (b) reconstructed (ε = 0.58π mm mrad).

Evaluation of the effect of space charge force

We varied the peak current of the beam to evaluate the effect of space charge force. Gaussian beams with rectangle-shaped temporal distributions (Fig. 12(a)) and mono-energetic distribution were assumed. The unnormalized emittance of the initial phase space distribution is 0.6π mm mrad (Fig. 12(b)). To clarify the effect of the two energy beams, 4 and 7MeV, we used two energy beams. 4MeV is the energy of the electron beam from a 1.6 cell BNL Gun-IV type photo-cathode rf gun and 7MeV is that from our 4.5 cell thermionic rf gun.

In Fig. 13, the reconstructed images of each peak current are shown. The reconstructed distributions were slightly rotated in the phase space as the peak current getting larger due to the space charge force. As shown in Fig. 14(a), the errors of calculated emittance became larger as the peak current getting larger. The force of transverse direction space charge effect is represented by Eq. (3). So x-axis of the Fig 14(b) is normalized by $(\gamma\beta)^3$. As shown in Fig 14(b), the errors of emittance were dominated by normalized peak current, so we could determine the tolerable normalized peak current about 0.05A to obtain less than 15% error.

$$\frac{d^2r}{dz^2} = \frac{qI(r)}{2\pi r m_0 c^2 (\beta\gamma)^3}\sqrt{\frac{\mu_0}{\varepsilon_0}} \qquad (3)$$

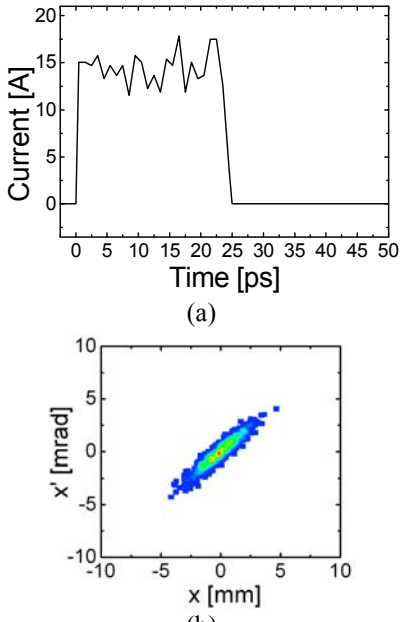

Figure 12: Gaussian beam with rectangle temporal distribution. (a) Temporal distribution, (b) phase space distribution.

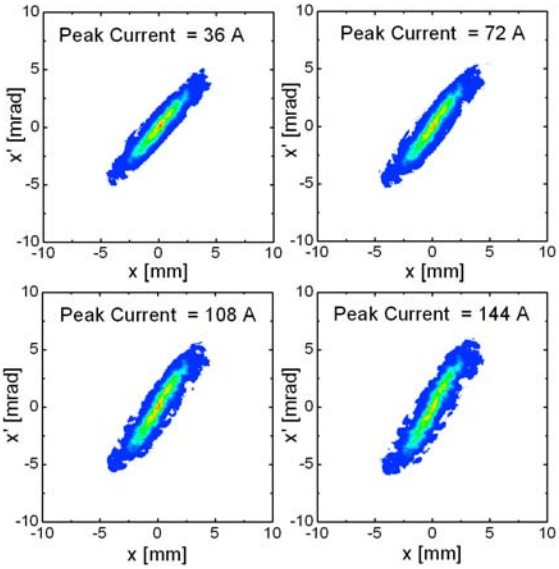

Figure 13: Reconstructed phase space distributions of Gaussian beam with rectangle-shaped temporal distribution with space charge calculation.

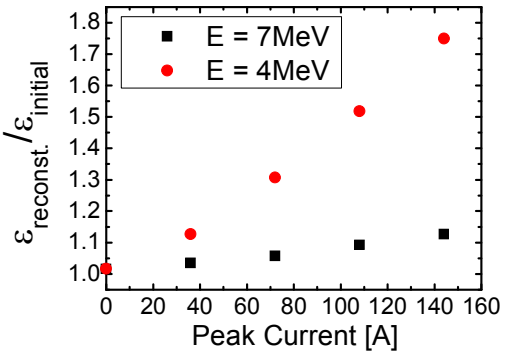

(a)

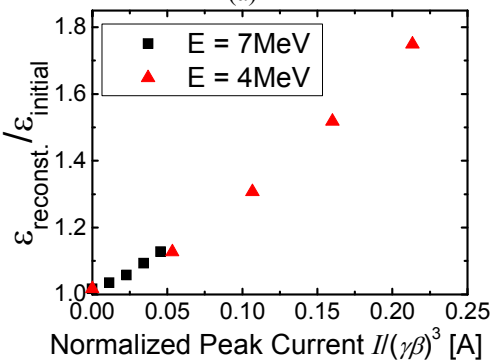

(b)

Figure 14: The ratios of the unnormalized emittances from the reconstructed phase space of Gaussian beams with rectangle-shaped temporal distributions to that from the initial one. (a) Dependence on the peak current. (b) Dependence on the normalized peak current (normalized by $(\gamma\beta)^3$).

CONCLUSION

The effect of energy distribution has been evaluated on the validity of the transverse phase space tomography by particle simulations. For a Gaussian beam with rectangle-shaped energy distribution the reconstructed image was distorted by the energy spread of the beam. However the error in the calculated emittance is less than 15 % when the energy spread is less than 15 %. For the beam which has a low energy tail the reconstructed image was severely distorted. By using 70 % energy cut-off, the reconstructed image is good enough in terms of emittance and phase space distribution. In practical use, the phase space distribution of the beam should be measured after the energy filtering section, such as a bending magnet and a slit. In terms of the space charge effect, the error in the calculated emittance is less than 15% if the normalized peak current was larger than 0.05A. To apply higher normalized peak current beam, we need some improvement of this method to reduce the effect of space charge.

REFERENCES

[1] C.B.McKee, et al, NIM A 358 (1995) 264.
[2] V.Yakimenko, et al, Pysical Review Special Topics – Accelerators and Beams, vol.6, 122801 (2003)
[3] H.Ohgaki, et al, NIM A 528 (2004) 366
[4] Lloyd M. Young, James H. Billen, LANL, LA-UR-96-1835 (2002)
[5] H.M. Hudson and R.S. Larkin, IEEE Trans. Med. Imaging, 13:601 (1994).
[6] Gengsheng L. Zeng, IEEE Transactions on Medical Imaging, vol. 19, No. 5, May 2000

ISOCHRONOUS TERAHERTZ RING PROJECT AT LNS, TOHOKU UNIVERSITY

Hiroyuki Hama#, Laboratory of Nuclear Science, Graduate School of Science, Tohoku University, 1-2-1 Mikamine, Taihaku-ku, Sendai 982-0826, Japan

Hitoshi Tanaka, Japan Synchrotron Research Institute (JASRI) /SPring-8, 1-1-1 Kouto, Mikaduki-cho, Sayo-gun, Hyogo-pref. 679-5198, Japan

Abstract

Theoretical and experimental studies concerning isochronous storage rings, so far, suggest nonlinear effect resulted from higher order dispersion declines the "complete" isochronous system, and thus an ultimate equilibrated bunch length would be limited [1]. In addition, we have recently found that path-length deviation originated from the betatron motion is a much seriouse obstacle for the isochronous system and preservation of the bunch length [2]. However, it has been found out that a careful lattice design for the path-length cancellation seems to be very promissing, at least for a wavelength region of THz. A concept to preserve bunch form-factor by using quasi-dispersion-free arcs and proper phase advances of the betatron oscillation to cancel out the path length deviation is discussed.

INTRODUCTION

An idea of isochronous storage ring for FEL to avoid bunch heating was proposed more than 20 years ago [3]. Quasi-isochronous (low momentum compaction factor) operations have been carried out to research beam dynamics in storage rings for reduction of equilibrium bunch lengths because the natural bunch length is proportional square root of momentum compaction factor (α).

Recently coherent mm range radiation has been observed on a 3rd generation light source, BESSY-II [4]. Because α on the 3rd generation rings are inevitably small and it shall be relatively easy to realize a quasi-isochronous system. On the other hand, recently a ring type SASE-FEL based on a complete isochronous transport arc has been proposed [5].

Another candidate for the next generation light source is high brilliant radiations from adiabatically damped beam via high-energy linacs connected with an extremely low emittance electron gun. For such a light source, energy recovery linacs (ERLs) are quite necessary to save consumed electricity. Isochronous system is also required by ERL to absorb the beam power correctly in the accelerating structure.

We have thought the X-rays source in not only the future light in various fields. To the contrary of approaching the X-ray targets, recent advanced linac beam is, however, able to give many scientific opportunities by means of low energy coherent photons such as terahertz (THz) radiations,

#hama@lns.tohoku.ac.jp

A concept developed by our group is combined use of the beam from an advanced linac with an isochronous ring type system to produce intense broadband coherent THz radiation from every bending magnet.

SHORT-BUNCH LIMIT ON STORAGE RINGS

The first order momentum compaction factor of the electron/positron ring accelerators is written as,

$$\alpha = \frac{1}{C}\oint_0^C \frac{\eta_x(s)}{\rho(s)}\,ds \quad \eta_x(s);\ \textit{energy dispersion function} \tag{1}$$

, where ρ is the bending radius and C is the ring circumference. In 90's, experimental attempts to reduce α in order to obtain equilibrium short bunch were studied on a couple of rings [6]. As one can notice that by introducing negative part of the term to be integrated in Eq. (1), 0 or negative α can be realized. However as the first order of α (α_0) is decreasing, the higher order terms become to dominate the pass length deviation, which is expressed by

$$\frac{\Delta C}{C} = \alpha_0 \frac{\Delta p}{p} + \alpha_1 \left(\frac{\Delta p}{p}\right)^2 + \alpha_2 \left(\frac{\Delta p}{p}\right)^3 + O(3) \quad . \tag{2}$$

The higher order momentum compaction factors are related higher order dispersion functions, respectively. Analytical estimation of the higher order dispersion was also developed. However actual complete correction of higher order effects may be impossible, so that it was concluded that the shorter bunch on the rings must be limited. In addition, the bunch lengthening occurs due to potential-well distortion. Consequently we are saying sub-picosecond bunch length containing certain electrons is probably impossible.

Furthermore an effect of coherent synchrotron radiation (CSR effect) seriously distorts the longitudinal phase space of the beam, which is recently investigated. This effect is very similar to a broadband impedance model for potential-well distortion. Here we are going to discuss phenomena of potential-well distortion shortly,

If the major broadband impedance can be expressed as

$$Z(\omega) = -i\,\omega L(\omega) + R(\omega) \quad , \tag{3}$$

where w is the frequency and L and R are inductive and resistive parts of the ring impedance, respectively. Thus the wake potential V_w is expressed as,

$$V_w(t) = -L\frac{d\,I(t)}{d\,t} + R\,I(t) \quad . \tag{4}$$

A conceptual figure of this impedance model is shown in Fig. 1.

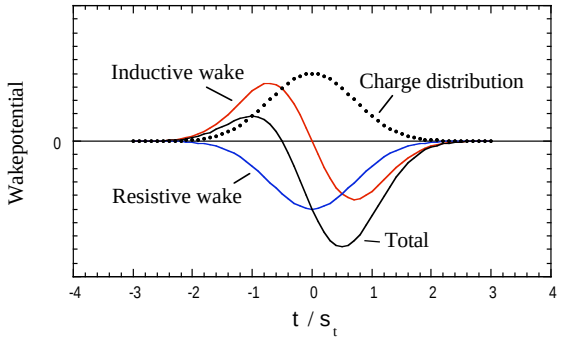

Figure 1: Dots show the shape of the bunch (here it is Gaussian. The inductive part and the resistive part of the wake potential are shown by a red line and a blue line, respectively. A total potential is indicated by a black line. However relative strengths of the impedances are depending on respective rings.

A conceptual figure of this impedance model is shown in Fig. 1.

Using the energy spread σ_{e0} and the bunch length σ_{t0}, a longitudinal Hamiltonian is written including the wake potential

$$H = -\frac{1}{2}\varepsilon^2 - \frac{1}{2}\tau^2 - \frac{e}{\alpha\,\sigma_{e0}^2\,E_0\,T_0}\int_0^t V_w(\bar{\tau})\,d\bar{\tau} \quad , \tag{5}$$

where $\varepsilon \equiv d\varepsilon/\sigma_{e0}$ and $\tau \equiv dz/\sigma_{z0}$, E_0 and T_0 are nominal energy and revolution time, respectively. By using Vlasov equation the distribution function ψ is obtained as

$$\psi(\tau) = K\exp\left(-\frac{1}{2}\tau^2 - a\,L\,N_p\,\psi(\tau) - a\,R\,N_p\int_0^\tau \psi(\bar{\tau})\,d\bar{\tau}\right) . \tag{6}$$

A parameter $a \equiv e^2/\alpha\,\sigma_{e0}^2\,E_0\,T_0$ is used. Equation (6) can be re-written as a differential equation

$$\frac{df}{d\tau} = -\frac{\tau f \pm \chi f^2}{1 \pm f} \quad , \tag{7}$$

where f is a normalized distribution function of the bunch, $f \equiv a\,L\,N_p\,\psi(t)$ and a strength ratio of the impedances

$$\chi \equiv R\,\sigma_{t0}/L \quad . \tag{8}$$

The – symbol in Eq. (7) stands for the negative α. This is one notation of famous Haissinski equation [7]. The normalized distribution function f has to satisfied a relation with the normalized beam current G as

$$G \equiv \int_{-\infty}^{+\infty} f\,d\tau = \frac{a\,Z\,N_p}{\sigma_{t0}} = \frac{\ddot{I}\,Z}{|\alpha|\,(E_0/e)\,\sigma_{e0}^2\sigma_{t0}} = \frac{\ddot{I}\,Z\,h}{2\pi f_{RF}^2\,V_{RF}\sigma_{t0}^3} \tag{9}$$

Since the total longitudinal coupling impedance is

$$Z \equiv L + \sigma_{t0}R \quad , \tag{10}$$

the normalized impedance is written as

$$\mathrm{Im}\left|Z/n\right| + \mathrm{Re}\left|Z/n\right| \equiv \frac{f_{rf}}{h}Z \quad , \tag{11}$$

the normalized current is also expressed as

$$G = \left(\mathrm{Im}\left|Z/n\right| + \mathrm{Re}\left|Z/n\right|\right)\frac{\ddot{I}\,h^2}{2\pi f_{RF}^3\,V_{RF}\sigma_{t0}^3} \quad . \tag{12}$$

The Haissinski equation can be numerically solved with under condition of satisfying the normalized current indicated by Eq. (12).

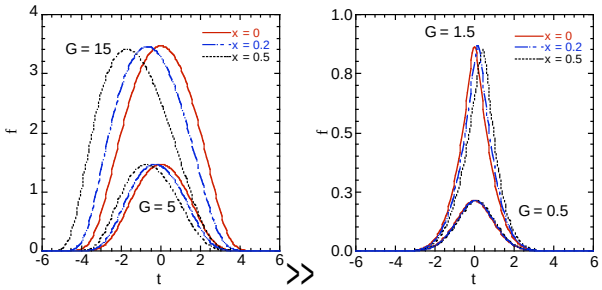

Figure 2: Examples of numerical solutions of the Haissinski equation. Left figure shows the bunch shape for various normalized current and L-R ratio χ. Right figure is same as the left one but for the negative α.

In general the bunch lengthening is dominated by the inductive impedance, meanwhile asymmetric shape results from strength of the resistive part. Particularly in the negative α mode, there is no solution of the Haissinski equation when $G > 1.55$. For the positive one, there is no bound for solution. However if we assume parabolic shape as the bunch, phase instability in an accelerating field appears at $G > \sim 17.5$. However if the bunch length is stretched by increasing the energy spread, the phase stability is recovered. This threshold current is well

agreed with Boussard criterion by taking the effect of potential-well distortion into account.

Taking look at Eq. (8), when the momentum compaction factor is reduced 1/100, the natural bunch length becomes 1/10, so that the ratio of the inductive and resistive impedances increases to 10 times more, if frequency dependence of the impedance is negligible.

Now we assume the normalized impedances are Im[Z/n] = 0.1 W and x is 0.2 for the nominal operation of 1.7 GeV BESSY-II storage ring. The normalized bunch shape at the normalized beam current of G = 10 is shown in Fig. 3, and that for the low a operation (1/100) is also shown. Note the natural bunch length of the low a mode is 10 times shorter than the nominal one, but the horizontal axis of the figure is normalized to the natural bunch length, and the vertical axis is also normalized to the G.

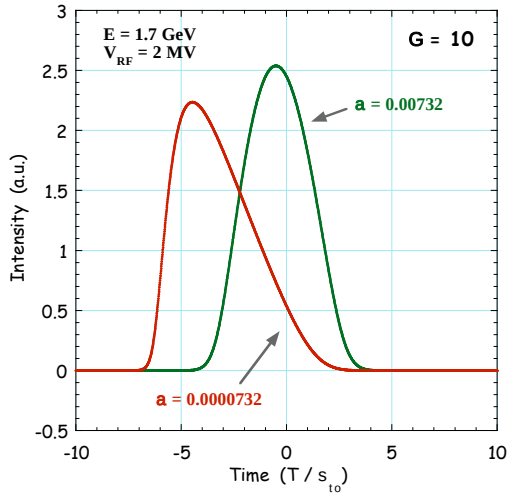

Figure 3: Calculated bunch shapes for the nominal (green) and the low a (red) mode. Parameters of the BESSY-II ring are quoted from the data book of synchrotron light source, v. 4, edited by Jim Murphy (BNL/NSLS).

In the low a mode, the bunch length is longer than 1 ps, even a is reduced to 1 % of the nominal value. If the bunch shape is nearly Gaussian, the coherent radiation of the wavelength longer than mm is only emitted. However as you can see, the bunch is strongly asymmetrically distorted, which means higher frequency component is included, so that shorter wavelength than mm range may be able to be emitted. The actual beam current in the low a mode is 1000 times lower than the nominal one as you notice from Eq. (12), so that the coherent light is not very strong.

Consequently, we concluded that the operation with low momentum compaction factor on storage rings is very difficult to be stable THz light source.

CONCEPT OF ISOCHRONOUS RING TO PRODUCE COHERENT TERAHERTZ SR

It is well known that the wavelength region of synchrotron radiation (SR) longer than the bunch length is emitted coherently [8]. A very simple expression for the intensity of coherent part of SR can be written as

$$I_{tot}(\omega) \propto I_{in\text{-}coh}(\omega)\left\{N_e + N_e^{\,2}\left|S(\omega)\right|^2\right\}, \qquad (13)$$

where N_e is the number of electrons and $S(\omega)$ is a form factor of the electron bunch. Ignoring transverse effect from the emittance, the bunch form factor is a Fourier transform of the bunch shape as

$$S(\omega) = \int \rho(z)\, e^{i\omega z/c}\, dz \qquad \left(\int \rho(z)\, dz = 1\right). \qquad (14)$$

For the Gaussian shape of the bunch, the standard deviation of the angular frequency is just the inverse of the bunch length, so that the bunch length of 100 fs corresponds ~ 1.6 THz (~188 mm). Consequently, the electron bunch length of 100 fs (standard deviation) is suitable to produce the coherent THz SR.

Recently the technical development of the linacs is very rapid, and already those advanced linacs brought new results such as proof of principle on SASE FEL [9]. A couple of bunch compress schemes have been deeply investigated. By using those bunch compressors and the photo-injector, the bunch length of around 100 fs with the bunch charge of ~ 1 nC is possible to be produced.

However such photo-injector cannot be operated with higher repetition rate. Though a very high charge bunch, the beam is operated at the single-bunch mode, in general.

On the other hand, the RF guns equipped with thermionic cathode have not been well studied so far. Although there may be a couple of reasons, the thermionic RF gun seems to have potential ability for short bunch production with multi-bunch mode, which is recently investigated by our group developing a new 3-D simulation code [10].

At the moment, we have obtained the shortest microbunch peak of 200 fs (fwhm) at the head of the continuum electrons extracted from a thermionic RF gun, which has been newly designed [11]. Details of the RF gun for short bunch production are found in the reference.

By using the very short bunch from advanced linacs, we may obtain intense THz light via synchrotron radiation, transition radiation and other radiation mechanisms. Normally these light sources are beam destructive, or the beam after photon emission does not remain the short bunch shape. This fact is quite unacceptable as an efficient light source.

As a breakthrough for the problem, we are proposing a novel idea to preserve the short bunch shape, which is a ring type THz light source with an isochronous optics.

Path length deviation due to momentum deviations of each electron in a ring can be written as Eq. (2). Although complete isochronous transport is impossible, a quasi-isochronous system that satisfy preservation of the short bunch length for coherent THz radiation seems to be realized.

Here we assume a very small average dispersion function of = 0.1 m and a very sharp relative energy spread of 5¥10^{-5} and the bunch length of 100 fs (standard deviation) for an injected beam from an advanced linac. If we use a bending radius of the ring dipoles of 3 m, the estimated path length deviation is only ~ 50 fs after passing a half of the ring, so that a convoluted bunch length is only 112 fs, which is not significant to obtain the coherent THz radiation.

The path length is estimated from an equation,

$$\Delta L = \int_0^C \frac{x}{\rho} ds + O(\Delta^2) \quad , \tag{15}$$

where C is the path length on the central orbit. The horizontal deviation from the central orbit, x, is coming from two physical aspects. One is of course the dispersion function, and another one is the betatron oscillation due to finite transverse emittance of the beam.

Assuming the horizontal emittance is 5 nm rad (the normalized emittance and the beam energy are assumed to be 2 p mm mrad and 200 MeV, respectively), the bending radius of 3 m and an averaged betatron function of 1.5 m, the path length deviation of 270 mm (~ 900 fs) is obtained for 180° bending, which is 20 times large than previous value resulted from the momentum deviation. It surely depends various parameters of the beam and the ring, at least we can conclude that cancellation of path length difference due to the betatron motion is significant for the isochronous transport system.

LATTICE EXAMPLE AND PROOF OF THE PATH LENGTH COMPENSATION

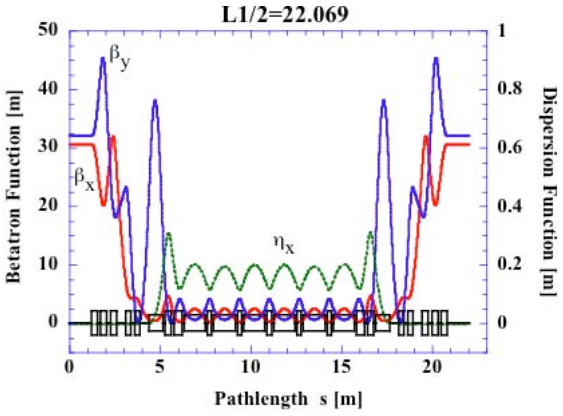

Figure 4 Example lattice of a half of the isochronous ring designed to cancel out the path length deviation due to the betatron oscillation.

Figure 4 shows an example of 180° lattice for cancellation of the path length deviation due to the betatron motion. All bending magnets include focusing quadrupole moment and may be sextupole one too. The bends at the dispersion suppressors include defocusing quad. We, of course, need certain length of the straight sections for beam injection and/or insertion devices, but we have not decided everything yet.

Because we introduce focus quad in the bend, the dispersion function is suppressed while keeping the horizontal beta function at lower. A final version will have positive and negative dispersion function alternately to reduce the momentum compaction factor.

In order confirm the path length compensation, we have numerical beam tracking by using Hamiltonian equations in Curvilinear system to reduce numerical errors.

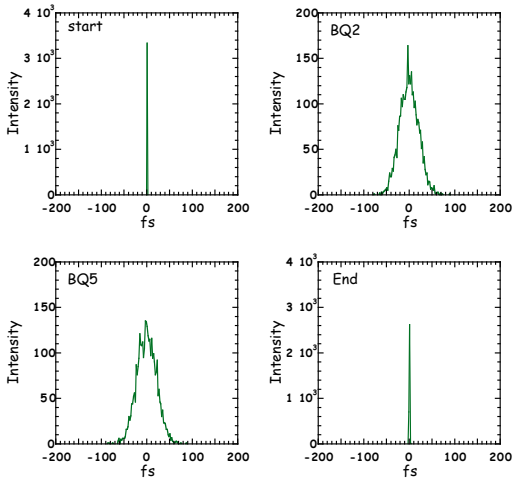

Figure 5: Tracking results for the path length deviation. Start (left-upper) and End (right-lower) mean the entrance and the exit of the 180° arc, respectively. BQ2 and BQ5 represent the middles of the 2nd bend and 5th bend in a half of the lattice, respectively.

It should be noted the d-function shape at the entrance becomes almost same as initial one at the exit. Even in the arc, the path length deviation is only ~ 20 fs (standard deviation). We can conclude that the 100 fs beam bunch can be mostly preserved, so that the coherent THz radiation may be emitted everywhere in the ring during at least one turn..

SIMULATION OF THE COHERENT SYNCHROTRON RADIATION

In general, the bunch form factor at a certain frequency is close to 1, the coherent radiation of the wavelength corresponds to the frequency can be emitted. However transverse effect is not negligible, so that actual spectrum of the coherent radiation is not easy to be predicted. In order to estimate what spectrum can be obtained from the lattice indicated in Fig. 4, a calculation for radiation was performed by using the integral of Lienard-Wiechert potential [12],

$$\frac{d^2I}{d\omega\, d\Omega} = \frac{e^2}{4\pi^2 c}\left| \int_{-\infty}^{\infty} e^{i\omega\left[t' + R(t')/c\right]} \frac{\boldsymbol{n} \times \left[(\boldsymbol{n}-\boldsymbol{\beta}) \times \dot{\boldsymbol{\beta}}\right]}{(1-\boldsymbol{\beta}\cdot\boldsymbol{n})^2}\, dt' \right|^2 . \tag{18}$$

The double differential equation, which is a power spectrum of the radiation, should be evaluated at the time of the retarded time $t + R(t')/c$, where R is the distance between the electron and the observation point at a moment of the photon emission.

Since the coherent radiation is brought by many-particle system, the incoherent part and the coherent part of SR is not normalized by an identical factor. However the interference with radiation emitted by a particle nearby can be seen if the bunch length is sufficiently short even small number of particles (in other words we do not have to employ actual huge number of electrons).

In this case the critical energy of SR is 5.9 eV (210 nm), which is clearly seen in spectra shown in Fig. 6, where R is 5 m for every bending angle. Intensity of the coherent part does not depend on the bending angle, which means the bunch is kept at an almost constant length.

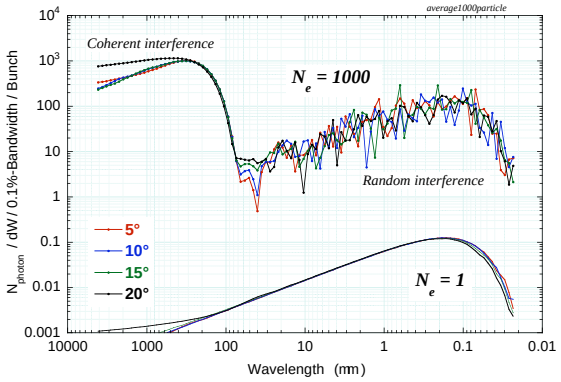

Figure 6: Calculated Spectra for different bending angles with single particle and 1000 particles. Intensity of coherent part is 10^6 times higher than that of one-particle is clearly seen.

SUMMARY AND PROSPECT

The significant path difference due to the betatron motion is discussed for the isochronous system. The isochronous ring may have higher potential for the coherent THz radiation. Further design of the ring and the RF gun are under way.

REFERENCES

[1] H. Hama, et al., Nucl. Instr. and Meth. A329 (1993) 29 – 36; H. Tanaka, et al., Nucl. Instr and Meth. A431 (1999) 396 – 408.

[2] H. Hama, " Dream of Isochronous Ring, Again", will be published in the Proc. 27th. Int. FEL Conf, Stanford, CA, (2005)..

[3] D.A.G. Deacon, Phys. Rep. 76 (1981) 349.

[4] M. Abo-Bakr, et al., Phys. Rev. Lett. 90 (2003) 94801.

[5] N.A. Vinokurov, et. al., Nucl. Insr. and Meth. A 528 (2004) 491-496.

[6] D. Robin, et al., Proc. of Micro Bunches Workshop, AIP Conference Proceedings No. 367 (AIP, New York, 1996) p150.

[7] J. Haissinski, Nouvo Cimento, 18B (1) (1973) 72.

[8] T. Nakazato et al., Phys. Rev. Lett. 63 (1989) 1245.

[9] Free Electron Laser World Wide Web Virtual library, http://sbfel3.ucsb.edu/www/vl_fel.html.

[10] H. Hama, et. al., Nucl. Instr. And Meth. A 528 (2004) 371-377.

[11] H. Hama et al., "Design study on an independently-tunable-cells thermionic rf gun", in these proceedings.

[12] J.D. Jackson, "Classical Electrodynamics", John Wiley & Sons, New York (1975) 2nd Edition.

BEAM STABILIZATION IN SPring-8 LINAC FOR TOP-UP INJECTIONS INTO STORAGE RINGS

H. Hanaki†, T. Asaka, H. Dewa, T. Kobayashi, A. Mizuno, S. Suzuki, T. Taniuchi, H. Tomizawa, K. Yanagida, JASRI/SPring-8, Sayo, Hyogo 679-5198, Japan

Abstract

The SPring-8 linac has been improved to realize stable top-up injection into the SPring-8 and the NewSUBARU storage rings. The beam energy instability of 0.02% rms in the long term was achieved by means of reducing RF variations, providing beam energy compensation, reinforcement of monitor systems and introduction of beam feedback controls: Variations in the RF power and phase have been reduced by improving the voltage regulation system for the klystron modulator, and by stabilizing the temperature drift of the atmosphere and cooling water in order to reduce the phase variation. A new synchronous oscillator synchronizes a beam trigger pulse and a 2856 MHz reference signal, reducing variation in the beam charge. A beam energy compression system (ECS) was installed to compensate for accidental energy variation and reduce the energy spread. Beam feedback controls compensate for residual long-term variations of beam trajectory and energy.

INTRODUCTION

SPring-8 and NewSUBARU storage rings have maintained the top-up operations since May 2004 and June 2003, respectively [1,2]. SPring-8 linac is now performing frequent beam injections into the two synchrotrons at short intervals to keep the stored current approximately constant. The present minimum injection interval is about 5 seconds for the parallel top-up operations and the constancy of the stored current is less than 0.1% for the SPring-8 storage ring, and less than 0.2% for the NewSUBARU.

The SPring-8 has supported the stable top-up operations with energy-stabilized beam injections; the energy instability has been improved to 0.02% rms in the long term. In this paper, we will introduce how the linac beam stability had been enhanced[3,4].

There are two general approaches to stabilization of a linac:

Stabilization of each device.
Introduction of feedback control.

The Spring-8 linac has fundamentally adopted the former approach and has introduced minimum feedback controls to reduce the long-term instability.

The following program has been our strategy for stabilizing the beam:

- Investigate the variation chains which result in beam instability
- Fix origins of the variation chains
- Synchronize the linac RF and the ring RF
- Install an energy compression system (ECS)
- Reinforce the monitor and control system
- Introduce beam feedback controls

A goal of the beam stability enhancement has been the energy variation range of ± 0.1%, which is provided by the NewSUBARU's practical beam acceptance to sustain the beam injection efficiency constant for the long term.

We have carried out this program step by step since 1998[3,4]. As a result, a minimum beam energy fluctuation of 0.02% rms in the long-term has been achieved. Present performance of the linac with an operation of the ECS is given in Table 1.

Note that we have a common parameter set for the top-up injections into the two synchrotrons as shown in Table 1. However, a slit in a beam transport line to NewSUBARU reduces the beam injection current by 1/3.

Table 1: Beam parameters for SPring-8 linac (with ECS)

	Synchrotron		Top-Up/ NewSUBARU
Pulse width	1 ns	40 ns	1 ns
Repetition	1 pps	1 pps	1 pps
Current	1.7 A	70 mA	660 mA
Energy	1 GeV	1 GeV	1 GeV
dE/E (FWHM)	0.45%	0.55%	0.32%
Instability (rms)			
Short term	0.02%	-	0.01%
Long term	0.02%	-	0.02%

Figure 1 shows a simplified diagram of the present linac's RF system. Thirteen 80 MW S-band klystrons feed pulsed RF power to the accelerating structures. The first klystron drives the next eleven klystrons via the 100 m-long waveguide drive line, as well as the injector section. A part of the RF power generated by the thirteenth klystron is also fed to the ECS. The ECS requires phase stability, and therefore the ECS's klystron is driven by a dedicated PLL-stabilized drive system.

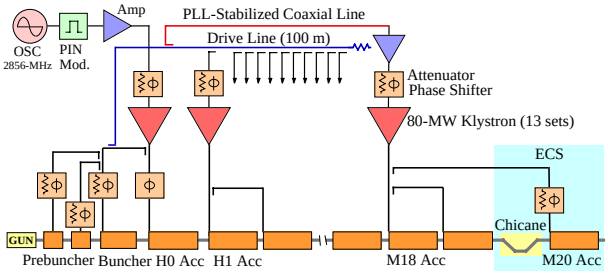

Figure 1: Diagram of improved RF system.

†hanaki@spring8.or.jp

LONG-PERIOD INSTABILITIES

Variation Chains and Their Sources [3]

The following items are the important primary sources of long-term variations in the SPring-8 linac:

1) Air temperature in a klystron gallery
2) Cooling water temperature
3) AC line for klystron modulators

Variations in these parameters cause the phase and power variations of the accelerating RF, and then result in the beam energy fluctuations as follows:

The air temperature dominates the electric length of the RF transmission line. The RF phase at the end of a transmission line consequently varies along with the temperature variation. The 100 m-long waveguide of the linac had not been temperature stabilized; the temperature coefficient of the RF phase at the end of the waveguide was approximately 2.5 deg./˚C [5].

It is well known that the temperature of a travelling wave structure has to be highly stable, to avoid causing variation of the phase shift. The RF phase of a klystron's RF output power is also sensitive to its body temperature. The temperature coefficient of the RF phase has been estimated to be 0.74 deg./˚C for an 80 MW klystron.

A cooling system for the SPring-8 linac's accelerating structures maintains its temperature at 30 ± 0.1 ˚C. The klystrons, however, had not been temperature stabilized; their temperature variation was approximately 3 ˚C [5].

The SPring-8 linac's klystron modulators adopt a conventional de-Q'ing circuit method. The circuit is designed to minimize the electric power loss, however, this power saving circuit degrades stability of a modulator's pulse forming network (PFN) voltage when the de-Q'ing rate is high. At the SPring-8 site, the AC line voltage varies by 5% throughout a day. This AC line variation directly appears in the DC high voltage of the modulator circuit. Therefore, the de-Q'ing rate had been set being around 7% to cover this variation range of 5%. This high de-Q'ing rate had thus resulted in variation of a modulator's PFN voltage. This PFN voltage variation often causes nonnegligible RF-amplitude and phase variations in a klystron's output.

Reduction of RF Phase Variation [3,4,5]

We have readjusted the air conditioners in the klystron gallery in 1998 to stabilize the room temperature. The temperature variation was consequently reduced to 1˚C[5]. In 2002, we reduced the RF repetition rate from 60 to 10 Hz for electric power saving. As a result, we re-experienced remarkable room temperature drifts in winter when the outdoor air temperature was low, because this power saving greatly reduced heat flow into the gallery air. The air conditioner system can only cool ventilated air and it also conducted the fresh outdoor air into the gallery. When the outdoor temperature was below 5˚C, 5˚C cooled water was forced into heat exchangers to prevent freezing of the cooled waters. This incorrect measure greatly decreased the ventilated air temperature. The gallery temperature fell accordingly below a set value in winter as shown in Fig. 2[4].

To reduce phase drift in the waveguide, we took the following four measures:

- The waveguide is covered with thermal insulation and warm water (27±1˚C) is circulated in pipes inside the cover.
- Outdoor air intakes are closed to prevent excessive reduction of the ventilated air temperature.
- For the freeze proofing, the air conditioner monitors the actual temperature of the air entering the heat exchanger, not the outdoor temperature.
- The pressure of nitrogen gas in the waveguide is stabilized to be less than 4 hPa by an automatic pressure controller to minimize variation of the nitrogen gas's permittivity which influences the wavelength.

The air temperature variations around the drive line have been consequently stabilized at ±1 ˚C as illustrated in Fig. 2 [4].

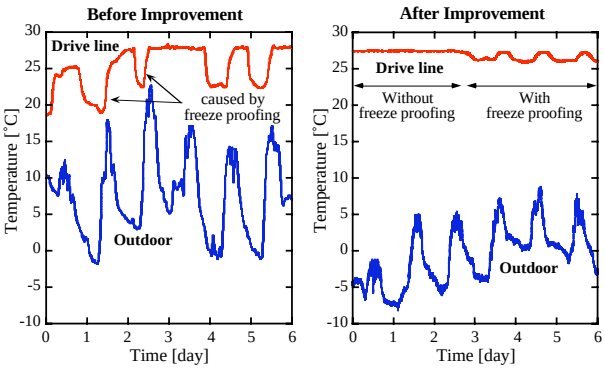

Figure 2: Variations of the air temperature around the drive line before and after improvement. In the right graph, the room temperature had been well stabilized during the former half period when the incorrect freeze proofing had been suspended. The later half period presents the temperature variations, however, the thermal insulators compressed the variation range by 1/3.

The temperature regulation of the water cooling system for the klystrons was improved by applying an inverter control method in the cooling unit. The improved regulation results in the phase variation of less than 0.5 degrees at the klystron's output [5].

Stabilization of Klystron Modulator [3]

In order to stabilize the modulator's PFN voltage, we improved the control of the induction voltage regulator (IVR), which coarsely adjusts the DC high voltage. The improved controller regulates the IVR's output voltage such that it is maintained within a 2.5% variation. This enhanced regulation consequently enabled the low de-Q'ing rate of 4%. The long-period variations of the PFN voltage have been reduced to 0.03% rms over a week-

long period, which corresponde to the RF power and phase variation of about 0.08% rms and 0.2 degrees rms, respectively.

These improvements realized the energy fluctuation of 0.03% rms for the short term; a full range of the variation, which can be assumed to be 6σ, satisfies the request mentioned in the section of introduction.

SYNCHRONIZATION OF RF AND BEAM

RF Asynchronousity Issue [6]

A trigger pulse for the electron gun is generated by counting the 508.58 MHz master signal for the ring. Therefore, a 1 ns beam ejected from the gun has not been synchronized with the linac's 2856MHz RF, which has no harmonic relation with the ring's frequency.

The asynchronous 2856 MHz RF formed two or three bunches along with the gun trigger timing. This unstable bunching caused random variation of the beam loading of accelerating RF field, and then the beam energy center was consequently varied shot by shot.

The SPring-8 linac also accelerates a 250ps beam and supplies a single-bunch beam to the synchrotrons. The RF asynchronousity mentioned above was not able to sustain the injection of the 250 ps beam at a specific phase of the RF fields in the buncher. That is, the buncher could not continuously capture the whole charge of the 250 ps beam, and thus the current of the accelerated single bunch beam consequently became unstable, as illustrated in Fig.4.

New Synchronous RF Reference [6]

A new method was developed to realize the complete synchronization of the beam trigger and the linac RF as expressed in Fig. 3[7]: A beam trigger of 1 Hz is produced by counting the 508.58 MHz reference for the ring. Sinusoidal waves of 89.25 MHz with duration of 290 μs, whose frequency is 2856 MHz divided by 32, are programmed in an arbitrary waveform generator. The 1 Hz beam trigger causes the generator to start oscillating by referring to the external 508.58-MHz clock, and thus a 89.25 MHz burst signal is created which synchronizes with the 508.58 MHz reference. This intermediate signal is filtered by a high-Q crystal filter with a bandwidth of 9.4 kHz, to reduce phase noises. Finally, the filtered signal is multiplied by 32 to generate the 2856 MHz burst signal as the reference.

RF signals generated by an oscillator system have phase noises around the center frequency. We actually observe the phase noises as the phase jitters of RF signals. The phase noises are amplified and filtered by an RF amplifier system and then fed to accelerating structures. The phase noises of the accelerating RF fields are transferred to electron beams in a buncher cavity, that is, the electron bunches have the timing (phase) jitters. Since the group velocity of RF signals transmitting to a downstream direction and the beam velocity are different, the beam bunches holding the timing jitters experience the relative phase jitter of RF fields in an accelerating structure downstream. The maximum relative phase jitters appear at a terminal accelerating structure. These phase jitters finally cause the beam energy fluctuations.

We evaluated the relative phase fluctuation at the ECS when using the new synchronous generator. Integration of the measured phase noise density S_{rf} in an appropriate frequency region[3] provided the relative phase fluctuation of 0.2 degrees rms.

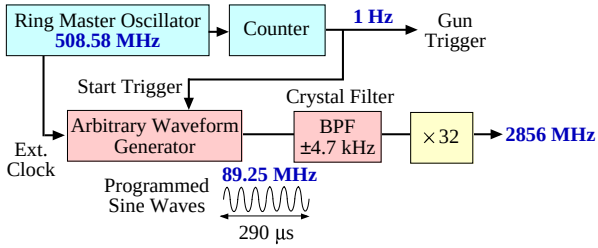

Figure 3: Block diagram of RF reference generator.

Figure 4 shows an example of beam current measurement during the single bunch acceleration mentioned above [6]. The fluctuation of current observed when using the previous asynchronous system does not appear in the new synchronous system. This measurement clearly demonstrates that the new 2856 MHz reference signal synchronizes with the beam trigger.

The RF synchronization also improves the beam energy stability since the beam loading remains almost constant: The energy fluctuation of 0.03% rms was reduced to 0.009% rms for the short term when the previous system was replaced with the new synchronous system.

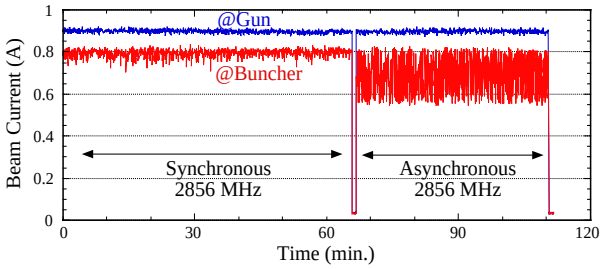

Figure 4: Current stability of single-bunched beam.

ENERGY COMPRESSION SYSTEM [8]

We introduced a conventional ECS which is mainly composed of a magnetic chicane section and an accelerating structure to provide the energy modulation of the electron bunches. The ECS compresses the energy spread from ±1.0% (full width) to ±0.4% (full width) for the 1 GeV beam with a bunch length of 20 ps, when the accelerating structure of the ECS holds the electric field strength of 6.9 MV/m.

The beam center energy varies along with the phase of the RF fed to the ECS's accelerating structure; the estimated rate is 0.35% per 1 degree. However, the minimum energy spread is estimated to continue over the range of 40˚ of the phase. Since the beam energy is

sensitive to the phase of the RF fed into the ECS's accelerating structure, this phase should be precisely synchronized with the phase of the beam bunches formed in the bunching section.

In order to reduce the phase fluctuation of the ECS's klystron, a phase-locked-loop technique was applied to an independent drive system for the klystron, as shown in Fig. 1. The PLL system was designed to maintain good stability of the RF phase in a 120 m coaxial cable that feeds the RF to an amplifier for the thirteenth klystron providing an RF power to the ECS.

We observed that the PLL achieved the phase stability of 0.2 degrees rms at the output of the klystron over a period of one week. The combination of this phase stability and the phase fluctuation of the new synchronous oscillator described in the former subsection gives the estimated total phase variation of 0.3 degrees rms, which results in the energy variation of 0.01% rms.

When the 40 ns beam at the high current of 350 mA was accelerated, we observed that the ECS compressed the full energy spread from 3.6% to 1.4% which is narrower than the synchrotron's energy acceptance, and consequently the injection current was doubled.

The ECS can also reduce the energy fluctuation according to the same principle. For example, Figure 5 presents that the ECS suppressed the energy variation of 0.06% rms down to 0.02% rms for the 1 ns beam of 1.9 A when the synchronous generator transmitted the reference RF. Thus the ECS is effective in maintaining both shot-by-shot and long-period beam energy stability.

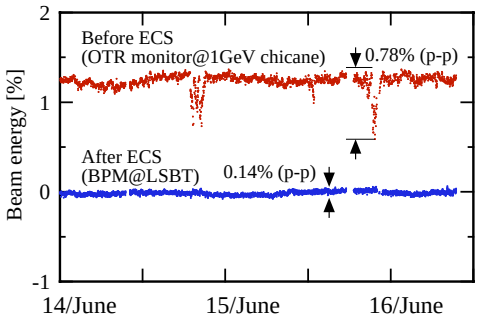

Figure 5: Beam energy variations observed during top-up injection. Accidental energy drops caused by modulator's failures were completely compensated by the ECS.

BEAM FEEDBACK CONTROL

The above improvements have enhanced beam energy stability. We, however, have observed residual long-term variations of the beam positions that degraded the injection efficiency of the NewSUBARU.

To improve the long-term stability, we introduced the following feedback controls:

- Beam position stabilization at three beam transport lines
- Beam energy stabilization by adjusting ECS

Beam position controls are carried out at the following three parts in the linac: 1) A drift space in the injector part, 2) a drift space of a transport line to the NewSUBARU storage ring and 3) a transport line between the ECS and a bending magnet downstream. These straight parts respectively contain two sets of steering magnet upstream and two sets of BPM downstream.

The control program adjusts the steering magnets and maintains beam positions within the position window at reference BPMs. The position window was determined to be ±30 μm, which is nearly double the standard deviation of the measured values. Figure 6 shows an example of the feedback control history at the third part; the beam position variations was 30 μm rms in the long term.

Beam energy is stabilized as follows: it is measured by BPMs installed at the dispersive sections of the beam transport line to the NewSUBARU or to the booster synchrotron. The program adjusts the RF phase of the ECS so that energy error remains within the energy window of ±0.03%.

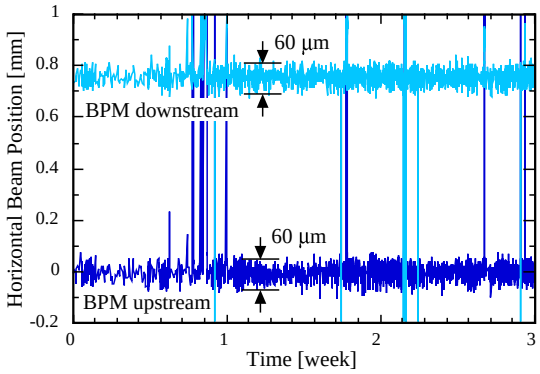

Figure 6: Beam positions stabilized by feedback controls.

REFERENCES

[1] H. Tanaka, et al., "Top-up operation at SPring-8 – towards maximizing the potential of a 3rd generation light", EPAC'04, Lucerne, Switzerland.

[2] Y. Shoji et al., "NewSUBARU Storage Ring: Operational Progress in These Three Years", APAC'04, Gyeongju, Korea.

[3] H. Hanaki et al., "Beam stabilization in the SPring-8 linac", APAC'04, Gyeongju, Korea.

[4] H. Hanaki et al., "Enhancements of Machine Reliability and Beam Quality in SPring-8 Linac for Top-Up Injection into Two Storage Rings", PAC'05, Knoxville, USA.

[5] T. Asaka et al., "Stabilization of the RF System at the SPring-8 Linac", NIM-A, 488 (2002) 26.

[6] T. Asaka et al., "Method for stabilizing beam intensity and energy in the Spring-8 linac", NIM-A, 516 (2004) 249.

[7] Y.Kawashima et al., "New synchronization method of arbitrary different radio frequencies in accelerators", Phys. Rev. ST Accel. Beams 4, 082001 (2001).

[8] T. Asaka et al., "Performance of the Energy Compression System at the SPring-8 Linac", 8th EPAC, Paris, June 2002.

ELECTRON BEAM COOLING AT A MAGNETIC STORAGE RING, TARN II, AND AN ELECTROSTATIC STORAGE RING

Tetsumi Tanabe, High Energy Accelerator Research Organization (KEK),
Accelerator Laboratory, 1-1 Oho, Tsukuba, Japan

Abstract

At the High Energy Accelerator Research Organization (KEK), a magnetic storage ring, TARN II, with an electron cooler was operated from 1989 to 1999, while an electrostatic storage ring with a small electron cooler has been operational since 2000. In this paper, the electron cooling at TARN II and the electrostatic storage ring is described.

INTRODUCTION

The aim of the magnetic storage ring TARN II was originally for studies of accelerator technology, like cooling techniques; later, the ring was used in atomic physics experiments, such as electron-ion collisions. The first electron cooling experiment at TARN II was performed in 1989 using a standard cooler in which the guiding solenoid field was uniform [1]. Then, in 1994 the electron gun region of the cooler was modified to a new one, which was an adiabatic expansion type with a higher magnetic field. Finally, the gun solenoid was further converted to a superconducting coil [2] in 1996. With this upgrade, the electron temperature was greatly decreased, resulting in faster cooling and better energy resolution. The cooling was performed for light atomic and molecular ions.

On the other hand, the electrostatic storage ring has been operational since 2000. The ring can store from light to heavy ions independently of their masses, and is also equipped with a small electron cooler of the adiabatic expansion type. However, the main purpose of the electron cooler is not ion-beam cooling, but as an electron target for studying electron-biomolecular ion collisions including protein and DNA. Although electron cooling is not the main theme, the cooling was tested for a proton beam [3] in order to check the electron beam quality and to calibrate the electron energies.

In this paper, the electron coolers and the cooling experiments at both TARN II and the electrostatic storage ring are described.

ELECTON COOLING AT TARN II

Electron cooling works in the merging region between electron and ion beams, and the mechanism underlying cooling is in the energy-loss of ion beams in a thin electron beam foil. In this way, ion beams are cooled both transversally and longitudinally. Beam phase-space compression with electron cooling in the transverse direction can be observed with a non-destructive residual-gas ionization beam-profile monitor. The beam size typically decreases from 10 mm to less than 1 mm [4]. On the other hand, longitudinal phase-space compression can be measured with Schottky signals. The momentum width decreased typically from 10^{-3} to the order of 10^{-5} [1]. Electron cooling has been widely used for beam stacking [4] as well as high-resolution experiments.

The cooling force (or drag force) is a function of the electron temperature, and increases with a decrease in the electron temperature. In the standard electron cooler, the electron beam is guided in a uniform solenoid field. In such a setup, the transverse temperature stays at the same value as the cathode temperature, while the longitudinal temperature decreases with an increase in the electron velocity due to a kinematical effect, Therefore, the velocity spread in both directions is quite unbalanced. The transverse velocity spread is much larger than the longitudinal one. This is called a flattened distribution. If we can reduce the transverse temperature, the cooling force will be greatly increased.

If we decrease the solenoid field along the electron trajectories instead of the uniform field, we can reduce the transverse electron temperature. This is called the 'adiabatic expansion method' because the electron-beam size expands along with a decrease in the solenoid field. In this method, the transverse temperature decreases according to equation (1), where R is the magnetic expansion factor, which is the ratio of the magnetic field in the gun region (B_{gun}) to the field in the cooling section (B_{cool}), given by $R = B_{gun} / B_{cool}$.

$$T_{\perp} = T_{\perp cath} / R \tag{1}$$

On the contrary, the longitudinal temperature increases with expansion due to energy conservation, as given by

$$T_{\parallel} = E\left[2+\frac{1}{E}\left\{T_{\parallel cath}+T_{\perp cath}\left(1-\frac{1}{R}\right)\right\}-2\sqrt{1+\frac{1}{E}\left\{T_{\parallel cath}+T_{\perp cath}\left(1-\frac{1}{R}\right)\right\}}\right]$$

$$\approx \left(\frac{1}{4E}\right)\left[T_{\parallel cath}+T_{\perp cath}\left(1-\frac{1}{R}\right)\right]^2 \tag{2}$$

where E is the electron energy. However, the increasing rate at high electron energies is negligibly small because of the kinematical effect. These equations are valid as long as the adiabaticity parameter given by $\xi = (\lambda_c / B)|dB/dz|$ (λ_c: spiral length) is sufficiently small. The electron temperatures calculated by Eqs. 1 and 2 are plotted as a function of the expansion factor in Fig. 1. As can be seen in the figure, the transverse temperature decreases with an increase in the expansion factor, while the longitudinal temperature increases and saturates. The longitudinal temperature is also a function of the electron energy. At high electron energies, it is negligibly small.

The electron cooling section is also an attractive research field for atomic physicists, where high-quality ion and electron beams collide. The charge-changed particles after

collisions deviate from the central orbit, and can be easily detected. The energy resolution in electron-ion collisions is improved with a decrease in the electron temperatures, as given by

$$\delta E = \frac{1}{2} kT_{\parallel} + kT_{\perp} \pm \sqrt{2E_r kT_{\parallel}}\,, \qquad (3)$$

where E_r is the relative energy between an electron and an ion.

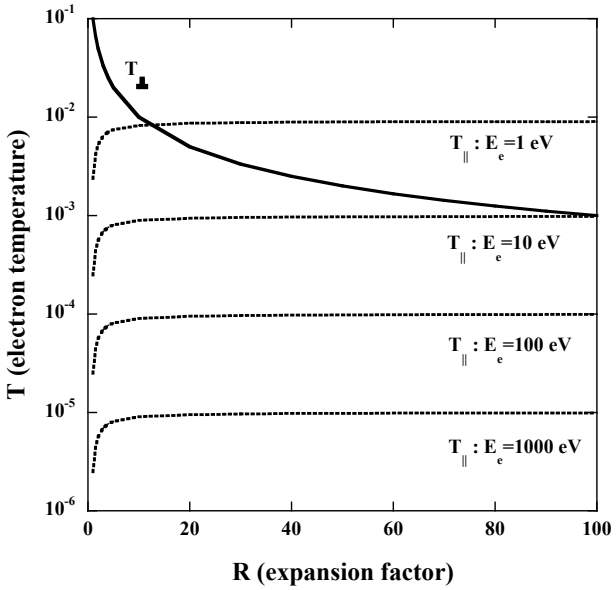

Figure 1: Transverse and longitudinal electron temperature as a function of the expansion factor.

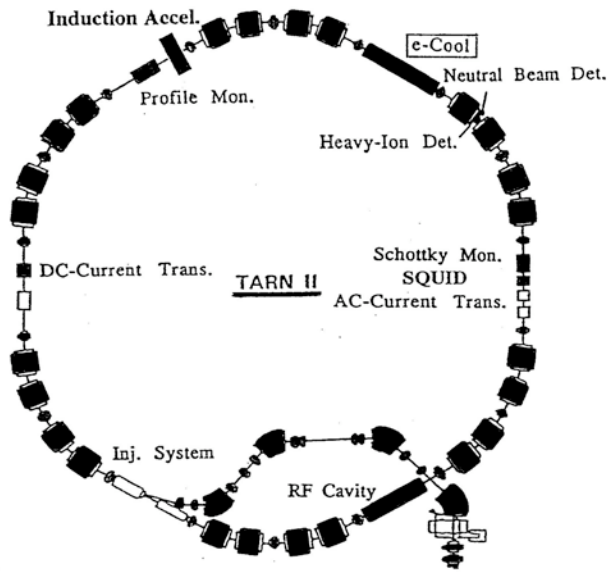

Figure 2: Layout of the magnetic storage ring TARN II.

Fig. 2 shows a layout of the storage ring TARN II [5] with a circumference of 78 m. Ions are produced with a PIG or ECR sources, and accelerated to energies on the order of 10 MeV by an SF cyclotron with a K-number of 68, and injected into the ring. The electron cooler was installed in one of the six straight sections. The solenoid field in the gun region of the cooler was changed three times. In the original cooler, the solenoid field was uniform and the maximum solenoid field was 0.6 kG. In 1994, we increased the solenoid field in the gun region to 5 kG using room-temperature coils and in 1996 further increased it to 35 kG using superconducting coils, leaving the other components unchanged. The magnetic expansion factor in these cases are 1, 10 and 100. Along with an increase in the expansion factor, the electron temperature decreases from 100 meV to the order of 1 meV.

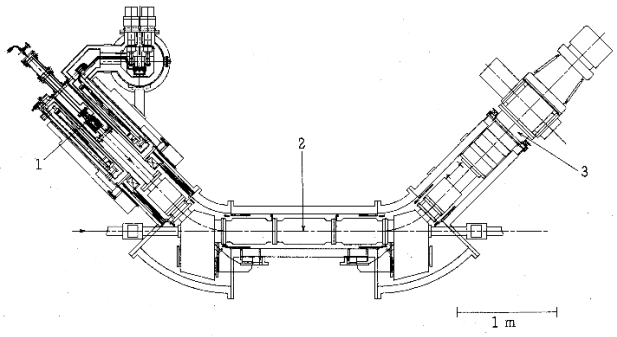

Figure 3: Liquid-helium-free superconducting electron cooler with (1) electron gun, (2) ion-electron interaction region and (3) electron collector [2].

Here, we introduce the liquid-helium free superconducting electron cooler with a cooling length of 1.5 m, as shown in Fig. 3 [2]. The gun field is 3.5 T, while the central field is 35 mT. This means that the expansion factor is 100. The ramping time up to 3.5 T is 30 min. The coil is cooled by two refrigerators consisting of 4 and 40 K stages. The cool-down time from room temperature to the final temperature is 10 days. Fig. 4 shows the electron trajectories, radial velocity and adiabaicity parameters in the gun region. Electrons are emitted from a 5 mm cathode and then expanded to 50 mm. Along with the expansion, the radial velocity spread decreases, while the adiabaticity parameter remains at less than 0.06. The maximum electron energy and current are 20 keV and 0.4 A, respectively.

An electron temperature decrease can be clearly seen by observing atomic physics phenomena. Figure 5 is the dissociative recombination spectra near to zero relative energies for HeH^+ [2]. HeH^+ captures an electron and dissociates accordingly to $HeH^+ + e \rightarrow He + H$. At a high electron temperature, as shown in Fig. 5 (a), the spectrum looks like a single peak with weak shoulder. However, with a decrease in the electron temperature, we can clearly observe the fine structure of the spectrum, as can be seen in close-up views of the central peak in Figs. 5 (b) and (c). This is clear evidence of a decrease in the transverse electron temperature.

Usually the circulating beam current is measured by a DC-current transformer (DCCT), in which the sensitivity is about 1 μA. However, the typical beam current for molecular ions is less than 1 μA. In order to measure such a low current non-destructively, we developed a unique current-measuring device using a superconducting quantum interference device (SQUID) [6]. In this device, the weak magnetic field produced by an ion beam is transferred to the SQUID by way of a superconducting shielding, in which the magnetic field is converted to a voltage proportional to the beam current. With this device, we can measure the beam current with a nano-ampere resolution non-destructively. The device was successfully used to determine absolute cross sections in atomic physics experiments.

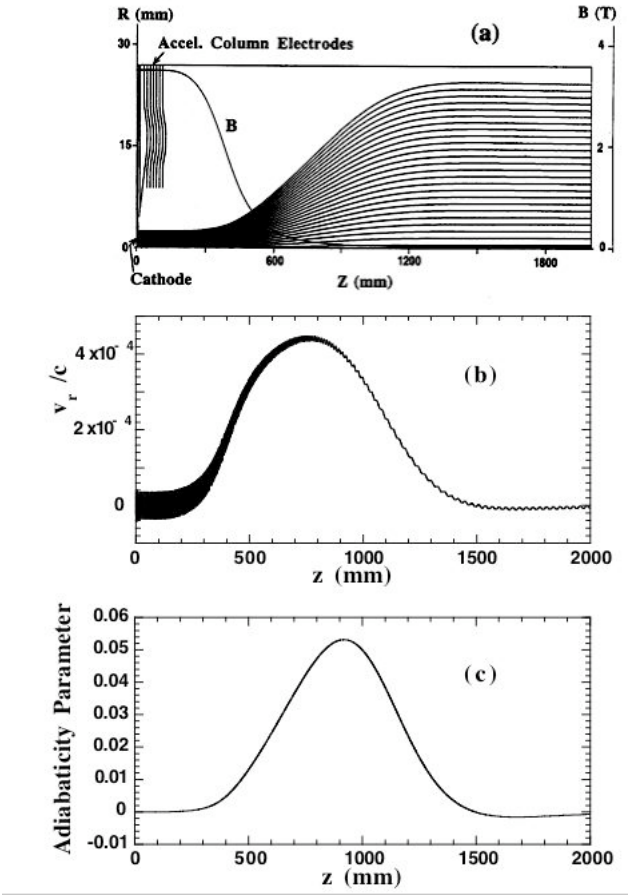

Figure 4: (a) Axial magnetic field and electron trajectories in the gun region at an energy of 2.5 keV and a current of 0.1 A, (b) radial velocity for an electron ray starting from a radius of 0.35 mm at the cathode, and (c) adiabaticity parameter for a 2.5 keV electron [2].

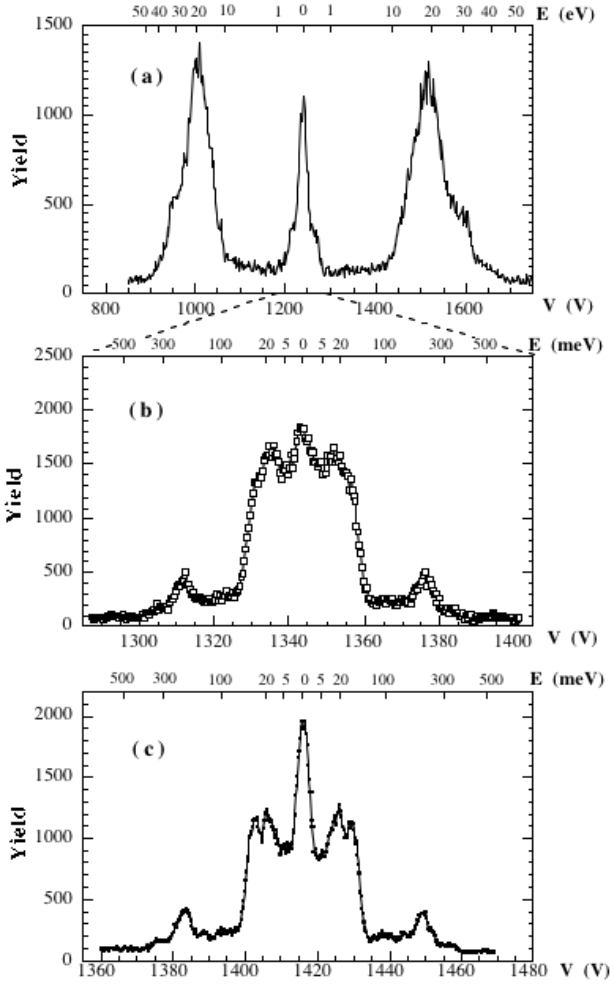

Figure 5: Comparison of the $^4HeH^+$ dissociative recombination rate as a function of the electron acceleration voltage (V) measured at different expansion factors (approximate resolutions) of (a) 1 (~0.1 eV), (b) 10 (~0.01 eV) and (c) 100 (~0.001 eV). The relative energies between electrons and ions are also shown on the upper horizontal axis [2].

ELECTRON COOLER AT THE ELECTROSTATIC STORAGE RING

Since the late 1980s, many ion storage rings with electron coolers have been constructed. Some of them have been used for atomic physics experiments, mainly for light ions. The features of this type of research can be summarized as high luminosity, high resolution, variable relative energy, low background and the quenching of vibrationally excited molecular ions. It is very interesting to expand this type of experiment to heavier macromolecules, such as biomolecules. For such a purpose, elecrostaic storage rings are more suitable than magnetic storage rings. In magnetic storage rings, the magnetic rigidity increases with an increase of the ion mass. We thus need a higher magnetic field for more massive ions. This is a disadvantage when we study

heavy mass ions in magnetic storage rings. On the other hand, the electrostatic rigidity does not depend on the ion mass. Therefore, we can store from light to heavy ions under the same operation parameters in electrostatic storage rings. Furthermore, if we use an electrostatic injector, the electrostatic rigidity is also independent of the ion charge. The first electrostatic ring was constructed in Brookhaven National Laboratory in the 1950s [7], and electron beams were accelerated from 1 MeV to 10 MeV. Then, in the late 1990s, an electrostatic storage ring for heavy ions was constructed in Aarhus, Denmark [8]. However, in the original Aarhus ring, there was a problem that the beam lifetime decreased with an increase in the ion intensity. This problem was overcome in our ring in 2000 by using cylindrical deflectors instead of spherical deflectors.

Figure 6 shows the layout of the electrostatic storage ring with a circumference of 8.1 m at KEK [9]. Light ions are produced by an ECR source. On the other hand, biomolecular ions are produced by an electrospray ion source (ESI) [10], and accelerated to 20 keV/charge. Ions are then injected into the electrostatic storage ring after being mass-analyzed. The electron cooler was installed in one of the two straight sections, as can be seen in Fig. 6. Neutral products emitted in collisions with electrons and residual gas are detected by a micro-channel plate installed in the vacuum extension.

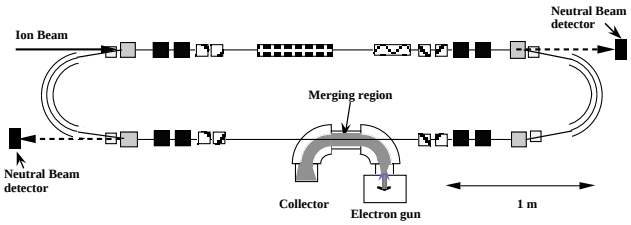

Figure 6: Layout of the electrostatic storage ring with an electron cooler. The electron cooler is rotated by 90° around the beam axis in order to help understanding.

The main purpose of the electron beam device is as an electron target for electron-ion collisions. Electron cooling for low-energy and heavy-mass ions is difficult, because electron energies with the same velocity as these ions are less than the thermal energy of the electron beam, which is about 0.1 eV, and velocity matching between electrons and ions is not practical. Furthermore, the cooling time is proportional to ion mass divided by the ion charge squared, which exceeds the beam lifetime in the ring for heavy ions. Therefore, electron cooling is limited to light ions [11].

We adopted an adiabatic expansion type for the cooler. As can be seen in Fig. 1, the longitudinal electron temperature increase due to expansion is not negligible at low electron energies. However, the total energy resolution given in Eq. 3 is still better than that for a non-expanded beam as long as the electron energy is higher than 1 eV. Other advantages of adiabatic expansion are a variable beam size in the merging region and less vacuum load due to the small cathode as well as a temperature decrease in the transverse direction.

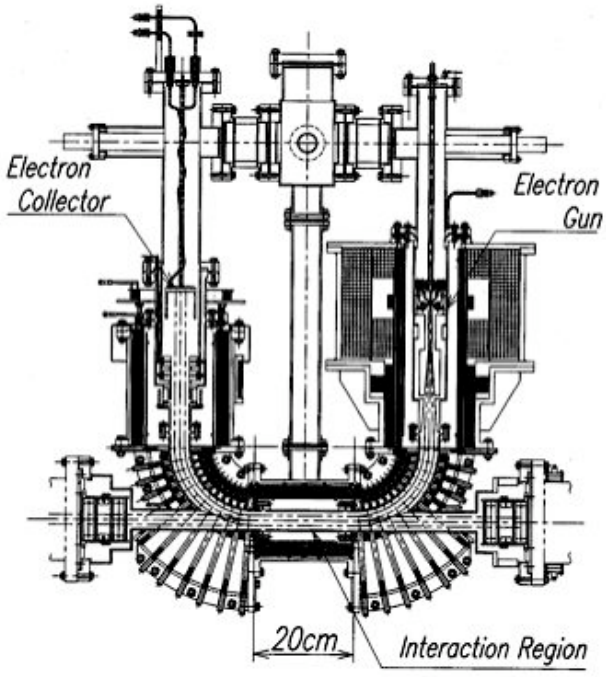

Figure 7: Layout of the electron cooler [3].

Figure 7 shows the layout of the electron cooler. Electrons are emitted from a thermo-cathode with a diameter of 3.5 mm in a solenoid field of 1 kG, and after acceleration the electron beam is expanded to a diameter of 20-35 mm in a magnetic field of 10-30 G. The electron beam is then bent by 90 degree and guided to the merging section. Ion beams pass through from right to left. The length of the merging region is only 20 cm, which is around an eighth of that of the TARN II electron cooler. The electron energy is variable from about 1 eV to 100 eV. The maximum electron current is 2 mA at the highest energy.

Figure 8 shows the result of electron-beam cooling. The proton beam with an energy of 20 keV was stored and merged with an adiabatically expanded electron beam by a factor of 33. The natural beam lifetime without an electron beam was about 2 s under a vacuum of 4×10^{-11} Torr. On the other hand, the lifetime increased by a factor of about 2 with a velocity-matched electron beam at an energy of 10.9 eV, as shown in Fig. 8. This clearly indicates that ions were cooled in the transverse direction [3].

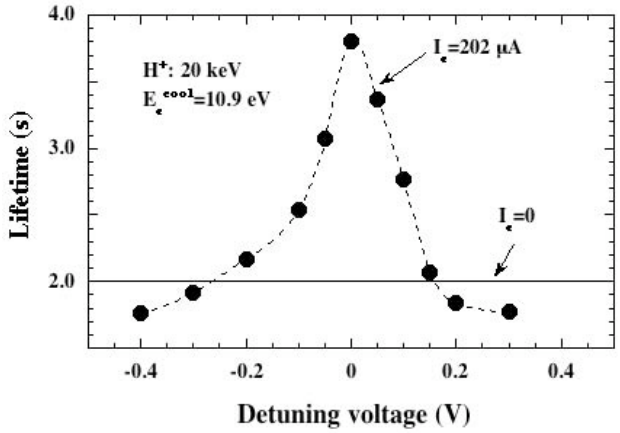

Figure 8: Lifetimes of 20-keV H^+ beam with and without electron beam as a function of detuning acceleration voltage of electrons. The tuned voltage is 14.5 V [3].

SUMMARY

In a magnetic storage ring, electron cooling is a powerful tool for compressing the beam phase spaces in both the transverse and longitudinal directions. This has realized high-quality ion beams, beam stacking and also high-precision atomic physics experiments for light ions.

In the electrostatic storage ring, an electron cooler has been used as a thick electron target for electron-biomolecular ion collision experiments. Electron cooling in the electrostatic storage ring was observed for the first time concerning a 20-keV proton beam. Thus, electron cooling for heavier ions is promising in electrostatic storage rings as well as in magnetic storage rings if we increase the ion beam energies as well as the effective length of the cooling section.

REFERENCES

[1] T. Tanabe, K. Noda, T. Honma, M. Kodaira, K. Chida. T. Watanabe, A. Noda, S. Watanabe, A. Mizobuchi, M. Yoshizawa. T. Katayama, H. Muto and A. Ando, Nucl. Instr. and Meth. A 307 (1991) 7.

[2] T. Tanabe, K. Noda, T. Yosiyuki, M. Hosino, I. Watanabe, K. Chida, T. Watanabe, T. Honma, I. Katayama, Y. Arakaki, Y. Haruyam, M. Saito, I. Nomura and K. Hosono, Nucl. Instr. and Meth. A 441 (2000) 326.

[3] T. Tanabe, K. Noda and E. Syresin: Nucl. Instr. and Meth. A 532 (2004) 105.

[4] T. Tanabe, I. Katayama, N. Inoue, K. Chida, T. Watanabe, Y. Arakaki, K. Noda, T. Honma, T. Shoji and Y. Sakawa, Proc. of the Workshop on Beam Cooling and Related Topics, Montreux, Switzerland, (1993), CERN 94-03 (1994) p. 312.

[5] T. Katayama, K. Chida, T. Hattori, T. Honma, M. Kanazawa, A. Mizobuchi, M. Nakai, A. Noda, K. Noda, M. Sekiguchi, F. Soga, T. Tanabe, N. Ueda, S. Watanabe, T. Watanabe and M. Yoshizawa, Part. Accel. 32 (1990) 105.

[6] T. Tanabe, K. Chida and K. Shinada, Nucl. Instr. and Meth. A 427 (1999) 455.

[7] G. K. Green and E. D. Courant: Handbuch der Physik, Band XLIV, Springer, Berlin, 1959, p. 218.

[8] S.P. Møller, Nucl. Instr. and Meth. A 394 (1997) 281.

[9] T. Tanabe, K. Chida, K. Noda and I.Watanabe, Nucl. Instr. and Meth. A 482 (2002) 595.

[10] T. Tanabe and K. Noda, Nucl. Instr. and Meth. A 496 (2003) 233.

[11] E. Syresin, K. Noda and T. Tanabe, Physica Scripta T 104 (2003) 185.

COMMISSIONING OF S-LSR *

T. Shirai#, S. Fujimoto, M. Ikegami, A. Noda, H. Tongu, M. Tanabe, H. Souda
ICR, Kyoto-U, Uji, Kyoto, Japan,
H. Okamoto, AdSM, Hiroshima-U, Kagamiyama, Higashi-Hiroshima, Japan
K. Noda, S. Yamada, NIRS, Anagawa, Inage, Chiba, Japan,
T. Fujimoto, H. Fujiwara, S. Iwata, S. Shibuya, A. Takubo, T. Takeuchi, S. Iwata
AEC, Anagawa, Inage, Chiba, Japan,
I. Meshkov, E. Syresin, I. Seleznev, A. Smirnov
JINR, Dubna, Moscow Region, Russia
H. Fadil, M. Grieser, MPI Kernphysik, Spaupfercheckweg, Heidelberg, Germany

.

Abstract

For the development of the new techniques of the beam cooling and for the beam physics of the cooled beam, a compact ion cooler ring, S-LSR was constructed in Kyoto University. It has an electron beam cooling device and a laser cooling system. The circumference is 22.557 m and the maximum magnetic rigidity is 1 Tm.

The beam comissioning of the ring was started from the beginning of October 2005. The 7 MeV proton beam is injected from the linac. The beam current is 8 μA and the pulse width is 50 μsec. The maximum storage beam current by the multi-turn injection is 300 μA and the lifetime is 550 sec when the average vacuum pressure was 5.7 x 10^{-8} Pa. The horizontal COD is +/-1.7 mm and the vertical one is +/-1.3 mm.

INTRODUCTION

An emittance of an ion beam in accelerators is large in general, compared with an electron beam, because the effect of the synchrotron radiation and the radiation damping are negligible. In order to obtain a small emittance and a small momentum spread of ion beams, a beam cooling is very important. The new ion cooler ring, S-LSR, is constructed at Kyoto University in order to develop the new beam cooling techniques for the medical applications and the fundamental science [1]. The beam physics of the ultra-cold ion beam, especially the realization of the crystalline beam is also an important subject of the ring [2][3].

Table 1 shows the main parameters of S-LSR. Figure 1 shows the layout. It has two cooling devices. One is an electron beam cooler. It is applied for 7 MeV proton beams, which is injected from the linac. The other is a laser cooling system using dye lasers. It is applied for the low energy heavy ions (Mg^+), which is injected directly from the ion source. Both beams are merged in the transport line and injected from the same injection line. The beam commissioning of the ring was started from the 7 MeV proton beam because the commissioning of the electron cooling was schedule after it.

The design of S-LSR is optimized for the beam cooling. The design features are following,

- Long straight sections for the electron beam cooler and laser cooling system,
- High super periodicity and the small betatron phase advance to avoid the resonance beam heating,
- Precise fabrication and the alignment of the magnets for the small stopband and closed orbit distortion,
- Electro-static deflector in the bending chamber to cancel the shearing force and control the dispersion.

The electrostatic deflector is shown in Figure 2. It is installed in the vacuum chamber for the bending magnet. The low energy heavy ion can be bended by not only the magnetic field but also the electrostatic field of the deflector. Using both fields, the dispersion function can be controlled and the cancel the shearing force to destroy the crystalline beam [4].

Table 1: Main Specifications of S-LSR

Ion species	
Proton	7 MeV
Mg^+	35 keV
Ring	
Circumference	22.557 m
Length of straight section	2.66 m
Number of periods	6
Max. magnetic rigidity	1 Tm
Bending magnet	
Maximum field	0.95 T
Curvature radius	1.05 m
Gap height	70 mm
Quadrupole magnet	
Length	0.20 m
Bore radius	70 mm

.

*Work supported by "Advanced Compact Accelerator Research Project" by Ministry of Education, Culture, Science and Technology and the 21st COE program, Centre for Diversity and Universality in Physics at Kyoto University
#shirai@kyticr.kuicr.kyoto-u.ac.jp

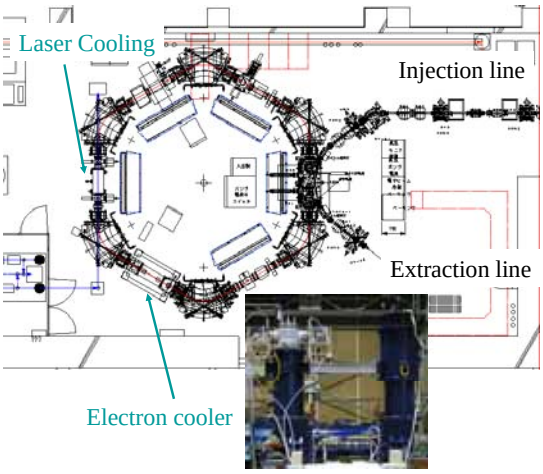

Figure 1: Layout of S-LSR.

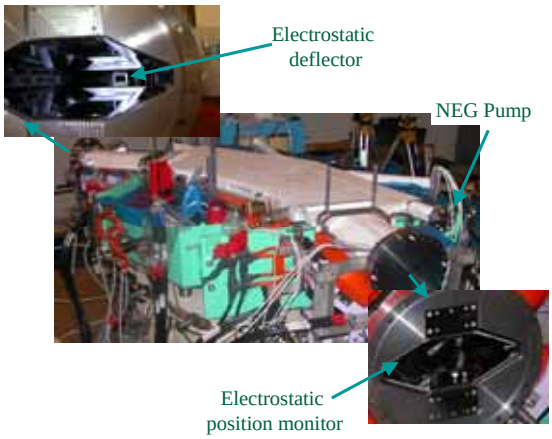

Figure 2: Vacuum chamber in the magnets. The electrostatic deflector, the electrostatic position monitors and NEG pumps are installed in the chamber.

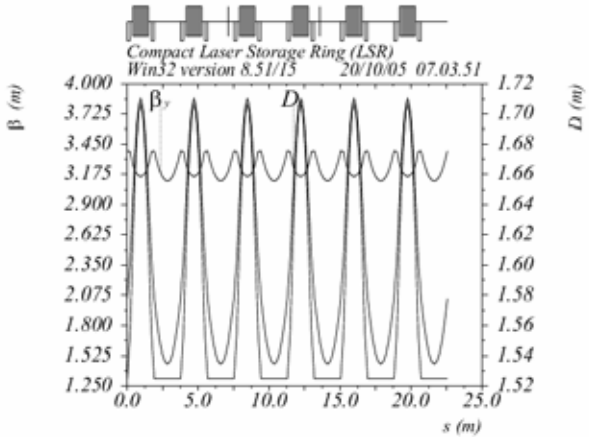

Figure 3:Lattice parameters in the ring at the commissioning. The betatron tune is (1.70, 1.11).

BEAM COMISSIONING OF THE RING

The low vacuum pressure is very important for the beam cooling because the beam lifetime must be longer than the cooling time and it is better to suppress the multiple scattering with the residual gas, which is a source of the beam heating. The vacuum chambers of the magnets are evacuated by the NEG pumps (see Fig.2). The straight sections in the ring are evacuated by 12 ion pumps and 5 Ti getter pumps. We started the beam commissioning two weeks after the vacuum chamber baking. The average vacuum pressure was 5.7 x 10^{-8} Pa at the time.

The beam injection test was started from the beginning of October, 2005. The typical beam current from the linac is 8 μA and the pulse width is 50 μsec. The beam energy is 7 MeV. The one set of the bump magnet is used for the multi-turn injection. The lattice parameters are shown in Fig.3. The horizontal and vertical tunes are 1.70 and 1.11, respectively. The first beam storage was observed at 10th, October. Figure 4 shows the Schottky signal of the stored beam. The beam current is 30 μA and the momentum spread is 0.6 %. Figure 5 shows the variation of the stored beam current measured by DC-CT after the beam injection. The injection current is 56 μA and the lifetime is 550 sec. The main source of the beam loss is multiple scattering with the residual gas. After the optimization of the injection, the maximum current reached to 300 μA.

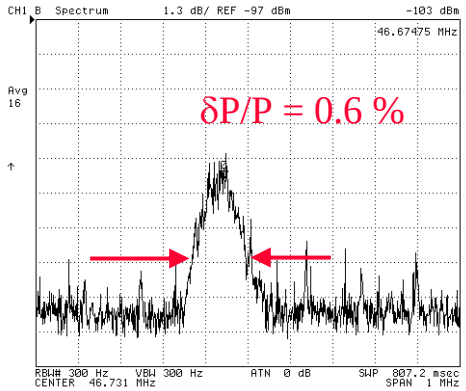

Figure 4: Schottky signal of the stored beam. The beam current is 30 μA and the momentum spread is 0.6 %

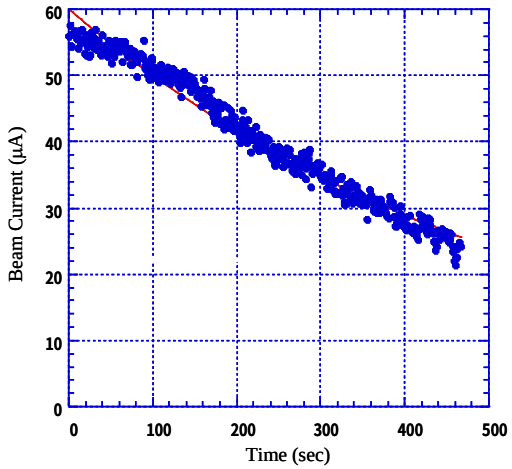

Figure 5: Variation of the stored beam current measured by DC-CT after the beam injection. The lifetime is 550 sec when the average vacuum pressure was 5.7 x 10^{-8} Pa.

The betatron tune of (1.70, 1.11) is one of the candidates for the electron cooling. The efficiency of the multi-turn injection is high and it is enough far from the strong resonances and the coupling resonance. Figure 6 shows the other operating points when the excitation current of the two families of quadrupoles are equal. The betatron tunes were measured by the transverse RF kicker. The line is calculated tune by MAD8. At some points, the measured lifetime is also shown. The lifetime is about 550 – 650 sec at the operating point far from the integer and half integer resonance lines.

The closed orbit distortion was measured by the electrostatic position monitors. The electrode of the monitor is shown in Fig.2. The 12 monitors were installed in the ring and 6 monitors were active at the commissioning. Figure 7 shows the measurement results. The horizontal COD is +/-1.7 mm and the vertical one is +/-1.3 mm. The expected COD is within +/-1 mm in the horizontal and +/-0.6 mm in the vertical direction when the electron cooler is off. The results means the unexpected COD sources exist.

SUMMARY

We succeeded to store the proton beam in S-LSR and the beam current increased up to 300 μA after the optimization of the parameters, when the injection beam current was 8 μA and the pulse width was 50 μsec. The lifetime was 550 sec when the average vacuum pressure was 5.7 x 10^{-8} Pa. The horizontal and the vertical COD are +/-1.7 mm and +/-1.3 mm, respectively. They are about 2 times larger than the expected values and the correction is necessary. We start the commissioning of the electron cooling as a next step and the injection of the low energy heavy ions and the laser cooling are preparing now.

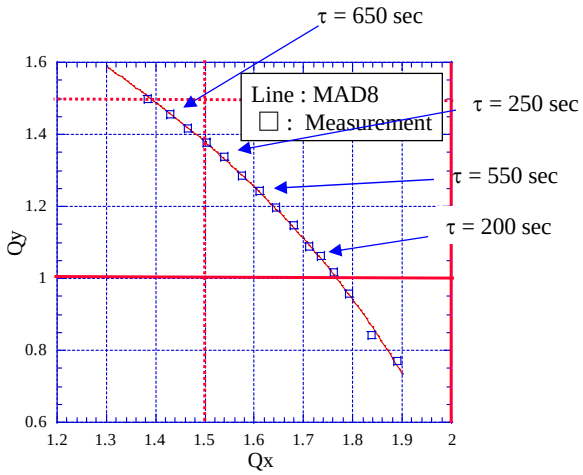

Figure 6: Operating points when the excitation current of the two families of quadrupoles are the same. The line is a calculation by MAD8.

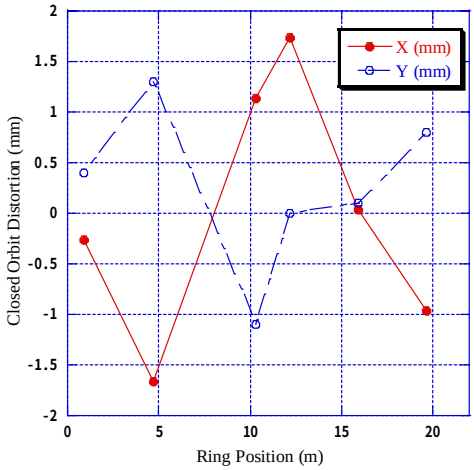

Figure 7: Measured COD in the ring when the electron cooler is off.

REFERENCES

[1] A. Noda et al., Proc. of EPAC 2002, Paris, France (2002) 2748.
[2] J.P. Schiffer and P. Kienle, Z. Phys. A321, 181 (1985).
[3] T. Kihara et al., Phys. Rev. E, 59, 3594-3604 (1999)
[4] M. Ikegami et al., Phys.Rev. ST-AB **7** (2004) 120101.

BEAM MONITORING SYSTEM AND ORBIT CORRECTION IN S-LSR*

S. Fujimoto, T. Shirai, H. Tongu, H. Souda, A. Noda,
ICR, Kyoto University, Uji, Kyoto, 611-0011, Japan
T. Takeuchi, AEC, Chiba, 263-8555, Japan
K. Noda, NIRS, Chiba, 263-8555, Japan

Abstract

Beam monitoring system of S-LSR consists of Direct Current Current Transformer (DCCT) to measure the circulating current in the ring, Schottky monitor for observation of momentum spread very low intensity coasting beam, beam profile monitor (BPM) with use of Micro channel plate and electro-static beam position monitor (ESBPM) for bunched beam. With DCCT and Schottky monitor, circulation current down to 1μA and frequency spectrum of Schottky signal for the intensity as low as $4x10^4$ protons were successfully measured. By the BPM with position resolution of 0.3 mm, the beam size of proton beam with 30 μA after electron beam cooling was measured to be 0.65 mm (one sigma). Closed orbit distortion was reduced from ±3mm to ±0.1mm by COD correction based on the COD measurement by ESBPM.

OUTLINE OF S-LSR

At ICR, Kyoto University, an ion storage and cooler ring, S-LSR has been constructed. S-LSR is a ring with the circumference of 22.56 m and radius of curvature of 1.05 m and aims at accumulation and cooling of 7 MeV proton, 24 MeV (2 MeV/u) $^{12}C^{6+}$ and 35 keV $^{24}Mg^{+}$[1]. Electron beam cooling is to be applied for proton and carbon beam while laser cooling will be applied for magnesium beam. In Fig.1, the layout of S-LSR is shown.

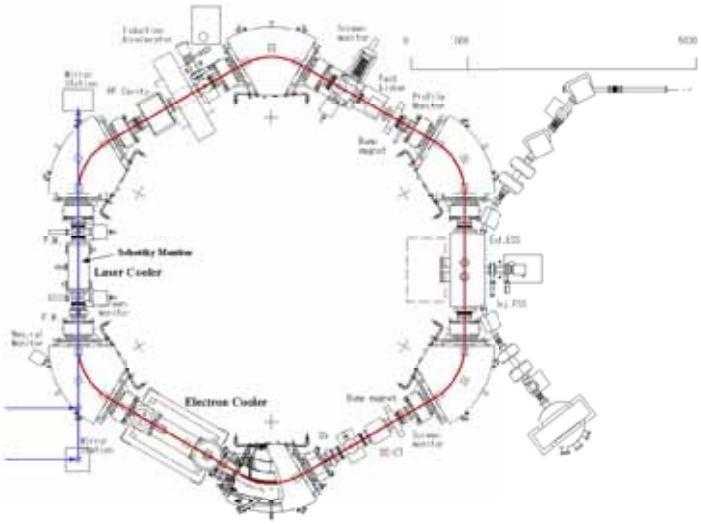

Fig.1 Layout of S-LSR

DIRECT CURRENT CURRENT TRANSFORMER (DCCT)

For the purpose of measuring the circulating current in the ring, DCCT is installed in S-LSR, which can sense the current down to 1 μA at minimum. In Fig.2, the overall

Fig.2 Photo of DCCT

view of DCCT installed into S-LSR is shown. In Fig. 3, the beam life of 7 MeV proton beam measured with the DCCT is shown, which gives the e-folding beam life ~300 seconds for the average vacuum pressure of 10^{-8} Pa.

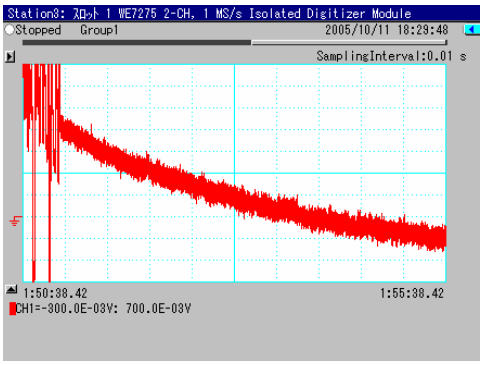

Fig.3 Decay of the 7 MeV proton beam current observed by the DCCT. The abscissa is 30 sec/div and ordinate is 10μA/div.

SCHOTTKY MONITOR

The circulating coasting beam is to be monitored by the Schottky pick up. The overall view of the outer conductor made of stainless plate which determines the earth potential of the picked up signal is shown in Fig. 4 (a), while the inner

*Work supported by Compact Accelerator Development by Ministry of Education, Culture, Sports, Science and Technology and the 21st COE program- Center for Diversity and Universality in Physics-at Kyoto University
#noda@kyticr.kuicr.kyoto-u.ac.jp

(a) Overall view of the outer conductor

(b) View of inner conductor from the beam entrance

Fig. 4 Photo of the Schottky pick up.

conductor utilizes the helically wound stainless ribbon as shown in Fig. 4 (b)[2]. The Schottky pick up is a travelling wave type signal detector with the characteristic impedance of ~100 Ω and picked up signal is fed to the low noise amplifier through

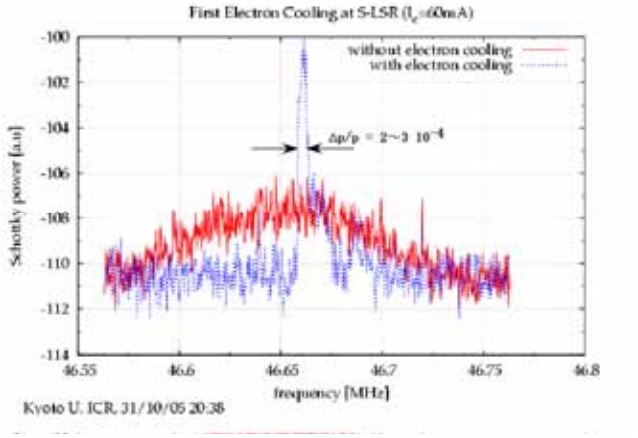

Fig.5 Frequency spectra observed by the Schottky pickup with and without application of electron cooling at S-LSR.

impedance converter. The harmonics of the revolution frequency is detected by the pick up and analyzed by a spectrum analyzer. The frequency spread gives us the information about momentum spread through the slip factor of the ring. In Fig.5, observed Schottky signals with and without the application of electron cooling are shown[3]. The fractional momentum spread of the 7 MeV proton beam is reduced to a few times 10^{-4} by the electron cooling[4].

BEAM PROFILE MONITOR

The horizontal profile of the circulating beam is monitored by the beam profile monitor as shown in Fig. 6. The geometrical apertures of the monitor are 12 cm and 5 cm in horizontal and vertical directions, respectively. In the electric field created by the electrodes shown in Fig.6 by the high voltage of 8 kV, the ionized ions by the charged particle beam in the residual gas are accelerated toward the micro channel plate with the dimension of 10 cm (horizontal direction) x 1.5 cm (beam direction) and are converted to the electric signal. The space resolution of the profile monitor is estimated to be 0.3 mm. The monitor is movable in horizontal direction as large as 27.5 cm with use of the driving mechanism by a pulase motor in order to cover full horizontal aperuture of S-LSR.

The horizontal beam profile has been monitored with this monitor through the electron beam cooling process. It is shown that the horizontal beam size has been safely reduced to 0.65 mm (1 sigma) for proton beam with intensity of 30 μA after cooling time about 10 seconds [3].

ELETRO-STATIC BEAM POSITION MONITOR (ESBPM)

For the purpose of monitoring the closed orbit and making its correction with use of adjustable fuction of each dipole excitation current, 12 electrostatic beam position monitors are istalled into the vacuum vessels set inside of all quadrupole magnets as shown in Fig. 8. The overall view of the monitor is shown in Fig. 9. The geometrical apertures of the monitor are 186 mm and 46 mm in horizontal and vertical directions, respectively, while the electrodes sizes are 200 mm (horizontal direction) and 100 mm (beam direction), respectively although they are cut to make triangles as seen in Fig. 9. Due to very limited geometrical size allowed for the beam

(a) Inner view of the aperture of the beam profile monitor

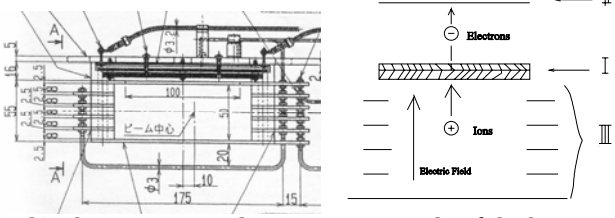

(b) The structure and operation principle of the beam profile monitor.

Fig.6 Beam profile monitor with use of MCP.

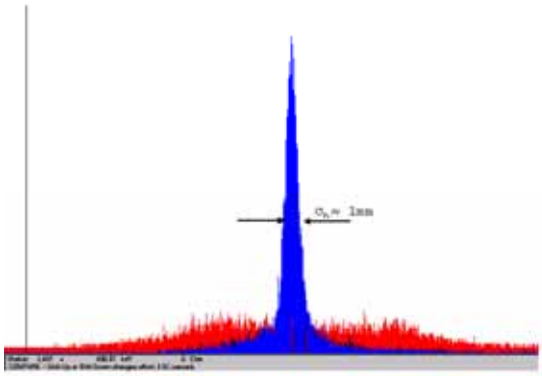

Fig. 7 Horizontal beam profile of the 7 MeV proton beam with and without electron beam cooling. Blue and red profiles indicate cases with and without electron beam cooling, respectively.

position monitor, each monitor is supported from one side utilizing the flange of the vacuum chamber as indicated in Fig. 10[5]. As the calibration of the monitor after the installation into the real space is impossible because of the severe restriction of the space, each monitor has been calibrated in a separate calibration chamber specially prepared together with peculiar preamplifiers. According

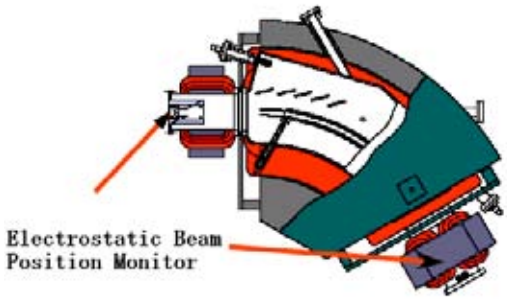

Fig. 8 Location of the electrostatic position monitors.

to the calibration results, the linearity of the position monitor is assured at least in±40 mm and ±15 mm in horizontal and vertical directions, respectively, which is found enough for the present situation although the position information can be available for much larger region to ~±100 mm.

Utilizing the picked up signals from these electro static beam position monitors, closed orbit of the S-LSR has been measured as shown in Fig. 11. For the purpose of realizing efficient cooling by electron cooling and laser cooling, it is desirable to reduce the distortion of the closed orbit (called closed orbit distortion-COD, hereafter) from the geometrical central orbit of the ring. By application of simplex algorithm, the COD can be

Fig. 9 Overall view of the beam position monitor.

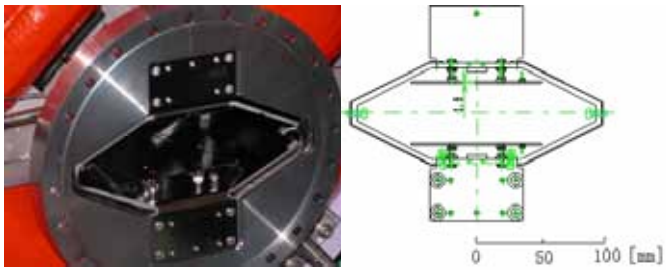

Fig. 10 Installation of the beam position monitor into the vacuum vessel.

reduced to less than ±0.1 mm after 3 times corrections [6].

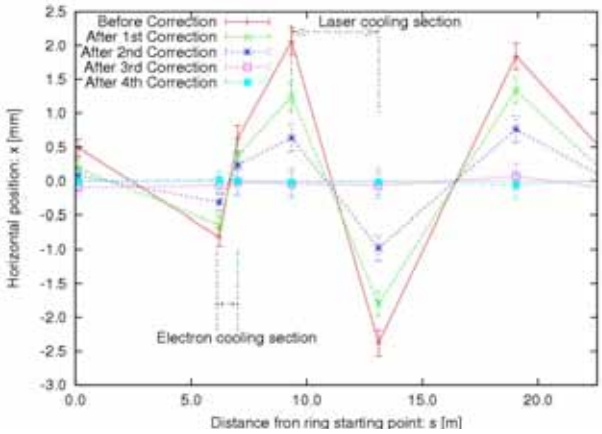

Fig. 11 COD of S-LSR before and after COD corrections.

SUMMARY

The beam monitoring system composed of DCCT, Schottky monitor, beam profile monitor and ESBPM has played an essential role to verify the good performance of S-LSR ring and electron cooling system, although further improvement in reduction of noise level is needed for demonstration of ordered state of the beam.

REFERENCES

[1] A. Noda, “Ion beam cooling at S-LSR project”, Nucl. Instr. And Meth. **A532** (2004) 150.

[2] H. Yonehara et al., ”Equipments for Momentum Cooling at TARN”, INS-NUMA49 (1983).

[3] T. Shirai et al., Proc. In this workshop

[4] H. Fadil et al., “Design of a compact electron cooler for the S-LSR”, Nucl. Instr. And Meth. **A532** (2004) 446

[5] S. Fujimoto et al., “Static beam position monitor for a small ion storage rings-LSR”, Proc. of the 2nd Annual Meeting of Particle Accelerator Society of Japan and the 30th Linear Accelerator Meeting in Japan, Tosu, Saga, Japan, (2005) 60 (in Japanese).

[6] H. Souda, „COD correction of heavy ion storage ring, S-LSR”, Maser Thesis submitted to Department of Physics, Faculty of Science, Kyoto University (in Japanese).

ELECTRON BEAM COOLING AND BEAM INSTABILITY ISSUES IN HIMAC SYNCHROTRON

T. Uesugi, K. Noda, NIRS, Japan
I. Meshkov, E. Syresin, JINR, Russia
S. Shibuya, AEC, Japan

Abstract

Experiments of electron cooling have been done with the HIMAC synchrotron in NIRS. Transverse coherent instabilities were observed when electron and ion densities were high. The instability was damped by applying rf-heating to decrease the peak ion-density. Limitation on cooled beam-sizes in longitudinal and transverse spaces were measured. The maximum volume density of bunched beams agreed with that of coasting beams.

INTRODUCTION

The heavy ion medical accelerator in Chiba (HIMAC) [1] is the accelerator complex constructed in national institute of radiological sciences (NIRS) for cancer therapy and other researches. Since 2000, electron cooling (EC) experiments have been carried out at the synchrotron in order to develop new technologies in heavy-ion therapy and related fields. One of the objectives of the HIMAC cooler is to increase the beam intensity of heavier ions, such as Fe, for risk estimations under low-dose exposure in space [2].

Such a high density beam includes strong space-charge effects. In the past experiments with the HIMAC synchrotron, the bunch length of cooled beams was meas measured for different ion-intensities and rf voltages to discuss the longitudinal cooling force, the heating force by intra-beam scattering (IBS) and space-charge effect [3]. The transverse beam-size was measured at cool equilibrium of a coasting beam in Ref. [4]. Analyzing the beam-size measurements during slow beam-loss, it was found that the beam-size was limited by the cross-section density at 0.9×10^8 ions/cm^2. Such a restriction on real-space density is related to some resonance conditions of betatron oscillation. At the intensity of less than $\sim 10^8$ ions/ring, there was a stronger limitation related to the phase-space density, which can be understood with the IBS [5].

The limitation of the transverse beam-size is generalized to a bunched beam. The longitudinal and transverse beam-sizes were simultaneously measured for weakly bunched beams, and volume density was compared with that of a coasting beam. The experimental result showed that the peak volume density was constant independent of the bunching factor.

EXPERIMENTAL APPARATUS

Experiments were done with coasting and bunched beams of Ar^{18+} ions at the injection energy of the HIMAC synchrotron. Experimental parameters ofthe HIMAC synchrotron are listed in Table 1.

The transverse ion distributions were non-destructively measured with gas-sheet beam-profile monitor (SBPM) [6]. The SBPM, at which the betatron amplitude function is (β_x, β_y)=(9 m,7 m), can measure the transverse ion-distribution with 0.8 mm resolution at full-width of half-maximum (FWHM). On the other hand, the longitudinal ion distributions are measured with sum-pickup of a beam position monitor (PON). The time resolution of the PON is estimated around 8 ns.

COASTING BEAMS

Coherent instability

Cool-stacking injections were done with coasting beam of Ar^18+ ions. A coherent instability was developed when ion and electron density were high. Figure 1 shows a typical waveforms from DC current monitor and vertical position pickup. As the Fig. 1, the instability was correlated with a vertical coherent oscillations. This instability can be explained by the coherent interaction between electron and ion beams, which lead to exponential growth of the transverse oscillations. The growth rate of the instability was high when the working point was near to a differential linear coupling line, $Q_x - Q_y = n$. One method to avoid

Table 1: Experimental conditions

Parameter	Value
Ring	
Circumference	$2\pi R$=129.6 m
Particle, energy	$^{40}Ar^{18+}$ 6 MeV/u
Betatron tune	(3.69 / 3.13) or (3.69 / 2.89)
RF frequency, harmonic no.	1042.1 kHz, h=4
RF voltage	$V_c \leq$130 V
Phase-slip factor	η=0.91
EC	
Current	0$\sim$100 mA
Cathode diameter	35 mm
Cathode temperature	100 meV
Solenoid field	0.05 T, 1.2 m
Magnetic expansion factor	3.3

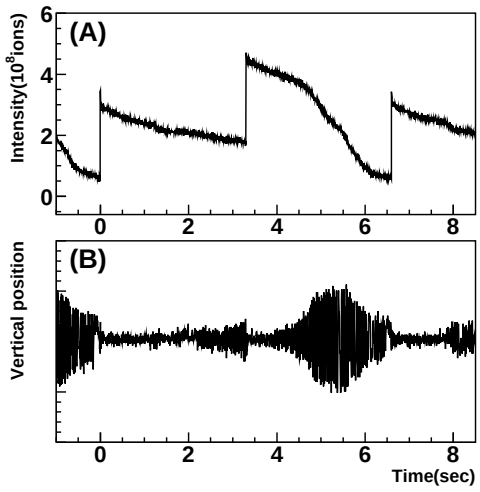

Figure 1: Transverse coherent instability.

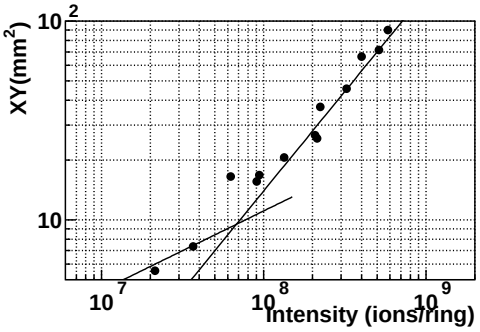

Figure 2: Products of the transverse FWHM beam-sizes of cool equilibrium (XY) at different intensity. SOlid lines corresponds to XY/N=1.1 $\times$ 10^{-7} mm^2 and $XY/N^{5/2}$=0.017 mm^2, respectively.

this instability is to replace the working point to sum resonance. The other is to reduce the peak density of ion beams by applying transverse rf-heating with very low amplitude ($\sim$1 V) around betatron frequency.

Limitation on cooling

The transverse ion-beam sizes and intensity was simultaneously measured during slow decay after high-intensity stacking. Figure 2 shows the product of horizontal and vertical FWHM beam-sizes as a function of ion intensity. It shows a linear dependence on ion intensity higher than $\sim$ 10^8 ions/ring, while it behaves as $N^{5/2}$ below that. The former corresponds to a constant real-space density, or the constant betatron tune-shift of ΔQ=0.03. The limit can be related to some betatron resonance. On the other hand, the dependence like $N^{5/2}$ corresponds to a constant phase-space density. This limit can be explained by the equilibrium between cooling force and intra-beam scattering (IBS).

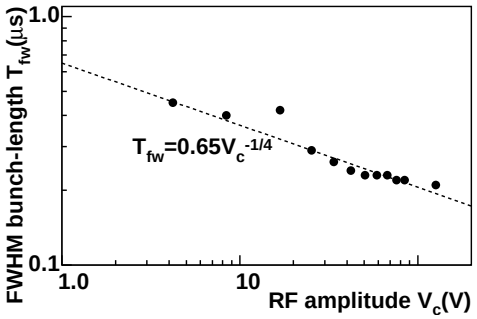

Figure 3: Bunch length at FWHM, as a function of rf voltage. Dashed line is.

BUNCHED BEAMS

Bunch length control by rf

First, we show in Fig. 3 the FWHM bunch length (T_{fw}) as a function of the rf voltage. Here, the ion-intensity was kept at 1.4×10^8 ions/ring. The bunch length was varied by twice by changing the rf voltage from 4.5 V to 130 V. The bunch length behaves as $V_c^{-1/4}$, as shown by the dashed line in Fig. 3. Since the longitudinal emittance is proportional to $\sqrt{V_c}T_{fw}^2$, if the space-charge force is neglected, the result means that the bunch length was shorten by the rf voltage as the longitudinal emittance was constant.

$$\varepsilon_{\parallel} = \frac{E_0\omega_s}{|\eta|c}\delta T^2 \qquad (1)$$

Transverse size

Now we investigate the limitation on the transverse size of a bunched beam at cool equilibrium. In the case of a coasting beam, the transverse size was limiited by the cross-section density at 0.9×10^8 ions/cm^2, which corresponds to the volume density of 2.3×10^8 ions/cm$^2\mu$s. We first calculate the peak volume density of a bunched beam at its equilibrium, taking into account the bunching factor, and compare it with that of a coasting beam.

On the assumption of Gaussian distribution in each spaces, the peak volume density (n_3) of a bunched beam is given by

$$n_3 = \left(\frac{dN}{dxdydz}\right)_{\rm peak} = \left(\frac{8\ln 2}{2\pi}\right)^{\frac{3}{2}} \frac{N/h}{X_{fw}Y_{fw}Z_{fw}}, \qquad (2)$$

where X_{fw} and Y_{fw} are the horizontal and the vertical FWHM beam-sizes, and $Z_{fw} = \beta cT_{fw}$ is the longitudinal FWHM size, respectively. In Fig. 4 the n_3 is plotted as a function of FWHM bunch length. The peak volume-density was about 1.75 μs independent of the bunch length, as shown by the solid line in Fig. 4. This value is nearly equal to the limit for a coasting beam (dashed line). Thus, the limitation on corss-section density of a coasting beam was generalized to a bunched beam in terms of the volume-density, 2.3×10^8 ions/cm$^2\mu$s.

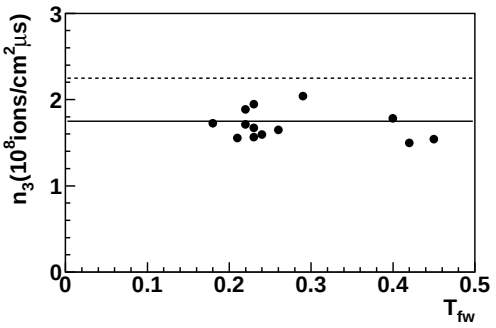

Figure 4: Volume density of a bunched beam as a function of bunch length.

CONCLUSION

The longitudinal and transverse sizes of a bunched beam at cool equilibrium was measured for different rf amplitude. The transverse size of a cool equilibrium was determined by the limitation on volume-density at 2.3×10^8 ions/cm$^2\mu$s, which agree with that of a coasting beam. Bunch length was varied by the rf amplitude, while the longitudinal emittance was kept constant.

REFERENCES

[1] Y. Hirao *et al.* , Nucl. Phys., **A** 538(1992) 541c.

[2] K. Noda *et al.* , NIM **A**441(2000), 159.

[3] K. Noda *et al.* , Nucl. Instr. and Meth in Phys. Res. **A** 532(2004) 129-136.

[4] T. Uesugi *et al.* , Nucl. Instr. and Meth in Phys. Res. **A** 545(2005) 45-56.

[5] T. Uesugi *et al.* , Proc. of PAC'05, Tenessee, (2005) *to be published*.

[6] Y. Hashimoto *et al.* , NIM **A**527 (2004), 289.

HIGH ENERGY BEAM OF LASER-ELECTRON PHOTONS AT SPRING-8 LEPS EXPERIMENT

Norihito Muramatsu, RCNP, Osaka University
For the LEPS Collaboration

Abstract

The LEPS collaboration produces a laser-electron photon beam up to 2.4 GeV by backward Compton scattering of Ar laser from 8 GeV electrons at SPring-8. The intensity is typically 10^6 /sec. The maximum energy of the photon beam has been extended up to 3.0 GeV by using deep UV laser. Possibilities of future beamlines are also described.

LASER ELECTRON PHOTON BEAM AT SPRING-8

A few GeV photon beam is a powerful tool to investigate hadron interactions at quark-nuclear scale through photoproductions of vector mesons, hyperons and exotics. For this purpose a laser-electron photon (LEP) beam is produced by injecting UV laser light into the storage ring at SPring-8. Fig.1 shows a plan view of the SPring-8/LEPS facility [1]. Ar laser light with the multi-wavelengths around 351.1 nm is focused at the 7.8 m-long straight section of the storage ring, which is located at the 35 m upstream from the laser hutch. The injected laser light is scattered by 7.960 GeV electrons toward the incoming direction (the backward Compton scattering), and its energy is magnified up to 2.4 GeV at maximum. The scattered photons make a narrow beam, and the size of the LEP beam is σ ~5 mm even at the experimental hutch, which is located at the 70 m downstream from the straight section. The energy of the LEP beam is measured by detecting the recoil electrons. The momenta of the recoil electrons are analyzed by the tagging system with 100 μ m-pitch silicon strips, which is placed just after the bending magnet of the storage ring. The energy spectrum measured with a $PbWO_4$ crystal at the experimental hutch is shown in Fig.2. The tagging system tags photons only above 1.5 GeV because of its geometrical acceptance. The LEP beam intensity is typically 10^6 /sec by colliding 6 W laser with a 100 mA electron beam. Since the laser light is linearly polarized, the LEP beam has high polarization degree. The state of the polarization vector is easily controlled by using wave plates. The polarized beam is a unique tool to measure spin observables in hadronic reactions.

The LEPS collaboration has carried out many physics programs by using the LEP beam mentioned above. The first evidence of the pentaquark baryon was obtained in the reaction of γ (n,K^-)X from the plastic scintillator [2]. Confirmations with the liquid deuteron target are now in progress. Measurements of cross sections and spin asymmetries in photoproductions of ϕ mesons [3,4] and Λ / Σ^0 hyperons [5] were also proceeded.

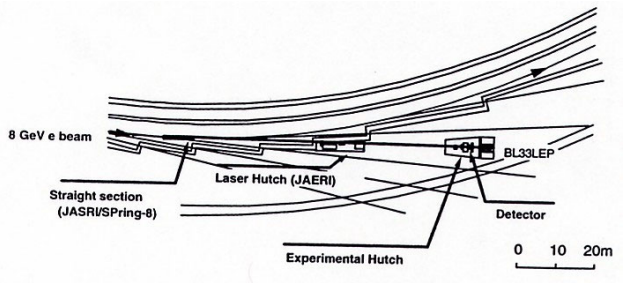

Figure1 : A plan view of the SPring-8/LEPS facility.

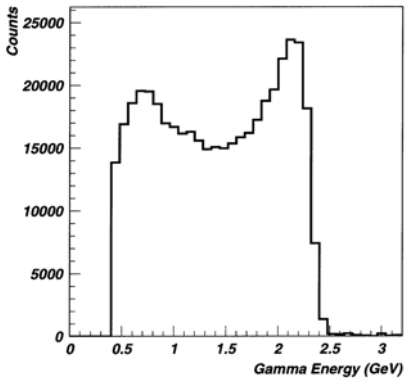

Figure2 : The energy spectrum of LEP beam measured with a $PbWO_4$ crystal at the experimental hutch.

PHOTON ENERGY UPGRADE

The maximum energy of the LEP beam, k_{max}, is calculated by the following equation:

$$k_{\max} = \frac{(E_e + P_e)k_{laser}}{E_e - P_e + 2k_{laser}} \cong \frac{4E_e^2 k_{laser}}{m_e^2 + 4E_e k_{laser}} \qquad (1)$$

where E_e, P_e, m_e are the energy, momentum and mass of electrons in the storage ring, respectively. k_{laser} represents the energy of the injected laser light. While the Ar laser (k_{laser}=3.5 eV) gives k_{max}=2.4 GeV, a deeper UV laser extends the maximum energy. Lasers with the wavelengths of 257 / 266 nm (k_{laser}=4.8 / 4.7 eV) are now available by the second harmonic generation from visible lasers with BBO crystals. The maximum energy of 3.0 GeV has been obtained by using those lasers at the LEPS facility. The typical intensity is 2×10^5 /sec because the power of the deep UV lasers are ~1 W. The higher energy LEP beam expands physics possibilities including the ω-mesic nuclei search and the $K^*(892)$ photoproductions.

FUTURE PROSPECTS

Possibilities to achieve higher intensities are now under considerations. The technique of the long range non-diffractive beam (LRNB) [6] is one of the candidates. The LRNB is generated as a result of interferences of lights from different apertures at a distorted spherical wave front, and forms a collimated beam in a long range. The length of the photon-electron scattering region can be extended so that the LEP beam intensity would be increased. This technique is being tested at the LEPS facility. Another candidate is the injection of multi-number of lasers into the storage ring. This option is also being tested.

Methods to produce photons with much higher energies are also desired. In case that 100 eV photons are injected to the storage ring, the maximum energy of the backwardly scattered photons exceeds 7 GeV. A small and high current accelerator with an undulator may be necessary to provide the 100 eV photons with high intensities. Feasibilities of higher energy options are now under considerations.

REFERENCES

[1] T. Nakano et. al., Nucl. Phys. A 684, 71 (2001).
[2] T. Nakano et. al., Phys. Rev. Lett. 91, 012002 (2003).
[3] T. Ishikawa et. al., Phys. Lett. B 608, 215 (2003).
[4] T. Mibe, W.C. Chang, T. Nakano et. al., Phys. Rev. Lett. 95, 182001 (2005).
[5] R.G.T. Zegers, M. Sumihama et. al., Phys. Rev. Lett. 91, 092001 (2003).
[6] T. Aruga, Appl. Opt. 36, 3762 (1997).

Development and application of Compton scattering hard X-ray source based on X-band electron linear accelerator

F. Sakamoto*[1], K. Dobashi[2], T. Miyoshi[2], A. Fukasawa[1], H. Ogino[1], K. Takao[1], D. Meng[1], T. Yamamoto[1], J. Urakawa[3], T. Higo[3], M. Akemoto[3], H. Hayano[3] and M. Uesaka[1]

[1]UTNS: Nuclear Professional School, the University of Tokyo
2-22, Shirakata-Shirane, Tokai, Naka, Ibaraki, 319-1188 JAPAN
[2]NIRS: National Institute of Radiological Sciences
4-9-1, Anagawa, Inageku, Chiba-shi, Chiba, 263-8555 JAPAN
[3]KEK: High Energy Accelerator Research Organization
1-1, Oho, Tsukuba-shi, Ibaraki, 305-0801 JAPAN

Abstract

Compton scattering hard X-ray source which consists of an X-band (11.424 GHz) electron linear accelerator (linac) and a YAG laser is under construction at Nuclear Professional School, the University of Tokyo (UTNS). Monochromatic hard X-rays are required for variety of medical and biological applications. Main advantage of our scheme is to produce monochromatic tunable hard (10-40 keV) X-rays with the intensities of 10^8-10^9 photons/sec. In addition, X-ray energy can be changed with rapidly by 40 msec by introducing two different wavelength lasers (YAG fundamental (1064 nm), 2nd harmonic (532 nm)) and optical switch. This quick energy change is indispensable to living specimens and very difficult by a large SR light source and others. Dual-energy X-ray CT and subtraction X-ray CT are available to determine 3D distribution of atomic number density and electron density, and specified atomic distribution, respectively. Here, the construction status of the X-band beam line and the application plan of the hard X-ray will be reported.

INTRODUCTION

Recently, hard X-rays of 10-40 keV have been used in medical science, biology and material sciences. Especially, monochromatic hard X-rays enable advanced diagnostics such as dual-energy X-ray CT [1] and subtraction X-ray CT. Intense monochromatic hard X-rays can be obtained by a third generation light source (SR) through a monochrometer. However, most SR sources are too large to be applied and used widely for public usage of the monochromatic hard X-ray. In addition, it is impossible to adapt the dual-energy X-ray CT to living specimens, because it takes a few minutes to change the energy of hard X-ray.

Compton scattering is one of the solution to obtain a monochromatic hard X-ray from a compact light source instead of the SR sources. We have developed a compact Compton scattering hard X-ray source. This system consists of a 35 MeV electron linac and YAG lasers. In order to realize more compactness, we adapt an X-band (11.424 GHz) linac and an X-band thermionic cathode RF gun to the X-ray source [2]. Main advantage of our scheme is the compactness of the whole system and to produce monochromatic tunable hard (10-40 keV) X-rays with the intensities of 10^8-10^9 photons/sec. In addition, X-ray energy can be changed with rapidly (40 msec) by introducing two different wavelength lasers (YAG fundamental (1064 nm), 2nd harmonic (532 nm)) and optical switch.

The test beam line to demonstrate production of Compton scattering hard X-ray is under construction at Nuclear Professional School, the University of Tokyo (UTNS). Conditioning of the X-band thermionic cathode RF gun is being performed.

In this paper, the construction status of the X-band beam line and the application plan of the hard X-ray will be reported.

SYSTEM OF COMPACT COMPTON SCATTERING HARD X-RAY SOURCE

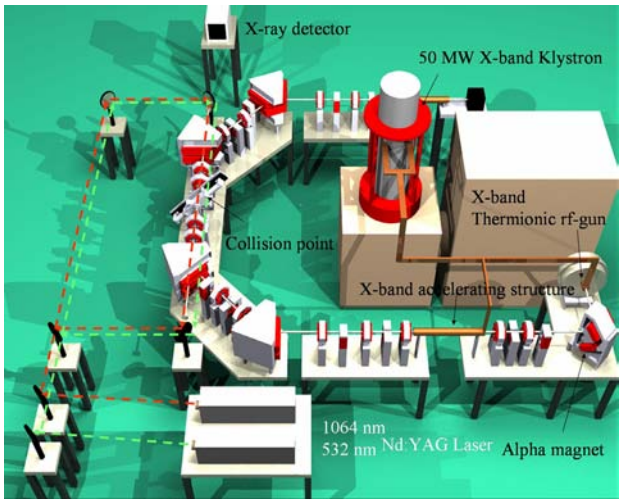

Figure 1: Schematic layout of the compact Compton scattering hard X-ray source based on X-band linac.

Compact hard X-ray source based on the X-band linac which we propose is shown in Fig.1. Multi-bunch electron beam is generated by the X-band thermionic

cathode RF gun and the beam is accelerated by the X-band accelerating structure. The beam is bent and focused at the collision point with a YAG laser. About 10 nsec hard X-ray is generated via Compton scattering on laser-electron collision.

Beam line of X-band electron linac

We applied the X-band linac to the compact hard X-ray source. The frequency of the X-band (11.424 GHz) is 4 times of the S-band (2856 MHz). However, the maximum field gradient of about 40 MV/m enables remarkable compactness. As shown in the Fig.1, the beam line of the X-band linac has the X-band 3.5 cells thermionic cathode RF-gun and an alpha magnet as an injector [3]. Figure 2 shows the cross sectional cut view of the X-band thermionic cathode RF gun. Design parameters of the RF gun are summarized in table 1. The alpha magnet acts as a magnetic bunch compressor and an energy selector with a pair of slits. The RDS (Round Detuned Structure) type X-band accelerating structure with 0.7 m long is used for this system. The technologies of the X-band accelerating structure that was developed for the future linear colliders at KEK and SLAC [4] are adapted for this system. The klystron for the RF gun and the accelerating structure is PPM (Periodic Permanent Magnet) type X-band klystron (E3168A). This is also designed for the future linear colliders [4]. Klystron modulator is designed to fit this system. RF power of 50 MW and pulse width of 1 μsec can be generated.

The beam optics of the beam line designed by SAD code is shown in Fig.3 [2]. Beam parameters at collision point (C.P.) are shown in table 2.

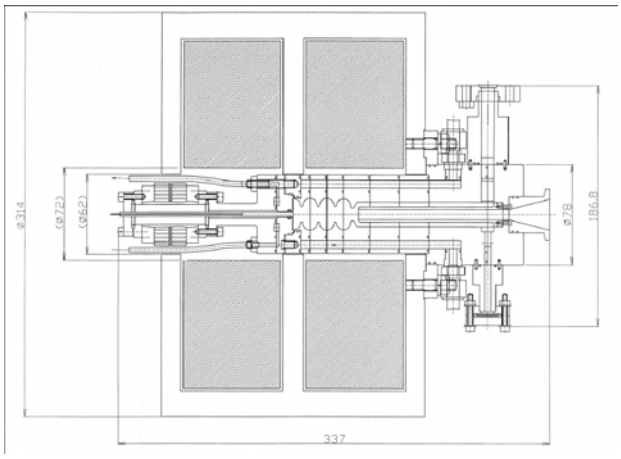

Figure 2: Cross sectional cut view of the 3.5 cells X-band thermionic cathode RF gun with a solenoid coil.

Table 1: Design parameters of the 3.5 cells X-band thermionic cathode RF gun.

Resonant frequency	11.424 GHz
Resonant mode	π mode
Number of cells	3.5 cells
Transit time factor	0.703
Q value	9350
Shunt impedance	2.46 MΩ
Filling time	80 nsec
Energy (7 MW feed)	3.5 MeV
Charge/bunch	86 pC/bunch (before AM) 20 pC/bunch (after AM)
Emittance (x, y)	15, 6.3 πmm-mrad (before AM) 10, 4.1 πmm-mrad (after AM)
Energy spread	2.3 % (before AM) 0.5 % (after AM)

AM : Alpha Magnet

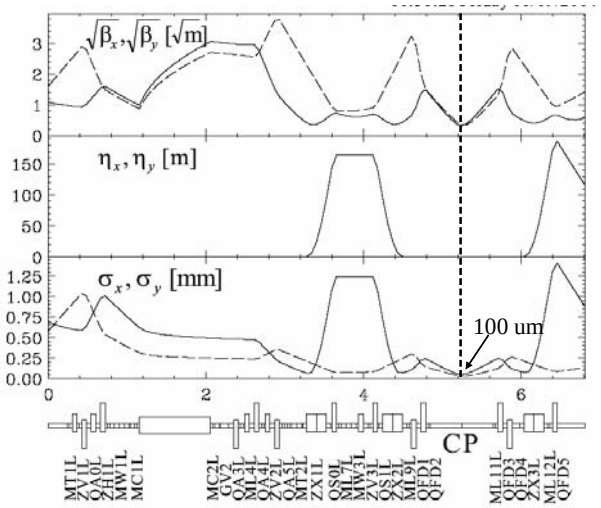

Figure 3: Beam optics of X-band linac designed by SAD code [2].

Table 2: Beam parameters at the collision point.

Beam energy	35 MeV
Charge/bunch	20 pC
Bunches/RF pulse	10^4
Beam size (rms), (x,y)	100, 100 μm

Laser system

To concentrate on the R&D of the linac, we chose a commercial and reliable laser for laser-electron collision. In order to realize the compactness of whole system, we adapt two Q-switch Nd:YAG lasers (fundamental (1064 nm) and 2nd harmonic (532 nm)). The energy of the lasers are 2.5 J/pulse for the fundamental and 1.4 J/pulse for the second harmonic, respectively. The repetition rate of each lasers are 10 pps and the pulse duration are 10 nsec (FWHM), respectively.

For the second step, in order to realize the fast switch of the X-ray energy, we add a dual-energy laser system. The concept of this laser system is illustrated in Figure 3. Each laser systems for fundamental and second harmonic are shot by turn. Then we can generate dual-energy monochromatic hard X-ray. In the case for the repetition rate of the linac is 25.0 Hz, the switching time of the X-ray energy becomes 40 msec. Advantage of this dual-energy system is that the dual-energy X-ray CT or subtract X-ray CT can be adapted to the living specimens.

In order to increase the intensity of the X-ray, we are

planning to adapt a circulation system of laser pulse. This system enhances the luminosity up to 10 times. Recently, we have demonstrated the proof-of-principle experiment using low energy YAG laser [5].

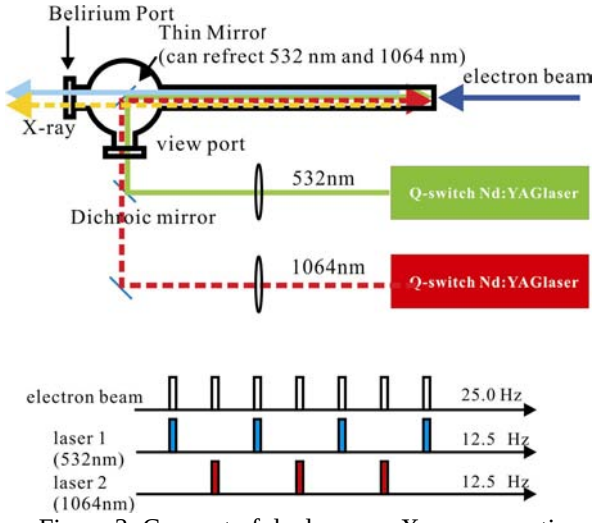

Figure 3: Concept of dual-energy X-ray generation system.

X-ray yield and properties

X-ray yield per bunch is estimated using a product of the cross section of Compton scattering and Luminosity. Figure 4 shows the intensity and scattering angle of Compton scattering as a function of the X-ray energy. In this figure, red line shows the case of the collision between fundamental (1064 nm) and 35 MeV electron beam, green one shows second harmonic (532 nm) with 35 MeV electron beam, respectively. Properties of the X-ray are summarized in table 3.

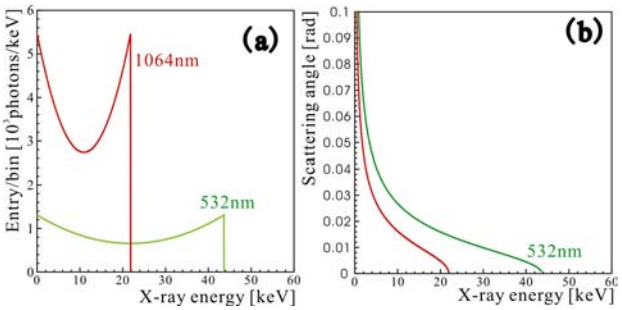

Figure 4: Energy spectrum (a) and scattering angle (b) of Compton scattering for laser wavelength of 1064 nm and 532 nm with electron energy of 35 MeV.

Table 3: Properties of generated X-ray with electron beam that energy of 35 MeV, charge of 20 pC per bunch.

Laser wavelength [nm]	1064	532
Pulse energy of laser [J/pulse]	2.5	1.4
X-ray intensity [photons/pulse]	$9.9*10^6$	$4.4*10^6$
Maximum X-ray energy [keV]	21.9	43.8

CONSTRUCTION STATUS OF X-BAND LINAC BEAM LINE

The RF generation and RF aging of the X-band klystron had been carried out until this March. The RF peak power reaches 20 MW and pulse width is 600 nsec under the repetition rate of 5 pps. The RF power of 7 MW and the pulse width of 400 nsec is required for the test of the X-band thermionic cathode RF gun [3]. The beam line for the test of the RF gun was installed in this April. Figure 5 is a picture of the test beam line. The test beam line consists of the X-band thermionic cathode RF gun, an alpha magnet, a quadrupole doublet, a steering magnet and 90 degree bending magnet. The beam current is measured by a pair of a current transformer which located just before and after the alpha magnet. This beam line has a diagnostics section which includes a screen monitor (luminescence screen) and a wire scanner monitor [6]. The beam profile and the emittance can be measured precisely by this diagnostics section. The energy of the electron beam will be measured by the 90 degree bending magnet and screen monitor.

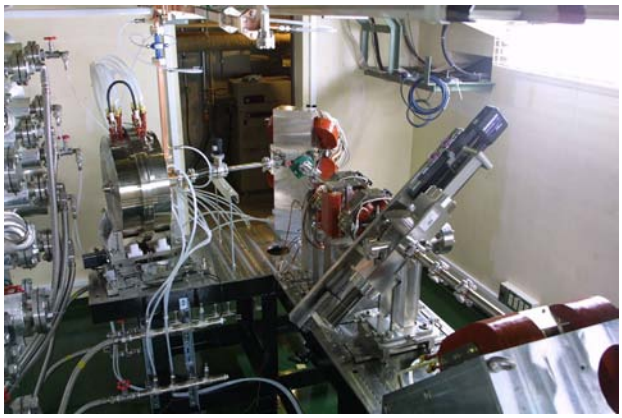

Figure 5: Test beam line for the X-band thermionic cathode RF gun.

Before the RF gun test, the RF conditioning of the gun cavity and RF windows at the waveguide must be required. We have been performing the RF aging of the RF gun cavity since this May. The RF power of 7 MW and pulse width of 200 nsec has proceeded to the gun cavity. Figure 6 shows the typical pulse shape of the RF. Last month, the breakdown occurred frequently at the RF window which locates just before the gun cavity. This breakdown is considered due to the multipactoring electrons. In order to avoid the breakdown, we changed the RF window to high power transmission one (>20 MW). Figure 7 shows the history of the RF aging of the cavity after changing the RF window. In this figure, the horizontal axis indicates the number of klystron shots, vertical axis of the left hand side (red line) shows the RF peak power in the unit of MW and the right hand side (blue line) is the RF pulse width in the unit of nsec.

After the test of the RF gun, klystron aging will be continued to reach the RF power up to 50 MW and pulse

width 1 μsec. In this December, the accelerating structure will be installed and the acceleration test will be carried out.

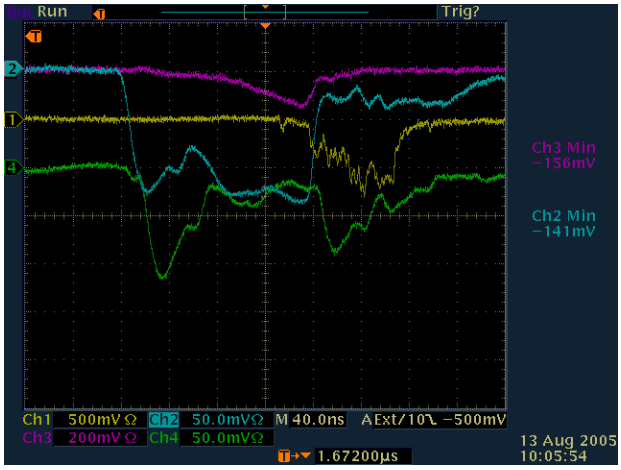

Figure 6: RF pulse shape of into (blue) the cavity and reflected (green) from the gun cavity. Pink one shows a signal of current transformer located just before the alpha magnet.

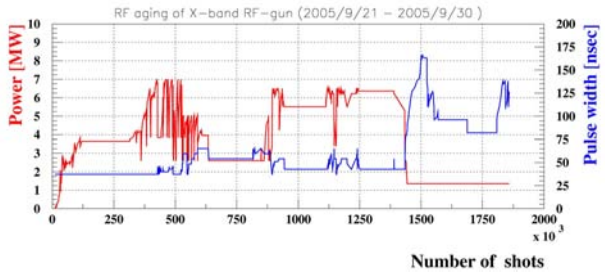

Figure 7: History of the RF gun aging.

APPLICATION

We are planning to carry out a deal-energy X-ray CT and subtraction X-ray CT using monochromatic hard X-ray, which enable us to obtain cross sectional image of a material based on effective atomic number Z_{eff} and electron density ρ_e. Figure 8 shows the principle of the dual-energy X-ray CT [1]. Experiments of the dual-energy X-ray CT has been performed utilizing SR light sources to measure electron density in biological materials. The electron density of a biological material was measured in agreement within 1 % of the theoretical one [1]. We will use the dual-energy X-ray CT for atomic number analysis in a material. For instance, the information on atomic number distribution in a tumor will contribute to treatment planning for advanced radiotherapy in medicine. Atomic number images in a plant are needed in plant physiology. In a nondestructive diagnostics of radioactive waste, we need to identify elements of a material. To apply the dual-energy X-ray CT for wide-range atomic numbers, we have carried out a numerical simulation and examined the applicability of the method by considering the X-ray profile of our scheme [7].

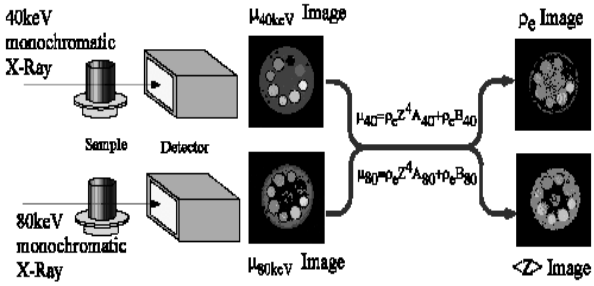

Figure 8: Principle of the dual-energy X-ray CT [1].

SUMMARY

In summary, we are developing a compact hard X-ray source by laser-electron collision (Compton scattering) based on the X-band linac at UTNS.

The RF aging of the X-band thermionic cathode RF gun has been carried out. The RF power of 7 MW and pulse width of 200 nsec has proceeded to the gun cavity. After the test of beam generation of the RF gun, the X-band accelerating structure will be installed to the beam line.

For the application of the hard X-rays, we are planning to carry out a deal-energy X-ray CT and subtraction X-ray CT using monochromatic hard X-ray. To apply the dual-energy X-ray CT for wide-range atomic numbers, we have carried out a numerical simulation.

ACKNOWLEDGMENT

The work on development of the monochromatic hard X-ray source is performed in the national project of Development of Advanced Compact Accelerators in Japan and partially supported from Research Program on Development Innovative Technology in Japan Science and Technology Agency. The study on applications of the monochromatic hard X-ray source is supported by the Japanese Ministry of Education, Culture, Sports, Sciences and Technology and the Japanese Ministry of Health, Labor and Welfare.

REFERENCES

[1]M. Torikoshi, et al., Phy. Med. Biol. 48,673(2003)
[2]K. Dobashi, et al., Jpn. J. Appl. Phys. 44(2005)4A pp.1995.
[3]A. Fukasawa, et al., Proc. of the Particle Accelerator Conference 2005 (WPAP019, 2005, May 16-22, USA)
[4]GLC report, KEK report 2003-7 (2003)
[5]F. Ebina, et al., Proc. of the CAARI 2005: 18th International conference on the application of Accelerators in Research and Industry (2004, Oct. /10-15, USA)
[6]F. Sakamoto, et al., Jpn. J. Appl. Phys. 44(2005)3 pp.1485.
[7]M. Uesaka, et al., Proc. of the Particle Accelerator Conference 2005 (RPAP012, 2005, May 16-22, USA)

BEAM MONITORING SYSTEM AND ORBIT CORRECTION IN S-LSR*

S. Fujimoto, T. Shirai, H. Tongu, H. Souda, A. Noda,
ICR, Kyoto University, Uji, Kyoto, 611-0011, Japan
T. Takeuchi, AEC, Chiba, 263-8555, Japan
K. Noda, NIRS, Chiba, 263-8555, Japan

Abstract

Beam monitoring system of S-LSR consists of Direct Current Current Transformer (DCCT) to measure the circulating current in the ring, Schottky monitor for observation of momentum spread very low intensity coasting beam, beam profile monitor (BPM) with use of Micro channel plate and electro-static beam position monitor (ESBPM) for bunched beam. With DCCT and Schottky monitor, circulation current down to 1μA and frequency spectrum of Schottky signal for the intensity as low as $4x10^4$ protons were successfully measured. By the BPM with position resolution of 0.3 mm, the beam size of proton beam with 30 μA after electron beam cooling was measured to be 0.65 mm (one sigma). Closed orbit distortion was reduced from ±3mm to ±0.1mm by COD correction based on the COD measurement by ESBPM.

OUTLINE OF S-LSR

At ICR, Kyoto University, an ion storage and cooler ring, S-LSR has been constructed. S-LSR is a ring with the circumference of 22.56 m and radius of curvature of 1.05 m and aims at accumulation and cooling of 7 MeV proton, 24 MeV (2 MeV/u) $^{12}C^{6+}$ and 35 keV $^{24}Mg^{+}$[1]. Electron beam cooling is to be applied for proton and carbon beam while laser cooling will be applied for magnesium beam. In Fig.1, the layout of S-LSR is shown.

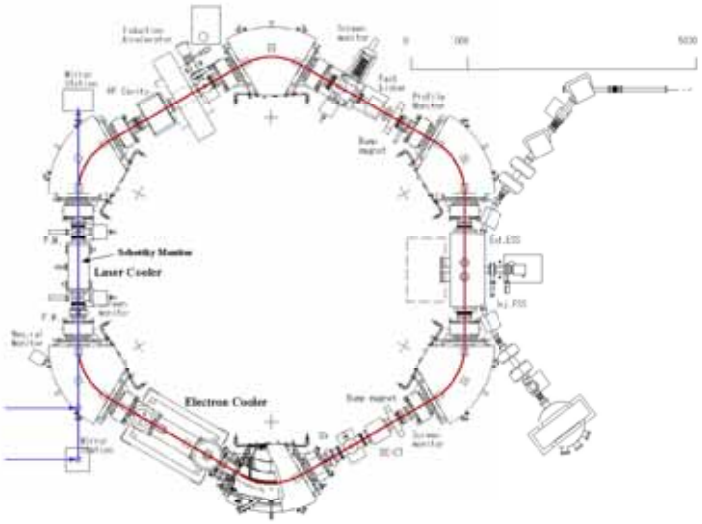

Fig.1 Layout of S-LSR

*Work supported by Compact Accelerator Development by Ministry of Education, Culture, Sports, Science and Technology and the 21st COE program- Center for Diversity and Universality in Physics-at Kyoto University
#noda@kyticr.kuicr.kyoto-u.ac.jp

DIRECT CURRENT CURRENT TRANSFORMER (DCCT)

For the purpose of measuring the circulating current in the ring, DCCT is installed in S-LSR, which can sense the current down to 1 μA at minimum. In Fig.2, the overall

Fig.2 Photo of DCCT

view of DCCT installed into S-LSR is shown. In Fig. 3, the beam life of 7 MeV proton beam measured with the DCCT is shown, which gives the e-folding beam life ~300 seconds for the average vacuum pressure of 10^{-8} Pa.

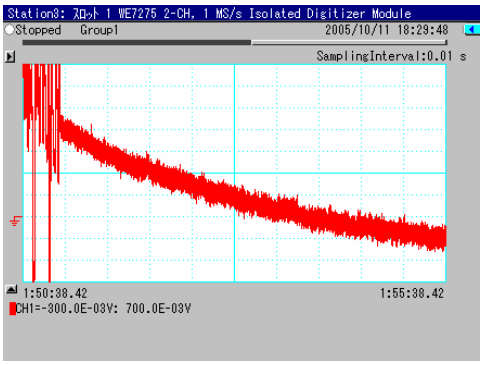

Fig.3 Decay of the 7 MeV proton beam current observed by the DCCT. The abscissa is 30 sec/div and ordinate is 10μA/div.

SCHOTTKY MONITOR

The circulating coasting beam is to be monitored by the Schottky pick up. The overall view of the outer conductor made of stainless plate which determines the earth potential of the picked up signal is shown in Fig. 4 (a), while the inner

(a) Overall view of the outer conductor

(b) View of inner conductor from the beam entrance

Fig. 4 Photo of the Schottky pick up.

conductor utilizes the helically wound stainless ribbon as shown in Fig. 4 (b)[2]. The Schottky pick up is a travelling wave type signal detector with the characteristic impedance of ~100 Ω and picked up signal is fed to the low noise amplifier through

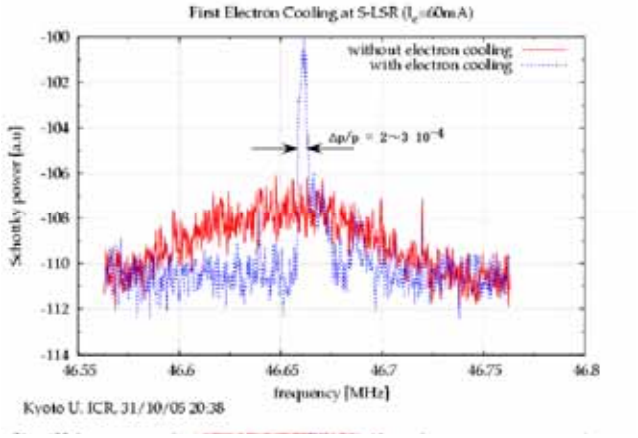

Fig.5 Frequency spectra observed by the Schottky pickup with and without application of electron cooling at S-LSR.

impedance converter. The harmonics of the revolution frequency is detected by the pick up and analyzed by a spectrum analyzer. The frequency spread gives us the information about momentum spread through the slip factor of the ring. In Fig.5, observed Schottky signals with and without the application of electron cooling are shown[3]. The fractional momentum spread of the 7 MeV proton beam is reduced to a few times 10^{-4} by the electron cooling[4].

BEAM PROFILE MONITOR

The horizontal profile of the circulating beam is monitored by the beam profile monitor as shown in Fig. 6. The geometrical apertures of the monitor are 12 cm and 5 cm in horizontal and vertical directions, respectively. In the electric field created by the electrodes shown in Fig.6 by the high voltage of 8 kV, the ionized ions by the charged particle beam in the residual gas are accelerated toward the micro channel plate with the dimension of 10 cm (horizontal direction) x 1.5 cm (beam direction) and are converted to the electric signal. The space resolution of the profile monitor is estimated to be 0.3 mm. The monitor is movable in horizontal direction as large as 27.5 cm with use of the driving mechanism by a pulase motor in order to cover full horizontal aperuture of S-LSR.

The horizontal beam profile has been monitored with this monitor through the electron beam cooling process. It is shown that the horizontal beam size has been safely reduced to 0.65 mm (1 sigma) for proton beam with intensity of 30 μA after cooling time about 10 seconds [3].

ELETRO-STATIC BEAM POSITION MONITOR (ESBPM)

For the purpose of monitoring the closed orbit and making its correction with use of adjustable fuction of each dipole excitation current, 12 electrostatic beam position monitors are istalled into the vacuum vessels set inside of all quadrupole magnets as shown in Fig. 8. The overall view of the monitor is shown in Fig. 9. The geometrical apertures of the monitor are 186 mm and 46 mm in horizontal and vertical directions, respectively, while the electrodes sizes are 200 mm (horizontal direction) and 100 mm (beam direction), respectively although they are cut to make triangles as seen in Fig. 9. Due to very limited geometrical size allowed for the beam

(a) Inner view of the aperture of the beam profile monitor

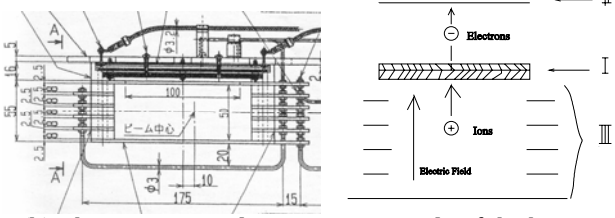

(b) The structure and operation principle of the beam profile monitor.

Fig.6 Beam profile monitor with use of MCP.

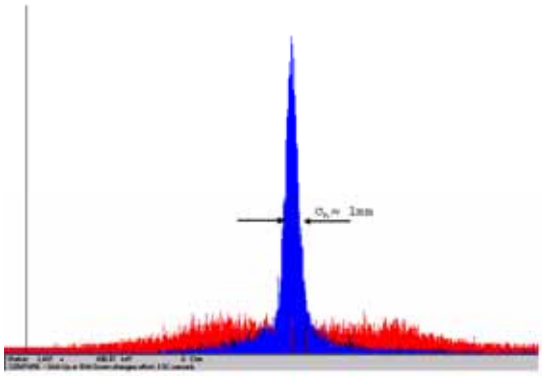

Fig. 7 Horizontal beam profile of the 7 MeV proton beam with and without electron beam cooling. Blue and red profiles indicate cases with and without electron beam cooling, respectively.

position monitor, each monitor is supported from one side utilizing the flange of the vacuum chamber as indicated in Fig. 10[5]. As the calibration of the monitor after the installation into the real space is impossible because of the severe restriction of the space, each monitor has been calibrated in a separate calibration chamber specially prepared together with peculiar preamplifiers. According

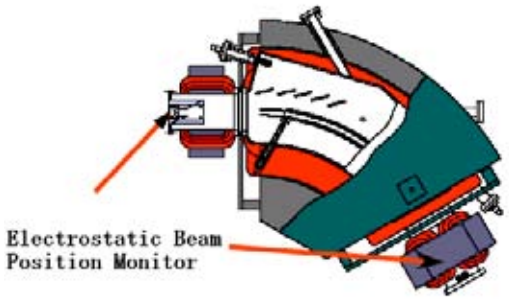

Fig. 8 Location of the electrostatic position monitors.

to the calibration results, the linearity of the position monitor is assured at least in±40 mm and ±15 mm in horizontal and vertical directions, respectively, which is found enough for the present situation although the position information can be available for much larger region to ~±100 mm.

Utilizing the picked up signals from these electro static beam position monitors, closed orbit of the S-LSR has been measured as shown in Fig. 11. For the purpose of realizing efficient cooling by electron cooling and laser cooling, it is desirable to reduce the distortion of the closed orbit (called closed orbit distortion-COD, hereafter) from the geometrical central orbit of the ring. By application of simplex algorithm,

Fig. 9 Overall view of the beam position monitor.

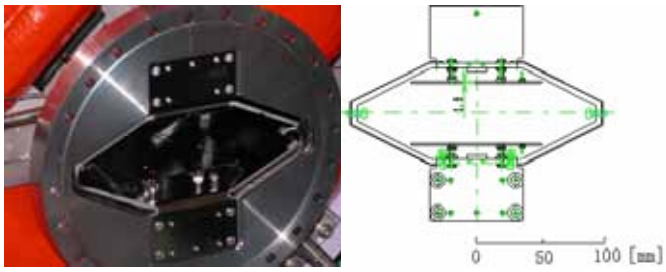

Fig. 10 Installation of the beam position monitor into the vacuum vessel.

the COD can be reduced to less than ±0.1 mm after 3 times corrections [6].

SUMMARY

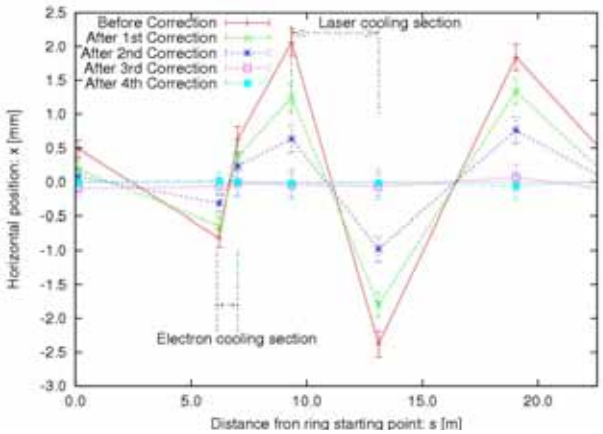

Fig. 11 COD of S-LSR before and after COD corrections.

The beam monitoring system composed of DCCT, Schottky monitor, beam profile monitor and ESBPM has played an essential role to verify the good performance of S-LSR ring and electron cooling system, although further improvement in reduction of noise level is needed for demonstration of ordered state of the beam.

REFERENCES

[1] A. Noda, “Ion beam cooling at S-LSR project”, Nucl. Instr. And Meth. **A532** (2004) 150.

[2] H. Yonehara et al., ”Equipments for Momentum Cooling at TARN”, INS-NUMA49 (1983).

[3] T. Shirai et al., Proc. In this workshop

[4] H. Fadil et al., “Design of a compact electron cooler for the S-LSR”, Nucl. Instr. And Meth. **A532** (2004) 446

[5] S. Fujimoto et al., “Static beam position monitor for a small ion storage rings-LSR”, Proc. of the 2nd Annual Meeting of Particle Accelerator Society of Japan and the 30th Linear Accelerator Meeting in Japan, Tosu, Saga, Japan, (2005) 60 (in Japanese).

[6] H. Souda, „COD correction of heavy ion storage ring, S-LSR”, Maser Thesis submitted to Department of Physics, Faculty of Science, Kyoto University (in Japanese).

THZ RADIATION IN KAERI

Young Uk Jeong#, Hyuk Jin Cha, Pildong Ahn, Seong Hee Park, Byung Cheol Lee,

KAERI, Daejon, Korea

Abstract

We have developed a high power terahertz (THz) radiation source by using a compact free electron laser (FEL). The FEL operates in the wavelength range of 100–1200 μm, which corresponds to 0.3–3 THz. The peak power of the FEL micropulse having 30 ps pulse duration is 1 kW and the pulse energy of the 3-μs-FEL-macropulse is approximately 0.3 mJ. The main application of the FEL is THz imaging and spectroscopy for bio-medical research and THz material study. We could get the transmitted THz imaging of several materials including bugs without being dryed by using the high power THz FEL. THz spectral characteristics of several materials have been studied by the FEL. We hope that the FEL can be upgraded for a practical source of medical and security inspections.

INTRODUCTION

T-ray which means THz radiation imaging technology was selected as one of '10 emerging technologies that will change your world' by a magazine named MIT's Technology Review of January 31, 2004. If we see the other selected technologies, e.g. universal translation, synthetic biology, and so on, the potentiality of the THz radiation technology might go beyond the usual understanding of us. THz radiation has several remarkable advantages for imaging compared with other conventional sources, such as safe energy range without ionization to the materials, foot-print spectral region of most chemicals and bio-materials, and relatively high spatial resolution for medical imaging.

There are several kinds of THz radiation sources [1–5]. Table-top THz sources generated by conventional lasers have been developed and used for various applications in the THz range [6–8]. However, advanced THz imaging such as tomography of living species requires much more power of the radiation to get information with better S/N ratio and higher speed of data acquisition. Inexpensive and compact THz FEL [5,9] can play the important role of encouraging the advanced THz applications due to its higher power and spectral brightness compared to the table-top sources.

We have developed a THz users facility based on a compact FEL [10-11]. The wavelength range of the FEL is 100-1000 μm and we could construct a users experimental stage for the wavelength of 100–300 μm. The THz FEL beam shows good performance in pulse-energy stability, polarization, spectrum and spatial distribution. We could get the 2-D imaging of various materials with the THz FEL beam. The measured coherence length of the THz FEL micropulses is 8-12 mm, which corresponds to 25-40 ps. In this paper we described the recent results of the THz application by the compact THz FEL.

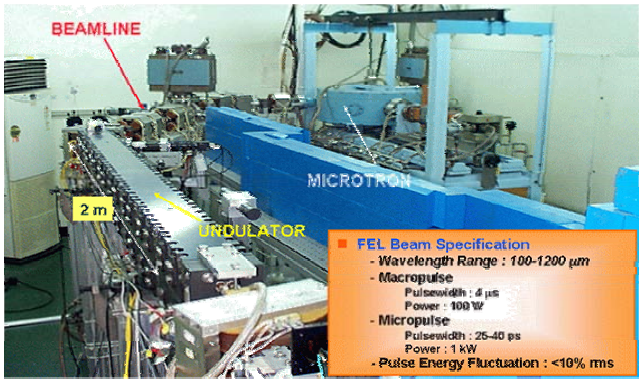

Figure 1: Photograph and specifications of the KAERI compact THz FEL.

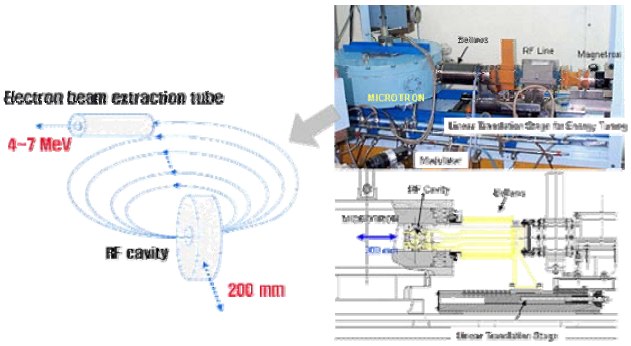

Figure 2: A microtron accelerator of the THz FEL. The electron energy of the microtron can be tuned in the range of 4-7 MeV by changing the position of a RF cavity.

A COMPACT WIDE-BAND THZ FEL

Main parameters and photograph of the FEL are shown in Fig. 1. A simple and cheap system providing motion of the accelerating cavity inside the microtron with the step of 0.1± 0.01mm along a principal diameter is used for variation of the energy of the microtron-injector by changing the orbit number, which is shown in Fig. 2. The system is based on a precise linear moving stage driven by a stepping motor. For each maximum orbit number the system keeps disposition of the axis of the RF-cavity in horizontal and vertical planes with accuracy better than 0.2 mrad. The microtron RF system including the RF cavity, RF-line elements and the magnetron has been

strongly mounted on the movable table of the stage. We can change the maximum orbit number in the microtron from 12 to 8 and it corresponds to the electron energy of 7 to 4.5 MeV. The measured current of the electron beam depending on its energy and the FEL wavelength calculated from the energy range are shown in Fig. 3.

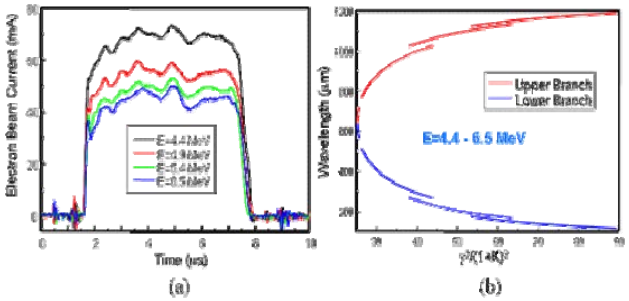

Figure 3: (a) Accelerated beam current from the microtron depending on the beam energy, (b) and its FEL wavelength calculated from the energy range.

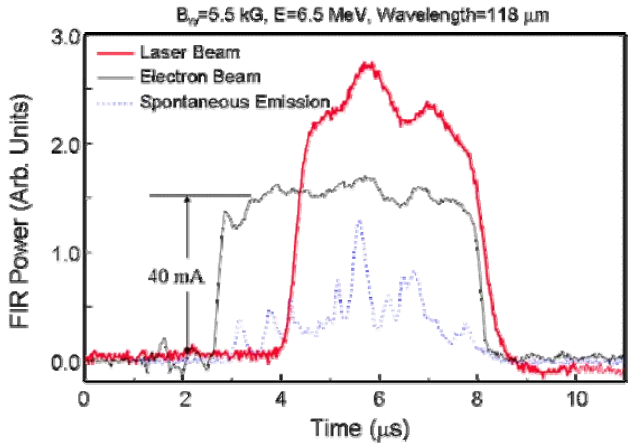

Figure 4: Typical waveform of the THz FEL pulse. For comparison, electron beam pulse and spontaneous emission pulse are placed in the same time structure. The power of the spontaneous emission is 10,000 times weaker than that of the FEL pulse.

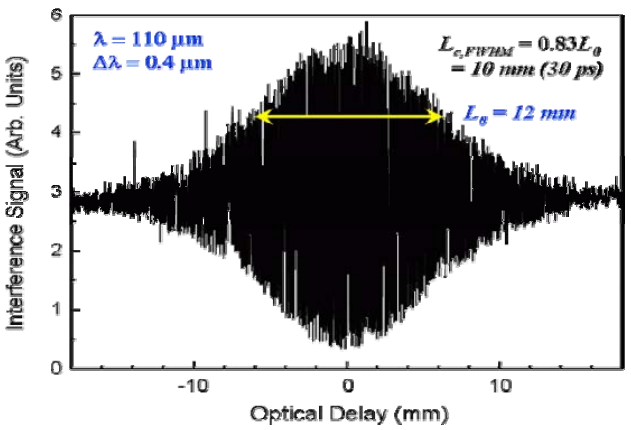

Figure 5: Measured pulse duration of the THz FEL beam by using linear autocorrelation method. The pulse duration is from 25 to 40 ps depending on the FEL oscillation condition.

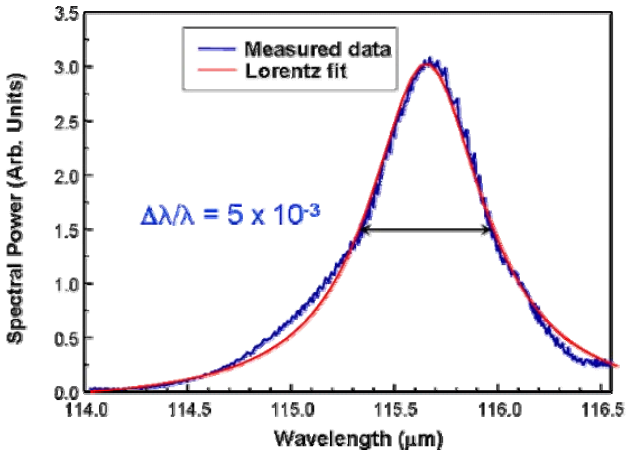

Figure 6: Measured spectrum of the FEL beam. The spectral line width of the FEL beam is depending on its cavity detuning.

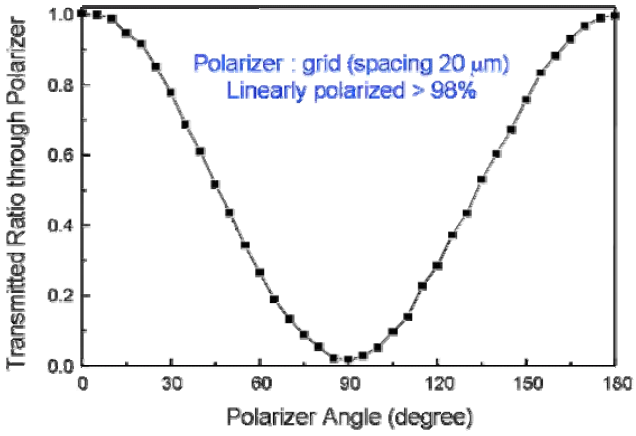

Figure 7: Measured polarization of the THz FEL beam by using a metal-wire polarizer having 20 μm spacing.

The measured results of the THz FEL beam parameters, pulse waveform, pulse duration, spectrum, and polarization, are shown from Fig. 4 to Fig. 7. The stability of the radiation pulse energy was monitored during several hours. We could not observe any drift of average value of the FEL pulse energy and the fluctuation of the pulse energy is less than 10% in r.m.s value. If we monitor and normalize the pulse energy fluctuation of the FEL beam, the measuring error is decreased to be less than 1%. With the stable THz pulses, we could measure 2-D scanned imaging, interference patterns, or spectroscopic information of species with high resolution.

We could understand that our THz FEL beam has excellent performance in power stability, polarization, spectral width, spatial distribution and wavefront. We hope that the THz radiation could be used for the advanced application of THz imaging for 3-D coherence tomography.

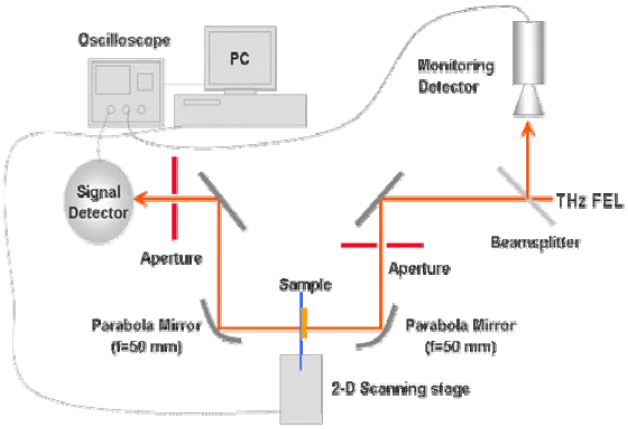

Figure 8: Schematics of the experimental setup for THz transmitted imaging with 2-D scanning of the samples.

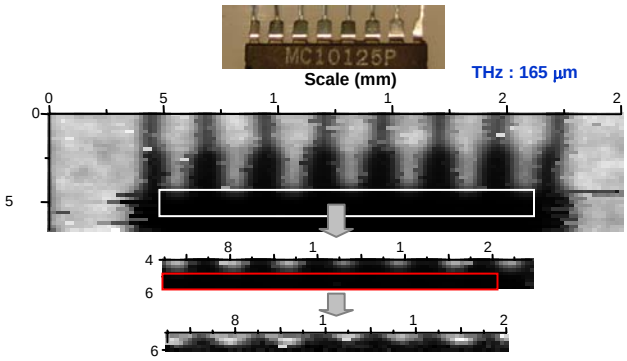

Figure 9: 2-D THz imaging of a microchip. From the experiment we could find the dynamic range of the THz imaging is much bigger than that of the usual vision recognition by human eyes. Even the dark part of the THz imaging inside the chip contains information on its structure.

2-D THZ IMAGING

Figure 8 shows schematics of the experimental setup for THz transmitted imaging with 2-D scanning of the samples. The 2-D scanning and data acquisition are automatically performed by a personal computer with a controller. For the first experiment on the THz imaging, we did not perform spectral study on the sample. Therefore the used wavelength for the THz imaging experiment was not optimised.

The first sample of 2-D THz imaging with our FEL was a microchip as shown in Fig. 9. From the experiment we could find the dynamic range of the THz imaging is much bigger than that of the usual vision recognition by human eyes. Even the dark part of the THz imaging inside the chip contains information on its structure. Figure 10 shows a transmitted THz imaging through an invisible paper box containing metal and silicon rings. We could see the shape of the rings clearly. Additionally the density information inside the silicon ring could be measured by the THz radiation, which means that the big dynamic range is very useful to recognize the nature of sample with THz spectral information. Without any additional processing of the imaging data, we could get the dynamic range of 10^5 for the measurements.

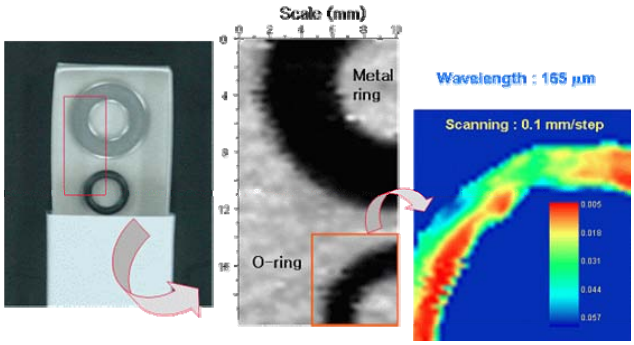

Figure 10: Transmitted THz imaging through an invisible paper box containing metal and silicon rings. From the THz transmitted imaging, we could get the density information of the silicon ring.

Figure 11 shows a THz imaging of a gingko leaf, which is compared with a visible transmitted imaging. You can see the difference between the visible and THz imaging clearly. The main difference is caused by 10^3-10^4 times difference in absorption coefficient of liquid water between the two frequencies.

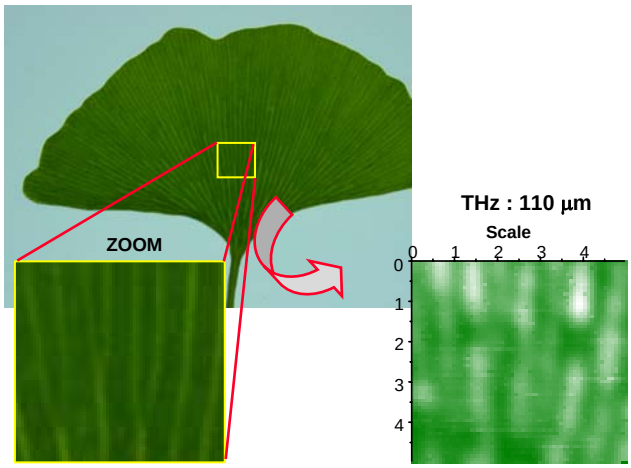

Figure 11: Transmitted THz imaging of a gingko leaf, which is compared with a visible transmitted imaging.

We have tested the FEL for transmitted imaging of bio-samples. Especially with 3 THz radiation the absorption in the water is the most severe except UV region. Fig. 12 and 13 show transmitted THz imaging of living bio-species by using the FEL light. The THz frequency of the imaging is 3 THz. We could get transmitted THz imaging of the bio-samples, even the image is not so clear. We hope the high power THz source can be used for an advanced imaging application like mammography

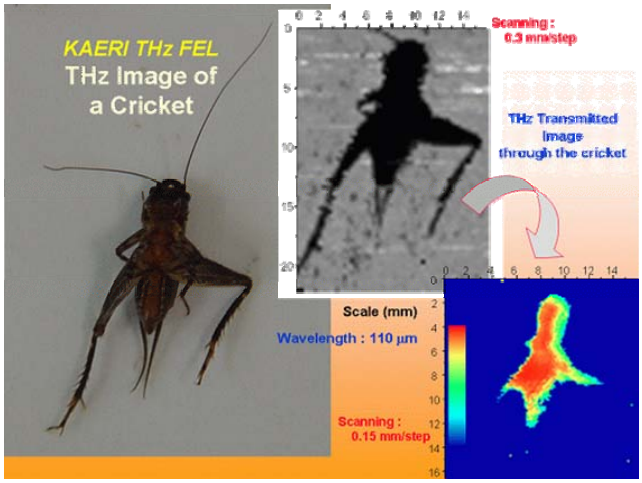

Figure 12: Transmitted THz imaging of a cricket. The sample was killed just before the measurement and the result is the first THz image of a bio sample not being dried.

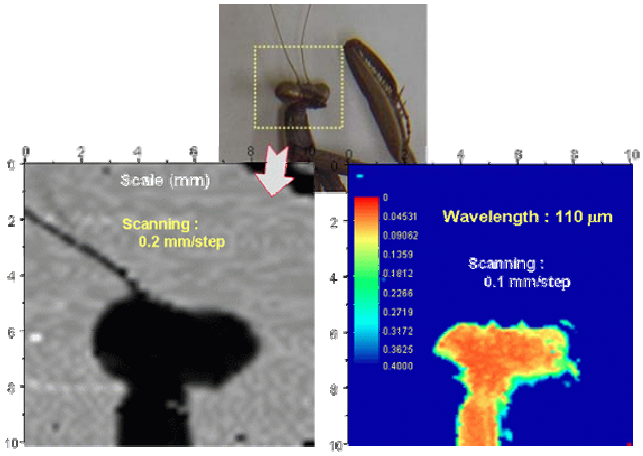

Figure 13: Transmitted THz imaging of the head part of a mantis. The sample was also killed just before the measurement.

CONCLUSION

We have developed a compact THz FEL and the main activity of its application for THz imaging is introduced in this paper. The FEL beam showed good performance in pulse-energy stability, polarization, spectrum and spatial distribution. We could get the 2-D imaging of various materials with the THz FEL beam. We hope to develop the technique for bio-medical application or non-destructive inspection.

ACKNOWLEDGEMENTS

This work was supported by Korea Research Foundation Grant (KRF-2004-042-C00053).

REFERENCES

[1] Rudeger Kohler, et al., Nature, 417 (2002) 156.
[2] Kodo Kawase, et al., Appl. Phys. Lett. 78 (2001) 2819.
[3] Q. Wu and X.-C. Zhang, Appl. Phys. Lett. 67, (1995) 3523.
[4] M. Abo-Bakr, et al., Phys. Rev. Lett. 88 (2003) 254801.
[5] Y.U. Jeong, et al., Nucl. Instr. and Meth. A 475 (2001) 47.
[6] D.M. Mittleman, et al., Appl. Phys. B 68 (1999) 1085.
[7] K. Kawase, et al., Opt. Express 11 (2003) 2549.
[8] T. Loffler, et al., Opt. Express 9 (2001) 616.
[9] Y.U. Jeong, et al., Nucl. Instr. and Meth. A 507 (2003) 125.
[10] Y.U. Jeong, et al., Nucl. Instr. and Meth. A 528 (2004) 88.
[11] Y.U. Jeong, et al., Nucl. Instr. and Meth. A 543 (2005) 90.

Tunable and monochromatic light sources at LEBRA in Nihon University

Y. Hayakawa*, I. Sato, K. Hayakawa, T. Tanaka, A. Mori[a], T. Kuwada, T. Sakai, K. Nogami, K. Nakao, M. Inagaki

Laboratory for Electron Beam Research and Application, Nihon University, Funabashi, 274-8501, Japan
[a]College of Pharmacy, Nihon University, Funabashi, 274-8555, Japan

Abstract

Two tunable light sources, a free electron laser (FEL) oscillator in the near infrared region and a Parametric X-ray (PXR) generator, have been developed on the basis of the 125-MeV electron linac in the Laboratory for Electron Beam Research and Application (LEBRA) at Nihon University. The saturated FEL lasing has been obtained in a wavelength range from 1 to 6 μm, with the maximum output energy of approximately 30 mJ per macropulse at around 2.4 μm. The property of the PXR generator has been investigated since the first observation of the PXR beam in 2004. The tunability of the device to the X-ray energy has been obtained in a range from 6 to 20 keV with the resolution of a few eV. Various application studies have been performed using the FEL or the PXR beam.

INTRODUCTION

In the Laboratory for Electron Beam Research and Application (LEBRA) at Nihon University, the development of a free electron laser (FEL) system and a monochromatic X-ray generator has been advanced based on the basis of 125-MeV electron linac. Table 1 shows the specification of the LEBRA linac. Although the linac is a conventional one with no sub-harmonic buncher nor RF-gun, it has relatively good performance as a middle-class one.

The FEL system is an oscillator type one and the first lasing of was achieved at the wavelength of 1.5 μm in 2001 [1]. Since the first lasing, a great effort has been spent for the improvement of the stability of the FEL system. As the results, the saturated FEL lasing can be obtained in a broad wavelength range from 1 to 6 μm and various application studies have been already performed using the fundamental FEL and the nonlinear higher harmonics since late 2003.

Table 1: Specification of the LEBRA linac

maximum energy	125 MeV
acceleration frequency	2856 MHz
klystron power	30 MW $\times$ 2
DC gun voltage	-100 kV
maximum pulse duration	20 μs
macropulse beam current	$\leq$ 200 mA
maximum repetition rate	12.5 Hz
normalized emittance (rms)	$\leq 20\pi$ mm mrad

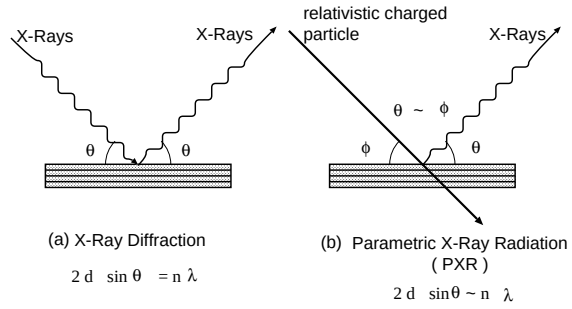

Figure 1: Schematic comparition between (a) Bragg diffraction and (b) Parametric X-ray radiation.

The monochromatic X-ray generator is on the basis of the phenomenon referred to as Parametric X-ray Radiation (PXR), which is schematically explained as shown in Fig. 1 [2]. The observation of the X-rays from this new source suceeded in April 2004 [3]. Application studies using the PXR beam such as radiography have been conducted since July 2004.

Figure 2 shows schematically the layout of two beam lines for FEL and PXR. Both of them are connected with the linac following the 90 $^\circ$ bending section.

STATUS OF THE FEL SYSTEM

Since the 90 $^\circ$ bending section acts a bunch compressor, an electron beam with a rather short bunch length can be obtained at the FEL undulator. Therefore, the FEL system has a relatively large FEL gain. For a wide tunability of the FEL wavelength, silver coated mirrors of copper substrates are used as the optical cavity mirror. With regard to shortest wavelength of the FEL system, the lasing at 800 nm has been barely observed using a 100 MeV electron beam at present. Stable and saturated lasing, however, have been obtained in a range from 1 to 6 μm. The specification of

* email: yahayak@lebra.nihon-u.ac.jp

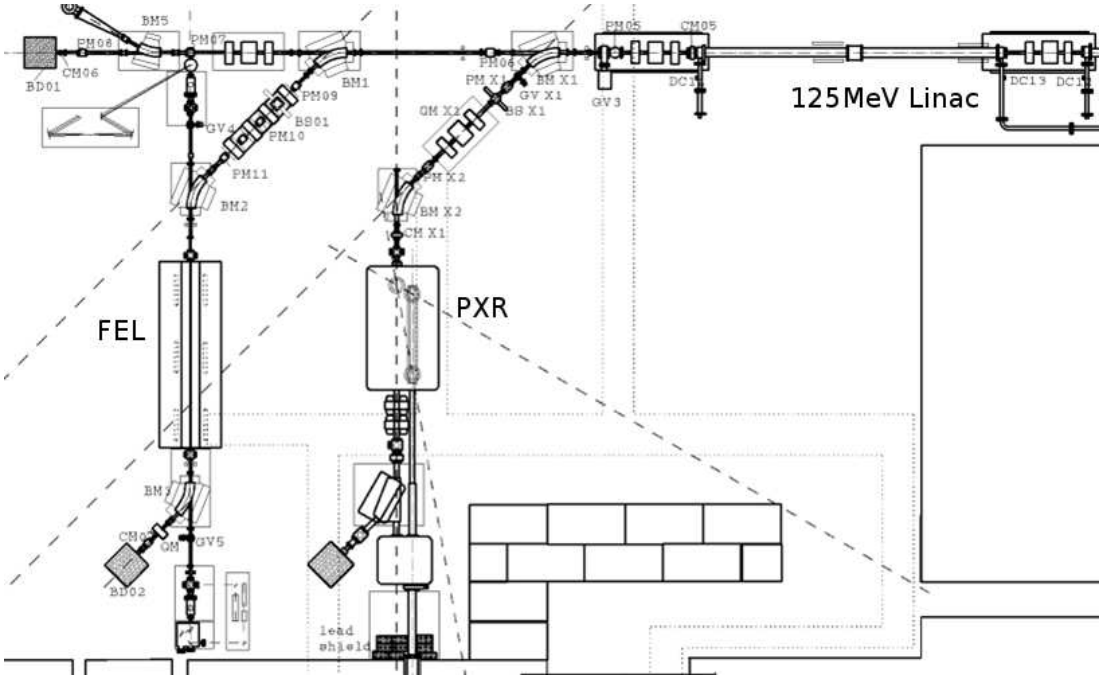

Figure 2: Beam lines for FEL and PXR connected with the 125 MeV electron linac.

the FEL system is shown in Table 2. In a wavelength range from 2.0 to 6 μm the most intense FEL beam can be extracted. The maximum output energy per macropulse at around 2.4 μm was estimated at approximately 30 mJ. The phase modulation of the linac, which corresponds to the dynamic cavity detuning during the macropulse, has been attempted in order to increase the optical energy [4]. Typical results of this experiment is shown in Fig. 3.

Because the diffraction due to the small coupling hole of the cavity mirror causes the optical beam loss during the transport, a beam expander system consisting of an elliptic and a parabolic mirrors was introduced into the guiding optics system for user's experimental facility [5, 6]. Thus far, various studies, such as the ablation effect of dental tissues and the synthesis of fullerene crystals, have been performed using the fundamental FEL and the nonlinear higher harmonics. Figure 4 shows an example of the ablation experiment for dental tissues using the FEL at the wavelength of 3 μm [7].

Table 2: Specification of the LEBRA FEL system

undulator period	48 mm
number of period	50
maximum K-value	2
electron bunch length (rms)	$\leq$ 1 ps
peak current	$\geq$ 20 A
FEL wavelength	0.8–6.1 μm

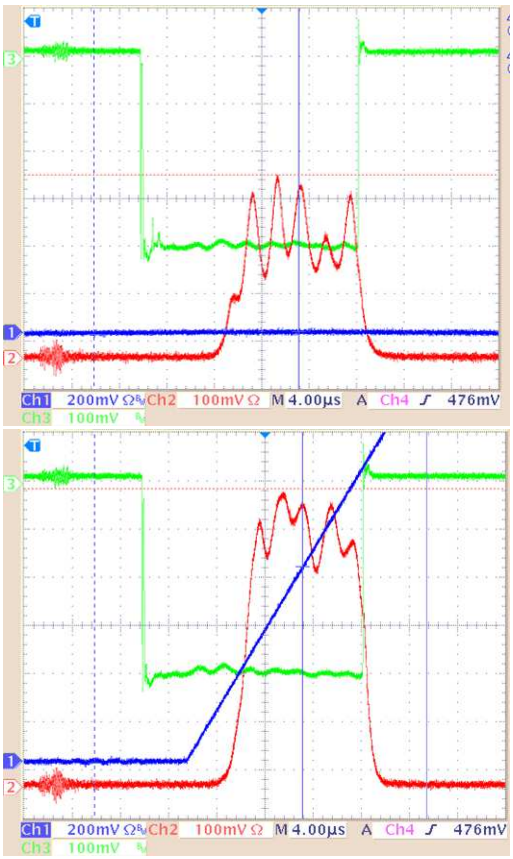

Figure 3: Typical shape of the FEL macropulse (upper) without and (lower) with the phase modulation.

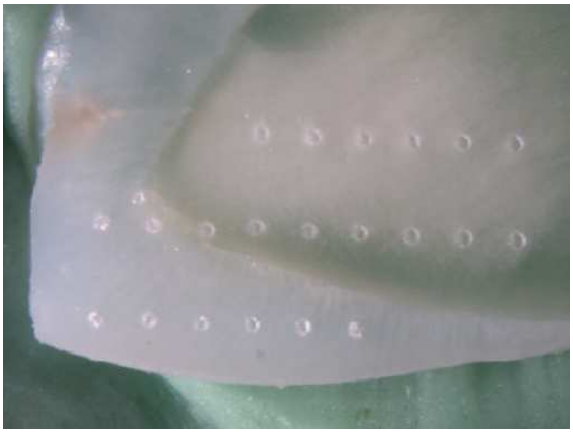

Figure 4: Ablation effect of dental tissues.

STATUS OF THE PXR GENERATOR

The PXR generator consists of two silicon perfect-crystal plates mounted on precise moving mechanisms with $(+,-)$ parallel arrangement to implement wide tunability. Figure 5 shows the concept of the system.

The property of the X-ray source has been investigated since the first observation of the PXR beam. The tunability of this device to the X-ray energy has been experimentally obtained in a range from 6 to 20 keV by use of Si(111) planes. Since the actual X-ray beam obtained from the PXR generator has a rather uniform spatial profile, the radiography is one of the most suitable applications of the PXR beam. Figure 6 shows the typical X-ray images taken using the PXR beam. These are raw images without any normalization except the white and black level adjustment. In addition to the monochromaticity of the X-rays, the positon resolution is rather fine because the electron beam spot on the target crystal behaves as a point-like source. Thus far, radiography for biological samples is the most popular application of the PXR beam.

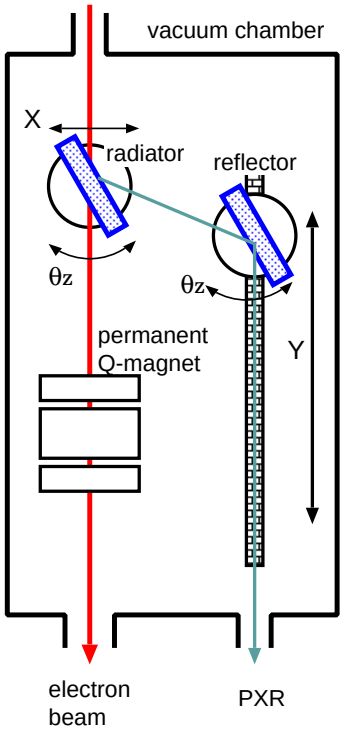

Figure 5: Scheme of the PXR generator. The generator consists of a double-crystal system in a vacuum chamber.

Table 3: Specification of the PXR generator

electron energy	100 MeV
average current	5 μA
target (radiator)	Si perfect crystal
target crystal thickness	0.2 mm
X-ray energy	
Si(111)	4–21 keV
Si(220)	6.4–34 keV

The PXR beam has an interesting property as shown in Fig. 7. The X-ray energy has the spatial distribution with a linear gradient horizontally. Figure 8 plainly demonstrates the effect of this property. The X-ray image explains that the X-ray absorption of copper discontinuously changes at the K absorption edge of 8.9 keV. Since the energy is lower than that of the K absorption edge of zinc, the absorption by a zinc foil is weak and flat. The rapid change of the X-ray absorption at the absorption edge suggest that the distribution of the PXR beam has the energy resolution of a few eV. Thus, the measurement of the X-ray absorption fine structure (XAFS) seems to be one of the most promising application of the PXR based source.

SUMMARY

The FEL oscillator in the near infrared region and the PXR generator have been developed on the basis of LEBRA linac and application studies have been already conducted. The FEL system cover the near infrared region from 1 to 6 μm and the application such as the ablation experiments have been actively performed. The investigation of the PXR property is in progress and preliminary application have been also attempted. In future, the development of applications , such as the tunability or the time structure of the light source, is expected.

ACKNOWLEDGMENTS

The development of this new x-ray source has been supported by the ”Academic Frontier” Project for Private Universities: matching fund subsidy from MEXT, 2000-2004. Part of the work was also supported by MEXT.KAKENHI (15760039).

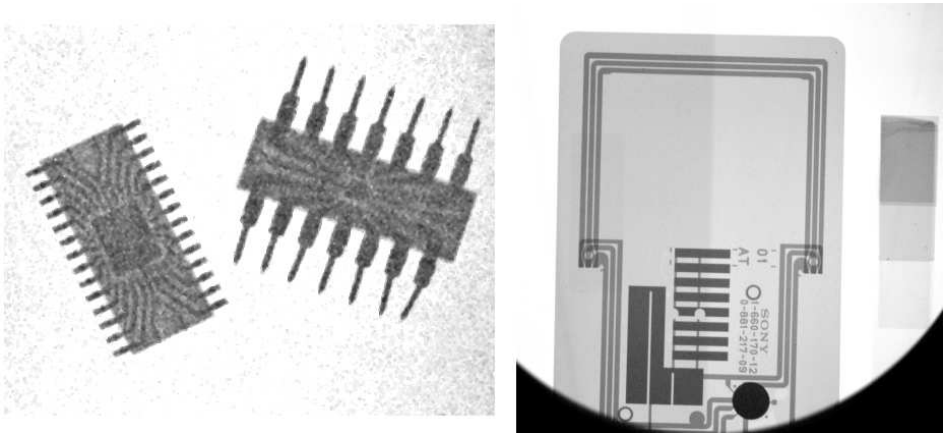

Figure 6: Examples of radiograph by the PXR beam.

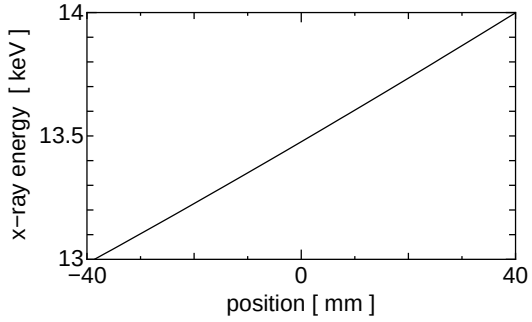

Figure 7: Spatial distribution of the PXR energy at the center energy of 13.5 keV. It has a linear gradient along the horizontal direction.

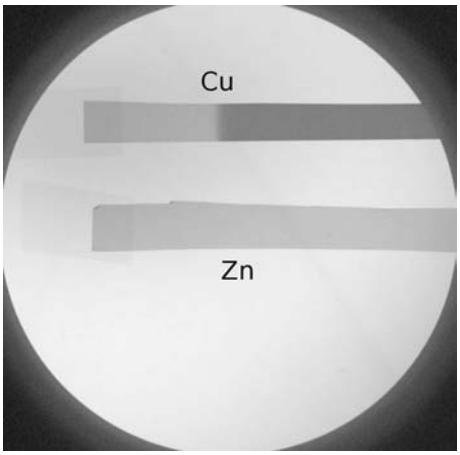

Figure 8: Demonstration of the effect attributed to the horizontal energy shift in the PXR profile in the case of the X-ray energy of 9 keV. Upper sample is a copper foil and lower is a zinc one.

REFERENCES

[1] Y. Hayakawa, I. Sato, et al.: Nucl. Instrum. & Methods A **483** (2002) 29.

[2] Y. Hayakawa, I. Sato, et al.: Nucl. Instrum. & Methods B **227** (2005) 32.

[3] Y. Hayakawa et al., Proc. of the 1st Annual Meeting of Particle Accelerator Society of Japan and the 29th Linear Accelerator Meeting in Japan, (2004) 60.

[4] K. Hayakawa, et al., Proc. of the 2ndt Annual Meeting of Particle Accelerator Society of Japan and the 30th Linear Accelerator Meeting in Japan, (2005) 117.

[5] T. Tanaka et al., Proc. of the 26th Int. Free Electron Laser Conf. and 11th FEL Users Workshop, (2004) 427.

[6] T. Tanaka et al., Proc. of the 2ndt Annual Meeting of Particle Accelerator Society of Japan and the 30th Linear Accelerator Meeting in Japan, (2005) 28.

[7] T. Sakae et al., Int. J. of Oral-Medical Sciences Vol.4 (2005) 8.

Exploring Fundamental Physics far beyond Standard Model by High Quality Laser †

M. Yoshimura
Department of Physics, Okayama University
Tsushima-naka 3-1-1 Okayama Japan 700-8530

ABSTRACT

Use of a high quality laser beam is advocated to explore physics far beyond the standard model of particle physics such as lepton and baryon nonconservation. The advantage is to activate electron capture processes by repeated compression and expansion of the electron cloud initiated by the continous irradiation of the laser beam.

Conventional means to explore the micro-world at shortest distance scale are either to go to the highest energy or to use a large amount of matter in precision experiments such super-kamiokande experiments. I would like to discusss yet another possible frontier using a high quality laser. The laser is used to activate atomic electron capture process otherwise difficult to detect. For instance electron capture by nucleus of the type $e^- \to e^+$ without neutrino emission and of the type $e^- + N \to \pi$'s immediately tells presence of lepton number nonconservation (LENNON) and baryon number nonconservation (BARNNON), both of which are of crucial importance to physics far beyond the standard model. If the idea of grand unification or the superstring theory is correct, there is no doubt of existence of these processes. The only crucial question is how large the rate is and how much the rate is enhanced by laser irradiation.

The activated reaction irradiated by laser has merits in two ways. First, a large number flux, $\approx 1.2 \times 10^{21} cm^{-2} s^{-1} (\frac{\omega}{eV})^{-1} (\frac{P}{W\, mm^{-2}})$, is expected with a moderate laser power P (ω is the photon energy). Secondly, an enlarged reaction time is available; one usually has time of order 1/photon frequency for a photon beam, but when the laser is continuously irradiated or the target

†Talk given at International Workshop on NANOBEAM 2005, 36th ICFA Advanced Beam Dynamics Workshop (held at Uji, Kyoto during October 17-21, 2005), and to appear in the Proceedings.

is put in a good quality resonator, it is enlarged to 1/ the Rabi frequency Ω_R, with $\Omega_R \approx 3 \times 10^{10} sec^{-1} \, (P/W\, mm^2)^{1/2} (\omega/eV)^{-3/2} (\gamma/10^9 s^{-1})^{1/2}$, with γ the transition rate between two relevant levels. This is the time scale of electron oscillation between tow activated levels.

As we shall discuss in the following, the passive rate without laser irradiation is enhanced by a multiplicative factor

$$Q \approx 1.6 \times 10^6 \, r \, (\frac{P}{W\, mm^{-2}}) (\frac{\omega}{eV})^{-4} (10^{-9} \frac{\omega}{\Delta\omega}) \, , \tag{1}$$

with $\Delta\omega$ the energy resolution and $r = |\psi_{ms}(0)|^2 / |\psi_{1s}(0)|^2$ is the wave function ratio squared where $m \gg 1$ is the principal quantum number relevant to the $ms \leftrightarrow mp$ dipole transition tuned by the laser beam. Thus a high quality laser of large $P/\Delta\omega$ may provide a large enhancement factor [1].

We consider for definiteness the atomic reaction process such as

$$laser + {}^A_Z X \rightarrow laser' + {}^A_{Z-2} W' + e^- + e^+ \, , \tag{2}$$

where the emitted e^+ has a few MeV energy (monochromatic), while the leftover e^- is almost at rest. This clearly violates the lepton number by two units. In a favorable nucleus the final nucleus may be in an excited state, in which case an additional nuclear gamma ray is emitted giving a good chance of simultaneous detection.

It is important to treat the laser-atom interaction as accurately as possible. The rest of the process, the electron capture by nucleus itself, may be treated by the perturbation theory. Restricting to the two level problem and adopting the rotating wave approximation, the interaction between the laser beam and one atomic electron can be treated analytically since the hamiltonian of this part is block-diagonal [2].

The subsequent capture process is assumed to go through one of two oscillating levels. We assume that the capture goes through via the lower energy ms electronic state of the target atom. For the photon state in the laser beam we take the coherent state, which can be decomposed in terms of states of definite photon numbers.

We shall first explain the physical picture of continuous laser irradiation in terms of the electron motion. Let us take for the simplest interpretation the laser irradiated state starting from the ineffective mp state, instead of a mixed state. The electron displacement is computed as

$$\approx \int d^3x \, r | \cos(\Omega_R t/2) \psi_{mp}(\vec{x}) - \sin(\Omega_R t/2) \psi_{ms}(\vec{x}) |^2 \, . \tag{3}$$

Unlike a pure mp or ms state, this state has a time dependent profile of the electron position. The electron motion in the radial direction is periodic and the electron can approach near the nucleus; it is closest to the nucleus when the two terms of the integrand of eq.(3) nearly cancells. If the wave functions of the two states are nearly equal, the electron is closest to the nucleus around $t = (n + 1/2)\pi/\Omega_R$. This coincides with the time of the maximal probability of the electron capture rate later given, which is directly $\propto \langle ms|\vec{x}|mp\rangle$. We propose to call this compression mechanism as PHIRAC to abbreviate PHoton IRrAdiated Compression of the electron cloud. The compression of the electron cloud occurs along the direction of the electric field of the laser.

We imagine that target atoms are put into a good quality resonator, and are irradiated by intense laser whose frequency is fine tuned to the energy level difference of target atom. Two electronic levels of the target atom are denoted by $|e\rangle$ taken as the upper energy p-state, and by $|g\rangle$ as the lower s-state. The system of laser and atom is then described by a Hamiltonian of the form [2],

$$H = \frac{\omega_{eg}}{2}\sigma_3 + \omega a^\dagger a + \tilde{s}(\sigma_+ a + \sigma_- a^\dagger)\,. \tag{4}$$

Here the Pauli matrices σ_i act on two levels of the ground $|g\rangle$ and the excited $|e\rangle$ state, and $\omega_{eg} = \omega_e - \omega_g$ is the energy level difference. The coupling strength s is given by

$$\langle e|\tilde{s}\sigma_+|g\rangle \equiv s = -\langle e|\vec{d}|g\rangle \cdot \vec{e}, \quad \vec{e} = i\frac{\omega}{\sqrt{2\omega V}}\vec{\epsilon}_k \tag{5}$$

for the dipole transtion, with $\vec{d}$ the dipole operator of atomic electron and $\vec{e}$ the electric field of a single photon beam with polarization $\vec{\epsilon}_k$. When multiplied by the average photon number N, this strength is expressed as $Ns^2 = \pi\gamma_d P/\omega^3$ where P is the laser power in the unit of energy/ (time *times* area). Throughout this paper we assume a linearly polarized beam of laser.

The effect of laser irradiation can be solved by decomposing the infinite dimensional Fock space into an infinite product of the mixture of two states, $|e\,,n\rangle = (a^\dagger)^n/\sqrt{n!}|e\rangle$ and $|g\,,n\rangle = (a^\dagger)^n/\sqrt{n!}|g\rangle$; $|\psi(t)\rangle = \sum_n (c_{g\,n+1}(t)|g\,,n+1\rangle + c_{e\,n}(t)|e\,,n\rangle)\,.$

It is reasonable under the continuous laser irradiation to assume that the target is initially in a superposed state of two levels, $|\frac{1}{2}\rangle \equiv \frac{1}{\sqrt{2}}(e^{i\delta}|g\rangle + |e\rangle)$ with $\delta = \pi/2$. The result is insensitive to the choice of this phase and the

initial condition as a whole. Time evolution of the mixed state is readily worked out, and the p-state component is given by

$$\langle e\,,n|\frac{1}{2}\,,n\,;t\rangle = e^{-i(n+1/2)\omega t}\cos(\frac{\Omega_n t}{2}-\frac{\pi}{4})\,c_n^{(\gamma)}(0)\,. \tag{6}$$

It is assumed that at a time t the electron in the mixed state absorbs the photon and is subsequently captured by nucleus. An example of subsequent rare X processes of this sort is LENNON electron capture of the kind $e^- \to e^+$, as discussed in [3]. The probability amplitude of the capture process has the factor of stimulated emission from $mp \to ms$, namely $\sqrt{n+1}$, and is given by

$$\sum_{n=0}^{\infty}\mathcal{M}_X(t)\frac{s\sqrt{n+1}}{\omega-\omega_{eg}+i\gamma/2}\langle e\,,n|\frac{1}{2}\,,n\,;t\rangle\,, \tag{7}$$

where $\mathcal{M}_X(t)$ is the amplitude for the rare X process originating from the ms state.

Computation of the discrete photon number (n) sum (7) is well approximated in the large N limit by a continuous n integral. Using the large n limit formula of $n!$, and the coherent state expression for $c_n^{(\gamma)}(0)$, the integrand is found to change violently, and one may estimate the integral by a gaussian approximation around the stationary phase, or the saddle point. The saddle point n_0 of the integrand is determined by the minimal variation of the exponent of the integrand and is given by taking the $n-$derivative of the exponent to vanish. A complex saddle is thus obtained; $n_0 \approx Ne^{-2i\omega t}$. Making the gaussian approximation around this saddle gives the rate formula [1],

$$\begin{aligned}\approx (\frac{\pi}{2})^{1/2}N^{3/2}&\frac{s^2\,|\mathcal{M}_X(t)|^2}{(\omega-\omega_{eg})^2+\gamma^2/4}\exp[-N(1-\cos 2\omega t)]\\ &\times[\sinh^2(\sqrt{N}st\sin\omega t)+\cos^2(\sqrt{N}st\cos\omega t+\frac{\pi}{4})]\,.\end{aligned} \tag{8}$$

The result is a periodic spiky function of time, of period $\approx 1/\,\omega$, whose amplitude is further modulated with a larger period of 1/the Rabi frequency, $\propto 1-\cos\Omega_R t$. The height of the spike is $\propto N^{3/2}$ and its width $N^{-1/2}$. Thus, the averaged rate over time $\gg 1/\Omega_R$ is in proportion to the single power of P. Convolution of the laser photon spectrum then gives the result, eq.(1), stated in the beginning.

The spiky time profile of the rate derived in of eq.(8) is semiclassically interpreted as follows. When the electron is closest to nucleus, its velocity v contributing to the flux factor for the electron capture is $\propto \Omega_R \propto \sqrt{P}$ in relation to the laser power P, hence the probability of photo-absorbed electron caputre is $vP \propto P^{3/2}$. This explains the height of the spike. On the other hand, the time spent near the nucleus is r_N/v, with r_N the nuclear radius, thus the time width of the electron capture is $1/\sqrt{P}$, explaining the narrowing of the spike.

LENNON process has been discussed in [3]. The event rate depends on the assumed Majorana mass of neutrinos. For instance, the LENNON rate of one event per year requires the Q-factor of order, $Q > 1 \times 10^7 |m_{ee}/0.1eV|^{-2}$ for $1gr$ of the isotope ${}^{112}_{50}Sn$ (one of the best isotopes for LENNON conversion), where m_{ee} is the neutrino mass combined with mixing for the $e^- \to e^+$ transition.

Baryon nonconservation may experimentally be investigated by searching for the atomic electron capture of the type, $e^- + N \to \pi + \pi$. Enhancement factor $\propto P$ may compensate the small nuclear overlap factor of order $(a_B m_\pi)^3 \approx 10^{-15}$ of atomic electrons that otherwise disfavors this process. A rough estimate of the rate gives the enhancement factor of order, $Q\,(r_A A^{1/3} m_\pi)^{-3}$, where the pion mass m_π times $A^{1/3}$ gives a measure of the inverse nuclear size, and r_A is the atomic size. It is important to go to a low frequency range for a large enhancement of order 10^{25}. Thus, the use of the Zeeman split hyperfine levels is promissing, which involves the microwave region.

References

[1] M. Yoshimura, "Photon Irradiated Compression as a Tool of Investigating Fundamental Physics beyond Standard Model" hep-ph/0507248 v3.

[2] For instance, C. Cohen-Tannoudji, J. Dupont-Roc, and G. Grynberg, *Atom-Photon Interactions*, Wiley-VCH(2004).

[3] M. Ikeda, I. Nakano, M. Sakuda, R. Tanaka, and M. Yoshimura, "New Method of Enhancing Lepton Number Nonconservation", hep-ph/0506062 v2.

Study of virtual vacuum polarizations in a strong electromagnetic field

K. Homma, Graduate School of Science, Hiroshima University and
T. Takahashi, Graduate School of Advanced Sciences of Matter, Hiroshima University

Abstract

A strong electromagnetic field may modify the refractive index of the normal vacuum which can be reduced to the light-light scattering amplitude via virtual vacuum polarizations in a microscopic sense. In order to observe the increase of the refractive index, Cherenkov light emissions associated with relativistic electrons into the strong field can be utilized as an experimental probe. In this letter, we will present a result of experimental search for Cherenkov emissions with a laser intensity of 10^{17}W/cm^2 with the wave length of 800 nm and electron beam of 35.4MeV/c, in which the expected Compton energy and a symptom of unexpected lower energies in visible range were observed.

MOTIVATION

Recently there are stimulating theories with varying velocity of light while the universe is evolving, which is well summarized in [1]. They naturally leads us to a question we have rarely asked; what does determine the physical propagation speed of light in a vacuum? Since we have knowledges that locally a vacuum has rich structures, we may have a hope that we can understand why the speed of light or vacuum permittivity became the present value based on the relation between local vacuum structures such as vacuum polarizations and the evolution of a system. Since our universe is expanding and it must have been a tiny system size with quite high energy density in the past, it raises a question; how are the local properties such as vacuum polarizations related with the system size and the energy density? Fig.1 shows a map of accessible system sizes and the energy densities of existing systems, where the nucleon energy density is a good reference point. Symbolic phenomena that a vacuum has surely rich structures can be seen in e^+e^- collisions at high energy circumstances, where various particles are produced via electromagnetic, weak and strong interactions. In a broad sense, it is related with degrees of vacuum polarizations via those types of interactions. However, the size is too small($< 10^{-18}cm$) to extend it to a macroscopic picture such as the physical propagation speed of light and we usually treat it as an instantaneous quantum fluctuation. What happens in hadron collisions? For example in heavy ion collisions, the size is expected to be of order of 10 fm and a thermodynamical picture with a volume can explain many body phenomena[2]. However, it is still too small to discuss the speed of light based on the degrees of vacuum polarizations and the phenomena are too dynamical where real vacuum polarizations cause complicated particle productions in a collision event. Then what happens in the other end, *i.e.* in the largest size of a vacuum? There is a proposal to measure the speed of light over a distance of 10^{10}ly from a gamma ray source by gamma ray bursts[3]. In this case, fluctuations due to quantum gravity during the long distance travel may cause the change of the dispersion relation in a vacuum, which would be observable by measuring a relation between arrival times and photon energies given an ideal situation that the burst occurs at a very short instant. Although we can expect all kinds of virtual quantum effects are involved in this case, we have to wait for those phenomena to occur accidentally in our universe. Is there a proper macroscopic vacuum which is experimentally controllable and not too dynamical to see a subtle effects on the vacuum permittivity. In this view point, an optical laser could be a good candidate as a macroscopic vacuum generator. Although J. Schwinger discussed the real vacuum polarization with a constant electromagnetic field[4] and it is still far from the present technology, the virtual vacuum polarization can be discussed with the currently achievable laser intensity. Therefore the high intense field provides us a chance to see a subtle change of the vacuum permittivity.

The change of the vacuum permittivity due to a strong electromagnetic field can be experimentally probed by observing Cherenkov emissions associated with a relativistic charged particle. There is a quantitative estimate on the Cherenkov emission[6] and more references are therein. In those calculations, only QED effects are taken into account. In this case, in order for Cherenkov lights to be emitted, we need a PW class laser and relativistic electrons above 45GeV/c. Such a facility does not exist in the world at this moment. However, a vacuum should contain richer structures and virtual contributions from QCD should be also taken into account. Discussion on the QCD effects in a constant electromagnetic field can be found in [7], which estimates photon-photon scattering amplitude via virtual quark polarizations originated from gluon condensates which has a finite vacuum expectation value as quantum fluctuations. In the calculation, a photon-photon scattering amplitude via quark polarizations overwhelms the amplitude with only electron polarizations strongly depending on the quark masses, which insists that the treatment of QED and QCD interference has not been settled yet theoretically. If the photon-photon scattering amplitude is drastically increased, there is a possibility for the Cherenkov threshold to be lowered by the QCD effects compared to only the QED effects. Therefore, we might have a chance to see the effect even with currently available facilities.

In this letter, we present a search for Cherenkov emissions in an intense electromagnetic field of 10^{17}W/cm^2

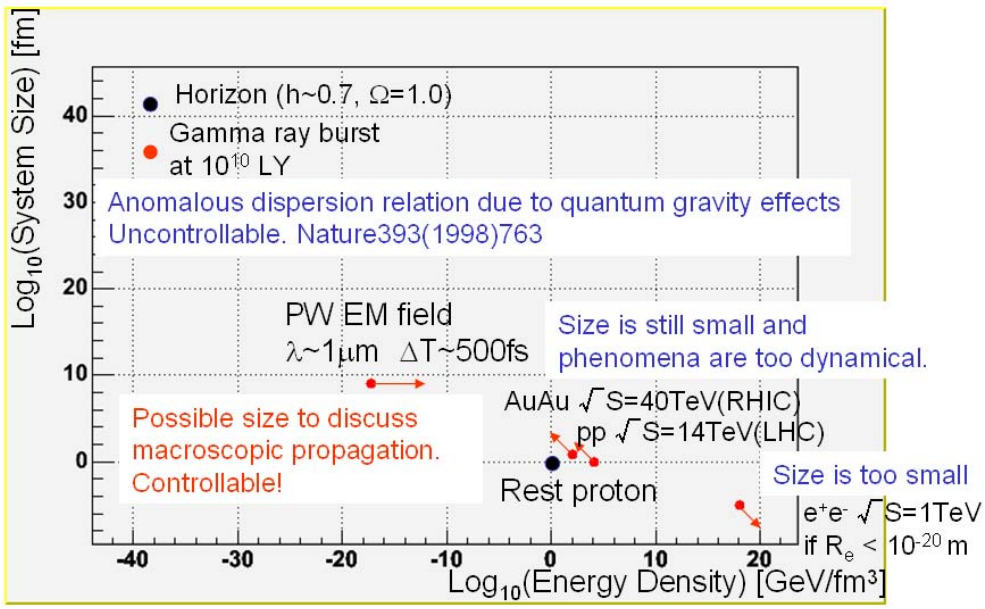

Figure 1: A map of accessible sizes and energy densities in various vacuum systems. Selected systems are; e^+e^- collider (Linear Collider) at the center of mass energy of $\sqrt{s} = 1$TeV assuming the size below 10^{-18}cm, pp collider at $\sqrt{s} = 14$TeV (Large Hadron Collider), Au+Au collider at $\sqrt{S_{NN}} = 200$GeV per nucleon pair (Relativistic Heavy Ion Collider), a rest proton, an optical laser pulse with $3 \times 10^{26}[W/m^2]$ and 500 fs duration (see parameters in [5]), and universe with $\Omega = 1.0$ and $h = 0.7$ in which gamma ray burst event might prove the variation of speed of light. Relevant comments in each system is found in the figure. The arrows indicate directions of possible uncertainties and future expectations.

laser with the wave length of 800nm by injecting relativistic electrons of 35.4MeV/c.

EXPERIMENTAL SETUP

Fig.2 shows a schematic view of the experimental setup. The parameters of a laser pulse and an electron bunch are summarized in Tab.1. Electron beam bunches and laser pulses are perpendicularly crossed, and Compton x-rays emitted to the forward direction of electrons are the focus of this experiment. Used electrons are bent by a bending magnet with a field strength of 0.3T, which causes synchrotron radiations with wave length greater than 4.9μm.

The aim of this experiment is to search for photons with energy different from known energies of linear and nonlinear Compton scatterings by rejecting background contributions from Bremsstrahlung radiations by interactions with residual gas in vacuum chambers and synchrotron radiations by bending magnets. Since the deviation of the refractive index from a pure vacuum is expected to be extremely small, the Cherenkov emissions are limited in the very forward region of incident electrons. Fig.3 shows an expected Compton x-ray energy spectrum simulated by CAIN235[8] based on the beam parameters in Tab.1. We put a narrow square slit of $1mm \times 1mm$ at the 5m downstream from the crossing point, where the expected Compton x-ray energy spectrum approaches to monochromatic one by narrowing the slit aperture. This setup enhances signals we search for in the forward region. The square slit is made of Ta with 3mm^t in both x and y directions, so that it is thick enough to suppress Compton x-rays outside the aperture.

Fig.4 shows a picture of the detector elements at the 5m downstream. A shielding wall made of SUS with a hole of 1cm$^\phi$ is located with a plastic scintillation counter in the upstream side of the wall to trigger x-rays. After the shielding wall, there is the square slit. Then Compton x-rays are measured by a x-ray detector XR-100CR of AMPTEK which has a energy resolution of 153eV to x-rays from 5 to 20keV with our readout system. In order to measure energies other than Compton x-rays, there is a photomultiplier(PMT) R7400U-04 of Hamamatsu Photonics after a mirror which reflects generated visible rays from the crossing point. The PMT has a fast rise time of 0.78 ns and sensitivities to wavelength from 200nm to 700nm with more than 10% quantum efficiency. Fig.5 shows a picture of the PMT part with a mirror and a wave filter which cuts off the 800nm wave length. Although there is a photo diode for soft x-ray detections in the picture, it was not used for the experiment this time.

MEASUREMENTS AND ANALYSIS

In order to confirm that we open a narrow slit in a correct geometrical position and guarantee an acceptance for single Compton ray per crossing, we need to check the end-point energy of the Compton scatterings. Before we narrowed the slit, we measured an energy spectrum with a larger slit size of about 1cm$^\phi$ at the 5m downstream.

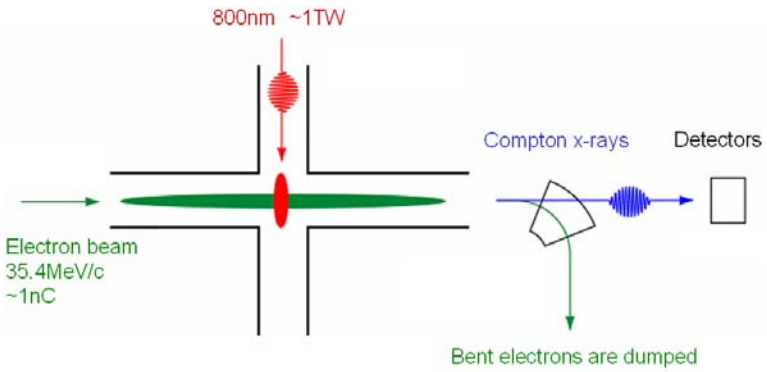

Figure 2: Schematic view of the experimental setup.

Electron momentum	$p_e = 35.4$MeV/c
Electron beam current	$I_e = 1$nC
Electron beam profile	$\sigma_x = \sigma_y = 50 \sim 70\mu$m, $\sigma_z = 3ps \times c$
Laser energy	$E = 40 \sim 135$ mJ
Laser pulse width	$\tau = 135$ fs in FWHM
Laser reputation rate	10 Hz
Laser power	$P = \frac{E}{\tau} = 0.3 \sim 1$TW
Laser profile	$\sigma = 28(FWHM)/2.35 = 12\mu$m
Laser power density	$S = \frac{P}{\pi\sigma^2} = 0.7 \sim 2.2 \times 10^{17}$ W/cm^2

Table 1: Electron and laser beam parameters.

Fig.6 shows the raw energy spectrum(ADC distribution), in which the pile up of multiple photons with the end-point energy can be seen.

In order to calibrate the X-ray detector, we used ^{109}Cd source with metal converters which can produce various characteristic X-rays to calibrate the energy of the detector. Fig.7 a) shows a merged X-ray spectrum with various converters. The converter materials are indicated in the figure. Fig.7 b) shows the calibration curve between the energy and the ADC channels in our setup.

In order to understand the background, filled and empty laser pulses are alternatively produced by synchronizing them to a basic 10 Hz clock. For the following explanations, we introduce four abbreviations; l_1 for filled laser pulses, l_0 for empty laser pluses, e_1 for filled electron bunches and e_0 for empty electron bunches. Fig.8 shows an energy spectrum of the end-point region of Compton scatterings with the narrow square slit size of $1mm \times 1mm$ at the 5m downstream from the crossing point, where the magenta solid line shows the spectrum in $l_1\&e_1$(signal + beam halo), blue dotted line shows the spectrum in $l_0\&e_1$(only beam halo), black dashed line shows the fit to only the right side of the peak, red points show a spectrum by subtracting the fit result from the spectrum with the magenta solid line. During the experiment, the laser wavelength fluctuated from 2 to 4% around 800nm. The energy resolutions of the detector is 1%. Since the expected fluctuations were not precisely known, a fit to the right part of the end-point peak was performed in order to check if the width is consistent with expected fluctuations approximately. The peak position and the width were obtained as 14.9 keV and 3.6%, respectively. The peak position is consistent with the expected end-point energy of 14.87 keV from linear Compton scatterings. The obtained width is also consistent with the expected fluctuations. The subtracted spectrum shows a symptom of nonlinear Compton effect with the increased effective electron mass. All energy spectra shown above were measured in 5m air and thin beryllium windows as absorbers before entering the detector.

After we confirmed the end-point energy of the single Compton X-ray, we measured arrival times of visible rays with respect to each basic clock to which electron bunches and laser pulses were synchronized, by the photomultiplier sensitive to visible rays. Fig.9 a) shows the arrival time distributions of visible lays, where the magenta solid line is the case 1) $l_1\&e_1$(signal + all backgrounds), the blue dashed line is the case 2) $l_1\&e_0$ (background mainly from laser leaks from the upstream after laser dumps), the green dotted line is the case 3) $l_0\&e_1$(background mainly from electron beam halos), and the black dash-dotted line is the case 4) $l_0\&e_0$ (only electrical backgrounds). Data sets of these four cases were alternatively taken and the laser intensity in each case have been corrected in pulse-by-pulse basis. Fig.9 b) is the difference of arrival time distributions between case 1) $l_1\&e_1$ and 2) $l_1\&e_0$, which corresponds to arrival times of visible rays other than known laser leaks

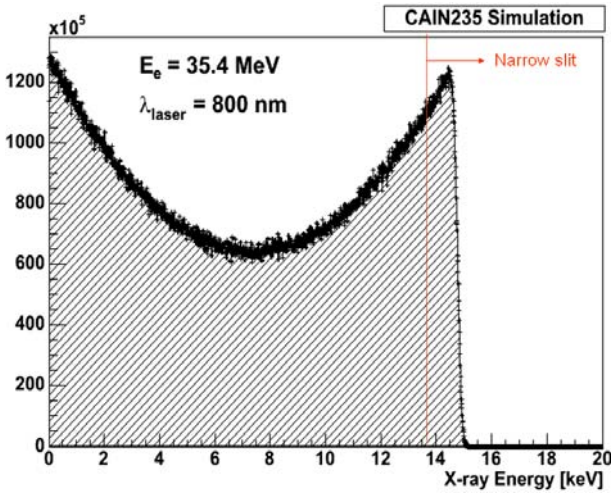

Figure 3: Energy spectrum of Compton x-ray simulated by CAIN235. Narrowing a slit aperture can select the end-point energy.

from the crossing point. Although the absolute time has no physical message, the excess of the intensity localized at the first arrival time of laser leak lights within a time jitter of PMT and electronics indicates that there exist additional photons in the visible range from the crossing point which should have almost the same arrival time as the laser leak photons within a few nsec. The second peak position is consistent with the time of flight of the reflection, in a path from the phototube to laser dump optics in the upstream and back to the phototube.

SUMMARY AND PROSPECT

By crossing laser pulses with the intensity of $10^{17}\mathrm{W}/cm^2$ and electron bunches with 35.4MeV/c perpendicularly, we have performed a search for photons other than Compton x-rays, synchrotron radiations and the other beam related backgrounds aiming at the observation of Cherenkov radiations. After we confirmed the end-point energy of single Compton x-rays, which guarantees that the detector is surely located at the true forward region of incident electrons where Cherenkov emissions are expected, we measured the arrival times of lights in the visible range. There is a symptom of an excess at the same arrival times as laser leak photons from the upstream due to laser beam dumping. This indicates that there are additional photons in the visible range at the crossing point. Since the symptom is still at the two sigma level, we must increase the statistics and check the reproducibility. Furthermore, the wavelength in other energy ranges should be scanned. In addition to the background discussed so far, there should be a physical background process such as a relativistic Larmor scattering. In order to separate the known process, it is necessary to measure the kinematic relation between scattered electrons and emitted photons. We hope that future facilities with stronger laser fields and more energetic electron beams realize this situation.

ACKNOWLEDGMENTS

We would like to thank F.Sakai, T.Nakajyo and T.Yanagida of Sumitomo Heavy Industries, Ltd. for giving us a chance to use their facility and full supports during the experiment. This work is financially supported by Research Foundation for Opto-Science and Technology.

REFERENCES

[1] Joao Magueijo. New varying speed of light theories. *Rept. Prog. Phys.*, 66:2025, 2003.

[2] K. Adcox et al. Formation of dense partonic matter in relativistic nucleus nucleus collisions at rhic: Experimental evaluation by the phenix collaboration. *Nucl. Phys.*, A757:184–283, 2005.

[3] G. Amelino-Camelia, John R. Ellis, N. E. Mavromatos, D. V. Nanopoulos, and Subir Sarkar. Potential sensitivity of gamma-ray burster observations to wave dispersion in vacuo. *Nature*, 393:763–765, 1998.

[4] Julian S. Schwinger. On gauge invariance and vacuum polarization. *Phys. Rev.*, 82:664–679, 1951.

[5] A. Ringwald. Pair production from vacuum at the focus of an x-ray free electron laser. *Phys. Lett.*, B510:107–116, 2001.

[6] I. M. Dremin. Cherenkov radiation and pair production by particles traversing laser beams. *JETP Lett.*, 76:151–154, 2002.

[7] Johann Rafelski. Electromagnetic fields in the qcd vacuum. *hep-ph/9806389*, 1998.

[8] P. Chen, G. Horton-Smith, T. Ohgaki, A. W. Weidemann, and K. Yokoya. Cain: Conglomerat d'abel et d'interactions nonlineaires. *Nucl. Instrum. Meth.*, A355:107–110, 1995.

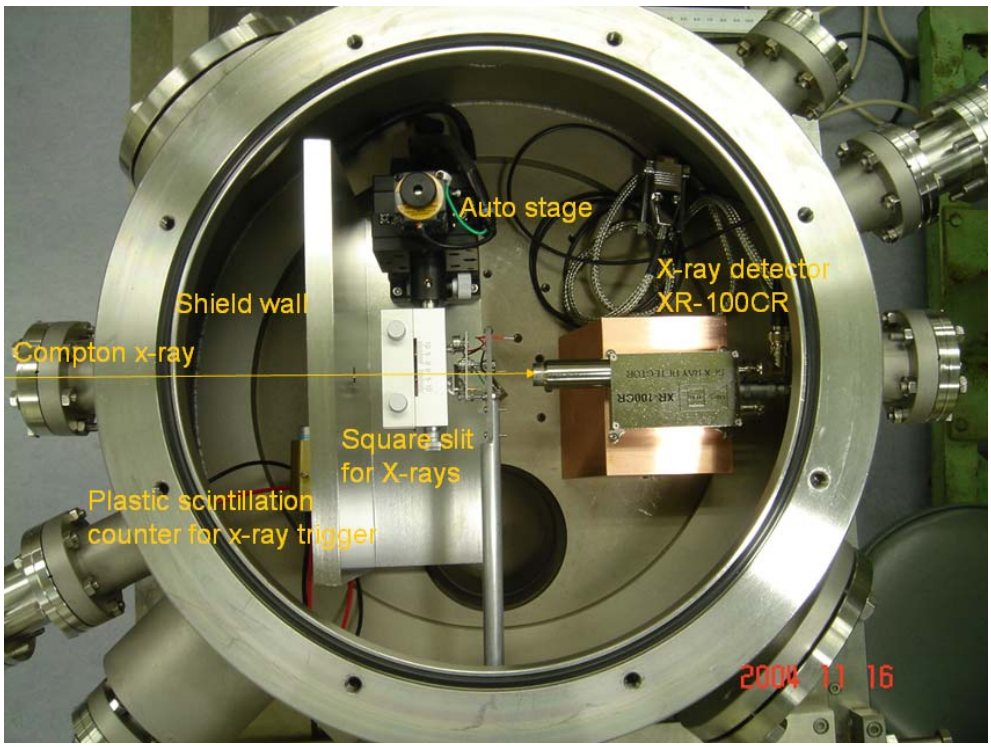

Figure 4: Picture of the detector elements at the 5m downstream. A shielding wall with a hole is located with a plastic scintillation counter in the upstream side of the wall to trigger x-rays. After the shielding wall, there is the square slit. Compton x-rays are measured by a x-ray detector XR-100CR of AMPTEK.

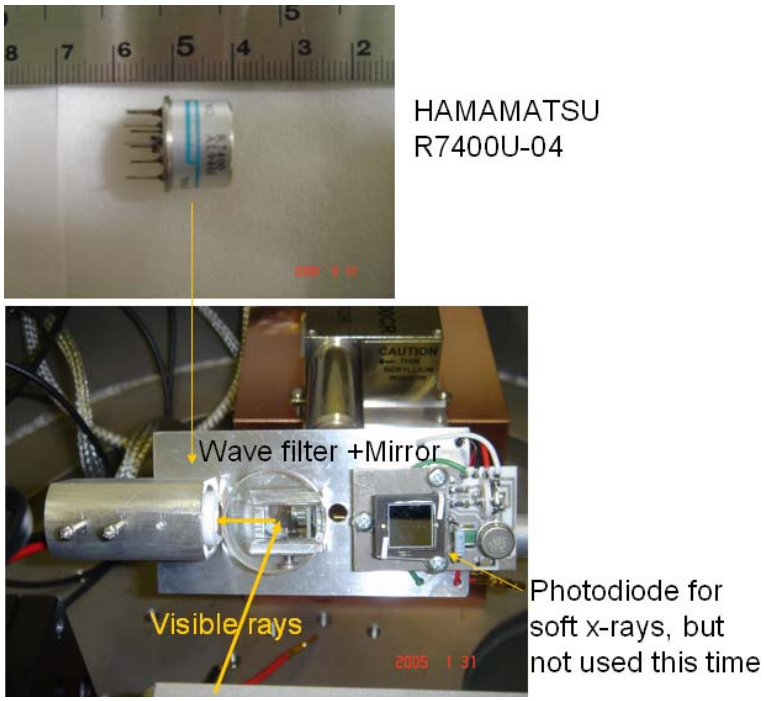

Figure 5: Picture of the PMT part with a mirror and a wave filter which cuts off the 800nm wave length. In order to measure energies other than Compton x-rays, photomultiplier(PMT) R7400U-04 of Hamamatsu Photonics is used after the filter and the mirror which reflects generated visible rays from the crossing point.

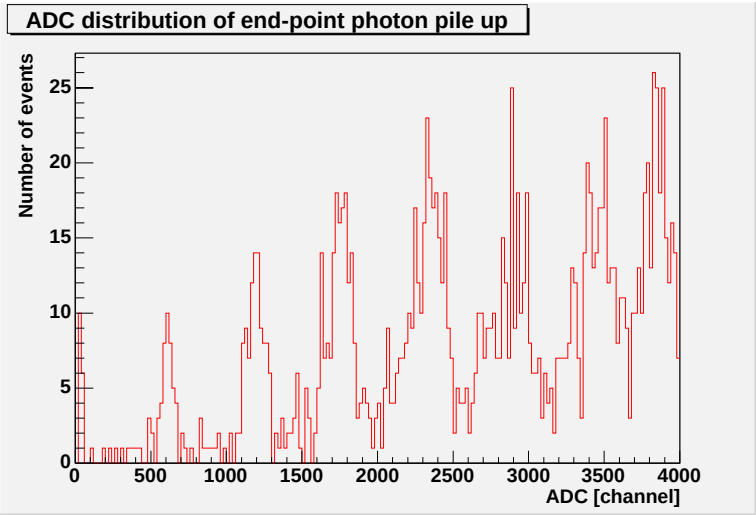

Figure 6: Piled up energy spectrum of end-point Compton x-rays, which was obtained by a larger aperture size of the square slit.

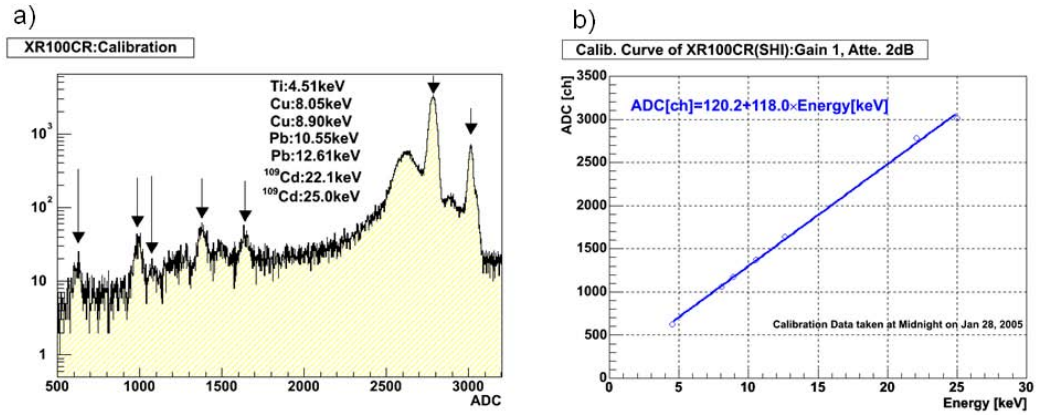

Figure 7: Calibration data for XR-100CR used for the Compton x-ray energy measurement. a) Merged raw energy spectrum with various metal converters with a ^{109}Cd source to produce characteristic x-rays. The converter materials are indicated in the figure. b) Calibration curve between the energy and the ADC channels in our CAMAC based readout system.

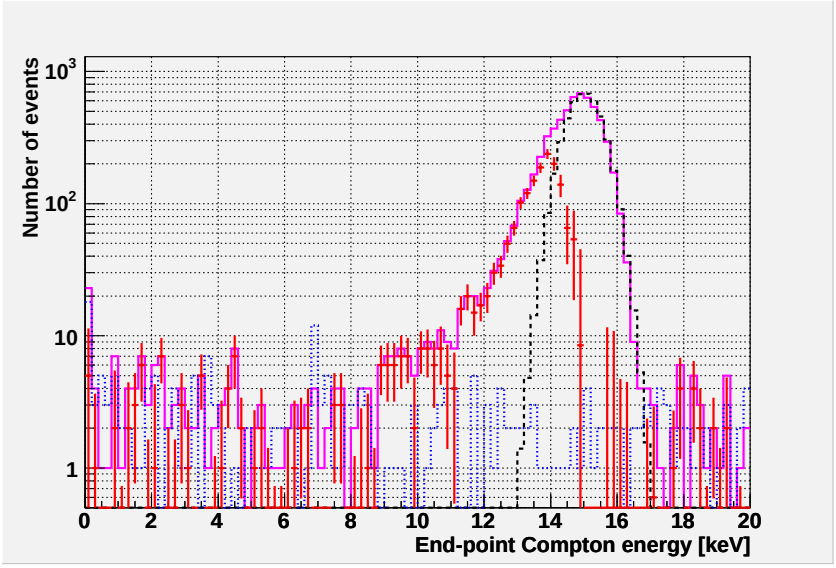

Figure 8: Energy spectra of the end-point region of Compton scatterings with the narrow square slit size of $1mm \times 1mm$ at the 5m downstream from the crossing point, where the magenta solid line shows the spectrum in $l_1 \& e_1$ (signal + beam halo), the blue dotted line shows the spectrum in $l_0 \& e_1$ (beam halo), the black dashed line shows the fit to only the right side of the peak, and the red points show a spectrum by subtracting the fit result from the spectrum with the magenta solid line.

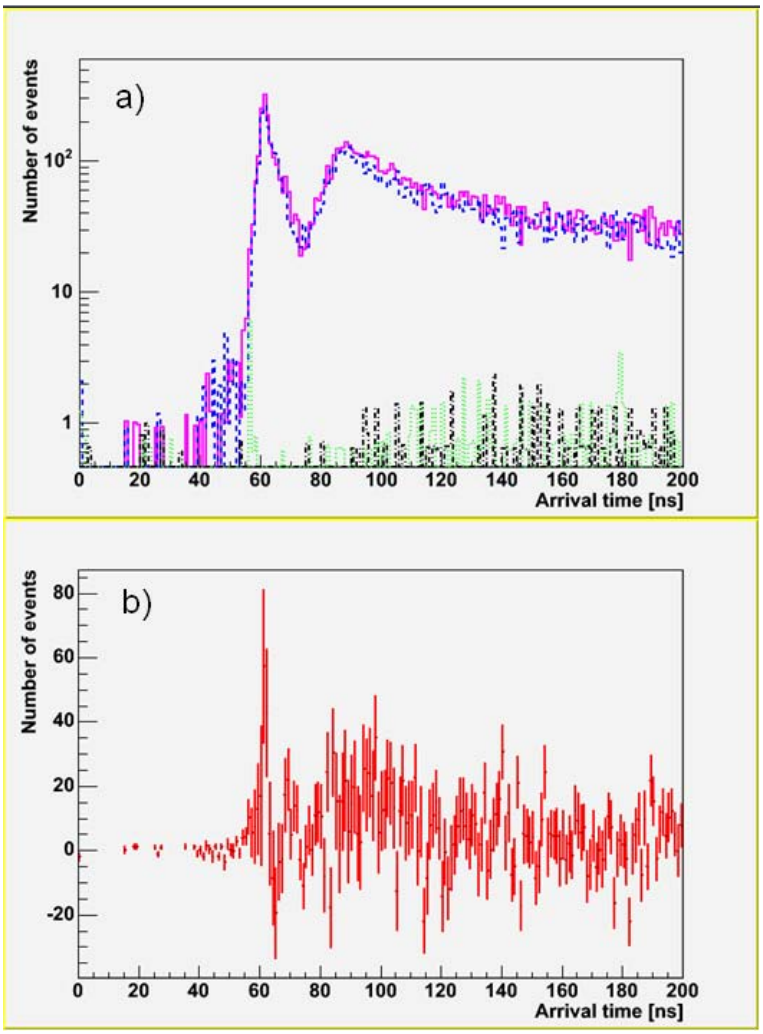

Figure 9: a) Arrival time distributions of visible lays, where the magenta solid line is the case 1) $l_1\&e_1$ (signal + all backgrounds), the blue dashed line is the case 2) $l_1\&e_0$ (background mainly from laser leaks from the upstream after laser dumps), the green dotted line is the case 3) $l_0\&e_1$ (backgrounds mainly from electron beam halos), and the black dash-dotted line is the case 4) $l_0\&e_0$ (only electrical backgrounds). b) Difference of arrival time distributions between case 1) $l_1\&e_1$ and 2) $l_1\&e_0$, which corresponds to arrival times of visible rays other than known laser leaks from the crossing point.

Energetic ion generation by Coulomb-explosion in cluster molecules with an intense femtosecond laser

S. Sakabe*, M. Hashida, and S. Shimizu

Advanced Research Center for Beam Science, Institute for Chemical Research

Kyoto University, Uji Kyoto 611-0011, Japan

* sakabe@laser.kuicr.kyoto-u.ac.jp

The energy distributions of protons emitted from the Coulomb explosion of hydrogen clusters by an intense femtosecond laser have been experimentally obtained. Ten thousand hydrogen clusters were exploded, emitting 8.1-keV protons under laser irradiation of intensity $6x10^{16}$ W/cm^2. The energy distributions are interpreted well by a spherical uniform cluster analytical model. The maximum energy of the emitted protons can be characterized by cluster size and laser intensity. The laser intensity scale for the maximum proton energy, given by a spherical cluster Coulomb-explosion model, is in fairly good agreement with the experimental results obtained at a laser intensity of 10^{16}–10^{17} W/cm^2 and also when extrapolated with the results of three-dimensional particle simulations at 10^{20} –10^{21} W/cm^2.

Recent progress in ultraintense femtosecond lasers has enabled the production of ionic radiation energetic enough to induce nuclear reactions, such as fusion, photofission, and electron-positron pair production. The generation of high-energy ion radiation by intense femtosecond laser plasma interactions can be effected by two mechanisms. One is by Coulomb explosion in a gas or underdense plasma, and the other is by acceleration in an electrostatic field induced by high-energy electrons driven by a ponderomotive force in an overdense plasma in thin foils[1]. In the present paper we focus on the first of the two mechanisms. Intense femtosecond lasers can expel electrons from molecules or clusters instantaneously without disassociating them, producing highly charged molecular or cluster (parent) ions, a process known as optical field ionization. The molecules or clusters subsequently explode because of the repulsive Coulomb force due to their own highly charged state. This phenomenon is called ‘‘Coulomb explosion.’’ During the Coulomb explosion of a parent ion cloud, the elemental ions acquire a high kinetic energy. In this paper, the energy distributions of protons emitted by the Coulomb explosion of hydrogen clusters in an intense femtosecond laser field are experimentally and analytically studied. An analytical model is shown to be able to predict the relationship between proton energy and laser intensity for a spherical uniform cluster.

Hydrogen clusters were generated from hydrogen gas(0.5–8.5 MPa of backing pressure) blown into a vacuum chamber (10^{-4} Pa) with a nozzle cryogenically cooled by liquid nitrogen[2]. The mean size of the clusters produced was measured by Rayleigh scattering [2,3]. The gas beam near the output of the gas-jet nozzle was irradiated with He-Ne laser light (wavelength 632 nm). The scattered light in the direction 90° to the laser beam was collected with a lens and imaged onto a photomultiplier tube through a spectrometer. The mean cluster size depends on the backing pres-sure and varied from $3x10^3$ to $2x10^5$ atoms/cluster for pressures ranging from

3.5 to 8.5 MPa. To be sure of the mean cluster size we employed the Hagena scaling law [4].

Laser pulses (wavelength 800 nm, pulse duration 130 fs, energy 200 mJ) from a chirped-pulse amplification Ti:sapphire laser [5] were focused onto the hydrogen cluster beam through an *f*=850 mm spherical concave mirror (*f* /17). The intensity profile of the laser focal spot size was measured separately (full width at half maximum 0.2 mm), and the averaged laser intensity at the laser-cluster interaction region, was 6×10^{16} W/cm^2, with an uncertainty of 20%. Protons exploded from the clusters were detected through a flight tube by a microchannel-plate detector located in the direction perpendicular to both the cluster beam and the laser beam propagation. The laser polarization was parallel to the time of flight axis. The flight times of the generated high-energy protons were reduced to an energy distribution.

Figure 1 shows the energy distributions of the protons at different backing pressures, taken from the time-of-flight spectra. As the proton energy increases, the number of pro-tons slowly increases up to a peak energy, and then rapidly decreases as the maximum energy is approached. The dependence of the maximum energy on the backing pressure (corresponding to cluster size) is shown in Fig. 2. For backing pressures smaller than 4 MPa the maximum proton energy increases as the backing pressure increases. For pressures over 4 MPa the maximum energy does not increase and plateaus at 8.1 keV. The reason for the leveling off of the maxi-mum proton energy above 4 MPa is that the laser intensity is insufficient to expel all electrons from the larger clusters produced at these pressures.

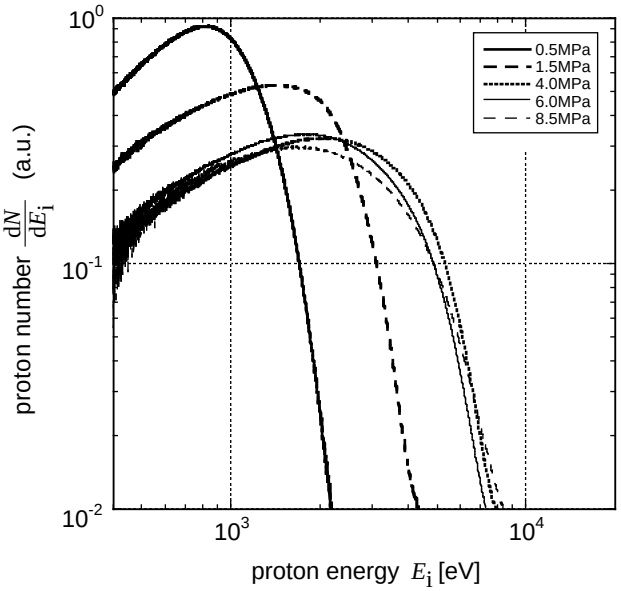

FIG. 1. Energy distributions of protons emitted from hydrogen clusters for varying nozzle backing pressures.

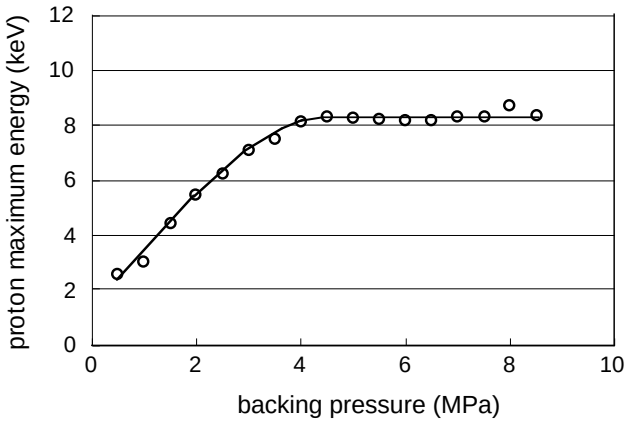

FIG. 2. Maximum proton energy as a function of backing pressure.

We can compare the experimental results with a uniform spherical non-neutral ion cluster model. The model is de-scribed in Ref. [6]. We consider a spherical cluster with a uniform density n and a radius R and assume equal electron and ion charge densities, with both components having zero temperature and being at rest initially. We first estimate the laser intensity required to expel all the electrons from the cluster. We introduce a normalized laser electric field amplitude $a=eE/m\omega c$, where e is the electron charge, E the electric field, m the electron mass, ω the laser frequency, and c the speed of light. For a laser with a wavelength of λ and an intensity of I, $a=0.85(I/10^{18}\ \mathrm{W/cm^2})^{1/2}(\lambda/\mu\mathrm{m})$. We assume a plasma that is transparent to the laser, i.e., ω is greater than the relativistic plasma frequency $\omega_{pe}=(4\pi ne^2/m\gamma)^{1/2}$, or the cluster is smaller than the Debye length $\lambda_D=[mc(\gamma-1)/4ne^2]^{1/2}$, where $\gamma=(1+a^2/2)^{1/2}$ for linearly polarized light. We can estimate the laser amplitude required for expelling all of electrons from the cluster as

$$a > \left(\frac{8\pi Ze^2 n}{3mc^2}\right)^{1/2} \equiv 34\left(\frac{Zn}{5\times 10^{22}\ \mathrm{cm}^{-3}}\right)^{1/2}\left(\frac{R}{1\mu\mathrm{m}}\right). \quad (1)$$

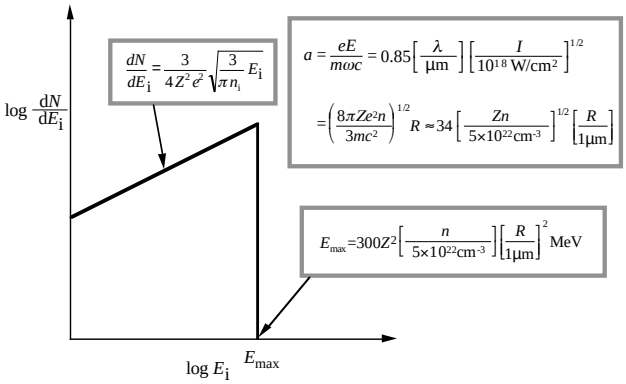

FIG. 3. Energy distribution for a uniform spherical cluster analytical model.

During the Coulomb explosion of a cluster, an ion obtains kinetic energy determined by its initial position in the cluster. Assuming a homogeneous distribution of the ion density n, the charge inside a radius r is given by $Q=4\pi Zer^3n/3$. If the ions peel off from the surface uniformly, an ion at the initial position r acquires an energy

$E_i=4\pi Z^2e^2nr^2/3$ at infinity. The maximum ion energy of a cluster with density n and radius R is given by

$$E_{\max} = 4\pi Z^2 e^2 nR^2/3 \approx 300 Z^2 \left(\frac{n}{5\times 10^{22}\ \mathrm{cm}^{-3}}\right)\left(\frac{R}{1\mu\mathrm{m}}\right)^2 \quad (2)$$

Since the number of ions within a radius r to $r+dr$ is $dN=4\pi nr^2dr$, the ion energy distribution function of a simple explosion can be given by

$$\frac{dN}{dE_i} = \frac{3}{4Z^2e^2}\sqrt{\frac{3E_i}{\pi n}} \quad (3)$$

The ion energy distribution is thus proportional to the square root of the energy. The energy distribution presented by this model is shown in Fig. 3. The distribution is examined by three-dimensional particle-in-cell (PIC) simulations in Ref.[6] as given later. A comparison between Fig. 1 and Fig. 3 shows qualitative agreement, that is, they both show an increase in proton number as the energy increases up to the peak energy. However, in Fig. 1 the proton number does not decrease as rapidly as it does in the model. This is due to the fact that the model considers only a single cluster size, whereas in the experiments there is a distribution of cluster sizes, which all contribute to the observed distribution.

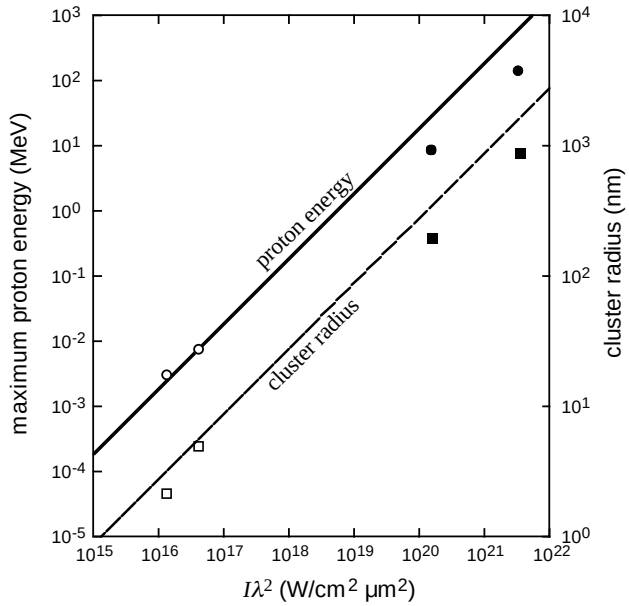

FIG. 4. Maximum proton energy (solid line) and cluster size (broken line) for the laser intensity given by a uniform spherical cluster analytical model. The horizontal axis shows the product of the laser intensity and the square of the laser wavelength.

Equation (2) gives the relationship between maximum energy and cluster size. For E_{max} =8.1 keV, as shown in Fig. 2, Eq. (2) give a cluster radius of 7.7 nm, which is in only fair agreement with the 4.8 nm measured by Rayleigh scattering. However, if we take the peak energy of the distribution, about 2.2 keV, to be the maximum

energy for an average-size cluster, the cluster radius given by Eq. (2) is 4.0 nm, which is in good agreement with the 4.8 nm Rayleigh scattering measurement. From Eqs. (1) and (2) the laser intensity for full ionization can be related to the maximum energy, a=1.97 $E_{max}^{1/2}$. For E_{max} =8.1 keV, the laser intensity is I=6.7x10^{16} W/cm^2 , which is very close to the intensity of 6x10^{16} W/cm^2 estimated from the focal spot size and laser energy. Note that the maximum energy is directly proportional to the laser intensity. We can conclude that the simple spherical cluster model can be used to determine the characteristics of high-energy ions emitted from a cluster exploded by an intense laser.

In the spherical cluster model, the exploded proton energy is proportional to the laser intensity, as shown in Fig. 4. Both the experimental results and predictions for higher intensities made using the three-dimensional PIC simulation are also given in Fig. 4. The PIC simulation is described in Ref. [6]. The present experimental results have shown the validity of the model, which will be useful for future experiments[7].

This work was partially supported by MEXT, Grant-in-Aid for Scientific Research on Priority Areas (15035207), and Grant-in-Aid for Creative Scientific Research (15GS0214).

[1] S. Okihara, Y. Sentoku, K. Sueda, S. Shimizu, F. Sato, N. Miyanaga, K. Mima, Y. Izawa, T. Iida, and S. Sakabe, J. Nucl. Sci. Technol. **39**,1(2002).

[2] R. A. Smith, T. Ditmire, and J. W. G. Tisch, Rev. Sci. Instrum. **69**, 3798 (1998).

[3] T. Ditmire, T. Donnelly, A. M. Rubenchick, R. W. Falcone, and M. D. Perry, Phys. Rev. A 53, 3379 (1996).

[4] O. F. Hagena, Rev. Sci. Instrum. **63**, 2374 (1992).

[5] H. Schillinger et al., Rev. Laser Eng. **25**, 890 (1997).

[6] K. Nishihara, H. Amitani, M. Murakami, S. V. Bulanov, and T. Zh. Esirkepov, Nucl. Instrum. Methods Phys. Res. A **464**, 98(2001).

[7] S. Sakabe, S. Shimizu, M. Hashida, F. Sato, T. Tsuyukushi, K. Nishihara, S> Okihara, T. Kagawa, Y. Izawa, K. Imasaki, and T. Iida, Phys. Rev. A 69, 023203(2004); M. Hirokane, S. Shimizu, M. Hashida, S. Okada, S.. Okihara, F. Sato, T. Iida, and S.Sakabe, Phys. Rev. A 69, 063201(2004).

EXPERIMENT ON NON-LINEAR COMPTION SCATTERING AND A LASER FACILITY AT THE ATF2

T. Takahashi*, Graduate School of Advanced Sciences of Matter, Hiroshima University, Higashi-Hiroshima, 739-8530, Japan

Abstract

We observed photon generation in the second harmonic region in collisions of 10 keV free electrons and the intense laser beam with the peak intensity of 4×10^{15}W/cm^2. Observed photon yield was 3 orders of magnitude higher than expectation from the nonlinear Compton scattering. The observation indicates necessity of further investigation and a laser facility at the ATF2 can be a suitable site if it will be constructed.

INTRODUCTION

Laser-electron scattering is a fundamental process in the interaction between photons and electrons and is well understood as Compton scattering. Recently, thanks to innovations of the laser and the electron beam technologies, the laser-electron scattering has got a lot of attention as a new kind of high energy photon sources [1]. In addition, by combining with accelerator technologies, its application expands into advanced beam technologies such as beam monitors. The intensity of an incident laser beam is getting higher to meet the requirement from applications. For example, photon colliders require laser power of O(5J/pulse) focusing down close to the diffraction limit. In these situation, the laser power density may exceed $O(10^{18})$W/cm^2 where nonlinear effects such as, higher order harmonic generation, will appear. Therefore, understanding of the nonlinear effect under the intense laser field is important for applications as it changes energy spectra of the generated photons as well as spent electrons.

The E144 experiment at Stanford Linear Accelerator Center observed nonlinear effects with the electron beam of 46.6 GeV and a 1 TW laser via energy spectra of the spent electrons off the laser beam [2]. The observations were consistent with the theoretical prediction based on the semi-classical formula given by Brawn and Kibble [3]. Englert and Rinehart reported the observation of second harmonic photons with the electron beam of 0.5 keV and 1.6 keV. They claimed that the results were consistent with theoretical predictions [4]. However, we believe that their arguments on comparison with theoretical predictions need careful verification [5].

These facts motivated an experiment with an intense laser and low energy electrons. As we discuss later, the results was not described by simple adaptation of the calculation for the non-linear Compton scattering. Therefore, we believe that, in addition to the high energy photon generation as a photon collider test bed, it is worth while constructing laser facility at the ATF2 where high quality electron beam is available.

In this paper, we first describe the experiment on non-linear Compton scattering at T6 laser system, then introduce a plan of a laser facility at the ATF2.

EXPERIMENT ON NON LINEAR COMPTIO SCATTERING

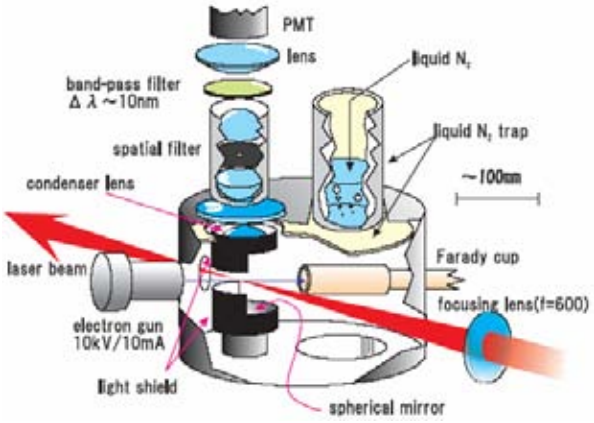

Figure 1: Schematic view of the target chamber.

The experimental setup is shown in figure 1. Detail of the apparatus and the results are described elsewhere [6]. The system consists of an electron gun of 10 keV beam energy and 10 mA or 5 mA beam current, an optical system for focusing the incident laser beam, and a photon detection system. The system was assembled in the target chamber in the experimental room of the T6 laser facility at the Institute of Laser Engineering in Osaka University [7]. The T6 laser system supplied intense laser pulses of 70.7 mJ/130 fs, which corresponds to the peak power of 0.544×10^{12} W, with the repetition rate of 10 Hz at the wavelength of 800 nm.

The laser beam is focused by a plano-convex fused silica lens mounted at the laser injection window of the target chamber. The sizes of the electron beam with 10 mA and with 5 mA were 0.98 mm and 0.33 mm in RMS, respectively at the interaction point in the chamber. The wavelength of the detecting photon was discriminated by bandpass filters with typical bandwidth of 10 nm. The detection efficiency was 1.26 ~ 3.04 × 10−3 depending on the wavelength of the photon. The target chamber was kept to high vacuum of 5×10^{-9} ~ 10×10^{-9} Torr.

The power of the laser pulses was measured throughout the experiment by a power meter positioned outside of the target chamber. The average of the laser power was 70.7 mJ/pulse with the pulse by pulse fluctuation of 4.2 mJ. The images of the laser pulse at the interaction point were

*tohru-takahashi @ hiroshima-u.ac.jp

transferred to a CCD camera set outside of the target chamber via a biconvex lens. The horizontal profile of the image was well fitted by a Gaussian distribution of a typical RMS of 0.0791 mm. The vertical profile was, on the other hand, shaped like a narrow peak on a wider base and rather fitted to a double Gaussian distribution. Typical RMSes of the distribution were 0.0153 mm and 0.0545 mm for the peak and the base portion, respectively. By combining the measurements for the laser power and the images, the peak power density at the interaction point was estimated to be $(4.0\pm0.1-1.3)\times10^{15}$ W/cm^2, where the first and the second error from variation of the laser power during the experiment and the ambiguity of the laser profile at the interaction point, respectively.

The photon counting scheme is shown in figure 2.

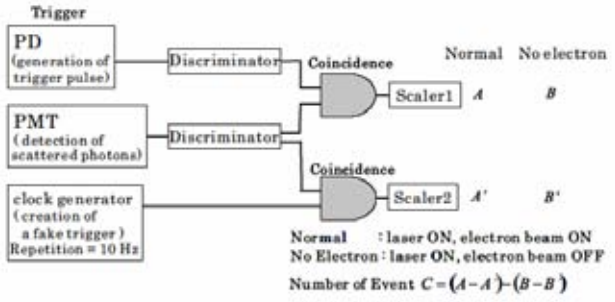

Figure 2: Diagram of photon counting.

The output pulses of the PMT were led to a discriminator followed by a coincidence circuit to count the number of pulses (A) exceeding the single photon threshold and satisfying the timing condition dictated by a gate signal. Background PMT pulses (A') disassociated with the laser pulses were subtracted off making use of another counts gated by fake signals at the timing in between the contiguous laser pulses. In order to eliminate the possible background (B) coming from the harmonic generation of residual gas and optical components irradiated with the strong laser beam, we also carried out a data taking run, referred to as No Electron-run, without turning on the electron gun. The net photon events (C) coming from the interaction of the laser and the electron beam are calculated as

$$C = (A - A') - (B - B') \quad (1)$$

where the photon counts in the measurement on and off timing with the laser pulse with the electron beam are denoted by A and A', respectively, while those without the electron beam are shown with B and B'. This method has been experimentally verified by observing the linear Compton scattering with the laser beam of 1.6×10^{14} W/cm^2 [7]. The spectrum in the second harmonic region was measured by changing the bandpass filters, whose central wavelength were 350 nm, 360 nm, 370 nm and 380 nm. Observed spectrum in the second harmonic region is shown in figure 3 together with the simulation.

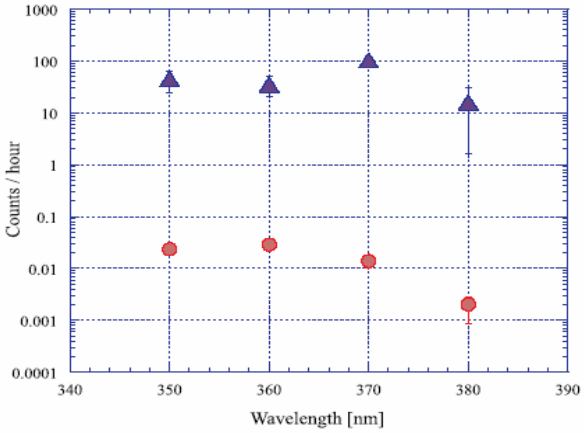

Figure 3: Spectrum of the observed photons. Solid triangles are the data and circles are simulations based on semi-classical model of nonlinear scattering. The error for the simulation was estimated by the statistics of the Monte Carlo and the ambiguities of the laser power density.

The yield in the second harmonic region was 3 orders of magnitude larger than the theoretical expectation of nonlinear Compton scattering. In contrast, we saw excellent agreement with the theoretical expectation at lower power density of the laser beam [6,7]. We also observed null results with the longer laser pulse of 200 ps at 131 mJ corresponding to the peak power density of 4.9×10^{12}W/cm^2, which ensures that our observation is related to the laser power density rather than the absolute power.

We considered possible reasons for this excess;

- Contamination of 400 nm component in the primary laser beam.
- Backgrounds from residual gases excited by the primary laser beam and by the electron beam.
- Contributions of phenomena which are not included in the simulation

The contamination of 400nm component was measured by a monochromator and found to be below the sensitivity of the monochromator, which is regarded as less than 10^{-3} of the incident beam. Backgrounds from residual gases excited by the primary laser beam and by the electron beam have been subtracted out by the procedure described in eq. (1). The remaining possibility is that the background arises only when both the laser and the electron beam exist. It could happen if the excitation of the residual gas by the electron beam assists conversion of incoming laser light to 370nm via appropriate excited energy levels of the gases. As the residual gases were bombard by 10 keV electrons, it, however, is natural to assume that the bombing process excited the gases to all possible levels with nearly equal probability and its contribution was subtracted as the count A'. It appears to be unlikely that a small additional assists by ≈ 1eV laser photons would be the reason of the observed photon yields. In addition, for nitrogen gas, the transition intensity generally becomes stronger as the wavelength

becomes shorter in the region of the wavelength from 350 nm to 390 nm, which does not agree with the observation.

If laser power exceeds the critical power Pc[8], it can be focused in the electron beam. However, with the electron beam density of 3.5×108 cm^{-3}, the critical power is 8.7×10^{22} W for the 800 nm laser, which is far more than the T6 laser(0.544×10^{12} W). Another possibility is dynamics of electrons under the intense laser field. Due to low energy of the electrons, the physical displacement of the electron in the laser pulse may not be small. This dynamical behaviour of the electron could lead density modulation of the electron beam and, if any, it depends on detail profile of the laser pulse. Our simulation is based on the particle in cell method and does not take into account the electron density modulation or electron displacement over cells. Recently, Matsukado performed a calculation included dynamical behaviour on electrons in a laser pulse. The spectrum for the 2nd harmonic region is shown in figure 4 [9].

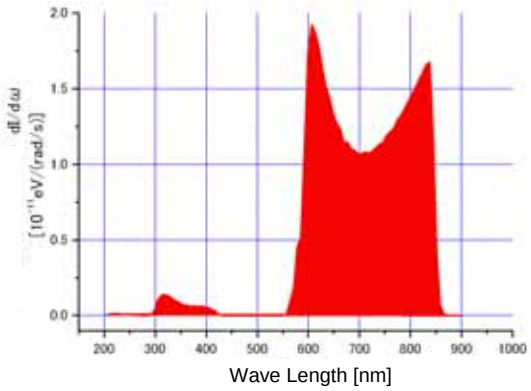

Figure 4: Calculated spectrum for 2nd harmonic region including electron behaviour in a laser pulse.

We found that the new calculation is consistent with those without the dynamical behaviour. Thus the reason of the observed excess is still open question.

Laser Facility at the ATF2

The ATF2 is a proposed beam line at the ATF in KEK to demonstrate the final focus system for the ILC [10]. Its primary goal is to focus electron beam down to 35 nm vertically with reasonably good stability. Once its goal is achieved, the ATF2 can be a prototype of the ILC interaction region.

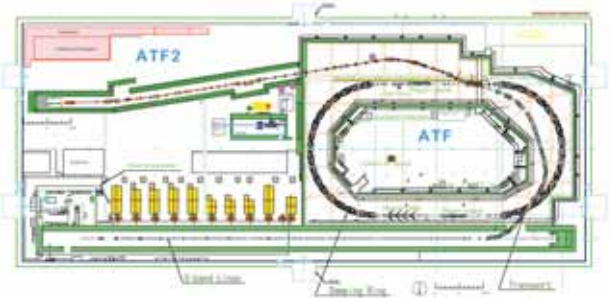

Figure 5: Layout of the ATF2.

On the other hand, the photon collider option need to bring high power laser pulses synchronizing with the electron bunches of 3000×5 repetition per second. According to recent discussion, a resonant cavity for pulse stacking is inevitable to fulfil requirements for the laser with affordable costs. Small scale pulse stacking cavities have been constructed at ATF but feasibility of large and high power stacking required for photon colliders are yet to be demonstrated. For this purpose, the laser facility for the ATF2 is proposed which is illustrated in figure 6.

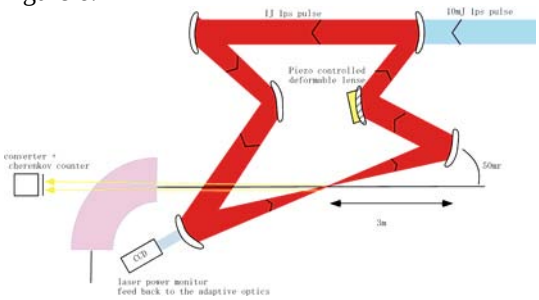

Figure 6: Schematic of the pulse stacking cavity at ATF2.

The purpose of the prototype is to demonstrate:

- Large scale of ~10m circumference cavity with Q~100
- Feed back system
- Focusing stability
- Long term stability

Once the prototype is successfully constructed, it will be where interaction between the electron and the intense laser beam happens. So that the site can be used for high energy photon source as well as for the study of fundamental interaction between an electron and a intense laser field.

SUMMARY

The interaction between an intense laser and an electron beam was performed at T6 laser system. The photon yield observed in the experiment was 3 orders of higher than simple expectation from the non linear Compton process. It is left open question and further investigation is desirable.

On the other hand, toward the realization of photon colliders, the large scale pulse stacking cavity has to be demonstrated. The ATF2 may be a suitable place to construct 10 m scale prototype for demonstration. Once it is constructed, the facility can be multi-purpose laser-facility which can be used for, high energy photon beam source, study of laser-beam interaction, etc. Participation of many interest parties are welcome.

The author would like to thank colleagues of the non linear Compton experiment as well as operation staff of T6 lasers. He also thank ATF2 group for valuable discussions.

REFERENCES

[1] See for examples Proc. 21st ICFA Beam Dynamics Workshop on Laser-Beam Interactions, (Stony Brook, New York) 2001.
[2] C. Bamber, et. al., Phys. Rev. D, 60, 092004(1999).
[3] L. S. Brown and T. W. B.Kibble, Phys. Rev. 133, A705(1964).
[4] T. J. Englert and E. A. Rinehart, Phys. Rev. A 28, 1539 (1983).
[5] According to parameters given in [4], the expected number of observed events is 0.027×10^{-2}L counts/pulse, where L [m] is length of the laser-electron interaction region and is not given in the reference. It has to be noted that L has to be 74 cm to reproduce reported event rate.
[6] K. Matsukado, I. Endo, T. Takahashi, and T. Tauchi, Rev. Sci. Instrum. 71, 369 (2000).
[7] K. Matsukado, I. Endo, T. Takahashi, M. Iinuma, S. Sakabe, F. Sato, Y. Izawa, and T. Tauchi, Nucl. Instr. and Meth. A455, 46 (2000).
[8] P. Sprangle, Cha-Mei Tang, and E. Esarey, IEEE. trans. plasma sci PS-15, 145 (1987).
[9] K. Matsukado, private communication.
[10] ATF2 Proposal, KEK Report 2005-2.

INDEX

Plenary Talks

Working Groups Summaries

Closing Remarks and Acknowledgements

WG1: Laserwire

WG2a : BDS Design and Interaction Region

WG2b : Stabilization and Beam Control

WG2c : Future R&D Plans

WG2d : Final Focus Q-magnets

WG3a : Low Emittance

WG3b : FELs/Radiation Sources

WG3c : Other Sources

WG4 : Physics with High Intensity Laser Beam